Jengnan Juang
Yi-Cheng Huang

Editors

Intelligent Technologies and Engineering Systems

Springer

Lecture Notes in Electrical Engineering 234

Jengnan Juang • Yi-Cheng Huang

Editors

Intelligent Technologies and Engineering Systems

Editors
Jengnan Juang
School of Engineering
Mercer University
Macon, GA, USA

Yi-Cheng Huang
National Changhua University of Education
Changhua City, Taiwan R.O.C.

Preface

Welcome Message from the ICITES 2012 General Chairs

On behalf of the organizing committee, we are pleased to extend our warmest welcome to all the participants of International Conference on Intelligent Technologies and Engineering System (ICITES 2012) at the National Changhua University of Education in Taiwan. The organizing committee has put forth an excellent technical program covering various aspects of Intelligent Technologies and Engineering Systems.

The primary objective of this conference is to bring together on a common platform academicians, researchers, application engineers, industry personnel, and the users of emerging intelligent technologies and engineering systems. Delegates and experts are invited to participate and present their work, and the conference will be of interest to a wide spectrum of professionals at all levels. The conference is intended to encourage and facilitate knowledge sharing, interactions, and discussions on future evolutions of new challenges in the twenty-first century. There will be keynote speeches, invited presentations, technical sessions, panel discussions, and local tours.

We have accepted 120 papers consisting of plenary sessions and technical sessions in which over 100 authors from several countries around the world will give their presentations. The organizing committee has tried its best to make the conference as comfortable as possible to all the participants.

We are grateful to the participants – in particular, those who organized sessions and presented papers. We would like to extend our sincere thanks to all the invited speakers, members of the organizing committee, review committee, local arrangement committee, and the persons from industries. We also would like to thank all the graduate and undergraduate students who are presenting their research work as well as volunteering to help in organizing this conference. We understand what it takes to put together an event such as this and would like to express our sincere thanks to all involved in the preparation of this conference. We also want to thank all of the colleagues and staff who worked on the conference technical program.

The success of this conference is due to those of you who planned and designed the technical program, participated in reviewing the manuscripts, coordinated the exhibit, and volunteered to moderate technical sessions.

We look forward to seeing you all again in the next conference.

Macon, GA, USA   Jengnan Juang
Changhua City, Taiwan R.O.C.   Yi-Cheng Huang

2012 First International Conference on Intelligent Technologies and Engineering Systems

Organization

Honorary Chair:

Yen-Kuang Kuo	National Changhua University of Education, Taiwan
Huey-Por Chang	Open University of Kaohsiung, Taiwan

General Chair:

Jengnan Juang	Mercer University, USA

General Co-chair:

Yi-Cheng Huang	National Changhua University of Education, Taiwan

International Program Committee:

Jer-Nan Juang	National Cheng Kung University, Taiwan
Chih-Chiang Hua	National Yunlin University of Science and Technology, Taiwan
Fuh-Shyang Juang	National Formosa University, Taiwan
Stephen D. Prior	Middlesex University, London, England
F. Frank Chen	The University of Texas-San Antonio, Texas, USA
Ekaterina Kostina	Marburg University, Marburg, Germany
Marvin Cheng	West Virginia University, USA
Yi-Cheng Huang	National Changhua University of Education, Taiwan
Benjamas Panomruttanarug	King Mongkut's University of Technology Thonburi, Thailand
Jeh Won Lee	University in Gyeongbuk, Korea
Jengnan Juang	Mercer University, USA
Richard W. Longman	Columbia University, USA
Hans Georg Bock	University of Heidelberg, Germany

Technical Program Committee:

Minh Q. Phan	New Hampshire, USA
R. Radharamanan	Mercer University, USA
Richard W. Longman	Columbia University, USA
Hans Georg Bock	University of Heidelberg, Germany

(continued)

Jeh Won Lee, Yeungnam	University in Gyeongbuk, Korea
Robert Howard	ATA, USA
Jengnan Juang	Mercer University, USA
Ghadir Radman	Tennessee Technological University, USA
J. Walton	The University of Edinburgh, UK
Soo cheol Lee	Daegu University, Korea
F. Frank Chen	The University of Texas – San Antonio, USA
Ekaterina Kostina	Marburg University, Germany
Cheng-Fu Yang	National University of Kaohsiung, Taiwan
Cheng-Yi Chen	Cheng Shiu University, Taiwan
Yi-Cheng Huang	National Changhua University of Education, Taiwan
Wing-Kwong Wong	National Yunlin University Scene, Taiwan
Wen-Chung Chang	Southern Taiwan University, Tainan, Taiwan

National Advisory Committee:

Yeong-Lin Lai, Chair	Dept. of Mechatronics Engineering, National Changhua University of Education, Taiwan
Jin-Jia Chen, Chair	Dept. of Electrical Engineering, National Changhua University of Education, Taiwan
Chi-Pan Hwang, Chair	Dept. of Electronic Engineering, National Changhua University of Education, Taiwan
Der-Rong Din, Chair	Dept. of Computer Science and Information Engineering, National Changhua University of Education, Taiwan
Der-Fa Chen, Chair	Dept. of Industrial Education and Technology, National Changhua University of Education, Taiwan
Yu-Wei Huang, Chair	Graduate Institute of Vehicle Engineering, National Changhua University of Education, Taiwan
Jenq-Shyong Chen	Director of The Center for Academia-Industry Collaboration and Intellectual Property Management, National Chung Hsing University, Taiwan
Ming-Chyuan Lu	Dept. of Mechanical Engineering, National Chung Hsing University, Taiwan
Shean-Juinn Chiou	Dept. of Mechanical Engineering, National Chung Hsing University, Taiwan
Wing-Kwong Wong	National Yunlin University of Science & Technology, Taiwan
Cheng-Fu Yang	Dept. of Chemical and Materials Engineering, National University of Kaohsiung, Taiwan
Cheng-Yi Chen	Dept. of Electrical Engineering, Cheng Shiu University, Taiwan
Wen-Chung Chang	Dept. of Electronic Engineering, Southern Taiwan University, Taiwan
Fuh-Shyang Juang	Dept. of Electro-Optical Engineering & Graduate Institute of Electro-Optical and Materials Science, National Formosa University, Taiwan
Hsin-Min Hsieh	Taiwan Invention Intellectual Property Association, Taiwan
Jian-Ji Huang, Chair	Dept. of Computer Science and Information Engineering, Chung Chou University of Science and Technology, Taiwan

(continued)

(continued)

Student Paper Competition Chair:
Jieh-Shian Young   National Changhua University of Education, Taiwan

Finance Chair:
Chih-Hsiung Shen   National Changhua University of Education, Taiwan

Finance Co-chair:
Shu-Jung Chen   National Changhua University of Education, Taiwan
Der-Jiunn Deng   National Changhua University of Education, Taiwan
Financial Sponsor Chair:
Kuan-Jung Chung   National Changhua University of Education, Taiwan

Registration Chair:
Ren-Der Chen   National Changhua University of Education, Taiwan

Poster Chair:
Ker-win Wang   National Changhua University of Education, Taiwan

Publication Chair:
Yeong-Lin Lai   National Changhua University of Education, Taiwan

Web Chair:
Po-Yueh Chen   National Changhua University of Education, Taiwan

Contents

Part I
Networking

Wireless Sphygmomanometer with Data Encryption

Hsien-Ju Ko and Kang-Ming Chang

Abstract A wireless physiological signal measurement system has been developed in which physiological signals can be transferred to a host server via a personal digital assistant (PDA) with wireless transmission using Bluetooth technology. The subject's personal information is also included with a radio frequency identification (RFID) tag. Both DES and RSA algorithms have been used to encrypt all the measured data and the key of DES algorithm to preserve the measured signal data with high security. This system is especially useful in the care and nursing environment, with efficient and high-accuracy security data transmission.

Keywords PDA • RFID • Bluetooth • Sphygmomanometer • Privacy • DES • RSA

1 Introduction

The increasing demands of health-care-based facilities are a major driving force of telemedicine. Due to the increasing percentage of elderly persons and decreasing percentage of newborn babies, telemedicine provides methods to take care of elders with more powerful facilities requiring fewer health-care personnel. The limitation of traditional bedside monitoring was wired facility, which also limited patient mobility. However, remote medical monitoring, consulting, and health care were increasingly developed with the advent of wireless technology [1]. Technology of the wireless sensor network was widely applied in health care [2]. Dittmar described four levels of telemedicine, from microsensor, wrist devices, and health smart

H.-J. Ko
Department of Photonics and Communication Engineering, Asia University, Taichung, Taiwan

K.-M. Chang (✉)
Department of Photonics and Communication Engineering, Asia University, Taichung, Taiwan

Graduate Institute of Clinical Medical Science, China Medical University, Taichung, Taiwan
e-mail: changkm@asia.edu.tw

clothes to health smart home [3]. Lin had integrated radiofrequency identification (RFID), Global Positioning System (GPS), and geographic information system (GIS) to construct a stray prevention system for elders with dementia [4]. Missing elders can be identified with mobile phone, PDA, notebook, personal computer (PC), and various mobile devices through the service platform.

Telemedicine for wireless biosignal monitoring involves the following issues: signal to be monitored, wireless transmission protocol, information transmission and representation media, and security protocol for Internet transmission. The biosignals to be monitored in this study were mainly vital sign signal, heart rate, and blood pressure. Vital sign monitoring was an important issue in telemedicine [5]. The wireless transmission protocol used in this study was based on Bluetooth technology, one of the famous transmission protocols [6]. The main advantage of Bluetooth is the low power consumption, high compatibility, and acceptable price. The other advantage of Bluetooth is its wide distribution in the commercial notebook or PDA. It is therefore more convenient for users to set up the required telemedicine function with handed facilities. Although there was only 10–100 m transmission range, it was acceptable and suitable for biosignal monitoring either in home care or in the hospital setting.

The medium employed for information transmission and representation was PDA, which was widely used [7], for example, for stroke patient monitoring [8]. Security is another important issue with telemedicine. Recently, privacy-preserving issues on wireless sensor networks and databases of telemedicine have become an attractive research area [9]. In this study, a joint security protocol, by mixing RSA [10] and DES [11], was employed for the coding and decoding of vital sign signal transmitted through Bluetooth. The motivation to develop such a protocol is in achieving higher computational speed and higher security of DES and RSA simultaneously. The aim of this study was to propose a vital signal monitoring system transmitted with Bluetooth embedded with PDA. Patient identification was also identified with RFID. Data transmission to the host server through the Internet was achieved with a security algorithm. The overall system was also implemented and examined.

2 Schematic Formulation of the System

Conventional sphygmomanometers in the hospitals are often of large size, are highly priced, and lack better operational efficiency. Recently, some improved sphygmomanometers that are smaller in size and easier to carry have been found in the retail markets. However, these kinds of devices are still without digital output ports for physiological data transmission, and therefore the measured data still rely on artificial processing such as handwrite, key-in, and related actions. Hence, this may reduce the efficiency of care for patients and the patients' privacy may not be preserved. Figure 1 demonstrates the main structure of the proposed system. Based on the system, the physiological data such as blood pressure of the people cared for can be transmitted wirelessly via Bluetooth. Sequentially, the PDA is designed as a
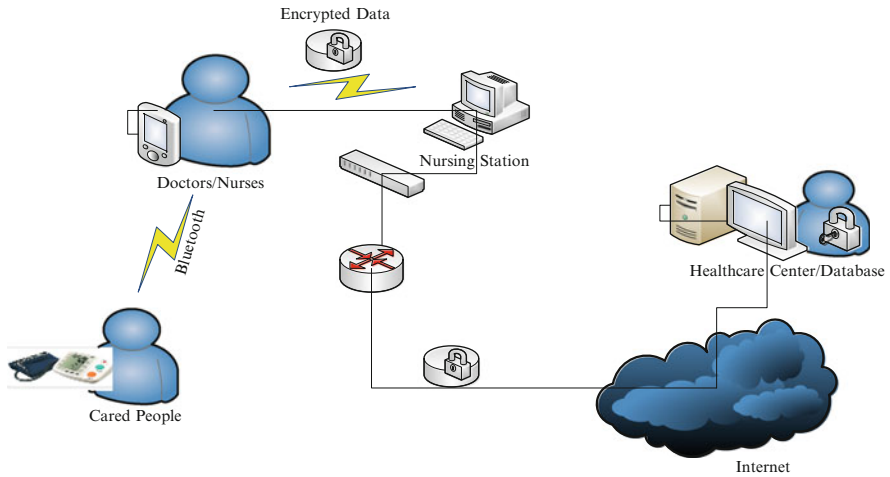
Fig. 1 The scenario of a wireless sphygmomanometer with data encryption

receiver that can receive data automatically with user-friendly interfaces. The received data will be inputted in the workstation at a nursing station via wired/wireless transmission with data encryption. Finally, the authorized data analyzer can decrypt the data from the health-care center or database.

2.1 Transmission

Bluetooth is a short-distance wireless transmission technology, with lower power consumption, tiny volume, and light weight. In addition, it uses a frequency-hopping technique to enhance the reliability and security of communications. In this article, the collected data were transferred by a Bluetooth transmitter bundled in the sphygmomanometer and received by a PDA with a specific program of receiving data. This program follows the communication protocol of sphygmomanometers. The advantages of using such a model are characterized as follows: A PDA with Bluetooth transmission module is of smaller volume, lighter weight, and lower power consumption than laptops. A general-purpose PDA is of a lower price than a special-purpose one. In contrast to usage in a special-purpose PDA, programmers may have higher degrees of freedom to use/design related functions.

2.2 RFID

For increasing efficiency and decreasing errors in data input of, for example, patients' ID/nurses' ID, we adopt RFID/infrared dual-mode reader (Socketscan) for the PDA to read information from the passive RFID tags attached to patients and

Fig. 2 The users'
interface for wireless
sphygmomanometers
in a PDA

care providers. These tags, which contain invisible information, are used to identify patients and care providers. Before receiving the physiological data, care providers will use the reader installed on the PDA to read both the tags attached to patients and care providers rather than directly input data using the touch panel of the PDA. The visible information about the IDs on the PDA is made up of just numbers or serial codes. The further process of information mapping will be done in the databases. This will improve the privacy protection for the cared patients. When the care providers complete the IDs input, they may start receiving the measured signals of blood pressures and heart beats of the patients from the sphygmomanometers. The care providers need only hit the "Receive Data" button on the touch panel of the PDA shown on the left side of Fig. 2. If the received data is properly displayed on the screen, the care provider may hit the "File" and "Save" buttons for saving data off-line, or may hit the "Send" button to directly transfer encrypted data to the remote servers. In practical usage experiences in hospitals, RFID tags are sometimes not the best solutions for person identification. The main reasons are the following: (1) Tags are more expensive than using barcodes; (2) the comfortableness of wearing a tag may concern the people; and (3) in practical usage, the antennas inside the tags are often broken after wearing for some days. To overcome these drawbacks, we adopt a RFID/infrared dual-mode reader to read RFID tags or barcodes for person identification.

3 The Encryption System of the Physiological Data

In this section, the authors propose a joint algorithm by using DES and RSA to perform data encryption. This algorithm is a compromise between the capability of computations of the PDA and the data security. In our designed scenario,

we suppose that the care providers may acquire the physiological data to the PDA from many patients at one time after they visit all the wards. Furthermore, due to the limitation of the computational capability of a PDA, we will use a DES algorithm to encrypt the acquired physiological data. However, DES is a symmetric-key algorithm, that is, the users have to use the same secret key during encryption and decryption processes. Thus, in this chapter, for the strength of data security, the secret key of DES will be encrypted by an RSA algorithm. Let patient_data be the data that include patients' ID, date, and physiological data, and Kdes be denoted as the secret key of the DES algorithm. Thus, one can obtain the encrypted data ENPdes by using DES encryption algorithm Edes:

$$Edes = Edes\,(patient\_data, Kes) \tag{1}$$

For the safety of transmitting data over a public channel, the secret key of DES should be encrypted by a public-key algorithm. Thus, an RSA algorithm is considered in this study. Let us define Eras and Krsa as the RSA encryption algorithm and the public key of the authorized organizations or care providers, respectively. Hence, one can obtain the encrypted secret key of DES ENPrsa as follows:

$$ENPrsa = ENPrsa\,(Kdes, Kpub) \tag{2}$$

When the authorized organizations or care providers receive the encrypted data from the public channel, they may recover the plain text by the following procedures. For recovering the secret key of DES, we shall use RSA decryption algorithm Drsa to decrypt ENPrsa by using the private key Kprv, which is only possessed by the authorized people. It can be described by the following equation:

$$Kdes = Drsa\,(Kprv, ENPrsa) \tag{3}$$

In addition, once the secret key Kdes is recovered, one can further use the DES algorithm yet again to decrypt ENPdes to obtain the plain text patient_data for further processing. This is characterized by the following equation:

$$patient\_data = Ddes\,(Kdes, ENPdes) \tag{4}$$

4   Results and Conclusion

For comparison with the conventional care mechanism, we adopt three approaches for measuring the blood pressure of the patients. The first is by using a laptop computer carried by a wagon. The second is by using a PDA by hand-take or putting it in the packet of a nurse. Both PDA and laptop receive data wirelessly from the Bluetooth sphygmomanometer. The third method is by using conventional

Table 1 Efficiency evaluation of three data input interfaces by PDA, by laptop computer, and by handwriting. The experiment was approved by the Institutional Review Board, China Medical University Hospital in Taiwan

	PDA		Laptop	Handwriting
	RFID	Barcode	RFID	Handwriting
Efficiency of data input (sec/person)	53.27	54.04	59.05	85.28
Correctness (total 50 measures)	96 %	98 %	98 %	NA.

handwrite recording. The results are listed in Table 1. From Table 1, we have some observations and explanations as follows: The efficiency of using a PDA or a laptop computer is much better than that of the handwrite. The correctness of the measured data transferred to a PDA or a laptop computer depends on the accuracy of reading the tag or bar code, operating the sphygmomanometer, and finally, transferring the data to the terminal devices (i.e., PDAs or computers). Thus, the correctness may be affected by one of these processes. In this experiment, all the errors occurred during the sphygmomanometer operations.

In summary, there are two major contributions in this article. The first is the implementation of the PDA program, which can receive physiological data wirelessly from a small-volume, light-weight, and Bluetooth-embedded sphygmomanometer. The second is that the security and privacy of the patients' personal information as well as confidential physiological data transmitting over a public channel can be ensured by using a joint algorithm of DES and RSA. By combining RFID and Bluetooth technologies, such a system may help care providers to avoid some artificial mistakes. Furthermore, it will increase the efficiency of caring for patients whether in the home or in the hospital. Further research about this topic may focus on IPv6 technology and improving the strength or efficiency of data encryption/decryption.

References

1. Tachakra S, Wang XH, Istepanian RS, Song YH (2003) Mobile e-health: the unwired evolution of telemedicine. Telemed J E Health 9(3):247–257
2. Alshehab A, Kobayashi N, Ruiz J, Kikuchi R, Shimamoto S, Ishibashi H (2008) A study on intrabody communication for personal healthcare monitoring system. Telemed J E Health 14(8):851–857
3. Dittmar A, Axisa F, Delhomme G, Gehin C (2004) New concepts and technologies in home care and ambulatory monitoring. Stud Health Technol Inform 108:9–35
4. Lin CC, Chiu MJ, Hsiao CC, Lee RG, Tsai YS (2006) Wireless health care service system for elderly with dementia. IEEE Trans Inf Technol Biomed 10(4):696–704

5. Anagnostaki AP, Pavlopoulos S, Kyriakou E, Koutsouris D (2002) A novel codification scheme based on the "VITAL" and "DICOM" standards for telemedicine applications. IEEE Trans Biomed Eng 49(12):1399–1411
6. Panescu D (2008) Wireless communication systems for implantable medical devices, IEEE Eng Med Biol Mag 27(2):96–101
7. Chang KM (2009) Portable obstructive sleep apnea screening system using overnight ECG and a PDA-based wireless transmission system. Telemed J e-Health 15(4):353–361
8. Kim DK, Yoo SK, Park IC, Choa M, Bae KY, Kim YD, Heo JH (2009) A mobile telemedicine system for remote consultation in cases of acute stroke. J Telemed Telecare 15(2):102–107
9. Hu F, Jiang M, Wagner M, Dong DC (2007) Privacy-preserving telecardiology sensor networks: toward a low-cost portable wireless hardware/software codesign. IEEE Trans Inf Technol Biomed 11(6):619–627
10. Kocarev L, Sterjev M, Fekete A, Vattay G (2004) Public-key encryption with chaos. Chaos 14(4):1078–1082
11. Bleumer G (1994) Security for decentralized health information systems. Int J Biomed Comput 35:139–145

Design and Implementation of Multimedia Social Services on Elgg

Meng-Yen Hsieh, Yin-Te Tsai, Ching-Hsien Hsu, Chao-Hung Hung, and Kuan-Ching Li

Abstract This chapter designs and implements multimedia social services over an open social network engine, denoted as Elgg. Elgg with basic elements such as blogging, e-portfolios, and file sharing possesses a plug-in architecture, so that developers can design plug-ins to provide particular social services. The three plug-ins about video, photo, and blog with a number of Elgg's APIs based on the Representational State Transfer architectural style are provided in the study. Therefore, external applications can easily announce and manage data on Elgg through these APIs. Not only providing details on the design of the Elgg APIs, but we also describe their request and response formats in REST styles. The prototype services are validated with a simple client. The data including text and multimedia from external applications can be automatically separated into the blogs and albums on Elgg.

Keywords Elgg • RESTful • Social media

M.-Y. Hsieh (✉) • C.-H. Hung • K.-C. Li
Department of Computer Science and Information Engineering, Providence University,
Taichung 43301, Taiwan
e-mail: mengyen@pu.edu.tw

Y.-T. Tsai
Department of Computer Science and Communication Engineering,
Providence University, Taichung 43301, Taiwan

C.-H. Hsu
Department of Computer Science and Information Engineering, Chung Hua University,
Hsinchu 30012, Taiwan

1 Introduction

Currently, most people surf social media on Internet in order to maintain individual data, share multimedia data with others, and harness real-time social activities of their friends. The users who have already authenticated can often maintain and announce their multimedia data of daily life with sharing permission in social media. Some textual descriptions or tags for multimedia data must be given in order to depict user context. Consequently, to provide convenient management services for multimedia in social media is significant. Due to mobile and wireless technologies, users operate multimedia data of social media through not only WEB but also mobile APP. Therefore, this study designs internal web services for external applications to deliver user's multimedia data to social networks. An open social network engine, denoted as Elgg, is used, where we have developed a number of plug-in functions, denoted as plug-ins, for multimedia services and open RESTful APIs for external applications. The plug-ins also support linking mechanisms with external social media on Internet. The chapter is organized as follows: we describe literatures and technologies related to our contribution in Sect. 2. Section 3 introduces the design issues of the plug-ins over Elgg for multimedia social sharing. The RESTful APIs are also described. The implementation results are presented and discussed in Sect. 4, and finally, Sect. 5 concludes this chapter.

2 Related Work

The RESTful style based on service-oriented architecture (SOA) uses a uniform resource locator (URL) address to determine resource in Web servers. External applications perform HTTP methods through URL addresses to operate Web resources. In the past, we have developed a Web application and mobile APP about tourism [1, 2]. The application provides some open Web services, and therefore, the mobile APP can use the services to exchange data with the application. Garrett et al. [3] have presented a design project on Elgg for general educations. The customized Elgg has blogs and wikis to assist students in collaborative and individual learning. The project allows students and teachers to customize their profile and to increase interaction, better than traditional course management systems without user interaction. In the experience result, only 15 % of the students reported low levels of satisfaction with the Elgg. More than 60 % of people reported that the Elgg helped them about course experience and social relationship. Weng et al. [4] have designed a social learning environment on Elgg. The social learning relations are divided into the four categories, Object2Object, User2User, Direct relation, and Composed relation, while user and object are defined as the two main portions in the Elgg.

3   Elgg Plug-ins for Multimedia Service

This study designs RESTful APIs for multimedia Web services over Elgg. Using the APIs with URLs, external applications can directly communicate with multimedia services through HTTP protocols with the four methods, POST, GET, PUT, and DELETE, corresponding to the basic operations, create, read, update, and delete (CRUD) for remote resources in backend servers. Two multimedia plug-ins named as Photo Albums and My Videos are proposed for individual multimedia management. Figure 1 depicts our Elgg platform with the plug-ins and RESTful APIs for multimedia services.

3.1   Photo Albums and My Videos Plug-ins

After setting up the Photo Albums, users own a photo board on the Elgg. Users can configure the board, such as the limited number of albums and access permission. Four alternative types of access permissions are provided, public, friend, authentication, and private. The Photo Albums plug-in supplies the functions:
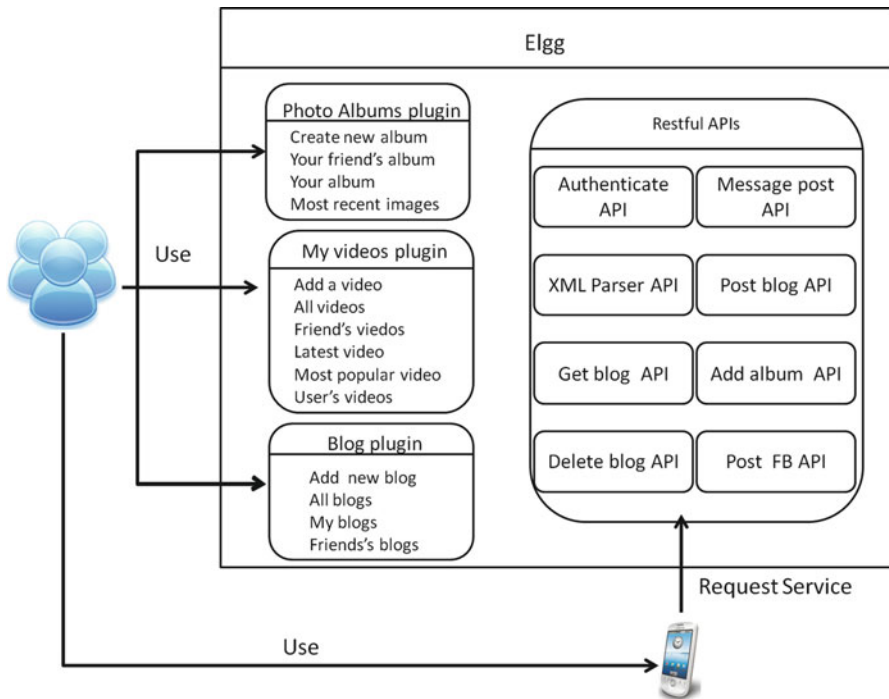
Fig. 1   Multimedia plug-ins and APIs on Elgg

Creating new albums. Users create a new album with initial descriptions including an album title, description, tags, and some configuration parameters. One of the configuration parameters is to set up access permissions on content in Photo Albums. Users can decide to upload images by one-by-one or batch mechanisms.

Browsing an album. Users easily open self or friend's album. Everyone who surfs the Elgg can browse the album, while the permission is set with the public privilege. Only friends open the album, while the owner configures the album with the friend privilege. Users that have been authenticated on Elgg are able to browse the albums with the authentication privilege.

Browsing the latest albums. Users browse the latest photos in the albums through a particular obvious link.

Maintaining an album. The authenticated users maintain their individual photos in the albums by the three functions, addition, edition, and deletion.

Like and sharing. Photos in an album are able to be shared to social networks, while users browse them and press the buttons linking to other social media. Users can press the "Like" button to show signs of liking some photos.

Downloading and commenting for photos. By this function, users comment on the photos that they saw in albums. Besides, the photos also can be downloaded easily.

The other plug-in, My Videos, assists users in announcing video data on Elgg. If one user steps up the plug-in in the Elgg's dashboard, his or her profile will present a window board for video presentation. The board can be set up with various presentation styles based on user preference. The plug-in includes the functions:

Uploading new videos. Owners upload video files to their video boards. The board embedded with a multimedia player includes simple functions, where users can play video. Each uploaded video is attached with one of the access permissions.

Browsing individual videos. The browsing function pattern presents that the users with different access permissions have different video files on their browsing pages. By linking functions, owners easily view the videos that they uploaded before. In addition, the videos with the private privilege are only presented for their owners.

Browsing all public videos. Another link denoted as "All videos," drives a browsing page to present all of the videos with the public privilege on Elgg.

Browsing friend's videos. Users can browse the videos in their friend boards, while the videos are set up with the friend privilege by their friends. A link denoted as "Friend's videos" drives the page listing with these videos.

Browsing latest videos. A user can browse the most new recent videos that other users announced with the public privilege recently, while pressing the link function denoted as "Latest videos."

Browsing most popular videos. A user can browse the most popular videos attaching with a high number of reviews. The page presents the popular videos in order based on how many times they have been seen.

Deleting a video. A valid user can delete his uploaded video when he is browsing it.

Table 1 Request and response data of the RESTful APIs

Services	Request format for service paths (URL)	Resp. (JSON)
Authentication	/json/?method=user.login&username={name}&password= {passwd}&api_key={key}	Token
Posting	/json/?method=travel.post&username={name}&title={title} &body={body}&api_key={key}&auth_token={token}	Success or fail
Getting	/json/?method=travel.get&guid={id}&api_key={key} &auth_token={token}	ID and title or blog article
Updating	json/?method=blog.delete&guid={id}&api_key={key} &auth_token={token}	Success or fail

3.2 RESTful APIs

Our Elgg provides not only the plug-ins but also Web services for multimedia management. External applications can maintain multimedia data of the plug-ins by the CRUD methods of HTTP protocol. We address that multimedia data for external applications consists of one XML-based description and some corresponding images.

The APIs are released for the Web services as follows:

Authentication service. The API, named as "user.login," supplies the authentication service. An external application must propose a login page to receive user's account and password in order to deliver a HTTP request to the API. The request URL follows a format described in Table 1, and the authentication data are included as some parameters in the request. The request has to be protected by SSL during delivery. The API will return a token, after checking that the authentication data is valid. The token is used by the application to contact with the other APIs.

Multimedia posting service. The three APIs for this service, denoted as XML parser API, Post blog API, and Add album API, are used to deliver multimedia data to Elgg. The service has three steps for posting, while receiving the multimedia files. First, the service interprets the description data through the XML Parser API to form a blog data. Second, the Post blog API announces the data to the blog of Elgg and forwards the ID and title of the blog article to the Add album API. Finally, the API creates a novel album related to the blog's ID and title and arranges the uploaded images into the album. The method for posting, named as "travel.post," is applied into the service.

Multimedia getting service. The API, denoted as "travel.get," assists external applications in searching and getting a blog article according to the article ID in the Elgg's blog. The service also provides all of the IDs and titles of blog articles, while the external application requests the service and sets the ID parameter to the particular value, "all." Generally, the external application shall get all of the IDs and titles for users, and they select an interesting article title to browse.

Multimedia updating service. The Elgg engine only supports HTTP get and post methods. We adopt the creation and deletion operations for the updating service. External applications update the same multimedia data according to the same identity of the multimedia description. While accepting the multimedia data with the same XML filename, the service deletes the old data by a method denoted as "blog.delete" and uses the Post blog API to create a novel announcement on the Elgg's blog.

Other services. The proposed architecture provides other services such as Message Post API and Post FB API to assist external applications in announcing message data to the wall pages of Elgg and Facebook.

4   Implementation

This section introduces the implemented services on Elgg. Figure 2 describes a sample of external applications as a client. The client must obey the request formats of the RESTful APIs in order to assist users in managing multimedia data to our Elgg. The three alternative methods, travel_post, travel_get, and travel_delete, are presented corresponding to the multimedia services of the Elgg, after users have been authenticated. Users will be able to announce a XML file with three image files to the Elgg, if performing the travel_post method. Figure 3a gave the interfaces of the four plug-ins on Elgg, and Fig. 3b presented a blog article with the title, Taichung 1D, from the XML file that the client had uploaded before. We give a description for the interface as follows:

Photo Albums (no. 1). The plug-in lists all of the albums with the photos public on Elgg. User can create an album though the admin. interfaces of the plug-in or the external applications supporting with the RESTful APIs, described in Sect. 3. Users announce photos with some alternative privileges in the albums.

Fig. 2 Example of a simple client supporting the RESTful APIs
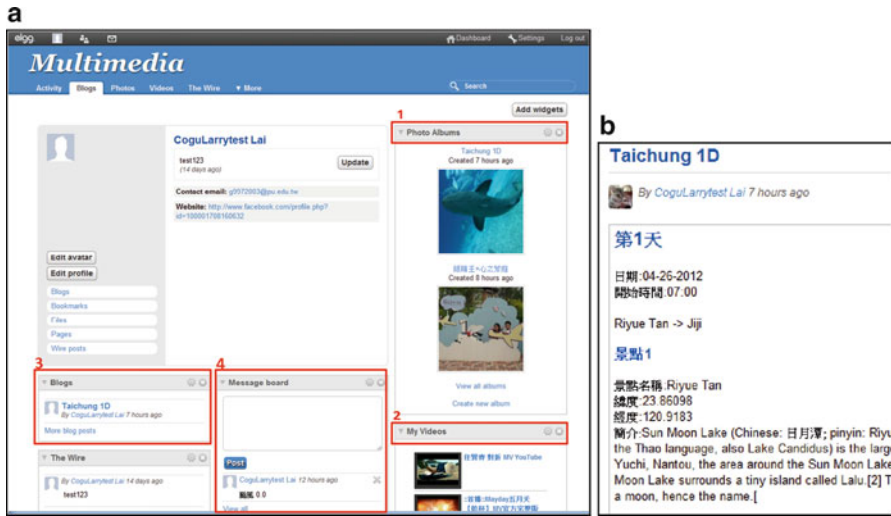
Fig. 3 Elgg for multimedia service: (**a**) the four plug-ins, blogs, message board, photo albums, and my videos; (**b**) a blog article for the multimedia description from external applications

My Videos (*no*. *2*). All videos without classification are involved in the plug-in. Users only manage videos through the admin. interfaces, after they have been authenticated on Elgg. Users announce videos with some alternative privileges.

Blogs (*no*. *3*). The plug-in as one of the basic functions on original Elgg lists all of the blog articles. The client in Fig. 2 can deliver a XML description with few photos to Elgg in order to create a blog article from the XML and an album with the photos.

Message board (*no*. *4*). The plug-in as one of the basic functions on original Elgg allows users to announce a short message on the board.

5 Conclusion

In this chapter, we develop two multimedia plug-ins and RESTful APIs on Elgg. The plug-ins service people to announce multimedia data in social networks. The RESTful APIs are proposed for that external applications can communicate multimedia data to the blogs and albums. The communication protocols are designed and acted based on the determined URL formats. In order to enhance social presence, the multimedia data on Elgg can also be linked with other social media.

References

1. Hsieh M-Y, Lin H-Y, Li K-C (2011) A web-based travel system using Mashup in the RESTful. Int J Comput Sci Eng 6(3):185–191
2. Hsieh M-Y, Lin H-Y, Yeh C-H, Li K-C, Wu BS (2012) A mobile application framework for rapid integration of ubiquitous web services. In: The 9th IEEE international conference on ubiquitous intelligence and computing, Fukuoka, 2012
3. Garrett N, Thoms B, Soffer M, Ryan T (2007) Extending the Elgg social networking system to enhance the campus conversation. In: Second annual design research in information systems (DESRIST), Pasadena, 2007, pp 14–15
4. Weng M, Chen Y-H, Yen N, Chang H-P, Shih T, Lin F (2012) A prototype of learning environment for social learning on Elgg social platform. In: IET international conference on frontier computing, Xining, 2012

On Migration and Consolidation of VMs in Hybrid CPU-GPU Environments

Kuan-Ching Li, Keunsoo Kim, Won W. Ro, Tien-Hsiung Weng, Che-Lun Hung, Chen-Hao Ku, Albert Cohen, and Jean-Luc Gaudiot

Abstract In this research, we target at the investigation of a dynamic energy-aware management framework on the execution of independent workloads (e.g., bag-of-tasks) in hybrid CPU-GPU PARA-computing platforms, aiming at optimizing the execution of workloads in appropriate computing resources concurrently while balancing the use of solely virtual or physical resources or hybridly selected resources, to achieve the best performance in executing application workloads and minimizing the energy associated with computation selected. Experimental results show that the proposed strategy can contribute to improve performance by introducing optimization techniques, such as workload consolidation and dynamic scheduling. We observed that workload consolidation can potentially improve performance, depending on characteristics of the workload. Also, the workload scheduling results present the importance of resource management by revealing the performance gap among different execution schedules for shared computing resources.

Keywords Virtualization • Workload consolidation • GPGPU • PARA-computing platforms

K.-C. Li (✉) • T.-H. Weng • C.-H. Ku
Department of Computer Science and Information Engineering, Providence University,
Providence, Taiwan
e-mail: kuancli@pu.edu.tw

K. Kim • W.W. Ro
School of Electrical and Electronic Engineering, Yonsei University, Seoul, Korea

C.-L. Hung
Department of Computer Science and Communication Engineering, Providence University,
Providence, Taiwan

A. Cohen
INRIA Saclay, Parc Club Orsay Université, ZAC des vignes, Orsay, France

J.-L. Gaudiot
Department of Electrical Engineering and Computer Science, University of California,
Irvine, CA, USA

1 Introduction

With the rapid increase in the number of high-performance computing environments, the way to place dynamically requested application workloads into available multi-core computing and storage resources has become an important topic. In that sense, GPGPU, short for general-purpose computation on graphics processing units, has already demonstrated its ability to accelerate the execution of scientific applications. These accelerated applications benefit from the GPU's massively parallel, multi-threaded multiprocessor design, combined with an appropriate data-parallel mapping of an application to it.

With the increasing number of this category of compute-intensive environments, we have observed there exist computing platforms composed by some high-end servers with hypervisors/VMs (virtual machines) while some other servers provide solely physical resources (e.g., ×86 cores and GPUs). In this way, virtual and physical resources coexist in the same environment, in which different ways of resources usage lead to different levels of energy consumption. For such a category of environment, the coauthors have named them as hybrid CPU-GPU PARA-virtualization environments.

Currently, the energy cost and resource utilization level have become important issues in maintaining these platforms [1–4]. In this trend, energy-efficient and sustainable computing have become active areas of research, motivated by environmental concerns as to limit the impact of computing on the ecosystem. A number of strategies have been proposed to optimize the resource utilization and reduce the total power usage. Power usage and system performance is another trade-off problem, especially when many new computing resources, such as multi-core systems and GPUs, have been deployed in current high-performance hybrid CPU-GPU environments.

2 Related Work

2.1 Virtual Machine (VM) Migration

Virtual machine (VM) technology has emerged as an essential technology for data centers and cloud systems, due to its capabilities of consolidating and migrating workloads and resources. Such an ability to migrate workloads seamlessly from one physical server to another physical resource (server, PC, among other computing resources) without significant downtime or noticeable disruption is one of the key features of virtualization [5]. Considering the performance of virtualization in computing environment, the amount of time it takes to migrate a virtual machine (VM) from one physical server to another resource is an important factor, particularly for heterogeneous virtualized environments.

2.2   Consolidation and Provisioning

Workload consolidation [6] is defined as to simplify and optimize end-to-end IT infrastructures with the goal of finding ways to better align the infrastructure to meet both current and future requirements. Although consolidation can substantially increase the efficient use of physical resources, it may also result in complex configurations of data, applications, and servers that can be confusing for the average user to contend with. To alleviate this problem, server virtualization may be used to mask the details of server resources from users while optimizing resource sharing. However, there exists inherent possibility of the performance degradation due to resource contention of physical resources among the users [7]. Therefore, workload scheduling is one of the key factors of workload consolidation. As an example, GPU workload management framework presented by Ravi et al. [8] demonstrated importance of workload consolidation optimization to improve the performance.

Resource provisioning [9, 10] in compute clouds often requires an estimate of the capacity needs of virtual machines (VMs). The estimated VM size is the basis for allocating resources commensurate with demand. A number of researches on how resources may be allocated to an application mix such that the service level agreements (SLAs) of all applications are met can also be found.

3   Proposed Research

Scientific and engineering workloads written as general-purpose computations on GPU and $\times 86$ multi-core processors are ever increasing, in efforts to obtain higher speedups. The way to obtain these computation results taking into consideration their performance, energy consumption, and energy efficiency is an important issue, that is, the exploration of the CPU and GPU design spaces – threads, blocks, and kernel launches – using CUDA and scheduling in $\times 86$ cores and their subsequent impact to produce better results. One final target of this proposed research may integrate all items listed into a single design. The goals in this research seek at some important issues, as listed below:

– Impact on the ability to execute computing workloads that demand excel management of VMs and servers toward high throughput at the cost of low power consumption and high device reliability
– Management and monitoring task support for energy-efficient scheduling of VMs on physical servers in a high-performance CPU-GPU PARA-virtualization computing environment toward energy-aware GPU and $\times 86$ computing, keeping resources utilization at a desired level
– Search and extract maximum amount of performance from the CPU processor cores which they are capable of delivering under inter – and intra-die process variations scheduled by OS, with migration of workloads appropriately decided by taking into consideration several of system factors

4 Experimental Results

4.1 Potential of Dynamic Workload Consolidation on GPU-Computing Environment

To investigate various aspects of designing CPU-GPU PARA-virtualized environment, we have conducted motivational experiments with a set of GPU applications. On virtualized environment, multiple VM instances share available physical GPU devices managed by hypervisor. However, we run experiments without virtualized layer in this chapter. In fact, one of the main goals of the virtualization layer is to provide additional abstraction and flexibility of shared resources to users, thereby ensuring transparent access as if the resource is dedicated to each user. In that sense, we believe that the virtualized configuration does not affect to reflect nature of the system that is intended to show in this chapter.

As experimental setup, we used Intel i5-2400 Quad-core PC with 8 GB main memory, NVIDIA GeForce GTX 550 GPU installed, running Ubuntu Linux 12.04 with kernel version 3.2.0. Application workloads are selected among NVIDIA CUDA SDK: *BlackScholes*, *scan*, *Interval*, and *radixSortThrust*. The applications are carefully selected to heavily utilize system resources, reflecting characteristics of CPU-GPU PARA-virtualized environment correctly.

To exploit parallelism, we increased the number of simultaneously executed application instances from one to five. Figure 1 shows how parallel execution of each workload improves performance compared to sequential execution. The result
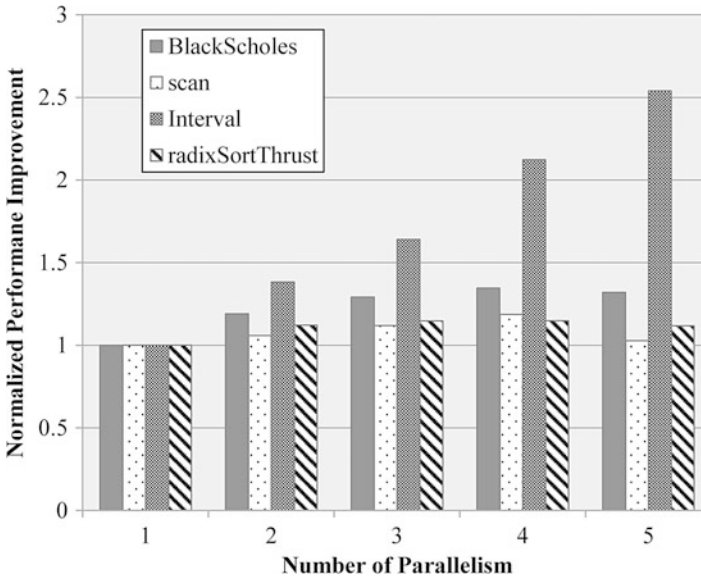
Fig. 1 Sequential vs. parallel execution: parallel performance improvement

Table 1 Impact on application pairs on performance

Case	Application pair	Sequential exec. time(s)	Parallel exec. time(s)	Speedup
A	(Interval, radixSortThrust)	1.51	1.06	1.42
B	(BlackScholes, scan)	4.51	3.63	1.24
C	(radixSortThrust, BlackScholes)	2.95	2.39	1.23
D	(Interval, scan)	3.1	2.58	1.20
E	(Interval, BlackScholes)	2.88	2.26	1.27
F	(radixSortThrust, scan)	3.16	2.88	1.10

implies the potential of workload consolidation. For applications like *Interval*, the performance is significantly improved up to $2.5\times$, which means it is possible to improve performance by consolidating these type of applications. On the other hand, application like scan does not show any remarkable improvement. Moreover, the performance was dropped when parallelism reaches five due to resource contention, since available CPU core is restricted to four in our configuration. This means workload like scan fully utilizes GPU resource; therefore there is no room left for consolidated execution. For these "heavy" workloads, consolidation would not impact the performance severely, which means the consolidation should be avoided to prevent performance degradation due to unnecessary overheads.

4.2 Maximize Performance with Workload Scheduling

In this section, we present an example to show how workload scheduling can impact performance in GPU-CPU PARA-virtualized environment. We assume that four virtual machine instances request to one shared GPU device at the same time. We also impose one more resource limitation to be considered by scheduler, which is shared GPU device can serve up to two applications simultaneously, due to its execution capability.

Given that we have to map four different applications into two available GPU space, there can exist six pairs of applications. Due to runtime behavior of applications, coexecution of each application shows different performance characteristics. We run experiments for all possible cases, in which result is presented in Table 1. Case A showed $1.42\times$ performance improvement when the application is run in parallel, which is the greatest value, while the minimum value is $1.1\times$ for case F.

The result implies that an effective scheduler can optimize execution performance. In detail, the optimal scheduling process can be described as follows. We find three valid combinations of application scheduling pairs which complete all four applications and which consisted of Case A + B, Case C + D, and case E + F, respectively. For each schedule, each pair executes application in parallel while the pairs are serialized due to resource constraint. Total execution time for each case

can be calculated from Table 1, which is 4.69, 4.97, and 5.14 s, respectively. In conclusion, we could observe that performance difference between worst and best schedules, which are 4.69 and 5.14 s, reaches up to 9.6 %.

5 Conclusions

The goals of this proposed research involves dynamic energy-aware management on the execution of independent workloads in hybrid CPU-GPU PARA-virtualization-computing platforms, aiming at optimizing the execution of workloads in appropriate computing resources concurrently while balancing the use of solely virtual or physical resources or hybridly selected resources, to achieve the best performance in executing application workloads and minimizing the energy associated with computation selected.

Essentially, the proposed research involves the search of strategies that best satisfies constraints of a multi-core computer system. We demonstrated how the optimized management strategy can impact performance in virtualized environment in which multiple virtual machines share physical devices. Workload consolidation increases resource utilization and improves performance by merging and executing workloads in parallel, considering the characteristics of workload. Dynamic scheduling improves performance based on resource constraint and coexecution characteristics of workloads. We prospect that the further investigation of various strategies can optimize considering performance, power and energy consumption, and resource utilization of PARA-virtualized computing platforms.

References

1. Qiu X, Fox G, Yuan H, Bae SH, Chrysanthakopoulos G, Nielsen H (2008) Parallel data mining on multicore clusters. In: Grid and cooperative computing, 2008. GCC'08. Seventh international conference on, Shenzhen, Oct 2008, pp 41–49
2. Asanovic K, Bodik R, Catanzaro BC, Gebis JJ, Husbands P, Keutzer K, Patterson DA, Plishker WL, Shalf J, Williams SW, Yelick KA (2006) The landscape of parallel computing research: a view from berkeley. Technical Report UCB/EECS-2006-183, EECS Department, University of California, Berkeley, Dec 2006
3. Li KC, Weng TH (2009) Performance-based parallel application toolkit for high-performance clusters. J Supercomput 48:43–65

4. Lee C, Ro WW, Gaudiot JL (2012) Cooperative heterogeneous computing for parallel processing on cpu/gpu hybrids. In: The 16th workshop on interaction between compilers and computer architectures (INTERACT-16), New Orleans, 2012
5. Clark C, Fraser K, Hand S, Hansen JG, Jul E, Limpach C, Pratt I, Warfield A (2005) Live migration of virtual machines. In: Proceedings of the 2nd conference on symposium on networked systems design & implementation, NSDI'05, vol 2, USENIX Association, Berkeley, 2005, pp 273–286
6. Srikantaiah S, Kansal A, Zhao F (2008) Energy aware consolidation for cloud computing. In: Proceedings of the 2008 conference on power aware computing and systems. HotPower'08, USENIX Association, Berkeley, 2008, pp 10–10
7. Yamagiwa S, Wada K (2009) Performance study of interference on gpu and cpu resources with multiple applications. In: Parallel distributed processing, 2009. IPDPS 2009. IEEE international symposium, Rome, May 2009, pp 1–8
8. Ravi VT, Becchi M, Agrawal G, Chakradhar S (2011) Supporting gpu sharing in cloud environments with a transparent runtime consolidation framework. In: Proceedings of the 20th international symposium on high performance distributed computing. HPDC'11, ACM, New York, 2011, pp 217–228
9. Yumerefendi A, Shivam P, Irwin D, Gunda P, Grit L, Demberel A, Chase J, Babu S (2007) Towards an autonomic computing testbed. HotAC II, USENIX Association, Berkeley, 2007, pp 1–1
10. Hsu C-H, Chen S-C, Lee C-C, Chang H-Y, Lai K-C, Li K-C Rong C (2011) Energy-aware task consolidation technique for cloud computing. In: Proceedings of the 3rd cloudcom'2011 I.E. international conference on cloud computing technology and science, Athens, 2011

A Case of Security Encryption Storage System Based on SAN Environments

Changyan Di, Kuan-Ching Li, Jason C. Hung, Qi Yu, Rui Zhou, Chao-Hung Hung, and Qingguo Zhou

Abstract SAN (storage area network) is a dedicated network that provides access to consolidated data storage and offers major advantages as simplified administration, high speed, and flexibility. This chapter proposes a security encryption storage system named ANGLE, which contains two major parts – the key management system (KMS) and the encryption engine (E-Engine). E-Engine is in charge to encrypt/decrypt storage disks under AES128 and SHA256 cryptographic algorithms, according to keys provided by KMS. These two parts communicate by IPsec protocols, and a well-defined UI (User Interface) for applications is provided. The proposed ANGLE system is implemented in both FC SAN and IP SAN, and performance tests show that the bottleneck of ANGLE's reading and writing throughput relies on data transmission speed of the storage network.

Keywords SAN • Encryption storage • Storage network

1 Introduction

SAN (storage area network) is a high-speed and dedicated network attaching servers and storage devices, offering more advantages such as better scalability, higher data throughputs, and easier management [1, 2]. It is often used in large-scale business

C. Di • Q. Yu • R. Zhou • Q. Zhou (✉)
School of Information Science and Engineering, Lanzhou University, Lanzhou, China
e-mail: zhouqg@lzu.edu.cn

K.-C. Li • C.-H. Hung
Department of Computer Science and Information Engineering (CSIE),
Providence University, Providence, Taiwan

J.C. Hung
Department of Information Management, Overseas Chinese University, Taichung, Taiwan

environment, which means that SAN systems are able to hold more critical data under severe security requirements. Besides, SAN is an open and available medium connecting servers and storage, making it vulnerable to various security threats like unauthorized access or hostile attack. Although SAN provides measures as LUN (logic unit number) and zoning schemes, it is far from enough due to malicious intrudes. In this case, encryption becomes the most direct and effective method to tackle data leaks. There is a number of software developed to secure storage units, such as BitLocker in Windows Vista/7, the open source encryption software Truecrypt, among others. Besides, SISWG (Security in Storage Working Group) under IEEE is working on the standardization project for encryption of stored data known as P1619 [3], and now P1619.1, P1619.2, and P1619.3 are issued.

In this chapter, a secured encryption storage system based on SAN named ANGLE is proposed, aimed to protect data from leaking in case of being stolen or lost in such server storage arrays. It is a kind of hardware-level encryption strategy, including two major parts – the encryption engine (E-Engine) and the key management system (KMS). ANGLE adopts FPGA as the hardware E-Engine with various cryptographic modes like XTS and CBC and cryptographic algorithms like AES (Advanced Encryption Standard) and DES (Data Encryption Algorithm) or blowfish, and encrypts data flowing in the block level. The architecture of KMS follows the standards of P1619 strictly. Finally, ANGLE is implemented in FC SAN and IP SAN. Performance evaluation shows that ANGLE's performance bottleneck lies in the data transmission speed of the storage network.

2 Design of Implementation of ANGLE

2.1 System Architecture

The schematic diagram of ANGLE is shown in Fig. 1. ANGLE adopts the hardware cryptographic mode that holds advantages as (1) the encrypting computing is processed by independent encryption hardware which does not affect the performance of SAN system and fits well in large-scale business environments and (2) the key management is tackled independently so as to provide better protection. ANGLE has embedded SHA256 and AES256 in FPGA to implement hardware encryption and, thus, increases data throughputs in SAN systems. In addition, AES256, SHA256, and random numbers are all produced by hardware that will extend system security.

The design of KMS is the most important yet difficult point in ANGLE. It is naive to say that data is secured, because it is encrypted in that this pushes the problem of securing the data to ensure that keys to decrypt or re-encrypt are only accessible in an authorized context [5]. Therefore, the design of KMS follows the P1619.3 International Standard, including key creation, destruction, usage, revocation, and update. ANGLE adopts various types of authorized schemes such as smart cards, traditional password, or biological characteristics.
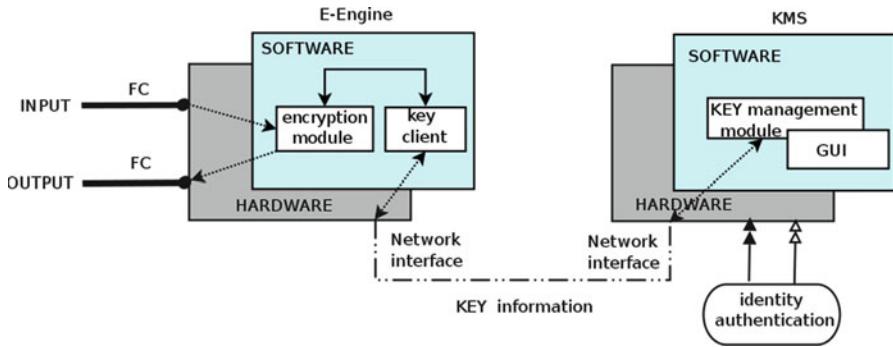
Fig. 1 Xilinx Virtex-4 FPGA device is applied as the E-Engine, which integrates cryptographic algorithms like SHA256 as IP cores [4]. A well-defined GUI provided in KMS includes system management and key management interface. E-Engine and KMS communicate with each other using IPSec protocols by PCIe ports under the slave-master mode
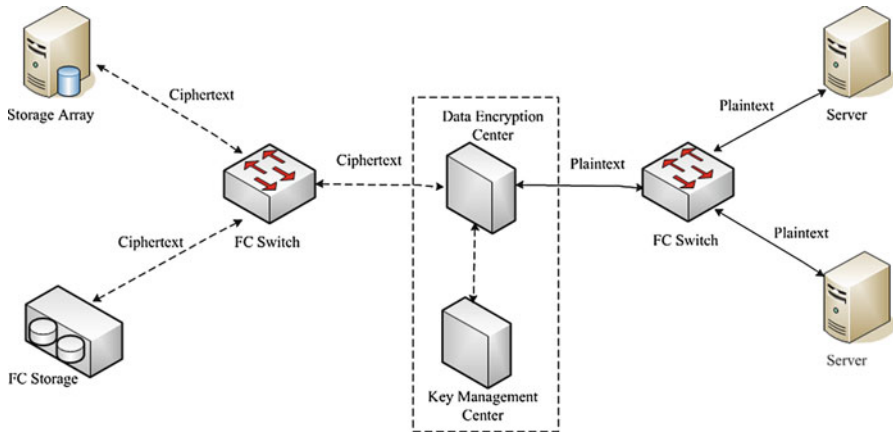
Fig. 2 In SAN, the network behind servers is usually applied to connect heterogeneous servers and storage resources. Several different components can be used in SAN's interconnection, like switches, and shown here as the implementation of ANGLE in FC SAN

2.2 Implementation of ANGLE in FC SAN and IP SAN

The term SAN is usually but not necessarily identified with block I/O services rather than file access services. Traditionally, the interconnections in SAN are based on fiber channel, whose advantages are high speed and higher level of security. Thus, FC SAN is very popular in mission-critical applications. Today, Internet Protocol (IP) has become an option to interconnect geographically separated SANs due its low cost, long distance, and also better interoperability.

As shown in Figs. 2 and 3, ANGLE is placed between storage arrays and servers and can be configured as the initiator or the target. Storage arrays are remapped by
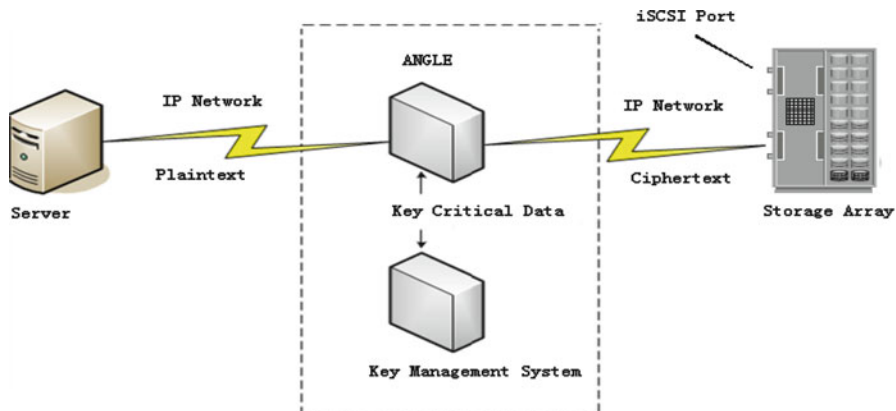
Fig. 3 IP SAN as alternative of FC SAN, it uses iSCSI protocol to encapsulate SCSI I/O over IP. As illustrated in this figure, IP traffic (*in the left of ANGLE, it is plaintext*) is routed over a network to an iSCSI storage array (*in the right of ANGLE, it is ciphertext*) that can handle the extraction and I/O natively

ANGLE and assigned to some certain servers. For every mapped disk, different keys are used to fulfill encryption and decryption requirements under some cryptographic algorithms, and applications can access the encrypted storage devices transparently. The investigations of iSCSI and FC communication protocols are fundamental in this point here, so that ANGLE can be applied in FC SAN and IP SAN seamlessly.

3   Experimental Results

As performance evaluation of ANGLE's reading and writing operations, Xilinx Virtex-4 FPGA with SHA256 IP core is used as the E-Engine with a 512-bit block size. Widely used open source software Bonnie++ [6] in UNIX is utilized to test data throughputs in different file sizes. Additionally, storage arrays are created by the *dd* command in Linux from the PC's disks. The remote encryption disks are tested in blocks of 2, 4, 8, and 16 GB at server's end with two-group comparisons, that is, (1) local non-encryption disks and (2) local encryption disks. In these tests, the server-side PC has the following configuration: one Intel Pentium Dual-core CPU E2200 2.20 GHz CPU, Linux Debian 2.6.39-dsi-new #1 i686 GNU/Linux, and 1 GB memory. After a total of over 30 tests performed, a conclusion has been drawn that the bandwidth of the storage network is the main factor affecting the performance of ANGLE, as depicted in Fig. 4.
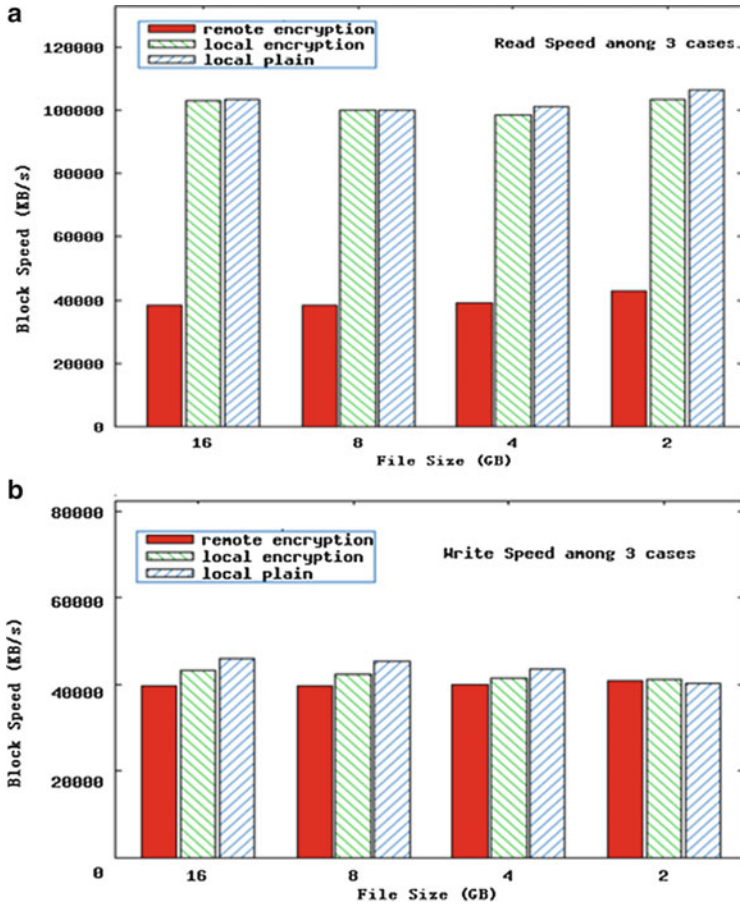
Fig. 4 *X*-axis refers to different block sizes while *Y*-axis refers to the reading or writing speed of each case in several different file block sizes. From the results shown in (**a**), reading performance between local encryption disks and non-encryption disks is almost the same when the file size is over 8 GB, but reading performance of remote encryption disks is less than 40 % of local disks and tends to be stable with the increase of the file size. Writing performance in (**b**) is smaller in remote encryption disks than that of local encryption disks, and additionally, the two are both less than that of local non-encryption disks

4 Conclusions and Future Work

In this chapter, a security storage system named ANGLE is proposed and has been implemented in FC SAN and IP SAN. The advantages of ANGLE include (1) ANGLE adopts a type of hardware encryption mode, whose encrypting speed is far higher than software encryption mode, and (2) random numbers and keys are produced by independent hardware which will provide better security. Moreover, the design of ANGLE follows P1619 International Standard.

As future work, encryption scheme at file level will be explored based on NAS. Since the concepts of Internet of Things are really popular nowadays, the way how to apply the architecture of ANGLE to intelligent mobile terminals will be investigated.

References

1. Somasundaram G, Ahrivastava A (2009) EMC education services: information storage and management. Wiley, Hoboken
2. Osama S (2011) Storage area network implementation on an educational institute network computer networking and communication. World Comput Sci Inform Tech J 1(7):292–296
3. IEEE P1619, http://en.wikipedia.org/wiki/IEEE_P1619
4. Li CJ, Zhou QG, Liu YL, Yao Q (2011) Cost-efficient data cryptographic engine based on FPGA. In: 4th international conference on Ubi-media computing, IEEE Computer Society, Sao Paulo, 2011, pp 48–52
5. Baldwin A, Shiu S (2002) Encryption and key management in a SAN. In: 1st international IEEE security in storage workshop, IEEE Computer Society, Washington, DC, 2002, pp 35–44
6. Bonnie++, http://en.wikipedia.org/wiki/Bonnie

Applying General Probabilistic Neural Network to Adaptive Measurement Fusion

Li-Wei Fong, Pi-Ching Lou, Kai-Yung Lin, and Chien-Liang Chuang

Abstract A neural-network-based adaptive state estimation is presented to measurement fusion for use of a multisensor system tracking a maneuvering target. The proposed approach consists of a group of parallel alpha-beta-gamma filters and a general probabilistic neural network (GPNN). By incorporating a general probabilistic formulation and Markov chain into a general regression neural network, GPNN is developed as a decision logic algorithm for online classification. Each activation function of GPNN is defined as Gaussian basis function whose smooth factor is a constant selected from filter's innovation covariance matrix by utilizing the parametric method. Based upon fused outputs of alpha-beta-gamma filters and a GPNN-based classifier, an adaptive alpha-beta-gamma filter is developed to improve tracking accuracy. The simulation results are presented to demonstrate the effectiveness of the proposed method.

Keywords Measurement fusion • General probabilistic neural network • Adaptive alpha-beta-gamma filter

1 Introduction

Multisensor measurement fusion [1] is one of the most powerful estimation techniques presented in many applications such as autonomous navigation and target tracking. In tracking situations, it is noted that modern targets may maneuver wildly to cause the tracking systems resulting in performance degradation, even in filter divergence. Recently, there were two adaptive methods for measurement

L.-W. Fong (✉) • P.-C. Lou • K.-Y. Lin • C.-L. Chuang
Department of Information Management, Yu Da University, Miaoli 36143, Taiwan
e-mail: fongliwei@ydu.edu.tw
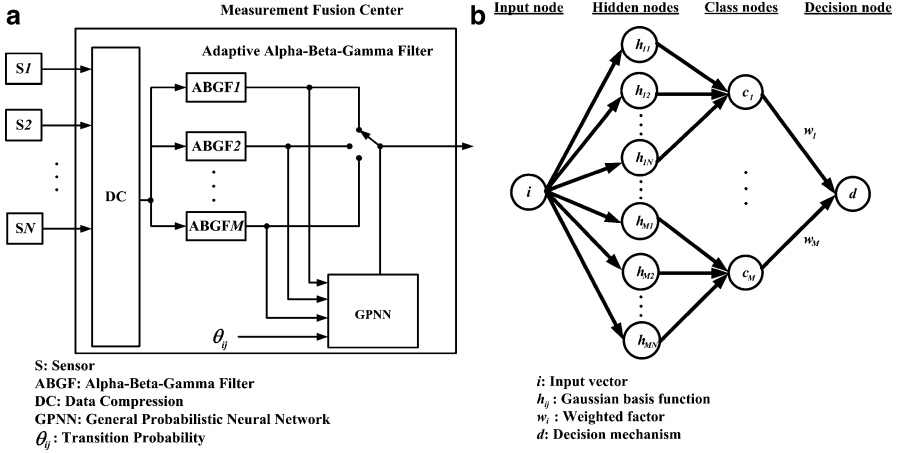
Fig. 1 (**a**) An adaptive alpha-beta-gamma filtering algorithm in the measurement fusion center and (**b**) the computational structure of general probabilistic neural network

fusion [2, 3] proposed to keep tracking in high accuracy. The first, so-called adaptive state estimator, was developed using the multiband standard Kalman filter (KF) and a traditional learning processor. The second, so-called adaptive KF, was devised that consists of a group of parallel filters and a Bayesian classifier constructed by the radial basis function network. However, these two methods still require a large amount of computation, not practical for real applications. To reduce the computational loads involved in physical implementation, alpha-beta-gamma filter (ABGF) [4] with decoupled tracking filtering technique [5] is proposed. The ABGF gains can be precomputed from three uncoupled one-dimensional filters by using closed-form equations in the line-of-sight Cartesian coordinate system (LCCS) and then transformed for use in the inertial Cartesian coordinate system (ICCS).

The main contribution of this chapter is that we join a general probabilistic formulation [6] into a general regression neural network [7] to develop a neural-network-based classifier so-called a general probabilistic neural network (GPNN) for solving online classification problems. By incorporating Markov chain into Bayesian estimation scheme, GPNN is used as a decision logic algorithm to classify which one of the candidates estimates for system output. In this chapter, an adaptive ABGF (AABGF) that consists of a group of parallel ABGFs and a GPNN-based classifier is developed for measurement fusion, as shown in Fig. 1a. Computational structure of GPNN-based classifier is shown in Fig. 1b. Each activation function of GPNN is defined as a Gaussian basis function whose smooth factor is a constant selected from filter's innovation covariance by off-line simulation through the parametric method. The resulting filter makes natural for target tracking that provides better tracking accuracy than each individual filter significantly.

2   Adaptive Measurement Fusion

In this section, the target model, measurement model, a group of parallel ABGFs, and a GPNN-based classifier are described. The candidate central fused estimates are produced by ABGFs. The classifier is used to classify which one of the candidate estimates for output only. Meanwhile, alpha-beta-gamma filtering approach is developed and outlined below briefly.

2.1   Target and Measurement Models

Assume that the target dynamics can be modeled by one of M hypothesis models. For the c-th hypothesized model, the target dynamics and the N sensor measurements are modeled by the discrete-time state-space model that can be consulted in [2]. By using data compression, the N sensor models can be obtained by weighted observation as the single model that can be found in [3]. Since the rotation of the coordinate system from the ICCS to LCCS (denoted as superscript L), the measurement noise correlation matrix $\boldsymbol{R}_{k+1}$ can be replaced by the measurement error variance matrix $\boldsymbol{R}_{k+1}^{(L)}$ in a diagonal matrix form as [5]

$$\boldsymbol{R}_{k+1}^{(L)} = \left[\sum_{i=1}^{N} \left(\boldsymbol{R}_{k+1}^{(i,L)} \right)^{-1} \right]^{-1} = \left[\sum_{i=1}^{N} \left(\mathrm{diag}\left\{ \left(\sigma_{\mathrm{j}}^{(\mathrm{i})} \right)^{2} \right\} \right)^{-1} \right]^{-1} = \mathrm{diag}\left\{ \sigma_{\mathrm{j}}^{2} \right\} \quad (1)$$

where $\sigma_j^{(i)}$ ($j = 1, 2, 3$) are the i-th sensor measurement error standard deviation and σ_j ($j = 1, 2, 3$) are the fused measurement error standard deviation in three axes of the LCCS.

2.2   Alpha-Beta-Gamma Filtering

The decoupled tracking filter is summarized in [5]. The filter structure shows that the estimates of states are calculated in the ICCS while the covariance matrices are calculated in the LCCS. Given the system model, the updated state equation of the c-th decoupled tracking filter is given by

$$\hat{\boldsymbol{x}}_{k+1}^{(c)} = \bar{\boldsymbol{x}}_{k+1}^{(c)} + \boldsymbol{M}\left(\bar{\boldsymbol{x}}_{k+1}^{(c)} \right) \boldsymbol{K}_{k+1}^{(c,L)} \boldsymbol{m}\left(\bar{\boldsymbol{x}}_{k+1}^{(c)} \right) \boldsymbol{d}_{k+1}^{(c)} \quad (2)$$

where

$$\bar{\pmb{x}}_{k+1}^{(c)} = \pmb{\Phi}_k^{(c)} \hat{\pmb{x}}_k^{(c)} \tag{3}$$

$$\pmb{d}_{k+1}^{(c)} = \pmb{z}_{k+1} - \pmb{H}_{k+1}\bar{\pmb{x}}_{k+1}^{(c)} \tag{4}$$

$$\pmb{M}\left(\bar{\pmb{x}}_{k+1}^{(c)}\right) = \mathrm{diag}\left\{ \pmb{m}\left(\bar{\pmb{x}}_{k+1}^{(c)}\right), \quad \pmb{m}\left(\bar{\pmb{x}}_{k+1}^{(c)}\right), \quad \pmb{m}\left(\bar{\pmb{x}}_{k+1}^{(c)}\right) \right\} \tag{5}$$

with subscript k represents the discrete-time index, $\bar{\pmb{x}}_{k+1}^{(c)}$ and $\hat{\pmb{x}}_{k+1}^{(c)}$ are predicted and updated state vectors, $\pmb{K}_{k+1}^{(c,L)}$ is the filter gain matrix, $\pmb{d}_{k+1}^{(c)}$ is the innovation, $\pmb{m}(\bar{\pmb{x}}_{k+1}^{(c)})$ is the 3×3 coordinate transformation matrix from the ICCS to the LCCS, $\pmb{\Phi}_k^{(c)}$ is the 9×9 state transition matrix, $\pmb{z}_k$ is the 3-dimensional fused measurement vector, and $\pmb{H}_k$ is the 3×9 observation mapping matrix.

As noted that the decoupled tracking filter has a linear structure and the state estimation, the filter gain is computed in the LCCS where the measurement noise covariance defined in (1) is diagonal. The filter gain defined in (2) with steady-state solution can be written as

$$\pmb{K}_{k+1}^{(c,L)} = \begin{bmatrix} \mathrm{diag}\left\{\alpha_j^{(c)}\right\} \\ \mathrm{diag}\left\{\beta_j^{(c)}/\mathrm{T}\right\} \\ \mathrm{diag}\left\{\gamma_j^{(c)}/\mathrm{T}^2\right\} \end{bmatrix}_{9 \times 3} \tag{6}$$

where $\alpha_j^{(c)}$, $\beta_j^{(c)}$, and $\gamma_j^{(c)}$ $(j = 1, 2, 3)$ are the optimal steady-state filter gain coefficients and T is a sampling period. A generalized solution for alpha-beta-gamma filter gains [4] has been derived based on the Tracking Index $\lambda_j^{(c)}$ expressed as

$$\lambda_j^{(c)} = \frac{\sigma_m^{(c)}}{\sigma_j} T^3 \tag{7}$$

2.3 General Probabilistic Neural Network

In the literature, there were two papers which generally discussed the design methods for neural-network-based classifiers. The first, Adali method [6], uses an extension of maximum likelihood, the partial likelihood theory to develop a general probabilistic framework for neural classifiers which is particularly suitable for application to problems in which time ordering is essential. The second, Specht method [7], describes a memory-based network that has an advantage of one-pass learning algorithm with a highly parallel structure. We combine the two methods

for constructing a classifier which is the so-called GPNN and used as a decision logic algorithm for solving online classification problems, as shown in Fig. 1b.

Suppose that the unknown target maneuver model switches randomly within a random time period between a finite set of M possible models. To begin with, we will treat each of the M reference models as a distinct class. A set of the M reference models is denoted as $\boldsymbol{\Psi}_{k+1} := \left\{ \boldsymbol{\Psi}_{k+1}^{(j)} | j = 1, 2, \ldots, M \right\}$ where the subscript of Ψ_{k+1} represents the time at $k + 1$. The random transitions among the reference models will be governed by an underlying Markov chain. Given the sequence of weighted observations $\boldsymbol{Z}^{(k+1)} : z_0, z_1, \ldots, z_{k+1}$, resulting from unknown target maneuvering pattern, decide which target maneuver model it belongs. The corresponding model probability $\mu_{k+1}^{(j)}$ of $\boldsymbol{\Psi}_{k+1}^{(j)}$ can be given by Bayes' rule as below:

$$\mu_{k+1}^{(j)} = \frac{w_{k+1}^{(j)} \cdot \prod\limits_{i=1}^{n} h_{ji}\left(z_{k+1}, \boldsymbol{H}_{k+1}\hat{\boldsymbol{x}}_{k+1}^{(j)}, s_i\right)}{\sum\limits_{j=1}^{M} w_{k+1}^{(j)} \cdot \prod\limits_{i=1}^{n} h_{ji}\left(z_{k+1}, \boldsymbol{H}_{k+1}\hat{\boldsymbol{x}}_{k+1}^{(j)}, s_i\right)} \tag{8}$$

where the i-th smooth factor s_i is a constant selected from filter's innovation covariance matrix by utilizing the parametric method and $w_{k+1}^{(j)}$ is the weighted factor, given by

$$w_{k+1}^{(j)} = \sum\limits_{l=1}^{M} \theta_{jl} \mu_k^{(l)} \quad \text{and} \quad \sum\limits_{l=1}^{M} \theta_{jl} = 1 \tag{9}$$

The θ_{jl} is the transition probability. Each hidden node h_{ji} is connected to a single class node c_j. The Gaussian basis function h_{ji} receives an input vector z_{k+1} and outputs an activation given by the function

$$h_{ji}(\boldsymbol{d}_{k+1}^{(j)}, s_i) = \left((2\boldsymbol{\pi})^3 |s_i| \right)^{-1/2} \cdot \mathbf{exp}\left(\frac{-1}{2} \left(\boldsymbol{d}_{k+1}^{(j)}\right)^{\mathrm{T}} s_i^{-1} \boldsymbol{d}_{k+1}^{(j)} \right) \tag{10}$$

In order to find the maximum probability over all possible models, the quantity has to be computed for each of the M reference models as below:

$$\mu_{k+1}^{(c)} = \max_{1 \leq j \leq M} \mu_{k+1}^{(j)} \tag{11}$$

Each class node c_j is connected to a single decision node with the corresponding weighted factor. According to (11), the decision node chooses the maximum probability over all the classes, and the final output filter state $\hat{\boldsymbol{x}}_{k+1}$ yields

$$\hat{\boldsymbol{x}}_{k+1} = \hat{\boldsymbol{x}}_{k+1}^{(c)}, \quad \text{if } \mu_{k+1}^{(c)} \text{ is the maximum probability.} \tag{12}$$

3   Simulation Results

The results of computer simulation are presented for the performance comparison of AABGF, low-level-band KF (denoted as KF1; maneuver variance given by 133 m^2/s^4), middle-level-band KF (denoted as KF2; maneuver variance given by 833 m^2/s^4), and high-level-band KF (denoted as KF3; maneuver variance given by 2133 m^2/s^4). During the initial transient period, each ABGF employs a piecewise linear approximation for approaching the optimal transient response of decoupled KF. The results of 100 runs of Monte Carlo simulation are processed in the following case study. The scenario of two maneuvering turns of the target trajectory is called circular-turn and U-turn as shown in [2, 3]. The smooth factors defined in (10) are selected as $[s_1, s_2, s_3] = [750, 550, 350]$ in m^2. The model switching probability matrix is a constant matrix with a large value 0.9999 on the diagonal elements, and the other elements are all the same value as 0.00005. The other system parameters are similar to but a little different in [3], [5]; the interesting readers may consult these papers for realizing the method of simulation processing. The performance is evaluated by using the root-mean-square error (RMSE). Averaged root-mean-square error (ARMSE) is defined as the performance index. For a quantitative performance comparison, the time average of estimation errors of the position velocity and acceleration is listed in Table 1. As shown, AABGF demonstrates adaptive capability in the tracking process and performs better tracking performance than KF1, KF2, and KF3.

4   Conclusion

In this chapter, an adaptive alpha-beta-gamma filter is developed to the measurement fusion for real applications in the multisensor tracking system. Simulation results are provided for comparison of tracking accuracy between proposed filter and each individual Kalman filter. Using target scenario with circular-turn and U-maneuvering turn for computer simulation, the proposed filter demonstrates better tracking accuracy than the average estimate of multi-model filter with about 9.91, 17.48, and 19.23 % improved in position, velocity, and acceleration, respectively. The results indicate that the proposed filter provides significant improvement performance and possible real-time applications because of using precomputed gains of alpha-beta-gamma filter.

Table 1 Time average of estimation errors

Method	Position (m)	Velocity (m/s)	Acceleration (m/s^2)
KF1	23.2723	32.7628	22.6795
KF2	21.0874	30.8301	23.3207
KF3	21.6405	34.0617	27.3572
AABGF	19.8198	26.8630	19.7502

References

1. Gan Q, Harris CJ (2001) Comparison of two measurement fusion methods for kalman-filter-based multisensor data fusion. IEEE Trans Aerosp Electron Syst 37(1):273–280
2. Fong L-W (2011) Multi-sensor measurement fusion via adaptive state estimator. In: international conference on electric and electronics 2011. LNEE, vol 100, Springer, Heidelberg, pp 455–462
3. Fong L-W (2012) On-line bayesian classifier design for measurement fusion. Adv Mater Res 461:826–829
4. Sudano JJ (1993) The α-β-Γ tracking filter with a noisy jerk as the maneuver model. IEEE Trans Aerosp Electron Syst 29(2):578–580
5. Fong L-W (2012) Decoupled adaptive tracking algorithm for multi-sensor measurement fusion. Appl Mech Mater 229–231:1235–1238
6. Adali T (1998) A general probabilistic formulation for neural Classifiers. In: Proceedings of the 1998 I.E. signal processing society workshop neural networks for signal processing VIII, pp 145–154
7. Specht DF (1991) A general regression neural network. IEEE Trans Neural Netw 2:111–121

Reorder Adapting TCP

Yi-Cheng Chan, Chien-Yu Chen, and Yu-Shuo Lee

Abstract Transmission Control Protocol (TCP) is the main transport protocol that provides reliable transmission in the current Internet. However, TCP still has problems that may affect its performance on various network environments. Packet reordering, which is one of the problems on TCP, refers to the out-of-order event of packets. There are many reasons that can cause packet reordering. In this chapter, we propose RA-TCP, a novel TCP variant which modifies the retransmission occasion and the congestion response of the traditional TCP mechanism, to improve the performance on packet reordering. In particular, we replace the three duplicate ACKs with a retransmission detection timer (RDT) for the trigger of fast retransmit. Our simulation studies reveal that RA-TCP performs consistently better than existing mechanisms that try to make TCP more robust to packet reordering.

Keywords TCP • Congestion control • Packet reordering • Out-of-order

1 Introduction

The congestion control of TCP adjusts the rate of data entering the network, keeping the data flow below a rate that would trigger collapse. It infers the network conditions between the sender and receiver depending on acknowledgments (ACK) and the timer. If a TCP sender detects a congestion event, it will limit the transmission rate of data entering the network by regulating the size of the congestion window (*cwnd*) and the number of unacknowledged packets allowed to be sent.

Y.-C. Chan (✉) • C.-Y. Chen • Y.-S. Lee
Department of Computer Science and Information Engineering, National Changhua University of Education, Changhua 50074, Taiwan
e-mail: ycchan@cc.ncue.edu.tw

Several congestion control algorithms, including slow-start, congestion avoidance, fast retransmit, and fast recovery, have been implemented in TCP. A new TCP connection starts from slow-start phase. In slow-start, the value of *cwnd* is incremented by one whenever the sender receives an ACK, until it reaches the slow-start threshold (*ssthresh*). After *cwnd* reaches *ssthresh*, the phase of TCP sender turns into congestion avoidance.

As long as non-duplicate ACKs are received, the *cwnd* is additively increased by one every round-trip time (RTT). In the other side, the TCP sender will resend the lost packet and decrease transmission rate by setting *cwnd* to half after the arrival of three duplicate ACKs. The response of retransmission, triggering by received three duplicate ACKs, is called fast retransmit. In addition to fast retransmit, there is another method for detecting network congestion. TCP uses a retransmission timer to ensure data delivery in the absence of any feedback from the remote data receiver. The duration of this timer is referred to as RTO. When the retransmission timer expires, the TCP sender will set the *cwnd* to one and restart from slow-start phase.

A packet loss event can be detected through a TCP sender that receives three duplicate ACKs. However, packet reordering can easily trigger the three duplicate ACKs. Packet reordering refers to the network behavior where the relative order of some packets transmitted in the network in the same flow is altered when these packets are relayed in the network [1]. When packet reordering occurs, the TCP sender may mistake the out-of-order event and transmit the redundant data packets unnecessarily. Worse is that the spurious packet retransmissions keep the *cwnd* small and lead a poor TCP performance.

There are many situations that may cause packet reordering, like packet-level multipath routing, route fluttering, inherent parallelism in modern high-speed routers, router forwarding lulls, and IP fast reroute. In view of this, we propose the scheme called reorder adapting TCP (RA-TCP) to improve the TCP performance for packet reordering. RA-TCP changes the conditions which trigger the fast retransmit. Besides, according to the network situation, we use the cost function to dynamically adjust the parameters of RA-TCP.

In the following sections, we describe the design of RA-TCP and compare it with the other recent TCP versions like TCP-PR [2] and TCP-NCL [3] for packet reordering via the simulation of ns-2.

2   The Proposed Method

When the out-of-order event arises on a connection, the TCP receiver sends the duplicate ACKs. In tradition, the three consecutive duplicate ACKs are regarded as the signal of packet loss, and the TCP sender triggers the fast retransmit. Nevertheless, packet reordering may lead to the false fast retransmit. Thus the basic idea of RA-TCP is to cancel the transmission effect about duplicate ACKs.

In RA-TCP, the retransmission detection timer (RDT) is used to replace three duplicate ACKs for the trigger of fast retransmit. We use the parameter *mxrtt*, which refers to the possible maximum round-trip time, to set RDT. If the TCP sender waits for a corresponding ACK for the period longer than the *mxrtt*, it performs the process of fast retransmit, and we suppose the packet loss event has occurred. Each time the TCP sender receives an ACK, the *mxrtt* is updated. The equation of *mxrtt* is presented as follows:

$$mxrtt = \alpha \times srtt, \tag{1}$$

where α is a positive constant larger than 1 and *srtt* is the smoothed round-trip time estimated by sender. In traditional TCP, the *srtt* is one of the variables for computing TCP's retransmission timer [4]. When a subsequent RTT measurement R' is made, the *srtt* can be computed as follows:

$$srtt = (1 - \beta) \times srtt + \beta \times R', \tag{2}$$

where β is set to one eighth in our experiments, just the same as the description in [4]. The retransmission detection timer decides the timing of retransmission. Therefore, it is significant to set RDT's countdown period appropriately.

The parameter α denotes the proportion between *mxrtt* and *srtt*. In fact, it is impossible to choose a proper fixed value of α that is suitable for all networks. According to this, we design the mechanism that allows a TCP sender to dynamically adjust the α value in a connection. The adjustment depends on the cost estimations of transmission. We use the concept of opportunity cost to design the cost function.

To ease the cost estimation, we choose to compute the most probable cost in all cases. There are two cases for the cost estimation. First, we consider the cost of a false fast retransmit. The false fast retransmit means the retransmit is triggered for an undropped packet. In other words, the RDT's countdown period is shorter than it should be. The TCP sender will receive the corresponding ACK later. A false fast retransmit causes an unnecessary retransmission and a window reduction by half.

For detecting false fast retransmit, we add the DSACK [5] function into RA-TCP. In a connection, the TCP sender detects false fast retransmit when it received the DSACK acknowledgement which contains the information about the duplicate data packets. The TCP sender always stores the *cwnd* value before fast retransmit. When false fast retransmit is detected by DSACK, the TCP sender restores the *cwnd* to original value that was just before the occurrence of false fast retransmit.

As illustrated in Fig. 1, we suppose that a TCP connection has a current congestion window size w and a smoothed RTT that refers to R. We maintain two exponentially weighted moving average parameters, including the fast retransmit recover duration D and the maximum window size W. The former indicates the period from the inception of retransmission to the next time of retransmission. The latter represents the top value of *cwnd* in general cases. For acquiring the most

Fig. 1 A simple diagram for the variation of *cwnd* to indicate the false fast retransmit
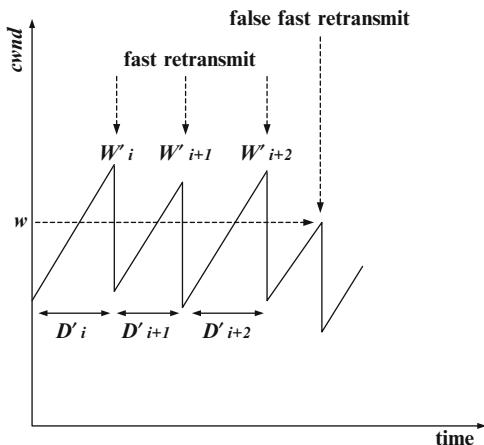
probable estimate, we set the exponential moving average duration between the occasions of fast retransmit as D. In other words, D is the duration between two consecutive fast retransmits. Whenever a fast retransmit is triggered, we get the duration D' from the moment of last fast retransmit to current time, and the equation of D can be presented as follows:

$$D = (1 - \beta) \times D + \beta \times D'. \tag{3}$$

The W is the common max value of *cwnd*; the fast retransmit is usually triggered whenever *cwnd* is greater than or equal to W. Because the packets which the TCP sender may transmit are not more than W per RTT, we choose W to estimate the cost as large as possible. We set the length of *cwnd* as W' when the retransmission arises, and the equation of W is as follows:

$$W = (1 - \beta) \times W + \beta \times W'. \tag{4}$$

With these parameters, we can discuss the cost estimation. For example, if D equals to R, the window was halved unnecessarily for only one RTT. Based on the assumption that there is no false fast retransmit during the period of D and the congestion window size is linearly increased per RTT until the *cwnd* gets up to W, the W is the maximum value of *cwnd* commonly. Therefore, C_{ffr}, the cost of a false fast retransmit, is $W - \dfrac{w}{2}$. When D is longer than R, the cost is greater because the reduced window is in effect for a longer period. Note that the cost in each subsequent RTT becomes less and less as the linear increase of congestion window is progressing. The original congestion window value may be restored after $\left(W - \frac{w}{2}\right)$ RTTs. Thus, for $k = \lceil D/R \rceil$, the cost of a false fast retransmit is bounded by $\left(W - \frac{w}{2}\right) + \left(W - \frac{w}{2} - 1\right) + \cdots + \left(W - \frac{w}{2} - (k-1)\right)$, or

$$C_{\text{ffr}} \leq \sum_{i=1}^{k-1} W - \frac{i(2W - w - i + 1)}{2} \tag{5}$$

packets. Note that we limit k to $W - \frac{w}{2}$ regardless of D for disposing the cost appropriately. Because D and R are estimated as exponentially weighted moving averages, their values are not instantaneously accurate. The cost of a false fast retransmit may lie between the cost estimation for $k = \lceil D/R \rceil$ and $k = \lceil D/R \rceil$.

We also consider the cost of the delay after packet loss, C_{dpl}. The opportunity cost is introduced in idle time when the RDT's countdown period is great. In this case, the TCP sender keeps idle and does not execute the fast retransmit even though the corresponding packets are indeed dropped.

Suppose that a TCP connection has a current congestion window size w, a smoothed RTT that refers to R. Before w is halved, the TCP sender is idle because the RDT is not expired after packet loss. Compared with the normal case, the TCP sender could send less packets. In the following, we try to estimate the cost for this situation.

We maintain another parameter I to indicate the supposed idle period for this connection. Theoretically, the I is less than *mxrtt*. To compute the most probable cost, we set I to *mxrtt* in our experiments. Whenever the TCP sender receives an ACK after the non-spurious retransmission, we could estimate the cost that the TCP sender may lack for delivering during the waiting time. In addition, we also need to consider the influence of limited transmit [6].

In modern TCP, limited transmit is the mechanism which lets the sender to transmit a new packet when it received a dup-ACK before fast retransmission and time-out. To take account of limited transmit, we count the number of further duplicate ACKs that return per idle period, d, before the occurrence of the next fast retransmit. These duplicate ACKs are not part of the opportunity cost in the idle period. Hence, the cost of this idle period is

$$C_{\text{dpl}} \leq \frac{I}{R} W - d \tag{6}$$

packets. Here W is the exponentially weighted moving average of the maximum window size, and R is the smoothed RTT.

After the calculations of C_{ffr} and C_{dpl}, the adjustment of α can be performed. Above all, the S is the fundamental parameter; through it we adapt the value of α. In the results presented herein, we set S to 0.01 which is chosen to acquire appropriate adjustment of α from the numerous simulation experiments. The rule for adapting α is described as follows. As false fast retransmit occurs, RA-TCP increases α by S. This leads a longer *mxrtt*. However, the cost of delay after packet loss cannot be ignored because it also grows when the value of *mxrtt* is large. Consequently, we should consider the two opposite sides of the α adjustment. In view of this, we decrease α after an idle period that leads $C_{\text{dpl}} > C_{\text{ffr}}$. Thus, when every idle period is over and the result corresponds to the condition that C_{dpl} is large than C_{ffr}, RA-TCP decreases α by

$$\frac{C_{\mathrm{dpl}}}{C_{\mathrm{ffr}}} \times S. \tag{7}$$

These rules dynamically adapt α in a way that maximizes throughput for a connection experiencing reordering. False fast retransmits cause a gradual increase in the α. If the α oversteps its suitable bounds, RA-TCP also decreases α depending on S and the ratio of the two cost estimations.

3   Performance Evaluation

Due to the page limitation, in this section, we only present the ns-2 simulation results on a simple wired network as shown in Fig. 2. It involves two end-systems (S1 and S2) and two routers (R1 and R2). The path between R1 and R2 models the underlying network path connecting R1 and R2. A single, long-lived TCP flow from S1 to S2 runs for 300 s. A total of ten runs are done to compute an average value of the performance metric. We take the throughput of a flow to make comparisons between four TCP variants; those are TCP SACK, TCP-PR [2], TCP-NCL [3], and the proposed RA-TCP.

To simulate packet reordering, we repeatedly change the path delay which is between R1 and R2 according to a uniform distribution. The minimum delay value between R1 and R2 is 20 ms, and the maximum value is configured from 20 to 500 ms depending on the simulation experiments. A larger maximum value will induce more variation in the path delay, thereby increasing the degree of packet reordering.

The Fig. 3 shows the throughputs of the four TCP variants when the maximum path delay varies between 20 and 500 ms. The throughput of SACK drops obviously as the maximum path delay is increased. The other three schemes have a relative good performance because they use the timers to trigger fast retransmission instead of three duplicate ACKs. However, RA-TCP's throughput outperforms that of TCP-PR and TCP-NCL when the maximum path delay is larger than 300 ms.

4   Conclusions

In this chapter, we propose a novel TCP variant, RA-TCP, as an efficient solution for packet reordering. Just like TCP-PR and TCP-NCL, we replace the three duplicate ACKs with the retransmission detection timer for the trigger of fast retransmit.
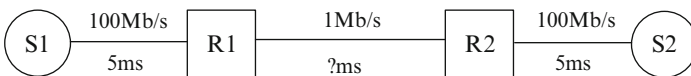
Fig. 2   A single three-hop wired network
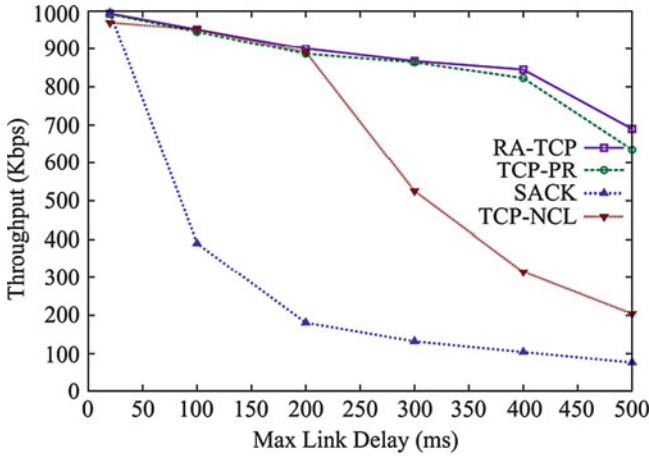
Fig. 3 Throughputs of the four TCP variants which are in different maximum path delays

For adapting the fluctuant network environment, we propose an adjustment algorithm, which refers to the cost functions of false fast retransmit and delay after packet loss, to adjust the timer fittingly. Our simulations show that RA-TCP has a significant performance improvement compared with that of SACK, TCP-PR, and TCP-NCL.

References

1. Leung K et al (2007) An overview of packet reordering in transmission control protocol (TCP): problems, solutions, and challenges. IEEE Trans Parallel Distrib Syst 18(4):522–535
2. Bohacek S, Hespanha JP, Lee J, Lim C, Obraczka K (2006) A new TCP for persistent packet reordering. IEEE/ACM Trans Netw 14(2):369–382
3. Lai C, Leung K-C, Li VOK (2010) Enhancing wireless TCP: a serialized-timer approach. IEEE INFOCOM 2010, pp 1–5
4. Paxson V, ACIRI, Allman M (2000) Computing TCP's retransmission timer, STD 7, IETF RFC 2988
5. Floyd S, Mahdavi J, Mathis M, Podolsky M (2000) An extension to the selective acknowledgement (SACK) option for TCP. IETF RFC 2883
6. Allman M, Balakrishnan H, Floyd S (2001) Enhancing TCP's loss recovery using limited transmit. IETF RFC 3042

A Novel and Feasible System for Rule Anomaly and Behavior Mismatching Diagnosis Among Firewalls

Chi-Shih Chao

Abstract While configuring firewalls, firewall rule ordering and distribution must be done cautiously on each of cooperative firewalls, especially in a large-scale network. However, network operators are prone to incorrectly configuring firewalls because there are typically hundreds of thousands of filtering rules (i.e., rules in the access control list file, or ACL for short) which could be set up in a firewall, not to mention these rules among firewalls could affect mutually. To speed up the crucial but laboring inspection of rule configuration on firewalls, this chapter describes our developed diagnosis system which can not only figure out anomalies among firewall rules effectively but also infer/correlate the main reasons from the diagnosed anomalies for filtering (behavior) mismatching between firewalls. At the end of this chapter, the system prototype is shown as a demonstration of our system implementation.

Keywords Firewall rule anomaly • Firewall behavior mismatching • Anomaly correlation • Diagnosis results reuse

1 Introduction

In the Internet, firewalls and their associated filtering rules should be discreetly deployed and configured for cooperative, integrated, and in-depth network security protection. Yet, in a large and complex enterprise network equipped with numbers of firewalls, it is very possible for a network manager to make mistakes while setting the firewall rules (i.e., ACL rules) since maintaining the security consistency between firewalls' rule configuration and the demands of network security policies is always time-consuming, laboring, and error-prone. Sometimes, the matter can go

C.-S. Chao (✉)
Department of Communications Engineering, Feng Chia University, Taichung 40724, Taiwan
e-mail: cschao@fcu.edu.tw

even worse when several managers with different levels of professional knowledge are assigned to do this job collectively.

The security inconsistency typically can be revealed by either the occurrence of anomalies between the firewall rules or demand mismatching of network security policies [1]. E. Al-Shaer and H. Hamed formally define an anomaly as a duplicate or multiple rule matching for a packet in a rule set. Based on the concept, they further define several different intra-/inter-ACL anomalies among the firewall rules [2–5]. However, because a finite-state-machine (or FSM)-based comparison between each pair of rules should be conducted for anomaly checking, their anomaly diagnosis will meet an inefficiency when the number of rules or firewalls get large.

To lower the comparison times between firewall rules needed in [4], Y. Yin et al. [6, 7] segment the IP address space formed by the source and destination networks into blocks where each block is precisely cut out by the IP addresses in the conditional field of each firewall rule. Utilizing these varying-sized blocks, a SIERRA tree is built and two conflict rules would be hanged on the same branch [8]. The network manager (or system) just needs to do the anomaly inspections/ checking on rules in the same spatial block(s), instead of wasting enormous time to conduct a comprehensive pair-wise rule comparisons. Yet, this approach would lead to a fatal drawback in a networking environment with frequent rule updates. A clean-slate reconstruction of the SIERRA tree is very possibly unavoidable if a simple rule deletion or insertion is performed. It is because space blocks are exactly sliced according to the IP addresses of each rule. So, once one rule changes, a change for the whole spatial rule relationship would occur, and the corresponding data structures could be reconstructed. This drawback also means the local diagnosis results, that is, the intra-ACL rule diagnosis results, can hardly be reutilized for the diagnosis of inter-ACL rule anomalies.

As to the demand mismatching of network security policies for the security inconsistency, many research results can be found for the past several years. Among them, some are noteworthy. Chao (this chapter's author) [9] first categorizes the filtering behavior (or effect) mismatchings between two firewalls into two different types: incorrectly blocking error and incorrectly admitting error. A formal high-level specification language is also designed to let managers describe the demand of the security policies [10]. The developed system can compare the high-level specification description file with the ACL file of any specific firewall for behavior mismatching check. Still, due to lack of sound linguistic validation for its high-level specification, by far, the system is not ready on the stage of practicability. In 2008, Alex Liu et al. [11, 12] propose firewall decision diagram (FDD) data structure as well as a similar high-level specification language called property rule. With their associated algorithm, the ACL file of filtering rules and the high-level specification file representing the demand of network security policies would be transformed to their FDD counterparts separately and then find the differences of their filtering effects. However, their implementations are viewed as far from being practicable either due to the lack of proof of solidness and completeness of the high-level logics they use to specify the firewall behavior.

   The rest of our chapter is organized as follows: Sect. 2 describes the novel data structure we use to achieve feasible and efficient rule anomaly diagnosis. In Sect. 3, we illustrate how the diagnosed rule anomalies are correlated and how we filter out the anomalies which actually lead to mismatching filtering effects among firewalls. Lastly, Sect. 4 gives a brief summary with a glance at our future work.

2 Firewall Rule Anomaly Diagnosis

For the anomalies between firewall rules, they are defined completely by E. Al-Shaer et al. and classified broadly into two types: anomalies within one single ACL (or called intra-ACL rule anomalies) and anomalies among different ACLs (or called inter-ACL rule anomalies). In this section, our RAR tree-based diagnosis approach is introduced and we will show how it can facilitate the diagnosis of firewall rule anomalies. To avoid the typical time-consuming pair-wise rule comparisons for anomalies checking [3], a 2-dimensional address space matrix is designed as a structural basis of our RAR tree to prune out those unnecessary comparisons in which there is no intersection between the IP address spaces of two rules. To do so, in our system, the IP address ranges of the source network domain and destination network domain are employed as two axes to form a rectangle plane which is further divided into a matrix containing fixed-sized blocks. Later, with the fields of <source_IP> and <destination_IP>, the IP address space of each ACL filtering rule can be represented as a smaller rectangle and drawn on some proper place of this matrix (see Fig. 1).

   After that, the address space of a rule can be recorded in our RAR tree in the form of, □—○—△ where □ contains the values of the conditional fields of the rule, ○ is used to indicate the matrix block(s) spanned by the address space of the rule, △ and shows the label (or the order) of the rule. By dealing with each rule in this fashion, the RAR tree depicting the structural configuration of Fig. 1 can be built as Fig. 2. From Fig. 2, it can be found that there are six branches containing more than one △ leaves, which indicates only the IP address spaces of those rules in these branches could have the chance to intersect with each other and hence incur intra-ACL rule anomalies. So, we simply have to do the pair-wise rule comparisons for anomaly checking on the rules at the same branch within these six branches. Comparing to [2], if the RAR tree is not introduced, then around three times rule pair-wise comparisons are required for anomaly checking.

   To isolate the inter-ACL (or even inter-firewall) rule anomalies, in our approach, it can easily be achieved by simply reutilizing the RAR trees built for the diagnosis of intra-ACL (or intra-firewall) rule anomalies. As network managers often do, for instance, we can first do the intra-ACL anomaly diagnosis for rules inside two designated firewalls individually, which will lead to the construction of two RAR trees separately for the diagnosis of intra-ACL rule anomalies. Later, to obtain the diagnosis of inter-firewall rule anomalies between these two firewalls, a tree integration can be made by simply collecting the leave △ nodes belonging to the
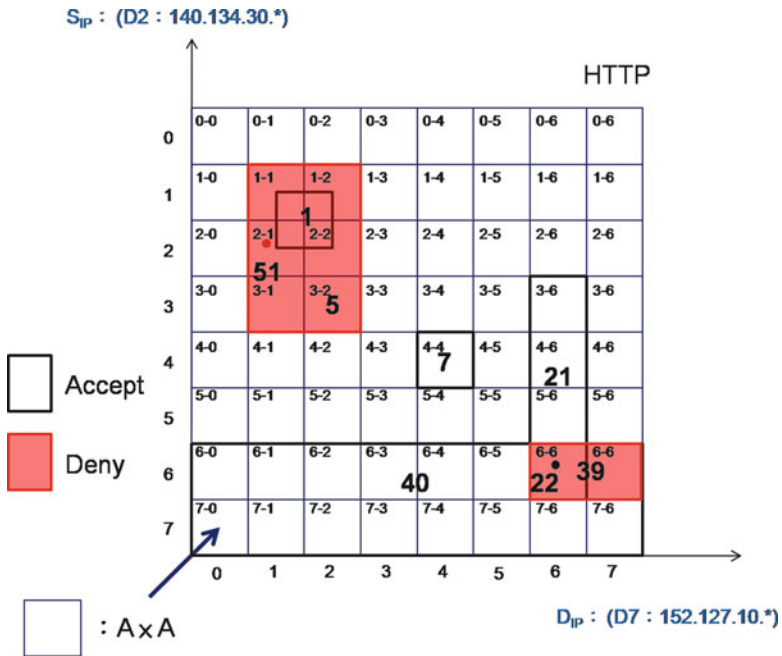
Fig. 1 2-dimensional address space matrix
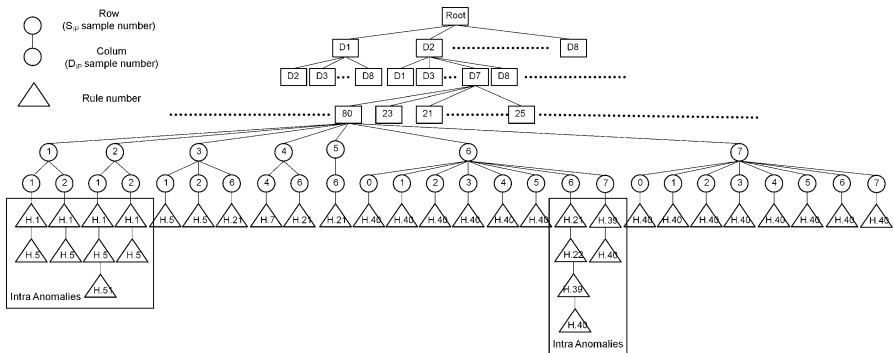
Fig. 2 The RAR tree of Fig. 3

same branch of the two individual RAR trees and putting them together under the same branch of a new RAR tree for inter-ACL rule anomaly diagnosis. And then, following the same logic (fashion) in our diagnosis for intra-ACL rule anomalies, the pair-wise comparisons for the diagnosis of inter-ACL rule anomalies would only be conducted for those rules which are under the same branch of the integrated RAR tree for inter-ACL rule anomaly diagnosis.

Two dominating advantages can be obtained by the introduction of our RAR tree:

1. Unlike the approaches in [6, 8], the local diagnosis results can be fully and easily reused. As described, the RAR trees built for intra-ACL rule anomaly diagnosis can be easily integrated for the use of the inter-ACL rule anomaly diagnosis. Comparing with the direct pair-wise-based solution in [2], our approach makes a huge saving of about 84 % time-consuming comparisons for inter-ACL rule anomaly checking.
2. By simple integration of RAR trees for intra-ACL rule anomaly diagnosis, our system can handle with ease the diagnosis of the inter-ACL rule anomalies among a large number of firewalls in an enterprise-level network, that is, our RAR tree-based diagnosis has superior capability of being up against network expansion. In fact, it can also be observed that it is quite easy for our approach to deal with the situation of network or firewall dynamic (e.g., a rule insertion or deletion). Other existing "clean-slate" approaches would do far more efforts on the rebuilding of data structures for the inter-ACL rule anomaly diagnosis. As a consequence, low system expansibility and scalability is incurred.

3   Behavior Mismatching Diagnosis

Besides anomalies among firewall rules, the other most noticeable problem with the security inconsistency while setting firewalls is the difference of filtering effects, say behavior mismatching, between two firewalls. In SOC, network managers often want to know if two of their equipped firewalls have the same filtering effect for unified in-depth protection [9]. To achieve the objective, a 3-dimensional Service Flow Space is devised, which is formed on the basis of the fields <order>, <Source IP>, <Destination IP>, and <Action> of each of filtering rules within the designated ACL of a firewall. Figure 3 shows two examples of 3-dimensional Service Flow Space for firewalls A and B. And their corresponding 2-dimensional counterparts can be drawn like those in Fig. 4, which reveal their actual filtering effects (or behavior), separately. As an example, in Fig. 4, we can indicate two of conflicting filtering regions: one marked as M_1 in $(S_{IP}, D_{IP}) = (192.168.0.0/27, 192.168.1.64/26)$ with incorrect blocking error and the other one M_2 located in $(S_{IP}, D_{IP}) = (192.168.0.128/27, 192.168.1.64/26)$ with incorrect admitting error, where firewall A is set as being upstream to firewall B.

To reason these two problematic regions, one thing should be highlighted first. According to the first matching scheme of firewalls [1], the actual filtering effect of an ACL can be formed by those rules which are not fully covered by any other firewall rules in the 3-dimensional Service Flow Space. Those rules in our work are termed as "significantly effective rules." Once the problematic regions fall in (or interest with) the IP addresses of the effective rules, it can be found that some
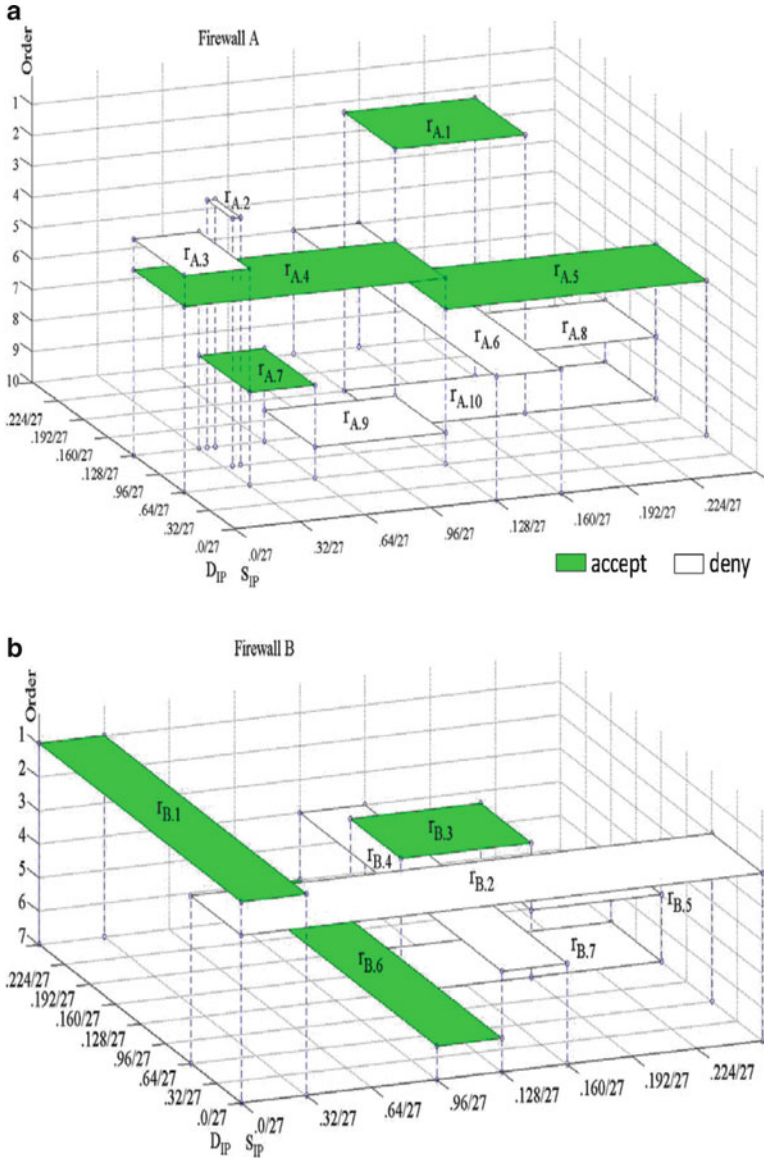
Fig. 3 3-dimensional service flow space

specific inter-ACL/inter-firewall anomalies will accompany. For example, for the region M_1 in Fig. 4, the filtering action of firewall A is to deny the traffic, but it is to accept the traffic for firewall B while the rule $r_{A.3}$ (the third rule of firewall A) and the rule $r_{B.1}$ (the first rule of firewall B) make an inter-ACL shadowing anomaly. Still, for rule $r_{A.4}$, although its IP address space also falls in M_1, its filtering effect on
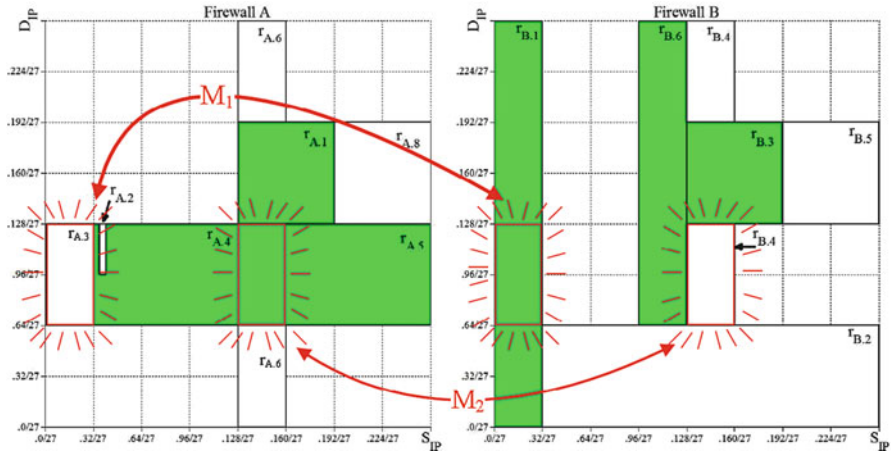
Fig. 4 Two conflicting filtering regions

M_1 can be neglected due to its lower priority in firewall A. It also means that network managers can ignore the inter-ACL generalization anomaly generated by $r_{A.4}$ and $r_{A.3}$. The same holds true for the case of region M_2. In the same fashion, rules $r_{A.5}$ and $r_{B.4}$ are the significantly effective rules for these two firewalls and also built the region M_2 with an inter-ACL correlation anomaly in which the <action> of $r_{A.5}$ is accept but $r_{B.4}$ is deny. In spite of the occurrence of another inter-ACL redundancy anomaly between $r_{A.6}$ and $r_{B.4}$ for region M_2, $r_{A.6}$ has a lower order than $r_{A.5}$ and will be not affect the M_2 at all. Thus, its effect is overlooked. Thus, in the above manner, we can effectively filter out the rule anomalies truly causing firewall behavior mismatching.

4 System Implementation and Future Work

Figure 5 shows the rule anomalies inferred by our developed diagnosis system with a well-designed GUI while those rule anomalies causing behavior mismatching are listed and indicated on Fig. 5b. In the near future, a 3D behavior mismatching diagnosis system will be developed and network managers can use it to make recommendations directly on the 3D visualized GUI by simply changing the shape of the problematic objects, regions, or icons. Additionally, we will also go deeper in exploration on the filtering effect relationships among multiple firewalls to let our developed system be more suited for the real challenges.
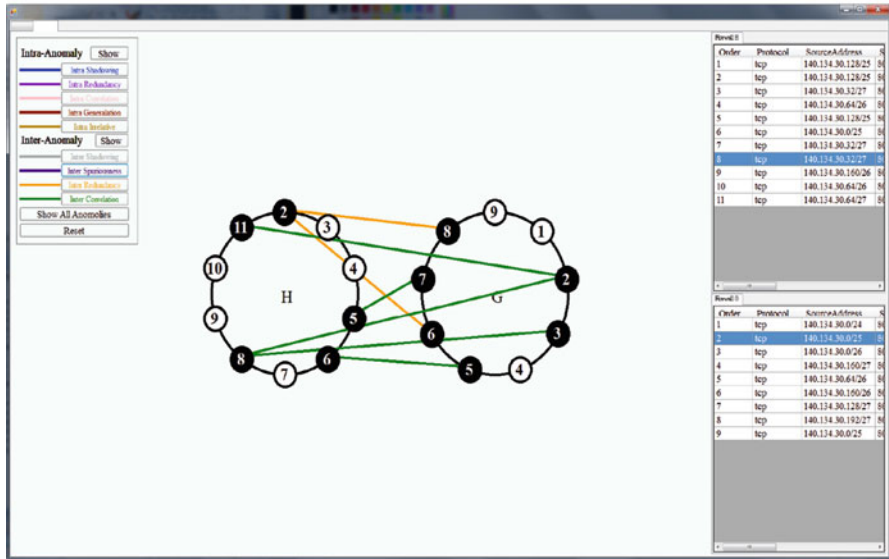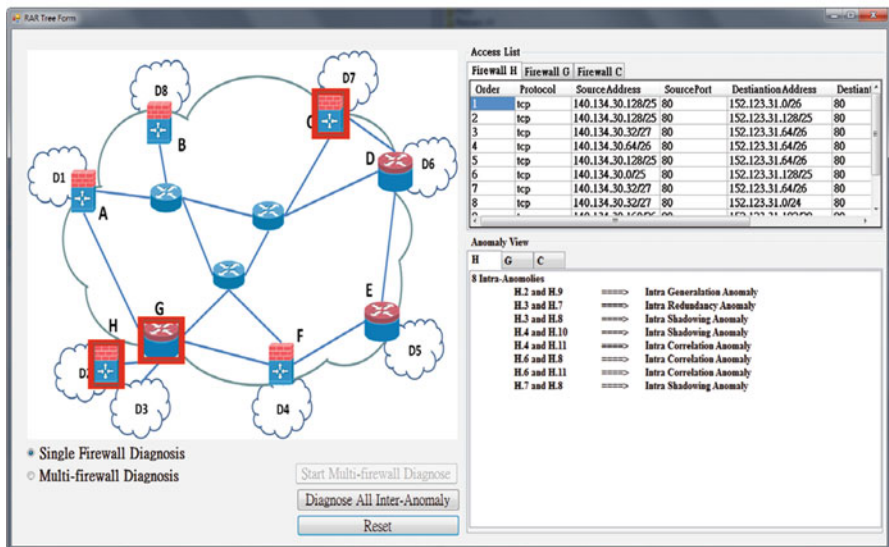
Fig. 5 Diagnosis results for (**a**) rule anomalies and (**b**) behavior mismatching

References

1. Hari B, Suri S, Parulkar G (2000) Detecting and resolving packet filter conflicts. Proc IEEE INFOCOM 3:1203–1212
2. Al-Shaer E, Hamed H (2004) Discovery of policy anomalies in distributed firewalls. In: Proceedings of the 23rd annual joint conference of the IEEE Computer and Communications Societies, vol 4, pp 2605–2616
3. Al-Shaer E, Hamed H (2003) Firewall policy advisor for anomaly discovery and rule editing, In: Proceedings of the 8th international symposium on integrated network management, pp 17–30
4. Al-Shaer E, Hamed H, Boutaba R, Hasan M (2005) Conflict classification and analysis of distributed firewall policies. IEEE J Selected Areas Commun 23(10):2069–2084
5. Al-Shaer E (2004) Managing firewall and network-edge security policies. In: Proceedings of network operations and management symposium, vol 1, pp 926–932
6. Yin Y, Katayama Y, Takahashi N (2008) Detection of conflicts caused by a combinations of filters based on spatial relationships. J Inf Process Soc Jpn 49:3121–3135
7. Thanasegaran S, Yin Y, Tateiwa Y, Katayama Y, Takahashi N (2009) Topological approach to detect conflicts in firewall policies. In: International workshop on security in systems and networks, proceedings of the of 23rd IEEE international parallel and distributed processing symposium, SSN-1569173665-paper-3.pdf
8. Yin Y, Bhuvaneswaran RS, Katayama Y, Takahashi N (2005) Implementation of packet filter configurations anomaly detection system with SIERRA. In: International conference on information, communication and signal processing, *LNC*S 3783, pp 467–480
9. Chao CS, Liu AC (2006) An internet firewall policy verification system. In: Proceedings of the 9th Asia-Pacific network operations and management symposium, Poster session 1, No. 4, Sept 2006
10. Chao CS (2007) An internet firewall policy validation system. In: Proceedings of the 10th Asia-Pacific network operations and management symposium, Oct 2007, pp 364–374
11. Liu A, Gouda MG (2008) Diverse firewall design. IEEE Trans Parallel Distrib Syst 19(9):1237–1251
12. Liu A (2009) Firewall policy verification and troubleshooting. Comput Netw 53(16):2800–2809

A Secure Routing Protocol to Prevent Cooperative Black Hole Attack in MANET

Nai-Wei Lo and Fang-Ling Liu

Abstract As a mobile ad hoc network (MANET) is dynamically formed by wireless mobile devices, which generally have limited computing resources, low network bandwidth accessibility, and limited power supply, and does not have any physical infrastructure and central base station, network management and operations are done cooperatively by all mobile devices in the network. In consequence, malicious mobile devices can easily join a MANET and launch attacks. Among those attacks, cooperative black hole attack requiring at least two malicious device nodes is a serious security threat since this attack is very easy to launch and hard to detect by other nodes. In this study, we introduce a secure routing protocol to defend against the cooperative black hole attack. Simulation experiments using QualNet has shown that our protocol provides up to 2.6 times performance in terms of the packet delivery ratio when comparing with AODV protocol under cooperative black hole attack.

Keywords Mobile ad hoc network • Cooperative black hole attack • Secure routing protocol

1 Introduction

Mobile ad hoc network (MANET) is dynamically formed by a set of mobile devices through their wireless communication capability. Therefore, MANET does not have physical infrastructure and central base station. Network topology will change any time due to dynamic movement of mobile devices and the wireless signal roaming range of each mobile device. Network management is dependent on the

N.-W. Lo (✉) • F.-L. Liu
Department of Information Management, National Taiwan University
of Science and Technology, Taipei 106, Taiwan
e-mail: nwlo@cs.ntust.edu.tw

cooperation among mobile nodes. In addition, the average life time of MANET is relatively short in comparison with wired network because mobile devices equip limited computing resources and battery power in general.

With increasing deployment and usage on military operations, enterprise meeting rooms, home networking, and vehicular traffic management systems, MANET security has become an important issue. Since network management and operations in MANET are dependent on cooperation of all mobile nodes, it is very easy for a MANET to encounter security threats and various attacks [1]. Malicious mobile devices can easily join a MANET and launch attacks. Among those attacks, cooperative black hole attack is a serious security threat since this attack is very easy to launch and hard to detect by other nodes [2]. To launch a cooperative black hole attack requires at least two malicious device nodes existing in the same MANET.

Since mobile devices have limited power supply, routing protocols used for MANET have to reduce energy consumption while establishing and maintaining packet (message) routes. From previous literature [3], it is shown that proactive protocols such as optimized link state routing protocol (OLSR) consume more energy than reactive protocols such as ad hoc on-demand distance vector protocol (AODV) [4] and dynamic source routing protocol (DSR) in general. In addition, regarding the two most dominant reactive routing protocols, AODV and DSR, AODV is more efficient and effective in comparison with DSR in general MANET environments [5]. Therefore, our study on cooperative black hole attack assumes AODV protocol is utilized in MANET.

Black hole attack is the simple version of cooperative black hole attack. When there is only one malicious node in MANET, this adversary can launch black hole attack by forging and replying the shortest packet transmission path, which will route through the malicious node itself, to the source node which is sending RREQ routing request control packets to establish a route for its destination. Once the source node selects the forged route and starts to use it as the delivering route for its data packets, the malicious node will deliberately drop all received data packets from the source node. In consequence, all data packets transmitted from the source node are vanished or absorbed by "a black hole" (the malicious node) and the destination node will never receive any data packet through the forged route. To defend against black hole attack, various mechanisms and protocols have been developed based on AODV [6–9]. In [6], three rules are set in each source node to assess plausibility of replied routes and select the target route. In [7], MOSAODV mechanism is proposed. Within MOSAODV, each source node will set a timer to collect all replied RREP packets and then discard those RREP packets with exceptionally high destination sequence numbers. In addition, the names of all identified malicious nodes will be stored in a blacklist table in each node. In [8], SAODV mechanism is introduced. Within SAODV, a source node collects routing information of its neighbors to determine which replied route it should select. Basically, the source node will select one of the replied routes in which all routes contain the same routing node as next hop, and the total number of these routes is the largest one compared to other possible routes. In [9], DPRAODV mechanism is introduced. In DPRAODV scheme, a threshold of valid RREP sequence number

is dynamically derived to evaluate the sequence numbers of received RREP packets for each wireless communication request process.

The attack model of cooperative black hole attack is the same as black hole attack. However, at least two malicious nodes are required to work together and launch a cooperative black hole attack. The two (or more) malicious nodes need to establish direct wireless communication link (hop) in advance. We refer the malicious node which is near the source node in terms of wireless connection path as the first malicious node. The other malicious node indicates as the second malicious node. The first malicious node tries to establish wireless communication route with the source node during the first step of cooperative black hole attack. Once the communication route passing through the first and second malicious nodes between the source node and the destination node is established, data packets will send through this route and reach the first malicious node. Then the first malicious node will forward the received data packets to the second malicious node along with their direct connected wireless link. Finally, the second malicious node drops the received data packets and successfully fulfills the cooperative black hole attack. As the first malicious node establishes data transmission route and the second malicious node drops transmitted data packets, it is more difficult to defend against cooperative black hole attack.

Several solutions have been proposed to defend against cooperative black hole attack in recent years [10–12]. In [10], Ramaswamy et al. proposed a solution to defend against cooperative black hole attack. A table containing data routing information (DRI) and a corresponding cross-checking method are installed at each mobile node. Each node observes its neighboring nodes and records whether its neighbors transmitting data packets to next corresponding nodes. All observed results are recorded in the DRI table, and each node determines which neighbors are not reliable based on its DRI table. Weerasinghe and Fu in [11] proposed an enhanced solution to identify and isolate nodes that invoke cooperative black hole attack using mechanisms proposed in [10] plus the usage of two new control packets: further request (FREQ) and further reply (FREP). In [12], Tamilselvan and Sankaranarayanan introduced a new concept called fidelity level to indicate the reliability of an observing node. A detection mechanism for cooperative black hole attack is developed by introducing a fidelity table into each node. An observing node with its fidelity level value 0 is considered as a malicious node, and all possible routing paths through this node will be eliminated by the observer (a mobile node). As the detection mechanism in [12] is derived based on AODV routing protocol, this mechanism will select a candidate route through a neighbor node with higher fidelity level for the observer if two RREP packets from different routing paths are received by the observer at the same time. In addition, the observer will broadcast the names of identified malicious nodes through ALARM control packets to other nodes in MANET.

In this study, we observed that previously proposed solutions require a lot of communications among nodes in MANET to observe neighboring nodes, identify malicious nodes, and broadcast the blacklist of detected malicious nodes. In consequence, control overhead can be very heavy. In addition, malicious nodes

may intentionally broadcast false blacklist to all nodes in MANET and easily paralyze the entire network. Therefore, we propose a new mechanism to resolve cooperative black hole attack without using blacklist or constant message (control packet) exchange.

2   The Proposed Detection Mechanism

For simplicity on detection mechanism description, we depict our detection methodology based on AODV routing protocol. The proposed detection mechanism is abbreviated as CBDAODV to indicate the full name of cooperative black hole attack detection mechanism based on AODV. We also define our attack model as follows. To form a cooperative black hole attack group, at least two malicious nodes can communicate to each other through one hop distance. For an attack group with two malicious nodes, either both nodes drop data packets or only the last (second) node drops data packets. Every node has its own blacklist but not broadcasts its blacklist to other nodes.

In a cooperative black hole attack, the first malicious node in the attack group will send out RREP control packets back to the source node who broadcasted RREQ connection requests. To increase the possibility that the RREP sent by the first malicious node is the earliest one to arrive at the source node, the best location for the first adversary is to become a neighboring node of the source node. In general, the false routing path replied by the first malicious node will pass through the first adversary and then reach to the second malicious node. Moreover, the second adversary does not actually have routes connecting to the destination node. Based on this observation, the concept of CBDAODV is developed. In CBDAODV, a source node will accept at least two RREP packets from different replying nodes; therefore, the source node knows two routes to reach the destination. By utilizing another routing path to verify the reliability of selected routing path, the source node itself can evaluate the currently selected routing path and make rerouting decision once it suspects the reliability of currently selected route. A confirmation control packet is invented by CBDAODV for the source node to send through another route, presumably a slower one than the selected one, to the destination node. The confirmation packet contains the name of the second malicious node which is observed and recorded by the source node when the first malicious node sends corresponding data packets to the second malicious node. Once receiving the confirmation packet, the destination node will reply it to indicate whether there exists a route between the destination node and the second malicious node. If the confirmation reply packet indicates there is no route between the destination node and the second malicious node, then the source node will know the second malicious node is a malicious node and it is executing a black hole attack. The source node now switches its routing path to another one and retransmits its data packets. At the same time, the source node will put the first malicious node into observation; if this malicious node regularly uses the second malicious node as its

next hop destination for all upcoming routing paths requested by the source node, then the source node can identify the first malicious node is belonging to the cooperative black hole attack group.

3 Simulation Results and Analysis

To evaluate the proposed CBDAODV mechanism, a set of simulation experiments are conducted by developing CBDAODV algorithm on QualNet 5.0 simulator. The simulated terrain area for a MANET is 800 m × 800 m, and there are 25 mobile nodes dynamically moving around for 600 s of simulation time. Two out of 25 nodes are defined as malicious nodes when necessary. The random waypoint model is used to model node mobility. The moving speed of each node is between 10 and 60 m/s. Packets transmitted among nodes are generated in constant bit rate (CBR). For each node, the pause time for change of moving speed and direction is 10 s. The wireless transmission range for a node is defined as 250 m. The size of data packet is 512 bytes. Regular AODV protocol without encountering cooperative black hole attack (AODV), AODV protocol with the occurrence of cooperative black hole attack (blackholeAODV), and AODV protocol implemented with our detection mechanism (CBDAODV) are compared in terms of packet delivery ratio and average end-to-end delay. From Fig. 1, when AODV is under cooperative black hole attack, the packet delivery ratio only has 20–40 %. With CBDAODV installed, the packet delivery ratio maintains at 70–80 % while suffering from the attack. That is, the CBDAODV mechanism effectively defends against cooperative black hole attack and provides up to 2.6 times packet delivery ratio in comparison with AODV without implementing any defense mechanism. In Fig. 2, CBDAODV has a slightly higher average end-to-end delay than regular
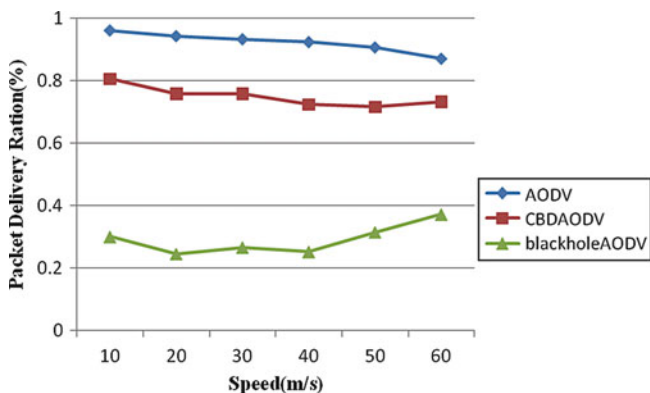
Fig. 1 Comparison on packet delivery ratio among three protocol conditions
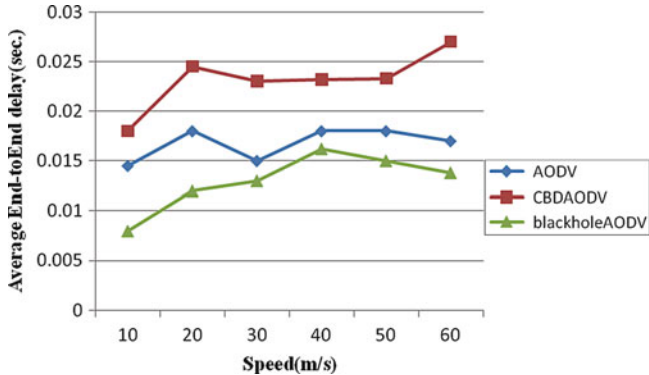
Fig. 2 Comparison on average end-to-end delay among three protocol conditions

AODV and AODV under the attack. This is because the nodes with CBDAODV wait for the second arriving RREP packet from different nodes to get the second routing path before sending data packets through the first selected routing path.

4 Conclusion

In this study, an effective detection mechanism for cooperative black hole attack is developed. This mechanism provides up to 2.6 times performance in terms of the packet delivery ratio when comparing with AODV protocol under cooperative black hole attack. In addition, no alarm packets broadcast or blacklist broadcast is required in our solution when malicious nodes were identified.

References

1. Deng H, Li W, Agrawal DP (2002) Routing security in wireless ad hoc networks. IEEE Commun Mag 40(10):70–75
2. Abusalah L, Khokhar A, Guizani M (2008) A survey of secure mobile ad hoc routing protocols. IEEE Commun Surv Tutor 10(4):78–93
3. Mbarushimana C, Shahrabi A (2007) Comparative study of reactive and proactive routing protocols performance in mobile ad hoc networks. In: 21st international conference on advanced information networking and applications workshops/symposia, IEEE Press, New York, pp 679–684
4. Perkins CE, Belding-Royer E, Das S (2003) Ad hoc on-demand distance vector (AODV) routing. The Internet Engineering Task Force (IETF) RFC 3561

5. Khatri P, Rajput M, Shastri A, Solanki K (2010) Performance study of ad-hoc reactive routing protocols. J Comput Sci 6(10):1159–1163
6. Medadian M, Yektaie MH, Rahmani AM (2009) Combat with black hole attack in AODV routing protocol in MANET. In: First asian himalayas international conference on internet, IEEE Press, New York, pp 1–5
7. Mistry NH, Jinwala DC, Zaveri MA (2009) MOSAODV: solution to secure AODV against blackhole attack. Int J Comput Netw Secur 1(3):42–45
8. Tamilselvan L, Sankaranarayanan V (2007) Prevention of blackhole attack in MANET. In: The 2nd international conference on wireless broadband and ultra wideband communications, IEEE Press, New York, pp 21–26
9. Raj PN, Swadas PB (2009) DPRAODV: a dynamic learning system against blackhole attack in AODV based MANET. IJCSI Int J Comput Sci Issues 2:54–59
10. Ramaswamy S, Fu H, Sreekantaradhya M, Dixon J, Nygard K (2003) Prevention of cooperative black hole attack in wireless ad hoc networks. In: The 2003 international conference on wireless networks, CSREA Press, Las Vegas, pp 570–575
11. Weerasinghe H, Fu H (2007) Preventing cooperative black hole attacks in mobile Ad Hoc networks: simulation implementation and evaluation. In: Future generation communication and networking. IEEE Press, New York, pp 362–367
12. Tamilselvan L, Sankaranarayanan V (2008) Prevention of cooperative black hole attack in MANET. J Netw 3(5):13–20

IP Address Management in Virtualized Cloud Environments

Chen-Hao Ku, Kuan-Ching Li, Ching-Hsien Hsu, Kuan-Chou Lai, Meng-Yen Hsieh, Tien-Hsiung Weng, and Hai Jiang

Abstract The ability to deploy resources and services in cloud computing utilizing virtualization technologies in a timely and cost-effective manner is important, bringing with it significant economical gain and business performance, yet accelerating the pace of innovation. Services in cloud platforms are scheduled and executed in optimized and on-demand resources, taking into consideration flexibility and scalability. Due to the existing limitation on the quantity of allocated IPv4 IP addresses, a number of alternatives have been discussed. In this chapter, we propose a novel yet low-overhead method for cloud service providers based on the concept of Infrastructure as a Service (IaaS) framework and network virtualization. The idea behind the design is to respond quickly to the infrastructure needs for the creation of virtual machines (VMs) that meet the capacity requirements of those cloud services as requested by users. It improves the utilization of providers' resources within this infrastructure as heterogeneous hardware resources are aggregated to the existing platform on demand. Testing on the prototype built demonstrates its effectiveness and performance.

Keywords Cloud computing • Virtual machine • IP address • Management

C.-H. Ku • K.-C. Li (✉) • M.-Y. Hsieh • T.-H. Weng
Department of Computer Science and Information Engineering, Providence University,
Providence, Taiwan
e-mail: kuancli@pu.edu.tw

C.-H. Hsu
Department of Computer Science and Information Engineering, Chung Hua University,
Hsinchu City, Taiwan

K.-C. Lai
Department of Computer and Information Science, National Taichung University,
Taichung, Taiwan

H. Jiang
Department of Computer Science, Arkansas State University, Jonesboro, AR, USA

1 Introduction

Most current cloud-computing systems are composed of large numbers of relatively inexpensive computers, interconnected by standard routers and a large number of disk drives. Virtualization is a fundamental technique in cloud computing that dynamically assigns and reassigns physical and virtual resources according to the service needs on demand. Network virtualization, as one of the key enabling technologies for clouds, has attracted extensive attention [1]. With this inclusion, it is possible to use cloud services to increase the overall QoS by delivering optimized resources, on-demand utilization, flexibility, and scalability [2].

As ways to decrease troubleshooting in such cloud environments, there exist a number of techniques for deploying and managing computing systems with minimal human involvement. Moreover, with the impressive increasing number of services, the number of virtual machines (VMs) is increasing at the same pace. With the increasing number of cloud platforms and the possibility to have private clouds in large public clouds, IPv4 is insufficient to meet the global demand, even with the presence of IPv6. The popularization of this mechanism is still a major concern, as difficulties are faced. Although there are already several technologies that can be used to transfer IPv6 into IPv4, their effectiveness is unclear. There is an urgent need to address the major problem of expanding the use of the limited IPv4.

This chapter addresses the architectural issues of virtual IP address assignment and management in an open source-based cloud platform by proposing an architectural solution for cloud service providers based on the concept of Infrastructure as a Service (IaaS) framework and IP network virtualization. Developers and users can easily create a VM based on the needs of the service. In addition, they may access this VM through any mobile device or lightweight notebook through a provided link.

A number of associated techniques and schemes have also been designed and implemented as building blocks for the proposed work, including resource description and abstraction mechanisms, virtual network request method, and a resource broker mechanism, to be able to respond quickly to the infrastructure and service needs and to meet capacity requirements of the cloud services requested [3, 4].

The remainder of this chapter is organized as follows. Section 2 provides background knowledge of resource and network virtualization and the approach of system design to aggregate techniques for this proposed method. In Sect. 3, the mechanism designed is presented and described, with some discussions on its performance and advantages. Finally, some concluding remarks of this work are given in Sect. 4.

2 Related Work

Virtualization technology is a technique based on the use of software that "partitions" a single computer to act as if it were several independent computers, allowing the system to run several different operating systems at the same time.

It offers powerful resource management mechanisms that include live migration and suspend/resume [5, 6].

In terms of network in the cloud environments, IPv4 is insufficient to meet the global demand. Although there are already several technologies that can transfer and convert IPv4 into IPv6, the effect is not yet clear. Avoiding a bloated use of IPv4 is a major problem that requires an effective solution.

With a ClassB IP (physical IP) separation of 256 ClassC IP (virtual IP), effective control can be achieved by a combination of NAT and DHCP [1]. In response to the widely concerned current energy-saving concept, this study will be about using virtualization technology to help enable a host machine to support multiple VMs. The research objectives of this chapter are focused on the cloud environment of IPv4 in distribution automation and are assigned to VM needs.

The ability to deploy new equipment and services in a timely and cost-effective manner – a quality known as network agility – is crucial to maintaining profitability. Bottlenecks that hinder deployment, reduce performance, or result in downtime add cost to every operation. As a result, organizations can only be as agile as their IP infrastructure can support. For example, managing thousands of IP addresses by hand creates bottlenecks during provisioning and troubleshooting as well as increases the possibility of service outages caused by human error [7].

3   Proposed Mechanism

In order to serve several users simultaneously in a model that dynamically assigns and reassigns virtual resources according to these consumers' needs by temporal demand, schemes have been designed as building blocks in the proposed method, including resource description and virtual network request mechanisms. The proposed method is able to respond quickly to the infrastructure needs for those cloud services through a real-time-based graphical interface. It improves the utilization of providers' resources, which allows the trading of IP network resources between infrastructure and services, an important and complementary innovation within the cloud landscape.

3.1   Environment Settings

In order to operate in a stable computing environment, we have made use of one 1U server containing two network interface cards (NICs) serving as a router. One of these NICs interconnects with the outside Internet, while the second card contains the functionality of a virtual switch. In the proposed environment, we have used a Ubuntu Linux 10.04 LTS server as the underlying system, enabling also the NAT and DHCP services in this environment. In addition, KVM and QEMU have also been installed in order to produce a reliable virtualization environment.
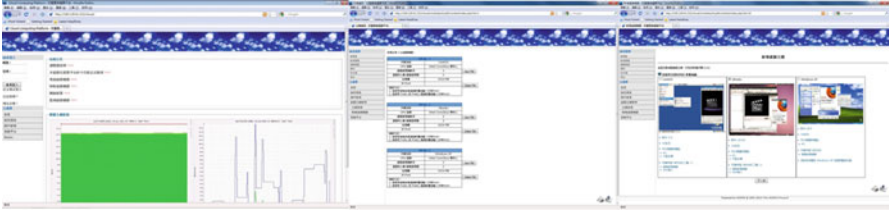
Fig. 1 Graphical user interface coupled with the proposed method

The proposed system with the implementation of a graphical interface is used to provide an easy alternative to users to specify virtual resources they plan to have in VMs being designed, as depicted in Fig. 1, such as the type of processor and number of cores, amount of memory, amount of storage, and finally the operating system. The 1U server used in our experiments is an IBM system x3550 M2, and its configuration includes 16 cores (2 CPUs/4 cores HT), 16 GB DDR3 memory, and 2 TB network storage systems.

3.2 Network Configuration

In the proposed method, each VM owns a particular configuration file, which records configuration information about this VM, including number of cores, amount of memory, and NIC information. The hypervisor will read the content of these files to emulate each one of the VMs. According to each of these files, as the number of cores or processors and amount of memory are configured by users, the virtual NIC is automatically assigned and configured by the proposed method.

3.2.1 Network Environment Configuration and Settings

Some steps to configure the 1U server were performed as follows:

– Rules to allocate a virtual IP: the system administrator needs to create in advance a virtual IP allocation file, containing VMAC, virtual IP, and port number.
– Creation of virtual network environment: a virtual switch needs to be created first, so that VMs can be added or removed from the virtual network area at anytime. Moreover, it helps dispatch the DHCP server and wait for VMs to request a virtual IP.

3.2.2 VM Deployment and Configuration

The following steps should be implemented during VM deployment and configuration processes:

– Check the virtual IP configuration file in the server in order to verify and avoid returning a VMAC not previously allocated. In an assignment case, this VMAC is marked as used and will not be assigned to other VMs coming in to be checked after the one that has just been checked.
– The configuration file generated upon creation of a VM records all virtual resource information, such as number of cores, amount of memory, and network interface, among others.
– Define transfer rules for packets to VM which include rules for firewall configuration that is resident in physical machines.
– The hypervisor will follow the configuration file of the VM to start this execution. At the same time, the virtual NIC and virtual switch will get interconnected.
– During the process of initialization of the VM, the DHCP client side is activated, sending also IP request packets to the physical server. As soon as such packets are received by the physical server's DHCP server and based on the VM's VMAC, such a virtual IP is set up in the VM.
– Once such a virtual IP is correctly assigned, users can make use of the remote connection mode to use such a VM created and its defined functions.
– At periodically defined intervals, the system checks the VM and the corresponding virtual IP for their connectivity activities. The system's cleanups such as the VM's firewall will remove and delete this virtual IP in the IP configuration file and unmark it as being available in the virtual IP address.

3.3 Network Architecture

As a cloud-computing environment is constructed and some VMs have been created and are in use, through the directives to the Linux operating systems' IPtable to configure a physical machine and VM packet transfer rule, the following connections are possible for any two VMs in the system, whether they are in the same network range or not, or a connection of a VM to the Web.

– Case 1: Inside the same network range, through a bridge, such a connection is feasible.
– Case 2: VMs with virtual IPs in different network ranges can make a connection feasible through a bridge and routing directed by servers.
– Case 3: Through a bridge and directed routing path, a VM can be connected to the Internet, as depicted in Fig. 2.

In a design which contains more than two physical servers, it is needed to configure the static routing table or, alternatively, to install the exiting routing software to provide such a dynamic routing service.
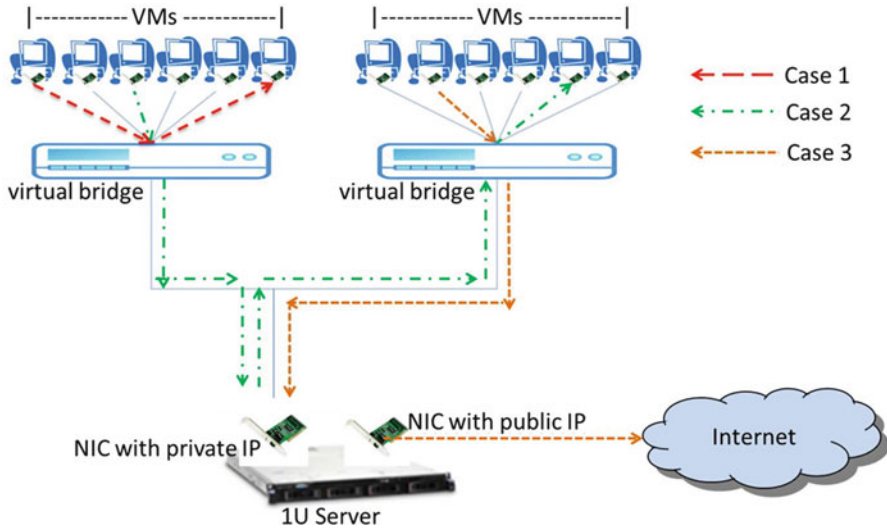
Fig. 2 Cloud environment routing schemes

4 Conclusions

With the number of cloud-computing environments being added each day, in parallel with the utilization of virtualization technologies to increase the usage of resources, the demand for available IPs is increasing, surpassing the total number of available ones. In this chapter, we propose an efficient method that manages the assignment of private IPs as virtual resources are created and returned to the management system if they are not used. With the automatic and efficient management of virtual IPs to VMs, we equip such a proposed system with a graphical interface in order to ease the creation and removal process of VMs, and diminish the drawbacks involved in the mentioned processes, by assigning and returning virtual IPs on a real-time basis.

From experimental results, the proposed method is satisfactorily efficient and available in most Linux-based systems. As for future work, this proposed method can be implemented in other Linux-based cloud environments, owned by VM hosting, universities and service centers, and also in applied science and engineering research projects distributed across different regions, as illustrated by Jacob et al. [8]. Moreover, issues in an autonomic system such as self-management, self-tuning, and self-configuration shall be considered and implemented to adapt its behavior and suit the context of use through appropriate methods that increase fault tolerance in cloud systems.

References

1. Antos D, Matyska L, Holub P, Sitera J (2009) VirtCloud: virtual network for user-controlled virtual clusters. Cesnet technical report 1/2009
2. Nagarajan AB, Mueller F, Engelmann C, Scott SL (2007) Proactive fault tolerance for HPC with Xen virtualization. In: ICS'2007. ACM, New York
3. Shin D, Wang Y, Claycomb W (2012) A policy-based decentralized authorization management framework for cloud computing. In: Proceeding of SAC'12 the 27th annual ACM symposium on applied computing. ACM, New York, pp 465–470
4. Li K-C, Weng T-H (2009) Performance-based parallel application toolkit for high-performance clusters. J Supercomput 48(1):43–65
5. Grit L, Irwin D, Yumerefendi A, Chase J (2006) Virtual machine hosting for networked clusters: building the foundations for 'autonomic' orchestration. In: Proceedings of the VTDC'06 international workshop on virtualization technologies in distributed computing. IEE Computer Society, Washington, DC
6. Hsu C-H, Chen S-C, Lee C-C, Chang H-Y, Lai K-C, Li K-C, Rong C (2011) Energy-aware task consolidation technique for cloud computing. In: Proceedings of The 3rd Cloudcom'2011 I.E. international conference on cloud computing technology and science. IEE Computer Society, Washington, DC
7. Bauer E, Adams R (2012) Reliability and availability of cloud computing. Wiley, Hoboken
8. Jacob JC, Katz DS, Berriman GB, Good JC, Laity AC, Deelman E, Kesselman C, Singh G, Su M-H, Prince TA, Williams R (2009) Montage: a grid portal and software toolkit for science-grade astronomical image mosaicking. Int J Comput Sci Eng 4(2):73–87

Part II
Signal Processing

A Fuzzy C-Means Method for Determining Motor's Quality Types Based on Current Waveforms

Yun-Chi Yeh, Yi Chu, Che Wun Chiou, and Hong-Jhih Lin

Abstract This study proposes fuzzy C-means method (FCMM) to analyze motor's current waveforms for determining the motor's quality types. The idea of the FCMM is to partition N input sampled vectors into c clusters by minimizing the objective function. The objective function is the sum of the squared Euclidean distances between each input sampled vectors and its corresponding cluster center, with the distances weighted by the fuzzy memberships. The proposed FCMM consists of three following main stages: (i) the preprocessing stage for enlarging motor's current waveforms' amplitude and eliminating noises, (ii) the qualitative features stage for qualitative feature selection of a motor's current waveform, and (iii) the classification stage for determining motor's quality types using the FCM algorithm. In the experiment, the error rates are 5.42 and 0.28 % for type A and B, respectively. The right rates are 94.58 and 99.72 % for type C and D, respectively.

Keywords Fuzzy C-means • Motor's current waveforms • Euclidean distances

---

Y.-C. Yeh • Y. Chu (✉)
Department of Electronic Engineering, Chien Hsin University of Science
and Technology, Jhongli 320, Taiwan

Department of Electrical Engineering, National Central University, Jhongli 320, Taiwan
e-mail: yichu@uch.edu.tw

C.W. Chiou • H.-J. Lin
Department of Computer Science and Information Engineering, Chien Hsin University
of Science and Technology, Zhongli 320, Taiwan

Department of Electrical Engineering, National Central University, Jhongli 320, Taiwan

1   Introduction

This study proposes a simple, fast, and reliable method called the fuzzy C-means method (FCMM) to analyze current waveforms for recognizing whether the motor is good or not. The FCMM is the best known and most widely used fuzzy clustering technique and was originally developed by Dunn in 1973 [1] and then improved by Bezdek in 1981 [2]. Several researchers use the FCMM for cluster analysis. For example, Chen and Wang [3] proposed a FCMM-based fragile watermarking scheme for image authentication. Lin et al. [4] proposed FCMM for estimating myocardial ischemia with pulse waveform analysis.

2   The Qualitative Features Stage

The features in the motor's current waveform are the location, duration, amplitudes, and shapes of the waves. These features can be recognized by the experienced operators for recognizing whether the motor is good or not. If it is defect, kind of defect is also determined. Table 1 and Fig. 1a list ten important test points of the motor's current waveform. Table 2 and Fig. 1b list six qualitative features based on many experiments; we judiciously chose the following values as features, which would be shown to be very effective by practical testing results. According to Table 2, classifier design for determining five kinds of defective motors is described as the following (see Fig. 2).

3   The Classification Stage: Fuzzy C-Means (FCM)

The idea of the FCM is to partition N sampled vectors into c clusters by minimizing the following objective function:

Table 1 Definition of the ten test points of the motor's current waveform

Test point serial no.	Test point description
1	The commuted point (up) of each cycle
2	The commuted point (down) of each cycle
3	The maximum value point of waveform 1 of each cycle
4	The minimum value point of waveform 1 of each cycle
5	The maximum value point of waveform 2 of each cycle
6	The minimum value point of waveform 2 of each cycle
7	The second point after the point 1
8	The second point after the point 5
9	The third point before the point 6
10	The third point after the point 6
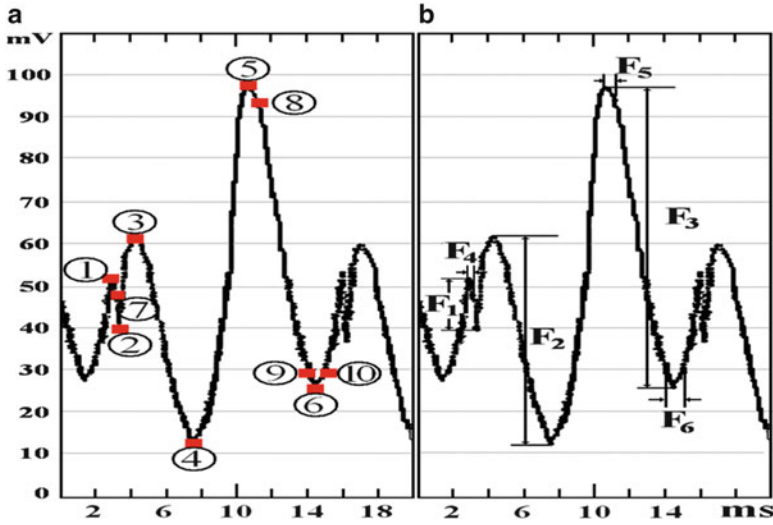
Fig. 1 The good motor's current waveform: (**a**) ten important test points of the current waveform; (**b**) six qualitative features (F1–F6)

Table 2 Definition of the six qualitative features

Feature's serial no.	Feature's symbol	Feature description	Units
F_1	$H_{1,\,2}$	The amplitude between point 1 and point 2 in Fig. 1b	mV
F_2	$H_{3,\,4}$	The amplitude between point 3 and point 4 in Fig. 1b	mV
F_3	$H_{5,\,6}$	The amplitude between point 5 and point 6 in Fig. 1b	mV
F_4	$T_{1,\,7}$	The time duration between point 1 and point 7 in Fig. 1b	ms
F_5	$T_{5,\,8}$	The time duration between point 5 and point 8 in Fig. 1b	ms
F_6	$T_{9,\,10}$	The time duration between point 9 and point 10 in Fig. 1b	ms
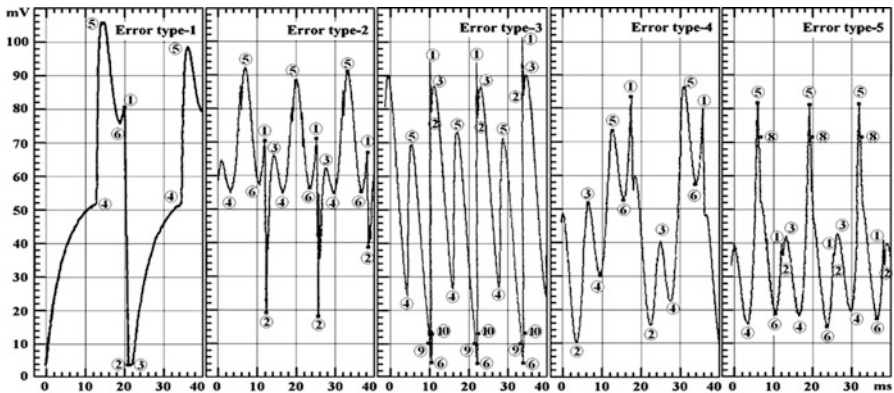
Fig. 2 The motor's current waveform for each quality type

$$J(X, U, V) = \sum_{i=1}^{c} \sum_{k=1}^{N} (u_{i,k})^m (d_{i,k})^2, \tag{1}$$

where $m\,(1 < m < \infty)$ is the weighting exponent which determines the fuzziness of the cluster and $d_{i,k}$ is the Euclidean distance between each measured data point X_k (p-dimensional) and its corresponding cluster center i. The Euclidean distance $d_{i,k}$ is calculated by the following equation:

$$d_{i,k} = \left[\sum_{j=1}^{p} \left| X_{k,j} - v_{i,j} \right|^2 \right]^{1/2} \tag{2}$$

The cluster center matrix V is given by

$$v_i = \frac{\sum_{k=2}^{N} (u_{i,k})^m (x_k)}{\sum_{k=1}^{N} (u_{i,k})^m}; \ 1 \le i \le c \tag{3}$$

where $U = (u_{i,k})_{c \times N}$ is the partition matrix and $u_{i,k}$ is the degree of membership of X_k in the cluster i, and the membership values satisfy the following two conditions:

$$\left\{ \begin{array}{l} 0 \le u_{i,\,k} \le 1, \ \ 1 \le i \le c, \ \ 1 \le k \le N \\ \text{and} \\ \sum_{i=1}^{c} u_{i,\,k} = 1, \ \ \ 1 \le k \le N \end{array} \right\} \tag{4}$$

The objective function is the sum of the squared Euclidean distances between each input measured data and its corresponding cluster center, with the distances weighted by the fuzzy memberships.

Minimization of the objective function (MinObjectFun) is an iterative optimization algorithm which can be summarized as the following steps [3]:

Procedure-MinObjectFun:
Step 1: Set each sampled vector of X_k
  Let $X = \{X_1, X_2, \ldots, X_N\}$ be a set of given sampled vectors, and assume each sampled vector $X_k = \left[X_{k1} X_{k2}, \ldots X_{kp} \right]^T$ has p qualitative features, where $X_k \in X$ and N represents the total number of sampled vectors.
Step 2: Select the weighting exponent m and the termination threshold ε (where $1 < m < \infty$ and ε is the prespecified small number representing the smallest acceptable change in U).

Step 3: Set the counter t to 0 (i.e., $t \leftarrow 0$), and initialize the membership matrix $U^{(0)}$ (Eq. 5) with random values between 0 and 1 such that constraints in Eq. 4 are satisfied.

$$U^{(0)} = \left(u_{i,k}^{(0)}\right)_{c \times N} = \begin{bmatrix} u_{1,1}^{(0)} & u_{1,2}^{(0)} & u_{1,3}^{(0)} & \cdots & u_{1,N}^{(0)} \\ u_{2,1}^{(0)} & u_{2,2}^{(0)} & u_{2,3}^{(0)} & \cdots & u_{2,N}^{(0)} \\ u_{3,1}^{(0)} & u_{3,2}^{(0)} & u_{3,3}^{(0)} & \cdots & u_{3,N}^{(0)} \\ \vdots & \vdots & \vdots & \cdots & \vdots \\ u_{c,1}^{(0)} & u_{c,2}^{(0)} & u_{c,3}^{(0)} & \cdots & u_{c,N}^{(0)} \end{bmatrix} \tag{5}$$

where $1 \leq i \leq c$ and $1 \leq k \leq N$.

Step 4: $t \leftarrow t + 1$.

Step 5: Compute the cluster center matrix $V(t)$.

Let $v_j^{(t)}$ be the obtained cluster center of the class i through t iterations. Given $U^{(t-1)}$ one can calculate $V^{(t)}$ by the following equation:

$$v_i^{(t)} = \frac{\sum_{k=1}^{N} \left(u_{i,k}^{(t-1)}\right)^m (x_k)}{\sum_{k=1}^{N} \left(u_{i,k}^{(t-1)}\right)^m}; \ 1 \leq i \leq c \tag{6}$$

Step 6: Update the membership values $U^{(t)} = \left(u_{i,k}^{(t)}\right)_{c \times N}$ by the following equation:

$$u_{i,k}^{(t)} = \frac{\left[\frac{1}{\left\|X_k - v_i^{(t)}\right\|^2}\right]^{1/(m-1)}}{\sum_{q-1}^{C} \left[\frac{1}{\left\|X_k - v_q^{(t)}\right\|^2}\right]^{1/(m-1)}}; \ 1 \leq i \leq c, 1 \leq k \leq N \tag{7}$$

where $\left\|X_k - v^{(t)}\right\|^2$ is the Euclidean distance between each sampled vector X_k and its corresponding cluster center i.

Step 7: If $\left\|U^{(t)} - U^{(t-1)}\right\| < \varepsilon$, then go to Step 8, otherwise go to Step 4.

Step 8: Classification.

The test sample vector TSV_k is assigned to the motor's error type z if its final $u_{i,k}^{(t)}$ has the maximum value for all cluster i, that is,

$$z = \arg_i \left\{\text{Max}(u_{i,k}^{(t)}), i = 1, 2, \ldots, c\right\} \tag{8}$$

Figure 3 shows the block diagram of the purposed FCMM, which consists of three stages: (i) the preprocessing stage for enlarging motor's current waveforms' amplitude and eliminating noises, (ii) the qualitative features stage for qualitative feature selection of a motor's current waveform, and (iii) the classification stage for determining motor's quality types using the FCM (Procedure-MinObjectFun).
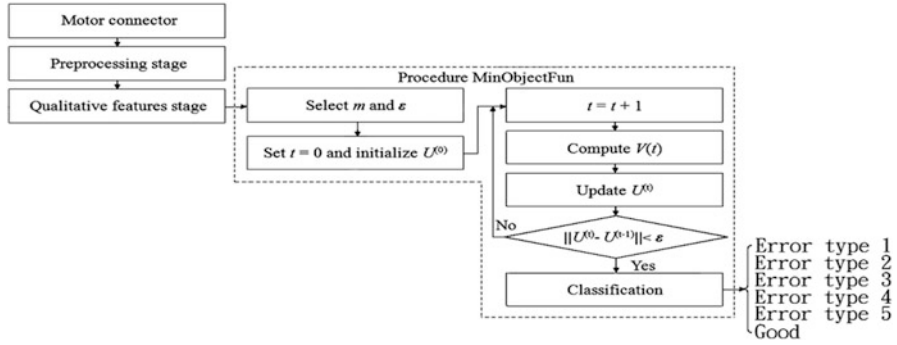
Fig. 3 The block diagram of the purposed FCMM

Table 3 The classified results of the experiment

Quality type	No. of test motors	Type A (error rate)	Type B (error rate)	Type C (right rate)	Type D (right rate)
Type-1	52	1	–	51	–
Type-2	26	2	–	24	–
Type-3	21	1	–	20	–
Type-4	32	3	–	29	–
Type-5	35	2	–	33	–
Good	29,834	–	82	–	29,752
Total	30,000	9	82	157	29,752
Rate	–	9/166 (= 5.42 %)	82/29,834 (= 0.28 %)	157/166 (= 94.58 %)	29,752/29,834 (= 99.72 %)

4   Evaluation

The experiment was performed to evaluate the performance of the proposed method. In the experiment, 30,000 motors are randomly selected as samples; 166 defective motors which have error type-1–5. The average processing time per motor is 0.5 s. The accuracy of classification is shown in Table 3. The error rates are 5.42 and 0.28 % for type A and B, respectively. The right rates are 94.58 and 99.72 % for type C and D, respectively. Where type A represents wrong judgment on defect motor to be determined as good, type B represents wrong judgment on good motor to be determined as defect, type C represents right judgment on defect motor to be determined as defect, and type D represents right judgment on good motor to be determined as good.

5 Conclusion

This study proposes a FCMM to analyze current waveform for determining the motor's quality types. The proposed method has the following advantages: (1) It can recognize good or defective motors as well as defect types in less than 0.5 s. (2) It has high good recognition performance, the error rates are 5.42 and 0.28 % for type *A* and *B*, respectively. The right rates are 94.58 and 99.72 % for type *C* and *D*, respectively. Where type *A* (*B*) represents wrong judgment on defect (good) motor to be determined as good (defect) and type *C* (*D*) represents right judgment on defect (good) motor to be determined as defect (good).

References

1. Dunn JC (1973) A fuzzy relative of the ISODATA process and its use in detecting compact well-separated clusters. J Cybern 3:32–57
2. Bezdek JC (1981) Pattern recognition with fuzzy objective function algorithms. Plenum Press, New York
3. Chen WC, Wang MS (2009) A fuzzy C-means clustering-based fragile watermarking scheme for image authentication. Expert Syst Appl 36:1300–1307
4. Lin SH, Chang KM, Tyan CC (2009) Fuzzy C-means clustering for myocardial ischemia estimation with pulse waveform analysis. Biomed Eng Appl Basis Commun 21:139–147

License Plate Recognition Based on Rough Set

Xin-Yan Cao and Chen-Ming Zhang

Abstract License plate recognition belongs to the field of computer vision and pattern recognition, and plays an important role in the field of intelligent transportation. The license plate location is a key technology in license plate recognition; the accuracy in the positioning of a license directly affects the accuracy of character segmentation and character recognition, and has a direct impact on the efficiency of the license plate recognition system. In this chapter, a plate positioning system is constructed based on the knowledge acquisition and knowledge reduction ability of a rough set, as well as the learning ability and generalization ability of a neural network,. By combining the rough set with neural networks and fuzzy logic, a rough fuzzy neural network recognition is proposed. The experimental results show that this system not only simplifies the structure of the system but also improves the generalization capability of knowledge, and improves the accuracy of character positioning.

Keywords Rough sets • License character recognition • Genetic methods • Neural network

---

X.-Y. Cao (✉)
School of Communication Engineering, Jilin University, Changchun,
Jilin 130022, China

College of Electronic and Information Engineering, Changchun University,
Changchun, Jilin 130022, China
e-mail: ccdxcaoxinyan@yahoo.com.cn

C.-M. Zhang
College of Electronic and Information Engineering, Changchun University,
Changchun, Jilin 130022, China

1 Introduction

The vehicle license plate recognition system is an important part of intelligent transportation systems. It is based on a computer vision system on vehicle licenses for a specific target and is one of the important research topics of computer vision and pattern recognition technology in the field of intelligent transportation applications. It can be widely used in automatic toll management systems of highways, bridges, tunnels, urban transport vehicle management, intelligent community, intelligent parking management, license plate validation, detection of stolen vehicle tracking, traffic statistics, and other fields; it has broad application prospects.

License plate location is finding the location of the vehicle license from the intake of car images and accurately segmenting the license plate from the region for use in character segmentation. Therefore, the determination of the license area is one of the important factors that affect system performance. The accuracy of license positioning directly affects the accuracy of character segmentation and character recognition, and has a direct impact on the efficiency of the license plate recognition system.

Vehicle images are collected from the natural environment in which the imaging conditions of the license plate and the background are generally not controlled, especially for lighting conditions and complex background information. This, coupled with the different shooting distances and angles, could result in significant difficulties to the target search. The plate area is very difficult to distinguish from the various interferences, and the special nature of the application requires that license plate location is completed quickly and accurately. So if there is no efficient search method, a lot of computing time and storage space will be consumed. License plate positioning technology has always been a difficult thing and is a key component of license plate recognition technology.

According to the different characteristics of the license plate, different positioning methods can be used. There are many ways of license plate positioning. The main license plate location methods are those based on edge detection and Hough transform [1], morphological processing and window searching [2], neural network [3], license plate of the scan line positioning, as well as the texture-based license plate location method [4]. This chapter combines rough set knowledge acquisition capability with neural network classification, and the study and implementation of an automatic positioning system for license plate images, and has a certain theoretical and practical value.

2 License Plate Image Acquisition

Before the previous license plate location, we must first obtain a license plate image. In the past, vehicle detection was mostly acquired by a pressure-sensitive coil embedded in a fixed location of the road. The disadvantages of this approach

are the complexity of the installation process, the device is easy to damage, there could be damage to the road surface, and it involves relatively high maintenance costs. With detection methods based on laser sensor and red sensor, human interference is relatively large. In comparison, the video-based road traffic monitoring system, which has a wide detection range, flexible installation, low maintenance costs, and easy application process, does not destroy the road surface, even though there are some defects, such as vulnerability to the impact of the external environment interference and low detection accuracy. With the continuous development of computer hardware and software technology, however, it has gradually become an emerging technology in detection of traffic parameters [5].

In dynamic vehicle license plate recognition, image acquisition and subsequent identification are closely linked in order to reflect the real time, without a long delay; otherwise, there is not much practical value. The sense coil and capture card, which is the core of the license plate collection system, consists of a lane before coil sensors, a capture controller, a CCD camera, a frame grabber, auxiliary lighting equipment, and industrial computer equipment. The lane before coil sensors uses the coil sensors to send signals to the capture controller, and the capture controller controls the vehicle images received by the image acquisition card and digitizes them into the computer in order to gain information on the license plate image.

3   License Plate Image Preprocessing

For these smudges and uneven illumination license plate images, image enhancement must be done to complete character segmentation. This chapter mainly conducts low-pass filtering and grayscale expansion treatment on these images [6]. We first make the segmented color car brand image gray, and then use Wiener filtering to remove noise from grayscale images, and, finally, we make the license clear through histogram equalization.

3.1   Grayscale Conversion

With the license plate image acquisition technology, the original images obtained are all colored. Colored images contain a large amount of color information, so they require large storage space, and this would mean spending a lot of system resources for processing, thus reducing the speed of system execution. So, we use grayscale images, with a 256 luminance value, to do colored image processing. The vehicle images captured by default are 24-bit true color images. First, the original image is transformed from RGB space to YCbCr space, and then only the Y component is extracted, thus generating grayscale images.

3.2   Wiener Filter

The image quality is reduced due to the interference of the license, so the image filtering denoising is necessary. This chapter adopts two-dimensional adaptive filtering, estimates according to the statistics of the local neighborhood of each image, and conducts pixel-adaptive Wiener filtering. The Wiener filter design steps are as follows:

Step 1: Digitizing samples on input signal $s(t)$
Step 2: Seeking the autocorrelation function of the input sample, thereby obtaining an estimate of $R_x(\tau)$
Step 3: Calculating the Fourier transform of $R_x(\tau)$ to obtain $P_x(s)$
Step 4: Digitizing a sample of the input signal in the case of no noise
Step 5: Obtaining the cross-correlation function of the signal samples and input samples, thereby estimating $R_{xs}(\tau)$
Step 6: Computing the Fourier transform of $R_{xs}(\tau)$ to draw the $P_{xs}(s)$
Step 7: Calculating the Wiener filter transfer function $H_0(s)$ with the formula

3.3   Grayscale Transformation Enhancement

Due to the limited brightness of the imaging system, there is often insufficient image contrast and the visual effect is poor, which will directly affect the subsequent processing of the image. The contrast can be enhanced by gradation transformation in order to improve the visual effect.

Grayscale Transformation. The gray transform method can enhance the grayscale range and enrich gray levels, so as to achieve the purpose of the enhanced image contrast. Using a linear single-valued function for the linear expansion on each of the pixels within the image will be effective to improve the visual effect of the image [7]. Let us consider the original image $f(x, y)$, where most of the pixels are within a relatively small range of gray levels. If we are interested on the gray level only in a certain range of the pixel, we set this grayscale range as $[a, b]$. After linear gradation transformation, the grayscale range $[a, b]$ can be extended to the image g (x, y) in a relatively large gradation range $[c, d]$, where the image after gradation conversion is $g(x, y)$, and $| d - c | > | b - a |$. The grayscale transformation relationship between $f(x, y)$ and $g(x, y)$ is formula (1):

$$g(x,y) = \begin{cases} c, & f(x,y) < a \\ \dfrac{d-c}{b-d}[f(x,y)-a]+c, & a \le f(x,y) < b \\ d, & f(x,y) \ge b \end{cases} \tag{1}$$

Histogram Equalization. If the grayscale images are concentrated in a narrow range causing the details to be fuzzy, in order to make the image details clear and some of

the objectives prominent for enhancing the image, we improve the ratio between the brightness of each part by implementing the histogram adjustment method. Setting the original total number of pixels as N, the histogram equalization calculation steps are as follows:

Step 1: List the original image gradation r_i, $i = 0,1, \ldots, L - 1$, where L is the number of the gray level.
Step 2: Define statistics of the gradation number of pixels $n(r_i)$, $i = 0,1, \ldots, L - 1$.
Step 3: Compute the respective gray level frequency of the original image histogram $P(r_i)$:

$$P(r_i) = \frac{n(r_i)}{N}, \quad i = 0, 1, \ldots, L - 1 \tag{2}$$

Step 4: Calculate for grayscale transformation function $T(r_i)$:

$$T(r_i) = \sum_{i=0}^{i} \frac{n(r_i)}{N}, \quad i = 0, 1, \ldots, L - 1 \tag{3}$$

Step 5: Calculate the gradation of the output image after mapping s_j:

$$s_j = \text{INT}[(s_{max} - s_{min})T(r_i) + s_{min} + 0.5], \quad i = 0, 1, \ldots, P - 1 \tag{4}$$

Step 6: Count each grayscale pixel number after statistical mapping $n(s_i)$
Step 7: Calculate the output image histogram $Q(r_i)$:

$$Q(r_i) = \frac{n(s_i)}{N}, \quad i = 0, 1, \ldots, P - 1 \tag{5}$$

Step 8: Use the r_i and s_i mapping relationship to adjust the gradation of the original image histogram, thus obtaining an approximately uniform output image distribution.

4 Plate Location Based on Rough Set and Neural Network

Given the computational complexity of the neural network and the long training time required, the learning process can be accelerated by using the rough set method to train data preprocessing, reducing the information table, eliminating redundant data input value, and decreasing input in the number of nodes and the right value, so that the learning time can be shortened. Using the knowledge of the rough set reduction capability for the training of data analysis in order to obtain an outline of the decision rules, and mapping these rules to the corresponding fuzzy

Fig. 1 RS-BP network model
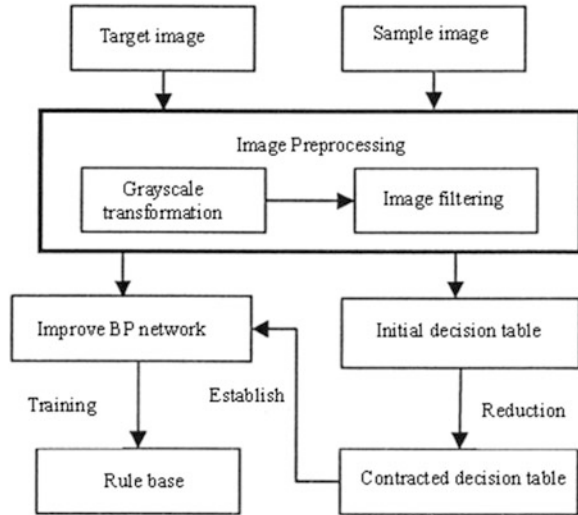
neural network model, or using the self-learning neural network and global approximation ability to optimize the rule parameters, may eventually solve the problem of optimal control rules [8]. The BP model is of great significance in every respect, and its application is very broad, but it also has some disadvantages. Therefore, it needs to be improved in order to locate the license plate more accurately and quickly. The rough set theory is introduced into the BP neural network, which will bring great improvement to the license plate positioning algorithm based on the neural network.

First, to improve the neural network appropriately, the output dynamic range generally needs enhancement, on the S-type compression function (0, 1), which is not necessarily superior. From the weight adjustment formula, we know that the changes in the value of the weights are also proportional to the output of the previous layer, and half of them tend to 0; this will cause a reduction in the amount of weight value adjusting or no adjusting, thereby lengthening the training time. To solve this problem, this chapter makes the output range of the S-type function become $(-1/2, 1/2)$. Experiments show that the improved activation function can significantly reduce the convergence time.

Although the rough set theory and BP neural network deal with the problem in two different ways, they have strong complementarity. Therefore, license plate positioning, which combines the two to deal with the technology of intelligent transportation systems in the complex environment, is of positive significance. This chapter presents a license plate positioning system based on rough sets and neural network theory; the model is shown in Fig. 1.

Target data and sample data after data cleaning, data discretization, and data reduction process in Fig. 1, in addition to the inconsistent and redundant data, trains the refined data as the target and sample data of the improved BP neural network and generates a control rule base. The rough set–neural network model of learning and testing processes is shown in Fig. 2.
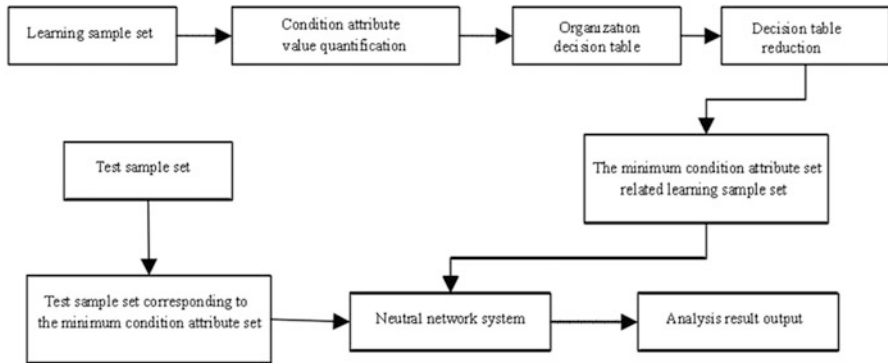
Fig. 2 Learning and testing processes of RS-BP

4.1 Neural Network Learning Algorithm

In this chapter, a dynamic adaptive network model is used, which is based on the nearest neighbor clustering algorithm. The algorithm is an online adaptive clustering linear algorithm and does not require a predetermined number of hidden layer units; the network obtained by clustering is optimal, and this algorithm is available through online learning. The specific process is as follows:

Step 1: Select an appropriate width of the Gaussian function r to define a vector A(l) used to store, which belongs to various types of output vectors, and a counter B (l) to count the number of various samples for statistics.

Step 2: From the start of the first data (x^1, y^1), establish a cluster center so $c_1 = x^1$, $A(l) = y^1$, $B(l) = 1$.

Step 3: Consider the second sample data (x^2, y^2), and make out the distance x^2 to c_1 of this cluster center: $| x^2 - c_1 |$.

If $|x^2 - c_1| \leq r$, c_1 is the nearest cluster of x^2, and make $A(l) = y^1 + y^2$, $B(l) = 2$.

If $|x^2 - c_1| > r$, and consider x^2 as a new cluster center, make $c_2 = x^2$, $A(2) = y^2, B(2) = 1$.

Step 4: If we consider the sample data k (x^k, y^k), $k = 3,4,\ldots,N$, there are m cluster centers, and its center is $c_1, c_2, \ldots, c_M$. Then make out the distance from x^k to m cluster centers, respectively: $| x^k - c_i |, i = 1,2,\ldots.M$.

If $|x^k - c_i| > r$, consider x^k as a new cluster center, make $c_{M+1} = x^k, M = M + 1$, $A(M) = y^k, B(M) = 1$.

If $|x^k - c_i| \leq r$, calculate as follows: $A(j) = A(j) + y^k, B(j) = B(j) + 1$. When $i \neq j, I = 1,2,\ldots,M$, maintain the value of A(i),B(i) as unchanged.

Step 5: According to the above established BP network, its output is

$$f(xk) = \frac{\sum_{i=1}^{M} w_i \exp\left(-\frac{|x^k - c_i|^2}{r^2}\right)}{\sum_{i=1}^{M} \exp\left(-\frac{|x^k - c_i|^2}{r^2}\right)} \tag{6}$$

4.2   License Plate Location

Based on the RS-BP model car license locator, which uses an M $\times$ N sliding window to traverse the preprocessed image pixel by pixel, producing data of the subimage within the window after normalizing the input to the neural network as the input vector, one can determine the location of the sliding windows either with a license plate if the neural network output is high, or otherwise without a license plate.

Sliding Window Selection. Based on the license plate characteristics, the sliding window should be a long strip, but not too large, or the neural network scale will be too large; the positioning accuracy is not high but at the same time it cannot be too small, or it will not be enough to make the network extraction license plate features achieve generalization.

Search Strategy. When using the sliding window traversal image, the search strategy should be paid attention to. No matter what the sliding window, there is a top-down or bottom-up traversal order. For the specific issues of license plate location, it should be said that the bottom-up traversal strategy is superior.

Image Normalization. The neutral network output must be normalized data. Therefore, the pretreated image should be normalized. The specific algorithm is formula (7):

$$\overline{f_d(x, y)} = \frac{f_d(x, y) - \min_{i,j} \{f_d(x, y)\}}{\max_{i,j} \{f_d(x, y)\} - \min_{i,j} \{f_d(x, y)\}} \tag{7}$$

License Plate Coarse Positioning. A normalized subimage is inputted to the neural network; if the output is high, it indicates that this region may have plates, and one must note down the coordinates of the upper left corner of this region as well as the neural network output values of this position. After the sliding window traverses the entire vehicle image, it may get some coordinates of the license plate image area, as well as the neural network output values. Remove the difference between the output value and a desired value in order to sort them. Mark the minimum

Table 1 Experimental results of license plate positioning

Collect environment	Total positioning	Accurate positioning	Positioning accuracy (%)
General situation	148	136	91.9
Rainy day or night	65	55	84.6
Comprehensive	213	191	89.4
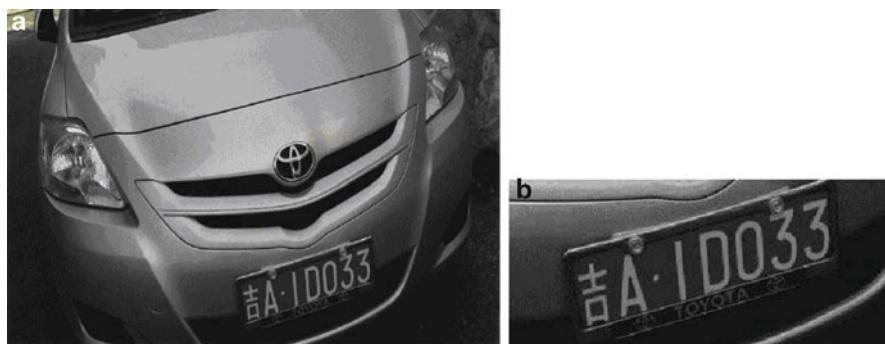
Fig. 3 License plate positioning result: (**a**) original car license image and (**b**) image after the positioning

coordinates of some locations for statistical processing, as this can determine the rough location.

Precise Positioning for License Plate. The exact coordinates of the license area location can be directly extracted from the original image using a threshold value.

4.3 Analysis on License Plate Positioning Results

With the help of the plate positioning system, we collected more than 100 sheets of vehicle images in a parking lot. The experimental test results on 213 vehicles containing license plate images are shown in Table 1.

Colored vehicle positioning input, through algorithm processing, and the final positioning of the license plate are shown in Fig. 3.

5 Conclusion

The automatic identification system of the license plate image is an important application of computer vision and pattern recognition technology in the field of intelligent transportation. The key technologies in the license plate recognition

system are vehicle location, character segmentation, and character recognition. License plate positioning is the premise and foundation of the last two steps, and has a direct impact on the processing effect of the last two steps. This chapter discussed the basic principles of a neural network and proposed the license plate positioning algorithm based on the combination of rough sets and neural networks. The experiments show that the license plate positioning achieved using this method is of high accuracy. The shape of the plate region, the proportion of the features, and the gray transition characteristics were used to achieve the precise positioning of the license plate.

References

1. Peng Jian-min (2006) In license plate recognition license plate localization and character if plate recognition engineering research and realization [D]. Hunan University, Changsha
2. Zhu Wei-jian, Xia Liang-zheng (2005) Practical and fast algorithm for character segmentation of license plate [J]. J Nanjing Univ Sci Technol S1:26–28
3. Xie Xiao-yan (2004) Vehicle plate automatic system research based on neural network [D]. Hunan University, Changsha
4. Yang Hai-ting (2005) License plate recognition system research and implementation based on texture features [D]. University of Electronic Science and Technology of China, Xi'an
5. Zhao Chun-xue, Qin Fei-hu (1998) Automatic recognition of vehicle license based on color segmentation [J]. Shanghai J Shanghai Jiaotong Univ 30(5):573–576
6. Rong Guan-ao (2000) Computer image processing [M]. Tsinghua University Press, Beijing
7. Wu Li-de (1993) Computer vision [M]. Fudan University Press, Shanghai
8. Wu Ming-fen (2002) Rough set theory and its present state and prospects [J]. J Wuyi Univ (Nat Sci Ed) 1(16):16–21

Electroencephalogram Lifting Recognition Using Unsupervised Gray-Based Competitive Clustering Networks

Chi-Yuan Lin, Yi-Fang Chen, and Sheng-Chih Yang

Abstract An analysis system for the single-trial electroencephalogram (EEG) recognition is presented. In combination with wavelet and amplitude modulation (AM), the gray-based competitive Hopfield clustering network (GCHCN) is applied to the clustering of left-finger lifting and resting. The fractal features in multiscale are extracted from the discrete wavelet transform (DWT) data by using fractal dimension. GCHCN is used for the recognition of features. GCHCN is an unsupervised clustering approach for the biomedical signals. Compared with popular supervised linear discriminant analysis (LDA) classifier and multilayer perceptron (MLP) classifier, GCHCN achieves promising results in lifting recognition.

Keywords Electroencephalogram • Discrete wavelet transform • Amplitude modulation • MLP classifier • Gray-based competitive Hopfield clustering network

1 Introduction

The aim of the brain–computer interface (BCI) is to provide a direct communication channel between a human and an external device for transmitting user intentions by analyzing specific mental tasks [1]. In recent years, the rapid development of BCI systems based on the analysis of single-trial electroencephalogram (EEG) associated with the hand movement has seen great improvement. The noninvasive EEG-based BCIs, which is the study of motor imagery, are of particular interest. It focuses on the discrimination of left and right MIs using the special characteristics of event-related desynchronization and synchronization (ERD and

C.-Y. Lin • Y.-F. Chen (✉) • S.-C. Yang
Department of Computer Science & Information Engineering, National Chin-Yi University of Technology, Taichung, Taiwan
e-mail: kzy0258@gmail.com

ERS, respectively) in µ(8–12 Hz) or β(18–26 Hz) rhythms over sensorimotor cortices [2, 3].

In this study, we use the Daubechies discrete wavelet transform (DWT) [4, 5] and amplitude modulation (AM) literature [6], which have investigated the offline classification of EEG signals by using adaptive autoregressive (AAR) parameters [7]. Among the various feature extraction techniques available, we have used DWT as a fast structured approach to ERP representation in selecting multiscale. In the feature extraction stages of BCIs, autoregressive (AR) models have proved to be popular. The all-pole AR model is appropriate for modeling EEG-filtered white noise with certain energy bands.

This study proposes a methodology that combines Daubechies DWT and AM to extract features and unsupervised classification scheme. However, the three goals of this study can be organized as follows: (1) describe data acquisition, (2) present feature extraction and unsupervised classifier, and (3) utilize other classifiers in comparison with our method.

2 Experiment and Method

2.1 Data Acquisition

The dataset was provided by the Department of Medical Informatics, Institute for Biomedical Engineering, Graz University of Technology. It consisted of three subjects, or three datasets were recorded.

They did not have the prior experience of BCI experiments. As shown in Fig. 1, they included five scalp EEG channels (C3, C5, FC3, C1, and CP3). These channels
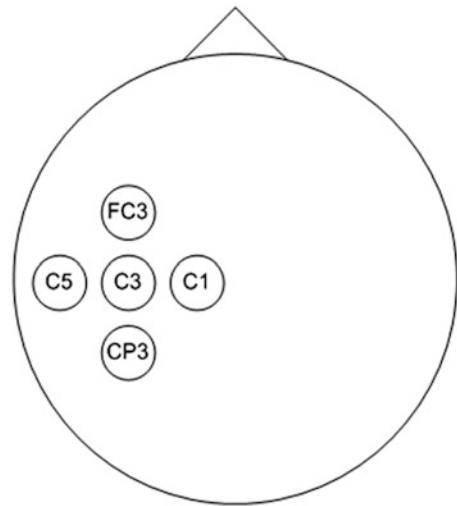

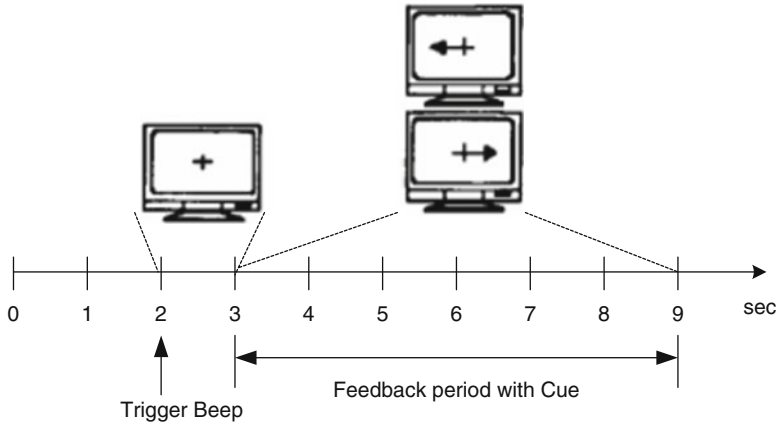**Fig. 1** EEG electrode locations used in this study

Fig. 2 Experimental paradigm of time scheme

were selected because they can be further enhanced by a surface Laplace operator; this part is discussed in the next section. In addition, the EMG channel for monitoring the right-side muscle activity and a channel on the forehead electrooculogram (EOG) artifacts recorded blinking during the trial. EEG was sampled at 125 Hz, and then filtered between 0.5 and 30 Hz.

Each trial lasted 9 s. During the experiments, for 3–9 s, the subjects were asked to do one of two mental tasks (Fig. 2). The experiment was divided into 7 runs with 40 trials each. Of the 280 trials available, 140 were used to train the classifier, whereas the remaining 140 trials were used in testing the generalization performance of the trained classifiers.

2.2 Data Preprocessing

To select a suitable of the EEG reference can greatly affect the classification accuracy and sensitivity to artifacts. EEG signals within the intervals of the artifacts were first excluded, and the derivation of the Laplacian operation was applied to obtain reference-free EEG data. The Laplacian method is presumed to be a superior ear reference method because it is a high-pass spatial filter that improves the focus of local sources of the activity and reduces the activity of wide distribution, including that from the far sources.

The Laplacian derivation of performance depends on the topographical size of the α- or β-rhythm control signals and also on the topographical sizes and locations of the various kinds of noise signals. The surface Laplacian can be considered as a spatial high-pass filter, which is necessary to further signal processing and feature extraction. It has already been proved to improve EEG spatial resolution, which is

a

b
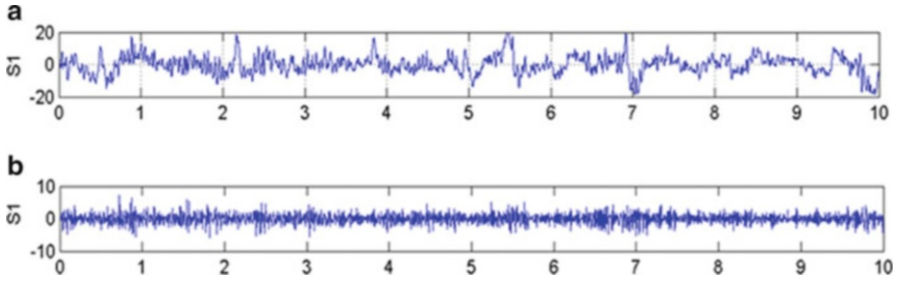
Fig. 3 The Laplacian filter experiments. (**a**) Raw EEG signal, (**b**) EEG signal after Laplacian filter
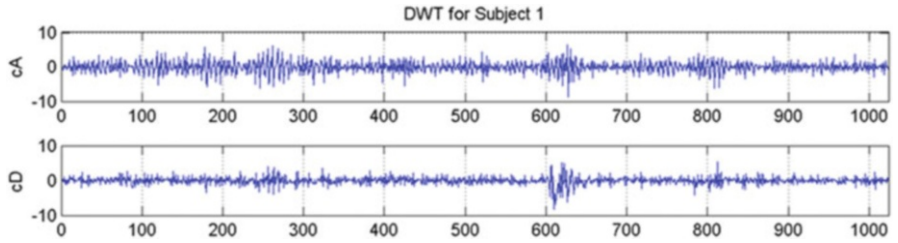
Fig. 4 DWT experiments

an effective approach [8]. For this reason, we have used the Laplacian operator to reduce the background wave and other interference waves (Fig. 3).

To calculate the Laplacian second derivative from the electrode of interest around a set of electrodes of average potential, the Laplacian was computed according to the formula

$$ E_i^{Lap} = E_i^{C_3} - \frac{\sum_{j=Si} E_j^{ref}}{N}, \tag{1} $$

where $E_i^{C_3}$ represents the signal measured from the electrode C3, E_j^{ref} stands for the signal measured from one of the other neighboring electrodes, and N stands for the number of electrodes in the montage (i.e., 4).

2.3 Feature Extraction

The wavelet packet analysis is a technique that provides the signal narrow information analysis method and its signal low-frequency and high-frequency parts of the decomposition (Fig. 4), which help analyze the characteristics of the signal, adaptively selecting the desired frequency band; the wavelet packet analysis has a wider range of applications.

Generally, the multi-resolution analysis of signal decomposition into countless resolutions, which represents a class of unique physical characteristics of each of the resolutions in the signal. That is, the signal and the preparation are characterized by decomposing it into a sub-band, and each sub-band can be handled separately, according to their characteristics.

The related event for each trial is represented by the DWT and can be defined as

$$x(t) = \sum_{k=-\infty}^{\infty} C(k)\varphi_k(t) + \sum_{j=0}^{\infty} \sum_{k=-\infty}^{\infty} D(k)\psi_{j,k}(t). \tag{2}$$

where $x(t)$ is the wavelet coefficient and $\psi_{j,k}(t) = 2^{J/2}\psi(2^j t - k)$ is the mother of the wavelet functions. The integers j and k mean decomposition scale and time shift, respectively.

Then, we used amplitude modulation to identify the signals. This practice can be found in the original signal of envelope and the amplitude envelope analysis, based on the Hilbert transform [9].

Each envelope, referred to as AM waveform, was computed based on

$$MC(k) = \sqrt{C(k)^2 + H(C(k))^2} \tag{3}$$

$$MD(k) = \sqrt{D(k)^2 + H(D(k))^2} \tag{4}$$

in which $C(k)$ and $D(k)$ are the single-trial bands that passed EEG signals, and $H(C(k))$ and $H(D(k))$ are the Hilbert transform of single trial of EEG signals.

3   Gray-Based Competitive Hopfield Clustering Network

The Hopfield neural network has been extensively studied for its features of simple architecture and parallel implementation [10–12]. A 2-D discrete competitive Hopfield neural network (CHNN) was proposed by Chung et al. [10], and it was applied for medical image segmentation by Cheng and Lin et al. [11]. They used the winner-takes-all learning to eliminate the need for finding weighting factors in the energy function.

For n training samples and c classes, the CHNN consists of $n \times c$ neurons, which can be conceived as a two-dimensional array. Each sample is iteratively trained to update the neurons' weights by using the nearest-neighbor rule. In a 2-D Hopfield neural network, let $v_{y,j}$ be the output state of the (y,j)th neuron and let $w_{x,i;y,j}$ represent the interconnected weight between neurons (x,i) and (y,j). The neuron (x,i) in the network receives weighted inputs $w_{x,i;y,j}$ from each neuron (y,j) and a bias $I_{x,i}$ from the outside. The total input to neuron (x,i) is computed as

$$Net_{x,i} = \sum_{y=1}^{n} \sum_{j=1}^{c} w_{x,i;y,j} v_{y,j} + I_{x,i}. \tag{5}$$

The Lyapunov energy function of the two-dimensional Hopfield neural network is given by [11]

$$E = -\frac{1}{2} \sum_{x=1}^{n} \sum_{y=1}^{n} \sum_{i=1}^{c} \sum_{j=1}^{c} v_{x,i} w_{x,i;y,j} v_{y,j} - \sum_{x=1}^{n} \sum_{i=1}^{c} I_{x,i} v_{x,i}. \tag{6}$$

The network reaches a stable state when the Lyapunov energy function is minimal.

In the CHNN, the competitive learning rule (winner-takes-all) is used for updating the weightings among the neurons. Therefore, only one of the neurons in each row that receives the maximum input would be the winner with its output being set to one. The outputs of all the other neurons on the same row would then be set zero. That is, the CHNN with a competitive learning rule is given as

$$v_{x,i} = \begin{cases} 1 & \text{if} \quad Net_{x,i} = \max\{Net_{x,1}, Net_{x,2}, \dots Net_{x,c}\} \\ 0 & \text{otherwise}. \end{cases} \tag{7}$$

The grey system is usually divided into several topics such as grey theory, grey mathematics, grey prediction, grey generating space, grey decision, and grey relational analysis. The grey relational theory demonstrates the measurement of similarity between the training samples and classes based on the grey relational space [13]. Let x_y be a training sample and w_j be a cluster centroid, then the grey relational grade between them is defined as

$$\gamma_{y,j} \equiv \gamma(x_y, w_j) = \frac{\Delta_{\min.} + \xi \Delta_{\max.}}{\Delta_{yj} + \xi \Delta_{\max.}}, \tag{8}$$

where $\Delta_{\min.} = \min|x_y - w_j|$, $\Delta_{\max.} = \max|x_y - w_j|$, $\Delta_{yj} = |x_y - w_j|$, and $0 < \xi < 1$ are the distinguished coefficients.

In order to update the training performance, the grey relation theory was embedded into a competitive Hopfield neural network (named GCHCN). Therefore, the simplified object function for GCHCN based on competitive learning can be modified as

$$E = \sum_{x=1}^{n} \sum_{y=1}^{n} \sum_{i=1}^{c} \sum_{j=1}^{c} V_{x,i} \gamma_{y,j} V_{y,j} \tag{9}$$

and

$$Net_{x,i} = \sum_{y=1}^{n} \sum_{j=1}^{c} \gamma_{y,j} V_{y,j}, \tag{10}$$

where $\gamma_{y,j}$ is a modified grey relational grade between training samples x_y and cluster centroids w_j and $I_{x,i} = 0$.

Using Eqs. (9) and (10), the Hopfield neural network based on competitive learning can be used for clustering in a parallel manner, which is given as follows:

Step 1: Input training samples $X = \{x_1, x_2, \ldots, x_n\}$ and the number of class c.

Step 2: Compute the grey relational grade matrix $\mathbf{R} = \left\{\gamma_{y,j}\right\}_{y=1,j=1}^{n,c}$ with training samples and cluster centroids.

Step 3: Set the initial number of the samples to be n. Each class contains at least one sample.

Step 4: Calculate the input to each neuron (x, i) by Eq. (10).

Step 5: Apply Eq. (7) to update the neurons' output states for each neuron in a row.

Step 6: Repeat Steps 4 and 5 for all rows and count the number of neurons for the new state. If no neuron is changed, go to step 7, otherwise go to step 4.

Step 7: Output the final clustering results.

4   Results and Discussion

In this study, an unsupervised method utilizing GCHCN is proposed for left-finger lifting and resting discriminant from single-trial EEG data. The GCHCN algorithm is implemented to recognize left-finger lifting and resting data without any training in advance. As GCHCN is an unsupervised approach that partitions a collection of feature vectors into a number of subgroups based on minimizing the trace of a within-cluster scatter matrix, it is adopted to automatically classify wavelet AM data into two clusters, left-finger lifting and resting. We use Daubechies DWT to decompose EEG signals into sub-bands, and then obtain multi-resolution envelope features by the AM methods. We perform experiments on three subjects to evaluate the performance of the proposed method. Table 1 and Fig. 5 show the comparisons of classification accuracy between the LDA, MLP, and GCHCN approaches. It can be concluded that GCHCN is appropriate for the recognition of nonstationary EEG signals since it can operate unsupervised. GCHCN is likely a potential unsupervised approach in the applications of mental tasks.

Table 1 Comparisons of classification accuracy among the LDA, MLP, and GCHNN approaches

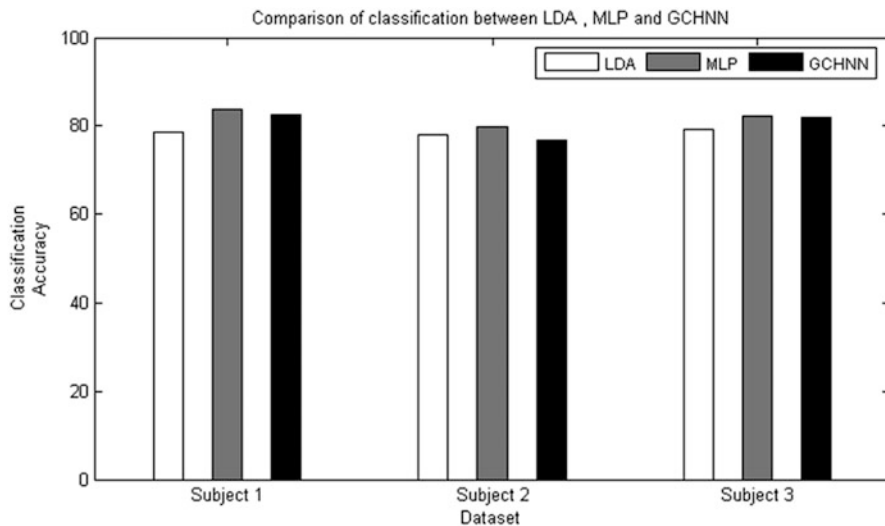| Dataset	LDA (%)	MLP (%)	GCHNN (%)
S1	78.6	83.8	82.6
S2	77.9	79.7	76.8
S3	79.3	82.9	81.9
Average	78.6	82.1	80.4

Fig. 5 Comparisons of classification accuracy among the *LDA*, *MLP*, and *GCHNN* approaches

5   Conclusion

We have proposed an analysis system for single-trial EEG discriminant in this study. The system that contains wavelet-based AM features and GCHCN clustering is present for the discrimination of left-finger lifting and resting. The features are extracted by AM method from the DWT data. These are good features that can improve the classification of the mental tasks. GCHCN is then used for the clustering of the EEG data. The experimental results show that the presented GCHCN method achieves promising results in lifting recognition.

References

1. Wolpaw J, Birbaumer N, McFarland D, Pfurtscheller G, Vaughan T (2002) Brain–computer interfaces for communication and control. Clin Neurophysiol 113(6):767–791
2. Pfurtscheller G (1977) Graphical display and statistical evaluation of event-related desynchronization (ERD). Electroenceph Clin Neurophysiol 43:757–760
3. Pfurtscheller G, Brunner C, Schlögl A, Lopes da Silva F (2006) Mu rhythm (de) synchronization and EEG single-trial classification of different motor imagery tasks. Neuroimage 31(1):153–159

4. Akay M (1998) Time frequency and wavelets in biomedical signal processing. Endorsed by IEEE Engineering in Medicine and Biology Society. IEEE Press, Piscataway, pp 192–207
5. Adeli H, Zhou Z, Dadmehr N (2003) Analysis of EEG records in an epileptic patient using wavelet transform. J Neurosci Methods 123(1):69–87
6. Hsieh IH, Saberi K (2010) Detection of sinusoidal amplitude modulation in logarithmic frequency sweeps across wide regions of the spectrum. Hear Res 262:9–18
7. Krusienski DJ, McFarland DJ, Wolpaw JR (2006) An evaluation of autoregressive spectral estimation model order for brain-computer interface applications. Conf Proc IEEE Eng Med Biol Soc 1:1323–1326
8. McFarland DJ, McCane LM, David SV, Wolpaw JR (1994) Spatial filter selection for EEG-based communication. Electroencephalogr Clin Neurophysiol 103:386–394
9. Clochon P, Fontbonne JM, Lebrun N, Etévenon PA (1996) A new method for quantifying EEG event-related desynchronization: amplitude envelope analysis. Electroenceph Clin Neurophysiol 98:126–129
10. Chung PC, Tsai CT, Chen EL, Sun YN (1994) Polygonal approximation using a competitive Hopfield neural network. Pattern Recognit 27:1505–1512
11. Cheng KS, Lin JS, Mao CW (1996) The application of competitive Hopfield neural network to medical image segmentation. IEEE Trans Med Imaging 15:560–567
12. Lin JS, Liu SH (2002) Classification of multispectral images based on a fuzzy-possibilistic neural network. IEEE Trans Syst Man Cybern 32(4):499–506
13. Lin CY, Chen CH (2003) A genetic grey-based neural networks with wavelet transform for search of optimal codebook. IEICE Trans Fundam E86-A(3):715–721

Adapting Intensity Degradation to Enhance Fisheye Images Shot Inside Cup-Shaped Objects

Chuang-Jan Chang, Chang-Min Cheng, Tsung-Kai Chou, and Shu-Lin Hwang

Abstract This chapter surveys the imaging properties inside cup-shaped objects. AOI is rarely discussed in this topic since the normally applied camera spans limited view angle and fails to capture images clearly if objects are inspected with ROI to a larger depth. Oppositely, fisheye cameras are a major issue, due to the inherently enormous scales of the focusing depth and the spanning view angle. Accordingly, closely placing a fisheye camera directly toward the bottom of a cup-shaped object, an exposure can cover the whole internal, including both the bottom and the sidewall. Through simple experimental implementation, this chapter surveyed the involved overall radial intensity degradation and the geometrically deformation profiles. The concluded photonic and morphological models are based to enhance the imaging fidelity and adapted to develop advanced images processing technologies.

Keywords Cup-shaped object • Fisheye camera • Intensity degradation

1 Introduction

As far as the image detection of machine vision is concern, cameras, light sources, and lens are important topics. The technology that is based on limited coefficients to map images from normal cameras to pinhole ones was called "camera calibration" [1]. Correctly calibrated parameters make cameras able to pose coordinates of targets in the 3-D space. Due to the daunted distortion involved, few literatures discuss the calibration of fisheye cameras, though it owns the smart properties of ultra-wide field and free-range focusable field. For instance, if aimed toward the global zenith, the objects, from nearest to farthest, covered with a 2π solid view

C.-J. Chang • C.-M. Cheng • T.-K. Chou • S.-L. Hwang (✉)
Department of Electronic Engineering, Ming-Chi University of Technology, Taishan, Taiwan
e-mail: hwangsl@mail.mcut.edu.tw

angle would map clearly an image of limited radius. However, the photograph generally with irregular distortion, so that the traditional AOI image processing technologies would fail.

2   Background and Motivation

Regular camera, armed with a rectilinear projection lens (RPL), owns a certain range of depth of field, ranging from submeter to about a few meters, and a limited view angle, spanning less than 60° angle. The extended depth of field was desirable and useful in many optical imaging systems – such as the independent robot vision and endoscopy medical imaging. As for the image processing part, the digital filter that is independent from focusing state is used to process the stepping intermediate image so as to obtain the image with high depth of field. However, the fisheye lens (FL) is superior in this aspect. It focuses free range and, moreover, spans view angle 180° or, with possibility, more.

Cup-shaped components were frequently found practically, but only few AOI literatures targeted for. These skillful systems used specifically designed parts if they wanted to view the bottom and the inner sidewall in one shot. However, it is straight to fisheye cameras by posing the lens closing to the rim of target. Unfortunately, the picture will look strange and difficult to interpret. Knowing the image more is beneficial in developing advance algorithm in the coming day. This chapter purposely studies the overall imaging signals inside the internal of a paper cup through a simple experimental setup [2].

3   Methods and Results

Our system setup, in some phase, was quite different from the usual AOI application. To an ideal AOI setup, the inspected region were, within a planar surface, placed in front of camera where the applied luminaires will cast constant illuminance over, and the image obtained will exactly reveal the morphologic information. Practically, a running system would go toward these criteria [3, 4]. With challenge, the involved arts cannot guide our study; the used components are the fisheye camera, the cup-shaped internal, and the nonconstant illuminance. Sequentially, our test procedures would be described latterly.

3.1   Intensity Degradations of the RPL Camera
and the Fisheye Lens Camera

The degradation of FL camera is heavier than that of RPL one. This optical property is analyzed and well discussed in the optical textbook. In this chapter a practical
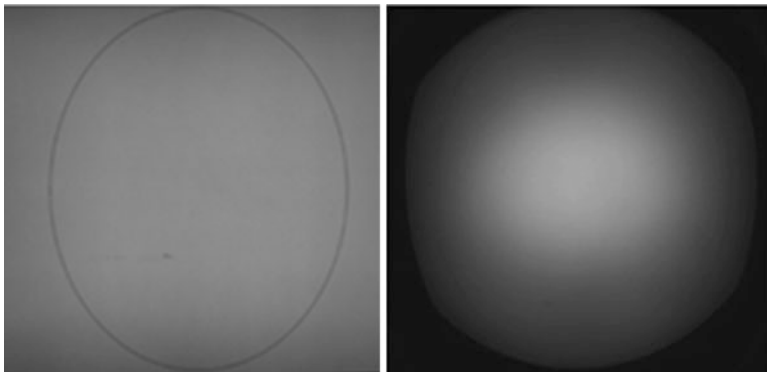
Fig. 1 Experimental environment

Fig. 2 Image captured by the RPL and FL

surveying had been processed, the test camera body respectively mounted the two test of different lenses, the first of RPL and the other fisheye lens. The experimental environment was set as shown in Fig. 1. A TFT panel was mounted in front of the test cameras. The panel worked as both roles: the tested object and the luminaire. The brightness distribution of images obtained with mean brightness by the rectilinear lens and fisheye lens will be discussed later. The used lens was respectively the fisheye lens and the rectilinear lens with 6 mm focal length. The test object was a white screen on which draw a black circle contour. This circle was used to define the ROI of the image shot and as the reference point for analysis.

Displayed on the screen, a white screen, the shot images by the RPL camera and the fisheye lens were photographed as shown in Fig. 2. Figure 3 showed the location of sampling line. The respected intensity profiles are shown in Fig. 4. The gray level
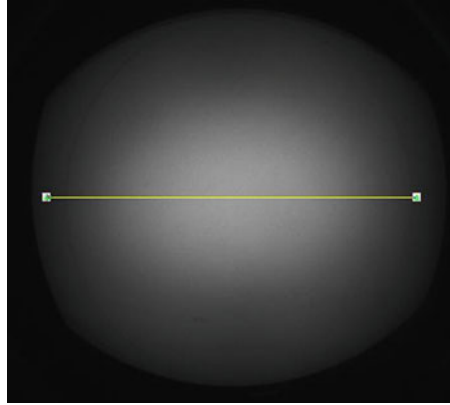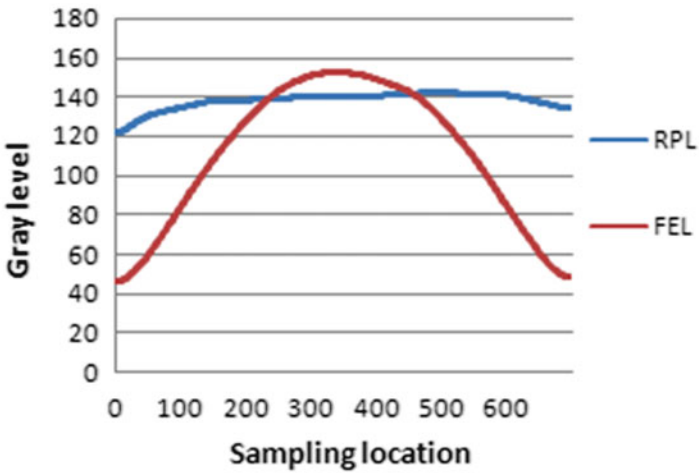
Fig. 3 Sampling method

Fig. 4 Brightness change of white target of RPL and FL

deviation of the image shot by the fisheye lens is far higher than that of the image shot by the rectilinear lens in degradation. The degradation is gradually growing from the central point to the border.

3.2 Calibration of Image Brightness

The brightness distortion calibration took the fisheye images as the reference brightness. The afterward brightness could calibrate to evaluate the sharpness of fisheye images. The sampling line was the same as the preceding section. The object to be tested is the concentric annulus in black and white, as shown. The thick of each annular contour is 100 pixels, and the center diameter is 200 pixels as shown

Fig. 5 Target calibration of horizontal image

Fig. 6 Photo of horizontal target by fisheye lens

in Fig. 5. The image shot was shown in Fig. 6. The aperture of lens is adjusted so that the gray level of the maximum intensity was lower than the saturated value of the analog signal. The change in the profile of the gray level was observed.

Figure 7 showed the intensity profiles of the target shot by the fisheye lens. From this curve, we found the radial degradation of the white brightness, but that of black brightness is not so clear. This experiment uses the brightness degradation contours as a reference to calibrate the imaging intensity. This will be simpler and accurate in processing the edge detection.

Figure 8 shows the signal degradation of the black screen and the white one. They will be based to calibrating the fisheye camera as black and white references. This experiment uses the two images as the reference points of the black and white of the fisheye image. The black and white gray level curves are as shown in Fig. 9. The above curve corresponding to the gray level curve of the target in Fig. 7 is used to obtain the calibrated gray level curve.
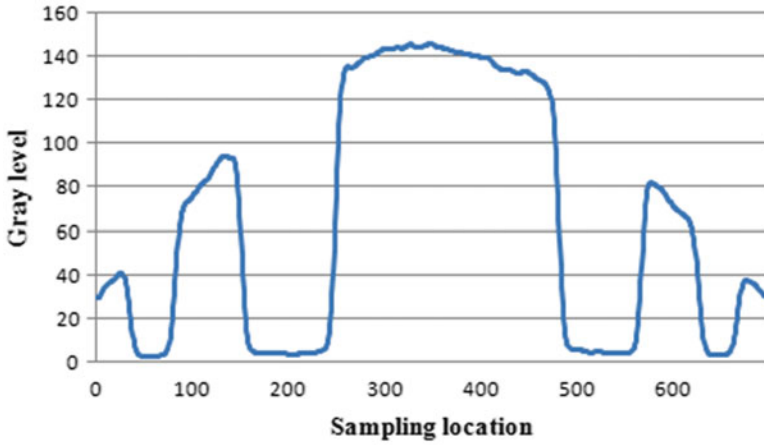
Fig. 7 Change in gray level curve of horizontal target by fisheye lens

Fig. 8 Calibrations of black and white targets

The white screen and the black one are respectively shot by the fisheye lens to obtain their brightness degradation curves. The saturated value is set to 1, and the darkest value is set to 0. The white degradation is visible by the fisheye lens, and it has a big difference from that of the rectilinear lens. The brightness degradation characteristics of the fisheyes are obtained. The characteristics are used to calibrate the gray level curve of the target that the brightness distortion occurred. The black gray level curves are deducted from both the target curve and the white curve. After
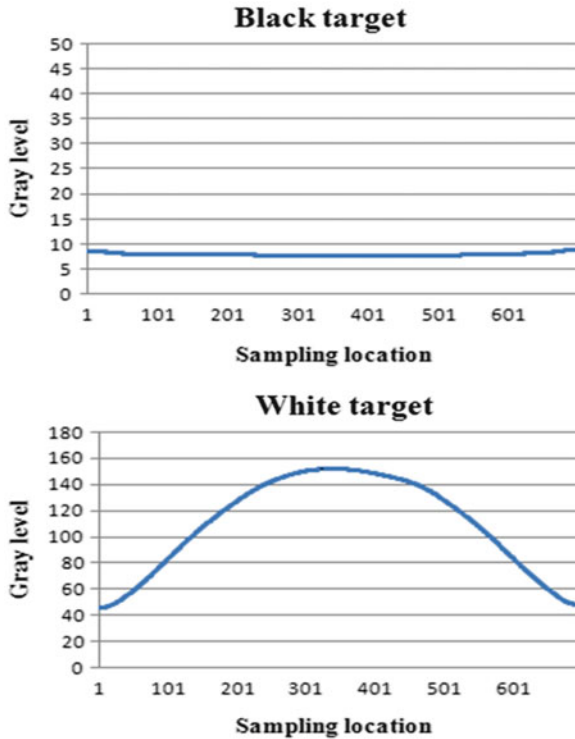
Black target

White target

Fig. 9 Gray level curves of black and white targets

removing the white curve from the target curve, the result is obtained as shown in Fig. 10. It is a square signal that is more convenient to process.

3.3 Imaging Signals Inside a Paper Cup

A paper cup painted multiple black squares on the sidewall, as shown in Fig. 11, in order to analyze objects with depth shot by the fisheye lens. All the square patterns are with size length of 2.85 cm, and the same to the each other separated as well as top one to the cup rim. Figure 12 shows the direct photo shot by the fisheye camera.

The lens aperture is adjusted to maximize the gray level of the image a little lower than the saturated value of the analog signal. The imaging signal from the cup rim to bottom is observed.

Figure 13 shows the intensity profiles extracted from an image of the target cup. The part of edge shot by the fisheye lens is mainly analyzed in this experiment. Bottom is not discussed in this experiment. The method stated in Sect. 3.2 is used to obtain the calibrated reference curve as shown in Fig. 14. Consideration shall be
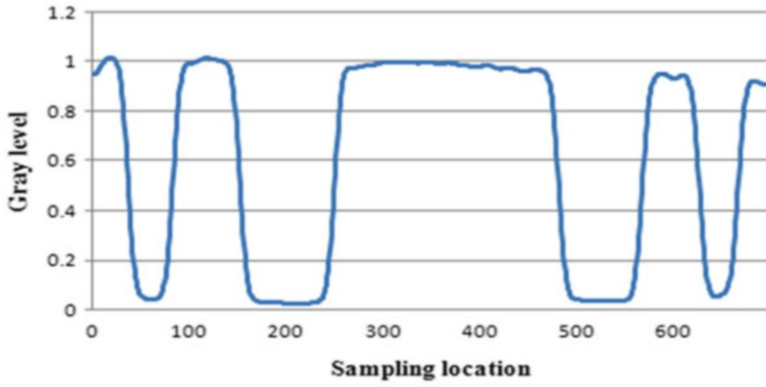
Fig. 10 Gray level curve after calibrating horizontal target shot by fisheye lens

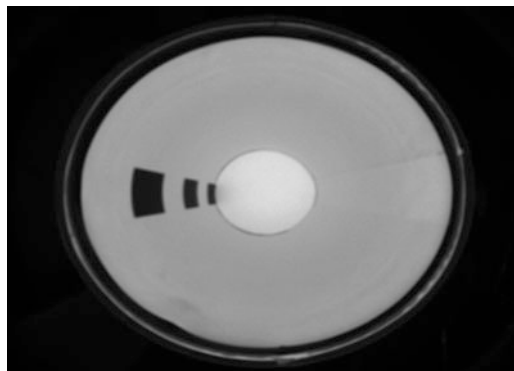

Fig. 11 Object to be tested

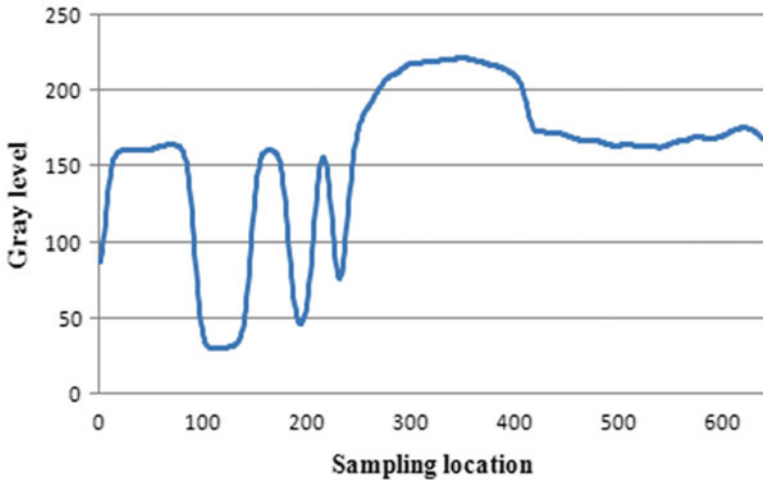**Fig. 12** Target of object with depth shot by fisheye lens

Fig. 13 Gray level curve of target with depth shot fisheye lens
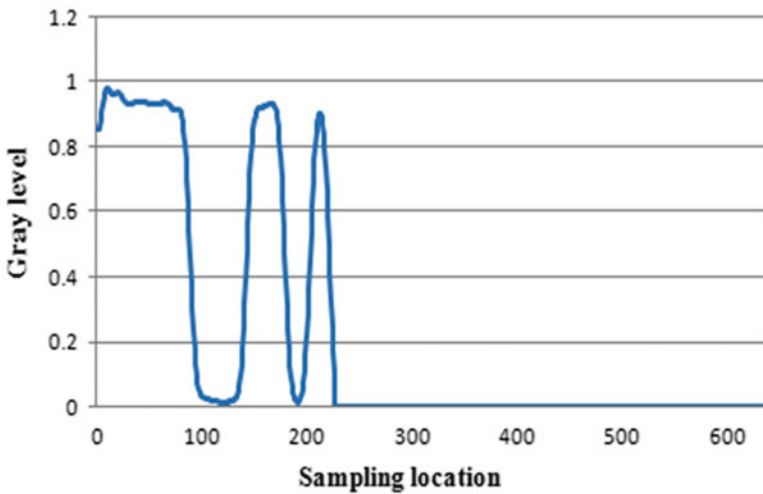
Fig. 14 Gray level curve after calibrating cup wall of target with depth shot by fisheye lens

taken into changes in the black and white curves because of degradation in the light source.

In this analysis, however, the white degradation is smaller than that of black. For lenses other than the rectilinear lens, the black and white degradations shall be taken into account. When the black and white targets are obtained, the influence from the degradation shall be minimized so that the black and white curves of the target are not the reference points we are looking for, and the recovered part shall use the black curve as a reference point of 0.

4 Conclusions

In this chapter, the ambient brightness is raised to calibrate images shot by fisheye lens and rectilinear lens. In different environments, the brightness degradation of each lens is different, so calibration shall be carried out in order to make discussion and evaluation before evaluating the correct square wave. Fisheye images are far superior to conventional images when presenting the inner of the cup-shaped object in the pattern distortion and the image quality. However, arrangement of the functional light source and image analytic technology are still the subject to be developed continuously in order to apply the fisheye imaging system to the AOI area.

References

1. Chang C-J (2002) Computer vision models of fisheye images and the 3D metrology. Doctoral dissertation, Graduate Institute of Electrical Engineering, National Taiwan University, Taipei
2. Lai S-H, Fu C-W, Chang S (1992) A generalized depth estimation algorithm with a single image. IEEE Trans Pattern Anal Mach Intell 14:405–411
3. Yao L, Zhang W, JunliLian (2004) "Application of AOI system in PCB", test & measurement technologies
4. Yang S-Y (2010) Imaging technologies to the inner surface of an opaque paper cup. Master dissertation, Department of Electronical Engineering, Ming Chi University of Technology, Taipei

A Method to Implementation of Lane Detection Under Android System Based on OpenCV

Xiao-Xu Wei and Lei Meng

Abstract Lane detection has drawn great attention in vehicle assistant driving and intelligent navigation systems, some of them are developed using Android operating system. This chapter presents a method to implementation of lane detection under Android system based on Open Source Computer Vision Library. To resolve the problem between C/C++ and Java mixed-language programming, the native code should be written using JNI with the Android NDK which makes available to use native code languages such as C/C++ in the Android at application level. Implementation of image processed with several processing techniques using OpenCV, such as RGB to grayscale conversion, set region of interest (ROI) crop, Canny edge detection, Hough transform, and linear fitness to detect the road lane. The method is verified on Android Virtual Device at the end of the chapter.

Keywords Lane detection • Android system • OpenCV • Android NDK

1 Introduction

With the development of society, traffic safety is attracting more and more attention and is becoming a key problem in automotive industry nowadays. Vision navigation system of intelligent vehicle is developed to remind drivers to avoid danger or to reduce accidents in advance [1]. Lane detection is becoming one of the most important parts in intelligent vehicle navigation systems, which should not be ignored in independence navigation.

X.-X. Wei (✉)
School of Automation, Wuhan University of Technology, Wuhan 430070, China
e-mail: weixiaoxu123123@163.com

L. Meng
School of Information Engineering, Wuhan University of Technology, Wuhan 430070, China

Now some of the vehicle navigation systems are developed on Android operating system. The Android platform has become more and more popular, which is a Linux-based operating system for mobile devices, especially on smart phones and tablet computers. So a method is provided to implement lane detection under Android system based on Open Source Computer Vision Library (OpenCV). Some people have achieved lane detection in Windows system [1]; the method in this chapter will try to achieve lane detection in Android system.

2 Works About Development Environment

Android applications are usually developed in the Java language by using the Android Software Development Kit (SDK) [2].

OpenCV is released under a BSD license and hence it is free for both academic and commercial use. It has C++, C, Python, and Java interfaces and supports Windows, Linux, Android, and Mac OS. If the code is written in optimized C/C++, the library can take advantage of multicore processing [3]. Therefore, the mixed-programming language involves C/C++ and Java direct function call to each other, the native code is written using Java Native Interface (JNI) and compiled through Android NDK.

Java language uses JNI to access codes written in other language (such as C/C++). Android NDK is a toolset which makes available to use native code languages such as C/C++ in the Android at application level [4]. Now most versions of the NDK provide a simplified build system through the new ndk-build build command. It adds support for easy native debugging of generated machine code on production devices through the new ndk-gdb command [5]. In addition, Cygwin is a collection of indispensable tools which provide a Linux look and feel environment for Windows. Android NDK can be used in Windows after installing Cygwin.

3 Implementation on Android Platform

To resolve the problem between C/C++ and Java mixed-language programming, the native code should be written by using JNI. Therefore, there are two parts to complete the implementation: firstly, algorithm of lane detection is written in C++ language by using JNI and then compiled by Android NDK to generate shared libraries that can be called through Java code; secondly, according to the Android application framework, Java code is written for showing processing results [6]. Figure 1 shows the processing of implementation.
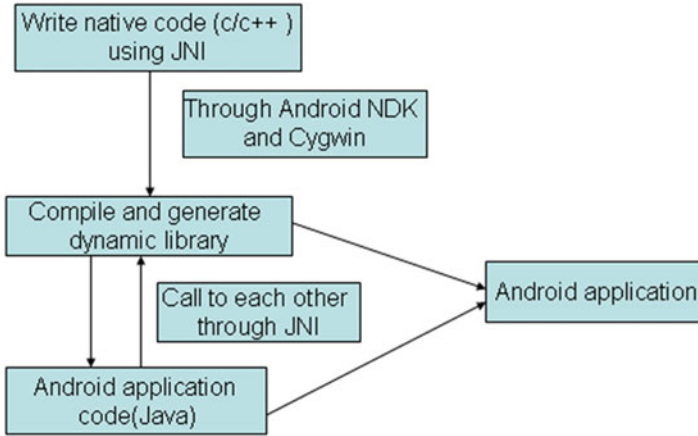
Fig. 1 Implementation process of the method

3.1 Algorithm of Lane Detection

The image processing algorithm of lane detection is implemented by OpenCV. There are several steps in this algorithm.

Load Image and Grayscale. This algorithm starts with loading image through JNI which is usually a path of temporary image. When the color image is loaded, it is converted to grayscale by a function in OpenCV. Grayscale gives the value of every pixel separate sample [7]. Grayscale image is base of edge detection.

Set the Region of Interest. In order to reduce redundant image data quantity based on effective information, the input image should be set on the region of interest (ROI). The ROI is set depending on specific conditions which are not hard absolute. In this chapter, the ROI is 2/3 of the image from the bottom, the remaining 1/3 of the image contains some useless elements (such as cars, buildings, and the sky). Setting the ROI is using the function of cvSetImageROI () in OpenCV [1]. After that, the processing algorithm will only deal with the ROI of the image, and the processing speed is also increased.

Edge Detection. Edge detection is an important technology in the preprocessing procedure. The main consideration in this algorithm is to save full information without missing any edges, so Canny operator is adopted to detect edges [7]. CvCanny () function in OpenCV library is used to implement edge detection, but the thresholds in the function are fixed experiential. To adapt the changing environment, Canny method adopts a self-adapting edge detection based on Otsu method to replace the two experiential thresholds in CvCanny function. Hough transform is adopted to gain the line of lane in edge space because of the character of traffic lane.

Hough Transform. At present, a common method to detect lines is Hough transform. In this part, cvHoughLines2 () function which is one of the image transform functions in OpenCV library is used to complete Hough transform on the image.

The function prototype is CvSeq * cvHoughLines2 (CvArr* image, void *line_storage, int method, double rho, double theta, int threshold, double param1 = 0, double param2 = 0). The detailed description of parameters is follows [8]:

Image: The input 8-bit single-channel binary image.

LineStorage: The storage for the lines detected.

Method: The Hough transform variant, there are CV_HOUGH_STANDARD of stander Hough transform (SHT), CV_HOUGH_PROBABILISTIC of progressive probabilistic Hough transform (PPHT), CV_HOUGH_MULTI_SCALE of multiscale variant of SHT [1].

Rho and Theta: The resolution desired for the lines.

Threshold: The value in the accumulator plane that can reach the routine to return a line.

Param1 and Param2: The parameters associated with the method of Hough transform. The parameters are not used because we use the SHT in algorithm of lane detection.

Lane Boundary Detection. This part tells how to realize lane boundary detection for middle lane. At first, we set the region of interest where middle lane is located as shown in Fig. 2a.

Then building *x*-0-*y* coordinates, respectively return much value of *Y* corresponding color to red point coordinates. In the actual operation, we find that the effective value point of R channel is in a range. If the three channel values of RGB image are, respectively: P[B], P[G] and P[R], the returning effective red pixels value should be satisfied condition:

$$90 < p[R] <= 255 \quad \&\& \quad p[G]! = 255 \quad \&\& \quad p[B]! = 255.$$

Average of multiple returned values is the *X* axis of central point, then linear fitting with least-square method. So the boundary of the liner fitting result is shown as Fig. 2b (green line is boundary).

The boundary is calculated with coordinates in ROI by the above method, and therefore it needs conversion of coordinate to fit the whole image. Slope of this linear fitting equation does not change, just changing coordinates according to coordinates of ROI movement.

The lane is shown in the initial image through each pair of points on the line. As is described in Fig. 3, the coordinate of point A, B, C, and D can be calculated according to the green line which was achieved in Fig. 2b. Then left and right lane boundary can be detected in the same way.

3.2 Compile Shared Library

At first, function declaration corresponding C/C++ should be established; the subject of the declaration is jstring Java_com_haveimgfun_LibImgFun_ImgFun
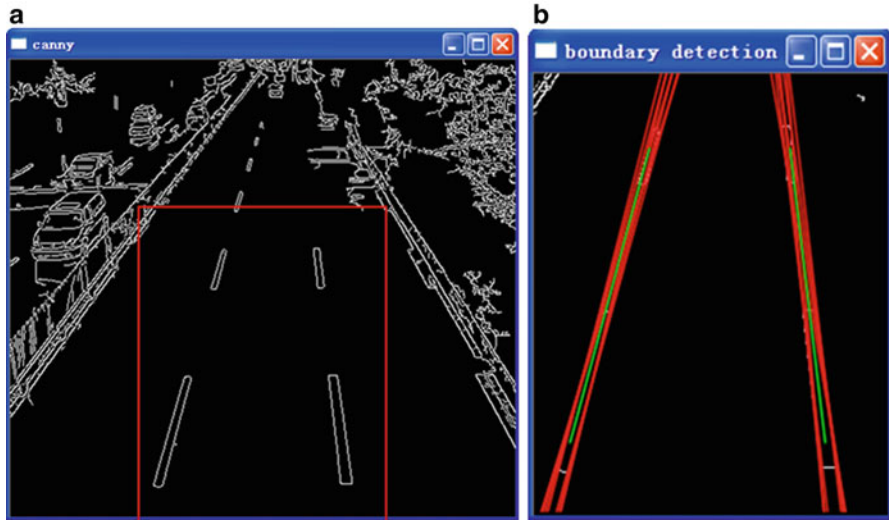
Fig. 2 (**a**) Set the region of interest. (**b**) Result of liner fitting
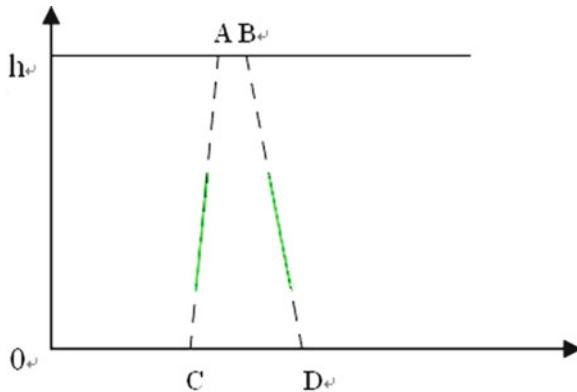

Fig. 3 Lane shown in the initial image

(JNIEnv* env, jobject thiz, jstring path, jstring path1), env points to environment of JAVA, and this represents Java class instance included in this native method. The next two parameters is the path of image. Then, a header file contained the function declaration can be generated through the tool of Java provided by Android JDK. The generated header file is copied to a folder named jni created under project directory. The C++ source files introduced that header file are created to write functions showing lane detection at the same time [6].

To compile shared library, two script files are needed to be written, which are Android.mk and Application.mk. The file of Android.mk describes source files that

Fig. 4 Result of this method running on the AVD, *top right* is the initial image

need to be compiled through NDK and components formed. The file of Application. mk describes some additional information to help compile about this application. The last step is to open Cygwin, enter into the folder called jni, and execute command of "$NDK/ndk-build." After that, a shared library libxxx.so will be generated finally so that the native method can be called in Java code for Android applications [6].

4 Verify on Android AVD

To verify the effectiveness and feasibility of the method in this chapter, an Android application was created on Android Virtual Device (AVD). An AVD is a device configuration for the Android emulator that allows to model different configurations of Android-powered devices.

Design code user program and UI according to the programming standard of Android SDK, and then package it as a file named xxx.apk, install file on the AVD [6]. When the AVD is loaded, a virtual SD card function should be created. It needed certain capacity to store the images. The results are shown in Fig. 4 after running the application.

5 Conclusion and Future Work

In this work, lane detection is implemented under Android platform based on OpenCV. The application in Java code can easily call the algorithm written in C/C++ code through Android NDK and JNI. In the future you can try to use this method in real-time lane detection. And we also can improve the detection algorithm to increase accuracy and reduce run time. Maybe your phone can be a navigation system of intelligent vehicle someday.

References

1. Ye W, Yuetian S, Yunhe X, Shu W, Yuchen Z (2010) The implementation of lane detective based on OpenCV. In: 2010 second WRI global congress on intelligent systems (GCIS). Wuhan, 2010, pp 278–281
2. http://developer.android.com/reference
3. OPENCV, http://opencv.org/
4. Paik JH, Seo SC, Kim Y, Lee HJ, Jung H-C, Le DH (2011) An efficient implementation of block cipher in android platform. In: 2011 5th FTRA international conference on multimedia and ubiquitous engineering (MUE), Crete, 2011, pp 173–176
5. Lee S, Jeon JW (2010) Evaluating performance of android platform using native C for embedded systems. In: 2010 international conference on control automation and systems (ICCAS), Gyeonggi-do, 2010, pp 1160–1163
6. Hongbin W, Denao L, Jumin Z, Yuhu X (2011) Implementation of human face detection based on OpenCV in android system. In: Computer engineering & software
7. Sankaraiah S, Deepthi RS (2011) Highly optimized OpenCV based cell phone. In: 2011 I.E. conference on sustainable utilization and development in engineering and technology, The University of Nottingham, Malaysia Campus, 2011, pp 47–52
8. http://www.emgu.com/wiki/

Automatic Broadcast Soccer Video Analysis, Player Detection, and Tracking Based on Color Histogram

Der-Jyh Duh, Shu-Yu Chang, Shu-Yuan Chen, and Cheng-Chung Kan

Abstract In this chapter, a broadcast soccer video analysis system is proposed for the detection and tracking of the players. Our method consists of two phases. The first one is the scene analysis phase which automatically classifies the video into different scenes based on 2-D Gaussian color model of hue and saturation. An adaptive incremental model update scheme is proposed so that even under shadow condition, good scene analysis result can still be provided. The second one is the player analysis phase. A color histogram-based method is proposed to classify the player with a decision tree, and a linear prediction model based on spatial similarity matrix (SSM) is used for tracking of the players. Experimental results show that the proposed method is simple yet effective.

Keywords Color histogram • Playfield segmentation • Player detection/tracking • Adaptive Gaussian color model update • Spatial similarity matrix (SSM)

1 Introduction

Automatic soccer video content analysis has become an extremely interesting research topic. Among the various features used in soccer scene classification, color information is most useful. The playfield color distribution and playfield ratio are often used for soccer video shot classification [1–3]. The color distance between a pixel and the mean value of the playfield is used to determine whether it belongs to the playfield or not [4]. Different color models and different

D.-J. Duh (✉)
Department of Computer Science and Information Engineering, Chien Hsin University of Science and Technology, Tao-Yuan 32097, Taiwan
e-mail: djduh@uch.edu.tw

S.-Y. Chang • S.-Y. Chen • C.-C. Kan
Department of Computer Engineering and Science, Yuan Ze University, Chung-Li 32003, Taiwan
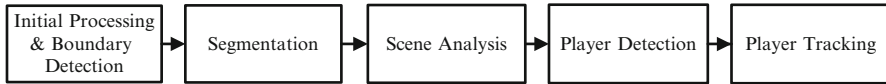
```
┌──────────────┐   ┌──────────────┐   ┌──────────────┐   ┌──────────────┐   ┌──────────────┐
│Initial Processing│ │              │   │              │   │              │   │              │
│ & Boundary   │──▶│ Segmentation │──▶│Scene Analysis│──▶│Player Detection│─▶│Player Tracking│
│  Detection   │   │              │   │              │   │              │   │              │
└──────────────┘   └──────────────┘   └──────────────┘   └──────────────┘   └──────────────┘
```

Fig. 1 The proposed system function blocks

segmentation scheme are used, such as simple thresholding method that chooses the color range for thresholding [5], color distribution of probability and statistics, and other solutions that use color histograms. Generally, the image is divided into several blocks, and the ratio between the blocks can be used to classify the scene.

After the playfield segmentation, player detection and tracking process is used. Most of the algorithms for moving object detection are mainly based on background subtraction. Features, such as edge, skeleton, shape, Haar features, and SVM classifier, are used to identify the true players. Multiple player candidates can be detected after the player detection in each frame. Many existing algorithms for the multiple target tracking in different frames are used, such as Kalman filter and Bayesian tracker.

Generally, when the playfield contains shadow, the results of segmentation and player detection are not good enough. A scheme for automatic playfield segmentation, shot classification, and player tracking in broadcast soccer video based on color histogram is proposed. The system function block diagram is shown in Fig. 1. The process is divided into three steps: playfield segmentation, shot classification, and player detection/tracking. During playfield segmentation step, HSV color space is used and 2-D H-S (hue and saturation) histogram is calculated for shot boundary detection. Shots are classified into three types based on the grass-like ratio. 2-mean clustering algorithm based on the H-S color histogram is used for player detection. The player tracking model using linear motion vector and prediction model modified from the SSM [6] are applied in order to handle multiple occluded player tracking.

The rest of the chapter is organized as follows. Section 2 describes in detail the playfield segmentation and shot classification process. Section 3 introduces the player detection, team classification, and player tracking scheme. In Sect. 4, the experimental results are shown. A conclusion is drawn in Sect. 5.

2 Playfield Segmentation and Classification

2.1 Playfield Segmentation

Shot boundary is detected first using the H-S color histogram. The chi-square distance between two nearby frames histogram is computed. When the distance value is greater than a predefined threshold, the current frame is defined as the shot boundary. Those frames classified as the shot boundary are not applied for the
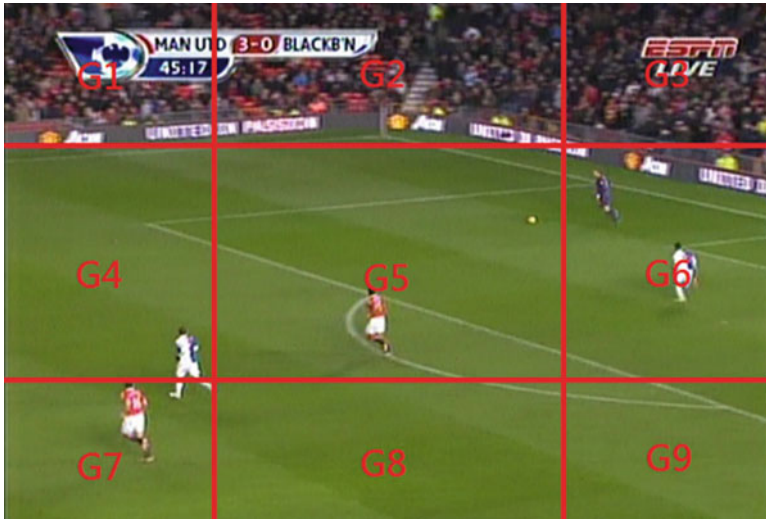
Fig. 2 The 3:5:3 block partition scheme

further playfield segmentation. To detect the first long view, if a frame with mean of hue between 12 and 17 and saturation greater than 20, the frame will be used and the first five frames that satisfied are used as the initial training frames. The initial playfield H-S Gaussian model can be estimated using those image pixels that satisfied the condition.

After initial training step, playfield candidate pixels using the derived playfield model are obtained and the area of playfield in each frame is calculated. An adaptive incremental 2-D H-S Gaussian model for playfield color is proposed, and the probability of each pixel belonging to the playfield is estimated based on the Gaussian model derived. Morphology operation is applied to the extracted playfield blob to remove the noises such as the soccer field lines and shadow of players.

Shot classification is applied to next decide the type of the clip between shot boundaries. In this study, three types of scene are considered: long view, middle view, and outfield view. The image after segmentation is divided into 3×3 blocks with size ratio of 3:5:3 as suggested in [3]. The playfield grass ratio, defined as G_1–G_9, of the number of playfield candidate pixels to the block size of each block is calculated as shown in Fig. 2. Two constraints are used to classify the shots. If Eq. 1 is satisfied, the scene is set to the outfield type:

$$\text{mean}(G_1, G_2, G_3) < 0.4 \text{ and mean}(G_4, G_5, G_6) < 0.4 \text{ and mean}(G_7, G_8, G_9) < 0.4$$

$$(1)$$

Fig. 3 Playfield segmentation results using proposed adaptive playfield model

For the long view scene, the scene of the image may contain one of the midfield, left corner, or right corner part of the playfield. The second constraint is based on the observation and the equations are shown as follows:

$$|G_4 - G_5| + |G_5 - G_6| < 0.2 \;\; \text{and} \;\; \text{mean}(G_1, G_2, G_3) > 0.35 \;\; \text{and} \;\; G_{7,8,9} > 0.35 \tag{2}$$

$$G_5 - G_4 > 0.05 \;\; \text{and} \;\; G_{8,9} > 0.85 \tag{3}$$

$$G_5 - G_6 > 0.05 \;\; \text{and} \;\; G_{7,8} > 0.85 \tag{4}$$

If any of the three conditions is satisfied, the scene is classified as long view type; otherwise it is classified as close-up type. If more than five frames after the shot boundary belong to the same type, the clip is classified as the same type of the five frames. This scene type detection is applied again if a new shot boundary is detected.

2.2 Adaptive GMM Updating

In order to adaptively handle the case when the playfield's conditions is changed during the game (such as shadow and color), an incremental training solution to generate adaptive Gaussian playfield model is proposed. Figure 3. gives the segmentation results using the proposed Gaussian model updating scheme.

During the initial phase, the initial Gaussian distribution is obtained. Then, for each testing frame, if more than five consecutive frames belong to the long view type, the playfield candidate pixels of these five frames are added to the training set and the Gaussian parameters is reestimated and updated. The new updated Gaussian distribution parameters are used for the segmentation of next input frame sequences.

Fig. 4 Segmentation and player blob detection results: (**a**) player with missed detection, (**b**) top boundary detection and outfield region remove, and (**c**) detection of the missing player

3 Player Detection and Tracking

3.1 Player Segmentation

The playfield and player blobs can be obtained using region growing after the playfield segmentation. The top boundary of the playfield needs to be detected first so that those player blobs connect to the outfield can be well isolated.

A simple and fast scheme to detect the top boundary is used. First, the largest nonplayfield region is located, and this region should be the outfield region. The points of lowest position of the leftmost and rightmost vertical line of this region are located. These two positions served as the starting and ending point of the top boundary. Median filter is applied to the positions of these two points of the current frame and the previous four frames. The point on this region boundary with the maximum distance to the line defined by the two reference points obtained above is located, and median filter is also applied to this point over the consecutive five frames. The two line segments constructed by these three points are defined as the top boundary of the playfield. Those pixels of nonplayfield blobs that lie above this boundary are deleted, and the rest of the blobs served as the possible player blobs. Figure 4 shows the result.

3.2 Player Detection and Tracking

After removing the outfield region, the bounding rectangle of each nonplayfield blob is detected, and a blob filter based on (1) blob size, (2) aspect ratio of the bounding rectangle, and (3) coverage ratio of the blob is applied to obtain the true player blobs. Then morphology operator is applied for noise reduction. From the start of the long view scene of the testing video, the jersey color of the first 1,000 player blobs detected are used for the player's training. The H-S histogram is calculated and 2-mean clustering algorithm is applied. Each frame belongs to the long view after the training phase is proceeded for player classification, and the

Fig. 5 SSM of two frames. *First row* shows players in merge state and *second row* with players in split state. *Third row* in disappearing state and *forth row* shows the normal case

probability of the blob belonging to the three clusters (team A, team B, and nonplayer) is calculated. A player tracking scheme based on the player blobs of consecutive frames is applied next in order to further eliminate the nonplayer blob. Inspired from [6], the construction of SSM is modified to indicate the correspondence of player blobs between consecutive frames. The distance between blobs of two consecutive frames is defined as the nearest Euclidean distance between the corner points of each blob. If the centroid of current blob falls inside of previous blob, the blob distance is set as 0. The SSM is constructed based on the distance. A total of five blob states can be defined: they are (1) normal, (2) merge, (3) split, (4) new player, and (5) missing state. Example of the SSM derived is shown in Fig. 5. Details of the construction of SSM are given in [7].

After all the states of player blobs are decided, player tracking process is applied. For those blobs in normal state, the displacement between the two centroids of the corresponding blobs is calculated and is used as the tracking position for the next frame. The probability of the team classification result of the current blob is updated based on the linear adaptive model and the player blob is reassigned to the team label with the highest probability. For the rest blobs, linear prediction of player blob's motion vector and position is applied to the blob of current frame and the player's pixel of the original segmented blob in the possible bounding window is used to form a new blob and the same process for team labeling mentioned above is applied.

4   Experimental Results

Four testing videos from Liga BBVA, Premier League, and World Cup 2010 are used. Two of the videos contain shadow in the playfield during the game. All together with about 1,600 frames are extracted for testing. The size of the video is 624*337 or 700*475. Comparison of the field segmentation result with [3] is made first and shown in Fig. 6. The result of segmentation using the proposed method is much better.

Fig. 6 Comparisons of playfield segmentation results between the proposed method and [2]. (**a**) Original image. (**b**) Our proposed method. (**c**) Results using ref. [2]

Table 1 Precision and recall rate of the proposed method

Testing sequence	Precision (%)	Recall (%)
A	99.74	85.66
B	91.00	94.47
C-1	97.75	92.96
C-2	94.47	95.46
D	92.73	92.02

The precision and the recall rate of the testing video are given in Table 1. The average precision rate is 95.14 % and the recall rate is 92.15 %. Precision rate is defined as $Precision = TP/(TP + FP)$ and recall rate is defined as $Recall = TP/(TP + FN)$, where TP is the number of true player detected in the testing video sequence, FP is the number of error detected player, and FN is the number of miss detected player.

5 Conclusion

In this chapter, a scheme for the broadcast soccer video analysis, player detection, and tracking is proposed. Our method consists of two phases: (1) automatic video scene analysis phase based on hue and saturation 2-D Gaussian color model. An adaptive color model update method is proposed so that it can deal with the scene even with shadow in the playfield, and (2) player analysis and tracking phase using color histogram, spatial similarity matrix, and linear prediction model is used for player tracking. Experimental results show that the method is simple yet effective. Future work will be focused on the player tracking schemes under much more complex scenes.

References

1. Pallavi V, Mukherjee J, Majumdar AK, Sural S (2008) Ball detection from broadcast soccer videos using static and dynamic features. J Vis Commun Image Represent 19(7):426–436
2. Tong X, Liu Q, Lu H (2008) Shot classification in broadcast soccer video. Electron Lett Comput Vis Image Anal 7(1):16–25
3. Ekin A, Tekalp AM, Mehrotra R (2003) Automatic soccer video analysis and summarization. IEEE Trans Image Process 12(7):796–807
4. Khatoonabadi SH, Rahmati M (2009) Automatic soccer players tracking in goal scenes by camera motion elimination. Image Vis Comput 27(4):469–479
5. Liu J, Tong X, Li W, Wang T, Zhang Y, Wang H (2009) Automatic player detection, labeling and tracking in broadcast soccer video. Pattern Recognit Lett 30(2):103–113
6. Junejo IN, Dexter E, Laptev I, Perez P (2008) Cross-view action recognition from temporal self-similarities. In: ECCV'2008, Marseille, vol 2008, pp 293–306
7. Chang S-Y (2011) Automatic broadcast soccer video scene analysis, player detection and tracking, Master thesis, Yuan-Ze University, Taoyuan

Conversion of 3D Triangular-Meshed Model to Dot Representation

Chih-Hung Huang, Cheng Wen, and Kuang-Chiung Chang

Abstract Dot representation is the only format accepted in a special 3D printing application called laser stippling, which outputs the shape and texture tone of a 3D model inside a lead glass by using laser beam. To fully utilize existing abundant and exquisite 3D triangular-meshed models, this study proposes a two-phase technique, i.e., a sampling phase followed by a halftoning phase, to convert models in triangular-meshed format to dot representation. The sampling phase generates a set of dense sample points that cover the entire surface of the model, and the halftoning phase removes some of the sample points to reflect the tone of the model's texture. The actual stippled results demonstrated the technique could deliver products in good quality.

Keywords Laser stippling • Triangular-meshed model • Dot representation

1   Introduction

Triangular-meshed representation and dot representation are two formats to represent three-dimensional (3D) models. Triangular-meshed models, with delicate textures applied on their surface, are usually created by modeling software. On the other hand, dot representation [1] uses a large number of small dots, collectively named as a point cloud, to represent a 3D model. Although the dot representation is less common and more storage consuming, it is the only acceptable format to a

C.-H. Huang
Department of Information Management, Lunghwa University of Science and Technology, Taoyuan 33306, Taiwan

C. Wen • K.-C. Chang (✉)
Department of Electrical Engineering, Lunghwa University of Science and Technology, Taoyuan 33306, Taiwan
e-mail: kcchang@mail.lhu.edu.tw
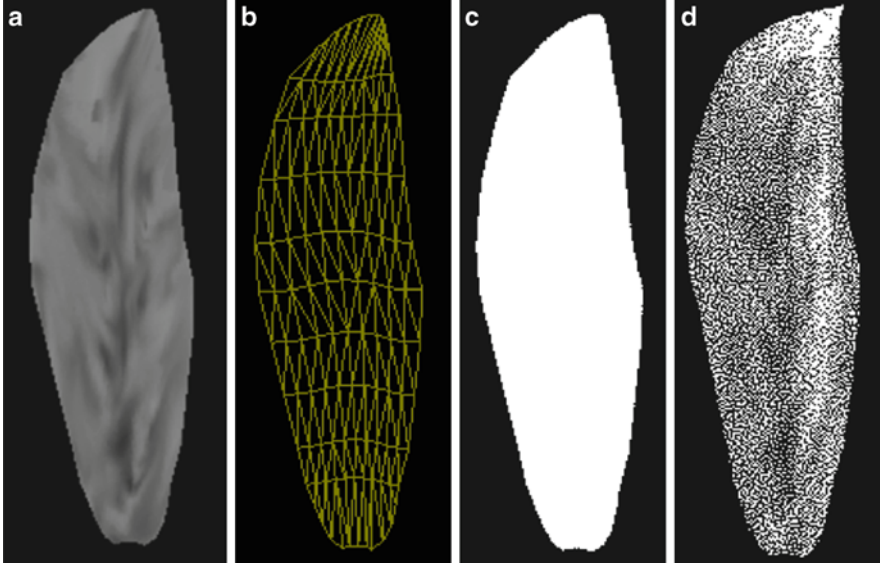
Fig. 1 Two phases of the conversion: (**a**) original textured petal model, (**b**) shown in triangular-meshed format, (**c**) output from 3D sampling phase, (**d**) final result from 3D halftoning phase

special 3D printing device called the laser engraving machine [2]. The laser engraving machine uses laser beam to stipple mono-color, fixed-sized, tiny dots inside a lead glass, according to the coordinates of points in a dot representation model. Unfortunately, 3D models in dot representation are rare. To fully utilize existing abundant and exquisite 3D triangular-meshed models, this study proposes a technique that can convert 3D triangular-meshed models to dot representation. The conversion process takes up two phases: a 3D sampling phase followed by a 3D halftoning phase. The quality of the conversion results are judged in two aspects: (1) the dots should fall on the outer surfaces of the model and (2) the distribution of dots should retain the grayscale tone of the model's texture. Figure 1a shows a textured petal of a flower model and Fig. 1b shows its triangular meshes. During the sampling phase, a set of densely, evenly distributed sample points are generated on the surface of the petal as shown in Fig. 1c. In the subsequent halftoning phase, the sample points are further processed to remove some of them. The points left from the halftoning phase are shown in Fig. 1d, which reflects the tone changes of the model's texture as compared to Fig. 1a.

2 Related Works

The 3D sampling phase is to place a set of sample points densely and evenly on the surface of the model. Previous approaches adopted a two-step strategy [3–7], i.e., a point creation step to generate a set of points densely and a relaxation step to

redistribute the sample points evenly. Turk's retiling of polygonal surfaces [3] started by randomly choosing a given number of points on the surfaces. The points were then relaxed by balancing the repelling forces between each other. Analogous to Turk's method, Pastor's approach [4] created point hierarchies by applying a series of subdivisions on the model surfaces. From these methods, it could be concluded that an easy sample point creation approach would generally require a complicated point relaxation. Besides, Nehab and Shilane [6] presented a stratified sampling strategy. The stratified sampling started like Lorensen's marching-cube method [8] that subdivided the sampling domain into nonoverlapping sample cubes and generated only one sample point in each cube.

The 2D halftoning technique with error diffusion was introduced by Floyd and Steinberg [9]. Regarding the 3D halftoning technique, Lou and Stucki [10] introduced a method to approximate a digital volumetric object to an ensemble of binary material volume elements. In Lou's approach, each voxel in the interior of 3D models was assumed to be solid, and the outer neighboring voxels around the center one were all assumed to be valid (not empty). However, the sample points generated from the 3D sampling phase are not necessarily at the geometrical centers of voxels, and errors are to be diffused only on the surface, not interior of the model. Therefore, developing a new 3D halftoning technique is required.

3   3D Sampling Phase

Since a triangular-meshed model can be decomposed into many triangles, the proposed sampling approach is to be applied on each triangle individually one after another. An easy but effective approach that generates evenly distributed sample points is called the square sampling. The square sampling takes the longest edge of the triangle in processing as the x axis of a Cartesian coordinate system and one of its vertexes as the origin. Through the origin, the y axis is perpendicular to the x axis. Both x and y axes are divided into line segments by a sampling distance d, which is a parameter representing the desired sampling density, except the first segment is $d/2$. Then, lines parallel to the x and y axes are drawn from each line segment as shown in Fig. 2a. The intersections inside the triangle are the sample points generated. It can be found that all distances between any two neighboring sample points remain constant, which maintain the uniformity.

The square sampling works well for most triangles. However, for those triangles with a small acute angle, it brings up a problem called the sampling hole. As the example shown in Fig. 2b, if the angle θ is between $\text{Tan}^{-1}(0.5d/2.5d)$ or $11.3°$ and $\text{Tan}^{-1}(0.5d/1.5d)$ or $18.4°$, the first sample point S is generated at position $(2.5d, 0.5d)$. As the angle θ becomes smaller, point S will be farther away from the vertex V. This could yield a situation that no sample points generated near the acute angle. Since a 3D model surface might contain a series of such triangles, the sampling result would create a blank area near the acute angles, as the shadowed area shown in Fig. 3.
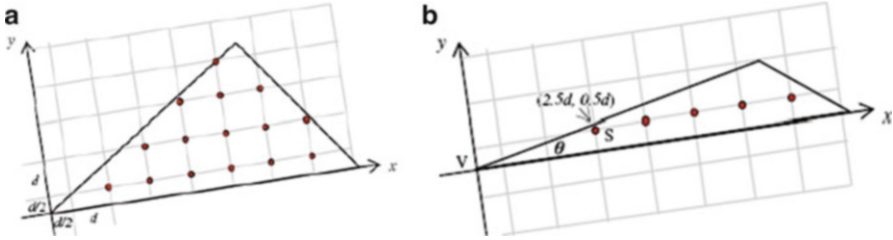
Fig. 2 Square sampling results of (**a**) an ordinary triangle and (**b**) a triangle with small acute angle
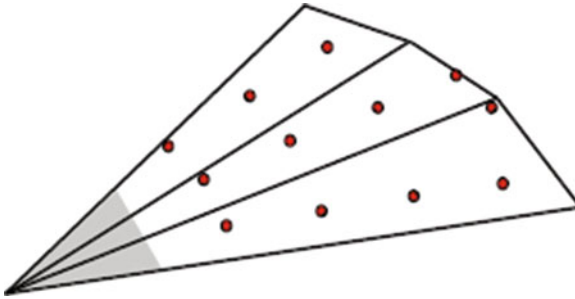

Fig. 3 Sampling-hole problem, no sample points generated in shadowed area

To overcome the sampling-hole problem, an extra relaxation step, which can slightly adjust the sample points toward the blank area, is needed. The step is called Voronoi relaxation, which is inspired from the Voronoi Diagram [11]. The Voronoi relaxation is not to subdivide a triangle into regions as the Voronoi Diagram does. Rather, the Voronoi relaxation moves and redistributes the sample points inside the triangle. The algorithm of the Voronoi relaxation is summarized as follows:

1. Assuming n sample points have been generated from the square sampling, record the position of each sample point x_i, $i = 1 \sim n$.
2. For every point y_j inside the triangle, find a sample point x_i, such that the distance between y_j and x_i is minimal. Record the position of y_j as a member point of x_i.
3. Compute the average $y_{i.\text{avg}}$ from all member points y_j of x_i, $i = 1 \sim n$, recorded.
4. Let $x_i = y_{i.\text{avg}}$, for every x_i, $i = 1 \sim n$.
5. Go to Step (2) until convergence is reached.

4 3D Halftoning Phase

Similar to the approach used in the marching cube [8], the first step in the 3D halftoning phase is to cut the model space into small cubes with edge length L. Depending on the geometry structure of the model, each cube may or may not
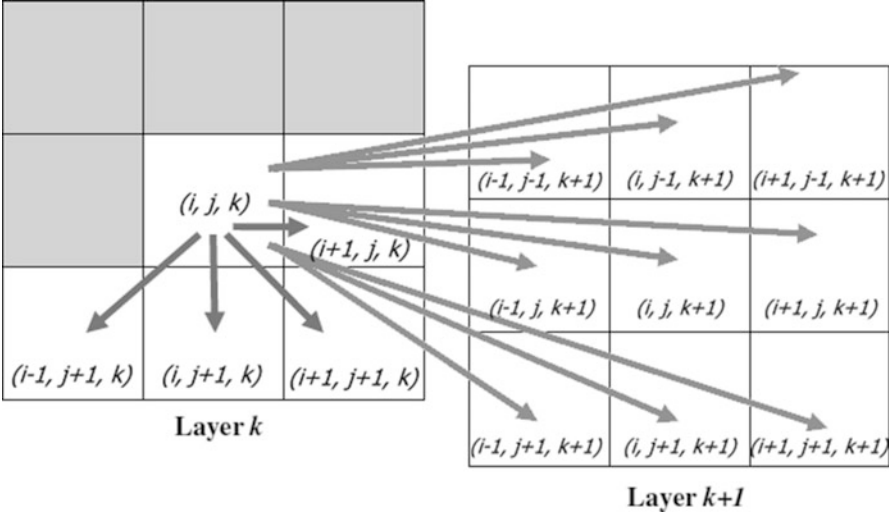
Fig. 4 Error diffusion for 3D surface halftoning

intersect the triangles that have been sampled; therefore, the number of sample points in each cube varies. Huang et al. [12] proposed an approach to determine a final sample point, if more than one sample point generated inside a cube. The cube that contains a final sample point is considered a valid cube, otherwise it is invalid. The grayscale value of a valid cube, which would be used in the subsequent 3D halftoning, is determined by the grayscale value on the texture where the final sample point locates.

The 3D halftoning technique, which is a modified version of the 2D halftoning [9], diffuses errors to final sample points in the neighboring cubes. Since cubes are in space, they are processed one at a time in a slice-wise linear manner, layer-to-layer, left-to-right, and up-to-down. As shown in Fig. 4, each square unit represents a cube and shadowed squares represent cubes that have been processed. At layer k, $Cube(i, j, k)$ is the current cube in processing. There are at most 13 neighboring cubes for $Cube(i, j, k)$. Let $P(i, j, k)$ and $P(x, y, z)$ be the final sample points of the current cube $Cube(i, j, k)$ and of one valid neighboring $Cube(x, y, z)$, respectively. The distance d_n is calculated individually as

$$d_n = |P(x, y, z) - P(i, j, k)| \ (n = 1 - 13 \text{ if valid}) \tag{1}$$

The error diffusion weighting w_n of $cube(i, j, k)$ to a valid neighboring cube is inversely proportional to the square of distance d_n and can be calculated by

$$w_n = \frac{\left(1 / d_n^2\right)}{\sum\limits_{\text{valid } d_n} 1 / d_n^2}. \tag{2}$$

5 Experimental Results

The algorithms for the 3D sampling and 3D halftoning were implemented to test their feasibility, and the results are demonstrated in this section. The resolution of the laser engraving machine was 300 dpi approximately; therefore, the sampling distance d was set to 0.7 mm and the cube edge length L was set to 0.8 mm throughout the tests.

The square sampling yielded pretty good results on most triangles, where the sample points were evenly distributed on the surface. However, if it was applied on a series of triangles, each of which had a small acute angle, a sampling hole appeared around the acute angles, as the enlarged view shown at the top of Fig. 5a. Since the Voronoi relaxation is a time-consuming process and is not required for all triangle sampling, the threshold to apply Voronoi relaxation was set to triangles with an acute angle less than 20°. The triangles in Fig. 5a met the criterion, thus they were further processed by the Voronoi relaxation, and the result is shown in Fig. 5b. It can be found from the enlarged view that the sampling points near the acute angles did move to cover the hole. Although other sample points move their positions as well, the uniformity did not change apparently.

An example of the 3D halftoning result is illustrated in Fig. 6. Figure 6a shows a textured flower model and Fig. 6b shows its triangular meshes. The model was
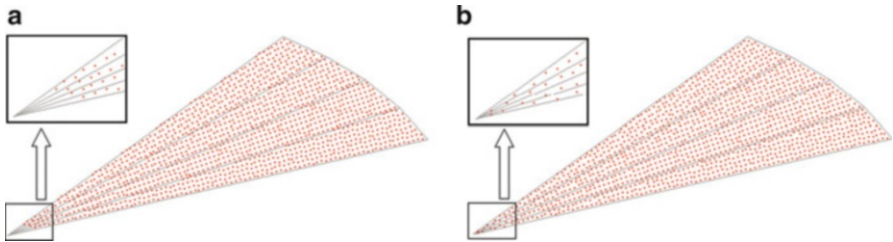
Fig. 5 3D sampling results: (**a**) sampling hole around small acute angles and (**b**) problem solved by Voronoi relaxation
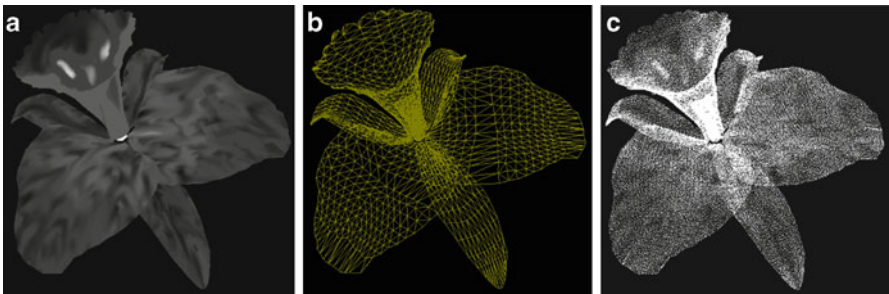
Fig. 6 3D halftoning result: (**a**) original textured flower model, (**b**) in triangular-meshed format, and (**c**) in dot representation after 3D halftoning

converted to dot representation by the square sampling (and Voronoi relaxation, if necessary) and finally by the 3D surface halftoning algorithm. The conversion result honestly reflects the tone of the model's texture, as shown in Fig. 6c.

6 Conclusion

This chapter proposes a two-step process that can convert 3D models in triangular-meshed format to dot representation. In the sampling phase, the square sampling generates a set of densely and evenly distributed sample points that cover the entire surface of the model. For those special triangles with a small acute angle, an extra Voronoi relaxation is applied to resolve the sampling-hole problem. In the halftoning phase, a 3D surface halftoning approach removes some sample points to reflect the tone of the model's texture. The actual stippled results demonstrate the feasibility of the proposed technique.

References

1. Secord AJ (2001) Fun with dots: non-interactive stippling of grayscale images and animations. Technique Report, UBC ID# 27984004
2. 3D Laser engraving machine, http://www.3dlasermachine.com/
3. Turk G (1992) Re-tiling polygonal surfaces. ACM Comput Graph 26(2):55–64
4. Pastor OM, Strothotte T (2002) Frame-coherent stippling. In: Proceedings of the eurographics, Pisa, 2002, pp 145–152
5. Kobbelt L, Botsch M (2004) A survey of point-based techniques in computer graphics. Comput Graph 28(6):801–814
6. Nehab D, Shilane P (2004) Stratified point sampling of 3D models. In: Eurographics symposium on point-based graphics, Zurich, 2004, pp 49–56
7. Quinn JA, Langbein FC, Martin RR (2007) Low-discrepancy point sampling of meshes for rendering. In: Proceedings of the eurographics/IEEE VGTC, Norrköping, 2007, pp 19–28
8. Lorensen WE, Cline HE (1987) Marching cubes: a high resolution 3D surface construction algorithm. ACM Comput Graph 4:163–169
9. Floyd RW, Steinberg L (1976) An adaptive algorithm for spatial grey scale. Proc Soc Inf Display 17:75–77
10. Lou Q, Stucki P (1998) Fundamentals of 3D halftoning. Lect Notes Comput Sci 1375:224–240
11. Aurenhammer F (1991) Voronoi diagrams – a survey of a fundamental geometric data structure. ACM Comput Surv 23(3):345–405
12. Huang CH, Chang KC, Wen C (2010) Non-iterative stippling of grayscale three-dimensional polygon meshed models. IET Comput Vis 4:138–148

Image Retrieval System Based on EMD Similarity Measure and S-Tree

Thanh Manh Le and Thanh The Van

Abstract This chapter approaches the binary signature for each image on the base of the percentage of the pixels in each color image and builds a similar measure between the images based on EMD (earth mover's distance). Next, it aims to create S-tree in a similar measure EMD to store the image's binary signatures to quickly query image signature data. Then, from a similar measure EMD and S-tree, it provides an image retrieval algorithm and CBIR (content-based image retrieval). Last but not least, based on this theory, it also presents an application and experimental assessment of the process of querying image on the database system over 10,000 images.

Keywords CBIR • Image retrieval • EMD • S-tree • Signature • Signature tree

1 Introduction

It is difficult to find images in a large database of digital images. There are two main approaches for querying the images: querying the images based on the keyword TBIR (text-based image retrieval) [1] and those based on the content CBIR (content-based image retrieval) [1, 2].

In recent years, there have been considerable researches regarding CBIR, such as the image retrieval system based on color histogram [1–4], the similarity of the

T.M. Le
Hue University, Hue, Vietnam

T.T. Van (✉)
Center for Information Technology, HoChiMinh City University of Food Industry,
HoChiMinh City, Vietnam
e-mail: thanhvt@cntp.edu.vn

images based on histogram and the texture [5], and using the EMD distance in image retrieval [6–8].

This chapter aims to create the binary signature of an image and describe the distribution of image's colors by a bitstring with a given size. It also aims to query "similar images" in a large image database system efficiently. Additionally, two major targets are used to reduce the amount of storage space and speed up the query image on large database systems.

2 The Related Theory

2.1 S-Tree

S-tree [2, 9] is a tree with many branches that are balanced; each node of the S-tree contains a number of pairs $\langle sig, next \rangle$, where sig is a binary signature and next is a pointer to a child node. Each node root of the S-tree contains at least two pairs and at most M pairs $\langle sig, next \rangle$, all internal nodes in the S-tree at least m and at most M pairs $\langle sig, next \rangle$, $1 \leq m \leq M/2$; the leaves of the S-tree contain the image's binary signatures sig, along with a unique identifier oid for those images. The S-tree height for n signatures is at most $h = \lceil \log_m n - 1 \rceil$. The S-tree was built on the basis of *inserting* and *splitting*. When the node v is full, it will be split into two.

2.2 EMD Distance

Setting I as a set of suppliers, J as a set of consumers, and c_{ij} as the transportation cost from the supplier $i \in I$ to the consumer $j \in J$, we need to find out flows f_{ij} to minimize the total cost $\sum_{i \in I} \sum_{j \in J} c_{ij} f_{ij}$ with the constraints [10] $f_{ij} \geq 0, \sum_{i \in I} f_{ij} \leq y_j$, $\sum_{j \in J} f_{ij} \leq x_i, i \in I, j \in J$. With x_i as the provider's general ability $i \in I$, y_j is the total need of the consumer $j \in J$. The feasible condition is $\sum_{j \in J} y_j \leq \sum_{i \in I} x_i$. The EMD distance [6, 7] is as follows: $\text{EMD}(x, y) = \left(\sum_{i \in I} \sum_{j \in J} c_{ij} f_{ij} \right) \Big/ \left(\sum_{i \in I} \sum_{j \in J} f_{ij} \right) = \left(\sum_{i \in I} \sum_{j \in J} c_{ij} f_{ij} \right) \Big/ \left(\sum_{j \in J} y_j \right)$

3 Building Data Structures and Image Retrieval Algorithms

3.1 Creating a Binary Signature of the Image Based on the Color Histogram

Step 1. Choose a standard color set $C = \{c_1, c_2, \ldots, c_n\}$ to calculate the color histogram of the images. To quantify the image I in order to retain only the dominant colors $C_I = \left\{c_1^I, c_2^I, \ldots, c_{n_I}^I\right\}$, the color histogram vector of image I is $H_I = \left\{h_1^I, h_2^I, \ldots, h_{n_I}^I\right\}$.

Step 2. Calculate the color histogram vector standardizes $H = \{h_1, h_2, \ldots, h_n\}$, where $h_i = h_j^I \big/ \sum_j h_j^I$ if $c_i \in C \cap C_I$, otherwise $h_i = 0$.

Step 3. Each color c_j^I will be described into a bitstring $b_1^j b_2^j, \ldots, b_m^j$. The binary signature of the image I will be $\mathrm{sig} = \mathrm{B}^1 \mathrm{B}^2 \ldots \mathrm{B}^n$, $B^j = b_1^j b_2^j \ldots b_m^j$, in which $b_i^j = 1$ if $i = \lceil h_i \times m \rceil$, otherwise $b_i^j = 0$.

3.2 Measuring Similar Image Based on EMD Distance

The weight of the component $B_I^j = b_1^j b_2^j \ldots b_m^j$ is $w_I^j = w\left(B_I^j\right) = \sum\limits_{i=1}^m \left(b_i^j \times (i/m) \times 100\right)$; the weight vector of the image I will be $W_I = \left\{w_I^1, w_I^2, \ldots, w_I^n\right\}$. J is the image that we need to calculate the similarity with the image I, so we need to minimize the cost $\sum\limits_{i=1}^n \sum\limits_{j=1}^n d_{ij} f_{ij}$, and $F = (f_{ij})$ is the matrix of color distribution flows from c_I^i to c_J^j and $D = (d_{ij})$ is the Euclidean distance matrix in the RGB color space from c_I^i to c_J^j. The similarity between two images I and J based on the EMD distance will minimize the value $\mathrm{EMD}(I, J) = \min\limits_{F = (f_{ij})} \left(\sum\limits_{i=1}^n \sum\limits_{j=1}^n d_{ij} f_{ij}\right) \Big/ \sum\limits_{i=1}^n \sum\limits_{j=1}^n f_{ij}$, with $\sum\limits_{i=1}^n \sum\limits_{j=1}^n f_{ij} = \min\left(\sum\limits_{i=1}^n w_I^i, \sum\limits_{j=1}^n w_J^j\right)$

3.3 Creating S-Tree Based on EMD Distance

Algorithm1. Gen-Stree(S, Root)
Step 1. v = Root;
      If S = ∅ **then** STOP;

```
        Else Choosing <sig,oid> ∈ S and S = S \ <sig,oid>;
        To go Step 2;
Step 2.If v is leaf then
        begin
                v = v ⊕ <sig,oid>; UnionSig(v);
                If v.count > M then SplitNode(v);
                To go back Step 1;
        end
        Else
        begin
                EMD(SIG₀→sig,sig)=min{EMD(SIGᵢ→sig,sig) |
                SIGᵢ∈ v};
                v = SIG₀→next; To go back Step 2;
        End
```

Splitting the node v based on $\alpha - seed$ and $\beta - seed$ in [2, 9] is done as follows:

```
Algorithm2. SplitNode(v)
Create the nodes vα and vβ contains α − seed and β − seed;
For (SIGᵢ ∈ v) do
Begin
    If(EMD(SIGᵢ→sig,α − seed)<EMD(SIGᵢ→sig,β − seed))then
        vα = vα ⊕ SIGᵢ;
    Else vβ = vβ ⊕ SIGᵢ;
    sα =⋃sigᵢᵅ, with sigᵢᵅ ∈ vα; sβ=⋃sigᵢᵝ, with sigᵢᵝ ∈ vβ;
    vparent = vparent ⊕ sα; vparent = vparent ⊕ sβ;
    If (vparent.count > M) then SplitNode(vparent);
End.
Procedure UnionSig(v)
Begin
s=⋃sigᵢ, with sigᵢ ∈ v;
If(vparent != null) then
begin
    SIGv = {SIGᵢ|SIGᵢ → next = v,SIGᵢ ∈ vparent};vparent → (SIGv → sig) = s;
    UnionSig(vparent);
end
End.
```

3.4 The Image Retrieval Algorithm Based on S-Tree and EMD Distance

```
Algorithm3. Search-Image-Sig(sig, S-tree)
v = root; SIGOUT = ∅ Stack = ∅ Push(Stack, v);
```

```
while(not Empty(Stack)) do
begin
  v = Pop(Stack);
  If(v is not Leaf) then
  begin
      For(SIG_i ∈ v and SIG_i→sig ∧ sig = sig) do
            EMD(SIG_0→sig,sig)=min{EMD(SIG_i→sig,sig)|
            SIG_i∈v};
      Push(Stack, SIG_0→next);
    end
    Else SIGOUT = SIGOUT ∪ {<SIG_i→sig,oid_i>|SIG_i∈v};
end
return SIGOUT;
```

4 Experiments

4.1 Model Application

Phase 1: *Perform Preprocessing* (Fig. 1)

Step 1. Quantize images in the database and convert to a color histogram.

Step 2. Convert the color histogram of the image in the form of binary signatures.

Step 3. Respectively calculate the similarity measure EMD distance of the image signatures and insert into the S-tree.

Phase 2: *Implementation Query*

Step 1. For each query image, calculate the color histogram and convert into binary signatures.

Step 2. Perform binary signature query on the S-tree consisting of the image signature, it is possible to find similar images at the leaves of the S-tree through the EMD measure.

Step 3. After finding similar images, conduct arrangement of similar levels from high to low and make the title match with the images arranged on the basis of similarity EMD distance.
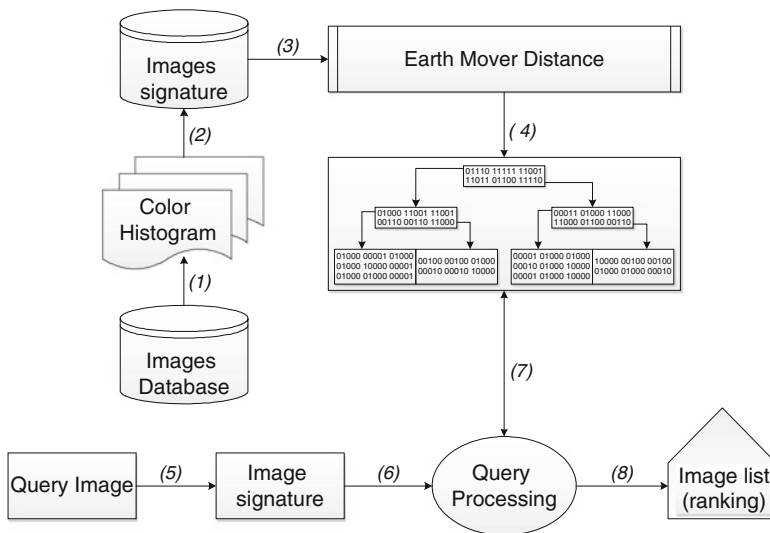
Fig. 1 Model image retrieval system

Fig. 2 A sample result of the process query image in image database over 10,000 images

4.2 The Experimental Results

Each image will calculate the color histogram based on 16 colors: black, silver, white, gray, red, orange, yellow, lime, green, turquoise, cyan, ocean, blue, violet, magenta, and raspberry (Figs. 2 and 3).
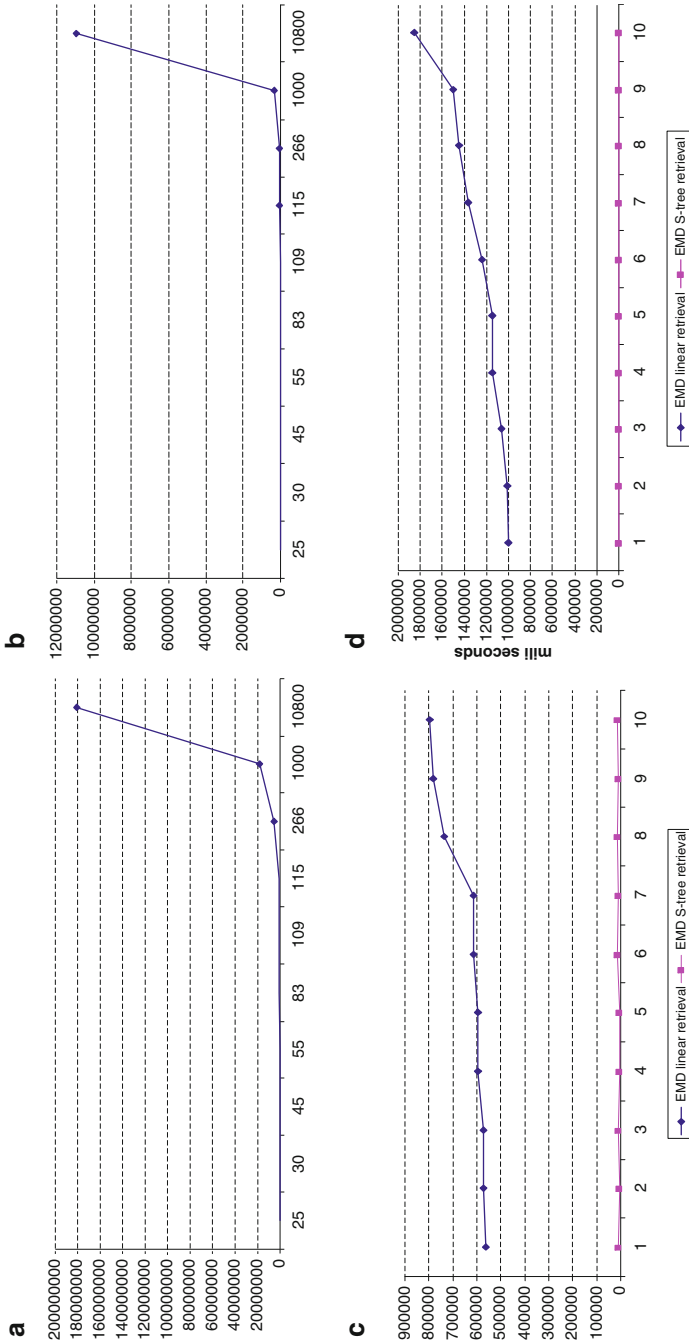
Fig. 3 (**a**) Number of comparisons to create S-tree. (**b**) The time to create S-tree. (**c**) Number of comparisons to query image in database over 10,000 images. (**d**) The time to query image in database over 10,000 images

5   Conclusion

This chapter creates algorithms in order to speed up the retrieval of similar images based on the image's binary signatures and then designs and implements the image retrieval model CBIR. As can be seen from the experiment, it takes a long time to create the S-tree from the image's binary signature, but the retrieval of the image that relies on the S-tree will be a lot faster than a linear search method based on EMD. However, using EMD to calculate the distribution of the image's colors will result in inaccuracy in the case of the images with the same percentage of color pixels, but the color distribution location does not correspond to each other. The next development will assess the similarity of the image through EMD distance with location distribution of the percentage of color pixels and compare the objects in the contents of the image to increase accuracy when querying the similar images.

References

1. Neetu Sharma S, Paresh Rawat S, Jaikaran Singh S (2011) Efficient CBIR using color histogram processing. Signal Image Process Int J 2(1):94–112
2. Nascimento MA, Tousidou E, Chitkara V, Manolopoulos Y (2002) Image indexing and retrieval using signature trees. Data Knowl Eng 43(1):57–77
3. Abuhaiba ISI, Salamah RAA (2012) Efficient global and region content based image retrieval. Int J ImageGraphics Signal Process 4(5):38–46
4. Yu J, Amores J, Sebe N, Radeva P, Tian Q (2008) Distance learning for similarity estimation. IEEE Trans Pattern Anal Mach Intell 30(3):451–462
5. Kavitha C, Babu Rao M, Prabhakara Rao B, Govardhan A (2011) Image retrieval based on local histogram and texture features. Int J Comput Sci Inf Technol 2(2):741–746
6. Rubner Y, Tomasi C, Guibas LJ (1998) A metric for distributions with applications to image databases. In: Proceedings of the IEEE international conference on computer vision, Bombay, India, 4–7 January 1998, pp 59–66
7. Abdelkhalak B, Zouaki H (2011) EMD similarity measure and metric access method using EMD lower bound. Int J Comput Sci Emerg Technol 2(6):323–332
8. Hurtut T, Gousseau Y (2008) Francis Schmitt: adaptive image retrieval based on the spatial organization of colors. Comput Vis Image Underst 112(2):101–113
9. Chen Y, Chen Y (2006) On the signature tree construction and analysis. IEEE Trans Knowl Data Eng 18:1207–1224
10. Konstantinidis K, Gasteratos A, Andreadis I (2005) Image retrieval based on fuzzy color histogram processing. Sci Direct Optics Commun 248(4–6):375–386

Tri-axis Accelerometer-Based Body Motion Detection System

Kang-Ming Chang, Sih-Huei Chen, and Chun-Lung Huang

Abstract Tri-axis accelerometers are widely used to detect physical activity. Three-axis accelerometers are sensing devices that measure gravitational changes. In this chapter, a body motion index was derived using an axis accelerometer with additional signal filtering and feature extraction. Various body motion factors, motion rates, motion angles, and directions were examined during an experiment. Six participants were recruited for this study. A TD1A system (K&Y Labs) was employed; this wireless system comprised one electrocardiogram (ECG) and tri-axis acceleration sensor. Using a belt, an amplifier was fixed to each participant in the same relative position between the abdomen and chest for each experimental measurement. The participants were instructed to move in both directions seven times for varying durations and at differing motion angles. Features were extracted from the motion index series. Both the mean and maximum values of the motion index series were used. The results showed that specific posture change patterns had corresponding axis acceleration variations. The influence of the motion angle on the motion index value was considerably greater than that of the motion rate. Higher motion angles were achieved with higher motion index values. Generally, anterior-posterior swaying caused greater motions than left-to-right swaying under the same motion conditions for angle and rate. Therefore, the proposed motion

K.-M. Chang (✉)
Department of Photonics and Communication Engineering, Asia University, Taichung, Taiwan

Graduate Institute of Clinical Medical Science, China Medical University, Taichung, Taiwan
e-mail: changkm@asia.edu.tw

S.-H. Chen
Department of Computer Science and Information Engineering, Asia University,
Taichung, Taiwan
e-mail: abbykayq@gmail.com

C.-L. Huang
Department of Mechanical and Automatic Engineering, Chung Chou University of Science
and Technology, Changhua, Taiwan
e-mail: clhuang@dragon.ccut.edu.tw

classification algorithm combined with a tri-axis accelerometer has significant potential for motion detection. However, the use of accelerometers has a number of limitations. In the future, a multi-sensor system will be employed to detect body movements.

Keywords Accelerometer • Body motion detection

1 Introduction

Accelerometers are low cost compared to other measurement systems [1, 2]. Tri-axis accelerometers contain a complementary metal-oxide semiconductor (CMOS) and measure the changes in capacitance caused by gravity. These gravitational changes are measured in three axes simultaneously and then reflected in output voltages. Tri-axis accelerometers are widely used to detect physical activity [3–5]. In this chapter, a body motion index was derived based on filtering and feature extraction.

2 Experiment

Six people participated in this study. These participants were required to abstain from consuming stimulating beverages, such as coffee and alcohol, during the day before the experiment. The participants recruited were college students. The experiment was conducted in a light and quiet environment. External noise was excluded to ensure the participants remained calm. A TD1A system (K&Y Labs) was employed because of its small size and reasonable cost. This wireless system comprised one ECG and tri-axis acceleration sensor. The acceleration specification was 0.73 G/cm, the size was 50*30*10 mm, and the weight was 11 g. The sampling frequency was 500 Hz. Using a belt, an amplifier was fixed to each participant in the same relative position between the abdomen and chest for each experimental measurement. The ECG measurements were performed using electrodes placed on the participants' left wrist and right ear bone. The analysis software used for coding was MATLAB®.

   The purpose of this experiment was to examine various body motion factors. The three factors investigated were the motion rate, motion angle, and direction. The participants were instructed to move in both directions (anterior-posterior and left-to-right) for varying durations (2, 3, 5, and 7 s) and at differing motion angles (10°, 15°, and 30°). The motion angle was marked on a board. The motion measurement process is shown in Fig. 1.
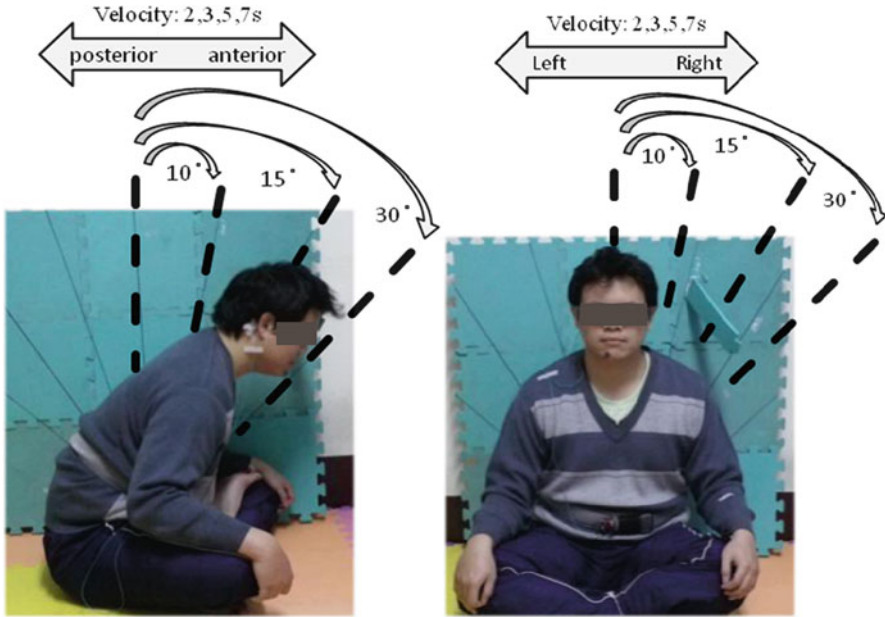
Fig. 1 Illustration of motion measurement environment

3 Motion Signal Analysis

Accelerometer data were transmitted wirelessly, saved on a host computer in text format, and then analyzed offline using an analysis program. The analysis process comprised several steps. The first step was raw data extraction, and the second step was preprocessing. By removing the DC component derived from the mode value of each axis, the motion index series was the sum of the square values for each axis. The final step involved extracting features from the motion index series. Both the mean and maximum values of the motion index series were used. The corresponding distribution percentage of each axis at the maximum point was also evaluated. Figure 2 shows the motion index estimation results, which indicate that the vibration period was significant.

4 Results

The motion index was defined as the square sum of the three axes' acceleration signals. Therefore, each axis contained major motion components. Specific posture change patterns had corresponding axis acceleration variations. The experiment results are listed in Table 1. The main motion axes of left-to-right swaying motion were the y- and z-axes, and the z-axis denoted anterior-posterior swaying motion. The influence of the motion angle on the motion index value was considerably
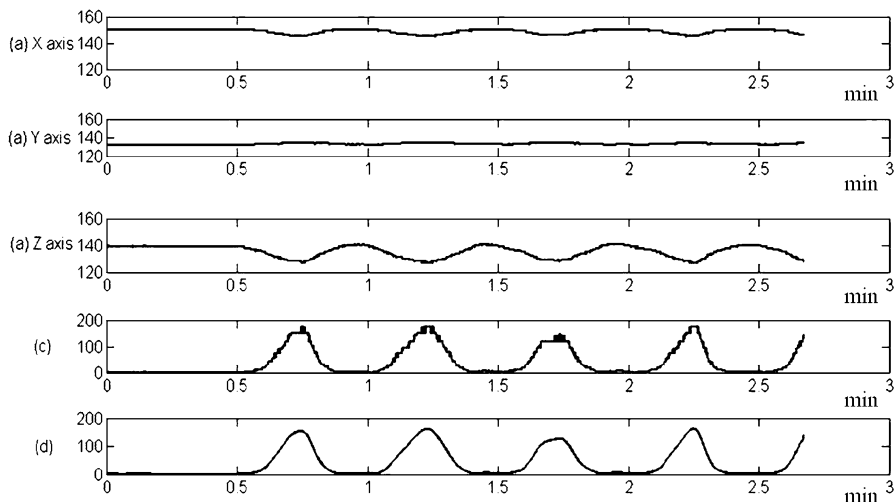
Fig. 2 Flowchart of motion index estimation. From top to bottom are tri-axis accelerometer signals, summation of square values of each axis. And final motion index series with smooth filtering

Table 1 Mean and maximum motion index of experiment 1c

Data	Mean motion	Max motion	X-axis % at max	Y-axis % at max	Z-axis % at max
A_10_2	1.05 ± 1.43	2.55 ± 3.37	0.20 ± 0.27	0.59 ± 0.38	0.21 ± 0.20
A_10_3	2.10 ± 2.46	3.88 ± 3.82	0.22 ± 0.40	0.53 ± 0.37	0.25 ± 0.26
A_10_5	1.43 ± 1.35	3.11 ± 2.11	0.03 ± 0.04	0.43 ± 0.17	0.54 ± 0.19
A_15_2	2.25 ± 2.24	4.78 ± 5.49	0.08 ± 0.15	0.54 ± 0.33	0.39 ± 0.31
A_15_3	2.95 ± 3.79	9.73 ± 16.85	0.15 ± 0.21	0.45 ± 0.35	0.41 ± 0.21
A_15_5	2.95 ± 1.66	10.85 ± 9.87	0.07 ± 0.14	0.59 ± 0.24	0.34 ± 0.18
A_30_3	14.10 ± 12.52	36.73 ± 31.12	0.19 ± 0.30	0.50 ± 0.25	0.31 ± 0.26
A_30_5	37.40 ± 53.05	63.0 ± 64.98	0.13 ± 0.18	0.57 ± 0.33	0.30 ± 0.36
A_30_7	16.45 ± 16.05	36.35 ± 36.62	0.12 ± 0.06	0.59 ± 0.38	0.29 ± 0.40
B_10_2	1.88 ± 1.30	4.43 ± 4.07	0.23 ± 0.20	0.13 ± 0.10	0.64 ± 0.18
B_10_3	2.95 ± 2.63	7.48 ± 6.59	0.13 ± 0.15	0.30 ± 0.29	0.57 ± 0.27
B_10_5	2.68 ± 2.54	6.21 ± 5.49	0.20 ± 0.22	0.04 ± 0.07	0.76 ± 0.26
B_15_2	3.01 ± 1.96	7.90 ± 5.26	0.10 ± 0.14	0.06 ± 0.06	0.84 ± 0.19
B_15_3	4.25 ± 2.54	11.88 ± 9.10	0.06 ± 0.08	0.04 ± 0.04	0.90 ± 0.07
B_15_5	4.26 ± 3.34	14.73 ± 10.0	0.05 ± 0.07	0.11 ± 0.20	0.84 ± 0.20
B_30_3	30.20 ± 21.24	112.73 ± 86.64	0.12 ± 0.05	0.18 ± 0.19	0.70 ± 0.19
B_30_5	37.61 ± 23.14	97.81 ± 68.40	0.07 ± 0.06	0.17 ± 0.19	0.76 ± 0.20
B_30_7	51.9 ± 25.94	107.4 ± 70.85	0.13 ± 0.13	0.16 ± 0.15	0.70 ± 0.25

First label is motion direction, the second is angle, and the third is sway number. For example, A_10_2 means left-to-right sway for seven times with 10° in 2 s

greater than that of the motion rate. Higher motion angles were achieved with higher motion index values. Generally, anterior-posterior swaying caused a greater motion than left-to-right swaying under the same motion conditions for angle and rate.

5 Discussion and Conclusion

The proposed motion classification method has a high application value. Considering the requirement of an economical and simple implementation process, wireless tri-axis accelerometers are an excellent choice. However, accelerometers have a number of limitations. Accelerometers should be mounted in the same orientation to retain the recorded data with concise directions on three axes. Local body movements caused by respiration may interfere with motion signals. For this experiment, wireless accelerometer sensors were fixed frontally between the participants' abdomen and chest. In the future, a multi-sensor system will be employed to detect body motion.

References

1. Farahmand F, Khadivi K, Rodrigues JJP (2009) Detecting intra-fraction motion in patients undergoing radiation treatment using a low-cost wireless accelerometer. Sensors 9:6715–6729
2. Betker AL, Moussavi ZM, Szturm T (2008) Ambulatory center of mass prediction using body accelerations and center of foot pressure. IEEE Trans Biomed Eng 55:2491–2498
3. Bouten CV, Koekkoek KT, Verduin M, Kodde R, Janssen JD (1997) A triaxial accelerometer and portable data processing unit for the assessment of daily physical activity. IEEE Trans Biomed Eng 44:136–147
4. Chang KM, Liu SH (2011) Wireless portable electrocardiogram and a tri-axis accelerometer implementation and application on sleep activity monitoring. Telemed J e-Health 17:177–184
5. van Hees VT, Renstrom F, Wright A, Gradmark A, Catt M, Chen KY, Lof M, Bluck L, Pomeroy J, Wareham NJ, Ekelund U, Brage S, Franks PW (2011) Estimation of daily energy expenditure in pregnant and non-pregnant women using a wrist-worn tri-axial accelerometer. PLoS One 6:e22922

On Mapping the Sorted-Set Intersection Problem onto a Graphics Processing Unit

Syun-Sheng Jhan, Liang-Tsung Huang, Lien-Fu Lai, Kai-Cheng Wei, Tsung-Yu Wei, and Chao-Chin Wu

Abstract The sorted-set intersection problem is important because it plays a key role in many algorithms. Instead of processing multiple short sorted-set intersections concurrently in previous work, this work focuses on how to efficiently find the intersection from two long sorted sets using emerging general-purpose graphics processing units (GPUs). We have implemented and evaluated four different algorithms to solve the set intersection problem. According to the experimental results, we identify which algorithm is the best choice based on the problem size.

Keywords Graphics processing unit • Set intersection • Parallel computing

1 Introduction

Sorted-set intersection is a crucial operation in the area of query processing such as databases and information retrieval. It accounts for a large fraction of the overall execution time for many algorithms, including inverted indexes in information retrieval, lists intersection in frequent-itemset mining, and merging of RID-lists in database query processing. In particular, major web search engines have to search billions of web pages for answering thousands of queries per second. Because the data sizes and query loads are growing at an exponential rate, how to

S.-S. Jhan
Department of Information Technology, Ling Tung University, Taichung City 409, Taiwan

L.-T. Huang
Department of Biotechnology, Mingdao University, Changhua 523, Taiwan

L.-F. Lai • K.-C. Wei • T.-Y. Wei • C.-C. Wu (✉)
Department of Computer Science and Information Engineering,
National Changhua University of Education, Changhua 500, Taiwan
e-mail: ccwu@cc.ncue.edu.tw

reduce query latencies becomes a key concern for these kinds of applications, making it very important to reduce the execution time of set intersection.

There has been a lot of research published with the goal of improving sorted-set intersection. Many approaches focus on speed up sequential intersection [1–6] by using efficient data structures or improved processing techniques. Some of them utilize modern hardware like multi-core CPUs [7, 8] and graphic processors (GPUs) [9–12] to exploit the thread-level and data-level parallelisms offered by these processors. In this work, we focused on how to efficiently map sorted-set intersection onto an NVIDIA GPU based on the observation that 3 out of top 5 supercomputers announced in the latest Top500 Supercomputers include NVIDIA GPUs in the systems. To fully exploit the computation capability of an NVIDIA GPU, we adopted the CUDA language to develop our proposed algorithms.

We implement four different approaches and compared their performances in this work. Experimental results give us an idea about which algorithm is the best choice when the problem size is given.

2   Related Work

Tsirogiannis et al. [8] studied lists intersection algorithms suitable for the characteristics of chip multiprocessors (CMP). They proposed a Dynamic Probes algorithm which takes advantage of multilevel cache hierarchies to reduce the overhead of random memory accesses. They also proposed a quantile-based algorithm that reduces the cost of intersection by a load-balancing algorithm. Ding and Konig [4] parallelized the lists intersection in their GPU search engine. They used the Parallel Merge Find algorithm to compute the intersection of k lists. This algorithm splits the lists into smaller segments and merges these smaller segments, respectively.

Wu et al. [11] have proposed an efficient GPU algorithm for high-performance intersection of inverted index lists. Their algorithm fed enough queries to GPU in batch, thus takes full advantage of GPU processor cores. They also proposed an input preprocessing method which alleviates load imbalance effectively. Instead using GPUs only, Wu et al. [12] later presented a CPU-GPU cooperative model which can dynamically switch between the asynchronous mode and the synchronous mode. In both modes, GPU plays an important role in efficient lists intersection. Note they focused on optimizing intersecting k ordered lists.

3   Four Algorithms

In this section we propose five algorithms for solving the sorted-set intersection problem. The two sorted sets are called Set A and Set B, respectively. The first algorithm is called *section-based search* (*SBS*). At first, Sets A and B are divided
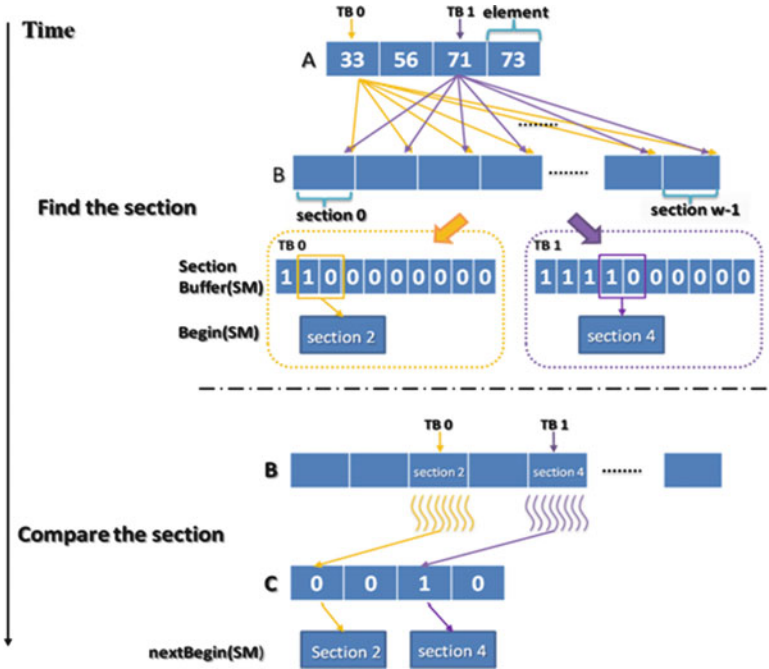
Fig. 1 An example for illustrating the section-based search algorithm

into T and W sections, respectively, where T is equal to the total number of thread blocks (TBs) and W is a user-defined parameter. Each TB will be responsible for one section of Set A. The elements in one section of Set A will be compared one by one from the beginning to the end by the responsible TB, and each run is for one element of Set A. The element in Set A to be compared with the elements in Set B in one run is called the target element. To reduce the total number of comparisons for each target element, we identify which section of Set B might contain the target element by comparing the target element with the last element in each section of Set B, which is called the candidate section. Next, we compare the target element with each element in this candidate section by a TB with many parallel threads. After an A element is compared, the beginning section of Set B to be searched for the next A element is the candidate section of Set B because the next A element is larger than or equal to the target element of Set A. Figure 1 shows an example, assuming there are two TBs.

The second algorithm is called *binary search* (*BiS*). In each run each thread in each TB will be assigned one element in A and uses binary search to determine whether the element is in Set B or not. After each run, the beginning element to be searched in the next run will be the one with the position that the last thread in the last TB identifies. In this way, the search space is reduced whenever a run is finished. For instance, assume Set A has 12 elements and each of the two TBs has two parallel threads, as shown in Fig. 2. In each run, four elements in A will be
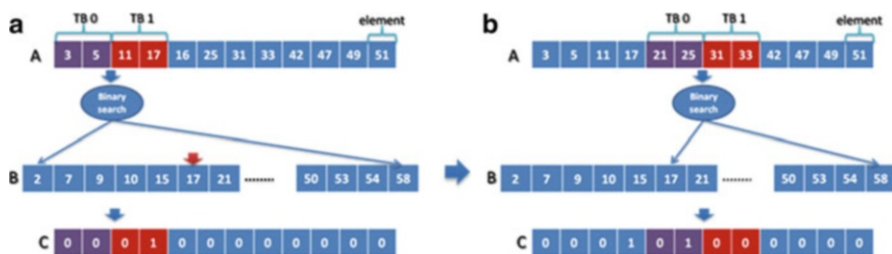
Fig. 2 An example for illustrating the binary search algorithm

searched in parallel. Each thread searches one element using binary search. In the end of the first run, the second thread of TB_1 will update the starting point to B [5] for the next run, as shown in Fig. 2a. In the second run, each thread will search from B [5], as shown in Fig. 2b.

In the third algorithm, called parallel-splitting search (PSS), we use binary search to partition Sets A and B into two smaller regions, respectively, after each run. Accordingly, each region of A will be contained in a region of B, thus reducing the search space gradually. At the beginning, the middle element in Set A is chosen to be searched among Set B, where Set B is divided into w equal-sized segments. One element in A is compared with the last element in each segment of Set B to determine which segment of Set B contains the element of A. After the segment of Set B is determined, we use binary search to find the element of A among the segment of Set B. Once the position of the target element of Set A is found, Set B is divided into two parts separated by the found position. In the next run, the elements on the left-hand side to the element of Set A will be searched among the left-hand side to the found position in Set B. Similarly, we use the same rule to process the elements on the right-hand side to the target element of Set A. The above procedure is repeated until all the elements in Set A are searched. Figure 3 demonstrates an example.

The fourth algorithm is called recursive binary search (RBS) [10]. The algorithm recursively finds the boundaries to be searched for a region of Set A. It consists of three steps. The first step divides Set A into equal-size regions and each TB is responsible for one region. Each region of Set A is divided into w sections further if there are w parallel threads in each TB. Each thread uses binary search to find the last element inside its assigned section among Set B and saves the result in the shared memory. Based on the search results of any two consecutive threads, we know the left and right boundaries of Set B to be searched for each section. The second step divides each section of A into two subsections, resulting in $2 \times w$ subsections. Each thread finds the last element in the first subsection among Set B according to the boundaries determined in the first step. The third step is to repeat the operations performed in the second step k times, where k is a user-defined parameter. Figure 4 shows an example.
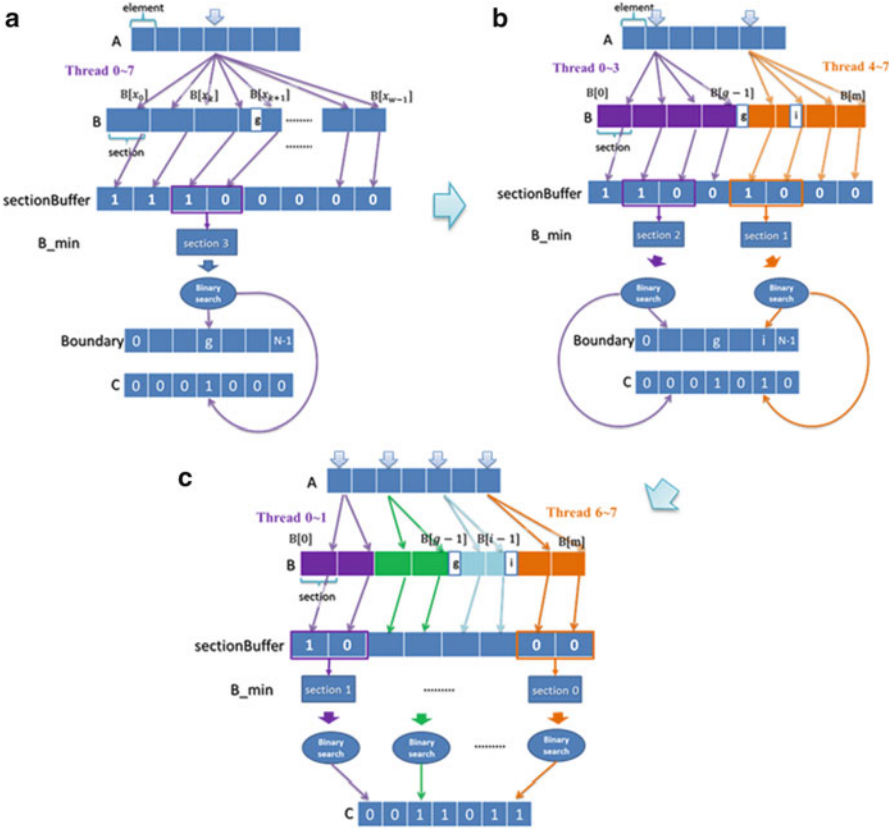
Fig. 3 An example for illustrating the parallel-splitting search algorithm

4 Performance Evaluations

We use CUDA version 3.2 to implement different algorithms for solving the optimal matrix parenthesization problem. The Dell Precision T5500 computer workstation is used as an experimental platform to evaluate our proposed algorithms, which consists of one Intel Xeon CPU and one NVIDIA Tesla C1060 GPU primarily. The compute capability of Tesla C1060 is 1.3. The operating system installed is Linux and its version is openSUSE 11.2 32-bit.

The experimental results are shown in Table 1. The SBS algorithm has poor scalability because the execution time increases significantly when the data size becomes larger. Similarly, the PSS algorithm cannot scale well even though it is better than SBS when the data size is large. The BiS algorithm is the best for most of the different data sizes. The BiS algorithm is worse than the RBS when the data size is 768,000 or 1,536,000. When the data size is large enough, it is worth finding more boundaries for smaller subsections and narrowing down the search space. However,

a

b
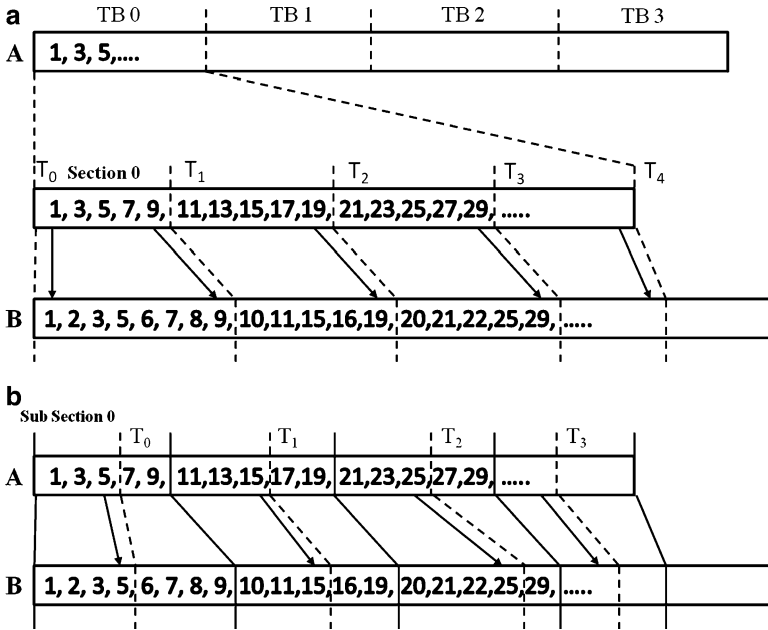
Fig. 4 An example for illustrating the recursive binary search algorithm

Table 1 Experimental results (ms)

Data size	3,000	6,000	12,000	24,000	48,000	96,000	192,000	384,000	768,000	1,536,000
SBS	59.42	59.33	60.32	62.86	65.95	74.57	93.49	147.98	328.40	823.90
BiS	**58.75**	**58.58**	59.41	58.67	**58.74**	**59.94**	**61.17**	**62.54**	65.19	71.14
PSS	59.93	59.63	60.08	62.00	64.01	67.90	77.29	94.13	128.70	199.93
RBS	58.84	58.63	**58.52**	58.53	59.45	60.14	61.23	62.83	**65.15**	**69.83**

if the data size is not large enough, it is better not to spend too much time in finding boundaries because the number of elements to be compared for each subsection is limited. However, RBS outperforms BiS for the cases of data sizes of 12,000 and 24,000 even though the data size is small. We are still trying to find the factors for them.

5 Conclusion

The inexpensive general-purpose GPUs give engineers a great choice to accelerate time-consuming applications. In this work, we discuss how to use an NVIDIA GPU to implement four different algorithms for solving the sorted-set intersection problem. In terms of the experimental results, we found that we should not spend

too much time in finding more boundaries for smaller sections of elements for small data sizes. However, it is better to recursively find the boundaries for each subsections if the data size is very large because it can guarantee the number of elements in a subsection is small enough.

References

1. Barbay J, Lopez-Ortiz A, Lu T (2006) Faster adaptive set intersections for text searching. In: WEA 2006. Springer, Berlin/New York, pp 146–157
2. Barbay J, Lopez-Ortiz A, Lu T, Salinger A (2010) An experimental investigation of set intersection algorithms for text searching. J Exp Algorithm 14(7):3.7–3.24
3. Demaine ED, Lopez-Ortiz A, Munro JI (2000) Adaptive set intersections, unions, and differences. In: SODA, Philadelphia, 2000, pp 743–752
4. Ding B, Konig AC (2011) Fast set intersection in memory. In: Proceeding of the VLDB Endow, Seattle, 2011, vol 4, pp 255–266
5. Hwang FK, Lin S (1972) A simple algorithm for merging two disjoint linearly-ordered sets. SIAM J Comput 1:31–39
6. Sanders P, Transier F (2007) Intersection in integer inverted indices. In: ALENEX. SIAM, Philadelphia, 2007
7. Tatikonda S, Junqueira F, Cambazoglu BB, Plachouras V (2009) On efficient posting list intersection with multicore processors. In: SIGIR '09, New York, 2009, pp 738–739
8. Tsirogiannis D, Guha S, Koudas N (2009) Improving the performance of list intersection. In: Proceedings of the VLDB Endow, Lyon, Aug 2009, vol 2, pp 838–849
9. Ao N, Zhang F, Wu D, Stones DS, Wang G, Liu X, Liu J, Lin S (2011) Efficient parallel lists intersection and index compression algorithms using graphics processing units. In: VLDB, Seattle, 5 Jan 2011
10. Ding S, He J, Yan H, Suel T (2008) Using graphics processors for high-performance IR query processing. In: WWW, New York, 2008, pp 1213–1214
11. Wu D, Zhang F, Ao N, Wang F, Liu X, Wang G (2009) A batched GPU algorithm for set intersection. In: Symposium on pervasive systems, algorithms, and networks, ISPAN '09, Washington, DC, 2009, pp 752–756
12. Wu D, Zhang F, Ao N, Wang G, Liu X, Liu J (2010) Efficient lists intersection by CPU-GPU cooperative computing. In: IPDPS workshops. IEEE, Atlanta, 2010, pp 1–8

A Novel Double Dynamic Stress Accelerated Degradation Test to Evaluate Power Fade of Batteries for Electric Vehicles

Yu-Chang Lin, Kuan-Jung Chung, and Chueh-Chien Hsiao

Abstract High-power lithium-ion batteries are being deployed in various transportation carriers such as hybrid, plug-in, or full electric vehicles recently. Power fade of lithium cells regarding temperature and charging and discharging rates are being the significant barrier that mitigates its widespread commercialization in the electric vehicle market. A novel double dynamic stress accelerated degradation test (D^2SADT) taking an advantage of closing the real driving conditions is developed to reduce the prediction error. The test contains two dynamic stress factors, temperature and cell charging and discharging currents, by which is implemented simultaneously. The test results show that the D^2SADT is capable of accelerating the battery degradation where the power of the test cell decreases near 10 % after 18 temperature cycles and 900 dynamic cell charging and discharging cycles. Compared to the traditional constant stress test, D^2SADT represents more realistic and efficient to evaluate the power fade of batteries used in the electric vehicles.

Keywords Accelerated degradation test • Power fade • Temperature cycling • Dynamic stress test

1 Introduction

The commercial market of lithium-ion batteries has been growing in these years due to their advantages of excellent energy density, long cycle life, and more safety for many applications, in particular portable electronic devices (phones, cameras, camcorders, laptops, etc.), hybrid/electric vehicles, and satellites. Battery power

Y.-C. Lin • K.-J. Chung (✉) • C.-C. Hsiao
Department of Mechatronics Engineering, National Changhua University
of Education, Changhua 50007, Taiwan
e-mail: kjchung@cc.ncue.edu.tw

fading, as usual, is the major concern of developing a high-performance electric vehicle since aging occurs when the cell is in charging-discharging cycles [1–3]. Many factors corresponding to the charging-discharging process, for instance, depth of discharge (DOD), state of charge (SOC), temperature, and charging-discharging rate, have been found to affect battery performance led by the degradation behavior of batteries. The mechanism of degradation can be divided by chemical and mechanical degradation. The former is caused by the formation of SEI (Solid Electrolyte Interface) films to impede deleterious degradation reactions within the cells; the latter is led by the cyclic expansion and contraction of insertion or alloy materials to induce cell cracking, fatigue, and structural distortion [4–7].

Many studies have been focused on the life prediction for the lithium-ion batteries. Ramadass et al. [8] developed a semiempirical prediction model to predict the capacity fade of Li-ion cells. Christensen and Newman [9] developed a model to simulate the influence of anode film resistance on charging/discharging process of a Li-ion battery, and then they were incorporated into the galvanostatic charging/discharging model previously developed by Doyle et al. [10]. Gang Ning et al. [11] developed a generalized first-principle-based charging/discharging model to simulate the cycle-life behavior of rechargeable Li-ion batteries. These models provide a scientific approach to predict the aging behavior of batteries, and some of them can be agreed by experimental data. However, traditional degradation tests to evaluate the battery power fade are based on the statistic charging-discharging process under a certain temperature that is far from the realistic situation, whereas the battery charging/discharging currents and temperature alter at all times when the electric vehicle is in use condition. An extra work has to be performed generally for modifying the prediction errors in order to match the real condition. Therefore, it increases the prediction complexity and cost.

In this study, a novel accelerated degradation test regarding double dynamic stresses, charging/discharging currents and temperature, is developed to approach the real condition of using the battery cells in the electric vehicles. The test is named D^2SADT. A great advantage of the new methodology is capable of implementing two dynamic stress factors simultaneously and one of the factors, temperature, is accelerated in advance to decrease the test duration dramatically. The test results demonstrate that D^2SADT has shorter test time than the traditional constant stress conditions of 1C/45°C in the ability of accessing a certain rate of battery power fading. It represents more realistic and efficient to evaluate the power fade of batteries in the electric vehicles.

2   Experiment Setup

Table 1 shows some significant specifications of devices under test (DUTs), a commercial high-capacity Li-ion battery usually used in the electrical vehicle. The whole system for D^2SADT, shown in Fig. 1, contains a thermal chamber, a battery test system, a data acquisition card (DAQ), and a PC with the controlled software (Labview).

Table 1 Certain specifications of the test vehicle

Cell brand and series #		Panasonic CGR-18650CH
Nominal voltage		3.6 V
Geometry		Cylinder
Weight		44 g
Nominal capacity[a]	Minimum	2,150 mAh
	Typical	2,250 mAh
Dimensions	Diameter × height	18.6 mm × 65.2 mm

[a]Charge: constant voltage/constant current, 4.2 V max. 1,500 mA, 110 mA cutoff
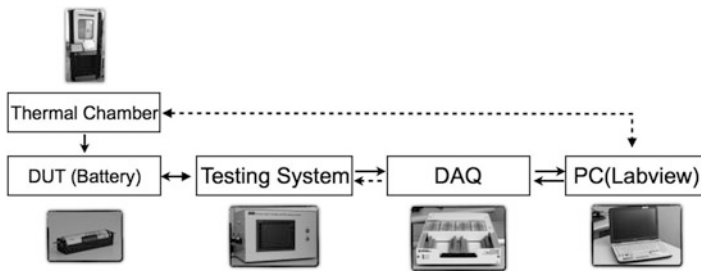
Fig. 1 The whole system for D^2SADT

The DUTs were housed in an environmentally controlled test chamber regarding temperature and humidity. The battery test system is capable of programming currents and time to pump/draw various currents to/from the cell and monitoring its terminal voltages as well as currents demand to perform the battery dynamic charge-discharge tests with cycling process. The software in PC simultaneously controls the test condition corresponding to thermal cycling and charging-discharging currents so that the DUTs are tested under various temperatures and charging-discharging currents in the same time, so-called double dynamic stress. The methodology is able to approach the realistic situation as batteries are used in electric vehicles.

Figure 2 shows the accelerated conditions of temperature cycling with dynamic stress charging-discharging tests (DSTs) for the battery degradation test. The temperature is from −15 to 45°C. There are three DSTs in a dwell time period and 2 DSTs in a ramp time duration so that a total of 10 DSTs are operated in a temperature cycling (two dwell times and two ramp times in a temperature cycle). On the other hand, Fig. 3 presents the DST profiles and Table 2 shows the test procedures. The total test time is 360 s, which is repeated end to end with no time delay between them. Prior to a fully charge, a battery was discharged by the DST power profile. Once the battery reached the cutoff condition or other criteria, the discharging process was terminated. Then the battery was charged immediately. Besides, a traditional constant charging/discharging stress test regarding a certain "C" rate and temperature combination was performed as a comparison test [14]. It represented to be 1C/45°C with the similar test conditions to D^2SADT.
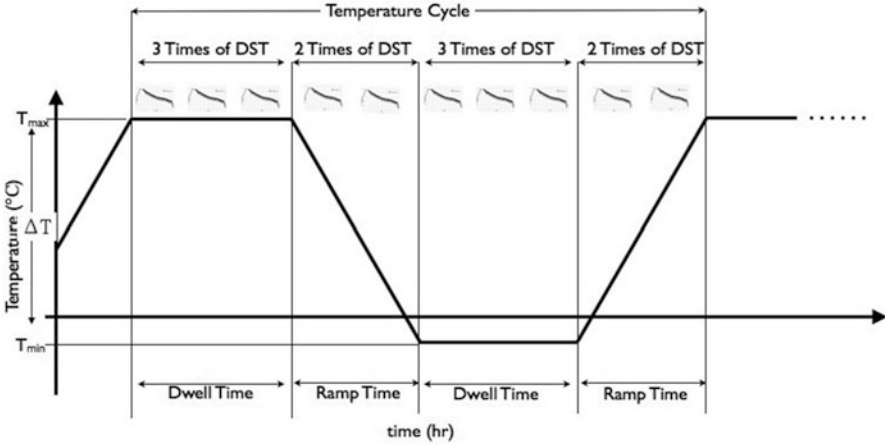
Fig. 2 The test conditions of D²SADT
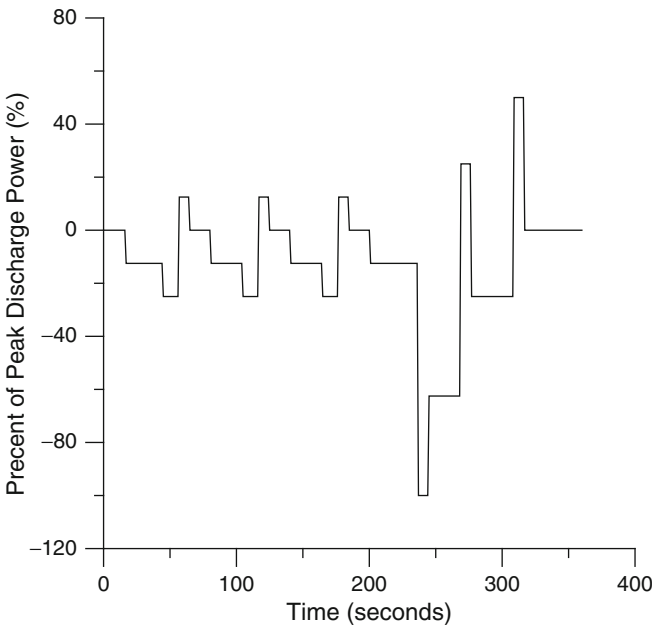
Fig. 3 DST profile

Further note, "1C" rate denotes a rate at which a fresh fully charged battery will be discharged to exhaustion in an hour at a specific temperature. Figure 4 presents the timing diagram of performing reference power test (RPT), which is applied to calculate the capacity of DUTs after certain temperature cycles and DSTs.

Table 2 DST test procedures

Step	Time (s)	%	Step	Time (s)	%
1	16	0	11	12	−25
2	28	−12.5	12	8	12.5
3	12	−25	13	16	0
4	8	12.5	14	36	−12.5
5	16	0	15	8	−100
6	24	−12.5	16	24	−62.5
7	12	−25	17	8	25
8	8	12.5	18	32	−25
9	16	0	19	8	50
10	24	−12.5	20	44	0
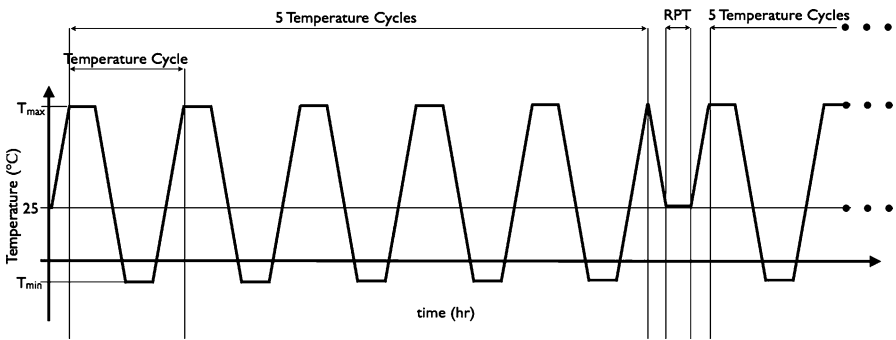
Fig. 4 Timing diagram of RPT

In this study, the RPT was performed when five temperature cycles had been finished each time. Further note, it has the same discharging rate currents with the constant stress test under the ambient temperature 25°C.

3 Results and Discussion

Figure 5 shows the RPT curves in various temperature cycles involving the discharging curve of a fresh battery (TC 0), which becomes an initial power without degradation. The discharging curve of performing 18 temperature cycling (TC 18) is obviously different from the curve of initial power (TC 0). Furthermore, the former represents a small area under the curve, where is the battery power (Ah) by calculating, to demonstrate that the power fade of the battery indeed exists after certain charging/discharging and temperature cycles. Table 3 presents the rate calculation of the battery power fade in various temperature cycles. The power fade (capacity loss) is defined by

Fig. 5 RPT curves in various temperature cycles
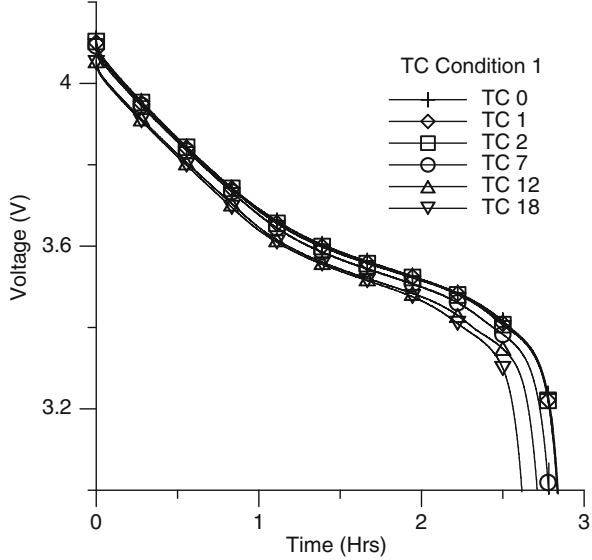
Table 3 The capacity calculation of the DUT in various temperature cycles

# of TC	Battery capacity (Ah)	Power fade (%)
0	2.137	0
1	2.135	0.09359
2	2.133	0.18718
7	2.090	2.19934
12	2.001	6.36406
18	**1.9344**	**9.48058**

$$\text{Power fade (\%)}$$
$$= \frac{|\text{The battery capacity of the nth temperature cycle} - \text{the initial battery capacity}|}{\text{The initial battery capacity}} \quad (1)$$

The battery capacity of TC 18 decreases about 9.5 % (power fade) compared to the initial capacity (TC 0). The test results demonstrate that the novel methodology is applicable of evaluating the battery power fade, and the aging phenomenon was found by observing the discharging curves in various temperature cycles. Furthermore, the calculation of battery power demonstrates that the capacity reduces when the cycles of the double stress factors increase. Figure 6 shows the comparison of the constant stress test and D²SADT. Compared to the traditional constant stress test done by our previous study [14], it is seen that D²SADT presents a dramatic decrease in the capacity loss along with the test duration (the constant stress test was terminated in the 35th days). The capacity losses of batteries in the D²SADT and the constant stress test are 5.2 and 0.13 %, respectively. Beyond the advantage of more realistic condition to test battery degradation for the electric vehicles, the novel D²SADT is more efficient than the constant stress test in evaluating the power fade of batteries.

Fig. 6 The comparison of constant stress test and D^{2}SADT
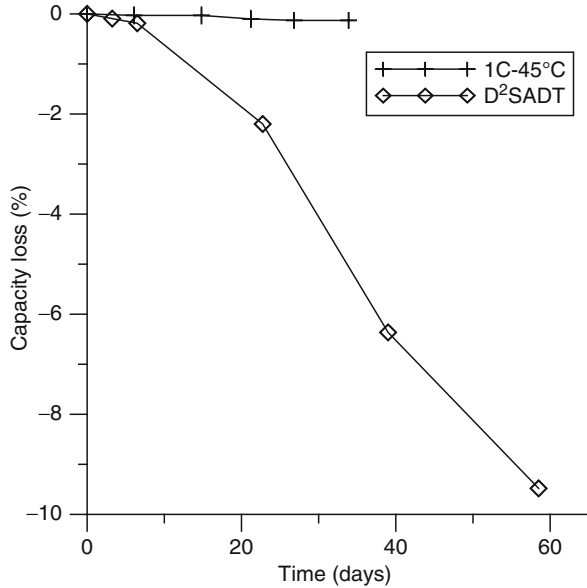
4 Conclusion

The novel D^{2}SADT involving two dynamic stress factors, charging/discharging currents and temperature, is successfully developed, and the degradation test was performed to validate its advantages. The test results represent that the novel methodology is applicable of evaluating the battery power fade, and the aging phenomenon was found by observing the discharging curves in various temperature cycles. The calculation of power fade demonstrates that the battery capacity dramatically decreases when the cycles of the double stress factors increase. Besides the advantage of more realistic condition of testing battery charging/discharging cycles in electric vehicles, the novel D^{2}SADT is more efficient than the traditional constant stress test in evaluating the power fade of batteries.

References

1. Kumaresan K, White R (2008) Parameter estimation and life modeling of lithium-ion cells. J Electrochem Soc 155(4):A345–A353
2. Thomas EV, Case H, Doughty D, Jungst R, Nagasubramanian G, Roth E (2003) Accelerated power degradation of Li-ion cells. J Power Source 124(1):254–260
3. Spotnitz R (2003) Simulation of capacity fade in lithium-ion batteries. J Power Source 113 (1):72–80
4. Ramadass P, Haran B, White RE, Popov BN (2003) Mathematical modeling of the capacity fade of Li-ion cells. J Power Source 123(2):230–240

5. Christensen J, Newman J (2003) Effect of anode film resistance on the charge/discharge capacity of a lithium-ion battery. J Electrochem Soc 150(11):A1416–A1420
6. Doyle M, Fuller TF, Newman J (1993) Modeling of galvanostatic charge and discharge of the lithium/polymer/insertion cell. J Electrochem Soc 140(6):1526–1533
7. Ning G, White R, Popov B (2006) A generalized cycle life model of rechargeable Li-ion batteries. Electrochim Acta 51(10):2012–2022
8. Tarascon J, Armand M (2001) Issues and challenges facing rechargeable lithium batteries. Nature 414:359–367
9. Ramadass P, Haran B, Gomadam P, White R, Popov B (2004) Development of first principles capacity fade model for Li-ion cells. J Electrochem Soc 151(2):A196–A203
10. Rong P, Pedram M (2006) An analytical model for predicting the remaining battery capacity of Lithium-ion batteries. IEEE Trans VLSI Syst 14(5):441–451
11. Oldham H, Myland J (1994) Fundamentals of electrochemical science. Academic, San Diego
12. Newman JS (1991) Electrochemical systems, 2nd edn. Prentice-Hall, Englewood Cliffs
13. Gu WB, Wang CY (2000) Thermal and electrochemical coupled modeling of a lithium-ion cell in lithium batteries. Proc ECS 99–25:748–762
14. Chueh-Chien Shiao, Kuan-Jung Chung (2012) Accelerated degradation assessment of 18650 Li-ion batteries. In: Proceedings of IEEE 2012 international symposium on computer, consumer, and control, Taichung, 4–6 June 2012, pp 930–933

The Development of Estimating Deviations Directly from Point Clouds

Cheng-Tiao Hsieh

Abstract A novel concept of computer graphics, point-based graphics, has grasped researchers' attentions in this decade. In 2000, the point rendering system QSplat was developed by a Stanford research team. It had successfully solved the rendering problem of point clouds. This has made point clouds very potential in 3D related computational applications, especially the applications in 3D scanning. For exploring advanced, possible, and practical applications of point clouds, this chapter proposed two methods for estimating deviations of two point clouds directly. The proposed methods are the Nearest Point method and the Neighborhood method. They were developed based on the Kd-tree structure and the concept of neighbor clusters. Those methods did not involve a complicated surface reconstruction, so they can be implemented to perform a virtual inspection efficiently.

Keywords Deviation estimation • Kd-tree • Point cloud library

1 Introduction

3D scanning technologies have been developed very successfully within this couple of decades. Their related applications have been widely applied in many areas such as industry, academics, and medicine. In 2009, author developed a digital face inspection for a dental application [1]. It was used to assist dentists to investigate the deviations of their patients' faces during an orthodontic treatment. This application has full functions and algorithms for a visual inspection. Its outputs provided dentists visual information to correct their treatments. Its

C.-T. Hsieh (✉)
Department of Industrial Design, Ming Chi University of Technology,
New Taipei City 24301, Taiwan
e-mail: cthsieh@mail.mcut.edu.tw
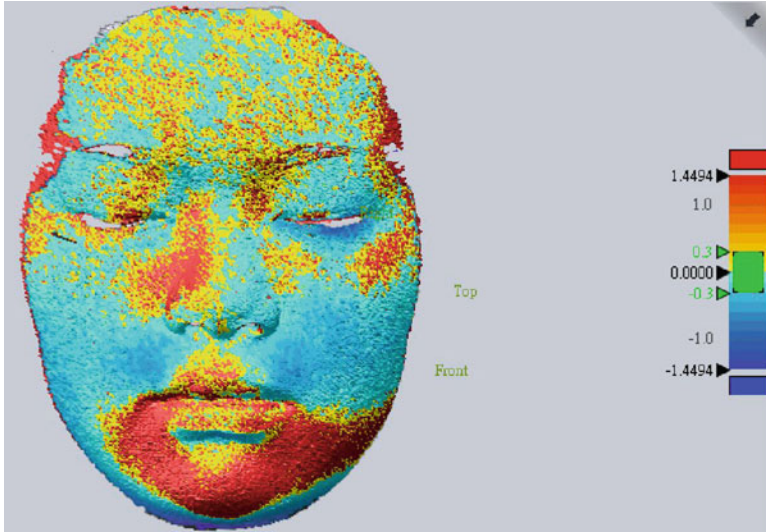
Fig. 1 The deviation estimation made by Rapidform

functions include surface registration, deviation estimation, and data visualization. The content of this chapter only includes a part of them, which is related of the deviation estimation. The entire computational procedure of a virtual inspection can be summarized in the following. In the first step, users utilized a 3D scanning device to capture patients' face shapes and saved them in a point cloud format. Two point clouds precisely described geometric shapes of patients' faces before/after an orthodontic treatment. Under a real scanning operation, two point clouds were captured under two independent scanning routines. This situation caused a well-known correspondence problem. For the event above, a correspondence registration was required before a deviation estimation [2]. In the first edition of our application, we attempted to avoid a complicated surface reconstruction. Therefore, our application only accepted an input with a specific format, i.e., STL. Most of reverse engineering (RE) and CAD software support an STL converter, such as *Rhino* and *Rapidform*. Most of raw data sets produced by 3D scanning systems are a set of unstructured point cloud [3]. Converting unstructured points to an STL format requires a complicated algorithm like the Delaunay triangulation method [4]. The algorithm is capable of constructing a triangle meshes perfectly fitted to point clouds. However, requiring extra software definitely consumes the cost of a virtual inspection. In this study, we proposed two methods for estimating deviations directly from two point clouds. The proposed methods will be described in later sections. Figure 1 shows a virtual inspection result that was created by a famous RE application, *Rapidform*. This result is the sample that was used to compare our results.
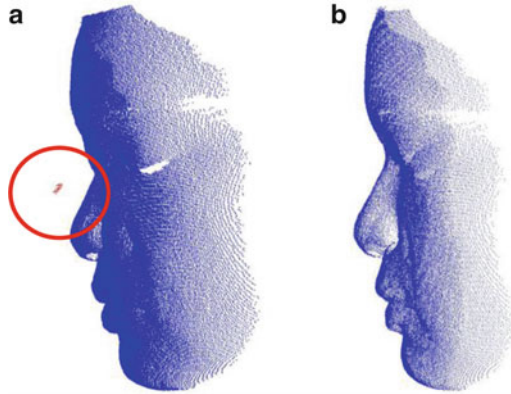
Fig. 2 (**a**) A point cloud with noisy points. (**b**) A new point cloud filtered by a statistical outlier removing process

2 Preprocess

Most of sources for obtaining point clouds are 3D scanners. There are many types of 3D scanning systems. They were developed with various scanning technologies used to capture surface information from physical objects, such as laser line scanning, structured lighting, and coordinate measuring machine (CMM). The sample point clouds we used in this study were generated by Vivid 910. The Vivid 910 is an optical scanner associated with a laser beam sectioning technology to capture surface information from an object. Because it utilized optical devices to capture surface information of target objects, it is hard to avoid scanning noises and errors. Especially, scanning errors always happen when a target object has black surface or locates in shaded area. Figure 2a shows our samples with noisy points. Noisy points were indicated by red color circles. Those noisy points absolutely affect the accuracy of deviation estimation. About this event, this study introduced a filter module of the PCL to detect and remove noisy points. The PCL is a well-known open source that has collected hundreds of computational processes and algorithms related to point cloud processing. It has a filter module which collected a lot of filters for handling outliers and noise points. The filter used in this study is a statistical outlier removal filter. Its filtering approach can be found in B. R. Rusu's dissertation [5].

3 The Nearest Point Method

3.1 Method Description

The Nearest Point method is a straightforward method for estimating the deviation directly from point clouds. Here, this chapter assumes that the deviation is the distance between a search point selected from one of the given clouds

and its correspondence point in the other cloud. This method also assumed that a search point and its correspondence point must have the smallest distance among its neighbor points. Its computational processes were summarized in the following. In the first step, this method arbitrarily selected one point from a point cloud, and the selected point was defined as a "search point." The cloud which a search point was selected from was defined as a "source cloud," and the other cloud was defined as a "target cloud." Once a search point is selected, an iterative loop including finding the nearest point and calculating a distance between two specific points will be started. The loop will be executed iteratively until all of points in source cloud had been selected as a search point. Obviously, the computational cost of this method is dependent on the size of source cloud. However, the size of our point cloud is always huge. For considering an efficient computation, this study implemented a Kd-tree structure to organize the data of a target cloud. It dramatically improves the searching ratio of a process in seeking the nearest point process. The Kd-tree is a well-known space partitioning data structure, and the description of its approach can be found in the reference [6]. A distance calculation follows behind after a particular nearest point is found. After all of required computations are completed, the estimated deviations will be visualized in color. This deviation visualization allows users to read and understand the deviation analysis easily and quickly. This visualization had been developed successfully by means of a visualization module of the PCL.

3.2 Discussion for the Nearest Point Method

Figure 3a shows the result estimated by the Nearest Point method. In this study, the point amounts of two sample point clouds are 61,670 and 60,115. From Fig. 3b, it clearly illustrated that 99 % of estimated deviations are distributed in the interval between −1.5 and +1.5. Regarding the above, this study assumed that the 1 % estimated deviations in outside of the interval were noisy points. For considering an accuracy estimation, those noisy points are needed to be removed. Thus, this study revaluated the deviations of noisy points up to the maximum (+1.5) or down to minimum (−1.5). Based on the setup above, the new result was generated as shown on Fig. 4. Since the range of a color bar was modified shorter, the visual feature of the deviations can be emphasized more clearly.
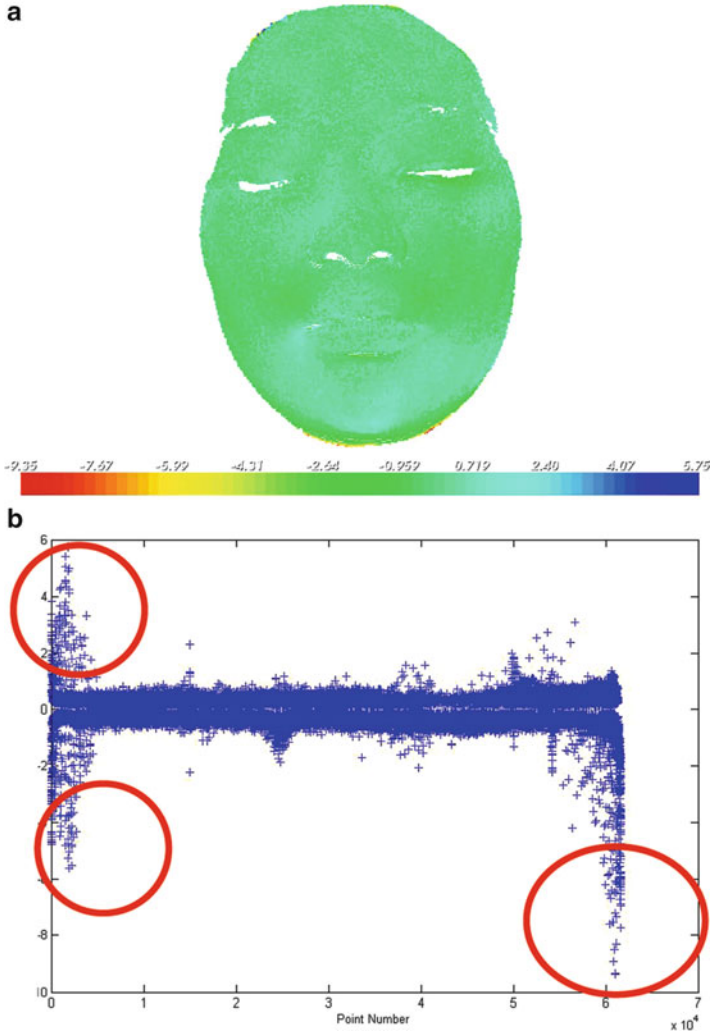
Fig. 3 (**a**) The deviations estimated by the Nearest Point method. (**b**) The deviation distribution in *XY* plot where the *X*-axis indicates the index of a point and the *Y*-axis indicates the deviation value
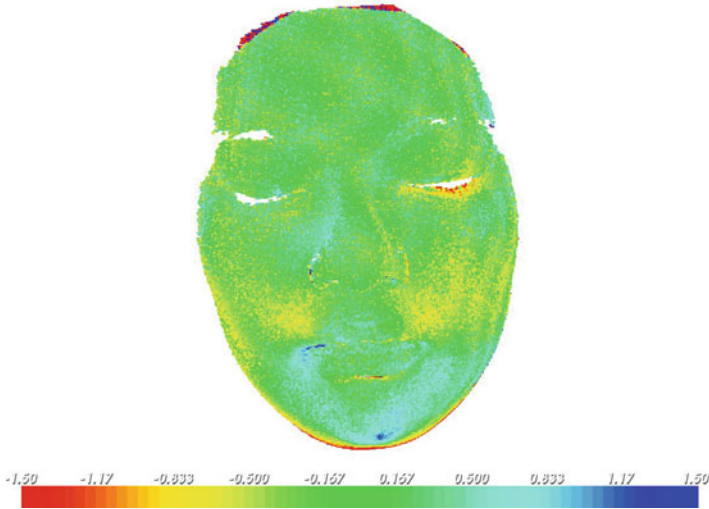
Fig. 4 The deviations for a specific interval between +1.5 and −1.5

4 The Neighborhood Method

4.1 Method Description

Actually, the Neighborhood method is an alternated Nearest Point method. Its approach is similar to that of the Nearest Point method. The Nearest Point method defined the nearest point of a search point as the correspondence point of a target cloud. But this method attempted to utilize a centroid of neighbor point cluster to replace the nearest point. In the first step, a parameter K must be identified and its value determines the amount of the neighbor points which are used to define a centroid. For considering an efficient computation, a Kd-tree data structure was also applied to organize the data of a target cloud. In this study, we set up the parameter K to 20. The value of the parameter K is sensitive to the efficiency and accuracy of this proposed method. Thus, this parameter is needed to be determined appropriately. This method had also been developed by the PCL.

4.2 Discussion for the Neighborhood Method

The deviations shown on Fig. 5a were estimated by the Neighborhood method with $K = 20$. The XY plot shown on Fig. 5b illustrates the distribution of the deviations. From the figures above, the maximum deviation is 6.602 and the minimum deviation is −11.775. Comparing the result of the Nearest Point method, the range
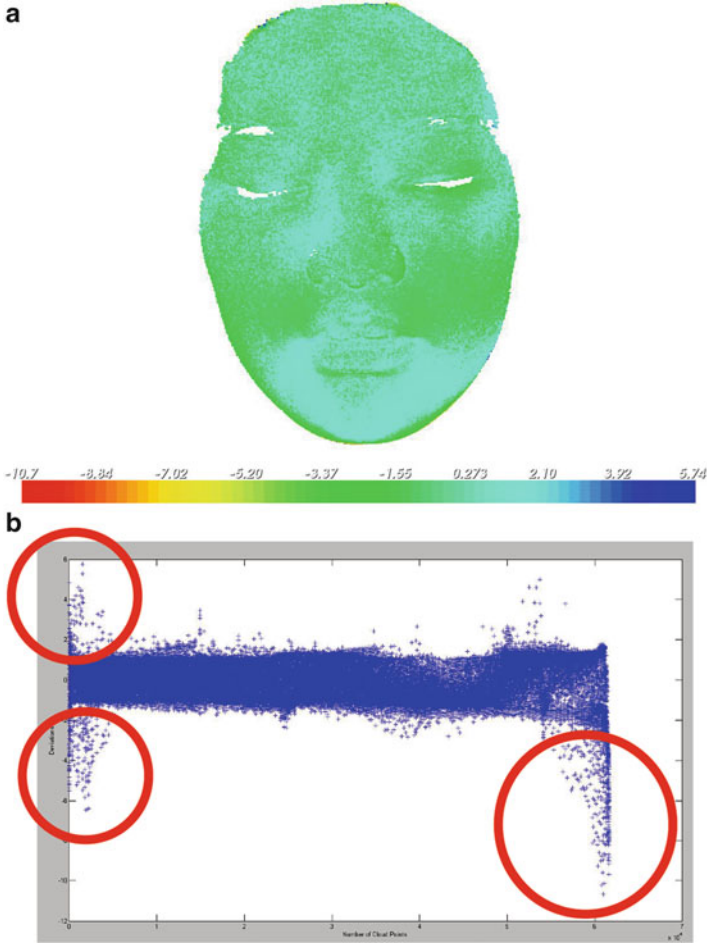
Fig. 5 (**a**) The deviations estimated by the Neighborhood method. (**b**) The deviation distribution presented in *XY* plot where the *X*-axis indicates the index of a point and the *Y*-axis indicates the deviation value

between the maximum and minimum was amplified. If it is required to have an interval the same as that on Sect. 3.2, then the amount of noisy points will be increased up to 2,722 (about 4.5 % of point cloud). For keeping the amount of noisy points less than 1 % of source cloud, an interval between −2.5 and +2.5 was used in this method. Based on the interval above, the amount of noisy points was reduced down to 694. Figure 6 shows the new result visually. Comparing to the result on Fig. 4, the new result is more similar to the result generated by Rapidform.
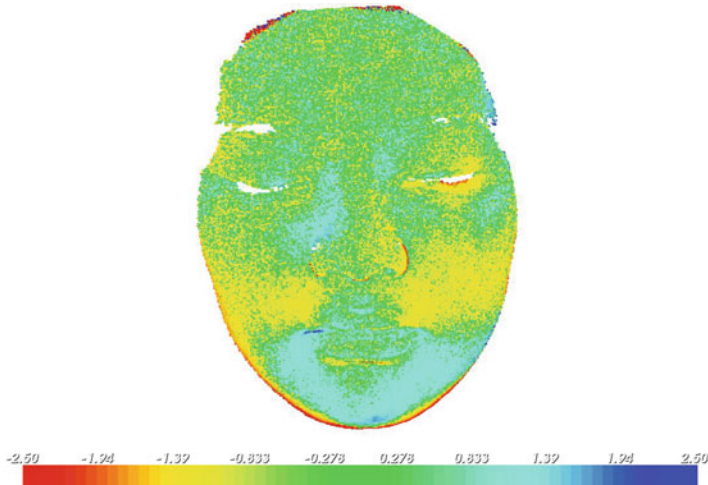
Fig. 6 The deviations ranged on the specific interval between +2.5 and −2.5

5   Conclusion

This chapter proposed two different methods for estimating deviations between two point clouds directly. Those methods had been developed successfully by the PCL. About an efficiency issue, a Kd-tree structure was implemented in both methods. Comparing to the Neighborhood method, the Nearest Point method is an efficient method. But unfortunately its result is less accurate than that of the Neighborhood method. Regarding users' requirement, users can select their appropriate method based on their needs to estimate deviations directly from two given point clouds.

References

1. Hsieh C-T (2009) Developing the digital face inspection application in VTK. In: International conference on manufacturing and engineering system. National Formosa University, Taiwan, 2009
2. Besl PJ, McKay ND (1992) A method for registration of 3-D shapes. IEEE Trans Pattern Anal Mach Intell 14(2):239–256
3. Varady T, Martin RR, Cox J (1997) Reverse engineering of geometric models – an introduction. Comput-Aided Des 29(4):255–268

4. Borouchaki H et al (1995) Reasonably efficient Delaunay based mesh generator in 3 dimensions. INRIA, Paris
5. Rusu RB (2009) Semantic 3D object maps for everyday manipulation in human living environments
6. Berg MD et al (1999) Computational geometry – algorithms and applications. Springer, Heidelberg

Using Modified Digital Halftoning Technique to Design Invisible 2D Barcode by Infrared Detection

Hsi-Chun Wang, Ya-Wen Cheng, Wan-Chi Huang, Chia-Long Chang, and Shih-Yun Lu

Abstract 2D barcode is an important interface to connect physical environment with virtual (digital) world. It is commonly presented at printing substrates whose embedded information can be captured through optical recognition system. Yet, for human perception, the black-and-white barcode is not only meaningless but also aesthetically displeasing. Therefore, this study utilized a modified digital halftoning technique to make 2D barcode invisible under normal reading condition; however, it can still be detected by infrared devices. The research composes halftone dots of both amplitude modulation (AM) and frequency modulation (FM) to create an infrared watermark due to the different absorption properties between K (black) ink and CMY (cyan, magenta, and yellow) inks under infrared light. The results show that the proposed method successfully avoids 2D barcode distracting people from normal reading. The method conforms to the existing printing process without requiring any special inks or materials. In the future, the technique can be applied to product packaging and brand protection.

Keywords Halftoning • 2D barcode • Infrared

1 Introduction

2D barcode has already been widely applied to our daily life. It is an important interface connecting physical environment with virtual (digital) world. Compared with 1D barcode, 2D barcode stores more information like texts, forms, and images. So far, it is mostly presented at printed paper or other substrates whose embedded information can be captured through optical recognition system, such as mobile

H.-C. Wang (✉) • Y.-W. Cheng • W.-C. Huang • C.-L. Chang • S.-Y. Lu
Department of Graphic Arts and Communications College of Technology,
National Taiwan Normal University, Taipei 10610, Taiwan
e-mail: hsiwang@ntnu.edu.tw

phones with built-in camera and webcams of notebooks or desktop computers. However, the black-and-white barcode is not only meaningless for human reading but also aesthetically displeasing. The occupied space often causes the inconvenience of graphic designing. Therefore, this study develops a data-hiding technique to make 2D barcode invisible under human perception; however, it can still be captured and detected by infrared devices.

With the progress of digital technology, copyright protection has become a significant issue. Therefore, many researchers have dedicated their efforts to data-hiding/watermarking techniques for audio, image, video, and other digital media. This kind of digital watermark can be directly input and recognized via computers. However, for the watermark existing on printed substrate, the encoding/decoding effectiveness involves more complex variables than that for digital media contents. Thus, the data-hiding techniques for printed documents remain an active topic for further research and development. MIT media lab once proposed the use of patchwork to embed data [1]. In Xerox, the displaced halftone dots are printed on both sides of the paper, whose embedded information can be perceived when the paper is held up against a light [2]. In other researches, the halftone dots are displaced to encrypt the embedded data, which can be decrypted through lenticular lens [3, 4]. Other researcher arranged halftone dots in an oblique manner to embed the information [5]. Most of the methods described above are using AM-based halftone dots for data encryption. In addition, there are also some data-hiding techniques proposed by utilizing FM halftone dots [6]. Our research team once presented a novel AM/FM hybrid halftone dot encoding technique to construct watermark [7]. In this research, this technique is further extended to use modified digital halftoning method with more inks, and the hidden 2D barcode pattern can be detected under infrared light.

2 Halftoning

Halftoning technique was first proposed by Frederic E. Ives at Cornell University in the nineteenth century. Since the output device can reproduce the image by limited tones, the continuous tone image has to be binarized before it is actually output. This process is called halftoning. Traditional halftoning technique utilizes a halftoning screen to transform continuous tone images into binary ones. With the rapid innovation of digital technology, digital halftoning has been widely adopted by printing industry. There are two major categories of digital halftoning technique. One is amplitude modulation (AM) and the other is frequency modulation (FM). The typical output images can be shown in Fig. 1.
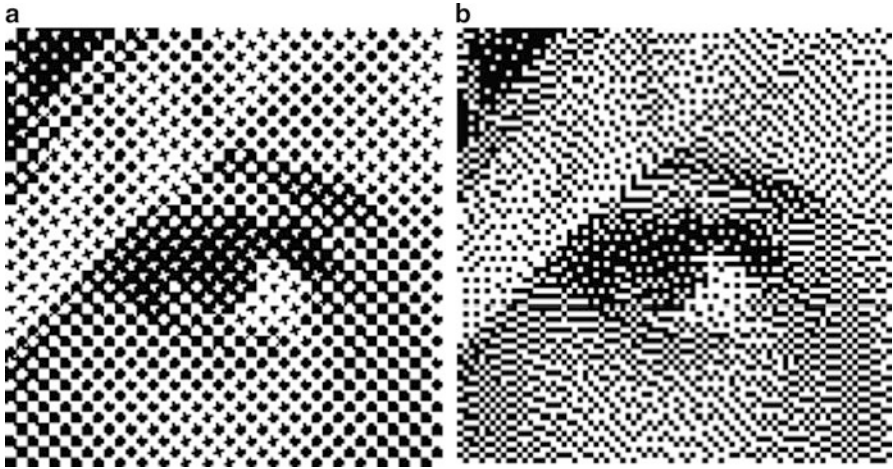
Fig. 1 Two typical halftone images by amplitude modulation (AM) and frequency modulation (FM). (**a**) AM halftone image generated by ordered dithering and (**b**) FM halftone image generated by error diffusion

2.1 Amplitude Modulation (AM)

The halftone images, constituting of AM halftone dots, simulate the continuous tone through the varied sizes of halftone dots. The spacing between each dot is fixed. Ordered dithering [8] uses a threshold matrix (8×8 as its typical size) to binarize the input continuous tone image into an AM halftone image. The values in the threshold matrix affect the dot shapes and the screen angle, while the size of the matrix and the DPI (dot per inch) of output device influence the LPI (line per inch) of output halftone images. For a grayscale image, $G(i,j)$, it uses Eq. (1) to convert its original grayscale value into value $X(m,n)$. N_1 and N_2 represent the length and the width of the threshold matrix $T(i,j)$.

$$X(m, n) = N_1 \times N_2 \times \left(1 - \frac{G(i,j)}{255}\right) \tag{1}$$

Equation (2) is applied to accomplish binarization, in which $H(i,j)$ denotes the converted value of output binary image and $T(i,j)$ indicates the values within the threshold matrix. Here, 1s (true) represent black pixels, while 0s (false) represent the white ones.

$$H(i,j) = \begin{cases} 1 \\ 0 \end{cases} \text{ when } \begin{matrix} X(m,n) \geq T(i,j) \\ X(m,n) < T(i,j) \end{matrix} \tag{2}$$
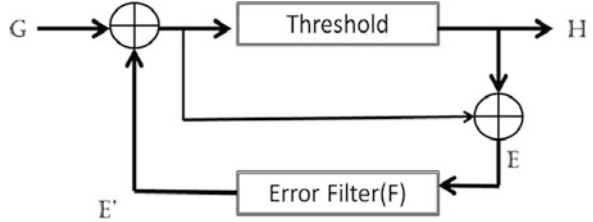
2.2 Frequency Modulation (FM)

FM halftone dots stay the same size and use different spacing between each dot to perform the tone of an image. Error diffusion, first proposed by Floyd and Steinberg [9], is the typical algorithm to generate FM halftone image. It converts a continuous tone image into a binary image and distributes the error, caused by the quantization, to neighboring pixels that have not yet been processed. The algorithm framework is shown in Fig. 2. After inputting the grayscale value of the continuous tone image G and comparing them with the threshold values T, the binary value H (by Eq. 3) and error E will be obtained. Then spread the error over neighboring pixel E' to complete quantization of that pixel. The process will be sustained until the binarizations of all pixels within the entire image have been done.

$$H(i,j) = \begin{cases} 1 \\ 0 \end{cases} \quad \text{when} \quad \begin{array}{l} G(i,j) \geq T \\ G(i,j) < T \end{array} \tag{3}$$

When each pixel has been compared with the threshold and already been decided to be black or white, the quantization error must be propagated based on the weightings through Eq. (4). The pixels are the basic units of the received halftone dots; therefore, the output images will be more delicate than using order dithering in AM.

$$\frac{1}{16} \begin{bmatrix} 0 & 0 & 0 \\ 0 & -16 & 7 \\ 3 & 5 & 1 \end{bmatrix} \tag{4}$$

3 The Optical Properties of Inks Under Infrared Light

Visible light refers to a certain section within the electromagnetic spectrum that human eyes can perceive, which generally corresponds to a wavelength (λ) range of 380–780 nm. In addition, the wavelength range between 0.78 and 1,000 μm is typically regarded as infrared range, which can be divided into three major regions: (a) near-infrared region ($\lambda = 0.78$–3 μm), (b) middle-infrared region ($\lambda = 3$–20μm), and (c) far-infrared region ($\lambda = 20$–1,000 μm). The near-, middle-, and far-infrared
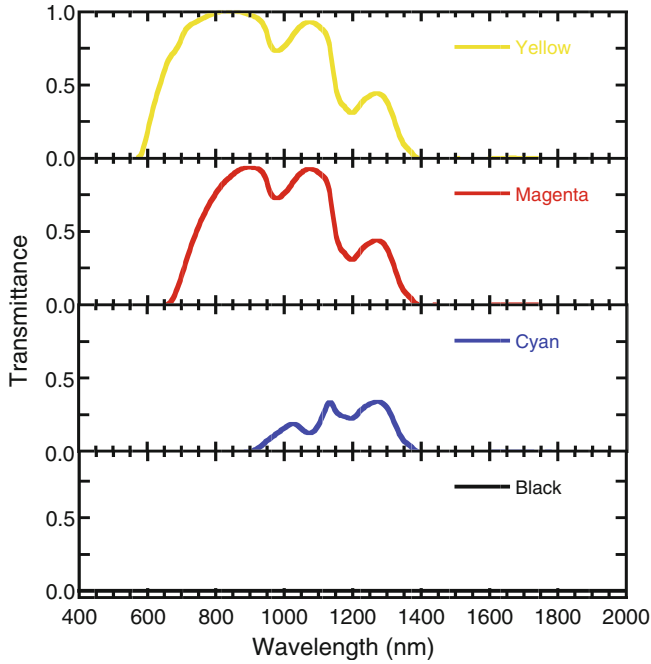
Fig. 3 The transmission percentage for each ink

regions that are mentioned above are defined by their distances with visible light region within the electromagnetic spectrum, in which near-infrared region is the closest of all. When the wave passes through an object, the energy will be transmitted to the object, causing the decline of the amplitude. If there is only a small part of energy that has been absorbed, the object will be seen as transparency to the radiation. By contrast, the object will be seen as opaque if most of the energy has been absorbed. Objects are selective in their absorption of light wavelengths, which means that they only absorb the radiation of certain wavelengths.

Most of the printers use inks of cyan (C), magenta (M), yellow (Y), and black (K) for color printing. Due to the fact that carbon black only exists in K ink, it shows greater absorption under near-infrared region. Although CMY inks have certain transmission percentage, all of them present certain extents of transparency under infrared detection (shown in Fig. 3). These diverse optical properties are utilized in this research to create the hidden watermark of 2D barcodes.

4 The Designing of Hidden Infrared Watermarks

This research adopts both AM and FM halftone dots to create watermark with 2D barcode pattern. In order to maintain neutral gray among AM/FM dots, the hidden watermark is coordinated with the pattern which is printed by carbon black ink and

Fig. 4 The density calibration chart with 3 % AM halftone dots (in K) and varied grayscale values of FM halftone dots (in YMC)

the remaining area which are printed by CMY inks. Then a density calibration chart is designed to match 3 % (dot area percentage) AM halftone dots (in K) in the foreground square shape with different grayscale values of FM halftone dots (in YMC) in the background, as shown in Fig. 4. The selected parameters are used as printer output. After comparing with the calibration chart, it is discovered that neutral gray between grayscale values 210–215 displays the slightest differences with 3 % halftone dots of K ink, which are the proper parameters to design hidden 2D barcode watermarks. The infrared watermark presents a consistent tone under normal light. However, the hidden 2D barcode image can still be detected and captured by the infrared webcam successfully.

In this study, a personal identity card is adopted as one of the examples. Observing by human eyes, the identity card still presents a consistent tone under normal light. Yet, observing by infrared detection with a CMOS camera, it can be obviously discovered that the pattern which is composed of K ink halftone dots presents opaque, while the neutral gray, combining with CMY inks as well as the cover image, is almost transparent, as shown in Fig. 5. The research applies the technique to a simulated 2010 Wimbledon quarterfinalist Yen-hsun Lu's player card. In Fig. 6, human eyes cannot perceive the 2D barcode under normal light. Therefore, the aesthetic design will not be affected. Under infrared light, the 2D barcode can still be recognized to enhance the functions and anticounterfeiting feature of player cards.
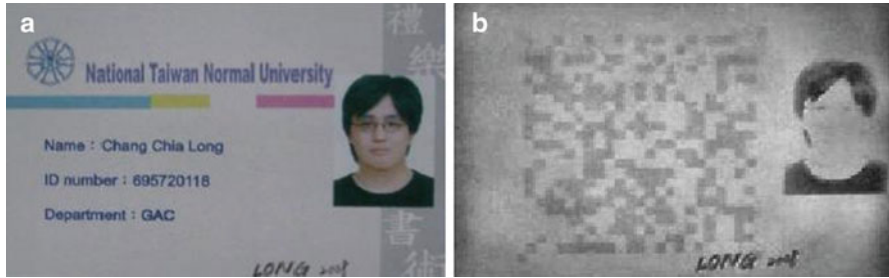
Fig. 5 The identity card contains the infrared watermark of 2D barcode. The image under (**a**) normal light and (**b**) infrared detection
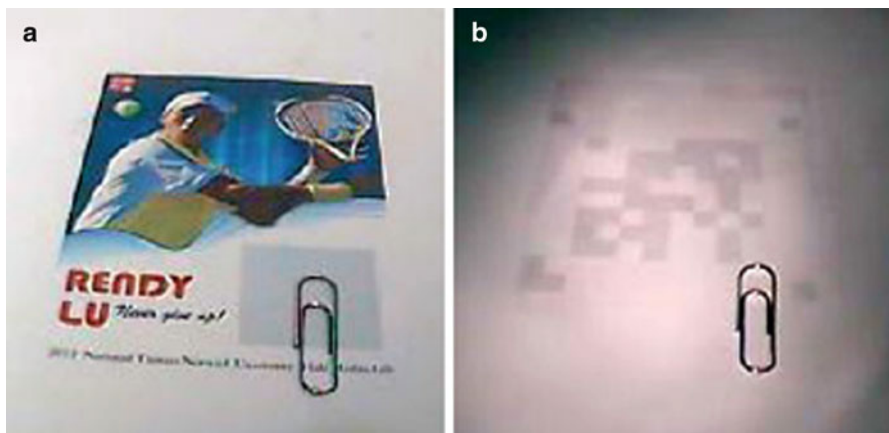
Fig. 6 The player card contains the infrared watermark of 2D barcode. The image under (**a**) normal light and (**b**) infrared detection

5   Conclusions

This research utilizes a modified digital halftoning technique as well as the varied optical properties of ink materials to create invisible 2D barcodes, whose embedded data can still be captured and detected by different light sources. The proposed method changes the way of displaying barcodes and allows them to fit in people's daily life with a more natural way. The results show that the invisible 2D barcodes can successfully be recognized by infrared detection to prove the feasibility of this method. In the research, we also apply this data-hiding technique to the designing of personal identity card and player card. Due to the fact that 2D barcode decoding technique has been quite matured already, in the future, the proposed method can be extended to other commercial 2D barcode specifications, such as QR code and DataMatrix, to enhance the packaging design and brand protection.

References

1. Bender W, Gruhl D, Morimoto N, Lu A (1996) Techniques for data hiding. IBM Syst J 35 (3&4):313–336
2. Sharma G, Wang SG (2004) Show-through watermarking of duplex printed documents. In: Proceedings of SPIE: security, steganography, and watermarking of multimedia contents VI, San Jose, 18–22 Jan 2004, vol 5306, pp 670–684
3. Huang S, Wu JK (2007) Optical watermarking for printed document authentication. IEEE Trans Inf Forensic Secur 2(2):164–173
4. Alasia AV (1976) Process of coding indicia and product produced thereby. United States Patent No. 3,937,565
5. Hecht DL (2001) Printed embedded data graphical user interfaces. IEEE Comput 34(3):47–55
6. Fu MS, Au OC (2002) Data hiding watermarking for halftone images. IEEE Trans Image Process 11(4):477–484
7. Wang HC, Hsiao PC, Lien CM (2009) Method of watermark with hybrid halftone dots. United States Patent No. 7,554,699
8. Ulichney R (1987) Digital halftoning. MIT Press, Cambridge
9. Floyd RW, Steinberg L (1976) An adaptive algorithm for spatial grayscale. Proc Soc Inf Disp 17 (2):75–77

Color Visual Evoked Potential Response for Myopia Subjects

Kang-Ming Chang, Chung-Yi Tsai, and Sih-Huei Chen

Abstract Visual evoked potential (VEP) by checkerboard stimulation with red, green, and blue color for myopia subject was investigated. There are 10 subjects involved. The average VEP pattern derived from 100 times stimulation showed that peak N2 latency and peaks P1 and P2 amplitude had significant variation among three colors. There was higher P2 amplitude response by red color than the other two colors. Myopia subjects without glasses had higher P1 and P2 amplitude response for green color.

Keywords Visual evoked potential • Color • Myopia

1 Introduction

Visual evoked potential (VEP) is often used to study visual processing mechanism under different physiological and psychological condition. Visual pathway under maturation and aging is also deeply investigated [1]. Different color stimulation had different response that is also proved as age-dependent changes during the school-age period [2–4]. Different stimulation pattern also had effects on VEP pattern. For example, there is major VEP pattern on P100 and N145 peaks with checkerboard pattern [5]. Stimulation strength is also affected for VEP. Myopia subject without glasses was a suitable model to examine this phenomenon. Previous study had been

K.-M. Chang (✉)
Department of Photonics and Communication Engineering, Asia University, Taichung, Taiwan
e-mail: changkm@asia.edu.tw

C.-Y. Tsai
Department of Digital Media Design, Asia University, Taichung, Taiwan

S.-H. Chen
Department of Computer Science and Information Engineering, Asia University, Taichung, Taiwan

investigated in the relation of binocular interaction with VEP [6]. This interesting study will investigate the basic VEP performance for three fundamental colors, red, green, and blue by checkerboard stimulation. Color areas were also important factor to be investigated. Color VEP response was also further applied for myopia subject.

2   Method

2.1   Subjects and EEG Recording

There were 10 volunteers mainly college students enrolled, 7 males and 3 females, age ranges 18–25 (mean age 22.4 and std 3.1). Subjects were all myopia patients. Subjects were sitting in a chair with comfortable posture. The EEG data was recorded in Asia University, Taiwan, by 32 channels SynAmps system produced by NeuroScan Inc. EEG data was recorded via unipolar connection, with Fpz as ground and A1/A2 as reference points. EEG channel impedance was adjusted until below 5 kΩ. A band-pass filter with 0.05–50 Hz was applied during recording. Sampling frequency was 1,000 Hz.

2.2   Experiment Procedures and Analysis

Experiment procedure was explained and under consent to each subject. There were 12 sessions in this study. The first nine sessions were applied to each subject with the aid of glasses. There are three colors combining with three check areas as experiment factors. Three colors are red, green, and blue. Three checkerboard areas are $5° \times 5°$, $10° \times 10°$, and $15° \times 15°$. Each session repeated 100 times with random color/area sequences. There was 50 s resting between each session. The other three sessions was with three colors by $15° \times 15°$ area checkerboard without the aid of glasses. Further VEP data was derived from Oz electrode by average of 100 times flash. There are four peaks used in the following analysis: N1, P1, N2, and P2. One-way ANOVA analysis was used to examine color and area size effect. Paired t-test was used to test the VEP difference for the same subjects with and without glasses.

3   Result

Grand average VEP responses for red, green, and blue stimulation of each checkerboard areas were illustrated in Fig. 1a–c. The corresponding VEP peak and latency distribution were shown in Tables 1 and 2.
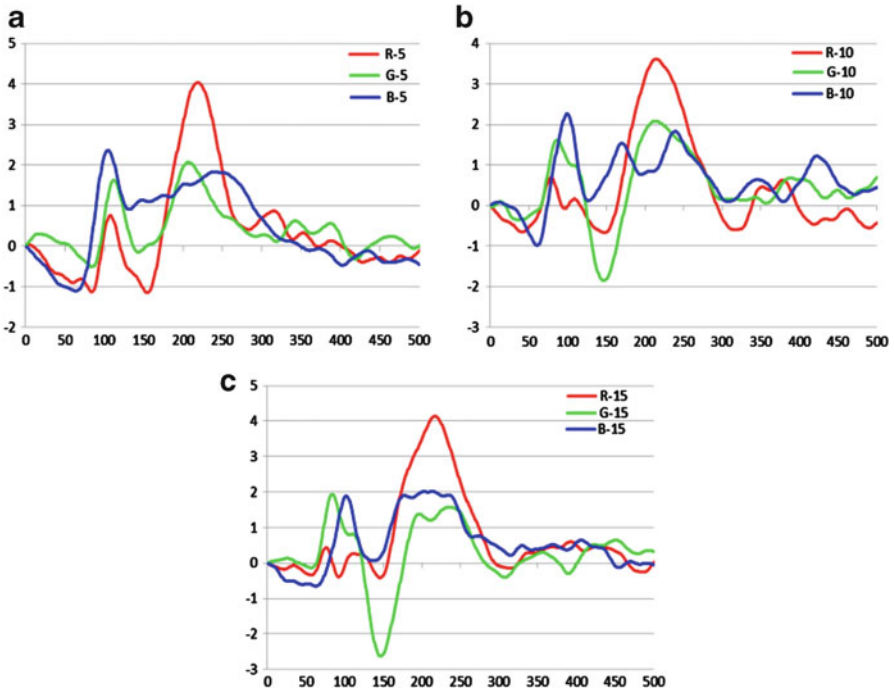
Fig. 1 Color VEP under various stimulation areas in Oz electrode. From *left* to *right* is for $5° \times 5°$, $10° \times 10°$, and $15° \times 15°$. The *x*-axis is ms and *y*-axis is uV. Label *R* is color *red*, *G* is color *green*, and *B* is color *blue* (Colour figure online)

Table 1 Color VEP peak latency distributions

Latency label	R	G	B	ANOVA
L_N1	87.1(24.6)	67.1(21.8)	69.8(14.3)	0.081
L_P1	123.6(27.9)	105.7(15.5)	103.6(13.9)	0.067
L_N2	160.2(19.6)	143.3(10.6)	137.6(15.3)	*0.008*
L_P2	208.7(19.9)	214.1(28.9)*	188.5(23.8)*	0.064
M_N1	75.6(20.5)	65.9(26.1)	65.7(15.7)	0.500
M_P1	113.8(30.9)	108(28.8)	106.9(18.5)	0.824
M_N2	148.8(25.0)	156.7(23.8)	139.9(22.7)	0.305
M_P2	214.9(20.4)	217.3(17.8)	219.1(30.5)	0.923
S_N1	85.3(23.5)	77.4(17.9)	70.1(14.3)	0.218
S_P1	119.4(20.2)	113.9(15.4)	110(15.4)	0.478
S_N2	155.1(22.4)	153.2(25.1)	148.8(28.5)	0.852
S_P2	219.8(17.7)	219.1(25.4)	211.9(36.4)	0.779

As shown in Table 1, there were significant latency variation on N2 among three colors ($p = 0.008$) for large area checkerboard. The average latency sequence was blue (137 ms) < green (143 ms) < red (160 ms). For the small and medium checkerboard area groups, there was no significant difference.

Table 2 Color VEP peak amplitude distributions

Amplitude label	R	G	B	ANOVA
L_N1	−1.9(2.7)	−1.0(1.2)	−1.4(1.8)	0.597
L_P1	2.8(1.7)	2.3(2.3)	2.9(2.3)	0.825
L_N2	−0.5(2.3)	−3.1(2.1)	−1.1(2.9)	0.063
L_P2	5.0(2.3)	2.3(1.3)	3.2(1.7)	*0.008*
M_N1	−1.7(2.3)	−0.4(1.2)	−1.4(0.9)	0.169
M_P1	2.2(2.3)	2.8(1.5)	3.2(2.3)	0.615
M_N2	−1.9(2.7)	−2.4(2.7)	−0.8(1.2)	0.329
M_P2	4.4(2.0)	2.7(2.3)	2.8(2.0)	0.147
S_N1	−2.7(3.0)	−1.7(1.6)	−1.8(2.2)	0.548
S_P1	1.6(2.8)	2.8(2.0)	3.6(2.1)	0.171
S_N2	−2.0(2.6)	−1.1(1.2)	−0.9(1.4)	0.389
S_P2	5.0(1.6)	2.8(1.9)	2.5(1.3)	*0.002*
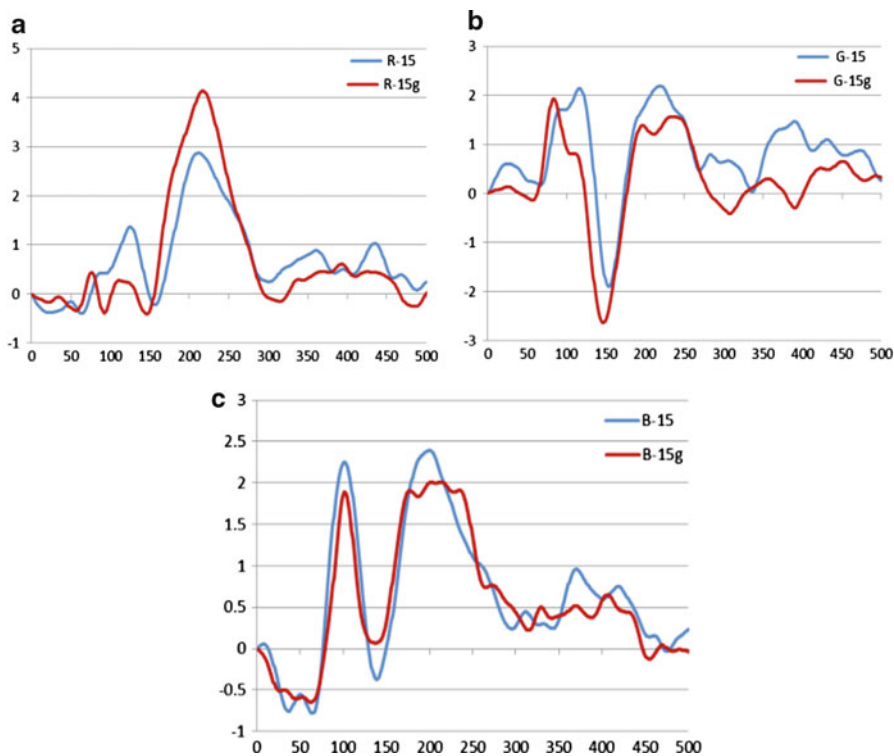
Fig. 2 Myopia color VEP with (end label with g, such as R-15g) and without glasses. From *left* to *right* for three colors, *red*, *green*, and *blue* (Colour figure online)

Results in Table 2 indicated that there was significant amplitude variation on P2 peak, both for large and small checkerboard area groups. P2 amplitude by red color stimulation was significantly higher than the other two colors. This phenomenon was also shown in Fig. 1.

Table 3 Color VEP peak latency distributions for myopia subjects

Label	Peak	R	G	B	ANOVA
Latency	N1	78.8 (16.3)	75.7 (15.8)	65.9 (12.1)	0.176
	P1	114.3 (19.1)	114.5 (12.8)	105.4 (15.7)	0.402
	N2	148.3 (21.8)	150.8 (11.6)	143 (15.7)	0.615
	P2	210.8 (17.8)	209 (16.4)	190.2 (13.2)	*0.018*
Amplitude	N1	3.8 (2.8)	−0.6 (2.4)	−1.6 (1.4)	0.441
	P1	2.6 (2.8)	4.1 (2.7)	3.4 (2.1)	0.444
	N2	1.1 (1.9)	−2.7 (2.0)	−1.2 (1.8)	0.165
	P2	3.8 (3.4)	2.9 (1.6)	3.2 (1.5)	0.740

Table 4 Myopia subjects *t*-test result of color VEP between with and without glasses

Label	Peak	R	G	B
Latency	N1	0.379	0.123	0.380
	P1	0.484	0.106	0.561
	N2	0.309	0.156	*0.048*
	P2	0.813	0.521	0.837
Amplitude	N1	0.872	0.580	0.704
	P1	0.749	*0.001*	0.587
	N2	0.533	0.477	0.918
	P2	0.223	*0.041*	0.998

Myopia's grand VEP with and without glasses for three colors was illustrated in Fig. 2a–c. The corresponding VEP peak and latency distribution were shown in Table 3. There was significant difference on peak P2 latency among three colors ($p = 0.018$).

Paired *t*-test result between with glasses and without glasses was listed in Table 4. Myopia patients had different VEP response for different colors without the aid of glasses. The difference was distributed on N2 peak latency ($p = 0.048$) for blue color and P1 and P2 peak amplitude for green color ($p = 0.001$ and $p = 0.041$). There was no significant difference for myopia with red color stimulation.

4 Discussion and Conclusion

Checkerboard area was one of the VEP performance factors. Large checkerboard area will be effective for different colors. The shortest latency response indicated a faster visual transmission rate for blue color. On the other hand, red color had higher P2 amplitude response. P2 amplitude is mainly involved with cognitive meaning. This result implied a stronger cognitive response for red color.

Myopia patients had slight different VEP response. Without the aid of glasses, there was no difference on VEP amplitude among three colors. Peak P2 latency

showed difference among colors that was different for peak N2 latency with glasses. Paired *t*-test result showed that there was no significant difference for myopia with red color stimulation. Without glasses, green color stimulation amplitude was mainly higher than that with glasses. This physiological mechanism is still open question and it is interesting to be further investigated.

References

1. Crognale MA (2002) Development, maturation, and aging of chromatic visual pathways: VEP results. J Vis 2:438–450
2. Pompe TA, Kranjc BS, Brecelj J (2006) Visual evoked potentials to red-green stimulation in schoolchildren. Vis Neurosci 23:447–451
3. Souza GS, Gomes BD, Lacerda EM, Saito CA, da Silva Filho M, Silveira LC (2008) Amplitude of the transient visual evoked potential (tVEP) as a function of achromatic and chromatic contrast: contribution of different visual pathways. Vis Neurosci 25(3):317–325
4. Tobimatsu S, Celesia GG (2006) Studies of human visual pathophysiology with visual evoked potentials. Clin Neurophysiol 117(7):1414–1433
5. Shawkat FS, Kriss A (2000) A study of the effects of contrast change on pattern VEPS, and the transition between onset, reversal and offset modes of stimulation. Doc Ophthalmol 101 (1):73–89
6. Di Summa A, Fusina S, Bertolasi L, Vicentini S, Perlini S, Bongiovanni LG, Polo A (1999) Mechanism of binocular interaction in refraction errors: study using pattern-reversal visual evoked potentials. Doc Ophthalmol 98(2):139–151

License Plate Recognition Under Nonuniform Illumination

Ren-Chao Shen and Day-Fann Shen

Abstract License plate recognition (LPR) is an important technique in automobile management and traffic control. Experiments show that the recognition rate dropped significantly when the illumination on the license plate is nonuniform. In this chapter, we proposed a simple block-based method to resolve the problem. Experiments show that the proposed method is not only fast but also outperforms well-known Otsu as well as state-of-the-art NiBlack and MAT, with recognition rate of 86 % for the 100 nonuniformly illuminated license plate test images.

Keywords License plate recognition • Registration • Block based • Edge detection • Nonuniform illumination • Character segmentation • Character recognition

1 Introduction

Experiments show that license plate recognition (LPR) under nonuniform illumination is a challenging task. In 1991, J. Parker [11] attacked the problem by using intensity gradient, noting levels correspond to an object as an initial guess of a threshold and then region grows the object using local image property. In 2005, Feixiang Yan et al. [1] proposed multistage adaptive thresholding (MAT) method; their method takes advantage of local thresholding and, at the same time, prevents over segmentation with the global image information.

To resolve the problem of license plate recognition under nonuniform illumination condition, we proposed a block-based approach with the assumption that illumination in the block is relatively even locally. The proposed method simply finds the local threshold for each block using the well-known thresholding method

R.-C. Shen (✉) • D.-F. Shen
Department of Electrical Engineering, National Yunlin University of Science
and Technology, Yunlin 64002, Taiwan
e-mail: shendf@yuntech.edu.tw

proposed by Otsu [2]. Hundred nonuniformly illuminated test images are generated to evaluate the performances of the proposed method as well as approach proposed by Niblack [3] and the multiple adaptive threshold (MAT) proposed by F. Yan et al. [1]. Experimental results show that the proposed block-based method with the recognition rate of 86 % not only outperforms the other two approaches but is also faster in terms of computation time due to its simplicity in nature.

2　Experimental Platform for LPR

The test LP images are characterized by (1) taken from cars registered in Taiwan (2) license plate of white background with black characters in 26 English alphabets and Arabic numbers 0–9. (3) Test LP images are taken from distance in the range of 2–3 m with camera angle within 5°. We implement a general license plate recognition process as the platform for experimental purpose. The flowchart is shown in Fig. 1.

2.1　LP Location [1]

Step 1. *Edge detection*. Apply Prewitt edge detector with threshold of 0.15 to find the vertical edge pixels (Fig. 2).
Step 2. *Morphological processing*. This step is to locate the LP in a test image through the use of morphological erosion with structure element [1 1 1] and closing with structure element 25 × 25.
Step 3. *Locate LP area*. Area of LP, as well as many nontrivial white areas, is obtained after step 2. The LP area distinguishes itself from other nontrivial areas in that it is the largest area with width highest ratio of 3.
Step 4. *Obtain grayscale LP contents*. The grayscale LP content is then extracted accordingly as shown in Fig. 3 using the information obtained in step 3.

Graylevel LP Image
↓
LP Location
↓
Character Extraction
↓
Character Normalization
↓
Character Recognition
↓
LPR Flowchart
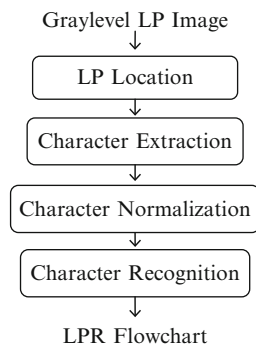
Fig. 1 LPR flowchart

Fig. 2 Prewitt edge detection

Fig. 3 Extracted grayscale
LP contents

Fig. 4 Character
segmentation
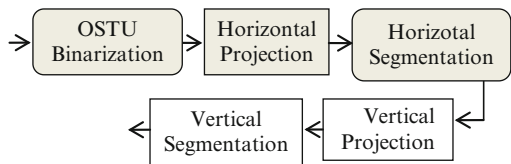
Fig. 5 Binary image
and horizontal projection

2.2 Character Segmentation

In this stage, the well-known Otsu method [2] is applied to the grayscale LP image to obtain the binary image as shown in Fig. 4. In addition to the desired characters (alphabets and numbers), the license plate binary image also contains unwanted information, such as city and bolts, in the upper and bottom areas. The horizontal projection method [4, 5] is then applied to obtain the histogram as shown in Fig. 5. The largest area in the center (h2) of the histogram is identified as the character area.

The vertical histogram is then obtained by applying the projection method [11] to the character area as shown in Fig. 6, where each character is separated by finding the locations of valleys in the histogram. The characters in the license plate are then obtained as shown in Fig. 7.
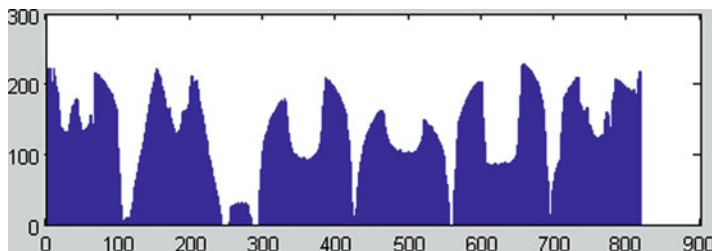
Fig. 6 Histogram by vertical projection

Fig. 7 Results of character segmentation

Fig. 8 36 Character template images (20×40)

2.3 *Character Normalization and Template Matching*

One template image for each possible character (26 English alphabets and 10-digit Arabic numbers) is pre-stored in the database; each input character image is then identified through the template matching process (Fig. 8). Since the picture-taking distances may be varied from image to image, the size in pixels of the extracted character may vary accordingly. This problem is resolved by normalizing (resize) the input character image to 20(W) $\times$ 40(H) pixels. The template matching process, the correlation between the normalized input character image $i(x,y)$, and each of the 36 templates $T_k(x,y)$ $k = 1\ldots36$ are calculated:

$$c_k = \sum_{y=0}^{h-1}\sum_{x=0}^{w-1} i(x, y)T_k(x, y) \tag{1}$$

where h and w are 40 and 20, respectively. The input character is identified as the kth character if it has the highest correlation with the kth template.

3   The Problem and Proposed Method

3.1   LPR Problems due to Nonuniform Illumination

In practice, nonuniform illumination may occur on LP images. By applying the well-known Otsu [2] thresholding method on the nonuniform illuminated LP image in Fig. 9a, we obtain the binary image in Fig. 9b, which is poor in quality and unable to proceed the LPR process. The leave shadowed LP image in Fig. 9c yields poor binary image quality, which also fails the consequent LPR process.

3.2   Nonuniformly Illuminated Test LP Images

The 20 test images of size 640 × 320 all feature nonideal illumination including leave shadowed image and dark images.

3.3   Proposed Block-Based Thresholding

The character segmentation process in Fig. 4 is modified to that in Fig. 10. We add histogram equalization in the beginning to resolve the problem of insufficient lighting condition. The Otsu thresholding is applied to the grayscale image on block basis rather than globally. The idea is simple that if we divide the nonuniformly illuminated LP into blocks, such that the illumination within each block is relatively uniform. The Otsu thresholding is then applied to each block for its binary representation.

Fig. 9 Nonuniform illuminated LP and their Otsu binary images. (**a**) Nonuniform illumination. (**b**) Binary by Otsu. (**c**) Nonuniform illumination. (**d**) Binary by Otsu
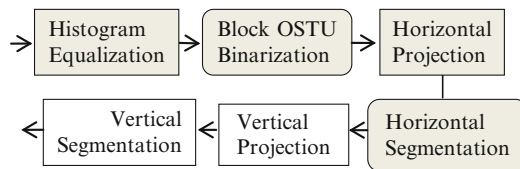
Fig. 10   Block-based character segmentation

Table 1 Effect of image size on LPR performance

Image size	Execution time (s)	Recognition rate (%)
640 × 320	0.682 (2.4)	95
320 × 160	0.284 (1.0)	95
160 × 80	0.092	80

Fig. 11 Effect of different block sizes. (**a**) Binary image (4 × 4). (**b**) Binary image (4 × 8). (**c**) Binary image (8 × 8). (**d**) Binary image (8 × 16)

Table 2 Effects of block size on LPR performance

Block size	Execution time (s)	Recognition rate (%)
4 × 4	0.138	75
4 × 8	0.284	95
8 × 8	0.512	80
8 × 16	0.976	70

3.4   On Image Size

Based on 20 test LP images, we conducted experiments to examine the effects of image size on performance, i.e., execution time and recognition rate. The results are shown in Table 1. Block size of 4 × 8 is adopted in the experiments.

The recognition rate for image size of 640 × 320 and 320 × 160 is the same at 95 %, while image size of 320 × 160 has a much faster execution time. Although image size of 160 × 80 is the fastest in execution due to smallest image size, the recognition rate drops to 80 %. Therefore, image size of 320 × 160 is recommended and used for the rest of the experiments.

3.5   On Size of Block

In this section, we examine the effect of block size on the binary image thresholding as well as the LPR performance. Block sizes of 4 × 4, 4 × 8, 8 × 8, and 8 × 16 are adopted in the experiments. The resulting binary images are shown in Fig. 11 and the execution time and recognition rate are listed in Table 2. We observe that block size 4 × 8 yields the best binary image (see Fig. 11) and therefore the best performance (Table 2).

4 Comparison with Other Methods

The performance of the proposed method is compared with the well-known Otsu method [80] as well as two well-known methods by Niblack [3] and MAT by F. Yan et al. [1] for nonuniformly illuminated images.

4.1 120 Test Images

120 test images are used in the experiments. The original test image plus 5 additional nonuniformly illuminated images are generated by *Photoshop* with five different parameters (UL, ULL, REL, EEL, LL) for each of the original 20 test images.

Two sets of license plate binary images obtained using different methods are shown in Fig. 12 for perceptual evaluation. Perceptually, both MAT and the proposed methods perform well in obtaining binary LP image. The general performance statistics in terms of recognition rate as well as execution time for the total 120 test images are shown in Table 3. The proposed method outperforms others in terms of recognition rate of 86 % with execution time of 0.284 s, while MAT ranked second in recognition rate with execution time of 0.371 s. The common used Otsu has the fastest execution time of 0.119 s, but its recognition rate is only 64 %.

5 Conclusion

The problem of license plate recognition under nonuniform illumination is studied in this chapter. We implemented a general license plate recognition system using existing techniques as the platform for experiments and improving. By observing

Fig. 12 (**a**) By Otsu. (**b**) By Niblack. (**c**) By MAT. (**d**) By proposed

Table 3 Comparison of LPR performances

Methods	Execution time (s)	Recognition rate (%)
Proposed	0.284	86
MAT	0.371	81
OTSU	0.119	64
Niblack	28.431	51

the nonuniform illuminated LP images, we propose a simple block-based method, where the LP image is divided into blocks such that the illuminations in a block are relatively uniform. The LP image size of 320×160 and block size of 4×8 are chosen for the best recognition rate as well as the fastest execution time based on 20 original LP test images.

Three well-known methods, namely, Otsu, MAT, and Niblack, are selected for comparison, while 20 original test images plus 100 additional Photoshop generated test images are used in the experiments for performance evolution. As a result, the proposed method with average recognition rate of 86 % and average execution time of 0.284 s outperforms MAT (81 %, 0.371 s), Otsu (64 %,0.119 s), and Niblack (51 %, 28.431 s). The proposed method, although simple in idea and implementation, provides very good performance for LPR under nonuniform illuminations.

References

1. Yan F, Zhang H, Ronald Kube C (2005) A multistage adaptive thresholding method. Pattern Recognit Lett 26:1183–1191
2. Otsu N (1979) A threshold selection method from gray-level histograms. IEEE Trans Syst Man Cybern 9(1):62–66
3. Niblack W (1986) An introduction to digital image processing. Prentice-Hall, Englewood Cliffs, pp 115–116
4. Rahman CA, Badawy W, Radmanesh A (2003) A real time vehicle's license plate recognition system. In: Proceedings of the IEEE conference on advanced video and signal based surveillance, Miami, 21–23,July 2003, pp 163–166
5. Juntanasub R, Sureerattanan N (2005) Car license plate recognition through hausdorff distance technique. In: Proceedings of IEEE 17th international conference on tools with artificial intelligence, Hong Kong, 14–16 Nov 2005, pp 647–651
6. Broumandnia A, Fathy M (2005) Application of pattern recognition for farsi license plate recognition. In: Proceedings of the international conference on graphics, vision and image processing, Cairo, 19–21 Dec 2005, vol 5, pp 25–31
7. Brugge MH Ter, Stevens JH, Nijhuis JAG, Spaanenburg L (1998) License plate recognition using DTCNNs. In: Proceedings of 5th IEEE international workshop on cellular neural networks and their applications, London, 14–17 Apr 1998, pp 212–217
8. Comelli P, Ferragina P, Granieri MN, Stabile F (1995) Optical recognition of motor vehicle license plates. IEEE Trans Veh Technol 44(4):790–799
9. Hussain B, Kabuka MR (Jan. 1994) A novel features recognition neural network and its applications to character recognition. IEEE Trans Pattern Anal Mach Intell 16(1):98–106

Part III
Artificial Intelligence

A Cross-Coupled MIMO Fuel Cell System Design by Using Intelligent Fuzzy-Neural Controller

Jium-Ming Lin and Cheng-Hung Lin

Abstract This chapter proposes a MIMO fuel cell design by integrating both Ziegler-Nichols-based PID and intelligent fuzzy-neural controllers. Comparing with the other PID methods by Matlab simulation, the proposed system performances are better and robust by using scaled conjugate gradient algorithm to determine the neural network weighting factors and biases; even the system has stack current disturbance variation and gas valve hysteresis effects.

Keywords Ziegler-Nichols PID method • Intelligent fuzzy-neural controller • Fuel cell • Hysteresis effect • Disturbance rejection

1 Introduction

Fuel cell system (FCS) is potentially intended for stationary and mobile power generations with low greenhouse emissions and high efficiency as in Ahmed and Krumpelt [1]. Brown's FPS (fuel processing system) [2] was to convert fossil and/or renewable fuel sources into suitable fuels, especially H_2-rich syngas. Of all primary fossil fuels as in Dicks [3], natural gas is the most environment-friendly and the cleanest fuel. Although it is a nonrenewable fuel resource, natural gas is naturally preferred as the first candidate of fuels because of sufficient infrastructure for refueling and storage [4]. Among all of the fuel reforming processes,

J.-M. Lin (✉)
Department of Communication Engineering, Chung-Hua University, Hsin-Chu 30012, Taiwan
e-mail: jmlin@chu.edu.tw

C.-H. Lin
Ph.D. Program in Engineering Science, College of Engineering, Chung-Hua University, Hsin-Chu 30012, Taiwan
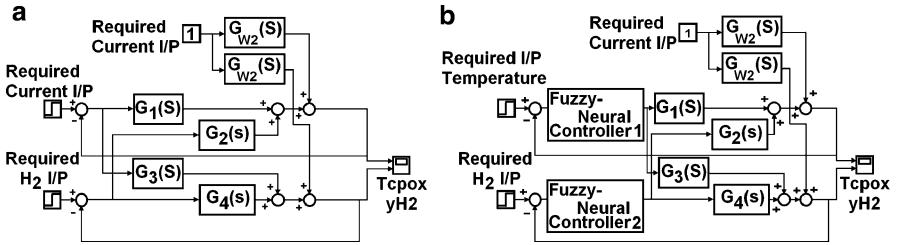
Fig. 1 (**a**) The fuel cell control system. (**b**) The proposed intelligent fuzzy-neural controller

catalytic partial oxidation (CPO) is the most suitable one for mobile applications with rapid start-up and good tracking ability of load variation. Pukrushpan and Stefanopoulou [5–7] applied linearization technique to obtain CPO-based system transfer function firstly as in Fig. 1a and then applied LQ method for the fuel regulation system design. Later Tsai and Lin [8, 9] used quadratic Gaussian methods; this method can achieve better performance than those obtained by the traditional LQ method. This motivates us to integrate both control methods of Ziegler-Nichols-based PID [10] and the intelligent fuzzy-neural [11, 12] control system design as in Fig. 1b to reserve both relative stability and disturbance rejection capability. Comparing with the PID method, one can see that the proposed system is more robust.

2　Review of Ziegler-Nichols-Based PID Controllers Design Method

The block diagram of a fuel cell control system is as in Fig. 1a. The temperature loop is designed firstly; Ziegler-Nichols method is to set both gains of I- and D-type controllers to zero and then adjust P-type control gain, until the system begins to oscillate as in Fig. 2a; thus, the critical gain K_{u1} and the period T_{u1} are, respectively, as 1 and 1.4. Similarly, next is to adjust P-type control gain of hydrogen supply loop, until the system begins to oscillate as in Fig. 2b; the critical gain K_{u2} and the period T_{u2} are, respectively, as 1 and 1.3. Then by Ziegler-Nichols design rule to calculate the PID controller gains of loops 1 and 2 as follows: loop 1 ($K_{p1} = 0.6$, $K_{u1} = 0.6$; $T_{I1} = 0.5$, $T_{u1} = 0.7$; and $T_{D1} = 0.125$, $T_{u1} = 0.175$) and loop 2 ($K_{p2} = 0.6$, $K_{u2} = 0.6$; $T_{I2} = 0.5$, $T_{u2} = 0.65$; and $T_{D2} = 0.125$, $T_{u2} = 0.1625$). The output responses of loops 1 and 2 by Matlab simulations are as in Fig. 3a and b respectively. The temperature overshoot is 45 %. The temperature rise and the settling times are 0.65 and 2 s, respectively. Thus, both temperature overshoot and settling time are too large for practical consideration.
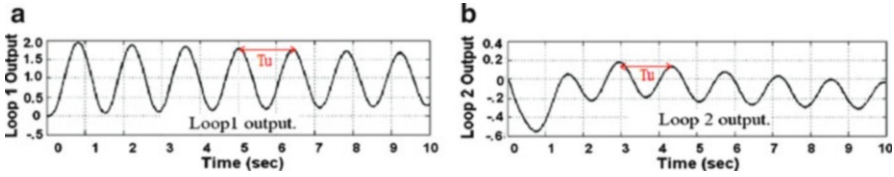
Fig. 2 Adjust the gains of the P-type controllers individually until the loops begin oscillation
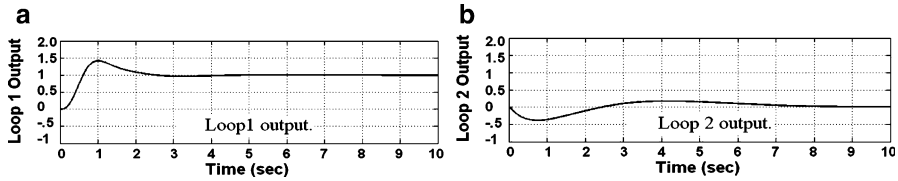
Fig. 3 The output responses of loops 1 and 2 with Ziegler-Nichols-based PID controller

3 Intelligent Fuzzy-Neural Controller Design

This section extends the PID controllers to the intelligent fuzzy-neural controllers as in Fig. 1b. The cross-reference rules and membership function parameters are defined in Tables 1 and 2, respectively. The triangular distribution functions are applied for membership functions to reduce the computation time.

Figure 4a and b shows the system output responses by using intelligent fuzzy PID controller. The overshoot of the temperature is 12 %, and the rise and the settling times are only 0.7 and 1 s, respectively. Thus, the improvements are very large.

However, if disturbance stack current is doubled, then the outputs by using PID and intelligent fuzzy controllers are as in Figs. 5 and 6, respectively. Note that large 60 % overshoots are produced by using PID controller. On the other hand, the overshoot is only 20 % for the intelligent fuzzy controller. Thus, the improvement is very dominant.

Moreover, if the hysteretic backlashes in the gas valves of both loops are as one-tenth of the inputs, i.e., 0.1 and 0.0088, respectively, then the results of PID and the fuzzy controllers are as in Figs. 7 and 8, respectively. Note that both methods cannot be accepted for the larger overshoots in the temperature loops. So the neural network is augmented to the fuzzy controller as in Fig. 9, in which three neurons are applied in the hidden layer. The output responses by using steepest descent algorithm of neural network method without and with disturbance variation and hysteresis effects are obtained as shown in Figs. 10 and 11, respectively. Note the overshoot effects are quietly reduced, but there are limit cycles in the outputs with both disturbance variation and hysteresis effects.

Similarly, the output responses by using variable learning rate algorithm of neural network method without and with disturbance variation and hysteresis

Table 1 Cross-reference rules

dE\E	NB	NM	NS	ZE	PS	PM	PB
NB	NB	NB	NB	NB	NM	NS	ZE
NM	NB	NB	NB	NM	NS	ZE	PS
NS	NB	NB	NM	NS	ZE	PS	PM
ZE	NB	NM	NS	ZE	PS	PM	PB
PS	NM	NS	ZE	PS	PM	PB	PB
PM	NS	ZE	PS	PM	PB	PB	PB
PB	ZE	PS	PM	PB	PB	PB	PB

Table 2 Parameters of membership functions

Item	Parameter E	Parameter ΔE	Parameter U
Negative big (NB)	[−1 −1 −0.75 −0.3]	[−0.5 −0.5 −0.375 −0.15]	[−2 −2 −1.5 −0.6]
Negative medium (NM)	[−0.75 −0.3 −0.15]	[−0.375 −0.15 −0.08]	[−1.5 −0.6 −0.3]
Negative small (NS)	[−0.15 −0.1 0]	[−0.1111 −0.05557 0]	[−0.3 −0.2 0]
Zero (ZE)	[−0.05 0 0.05]	[−0.02778 0 0.02778]	[−0.1 0 0.1]
Positive small (PS)	[0 0.1 0.15]	[0 0.05557 0.1111]	[0 0.2 0.3]
Positive medium (PM)	[0.15 0.3 0.75]	[0.08 0.15 0.375]	[0.3 0.6 1.5]
Positive big (PB)	[0.3 0.75 1 1]	[0.15 0.375 0.5 0.5]	[0.6 1.5 2 2]
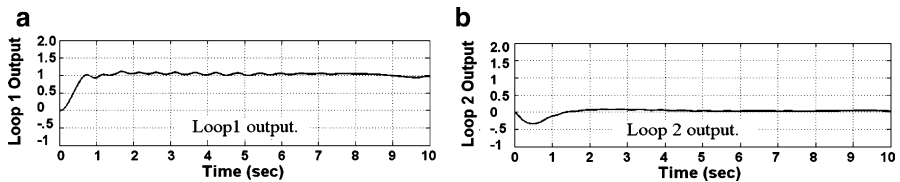
Fig. 4 The output responses with Ziegler-Nichols-based intelligent fuzzy PID controller
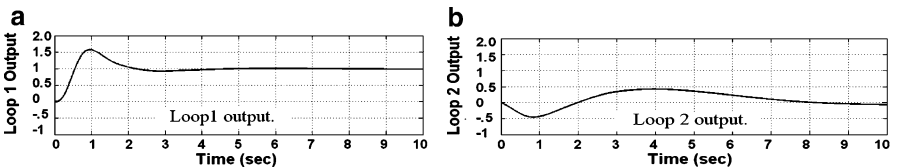
Fig. 5 The output responses by using PID controller with stack current doubled
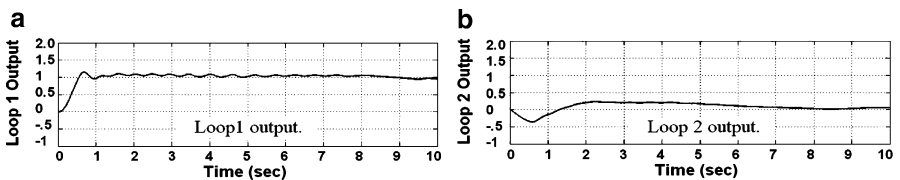
Fig. 6 The output responses by using intelligent fuzzy controller with stack current doubled
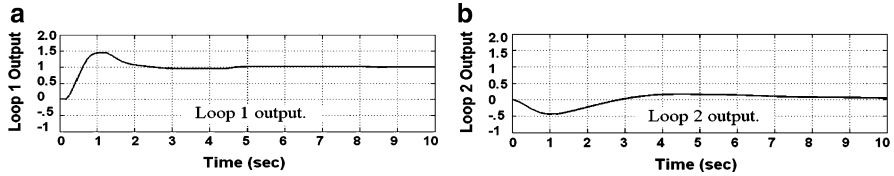
Fig. 7 The output responses by using PID controller with hysteresis effect
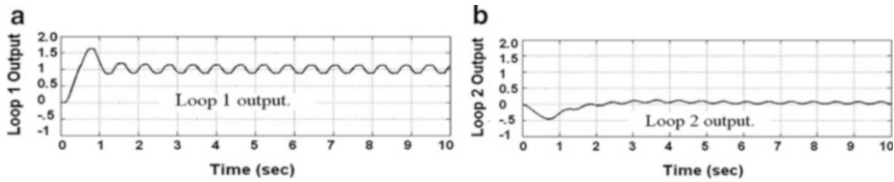
Fig. 8 The output responses by using fuzzy PID controller with hysteresis effect
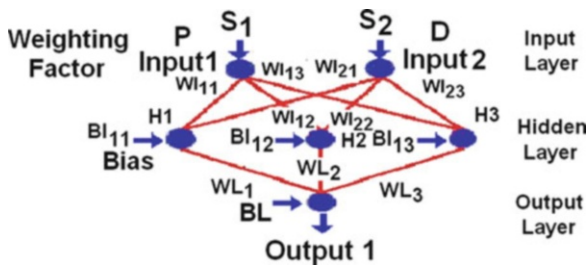
Fig. 9 The model of neural network controller
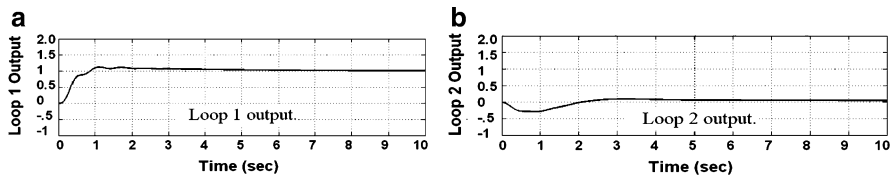
Fig. 10 The output responses by using steepest descent algorithm of neural network method
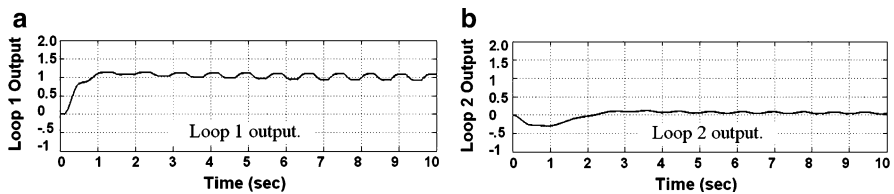
Fig. 11 The output responses by using steepest descent algorithm of neural network method with both disturbance variation and hysteresis effects
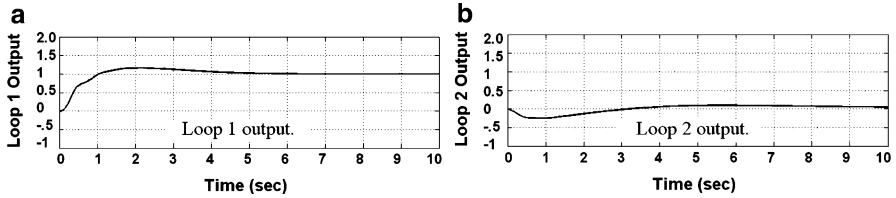
Fig. 12 The fuel cell output responses by using variable learning rate algorithm of neural network method without disturbance variation and hysteresis effects
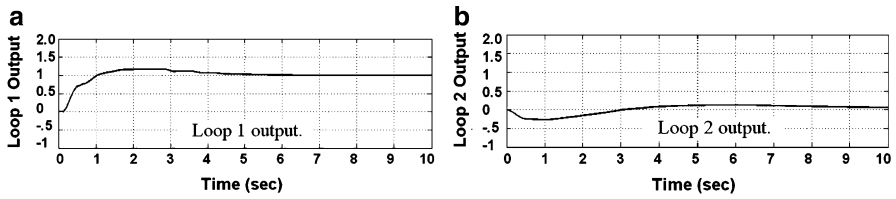
Fig. 13 The fuel cell output responses by using variable learning rate algorithm of neural network method with both disturbance variation and hysteresis effects
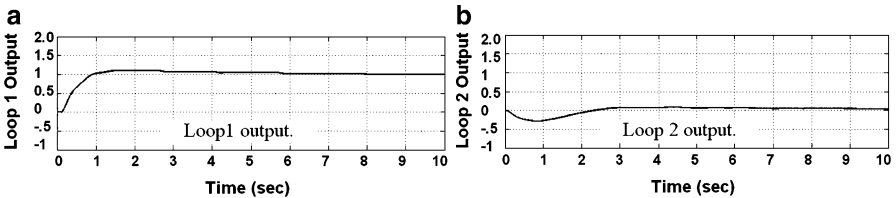
Fig. 14 The fuel cell output responses by using scaled conjugate gradient algorithm of neural network method with both disturbance variation and hysteresis effects

Table 3 Neural network weighting factors and biases with scaled conjugate gradient algorithm

	P input ($WI1,j$)			D input ($WI2,j$)			Weighting factors ($WL1,j$)	−0.5521 1.6540 −0.5301
Weighting factors	25.9712	2.0710	25.7526	−26.3687	2.4974	−26.0744		
Bias (BIj)	−20.4571	0.0022	20.2284				Bias (BL)	−0.0245

effects are obtained as shown in Figs. 12 and 13, respectively. Note that the overshoot and the limit cycle effects in the temperature loop are reduced.

Finally, the scaled conjugate gradient algorithm is also applied; the results are as shown in Fig. 14. Note that the system performances are very good even with both disturbance variation and hysteresis effects. The neural network weighting factors and biases obtained by the scaled conjugate gradient algorithms are also listed in Table 3 for reference.

4 Conclusion

This research integrates both Ziegler-Nichols-based PID and intelligent fuzzy-neural control methods for a fuel cell design. The gas valve hysteresis and the stack current command parameter variation effects are taken into consideration. Comparing with PID controllers also made by Matlab simulation, one can see the system performances, obtained by Ziegler-Nichols-based intelligent fuzzy-neural PID controller and by using scaled conjugate gradient algorithm to determine the weighting factors and biases is better even with disturbance variation and hysteresis effects.

References

1. Ahmed S, Krumpelt M (2001) Hydrogen from hydrocarbon fuels for fuel cells. Int J Hydrogen Energy 26:291–301
2. Brown LF (2001) A comparative study of fuels for on-board hydrogen production for fuel-cell-powered automobiles. Int J Hydrogen Energy 26:381–397
3. Recupero V, Pino L, Leonardo RD, Laganà M, Maggio G (1998) Hydrogen generator, via catalytic partial oxidation of methane for fuel cells. J Power Sour 71:208–214
4. Pukrushpan JT, Stefanopoulou AG, Varigonda S, Pedersen LM, Ghosh S, Peng H (2003) Control of natural gas catalytic partial oxidation for hydrogen generation in fuel cell applications. In: Proceedings of American control conference, Denver, 4–6 June 2003, vol 3, pp 2030–2036
5. Pukrushpan JT, Stefanopoulou AG, Varigonda S, Pedersen LM, Ghosh S, Peng H (2005) Control of natural gas catalytic partial oxidation for hydrogen generation in fuel cell applications. IEEE Trans Control Syst Technol 13:3–14
6. Pukrushpan JT, Stefanopoulou AG, Varigonda S, Eborn J, Haugsteretter C (2006) Control-oriented model of fuel processor for hydrogen generation in fuel cell applications. Control Eng Pract 14:277–293
7. Tsai HL (2008) Optimal control design of fuel processing system by linear quadratic Gaussian and loop transfer recovery method. J Chin Inst Eng 31:369–378
8. Tsai HL, Lin JM (2010) Optimal control of fuel processing system using generalized linear quadratic Gaussian and loop transfer recovery method. Asia J Control 12:1–10
9. Ziegler JG, Nichols NB (1942) Optimum settings for automatic controllers. Trans ASME 64:759–768
10. Zhang H, Liu D (2006) Fuzzy modelling & fuzzy control. Springer, New York
11. Rehman HU, Linkens DA, Asbury AJ (1993) Neural networks and nonlinear regression modelling and control of depth of anaesthesia for spontaneously breathing and ventilated patients. Comput Method Prog Biol 40(4):227–247
12. Rusu P, Petriu EM, Whalen TE, Cornell A, Spoelder HJW (2003) Behavior-based neuro-fuzzy controller for mobile robot navigation. IEEE Trans Instrum Meas 52(4):1335–1340

Development of Fuzzy Comprehensive Evaluation and Approaching Degree Toolbox via Matlab

Yaug-Fea Jeng, Ting-Hui Hsu, Kun-Li Wen, and Rui-Xiang Chen

Abstract In the twenty-first century, for the science and technology peripheral auxiliary, mostly computer software are used to do a bulk of numerical analysis and verification, especially in soft computing calculation after the 1990s. Currently, for the studies on the related soft-computing field, auxiliary calculation software are available. However, through the actual validation, it is a very professional software system. Hence, the goals of this chapter are extensiveness and practicability. By using the powerful engineering function in Matlab, it is possible to develop an auxiliary computer toolbox of comprehensive evaluation and approaching degree in the fuzzy system theory. Through experimental validation, it not only helps in calculation and validation but also enhances the popularity and practicability of comprehensive evaluation and approaching degree in the field of soft computing.

Keywords Soft computing • Matlab • Fuzzy system theory • Comprehensive evaluation • Approaching degree • Toolbox

Y.-F. Jeng
Department of Automation Engineering and Institute of Mechatronoptic Systems,
Chienkuo Technology University, Changhua 500, Taiwan

T.-H. Hsu
Department of International Business Administration, Chienkuo Technology University,
Changhua 500, Taiwan

K.-L. Wen (✉) • R.-X. Chen
Department of Electrical Engineering, Chienkuo Technology University,
Changhua 500, Taiwan
e-mail: klw@ctu.edu.tw

1 Introduction

Due to the development of science and technology, the mathematics analytical methods are generated. Hence, how to combine them together and apply them to human civilization has become the research topic for the past 100 years. With the invention of the computer in the middle of the twentieth century, it can now solve the problems that were earlier solved manually and has made significant progress as well. The development of science and technology also promotes the tremendous progress of the software. Therefore, the twentieth century is said to be the period of rapid development of accurate scientific methods [1]. L. Zadeh proposed the fuzzy system theory in 1965, and the theory is to use mathematics method research to deal with fuzzy mathematics, that is, to understand the uncertainty of differences in objective things [2]. After half a century's development, it is now used in many fields [3–8]. Though there are many research fields in the fuzzy system theory with relevant software, they are quite a professional software system [9]. Therefore, the goals of this chapter are extensiveness and practicability, and the chapter complements a huge number of analysis and calculation as a starting point [10–13]. By using the powerful engineering function in Matlab [14], it is possible to develop the auxiliary computer toolbox of comprehensive evaluation and approaching degree in the fuzzy system theory [15].

Section 2 describes the mathematical model of comprehensive evaluation and approaching degree in fuzzy system theory. Section 3 discusses the devolvement of the Matlab toolbox, including the calculation steps. The final section consists of conclusion and recommendations for future research.

2 The Mathematics Model

2.1 Fuzzy Comprehensive Evaluation

The basic concept of fuzzy comprehensive evaluation is introduced below [16]:

1. Build up the evaluation factor set:

$$A = (A_1, A_2, A_3, \ldots, A_m) \tag{1}$$

2. Build up the judgment set:

$$V = (v_1, v_2, v_3, \ldots, v_n) \tag{2}$$

3. Build up the single-factor fuzzy comprehensive matrix:

$$R = \begin{bmatrix} r_{11} & r_{12} & \cdots & r_{1n} \\ r_{21} & r_{22} & \cdots & r_{2n} \\ \vdots & \cdots & \ddots & \vdots \\ r_{m1} & r_{m2} & \cdots & r_{mn} \end{bmatrix} \tag{3}$$

4. The operation of fuzzy comprehensive evaluation is

$$B = A \circ R = (b_1, b_2, b_3, \ldots, b_n) \tag{4}$$

Use four types of methods:

$$B_1 = \bigwedge_{i=1}^{m} (A_i \wedge r_{ij}), \quad j = 1, 2, 3, \ldots, n \tag{5}$$

$$B_2 = \bigwedge_{i=1}^{m} (A_i \vee r_{ij}), \quad j = 1, 2, 3, \ldots, n \tag{6}$$

$$B_3 = \bigvee_{i=1}^{m} (A_i \vee r_{ij}), \quad j = 1, 2, 3, \ldots, n \tag{7}$$

$$B_4 = \bigvee_{i=1}^{m} (A_i \wedge r_{ij}), \quad j = 1, 2, 3, \ldots, n \tag{8}$$

Equations (5), (6), (7). and (8) are called fuzzy comprehensive evaluation model.

2.2 Fuzzy Approaching Degree

For fuzzy identification, consider the close degree of two fuzzy subsets. Suppose that there are m fuzzy subsets $A_1, A_2, A_3, \cdots, A_m$ in universal $U = (u_1, u_2, u_3, \ldots, u_m)$ to constitute a standard model base. If the identified object B is also a fuzzy subset, which is the closest between B and A_i $(i = 1, 2, 3, \cdots, m)$. First, the inner product and cross-product of fuzzy vector are explained as follows [17]:

1. The inner product of fuzzy sets A and B is

$$A \circ B = \bigvee_{\text{all x}} (A(x) \wedge B(x)) \tag{9}$$

2. The cross-product of fuzzy sets A and B is

$$A \otimes B = \bigwedge_{\text{all x}} (A(x) \vee B(x)) \tag{10}$$

and the approaching degree of fuzzy sets A and B is

$$\sigma_T(A, B) = \frac{1}{2}[(A \circ B) + (1 - A \otimes B)] \tag{11}$$

Besides, Professor Wang also proposed a modified approaching degree, which is shown in Eq. (12) [18]:

$$\sigma_W(A,B) = (A \circ B) \wedge (A \otimes B)^c \qquad (12)$$

3 The Toolbox

3.1 The Characteristics of Toolbox

There are some features of fuzzy comprehensive evaluation and approaching degree toolbox [19]:

1. By using the Matlab GUI interface, it is possible to present the whole data on the interface and input the multi-data user-friendly. Moreover, Microsoft Office provides the functions cut, paste, copy, save, print, etc. Users can access the data easily, which is a great deal of help when processing papers.
2. The system requirements are as follows:
   Windows XP version or upgrade version, Matlab R2007/a version, Microsoft Excel 2000 version or upgrade version, and screen resolution, at least $1{,}024 \times 768$.

3.2 Fuzzy Comprehensive Evaluation

Example 1 For $A = (0.13, 0.13, 0.13, 0.08, 0.08, 0.13, 0.04, 0.08, 0.08, 0.04, 0.13)$, and

$$B = \begin{pmatrix}
0.24 & 0.69 & 0.07 & 0 & 0 \\
0.22 & 0.62 & 0.16 & 0 & 0 \\
0.27 & 0.60 & 0.33 & 0 & 0 \\
0.24 & 0.49 & 0.27 & 0 & 0 \\
0.13 & 0.47 & 0.33 & 0 & 0 \\
0.25 & 0.62 & 0.13 & 0 & 0 \\
0.11 & 0.65 & 0.22 & 0.2 & 0 \\
0.14 & 0.53 & 0.33 & 0 & 0 \\
0.14 & 0.65 & 0.16 & 0.5 & 0 \\
0.11 & 0.45 & 0.44 & 0 & 0 \\
0.13 & 0.41 & 0.40 & 0 & 0
\end{pmatrix}.$$

Taking min . min . $\quad b_1 = \overset{m}{\underset{i=1}{\wedge}} (A_i \wedge r_{i(11)}),$
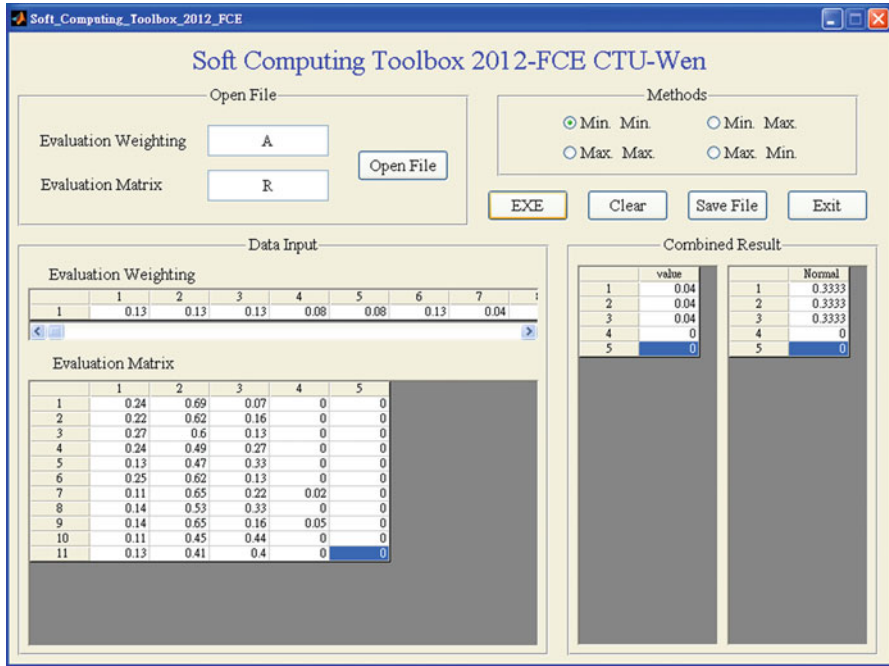
Fig. 1 The result of min.min. method

the results are (0.04, 0.04, 0.04, 0, 0), and after normalized, the weightings are (0.3333, 0.3333, 0.3333, 0, 0). The same as the calculation steps of min.min., the results of other states can be found, and when verified by the toolbox, the results are shown in Fig. 1.

3.3 Fuzzy Approaching Degree

Example 2 For $A = (0.13, 0.13, 0.13, 0.08, 0.08, 0.13, 0.04, 0.08, 0.08, 0.04)$, and

$$B = \begin{pmatrix} 0.24 & 0.22 & 0.27 & 0.24 & 0.13 & 0.25 & 0.11 & 0.14 & 0.14 & 0.11 \\ 0.69 & 0.62 & 0.60 & 0.49 & 0.47 & 0.62 & 0.62 & 0.53 & 0.65 & 0.45 \\ 0.07 & 0.16 & 0.33 & 0.33 & 0.33 & 0.13 & 0.22 & 0.33 & 0.16 & 0.44 \end{pmatrix}.$$

1. The first row in B: Through Eqs. (9) and (10), we can get

$$A \circ B_1 = \bigvee_{\text{all } x} (A(x) \wedge B(x)) = 0.13 \quad \text{and} \quad A \otimes B_1 = \bigwedge_{\text{all } x} (A(x) \vee B_1(x)) = 0.11;$$

then by substituting into Eqs. (11) and (12), the approaching degrees are
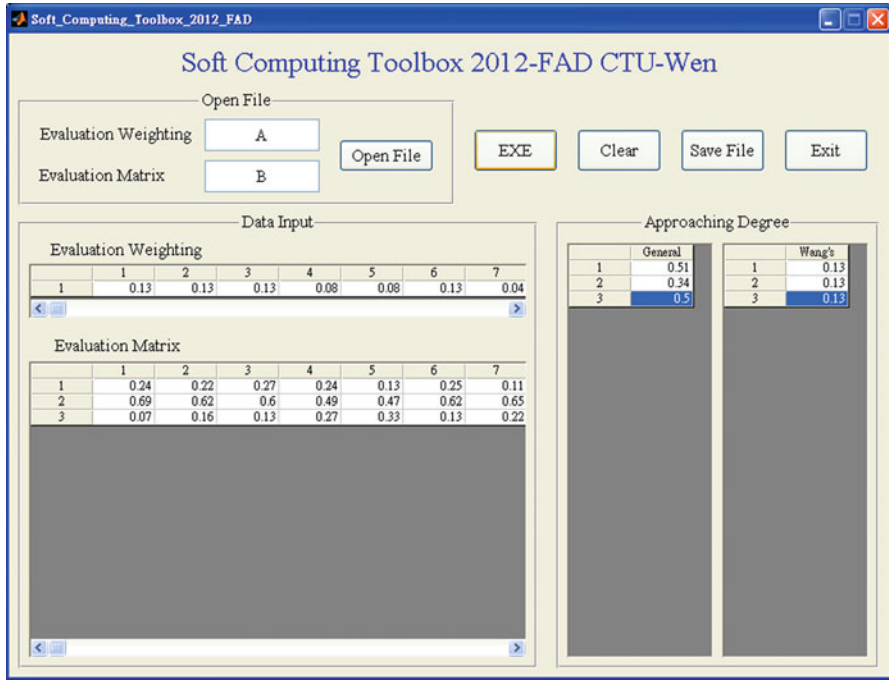
Fig. 2 The result of general and Wang's method

$$\sigma_T(A, B_1) = \frac{1}{2}[(A \circ B) + (1 - A \otimes B)] = \frac{1}{2}[0.13 + (1 - 0.11)] = 0.51$$

and $\sigma_W(A, B_1) = (A \circ B_1) \wedge (A \otimes B_1)^c = 0.13 \wedge 0.11^c = 0.13$, respectively.

2. The second row in B: Same as the calculation steps,

$A \circ B_2 = \underset{all\ x}{\vee} (A(x) \wedge B(x)) = 0.13$ and $A \otimes B_2 = \underset{all\ x}{\wedge} (A(x) \vee B_1(x)) = 0.45$,

then $\sigma_T(A, B_2) = 0.34$ and $\sigma_W(A, B_2) = 0.13$

3. The third row in B: Same as the calculation steps,

$A \circ B_3 = \underset{all\ x}{\vee} (A(x) \wedge B(x)) = 0.13$ and $A \otimes B_3 = \underset{all\ x}{\wedge} (A(x) \vee B_1(x)) = 0.13$,

then $\sigma_T(A, B_3) = 0.50$ and $\sigma_W(A, B_3) = 0.13$.

The use of Matlab to verify the results is shown in Fig. 2.

4 Conclusions

In the current engineering calculations, software are often used to assist and analyze the data. In the past, there were lots of achievements in software development, but lacked the discussion of the Matlab GUI toolbox to integrate fuzzy comprehensive evaluation and approaching degree. The proposed toolbox in this chapter aims to assist analysis and validation. The chapter uses the GUI software, which is not only user-friendly but also has powerful analytical functions. However, the limitation of this chapter is that the Matlab GUI function is limited to the resolution of the graphics, which cannot present the whole analysis process. In the future research, it is suggested that it be compared to other toolboxes of relevant theory to have a better effect.

References

1. Wiki (2012) http://en.wikipedia.org/wiki/Soft_computing
2. Zadeh LA (1965) Fuzzy sets. Inf Control 8:338–353
3. Lee J, Wang HF, Su MC (2005) Fuzzy set theory and its application. CHWA, Taipei
4. Ang K, Chong G, Li Y (2005) PID control system analysis, design and technology. IEEE Trans Control Syst Technol 13:559–576
5. Wang AM, Liu LX (2008) The giant complex system research based on fuzzy theory and intelligent decision support system IDSS. In: International symposiums on information processing. IEE Computer Society, Los Alamitos, pp 229–235
6. Huang LJ, Wang W, Wu ZS, Xu LJ (2008) Research on the model of HV SF6 circuit breaker fault diagnosis based on fuzzy theory. In: International conference on condition monitoring and diagnosis, pp 428–431
7. Wang HA, Dong ZC, Wu Z (2008) Research on multi-system coupling system dynamics model simulation combining with fuzzy theory. In: International conference on intelligent computation technology and automation. IEE Computer Society, Washington, DC, pp 920–924
8. Ross TJ (2010) Fuzzy logic-with engineering applications, 3rd edn. Wiley, Chichester
9. Zhai XF, Zhang JH, Zhao JH (2006) The MATLAB simulation of the permanent magnetic linear synchronous motor and positioning experiment. Marine Electr Electron Technol 26(4):6–9
10. Li C, Duanmu JS, Wang Q (2012) Organizational safety culture assessment method based on fuzzy proximity. China Safety Sci J 22(1):131–136
11. Liu Y, Xia Y (2003) The application of fuzzy comprehension decision method to assessing inter-risk control. Value Eng 2(49):49–52
12. Li K, Chen YX, Shi MC (2008) Weapon efficiency evaluation based on fuzzy approaching degree. Electron Opt Control 4:23–26
13. Han JH, Guo Y (2008) Reliability prediction of product based on fuzzy approaching degree. Mech Manage Dev 23(3):49–50
14. Jang JSR (2008) Matlab program design. TeraSoft Inc, Hsinchhu

15. Wu XL (2002) Design of auxiliary fuzzy system in MATLAB. Xi'an University of Electronic Science and Technology Press, Xi'an
16. Wen KL, Lu HT, Wu JH (1997) The research of student responses of teaching based on weighted average, fuzzy evaluation and grey relational grade. In: The grey system theory and application conference, pp 250–256
17. Feng GC, Chao JS, Chang HC, Wen KL (2007) Fuzzy theory and its application. New Wun Ching Developmental Publishing Co. Ltd, Taipei
18. Wang PZ, Lee HS (1995) The design of fuzzy computer. J Beijing Normal Univ (Nat Sci) 2
19. Wang BT, Wang JR, Wen KL, Nagai MT, Liang JC (2011) Kansei engineering fundamentals. Taiwan Kansei Information Association, Taichung

Deploying Autonomous Coordinating Agent for Assessment Model in Smart Urban Space: A Case Study of Cozy Space Design Pattern

Chiung-Hui Chen

Abstract This research proposes an effective method for assessing the design of the coordination of autonomous agents, which can be applied to urban outdoor space design based on the developed "cozy place" model base. The purpose of this research is to assess the coordination effectiveness of coordination agents during the interaction process of the design model. This project adopts autonomous coordination agents to simulate the design goal, constructs a coordination model, defines the coordination collections of agent groups, and regards the conflicts in the coordination process as the coordination problems of agents in each group. Finally, this research used the design model of the coordination mechanism of cozy place design as an example to verify the assessment method proposed by this research.

Keywords Coordinating agent • Cozy place • Assessment model • Autonomous

1 Introduction

Outdoor activities in a relaxed atmosphere cannot only increase an individual's interaction with others but they can also practice and enhance their own values of life. Hence, good places in a city have gradually become main fields for people to have leisure activities. According to the agent-based theory, Chen [1, 2] proposes an interactive agent model in which the design is pattern-oriented, with the socially open space in the cities being main observation subjects. In that essay, the relationships between the design pattern and the agent-based model are mainly explored. As the agent-based theory is suitable for the acquisition and analysis of planning needs in the interactive coordination, the ways other agents should present are controlled by

C.-H. Chen (✉)
Department of Digital Media Design, Asia University, Taichung 41354, Taiwan
e-mail: 7451616@gmail.com

setting up their locations and spreading attraction in terms of the scale-distance relationships among various qualitative agents in that essay. Then, each design object in the space is regarded as an agent. Its major contribution is to develop a script-based agent pattern database of spatial object. In the essay, assuming that if each agent of design object possesses his own behavioral mechanism, it is to complete a design goal when a script function is executed. During the process in which action dependencies among agents are researched, it is discovered that coordinating agents need to be added to be responsible for the coordination of behaviors and functions, if good communication and coordination are produced to reach the design goal. Based on the above research background, it is considered in this study that an assessment model must be further developed and built.

2 Exploration of Relevant Theories

2.1 Characteristics of Coordination

According to the term "coordination" described by Malone [3], a task must be completed together by more than two people, and the communication activity generated in this process is coordination. Meanwhile, Malone and Crowston [4] give more clear definitions regarding the application of the coordination theory in the field of collaborative design. According to their research, the combination of coordination can be divided into four elements: *goal*, *activities*, *actors*, and *interdependencies*. The dependencies among actors must be dealt with when a variety of activities are held to reach common goals. And this necessary behavior is a kind of coordination. Regarding the cooperation problem among agents, Conte et al. [5] think that the cooperation among agents can be viewed as the adjustment for common goals. Furthermore, the complete cooperation is employed in solving cooperative problems. None of the agents have sufficient abilities or resources to independently solve problems. Hence, through each other's cooperative mechanism, the problems are broken down into tasks which are separately completed. Genesereth et al. [6] research into a variety of scenarios in which multiagents are from complete cooperation to competitive hostility. In the model of complete cooperation, it is necessary to be premised on the assumption that agents are altruistic. However, in reality, the conflicts among agents are inevitable. Hence, coordination and negotiation are further required to solve the problem of goal conflict among one another.

2.2 Design and Coordinating Agent

The establishment of the agent architecture is mainly decided on the problem of its own field as well as on the dispersal behavior of groups. For instance, the spatial

objects proposed by Aly and Krishnamurti [7] are the active concepts of agents. The doors and windows in the design are regarded as agents. These object agents form a cooperative system on their own and can interact with designers. Liu et al. [8–10] create a cooperative design environment, providing designers and software agents to have interactive behaviors such as information exchange in the design process. By building a stratified multiagent system as well as agent dynamic and static knowledge structure, a cooperative model of dynamic management agent is generated. In the abovementioned multiagent framework, each agent can automatically respond to design scenarios and other agents' knowledge. Meanwhile, cooperation among agents also accordingly forms a dispersive knowledge connection relationship. To establish these dispersive knowledge connection relationships, communication among agents is an important normalization mechanism. This mechanism which is the major computing mechanism of agents controls the coordinative relationships of interplay.

2.3 Interactive Connection Pattern of Coordinating Agent Community

Bryan [11] thinks that a multiagent system is like the human organization. There are differences in statically or dynamically formed organizations. There are flat, hierarchic, nest-shaped organizational structures. There are organizational designs in different freedom levels such as control and society. There are organizational structures of parallel processing and centralized distribution. These create various organizational forms of multiagents. However, no matter if it is the static formation or the dynamic one, there are no consistent viewpoints regarding what forms of agent organizations will be most suitable for solving problems in relevant studies. Guimera et al. [12] think that various scenarios and problems should be considered to choose a suitable form of organization. No organizational form is particularly prominent enough to dominate other forms of organizations. For instance, Klein et al. [13, 14] propose that, basing the connection establishment on design problems, each agent solves different design problems and thus generates the connections based on groups or clumps, further forming the interactive coordinating connection pattern of communities. How to evaluate function rules is also defined, generating an assessment approach to utility value optimization design.

3 Research Methods

Based on the abovementioned important literature analyses and research purposes, the agent coordination mechanism defined in this model is to view the cooperation as the operation mechanism. The research approach to theoretical modeling is summarized as follows:

ME   MainEntrance
AB   Advertisement Board
UL   Up-Lighting
ST   Seat
PT   Plant
BL   Bottom-Lighting
GC   Garbage Can
MT   Movie Timetable
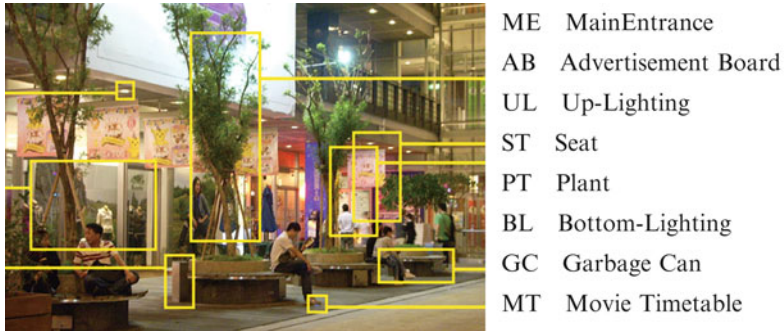
Fig. 1 Example of good-place design pattern: not just for entertainment purposes only

3.1   Autonomous Agent Coordination Issue

A title "Not Just For Entertainment Purposes Only" is as low profile as the privacy of its location; a semicircular open-air plaza is hidden in the community. As shown in Fig. 1, the "Not Just For Entertainment Purposes Only" contains two kinds of solid wooden chairs: seven round chairs and seven square ones. Of all, seven solid wooden chairs are colored with red, orange, yellow, green, blue, indigo, and violet, while the other seven ones remain unchanged. From the inside come the singing voices and the sounds of musical instruments. It turns out that these voices and sounds come from the little stage with one step rising from the center. People are invited to enter this half-open, half-private space. Sitting on solid wooden chairs of various colors, people listen to, watch, and enjoy the sounds, colors, and atmospheres belonging to this field. At night, solid wooden chairs and the little stage slightly protruding from the center are installed with projection lamps and punctual illumination. They are surrounded by Madagascar almond which is as high as a one-story building to form an open-air theater. Resonance is established among people. Life experiences of middle-aged people are shared with one another. The information closely related with people is provided. In the real world, people let themselves enter into a state of encounter. A venue full of reality is the good-place design pattern with real contents.

3.2   Autonomous Agent Coordination Framework

The above issues are divided into the main concept group and small concept groups; that is, they are broken down into different design object agent groups, as shown in Fig. 2. Interactive connection will be generated among agent groups because of the intervention of coordinating agents, as shown in Fig. 3. A good-place design pattern
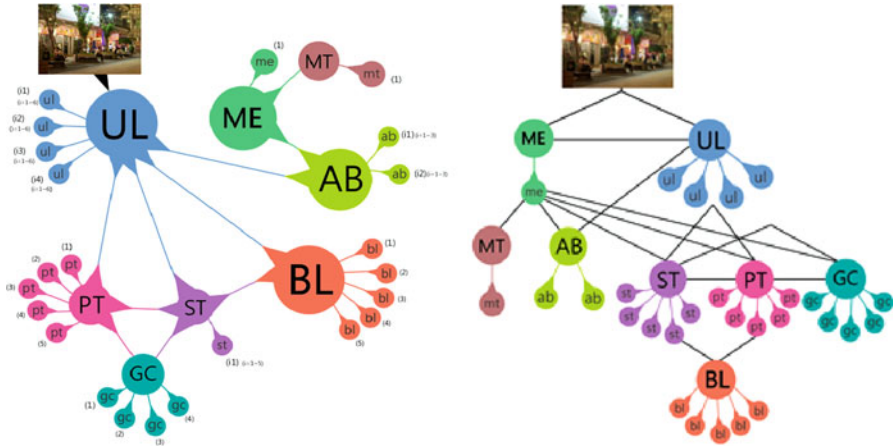
Fig. 2 Design object agent groups of "Not Just For Entertainment Purposes Only"
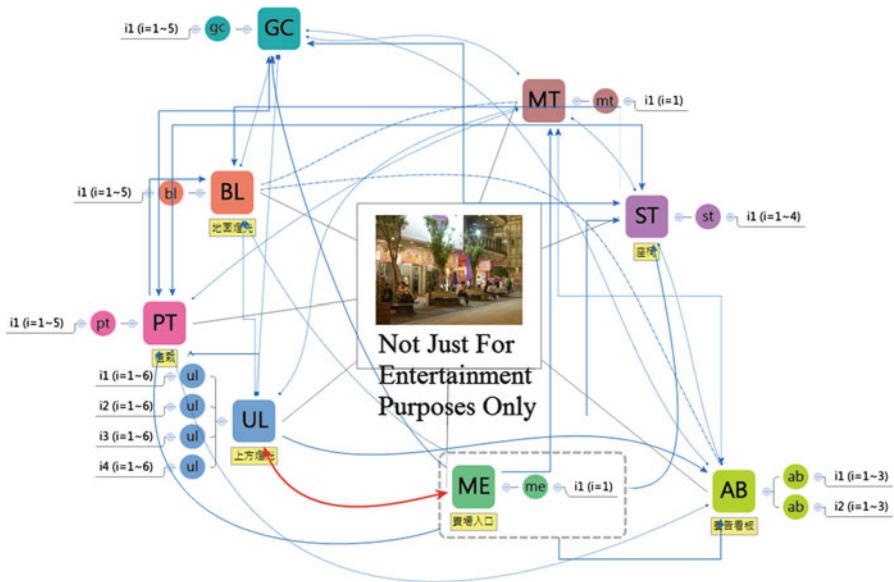
Fig. 3 Interactive connection is generated between two different design object agent groups because of the intervention of coordinating agents

is made up of several design object agent groups. Agents of each group must coordinate the constituent sequence. The agent coordinating algorithm is taking all the constituent sequences of this pattern into consideration. Coordinating agents propose the best sequence for bargaining. Here, three kinds of ways are set for the connection principle:

- When individuals are linked to the main group, connection will be formed among them to form a group.
- When individuals are not linked to the main group, connection will also be formed among them. A group is formed, too.
- When individuals are correlated with other main groups (including individuals), connection will also be formed. Groups are divided according to the procedure.

4 Discussions and Subsequent Studies

Linkography [15, 16] is a process in which the evolution of design ideas is recorded. Through image links, the correlation of each idea is recorded, like a chess move, which is a continuous activity. Hence, in this chapter, the propagation steps generated by coordinating agents are taken as a basis, besides referring to the link index of Goldschmidt and the way of link density of van der Lugt. Design effectiveness and link density are correlated with the number of key moves. It shows that the higher the number of these two is, the more productivity there is in this design process. We can calculate the relationships between the number of moves and the link density through linkography to explore the content of information implied in various linkographies. When the model is built in this study, the focus is on the link effectiveness of coordinating agents. Therefore, the link index can provide a major way to evaluate the combination link effectiveness of this model. Here, life cycle of coordinating agent, total value of links, link depth, and link index are the quantified measurement indices.

References

1. Chen CH (2011) Attention theory-based agent system: using shopping street design simulation as an example. J Chin Inst Eng 34(1):155–168
2. Chen CH (2011) Behavioral mechanism-advancing a design state with multi-agents coordinating. Appl Mech Mat 148–149:789–794
3. Malone TW, Crowston K (1990) What is coordination theory and how can it help design cooperative work systems. In: Proceedings of the 3rd conference on computer-supported cooperative worked,. ACM Press, New York, pp 357–370
4. Malone TW, Crowston K (1994) The interdisciplinary study of coordination. ACM Comput Surv 26(1):87–119
5. Conte R, Miceli M, Castelfranchi C (1991) Limits and levels of cooperation: disentangling various types of prosocial interaction. In: Demazeau Y, Muller JP (eds) Decentralized artificial intelligence, vol 2. North Holland, Amsterdam

6. Genesereth MR, Ginsberg ML, Rosenschein JS (1986) Cooperation without communication. In: Proceedings of American Association on Artificial Intelligence, Philadelphia, Aug 1986, pp 51–57
7. Aly S, Krishnamurti R (2002) Can doors and windows become design team player. In: Agents in design, pp 3–22
8. Liu H, Tang M, Frazer JH (2002) Supporting evolution in a multi-agent cooperative design environment. Adv Eng Softw 33(6):319–328
9. Liu H, Tang M, Frazer JH (2002) A knowledge based collaborative design environment. In: Gero JS, Brazier FMT (eds) Agents in design. Key Centre of Design Computing and Cognition, University of Sydney, Sydney, pp 233–246
10. Liu H, Tang M (2006) Evolutionary design in a multi-agent design environment. Appl Soft Comput J 6(2):207–220
11. Bryan H, Victor L (2005) A survey of multi-agent organizational paradigms. Knowl Eng Rev 19(4):281–316
12. Guimera R, Uzzi B, Spiro J, Amaral L (2005) Team assembly mechanisms determine collaboration network structure and team performance. Science 308(5722):697–702
13. Klein M, Sayama H, Faratin P, Bar-Yam Y (2002) A complex systems perspective on how agents can support collaborative design. In: Gero JS, Brazier FM (eds) Agents in design. Key Centre of Design Computing and Cognition, Cambridge, MA, pp 95–111
14. Klein M, Sayama H, Faratin P, Bar-Yam Y (2002) A complex systems perspective on computer-supported collaborative design technology. Commun ACM 45(11):27–32
15. Goldschmidt G (1990) Linkography-assessing design productivity. In: Trappl R (ed) Cybernetics and systems'90. Proceedings of the tenth European meeting on cybernetics and systems research. World Scientific, Singapore, pp 291–298
16. Goldschmidt G, Tatsa D (2005) How good are good ideas? Correlates of design creativity. Des Stud 26:593–611

Quantum-Membership-Function-Based Adaptive Neural Fuzzy Inference System

Cheng-Hsiung Chiang

Abstract The well-known ANFIS (adaptive-network-based fuzzy inference system) has demonstrated good performance and applicability. This chapter presents a quantum version of ANFIS model, namely, qANFIS, whose network structure is similar to ANFIS but it is with quantum membership functions (qMF). A hybrid learning procedure is proposed to update the parameters. First, we develop a genetic algorithm with trimming operator to determine the number of quantum levels in qMF. Second, the least squares estimate method is applied to update the consequent parameters. Finally, we introduce two methods to update the qMF parameters, the gradient descent and the quantum-inspired particle swarm optimization methods, and one of them is selected for training purpose. The simulation results of path planning had demonstrated that the proposed method could reach satisfactory performance and smaller error measure as compared with ANFIS.

Keywords ANFIS • Genetic algorithm • Neuro-fuzzy system • Path planning • Quantum function • Quantum particle swarm optimization

1 Introduction

The neuro-fuzzy systems that combine fuzzy systems and neural networks demonstrate several advantages, e.g., tuning membership functions and fuzzy rules by neural networks and getting a more clear understanding of mapping rules in the network.

C.-H. Chiang (✉)
Department of Information Management, Hsuan Chuang University,
Hsinchu City 300, Taiwan, Republic of China
e-mail: chchiang@hcu.edu.tw

The Takagi-Sugeno-Kang (TSK) system whose fuzzy rules are linear combinations of their preconditions has been proven that it can approximate every plant. ANFIS proposed by Jang [5] is a TSK-type fuzzy system that has been successfully applied to many fields such as [6]. ANFIS is a five-layered feed-forward network where each node within the network performs a particular function on incoming signals. To perform desired input-output characteristics, the parameters are updated based on gradient descent (GD) learning rules and/or least squares estimate (LSE) method [5].

Several literatures have reported the other evolutionary computation approach-based learning algorithms for ANFIS, such as genetic algorithms (GAs) and particle swarm optimization (PSO), to reduce model training errors and testing errors. Lu and Wang [7] had reported that the parameter learning of PSO-based ANFIS had better performance than GA-based ANFIS.

With regard to the different types of node function in the network of ANFIS, Chai et al. [1] presented Mamdani model-based ANFIS, i.e., M-ANFIS, whose consequent part adopted the Mamdani-type fuzzy rules. In the application of evaluating traffic level of service, M-ANFIS has been proven that it is more effective than ANFIS in small-scale sample data. To our best knowledge, no studies have investigated quantum-membership-function (qMF)-based ANFIS.

The qMF is a multilevel membership function, and the traditional membership function may be considered as a special case of qMF. This chapter proposes the qMF-based ANFIS, namely, qANFIS, whose structure is similar to ANFIS but its premise fuzzy sets in Layer 1 adopt the qMFs. A hybrid learning algorithm with three main processes is presented to tune the parameters: (1) The trimming operation-based GA (tGA) is proposed to discover a better number of quantum levels for qMF, (2) the LSE approach is applied to update the consequent parameters, and (3) one of the GD method or quantum-inspired PSO (qPSO) method is selected to adjust the premise parameters. The simulation results of path planning have demonstrated the performance of the proposed methods by comparing with ANFIS.

2 Quantum Membership Function

The qMF used in qANFIS has the following form [2]:

$$
\mu_{A_i}(x) = \frac{1}{ns_i} \sum_{\alpha=1}^{ns_i} \left[\frac{1}{1 + \exp\{-\beta_i(x - c_i + |\theta_i^\alpha|)\}} \cdot U(x; -\infty, c_i) \right.
$$
$$
\left. + \frac{\exp\{-\beta_i(x - c_i - |\theta_i^\alpha|)\}}{1 + \exp\{-\beta_i(x - c_i - |\theta_i^\alpha|)\}} \cdot U(x; c_i, \infty) \right],
$$

(1)

Fig. 1 It is an example of quantum membership function. The number of levels $ns = 3$, the center $c = 0$, the slope factor $\beta = 2$, and the quantum intervals $\theta = [5, 15, 25]$
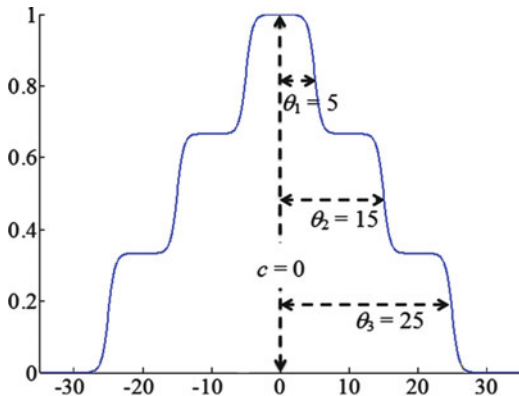
where $\mu_{A_i}(x)$ is the ith qMF of input variable x and $U(x; a, b) = \begin{cases} 1, & \text{if } a \leq x_i < b \\ 0, & \text{otherwise} \end{cases}$.

For node i, c_i is the center of qMF, β_i is the slope factor, ns_i denotes the number of levels in the qMF, and θ_i^α is the αth quantum internal. Figure 1 illustrates a three-level qMF.

3   Hybrid Learning Algorithm for qANFIS

The task of the learning algorithm is to determine that the modifiable parameters to make the actual output of qANFIS match the desired output of training data. We expand the hybrid learning algorithm proposed by Jang [5] to develop a new learning procedure for qANFIS as shown in Algorithm 1.

Initially, let $ns_i = 1$. The initial qMFs are distributed uniformly on [0, 1]. The initial β_i and θ_i^α are determined as $\beta_i = 12/\text{width}$ and $\theta_i^\alpha = \text{width}/2$, where width $= 1/(n - 1)$ and n is the number of qMFs. After calculating the output of Layer 3, the sequential LSE method [5] is then employed to determine the initial consequent parameters. Before training, the proposed tGA is used to find the number of quantum levels ns_i, and the αth quantum interval is then obtained by $\theta_i^\alpha = (1/ns_i) \cdot \alpha \cdot (\text{width}/2)$.

In Lines 6–10, we first carry out the sequential LSE method to determine the consequent parameters and fix the obtained parameters. We introduce two schemes to update the qMF parameters, i.e., GD and qPSO approaches. Once we choose one of them to update parameters, we have to use it for all training epochs. The root mean square error (RMSE) is applied to pick out a better parameter set as stated in Line 9. After performing *nEpochs* iterations, we can get the best parameter set of qANFIS.

Algorithm 1: Hybrid Learning Algorithm of qANFIS

1: Normalize the training data into [0, 1]
2: Establish initial qMF parameters: $\{ns_i, c_i, \beta_i, \theta_i^\alpha\}$
3: Calculate initial consequent parameters $\{p_i, q_i, r_i\}$ using sequential LSE method
4: Find best ns_i and θ_i^α using ***tGA*** and then fix ns_i
5: Let bestRMSE be a big positive number
6: **for** $t = 1$ to *nEpoch* **do**
7:       Apply sequential LSE method to update the $\{p_i, q_i, r_i\}$ parameters
8:       Adjust the parameters $\{ns_i, c_i, \beta_i, \theta_i^\alpha\}$ using ***qPSO*** or ***GD*** method
9:       If current RMSE $<$ bestRMSE, then record bestRMSE and *best parameters*
10: **end_for**
11: Return the *best parameters*

Algorithm 2: Trimming-Operator-Based Genetic Algorithm (tGA)

1: Determine the initial parameters
2: Randomly generate initial population $\boldsymbol{P} = \{p_1, \ldots, p_N\}$ with N chromosomes
3: **for** $t = 1$ to *maxGen* **do**
4:       Evaluate $\boldsymbol{P}$, and store the best m individuals into $\boldsymbol{P_{best}}$
5:       $\boldsymbol{sP} \leftarrow$ SELECTION($\boldsymbol{P}$)
6:       $\boldsymbol{cP} \leftarrow$ CROSSOVER($\boldsymbol{sP}$) and $\boldsymbol{mP} \leftarrow$ MUTATION($\boldsymbol{sP}$)
7:       $\boldsymbol{mergeP} \leftarrow \{\boldsymbol{P_{best}} \cup \boldsymbol{sP} \cup \boldsymbol{cP} \cup \boldsymbol{mP}\}$
8:       $\boldsymbol{trimP} \leftarrow$ TRIMMING($\boldsymbol{mergeP}$)
9:       $\boldsymbol{P} \leftarrow$ find the best N individuals from $\boldsymbol{trimP}$
10: **end_for**
11: Output the best one obtained from $\boldsymbol{P_{best}}$

3.1 tGA Approach

GA is an optimization method based on the ideas of natural selection and evolutionary processes. We developed a new GA with trimming operator (tGA) to find the fittest ns_i for ith qMF as presented in Algorithm 2.

In the beginning, we have to settle the initial parameters including the probabilities of doing crossover and mutation operations, the number of chromosomes N, the number of remained elite in a population m, and the maximal number of evolution *maxGen*. The symbol $\boldsymbol{y} \leftarrow$ FUNCTION($\boldsymbol{x}$) means that the output $\boldsymbol{y}$ is obtained by performing the FUNCTION given the input $\boldsymbol{x}$, as shown in Lines 5, 6, and 8. We apply the roulette-wheel selection, two-point crossover, and bit-flipping-based mutation [4]. The trimming operator, in Line 8, is to randomly regenerate the chromosomes whose binary strings are the same.

3.2 GD Approach

The objective is to minimize the overall error measure E between the actual output and desired output in order to adjust the qMF parameters. To minimize E, we have to calculate gradient vector $\partial E / \partial \omega$ defined as

$$\Delta\omega = -\eta\frac{\partial E}{\partial \omega}, \tag{2}$$

where ω represents an adjustable qMF parameter. The update formula of ω is

$$\omega(t+1) = \omega(t) + \Delta\omega. \tag{3}$$

3.3 PSO Approach

The PSO simulates the social behavior of a bird swarm, and it optimizes a problem by evolution. A number of literatures have reported on the ANFIS training task using PSO [6]. In addition, several literatures demonstrated that quantum-behavior-inspired PSO (QPSO) is more efficient than PSO in specific problems such as [8]. The QPSO guides all particles moving based on quantum behavior instead of the linear motion. In this chapter, we apply an improved QPSO, i.e., qPSO, proposed by Chiang [3] to discover the best qMF parameters. We employ the RMSE to evaluate the solution quality of a particle that represents a qMF parameter set.

4 Simulation Results of Robotic Path Planning

In order to demonstrate our proposed model, we apply qANFIS to the robotic path-planning problem. To control the robot moving to the target, we employ the design of robotic controller proposed by Chiang [3]. The input variables of qANFIS are d and φ which are the distance and included angle between the robot and target, respectively. The output variable θ is the steering angle of the robot. The qANFIS models have two types: (1) GD-qANFIS whose qMFs are updated by GD approach and (2) qPSO-qANFIS whose qMFs are adjusted by qPSO approach. Two simulation results are described as follows.

4.1 Case 1

Figure 2a shows that all methods can successfully reach the target without collision, and the trajectories obtained by them are very close. The RMSE values resulted by the three methods are listed in Table 1. The GD-qANFIS has the smallest RMSE,
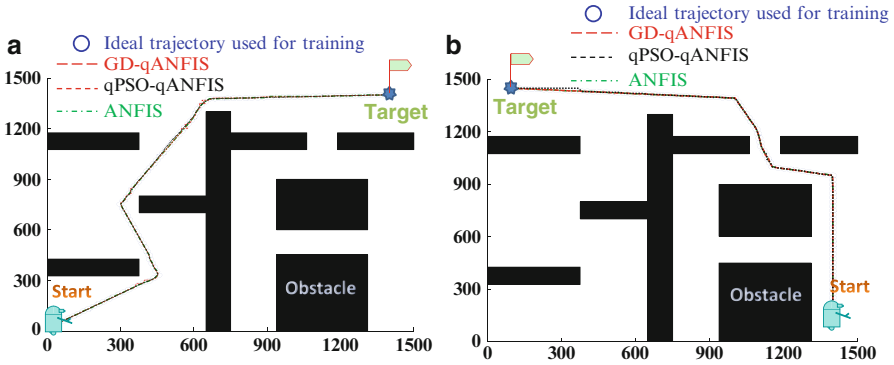
Fig. 2 Comparison results of the three methods: GD-qANFIS, qPSO-qANFIS, and ANFIS. (**a**) Case 1; (**b**) Case 2. The robotic trajectories of the three approaches are very close in Case 1 and Case 2

Table 1 The best RMSE values after 2000 training epochs of the three methods

	RMSE	
Method	Case 1	Case 2
GD-qANFIS	*0.00230*	0.00841
qPSO-qANFIS	0.00232	*0.00360*
ANFIS	0.00839	0.01262

0.00230, and its RMSE is close to that of qPSO-qANFIS. In respect to the path length, both ANFIS and qPSO-qANFIS guided the robot moving 96 steps to reach the target, but GD-qANFIS required 101 steps.

4.2   Case 2

Figure 2b also reveals that the three approaches have the approximate trajectories. The training error listed in Table 1 shows that qPSO-qANFIS is with the smallest value, 0.00360, and ANFIS is with the biggest, 0.01262. In terms of the path length, both GD-qANFIS and ANFIS required 97 steps to lead the robot reaching the target, and qPSO-qANFIS requires 98 steps.

4.3   Discussion

The trajectories of all methods are approximate, but in terms of the training error, qPSO-qANFIS almost performed the best. However, qPSO-qANFIS required much CPU time for training 2000 epochs, i.e., several hours, but the other two methods only took hundreds of seconds. Thus, if we consider the smaller training error and acceptable outcomes, *the GD-qANFIS is the better choice*.

5 Conclusion

This chapter has proposed the quantum-membership-function-based ANFIS, namely, qANFIS. The presented hybrid learning algorithm contains three major processes: (1) The proposed tGA determines the number of quantum levels, (2) the LSE method updates the consequent parameters, and (3) one of the GD or qPSO approach is selected to adjust the qMF parameters. The simulation results of path planning showed that the GD-qANFIS is a better choice among the three methods. In future study, we may investigate the issue of rule reduction of qANFIS to enhance the efficiency.

References

1. Chai Y, Jia L, Zhang Z (2009) Mamdani model based adaptive neural fuzzy inference system and its application. Int J Comput Intell 5:22–29
2. Chen C-H, Lin C-J, Lin C-T (2008) An efficient quantum neuro-fuzzy classifier based on fuzzy entropy and compensatory operation. Soft Comput 12:567–583
3. Chiang C-H (2008) A symbolic controller based intelligent control system with quantum particle swarm optimization based hybrid genetic algorithm. In: Congress on evolutionary computation. IEEE Press, New York, pp 1356–1363
4. Goldberg DE (1989) Genetic algorithms in search, optimization and machine learning. Kluwer Academic, Boston
5. Jang J-SR (1993) ANFIS: adaptive-network-based fuzzy inference system. IEEE Trans Syst Man Cybern B Cybern 23:665–685
6. Jiang HM, Kwong CK, Ip WH, Wong TC (2012) Modeling customer satisfaction for new product development using a PSO-based ANFIS approach. Appl Soft Comput 12:726–734
7. Lu KZ, Wang RC (2008) Application of PSO and QPSO algorithm to estimate parameters from kinetic model of glutamic acid batch fermentation. In: 7th world congress on intelligent control and automation. IEEE Press, New York, pp 8968–8971
8. Mikki SM, Kishk AA (2006) Quantum particle swarm optimization for electromagnetics. IEEE Trans Antenna Propag 54:2764–2775

A Set-Checking Algorithm for Mining Maximal Frequent Itemsets from Data Streams

Ye-In Chang, Meng-Hsuan Tsai, Chia-En Li, and Pei-Ying Lin

Abstract Online mining the maximal frequent itemsets over data streams is an important problem in data mining. In order to solve mining maximal frequent itemsets from data streams using the Landmark Window model, Mao et al. propose the INSTANT algorithm. The structure of the INSTANT algorithm is simple and it can save much memory space. But it takes long time in mining the maximal frequent itemsets. When the new transaction comes, the number of comparisons between the old transactions of the INSTANT algorithm is too much. Therefore, in this chapter, we propose the Set-Checking algorithm to mine frequent itemsets from data streams using the Landmark Window model. We use the structure of the lattice to store our information. The structure of the lattice records the subset relationship between the child node and the parent node. From our simulation results, we show that the process time of our Set-Checking algorithm is faster than that of the INSTANT algorithm.

Keywords Data stream • Itemset • Landmark Window model • Lattice • Maximal frequent itemset

1 Introduction

Traditional database management systems expect all data to be managed within some forms of persistent data sets. For many recent applications, the concept of a data stream, possibly infinite, is more appropriate than a persistent data set. A data stream is an order sequence of transactions that arrives in a timely order. Different from data in traditional static databases, data streams have the following

Y.-I. Chang (✉) • M.-H. Tsai • C.-E. Li • P.-Y. Lin
Department of Computer Science and Engineering, National Sun Yat-Sen University,
Kaohsiung, Taiwan, R.O.C.
e-mail: changyi@mail.cse.nsysu.edu.tw

characteristics [1–6]. First, they are continuous, unbounded, and usually come with high speed. Second, the volume of data streams is large and usually with an open end. Third, the data distribution in streams usually changes with time. A maximal frequent itemset is the itemset which is not the subset of other frequent itemset and the support is large or equal to the mining support. Therefore, the result of maximal frequent itemsets is more compact than the result of frequent itemsets. The INSTANT algorithm [5] uses a compact data structure to mine maximal frequent itemsets from data streams based on the Landmark Window. In the Landmark Window model, knowledge discovery is performed based on the values between the beginning time and the present. The advantage of using the Landmark Window model is that the results are correct as compared to the other models. The structure of the INSTANT algorithm is simple so that it can save the memory space. However, in the part of the itemset comparison, the INSTANT algorithm will take long time. Therefore, in the chapter, we propose the Set-Checking algorithm. In our structure, we add the link between the set and its subsets to show the relation between itemsets. When the new transaction comes, we will check the relation between the new transaction and the old transaction. Because of this links between the set and the subset, there are two advantages. First, we can decrease the number of comparisons between the new transaction and the old transactions. Second, when the support increases, the lattice structure does not change. From our simulation results, we show that the process time of our Set-Checking algorithm is faster than that of the INSTANT algorithm. The rest of the chapter is organized as follows. Section 2 gives a survey for mining association rules related problem. Section 3 presents the proposed Set-Checking algorithm. In Sect. 4, we study the performance. Finally, Sect. 5 gives the conclusion.

2   The Related Work

In this section, we describe some well-known data mining algorithms for association rules related problems in the traditional database and data streams [1–6].

Maximal frequent itemsets mining is one of the most important research issues in data mining. Take Transaction Database T in Fig. 1a as an example; Fig. 1b shows the frequent itemsets of Transaction Database T, where the value of the minimal support is 2. In Fig. 1c, large itemset "CD" and "ABC" is a maximal frequent itemset, because there is no superset which contains it. Itemset "AB" is not a maximal frequent itemset, because the frequent itemset "ABC" contains it.

The INSTANT algorithm [5] is a single-phase algorithm for mining maximal frequent itemsets from data streams. Given a continuous data stream, a user-specified minimum support count δ, and a shedding condition, the INSTANT algorithm consists of four steps: Step 1: generate a sorted itemset α from the current transaction of the data stream. Step 2: form new frequent itemsets and update the set of frequent itemsets. Step 3: modify information about infrequent elements and their supports based on α. Step 4: execute a shedding plan to maintain search efficiency and memory usage.

a

TID	Items
1	ABC
2	CD
3	ABC
4	ACD

b

L1	A : 3
	B : 2
	C : 3
	D : 2
L2	AB : 2
	AC : 3
	BC : 2
	CD : 2
L3	ABC : 2

c

L2	CD : 2
L3	ABC : 2

Fig. 1 An example: (**a**) Transaction Database T; (**b**) Frequent itemsets of Transaction Database T with the minimal support $= 2$; (**c**) Maximal frequent itemsets of Transaction Database T with the minimal support $= 2$

3 The Set-Checking Algorithm

One of the well-known models for data streams is the Landmark Window model. In this section, we present our algorithm based on the Landmark Window model.

3.1 The Proposed Algorithm

We first define some basic definitions and notations and then describe how to use them to find the maximal frequent itemsets and organize the maximal frequent itemsets in a lattice. According to the characteristic of the maximal frequent itemsets, we propose the Set-Checking algorithm. We can check the relation between the new transaction and old transactions and then build the lattice. The variables used are defined as follows. *minsup* is the minimal support. *Sup* is a transaction's support. *f_list* is the maximal frequent itemsets.

Our algorithm has three steps. Step 1: transform the itemset to the bit pattern. Step 2: check the relation between new transaction and old transaction. There are five cases in the relations. Case 1: equivalent. This case only updates the support of the old transaction. Case 2: superset. This case will update the support of the old transaction and the old transaction becomes the child of the new transaction. The new transaction will be inserted into the lattice. Case 3: subset. The new transaction will become the child of old transaction. Case 4: intersection. There are two situations. Case 4-1: the node is the intersection of the old transaction and the new transaction is not in the lattice. This case will insert the new transaction and intersected node. Case 4-2: the node which is the intersection of the old transaction and the new transaction is in the lattice. This case will insert the new transaction and update the support of intersected node. Case 5: empty set. The new transaction will

a

Tid	Itemset	Bit-Patten
1	1, 2, 3	111000
2	3, 4, 5	001110
3	3, 6	001001
4	1, 2, 3, 4, 5	111110
5	2	010000
6	1, 2, 3, 4, 5	111110

b

root

111000, Sup(1)

c

root

1,2,3   3,4.5
111000, Sup(1)   001110, Sup(1)

3
001000, Sup(2)
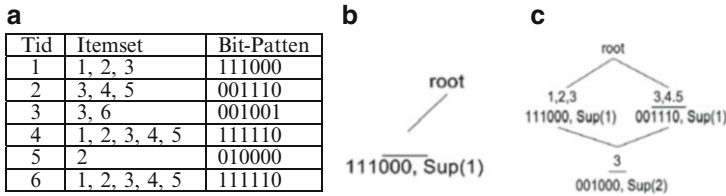
Fig. 2 An example: (**a**) an example of the data stream; (**b**) insertion of transaction Tid_1 into the lattice; (**c**) insertion of transaction Tid_2 into the lattice

be inserted into the lattice. Step 3: examine which transaction is the maximal frequent itemsets. If the frequent node is not the subset or equal to the *f_list*, we can add the frequent node to *f_list* and delete the node which is the subset of the frequent node from *f_list*.

3.2 Data Structure

In our algorithm, we propose a lattice structure. The lattice structure has two advantages. First, we can know the relation between the new transaction and the present transactions easily. Second, we can update the support of the transaction efficiency. We also build *f_list* to store the maximal frequent itemsets. The lattice structure contains the root, nodes, and child link. The root is the start point. It has no information. When a new transaction is coming, we start to search them from the root. The nodes are infrequent itemsets. Each node has some information: (1) *Bit pattern* represents itemset and (2) *Sup* represents the support of the itemset. The child link is the node link to subset nodes. Building the child link has many advantages. First, we can check the node's relation and insert the node into the tree easily. Second, we can increase the node's support easily. Our lattice structure has two characteristics. First, the high-level nodes are the subset of low level nodes. Second, the supports of high-level nodes are larger than that of the low level nodes.

3.3 Data Insertion

We use an example to illustrate our algorithm. Figure 2a shows an example of the data stream. The maximal length of bit length is 5 and the *minsup* is 6. Transaction Tid_1 {1, 2, 3} is the first transaction of the data stream. The root does not have a child, so the itemset is inserted into the root's child directly as shown in Fig. 2b. When transaction Tid_2 {3, 4, 5} comes, we will check whether the itemset is in the lattice or not. Obviously, transaction Tid_2 is not in the lattice. Then, we will check the relation between transaction Tid_1 and transaction Tid_2. We find that Tid_2

Fig. 3 Data insertion: (**a**) insertion of transaction Tid_3 into the lattice; (**b**) the final lattice
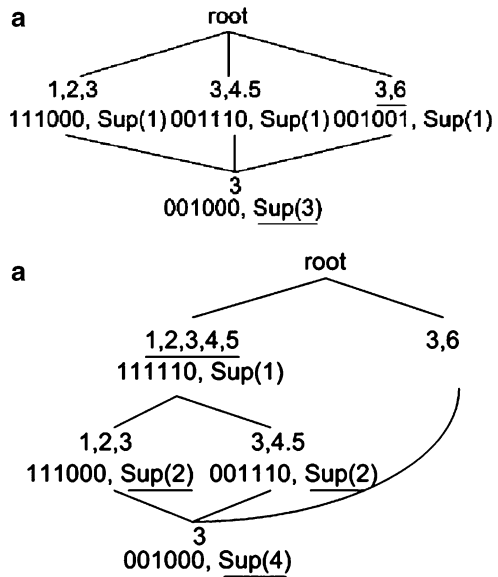
intersects with Tid_1 and intersected node {3} is in the lattice. So node {3} becomes the child of node {1, 2, 3} and node {3, 4, 5}. The support of node {1, 2, 3} which is in the lattice is increased. When we process the last child, we insert Tid_2 {3, 4, 5} into the lattice as shown in Fig. 2c. When transaction Tid_3 {3, 6} comes, we find that the intersected node {3} is in the lattice. Node {3} becomes the child of node {3, 6} and the support of node {3} is increased. Consider that when the new data stream comes, the support of each node in the lattice is increased at once. Because transaction Tid_3 {3, 6} is not in the lattice, when we process the last child, we insert transaction Tid_3 {3, 6} into the lattice as shown in Fig. 3a. Finally, the lattice will be built as shown in Fig. 3b.

3.4 The Maximal Frequent Itemsets

When the support of the transaction is larger than or equal to the minimal support, we can add this transaction to f_list. Figure 2a shows an example of the data stream. Let the minimal support = 3. When transaction Tid_1 {1, 2, 3} and Tid_2 {3, 4, 5} comes, the lattice will be built as shown in Fig. 2c. When transaction Tid_3 {3, 6} comes, the support of item {3} becomes 3. It equals the minimal support. So we can add item {3} to f_list as $f\_list \rightarrow 3(001000)$.

4   Performance

In this section, we describe how to generate the synthetic data which will be used in the simulation. Then, we study the performance of the INSTANT algorithm and our proposal Set-Checking algorithm.

4.1   The Simulation Model

We describe the way to generate synthetic transaction data from the IBM synthetic data developed by Agrawal and Srikant [1]. The parameters used in the generation of the synthetic data are as follows. $|T|$ is the average size of transactions. $|MT|$ is the maximum size of transactions. $|I|$ is the average size of maximal potentially frequent itemsets. $|D|$ is the number of transactions and $|MI|$ is the maximum size of potentially frequent itemsets. $|SD|$ is the size of added data and *corr* is the number of the correlation level.

First, the length of a transaction is determined by the Poisson distribution with a mean which is μ equal to $|T|$. The size of a transaction is between 1 and $|MT|$. The transaction is repeatedly assigned items from a set of potentially maximal frequent itemsets F while the length of the transaction does not exceed the generated length. Then, the length of an itemset in F is determined according to the Poisson distribution with a mean μ which is equal to $|I|$. The size of each potentially frequent itemset is between 1 and $|MI|$. To model the phenomenon that frequent itemsets often have common items, some fraction of items in subsequent itemsets are chosen from the previous itemset generated. We use an exponentially distributed random variable with a mean which is equal to the *correlation level* to decide this fraction for each itemset. The *correlation level* was set to 0.5. The remaining items are chosen randomly. Each itemset in F has an associated weight that determines the probability that this itemset will be chosen. The weight is chosen from an exponential distribution with a mean equal to 1.

4.2   Experiment Results

In this section, we show the experiment results. Figure 4a shows the comparison of the processing time under different minimum supports. The synthetic data is T3. MT10.I10.MI20.D10k. The number of item is 1,000 and the minimum support threshold is changed from 0.2 to 1 %. We can build 9k data then add 1k data to the data which we build. From the figure, we can find that the Set-Checking algorithm is faster than the INSTANT algorithm. Because the number of the itemset comparisons of the Set-Checking algorithm is less than that of the INSTANT algorithm, Fig. 4b shows the comparison of the processing time under different size of data. The minimum support threshold is 0.4 % and the number of items is 1,000.
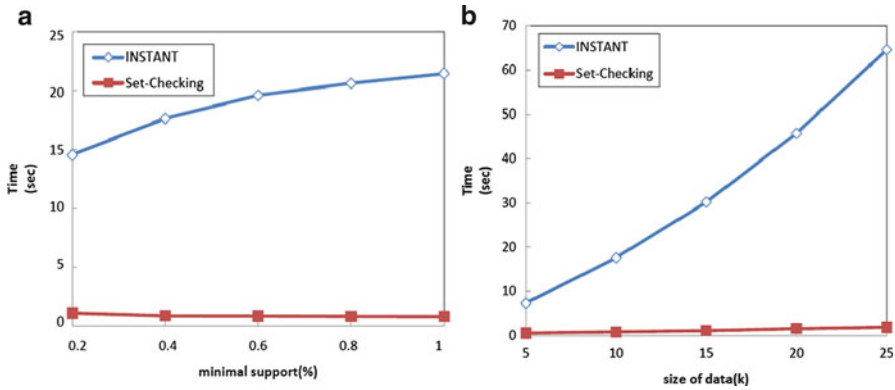
Fig. 4 A comparison of the processing time under (**a**) different minimum supports and (**b**) different size of the data

5 Conclusion

In this chapter, we have proposed the Set-Checking algorithm that could efficiently mine maximal frequent itemsets in data streams. When updating the transaction data streams occur, how to maintain these rules efficiently is the key point of stream mining. The simulation results have shown that the proposed Set-Checking algorithm outperforms the INSTANT algorithm.

References

1. Agrawal R, Srikant R (1994) Fast algorithm for mining association rules in large databases. In: 20th international conference on very large data bases. Morgan Kaufmann, San Francisco, pp 487–499
2. Li H, Zhang N (2010) Mining maximal frequent itemsets over a stream sliding window. In: IEEE youth conference on information computing and telecommunications. IEEE Press, New York, pp 110–113
3. Li JW, Lee GQ (2009) Mining frequent itemsets over data streams using efficient window sliding techniques. Int J Expert Syst Appl 36(2):1466–1477. Pergamon Press, New York
4. Lin KC, Liao IE, Chen ZS (2011) An improved frequent pattern growth method for mining association rules. Int J Expert Syst Appl 38(5):5154–5161. Pergamon Press, New York
5. Mao G, Wu X, Zhu X, Chen G, Liu C (2007) Mining maximal frequent itemsets from data streams. J Inf Sci 33(3):251–262. Sage, Thousand Oaks
6. Xin JW, Yang GQ, Sun JZ, Zhang YP (2006) A new algorithm for discovery maximal frequent itemsets based on binary vector sets. In: 5th international conference on machine learning and cybernetics. IEEE Press, New York, pp 1120–1124

Parallel Matrix Transposition and Vector Multiplication Using OpenMP

Tien-Hsiung Weng, Delgerdalai Batjargal, Hoa Pham, Meng-Yen Hsieh, and Kuan-Ching Li

Abstract In this chapter, we propose two parallel algorithms for sparse matrix transposition and vector multiplication using CSR format: with and without actual matrix transposition. Both algorithms are parallelized using OpenMP. Experimentations are run on a quad-core Intel Xeon64 CPU E5507. We measure and compare the performance of our algorithms with that of using CSB scheme. Our experimental results show that actual matrix transposition algorithm is comparable to the CSB-based algorithm; on the other hand, direct sparse matrix-transpose-vector multiplication using CSR significantly outperforms CSB-based algorithm.

Keywords OpenMP • Sparse matrix transposition

1 Introduction

The sparse matrix transposition and vector multiplication are important among many scientific computing applications. CSR (compressed sparse row) and CSC (compressed sparse column) are the simplest formats. Many parallel matrix-vector multiplications using CSR have been proposed [1, 2], but the matrix transposition is also important in many scientific computations such as iterative linear solvers. An efficient matrix transposition and vector multiplication algorithm has been actively researched, and most of the recent works have been using CSB (*compressed sparse block*) format [3]. Mateescu et al. [4] develop a dense matrix transpose rather than sparse that runs on POWER7 machine by utilizing its cache model and prefetching technique. Gustavson [5] proposed two fast serial algorithms for sparse matrix multiplication and permuted transposition using CSR; they were serial codes.

T.-H. Weng (✉) • D. Batjargal • H. Pham • M.-Y. Hsieh • K.-C. Li
Department of Computer Science and Information Engineering, Providence University, Taichung 43301, Taiwan
e-mail: thweng@pu.edu.tw

In this chapter, we proposed two algorithms for sparse matrix transposition and vector multiplication using CSR: with and without actual transposition. We use OpenMP [6] because it requires less effort and it is portable across shared memory environment. Other advantages include incremental parallelization and easier to program, debug, understand, and maintain. We compare ours to the previous research work on parallel sparse matrix-vector multiplication which used the CSB by Buluç et al. [3]. This CSB scheme requires no actual transposition, and is implemented using Cilk++ [7] and written in C++ in recursive style, and can be downloaded from [8].

2 Sparse Storage Format

In this section, we introduce CSR and CSB sparse matrix formats. CSR consists of three arrays, namely, *val*, *idx*, and *ptr*, as shown in Fig. 1a. Let *A* be a sparse matrix whose order is *r* by *c* and *NNZ* is the number of nonzero of *A*. The value of nonzero elements is stored in a double-precision array *val* of length *NNZ*. The column indices for each nonzero element are stored in the integer array *idx* of length *NNZ*. The pointers to each starting row in arrays *idx* and *val* are stored in integer array *ptr* of length *c*.

Figure 1b is the CSB representation of the sparse matrix *r* by *c* which is divided into sub-matrices ($\beta \times \beta$). It is called *blocks*. CSB is very similar to CSR or CSC. But CBS uses an extra array *blk_ptr* that contains the pointer to the nonzero block arrays.

3 Implementation of Parallel Algorithms

We named our first and second algorithm as CSR1 and CSR2, respectively. Both algorithms read matrix market file into its triplet format, and then it is converted to CSR format. After that CSR1 performs actual transposition and then $A^{T}x$; on the other hand, CSR2 performs $A^{T}x$ directly without performing actual matrix
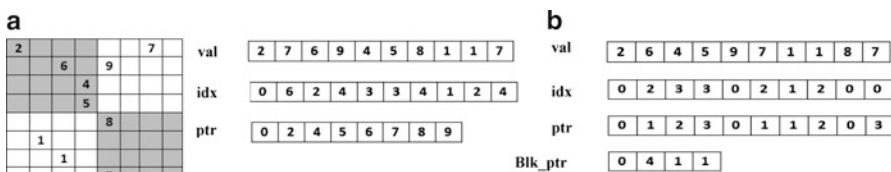
Fig. 1 A matrix example and its CSR and CBS formats. (**a**) CSR, (**b**) CSB

```
01 #pragma omp parallel for
02 for i=0 to c-1 do
03     count[i]=0;
04 enddo
05 for i=1 to NNZ-1 do in serial
06     off[i]= count[A.idx[i]]++;
07 enddo
08 Aᵀ.ptr[0]=0;
09 nad[0]=0;
10 for i=1 to c do in serial
11     Aᵀ.ptr[i]= Aᵀ.ptr[i-1] + count[i-1];
12 enddo
13 #pragma omp parallel
14 {
15   #pragma omp for nowait
16   for k=0 to c-1 do
17     for i=A.ptr[k] to (A.ptr[k+1])do
18         Aᵀ.idx[Aᵀ.ptr[A.idx[i]]+off[i]]=k;
19     enddo
20   enddo
21   #pragma omp for
22   for i=0 to NNZ-1 do
23       Aᵀ.val[Aᵀ.ptr[A.idx[i]]+off[i]]=A.val[i];
24   enddo
25 }
26 #pragma omp parallel for private(i,k,t)
27 for i=0 to c-1 do
28     t=0;
29     for k=A.ptr[i] to A.ptr[i+1] do
30         t+=Aᵀ.val[k]*x[Aᵀ.idx[k]];
31     enddo
32     b[i]=t;
33 enddo
```

Fig. 2 The OpenMP matrix transposition and vector multiplication (CSR1)

transposition. CSR2 is expected to get better performance since it has less memory accesses than the actual transposition.

The actual transposition in CSR1 is started by computing the number of nonzero for each column and stores it in the temporary array **count** and also computes the new address (stored in $A^T.ptr$); after that the combination of the offset and the new address can be used for one-to-one mapping and to target address of both **idx** and **val** of A^T. The actual matrix transposition and the $A^T x$ are done in parallel using OpenMP.

In the previous research work using CSB by Buluç, it consists of four steps: (1) reading matrix from a file of the matrix market format into triplet, (2) converting triplet into CSC format, (3) converting CSC to SCB, and (4) performing $A^T x$ in parallel using Cilk++.

CSR1 in Fig. 2 first initializes the array **count** to zeros in parallel, where **count**[i] represents the number of nonzero in ith column and where i is from column 0 to $c - 1$ and c is the total number of column in array A. The second loop shown in

Fig. 3 CSR2 algorithm

```
01  #pragma omp parallel for private(k)
02  for(i = 0; i < r; i++)    {
03      for(k= A.ptr [i]; k < A.ptr [i+1]; k++) {
04          yᵀ[A.idx [k]] += A.val[k] * x[i];
05      }
06      #pragma omp barrier
07  }
```

lines 5–7 computes the *offset* of the target transposition for each nonzero ith element of array A and stores in *off*[i], while *count*[$A.idx$[i]]++ is incremented for the column index stored in idx[i], as the resulting total number of nonzero element for each column is obtained.

The third loop calculates the starting addresses of each targeted nonzero of A for AT; the result is stored in AT.ptr. It is a serial loop, since line 11 is the statement with true loop dependences. New target starting address for each column i is computed and stored in array AT.ptr[i]. The target transposed array AT.ptr is generated, which stores pointers to the beginning of each row in the array values idx and val. Hence, it has two serial loops: the first loop takes O(NNZ) where NNZ is the number of nonzero and the second loop takes O(c) where c is the number of column.

A *pragma omp parallel* directive is inserted to create a parallel region to distribute works for transposition of the sparse matrix. An OpenMP NOWAIT clause is declared in line 15 of the parallel loop to remove the barrier since the data access between two loops is independent and because the loop in line 16 writes access to $A^T.idx$, whereas the next loop writes to $A^T.val$. In order to accomplish this actual transposition, $A^T.idx[A^T.ptr[A.idx[i]] + off[i]] = k$ is used to set the row of array A as a column of A^T as shown in line 18, so the combination of the new address and its offset is applied as a one-to-one mapping and for the correct address of *idx* of A^T. Similarly, in line 23, $A^T.val[A^T.ptr[A.idx[i]] + off[i]] = A.val[i]$, the nonzero of array A, is copied to correct address of A^T. The transposition from A to A^T generates three vectors, namely, *ptr*, *idx*, and *val*. Parallel matrix-vector multiplication is shown in lines 26–33 and this portion of code is similar to the one proposed by [3].

CSR2 algorithm shown in Fig. 3 computes $y^T = A^T x$, after matrix A is in CSR format, and since line 4 write accesses to y^T, it may write to the same memory between iterations; hence, the barrier synchronization is required.

4   Experimental Results

Our experimental results run on a quad-core CPU 2.27 GHz Intel(R) Xeon(R) CPU E5507 platform with 12 GB of main memory, 256 KB L1 cache, 1 MB L2 cache, and 4 MB L3 cache. We compile the parallel version of our code with
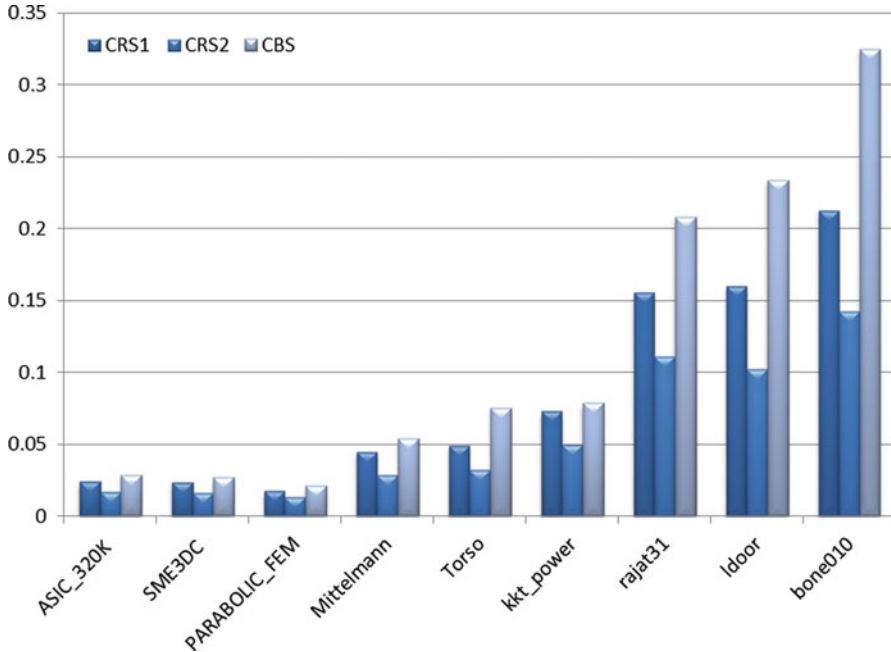
Fig. 4 Total serial execution time for three schemes

GNU g++ OpenMP compiler version 3.1 with flag -fopenmp -O2 -fno-rtti-fno-exceptions and run on Linux CentOS. The matrix-transpose-vector multiplication using CSB code is compiled with Cilk++ [7], with the same version of g++, and the same flag -O2 -fno-rtti -fno-exceptions.

We run programs with nine different matrices from the University of Florida sparse matrix collection [10]. Figure 4 shows the total execution time of CSR1, CSR2, and CSB scheme using one thread. Both our code and Cilk++ CSB code input a matrix from matrix market file to triplet of (row, col, and val); this part has the same execution time. Therefore, we measure the execution time in seconds starting from the conversion from triplet to CSR until the end of the matrix multiplication. The results from running these nine matrices show that our sequential code is faster than that of CSB scheme as the matrix gets larger. CRS2 gives the shortest execution time among the schemes.

The result of running nine matrices using 1 and 4 threads is shown in Fig. 5. The performance is measured in MFLOPS (millions of floating-point operations per second). Since the matrix transposition and vector multiplication take $2*NNZ$, this value is divided by its parallel execution time. The CSB scheme achieves better performance than ours in two matrices, PARABOLIC_FEM and Rajat31. Our algorithm achieves the better performance on other matrices. Since CSR2 takes very short execution time, it gives better speedup on large matrix such as Bone010.
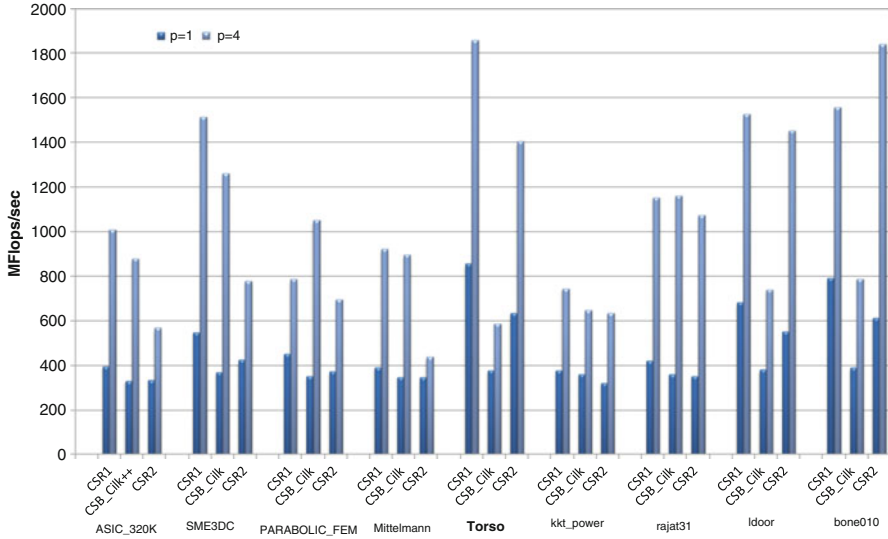
Fig. 5 Performance comparison between parallel code of CSR1, CSR2, and CSB

5 Conclusions and Future Work

In this chapter, we present two parallel algorithms using OpenMP to compute $y^{\mathrm{T}} = A^{\mathrm{T}}x$. First algorithm involves actual matrix transposition; after that the resulting transpose matrix can then be multiplied by a vector in parallel. The second algorithm is performed without actual matrix transposition. We compare their performance with the CSB scheme proposed by Buluç [8]. With all algorithms, the timer is started just after reading a matrix market file into triplet format. The experiments show that our algorithms give shorter execution time than that of using CSB scheme on serial code and better performance on processing larger matrices. Our ongoing work will focus on porting our algorithm to run on distributed environment using hybrid model of OpenMP and MPI as well as distributed GPU machines, taking into consideration the use of programming environment tools toward performance analysis, as those presented in [9, 11].

References

1. Kotakemori H, Hasegawa H, Kajiyama T, Nukada A, Suda R, Nishida A (2008) Performance evaluation of parallel sparse matrix-vector products on SGI Altix3700. In: Proceedings of the 2005 and 2006 international conference on OpenMP shared memory parallel programming, LNCS, West Lafayette, 12–14 May 2008, vol 5315, pp 153–163
2. Godwin J, Holewinski J, Sadayappan P (2012) High-performance sparse matrix-vector multiplication on GPUs for structured grid computations. In: Proceedings of the 5th annual workshop on general purpose processing with graphics processing units, New York, 2012, pp 47–56
3. Buluç A, Fineman JT, Frigo M, Gilbert JR, Leiserson CE (2009) Parallel sparse matrix-vector and matrix-transpose-vector multiplication using compressed sparse blocks. In: Proceedings of the 21th annual symposium on parallelism in algorithms and architectures, Calgary, 11–13 Aug 2009, pp 233–244
4. Mateescu G, Bauer GH, Fiedler RA (2011) Optimizing matrix transposes using a POWER7 cache model and explicit prefetching. In: Proceedings of the second international workshop on performance modeling, benchmarking and simulation of high performance computing systems, Seattle, 12–18 Nov 2011, pp 5–6
5. Gustavson FG (1978) Two fast algorithms for sparse matrices: multiplication and permuted transposition. ACM Trans Math Softw 4(3):250–269
6. OpenMP Architecture Review Board, Fortran 2.0 and C/C++ 1.0 specifications. Available at: www.openmp.org
7. Cilk Arts, Inc. (2009) Cilk++ Programmer's Guide. Cilk Arts, Inc., Burlington. Available at: http://www.cilk.com
8. Buluç A (2011) Parallel SpMV and SpMVT using CSB, research software. Available at: http://gauss.cs.ucsb.edu/~aydin/software.html
9. Li K-C, Weng T-H (2009) Performance-based parallel application toolkit for high-performance clusters. J Supercomput 48(1):43–65
10. Davis TA (1994) University of Florida sparse matrix collection. NA Digest 92
11. Li K-C, Chang H-C (2007) The design and implementation of Visuel performance monitoring and analysis toolkit for cluster and grid environments. J Supercomput 40(3):299–317

Designing Parallel Sparse Matrix Transposition Algorithm Using CSR for GPUs

Tien-Hsiung Weng, Hoa Pham, Hai Jiang, and Kuan-Ching Li

Abstract In this chapter, we propose a parallel algorithm for sparse matrix transposition using CSR format to run on many-core GPUs, utilizing the tremendous computational power and memory bandwidth of the GPU offered by parallel programming in CUDA. Our code is run on a quad-core Intel Xeon64 CPU E5507 platform and a NVIDIA GPU GTX 470 card. We measure the performance of our algorithm running with input ranging from smaller to larger matrices, and our experimental results show that the preliminary results are scaling well up to 512 threads and are promising for bigger matrices.

Keywords CUDA • Sparse matrix transposition • Parallel programming

1 Introduction

Matrix transposition is a basic operation in linear algebra that can be found in software packages such as MATLAB and LINPACK. The most recent works on parallel sparse matrix–transpose–vector multiplication using CSB were proposed by Buluç et al. [2]; it is implemented using Cilk++ [3] in recursive style with no actual matrix transposition required. However, it needs more effort to port it for GPU. Krishnamoorthy et al. [4] proposed an efficient parallel algorithm for out-of-core matrix transposition, where a large dense matrix is stored in disk. When the main memory has not enough memory to hold the whole matrix, the transposition is done by reading a part of the matrix at any time, and its goal is to minimize the

T.-H. Weng (✉) • H. Pham • K.-C. Li
Department of Computer Science and Information Engineering, Providence University,
Taichung, Taiwan
e-mail: thweng@pu.edu.tw

H. Jiang
Department of Computer Science, Arkansas State University, Jonesboro, AR, USA
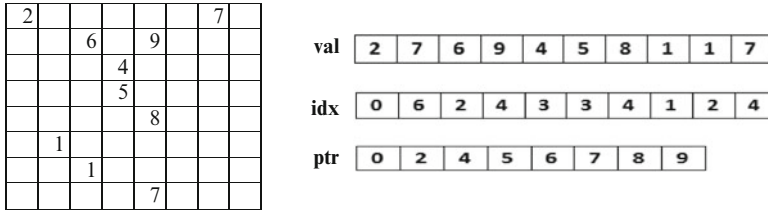
Fig. 1 A matrix example and its CSR sparse format

number of I/O operations. Mateescu et al. [5] developed a dense matrix transpose to run on POWER7 machine by utilizing its cache model and prefetching technique. Stathis et al. [6] proposed the parallel transposition of matrix using special hardware mechanisms on vector architecture. Gustavson et al. [7] proposed two fast serial algorithms for sparse matrix multiplication and permuted transposition using CSR, but they were not parallelized.

Among the sparse formats, CSR (compressed sparse row) and CSC (compressed sparse column) are the simplest and easy to understand and maintain. The CSR sparse format consists of three arrays, namely, val, idx, and ptr, as shown in Fig. 1. Let A be a sparse matrix whose order is r by c and NNZ is the number of nonzeros of A. The values of the nonzero elements are stored in a double-precision array val of length NNZ. The column indices for each nonzero element are stored in the integer array idx of length NNZ. The pointers to each starting row of arrays idx and val are stored in integer array ptr of length r. Our algorithm converts a sparse matrix stored in the CSR format into its transpose equivalence. The output is also in the same CSR form, which is convenient for later parallel vector matrix multiplication or whatever it fits the purpose. The input can be asymmetric. The reason we use CSR is that many existing applications have been designed in this format; when other library functions that adapt other sparse formats are used, it is a further burden on the programmer to modify or write the conversion code.

2   Parallel Algorithm Using CUDA

The matrix transposition algorithm is a memory-access-bound code. Our strategy is to reduce the memory access latency. We select the sparse matrices to reside in the texture memory with on-chip cache and smaller read-only data to reside in the constant memory, because the texture memory has larger memory than the constant memory and has faster read and write access than the global memory.

Matrix A is read into the main memory of the CPU (host) as three one-dimensional arrays, ptr, idx, and val, as shown in Fig. 1. Next, data extraction is performed in host; it computes (1) the offset calculation and (2) the new address of the target index for each nonzero element calculation, and the result is stored in AT. ptr, which is a partial transposition of A. The corresponding code is shown in

```
01 Declare texture reference
02 Define the grid size and the number of threads
03 for  i=1  to  NNZ-1  do  l
04      off [i]= count[A. idx[ i ] ]++;
05 enddo
06 A^T.ptr  [0]=0;
07 for  i=1  to  c  do  //row pointer for AT
08   A^T.ptr[i] = A^T. ptr[i-1] + count[i-1];
09 enddo
10 h = 0;
11 for k=0 to r-1 do
12   for i= A^T.ptr [k] to A^T.ptr [k+1]do
13     idxtemp [h++] = k;
14   enddo
15 enddo
16 move arrays to device memory and bind as texture
17 Allocate A^T.idx , A^T.val , y^T in device memory and
   bind them as texture
18 transp<<< dimGrid , dimBlock>>>(dev _ A^T.idx,);
19 cudaThreadSynchronize();
```

Fig. 2 Main program for sparse matrix transposition on CUDA

```
01 __ global__ void transp (int *A^T.idx, ……) {
02 tid = blockIdx.x * blockDim.x + threadIdx.x ;
03 while (tid < NNZ) {
04    temp = tex1Dfetch (tex_A^T .prt ,A. idx[tid ] ) +
                                  tex1Dfetch (tex_off , tid);
05    A^T. idx [temp] =tex 1Dfetch (tex_idxtemp, tid );
06    A^T.val [temp] =tex1Dfetch (tex_A.val, tid );
07    tid += THREADS;
08 } // endwhile
09 }
```

Fig. 3 CUDA kernel function for the sparse matrix transposition code

lines 1–15 of Fig. 2, and it is best done in the host (CPU). The texture reference variables are declared by using keyword texture. The data are extracted and stored in arrays count, off, idxtemp, and AT.ptr; we transfer arrays off, A.idx A.val, and AT.ptr, idxtemp, and x, except count, A.ptr from host to device memory by invoking the cudaMemcpy() function; then we bind these variables as the texture memory by the cudaBindTexture() function. The arrays AT.idx and AT.val are directly allocated from the device memory by invoking cudaMalloc(). These two arrays are also bound to the texture memory. Then transp <<<…>>> is invoked to launch the kernel transpose function shown in Fig. 3. We assign threads a finer granularity as possible by assigning a group of threads so that consecutive threads access consecutive rows of sparse matrix A and the remainder is assigned similarly in a cyclic fashion.

The number of blocks and threads per block is shown in line 2 of Fig. 2. The built-in variable, dimGrid, is determined by taking the ceiling of the total number of threads/number of threads per block; dimBlock provides the dimension of the block,

Fig. 4 Fine-grain thread mapping of our parallel transpose

T_0	T_1	T_2	T_3	T_0	T_1	T_2	T_3	T_0	T_1	T_2	T_3
0	1	2	3	4	5	6	7	8	9		
4	6	8	3	2	9	1	7	0	5		

which is the number of threads per block. We set dimBlock to (512, 1, 1). The kernel function of matrix transposition is declared using the keyword __global__ to specify the function is a kernel entry point, and a function called transp $<<<$ dimGrid, dimBlock $>>>$ is used to launch from host in parallel across blocks of threads in the device kernel.

Our parallel algorithm is designed to assign threads a finer granularity in which it processes one element at a time. We make sure that the remaining elements are accessed correctly within the array bound by a conditional while loop to check if the thread identification (tid) is less than the total number of nonzeros, as shown in line 3 of Fig. 3. The keyword *tex1Dfetch()* is used to load the data from the texture memory. Since the array indices in statements 5–6 are read accesses to both arrays *off* and A^T.*ptr*, we reduce the read reference twice by assignment statement of read access of both arrays and add the two values and store in the register variable *temp* at line 4 of Fig. 3, so that lines 5 and 6 do not need to reaccess them from the memory. When the *transp* kernel is launched, its *tid* is obtained from the CUDA runtime system, as shown in line 2. Then it accesses an element of an array; after that the statement *tid* is incremented by (THREADS) the total number of threads as shown in line 7, which serves as the step size, so that this thread accesses the next element, that is, THREADS-th elements, away in a cyclic fashion. As a result, consecutive threads will process consecutive elements in a cyclic fashion. For example, suppose we have *NNZ* equal to 10, and THREADS is set to 4; the mapping of threads for our *transp* kernel function is shown in Fig. 4. The *transp* kernel function will be invoked by these four threads, whose thread ID is from 0 to 3, threads labeled as T_0 to T_3. T_0 will access array element index 0, 4, and 8, since the step size is 4. T_2 will access element index 2, 6, and 10, but since 10 is not less than 10 (*NNZ*), T_2 is now terminated; hence, T_2 only processes element index 2 and 6.

3 Experimental Results

We evaluated our code on a quad-core Intel Xeon64 CPU E5507 platform with 12 GB of main memory, 256 KB L1 cache, 1 MB L2 cache, and 4 MB L3 cache and an NVIDIA GPU GTX 470 which has 448 cores with graphics clock of 607 MHz, processor clock 1,215 MHz, and memory bandwidth of 133.9 GB/s. We compiled the parallel code with GNU nvcc compiler version 4.1 with flag -O2—use fast math and -arch sm_13 to use the fast math library and enable double precision on Linux. We ran our code with 11 different sparse matrices from the University of Florida sparse matrix collection [8] ranging from smaller to larger matrices. Figure 5 shows
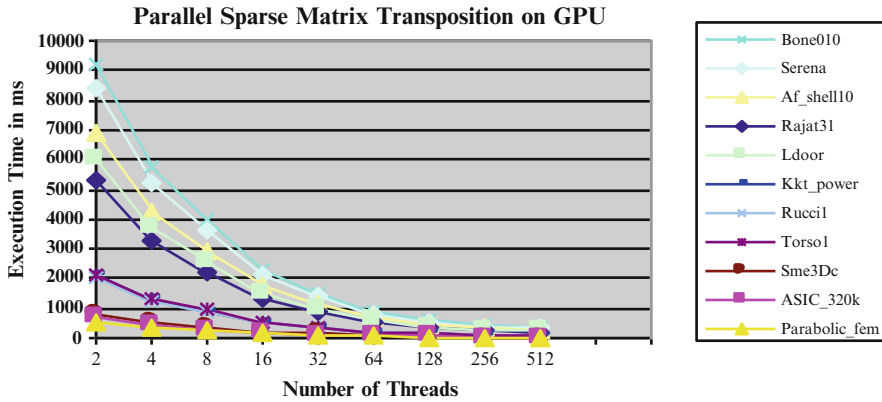
Fig. 5 The performance of the parallel sparse matrix transposition on GPU

the total execution time of our parallel sparse matrix transposition using two threads up to 512 threads. The timer was taken after reading a matrix file until sparse matrix transposition; it was obtained by putting the timer between lines 1 and 2 in Fig. 2 of our main program and at the end of line 19. The results from running these 11 matrices show that the execution time of our code is scalable as the matrix gets larger.

In this experiment, we intend to write our code in such a way that it runs on different number of threads to observe scalability, but in CUDA, creating many threads is inexpensive. Thus, when we run our code using two threads, for instance, our kernel function code is actually launched by specifying the number of blocks equal to one and 512 threads per block, but then only two threads are performing the computation. This is done by controlling our code while using the loop shown in lines 3 and 7 of Fig. 3, while the other threads will terminate their execution. We did not run using one thread because the system watchdog timer will interrupt and give timeout error when a thread executes a kernel code for more than 7 or 9 s on a GPU in order to protect the GPU from being frozen.

Table 1 shows the name, size, number of nonzeros, and shapes of the matrices as well as details of the execution time using two and 512 threads. The matrices are listed from smaller size of nonzero values to larger. Most matrices are square matrices, except Rucci1. The third and fourth columns of the table show the total execution time of sparse matrix transposition in milliseconds (ms) using 2 and 512, respectively. The execution time includes the sequential part and data transfer from CPU to GPU device memory that we discussed earlier on how we measure the time. In the case of the Serena matrix, it is a 1.4M × 1.4M matrix with 64.13M of nonzero values, which is the biggest of the 11 matrices; our parallel matrix transposition takes 8,412 ms using two threads and reduces to 313 ms using 512 threads.

Table 1 Total execution time of parallel sparse matrix transposition on GPU using two and 512 threads

Name	Size	NNZ	Two threads	512 threads
Asic_320k	321K × 321K	1,931K	683	29
Sme3Dc	42K × 42K	3,148K	801	30
Parabolic_fem	525K × 525K	3,674K	560	26
Rucci1	1,977K × 109K	7,791K	1,994	85
Torso	116K × 116K	8,516K	2,161	78
Kkk_power	2.06M × 2.06M	12.77M	2,118	95
Rajat31	4.69M × 4.69M	20.31M	5,320	214
Ldoor	952K × 952K	42.49M	6,083	225
Bone010	986K × 986K	47.85M	9,242	337
af_shell10	1.5M × 1.5M	52.26M	6,915	268
Serena	1.4M × 1.4M	64.13M	8,412	313

4 Conclusions and Future Work

In this chapter, we present our newly designed algorithm to explicitly perform the matrix transposition using the CSR format with CUDA on GPU. Our experimental result shows that even though it does not give linear speedup because of its serial part and the data transfers from host to device and device to host, it is scalable as the number of nonzeros is growing. In the implementation, it only requires a minimum effort to port it to the CUDA code; therefore, we also believe it will be relatively easy to port it to OpenCL as well. Because our host memory has only 12 GB, we can only process the sparse matrix up to 64.13 million of nonzero. The execution time of the sparse matrix transposition using 512 threads only takes 313 ms. Since our CUDA implementation may not be an optimal code, our future work includes optimization of this program by accessing on-chip shared memory and avoiding memory bank conflict.

References

1. NVIDIA (2008) CUDA programming guide. NVIDIA Corporation, June, 2008, version 2.0.
2. Buluç A, Fineman JT, Frigo M, Gilbert JR, Leiserson CE (2009) Parallel sparse matrix-vector and matrix-transpose-vector multiplication using compressed sparse blocks. In: Proceedings of the 21th annual symposium on parallelism in algorithms and architectures, Calgary, 2009, pp 233–244
3. Cilk++ programmer's guide (2009) Cilk Arts, Inc., Burlington. Available at: http://www.cilk.com

4. Krishnamoorthy S, Baumgartner G, Cociorva D, Lam C-C, Sadayappan P (2004) Efficient parallel out-of-core matrix transposition. Int J High Perform Comput Netw 2(2–4):110–119
5. Mateescu G, Bauer GH, Fiedler RA (2011) Optimizing matrix transposes using a POWER7 cache model and explicit prefetching. In: Proceedings of the second international workshop on performance modeling, benchmarking and simulation of high performance computing systems, 2011, pp 5–6
6. Stathis P, Cheresiz D, Vassiliadis S, Juurlink B (2004) Sparse matrix transpose unit. In: Proceeding of the 18th international conference on parallel and distributed processing symposium (IPDPS), 2004
7. Gustavson FG (1978) Two fast algorithms for sparse matrices: multiplication and permuted transposition. ACM Trans Math Softw 4(3):250–269
8. Davis TA (1994) University of Florida sparse matrix collection. NA Dig 92
9. Li K-C, Weng T-H (2009) Performance-based parallel application toolkit for high-performance clusters. J Supercomput 48(1):43–65

Analysis of USDA Food Classifications Using Neural Network Classifier

Thomas Evans and Anthony Choi

Abstract Neural networks have the potential to analyze many possible situations and learn the correct information through training, learning, and validation. The development of a neural network that is capable of replicating the food groupings in the United States Department of Agriculture's National Nutrient Database will be analyzed. This database contains 7,906 food items that are grouped into several different categories such as fats and oils, breakfast cereals, and pork products. A single-layer perceptron network is then created to analyze this data and train the network to classify the food items correctly. The neural network data is divided into three categories. Seventy-five percent of the data is used for training the neural network, 15 % is used for validation, and 10 % is used for testing. The results of the network show that certain food groups were harder to classify correctly than others, but overall, the entire testing data set had a misclassification of approximately 10 %. There is still much potential for this network to become better. Expanding the data set in certain categories should help the classification error to decrease even more.

Keywords Neural network • Food classification • USDA • Kohonen map • MATLAB • Self-organizing map

1 Introduction

The first neural computing model was introduced in the 1940s by McCulloch and Pitts. In the past 70 years, many variations and improvements have been made to this model. This includes adding hidden layers, varying the number of nodes in the hidden layers, changing the activation function of the neurons, implementing momentum to avoid local minima, and developing numerous training methods.

T. Evans • A. Choi (✉)
Electrical and Computer Engineering, Mercer University, Macon, GA 31207, USA
e-mail: choi_ta@mercer.edu

All of these factors influence the performance of the model, but there is no one optimal structure [1–5]. This chapter has concentrated on exploring how these factors influence the performance of a classifier, a neural network used to classify items into predetermined groupings.

Artificial neural networks (ANNs) have been used for analyzing many unique cases ranging from analysis to classification. ANNs have been shown to produce better results than most statistical classification techniques. Some previous work completed in the classification area includes analyzing pistachios. Using ANNs, different varieties are capable of being determined by this "computer program" with rather accurate results. By using this program, certain attributes of the pistachio were analyzed and classified based on length and diameter. With this data sample of 5 different varieties, each with 100 samples, the NN was capable of achieving nearly 100 % accuracy. Only 3 pistachios out of 500 were misclassified [6].

Neural networks have been used in many different types of classification situations as well. For example, an ANN has been used to classify the quality of tea by measuring the color. This neural network uses a matching system that detects the completion of the fermentation process. Using this process, Borah, Bhuyan, and Saikia achieved 94 % accuracy in their results [7]. Another capability of ANNs is measuring the surface area of guava. The ANN trained by Chokananporn and Tansakul was accurate to within 0.05 % [8]. Yet another ANN classification example is geographical classification. ANNs are capable of classifying geographic origins of potatoes by measuring the elements in the potatoes. By using this information, geographical origins of the potatoes can be determined with an accuracy of 96 % [9].

Grain samples can also be analyzed by an ANN. Three thousand grain samples, collected by Anami and Savakar, were analyzed by visual standards. The RGB (red, green, blue) colors are analyzed in the images to better analyze the differences in grain samples [10]. Another example involves Duroc and Iberian pork. Different types of pork were successfully classified by using an ANN. This data set encompassed a small sample size, but an ANN was still capable of achieving accurate results [11]. Meat classification can even be done by computer imaging for quality assessment [12]. Analyzing certain conditions or attributes of food can tell ANN information that can be used to better understand and classify the issue that needs to be resolved. Temperature and humidity is another example that can be monitored to determine the reliability of the food transportation system [13]. A few more ways that neural networks can be used include predicting the quality of drying apples, using decision trees to classify where wine was cultivated, using the thermal conductivity of food, and even predicting the safety and quality of canned foods [14–17].

An interesting development in the field of ANNs is using the electronic nose to analyze data. An electronic nose is a digitized system that functions as a human nose and is composed of metal oxidized sensors or conducting polymers. This nose is capable of analyzing flavors and concentrations of food. With this sensor, real-time information about various characteristics of food can be analyzed. Electronic nose can be used to analyze the shelf life of soy milk, determine the geographical

origin of honey, identify different odors in tea, and monitor the quality of cocoa beans to name a few [18–21].

Another development in the NN field is the invention of DiaWear. DiaWear is a context-aware wearable food and activity recognition system. This device is capable of analyzing patients' calories burnt through wearable sensors, and it will assist the user regarding how much food to eat. Using DiaWear and an ANN to analyze certain data from food-like image classification, this will assist medical professionals to provide more accurate forms of treatment, especially for one of today's health crisis, diabetes [22].

Inspired by the success of the surveyed papers, this chapter takes a holistic approach to food categorization. Food group categories, provided by the United States Department of Agriculture (USDA), can be confusing and misleading. Although most food is reasonably categorized, some foods are categorized in a very peculiar way. This chapter proposes a scientific and rigorous method to food categorization. By using physical and measureable properties of foods and by using an unbiased ANN for categorization, consumers can gain better understanding of the foods they consume and also lead to better understanding of our current food groups provided by the USDA.

The classification problem chosen was to develop an ANN capable of replicating the food groupings found in the United States Department of Agriculture's National Nutrient Database. This database is updated annually and contains 7,906 food items. For each food item, the content of 47 nutrient values in 100 g of the items is provided. These food items are concentrated into the following groupings: Dairy and Egg Products, Spices and Herbs, Baby Food, Fats and Oils, Poultry Products, Soups, Sauces and Gravies, Sausages and Luncheon Meats, Breakfast Cereals, Fruits and Fruit Juices, Pork Products, Vegetables and Vegetable Products, Nut and Seed Products, Beef Products, Beverages, Finfish and Shellfish Products, Sweets, Cereal Grains and Pasta, Fast Foods, Meals, Entrees, and Side Dishes, Snacks, Ethnic Food, and Restaurant Food.

2   Network Structure

Three network structures were developed and tested in order to gauge their effectiveness as a classifier. These include a perceptron, a multilayer perceptron, and a self-organizing map (SOM) or Kohonen map. All of these networks can be modeled using MATLAB's Neural Network Toolbox. The two perceptron networks were modeled using the ANN graphical tool, as shown in Figs. 1 and 2, and the Kohonen map using the clustering tool [23, 24].

These structures were implemented, trained, and tested with a wide range of parameters. Each version varied by the number of neurons and training algorithms utilized. The training algorithms used were gradient backpropagation with momentum, Levenberg-Marquardt, and resilient backpropagation.
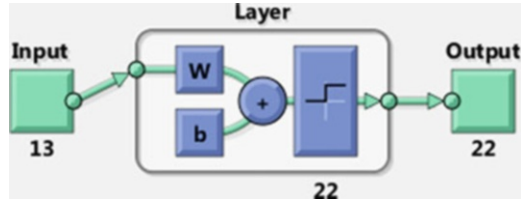
Fig. 1 Single-layer perceptron
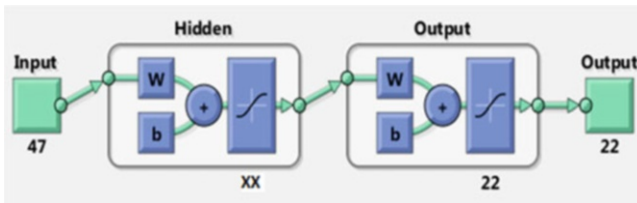
Fig. 2 Multilayer perceptron

3   Input Data Sets

The most influential factor in the performance of an ANN is the detail and applicability of the input data to the problem. This is because everything the ANN "learns" comes directly from this input data. For this reason, various preprocessing techniques on the raw nutrition data to develop separate input data sets to train and test the networks are used. In the end, six data sets were used with the various ANNs.

A data set is labeled full, containing all of the food items, or incomplete, filtered to remove the food item that contained incomplete nutrient data (nutrient represented by a negative one). Filtering the data removed two-thirds of the food items; this is a significant reduction in the amount of data. For both full and incomplete data, there is a set that contains the raw data, normalized data, and data generated using the principle component analysis (PCA) technique. PCA involves translating the input data onto another basis that maximizes the variability in one dimension. This allows the ANN input layer to be decreased in size, reducing the dimensionality of the problem.

4   Results

The food items data set was divided into three categories for the neural network. Seventy-five percent of the data was used to train the ANN. Fifteen percent of the data was used to validate the ANN to check and see the progress. The final 10 % of
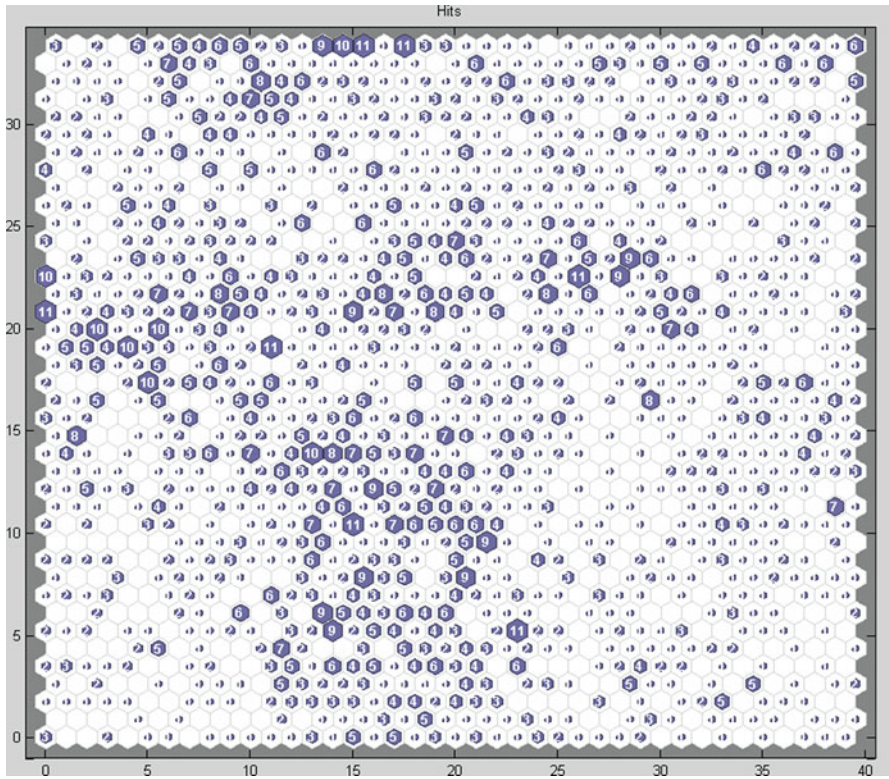
Fig. 3 Hits map from incomplete data set

the data was used to test the network. These percentages were chosen based on prior journal articles and the achieved better results of the analyzed data.

The result of using a SOM was best interpreted using the hit map and the weights distance map figures generated by MATLAB. These figures display the clustering of the input vectors and the distance between nodes, respectively. Since SOMs are trained using unsupervised methods, these figures show the natural grouping of the data. The data set that showed the most natural separation was the incomplete data sets. These results can be seen in Figs. 3 and 4. While a SOM may not be applicable as a classifier, the results do provide a useful way of judging the natural separation of the data set.

The data set that was able to most accurately model the classifications was the full normalized set. Each ANN perceptron structure was trained and tested using each of the data sets while varying the hidden node count and training method. The best performing single-layer perceptron network resulted in 60 % error. The multilayer networks using the resilient learning training technique had universally lower error on all structures and data sets. The network structures that contain 60 hidden nodes classified with the least amount of error. Tables 1, 2, and 3 contain
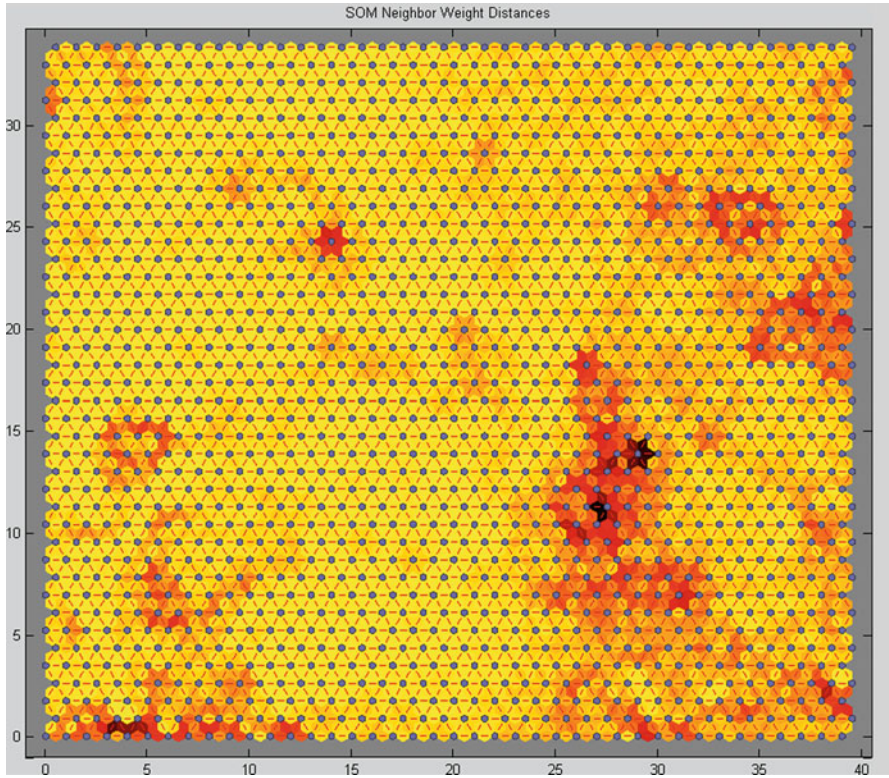
Fig. 4 Weight distances from incomplete normed data set

Table 1 Full normalized data set error rates

Number of hidden nodes	Gradient descent with momentum (%)	Resilient learning (%)
25	70.00	19.00
40	73.00	19.80
50	61.00	13.00
60	55.00	11.70
75	50.00	15.30

Table 2 Incomplete normalized data set error rates

Number of hidden nodes	Gradient descent with momentum (%)	Resilient learning (%)
25	94.00	32.00
40	95.60	24.30
50	99.20	21.50
60	94.30	20.80
75	92.30	23.40

Table 3 PCA data set error rates

Number of hidden nodes	Gradient descent with momentum (%)	Resilient learning (%)
25	69.00	48.80
40	73.50	41.40
50	69.00	42.00
60	69.40	40.00
75	70.00	41.80

sample error rates achieved when using the multilayer perceptron networks to perform the classification for full normalized, incomplete normalized, and PCA data, respectively.

5 Conclusion

The failure of the single-layer perceptron ANN to accurately classify these food groups implies that this classification problem is nonlinear and therefore requires multiple layers. The factor that had the most impact on the performance of the network was preprocessing techniques used on the data set. Normalizing the data removed the effect of any large nutrient group from having a larger influence on final result.

While the PCA data sets did reduce the dimensionality of the input data, the correlation between the nutrient fields was weak and the PCA did not result in data that contained the patterns required for proper classification.

Surprisingly, even though the full data set contained incomplete nutrient data for some food items, which are shown as a −1 value, having these items in the set proved to be beneficial. Neural networks have the power to adapt to a given problem; even though the −1 value did not follow the standard pattern, the ANN learned to interpret them. The key to their performance is the size of the data set. Therefore, including even the incomplete data in the set reduced the error rate in half.

Classification is a very common application for an ANN. When using MATLAB, the best performing network using one hidden layer with the number of nodes calculated using the geometric mean of the input and output layer achieved the best result.

References

1. Debska B (2011) Application of artificial neural network in food classification. Anal Chim Acta 705(1):283–291
2. Nazari J, Okan E (1992) Implementation of back-propagation neural networks with MATLAB. ECE technical reports, Purdue University, West Lafayette, pp 1–26

3. Hamza A (2008) Back propagation neural network Arabic characters classification module utilizing Microsoft word. J Comput Sci 4:744–751

4. Rimer M (2007) Improving neural network classification training. Brigham Young University, Provo, pp 1–265

5. Zhang G (2000) Neural networks for classification: a survey. IEEE Trans Syst Man Cybern 30(4):451–462

6. Kouchakzadeh A, Brati A (2012) Discrimination of pistachio varieties with neural network using some physical characteristics. Int J Emerg Sci 2(2):259–267

7. Borah S, Bhuyan M, Saikia H (2002) Ann based color in tea fermentation. Allied Publishers Private Limited, Karachi, pp 1–4

8. Chokananporn W, Tansakul A (2008) Artificial neural network model for estimating the surface area of fresh guava. Asia J Food Agro-Ind 1(3):129–136

9. Anderson K, Magnuson B, Tschirgi M, Smith B (1999) Determining the geographical origin of potatoes with trace metal analysis using statistical and neural network classifiers. J Agric Food Chem 47:1568–1575

10. Anami B, Savakar D (2009) Effect of foreign bodies on recognition and classification of bulk food grains image samples. J Appl Comput Sci 6(3):77–83

11. Moral F, Guillen A, Moral L, O'Valle F, Martinez L, Moral R (2008) Duroc and Iberian pork neural network classification by visible and near infrared reflectance spectroscopy. J Food Eng 90(4):540–547

12. Valous N, Mendoza F, Sun D, Allen P (2010) Supervised neural network classification of pre-sliced cooked pork ham images using quaternionic singular values. Meat Sci 84:422–430

13. Jabbari A, Jedermann R, Lang W. Neural network based data fusion in food transportation system. In: International conference on information fusion, vol 11, pp 1249–1256

14. Scala K, Meschino G, Vega-Galvez A, Vergara J, Roura S, Mascheroni R (2010) Prediction of quality indices during drying of apples using artificial neural network models for process optimization. In: International conference on food innovation, Bangna, 25–26 Oct 2010, pp 1–4

15. Chandra R, Chaudhary K, Kumar A (2010) The combination of comparison of neural networks with decision trees for wine classification. School Sci Technol 10–17

16. Rahman M, Rashid M, Hussain M (2012) Thermal conductivity prediction of foods by neural network and fuzzy (ANFIS) modeling techniques. Food Bioprod Process 90:333–340

17. Kseibat D, Mittal G, Basir O (2004) Predicting safety and quality of thermally processed canned foods using a neural network. Trans Inst Meas Control 26(1):55–68

18. Ko S, Park E, Han K, Noh B, Kim S (2000) Development of neural network analysis program to predict shelf-life of soymilk by using electronic nose. Food Eng Prog 4(3):193–198

19. Benedetti S, Mannino S, Sabatini A, Marcazzan G (2004) Electronic nose and neural network use for the classification of honey. Apidologie 35:1–6

20. Sharma S (2010) Implementation of artificial neural network for odor identification using e-nose. In: National conference on computational instrumentation, Chandigarh, 19–20 Mar 2010, pp 187–190

21. Olunloyo V, Ibidapo T, Dinrifo R (2011) Neural network-based electronic nose for cocoa beans quality assessment. Agric Eng Int 13(4):1–17

22. Shroff G, Smailagic A (2009) Neural network based food recognition and calorie calculation for diabetes patients. CSD senior thesis extended abstract, pp 1–8

23. Beale M, Martin H, Howard D (2011) Neural network toolbox user's guide. Math Work 8(1):1–420

24. Jordan S. Classification of food groups. http://www.livestrong.com/article/299591-classification-of-food-groups/

Optimization Path Programming Using Improved Multigroup Ant Colony Algorithms

Wen-Jong Chen, Li-Jhen Jheng, Yan-Ting Chen, and Der-Fa Chen

Abstract The main purpose of this chapter proposes an improved multigroup ant colony optimization (IMG-ACO) algorithm to improve the traditional ant colony optimization (TACO) algorithm and traditional multigroup ant colony optimization (MG-ACO) for dealing with the optimization path problem. The TACO and MG-ACO algorithms have exhibited good performance on searching the shortest path. But on the search space, it tends to suffer from premature convergence and fall into local optimal. In this study, the IMG-ACO algorithm utilizing traditional multigroup framework and mutation mechanism performs the virtual parallel optimization algorithm. Compared with the MG-ACO, the results show that the shortest path improved by about 11.5, 16.8, and 9.1 % for 60, 90, and 120 nodes, respectively. This indicates that IMG-ACO can quickly obtain the optimal or nearly optimal solutions to the path programming problem.

Keywords ACO • IMG-ACO • Shortest path • Optimization

1 Introduction

Ant colony algorithm is a metaheuristic inspired by the foraging behavior of ants. It is an effective method to solve the combinatorial optimization problems and to find optimal solutions for difficult discrete optimization problems, especially in the shortest path planning. An ant system (AS) algorithm, which is used to find the optimal path of probability-based algorithm, is first proposed by Dorigo [1]. It updates the pheromone of the paths passing through the segment path for each ant. For obtaining the more superior solutions, the ant colony system (ACS) based

W.-J. Chen (✉) • L.-J. Jheng • Y.-T. Chen • D.-F. Chen
Department of Industrial Education and Technology, National Changhua University
of Education, Changhua 50007, Taiwan
e-mail: wjong@cc.ncue.edu.tw

on AS algorithm was provided with the methods of local and entire updating of pheromone and a new transition rule instead of transition probabilities [2]. However, the above methods easily fall into local optimization and suffer from premature convergence in the search region [3, 4]. Therefore, [5] provided a max-min AS (MMAS) to improve the AS and ACS. However, all ants of MMAS cannot expand the search regions; the solutions are also trapped into local optimum. In recent years, multigroup ant colony algorithms (MG-ACO) have been developed for TSP. It depends on the information exchange of multigroup ant to update the solutions for finding the shortest path [6, 7]. This algorithm avoids some defects of ACS and MMAS. However, traditional multigroup ant colony (MG-ACO) is still trapped into local optimization when the solution of each group conducts premature converge in search space. This study provides an improved multigroup ACO (IMG-ACO) with mutation to perform the job-share mechanism for computing the optimal path. The ants in this work are divided into three groups in the search region. In each group, ants update their pheromone respectively with the initial pheromone and mutate the nodes for each path per iteration. Each group exchanges the information with each other. It is not only to search all possible solutions but also to avoid falling into the local optimum. Simulation results demonstrate that the developed approach proposed in this chapter possesses superior ability in determining the optimal solution, compared to the MG-ACO algorithm.

2 Traditional Ant Colony Optimization Algorithms (TACO)

Traditional ant colony optimization algorithms (TACO) [1] were inspired by the ants finding the shortest path between food sources and nests. The TACO algorithm modeling the behavior of real ant colonies is to rapidly find the shortest path, as shown in Fig. 1. When foraging, ants release a chemical pheromone trail on the ground. Numerous ants follow the pheromone-rich trail, and the probability of the trail being followed by other ants is further enhanced by increased trail deposition. The ant system algorithms were based on the indirect communication capabilities between the ants via the pheromone trails allowing them to find shortest paths. Artificial ants in the ACO algorithms are deputed to generate rules by using heuristic information or visibility and by using the principle of indirect pheromone communication capabilities for iterative improvement of rules. The descriptions are presented as follows:
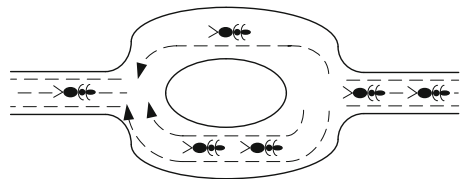
Fig. 1 Real ants find a shortest path

$$P_{ij}^k(t) = \begin{cases} \dfrac{[\tau_{ij}(t)]^\alpha \times [\eta_{ij}]^\beta}{\sum_{m \in J_k(i)} [\tau_{im}(t)]^\alpha \times [\eta_{im}]^\beta}; & \text{if} \quad j \in J_k(i), \\ 0; & \text{others,} \end{cases} \tag{1}$$

where i is the current node, j is the next node, $P_{ij}{}^k(t)$ is the probability of choosing for the kth ant at time t, $\tau_{ij}(t)$ is the pheromone level between node i and node j at time t, η_{ij} is the inverse of the distance between node i and node j, $J_k(i)$ is the set of nodes that remain to be visited by the kth ant positioned on node i, and α and β are the parameters that determine the relative importance of pheromone level versus distance. All of the ants are put on randomly chosen nodes. Each ant starts from its node and obtains the probability to select the next node through the probability $P_{ij}{}^k(t)$. The optimal path is updated and is chosen within all of the paths passed by the ants. Through the iterative computation, the algorithm will stop when the iteration arrives at the maximal iterative set number or converges to the optimization solution.

3 MG-ACO and IMG-ACO

To avoid premature convergence in TACO, a multigroup ant colony (MG-ACO) algorithm based on the job-share mechanism is provided to solve the optimization path problem. The multigroup ant colony approaches let several groups of ants cooperate to find good solutions [6]. However, the final solution is led to the premature convergence due to each group suffering from the local optimization. In this study, improved multigroup ant colony algorithms with mutation (IMG-ACO) are presented to avoid the defects of MG-ACO algorithm. All the ants in IMG-ACO algorithm divide into several groups and each group has the same number of ants. In the process of IMG-ACO algorithm, each group performs a mutation for different paths respectively. Each of the nodes is almost always passed and thus the pheromone concentrations of each path are almost equal. The path of each iteration of each group is randomly mutated by exchanging the sequence of nodes. Therefore, the path can escape from the local optimization via mutation. It shows that the global optimal solutions can be preserved in the search process and are not lost. In this work, all ants are divided into three groups to search the global shortest path through the exchanged information between the groups. The flowchart of the IMG-ACO algorithms is shown in Fig. 2, where τ_i is a random global pheromone and G_1, G_2, and G_3 represent the three groups of ants, respectively. $\Delta\tau_{G1}$, $\Delta\tau_{G2}$, and $\Delta\tau_{G3}$ are the increments of pheromone for each group of ants, respectively:

$$G_1 \cup G_2 \cup \ldots \cup G_Z = \overset{z}{\underset{d}{\cup}} G_d = T_{\text{ant}} \tag{3}$$

$$|G_d| = \frac{|T_{\text{ant}}|}{z} \tag{4}$$
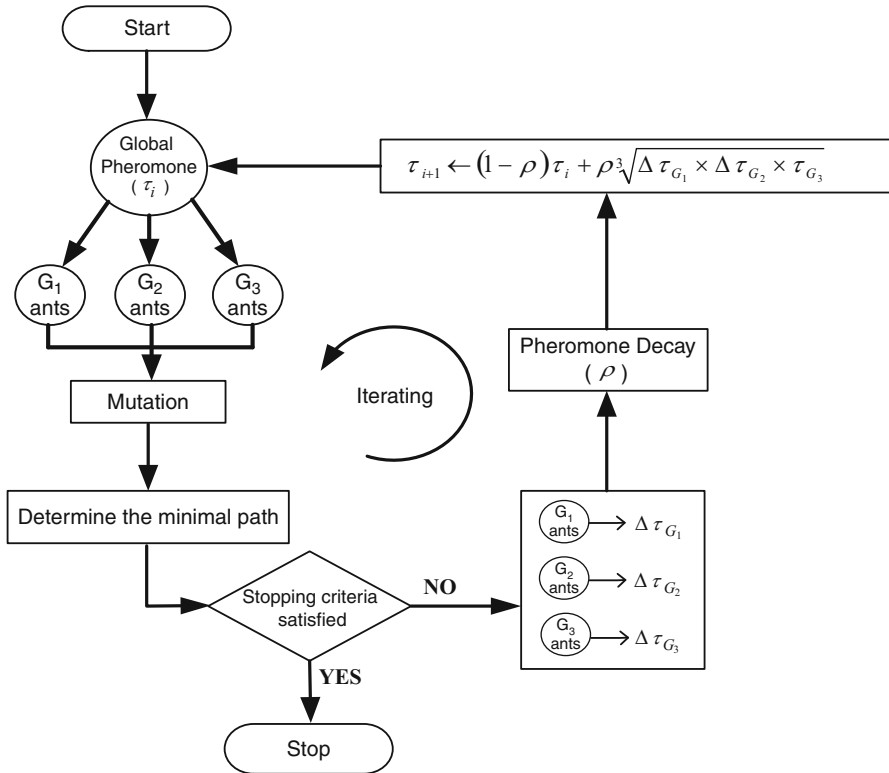
Fig. 2 The flowchart of the IMG-ACO algorithms

$$\tau_{i+1} \leftarrow (1 - \rho) \cdot \tau_i + \rho \sqrt[3]{\Delta\tau_{G_1} \times \Delta\tau_{G_2} \times \Delta\tau_{G_3}} \qquad (5)$$

$$\Delta\tau = \begin{cases} \displaystyle\sum_{C=1}^{T_{\text{ant}}} \frac{Q}{L_{ij}^{\ c}} & \text{if } (i,j) \text{ belong to the best tour} \\ 0 & \text{Otherwise} \end{cases} \qquad (6)$$

where G_d represents the dth group of ants, $|G_d|$ is the number of the dth group of ants, and T_{ant} and $|T_{\text{ant}}|$ are the set and number of all ants, respectively; Z is the number of ants; Q is a parameter of the pheromone strength and $L_{ij}^{\ c}$ represents the length between nodes i and j visited by the cth ant for each group. Within the exchange process of information, the nodes of the optimal trajectory of each group at tth iteration perform the random-exchange mutation. Equation (7) shows that the formulation of mutation is derived from the probability of density function (PDE):

$$P(t_{\text{mutation}}) = \frac{1}{(2|T_{\text{ant}}| - 4)t^2 / Nt_{\text{total}}^2 - (2|T_{\text{ant}}| - 4)t/t_{\text{total}} + |T_{\text{ant}}|/2 + 1} \qquad (7)$$

where $t_{mutation}$ is the mutation number of the tth iteration, $P(t_{mutation})$ is the probability of $t_{mutation}$, and t_{total} is the total number of iterations.

4   Results and Discussions

In this study, we used 30, 60, and 120 nodes to verify the difference between the MG-ACO and IMG-ACO algorithms. The degenerating parameter of the pheromone ρ and the parameter α was randomly set in [0,1] per iteration. β was set to $(1 - \alpha)$. The number of ants is 60 and is divided into three groups. Figures 3a–c and 4a–c show the convergence diagrams of 30, 60, and 120
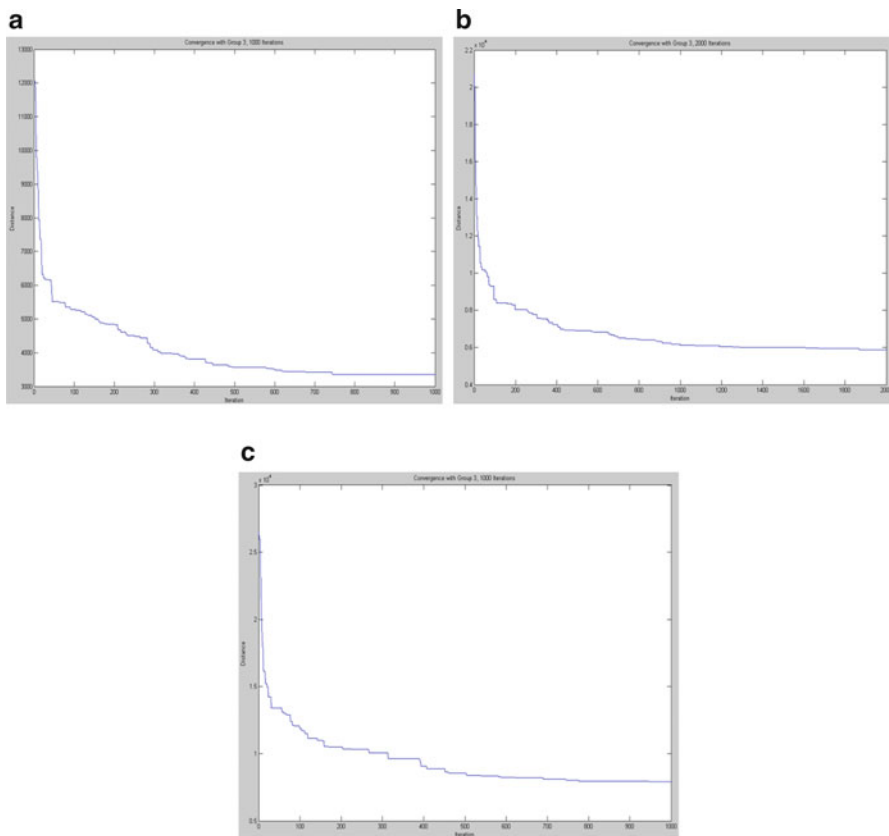
Fig. 3 Convergent diagram of MG-ACO. (**a**) 60 nodes, (**b**) 90 nodes, and (**c**) 120 nodes
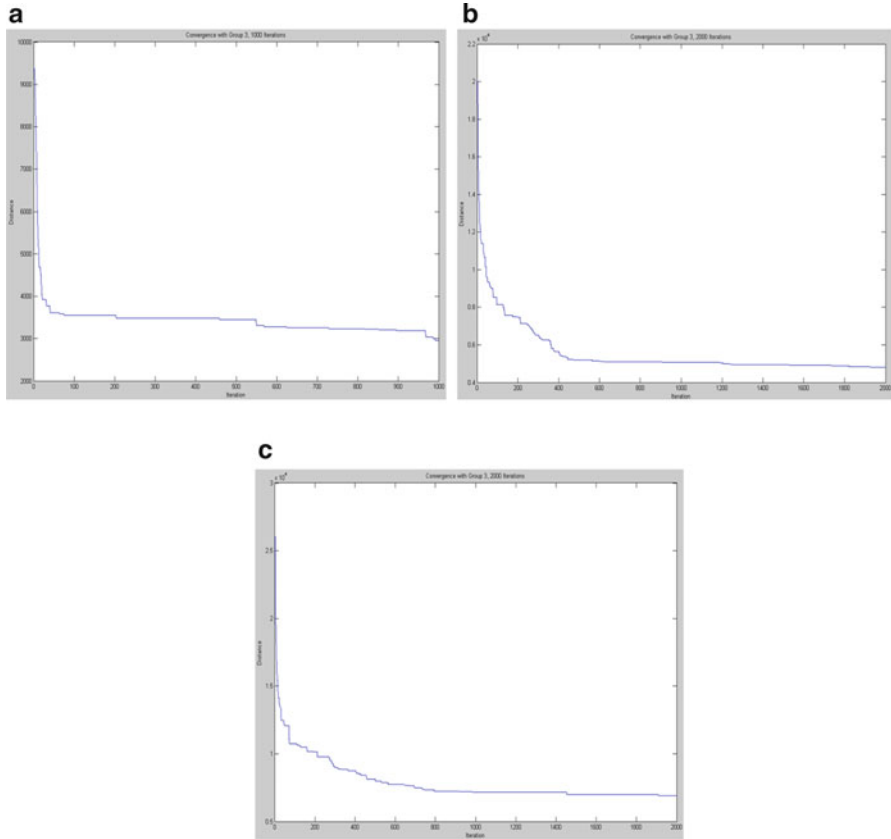
Fig. 4 Convergent diagram of IMG-ACO algorithms. (**a**) 60 nodes, (**b**) 90 nodes, and (**c**) 120 nodes

nodes of MG-ACO and IMG-ACO algorithms. They illustrate that the speed of convergence of IMG-ACO is faster than that of MG-ACO. The trajectories of MG-ACO and IMG-ACO are shown in Figs. 5a–c and 6a–c, respectively. Table 1 shows the comparison of the path lengths of MG-ACO and IMG-ACO. The results depict that the shortest path lengths of IMG-ACO are better than those of MG-ACO. Compared with the MG-ACO for 30, 60, and 120 nodes, the shortest path lengths improved by about 11.5, 16.8, and 9.1 %. It can be observed that the IMG-ACO algorithm greatly improves its global search capability without losing its fast convergence property.
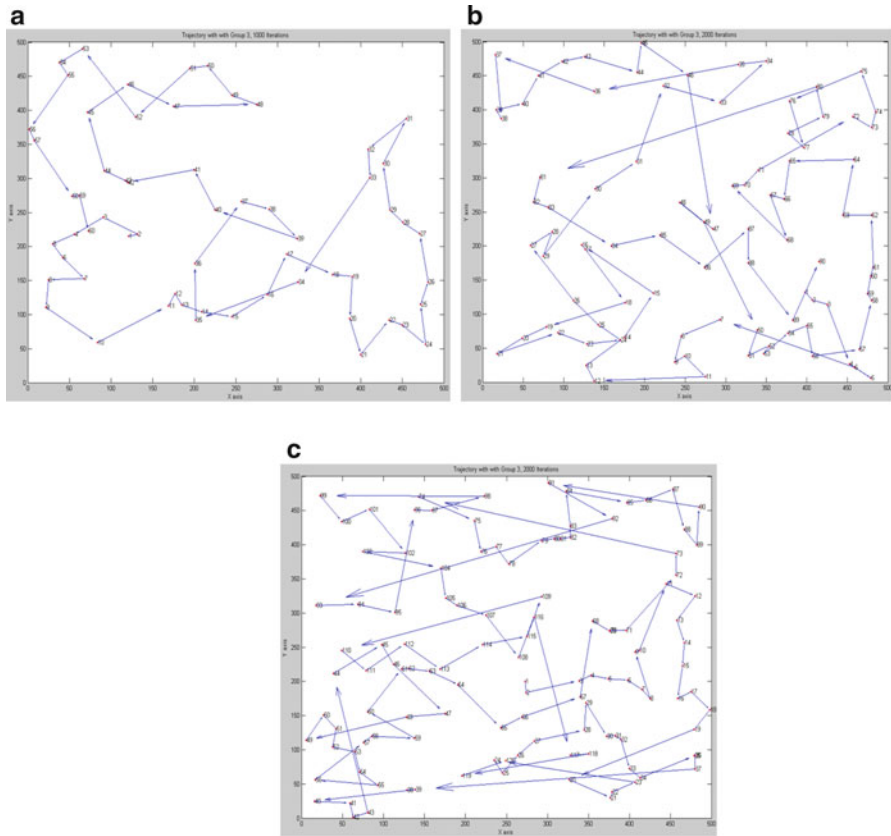
Fig. 5 The shortest trajectory of MG-ACO algorithms (unit: cm). (**a**) 60 nodes, (**b**) 90 nodes, and (**c**) 120 nodes

5 Conclusions

As the defects of the MG-ACO algorithm are easily trapped into the local optimum and converge slowly, this chapter provides an improved multigroup ant colony approach by virtual parallel optimization algorithm. The proposed approach creates the various groups of ants to iterate and exchange information. The more divided the group is, the more excellent the solutions are. The results can be widely used in different engineering fields via the superior abilities in finding the globally optimal solution.
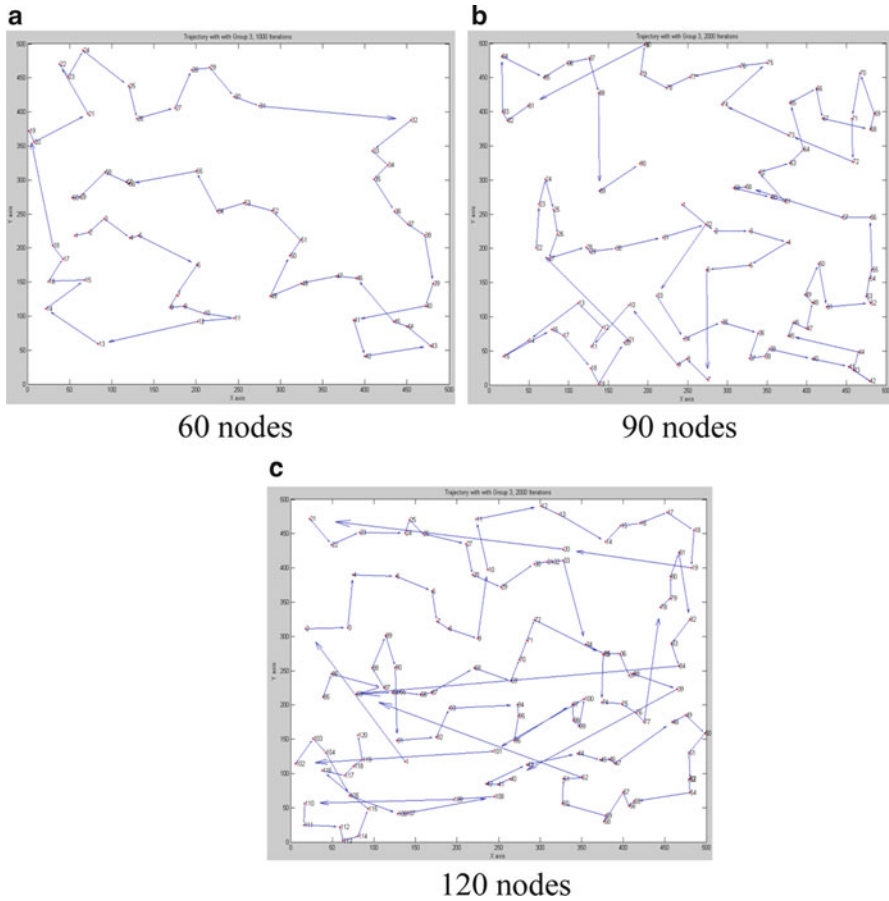
Fig. 6 The shortest trajectory of IMG-ACO algorithms (unit: cm). (**a**) 60 nodes, (**b**) 90 nodes, and (**c**) 120 nodes

Table 1 Comparisons of MG-ACO and IMG-ACO for the shortest path

Nodes	MG-ACO (cm)	IMG-ACO (cm)
60	3346.55	2962.63
90	5773.64	4801.95
120	7595.97	6906.03

References

1. Dorigo M (1997) Luca Maria Gambardella: ant colony system: a cooperative learning. IEEE Trans Evol Comput 1:53–66
2. Chen L, Sun HY, Wang S (2012) A parallel ant colony algorithm on massively parallel processors and its convergence analysis for the travelling salesman problem. Inf Sci 199:31–42

3. Pan J, Wang XS, Cheng YH (2012) Improved ant colony algorithm for mobile robot path planning. J China Univ Min Technol 41:108–113
4. Wong KY, Phen CS (2009) A new minimum pheromone threshold strategy (MPTS) for max-min ant system. Appl Soft Comput 9:882–888
5. Stutzle T, Hoos H (2000) MAX-MIN ant system. Future Gener Comput Syst 6:889–914
6. Liu XH, Zhang X, Liu WJ (2008) Multi-process paths decision-making methodology based on improved max-min ant system. Comput Integr Manuf Syst 14:2414–2420
7. Ouyang J, Yan GR (2004) A multi-group ant colony system algorithm for TSP. In: Proceedings of the third international conference on machine learning and cybernetics, Shanghai, 2004, pp 26–29

Conceptual Information Retrieval System Based on Automatically Constructed Semantic Word Network

Ko-Li Kan and Hsiang-Yuan Hsueh

Abstract This chapter describes a method to dynamically generate a semantic word network which can properly reflect the semantic status. A conceptual information retrieval system based on the method is also described. The method started with the determination of keywords in a textbase. Keywords can then be clustered using analysis methods. For each cluster of keywords, the hierarchical and sibling interrelationships then are statistically inferred, so that the semantic word network can be dynamically established. The method can be formed as a module in concept information retrieval (IR) system. The query expansion function can be implemented with the module, so that the recall and precision of query result can be improved.

Keywords Information retrieval • Semantic word network

1 Introduction

With the popularity of computers and Internet, the electronic data becomes more and more important for both organizations and individuals. Among the different types of data, unstructured data management is always a big challenge because it is very hard for machine to automatically understand and utilize the content of unstructured data with semantic manners.

Traditionally, information retrieval (IR) system is a solution for utilization of unstructured data. By inventing keywords as query string, data or documents which have potential to relate to users' request will be acquired, so that users' problems or questions can be solved or answered by reviewing the data or documents provided

K.-L. Kan (✉) • H.-Y. Hsueh
Information & Communication Research Lab, Industrial Technology Research Institute, Taiwan, R.O.C.
e-mail: kankoli@itri.org.tw

by IR system. Currently, it is proved that IR system can support the full-text search smoothly, such as Google or Yahoo! search engine.

However, with respect of problem-solving purposes, the effectiveness of IR system is still always a problem. According to Van Rijsbergen [1], the problem occurred owing to the trade-off between precision and recall factors. It invents the result that users cannot find result completely, precisely and concisely. One solution is the utilization of query expansion mechanism [2] to predict the exact query string users preferred; however, current approaches of query expansion are based on the query history. With respect to the concept retrieval or question-answering purposes, current solutions cannot always satisfy users.

This chapter describes a method to dynamically generate a semantic word network from textbase which can properly reflect the semantic status. A conceptual information retrieval system based on the method is also described. Strategically, the method started with the determination of keywords of each document in the universal textbase. Keywords can then be clustered using analysis methods such as latent semantic analysis (LSA). For each cluster of keywords, the hierarchical and sibling interrelationships then are statistically inferred, so that the semantic word network can be dynamically established. The method can be formed as a module in concept information retrieval (IR) system. The query expansion function can be implemented with the module, so that the recall and precision of query result, which can also impact the users' experience, can be improved.

2 Solution

The proposed mechanism in this chapter can be shown in Fig. 1.

In this chapter, we proposed a 4-step mechanism for systematically and dynamically generating semantic word network among keyword from textbase:

2.1 Keyword Identification

Having the textbase, the potential keywords must be found. Here, we can reference the existing keyword extraction mechanism and indicators, such as TF-IDF. Text weights can be quantitatively calculated, and a candidate set of keywords from the textbase can be found by a reasonable threshold for candidate keyword weights. It should be noted that the keyword excavated methods, including the tokenization, the text weighting indicators, and the keyword determination threshold, are not in the scope of the chapter. Further, under the consideration of efficiency, performance and scalability, the keywords filtered out in this step are a collection of "candidate set of keywords."
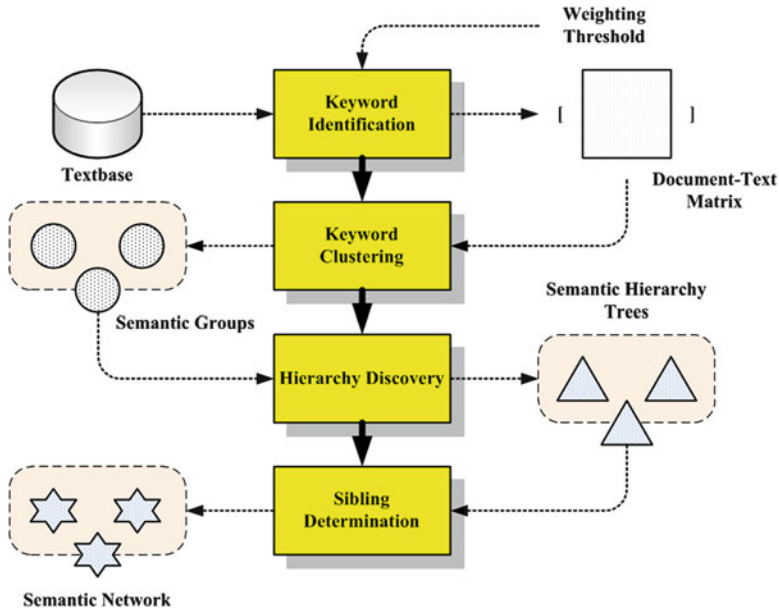
Fig. 1 The proposed mechanism

Therefore, after this step, a matrix $M: D \times K$ can be obtained, wherein D represents a number of documents in the textbase, K represents the number of candidate keyword set, and each element of M represents the quantitative weight of a candidate keyword in a document.

2.2 Keyword Clustering

In this step, the keywords will be clustered based on similarity in matrix M. Candidate keyword clustering involves preprocessing of document candidate keywords to filter the semantic noise so that the complexity of semantic analysis can be reduced. In this step, we invent the latent semantic analysis (LSA) [3] for eliminating the dimension and semantic noise in M. After reducing the semantic dimension with ignorable impact, K can be simplified to the actual set of keywords RK. In other words, after preprocessing, it can get the matrix RM which is similar to matrix M and with dimension $D \times RK$, where $RK \ll K$. Given RM, the degree of similarity between keywords in RK can be calculated. In this chapter, we measure the angle between keyword vectors in RM matrix in the space:

$$Sim(t_p, t_q) = \frac{\overrightarrow{t_p} \cdot \overrightarrow{t_q}}{\left|\overrightarrow{t_p}\right| \times \left|\overrightarrow{t_q}\right|} = \frac{\sum\limits_{i=1}^{D}(t_{pi} \times t_{qi})}{\sqrt{\sum\limits_{i=1}^{D} t_{pi}{}^2} \times \sqrt{\sum\limits_{i=1}^{D} t_{qi}{}^2}}, \ p, q \in N, \ p, q \le RK \qquad (1)$$

Finally, the degree of similarity between the keywords can be integrated into a symmetric matrix *FK*: *RK* × *RK*. This matrix can be used as the input of text clustering method to clustering keywords.

The final result of this step is a set of keyword group as semantic group *U*.

2.3 Hierarchy Discovery

The hierarchical relationships among keywords in a cluster of *U* should be determined in this step. Hierarchical relationship means hypernym and hyponym relationship between keywords. If the semantic of keyword *A* can include the keyword *B*, *A* is a hypernym of *B*. In other words, *A* is more general than *B*, which in turn says *B* is a hyponym of *A*.

In this chapter, the determination method of the hierarchical relationships bases on Invert Document Factor (IDF) is proposed. The main spirit of this method is that if IDF value is smaller, this keyword is more popular in the document of textbase. Such feature can be applied and inferred that the IDF value of the keyword is lower, this keyword is more general. On the other hand, if the IDF value is higher, it may be regarded as hyponym.

The proposed method started from navigating the sets of keywords with highest and secondary high IDF value, *WA* and *WB*, respectively. For each term *a* in *WA*, find *b* in *WB* so that the occurrence state of *b* can contain or fully explain the occurrence state of *a*. In such case, *b* is hypernym, and *a* is hyponym. The interrelationship can be expressed as

$$b \to a \qquad (2)$$

The iteration exits as all keywords are investigated. Such approach can be formalized as the following algorithm:

```
float IDF = MAX_VALUE_OF_IDF;
while (IDF > = 0) begin
    list all keyword set A whose idf value = IDF;
    find the maximum available idf value in keyword set
IDF' < IDF;
    list all keyword set B whose idf value = IDF';
    foreach keyword a in A and keyword b in B begin
        if document set C with keyword a can be included in
document set D with keyword D then begin
```

```
                    Add a hierarchical relationship a → b;
            end
        end
        Combine isolated keywords in A to B;
        IDF = IDF';
    end
```

The execution results of the above algorithm will be a collection of keywords in a cluster tree. It should be noted that the definition of "occurrence in documents can be contained completely" may be defined by document training set or the system administrator.

2.4 Sibling Determination

Determination of relationships among keywords in a cluster, the non-direct subordination of the hypernym and hyponym, will be processed in final step. If the co-occurrence probability of any two non-directly subordinate relationships of the glossary text a and b in a document set exceeds a specific threshold value, we can create a parallel relationship between a and b.

After the results of the four implemented steps, a semantic network between keywords will be dynamically generated for the textbase. The interrelationship can be expressed as

$$b \longleftrightarrow a \tag{3}$$

It should be noted that the co-occurrence probability of a specific threshold value can be defined by document training set or system administrator.

The following Fig. 2 illustrates a simple example of discovered semantic networks, which reflect the astronomy domain knowledge, with both hierarchical and sibling relationships among keywords in a textbase:

3 Referential Architecture of Conceptual IR System

In this chapter, a referential architecture for conceptual IR system can be illustrated as shown in Fig. 3.

In this chapter, the conceptual retrieval system should be a dynamic creating text semantic network to help improve user retrieval query. Compared to general IR system, some components might be different from traditional approaches in order for conceptual IR query:
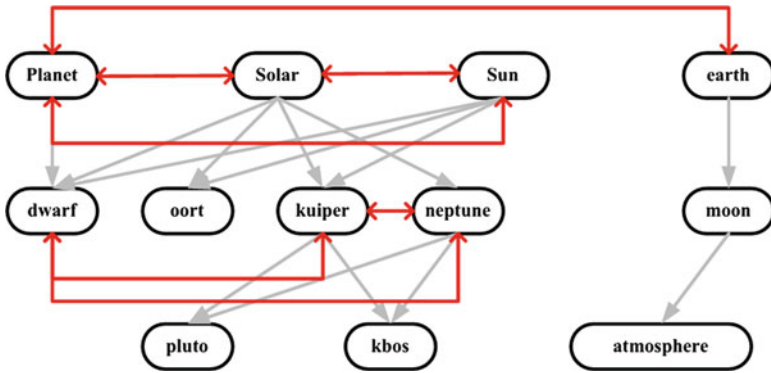
Fig. 2 Semantic network sample
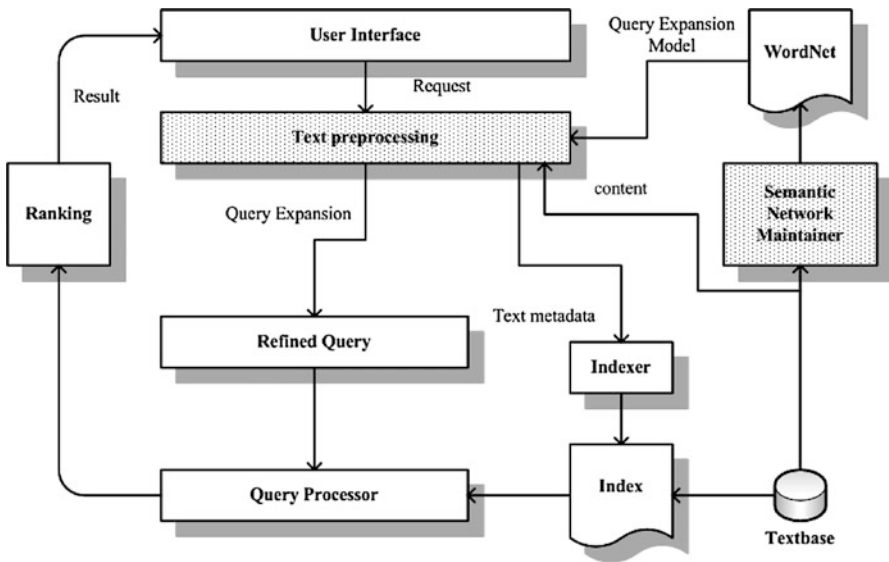
Fig. 3 The conceptual IR systems architecture based on semantic network

3.1 Semantic Network Maintainer

The semantic network will be generated in a background service module. This background service applies the proposed method that dynamically generates the semantic network from textbase.
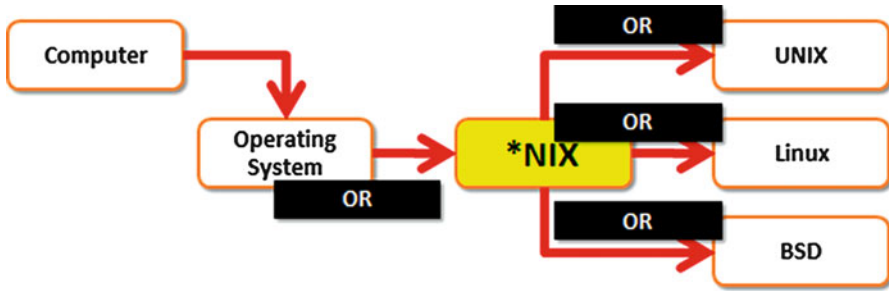
Fig. 4 Expanding query by OR operators and a domain semantic network

3.2 Text Preprocessing Module

The text preprocessing module is responsible to refine the query using the information in the semantic network. We recommend that the query should be refined, or expanded, using OR operator instead of AND operator which is commonly adopted in current query expansion modules such as Google or Yahoo!. The completeness of query result will be improved since some semantically related documents without the original query terms can also be acquired. The following Fig. 4 shows such effect by expanding a query {*NIX*} using discovered semantic network:

4 Conclusion Remarks

In this chapter, we proposed a method to dynamically generate a semantic word network which can properly reflect the semantic status of a textbase. A conceptual IR system based on the method is also described. Applying the mechanism in IR system, the method can be formed as a module in concept information retrieval (IR) system for semantic network generation and query expansion. Different from traditional approach, such as study from Kasperski et al. [4], the query expansion function can be implemented with semantic manners, so that the recall and precision of query result can be improved.

References

1. Van Rijsbergen CJ (1979) Information retrieval, 2nd edn. Butterworth-Heinemann, London
2. Qiu Y, Frei H (1993) Concept based query expansion. In: Proceedings of the 16th annual international ACM SIGIR conference on Research and development in information retrieval, Pittsburgh, 27 June–1 July 1993, pp 160–169
3. Dumais ST (2004) Latent semantic analysis. Ann Rev Inf Sci Technol 38(1):188–230
4. Kasperski R, Borkovsky A, Rabbat RR (2010) Alternative search query prediction, US Patent no. 7747639

An Intelligence-Based Approach to Optimal Power Flow Control Considering Flexible AC Transmission Systems

Chao-Ming Huang, Yann-Chang Huang, and Shin-Ju Chen

Abstract This chapter proposes an intelligence-based approach to solve the optimal power flow (OPF) problem considering flexible AC transmission system (FACTS). FACTS plays an important role in dynamic stability and steady-state control of power systems. This chapter aims at the study of steady-state control which determines the optimal location of FACTS devices and their associated values in the transmission lines. To determine the optimal solution of FACTS, this chapter presents an improved differential evolution (IDE) approach to deal with the OPF problem. The IDE uses a variable scaling mutation operation to enhance the global search capability of basic DE. Therefore, it is very appropriate to solve the OPF problem. The proposed method is verified on an IEEE 30-bus 41-transmission line system. Results show that the proposed approach can save more active power transmission loss and provides better convergence performance than the existing methods.

1 Introduction

Based on the developments of both semiconductor technology and electric power devices, FACTS has been widely applied to improve power flow control and increases the loadability of transmission systems. FACTS is an advanced technique that plays an important role in dynamic stability and steady-state control. The control of dynamic stability focuses on the design of FACTS controllers

_____

C.-M. Huang (✉) • S.-J. Chen
Department of Electrical Engineering, Kun Shan University, Tainan 71003, Taiwan
e-mail: h7440@ms21.hinet.net

Y.-C. Huang
Department of Electrical Engineering, Cheng Shiu University, Kaohsiung 83347, Taiwan

which dynamically adjust FACTS devices to change the structure of transmission network and enhance the capability of transient stability. This chapter aims at the study of steady-state control which determines the optimal location of FACTS devices and their associated values. For a meshed transmission network, an optimal location of FACTS devices can control power flow and increases system loadability. However, because the power system is composed of many buses and transmission lines, it is difficult, time consuming, and a work of challenge to search for the optimal location of FACTS devices by system operators.

Much research has been proposed to coping with OPF considering FACTS. These methods include Newton method [1], interior method [2], Tabu search method [3], genetic algorithm [4], evolutionary programming method [5], and particle swarm optimization (PSO) method [6]. These techniques have served as effective tools to deal with OPF considering FACTS devices.

In this chapter, an intelligence-based approach using IDE is presented to solve the OPF problem. The basic DE [7] has rapid convergence and easy implementation natures. However, the operations of single mutation used in DE may easy to fall into local minima. To improve the drawbacks, this chapter uses a variable scaling mutation operation to enhance the global search capability of DE. Since IDE is a superior optimization technique, it is very appropriate to solve the OPF problem and to offer higher probability of converging toward global solution than the existing methods.

2 Problem Formulation

2.1 Objective Function

The objective function considered in this chapter is the minimization of active power transmission loss as follows:

$$
\min P_{\text{loss}} = \min \sum_{k \in (i,j)} P_{l,k}
$$

$$
= \min \sum_{i=1}^{L} \sum_{j=1}^{L} \left[g_{ij} \left(|V_i|^2 + |V_j|^2 - 2|V_i||V_j| \cos (\delta_i - \delta_j) \right) \right] \quad (1)
$$

where P_{loss} is the active power transmission loss, $P_{l,k}$ is the active power transmission loss of branch k, L is the number of transmission lines, $|V_i|$ is the voltage magnitude at bus i, g_{ij} is the conductance between bus i and j, and δ_i is the voltage phase angle of bus i.
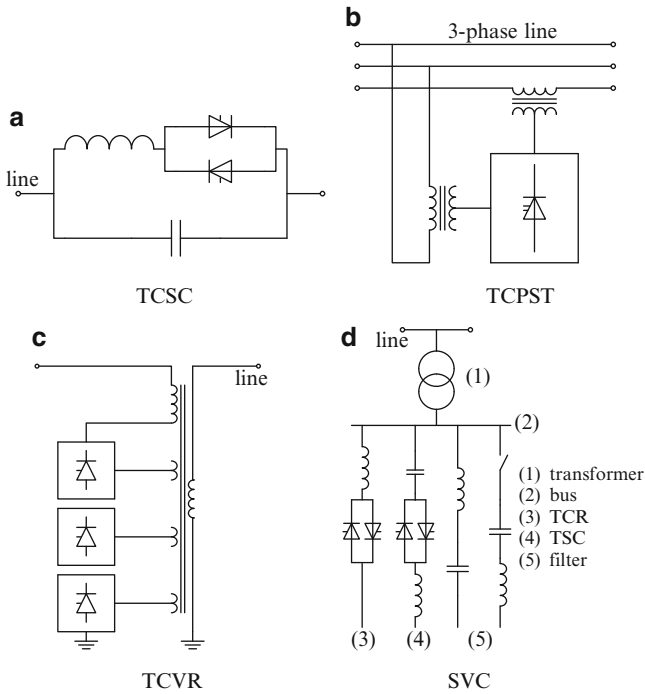
Fig. 1 Configuration of FACTS devices. (**a**) TCSC. (**b**) TCPST. (**c**) TCVR. (**d**) SVC

The objective function of model (1) must satisfy a number of constraints, including power balance constraint, reactive generation constraint, bus voltage constraint, and capacitor and transformer tap setting constraints [8].

2.2 FACTS

The FACTS can be categorized into four types in accordance with their configuration, as follows:

1. Thyristor-Controlled Series Capacitor (TCSC)
   As shown in Fig. 1a, TCSC is composed of a capacitor, an inductor, and a short-circuit line. In order to prevent resonance, only one component is permitted to be energized at one time.
2. Thyristor-Controlled Phase-Shifting Transformer (TCPST)
   TCPST is used to control the angle of bus voltage. As shown in Fig. 1b, TCPST uses an ideal phase shifter with zero impedance to insert to the system. The range of control angle is set between $-5°$ and $+5°$.
3. Thyristor-Controlled Voltage Regulator (TCVR)

Figure 1c is the configuration of TCVR, which is mainly used to tune bus voltage amplitude. The TCVR is connected to main bus in order to change voltage amplitude, i.e., an ideal tap transformer whose turn ratio is set from 0.9 to 1.1 (p.u.).

4. Static Var Compensator (SVC)

SVC is a static compensation device of reactive power. To control bus voltage, the output of SVC can be switched to be a capacitance or an inductance. As shown in Fig. 1d, the SVC is composed of a thyristor-switched capacitor (TSC), a thyristor-controlled reactor (TCR), and a filter. The SVC usually connects in parallel to the center of transmission line to inject (absorb) reactive power to (from) the bus.

3 The Proposed IDE Algorithm

Based on the basic evolutionary strategies, the proposed IDE approach achieves the fittest individual after repeated initialization, variable scaling mutation, recombination, and selection operations as follows:

3.1 Initialization

Let $p_i = [p_{i1}, p_{i2}, \ldots, p_{iM}]$ be a trial vector representing the ith individual ($i = 1, 2, \ldots, P$) of the population to be evolved, where P is the population size and M is the dimension of each individual. The elements in vector p_i represent the decision variables (genes) which are randomly generated as follows.

$$p_{ij} = p_{ij,\min} + \sigma \times (p_{ij,\max} - p_{ij,\min}), \quad j = 1, 2, \ldots, M \tag{2}$$

where p_{ij} represents the jth gene of the ith individual; $p_{ij,\min}$ and $p_{ij,\max}$ mean the lower and upper bounds of p_{ij}, respectively; and σ represents the uniform random number between 0 and 1. In this chapter, the trial vector p_i represents the location of FACTS devices and their associated values in the transmission lines.

3.2 Variable Scaling Mutation

The mutation operation of basic DE is performed by adding a differential vector to the parent individual as follows.

$$p_i' = p_i + f_m \times (p_i^a - p_i^b) \tag{3}$$

where p_i^a and p_i^b are the randomly selected individuals in the parent population and $f_{\mathrm{m}} \in [0, 1]$ represents the mutation factor.

To increase the diversity of the population, a variable scaling mutation (VSM) based on 1/5 success rule is used in this chapter. VSM varies the mutation factor according to the frequency of successful mutations to avoid falling into local minima and save more computational time. The rule of updating mutation factor is as follows.

$$f_{\mathrm{m}}(t+1) = \begin{cases} k_d \times f_m(t), & \text{if } p_s(t) < 1/5 \\ k_i \times f_m(t), & \text{if } p_s(t) > 1/5 \\ f_{\mathrm{m}}(t), & \text{if } p_s(t) = 1/5 \end{cases} \tag{4}$$

where k_d and k_i are the scaling factors and $p_s(t)$ is the frequency of successful mutations. The successful mutations define the objective function of the best individual in the next generation as being better than the best individual in the current generation.

3.3 Recombination

In essence, the mutant individual in (3) is a noisy replica of p_i. To extend the local diversity of the mutant individuals, a recombination operation is introduced as follows:

$$p_{ij}' = \begin{cases} p_{ij}, & \text{if } \mathrm{rand}_{ij} > R_r \\ p_{ij}', & \text{if } \mathrm{rand}_{ij} \leq R_r \end{cases} \tag{5}$$

where p_{ij} is the jth gene of the ith individual before mutation, p_{ij}' represents the jth gene of the ith offspring individual following mutation, rand_{ij} is a random number with normal distribution, and $R_{\mathrm{r}} \in [0, 1]$ is a recombination factor.

3.4 Selection

The basic DE uses one-to-one competition to retain its offspring. Each offspring individual must compete against its parent individual based on the objective values as follows.

$$p_i'(t+1) = \begin{cases} p_i(t+1), & \text{if } F_i(t+1) > F_i(t) \\ p_i(t), & \text{otherwise} \end{cases} \tag{6}$$

where $F_i(t + 1)$ and $F_i(t)$ represent the objective values of the ith individual at $t + 1$ and t iteration, respectively. As shown in (6), it is observed that any parent individual will be replaced by its offspring individual if the objective value of the parent individual is worse than that of its offspring individual.

4   Numerical Results

The proposed approach was verified on an IEEE 30-bus 41-transmission line system. The schematic diagram of this system can be found in [8]. For comparison, the PSO [6] and basic DE [7] methods were also tested using the same database.

In this case, the bus 1 is slack bus; buses 2, 5, 8, 11, and 13 are generation bus; and the others are load bus. The control variables are the location of FACTS devices and their associated values in the transmission lines. Table 1 shows the control range of FACTS devices. The population size and the number of maximum iteration of each method are set at 30 and 500, respectively. In the optimization process, four observations are hypothesized as follows:

- Each FACTS is tuned with discrete value.
- The TCVR and SVC do not install in PV buses.
- The TCSC whose line reactance is lower than 0.1(p.u.) does not install in transmission line.
- Each transmission line or bus only installs one FACTS device.

Table 2 shows the comparison of different methods with eight FACTS devices, where the basic load flow solution is regarded as the benchmark. The results reveal the proposed IDE can save more active power transmission losses than basic DE

Table 1 Range of FACTS devices

FACTS devices	Adjust items	Range
TCSC	Series capacitance	0.01–0.50 pu
TCPST	Shift-transformer angle	$-5°$ to $+5°$
TCRV	Voltage amplitude of regulator	0.95–1.05 pu
SVC	Compensation value of reactive power	1–10 MVar

Table 2 Results of different methods with eight FACTS devices

Method	P_G (MW)	Q (MVar)	P_{loss} (MW)	Q_{loss} (MVar)	ΔP_{loss} (%)
Load flow solution	288.6830	102.766	5.2830	−23.4340	None
DE	285.638	68.471	2.2377	−25.249	57.64
PSO	285.834	73.181	2.4345	−24.717	53.92
IDE	284.021	74.635	1.0966	−19.432	79.24

Table 3 Locations and associated values of different methods

FACTS	DE		PSO		IDE	
TCSC	Line 12–14	0.1 pu	Line 6–11	0.1 pu	Line 12–14	0.1 pu
	Line 23–24	0.2 pu	Line 4–12	0.1 pu	Line 27–30	0.1 pu
TCPST	Line 14–15	+5°	Line 12–15	+5°	Line 3–4	+5°
	Line 15–23	+5°	Line 10–17	+5°	Line 1–3	+5°
TCVR	Line 18–19	1.02 pu	Line 15–23	1.02 pu	Line 10–21	1.02 pu
	Line 21–22	0.99 pu	Line 21–22	0.98 pu	Line 15–23	0.99 pu
SVC	Bus 14	5 MVar	Bus 15	3 MVar	Bus 19	5 MVar
	Bus 15	4 MVar	Bus 26	3 MVar	Bus 23	4 MVar

and PSO methods. The obtained locations and associated values of each FACTS device are shown in Table 3. The average execution times for DE, PSO, and IDE methods through 30 random runs are 3.91, 3.88, and 3.24 s, respectively.

5 Conclusions

An intelligence-based algorithm to solve the OPF considering FACTS has been proposed and implemented in this chapter. The chapter first introduced the formulation of FACTS problem. Then the proposed IDE for determining the OPF considering FACTS problem was briefly reviewed. Owing to the near global search scheme, the proposed IDE algorithm can offer higher probability of converging toward global solution than the other methods. Testing on the IEEE 30-bus 41-transmission line system has shown that the proposed IDE can save more active power transmission losses with better convergence performance than the basic DE and PSO methods.

References

1. Abdel-Moamen MA, Padhy NP (2003) Power flow control and transmission loss minimization model with TCSC for practical power networks. In: Proceedings of IEEE Power Engineering Society, general meeting, Toronto, 2003, vol 2, pp 880–884
2. Xiao Y, Song YH, Liu CC, Sun YZ (2003) Available transfer capability enhancement using FACTS devices. IEEE Trans Power Syst 18(1):305–312
3. Mori MY (2006) Application of two-layered tabu search to optimal allocation of UPFC for maximizing transmission capability. In: Proceedings of IEEE international symposium on circuits and systems, Island of Kos, 21–24 May 2006, pp 1699–1702
4. Gerbex S, Cherkaoui R, Germond AJ (2001) Optimal location of multi-type FACTS devices in a power system by means of genetic algorithms. IEEE Trans Power Syst 16(3):537–544

5. Hao J, Shi LB, Chen C (2004) Optimising location of unified power flow controllers by means of improved evolutionary programming. IEE Proc Gen Transm Distrib 151(6):705–712
6. Saravanan M, Slochanal SMR, Venkatesh P, Prince Stephen Abraham J (2007) Application of particle swarm optimization technique for optimal location of FACTS devices considering cost of installation and system loadability. Electr Power Syst Res 77(3–4):276–283
7. Storn R, Price K (1995) Differential evolution: a simple and efficient adaptive scheme for global optimization over continues space. Technique report TR-95-012, International Computer Science Institute, Berkeley
8. Zhao B, Guo CX, Cao YJ (2005) A multiagent-based particle swarm optimization approach for optimal reactive power dispatch. IEEE Trans Power Syst 20(2):1070–1078

Modern Heuristic Optimization Approaches for Electrical Power System Applications

Yann-Chang Huang, Chao-Ming Huang, and Chien-Yuan Liu

Abstract This chapter reviews modern heuristic optimization approaches for unit commitment (UC) scheduling problem in electrical power system planning, operation, and optimization by discussing recent and historical developments. The purpose of this chapter is to illustrate the potential application of the modern heuristic optimization approaches in the optimization of UC scheduling and the advantages of such methods. Relevant publications from international journals covering a broad range of modern heuristic optimization methods applied to UC problems are reviewed. Recent advances and development trends in applying the modern heuristic optimization approaches to solving UC problem are summarized in the conclusions.

Keywords Modern heuristic optimization approaches • Electrical power system optimization

1 Introduction

In the last decade, many heuristic methods have evolved for solving optimization problems that were previously difficult or impossible to solve. These methods include simulated annealing (SA), tabu search (TS), genetic algorithm (GA), differential evolution (DE), evolutionary programming (EP), evolutionary strategy

Y.-C. Huang (✉)
Department of Electrical Engineering, Cheng Shiu University, Kaohsiung, Taiwan
e-mail: huangyc@csu.edu.tw

C.-M. Huang
Department of Electrical Engineering, Kun Shan University, Tainan, Taiwan

C.-Y. Liu
Department of Computer Science and Information Engineering, Cheng Shiu University, Kaohsiung, Taiwan

(ES), ant colony optimization (ACO), and particle swarm optimization (PSO). These methods skillfully simulate physical phenomena, natural evolution, and mathematical heuristics and yield good results when applied to the combinatorial optimization problems. These methods are referred to as "modern heuristic approaches" or "meta-heuristic approaches."

Many applications of modern heuristic approaches to power systems have been proposed in the past 20 years, especially in unit commitment and economic dispatch applications. In this chapter, articles that have been published on the use of SA, TS, GA, DE, EP, ES, and combinations thereof in relation to UC scheduling in power systems are systematically reviewed. These articles were published in international journals and cover a broad range of modern heuristic optimization approaches.

This chapter discusses recent and historical developments for modern heuristic optimization approaches applied to the UC scheduling problem in electrical power systems. Moreover, this chapter aims to review the potential application of the modern heuristic optimization approaches in the optimization of the UC scheduling and the advantages of such methods. Finally, recent advances and development trends in applying the modern heuristic optimization approaches to solving the UC problem are summarized in the conclusions.

2 Power System Optimization Problems

Many optimization problems in power system planning, control, and operation can be formulated mathematically as follows:

$$
\begin{aligned}
&\text{Minimize } f(x) \\
&\text{subject to } g_i(x) = 0, \quad i = 1, 2, \ldots, I \\
&\qquad\qquad\; h_j(x) \geq 0, \quad j = 1, 2, \ldots, J
\end{aligned}
\tag{1}
$$

where $x^{\mathrm{T}} = [x_1, x_2, \ldots, x_N]$ and the elements of x are the decision variables that are to be determined. The constrained optimization problem that is described by (1) can be transformed to an unconstrained optimization problem using the penalty method. With the equality constraints represented as inequality constraints, the unconstrained optimization problem can be formulated as

$$
\text{Minimize } f(x) + p \sum \Theta[h_i(x)]
\tag{2}
$$

where p is the penalty coefficient and Θ is the penalty function. When $f(x)$ is multimodal, modern heuristic optimization approaches can be used to find the global optimal values of the decision variables x that are described in (2). Let x_{d} be a dependent parameter in a constrained problem that is randomly selected at any stage in the optimization process. The constrained problem can thus be formulated as

$$\text{Minimize } f(x', x_{\text{d}})$$
$$\text{subject to } h_j(x) \geq 0, \quad j = 1, 2, \ldots, J \tag{3}$$

where x' is x excluding x_{d}. In minimizing the objective function in (3), the values of the nondependent parameters in x' are firstly determined in each iteration of the optimization process. When the values of the parameters in x' are known, x_{d} can be determined by applying the relationship between the dependent and nondependent parameters:

$$x_{\text{d}} = g'(x') \tag{4}$$

This chapter reviews modern heuristic optimization approaches for solving the constrained optimization problem that is formulated as (3) and (4).

3   Unit Commitment Applications

The main objective of unit commitment (UC) is how to schedule the on/off status of the generators to minimize the production cost of electricity. A typical UC problem is combinatorial and involves a large set of physical, operating, and contractual constraints, making the problem difficult to solve. The SA method was originally proposed to solve the UC problem [1]. It is highly flexible in handling UC constraints, and numerical results on test systems of up to 100 units were reported.

A short-term hydrothermal UC based on the SA method was proposed [2]. In the algorithm, the power balance constraint, total water discharge constraint, reservoir volume limits, and constraints on the operational limits of the hydrothermal generator and the thermal generator are fully considered. The relative operational capacities of the hydroplant and the thermal plant are also considered. A coarse-grained parallel SA algorithm was presented for short-term hydrothermal UC [3]. The design of the algorithm considers load balancing, processor synchronization reduction, communication overhead reduction, and memory contention elimination. The test results were compared with those obtained using a sequential algorithm, and the results revealed that the proposed method provides an almost linear reduction in computation time. Two parallel SA concepts, speculative computation and serial subset, were proposed to the UC [4]. A combined scheme in which speculative computation is used in the initial phase and the serial subset is used in the final phase. The test results revealed that the proposed parallel schemes greatly improved the computing performance of SA.

A hybrid GA/SA method was developed to the UC [5]. That method can typically provide feasible schedules in the solution process. The hybrid method can handle the non-convexity of the UC. The authors subsequently provided a new formulation for short-term UC with a take-or-pay fuel contract [6] and used a fuzzy set approach to help to find schedules that yield, as closely as possible,

the take-or-pay fuel consumption. They extended the formulation to cover the economic dispatch problem when fuel consumption exceeds the agreed amount in the take-or-pay contract, and the extended formulation was combined with the GA and SA algorithms for determining the UC.

A new formulation for short-term multiple-fuel-constrained UC was presented [7]. In the formulation, the power balance constraint, operating limits of the generators, fuel availability factors of the generators, efficiency factors of the fuels, and the supply limits of the fuels are fully considered. They combined the new formulation with GA, SA, and hybrid GA/SA methods to establish new algorithms. They demonstrated the new algorithms by using them to determine the most economical generation schedule for 25 generators in a local power system and the schedule of the system for four fuels.

An enhanced SA was adopted to solve the UC by applying mechanisms to ensure that the generated candidate solutions are feasible and satisfy all of the constraints [8]. The performance of the enhanced SA was demonstrated and compared with that of conventional methods. The UC was divided into two subproblems: a combinatorial optimization problem and a nonlinear programming problem [9]. They solved the former using the SA and the latter using a quadratic programming routine. Numerical results revealed an improvement in the cost associated with the solutions.

A new algorithm based on integrating GA, TS, and SA methods to solve the UC was presented [10]. The core of the proposed algorithm is based on GA. TS is used to generate new population members in the reproduction phase of the GA. The SA is used to accelerate the convergence of the GA by applying the SA test for all the population members. Numerical results showed the superiority of the solutions thus obtained over those obtained using GA, TS, and SA methods and two exact algorithms.

An extended mean field annealing neural network (NN) approach was presented to short-term UC [11]. The annealing NN provides the high solution quality for SA with the rapid convergence for the NN. Test results confirmed that their approach was very effective in finding the optimum solution to the UC. An approach combining the feed-forward NN and the SA method was presented to solve UC [12]. The NN is used to determine the discrete variables that correspond to the state of each unit at various times. The SA is used to generate the continuous variables that correspond to the power output of each unit and the production cost. A set of load profiles as inputs and the corresponding UC schedules as outputs that satisfy the minimum up-down times, spinning reserve, and crew constraints were used to train the NN. The experimental results demonstrate that the proposed approach can solve the UC in a reduced computational time.

A combined SA and TS approach was used to solve the UC [13]. In their stochastic extended neighborhood algorithm, SA is the main stochastic algorithm, and TS is used to perform an extended neighborhood search and thus locally improve the solution obtained by SA. The neighborhood search uses local domain knowledge, resulting in rapid convergence of the SA. The results obtained for many example systems illustrate the potential of the hybrid approach. The SA with local

search hybrid algorithm was proposed to solve the UC [14]. The hybrid algorithm is robust and provides faster convergence than earlier algorithms. The results verified its potential for solving the UC.

A scheduling method for representing the thermal stress of turbine shafts as ramp rate constraints in the UC [15]. In the UC, thermal stress over the elastic limit is used to calculate the ramping cost. Determination of the contribution of the thermal stress to the generation cost requires that a set of solution that includes thermal stress at the end of each time step be calculated; this requirement establishes a complex problem that cannot be solved using an ordinary optimization method. An improved SA was used to determine the optimal trajectory of each generating unit, and they elucidated the economics of frequently ramping up/down of low-cost generating units in relation to the cost of replacing their turbine rotors with a shorter life span. The results demonstrated the effectiveness of the proposed method.

A new SA combined with a dynamic economic dispatch method was designed to solve the short-term UC [16]. SA was used to schedule the generating units, while a dynamic economic dispatch method, incorporating the ramp rate constraints, was used to solve the UC. The ramp rates are considered by performing either a backward or a forward sequence of conventional economic dispatches with modified limits on the generating units. The proposed algorithm is relatively fast and provides feasible near-optimal solutions. A new method for the incorporation of the unit unavailability and the uncertainty of the load forecast in the solution of the short-term UC solved by the SA was presented in [17]. The required spinning reserve capacity was conducted by imposing reliability constraints, based on the expected unserved energy and the loss of load probability indices. Numerical simulations demonstrated the efficiency of the proposed method.

An absolutely stochastic SA method was proposed to UC [18] and Fuzzy UC using the absolutely stochastic SA was presented [19]. In both chapters, all of the solutions that involved high and low costs are associated with acceptance probabilities and an early jump from one local minimum to another, enabling more local minima to be found and compared in a particular time or number of iterations. The number of bits to be flipped is determined by the appropriate control of parameter. Excess units with a system-dependent probability distribution handle constraints efficiently. The sensitivity of the distribution parameters is satisfactory. To reduce the number of required economic load dispatch calculations, a sign bit vector was introduced. Numerical results indicate an improvement in the cost and time required to find a solution relative to those using the proposed algorithms.

Besides, an EP-based SA was proposed to the short-term UC [20] and the UC using SA-embedded EP approach was presented to hydrothermal UC [21]. Numerical results are used to compare the costs of the solutions and computation times obtained when the proposed approaches and conventional methods are used to determine the optimal UC.

4 Conclusions

This chapter reviewed journal chapters that have presented the applications of modern heuristic optimization approaches to solving UC problem in electric power systems. The modern heuristic optimization approaches have the following advantages. They may find a global optimum; they can produce a number of alternative solutions, no mathematical restrictions on the problem formulation exist, and they are relatively easy to program and numerically robust. The purpose of the review of chapters and example applications in this chapter is to illustrate the potential application of the modern heuristic optimization approaches in the optimization of electric power systems and the advantages of such methods. Recently, these new heuristic tools have been combined with each other and with knowledge to solve extremely challenging problems. Hybrid approaches typically seem both to combine complementary strengths and to overcome the drawbacks of single methods by embedding in them one or more steps that involve different techniques. Developing solutions using such tools provide two major advantages: development time is much shorter than when more traditional approaches are used, and the solutions are very robust.

References

1. Zhuang F, Galiana FD (1990) Unit commitment by simulated annealing. IEEE Trans Power Syst 5:311–318
2. Wong KP, Wong YW (1994) Short-term hydrothermal scheduling. Part I: simulated annealing approach. IEE Proc Gen Transm Distrib 141:497–501
3. Wong KP, Wong YW (1994) Short-term hydrothermal scheduling. Part II: parallel simulated annealing approach. IEE Proc Gen Transm Distrib 141:502–506
4. Annakkage UD, Numnonda T, Pahalawaththa NC (1995) Unit commitment by parallel simulated annealing. IEE Proc Gen Transm Distrib 142:595–600
5. Wong KP, Wong YW (1995) Thermal generator scheduling using hybrid genetic/simulated-annealing approach. IEE Proc Gen Transm Distrib 142:372–380
6. Wong KP, Wong YW (1996) Combined genetic algorithm/simulated annealing/fuzzy set approach to short-term generation scheduling with take-or-pay fuel contract. IEEE Trans Power Syst 11:128–136
7. Wong KP, Wong YW (1997) Hybrid genetic/simulated annealing approach to short-term multiple-fuel-constrained generation scheduling. IEEE Trans Power Syst 12:776–784
8. Wong YW (1998) An enhanced simulated annealing approach to unit commitment. Int J Electr Power Energy Syst 20:359–368
9. Mantawy AH, Abdel-Magid YL, Selim SZ (1998) A simulated annealing algorithm for unit commitment. IEEE Trans Power Syst 13:197–204
10. Mantawy AH, Abdel-Magid YL, Selim SZ (1999) Integrating genetic algorithms, tabu search, and simulated annealing for the unit commitment problem. IEEE Trans Power Syst 14:829–836
11. Liang RH, Kang FC (2000) Thermal generating unit commitment using an extended mean field annealing neural network. IEE Proc Gen Transm Distrib 147:164–170

12. Nayak R, Sharma JD (2000) A hybrid neural network and simulated annealing approach to the unit commitment problem. Comput Electr Eng 26:461–477
13. Purushothama GK, Narendranath UA, Jenkins L (2003) Unit commitment using a stochastic extended neighbourhood search. IEE Proc Gen Transm Distrib 150:67–72
14. Purushothama GK, Jenkins L (2003) Simulated annealing with local search-a hybrid algorithm for unit commitment. IEEE Trans Power Syst 18:273–278
15. Li Z, Shahidehpour M (2003) Generation scheduling with thermal stress constraints. IEEE Trans Power Syst 18:1402–1409
16. Simopoulos DN, Kavatza SD, Vournas CD (2006) Unit commitment by an enhanced simulated annealing algorithm. IEEE Trans Power Syst 21:68–76
17. Simopoulos DN, Kavatza SD, Vournas CD (2006) Reliability constrained unit commitment using simulated annealing. IEEE Trans Power Syst 21:1699–1706
18. Saber AY, Senjyu T, Miyagi T, Urasaki N, Funabashi T (2007) Unit commitment by heuristics and absolutely stochastic simulated annealing. IET Gener Transm Distrib 1:234–243
19. Saber AY, Senjyu T, Miyagi T, Urasaki N, Funabashi T (2006) Fuzzy unit commitment scheduling using absolutely stochastic simulated annealing. IEEE Trans Power Syst 21:955–964
20. Christober Asir Rajan C, Mohan MR (2007) An evolutionary programming based simulated annealing method for solving the unit commitment problem. Int J Electr Power Energy Syst 29:540–550
21. Christober Asir Rajan C (2011) Hydro-thermal unit commitment problem using simulated annealing embedded evolutionary programming approach. Int J Electr Power Energy Syst 33:939–946

A New Product Design Process: Combining the System Model and VRTC

Hsiao-wen Wu, Jin-Jen Wang, and Wen-Chih Wang

Abstract A new product design process, the virtual reality transferred by correlation (VRTC) is presented to lower the cost and shorten the product development process. The workflow is based on the comprehensive analysis of the problem to build a simulation-driven design process, which is used for both decisions of making the design parameters and minimizing the need for tests. By combining the VRTC with a system model, the designers can make a quick assessment for the design for the whole system and shorten the product's time for market with an improved quality. A vibro-acoustic analysis on a loudspeaker diaphragm is presented to show the effectiveness of the workflow. By measuring the mode shapes and sound pressure, the relation between vibrations of diaphragm and sound generated can be found, and then we can redesign the speaker's structure to generate desired sound quality.

Keywords System model • Reversed engineering • Vibro-acoustics • Workflow

1 Introduction

Product development is a long and costly process, which usually includes redesign and extensive tests. However, as the competition grows, many companies have begun to shorten the product development cycle to reduce the time for market. Many have tried on reducing the time in new product development process via the management of the process or organization; however, it causes more than just management problems. Griffin [1] showed that many had tried to reduce the product development time and end up failed in market due to a lower product quality.

H.-w. Wu
Department of Electronics Engineering, TungNan University, New Taipei City 22202, Taiwan

J.-J. Wang (✉) • W.-C. Wang
Engineering Service Team, Samwell Testing Incorporation, New Taipei City 22180, Taiwan
e-mail: dave@samwells.com

Mallick and Schroeder [2] mentioned that the major challenge in managing new product development is not only to reduce the cost and time but also on the product performance and the long-term goal of the company. These studies concluded that the efficiency of new product development is not solely achieved by reducing the time, we need a workflow that can solve the time, cost, and quality problem once and for all.

In this study, VRTC (virtual reality transferred by correlations) workflow is presented to reduce time and cost in product development without sacrificing the quality of the work. It is done by improving the model through correlation analysis and will build an analysis model-driven process. In addition, a system model is used to give a quick evaluation on design parameters. The key is to validate the analytical model via test in each design process. An example of speaker diaphragm design will also be presented to show how effective VRTC is to reduce the development time and cost.

2 Principles and Concepts

2.1 System Model

A system model describes the responses of a system corresponding to the parameter change and time. It can offer the designers a comprehensive view on how the product works as a whole system and is very useful in assessing the dynamic behavior of the design. A system model can assess the combined effect of a system on its functions, and it is regularly used to evaluate the design parameters before the designers conduct the detailed design and analysis.

Since a system model simulates the responses of a system caused by an input, the modules in the model can be black boxes. It provides us two advantages in designing. Firstly, the designers do not need to know all details at the beginning; the model will provide the information on the nature of the problems. The product design will be more flexible with a system model since the designers only need to decide the specifications and functions of the products, and it will show where and what area they need to work. Secondly, a system model can offer a quick assessment on design parameters. The parameters like forces, friction coefficients, and stiffness can be evaluated quickly because the analysis is not a 3-D PDE problem. The parameters can be used as boundary conditions and loads in 3-D analysis and will greatly reduce the time for simulations.

A system model can also validate the design results that combined with part or assembly from other sources. The parameters obtained for the optimal design can also be used to evaluate if the outsourcing parts or assembly meets the requirements. This will greatly reduce the work in validation stage since the prototype testing and redesigning can be minimized by system model's evaluations. Thus, a system minimizes the time and cost of the design while improving the product quality by simulations on the whole system of a product.

2.2   Coupled Engineering and Hybrid Engineering

Coupled engineering refers to those methods that involve the analysis or tests that involve more than one physical domains [3, 4], and hybrid engineering refers to the analysis methods that use the test results to modify the analytical models [5]. These methods will be frequently applied in VRTC workflow.

The coupled engineering method is used to analyze the problem from the aspects of different physics. Such method can usually show us alternative ways to solve the problem, for instance, to suppress the noise by altering the structural vibration characteristics. In simulations, coupled analysis can also provide the interactions between two different physical properties which can offer comprehensive information on the full-field scope. The hybrid engineering improves the analytical model via tests; the model is modified and validated based on the test results, and sometimes the test results are applied as analytical conditions directly which generates highly accurate models. These models can help the designers to find the optimal product design simply by simulations.

2.3   VRTC and the New Process

VRTC is a workflow based on a comprehensive examination on the problem, and thus we can find all problems with less tests and analysis. The coupled engineering method is adopted to provide thorough observations, and hybrid engineering method is used to provide accurate models for analysis, which will make the development process more efficient since most of the designs can be based on the simulation results. In the new process, we combine a system model in VRTC, which can make the process more efficient by providing quick evaluations on parameters in the view of the whole system. Thus, the new workflow can give the designers an edge because of its thoroughness and efficiency.

The main purpose of VRTC workflow is to obtain an analysis-driven design process. In order to provide accurate and realistic predictions, all analytical models are validated thoroughly in multi-physical domain correlation analysis, and thus the need for tests in the subsequent product development process is minimized. The models are to be updated after each test in the workflow, so not only the tests but also the cost and time will be minimized in the following work. By applying a system model in VRTC workflow, the decision making for design parameters can be hastened, and the ideal of a shorter time for market with a high-quality product can be achieved.

3   Example: Development of a Loudspeaker

3.1   Experimental Methods

Since the process of the sound generated by a loudspeaker membrane is a
vibro-acoustic-coupled problem, the experiments are conducted by measuring the
vibrations and sound. The vibrations of the membrane in operation is measured with
a Polytec laser Doppler vibrometer, which scans the membrane surface with a laser
beam and the vibrations is measured with Doppler effect. The vibration mode shapes
and frequencies are then used to compare with simulation results for validation. The
sound is measured by a Microflown sensor, which scans the membrane surface and
measure the motion of the air particles and the sound above it. By comparing the results
of vibrations and air particle motion, we can find the relation between the membrane
vibrations and the sound emission, as well as validating the analytical model. The
comparison of vibrations and air particle velocity is shown in Fig. 1, and the spectrum
of sound pressure is shown in Fig. 2.

3.2   Analytical Methods

A loudspeaker generates sounds by vibrating the air via membranes. The membrane
is driven by an actuator which causes the vibrations on the membrane and then
drives the nearby air to move. The vibrations of a membrane can be described by
Helmholtz equation:
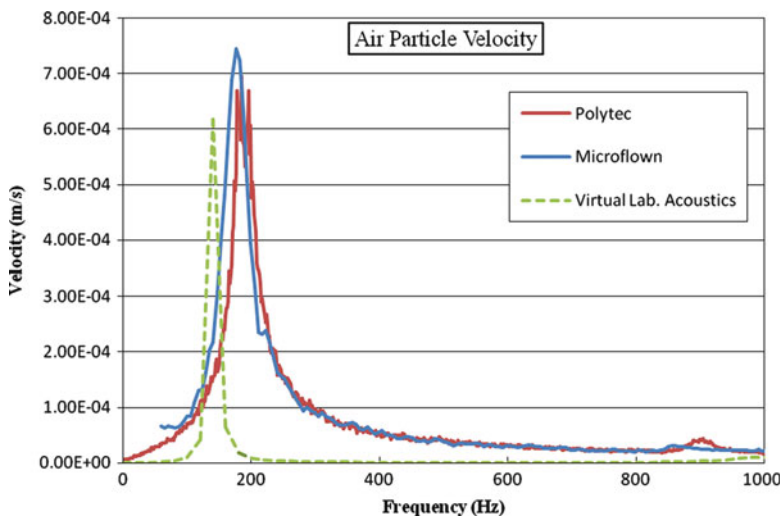
Fig. 1 Simulation and test results
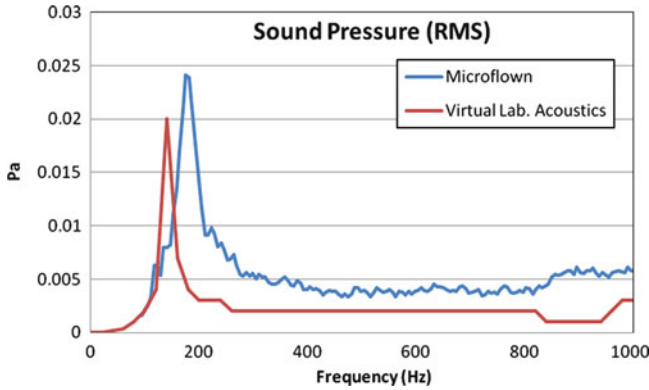
Fig. 2 The spectrum of sound pressure
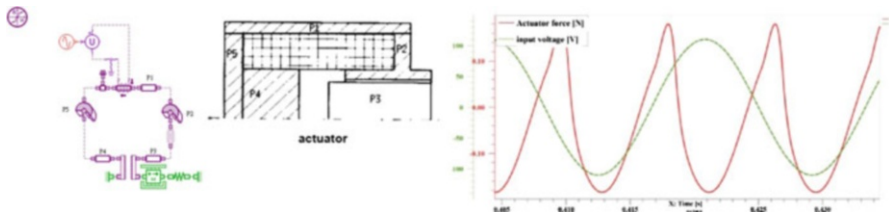
Fig. 3 System model of the actuator

$$\nabla^2 \psi(p) + k^2 \psi(p) = 0 \tag{1}$$

where $\psi(p)$ and k are the velocity potential function and wave number, respectively. Since the nearby air particles are driven by the vibrating membrane, the air particles near the membrane surfaces should vibrate at the same way as the membrane. In the vibro-acoustic problem, the acoustic fluid is assumed to be homogeneous and isotropic fluid, and the sound generated by the vibrations will have the same frequency as the vibrations.

The membrane is controlled by an actuator, and the actuator is a magnetic-mechanical problem which is a complex coupled-field problem. In this case, a system model is used for simulations on the output forces of the actuator as shown in Fig. 3. In this study, LMS Imagine Lab. AMEsim is used to provide the system analysis, and the vibro-acoustic simulations are conducted by LMS Virtual Lab. Acoustics.

3.3 Discussions

The system model in Fig. 3 provides an alternative way for actuator simulations. The membrane is the target of design in the example, and the system model saves time with a quick simulation on the actuator force. The system model also provides us a way to conduct the parameter analysis for the actuator design, which may provide us more options on actuator response design.

By comparing Figs. 1 and 2, it shows that the vibrations of membrane does affect the sound generated by a loudspeaker, since the spectrum measurement of vibrations and sound pressure shows the same pattern. The results also show that the peaks in both spectrum show the same frequencies, so observations in one can represent the other in the vibro-acoustic problems. This means the measurement of both sound and vibrations will help us greatly with the noise and vibration problems. The results can also be processed by sound quality analyzer such as ACQUA for sound quality design of a loudspeaker.

Since the vibrations of the membrane are decided by its mode shapes, the analytical model is modified by comparing the mode shapes at the corresponding frequencies. In Fig. 2, the frequency spectrum of the speaker predicted by the model is close to the test results and can hasten the following designing work since most of it can refer to simulations. The analytical model can be used to offer redesign suggestions with the information of sound quality analyzers. The concepts can be used in reversed engineering to help the developers gain more information in the process [6].

4 Concluding Remarks

This study presents the VRTC workflow which can reduce the product development time and cost by providing an analysis-driven product development process. The analytical model proves to be able to provide accurate predictions after validations, and the need for tests is reduced in product development. With the help of the system model analysis, VRTC will make the development of complex product more efficient and flexible. The designers will benefit from the new process by a shorter time for market and less cost.

References

1. Griffin A (1993) Metrices for measuring product development cycle time. J Prod Innov Manag 10:112–125
2. Mallick DN, Schroeder RG (2005) An integrated framework for measuring product development performance in high technology industries. Prod Oper Manag 14(2):142–158

3. Taylor CA et al (2006) A coupled momentum method for modeling blood flow in three-dimensional deformable arteries. Comput Method Appl Mech Eng 195(41–43):5685–5706
4. Herbruggen J, Deblauwe F, Kühn R (1998) Engine test bed application and comparison of sound intensity and acoustic holography. In: Proceedings of Euro noise 98, Munich, 1998
5. Gérard F, van der Linden PJG, Storer D (2000) Interior noise investigation of a vehicle by means of hybrid calculation procedures and modal contribution analysis. In: Proceedings of IMechE-2000: European conference for noise and vibration 2000, London, 2000
6. Wu HW et al (2012) Reversed system engineering – an approach for Taiwan's car electronics industry to gain competitive advantages. In: The 20th national conference on sound and vibration, Changhua, 2012

Part IV
Control and Software Engineering

The Study of Permanent Magnetic Synchronous Motor Control System Through the Combination of BP Neural Network and PID Control

Lin Zhang, Bao-Jie Xu, Kun-Li Wen, and Yuan-Hui Li

Abstract   Modern manufacturing is not only more demanding on machining accuracy but also requires the equipment to have a better degree of wisdom. For PMSM control system, it generally uses traditional PID control method due to the control advantages of traditional PID control which are simple algorithm, strong bond, and high reliability. However, the actual industrial processes are often nonlinear, and many nonlinear systems have difficulties to determine the precise mathematical model, which causes PID controller to not achieve ideal control effect. Because BP neural network has arbitrary nonlinear express ability which can achieve the best combination of PID control through the study of system performance. Hence, the control accuracy, robustness, and adaptive capacity of the control system for permanent magnet synchronous motors are improved. Also, PMSM vector control model is established to be a controlled subject. The chapter proposes the advantages of PID control and BP neural network to develop BP neural network PID controller. By using double-layer neural network controller with three inputs and three outputs, and the input refers to deviation, input signal and system output. After correcting the weightings and adjusting the three parameters of PID controller, the purpose of eliminating transient error rapidly and reaching steady state can be achieved. The practical simulation results find that the proposed BP neural network PID controller has parameter self-tuning function, short system response time, no over shooting phenomenon, and stronger robustness.

L. Zhang • B.-J. Xu
Mechanical & Electrical Engineering School, Beijing Information Science & Technology University, Beijing 100192, China

K.-L. Wen (✉)
Department of Electrical Engineering, Chienkuo Technology University,
Changhua 500, Taiwan
e-mail: klw@ctu.edu.tw

Y.-H. Li
Manufacturing Engineering Department, Beijing Foton Cummins Company,
Beijing 102206, China

1 Introduction

When it comes to control theory, the traditional PID control has advantages such as good intuitiveness, simple, highly reliable, and excellent robustness. It has been widely used in industrial control, especially for the uncertainty system of the precise mathematical model [1]. But the modern industry has a very complex process mechanism which consists of nonlinear, variable parameters and variable structure uncertainty making it difficult to determine the precise mathematical model; thus, it is hard to obtain a satisfactory control effect using the traditional PID control [2]. In addition, the traditional PID control has a form of fixed control parameters, also it is difficult to adjust the line with long adaptation processes and parameter interaction problems which impact the effectiveness of the PID control [3].

In order for the controller to have better adaptability to achieve automatic adjustment of the control parameters, the concept of control by neural network was used as a starting point [4–7]. By using a integration of the BP neural network control and the traditional PID control based on the self-learning and optimal capacity finding ability of the BP neural network, [8] to combine the advantages of both ways which makes the system self-adaptive, automatically adjusting the control parameters to adapt to the changes of the controlled process, improving the control performance and reliability. The system not only has a better robustness and shorter system response time but also contains less swing than the PID controller.

Section 2 of this chapter contains the mathematical model of the PMSM model. It introduces the basic mathematical models and calculation methods. Section 3 is the author's development of the neural network PID controller. This shows the advantages of the fuzzy PID controller over the traditional PID controller via mathematical derivations and simulation experiments. Lastly, the results come to a conclusion with proposed future research recommendations.

2 The Mathematical Model of PMSM

The PMSM stator is similar to that of an electrically magnetized three-phase synchronous motor [3]. The induced electromotive force (EMF) generated by the permanent magnet is a sine wave form. In the derivation of the mathematical model of the PMSM, have some assumptions, and the equations are listed below.

$$u_q = R_s i_q + p\psi_q + \omega_r \psi_d, \quad u_d = R_s i_d + p\psi_d - \omega_r \psi_q \tag{1}$$

$$\psi_q = L_q i_q, \quad \psi_q = L_q i_q + \psi_f \tag{2}$$

$$T_{em} = p_n(\psi_d i_q - \psi_q i_d), \quad T_{em} = p_n[\psi_f i_q - (L_d - L_q)i_d i_q] \tag{3}$$

Therefore, the equation of the motor motion is

$$T_{em} = T_l + B\omega_r + Jp\omega_r \tag{4}$$

The voltage equation, torque equation, and the motion equation mentioned above constitute the mathematical model of the PMSM. Of which u_d, u_q as d, q axis voltage; i_d, i_q as d, q axis current; L_d, L_q as d, q axis inductance; R_s as the stator resistance; ω_r as the electrical angular velocity of the rotor; ψ_f for the flux of the fundamental permanent magnet's excitation magnetic field over the stator windings; and p as the differential operation. T_l as the load torque; B as the viscous friction coefficient; Ω_r as mechanical angular velocity; J as the total moment of inertia of the rotor and the load carried. In order to facilitate the simulation study, the voltage equation and the equation of motion can be written in the form of the equation state:

$$\begin{cases} pi_d = \left(u_d - R_s i_d + \omega_r L_q i_q\right)/L_q \\ Pi_q = \left(u_d - R_s i_d - \omega_r L_d i_d - \omega_r L_{md} i_f\right)/L_q \\ p\omega_r = \left(p_n T_{em} - p_n T_l - B\omega_r\right)/J \end{cases} \tag{5}$$

In general, control $i_d = 0$ to complete the so-called steady state of the decoupling control. In such cases, we can obtain the stator current i_q:

$$\begin{cases} pi_q = \frac{u_q}{L_q} - \frac{R_s}{L_q} i_q - \frac{\omega_r \Phi_f}{L_q} \\ p\omega_r = -\frac{B}{J}\omega_r + \frac{K_t}{J} i_q - \frac{T_l}{J} \end{cases} \tag{6}$$

Similarly, by selecting i_q and ω_r, we can obtain the dynamic mathematical model of the permanent magnet synchronous motor:

$$\begin{pmatrix} \dot{i}_q \\ \dot{\omega}_r \end{pmatrix} = \begin{pmatrix} -\frac{R_s}{L_q} & -\frac{\Phi_f}{L_q} \\ \frac{K_t}{J} & -\frac{B}{J} \end{pmatrix} \begin{pmatrix} i_q \\ \omega_r \end{pmatrix} + \begin{pmatrix} \frac{u_q}{L_q} \\ -\frac{T_l}{J} \end{pmatrix} \tag{7}$$

3 BP Neural Network PID Controller

3.1 Controller Structure and Working Principle

The BP neural network adaptive PID controller structure is shown in Fig. 1 [8]. It uses a double-layer neural network controller with three inputs and outputs, with the error, input signal r_{in}, and the system output y_{out} as the input for the neural network controller. Adjusting the three parameters K_P, K_I, and K_D of the PID
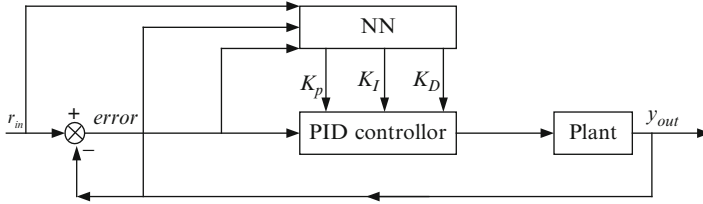
Fig. 1 The adaptive PID controller structure based on the BP neural network

controller according to the system operation state, through a series of amendments to right the weight values to achieve the purpose of rapid elimination of transient errors and steadying the system state. Through the BP neural network's self-learning and adjustment of the weighting factors, the neural networks output corresponds to the optimal control rate of the PID controller parameters.

3.2 BP Neural Network Structure and Algorithm

The algorithm of the BP neural network error reverse spread is referred to as the BP algorithm; it mainly uses the least squares algorithm and the gradient search technique so that the actual output value and the desired output value of the error mean square value are at a minimum. The learning process of the BP algorithm is composed of two parts: the forward pass and reverse pass. During the forward pass process, information enters from the input layer with a hidden layer containing layer-by-layer processing, then it is transferred to the output layer; the neurons (node) of each layer can only influence the state of the next layer of neurons. If the output layer gives an expected result with an unacceptable error as an output, then it is turned into a reverse pass, returning the error signal along the original connection path. With the use of the gradient search method, the weight value to achieve a decreased error is found. So through repeated modification of the weight values of the layers of neurons, the error signal is kept at a minimum. The overall structure is shown in Fig. 2 [8].

From Fig. 2, the input of the network hidden layer is

$$Q_j^{(1)} = x(j), \quad j = 1, 2, 3, \ldots, m \tag{8}$$

The input and output for the network hidden layer is

$$net_i^{(2)}(k) = \sum_{j=0}^{m} w_{ij}^{(2)} O_j^{(1)}, \quad \text{in which} \quad O_i^{(2)}(k) = f(net_i^{(2)}(k)),$$

$$i = 1, 2, 3, \ldots, q \tag{9}$$

Fig. 2 BP network structure
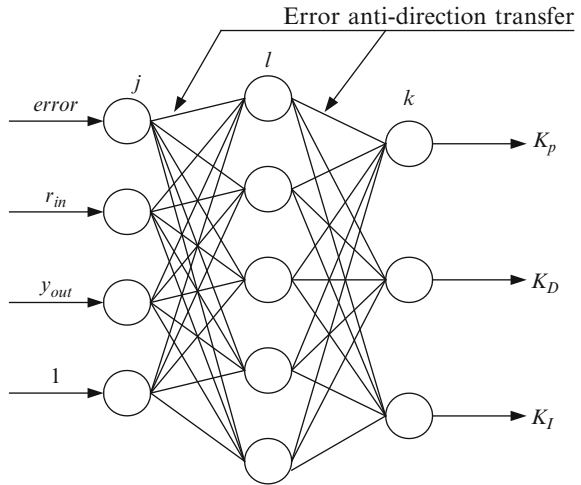
Among this, $w_{ij}^{(2)}$ is the hidden layer weight factor; the superscript represents the input layer, hidden layer, and output layer. $f(x)$ is the hyperbolic function, so that $f(x) = \frac{(e^x - e^{-x})}{(e^x + e^{-x})}$; lastly, the input and output of the three nodes of the last network output layer is

$$net_l^{(3)}(k) = \sum_{i=0}^{q} w_{li}^{(3)} O_i^{(2)}(k), \quad \text{in which} \quad O_l^{(3)}(k) = g(net_l^{(3)}(k)),$$

$$l = 1, 2, 3 \tag{10}$$

At this point,

$$O_1^{(3)}(k) = K_P, \quad O_2^{(3)}(k) = K_I, \quad O_3^{(3)}(k) = K_D \tag{11}$$

with $w_{li}^{(3)}$ as the output layer weighting factor; the output layer neuron activation function taken as a nonnegative Sigmoid function $g(x) = e^x/(e^x + e^{-x})$ takes the performance index function:

$$E(K) = \frac{1}{2}(r_{in}(k) - y_{out}(k))^2 \tag{12}$$

In accordance to the gradient descent algorithm to amend the network weight coefficients, that is, to adjust the negative gradient direction search according to $E(k)$ weighting coefficients, we get

$$\Delta w_{li}^{(3)}(k) = -\eta \frac{\partial E(k)}{\partial w_{li}^{(3)}} + \gamma \Delta w_{li}^{(3)}(k-1) \tag{13}$$

where η as the learning rate and γ as the inertia coefficient, then

$$\frac{\partial E(k)}{\partial w_{li}^{(3)}} = \frac{\partial E(k)}{\partial y(k)} \cdot \frac{\partial y(k)}{\partial u(k)} \cdot \frac{\partial u(k)}{\partial O_l^{(3)}} \cdot \frac{\partial O_l^{(3)}(k)}{\partial net_l^{(3)}} \cdot \frac{\partial net_l^{(3)}(k)}{\partial w_{li}^{(3)}} \tag{14}$$

variable needed by the (14) form $\frac{\partial y(k)}{\partial u(k)}$, due to $\frac{\partial y(k)}{\partial u(k)}$ being unknown, an approximation is used as a replacement.

$$\frac{\partial u(k)}{\partial O_1^{(3)}} = e(k) - e(k-1), \frac{\partial u(k)}{\partial O_2^{(3)}} = e(k),$$
$$\frac{\partial u(k)}{\partial O_3^{(3)}} = e(k) - 2e(k-1) + e(k-2) \tag{15}$$

Imprecise effect resulted from this process can be compensated by adjusting the learning rate [9], and then we can get the BP neural network output layer weight formula:

$$\Delta w_{li}^{(3)}(k) = \eta \delta_l^{(3)} O_i^{(2)} + \gamma \Delta w_{li}^{(3)}(k-1) \tag{16}$$

$$\delta_l^{(3)} = e(k) \cdot \frac{\partial \hat{y}(k)}{\partial u(k)} \cdot \frac{\partial u(k)}{\partial O_l^{(3)}(k)} \cdot g(net_l^{(3)}(k)), \quad l = 1, 2, 3 \tag{17}$$

Similarly, the hidden layer weight is calculated as

$$\Delta w_{li}^{(2)}(k) = \eta \delta_l^{(2)} O_j^{(1)} + \gamma \Delta w_{li}^{(3)}(k-1) \tag{18}$$

$$\delta_i^{(2)} = f'(net_i^{(2)}(k)) \sum_{l=1}^{3} \delta_l^{(3)} w_{li}^{(3)}(k), \quad i = 1, 2, 3, \ldots, q \tag{19}$$

4   Simulation

Using the c2d function in Matlab, we were able to discrete the permanent magnet synchronous motor vector mathematical model into bytes in the control object [9, 10]. Then construct an AC permanent magnet synchronous motor using a neural
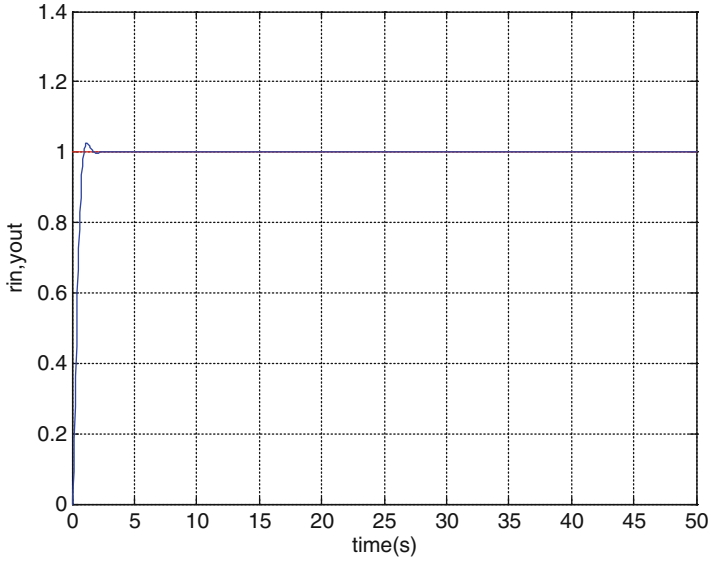
Fig. 3 System step response
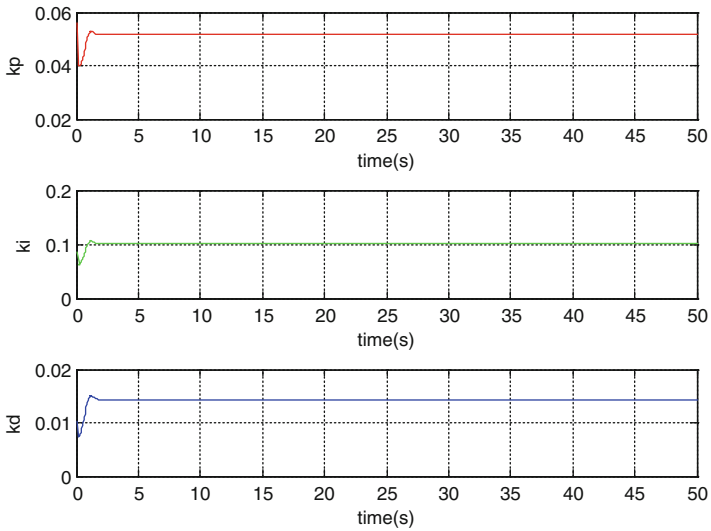
Fig. 4 Mapping the neural network auto-tuning PID curve

network PID control system model shown in Fig. 1, in Matlab, to perform simulation tests. Figs. 3 and 4 show BP neural network PID step response and the PID parameter curve.
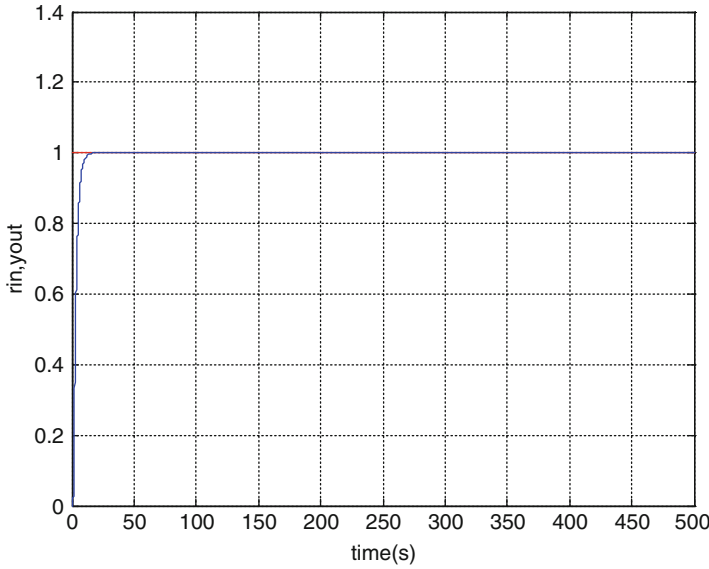
Fig. 5 System step response after adjusting learning rate
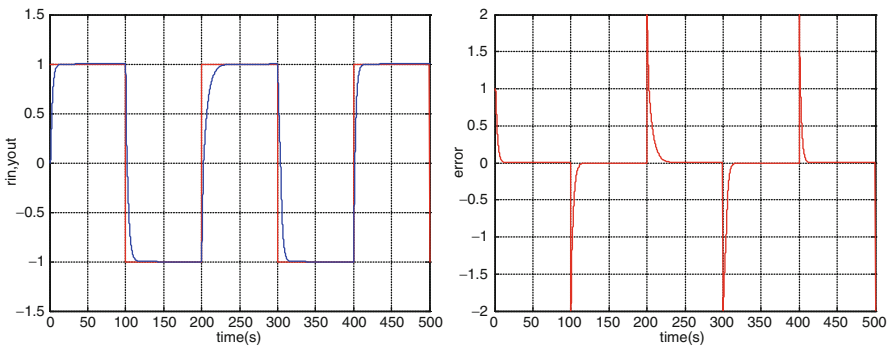
Fig. 6 Square wave signal system response curve and error curve

System can also be adjusted according to the calculation speed of its own hardware cycle and the learning rate; the smaller the learning rate, the less prone it is to pendulum. Figure 5 is the system step response after adjusting learning rate in order to reflect the control system's antijamming capability and the ability to adaptive control nonlinear systems; the input signal at this point is $r_{\text{in}}(k) = \text{sign}$ $(\sin (0.01 \times \pi \times k \times t_{\text{s}})$. Observe the square wave signal response curve and the mapping of system error; the results are as shown in Fig. 6.

5 Conclusions

In traditional PID control, the parameter values K_P, K_I, and K_D are fixed. Therefore, even if reasonable adjustments were made, these parameters still cannot satisfy the requirements of the permanent magnet synchronous motor servo system because the motor is highly nonlinear and contains some uncertainties in the system such as load changes and external interference. This chapter integrates traditional PID control with the advantages of a BP neural network control to design and develop a neural network PID controller with the simplified vector control model of the AC permanent magnet synchronous motor as the charged object. It is shown through simulation experiments that using the BP neural network PID controller researched and developed in this chapter, online automatic adjustment of the parameters can be achieved giving it a wider applicability, and the overswing phenomenon almost disappears. In addition, users can also adjust the sampling period and the value of learning rate according to the computing speed of the hardware and the control accuracy of the demand conditions to adjust the system's transient response time and overswing amount. Also, different transient response times and overswing standard requirements selected by the sampling period and the value of learning rate adaptation can be based on the control accuracy. Only those requirements of the selected hardware for the chosen calculation speeds are different for each sample period and learning rate. The inadequacies of this chapter lie within the three PID parameters that cannot be controlled and optimized manually. Therefore, integration with other soft methods such as the fuzzy theory is the future research orientation and recommendation of this chapter.

References

1. Ang K, Chong G, Li Y (2005) PID control system analysis. Design and technology. IEEE Trans Control Syst Technol 13:559–576
2. Shitao H, Zhijing F (2006) Design of optimal PID controller for liner servo system based on LQR approach. Manuf Technol Mach Tool:33–35
3. Jeng YF, Zhang L, Xu BJ, Wen KL (2012) The study of fuzzy PID controller in permanent magnetic synchronous motor. In: International conference on ICADE, pp 176–180
4. Hu HJ (2001) Stable and adaptive PID control based on neural network. J Beijing Univ Aeronaut Astronaut 27(2):153–156
5. Chen WB, Zeng GH, Zou HJ, Zhang HB, Tan CW (2012) Study of a single neuron fuzzy PID DC motor control method. In: International conference on intelligent systems design and engineering application, pp 1125–1128
6. Ablameyko S, Goras L, Gor M (2001) Neural networks for instrumentation. Measurement and related. Ios Press, Amsterdam

7. Chen YL, Chen WL et al (2005) Development of the FES system with neural network + PID controller for the stroke circuits and systems. In: International conference on IEEE ISCAS, Kobe, 2005, pp 5119–5121
8. Guo BT, Liu HY, Luo Z, Wang F (2009) Adaptive PID controller based on BP neural network. In: International joint conference on artificial intelligence, Pasadena, 2009, pp 148–150
9. Jang JSR (2008) Matlab program design. TeraSoft Inc, Hsinchhu
10. Lee YD (2011) The design and simulation of control system: use Matlab/Simulink. CHWA, Taipei

Power Compensation Methodology for Electric Vehicles

Chien-An Chen and Ming-Chih Lin

Abstract A dynamic compensation strategy to enhance the driving quality of electric vehicle (EV) is proposed. Statuses of vehicle, road conditions, and vehicle operation scenarios are taken into consideration to account for the undesired vehicle behaviors, such as start slowing, weak acceleration, and time-varying loads. At the instant of starting, an extra power is added against static frictional force. An additional power is considered while there is an extra loading or vehicle is under creeping. Besides, for comprehending the limitation of power output, the behaviors among battery, inverter, and motor are also unveiled to promote the proposed compensation strategy. Finally, the proposed compensation strategy is implemented on *i*-EV developed by Automotive Research & Testing Center to validate the feasibility.

Keywords Electric vehicle • Power compensation • Vehicle behavior

1 Introduction

A Vehicle Control Unit (VCU), which is electric vehicle control kernel, consists of controlling and management of power, energy, auxiliary subsystems, and other subsystems. In recent years, although the conventional vehicle technologies had matured, however, dynamic control for electric vehicle applications is still exciting some issues to be solved. Hence, the development status, the control strategies, and the strategies of VCU are discussed.

Presently, the VCU development conditions are still under research and development. Besides AC Propulsion (ACP), Curtis, and BRUSA, whose products

C.-A. Chen (✉) • M.-C. Lin
Technical Development Group, Green Vehicle Development Division,
Automotive Research & Testing Center, Changhua 50544, Taiwan
e-mail: chienan@artc.org.tw

possess VCU functions, most of developers focus on the management of drive unit, i.e., Power Control Module (PCM):

1. ACP [1]: It processes the functions of motor drive control, smooth operation under any driving conditions, adjustable braking to regenerate, torque/speed control, RS232 communication interface, battery management system, charging status display, wireless communications, and diagnosis.
2. Curtis [2]: Acceleration or deceleration, downhill or uphill, half throttle or full throttle control, VCL (Vehicle Control Language) to develop control algorithms, and built-in FLASH can be easily upgraded in the file.
3. BRUSA [3]: To provide easy driving mode, i.e., energy-saving, normal and sport, judgment to drive command, control, and coordination functions. The main features are described as follows:

   (a) CAN communicated interface, inverter, charger, DC/DC converters, and battery management are constructed for surveillance, control, and coordination.
   (b) The position of pedal, battery power, instantaneous driving state, given desired speed, and desired torque command are transferred to driver.

4. California Motors [4]: To provide users CAN (Controller Area Network) interface for transmission and hybrid control function.

Overviewing the international product development status, the current products already had basic performance, communication, and monitoring functions. However, how to integrate those functions and even development of new strategies to meet the overall demand for electric vehicles to follow-up required are the pending problems.

2 Vehicle Control Unit Functions

In the performance requirements in the electric vehicle propulsion system, the development engineers generally focus on the dynamic response to meet the vehicle performance index, i.e., acceleration, grade ability, and mileage. However, for the completeness of control strategy design, in addition to meeting basic performance requirements, it still needs to consider system corresponding strategy based on function failures and fault diagnosis functions.

For vehicle starting control process, it not only needs to go through in the first position of the key switch and shift gear confirmation, but it also needs to follow the required power status of the battery (i.e., voltage, current, temperature, and state of charge) and other subsystem status determined. When it completes the boot process, a Motor Control Unit (MCU) is in accordance with driver's operation mode (acceleration and braking) and external environment (climbing, downhill, and severity of the load) to exert control commands. However, the above-maintained control flow is constructed in the normal operation of the system

function and condition. Since the vehicle propulsion system is to be repeatedly used and perhaps had parts damaged, functional failures may be the cause. Therefore, how to introduce the failure mode of the corresponding decision-making in normal mode is an important consideration of vehicle traveling security.

State analysis and detection, discrimination of the operating environment, failure mode discrimination, safety protection, analysis, decision-making, etc. are also joined for fault diagnosis and energy management technology. These will enable more complete control functions of propulsion system so as to achieve security reasons, failure mode, and good dynamic performance. Hence, the complete vehicle control should consist of power control, safety protection, status monitoring, diagnosis and failure warning, communications, and parameter tuning [5].

3   Power Compensation Methodology Design

The conventional power control device has the following drawbacks:

1. When the electric vehicle starts, a static friction force must be overcome. If the electric vehicle does not have a slow-movement design, the conventional power control scheme may result in a slow start, especially for a heavy electric vehicle.
2. When the electric vehicle accelerates, the conventional power control device may not result in an obvious feeling of acceleration because of a small accelerating force of the electric vehicle.
3. When the accelerated pedal depth is not to be changed, a change of a road slope may result in a load change of the electric vehicle so that the torque output signal from the conventional power control device may be too large or too small, resulting in undesired speed change of the electric vehicle.

Therefore, in order to make good decisions of VCU and excellent dynamic performance of electric vehicles, power control compensation planning is followed as the three control compensation strategies:

1. Start Compensation: in order to reduce energy consumption, idle mode is excluded. Besides, for overcoming the static friction resistance while starting, motor needs to be provided immediate torque required to reduce the start-up time.
2. Accelerated Compensation: to follow-up the accelerating demand of driver, the power output is also immediate compensation the amount of power so as to make the vehicle has a good dynamic performance.
3. Load Compensation: while vehicle under climbing road, the required power output is much than that of flat road, the power is compensated when the vehicle is under climbing.

Fig. 1 Start compensation
function
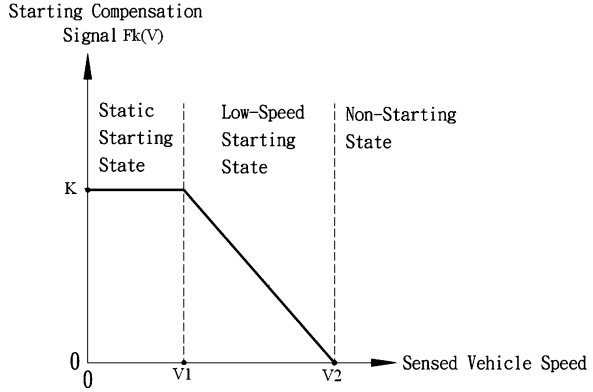
3.1 Start Compensation

In the compensation strategy, the start judgment of the situational judgment unit is that if the sensed vehicle speed (V) is less than the first preset speed ($V1$), it is judged in a stationary starting situation; if the sensed vehicle speed is between the first preset speed and the second between two preset speeds, it is judged that an electric vehicle is in the low-speed starting contexts; otherwise, it is determined in a non-starting contexts. Its relationship is shown in Fig. 1. The second preset velocity ($V2$) is greater than the first preset velocity ($V1$) and is described as follows:

$$Fk(V) = \begin{cases} K, & V \leq V1 \\ K \cdot d(V) & V1 < V \leq V2 \\ 0, & V > V2 \end{cases} \tag{1}$$

where K is a constant value and $d(V)$ is a decaying function between k and 0.

3.2 Acceleration Compensation

In the compensation strategy, for making the judgment of the acceleration condition, the acceleration condition judging unit operates as follows:

1. The acceleration condition judging unit judges that an electric vehicle is in the accelerating state when the depth variation value of the pedal is greater than a preset value and sets an initial pedal depth using the reference pedal depth when the condition judging module judges that the electric vehicle has changed from the non-accelerating state to the accelerating state.
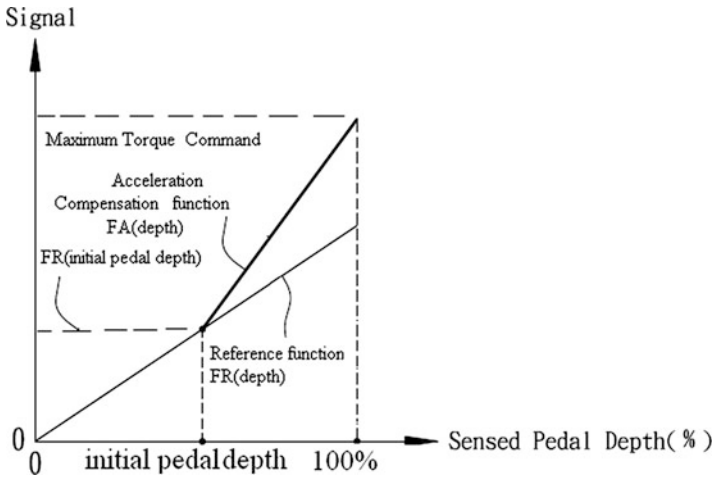
Fig. 2 Acceleration compensation function

2. The acceleration condition judging unit judges that the electric vehicle is in the accelerating state when the depth variation value is less than the preset value and the sensed pedal depth is greater than the initial pedal depth.
3. The acceleration condition judging unit judges that the electric vehicle is in the non-accelerating state and sets the initial pedal depth as 0 when the depth variation value is less than the preset value and the sensed pedal depth is less than the initial pedal depth.

Its relationship is shown in Fig. 2.

3.3 Load Compensation

In the compensation strategy, the load condition judging unit has information of a reference curve of vehicle speed. The reference curve of vehicle speed describes a preset relation between the pedal depth of the accelerator pedal and the vehicle speed of an electric vehicle. For making the judgment of the load condition, the load condition judging unit operates as follows:

1. The load condition judging unit judges that the electric vehicle is in the light load state when the sensed vehicle speed is larger than at least a preset difference from a preset speed that corresponds to the sensed pedal depth according to the reference curve of vehicle speed.
2. The load condition judging unit judges that the electric vehicle is in the heavy load state when the sensed vehicle speed is smaller than at least the preset difference from the preset speed that corresponds to the sensed pedal depth according to the reference curve of vehicle speed.

3. The load condition judging unit judges that the electric vehicle is in the preset load state when the sensed vehicle speed is not larger by at least the preset difference from the preset speed that corresponds to the sensed pedal depth according to the vehicle speed reference curve and is not smaller by at least the preset difference from the preset speed that corresponds to the sensed pedal depth according to the vehicle speed reference curve.

4 Verifying Results and Conclusion

Through the above analysis and discussion, the power control compensation in this chapter is finished by the proposed design strategies. It has been proved through several tests and is shown as follows:

- Start Compensation Test (Fig. 3)
- Acceleration Compensation Test (Fig. 4)
- Load Compensation Test (Fig. 5)

In this chapter, the power compensation methodology for electric vehicles is presented. The analysis, design, and power compensation methodology are implemented and validated to overcome the drawbacks of the conventional power control drive. Therefore, the proposed power control compensation can effectively be applied to EV.
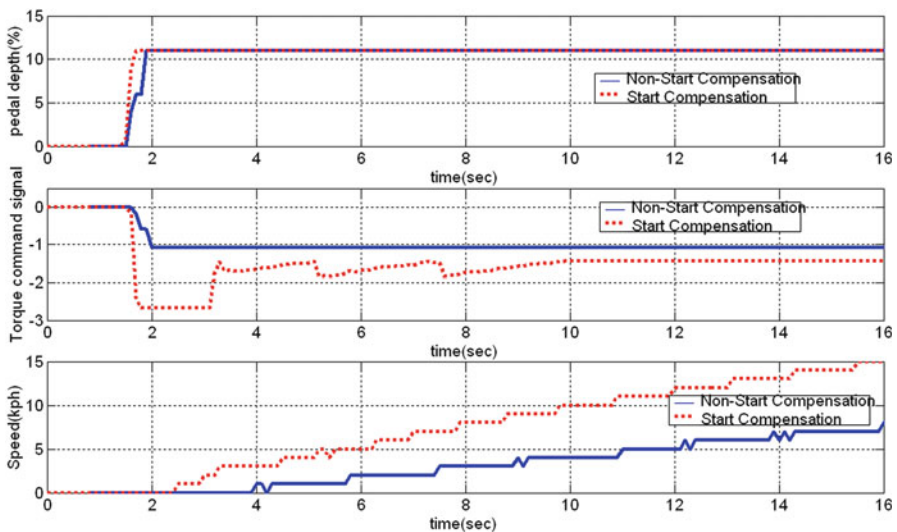
Fig. 3 Start compensation response
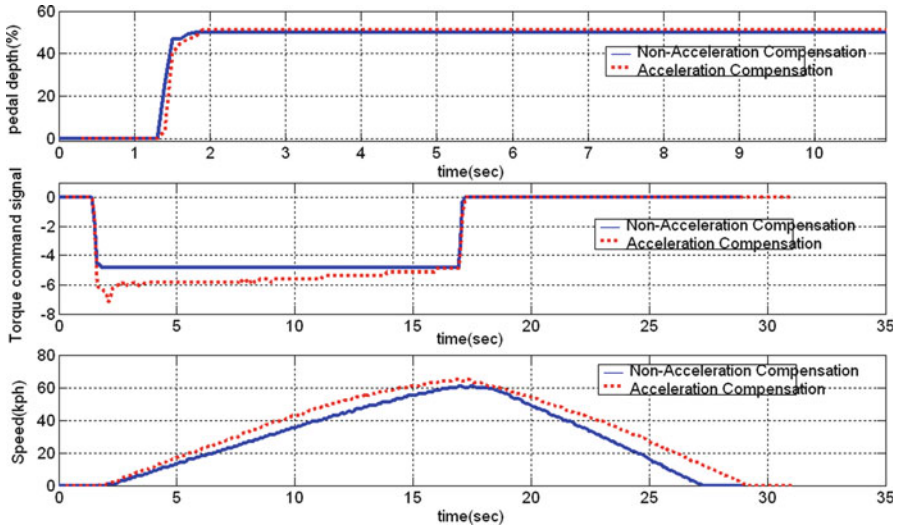
Fig. 4 Acceleration compensation response
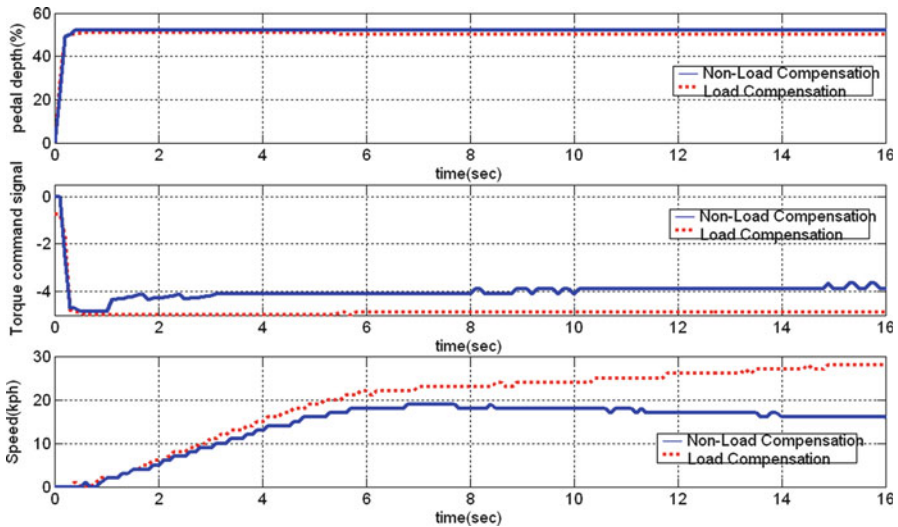
Fig. 5 Load compensation response with gradients of 12 %

References

1. http://www.acpropulsion.com/products-tzero.html
2. http://curtisinstruments.com/index.cfm?fuseaction=cProducts.dspMotorControllers
3. http://www.brusa.biz/products/e_vcu200413.htm
4. http://www.calmotors.com/
5. Mikhail G, Ibrahim D, Marc AR (2006) Economic and environmental comparison of conventional, hybrid, electric and hydrogen fuel cell vehicles. J Power Source 159(9):1186–1193

Model-Based Robust Control for Nonlinear Networked Control Systems

Cheng-Fa Cheng and Cheng-Han Yang

Abstract In this chapter, a nonlinear model-based networked control system (MB-NCS) will be proposed to reduce the packet rate and network usage. A model plant that approximates the nonlinear plant dynamics via a transmission attenuation path and makes possible stabilization of the nonlinear plant will be introduced. The comparison system whose states as well as the nonlinear MB-NCS states will be developed such that the stability of the original system can be guaranteed. And then the robust stabilization problems of the nonlinear time-variant MB-NCS with time-variant transmission attenuation will be investigated. Finally, an example with simulation results is given to exemplify the implementation of the proposed controller design technique.

1 Introduction

Recently, the development of the digital systems and communication networks has increased rapidly. In particular, networked control system (NCS) [1, 2] has gained a significant amount of attention in the control society. To exchange the information and to complete the control task [3], engineers would like to incorporate the real-time communication channel into a digital system. The networked control architecture owns many advantages over a traditional point-to-point design [3]. Control community has aimed to model, analyze, and control the networked control systems with the limited communication capability [3–6].

C.-F. Cheng (✉) • C.-H. Yang
Department of Communications, Navigation and Control Engineering,
National Taiwan Ocean University, Keelung 20224, Taiwan
e-mail: cfcheng@ntou.edu.tw

It is usually a trade-off between the stability and performance of the control system and bandwidth usage [7]. The uses of communication networks are always constrained by the bandwidth [8]. When the communication channel is noisy, the deterministic real-time communications cause important restrictions on the available bandwidth. Good performance and large stability margins can be obtained by having accurate sensor measurements that are communicated to the controller in a timely manner, and one of the main problems to be addressed when considering a networked control system is the size of the bandwidth required by each subsystem. It is clear that the reduction of bandwidth necessitated by the communication network in a NCS is a major concern.

In this chapter, we consider the major problem of reducing the bandwidth necessitated of a nonlinear NCS using a novel approach called model-based network control system (MB-NCS). At each transmission times, the plant model is updated with the measured nonlinear plant state, and this control architecture has as its main objective the reduction of the data packets transmitted over the network. In addition, the effect of the transmission attenuation for analyzing the stability of the nonlinear time-variant MB-NCS using a comparison principle will be proposed. We will also further explore the robust stabilization problems of nonlinear time-invariant MB-NCS with time-variant transmission attenuation using a novel comparison method in this chapter.

2 Systems Description and Problem Formulation

The system dynamics are given by [9]:

$$\text{Plant}: \dot{x}(t) = A(t)x(t) + B(t)u(t) + f(t, x(t)), \tag{1a}$$

$$\text{Model}: \dot{\hat{x}}(t) = \hat{A}(t)\hat{x}(t) + \hat{B}(t)u(t), \tag{1b}$$

$$\text{Controller}: u(t) = K(t)\hat{x}(t), \tag{1c}$$

where $A(t) \in R^{n \times n}$ and $B(t) \in R^{n \times p}$ denote the nominal system matrix and input connection matrix of the plant, respectively, and $\hat{A}(t) \in R^{n \times n}$ and $\hat{B}(t) \in R^{n \times p}$ denote the nominal system matrix and input connection matrix of the model, respectively. $f(t, x(t)) \in R^n$ is a nonlinear function which satisfies

$$\|f(t, x(t))\| \leq \ell(t)\|x(t)\|^m, \tag{2}$$

where $m \geq 1$ is a constant and the function $\ell(t) \geq 0$, $t \geq 0$. The update times are denoted as τ_k, and $\tau_0 < \tau_1 < \tau_2 < \cdots$, $\lim_{k \to \infty} \tau_k = \infty$. The update intervals are $h_k = \tau_k - \tau_{k-1}$ for all $k \in \mathrm{N}$, where N is the set of the natural number. Due to the

long-distance transmission, the signal $x(t)$ will be attenuated with the attenuation ratio ϖ_k before entering the model (1b) for $0 < \varpi_k \leq 1$. Furthermore, the plant (1a) will be updated with the update factor χ_k, where $\chi_k \in \mathrm{R}$. Assume

$$x(\tau_k) = (\chi_k + \Delta\chi_k)x(\tau_k^-) \tag{3a}$$

$$\hat{x}(\tau_k) = (\varpi_k + \Delta\varpi_k)x(\tau_k^-) \tag{3b}$$

for all $k \in N$, where $\Delta\chi_k$ and $\Delta\varpi_k$ are the update uncertainties of the plant and the model, respectively, and they are bounded by $\|\Delta\chi_k\| \leq r_1$ and $\|\Delta\varpi_k\| \leq r_2$.

Let us define the state error as $e(t) = x(t) - \hat{x}(t)$ which represents the difference between the plant state and the model state. $\tilde{A}(t) = A(t) - \hat{A}(t)$ and $\tilde{B}(t) = B(t) - \hat{B}(t)$ represent the difference between the plant and the model. Denoting $z(t) = \begin{bmatrix} x(t) \\ e(t) \end{bmatrix}$,

$\Lambda(t) = \begin{bmatrix} A(t) + B(t)K(t) & -B(t)K(t) \\ \tilde{A}(t) + \tilde{B}(t)K(t) & \hat{A}(t) - \hat{B}(t)K(t) \end{bmatrix}$, $G = \begin{bmatrix} I \\ I \end{bmatrix}$, $M_k = \begin{bmatrix} (\chi_k - 1)I & 0 \\ (\chi_k - \varpi_k)I & -I \end{bmatrix}$,

$R_k = \begin{bmatrix} \Delta\chi_k & 0 \\ \Delta\chi_k - \Delta\varpi_k & 0 \end{bmatrix}$, and $\Delta z = z(\tau_k) - z(\tau_k^-)$, for $t = \tau_k$, system (3) can be rewritten as

$$\begin{cases} \dot{z}(t) = \Lambda(t)z(t) + Gf(t, x(t)), & t \neq \tau_k \\ \Delta z(t) = M_k z(t^-) + R_k z(t^-), & t = \tau_k \end{cases} \tag{4}$$

for $k \in N$ with initial condition $z(t_0) = \begin{bmatrix} x(t_0) & 0 \end{bmatrix}^\mathrm{T} = z_0$.

3 Nonlinear Network Control

Let $\Phi(t, s)$ be the fundamental matrix of the system $\dot{z}(t) = \Lambda(t)z(t)$ which satisfies

$$\|\Phi(t, s)\| \leq \phi_1(t)\phi_2(s) \tag{5}$$

with $\phi_1(t) > 0$, $\phi_1(\tau_k^+) > 0$ and $\phi_2(t) > 0$, $\phi_2(\tau_k^+) > 0$ for $\tau_{k-1} < s \leq t \leq \tau_k$ and $\Psi(t, s)$ be the Cauchy matrix of reference system

$$\begin{cases} \dot{z}(t) = \Lambda(t)z(t), & t \neq \tau_k \\ \Delta z(t) = M_k z(t^-), & t = \tau_k \end{cases} \tag{6}$$

for $k \in N$, then we have the following result:

Theorem 1. *The uncertain MB-NCS (1) will be asymptotically stable:*

(a) For $m > 1$, if there exists $\hbar = \hbar(\varepsilon, t_0)$ for any $\varepsilon > 0$ such that

$$\int_0^\infty \left\{ \prod_{0 < \tau_k < s} (\sqrt{v_k} + r)\phi_1(\tau_k)\phi_2(\tau_k^+) \right\}^{m-1} \phi_1^m(s)\phi_2(s)\sqrt{2}\ell(s)ds < \infty \quad (7)$$

and

$$\phi_1(t) \prod_{0 < \tau_k < s} (\sqrt{v_k} + r) < \varepsilon. \quad (8)$$

(b) For $m = 1$, if there exists $\hbar = \hbar(\varepsilon, t_0)$ for any $\varepsilon > 0$ such that

$$\phi_1(t)\phi_2(t_0) \prod_{0 < \tau_k < s} \left\{ (\sqrt{v_k} + r)\phi_1(\tau_k)\phi_2(\tau_k^+) \right\} \exp\left\{ \int_0^t \sqrt{2}\phi_1(s)\phi_2(s)\ell(s)ds \right\} \leq \varepsilon \quad (9)$$

for $t \geq t_0 + \hbar$, where $v_k = \chi_k^2 + (\chi_k - \varpi_k)^2$ and $r = \sqrt{r_1^2 + (r_1 + r_2)^2}$.

Proof. Since $\Psi(t, s)$ is the Cauchy matrix of the reference system (6), then

$$\|\Psi(t, s)\| \leq \phi_1(t)\phi_2(s) \prod_{s \leq \tau_k < t} \left\{ \sqrt{v_k}\phi_1(\tau_k)\phi_2(\tau_k^+)) \right\}. \quad (10)$$

The solution of (4) can be represented as

$$z(t) = \Psi(t, t_0)z(t_0) + \int_{t_0}^t \Psi(t, s)Gf(s, x(s))ds + \sum_{t_0 < \tau_k < t} \Psi(t, \tau_k^+)R_k z(\tau_k). \quad (11)$$

It follows from (2), (10), and (11) that

$$\begin{aligned}
\left\| \breve{z}(t) \right\| &\leq \phi_2(t_0^+)\|z(t_0)\| \prod_{t_0 < \tau_k < t} \sqrt{v_k}\phi_1(\tau_k)\phi_2(\tau_k^+) \\
&\quad + \int_{t_0}^t \left(\prod_{t_0 < \tau_k < t} \sqrt{v_k}\phi_1(\tau_k)\phi_2(\tau_k^+) \right) \sqrt{2}\ell(s)\phi_1^m(s)\phi_2(s)\breve{z}^m(s)ds \\
&\quad + \sum_{t_0 < \tau_k < t} r\phi_1(\tau_k)\phi_2(\tau_k^+) \prod_{\tau_k < \tau_i < t} \sqrt{v_i}\phi_1(\tau_i)\phi_2(\tau_i^+)\breve{z}(\tau_k),
\end{aligned}$$

where $\breve{z}(t) = \dfrac{\|z(t)\|}{\phi_1(t)}$.

(a) For $m > 1$. By using Theorem A.3.2 and Lemma A.1.1 of [10], we have

$$\|z(t)\| \leq \phi_1(t)\phi_2\left(t_0^+\right)\|z(t_0)\| \prod_{t_0 < \tau_k < t}$$

$$\left(\sqrt{v_k} + r\right)\left\{1 - (m-1)\left[\phi_2\left(\tau_0^+\right)\|z(t_0)\|\right]^{m-1}\varphi(t_0, t)\right\}^{\frac{1}{1-m}}$$

for all $t > t_0$ such that $(m-1)\left[\phi_2\left(\tau_0^+\right)\|z(t_0)\|\right]^{m-1}\varphi(t_0, t) < 1$ where

$$\varphi(t_0, t) = \int_{t_0}^t \left(\prod_{t_0 < \tau_k < s} \left(\sqrt{v_k} + r\right)\phi_1(\tau_k)\phi_2\left(\tau_k^+\right)\right)^{m-1} \sqrt{2}\ell(s)\phi_1^m(s)\phi_2(s)ds.$$

It follows from Theorem 8.3 of [25] that the proof can be completed immediately.

(b) For $m = 1$. By using Lemma 1.7.1 of [11], we have

$$\|z(t)\| \leq \phi_1(t)\phi_2\left(t_0^+\right)\|z(t_0)\| \prod_{0 < \tau_k < s} \left\{\left(\sqrt{v_k} + r\right)\phi_1(\tau_k)\phi_2\left(\tau_k^+\right)\right\}$$

$$\exp\left\{\int_0^t \sqrt{2}\phi_1(s)\phi_2(s)\ell(s)ds\right\}$$

$t > t_0$. It follows from Theorem 8.5 of [12] that the uncertain MB-NCS (1) is asymptotically stable if (9) holds.

Next, for the nonlinear time-invariant MB-NCS

$$\begin{cases} \dot{z}(t) = \Lambda z(t) + Gf(x(t)), & t \neq \tau_k \\ \Delta z(t) = M_k z(t^-) + R_k z(t^-), & t = \tau_k \end{cases}, \tag{12}$$

we have the following theorem by using the comparison principle:

Theorem 2. *Assume the matrix P is symmetric and positive definite and $\lambda_1 > 0$, $\lambda_2 > 0$ are the smallest and the largest eigenvalues of P, respectively. Let*

$$Q = \Lambda^T P + P\Lambda \tag{13}$$

and λ_3 be the largest eigenvalue of $P^{-1}Q$. The nonlinear time-invariant MB-NCS (1) is asymptotically stable if

$$\tilde{\sigma}(\tau_{k+1} - \tau_k) + \ln(d_k) < 0, \tag{14}$$

where $\tilde{\sigma} = \left(\lambda_3 + 2\bar{\ell}\frac{\lambda_2}{\lambda_1}\right)$ and $d_k = (1 + a_k)m_k + \frac{r^2}{(1 + a_k)}\frac{\lambda_2}{\lambda_1}$, m_k is the largest eigenvalue of the matrix $P^{-1}\left(I + M_k^T\right)P(I + M_k)$, and a_k are arbitrary constants for all $k \in \mathbb{N}$.

Remark 1. It follows from Theorem 4.6 of [10] that for any given positive definite symmetric matrix $-Q$, there exists a positive definite symmetric matrix P that satisfies the Lyapunov equation (27) if and only if the matrix Λ is Hurwitz. Let us denote $\bar{\Lambda} = \begin{bmatrix} A & 0 \\ \tilde{A} & \hat{A} \end{bmatrix} \in \mathrm{R}^{2n \times 2n}$, $\bar{B} = \begin{bmatrix} B \\ \hat{B} \end{bmatrix} \in \mathrm{R}^{2n \times p}$, $\bar{C} = \begin{bmatrix} I & -I \end{bmatrix} \in \mathrm{R}^{p \times 2n}$, then Λ can be rewritten as $\Lambda = \bar{\Lambda} + \bar{B}KC$ which is analogous to the static output feedback control problem. Since the output controllability matrix is

$$\begin{bmatrix} \bar{C}\bar{B} & \bar{C}\bar{\Lambda}\bar{B} & \cdots & \bar{C}\bar{\Lambda}^{2n-1}\bar{B} \end{bmatrix} = \begin{bmatrix} \tilde{B} & \hat{A}\tilde{B} & \cdots & \hat{A}^{2n-1}\tilde{B} \end{bmatrix} = C,$$

if we choose $\hat{A}$ and $\hat{B}$ appropriately such that $\mathrm{rank}(C) = p$, then there exists a matrix K such that the eigenvalues of the matrix Λ can be assigned arbitrarily.

4   Illustrative Example

Consider the nonlinear time-invariant MB-NCS (1) with unstable plant

$$A = \begin{bmatrix} 0.9 & 0.3 \\ -0.5 & 0.8 \end{bmatrix}, \quad B = \begin{bmatrix} 0.8 \\ 0.1 \end{bmatrix}$$

and nonlinear function bound $l = 1$. Usually it is assumed that the actuator/controller will hold the last value received from the sensor until the next time the sensor transmits. The model (1b) is chosen as

$$\hat{A} = \begin{bmatrix} -1.4493 & -0.1867 \\ 1.9492 & -1.6888 \end{bmatrix}, \quad \hat{B} = \begin{bmatrix} 0.5351 \\ 0.7726 \end{bmatrix}.$$
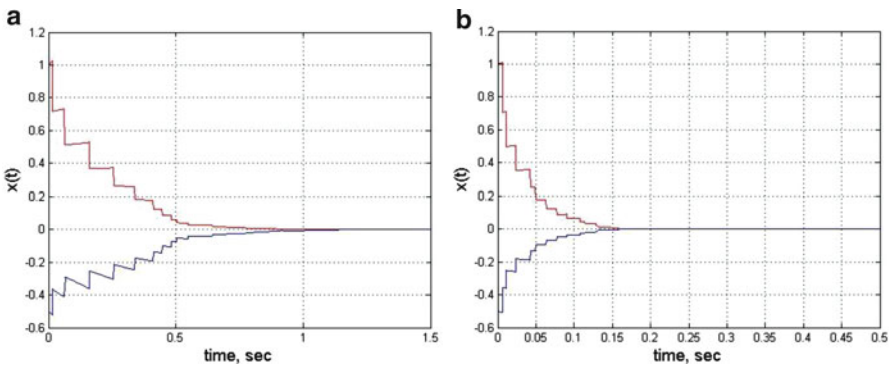
Fig. 1   State responses of the nonlinear MB-NCS (1) with $\chi_k = 0.7$ and (**a**) $\varpi_k = 0.8$, (**b**) $\varpi_k = 0.4$ for all $k \in N$

Throughout this section, we will use the state feedback controller (1c) with $K = [-1.7 \quad 0.2]$. With $P = \mathrm{diag}[0.86 \quad 0.77 \quad 0.91 \quad 0.84]$, we have $\lambda_1 = 0.77$, $\lambda_2 = 0.91$, and $\lambda_3 = 2.8416$. For the case that $\chi_k = 0.7$ for all $k \in \mathbb{N}$, the state responses of the nonlinear MB-NCS (1) are plotted in Fig. 1 with the nonlinear function $f(t, x(t)) = [x_1(t)sin(x_1(t)) \quad x_2(t)sin(x_1(t))]^{\mathrm{T}}$, the initial condition $[x(t) \quad \hat{x}(t)] = [1 \quad -0.5 \quad 0 \quad 0]$, and the random update intervals $h_{\max} = 0.1015$ for $\varpi_k = 0.8$ and $h_{\max} = 0.0201$ for $\varpi_k = 0.4$.

5 Conclusion

In this chapter, the problem of reducing the data transfer rate as much as possible with a nonlinear NCS using the model-based approach has been investigated. The robust stabilizability of the nonlinear time-variant MB-NCS with time-variant transmission attenuation using the comparison principle has been explored. The close relationship among the signal attenuation ratio, the update factor, and the upper bound of admissible update intervals has been established. An example with simulation results is illustrated to demonstrate the effectiveness and flexibility of the proposed techniques.

References

1. Walsh GC, Ye H, Bushnell LG (2002) Stability analysis of networked control systems. IEEE Trans Control Syst Technol 10:438–446
2. Kim WJ, Ji K, Ambike A (2006) Real-time operating environment for networked control systems. IEEE Trans Autom Sci Eng 3:287–296
3. Zhang W, Branicky MS, Phillips SM (2001) Stability of networked control systems. IEEE Control Syst Mag 21:84–99
4. Brockett R, Liberzon D (2000) Quantized feedback stabilization of linear systems. IEEE Trans Autom Control 45:1279–1289
5. Elia N, Mitter SK (2001) Stabilization of linear systems with limited information. IEEE Trans Autom Control 46:1384–1400
6. Antsaklis P, Baillieul J (2004) Guest editorial: special issue on networked control systems. IEEE Trans Autom Control 49:1241–1243
7. Bondi AB, Simon CS, Anderson KW (2005) Bandwidth usage and network latency in a conveyor system with ethernet-based communication between controllers. In: IEEE Pacific Rim conference on communications, computers and signal processing, pp 9–12
8. Sozer E, Stojanovic M, Proakis J (2000) Underwater acoustic networks. IEEE J Ocean Eng 25:72–83
9. Montestruque LA, Antsaklis P (2004) Stability of model-based networked control systems with time-varying transmission times. IEEE Trans Autom Control 49:1562–1572
10. Khalil HK (2002) Nonlinear systems, 3rd edn. Prentice Hall, Upper Saddle River
11. Yang T (1999) Impulsive control. IEEE Trans Autom Control 44:1081–1083
12. Bainov D, Simeonov PS (1989) Systems with impulse effect: stability, theory and applications. Halsted, New York

Control Strategies Development for a Series Hydraulic Hybrid Vehicle Based on Engine Experimental Map

Chih-Keng Chen, Tri-Vien Vu, Chih-Wei Hung, and Chuan-Sian Wang

Abstract As a branch of the hydraulic hybrid vehicle (HHV) technology, series hydraulic hybrid vehicle (SHHV) has been an important research object of institutions and automotive manufacturers all over the world. Based on the engine experimental map, several control strategies are developed and applied on the system with an expectation that the engine will be controlled to operate in its optimal operation regions where fuel consumption and emissions of the engine are minimized. Simulation results of the system over the Japan 10–15 driving cycle indicate that the engine can be controlled to follow its optimal BSFC line most of the working times. Those results also represent a significant fuel economy improvement in comparison to the vehicle with standard conventional and hydrostatic transmission systems. With different control strategies, the improvement can be up to 80 % compared with a traditional hydrostatic control strategy and up to 60 % compared with a high-quality standard.

Keywords Control strategy • Series hydraulic hybrid • Engine map

1 Introduction

The development of the automobile industry has made great contributions to the growth of modern society by providing the mobility for everyday life. Along with the increase in the number of vehicle holders, the automobile industry has become a

---

C.-K. Chen (✉) • T.-V. Vu • C.-W. Hung
Department of Mechanical and Automation Engineering, Dayeh University,
Changhua 51591, Taiwan
e-mail: ckchen@mail.dyu.edu.tw

C.-S. Wang
Environment & Energy Research Section, Automotive Research and Testing Center,
Changhua 51591, Taiwan

big customer that consumes a large part of fossil fuel which is about to be depleted in the near future [1]. Vehicle emissions were one of the main air pollution sources since in 2009 about 27 % of US greenhouse gas emissions were generated from the transportation sector [2]. Nowadays, the automobile industry is faced with the requirement of fuel economy improvement and the legislation of emission pollution as well.

In all types of hybrid vehicles, the main function of supervisory controller is to coordinate multiple power sources to satisfy the power demand of the driveline with minimum fuel consumption in the most convenient way. In general, control strategies of the hybrid propulsion systems can be classified into three categories: rule-based, semi-optimal, and global optimal. Among these, the rule-based control strategy is a real-time implementable power management. The rule-based strategy uses several rules to determine the control output according to preset conditions. Most papers regarding the rule-based control strategy for hydraulic hybrid vehicle (HHV) have used the state of charge of accumulator as the sole state variable for the determination of engine power [3–6].

In this work, a physical-based, forward simulation model of a class II light-duty series hydraulic hybrid vehicle (SHHV) with a mass of 3.5 t has been established based on the components derived from the MATLAB/Simulink Simscape library. In accordance with the engine experimental map, different rule-based control strategies were applied to the system to analyze their effects on the fuel economy. The control strategies were named as hydrostatic, thermostatic SOC, and modulated SOC, respectively. The average required fuel economy of 11.42 km/L was selected as the baseline value for calculating the improvement of the proposed system with different control strategies under the Japan 1015 drive cycle. This value was extracted from MY 2012–2016 standards [7].

2 System Configuration and Modeling

This chapter proposes a configuration of SHHV for a rear-wheel-drive 3.5 t light-duty class II truck. The schematic and control signal path of the system is shown in Fig. 1, and the corresponding Simulink model is shown in Fig. 2. The component models were used directly from the built-in library of Simulink/Simscape environment. The details of vehicle specification, component selection, and parameter setting for the proposed model can be found in [8]. In this configuration, diesel engine E was connected to hydraulic pump P1. P/M unit P2 was connected to the rear wheels through differential DF. Low-pressure accumulator A2 was used to provide the needed fluid for the hydraulic system. High-pressure accumulator A1 functions as a secondary power source of SHHV system. The stored energy in A1 can be the recovered energy from vehicle deceleration or the charged energy by the diesel engine E. The directional valves V1, V2, and V3 were used to control the flow direction within the hydraulic system.
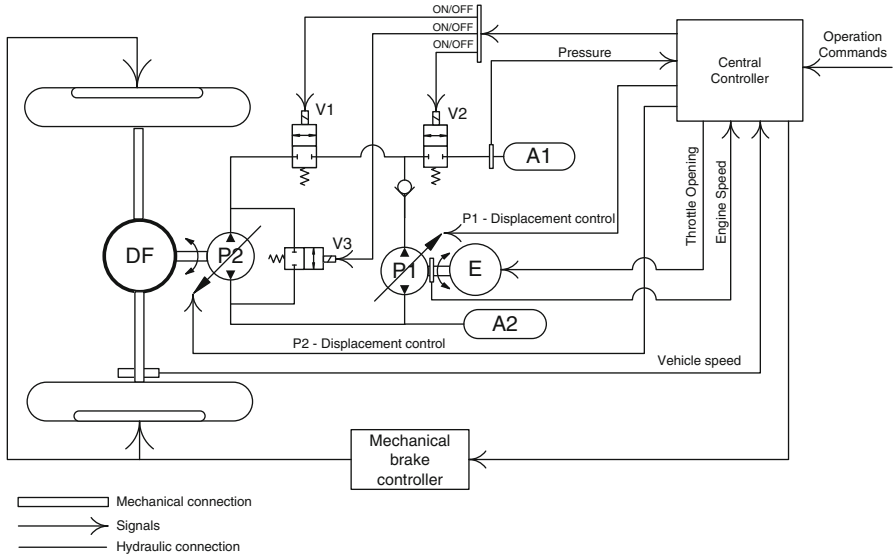
Fig. 1 Schematic and control signal paths of SHHV
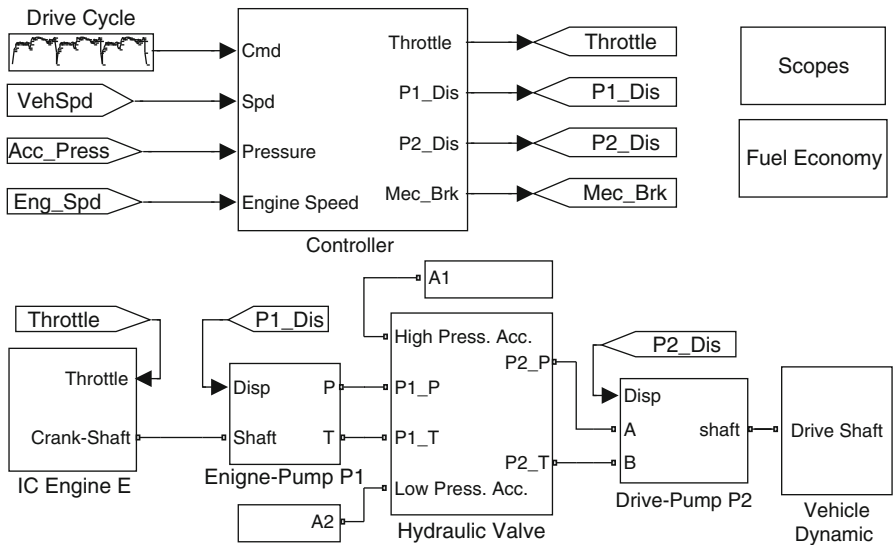
Fig. 2 Simulink model of SHHV

In this system, the inputs of the center controller were the pedal position signal, the current measured data-vehicle angular speed, engine angular speed, and accumulator pressure. The outputs of this controller were the signals to activate or

deactivate the subcontrollers: hydraulic valve, drive, and frictional brake controller. In accordance with the inputs, the central controller output commands depended on the applied control strategy, which will be discussed in the next section.

3 Control Strategy and Fuel Economy

As mentioned earlier, the main function of the power management system is to apply a proper control strategy not only for ensuring safe operation regardless of the driver demand and vehicle states but also with minimum fuel consumption. In order to develop the control strategy for the proposed system, an experimental map of the engine is necessary. The experiment was conducted by ARTC Taiwan, and the brake-specific fuel consumption map of the engine is shown in Fig. 3. There are three controllers that were used in the proposed system. The first controller determines the engine power demand based on the SOC in the accumulator. The second controller controls the operation of the engine to meet the desired power with minimum specific fuel consumption. The third controller controls the displacement of the pump/motor P2, ensuring that the vehicle follows the desired speed profile.

Regardless of the capability of energy regeneration of the accumulator, the series hybrid hydraulic propulsion system can be considered as a pure hydrostatic transmission system. Hence, in the first control strategy, namely, hydrostatic, the braking energy will not be captured and the accumulator A1 will just function as in a traditional power fluid system. Because the accumulator capacitor in a hydraulic
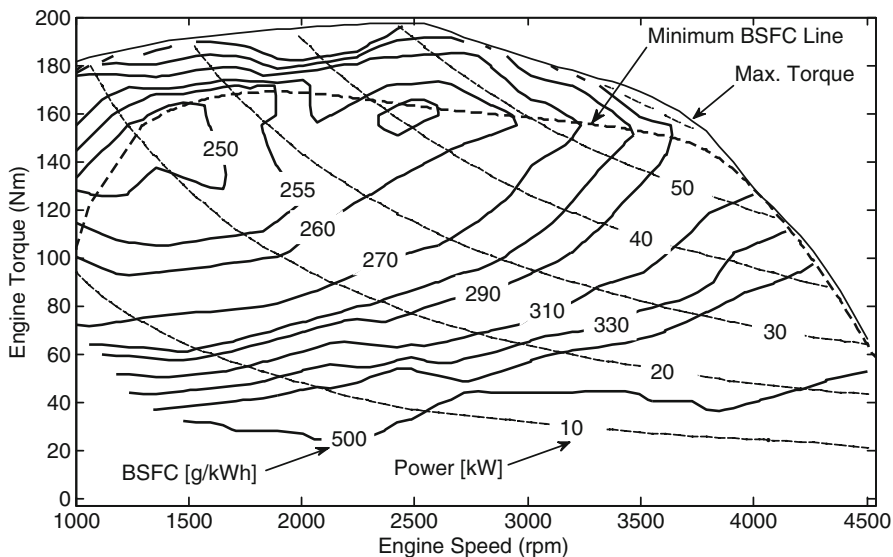
Fig. 3 The brake-specific fuel consumption map of an engine with the minimum BSFC trajectory

hybrid system is normally larger than the one in a traditional hydrostatic system, SHHV can achieve a better performance even in hydrostatic mode. This is due to the fact that the accumulator can be used as an energy buffer that helps the engine work at the efficient region most of the time. If the power demand is low, the surplus engine power will be absorbed by the accumulator. For the case of high-power demand or hard acceleration, the accumulator will discharge to act as the secondary power source to support the exceeded power demand.

One of the advantages of the hydraulic accumulator compared with the electric battery is that it can charge and discharge with a very high frequency. Besides, the accumulator can be charged to the full state or discharged to the zero state. The full state is when the pressure of the accumulator reaches its highest working value, and the zero state is when there is no available fluid stored in the accumulator. In the thermostatic control strategy, the first controller either uses the SOC of accumulator A1 or the driver's command for determining the engine's ON/OFF state. If the controller only uses the SOC as the state variable, it is called *pure-thermostatic* mode. In this case, whenever the accumulator is depleted, it will be charged by the engine until it reaches the full state. In the *acceleration-thermostatic* mode, the accumulator will be charged whenever it is depleted and the acceleration of the vehicle is greater than zero. In the last case, the charging of the accumulator can be happen if the condition of SOC is met and the acceleration of the vehicle is greater or equal to zero. This is called the *with-idle-thermostatic* mode.

The benefit of the pure-thermostatic mode is that the pressure in the accumulator is at a high value most of the time, which supports the system to meet the driver's request under any condition. However, higher pressure also means smaller available space reserved for regenerative braking. Hence, the efficiency of the system may be reduced. On the other hand, in the acceleration-thermostatic mode where the energy buffer capable of accumulator may not be used, the engine operating points will be shifted apart from its optimal region due to the high-power demand from the driver. Inherently, the with-idle-thermostatic mode is the best candidate since the engine can charge the accumulator when the vehicle is standstill to ensure that the accumulator can function as a secondary power source for a hard acceleration and also have efficient space for braking energy recovery later.

The optimal-thermostatic control strategy originated from the idea that maintaining the SOC within a specific range will improve fuel economy by avoiding unnecessary energy conversion from charging accumulator using engine. With a proper selection, keeping SOC at the predesigned low level before braking can also help store the regenerative braking energy effectively. As in the thermostatic control scheme, three modes of optimal-thermostatic control scheme are investigated. An example of the optimal-thermostatic control strategy on the with-idle mode under the Japan 1015 drive cycle is shown in Fig. 4. In this case, the pressure of the accumulator is maintained within 150 and 200 bar. When the high-power demand occurs, the pre-charge energy in accumulator will be used to provide the exceeded power; hence, the engine will not necessary be shifted to the higher power region. Also, the pressure of the accumulator is kept at a low value before the hard braking is applied.
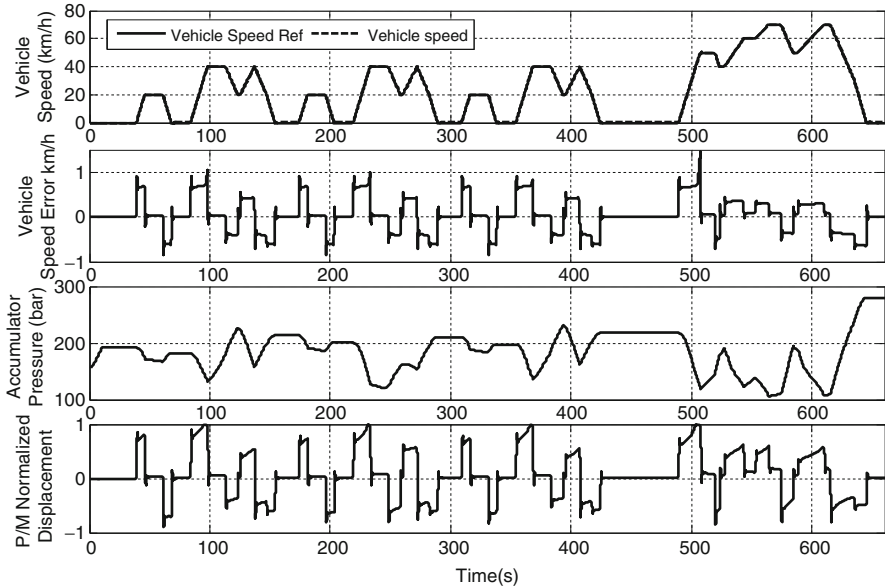
Fig. 4 System behavior of the optimal-thermostatic control strategy

Table 1 Summary of SHHV predicted performance and fuel economy improvement

No.	Name	Fuel economy (km/L)	Fuel economy improvement (%)	
			Criterion 1	Criterion 2
1	Hydrostatic	10.15	–	–
2	Thermostatic			
2.1	Acceleration	12.01	18.33	5.17
2.2	Pure	12.71	25.22	11.30
2.3	With-idle	13.28	30.84	16.29
3	Optimal-thermostatic			
3.1	Acceleration	16.36	61.18	43.26
3.2	Pure	17.79	75.27	55.78
3.3	With-idle	18.13	78.64	58.76

A summary of the effects of different control strategies over the performance and the fuel economy improvement of the proposed SHHV system is given in Table 1. The fuel economy improvement of the system is estimated with two different criteria. In the first criterion, the fuel economy of the system working on hydrostatic is selected as the baseline to estimate the fuel economy improvement of the system with the thermostatic and optimal-thermostatic control strategies. In the second criterion, the fuel economy of 11.42 km/L is selected for estimating the process.

4 Conclusion

In this work a physics-based forward-facing simulation model of SHHV has been established. Important design and control parameters have been discussed and tailored for a certain application of SHHV. The improvement of fuel economy of the proposed system has been investigated under the Japan 1015 drive cycle with different control strategies. Simulation results show that the fuel economy improvement of the proposed system can be up to 80 % compared with a traditional hydrostatic control strategy and up to 60 % compared with the MY 2012–2016 standards. In the future, global optimized power management such as the dynamic programming technique will be applied to provide a benchmark power management that can be learned or at least be compared with the rule-based control strategies.

References

1. Léon A, Tanoue K, Yanagihara H, Kusumi H (2008) Hydrogen technology mobile and portable applications. Springer, Berlin
2. U.S. EPA (2001) Clean automotive technology: progress report on clean and efficient automotive technologies under development at EPA. Interim technical report
3. Wu B, Lin C-C, Filipi Z, Peng H, Assanis D (2004) Optimal power management for a hydraulic hybrid delivery truck. Vehicle Syst Dyn 42:23–40
4. Filipi Z, Loucas L, Daran B, Lin C-C, Yildir U, Wu B, Kokkolaras M, Assanis D, Peng H, Papalambros P, Stein J, Szkubiel D, Chapp R (2004) Combined optimization of design and power management of the hydraulic hybrid propulsion system for the 6x6 medium truck. Int J Heavy Veh Syst 11:371–401
5. Kim Y, Filipi Z (2007) Series hydraulic hybrid propulsion for a light truck – optimizing the thermostatic power management. SAE technical paper 2007-24-0080
6. Tavares F, Johri R, Salvi A, Baseley S et al (2011) Hydraulic hybrid powertrain-in-the-loop integration for analyzing real-world fuel economy and emissions improvements. SAE technical paper 2011-01-2275
7. U.S Department of Transportation and Environmental Protection Agency. Joint rulemaking to establish CAFE and GHG emission standards, MY 2012-2016 – the final rule. http://www.nhtsa.gov/staticfiles/rulemaking/pdf/cafe/CAFE-GHG_MY_2012-2016_Final_Rule_FR.pdf
8. Vu TV (2011) Simulation and design of hydraulic hybrid vehicle. M.S thesis, Da-yeh University, Taiwan

Japanese Calligraphy Using Whole Body Motion of a Humanoid Robot

Seiji Sugiyama, Ikuma Oshita, and Tsuneo Yoshikawa

Abstract In this research, a system for writing Japanese calligraphy using the whole body motion of a humanoid robot has been developed. It consists of an instruction system using a virtual haptic interface and a humanoid robot with a brush on its right hand. The trajectory of human handwriting is given by the instruction system. The humanoid robot can write characters larger than its own size with a walking motion. The experimental results using a humanoid robot Hoap-2 are presented.

Keywords Humanoid robot Hoap-2 • Mobile manipulation • Haptic

1 Introduction

Recently, there is a lot of research about walking technology for humanoid robots. Although low-cost small bipedal locomotion platforms are sold on the market from several companies, most of them only have a simple arm-hand mechanism. In order to make humanoid robots more useful, they require not only an improvement of their walking technology but also the ability to work using arms and hands.

Yoshida et. al. proposed the Mobile Manipulation for humanoid robots and analyzed the demanded leg function [1]. In this work, only simulations were given. No application to a hardware system has been performed.

There is already a lot of research about Japanese or Chinese calligraphy using industrial robot arms [2–4]. Even though they can write beautiful characters by controlling the position and the power, they cannot walk.

S. Sugiyama (✉) • I. Oshita • T. Yoshikawa (✉)
Department of Human and Computer Intelligence, College of Information Science
and Engineering, Ritsumeikan University, Shiga 525-8577, Japan
e-mail: seijisan@is.ritsumei.ac.jp; yoshikaw@is.ritsumei.ac.jp

An example of Japanese calligraphy by a humanoid robot (2011) is found [5]. In this work, only limited characters can be written. Big characters beyond the movable range of the arm cannot be written, because it does not walk.

In this chapter, a system for writing Japanese calligraphy using the whole body motion of a humanoid robot is proposed. The control method for writing a big character beyond the movable range of the arm on bigger paper than the robot's size is given. It consists of an instruction system using a virtual haptic interface and a humanoid robot with a brush on its right hand. The trajectory of human handwriting is given by the instruction system. Our humanoid robot can write the calligraphy by referring to the instruction system.

There are two types of geometric translation styles. One is that the size of the character that the human wrote is converted into the movable range of the robot arm. Using this style, our humanoid robot can write several basic skills of Japanese calligraphy: dot, horizontal, vertical, hook, break, throw away and press down [6]. The other is that its size is converted to more than the movable range of the robot arm. Using this style, our humanoid robot can write characters larger than its own size with a walking motion. The results of these experiments using a humanoid robot Hoap-2 are presented in this chapter.

2 System Configuration

Figure 1 shows an instruction system for entering a character's shape using a pen style haptic device, PHANToM OMNI. A virtual paper space is constructed vertically between the user and the pen. The character is displayed by drawing white circles in proportion to the pressures to the space. The flush rate is 100 Hz. The trajectory and pressure data of human handwriting is given by this system.

Figure 2 shows a humanoid robot Hoap-2 (Fujitsu Automation Inc.) with a brush. The height is 500 mm and the weight is 7 kg. The degree of freedom is 25 (neck:2, right arm:4, left arm:4, right hand:1, left hand:1, waist:1, right foot:6, and left foot:6). It has four kinds of sensors: joint angular sensor, 3-axis acceleration sensor, 3-axis angular velocity sensor, and sole pressure sensor.

Hoap-2 cannot grasp a brush strongly because the hand power is weak. To cope with the difficulty, an attachment as shown in Fig. 3 is equipped on the right hand.

Fig. 1 Instruction system

Fig. 2 Hoap-2

Fig. 3 Attachment

Two duracon plates can fix the hand and an aluminum cylinder can fix a brush. The diameter of this brush is 18 mm and the height is 284 mm.

3 Trajectory Planning in the Movable Range

To maintain a brush vertically on a paper is necessary not only when writing Japanese calligraphy but also when raising and lowering a brush. The raising and lowering brush motions are realized by only performing knee bends, because the degree of freedom for the Hoap-2's right arm is not enough. The trajectory of right arm end in horizontal plane equals the writing trajectory on a paper.

Figure 4 shows the movable range of right arm in top view. It is calculated by using forward kinematics for two link mechanisms. In this figure, the coordinate system XY on the right shoulder is considered. The right arm end position (x, y) is represented by

$$x = -l_2 \sin \theta_1 \sin \theta_3 - (l_1 + l_2 \cos \theta_3) \cos \theta_1, \tag{1}$$

$$y = -(l_1 + l_2 \cos \theta_3) \sin \theta_1 + l_2 \cos \theta_1 \sin \theta_3, \tag{2}$$

where l_1 and l_2 denote the lengths of the first and second links from the right shoulder, respectively, and θ_1 and θ_3 denote the angles of pitch and yow, respectively. The reversed kinematics is represented by

Fig. 4 Movable range
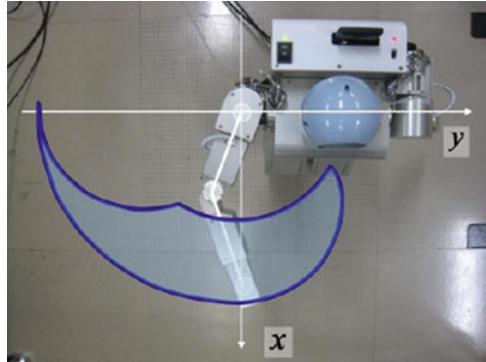
Fig. 5 Experiments for writing several basic skills of Japanese calligraphy in the movable range
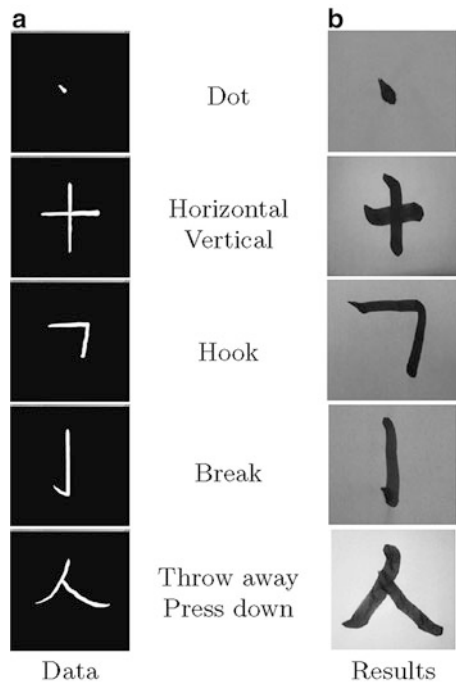
$$\theta_1 = \tan\left(-\frac{y}{x}\right) \mp \cos^{-1}\left(\frac{l_1 + l_2 \cos\theta_3}{\sqrt{x^2 + y^2}}\right), \tag{3}$$

$$\theta_3 = \pm\cos^{-1}\left(\frac{x^2 + y^2 - (l_1^2 + l_2^2)}{2l_1 l_2}\right). \tag{4}$$

If a character size on a paper is within this area, a walking motion is not necessary. On the other hand, if it exceeds, a walking motion is necessary.

In the movable range, when the instruction data as shown in Fig. 5a is entered, our humanoid robot can write several basic skills of Japanese calligraphy as shown
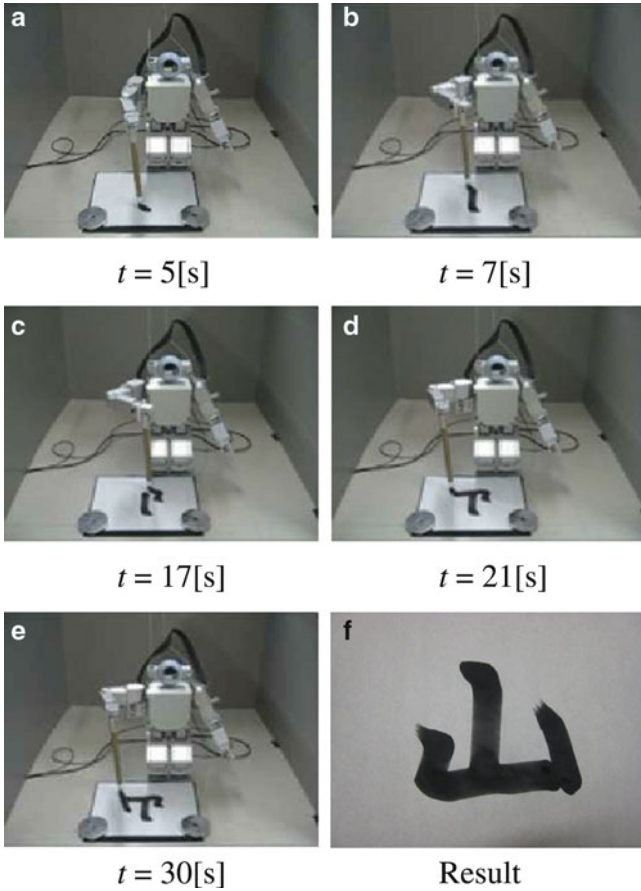
Fig. 6 Captured images of the video for writing a Japanese calligraphy in the movable range

in Fig. 5b. Figure 6a–e show the captured images of the sample video. Figure 6f shows the writing result. No walking motion is performed in these experiments. Only performing knee bends motion is utilized.

4 Center of Gravity Shifting

The center of gravity always changes while walking as shown in Fig. 7. In the right side figures, d denotes the shifting distance. The right arm end position can be fixed by calculating Eqs. 3 and 4 after changing (x, y) into $(x, y - d)$. To maintain the
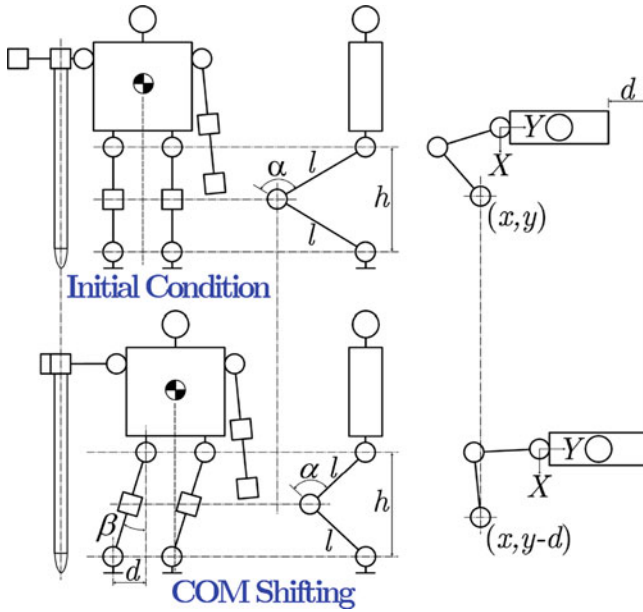
Fig. 7 Center of gravity shifting

height of humanoid robot while walking, $d = h \tan\beta$ can be given by the geometric relations, where h denotes the height between the ankle joint and the hip joint when the brush is contacting with the paper, and β denotes the tilt angle of hip joint. The joint angle α is represented by

$$\alpha = \frac{1}{2} \cos^{-1}\left(\frac{h}{2l\cos\beta}\right),\tag{5}$$

where l denotes the length between the hip joint and the knee joint. Using Eq. 5, the brush height and its position on a paper can be controlled.

Figure 8a–d show the captured images of the sample video. It has been verified that the brush end on the paper can always be fixed at the same position while shifting the center of gravity. In addition, the reciprocating motions were thrice successful in this experiment.

5 Trajectory Planning Using Walking Motion

The size of the virtual paper space on the instruction system is transferred to that of the paper on the ground. The human handwriting trajectory can also be transferred to the real paper size called 'PHANToM DATA' as shown in Fig. 9 using a dotted
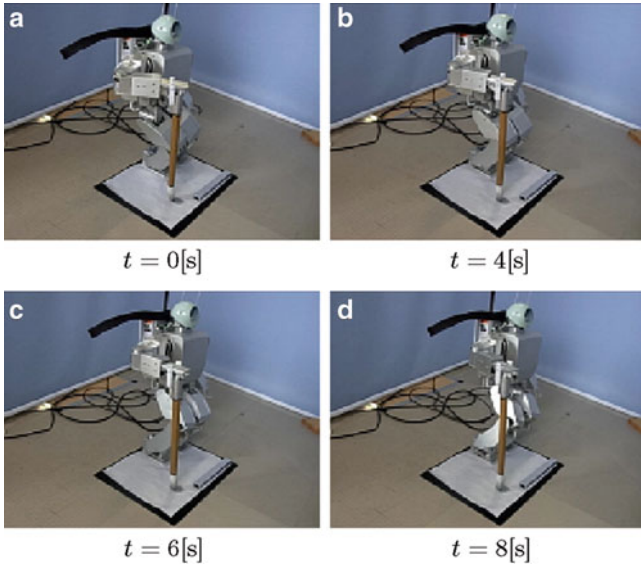
Fig. 8 Captured images of the video for shifting the center of gravity
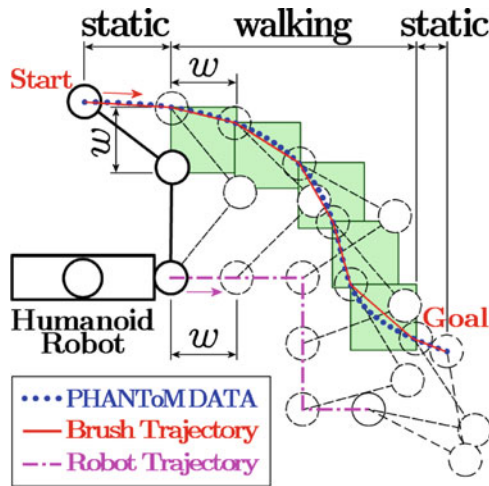
Fig. 9 Writing method while walking

line. This data is thinned out and becomes simple and is shown by a broken line called 'Brush Trajectory' in this figure.

One segment of the broken line is automatically generated in the range which does not exceed a square of side w that equals the maximum length of
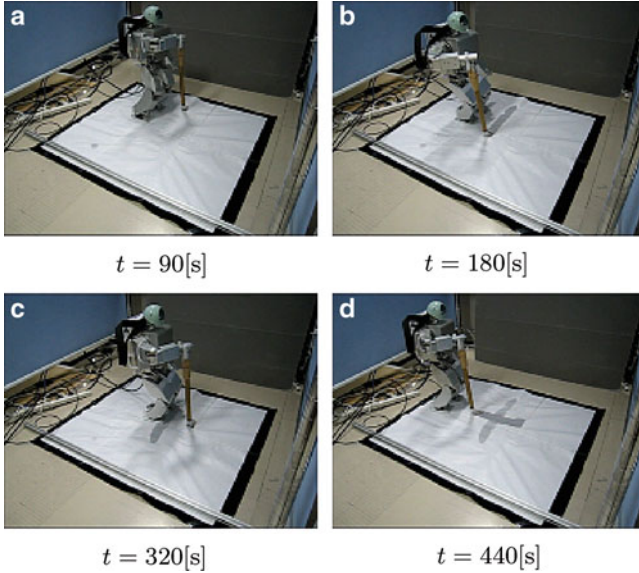
Fig. 10 Captured images of the video for writing horizontal and vertical segments while walking

a step of a humanoid robot. When this segment goes to the vertical side of the square, the robot walks a step horizontally. On the other hand, when it goes to the horizontal side, the robot walks a step vertically. This 'Robot Trajectory' is shown by using a dash-dot line. The diagonal factor is corrected by using the arm's motion.

This planning is very simple to control. In addition, the start and the finish areas can be written by just the arm's motion (without walking). In this figure, the robot only walks two horizontal steps, two vertical steps and one horizontal step.

Figure 10a–d show the captured images of the video for writing horizontal and vertical segments while walking: (a) The humanoid robot only walked toward the start point (left side on the paper). (b) It could write the horizontal segment while walking toward the right. (c) It only walked toward the next start point. (d) It could write the vertical segment while walking toward the bottom. It took 440 s in this experiment. The paper size is 210 ×272. 6 mm.

Figure 11a, b show the entering data of a curve. (a) denotes the human handwriting trajectory and the generated robot trajectory. (b) denotes the human handwriting pressure data for controlling the height of the brush.
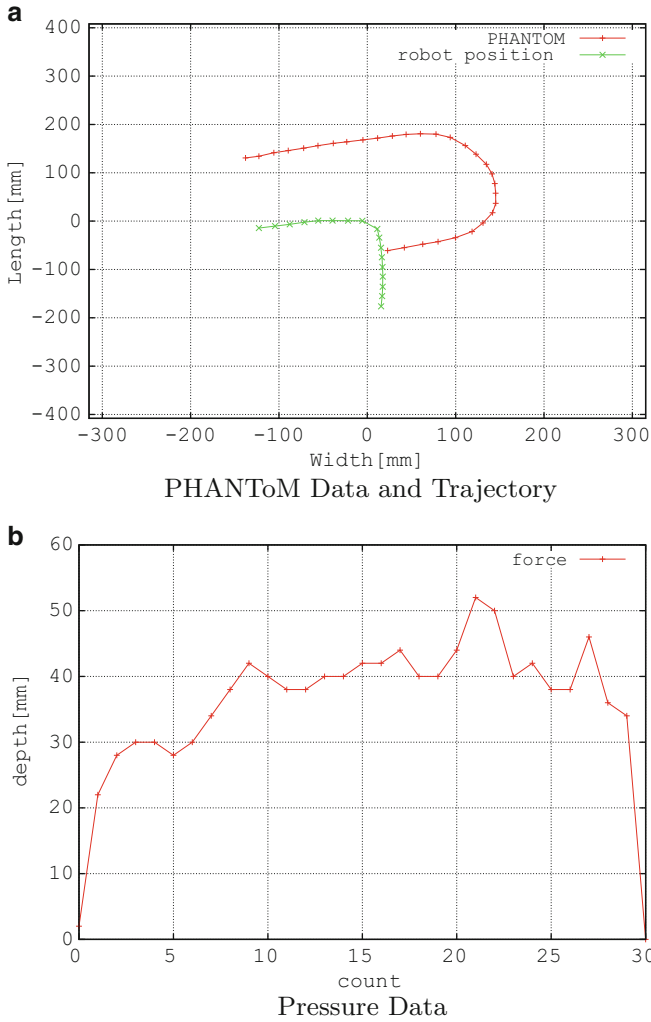
Fig. 11 Entering data of a curve

Figure 12a–e show the captured images of the video for writing a curve while walking using the entering data. This curve is Japanese Hiragana character 'TSU': (a) The humanoid robot only walked toward the start point. (b–d) It could write the curve while walking using arm's motion. (e) It could write the end area without walking. Figure 12f denotes the writing result.
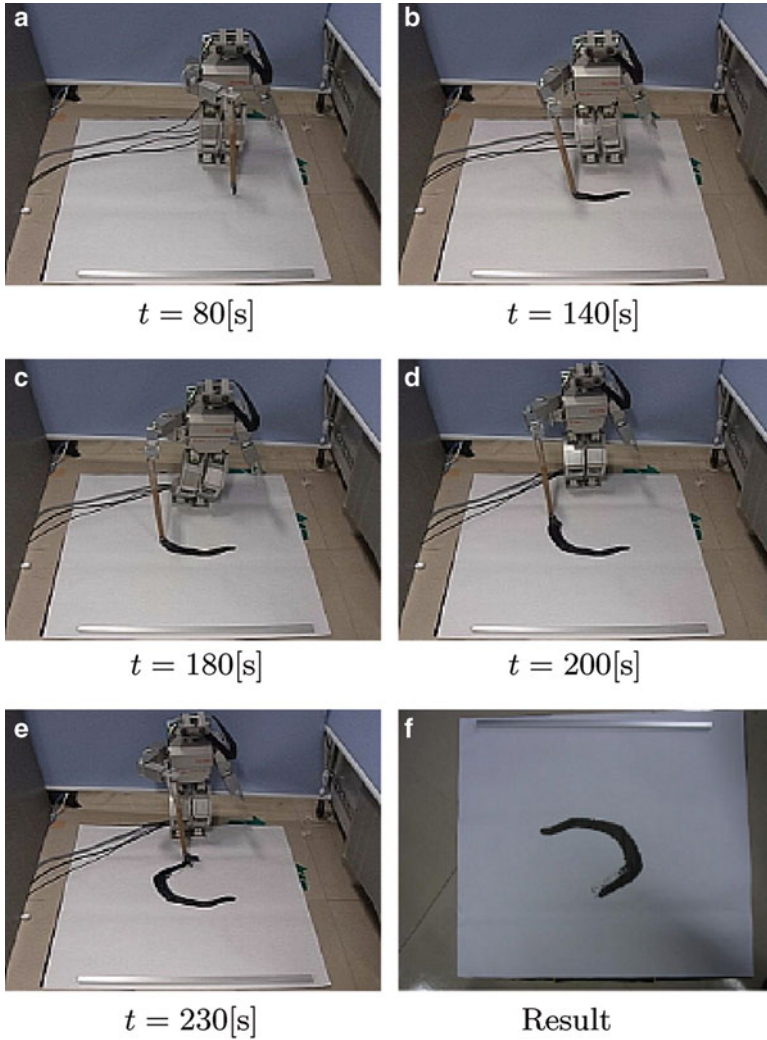
Fig. 12 Captured images of the video for writing a curve while walking

6   Conclusion

In this chapter, a system for writing Japanese calligraphy using the whole body motion of a humanoid robot has been developed. It has been verified that the robot could write Japanese calligraphy while walking in basic experiments. The walking speed is very slow because the calligraphy paper and mat are very soft. Our future research will be conducted to improve the performance of this system.

References

1. Haruyuki Yoshida, Kenji Inoue, Tatsuo Arai, Yasushi Mae (2002) Mobile manipulation of humanoid robots: optimal posture for generating large force based on statics. In: Proceedings of international conference robotics and automation, pp 2271–2276
2. Fenghui Yao, Guifeng Shao, Jianqiang Yi (2004) Extracting the trajectory of writing brush in Chinese character calligraphy. In: Engineering application of artificial intelligence, vol 17, pp 631–644
3. Nico Huebel, Elias Mueggler, Markus Waibel, Raffaello D'Andrea (2012) Towards robotic calligraphy. In: Proceedings of international conference on intelligent robots and systems, WedFVT9.5
4. Seiichiro Katsura (2012) Motion copy system (in Japanese). http://www.keio.ac.jp/ja/press_release/2012/kr7a4300000b0lus-att/120927_1.pdf. The sample video (in Japanese): http://www.youtube.com/watch?v=ZeHEsb7XdWM
5. Teaching the NAO robot Japanese calligraphy. http://www.robots-dreams.com/2011/07/teaching-the-nao-robot-japanese-calligraphy.html
6. Suzuki S (1983) Shodo Nyumon (Kaisyo hen) (in Japanese), Kin-en-sya

Design and Experiment of the Auto-alignment Control System for TPS Storage Ring Girder

Meng-Hsiu Wu, Wei-Yang Lai, Tse-Chuan Tseng, Mei-Ling Chen, Huai-San Wang, His-Chou Ho, Chia-Jui Lin, Hung-Ming Luo, Shen-Yaw Perng, Pei-Lun Sung, Chang-Sheng Lin, Hsueh-Cheng Lin, and June-Rong Chen

Abstract The auto-alignment system is designed for aligning the magnet girder system with little manpower and time as well as improving the accuracy of girder system in the whole storage ring simultaneously. The system consists of absolute length gauges between two consecutive girders, laser position-sensitive devices (PSD) between two straight-section girders, and a precision inclination sensor on each girder. The more precise angle and length between two girders obtained from these sensors module, the more precise position that can then be located. A magnet girder system with six cam movers on three pedestals is designed to provide precise adjustments of six axes and align girders automatically driven by six electric motors. This chapter consists of the construction of system, auto-alignment process, and experimental results. In the auto-alignment process, a laser tracker is employed to acquire the data as the feedback one in auto-alignment process to locate the position of girders and to simulate the status of the whole TPS storage ring. Further verification of the proposed technique of auto-alignment based on the results of several experiments in this chapter is merited.

Keywords TPS • Auto-alignment • PSD

M.-H. Wu (✉) • W.-Y. Lai • T.-C. Tseng • M.-L. Chen • H.-S. Wang • H.-C. Ho
• C.-J. Lin • H.-M. Luo • S.-Y. Perng • P.-L. Sung • C.-S. Lin • H.-C. Lin
National Synchrotron Radiation Research Center, No. 101, Hsin-Ann Road,
Hsinchu 30076, Taiwan
e-mail: wu.thomas@nsrrc.org.tw

J.-R. Chen
National Synchrotron Radiation Research Center, No. 101, Hsin-Ann Road,
Hsinchu 30076, Taiwan

Department of Biomedical Engineering and Environmental Sciences, National Tsing-Hua
University, Hsinchu, Taiwan

1 Introduction

Taiwan Photon Source (TPS) is a new 3-GeV ring under construction at the NSRRC site in Taiwan with circumference of 518.4 m and 24 double-bend cells. Based on the consideration of stability, the entire building is being constructed half underground at depth of 12 m [1, 2]. The measured area is wide, and survey network is hard to be connected in the ring. Besides, the structure and environment of storage ring in TPS is unstable in the initial constructing stage. Therefore, the auto-alignment control system is proposed to improve the precision of survey in TPS construction.

TPS auto-alignment control system is designed for aligning the magnet girder system with little manpower and time and improving the accuracy of girder system in the whole storage ring simultaneously. This chapter consists of the construction of system, auto-alignment process, and experimental results. Hardware construction includes pedestals, girders, cam movers, precision inclination sensors, laser PSD, a laser tracker, and absolute length gauges. The process of auto-alignment is described as follows: Coordinates and angular deviation of adjacent and straight-section girders could be measured by absolute length gauges and laser PSD after assembling, calibration, and location of the mechanism and optical components. Pitch and roll angles of girders are measured by precision inclination sensors. In the following, updated positions of girders are calculated in auto-alignment process with above measured data. Finally, girders are aligned to updated positions by cam movers accordingly. In the experiment of this chapter, there are only six girders equipped; therefore, a laser tracker is employed to acquire the data as the feedback one in auto-alignment process to form a closed loop.

2 Construction of System

The hardware construction of TPS auto-alignment system in our experiment is shown in Fig. 1. There are two double-bend cells SR1 (storage ring 1) and SR2 (storage ring 2) in the experimental construction. Each girder is located on six cam movers. Angular deviation between two double-bend cells is measured with a laser PSD system. Relation of positions between adjacent girders can be obtained from absolute length gauges. The laser tracker is employed to acquire the data as the feedback one in auto-alignment process. The data could be used to locate positions of girders and to form a closed-loop feedback.

The control system of Leica laser tracker is shown in Fig. 2. It is controlled by a system controller to measure. A laser tracker connected to the system controller by one cable. The application PC communicated with the system controller by a network switcher. A control GUI (graphical user interface) is installed on the application PC. The control GUI is shown in Fig. 3, which could acquire data and environmental parameters by sending various commands from the system controller of the laser tracker.
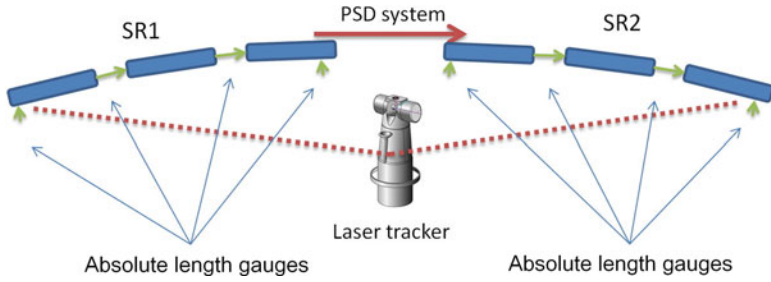
Fig. 1 The illustration of auto-alignment system in TPS
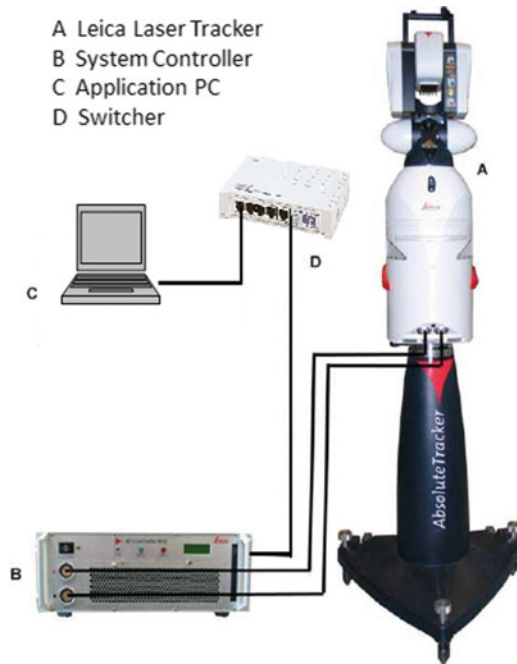
Fig. 2 The control system of Leica laser tracker

3 Auto-alignment Process

The structure of auto-alignment process is shown in Fig. 4. The symbols $G_{(n-1)L}(X, Y, Z)_i$, $G_{(n-1)R}(X, Y, Z)_i$, $G_{(n)L}(X, Y, Z)_i$, and $G_{(n)R}(X, Y, Z)_i$ mean fiducial points of girders; $S_{(n-1)}(X, Y, Z)$, $S_{(n)}(X, Y, Z)$, and $S_{(n-1)n}(X, Y, Z)$ mean deviations of pin hole in X, Y, and Z directions, respectively. In the preceding symbols, n is number of a girder. R/L means right/left side of a girder. The symbol i means the number of iteration sequence.
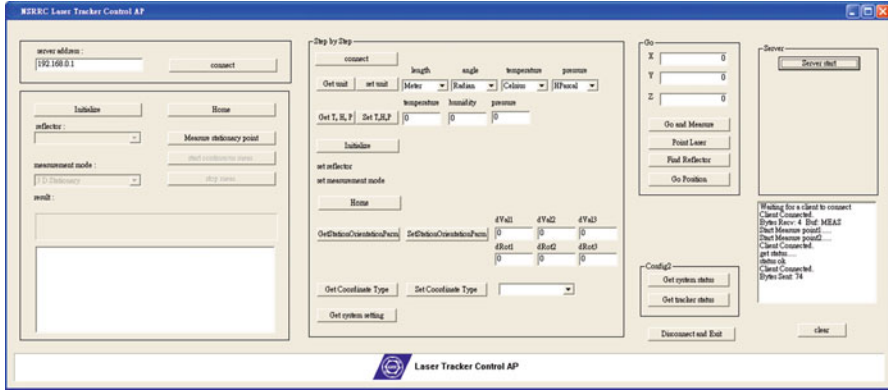
Fig. 3 GUI (graphical user interface) on an application PC
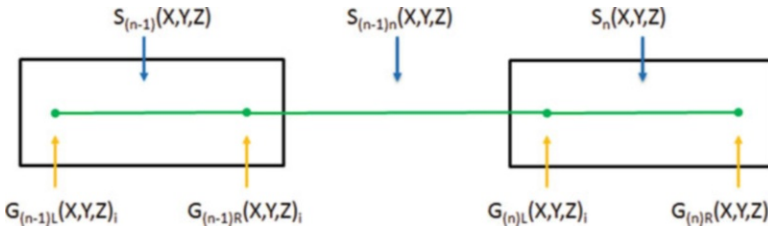
Fig. 4 The structure of auto-alignment process

The result of updating fiducial points is satisfactory with the selection of the number of W as 0.5 in the process. Fiducial points are updated as following equation (1):

$$
\begin{aligned}
G_{(n)\mathrm{L}}(X,Y,Z)_{i+1} = \big\{ & \big[G_{(n-1)\mathrm{R}}(X,Y,Z)_i + W\big(S_{(n-1)n}(X,Y,Z) \\
& + (1-W)G_{(n)\mathrm{L}}(X,Y,Z)_i - (1-W)G_{(n-1)\mathrm{R}}(X,Y,Z)_i\big] \\
& + \big[G_{(n)\mathrm{L}}(X,Y,Z)_i - WS_{(n)}(X,Y,Z)_i - (1-W)G_{(n)\mathrm{R}}(X,Y,Z)_i \\
& + (1-W)G_{(n)\mathrm{L}}(X,Y,Z)_i \big] \big\}/2
\end{aligned}
$$

$$(1)$$

Through the combination with survey network and auto-alignment process, the laser tracker provided initial location of the girders. The auto-alignment process is scheduled as shown in Fig. 5. In the process, the laser tracker also provided feedback data in the second step. The process would be continued interactively until the translation and rotation varying values converged to less than 10 μm and 2.5 μrad, respectively.
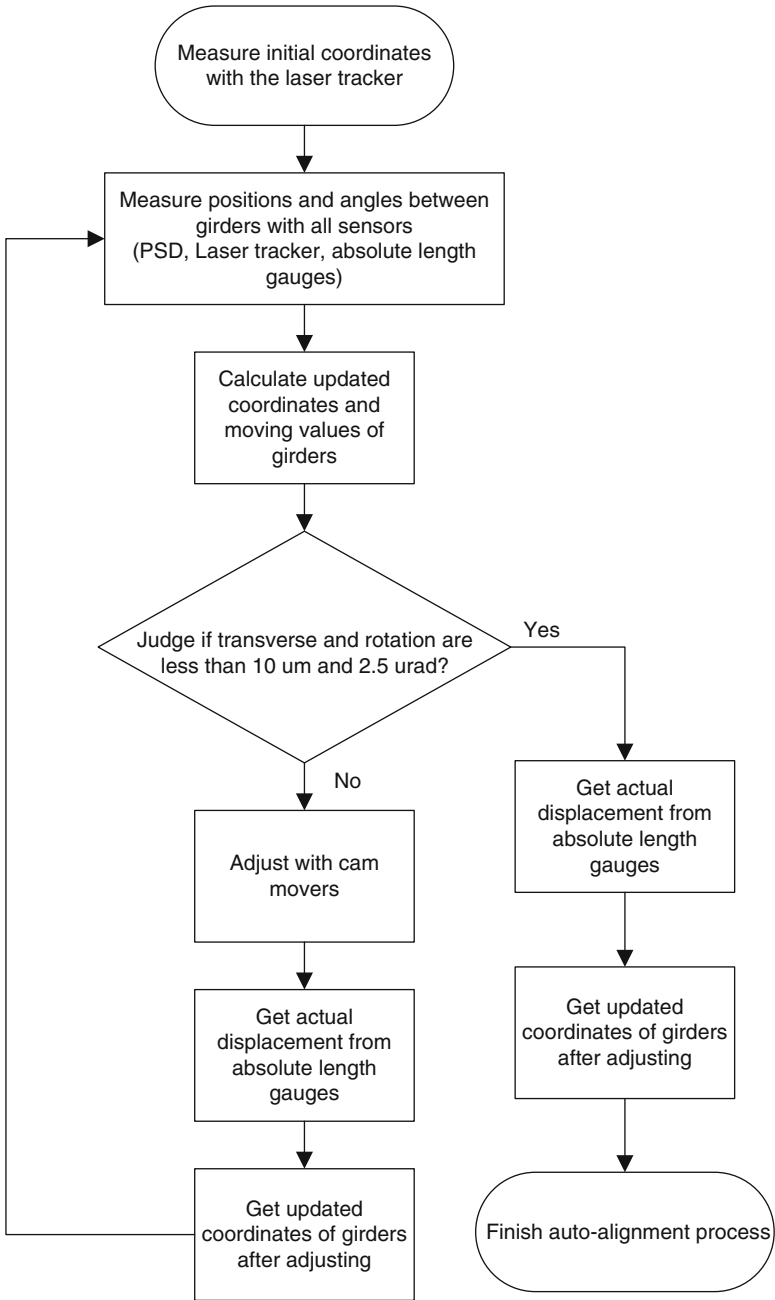
Fig. 5 The flowchart of auto-alignment process

4 Experimental Results

All the mechanisms and devices are located in a laboratory. For the stability of experimental condition, it is necessary to maintain the consistent temperature to 25 °C. It is shown in Fig. 6. The record of temperature varied around 1.3 °C during 24 h. Stabilities of various sensors in transverse direction are shown in Fig. 7. The drift of PSD is 3.85 μm; the drift of absolute length gauge is 0.16 μm; drifts of precision inclination sensor in pitch and roll angle are both 0.2 μrad. The recording period is chosen as 1 min due to that the measuring time of instruments is 1 min in a cycle of auto-alignment process.
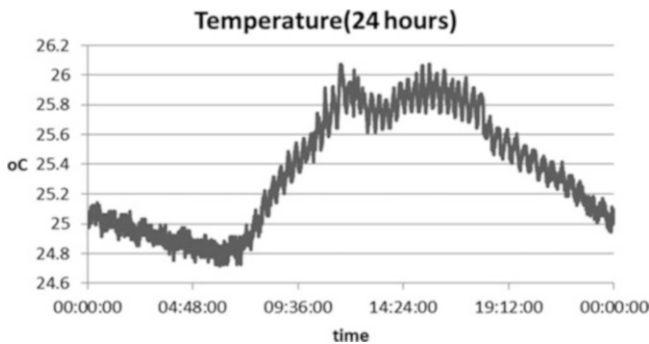
Fig. 6 The record of temperature variation during 24 h
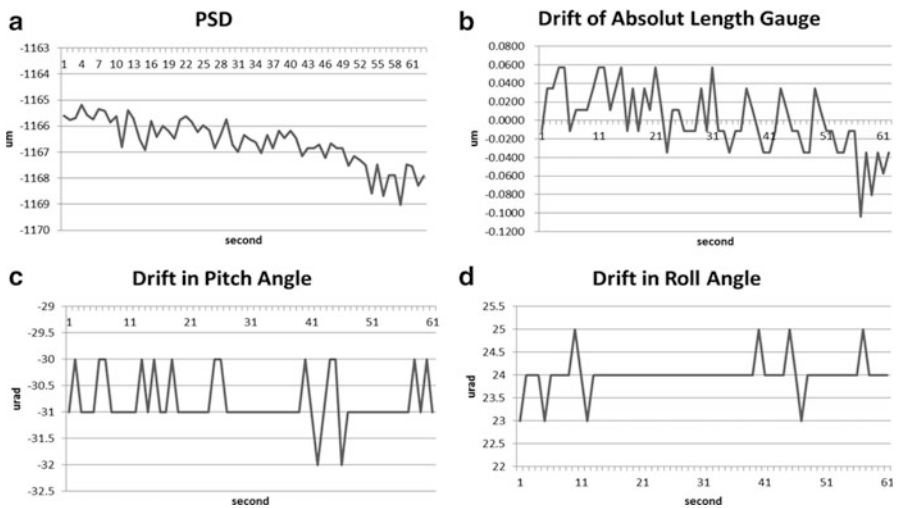
Fig. 7 (**a**) The drift of PSD. (**b**) The drift of absolute length gauges. (**c**) The drift of precision inclination sensor in pitch angle. (**d**) The drift of precision inclination sensor in roll angle
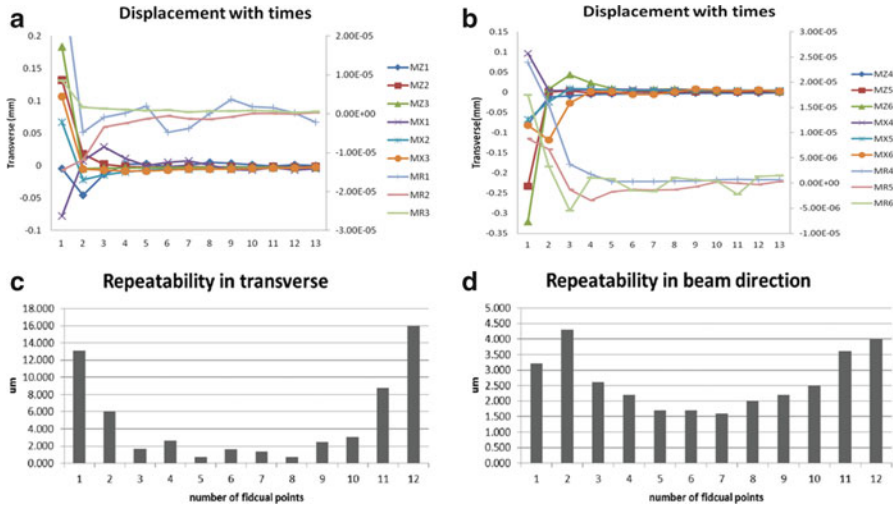
Fig. 8 (**a**) Variation of the first bend cell. (**b**) Variation of the second bend cell. (**c**) Repeatability in transverse. (**d**) Repeatability in beam direction

The adjustments of the auto-alignment system converged to target within 6 rounds as shown in Fig. 8a, b. For observing adjustment results and ensuring all the system trustworthy, the experimental process is extended to 13 rounds.

The symbols MX, MZ, and MR are the adjusting values in transverse, beam direction, and yaw. The subscripts of MX, MZ, and MR mean the assigning numbers of girders. The accuracy of the laser tracker is worse than other sensors, so adjustments of the first and last girder are comparatively larger than other girders. The moving values are varied obviously as shown in Fig. 8a, b. However, the translation and rotation deviations of the system could still be less than 10 μm and 2.5 μrad, respectively. The repeatability of the system that is tested 10 times is within 10 μm except the first and last point, which is shown in Fig. 8c, d. It is better than previous testing [3].

5 Conclusions

The experimental results of auto-alignment system reveal that the translation and rotation of the girders converge within 6 μm and 2.1 μrad even with a laser tracker for forming a closed loop. The repeatability of the system is under 10 μm except the first and last point and improves the problems of previous testing [3]. The auto-alignment system shows good convergence and repeatability from experiments [4]. The process will be applied, while the TPS storage ring installation and the experiment will be more complete.

References

1. Tse-Chuan Tseng (2006) A precise 6-axis girder system with can mover mechanism, MEDSI
2. Tse-Chuan Tseng (2008) Design and prototype testing of the girder system for TPS, SRI
3. Wei-Yang Lai (2011) From survey alignment toward auto-alignment for the installation of the TPS storage ring girder system, PAC11, 559–561
4. Wei-Yang Lai (2012) Auto-alignment system and calibration procedure in TPS girder system, PAC12

A Proposed System for Practicing Industrial Robot Remotely

Fu-Hua Jen and The Can Do

Abstract This research proposed a system combining NI Smart Camera, PLC, and KUKA robot for remote control. It lets students manage operating process of an industrial robot in a laboratory through the Internet at anytime and everywhere. It also provides a new solution to manage production line remotely. This system can help students viewing exact status of the robot everywhere when practicing on the robot without being in the laboratory and waiting for available shifts.

In the system, NI Smart Camera will transfer videos about the operating process of system to a central computer. All output and input signals from I/O devices will be integrated on the PLC for building up a human machine interface (HMI) in the central computer. The students can interact with the HMI on the central computer to control and monitor the system. They can also access the central computer to write program for KUKA robot. All data from NI Smart Camera and HMI will help students review their works.

Keywords Smart camera • PLC • KUKA robot • Human machine interface

1 Introduction

Nowadays many industrial robots such as KUKA robot and DENSO robot transferred to universities for training courses. However, these devices are very expensive and the exploitation costs are also expensive. So the number of

---

F.-H. Jen (✉)
Department of Mechanical Engineering, Minghsin University of Science and Technology,
Xinfeng, Hsinchu 30401, Taiwan, R.O.C.
e-mail: alanjen@must.edu.tw

T.C. Do
Institute of Precision Mechatronic Engineering, Minghsin University of Science and Technology,
Xinfeng, Hsinchu 30401, Taiwan, R.O.C.

industrial robots transferred to universities is limited. Especially, the student can only practice on the robot arms such as KUKA robot in laboratory on the working hours. Therefore, the opportunities for students to study and practice on these devices are limited. To resolve the above problem, one study developed remotely controlled and monitoring features for robot system [1]. Some research used KUKA robot with a regular personal computer to achieve monitoring process remotely [2]. Some research did remote control of CAN-based industrial equipment using Internet technologies [3]. In this study we want to propose another solution with technological applications to control and monitor industrial robot remotely. This system has combined an NI camera, a PLC, and a KUKA robot. This system allows the user to remotely write programs and monitor system through the Internet. In order to design and build up the system, many challenges have been encountered about hardware and software. First of all, what way is used to control and write program remotely for a KUKA robot when the system setup signal and programming start/stop signal have been available on the teach pendant of robot. Another challenge of the system is the data transmission method with which students can remotely write program and monitor system through the Internet. All challenges above have gradually resolved to build a remotely controlled system for industrial robots.

The study has been successfully implemented in the MUST. It opened up a great opportunity for students in the department of mechanical engineering to practice on production line with the participation of industrial KUKA robot.

2   Methodology for Control

The structure of remotely controlled system includes three components as shown in Fig. 1: One is the computer of user (client), the second one is the KUKA controller (client), and the third is the central computer (local server). These three components have different functions. At the computer of user, the user can set the experiment parameters and remotely watch, program, and control the experimental process through an HMI and on-site video camera. At the same time the user can obtain the experimental data. For the central computer, it includes three main parts: an OPC server, an HMI, and a video monitoring camera system. The KUKA controller controls KUKA robot and connects I/O device to receive control signals from the central computer.

Signals from buttons on HMI exchange for the controls signals on the teach pendant of KUKA robot. The user can access the central computer by TeamViewer software and click buttons on HMI desktop to control KUKA robot.
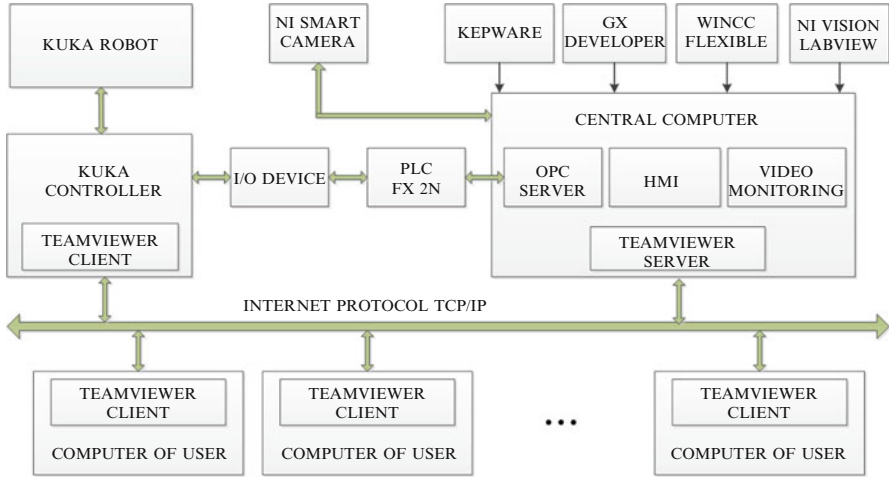
Fig. 1 The remote control construction
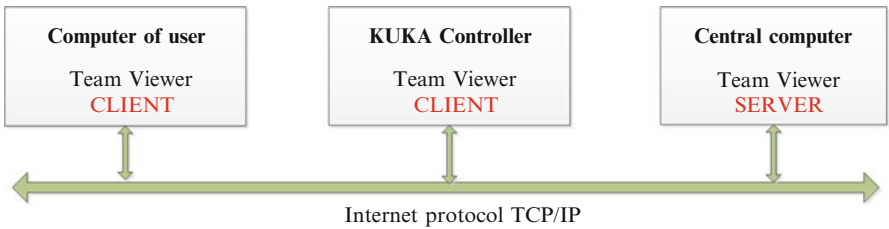
Fig. 2 TeamViewer connection

2.1 Desktop Sharing and Remote PC with TeamViewer

Three components of system transfer signals through the Internet by TeamViewer software as shown in Fig. 2. The user who can access the central computer needs the manager to provide IP address and password. The user will access the central computer to control and monitor system through TeamViewer window.

The user will write program directly on hard driver of KUKA controller. When interacting with the HMI to monitor and control robot, the user can monitor operating process of system with camera window on desktop of the central computer.

2.2 Robot Controlling by HMI Through Serial Port

The HMI shows all control buttons and monitor output signal. The control and monitor signal on the central computer will be transferred to KUKA controller
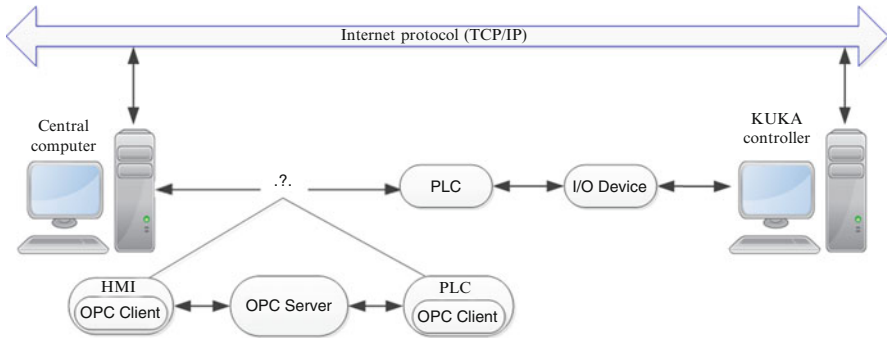
Fig. 3 OPC server communication

through serial port by I/O device and PLC FX2N. Figure 3 depicts the view on how the PLC is connected to HMI server. The OPC server is in the middle connecting to the PLC with native protocol on one side and connecting to other OPC client, say HMI on the other side.

3   Structure of Hardware

The hardware structure of this study is equipped with various modules such as KUKA robot, I/O devices, Mitsubishi PLC FX2N, PC, NI Smart Camera, solenoid valves, and pistons, as shown in Fig. 4.

In this study KUKA KR5 sixx R650 robot is controlled directly from KUKA controller. All input and output signals of KUKA robot are transmitted to the PLC FX2N through WAGO I/O devices. PLC FX2N will collect all output signals from KUKA and transmit to the central computer. Moreover, the PLC will control operating process of solenoid valves and pistons for the production line.

All data from KUKA and PLC will be transferred to the central computer to build a HMI with WinCC flexible software. The NI 1742 Smart Camera is connected directly to the central computer for transferring video. The smart camera provides automatic MDI/MDI-X correction, so we can use either a standard Ethernet cable or a crossover Ethernet cable to connect to the central computer. If the central computer is configured on a network, we must configure the smart camera on the same network as a subnet.
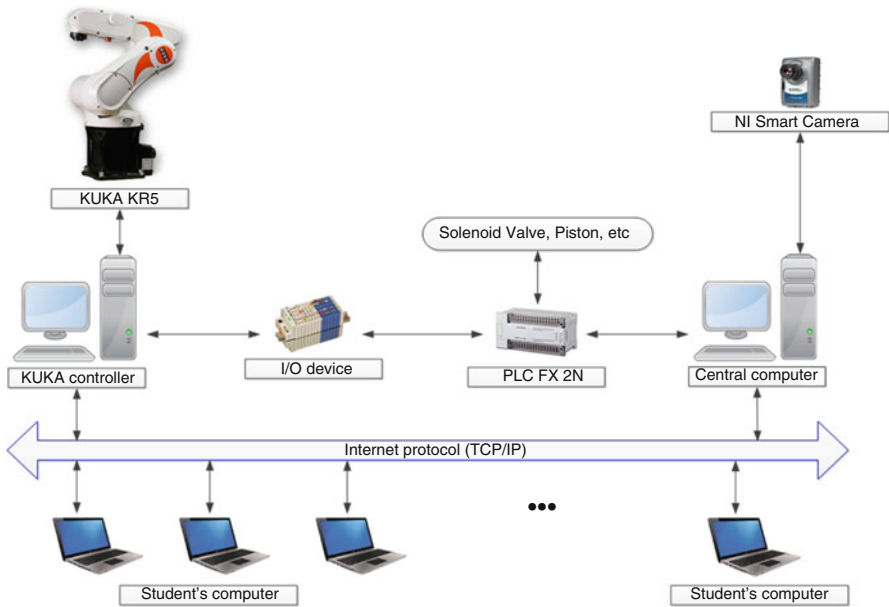
Fig. 4 Hardware structure of system

4 Communication Setup and HMI Designing

The main steps necessary to initialize the communication through serial port are listed below:

1. In the KUKA control panel [4], switch the mode selector to "automatic external." Configure automatic external inputs suitable with output signal of PLC and input signal of OPC server.
2. Start GX Developer to write/load program for PLC.
3. Start Kepware and set up an OPC server connection to connect HMI and PLC.
4. Start WinCC flexible and design a HMI with all necessary keys for controlling robot.
5. Click buttons on HMI Runtime window to control robot.
6. Check whether the communication is established. If not, return to step 3.

4.1 Communication Setup with KEPServerEX V4.0 OPC Server

The main steps to design tags on OPC are follows:

1. Start OPC server.
2. Make a new project using driver PLC FX 2 N.
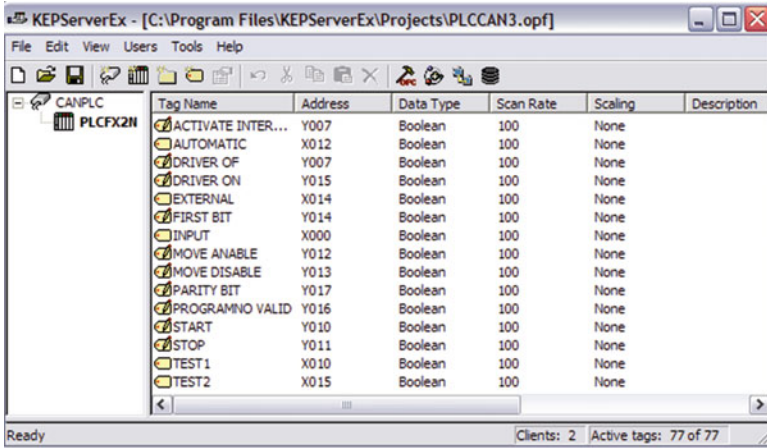
Fig. 5 OPC Quick Client
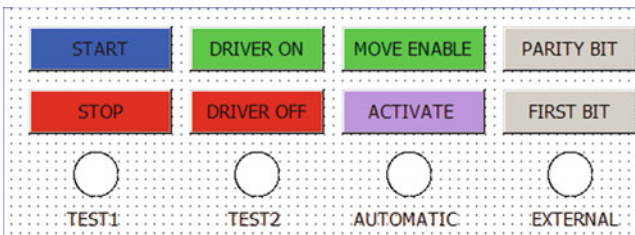
Fig. 6 Design HMI with WinCC flexible

3. Set up tags with address and data type suitable with PLC as shown in Fig. 5.
4. Start OPC Quick Client to testing connection.

After running OPC Quick Client, the OPC Quick Client window will display quality of connection. We can change update count to check if the connection is good or bad. If all tags connected to PLC are good, this means that OPC server completed connection with PLC and it can access memory areas of PLC to read/write data.

4.2 Design a HMI with WinCC Flexible

WinCC flexible [5] is ideal for use as the HMI software in all applications in which operator control and monitoring is required on-site – whether in production or process automation. To remotely control robot, we need to design a HMI with enough buttons as shown in Fig. 6 that can exchange for control buttons on teach pendant of robot.

The main steps to design a HMI are as follows:

1. Start WinCC flexible.
2. Design a new project and choose OPC communication to connect HMI with PLC.
3. Design all buttons necessary to control robot.
4. Make tags to connect to OPC. Address on tags is the same with address on OPC.
5. Connect buttons to tags of HMI.
6. Start WinCC flexible Runtime.
7. Click buttons on HMI simulation to testing connection.

5   Conclusion and Future Work

There are many ways to build a remotely controlled robot system. Much work has been done in recent years. The different purposes of application give the different methodologies to design the system. The remotely controlled robot system in this study is expected to become a device for the robotic class and can be used in industry. Methodology for control developed in this study is also simple for students who can understand and easily use. They can practice programming for PLC, designing HMI with WinCC flexible, building solution for NI Vision system, controlling solenoid valves, etc. It can help students improve skills on controlling industrial devices and understand in depth about communication between devices. Successful implementation of this proposed system will decrease investment cost on educational equipment. Increasing opportunities for students in practicing on production line provides better training for an integrated industrial robot system.

The study has been successfully applied in the laboratory. The results clearly indicate that this system achieves to fulfill the original purpose. When all necessary software used on central computer is ready, the student only needs to access the central computer by TeamViewer to control the robot.

For the future work, we would like to develop monitoring function with vision system and increase safety of working environment. Building a SCADA system offers maximum functionality and a user-friendly interface.

References

1. Björn Ostermann (2009) Industrial jointed arm robot evading dynamic objects, Sankt Augustin
2. Francesco Chinello, Stefano Scheggi, Fabio Morbidi, Domenico Prattichizzo (2010) A MATLAB toolbox for motion control of KUKA robot manipulators. In: Proceedings – IEEE international conference on robotics and automation, Alaska, 2010

3. Gerhard Gruhler (2003) Remote control of CAN-based industrial equipment using Internet technologies. In: Proceedings – international conference on communications ICC, Alaska, 2003
4. KUKA's Technical support. http://www.kuka.be/main/cservice/faqs/software/KUKA-Control Panel.pdf
5. SIEMENS automation technology. http://www.automation.siemens.com/salesmaterial-as/brochure/en/brochure_simatic-wincc-flexible_en.pdf

An Intelligent Sensorless Drive Strategy for a Brushless DC Motor Based on Back-EMF Detection

Seng-Chi Chen, Ying-Jyh Lin, Ming-Mao Hsu, and Yung-Nan Hu

Abstract This investigation describes a permanent magnet brushless direct current motor (PMBLDCM) that is based on an intelligent sensorless driver controller. Digital signal processing integrated circuit (DSPIC) is used as the core of the driver since it exploits microcontroller unit (MCU) and digital signal processor (DSP) technology, has the capacity for high-level computing, and is reliable. Not only sample the back electromotive force (back-EMF) by analog-to-digital converter ADC but also a virtual neutral voltage is retrieved from the lead of the motor during the non-driven sector for a particular phase. An intelligent control law that combines Cerebellar Model Articulation Controller (CMAC) with the PI controller proposes to control a driver. The drive controller allows the PMBLDCM to reach the rated speed rapidly. However, when a mechanical load is applied, having good speed regulation response is obtained by the developed motor drive. The controller realizes the self-adjustment pursuit of the speed control to a better performance.

Keywords PMBLDCM • Intelligent sensorless drive controller • CMAC • Back-EMF

1 Introduction

PMBLDCM has been extensively adopted in factory and office automation equipment, owing to its high efficiency, power density, and easy of control. In PMBLDCM, electronic commutation eliminates brushes and mechanical commutator. Information of the rotor position that identifies the commutation points is obtained using Hall-effect sensors placed within the motor. However, Hall sensors

S.-C. Chen (✉) • Y.-J. Lin • M.-M. Hsu • Y.-N. Hu
Department of Electrical Engineering, Da-Yeh University, Changhua 51591, Taiwan
e-mail: amtf.csg@mail.dyu.edu.tw

are temperature sensitive. Their misalignment in mechanical installation and additional wiring degrade system reliability, subsequently limiting the operations of the motor in harsh environments. Therefore, although capable of reducing the component count, overall axial length of the motor, and increasing reliability, a position sensorless PMBLDCM is more difficult to control than position sensor PMBLDCM. Recent research on sensorless methods for PMBLDCM is thoroughly reviewed in [1, 2].

This work presents a novel sensorless PMBLDCM drive and an intelligent control scheme. The drive system is based on detection of back-EMF zero-crossing point (ZCP) from the terminal and neutral voltages of the motor windings. Once the motor is started from standstill up to a certain speed, the sensorless method can detect the correct commutation instants. Running the motor in the sensorless mode involves delaying the switching signals by 30 electrical degrees from the ZCP of the back-EMF.

To comply with controller design, this work adopts an intelligent control strategy, in which the intelligent control algorithm consists of a CMAC and a proportional-integral (PI) controller. CMAC plays a critical role in estimating plant parameters and regulating PI controller gains online. The velocity control loop is realized using C-language in a DSPIC-based control system.

Developed by Albus [3], CMAC is a self-adaptive neural network that imitates the functions of the human cerebellum, which has a perceptron-like associative memory with overlapping receptive fields. CMAC can both express complex nonlinear functions by lookup tables and modify the table contents through self-learning. CMAC is superior in many ways to other neural networks in control engineering applications, including learning quickly online, computationally easy weight update operations, and local generalization ability. In this work, CMAC also operates as an estimator to predict unknown plant parameters, providing potentially rich information and knowledge that represents the relationships between input and output vectors. Additionally, designed to compensate for the conventional PI controller, CMAC improves the property of disturbance rejection and diminishes the effects of nonlinearities and system uncertainties on stability.

In this work, a sensorless PMBLDCM driving system is implemented by measuring terminal and virtual neutral voltages, and filter and phase-shift circuits detecting ZCP. An intelligent controller is then designed, in which CMAC and PI controllers are integrated to achieve improved system performances. Finally, experimental results of motor starting, running, velocity tracking control, and disturbance rejection capabilities demonstrate the effectiveness of the proposed sensorless PMBLDCM drive and the intelligent control scheme.

2 Sensorless PMBLDCM Drive Architecture, Back-EMF Detection, and Commutation Strategy

The proposed motor control architecture shown in Fig. 1 consists of dsPIC microcontroller, gate drive circuit, three-phase inverter, a virtual neutral point n' composed of R'_a, R'_b, R'_c, back-EMF filtering, and detection circuit. Motor winding of the motor stator is three-phase Y configurations. When motor rotor is rotated, according to the law of Faraday and Lenz, back-EMF is generated in each phase of winding. Back-EMF is detected when the phase is unexcited and synchronously sampled. Back-EMF signals pass through the resistor R_1–R_4, capacitor circuit (C), and are directly fed to the ADC pin of the DSPIC for processing.

Figure 2 schematically depicts three-phase terminal voltages and currents waveforms. The excitation current is assumed here to be a six-step square wave, and the conduction angle is 120 electric degrees. Efficient torque production relies on forcing the current into the motor such that it is in phase with the terminal voltage waveform. One full electrical period is divided into six regions, denoted as ①–⑥ sectors shown in the horizontal coordinate. The ZCPs are also displayed in the unexcited sector.

Only balanced windings are considered. Three-phase windings have the same resistances R_s and inductances L_s. Three-phase voltages of the motor are expressed as follows:
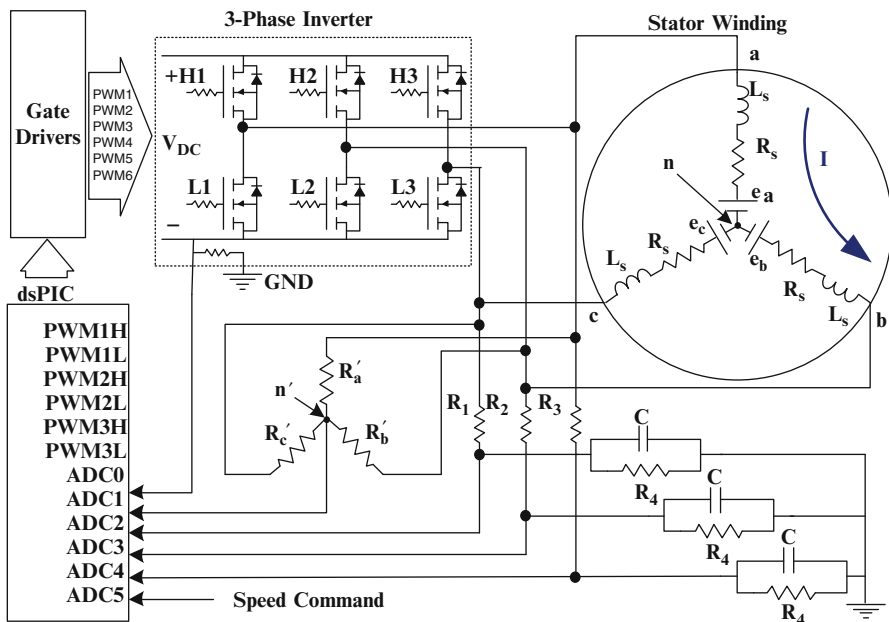
Fig. 1 Sensorless control of PMBLDCM drive hardware architecture
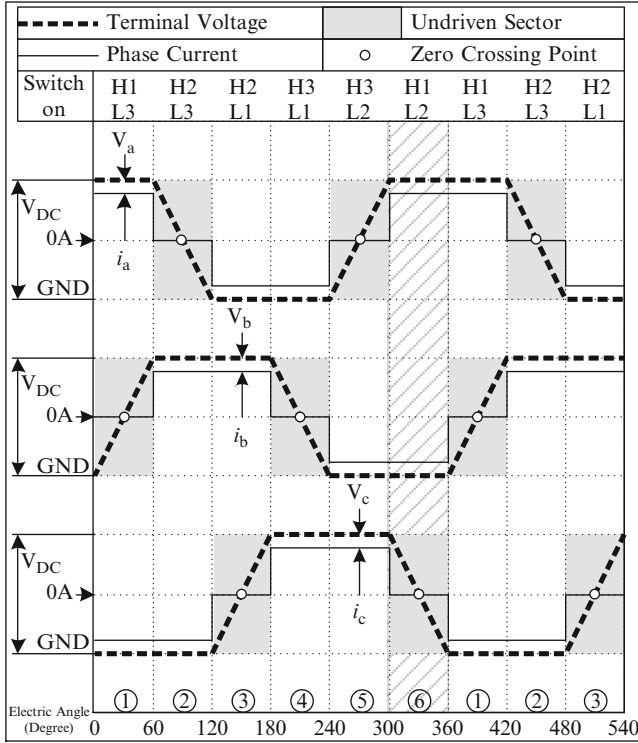
Fig. 2 Back-EMF zero-crossing detection

$$V_j = V_n + V_{jn} = V_n + R_s i_j + L_s \frac{di_j}{dt} + e_j, \quad (j = a, b, c) \tag{1}$$

where V_j denotes three-phase terminal voltages $(V_j = V_a, V_b, V_c)$ with respect to DC bus ground; V_n represents voltage of neutral point (n) to DC bus ground; V_{jn} denotes voltage of each phase winding to the neutral point; and e_j refers to back-EMF of each phase winding. The sum of the three-phase terminal voltages can be obtained as follows:

$$\sum_{j=a,b,c} V_j = V_a + V_b + V_c = (V_{an} + V_{bn} + V_{cn}) + 3V_n \tag{2}$$

Figure 2 reveals an unexcited phase at any instant. When power transistor switches H1 and L2 are conducted, denoted as ⑥ region in Fig. 2, then the current flows from phase a to phase b. At this time, i_a is equal to $-i_b$, and $i_c = 0$. Incorporating i_a, i_b, i_c into (1), followed by rearranging, yields $V_{an} = -V_{bn}$ and $V_{cn} = e_c$, subsequently leading to

$$V_{\mathrm{n}} = \frac{(V_a + V_b + V_c - e_{\mathrm{c}})}{3} \qquad (3)$$

In this region, the c phase current is zero. Then, according to (1) and (3), back-EMF of phase c is simplified by rearranging and is expressed as

$$e_c = \frac{3[V_c - (V_a + V_b + V_c)/3]}{2} \qquad (4)$$

In this sector, $e_c = 0$ in ZCP position, in which Eq. (4) indicates that ZCP occurs in $V_c = (V_a + V_b + V_c)/3$. At this time, $V_a = V_{\mathrm{DC}}, V_b = 0, V_c = e_c + V_{\mathrm{n}}$ are given. By assuming that no voltage drop occurs on the inductor, the above described phase current relationship has $i_a = -i_b$. By rewriting Eq. (3), the voltage of the neutral point is $V_{\mathrm{n}} = [V_{\mathrm{DC}} - (e_a + e_b)]/2$. For a motor with sinusoidal back-EMF waveforms, $e_a + e_b + e_c$ is equal to zero. Once ZCP occurs, then $e_c = 0$, and $e_a + e_b = 0$, are given. The terminal voltage in phase c is

$$V_c = V_{\mathrm{n}} = \frac{V_{\mathrm{DC}}}{2} \qquad (5)$$

Therefore, the above described sensorless brushless motor commutation strategy is feasible. By detecting the terminal voltage of unexcited phase, ZCP appears when this voltage is equal to $V_{\mathrm{DC}}/2$ and also equals the neutral point voltage V_{n}. After ZCP is determined by measuring the terminal voltage and the voltage of neutral point, ZCP delayed by 30° electrical angle is the right time with correct commutation. Therefore, the sensorless PMBLDCM can operate continuously and produce the maximum torque.

3 Intelligent Controller Design

The kernel of control algorithms is based on an intelligent controller developed in this work. Figure 3 depicts the detailed system block diagram, where $G_{\mathrm{c}}(z)$ denotes a discrete PI controller with a z-transfer function $G_{\mathrm{c}}(z) = (q_0 + q_1 z^{-1})/(1 - z^{-1})$, in which q_0, q_1 represents the PI controller parameters. The controlled system consists of a digital-to-analog converter (DAC) and the motor driver system, in which the dynamic model of the plant can be described as $G_{\mathrm{p}}(z) = (b_1 z^{-1})/(1 + a_1 z^{-1})$, with $a_1 = -e^{-T/\tau}$ and $b_1 = K_{\mathrm{m}}(1 - e^{-T/\tau})$, wherein T, τ, and K_{m} refer to the sampling time, electric time constant, and motor constant, respectively.

CMAC plays multifunctional roles in this system: as a velocity estimator to predict motor velocity based on ZCP timing and calculating counts from motor driver, as an estimator identifying motor speed and the controlled system states, and
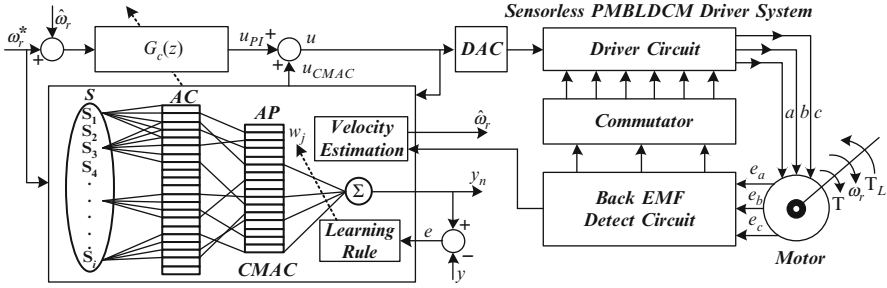
Fig. 3 Intelligent control system for a sensorless PMBLDCM drive

as a learning feedforward neural network and adaptive tuning of the PI controller parameters by optimum performance index. CMAC design procedures are described as follows. The first layer is a conceptual mapping, which is the mapping from an input state space S onto a conceptual memory AC. Next, considering the case of single input mapping, in which each state activates c memory cells in AC simultaneously. Additionally, $\omega_r^*(k)$ is the input of the CMAC, and the input state is quantized using a linearization function [4, 5]

$$q_i(k) = Q\left((\omega_r^*(k) - x_{\min})\frac{M}{x_{\max} - x_{\min}}\right) + i, \quad i = 1, 2, \ldots, c \tag{6}$$

where $q_i(k)$ denotes the mapping address; $x_{\min}$ and $x_{\max}$ represent maximum and minimum values of the input state, respectively; M refers to the corresponding initial address of $x_{\max}$ after the quantized process; and $Q(\cdot)$ denotes rounding of the input value to the nearest integer.

The second layer maps c memory cells in AC onto another c cells of an actual memory AP; in addition, the c cells in AP store the corresponding weighting values. In this procedure, the actual mapping is mapped using a "modulus after the division" method of Hash-coding techniques. While assuming that Hash-table length is m, the actual mapping is given by

$$\text{ad}(i) = \text{MOD}\left(q_i(k), N\right) + 1, \quad i = 1, 2, \ldots, c. \tag{7}$$

where $\text{ad}(i)$ denotes the Hash address, N represents a number which is typically in the range $c \leq N \leq M$, and $\text{MOD}(a, b)$ refers to the "modulus after division" function.

The output layer for a single-input state is given by $y_n = \sum_{i=1}^{c} w(\text{ad}(i))$, in which the weights stored in the Hash addresses are accumulated. The CMAC learning rules are expressed as

$$w_j(t) = w_j(t-1) + \Delta w_j(t) + \alpha\left[w_j(t-1) - w_j(t-2)\right] \tag{8}$$

in which the index $j = \text{ad}(i)$, $i = 1, 2, \ldots, c$, α denotes a momentum, in the range $0 \leq \alpha < 1$, in which the amount is determined by which previous weight changes affect the actual weight change. The change of the weights based on a gradient decent method can be expressed as

$$\Delta w_j(t) = -\eta \frac{\partial E}{\partial w_j} = \eta e(t) \tag{9}$$

where E is an updating weight performance index, is set as $E = e(t)^2/2$, and η is a learning rate.

Additionally, CMAC identifies the plant dynamics and produces a feedforward control effort $u_{\text{CMAC}}(k) = K_{\text{F}}\left[\omega_r^*(k+1) - \omega_r^*(k)\right]/T$, the feedforward control enhances the initial response to step commands, and the gain K_{F} is normally set to lower than 1. The PI controller $G_{\text{c}}(z)$ is designed to satisfy the stability criteria by using bilinear transformation [6]. The stability conditions are

$$q_0 > -q_1, \quad q_0 < q_1 + 2(1 - a_1)/b, \text{ and } q_1 < (1 + a_1)/b_1 = 1/K_{\text{m}} \tag{10}$$

PI control efforts $u_{\text{PI}}(k) = u_{\text{PI}}(k-1) + (q_0 + q_1)\, e\,(k-1)$; the intelligent control law that combines CMAC with the PI controller can be expressed as

$$u(k) = u_{\text{PI}}(k) + u_{\text{CMAC}}(k) \tag{11}$$

4 Experimental Results

In this work, the motor has a 12-slot 10-pole structure; the rated voltage is 24 VDC, rated current is 2 A; the rated speed is 2,000 rpm; the terminal resistance is 2.1 Ω; the terminal inductance is 580–630 μH; and back-EMF constant is 0.049 Vs/rad. The CMAC selects control parameters as follows:

$$T = 0.001\, s, \ M = 200, \ N = 150, \ c = 5, \ \eta = 0.6, \text{ and } \alpha = 0.06$$

According to Fig. 4, terminal voltage and phase current of phase a, virtual neutral-point voltage waveforms are displayed corresponding to the sensorless motor rotating from stop to a lower speed in a synchronous mode. When the motor speed reaches around 150 rpm, the motor generates a sufficiently large back-EMF to detect ZCP in an unexcited sector to obtain the correct commutation. Figure 5 illustrates the waveforms corresponding to motor operating at the rated speed and carried a rated load 2 A. Figure 6 plots the system performance using the proposed intelligent control.
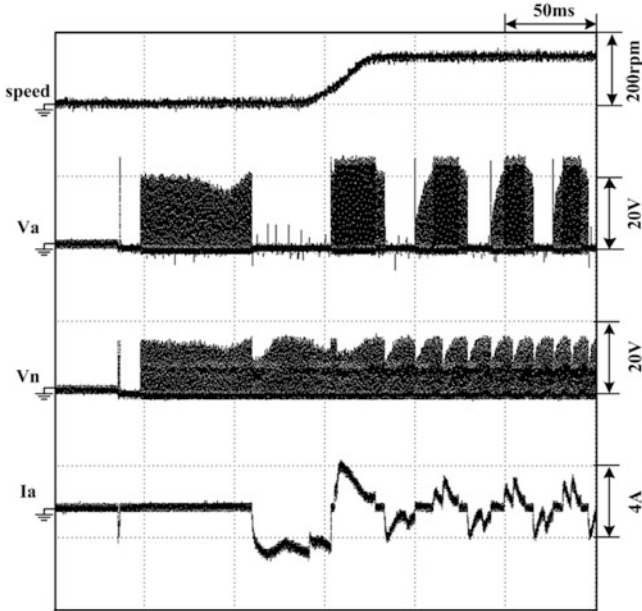
Fig. 4 Start-up characteristics of sensorless PMBLDCM
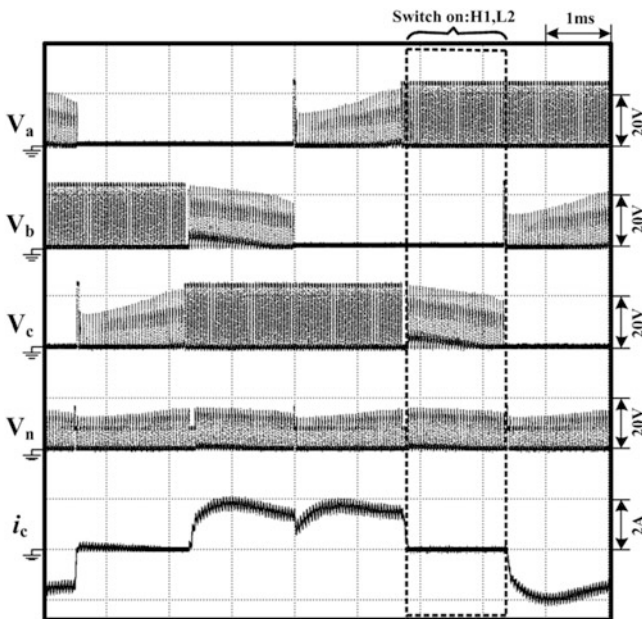
Fig. 5 Three-phases terminal voltages, currents, and neutral voltage waveforms with rated load
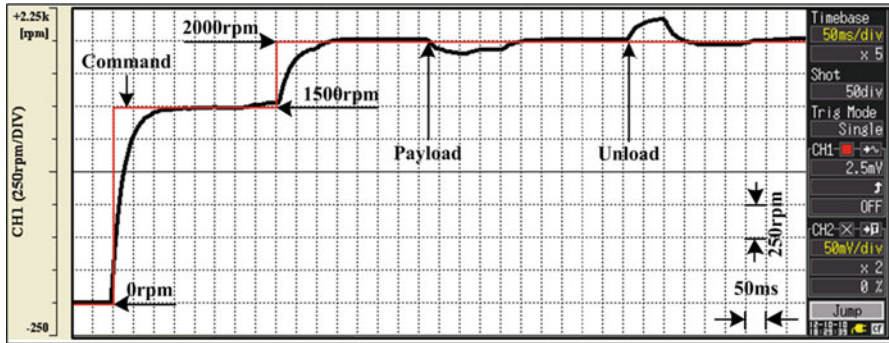
Fig. 6 Motor from standstill to 1,500 rpm and then from 1,500 to 2,000 rpm. When 2,000 rpm, motor loading and unloading

The motor accelerates in speed from 0 to 1,500 rpm and then to 2,000 rpm. When the motor speed reaches a steady-state value, a fixed load (2 A) is loaded and then unloaded. Experimental results demonstrate that the proposed intelligent controller has a rapid response, speed regulation, and satisfactory performance under applying load condition.

5 Conclusions

This work presents an intelligent controller for a sensorless PMBLDCM velocity control system. The proposed controller has many advantages over the conventional controller, including a simpler structure, faster self-learning capability, and more easy implementation. The controlled motor performs satisfactorily in the case of starting, velocity regulation, and adding a rated load. Experimental results also confirm that ZCP detecting method is highly reliable. Importantly, the proposed sensorless motor control method has a satisfactory speed dynamic response, in which the system performance approximates that of motor control with sensors.

References

1. Damodharan P, Vasudevan K (2010) Sensorless brushless DC motor drive based on the zero-crossing detection of back electromotive force (EMF) from the line voltage difference. IEEE Trans Energy Convers 25(3):661–668

2. Fu YJ, Huang LT, Lin RY, Chen CH (2012) Reliable starting method for sensorless brushless DC motor drive. In: The 2012 IEEE/ASME international conference on advanced intelligent mechatronics, Kaohsiung, 11–14 July 2012, pp 1005–1010
3. Albus JS (1975) A new approach to manipulator control: the Cerebellar Model Articulation Controller (CMAC). ASME J Dyn Syst Meas Control 97:220–233
4. Liu JK (2009) Intelligent control (in Chinese). Publishing House of Electronics Industry, Beijing
5. Zheng L (2009) CMAC neural networks based combining control for BLDC motor. In: International workshop on intelligent systems and applications, Wuhan, 23–24 May 2009, pp 661–668
6. Isermann R (1989) Digital control systems, vol 1, Fundamentals, deterministic control. Springer, Berlin/Heidelberg

Establishment of the Photovoltaic Simulation System Using Mixed Programming with LabVIEW and Simulink

Ting-Chung Yu, Yih-Bin Lin, and Fu-Sheng Chang

Abstract The purpose of this chapter is to establish a photovoltaic simulation system using mixed programming with LabVIEW and Simulink and compare the simulation results of three maximum power point tracking (MPPT) algorithms for the photovoltaic simulation system. The Matlab/Simulink is used in this chapter to establish the component models of the proposed photovoltaic simulation systems. LabVIEW is responsible for developing the virtual control interface and connects it with Simulink to perform simulation and analysis tasks. The proposed photovoltaic simulation system is developed by combining the models of solar modules and DC-DC boost converter with the tracking algorithms of perturbation and observation (P&O), incremental conductance (INC), and hill climbing (HC), respectively. The system will be simulated and analyzed under different weather conditions and MPPT algorithms. The simulation results will be shown on the interface of LabVIEW by mixed programming method. According to the comparisons of the simulation results, it can be observed that the photovoltaic simulation system can track the maximum power accurately using the three different MPPT algorithms, respectively. The simulation results can also be successfully displayed on the LabVIEW interface. The correctness and feasibility of the proposed photovoltaic simulation system is then validated.

Keywords Photovoltaic simulation system • Maximum power point tracking (MPPT) • Perturbation and observation • Incremental conductance • Hill climbing

T.-C. Yu (✉) • Y.-B. Lin • F.-S. Chang
Department of Electrical Engineering, Lunghwa University of Science and Technology, Taoyuan 33306, Taiwan
e-mail: tingyu@mail.lhu.edu.tw

1   Introduction

In addition to the excellent geographical conditions, it is very important to have an effective maximum power point tracking algorithm for the photovoltaic system. The photovoltaic system can generate maximum power and efficiency, while an appropriate MPPT algorithm is used with the system under any weather condition. Many scholars and researchers had devoted to explore effective MPPT algorithms [1–5], such as voltage feedback, perturbation and observation, incremental conductance, linear approximation, practical measurement, hill climbing, and fuzzy logic.

In the research [3] done by F. Liu et al., the response speed and applicability of the P&O and HC algorithms are compared for the grid-connected system. Moreover, C. C. Hua, J. R. Lin [4], and W. Xiao [5] improve the efficiency of the P&O and HC algorithms in their researches.

Most of the researchers used Matlab/Simulink to implement the simulation tasks of photovoltaic systems. Although Matlab/Simulink is a powerful industry-standard software, it is difficult to begin and use for the common novices and users. Based on the above reason, a technique of mixed programming with LabVIEW and Matlab/Simulink [6–8] is proposed in this chapter to establish the photovoltaic simulation system. By LabVIEW's user-friendly virtual instrument interface and Simulink's powerful modeling and calculating capability, the proposed system can simulate the power generation of the photovoltaic system with different MPPT algorithms and weather conditions and show the results on the LabVIEW's interface.

S. K. Huang, Y. N. Peng, S. P. Xie, and D. H. Wei introduced a mixed programming [6] with LabVIEW and Matlab/Simulink and applied this technology to examples of fuzzy and self-adaptive PD controllers to develop intelligent virtual instrument and control systems in their research. S. Vergura and E. Natangelo [7] proposed the design of a LabVIEW interface for acquiring, preprocessing, processing, and visualizing data deriving from photovoltaic plants. The procedures for monitoring the energy performances of PV plants and implemented in Matlab environment have been integrated in the operation of the proposed interface. The function of Matlab in their research was only to execute the statistical analyses.

This chapter is organized as follows: Sect. 2 introduces three MPPT algorithms used in this chapter, Sect. 3 proposes the integration of the Simulink models in LabVIEW environment, Sect. 4 presents the power generation results of the proposed photovoltaic simulation system under different MPPT algorithms and weather conditions, while Sect. 5 reports the conclusions.

2   Maximum Power Point Tracking Algorithms

The requirements of implementing maximum performance of a photovoltaic system are not only good weather conditions but also the appropriate MPPT method. Three power-feedback-type MPPT algorithms, including P&O, INC, and HC algorithms, are used in this chapter to implement MPPT tasks.
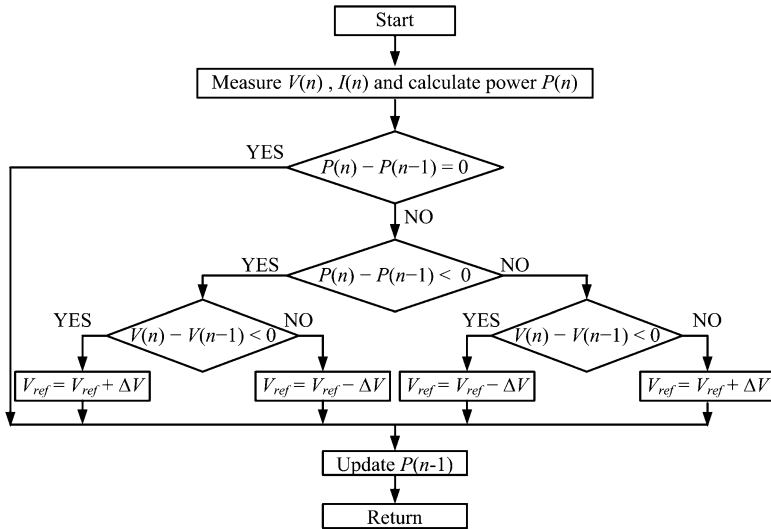
Fig. 1 The flow diagram of the P&Q algorithm

2.1 Perturbation and Observation (P&O) Algorithm

P&O algorithm [3, 4, 9–11] is the most frequently used algorithm in all of the MPPT algorithms. This algorithm can find the maximum power point of PV modules by means of iteratively perturbing, observing, and comparing the power generated by the PV modules. It is widely applied to the maximum power point tracker of the photovoltaic system owing to its features of simplicity and convenience.

From the P-V characteristic diagram of PV modules, it can be observed that regardless of the magnitude of sun irradiance and terminal voltage of PV modules, the maximum power point is obtained, while the condition $dP/dV = 0$ is accomplished. The slope of the power can be calculated by consecutive output voltages and output currents and is expressed as follows:

$$\frac{dP}{dV}(n) = \frac{P(n) - P(n-1)}{V(n) - V(n-1)} \tag{1}$$

The basic operating procedure of P&O algorithm is shown in Fig. 1. In a fixed period of time, the load of the PV system is adjusted in order to change the terminal voltage and output power of the PV modules. The variations of the output voltage and power before and after changes are then observed and compared to be the reference for increasing or decreasing the load in the next step. If the perturbation in

this time results in greater output power of PV modules than that before the variation, the output voltage of PV modules will be varied toward the same direction. Otherwise, the varying direction in the next step should be changed. The maximum output power point of a PV system can be obtained by using these iterate perturbation, observation, and comparison steps.

2.2 Incremental Conductance (INC) Algorithm

The theory of the INC algorithm [9–13] is to determine the variation direction of the terminal voltage for PV modules by measuring and comparing the incremental conductance and instantaneous conductance of PV modules. If the value of incremental conductance is equal to that of instantaneous conductance, it represents that the maximum power point is found.

When the operating point of PV modules is exactly on the maximum power point, the slope of the power curve is zero ($dP/dV = 0$) and can be further expressed as follows:

$$\frac{dP}{dV} = \frac{d(VI)}{dV} = I\frac{dV}{dV} + V\frac{dI}{dV} = I + V\frac{dI}{dV} \tag{2}$$

By the relationship of $dP/dV = 0$, (2) can be rearranged as follows:

$$\frac{dI}{dV} = -\frac{I}{V} \tag{3}$$

where dI and dV represent the current divergence and voltage divergence before and after the increment, respectively. The static conductance (G_s) and the dynamic conductance (G_d, incremental conductance) of PV modules are defined as follows:

$$G_s = -\frac{I}{V}; \quad G_d = \frac{dI}{dV} \tag{4}$$

When the equation in (3) comes into existence, the maximum power point is then tracked by MPPT system. Figure 2 is the operating flow diagram of the incremental conductance algorithm. The main difference between incremental conductance and P&O algorithms is the judgment for determining the direction of voltage perturbation. When static conductance G_s is equal to dynamic conductance G_d, the maximum power point is found [8].
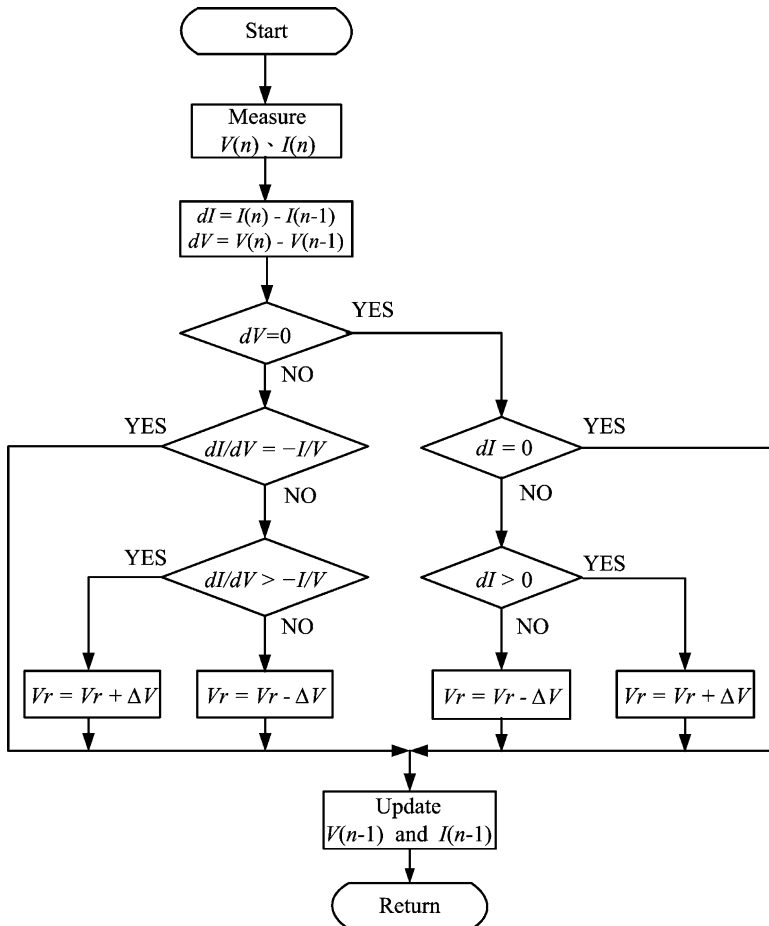
Fig. 2 The flow diagram of the INC algorithm

2.3 Hill Climbing (HC) Algorithm

The basic operating theory of the HC algorithm [3, 5, 10, 11] is similar to that of the P&O algorithm. Both algorithms use the condition whether $P(n)$ is greater than $P(n-1)$ or not to make the judgment. As described in previous section, the P&O algorithm uses the condition dP/dV to determine whether the maximum power point has been found or not. However, the HC algorithm uses the condition dP/dD to judge. In most applications, DC-DC converters and DC-AC inverters are usually used as the power interface devices between PV modules and loads. The HC algorithm uses the duty cycle (D) of these switching mode power interface devices as the judging parameter when the task of the maximum power point

Fig. 3 The flow diagram
of the HC algorithm
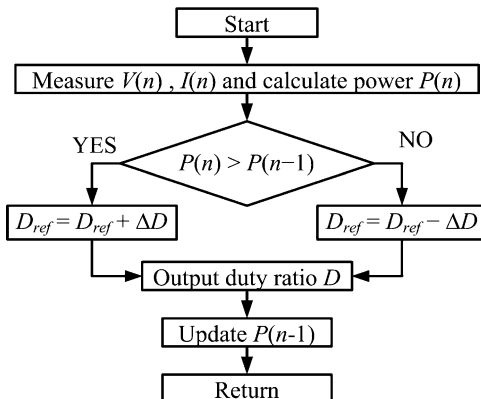
tracking is implemented. When the condition $dP/dD = 0$ is accomplished, it represents that the maximum power point has been tracked. The flow diagram of the HC algorithm is shown in Fig. 3.

The duty cycle is determined by comparing the powers at present time and previous time in each sampling period. If the incremental power $dP > 0$, the duty cycle should be increased in order to make $dD > 0$. If $dP < 0$, the duty cycle is then reduced to make $dD < 0$.

3 LabVIEW-Simulink Integration Interface

According to the model of the photovoltaic simulation system established by Matlab/Simulink that is more complicated, it is difficult to use for the beginners. In order to help them to learn the knowledge of photovoltaic system, a simulation interface with mixed programming of LabVIEW and Simulink is proposed to operate and control easily. After connecting LabVIEW with Simulink model by Simulation Interface Toolkit, the LabVIEW model of the proposed system is shown in Fig. 4. Figure 5 is the corresponding diagram of LabVIEW-Simulink integration virtual instrument interface.

Except data of power generations, the maximum power point tracking waveforms can also be displayed on the LabVIEW interface as shown in Fig. 6.

4 Analysis and Discussion of Simulation Results

Sanyo HIP-200NHE1 PV module is used in this chapter as a simulation example. The electric specifications of the PV module measured by Sanyo under standard conditions of 1,000 W/m^2, AM1.5, and 25 °C are listed in Table 1.
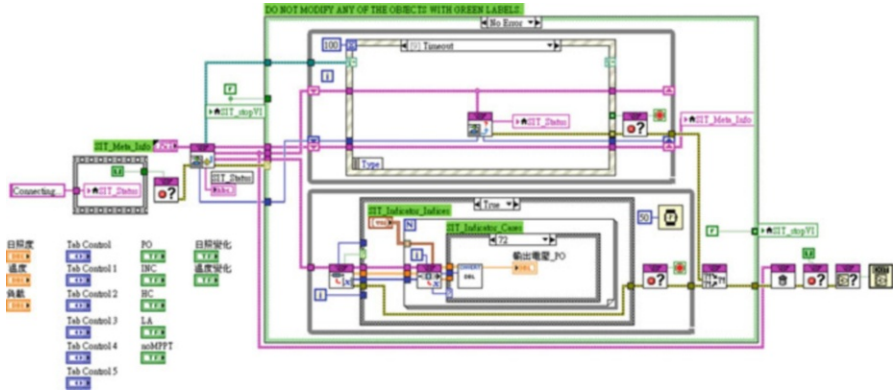
Fig. 4 Block diagram of the LabVIEW model
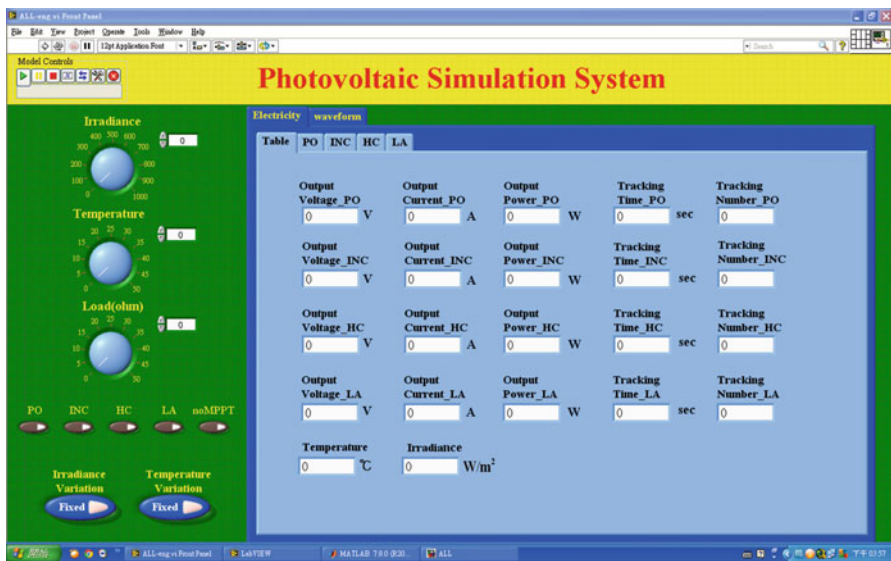
Fig. 5 LabVIEW interface of the proposed photovoltaic simulation system

The weather condition of the simulation test case starts from 1,000 W/m^2/40 °C, and gradually goes down to 500 W/m^2/25 °C, and then goes up back to 1,000 W/m^2/40 °C finally. The voltage increment in each time step for P&O and INC algorithms is set to be 0.3 V, and the duty-cycle increment for HC algorithm is set to be 0.01. Figure 7 is the simulation comparison results of Matlab and LabVIEW under three MPPT algorithms for two weather condition cases.

According to the results of Fig. 7, it can be found that the output power of three MPPT algorithms would approach their ideal maximum power. The output power waveforms shown in Matlab diagram are truly presented in the LabVIEW interface.
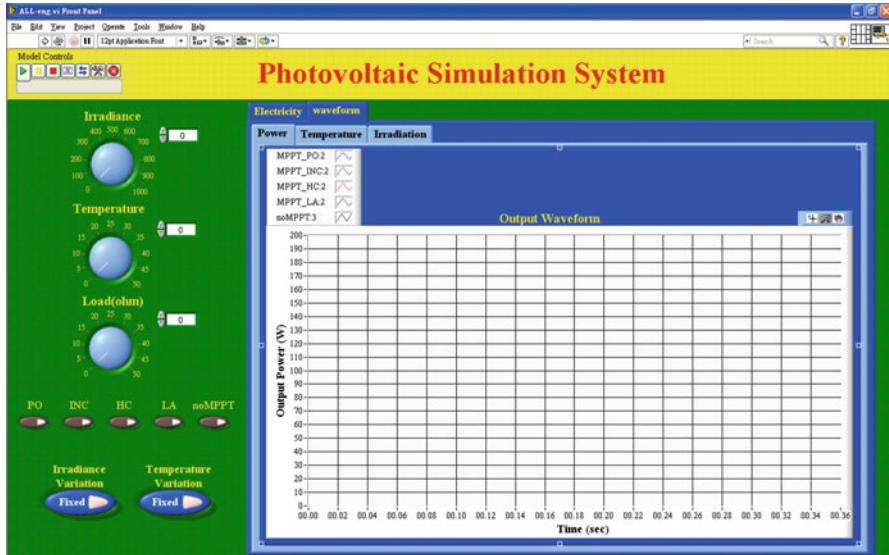
Fig. 6 LabVIEW interface with output power waveforms

Table 1 Electric specifications of Sanyo HIP-200NHE1

Parameter	Value
Maximum power (P_{max})	200 (W)
Max. power voltage (V_{mp})	40.0 (V)
Max. power current (I_{mp})	5.00 (A)
Open-circuit voltage (V_{OC})	49.6 (V)
Short-circuit current (I_{SC})	5.50 (A)
Temperature coefficient of I_{SC}	1.65 (mA/°C)
Temperature coefficient of V_{OC}	−0.129 (V/°C)

The tracking speed of HC algorithm is superior to the other two algorithms. However, the output power perturbations of the HC algorithm are also much greater than those of the other two MPPT algorithms.

In order to reduce the output power perturbations of HC algorithm to close to those of P&O and INC algorithms, a smaller duty-cycle perturbation was used in the following simulations. The voltage increment for P&O and INC algorithms is still set to be 0.3 V; however, the duty-cycle increment for HC algorithm is set to be 0.005. Figure 8 is the simulation comparison results of Matlab and LabVIEW under three MPPT algorithms after changing the perturbation.

According to the results of Fig. 8, the power perturbations of the HC algorithm are adjusted to close to those of P&O and INC algorithms when they reach their maximum power. However, the tracking speed of HC algorithm is apparently reduced. In summary, HC algorithm possesses better dynamic responses in the system which is not required precise output stability. INC algorithm has the best accurate results under rapid changing weather conditions.
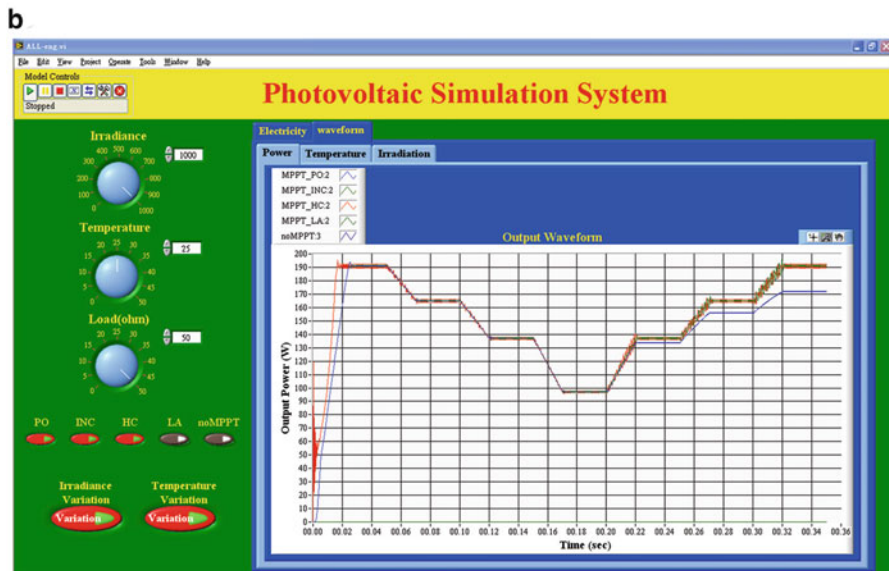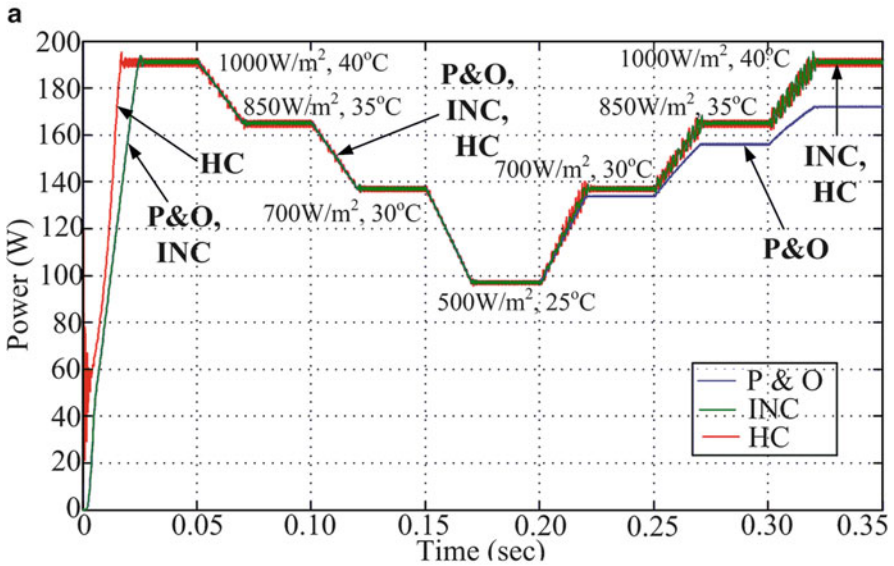
Fig. 7 Comparisons of output power of PV simulation system for the test case. (**a**) Comparison of output power – Matlab. (**b**) Comparison of output power – LabVIEW

a

b
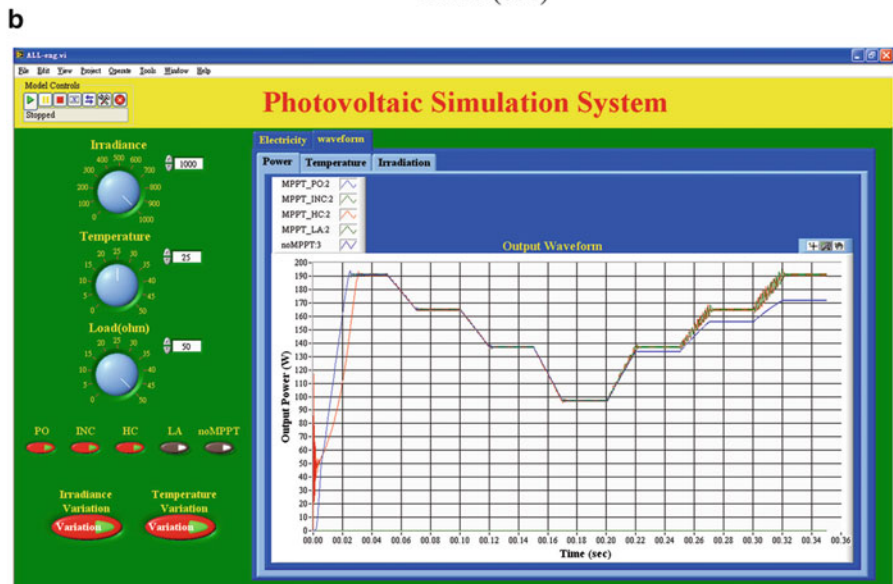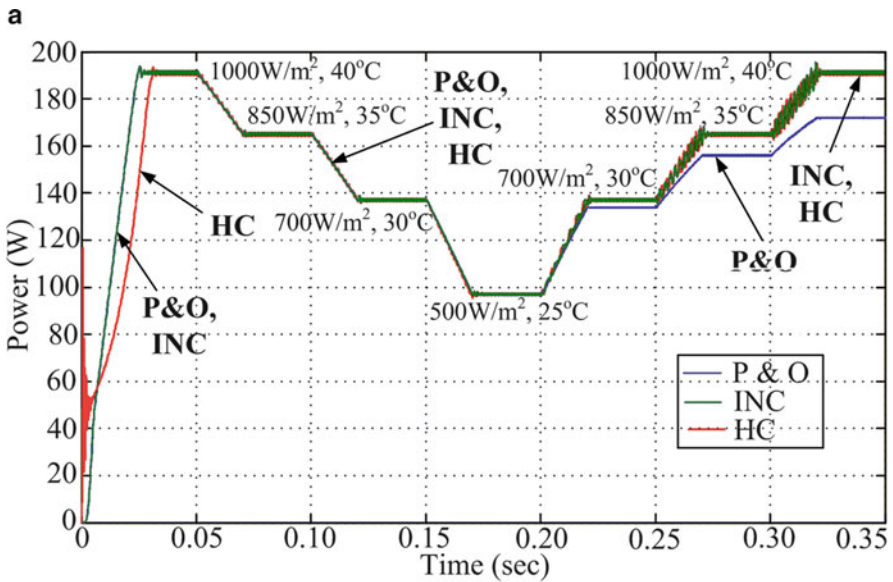
Fig. 8 Comparisons of output power of PV simulation system after changing the perturbation. (**a**) Comparison of output power – Matlab. (**b**) Comparison of output power – LabVIEW

5 Conclusion

The purpose of this chapter is to establish a photovoltaic simulation system using the technique of mixed programming with LabVIEW and Simulink. The component models of the proposed photovoltaic simulation system are first developed by Matlab/Simulink and then connected with LabVIEW to establish a user-friendly virtual instrument interface.

After comparing and analyzing the simulation results, it can be found that all the three MPPT algorithms can approximately track their maximum powers under continuously varied weather conditions. The simulation results of the three MPPT algorithms can be controlled and truly displayed on LabVIEW interface. The HC algorithm has the fastest tracking speed; however, its output powers are severely oscillated and unstable when they reach their maximum values. The output power oscillations of P&O algorithm are much smaller than those of HC algorithm. However, the tracking accuracy of P&O algorithm is the worst under rapid changing weather conditions. The simulation time of tracking maximum power for INC algorithm is the longest due to its complicated judgment process. However, INC algorithm has the advantages of exact direction in the tracking process and highest accuracy under rapid changing weather conditions.

After optimizing the duty-cycle perturbation of HC algorithm, its oscillated amplitude is obviously reduced; nonetheless, the tracking time is longer than before. In conclusion, HC algorithm is suitable for the system that the stable output power is not the priority consideration. For the system with the sophisticated equipment in the environment of rapid changing weather conditions, INC algorithm may be the best choice.

References

1. Tavares CAP, Leite KTF, Suemitsu WI, Bellar WI (2009) Performance evaluation of photovoltaic solar system with different MPPT methods. In: 35th annual conference of IEEE (IECON '09), Porto, 3–5 Nov 2009, pp 719–724
2. Hua C, Lin J, Shen C (1998) Implementation of DSP-controlled photovoltaic system with peak power tracking. IEEE Trans Ind Electron 45(1):99–107
3. Fangrui Liu, Yong Kang, Yu Zhang, Shanxu Duan (2008) Comparison of P&O and hill climbing MPPT methods for grid-connected PV converter. In: 3rd IEEE conference on industrial electronics and applications 2008 (ICIEA 2008), Singapore, 3–5 June 2008, pp 804–807
4. Hua CC, Lin JR (2001) Fully digital control of distributed photovoltaic power systems. In: IEEE international symposium on industrial electronics (ISIE 2001), Pusan, June 2001, vol 1, pp 1–6
5. Xiao W (2003) A modified adaptive hill climbing maximum power point tracking control method for photovoltaic power system. Master thesis, The University of British Columbia, British Columbia, July 2003
6. Huang SK, Peng YN, Xie SP, Wei DH (2009) Methods and application of mixed programming with LabVIEW and Matlab. Res Explor Lab 27(7):67–71

7. Vergura S, Natangelo E (2010) LabVIEW-Matlab integration for analyzing energy data of PV plants. In: International conference on renewable energies and power quality, Granada, 2010
8. Brezina L, Andrs O, Brezina T (2008) NI LabView – Matlab SimMechanics Stewart platform design. Appl Comput Mech 2:235–242
9. Zhuang J-C (1997) Photovoltaic engineering-solar cells. Chuan Hwa Book CO. LTD, Taipei
10. Hohm DP, Ropp ME (2003) Comparative study of maximum power point tracking algorithms. Prog Photovolt Res Appl 11(1):47–62
11. Esram T, Chapman PL (2007) Comparison of photovoltaic array maximum power point tracking techniques. IEEE Trans Energy Convers 22(2):439–449
12. Lee J-H, Bae HS, Cho B-H (2006) Advanced incremental conductance MPPT algorithm with a variable step size. In: 12th international conference on power electronics and motion control, Poznan, 30 Aug–1 Sept 2006, pp 603–607
13. Yusof Y, Sayuti SH, Latif MA, Wanik MZC (2004) Modeling and simulation of maximum power point tracker for photovoltaic system. In: Power and energy conference (PECon 2004), Kuala Lumpur, 29–30 Nov 2004, pp 88–93

Implementation of Fuzzy Force Control for an Electrohydraulic Servo Press System

Hong-Ming Chen, Chun-Sheng Shen, and Guo-Wei Yang

Abstract In this chapter, based on the fuzzy method, a PC-based precision force control scheme is proposed for the electrohydraulic servo press system. The main feature of proposed scheme is to develop a composite control of relief valve and flow servo valve. With the feedback of force sensor, the fuzzy-based control system is realized by LabVIEW for achieving the precision force control of hydraulic cylinder. In the experimental testing, a practical platform of hydraulic servo press system is used to demonstrate the effectiveness of proposed scheme. The testing results indicate the accurate output responses.

Keywords Force control • Electrohydraulic servo press system • Composite control • Relief valve • Flow servo valve • LabVIEW

1 Introduction

In general, the motor is always the main power source of mechanical system. Instead of manpower, the motors are used to accomplish many kinds of tasks. According to the different transportation ways, the mechanical systems possess different properties. The precision of position control is relating to the property and mechanical architecture of motor. Unfortunately, some motors are not satisfied for the market requirements because of its horsepower and volume. Therefore, the hydraulic system [1] has been widely applied in the case of small volume and large horsepower.

H.-M. Chen (✉) • C.-S. Shen • G.-W. Yang
Department of Electronic Engineering, Chienkuo Technology University,
Changhua 50094, Taiwan
e-mail: steven@ctu.edu.tw

The transportation media of hydraulic system is based on liquid. In early stage, the hydraulic cylinder just can be controlled by the ON/OFF switch due to components' property. Moreover, the pressure of hydraulic cylinder is produced by spring and is regulated by human. The system is inflexible and unavailable for fine tuning. The efficiency of precision control for the hydraulic system is also restricted.

In recent years, various precise sensors and servo valves are popularly produced because of the mutual development of semiconductor technology. Accordingly, the high-precision position and force control of hydraulic system [2] can be performed by controlling the movement and liquid flow rate of hydraulic cylinder via servo valves. However, the hydraulic system has the disadvantages of leakage and variation due to the compressibility of oil. The property of system is also changed with the temperature variation of oil. Moreover, the proportional servo valve possesses the problems of dead zone and delay phenomenon. The general linear control schemes are not available to deal with these problems. Therefore, various methods [3] are proposed for achieving the effective control of hydraulic system. Among proposed methods, the fuzzy control is a nonlinear and useful one in the industrial applications [4]. Even without of certain system model, the fuzzy control law is designed by the expert rule base. Compared with other advanced control schemes, the fuzzy control is much easier in the design and implementation. Consequently, we propose a composite control law with fuzzy method for the hydraulic servo system and implement the controller in LabVIEW.

By the examination of a practical hydraulic servo press platform, the experimental results indicate the force outputs of relief valve and servo valve could be controlled accurately.

2 Hydraulic Servo Force Control System

2.1 Hydraulic Servo Press System

In this investigation, we use a vertical-type hydraulic servo press system which structure is depicted in Fig. 1. The hydraulic servo system is composed of servo valve, relief valve, hydraulic cylinder, linear scale, force sensor, spring load, computer, and data acquisition (DAQ) card. The hydraulic cylinder acts up and down, which stroke is 20 cm. In this hydraulic servo system, the AC motor drives the hydraulic pump and the relief valve adjusts the inner pressure of hydraulic cylinder. Adjusting the direction and oil flow of hydraulic cylinder by servo valve, the position and force of hydraulic cylinder could be controlled.

The power of hydraulic servo system is supplied by the hydraulic cylinder which is driven by the motor and pump. Therefore, we design a PC-based fuzzy controller to achieve the precision force control of hydraulic cylinder. In the designed system, the pressure and force states of hydraulic cylinder are measured by the relating
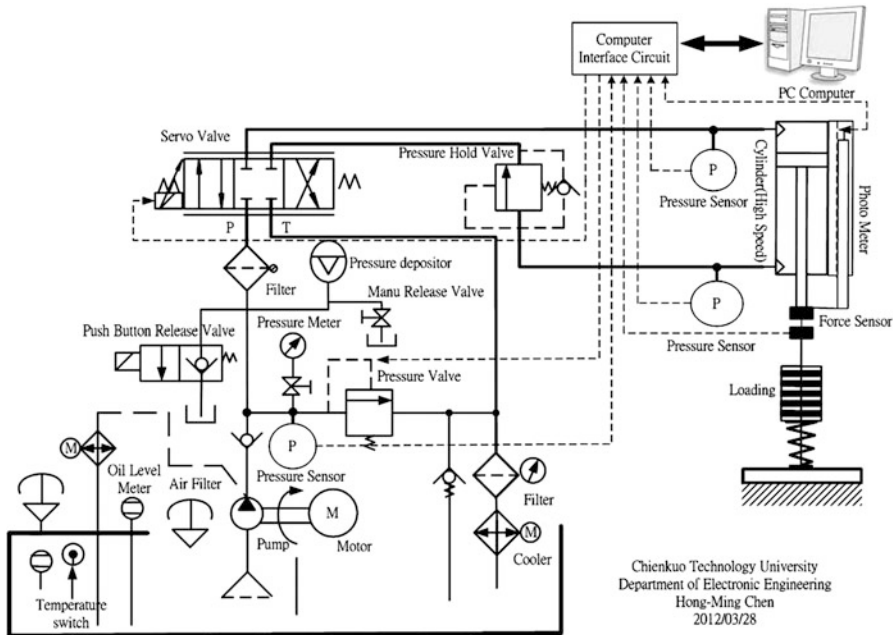
Fig. 1 The structure of hydraulic servo press system

sensors and are transferred to computer by PCI-6221 interface card. Based on the proposed control law, the control values of force and oil flow are calculated by LabVIEW software and are exported to relief valve and flow servo valve, respectively. With the composite control of relief valve and flow servo valve, the precision force control could be performed for the hydraulic servo system.

2.2 Hydraulic Cylinder Servo System

The hydraulic cylinder servo system is composed of servo valve and hydraulic cylinder. The relating structure is illustrated in Fig. 2. The purpose of control is to make the flow rate approach the expected value Q_L as fast as possible. By the orifice law [6, 7], the relation between spool position (x_v) and flow rate (Q_L) is explained in the following equation:

$$Q_L = k_q x_v - k_c P_L \tag{1}$$

with

$$k_q = k_v C_d w \sqrt{\frac{1}{\rho}} \sqrt{P_S - \text{sgn}(x_v) P_L} \tag{2}$$
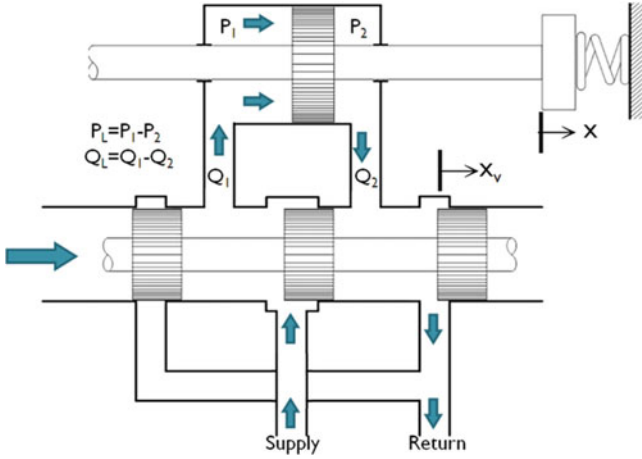
Fig. 2 The structure of hydraulic cylinder servo system

where P_S is input pressure, C_d is hydraulic emission factor, w is the area gradient of servo valve, x_v is the displacement of servo valve, ρ is oil density, P_L is the difference in pressure between both sides of hydraulic cylinder, k_v is the gain of servo valve, and k_c is the constant of difference in pressure.

In general, the moving rate of hydraulic cylinder is available for the servo valve. We can regard the servo valve as a zero-order system. The proportional equation of x_v and k_v is represented by

$$x_v = k_a u \tag{3}$$

where k_a and u are the gain and control inputs of servo valve. The internal oil leakage and compressibility of hydraulic system can be observed from the flow equation [6], which is represented by

$$Q_L = A\dot{x} + \frac{V_t}{4\beta_e}\dot{P}_L + C_t P_L \tag{4}$$

where A is the effective sectional area of hydraulic cylinder, V_t is the effective volume of hydraulic system, β_e is the compressibility modulus of hydraulic oil, and C_t is the total leakage factor of hydraulic cylinder. With the Eqs. (2) and (4), the equation of system model can be rewritten by

$$\dot{F}(t) = -A^2\frac{4\beta_e}{V_t}\dot{x} - (C_t + K_c)\frac{4\beta_e}{V_t}F(t) + AK_qK_a\frac{4\beta_e}{V_t}u \tag{5}$$

As can be known from Eq. (5), the hydraulic cylinder force servo system is a nonlinear system with variable parameters. The precision control is hardly approached by the traditional control scheme in switch ON or OFF. Therefore, we propose to design a fuzzy controller for hydraulic cylinder servo system to achieve precise force servo control.

3 Fuzzy Controller Design

In this chapter, the main purpose is to design a fuzzy controller for the hydraulic servo platform. The essential composition of fuzzy control system includes four parts [5]: *fuzzification*, *fuzzy rule base*, *fuzzy inference engine*, and *defuzzification*. The structure of fuzzy control system is depicted in Fig. 3. First, the error and change of error variables are used for the two inputs of fuzzy control system. The input variables in a fuzzy control system are in general mapped into fuzzy sets by membership functions. The process of converting a crisp value to a fuzzy value is called *fuzzification*. The *rule base* is established by the experts' knowledge and experiences, which is represented in the form of if-then statements. Then, the process of *fuzzy inference engine* is to invoke each appropriate rule for generating a result for each and combine the results of the rules. Finally, the process of *defuzzification* is to convert the combined result into a specific control output value.

To ensure the input variables are within the universe of discourse, two scaling gains *K1* and *K2* are cascaded in front of the fuzzification process. Similarly, a scaling gain *K3* is cascaded in back of defuzzification process to adapt the control output.

4 Experimental Results

In the experiments, a practical equipment of hydraulic servo press system displayed in Fig. 4 is utilized to verify the effectiveness of precision force control. We propose a composite control scheme to achieve the precision force control of hydraulic servo system. The structure of proposed scheme is illustrated in Fig. 5, where the controller is designed based on fuzzy method and is implemented by LabVIEW.

In order to demonstrate the superiority of proposed scheme, we do the comparison of developed control law and traditional PID control law. With the Ziegler-Nichols method and trial and error, the parameters of PID controllers are defined as follows: $K_p = 0.015$, $K_i = 0.00237$, $K_d = 0.00023$ for relief valve, and $K_p = 0.023$, $K_i = 0.01115$, $K_d = 0.00985$ for servo valve. Accordingly, the comparison results are represented in Fig. 4, where black, red, and green curves
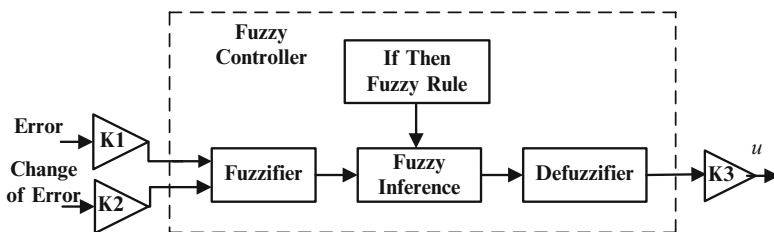
Fig. 3 The fuzzy controller block diagram
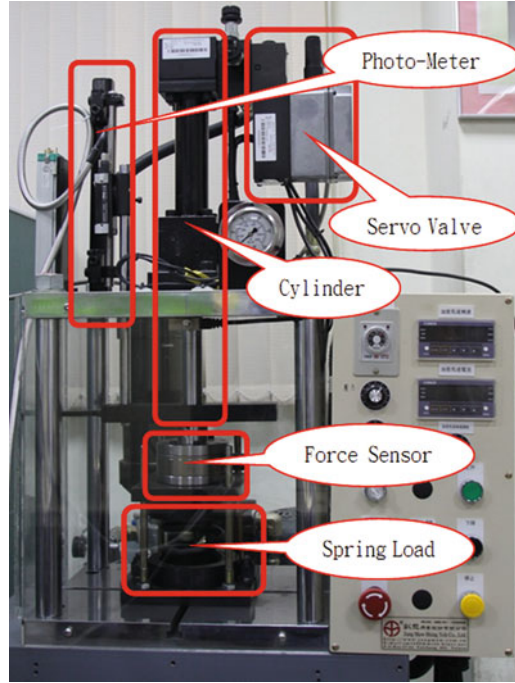
Fig. 4 The real press system
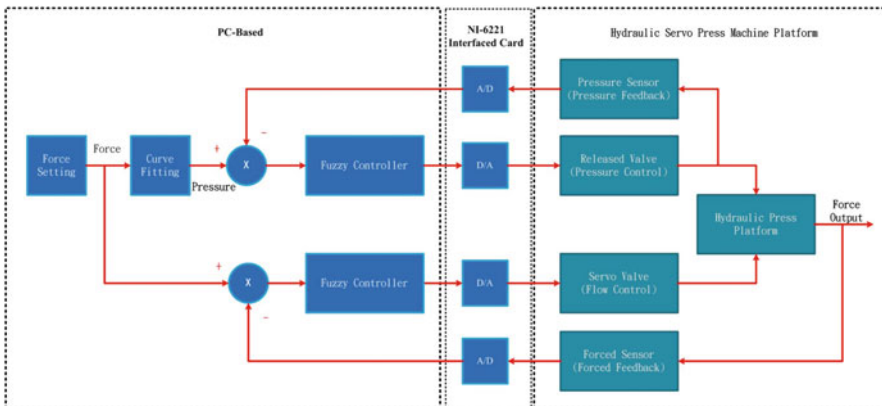
Fig. 5 The architecture of composite control scheme

are the output responses of desired signals, PID controllers, and fuzzy controllers, respectively. Figure 6 indicates the output force responses of multiple force increasing steps. The initial force is 500 kgf and is increased 100 kgf every 10 s until 1,000 kgf is reached. Figure 7 indicates the error responses of multiple force increasing steps. As can be observed, the output force errors of fuzzy controller are
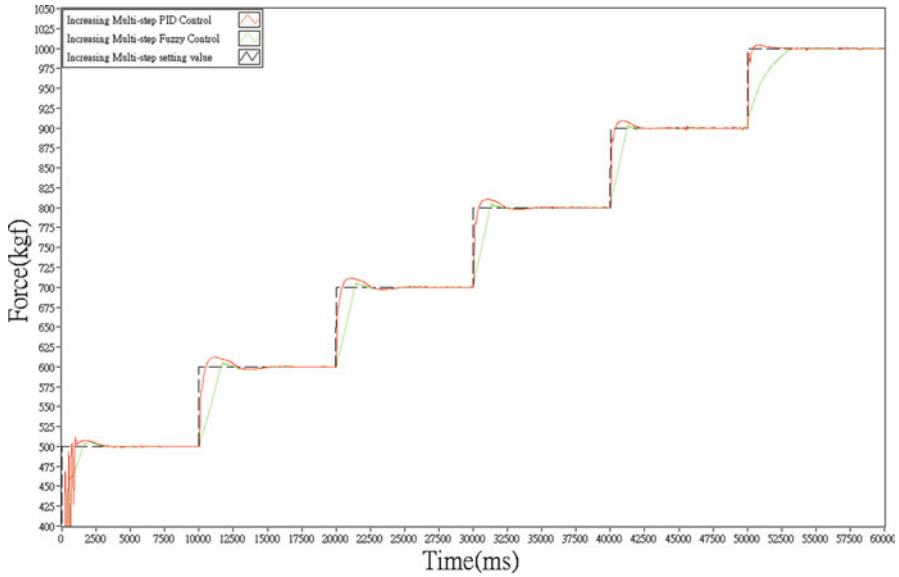
Fig. 6 The multistep responses
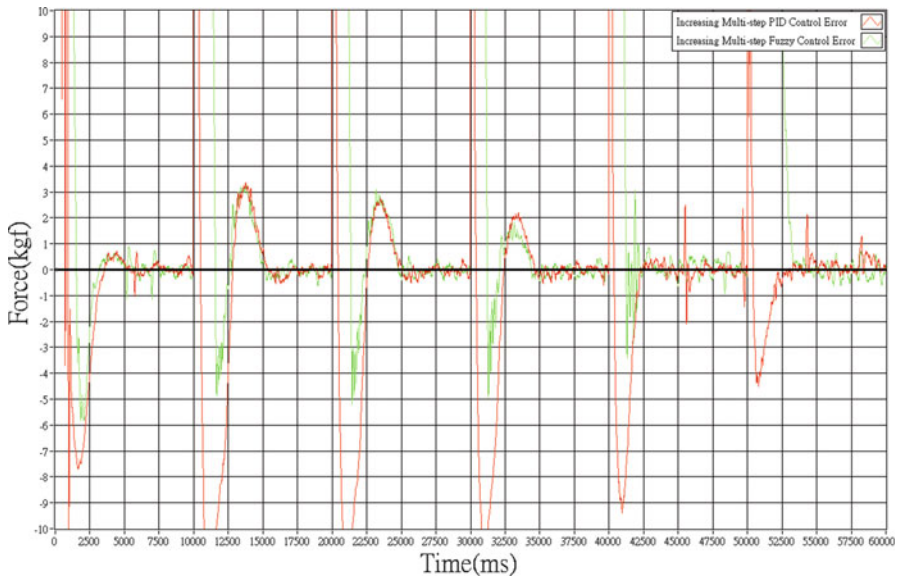
Fig. 7 The error multistep responses

within ±0.5 kgf which are less than those of PID controller. Otherwise, we have done various testing under different conditions. The numerical comparisons are collected in Tables 1 and 2. Obviously, the performance of fuzzy controller is much better than that of PID controller, especially in maximum overshoot.

Table 1 The comparison of maximum overshoot

	Single step	Multiple increasing step	Multiple decreasing step	Force sine wave	Repeating load
PID	12.25	11.8	5.5	9	12.8
Fuzzy	0.5	5.8	4.8	9.5	10.4

Table 2 The comparison of steady-state error

	Single step	Multiple increasing step	Multiple decreasing step	Force sine wave	Repeating load
PID	<0.5	<0.5	<5	<2	<0.5
Fuzzy	<0.5	<0.5	<5	<3	<0.5

5 Conclusion

The most important thing for the force control is that the maximum overshoot could not be large because the loaded object could be possibly broken by the large overshoot. By the consideration of the press testing instrument, the unit under test (UUT) could be also possibly damaged by the large overshoot. Accordingly, we have proposed to design fuzzy controllers for the hydraulic servo system. With the composite control of relief valve and flow servo valve, the force output could be controlled accurately. The experimental results indicate that the fuzzy controller provides better effect for the overshoot restriction. Due to the sensitivity of used force sensor is within ± 1 kgf, we have successfully achieved the practical implementation of the precision force control for the hydraulic servo press system.

References

1. Nielsen RJ, Bruning JH, Richman RM, Biddick CJ, Giacchi J, Kossyk GJW, Bush DR, Barna SJ, Alles DS (1987) A hydraulic X-Y stage system for applications in electron beam exposure systems. J Vac Sci Technol B Microelectron Nanometer Struct 5:57–60
2. Kularatna N, Mcdowall J, Melville B, Kularatna-Abeywardana D, Hu AP, Dwivedi A (2010) Low-cost autonomous 3-D monitoring systems for hydraulic engineering environments and applications with limited accuracy requirements. IEEE Sens J 10:331–339
3. Lischinsky P, Canudas-de-wit C, Morel G (1999) Friction compensation for an industrial hydraulic robot. IEEE Control Syst 19:25–32
4. Liao H, Roelle MJ, Chen JS, Park S, Gerdes JC (2011) Implementation and analysis of a repetitive controller for an electro-hydraulic engine valve system. IEEE Trans Control Syst Technol 19:1102–1113
5. Wang LX (1997) A course in fuzzy system and control. Prentice Hall International, Inc., Upper Saddle River
6. Merrit HE (1967) Hydraulic control system. Wiley, Hoboken
7. Chen HM, Su JP, Renn JC (2002) A novel sliding mode control of an electro-hydraulic position servo system. IEICE Trans Fundam E85-A:1928–1936

Sizing Cloud Applications with ISO/IEC 19761: A Case Study

Wen-Ming Han and Wei-Tso Chen

Abstract Despite business opportunities created by cloud software development becoming an irresistible trend, enterprises are daunted by the high complexity of managing cloud software development. Accurate cost estimations and time scheduling are essential to successfully manage cloud software development; quantification of the size of cloud software has a key role in supporting decisions that may occur. The international standard ISO/IEC 1976-1, a widely used functional-size measurement method, has the advantage of being able to be applied to real-time systems and more easily performing quantitative calculations. Using a case study method, this study guides and explains how to use ISO/IEC 1976-1 to measure the functional size of cloud software. The contributions of this research are primarily divided into the following three points: (a) introducing ISO/IEC 1976-1 to provide practical fields a systematic method to quantitatively measure the functional size of cloud software to support managerial decision-making, (b) using ISO/IEC 1976-1 as a practical guide and system for the management and applications measuring the size of cloud software, and (c) verifying the usability of ISO/IEC 1976-1 on size measurement of cloud software.

Keywords Cloud software • Software measurement • ISO/IEC 19761 • Functional-size measurement

W.-M. Han (✉)
Department of Management Information Systems, Takming University of Science and Technology, Taipei 11451, Taiwan
e-mail: wmhan@takming.edu.tw

W.-T. Chen
Graduate Institute of Information Technology and Management, Takming University of Science and Technology, Taipei 11451, Taiwan

1 Introduction

Cloud computing has become an irresistible trend for enterprises to create commercial opportunities without national boundaries. According to the market research institute International Data Corporation [1], the market for cloud services in 2015 will be 72.9 billion US dollars, nearly three-fourths of which will be accounted for by cloud software. Forrester Research's data suggest that cloud software market revenues will grow from 21.2 billion US dollars in 2011 to 92.8 billion US dollars in 2016 [2]. A Gartner survey report states that 43 % of CIOs believe that more than half of their enterprise's internal applications will turn to cloud by 2015 [3]. These information imply that cloud software will become ubiquitous.

Software metrics has become a well-known professional discipline in both academic and commercial sectors in recent years [4]. It involves quantifying the relevant elements for software development via regular measurement procedures during the analysis in order to produce meaningful information to support decision-making. The software metrics frequently used include defect density, test coverage rate, and software size. Of these, software size is the most important since it is reflective of the basic metric values used for obtaining the necessary data elements, which are used for determining derived measures (such as unit cost). In addition, this parameter facilitates objective decision-making with regard to resource allocation, cost estimates, and delivery schedule.

Before 1980s, we often used the number of lines to represent software size. But the programming style will inflate the values by 20–40% [4]. Nowadays, ISO has developed the international standards of five quantitative software sizes, including ISO/IEC 19761 [6], ISO/IEC 20926 [7], ISO/IEC 20968 [8], ISO/IEC 24570 [9], and ISO/IEC 29881 [10], of which ISO/IEC 19761 catches more attention and proves more applicable. This is because its measurement framework adopts both developers' as well as a users' point of view; it is also applicable to functional-size assessment on the commercially used system and real-time system. Therefore, many researchers adopt ISO/IEC 19761 to measure the size of various software applications [11, 12]. Unfortunately, as of now no applicable ISO/IEC 19761 has ever been developed to quantify the functional size of cloud software so as to further verify and analyze its feasibility and applicability.

2 ISO/IEC 19761

The quantitative information of software size is an important parameter to the cost and delivery schedule estimates. Ever since ISO/IEC 14143 [13] defines the design principles and structure of FSMM, to extend or develop new FSMM has become a hot issue discussed nowadays. As of now, five FSMM international standards have been developed, including ISO/IEC 19761, ISO/IEC 20926, ISO/IEC 20968, ISO/IEC 24570, and the ISO/IEC 29881, of which ISO/IEC 20926 and ISO/IEC 19761
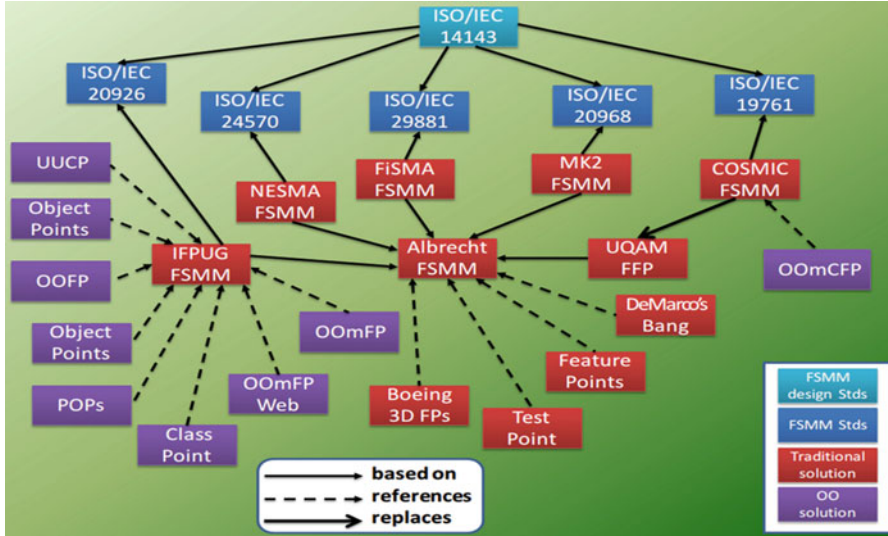
Fig. 1 The heritage of FP-like metrics in 2012

have been highly used. This is because the above two international standards have their respective dedicated organizations to push forward the organization, the training courses, and professional certification served to guide the practical application of information personnel and to maintain the measurement principles update.

ISO/IEC 20926, formerly known as Functional Point Analysis [14] developed by Albrecht in 1979, was first approved in 2006 and updated in 2009. The major difference between the standard and the functional point analysis depends on whether it bears the algorithm of GSC. In ISO/IEC 20926, the size measurement has ruled out GSC algorithm in order to avoid the size quantification of quality and technical issues and to accord with the definition of ISO/IEC 14143. The predecessor of ISO/IEC 19761, COSMIC, was developed to carry out complex logic processing function, which was first approved in 2003 and updated in 2011. The basic measurement unit is "CFP," a simplified form of "Cfsu." Figure 1 presents the heritage of FP-like metrics.

ISO/IEC 19761 is not applicable to the systems of complex mathematical algorithm nature like simulation software and self-learning software and the systems for processing continuous variables such as computer game software and musical instruments. This shortfall is similar to other four kinds of international standards. Standard ISO/IEC 19761 is applicable to and defines the functional-size measurement of the following three types of software: (1) business application software which is a type of software that is typically used to support business operation and management and requires the characteristics of managing large amount of data, such as banks, financial affairs, personnel, procurement, delivery, and manufacturing; (2) real-time software which is a type of software that is able to control or trigger a real-world event,
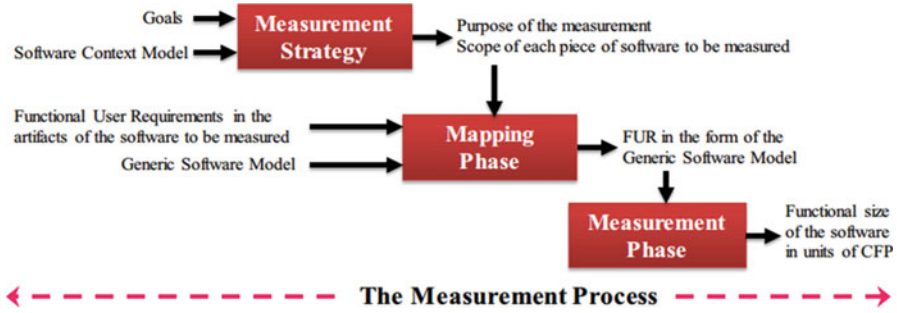
Fig. 2 The ISO/IEC 19761 measurement process

such as information appliances, elevators, engines, and aircraft; and (3) the applications of mixing above applicable systems, such as airlines' and hotels' real-time ticket reservation and purchase system. Figure 2 shows the measurement process of the ISO/IEC 19761, covering, respectively, a measurement strategy stage, a mapping stage, and a measurement stage. The main work of the various stages is outlined as follows:

The focus of measurement strategy stage is to determine the functional-size measurement scope of the software. At this stage, users must clarify and answer four important issues: (1) What is the reason to conduct this measurement? (2) Which functional features need to be included into or excluded out from the measurement range? (3) Who is the functional user? (4) How accurate level is needed for the level of measurement? When the above four issues can be clearly defined, the measurement results can then be consistently explained.

The focus of mapping stage is to make the measurement functional size of software documents (such as requirement specifications) corresponding with what ISO 19761 defined measurement framework so that the rules defined by ISO/IEC 19761 can be used to identify how many functional processes of this software.

The focus of the measurement stage is to identify all functional processes in the basic functional elements, including inflow, outflow, write out, and read. The main difference of all these four basic functional elements comes from the movement process of data group in the functional process and continuous storage media. The final total sum of all basic functional elements can then result in CFP points.

3 Case Study

When a multinational enterprise adopts a decentralized management strategy, its personnel management is usually managed by regional business units. However, in the context of time and space, the variety and heterogeneity of human resource (HR) systems also contributes to the difficulties of information exchange and application integration among different systems. For example, an enterprise cannot

Table 1 Functional requirements for this cloud software

No.	Functional description
1	Using web service manner for consistent data-exchange formats
2	Listing the group subsidiaries and regional queries
3	Data-exchange version control and journal queries
4	The automatic scheduling mechanism
5	Providing data-exchange network topology and service health signaling
6	Allowing daily data backup and mutual redundancy across units
7	Integrating regional information together as personnel basic information, list of organizational relationship, general table for role relationship, and list of levels
8	Building a trigger device for information update in a real-time manner, initiate personnel change status update, and role relationship and level change update
9	Providing real-time download and manual upload interface
10	Providing multi-language interface and conversion of various time zones
11	Using digital signature for information/data transmission encryption
12	Building access control lists to control information fields and access to the source system

grasp the personnel changes in real time and, thus, is unable to perform proper manpower adjustments for the latest manpower shifts. Therefore, to facilitate operations across five major business areas (Pan Americas, Europe, China, Australia, and newly emerging regions) and to facilitate the seamless management of personnel changes, D company is planning to construct a set of cloud-based integration personnel resource services. The personnel resource application cloud consists of the following three parts: (a) it integrates headquarters (HQ) and various BU resource information centers; (b) it creates regional service agents for conducting lease verification and service content guidelines; and (c) it provides information management systems to implement Web interfaces for platform maintenance and lease-content drafting.

When the personnel in a region change, various regional HR systems are triggered in a real-time manner to conduct data-exchange procedures, and exchange information with resource centers through Web services. Upon completion, service agents notify the application system to draft leases. The leased resources are updated, and are then used and sent to the relevant application systems (e.g., payroll systems) through automatic scheduling and transmission mechanisms. Furthermore, managers can perform system-lease management, lease-service content maintenance, health status data exchanges for queries, and information backup work through the Web interface. The requirements and size distributions of this cloud application are shown in Tables 1 and 2.

4 Conclusions and Future Work

We demonstrate the functional-size measurements of ISO/IEC 1976-1 in the cloud through a case study. In addition, we discuss the feasibility and applicability of applying the standards using an empirical approach. The R&D team of D company

Table 2 Distribution of size units

No.	Functional process name	Data movement types				CFP	%
		E	X	R	W		
1	Trigger message	1	2	0	0	3	6
2	Reply message	1	2	1	0	4	9
3	Upload change information	1	2	0	1	4	9
4	Check and inform service change	3	2	2	1	10	19
5	Reply message	1	2	0	0	3	6
6	Auto update or download	1	2	0	0	3	6
7	Reply message	1	3	0	1	5	9
8	Maintain contract	2	1	1	1	5	9
9	Inform contract enable	1	2	1	0	4	7
10	Reply service request	1	2	0	0	3	6
11	Auto upload or download	1	2	0	0	3	6
12	Reply message	1	3	0	1	5	8
Total		15	27	5	5	52	100

for this case study holds a positive attitude toward the application of the ISO/IEC 1976-1 measurement mechanism. Moreover, the firm plans to include the ISO/IEC 1976-1 measurement mechanism in the original standard operating process to facilitate the application of all company R&D projects. Finally, the accuracy of measurement must build on the integrity of the requirement documents. In other words, incomplete, vague, and improper requirement documents are confusing. The application deviation of new technologies gradually converges and improves through continuous use and experience feedback. However, for the following measurement and analysis applications, it is fundamental to write a strong requirement specification paper (e.g., the IEEE 830 format).

References

1. International Data Corporation (2011) Worldwide and regional public IT cloud services 2011–2015 forecast, pp 1–32
2. Forrester Research (2011) Sizing the cloud: understanding and quantifying the future of cloud computing
3. Gartner. Gartner outlines cloud computing trends through to 2015, http://midsizeinsider.com/en-us/article/gartner-outlines-cloud-computing-trends
4. Fenton NE, Pfleeger SL (1998) Software metrics: a rigorous and practical approach. PWS Publ., Boston
5. Jones C (2008) A short history of lines of code (LOC) metrics. Capers Jones & Associates LLC, Narragansett, pp 1–12
6. ISO/IEC: 19761 (2011) Software engineering – COSMIC-FFP: a functional size measurement method, pp 1–14

7. ISO/IEC: ISO/IEC 20926 (2009) Software and systems engineering – software measurement – IFPUG functional size measurement method, pp 1–24
8. ISO/IEC: ISO/IEC 20968 (2002) Software engineering – Mk II function point analysis – counting practices manual, pp 1–93
9. ISO/IEC: ISO/IEC 24570: (2005) Software engineering – NESMA functional size measurement method version 2.1 – definitions and counting guidelines for the application of function point analysis, pp 1–124
10. ISO/IEC: ISO/IEC 29881 (2010) Information technology – software and systems engineering – FiSMA 1.1 functional size measurement method
11. Santillo L (2007) Seizing and sizing SOA applications with COSMIC function points. In: Proceedings of the software measurement European forum, Rome, 9–11 May 2007
12. Software Engineering Research Laboratory (2003) Software functional size with ISO 19761: COSMIC-FFP measurement method – proposed measurement etalon: C-registration system, Université du Québec (Canada), pp 1–47
13. ISO/IEC: ISO/IEC 14143-1 (2007) Information technology – software measurement – functional size measurement – part 1: definition of concepts, pp 1–6
14. Albrecht AJ (1979) Measuring application development productivity. In: Proceedings of the joint SHARE/GUIDE/IBM symposium on application development, Monterey, 1979, pp 83–92

Development of a Fuzzy-Control-Based Battery Charging Technique for Li-Ion Battery Module for Light Electrical Vehicles

Yi-Hsun Chiu, Chun-Liang Liu, Yi-Feng Luo, Jung-Hsien Chen, and Yi-Hua Liu

Abstract The island nation of Taiwan is perfectly suited to design and develop light electric vehicles (LEV) for use in urban areas. In this chapter, a fuzzy-control-based battery charger is proposed. The proposed charger takes the temperature and state-of-charge (SOC) information into account and adjusts the charging current accordingly. According to the experimental results, the performance of the proposed charger can be improved.

Keywords Light electrical vehicle • Battery charger • Fuzzy control

1 Introduction

Today's concerns about the environment, particularly noise and exhaust emissions, coupled with new developments in batteries make electric vehicles (EV) favorable. The island nation of Taiwan is perfectly suited to design and develop light electric vehicles (LEV) for use in urban areas. Lithium-ion (Li-ion) batteries have emerged as the major power source for today's LEV because they can offer advantages such as high energy density, low maintenance requirement, high open-circuit voltage (OCV), low self-discharge rate, and lack of memory effect. To make full use of the battery, high-performance charger is often required. The traditional method of

Y.-H. Chiu (✉) • C.-L. Liu • J.-H. Chen • Y.-H. Liu
Department of Electrical Engineering, NTUST, Taipei, Taiwan, R.O.C.
e-mail: D10107203@mail.ntust.edu.tw

Y.-F. Luo
Division for Biomedical and Industrial IC Technology, Green Electronics Design
and Application Department, ICL, ITRI, Hsinchu, Taiwan, R.O.C.

charging Li-ion batteries is to apply constant current followed by a constant voltage. This method is often called constant current-constant voltage (CC-CV) charging method. Constant current is applied at the beginning of a battery charging when the battery voltage is low. When the battery voltage rises to a predefined value (4.1 or 4.2 V), the charger switches to constant voltage until the charging current decreases to a predetermined small value. During the constant-voltage phase, current drops exponentially due to the sum of battery resistance and any resistance in series with the battery. Therefore, full charge takes a long time. Moreover, the constant-voltage charging reduces the cycle life of the battery.

The performance and life span of Li-ion batteries are closely related to the quality of their charger [1–3]. Therefore, an advanced charger is essential for Li-ion batteries to achieve shorter charging time and longer cycle life [4–6]. The main objective of an advanced charger includes high charging efficiencies and improved battery cycle life. In this chapter, a fuzzy-control-based battery charger (FCBBC) which can be embedded into the Li-ion battery pack for LEV is proposed [7, 8]. The proposed embedded battery charger can charge the Li-ion battery pack using the commercially available adaptor as the power source and charge the battery according to the chemical requirement. The hardware and firmware parts of the proposed system will be described in detail. In this chapter, the power stage is implemented using the boost converter and a temperature-sensing circuit. The software consists of a digital compensator, a digital filter, and a fuzzy controller and is realized using the dsPIC33FJ16GS502 microcontroller from Microchip Corp. The proposed FCBBC takes the temperature and state-of-charge (SOC) information into account and adjusts the charging current accordingly. In order to validate the effectiveness of the proposed system, experiments on Li-ion battery module for LEV are carried out. According to the experimental results, the performance of the proposed charger can be improved.

2 Hardware Configuration

Figure 1 shows the block diagram of the proposed charger system. In Fig. 1, the input power of the proposed Li-ion battery charger is a commercially available adaptor for notebook computer, and the battery pack used is a 52 V, 17.6 Ah lithium-ion battery module for light electric vehicles. In Fig. 1, low-voltage DC link (adaptor output voltage) is converted into high-voltage DC to charge the battery pack by the power converter. The gating signals of the power converter are supplied by the dsPIC microcontroller from Microchip Corp. The charging current is controlled by the proposed fuzzy-control-based charging algorithm.

Figure 2 shows the hardware configuration of the proposed charger. In Fig. 2, the dsPIC33FJ16GS502 microcontroller from Microchip Corp. is used to implement
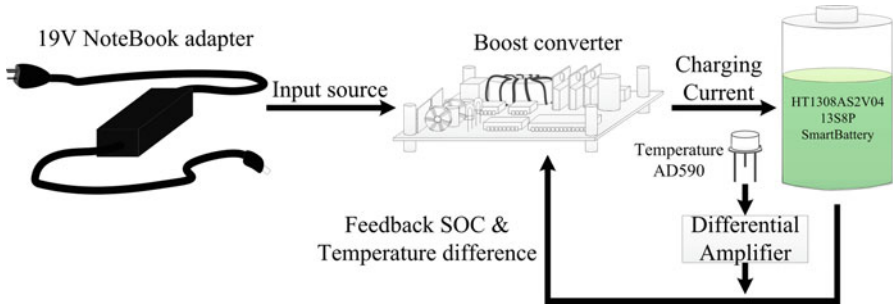
Fig. 1 Block diagram of the proposed charger
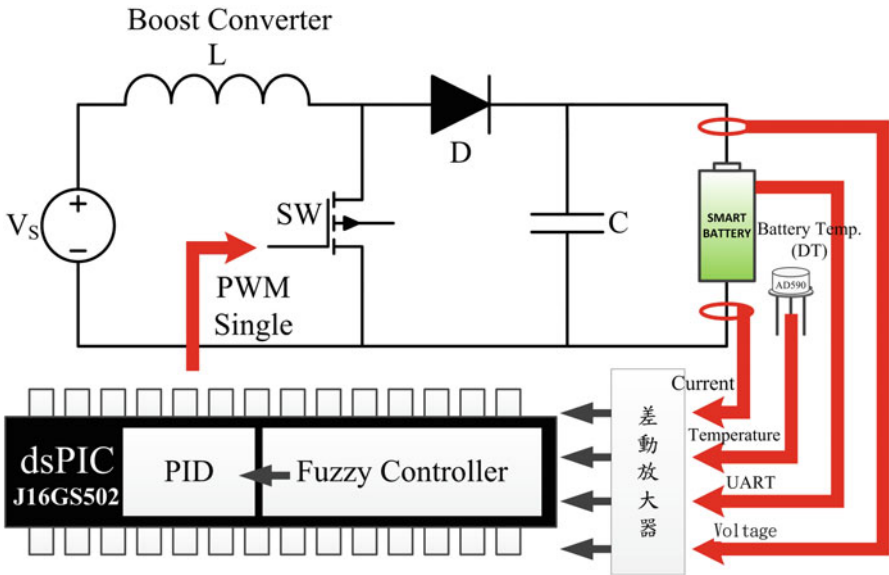
Fig. 2 Hardware configuration of the proposed charger

the charging algorithm, provide the required gating signals for the power switches in the power source, and then gather and analyze data from the data acquisition circuit. PWM modulation strategies and interfacing IC driving signal are also realized using the dsPIC chip to achieve better performance. The proposed dsPIC controller attempts to meet the flexibility, ease of use, and low cost requirements for most consumers and industrial applications. From Fig. 2, the whole system can be divided into three major parts: input/output interfacing unit, digital control unit, and energy conversion unit. Detailed descriptions about each unit will be given in the following sections:

(a) Input/output interfacing unit: I/O interfacing unit includes display circuits which display the charger status; feedback circuit which is used to measure the voltage, current, temperature, and SOC information from the output side (battery side) of the energy conversion unit; and signal conditioning circuits which performs amplification and range adaptation on feedback signals.

(b) Main control unit: main control unit controls the voltage/current command according to the measured data. dsPIC gathers and analyzes battery status data (voltage, current, temperature, and SOC). After obtaining the required charging status, necessary charging current is then determined through the proposed fuzzy controller. The digital PID control algorithm is also implemented in the dsPIC controller. dsPIC controller computes the gating signals of power converter according to the feedback current command and current feedback information.

(c) Energy conversion unit: energy conversion unit is used to supply the electric power to Li-ion batteries. As shown in Fig. 2, a simple boost-type DC/DC converter is used as the charging unit. By adequately controlling the PWM gating signal, the energy conversion unit can transfer the required energy to the Li-ion battery pack.

3 Software Configuration

In this section, the software configurations of the proposed charging system will be provided. Figure 3 shows the software flowchart of the proposed controller. From Fig. 3, the main tasks of the dsPIC controller include:

- Performing digital filter and digital controller
- Providing the gating signals of boost converter
- Performing fuzzy controller
- Controlling the interfacing circuits

The digital filter and digital controller are performed every 10 μs. Therefore, the switching frequency of the proposed power stage is 100 kHz. The digital filter used in the proposed system is a 16-order finite impulse response (FIR) filter. The equation describing a FIR filter can be expressed as in (1):

$$y[n] = \sum_{k=0}^{T-1} a_k x[n-k] \tag{1}$$

where x is the filter input, y is the filter output, and a_k is the corresponding coefficient of the designed FIR filter.
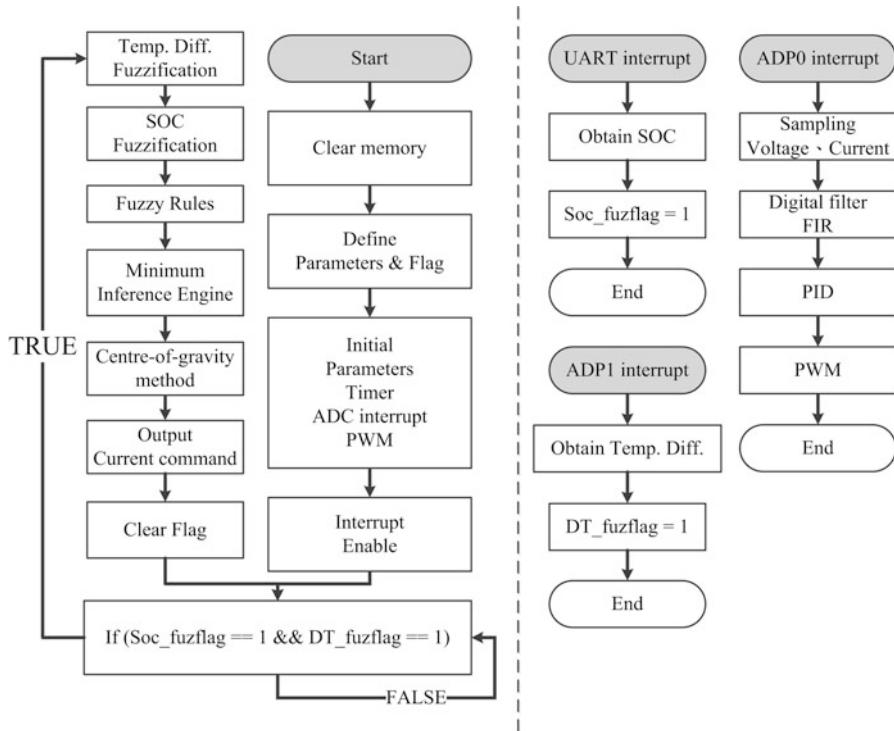
Fig. 3 Software flowchart of the proposed charger

The digital controller is used to calculate the required PWM command. A simple PID controller is utilized in this chapter and the PID control algorithm can then be designed as in (2):

$$u(n) = K_P \times e(n) + K_I \times \sum_{i=0}^{n} e(i)T + K_D \times \frac{e(n) - e(n-1)}{T} \tag{2}$$

where $e(n)$ is the error signal, T is the sampling time, and $u(n)$ is the output of the PID controller.

To achieve higher charging efficiency, a fuzzy controller is used in this chapter to determine the charging-current setting level. The fuzzy controller is calculated every 1 s. Figure 4 shows the block diagram of the implemented fuzzy controller. In this chapter, the input of the fuzzy controller is the temperature rise T and the state of charge (SOC). The membership function of the inputs T and SOC for the proposed charger is illustrated in Fig. 5. Figure 5a shows the membership function of the input variable T and Fig. 5b depicts the membership
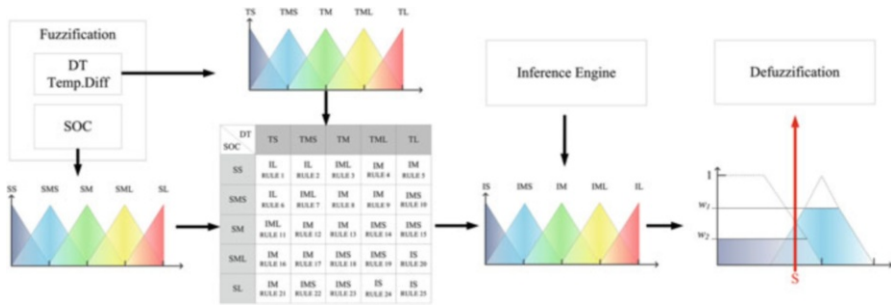
Fig. 4 Block diagram of the implemented fuzzy controller
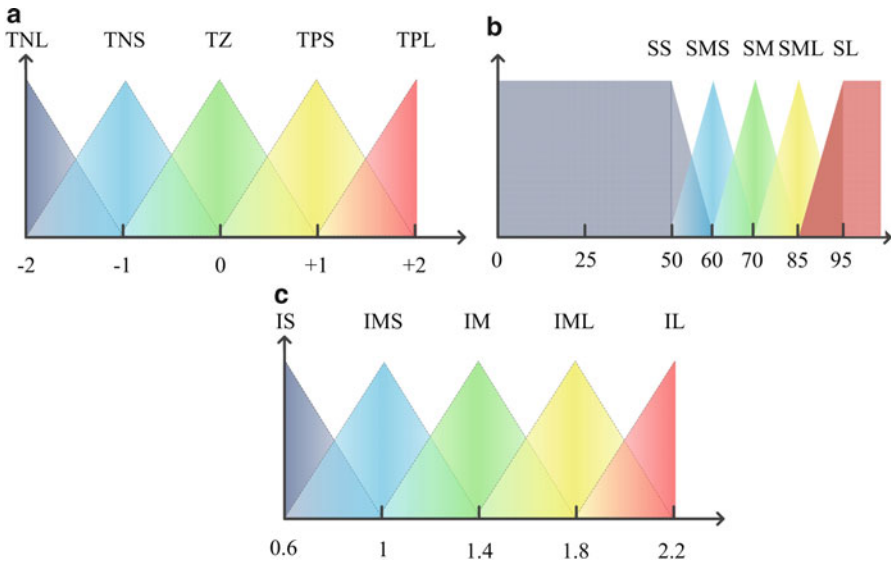
Fig. 5 Membership functions of (**a**) temperature T, (**b**) SOC,and (**c**) output current I_o

function of the input variable SOC, respectively. Figure 5c is the membership function of the output current command. The membership function T, SOC, and I_o are all in triangular form.

From Fig. 5, each of the input variables T and SOC is mapped into five different linguistic values. Therefore, the proposed fuzzy rule will consist of 25 different rules. The complete set of fuzzy control rules for the proposed system is tabulated in Fig. 6. The defuzzification method used in this chapter is the commonly used center of gravity method and is shown in (3):

DT SOC	TS	TMS	TM	TML	TL
SS	IL RULE 1	IL RULE 2	IML RULE 3	IM RULE 4	IM RULE 5
SMS	IL RULE 6	IML RULE 7	IM RULE 8	IM RULE 9	IMS RULE 10
SM	IML RULE 11	IM RULE 12	IM RULE 13	IMS RULE 14	IMS RULE 15
SML	IM RULE 16	IM RULE 17	IMS RULE 18	IMS RULE 19	IS RULE 20
SL	IM RULE 21	IMS RULE 22	IMS RULE 23	IS RULE 24	IS RULE 25

Fig. 6 The complete set of fuzzy control rules for the proposed system

$$y = \frac{\sum_{i=1}^{n} W_i B_i}{\sum_{i=1}^{n} W_i} \tag{3}$$

where W_i is the inference result of rule i, B_i is the corresponding output of rule i, and y is the output.

4 Experimental Results

In order to validate the effectiveness of the proposed method, experiments are carried out on commercially available Li-ion battery packs. Figure 7 shows the measured full-load charging-current waveform of the proposed system when battery pack voltage is at maximum (55 V) and minimum (39 V). From Fig. 7, the proposed charger can provide stable charging currents. Figure 8 shows the measured charging current profile under different SOC value. From Fig. 8, the proposed charger can adapt the charging current according to the measured temperature and SOC value. Also from Fig. 8, the charging current will decrease when the measured temperature rises; this will improve the charging efficiency.
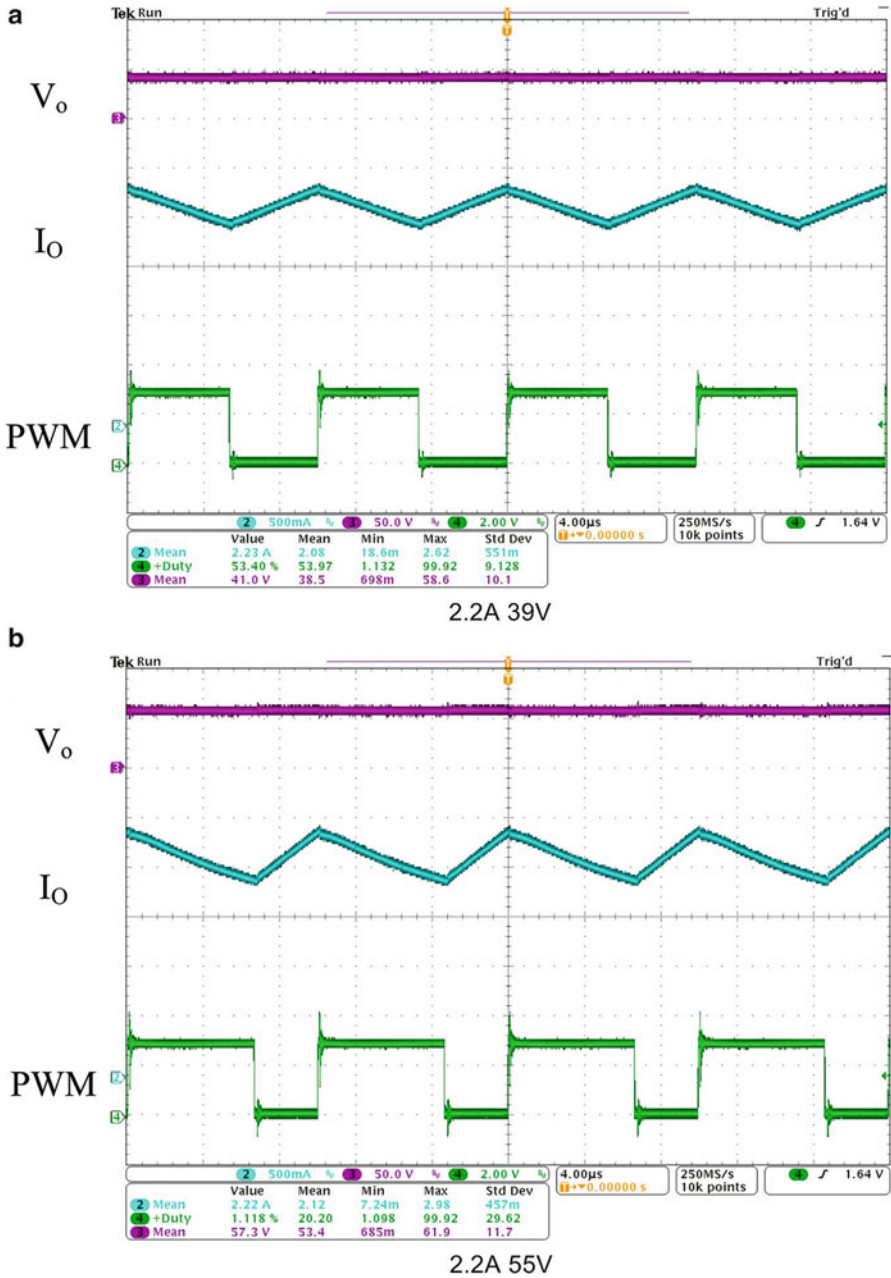
Fig. 7 Measured full load charging current waveform of the proposed system (CH2:0.5 A/div, CH3:50 V/div, CH4:2 V/div)
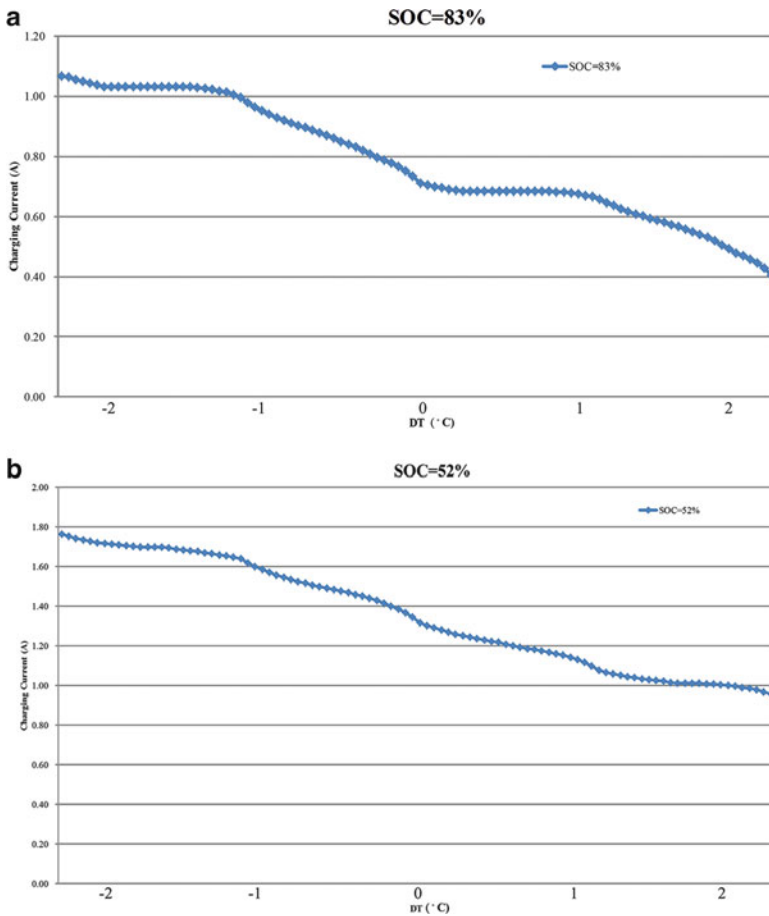
Fig. 8 Measured charging-current profile under different SOC values

5 Conclusion

In this chapter, a fuzzy-control-based battery charger is proposed. The proposed charger utilizes commercially available adaptor as the power source, therefore increasing the convenience of the propose charger. The proposed fuzzy-control algorithm takes the temperature and state-of-charge (SOC) information into account; the charging current will decrease when the measured temperature or battery SOC rises. Therefore, the charging efficiency can be improved.

References

1. Chen L-R, Hsu RC, Lii C-S (2008) A design of a grey-predicted Li-ion battery charge system. IEEE Trans Ind Electron 55:3692–3701
2. Wen S (2009) Cell balancing buys extra run time and battery life. Texas Instrum Analog Appl J
3. Malekjamshidi Z, Jafari M (2009) Design, simulation and implementation of an intelligent battery charging system. IEEE Comput Elect Eng 2:242–246
4. Chen LR (2007) A design of an optimal battery pulse charge system by frequency-varied technique. IEEE Trans Ind Electron 54:398–405
5. Liang-Rui C, Liu C-S, Chou J-J (2009) Improving phase-locked battery charger speed by using resistance-compensated technique. IEEE Trans Ind Electron 56:1205–1211
6. Chen L-R, Chen J-J, Chu N-Y, Han G-Y (2008) Current-pumped battery charger. IEEE Trans Ind Electron 55:2482–2488
7. Cheng M-W, Wang S-M, Lee Y-S Hsiao S-H (2009) Fuzzy controlled fast charging system for lithium-ion batteries. IEEE Power Electron Drive Syst, 1498–1503
8. Hsieh GC, Chen LR, Huang KS (2001) Fuzzy-controlled Li-ion battery charge system with active state-of-charge controller. IEEE Trans Ind Electron 48:585–593

Low-Cost and High-Speed Eye Tracker

Chi-Wu Huang, Zong-Sian Jiang, Wei-Fan Kao, and Yen-Lin Huang

Abstract This chapter presents the integration of hardware and open-source software to build a low-cost (US$100) and high-speed eye tracker. With minor modifications of PlayStation 3 Eye (PS3 Eye) camera as the main hardware component and the proper coding adjustments in software interface to CL Eye Platform Driver, offered by open-source Code Laboratories, our low-cost eye tracker runs at the speed of 187 frames per second (fps) in 320 × 240 resolution, which is at least three times faster than the ordinary low-cost eye trackers usually running between 30 and 60 fps. We have also developed four application programs, which are ISO 9249-Part 9, Gaze Replay, Heat Map, and the Areas of Interest (AOI). Our design is then compared with the low-cost KSL-240 and commercially available high-price (over US$5,000) Tobii under ISO 9249-Part 9 eye-tracking test. The test performance favored ours in terms of response time and correct response rate.

Keywords Eye tracker • Open source • Glint • Bright pupil • Dark pupil • Fixation • Saccade

C.-W. Huang
Department of Industrial Education, National Taiwan Normal University,
Taipei 10610, Taiwan

Z.-S. Jiang (✉) • W.-F. Kao • Y.-L. Huang
Department of Applied Electronics Technology, National Taiwan Normal University,
Taipei 10610, Taiwan
e-mail: q7049527@hotmail.com

1 Introduction

1.1 Eye-Tracker Overview

An eye tracker is a device used to analyze eye movements, as the eye scans the environment or fixates on particular objects in the scene, and to simultaneously localize the eye position in the image and track its movement from one location to another over time for determining the gaze direction. Eye-tracking technology is a specialized application of computer vision to do such analyses. However, this technology needs sophisticated software to process each image, captured by a high-speed camera, so that the gaze direction (estimated by the pupil center) is obtained, and the mapping from the gaze direction in the image to the screen is calculated to predict the gaze location on the screen. The mapping between the image and the screen is depicted in Fig. 1. The original gazing point A on screen, captured in the image I, constitutes vector GP, which is mapped back to obtain vector OS on the screen. The coordinates of $S(sx,sy)$ and mapping error Err° (in angle degree) between S and A can be calculated from the coordinates of $G(x,y)$. The mapping calculation is discussed in more detail in the next section [1].

1.2 Cameras and Open-Source Software

Observing from the eye-tracker overview, the high-speed camera and the R&D in software integration might be the main costs to keep the commercial eye-tracker
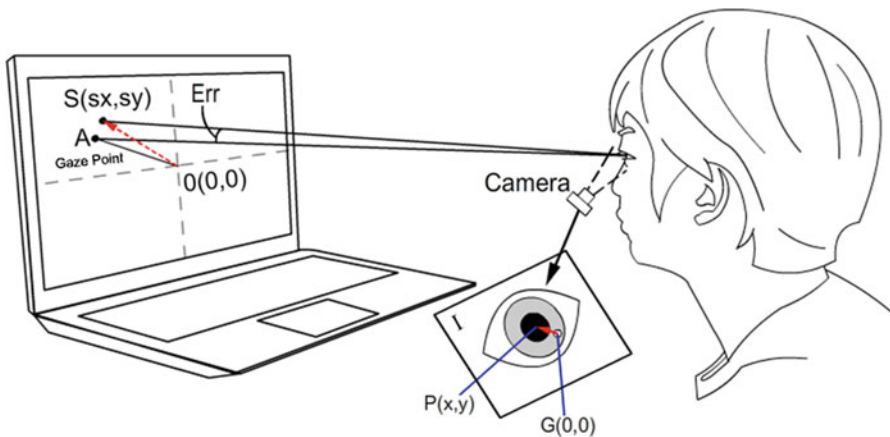
Fig. 1 Mapping from the pupil center to screen

Table 1 Low-cost and commercial eye trackers

Eye tracker	Hardware	Software	Frame rate (fps)	Price
Hiley et al. [4]	*QuickCam Pro 4000*	*MATLAB*	30	US$130
DIY eye tracker [5]	*MS LifeCam VX-1000*	*MATLAB, ITU Gaze*	30	€30
KSL-240 [6]	*Sony PS3 Eye cam*	*OGAMA*	125	Not available
Tobii 1750	*Tobii Corporation*	*Tobii Corporation*	50	Over US $5,000
Ours	*Sony PS3 Eye cam*	*CL Eye Platform Driver, AForge.NET, OpenCV*	187	US$100

devices at a high price in the market. However, rather cheap commercial over-the-shelf (COTS) cameras and open-source software are now available in the web; some of these are listed as follows:

COTS camera	*QuickCam Pro 4000, MS LifeCam VX-1000, Sony PS3 Eye cam*
Open source	*ITU Gaze* [2]*, CL Eye Platform Driver* [3]*, AForge.NET, OpenCV*

By minor modifications of the COTS camera and integration with open-source software, some low-cost eye-tracker devices have been developed, as shown in Table 1.

This chapter presents a low-cost (US$100) eye tracker using Sony PS3 Eye camera combining the open-source Code Laboratories [3], which achieved high-speed image capturing of 187 frames per second (fps); a more detailed description is given in the next section. The chapter is organized as follows. Section 2 describes the hardware configuration and background technology. Section 3 describes the integration software. Section 4 presents the application examples. Finally, Section 5 presents the conclusion as well as future works.

2 Hardware Configuration and Background Technology

2.1 Hardware Configuration

The Sony PS3 Eye is reconstructed to become infrared (IR) sensitive only and two IR-LEDs (850 nm) are appended for the dark pupil tracking process. USB 2.0 was used for the communication with the computer. Figure 2 shows our glass-like head-mounted tracking hardware.
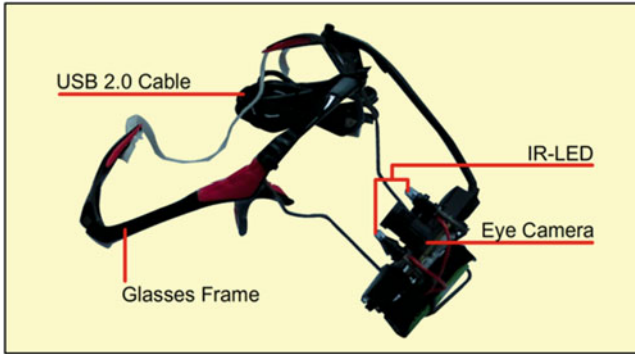
Fig. 2 Modified Sony PS3 eye-tracker hardware
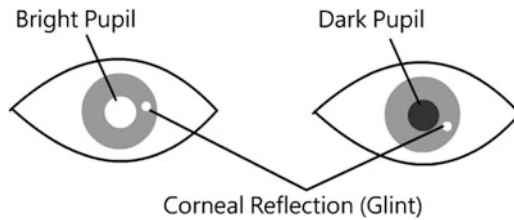
Fig. 3 Bright pupil, dark pupil, and corneal reflection of an infrared camera image

Fig. 4 Three glint–pupil difference vectors (*GP*s)

2.2 Background Technology

Glint, Bright Pupil, and Dark Pupil. The light reflected from the IR-LED beside the camera caused a white speck on the iris called glint. If the IR light source coax with the camera, most of the light is reflected back, causing a bright pupil; otherwise the pupil is rather dark [5] as shown in Fig. 3.

Glint–Pupil Difference Vector. A camera was used to track the location of the pupil center with reference to the glint of the IR light. Since the cornea of an eye is nearly spherical, the position of the glint remained more or less fixed as an eye moves to focus on different points of regard (POR) and the difference vector between glint and pupil is resulted as shown in Fig. 4. Eye tracker uses these difference vectors

(*GP*s) in the image to determine the gaze vectors (*OS*s) on screen; a more detailed description of screen mapping is presented next.

Screen Mapping. After the point $P(x,y)$ is calculated in the image, our design used the following least-square polynomial equations to map the estimated gaze point S (sx,sy) on the screen as shown in Fig. 1:

$$sx = a_0 + a_1x + a_2y + a_3xy + a_4x^2 + a_5y^2 \qquad (1)$$

$$sy = b_0 + b_1x + b_2y + b_3xy + b_4x^2 + b_5y^2 \qquad (2)$$

Calibration. The coefficients a_0–a_5 and b_0–b_5 of the aforementioned equations have to be determined before tracking is started. Therefore, at the beginning of the eye-tracking process, the user is asked to look at a set of known position points on the screen, to make the values of (sx,sy) and (x,y) become known, in Eqs. 1 and 2, such that the coefficients a_0–a_5 and b_0–b_5 can all be solved.

3 Integration Software

A sophisticated software system should be developed to control the camera operation in accordance with the related fast image capturing, glint–pupil detection, calibration, and mapping calculation. The above-mentioned open source offered such integrating services.

With minor modifications of the PS3 Eye camera as the main hardware component and proper coding adjustments in the software interface to the CL Eye Platform Driver, offered by the open-source Code Laboratories [3], our low-cost eye tracker runs at the speed of 187 fps in 320 × 240 resolution, which is at least three times faster than the ordinary low-cost eye trackers usually running between 30 and 60 fps [4, 5].

4 Application Examples

4.1 High-Speed Demonstration in ISO Test

ISO test requires that if the participant can make eye movement between two predefined locations on screen within 2,000 ms, it achieves a correct response trial and its response time is recorded. There are 5 sessions with 16 trials each. The rate of correct response trials and its average (correct) response time are displayed in Fig. 5.
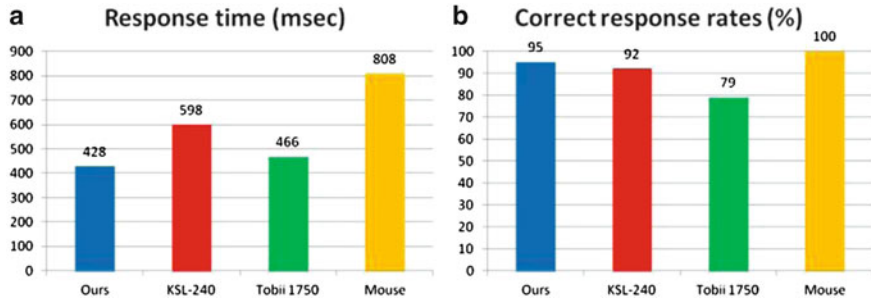
Fig. 5 (**a**) Response time comparison, (**b**) Correct response rate comparison
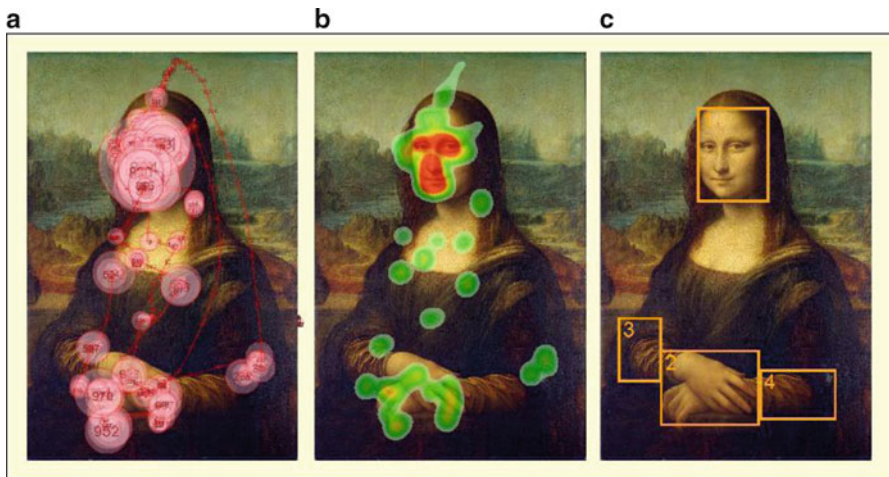
Fig. 6 (**a**) Gaze replay, (**b**) Heat map, (**c**) AOI

After having developed the ISO test application program, our design was then compared with the low-cost KSL-240 and commercially available high-price (over US$5,000) Tobii under the ISO 9249-Part 9 eye-tracking test [4, 6]. The test performance favored ours in terms of response time and correct response rate as shown in Fig. 5.

4.2 Gaze Replay, Heat Map, and AOI

The applications Gaze Replay, Heat Map, and Areas of Interests (AOI) were also developed, whose performances are explained next.

Gaze Replay. Gaze Replay is able to display dynamically the sequence of gaze path as shown in Fig. 6a, where the circle denotes the gaze position while the size of circle is proportional to the gaze time. The numbers in all circles represent their timing sequence.

Heat Map. Heat Map is able to display the total gaze time at each gaze area using "d" magnitude levels as shown in Fig. 6b. The basic gaze unit is 5 ms. By using "d = 3" in this experiment, the area obtained the maximum number of accumulated gaze units assigned red color, the minimum assigned green, and the middle assigned yellow. The number of "d" and the related colors are users' choices.

AOI. AOI is able to select the areas according to the user's interests for further processing by using squares, as shown in Fig. 6c, where the data in each AOI are then transformed to Microsoft Excel for further processing in terms of saccade and fixation.

5 Conclusion and Future Works

We have been building a low-cost and high-speed eye tracker, which is a sort of hardware and software integration, and some application programs have been running in the system. Three application results are displayed in Figs. 5 and 6. Currently, we are developing a tracking accuracy application test.

The future work will include head movement estimation. This will require the development of control software involving the complicated issues concerning the measurement of distances and angles through image processing [8]. However, if it is successfully implemented, then the chin rest used in the experiments would become unnecessary.

References

1. Hansen DW, Ji Q (2010) In the eye of the beholder: a survey of models for eyes and gaze. IEEE Trans Pattern Anal Mach Intell 32(3):478–500
2. ITU GazeGroup. http://www.gazegroup.org
3. Code Laboratories. http://codelaboratories.com
4. Hiley JB, Redekopp AH, Fazel-Rezai R (2006) A low cost human computer interface based on eye tracking. In: Engineering in medicine and biology society, 2006. EMBS'06. 28th annual international conference of the IEEE, New York City, NY
5. Kowalik M (2011) Do-it-yourself eye tracker: eye tracking accuracy. In: Wimmer M, Hladůvka J, Ilčík M (eds) The 15th central European seminar on computer graphics. University of Technology, Institute of Computer Graphics and Algorithms, Vienna, pp 67–73
6. Lee S, Shon Y-J, Jung Y-M, Chang M-S, Kim SY, Kwak H-W (2011) Verification of the low-cost eye-tracker KSL-240. In: 2011 5th international conference on new trends in information science and service science, Macao, pp 90–92
7. Zhang X, MacKenzie IS (2007) Evaluating eye tracking with ISO 9241 – part 9. In: HCI International 2007. Springer, Heidelberg, pp 779–788
8. Zhu Z, Ji Q (2007) Novel eye gaze tracking techniques under natural head movement. IEEE Trans Biomed Eng 54(12):2246–2260

Using Hedge Algebra to Control Varied-Parameter Object

Trung Kien Ngo, Duy Tien Nguyen, Tuan Quoc Duong, Huy Ngoc Vu, and Tan Duc Vu

Abstract This chapter presents a controller using Hedge Algebra to control nonlinear object. Then, it opens the possibility for a reasonable application of new theory in the design of automation systems in the industry, suitably for nonlinear objects with variable parameters. The method with a new flexible tool based on quantifying linguistic domains can calculate with higher accuracy than the fuzzy controller.

Keywords Hedge algebra • Fuzziness measures • Varied-parameter object

1 Introduction

The design of the controller tracking the direction of the sun in order to achieve high performance has been much researched by scientists with many controlling methods [1, 2]. The quality of the system has been improved by applying the controllers such as PID controller and fuzzy controller, and each controller has its own advantage and is calculated for a specific working mode of the system, respectively [1, 3]. However, a high-quality controller needs to ensure good controlling quality when the parameters of objects constantly vary. By applying Hedge Algebra, a new simple flexible and high-accuracy calculation tool, this chapter offers a control method to ensure constantly controlling quality for solar tracking system when the moment of inertia J and armature resistor R_{u} are varied parameters.

T.K. Ngo (✉) • D.T. Nguyen • T.Q. Duong • H.N. Vu • T.D. Vu
Department of Electrical Engineering, Thai Nguyen University of Technology,
Thai Nguyen, Vietnam
e-mail: trungokien@tnut.edu.vn

2 Using Hedge Algebra for Control Problem

2.1 Introduction of Hedge Algebra

Hedge Algebra is the development basing on the logic perception of linguistics [4].

The input/output relationship in fuzzy logic must define membership functions discontinuously, whereas Hedge Algebra creates an algebraic structure in terms of functions of linguistic input/output variables.

Example

Consider a set of linguistic intervals which is a linguistic domain of TEMPERA-TURE truth variable including T = dom(TEMPERATURE) = {Large, Small, very Large, very Small, more Large, more Small, approximately Large, approximately Small, little Large, little Small, less Large, less Small, very more Large, very more Small, very possible Large, very possible Small,...}.

Then the linguistic domain T = dom(TEMPERATURE) can be considered as an algebraic structure AT = (T, G, H,≤), where T is the based set of AT, G is the set of generators (Large, Small), H is the set of linguistic hedges (Very, Little, Less...), and ≤ is an semantically ordering relation (Small ≤ Large, more Large ≤ very Large...).

Definition 1 A given *HA: AT = (T, G, H, ≤), f: T →* [0, 1] is the set of semantic quantifying mapping (SQM) of *AT* if $\forall h, k \in H+$ or $\forall h, k \in H-$ and $\forall x, y \in T$; then

$$\left|\frac{f(hx) - f(x)}{f(kx) - f(x)}\right| = \left|\frac{f(hy) - f(y)}{f(ky) - f(y)}\right| \tag{1}$$

Considering intervals (*Large, very Small...*) and according to the viewpoint of *HA*, fuzziness can be defined quite clearly basing on the size of the set $H(x)$ shown in Fig. 1.

A given semantic quantifying mapping *f* of *X* and considering $\forall x \in$ X, fuzziness of *x* can be measured by the diameter of $f(H(x)) \subseteq$ [0, 1].

Definition 2 Fuzziness measures
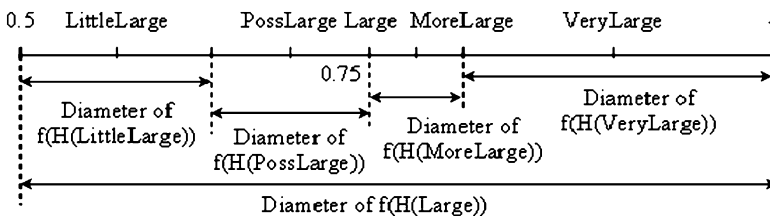
Fig. 1 Fuzziness of linguistic intervals

A function $f_m: T \to [0, 1]$ is said to be a fuzziness measure if $f_m(c^-) = \theta > 0$ and $f_m(c^+) = 1 - \theta > 0$, whereas c^- and c^+ are negative and positive generating elements. Assume set of hedges $H = H + \cup H-$, $H- = \{h_1, h_2 \dots, h_p\}$ with $h_1 > h_2 > \dots > h_p$, $H+ = \{h_{p+1}, h_{p+2}, \dots, h_{p+q}\}$ with $h_{p+1} < h_{p+2} < \dots < h_{p+q}$. Then $\forall x, y \in T$, $\forall h \in H$, $f_m(hx)/f_m(x) = f_m(hy)/f_m(y)$. This equation does not depend on specific elements and it is called the fuzziness measure of the hedge h and denoted by $\mu(h)$.

Clause 2.1 Propositions of $f_m(x)$ and $\mu(h)$

$$f_m(hx) = \mu(h)f_m(x), \quad \forall x \in T \tag{2}$$

$$\sum_{i=1}^{p+q} f_m(h_i c) = f_m(c), \quad \text{with } c \in \{c^-, \ c^+\} \tag{3}$$

$$\sum_{i=1}^{p+q} f_m(h_i x) = f_m(x) \tag{4}$$

$$\sum_{i=1}^{p} \mu(h_i) = \alpha, \ \sum_{i=p+1}^{q} \mu(h_i) = \beta \text{ with } \alpha, \beta > 0 \text{ and } \alpha + \beta = 1 \tag{5}$$

Clause 2.2 Construction of SQM Based on the Basics of Fuzziness Measure of Hedges

Assume fuzziness measures of hedges $\mu(h)$ and fuzziness measure intervals of base terms $f_m(c^-), f_m(c^+)$ are given and θ is the neutral terms.

A semantic quantifying mapping v of T is constructed as follows with $x = h_{im} \dots h_{i2} h_{i1} c$:

$$v(c^-) = \theta - \alpha f_m(c^-), v(c^+) = \theta + \alpha f_m(c^+), f_m(x) = f_m(h_{im} \dots h_{i2} h_{i1} c)$$
$$= \mu(h_{im}) \dots \mu(h_{i2}) \mu(h_{i1}) f_m(c),$$
$$v(h_j x) = v(x) + \text{sgn}(h_j x)$$
$$\times \left[\sum_{i=j}^{p} f_m(h_i x) - \frac{1}{2}(1 - \text{sgn}(h_j x) \, \text{sgn}(h_{p+q} h_j x)(\beta - \alpha)) f_m(h_j x) \right] \text{if } j < p$$
$$v(h_j x) = v(x) + \text{sgn}(h_j x)$$
$$\times \left[\sum_{i=p+1}^{j} f_m(h_i x) - \frac{1}{2}(1 - \text{sgn}(h_j x) \text{sgn}(h_{p+q} h_j x)(\beta - \alpha)) f_m(h_j x) \right] \text{if } j > p \tag{6}$$

2.2 Hedge Algebra-Based Controller

From theories of HA, the design of a Hedge Algebra-based controller (HAC) include the following steps:

Step 1, Semantization: determining the input variable, state variable, control variables (output variables), and the working range of variables. Identifying calculated conditions (choosing the calculated parameters of HA). Calculating the values of semantic quantifying of input variable, state variable, and control variable (apply hedges on the working range of the variables).

Step 2, Semantic Quantifying Mappings (*SQMs*): changing fuzzy control rules to control rules with semantic quantifying parameters of HA. Solving the approximated problems based on HA to determine the semantic quantifying of control states. Combining the semantic quantifying values of controls and building semantic quantifying curve.

Step 3, Desemantization: basing on the initial conditions of the control problem to solve semantic quantifying curve interpolation and determine the real control value.

3 Design the HA-Based Controller to Control Solar Tracking System

3.1 Model of Solar Tracking System

The system (Fig. 2a) includes a curved reflecting mirror, heat collecting pipe, sunlight receiver, and drive system. Sunlight receiver has two light sensors, CB1 and CB2 mounted on the solar mirror, and they are arranged to track the sun; each sensor is placed in a cylindrical tube. The output signal of each sensor is associated with a differential amplifier. Output voltage (corresponding to the deviation from the applied voltage) determines the feedback response used as input variables for the controller to generate the desired control parameters. Hence, controlling the speed and direction for the DC motor is suitable. This control system uses a motor
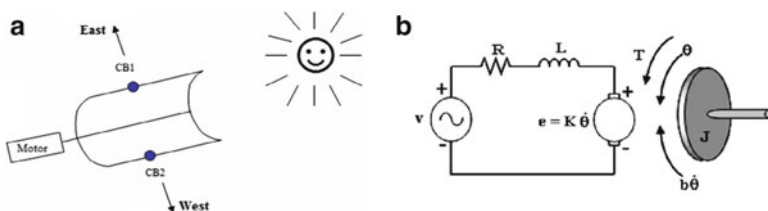
Fig. 2 The solar tracking system: the system model (**a**) and the DC motor (**b**)

to adjust the direction of rotation of the mirror to control DC motor position. Position control of DC motor's model is illustrated in Fig. 2b.

Differential equation describing Fig. 2b is as follows:

$$\frac{L}{K}\dddot{\theta}(t) + \frac{LB + RJ}{K}\ddot{\theta} + \frac{BR + K^2}{K}\dot{\theta} = v(t) \tag{7}$$

3.2 Design the FLC, HAC, and HAC1

Design a PD-fuzzy controller and two HACs to control position of a DC motor with parameters $B = 0.1$(Nms), damping ratio of the mechanical system; $K = 0.01$(Nm/ Amp), electromotive force constant; $L = 0.5$(H), armature inductance; $J = 0.01$ (kg m^2/s^2), inertia moment; and $R_u = 1(\Omega)$, armature resistance. Controller includes two inputs and one output: U_h (the first input) is voltage put in controller, dU_h (the second input) is derivative of the U_h, and U (the output) is DC voltage value:

(a) Designing PD-fuzzy controller (FLC) [5].
(b) Designing HAC ($\alpha = \beta$):
   $Step1$: choosing set of calculated parameters:

$$G = \{0, \text{Small}, W, \text{Large}, 1\}; \ H^- = \{\text{Little}\} = \{h_{-1}\}; \ q = 1;$$
$$H^+ = \{\text{Very}\} = \{h_1\}; \ p = 1;$$

$$f_m(\text{Small}) = \theta = 0.5; \ \mu(\text{Very}) = \mu(h_1) = 0.5; \ \mu(\text{Little}) = \mu(h_{-1}) = 0.5.$$

So $\alpha = \beta = 0.5; \ f_m(\text{Large}) = 1 - f_m(\text{Small}) = 0.5.$

$Step\ 2\ and\ step\ 3$: change fuzzy linguistic labels to HA linguistic labels for U_h, dU_h, and U. Then, we will calculate linguistic quantifying values for these variables.

$Building\ Semantic\ Quantifying\ Curve$: from the linguistic quantifying values, using $product\ (and)\ calculation$ in conditional statements of rule bases, coordinates of points in real plane are calculated. Then determine real curve from all above points
   The semantic quantifying curve in Fig. 3a is a sectional linear curve built by average point laws.

(c) Designing HAC1 ($\alpha \neq \beta$), the semantic quantifying curve is shown in Fig. 3b.
(d) Using Matlab and Simulink to perform simulation as in Fig. 4:
   Simulation with $J = 0.01$(kgm^2/s^2), $R_u = 1(\Omega)$, the system output and control signal are shown in Fig. 5a, b.
   Simulation with the varied inertia moment J and varied electric resistance R_u are shown in Figs. 6 and 7.
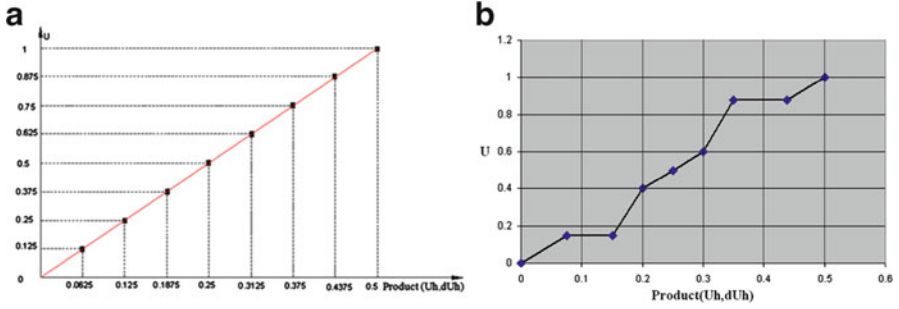
Fig. 3 Semantic quantifying curve of HAC (**a**) and HAC1 (**b**)
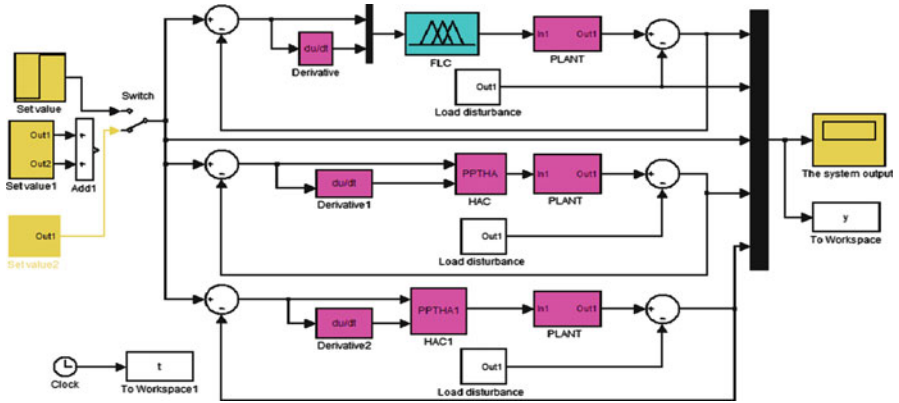
Fig. 4 Fuzzy controller and two hedge algebra controllers
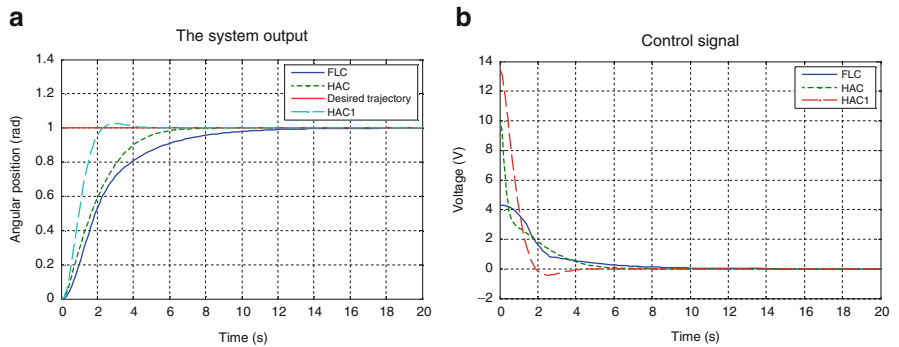
Fig. 5 Unit step tracking (**a**) and respective step control signal (**b**)
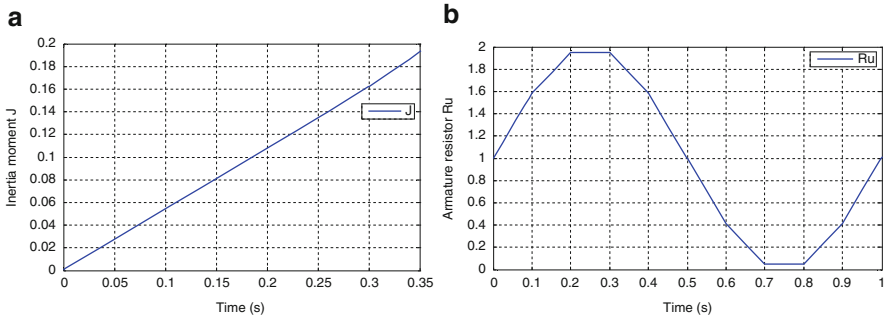
Fig. 6 Varied parameters: Inertia moment J (**a**) and armature resistance R_u (**b**)
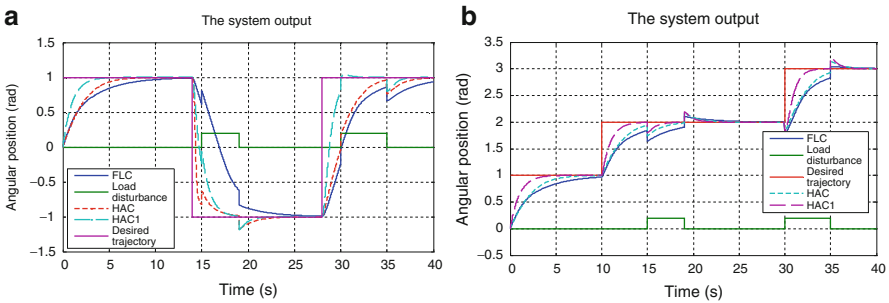
Fig. 7 Rectangular tracking (**a**) and stair tracking (**b**) with load disturbance

4 Conclusions

Successfully study a new method in controlling automation system based on the basis of the general theory of Hedge Algebra called HAC, and this method has the ability to control with higher accuracy than fuzzy method.

Successfully investigate and select α and β for HAC1 to ensure quality when the nonlinear object's parameters vary. The simulation results show that the algorithms and method to design Hedge Algebra controller for solar tracking system are proper.

References

1. Louchene A, Benmakhlouf A, Chaghi A (2007) Solar tracking system with fuzzy reasoning applied to crisp set. Revue des Energies Renouvelables 10(2):231–240
2. Cong NH, Trung NK, Duy NT, Ha LTT (2010) A research on parabolic trough solar collector system control based on hedge algebra, In: The 11th international conference on control, automation, robotics and vision – ICARCV, Singapore, 2010

3. Lan VN, Hung VC, Phu DT (2005) Application of hedge algebras to fuzzy control problems. Adv Nat Sci 6(3):1–16
4. Ho NC, Wechler W (1990) Hedge algebra: an algebraic approach to structures of sets of linguistic truth values. Fuzzy Set Syst 35:281–293
5. Trung NK (2009) Research the model of intelligent controller using hedge algebra to control nonlinear object. Scientific and technology theme in Ministry level

Variable-Speed Wind Generator System with Maximum Output Power Control

Yoko Amano

Abstract To achieve maximum output power from wind generator systems, the rotational speed of wind generators should be adjusted in real time according to natural wind speed. This chapter pays attention to an optimum rotational speed of a single-phase AC (SPAC) generator that can obtain maximum output power with natural wind speed. A high-performance online maximum output power control using the optimum rotational speed to obtain maximum output power is proposed for the SPAC generator system. Moreover, an original generated power brake is introduced in the variable-speed wind generator system. By experimental results, the validity and the practicality of the proposed method are confirmed and can be of practical use in the near future.

Keywords Maximum output power control • Variable-speed wind generator system • Small wind turbine generator • PWM control • Generated power brake

1 Introduction

In recent years, wind energy has greatly attracted researcher's attention because it is an important inexhaustible clean energy and renewable resource. Since the wind energy density does not spread at least 1/800 compared with water energy and the natural wind speed is variably irregular, various efficient control methods were proposed as variable-speed wind generator (VSWG) systems with obtaining maximum output power [1–3].

Y. Amano (✉)
Graduate School of Electrical and Electronics Engineering, Department
of Electrical and Electronics Engineering, College of Engineering, Nihon University,
Chiyoda, Tokyo 963-8642, Japan
e-mail: amano@ee.ce.nihon-u.ac.jp

The above-mentioned methods are expensive to make and should be used for a long time to training the neural networks. Generally, the characteristic of the VSWG system changes a lot according to the natural wind speed and has a nonlinear nature; it is difficult to decide the optimum operating point in the VSWG systems.

This chapter pays attention to the optimal rotational speed of the SPAC generator that can obtain the maximum output power according to the natural wind speed. A secondary polynomial approximate technique is carried out between the wind speed and the optimum rotational speed. A variable-speed wind generator system with maximum output power control is proposed, which adjusts the rotational speed of the SPAC generator to the optimum rotational speed.

In order to realize the adjustment of variable-speed wind online, a new generated power brake is directly linked with the SPAC generator, and the rotational speed of the SPAC generator is adjusted by controlling the generated current flowing on the generated power brake. The generated power brake is constituted by the field-effect transistor (FET) device and introduces the pulse-width modulation (PWM) controller to control the FET device for reducing its heat loss.

2 Maximum Output Power Control

An output power P is obtained by the VSWG system that consists of the wind turbine rotor linked directly and the SPAC generator is expressed as

$$P = \eta \times C_{\mathrm{P}} \left(\frac{1}{2} \rho A V_{\mathrm{w}}^3 \right) \tag{1}$$

where η is the efficiency of the direct drive turbine, C_{P} is the power coefficient, ρ is the air density (kg/m^3), A is the swept area (m^2), and V_{w} is the wind speed (m/s).

When a pitch angle is fixed, the power coefficient C_{P} becomes the function of only the tip-speed ratio λ defined by $\lambda = r\omega/V_{\mathrm{w}}$; r and ω express a windmill radius (m) and a rotation angular speed (rad/s) of the SPAC generator, respectively.

In order to obtain the maximum output power P_{max}, if the efficiency $\eta = 1$ is assumed and the speed ratio is set with λ_{opt}, the optimum rotation angular speed that obtains the maximum output power from the wind speed V_{w} will become

$$\omega_{\mathrm{opt}} = \frac{\lambda_{\mathrm{opt}} V_{\mathrm{w}}}{r} \tag{2}$$

The control purpose of the maximum output power is expressed as a rotational speed control; this rotational angular speed ω is made to follow the target value ω_{opt}.

However, the large deviation of the efficiency η arises with actual wind turbines and generators; furthermore, the efficiency η is the nonlinear function related to the

wind speed V_w and has a large gap between the practical measured value and the theoretical calculation value. It is difficult to find the identification of the efficiency η about the VSWG system for the variable-speed natural wind.

3 VSWG Systems

The present composition of the Aerogen 2 wind generator is an open-loop system [4]. The exchange of electric power from the wind turbine connected with the SPAC generator is transformed into direct-current (DC) electric power, which flows through a rectifier and a DC load or a battery. Conventionally, the output power of the Aerogen 2 wind generator with an open loop depends upon the natural wind speed; the stabile maximum output power cannot be obtained.

3.1 Configuration of the Proposed Method

The composition of the VSWG system proposed in this chapter is shown in Fig. 1, which includes a laser sensor, a wind speed sensor, a speed converter, a controller, a PWM controller, and a FET device.

The natural wind speed is measured by the wind speed sensor and becomes the optimum rotational speed N_r^* by the speed converter of wind speed vs. rotational speed. The rotational speed N_r of Aerogen 2 is measured by the laser speed sensor and compares N_r^*; it becomes the speed deviation e_N. The controller outputs a control signal to lost e_N, and the PWM controller adjusts the generated current that flows through the FET device. When the generated current is changed, the load and the rotational speed of Aerogen 2 change at the same time.
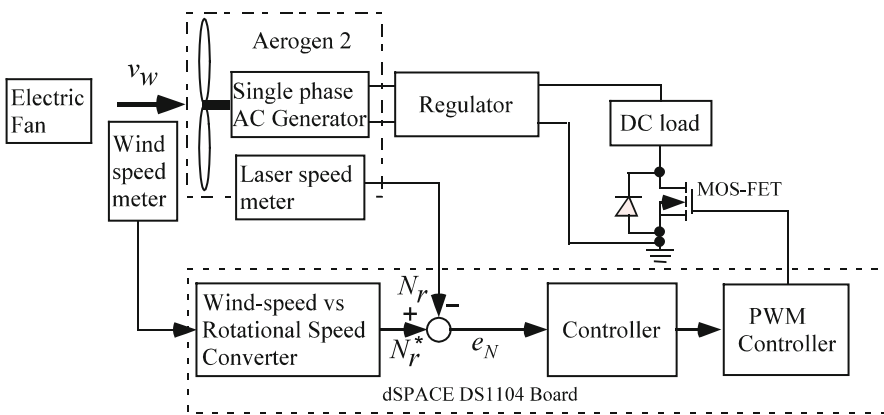
Fig. 1 Configuration of the proposed method

4 Experimental System

The Aerogen 2 wind generator with the specification shown in Table 1 is taken as a control object in the proposed VSWG system with maximum output power control. Moreover, the characteristic measurement result of output power vs. rotational speed is shown in Fig. 2 and is included in the efficiency η of the formula (1).

By Fig. 2, the optimum rotational speed obtaining the maximum output power to every wind speed is shown in Fig. 3. The relationship between the optimum rotational speed and the wind speed is interesting as the alignment within the theoretical formula (2).

In order to obtain optimum rotational speed from the natural wind speed, the characteristic curve of Fig. 3 is approximated by the following secondary polynomial:

Table 1 Specifications of the Aerogen 2 generator

Item	Specification
Rated output@rated wind speed	20 (W) @10.5 (m/s)
Generator	Single-phase AC generator
Blade diameter	580 mm
Blade number	5
Weight	5 kg
Output voltage	12 (V)
Survival wind-speed	40 (m/s)
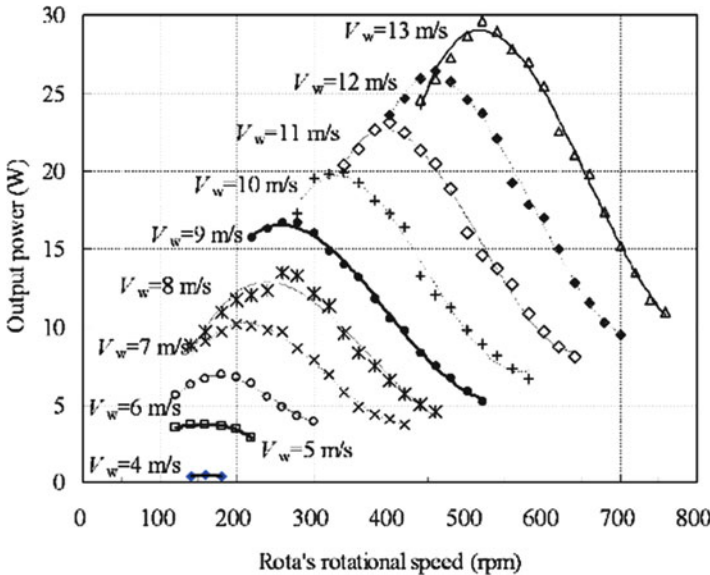
Fig. 2 Output power vs. rotational speed

Fig. 3 Optimum rotational
speed N_r^* vs. wind speed V_w
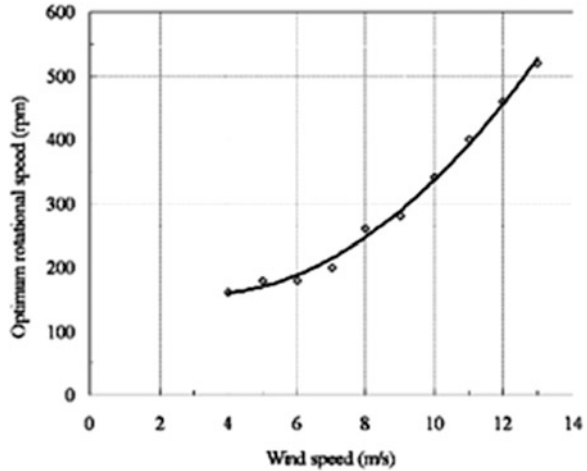
$$N_r^* = 3.7879V_w^2 - 23.545V_w + 193.21 \qquad (3)$$

4.1 Composition of Experimental Equipment

The natural wind is generated using an electric fan shown in Fig. 1, and the wind
speed can be arbitrarily adjusted by changing the input voltage of the electric fan
using control programmes.

Since the high-speed response is required for the maximum output power
control, the operation of the controller adopted PID control with sufficient effect.
In order to reduce exothermic loss of the FET device, the experimental system is
conducted by the "PID + PWM" control type that added the PWM controller with
20 kHz carrier frequency.

4.2 Experimental Results

The output power for the wind speed from 4 (m/s) to 13 (m/s) of the Aerogen
2 wind generator is shown in Fig. 4; the white bar graph represents the Aerogen 2
wind generator and the black bar graph represents the Aerogen 2 wind generator
using the proposed method. It can be clarified that the black bar graph is 1.07 times
more than the white bar graph.

Moreover, the generated power data and its standard deviation with the wind
speed at 10 (m/s) in 24 h are shown in Fig. 5; the dotted line and the solid line
express the generated electric power and the range of its standard deviation value
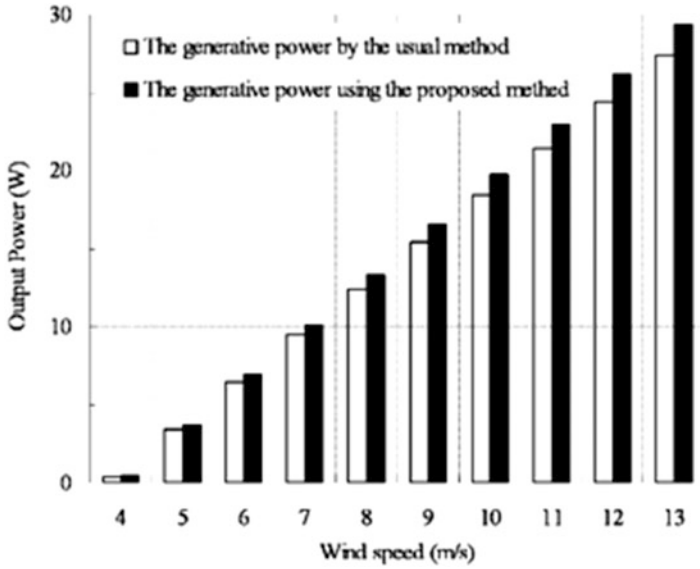
Fig. 4 The wind output power comparison
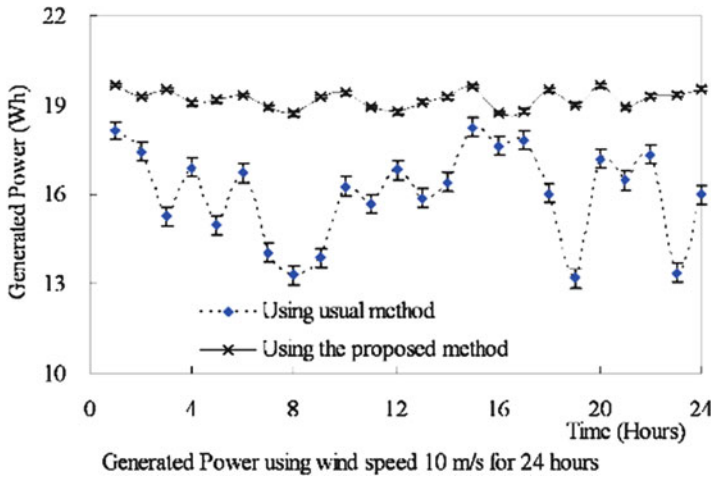
Fig. 5 The generated power comparison

for every hour of the Aerogen 2 wind generator and the Aerogen 2 wind generator with the proposed method, respectively.

From Fig. 5, the average value of the generated electric power by the Aerogen 2 wind generator is 16.04 (Wh), but the average value of the Aerogen 2 wind generator with the proposed method is 19.22 (Wh), which is 1.20 times more than the Aerogen 2 wind generator.

   Furthermore, the standard deviation of the Aerogen 2 wind generator is 1.56, and the standard deviation of the Aerogen 2 wind generator with the proposed method is 0.30, which is 0.19 times more than the Aerogen 2 wind generator.

   From the comparison result of Fig. 5, the Aerogen 2 wind generator with the proposed method can generate electric power up to 1.20 times more, and the standard deviation of the generated electric power is 1/5 lesser than the Aerogen 2 wind generator, where the maximum output power can be obtained.

5   Conclusion

In order to utilize the thin energy density of wind energy, the maximum output control for the VSWG system with the SPAC generator is proposed in this chapter, and the relationship between the optimal rotational speed and the wind speed is introduced. Moreover, PWM control was introduced in order to reduce the exothermic loss of the FET device as the generated power brake. Finally, the experimental system of the proposed method was built, which were then examined and confirmed that the proposed method is valid and practical.

References

1. Sperling K, Hvelpund F, Mathieses BV (2010) Evaluation of wind poser planning in Denmark-towards an integrated perspective. Energy 35:1–12
2. Ibrahim AO, Nguyen TH, Lee DC (2011) A fault ride-through technique of DFIG wind turbine systems using dynamic voltage restores. IEEE Trans Energy Conver 26(3):871–882
3. Lin WM, Hong CM, Chen CH (2011) Neural-network-based MPPT control of a stand-alone hybrid power generator system. IEEE Trans Power Electron 26(12):3571–3581
4. http://www.wirefreedirect.com/aerogen_wind_generators.asp

FPGA-Based Control for a Boost PFC Converter with Improved Dynamic Performance

Shin-Ju Chen, Sung-Pei Yang, Chao-Ming Huang, and Ruei-Hong Wong

Abstract A field-programmable gate array (FPGA)-based digital control boost power factor correction (PFC) AC-DC converter with average current-mode control (ACC) and load-current-injection control is proposed to achieve high power factor and to improve dynamic performance. The ACC-controlled converter includes a fast inner current loop and a slow outer voltage loop. The current loop regulates the input current such that input average current follows the input voltage to comply with the current standards on power factor and input current distortion of power supplies. The outer voltage loop maintains the output voltage at a reference level against load variation and line voltage fluctuation. The main limitation of the ACC-controlled PFC rectifiers is that the bandwidth of the voltage loop is only about 10–20 Hz. The technique of load-current-injection control is applied to speed up the output voltage response to load variation. A 350 W prototype of boost PFC converter is built to validate the dynamic performance. The experimental results are provided to verify the high power factor complying with IEC 61000-3-2 Class D and fast output voltage regulation against the load variation.

Keywords Boost converter • FPGA • Average current-mode control • Load-current-injection control • Power factor correction

1 Introduction

The harmonic reduction requirements imposed by relative regulations, such as IEC 61000-3-2, have accelerated interest in active PFC AC-DC preregulator for switching power supply. The continuous-conduction-mode (CCM) boost topology is a popular choice for a PFC converter with high power rating because the

S.-J. Chen (✉) • S.-P. Yang • C.-M. Huang • R.-H. Wong
Department of Electrical Engineering, Kun Shan University, Tainan 71003, Taiwan
e-mail: sjchen@mail.ksu.edu.tw
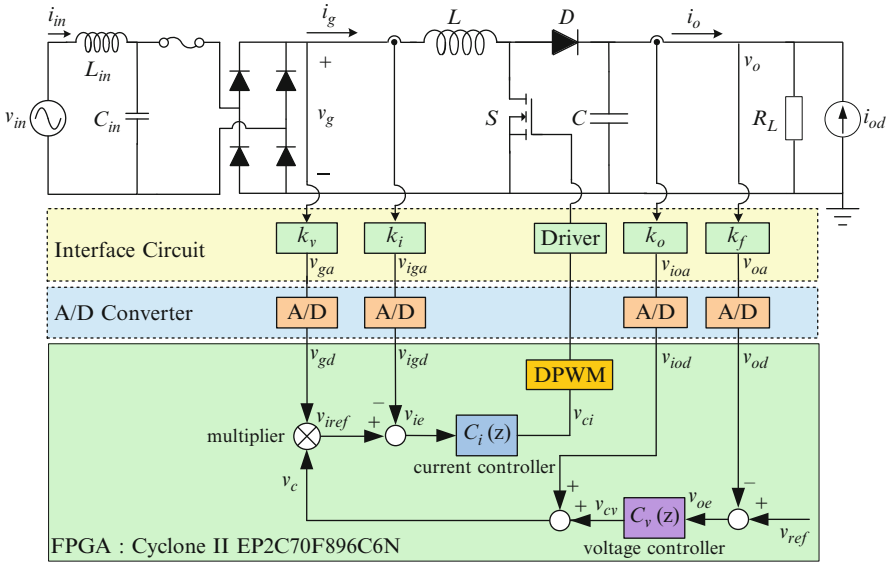
Fig. 1 FPGA-based digital control of a boost PFC converter

inductor current ripple is small, and the converter has low current stress as well as a small filter for electromagnetic interference (EMI). In order to achieve a low input line current harmonics, the average current-mode control (ACC) scheme is generally used in practice. However, the main disadvantage of the ACC-controlled PFC rectifiers is that the bandwidth of the voltage loop is only about 10–20 Hz to attenuate the contents of the second line harmonic in the control signals [1]. Therefore, the dynamic response of the output voltage to load variation is generally slow.

Some researches have been proposed to overcome this problem, such as notch filter approach and ripple compensation approach [2, 3]. However, the relatively complex control circuit is the main drawback. In this chapter, the ACC scheme is combined with load-current-injection control [4] to achieve fast response of the output voltage to load variation and keep low distortion of the input current.

The PFC control is usually based on analog commercial solution. However, the emergence of powerful, low-cost digital signal processors (DSP), microcontroller, and FPGA has made it possible for the digital control to become a competitive option. The FPGA is a programmable digital logic device by software. Thus, it can perform any logic function such as digital interface, controllers, numeric processors, and decoders in a single IC. Therefore, there are some researches on the digital control of AC-DC PFC converter based on FPGAs [5–7].

In this chapter, the analysis and synthesis of FPGA-based digital control for PFC boost converters with ACC and load-current-injection scheme are proposed. The digital control scheme is shown in Fig. 1. The small-signal model of outer

voltage loop for the PFC converter is presented for the controller design. Finally, the experimental results based on a 350-W prototype are given to validate the static and dynamic performances.

2 System Configuration and Modeling

The scheme of introducing an ACC-controlled PFC boost converter with load-current-injection control is shown in Fig. 1. In outer voltage loop, the output voltage is sensed and compared with the voltage reference v_{ref}. The error v_{oe} becomes the input of the voltage controller. The controller output v_{cv} and the "load following" control voltage v_{iod} (dependent on the sensed load current) are added to be the scaling factor for the rectified voltage v_{gd}. The output of the multiplier is the current reference v_{iref}. The inner current loop containing current controller and DPWM shapes the average inductor current to follow the reference current and results in the input current to be a sinusoidal shape in phase with the AC line voltage.

Assume that the boost converter operates in CCM mode. If the inner wide-bandwidth current controller is well designed, then the average input current follow the waveform of input voltage. The outer voltage control loop is designed to maintain the output voltage equal to the reference voltage. In general, the bandwidth of the outer voltage control system is low, so that the control signal v_{c} in Fig. 1 has a small ripple of the second line harmonic frequency to avoid the distortion of the input line current. Let $v_{\text{in}}(t) = V_{\text{m}} \sin(\omega t)$. Based on the average power balance of input and output, the transfer functions of power stage and output impedance can be obtained as follows [7]:

$$G(s) = \left. \frac{\tilde{v}_{\text{o}}(s)}{\tilde{v}_{c_{\text{v}}}(s)} \right|_{\tilde{i}_{\text{od}}=0} = \frac{\frac{k_{\text{v}} V_{\text{m}}^2}{2 k_{\text{i}} v_{\text{o}} C}}{s + \frac{2}{R_{\text{L}} C}} \tag{1}$$

$$Z_{\text{o}}(s) = \left. \frac{\tilde{v}_{\text{o}}(s)}{\tilde{i}_{\text{od}}(s)} \right|_{\tilde{v}_{c}=0} = \frac{1}{Cs + \frac{2}{R_{\text{L}}}} \tag{2}$$

To account for the load variation, an exogenous current source i_{od} regarded as load disturbance is added to the nominal resistance R_{L}. Thus,

$$i_{\text{o}}(t) = \frac{v_{\text{o}}(t)}{R_{\text{L}}} - i_{\text{od}}(t) \tag{3}$$

The small-signal block diagram of the outer voltage loop with load-current-injection scheme in continuous-time domain is shown in Fig. 2, where k_{f} and k_{o} are the output voltage sensing gain and load-current-injection gain, respectively. $C_{\text{v}}(s)$ is the voltage controller. The resulting closed-loop output impedance is
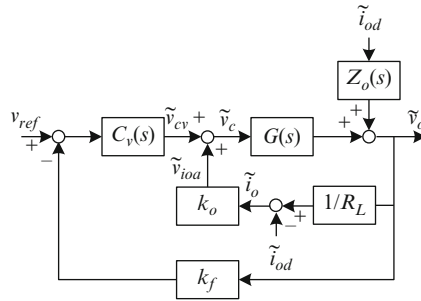
Fig. 2 Block diagram of outer voltage loop
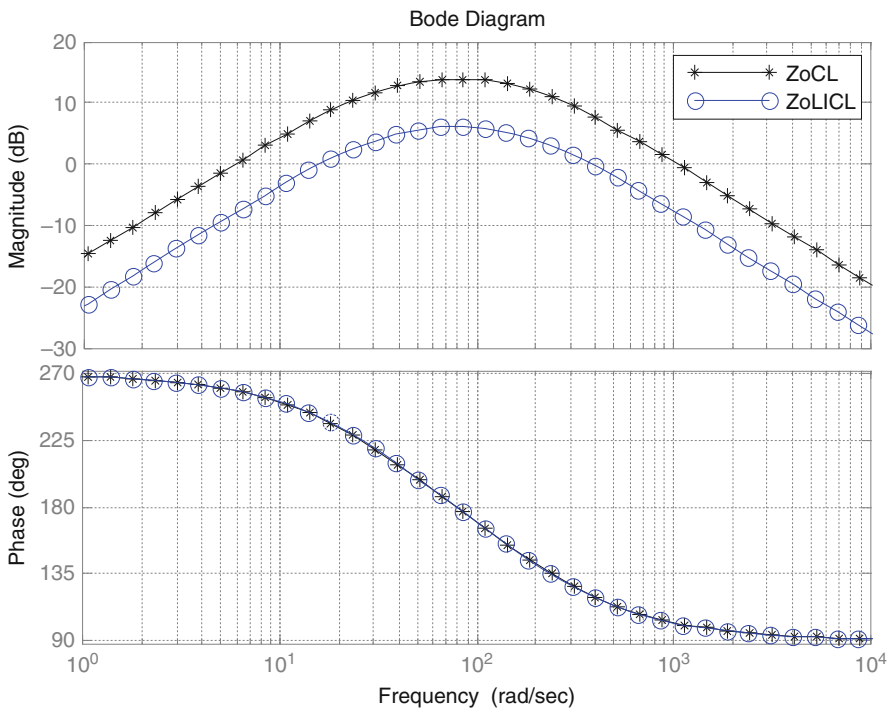
Fig. 3 Bode plots of $Z_{\text{oCL}}(s)$ and $Z_{\text{oLICL}}(s)$

$$Z_{\text{oLICL}}(s) = \frac{\tilde{v}_{\text{o}}(s)}{\tilde{i}_{\text{od}}(s)} = \frac{Z_{\text{o}}(s) - k_{\text{o}}G(s)}{1 + k_{\text{f}}C_{\text{v}}(s)G(s) - \frac{k_{\text{o}}}{R_{\text{L}}}G(s)} \tag{4}$$

It is worth noting that there is no inner feedback path in Fig. 2 for the conventional ACC-controlled system. Let $Z_{\text{oCL}}(s)$ be the closed-loop output impedance of the conventional ACC-controlled system. With the parameters of experimental proto-type, the Bode plots of $Z_{\text{oCL}}(s)$ and $Z_{\text{oLICL}}(s)$ are shown in Fig. 3. It is seen that the

closed-loop output impedance of the considered system in this chapter is lower than that of conventional ACC-controlled system [7]. The improvement is of about 10 dB in a wide range of frequency. Therefore, the dynamic reponse of the output voltage to load varition can be improved.

3 Controller Design and Implementation

The controller parameters are designed using a continuous-time model and then the discrete-time model in z-domain can be obtained by using the Tustin's transform. For the inner current loop, the PI controller is designed such that the bandwidth of input current control system is 4.95 kHz which is much more than twice line frequency. For the outer voltage loop, the PI controller is designed such that the bandwidth of the output voltage control system is 13.2 Hz which is much less than twice line frequency.

The sampling frequency for the inner current loop is chosen as 100 kHz and the output voltage sampling is 10 kHz. The difference equations that represent the current and voltage controllers can be respectively expressed as

$$v_{ci}(n) = v_{ci}(n-1) + 3.2501 \times v_{ie}(n) - 3.2498 \times v_{ie}(n-1) \tag{5}$$

and

$$v_{cv}(n) = v_{cv}(n-1) + 0.37501 \times v_{oe}(n) - 0.37498 \times v_{oe}(n-1) \tag{6}$$

Owing to the quantization effect of fixed-point arithmetic, the control gains can not be realized precisely. In order to reduce the calculated error, the result of the subtraction between the reference input $v_{ref}(n)$ and measured output $v_{oa}(n)$ has to be premultiplied by a constant. The final result is then divided by the same constant. In the case the constant is 2^{16}. The voltage loop control is implemented as shown in Fig. 4 with $a_0 = 0.37501 \cong 2^{-2} + 2^{-3} + 2^{-16}$ and $a_1 = 0.37498 \cong 2^{-2} + 2^{-3} - 2^{-16}$. The calculations in the FPGA development are subtraction, shifting operation, and addition. In the similar manner, the current-loop controller can be implemented.
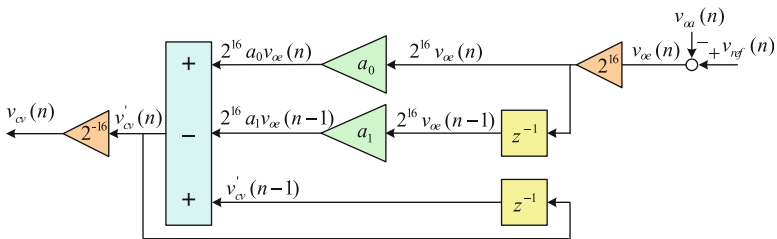
Fig. 4 The representation of the voltage loop controller

In the implementation of the digital control, the FPGA kit ALTERA DE2-70 has been employed. This board has a 50-MHZ Cyclone II EP2C70F896C6N FPGA. The main software used is the ALTERA Quartus II. The hardware description language of Verilog is used to program the control algorithm. The DPWM is achieved by three basic blocks: a register to hold the duty ratio value, a triangular carrier with the up/down counter to be compared with the duty ratio value, and the comparator block.

The interface circuits include scaling circuit, Butterworth low-pass filter, and current-sensing circuit. There are four A/D converters by IC ADC 7822 (8-bit, conversion time 420 ns) used for the scaling input current, output current, input voltage, and output voltage. The control algorithm is then performed by FPGA chip.

4   Experimental Results

To validate the performance of the converter system, a prototype of the boost PFC converter is built with the following parameters: input line voltage $v_{in} = 90 - 130$ Vac, output voltage $v_o = 312$ V, rated output power $P_o = 350$ W, inductor $L = 2$ mH, output capacitor $C = 940$ μF, switching frequency $f_{sw} = 100$ kHz, and sensing gains $k_v = 1/156$, $k_i = 0.2$, $k_o = 0.06$, and $k_f = 1/621$.

Static and dynamic tests have been performed with the prototype. In the steady-state operation, the measured results of input current i_{in}, input voltage v_{in}, and output voltage v_o at full load are depicted in Fig. 5. The power factor is 0.981. The comparison with the IEC 61000-3-2 Class D standard is shown in Fig. 6. It reveals that the input line current satisfies current harmonic standard. The measured results of power factor at different load levels are listed in Table 1.

To verify the improvement achieved by ACC with load-current-injection scheme, the comparative experimental response of the output voltage to a load variation from 350 to 175 W with conventional ACC scheme [7] is depicted in Fig. 7. It is seen that the setting time is improved from 300 to 50 ms, and the peak of the output voltage deviation from the steady-state value is improved from 6 to 3 V. It shows that the used scheme indeed speeds up the output voltage response to load variation, but it does not affect the harmonic currents of the input current.
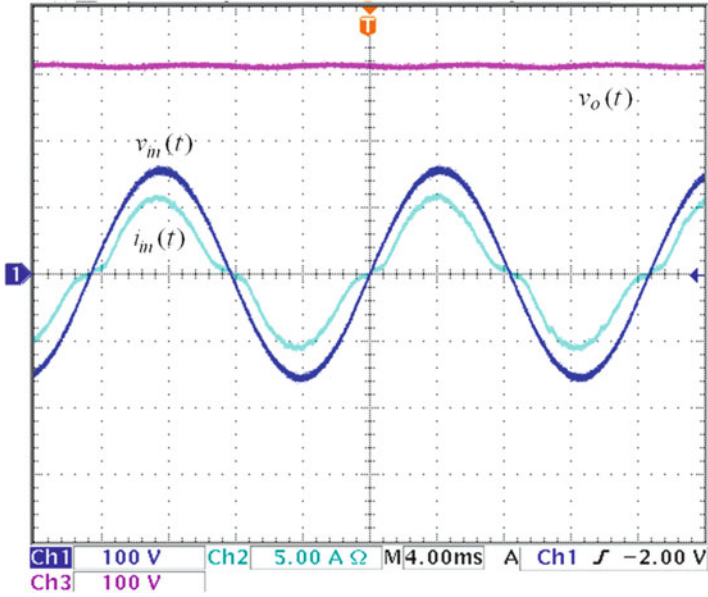
Fig. 5 Waveforms of i_{in}, v_{in}, and v_o at full load
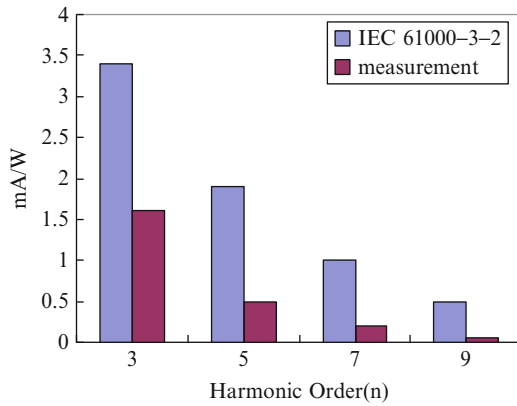
Fig. 6 Comparison of measurement with standard

Table 1 Measured power factor at different load levels

P_o (W)	100	150	200	250	300	350
Power factor	0.970	0.975	0.979	0.980	0.981	0.981
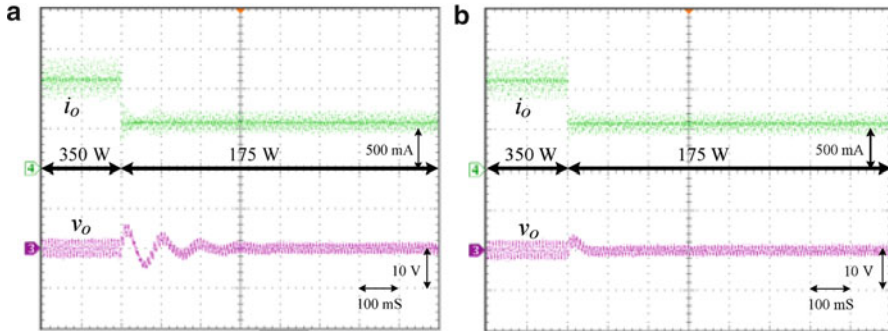
Fig. 7 The output voltage response to a load variation. (**a**) Conventional ACC scheme. (**b**) ACC with load-current-injection scheme

5 Conclusions

The FPGA-based digital control for a PFC boost converter with ACC and load-current-injection scheme is implemented to improve the dynamic performance. The required current and voltage controllers are designed. A 350-W prototype is built to evaluate the performance. The experimental results are provided to verify the high power factor and comply with current harmonic standard. The control scheme indeed speeds up the output voltage response to load variation.

References

1. Jovanovic ZM (1992) Design trade-offs in continuous current-mode controlled boost power factor correction circuits. In: Proceedings of the HFPC, San Diego, 1992, pp 209–220
2. Buso S, Mattavelli P, Rossetto L, Spiazzi G (1998) Simple digital control improving dynamic performance of power factor preregulators. IEEE Trans Power Electron 13:814–823
3. Eissa MO, Leeb SB, Verghese GC, Stankovic AM (1994) A fast analog controller for a unity-power factor AC/DC converter. In: Proceedings of the IEEE APEC, 1994, pp 551–555
4. Figures E, Benavent JM, Garcera G, Pascual M (2007) A control circuit with load-current injection for single-phase power factor correction rectifiers. IEEE Trans Ind Electron 54:1272–1281
5. Zhang W, Liu YF, Wu B (2006) A new duty cycle control strategy for power factor correction and FPGA implementation. IEEE Trans Power Electron 21:1745–1753
6. Alcalde ALP, Ortmann MS, Mussa SA (2008) NIOS II processor implemented in FPGA an application on control of a PFC converter. In: Proceedings of the IEEE PESC, Rhodes, 2008, pp 4446–4451
7. Chen SJ, Yang SP, Wong RH (2012) FPGA-based digital control for boost converters with power factor correction. In: Proceedings for the IEEE ICIEA, 2012, pp 1089–1093

Robotic Manipulator Trajectory Tracking Using Direct Collocation

Cheng-cai Mei, Xiu-qiang Pan, Satya Prakash, Jyun-jye Felipe Chen, and Xiu-long Wu

Abstract This study applies a five-linked robotic manipulator to track prespecified trajectories in the workspace. It is authors' intent to see how adequate the method of direct collocation and nonlinear programming (DCNLP) can be in enhancing the capability of robotic manipulator. Creative dig-ins may excavate useful robotic applications not only in welding industry but also in medical-home health caring applications. In this study, the dynamics of the manipulator is constructed by Lagrange-Euler (L-E) formulation and the geometry of the manipulator is defined according to the Denavit-Hartenberg convention. Once the EOM are available, the optimal control theory takes over and the necessary conditions (NCs) confine the manipulator system to the optimality condition of least-energy maneuvering. However, NCs inevitably evoke the two-point boundary-valued problem (TPBVP). The method of DCNLP will convert a TPBVP into a nonlinear programming problem. It assures the certainty of obtaining optimal solutions for TPBVP.

C.-c. Mei (✉) • X.-q. Pan • J.-j.F. Chen • X.-l. Wu
College of Information and Communications, Zhejiang Industry and Trade
Vocational College, Wenzhou, Zhejiang 325003, China
e-mail: gmmeichengcai@126.com

S. Prakash
Department of Electrical Engineering, Parala Maharaja Engineering College,
Brahmapur, Odisha, India

1   Introduction

This study applies optimal control to a five-linked manipulator and tries to design
the least-energy maneuvering sequences for its five joint actuators. In the mean-
time, the end-effectors of the manipulator are required to track along a prespecified
curve in 3-D workspace. This requirement serves as a path constraint while the
manipulator finds the optimal solution for the maneuvering.

Since it is an articulated body, the Lagrange-Euler formulation is adopted to
describe its dynamics. Once the optimal control theory takes over the problem, the
necessary conditions (NCs) immediately define how the optimality should look
like when optimality appears. The method of direct collocation and nonlinear
programming (DCNLP) is thus introduced in order to locate the numerical
solution. DCNLP transforms a two-point boundary-value problem (TPBVP)
into an ordinary nonlinear programming problem. Runge–Kutta often fails to
solve TPBVP. DCNLP appears to be the right tool in this case if provided with
large memory and fast CPU.

2   Dynamics and Equations of Motion

The manipulator at its parking position is given in Fig. 1.
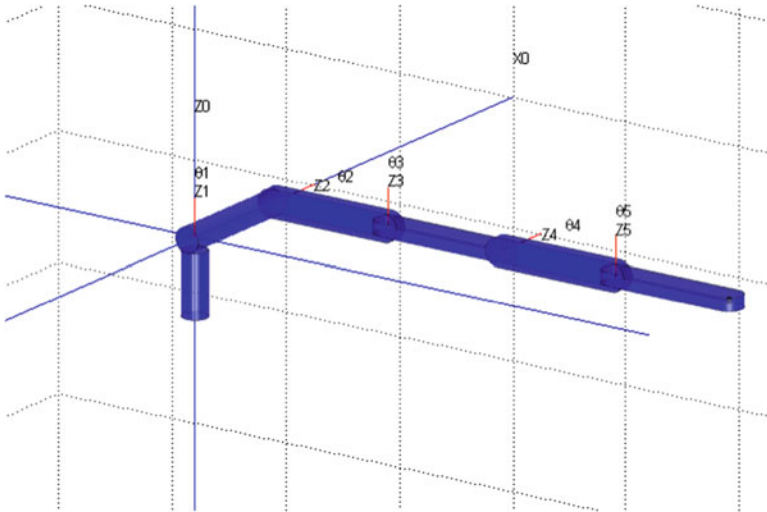
Fig. 1   Configuration of the five-linked manipulator

$$
{}^0A_1 = \begin{bmatrix} \cos\theta_1(t) & -\sin\theta_1(t) & 0 & 0 \\ \sin\theta_1(t) & \cos\theta_1(t) & 0 & 0 \\ 0 & 0 & 1 & 0 \\ 0 & 0 & 0 & 1 \end{bmatrix} \tag{1}
$$

$$
{}^1A_2 = \begin{bmatrix} 0 & 0 & 1 & L_1 \\ -\cos\theta_2(t) & \sin\theta_2(t) & 0 & 0 \\ -\sin\theta_2(t) & -\cos\theta_2(t) & 0 & 0 \\ 0 & 0 & 0 & 1 \end{bmatrix} \tag{2}
$$

$$
{}^2A_3 = \begin{bmatrix} \cos\theta_3(t) & -\sin\theta_3(t) & 0 & L_2 \\ 0 & 0 & -1 & 0 \\ \sin\theta_3(t) & \cos\theta_3(t) & 0 & 0 \\ 0 & 0 & 0 & 1 \end{bmatrix} \tag{3}
$$

$$
{}^3A_4 = \begin{bmatrix} \cos\theta_4(t) & -\sin\theta_4(t) & 0 & L_3 \\ 0 & 0 & -1 & 0 \\ -\sin\theta_4(t) & -\cos\theta_4(t) & 0 & 0 \\ 0 & 0 & 0 & 1 \end{bmatrix} \tag{4}
$$

$$
{}^4A_5 = \begin{bmatrix} \cos\theta_5(t) & -\sin\theta_5(t) & 0 & L_4 \\ 0 & 0 & -1 & 0 \\ -\sin\theta_5(t) & -\cos\theta_5(t) & 0 & 0 \\ 0 & 0 & 0 & 1 \end{bmatrix} \tag{5}
$$

$\theta_1(t), \theta_2(t), \theta_3(t), \theta_4(t)$, and $\theta_5(t)$ are the five joint angles. L_1, L_2, L_3, L_4, and L_5 are the lengths of the five links. The Lagrange-Euler formulation (6) describes the dynamics [1]:

$$
\vec{\tau} = \frac{d}{dt}\left(\frac{\partial L}{\partial \dot{\vec{\theta}}}\right) - \frac{\partial L}{\partial \vec{\theta}} \tag{6}
$$

$$
L = \frac{1}{2}\sum_{i=1}^{5}\sum_{j=1}^{i}\sum_{k=1}^{i}\left[Tr\left(U_{ij}J_iU_{ik}^T\right)\cdot\dot{\theta}_j\dot{\theta}_k\right] + \sum_{i=1}^{5}m_i\vec{g}\left({}^0A_i \cdot {}^ir_i\right) \tag{7}
$$

$$
J_i = \begin{bmatrix} \frac{1}{3}m_iL_i^2 & 0 & 0 & \frac{1}{2}m_iL_i \\ 0 & 0 & 0 & 0 \\ 0 & 0 & 0 & 0 \\ \frac{1}{2}m_iL_i & 0 & 0 & m_i \end{bmatrix} \tag{8}
$$

$$U_{ij} = \begin{cases} {}^0 A_{j-1} Q_j{}^{j-1} A_i & 0 \le j < i \\ 0 & j > i \end{cases}, 0 \le i,j \le 5, \frac{d^{j-1} A_i}{d\theta_i} = Q_i{}^{j-1} A_i \qquad (9)$$

where $\vec{g} = \begin{bmatrix} 0 & 0 & -9.81 & 0 \end{bmatrix}$ is the gravity acceleration, $\vec{\tau}$ is the joint actuator inputs, and m_i is the mass of the ith link. L is the Lagrangian function of the system. Symbolic language technique is applied to help derive the L-E equation and it yields

$$\ddot{\vec{\theta}}(t) = D^{-1}\left(\vec{\theta}\right) \cdot \left(-\vec{h}\left(\vec{\theta}, \dot{\vec{\theta}}\right) - \vec{c}\left(\vec{\theta}\right) + \vec{\tau}(t)\right) \qquad (10)$$

3 Direct Collocation and Nonlinear Programming

The state vector is $\vec{x}(t) = \begin{bmatrix} \theta_1(t) & \omega_1(t) & \theta_2(t) & \omega_2(t) & \cdots & \theta_5(t) & \omega_5(t) \end{bmatrix}^{\mathrm{T}}$. According to Bryson and Ho [2], the optimality situation appears when the following necessary conditions satisfy:

$$\dot{\vec{x}}(t) = \vec{f}_{10 \times 1}(\vec{x}(t), \vec{\tau}(t), t), \qquad (11)$$

$$\dot{\vec{\lambda}} = -\frac{\partial H}{\partial \vec{x}^*}, \qquad (12)$$

$$0 = \frac{\partial H}{\partial \vec{\tau}^*}, \qquad (13)$$

$$\vec{\lambda}(t_{\mathrm{f}}) = \left(\frac{\partial \phi}{\partial \vec{x}^*(t_{\mathrm{f}})}\right) \text{ and some } x_i(t_0), x_j(t_{\mathrm{f}}), \text{ and } \lambda_k(t_{\mathrm{f}}) \text{ are given} \qquad (14)$$

where * denotes optimality situation, H is the Hamiltonian, ϕ is the final constraint, and $\vec{\lambda}(t)$ is the Lagrange multiplier vector.

3.1 Direct Collocation

The time history is divided into $n = 100$ segments. DCNLP transforms the 10 first-order differential equations as is in (10) into a set of 1,000 difference equations [3]. The new states are regrouped into $\vec{X}_{i(15 \times 1)} = \begin{bmatrix} \vec{x}_i & \vec{\tau}_i \end{bmatrix}^{\mathrm{T}}$. We use Hermite-Simpson's interpolation and define a cubic polynomial cutting through the end points at each segment. At the center of the segment, the slope of the

cubic polynomial is x'_c. In the same segment, the value of the differential equation f_c can be determined from (11):

$$x_c = \tfrac{1}{2}(x_i + x_{i+1}) + \tfrac{T}{8}(f_i - f_{i+1})$$ (15)

and

$$x'_c = -\tfrac{3}{2T}(x_i - x_{i+1}) - \tfrac{1}{4}(f_1 + f_2)$$ (16)

x'_c is available from (16). DCNLP compels the difference between f_c and x'_c to zero. The difference $\Delta_i = f_c - x'_c = f_c + \tfrac{3}{2T}(x_i - x_{i+1}) + \tfrac{1}{4}(f_i + f_{i+1})$ is called defect function [3]. As soon as the right combination of $\vec{X}_i$ appears, $\vec{\Delta}_{1000 \times 1}$ vanishes to a zero vector, and then the optimal solution $\vec{X}_i$ is found where $i = 1 - 100$.

3.2 Constraint Functions of Trajectory Tracking

The coordinate of the end-effectors at any time is defined as follows:

$$\vec{r}_5 = [\,x_R \quad y_R \quad z_R \quad 1\,]^T = {}^0A_1 \cdot {}^1A_2 \cdot {}^2A_3 \cdot {}^3A_4 \cdot {}^4A_5 \cdot {}^5\vec{r}_5$$ (17)

where ${}^5\vec{r}_5 = [\,1.0 \quad 0.0 \quad 0.0 \quad 1.0\,]^T$. $\vec{G}(t) = [\,G_x(t) \quad G_y(t) \quad G_z(t)\,]$ is the equation of the prespecified trajectory that the end-effectors are requested to track. Let $\Delta_x(t) = x_R(t) - G_x(t)$, $\Delta_y(t) = y_R(t) - G_y(t)$, and $\Delta_z(t) = z_R(t) - G_z(t)$. Forcing the three quantities to zero is equivalent to driving the end-effectors to track the trajectory. It adds up another 300 equality constraints. Finally, the cost function is defined as follows:

$$J = \frac{1}{2} \sum_{k=1}^{100} \left(\tau_1^2[k] + \tau_2^2[k] + \tau_3^2[k] + \tau_4^2[k] + \tau_5^2[k] \right) \cdot \frac{t_f}{100}$$ (18)

4 Simulations: Tracking Along a Heart Curve

This case requests the end-effectors to track along a heart curve. The trajectory equations are [4]:
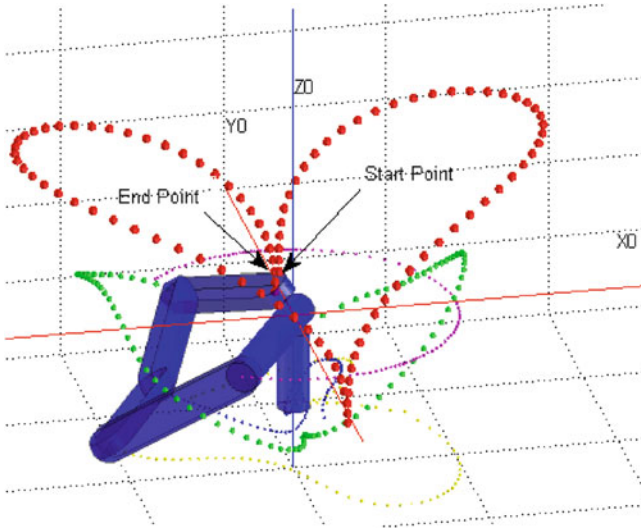
Fig. 2 The traces of the end-effectors and four joints
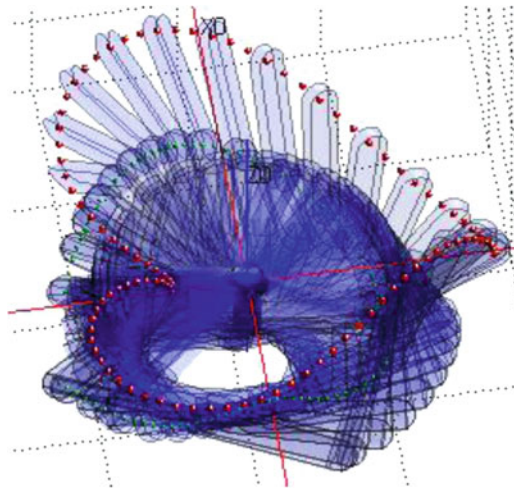
Fig. 3 Motion-still diagram of the end-effectors

$$G(t) : \begin{pmatrix} x = \frac{16}{10}\sin^3(t) \\ y = \frac{1}{10}(13\cos(t) - 5\cos(2t) - 2\cos(3t) - \cos(4t)) \\ z = \pm\sin(t) \end{pmatrix} \text{where } t \in [0, 2\pi] \quad (19)$$

Note that $z = \sin(t)$ if $t \in [0, \pi]$ and $z = -\sin(t)$ if $t \in [\pi, 2\pi]$. This generates a non-differentiable point at $t = \pi$ for DCNLP to handle (Figs. 2 and 3).
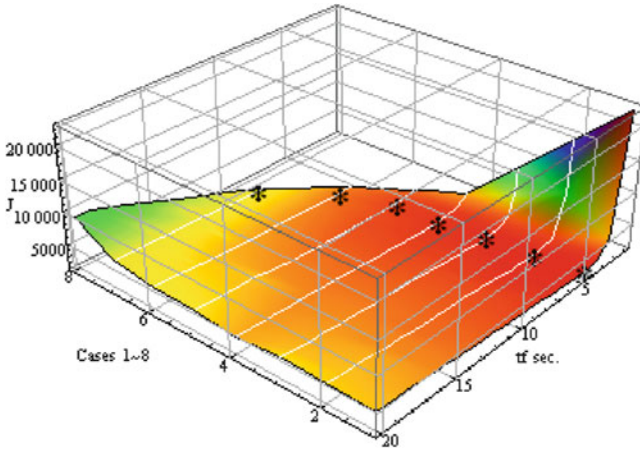
Fig. 4 Cost index subjected to various angular velocity constraints and t_f

Eight different sets of bound on angular velocities are applied. The angular velocity of Case 1 is set unbounded. The angular velocity of Case 2 is bounded between $\pm 180°/s$; and Case 3, $\pm 150°/s$; Case 4, $\pm 120°/s$; Case 5, $\pm 90°/s$; Case 6, $\pm 60°/s$; Case 7, $\pm 36°/s$; and Case 8, $\pm 18°/s$. Several iterations are conducted at various t_f s in each case. The results are shown in Fig. 4. The cost index rises sharply if t_f is decremented. See the upper right corner of Fig. 4. On the other hand, the excessive t_f keeps the four actuators consuming electric power in order to counteract the gravity force. See the lower left corner of Fig. 4. DCNLP also detects a "valley of local minimum J^*." See the seven asterisks meandering in Fig. 4.

5 Conclusion

Genetic Algorithm [5] depends on the evaluation of the fitness function on every possible existing solution. The most fitted individuals are repeatedly selected until the optimality appears. In this chapter, the NCs and DCNLP provide a unique approach [6] to the solution. This approach allows the solution process to be deterministic instead of stochastic. According to Sect. 4, DCNLP proves to be capable of finding optimal solutions and, in the mean time, demonstrating genuine quality of "intelligence" by clinging to the elegance of optimization. According to Sect. 4, DCNLP does not discriminate if non-differentiable points exist or not in the constraints. This counts as another token of DCNLP in hunting down the solution.

References

1. Fu KS, Gonzalez RC, Lee CSG (1987) Robotics: control, sensing, vision, and intelligence. McGraw-Hill Book Company, New York
2. Bryson AE Jr, Ho Y (1975) Applied optimal control. Hemisphere Publishing Corporation, New York
3. Gill PE, Murray W, Saunders MA (1998) User's guide for SNOPT 5.3: a fortran package for large-scale nonlinear programming. Stanford Business Software, Inc., Stanford
4. Weisstein EW Heart curve. From MathWorld – a wolfram web resource, http://mathworld.wolfram.com/HeartCurve.html
5. Meghdari A, Naderi D, Eslami S (2006) Optimal stability of a redundant mobile manipulator via genetic algorithm. Robotica 24:739–743
6. Geiger BR, Horn JF, DeLullo AM, Long LN (2006) Optimal path planning of UAVs using direct collocation with nonlinear programming. In: AIAA GNC conference, Paper No.2006-6199, Keystone, Aug 2006

Objective Function Design in Real-Number-Coding Genetic Algorithm for Laser-Cutting Tool-Path Minimization

Wei-Kai Hu and Kerwin Wang

Abstract Laser-cutting path arrangements are constrained multimodal optimization problems. In solving these continuous-path control problems, one can improve the time efficiency and power consumption of laser-cutting process. This chapter presents a simplified objective function design methodology for real-number-coding genetic algorithm. In the cutting route determination stage, all the cutting starting and ending points are placed in a plane at the same place to facilitate the completion of routing. These objective functions can be used for path finding in practical laser-cutting assignments.

Keywords Path minimization • Genetic algorithm • Tool-path

1 Introduction

It is important to have a minimized tool-path in a laser-cutting system to save process energy and time. Many similar problems have been studied using genetic algorithms. As a branch of evolutionary programming, they perform a multiple directional search by maintaining a population of potential solutions. At each generation of a population, the relatively good solutions are reproduced and selected to reproduce the next generation of a population. The process uses probabilistic transition rules; it can guide their search toward favorable regions. They can solve problems without relying on gradient information of an objective function; it is suitable for discrete objective functions. State-of-the-art genetic algorithms can solve many global optimization problems much faster than random search or dynamic annealing methods. Tate and Smith applied genetic algorithms to shape

W.-K. Hu • K. Wang (✉)
Department of Mechatronics Engineering, National Changhua University
of Education, Changhua 50007, Taiwan
e-mail: kerwin@cc.ncue.edu.tw

constrained area facility layout problems [1]. Lim and Chew proposed a genetic algorithm for the joining compacted cells [2]. Previous works already found that genetic algorithms can produce good results in a reasonable time when solving these kinds of problems by implementing real encoding methods and enlarging the sampling space. It is also possible to add directional searching operators in genetic algorithm to improve its time efficiency [3]. As a branch of evolutionary programming, genetic algorithms (GA) perform a multidirectional optimization search. It can handle different types of objective functions and constraints (i.e., linear or nonlinear, continuous or discontinuous). Existing genetic algorithms can solve many different engineering problems faster than random search or dynamic annealing methods; however, without well-defined objective function, genetic algorithms can take a large amount of time to converge to global solutions in multimodal problems. In this chapter, a simplified objective function for solving a laser-cutting tool-path minimization problem is proposed and solved by a real-number-coding genetic algorithm.

2   Objective Function Design

In general, a series of laser-cutting commands will tell the laser head move from element node to node and where it needs to fire. Laser head moves without cutting when it is moved from pattern to pattern. It is called air move (fly mode). An air move would require less time than a cut move (process mode).

A laser-cutting tool-path minimization problem is similar to a generalized traveling salesman problem [4]. However, it involves arbitrary pattern cutting. If there is no internal contour, each pattern is surrounded by one contour only. Each contour consists of one entering point and one identical exiting point. The following assumptions have to be made in defining this problem.

Assumptions:

1. All the patterns have predetermined positions.
2. All the tool-paths are two dimensional.
3. A contour has to be fully cut before moving to a next contour.
4. The laser cutter head can stop cutting when moving between different contours (under fly mode).
5. Entering point and exiting point are identical, which means if a contour is entered by a laser cutter head, it has to be exited.
6. Every element on a contour has been passed once only, except entering points.

Under these assumptions, the total cut move length, required to complete a cutting task, is independent of the chosen tool-path. Using these assumptions, a genetic algorithm can then be applied without additional constraints. In order to do this efficiently, an indicator is defined as the sum of serially connected piece-wise-continuous sections on the circumference from entering/exiting points to a given starting point. It is a percentage number which can represent the ratio of
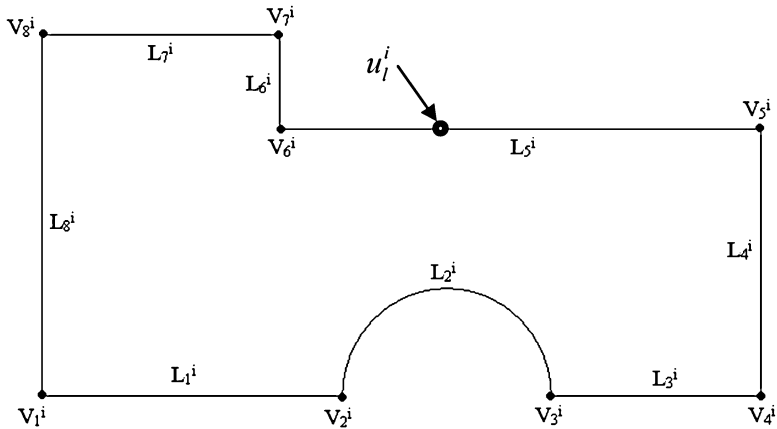
Fig. 1 Nodes and piecewise-continuous sections of an arbitrary pattern

partial piecewise-continuous section to the circumference of a given pattern. That means each pattern offers only one searching dimension.

Every time the laser head needs to start cutting in a new piecewise-continuous section of the pattern, an initial cut of a pattern can be made "on the fly." The fly mode allows the laser-cutting head to pass an element where it has to start cutting later. The goal of the laser-cutting tool-path problem is to minimize the total tool-path length required to cut all parts. The total path consists of the sum of the actual cutting path length and flying distance. One can calculate the total flying distance among entering/exiting points and estimate the circumference from the sum of the partial integration of these patterns. A pattern consists of several piecewise-continuous sections (shown in Fig. 1). They are connected into a topologically closed contour. This arrangement allows us to design a simplified objective function. The simplified objective function is evaluated by calculating the summation of the distance among entering/exiting points, in which coordinates can be derived from the indicator of each pattern.

V_k^i = pattern i and kth node ($i = 1,\ldots, m; k = 1,\ldots, n$)

L_l^i = pattern i and lth section ($i = 1,\ldots, m; l = 1,\ldots, n$)

u_l^i = one-dimensional position ratio of an entering/exiting point on pattern i at section l ($0 \leqq \%u_l^i \leqq 100 \%$)

$P^i(u_l^i)$ = coordinate of an entering/exiting point of pattern i

$d_{ij}(u_i, u_j) = \left\| P^i(u_l^i) - P^j(u_l^j) \right\|$

$d_{ij}(u_i, u_j)$ = distance between entering and exiting points of two selected patterns, i and j

The objective function then evaluates the sum of the total path length for all patterns. A distance matrix is prepared. d_{ij} equals the path length required to move from an entering/exiting point of a selected pattern to another. The objective function then minimizes the sum of the total traveled path length. It can be converted into required time for processing.

3   Real-Number-Coding Genetic Algorithm

Goldberg [5] describes the usual form of genetic algorithm. This is based on the mechanism of natural selection and natural genetics. Genetic algorithms start with some initial random starting points called population or parents (chromosomes). They are encoded from the parameters or design chosen. A chromosome is a string of symbols; it could be a binary bit string, number, or text. The chromosomes evolve through successive iteration, called generation. During each generation, the chromosome will be evaluated and selected by using fitness evaluation. In the selection process, better parents will be assigned higher probabilities of being selected. The selected chromosome (parents) will be "calculated" by genetic operators (crossover and mutation) and create (born) the next generation (offspring). After several generations, hopefully, the algorithms converge to the best chromosome, which represents the optimal solution to the problem. It is an effective approach for solving optimization problems.

However, there are many situations in which the simple genetic algorithm does not perform particularly well. Various hybridization methods have been proposed. For example, Ackley recommended genetic hill climbing, in which crossover operators play a rather less dominant role [6]. On the other hand, binary coding methods have their own limitation because their accuracy is limited by its resolution. Real-number-coding methods (Fig. 2) would be better than binary coding for different optimization problems.

The real-number-coding (also known as floating-point representation [7]) technique is used to represent the solution of this path minimization problem. In this proposed real-number-coding genetic algorithm, all the binary chromosomes are encoded as a vector of real numbers; it has same lengths as the solution vector. It involves four stages: (a) binary chromosome to real-number conversion, (b) population initialization, (c) operator calculation, and (d) chromosome evaluation.

4   Results

The proposed objective function works well with real-number-coding technique. It provides accurate results (shown in Fig. 3). Genetic algorithm is not dependent on gradient-based searching methods. One thing to be careful of is to prevent a super
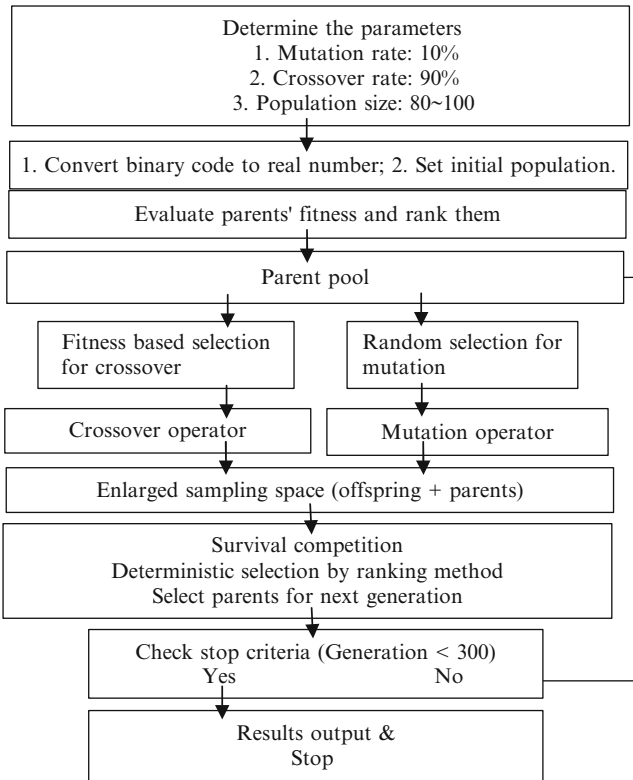
Fig. 2 Structure of real-coding genetic algorithm
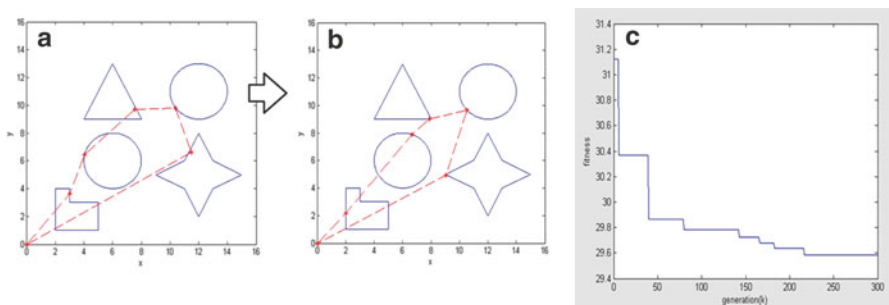
Fig. 3 (**a**) Path minimization progress and (**b**) results using simplified objective function and real-coding genetic algorithm and (**c**) the evolution process

gene from dominating the solution process, which could result in converging on a local optimal. Therefore, the proper fitness and selection pressure need to be assigned. In practical applications, the power and speed of laser-cutting toolhead

would need to be taken into consideration to avoid overheating. An incomplete cutting path of a contour would also be needed to leave uncut small joints to prevent patterns detaching from the plate.

5 Summary

A simplified objective function design strategy for tool-path minimization of a laser-cutting process using real-number-coding genetic algorithm is introduced. The algorithm converts binary coding chromosome to a real-number-coding system. This technique is used to represent the solution. The efficiency and accuracy of optimized results are verified. It can be easily implemented in a variety of path optimization problems.

References

1. Tate D, Smith A (1995) Unequal-area facility layout by genetic search. IE Trans 27:465–472
2. Lim A, Chew H-K (1997) Joining of compacted cells using genetic algorithm. Electron Lett 33 (23):1944–1945
3. Wang, K (1998) The development of real coding genetic algorithms and their applications. A paper in partial fulfillment of the requirements for the Degree of Master of Science, University of New York, Buffalo, 21 Dec 1998
4. Dewil R, Vansteenwegen P, Cattrysse D (2012) Heuristics for laser-cutting tool-path generation. In: Applied mathematical optimization and modeling, Paderborn, 28–30 Mar 2012, pp 210–216
5. Goldberg D (1989) Genetic algorithm in search, optimization and machine learning. Addison-Wesley, Reading
6. Ackley D (1987) A connectionist machine for genetic hill-climbing. Kluwer Academic Publishers, Boston
7. Michalewicz Z (1994) Genetic algorithm + data structure = evolution programs, 2nd edn. Springer, New York

A Fuzzy Control Load Balancing Method for Dual CAN Bus

Yu-Wei Huang and Chih-Hung Wu

Abstract This chapter presents a load balancing method for dual CAN bus to maximize the use of network bandwidth. The CAN (controller area network) is a serial communication protocol gaining widespread acceptance in automotive and automation industry. The network uses dual bus to improve network bandwidth and performance. The data traffic of CAN bus is degraded on high-load conditions. This chapter proposes a load balancing allocation algorithm using fuzzy control to obtain the maximum data traffic. The load balancing allocation algorithm introduced in the chapter is validated on a four-node dual CAN bus system. Each CAN node uses a LPC2119 ARM development board as hardware platform. The chip LPC2119 is based on the ARM7 CPU core with 2 CAN channels. Experiment results show that the fuzzy control is quite suitable for the load balancing control to improve the performance of dual CAN bus at high-load conditions.

Keywords Dual CAN bus • Fuzzy control • Load balancing

1 Introduction

In order to solve the problem of exchanging data between the car controllers with many sensors, Bosch proposed the CAN bus (controller area network bus) solution. CAN is extensively used in automobiles and trucks but has found applications

Y.-W. Huang
Graduate Institute of Vehicle Engineering, National Changhua University of Education, Changhua 50007, Taiwan

C.-H. Wu (✉)
Department of Game and Product Design, Chienkuo Technology University, Changhua 50094, Taiwan
e-mail: zhwu@ctu.edu.tw

everywhere. Its domain of application ranges from high-speed networks to low-cost multiplex wiring.

A CAN network consists of at least two nodes connected together with a twisted pair of wires. It is relatively easy to construct a network consisting of 20 nodes (or more) with a given maximum 1 Mbps speed and a bus length up to 40 m. Any node can broadcast a message using a CAN frame on a bus. Every node will see this message.

Many CAN networks work on a bus loading from 15 to 35 % and this is increasing [1]. A higher bus loading can cause lower-priority messages to be delayed but these messages will still get through in a timely fashion [2]. It is possible to get very high bus loads for a very short period of time in any CAN network [3]. CAN does not automatically space out messages. It is possible to get a series of back-to-back messages that will equal nearly 100 % bus loading.

This chapter proposed a fuzzy control load balancing allocation method for dual CAN bus system [4, 5]. The results of experiments and tests show that the proposed method can take full advantage of dual bus transfer and improve the performance of dual CAN bus at high-load conditions.

2 Load Balancing Algorithm Based on Fuzzy Control

This study primarily designs a dual CAN bus load balancing allocation mechanism, as shown in Fig. 1. In this chapter, the load balancing control is based on loading difference between buses and change rate of deviation. The host reads current loading of each bus to calculate loading situation. The fuzzy control predicts loading trend of each bus to decide which bus sends data in order to achieve load balancing.

This study uses fuzzy control to solve the problem of load balancing allocation for dual CAN bus. The inputs of the fuzzy control are loading difference between buses and change rate of deviation. The output is one of dual CAN bus. The interval
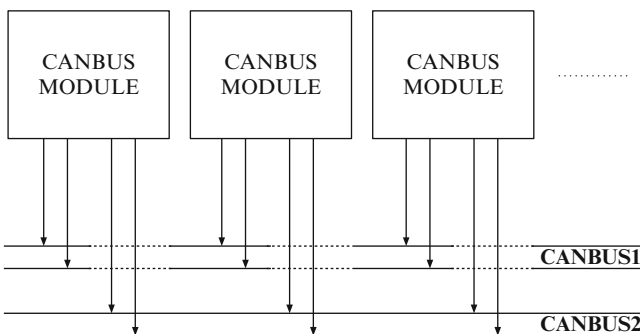
Fig. 1 Dual CAN bus system
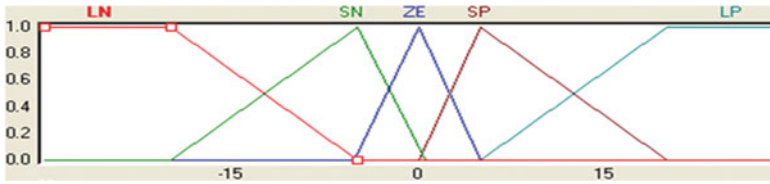
Fig. 2 Membership function of CAN bus loading difference
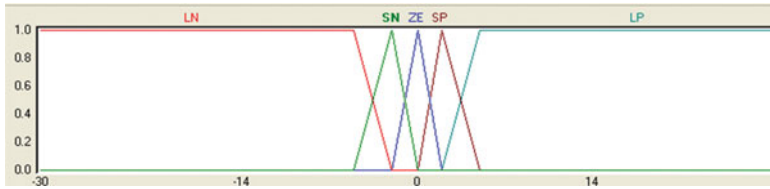
Fig. 3 Membership function of change rate of deviation

Table 1 Fuzzy control rules

A/B	LN	SN	ZE	SP	LP
LN	LN	LN	SN	SN	ZE
SN	LN	SN	SN	ZE	SP
ZE	SN	SN	ZE	SP	SP
SP	SN	ZE	SP	SP	LP
LP	ZE	SP	SP	LP	LP

A is a loading difference between buses
B is the change rate of deviation

of loading difference can be discretized into five points: $[-20, -5, 0, +5, +20]$, as shown in Fig. 2. The interval of change rate of deviation can be discretized into five points: $[-5, -2, 0, +2, +5]$, as shown in Fig. 3. Language variables are expressed as [LN, SN, ZE, SP, LP].

When the loading difference is large, the output of fuzzy control should eliminate the difference as soon as possible. When the loading difference is small, the output of fuzzy control should prevent overshoot. According to characteristics of dual CAN bus, the fuzzy control rules can be set up as shown in Table 1.

After the completion of the fuzzy inference, the result shows the membership degrees of the fuzzy sets. The interval of output can be discretized into five points: [20, 40, 50, 60, 80], as shown in Fig. 4. The output should be interpreting the membership degrees of the fuzzy sets into a specific decision or real value. If the output value is greater than 50, it will transmit data from CAN bus 1. Otherwise, it will select CAN bus 2 to transmit data.
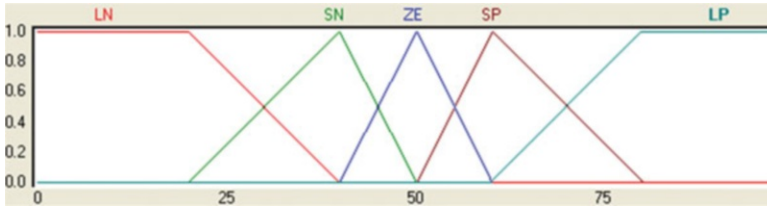
Fig. 4 Membership function of output

3 System Design and Architecture

Based on studying CAN bus load balancing deployment mechanism, the hardware system architecture is presented as shown in Fig. 5. Each CAN bus node uses a development board with core chip LPC2119. Chip LPC2119 has embedded 2 CAN controllers, but it must be connected to the CAN transceiver to transmit and receive CAN signals. The TJA1050 transceiver provides a communication interface between the CAN controller and CAN bus. The signals CAN_H and CAN_L from transceiver form a dual CAN bus.

Each CAN controller of LPC2119 has a register structure and the PeliCAN Library block. The CAN controller needs only to register configuration at initialization process. The initialization of CAN controller includes the following task: pin function, error warnings, baud rate, acceptance filter, and interrupt.

To develop test program of the proposed method, the Keil software development tool is selected. The test program contains the initialization part and the main loop part. The main loop part consists of three tasks: the core function, the receive function, and the transmit function. The core function is designed according to the proposed method.

A transmit function has been programmed to carry out the tasks of transmit messages. Any node can start sending a CAN frame when the bus is idle. All other nodes start receiving it except those that also start transmitting at the same time. The node with the highest priority continues on and those with a lesser priority stop sending. When the transmitting node has completed sending its message, it waits 1 bit ACK field to signify the frame was received without errors. If this happens, the transmitting node sends the end-of-frame bits. The CAN bus is idle again. If an error condition is detected, the message will be resent but only for a certain number of times.

In CAN bus, all nodes except those currently transmitting frame are in listening mode. A transmitted frame is received by all listening nodes. When a CAN controller has received a complete frame, it signals the acceptance filter. The receive frame contains identifier, data, and other information. The acceptance filter reads the CAN message. It then proceeds to determine whether the message should be received or ignored. If accepted, it is sent to the controller and stored in FIFO memory. The processor is alerted by an interrupt or a flag. This frame must be read as soon as possible. A receive function has been programmed to carry out the tasks. The interrupts of receive message cause the processor to jump to the receive function where the frame is read from the controller.

Fig. 5 System architecture diagram
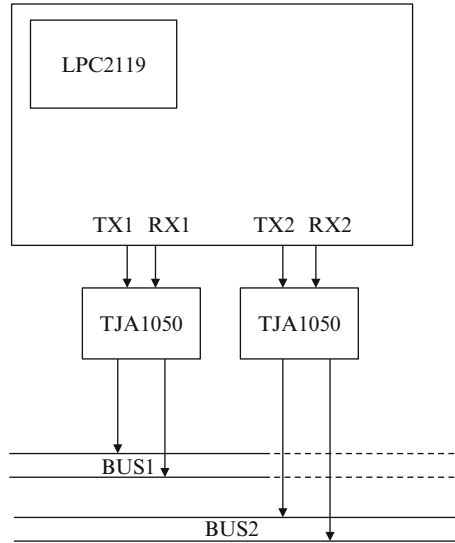
4 System Test and Result

This chapter proposed a fuzzy control load balancing method for dual CAN bus system according to the CAN bus protocol, dual CAN bus architecture, and fuzzy theory. The main purpose in this chapter is to achieve dual CAN bus load balancing based on fuzzy control. The test will continue to transmit message during a fixed period of time. The results compare the transmit message number between CAN buses 1 and 2. The test measurement and analysis are on different bus loadings.

A hardware system is implemented to test results. A dual CAN bus system consists of four operation nodes and a monitor node. The monitor node only receives CAN frame. It is mainly used to observe and record CAN frame from the other four nodes. The identifier of nodes 1, 2, 3, and 4 is assigned to 0×49, $0 \times 59, 0 \times 69$, and 0×79, respectively. The test data field length is 8 bytes. Each loading condition was measured four times. Each time was 10 min. The result is average of the four times.

A waveform of CAN bus transmission is shown in Fig. 6. The first and second channels at the top of Fig. 6 are messages at CAN buses 1 and 2, respectively. The remaining channels (D7–D0) below channels 1 and 2 are transmitting frames at CAN buses 1 and 2 for each node, respectively.

This first experiment tests whether dual CAN bus reached load balancing under different sending nodes. In the first case, only one node sends CAN messages, and then two nodes, three nodes, and four nodes send messages in order. The test is performed four times, each time sending the same data every 10 min. The result is shown in Table 2. The traffic difference between CAN buses 1 and 2 is small enough.
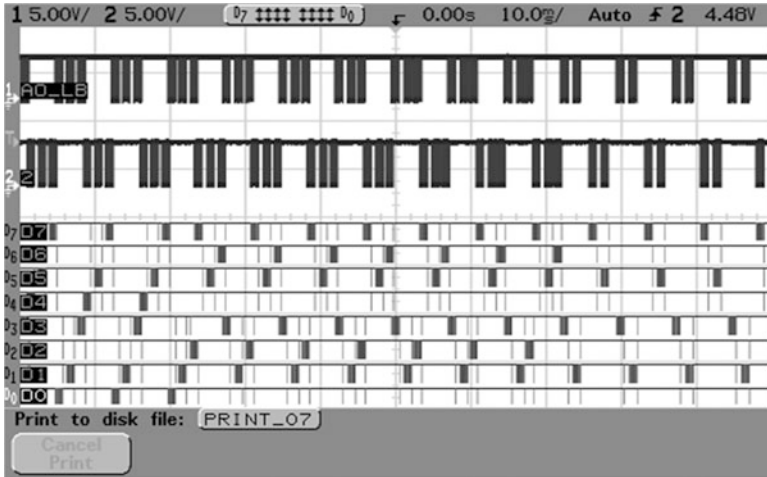
Fig. 6 Actual measurement of CAN bus

Table 2 Loading balance test for different node numbers

No. of transmit node	CAN bus 1	CAN bus 2	Difference between CAN buses 1 and 2 (%)
1 node	132,453	132,456	0.00
2 nodes	267,077	266,099	0.37
3 nodes	373,471	374,502	0.28
4 nodes	456,319	456,237	0.02

Table 3 Loading balance test for different loading

Loading condition	CAN bus 1	CAN bus 2	Difference between CAN buses 1 and 2 (%)
Low	96,114	96,117	0.00
Medium	262,573	262,776	0.08
High	456,320	456,237	0.02

This second experiment tests whether dual CAN bus reached load balancing under different loadings. The first case is low loading at CAN bus, then medium loading and high loading in order. The test is performed four times, each time sending the same data every 10 min. The result is shown in Table 3. The traffic difference between CAN buses 1 and 2 is small enough.

The results from the above experiments show good results under different loadings or nodes. The loading difference between CAN buses 1 and 2 is less than 0.37 %.

In order to understand transmission efficiency, the proposed method is compared with alternate bus method. The alternate bus method sent data to different CAN buses in turn. In theory it is load balance naturally. The following experiments compared

Table 4 Loading balance for different loadings

Loading condition	CAN bus	The proposed method	Alternative bus method	The proposed method vs. alternative bus method (%)
Low	CAN bus 1	96,110	95,773	0.35
	CAN bus 2	96,126	95,786	0.35
Medium	CAN bus 1	262,537	252,554	3.80
	CAN bus 2	262,813	252,726	3.84
High	CAN bus 1	456,288	426,203	6.59
	CAN bus2	455,963	427,694	6.20

different methods for the transmission efficiency of dual bus load balancing. This section will be carried out to several cases. Each case tests five times. Each time was 10 min. The result is shown in Table 4. In high-loading situations, the transmission rate of the proposed method is more than 6.5 %. These results show that the proposed method transmits more data than alternative bus method regardless of load transfer rate.

5 Conclusion

The proposed method uses fuzzy control to balance dual CAN bus load. In this study, load balancing mechanism determines which bus is selected according to loading difference between the buses and loading change rate. Via the above tests and comparison, the proposed method can achieve load balancing requirements and higher transmission rates regardless of loading rate.

References

1. Gao X, Li L (2011) Analysis and research of real time ability of message transmission in CAN bus. In: International conference on control, automation and systems engineering (CASE), IEEE Press, New York, 2011, pp 1–3
2. Nolte T, Hansson H, Norstrom C (2003) Probabilistic worst-case response-time analysis for the controller area network. In: The 9th IEEE real-time and embedded technology and applications symposium, IEEE Press, New York, 2003, pp 200–207
3. Davis RI, Navet N (2012) Controller area network (CAN) schedulability analysis for messages with arbitrary deadlines in FIFO and work-conserving queues. In: 2012 9th IEEE international workshop on factory communication systems (WFCS), EEE Press, New York, 2012, pp 33–42

4. Jun Y, Kai X (2010) The application of fuzzy control in solar heat supply and storage system. In: 2010 international conference on computer, mechatronics, control and electronic engineering (CMCE), IEEE Press, New York, 2010, pp 179–182
5. Guo Y, Zhao Y, Lu Z, Liu J (2008) The design of improved fuzzy controller based on MCU for central air conditioner. In: International symposium on intelligent information technology application workshops, IEEE Press, New York, 2008, pp 197–200

Backup Host Plan for Banking Information System Based on Capacity on Demand Model

Ming-Tsung Yeh, Wan-Chun Liu, and Yi-Nung Chung

Abstract The financial information's operation of banking cannot allow the services to discontinue and lose data. To reduce the banking service impact because of unexpected disasters, this study plans to use the composite remote backup model and proposes to use the CoD (capacity on demand) model to design the backup center's host to protect the information system that is suitable to the recovery requirement for banking. This study uses the analysis of variance method to census and analyze the fault factors of some banks' information system and derives the equation of estimation to calculate how much redundancy capacity to purchase for the remote host. This should reduce the setup cost substantially than is possible using the traditional model.

Keywords CoD model • Remote backup • Fault factor analysis

1 Introduction

Nowadays, banking use the information system for business operations daily. This will reinforce the dependence on the computer system. However, natural disasters and artificial negligence that bring the system down cannot be avoided from happening in the data center. Many redundancy mechanisms are present in the information industry, including local dual host mode, remote dual host mode, and hybrid backup model [1].

M.-T. Yeh • Y.-N. Chung (✉)
Department of Electrical Engineering, National Changhua University
of Education, Changhua 50007, Taiwan
e-mail: ynchung@cc.ncue.edu.tw

W.-C. Liu
Department of Information Engineering, Kun Shan University, Tainan 710, Taiwan

Nowadays, mainframe systems control the host performance by the key mode, and the vendors offer the same system hardware platform; with the performance capacity purchased by a customer's need, this can be increased by paying anytime. This makes the whole system to operate in a more flexible capacity demand, capacity on demand (CoD), which is defined as follows: Customers receive the purchase host because of its more processing capacity, storage space, and the other higher performance than the specifications required for the machine, and these additional capacities will be retained. When a customer needs more efficacies, they pay the vendor to obtain other key opened more performances that can be cost-effective and time-saving [2].

This should be expensive to set up the remote backup host if we use the traditional model, which needs to buy other same level host with the production host. The backup hosts based on the CoD model only spend the basic hardware and performance key price demanded for backup. This should reduce the setup cost in remote site.

2 Information Disaster

The data center is the core of the business operation for the banking. These have many artificial negligence and natural disasters that bring the system down.

This chapter refers to some literatures [1] discussing information risks and threats. Figure 1 shows the analysis chart depicting the cause of information disaster and the first five items to cause the information disaster that happened.
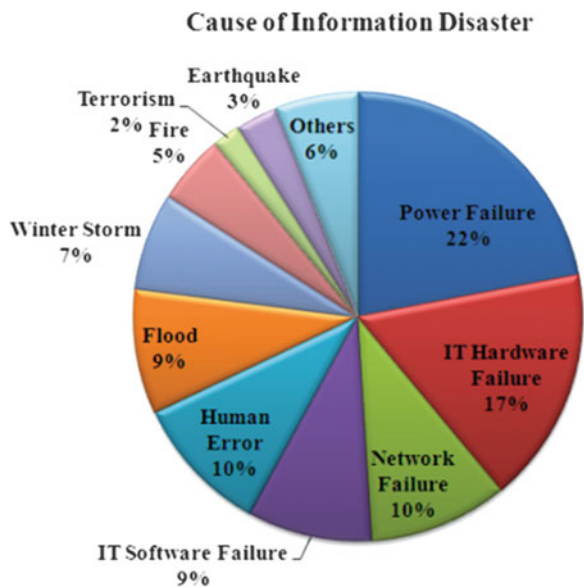
Fig. 1 The cause of information disaster (Source: Forrester Research Inc.)
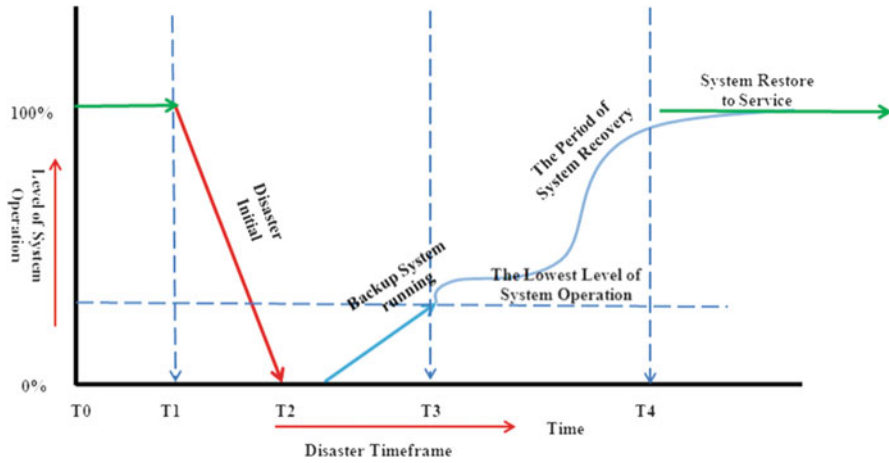
Fig. 2 Information disaster restoration timeframe

These items are power fault, hardware error, network malfunction, software error, and artificial out of operation, which are common faults in the data center.

In general, the disaster recovery timeframe can be divided into four time phases from initial disaster to normal state. Figure 2 shows the timeframe chart to explain the disaster recovery processes.

In the figure, T0–T1 is the normal operation state, T1–T2 is the system crash that causes the service to stop, T2–T3 is the system transit to the backup system that can provide some essential services, and T3–T4 is the recovery phase that primary system restores in progress and the service will restore to normal gradually [3].

Disaster recovery mechanism is devoted to shorten the timeframe T1–T4. The best ideal backup plan will cause this time to become almost zero that should transfer the service supplier to the backup system seamlessly if a disaster happens.

3 Remote Host Plan Based on the CoD Model

For banking special requirement, this chapter plans to use the composite remote dual host backup model. Refer to Fig. 3, which is the framework. This mode will set up other host with the same performance level of the production host in the remote site. The backup host will take over all the services of the primary site host provided disasters happened. This action is called as "fail over" to remote site [4, 5].

There are many factors that cause the failure of the bank's information center. This chapter refers and analyzes a number of events that are the routine operation logs in bank's data centers and the computer company's service records, which categorize the system failure analysis into seven categories, as shown in Table 1. This chapter will only analyze the fatal failures that cause the service to stop. The
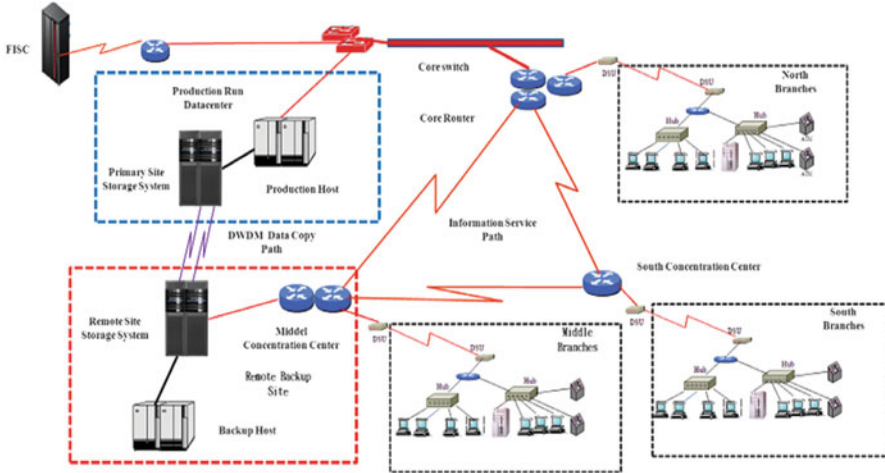
Fig. 3 The framework of remote backup center

failure information of case banks can be arranged as shown in Table 1, which shows each fault percentage of the entire disability rate.

For the planning backup host based on CoD mode, we first need to know how much performance capacity to buy for this host. The disaster recovery capacity is defined as how many days the backup host can open annually and which performance level is the same as the production host.

The disaster recovery capacity of the backup host should estimate the amount of frequency of occurrence of failure factor in a data center each year; thus, the data center must census and analyze the annual average of occurrences of each failure factors. In accordance with the importance of each failure factors offer weight to that. The disaster recovery capacity is obtained from the annual average of failure factors multiplied by its weight and then sum all. The estimation equations are presented as follows:

$$DRc = \sum_{i=1}^{n} FA_i \times W_i \qquad (1)$$

where DRc is the disaster recovery capacity, FA is the failure factors annual average by days, and W is the weight. The failure factor weights are shown in Table 2. The weights are based on the importance and influence of each failure factor and recovery processing time.

We can obtain how many DRc are used by using (1) that requires backing up the production host after getting the annual average of fault factors, and stand on this data to purchase the disaster recovery key for the backup host. The disaster recovery capacity calculated for the case banks is shown in Table 3.

Table 1 Casebanks fatal failure percentage

Failure factor Bank	Host hardware failure (%)	System software failure (%)	Application software failure (%)	Human error (%)	Network failure (%)	Facility failure (%)	Natural disaster (%)	Fatal error quantity (%)
A	12.24	16.33	26.53	14.29	14.29	14.29	2.04	49
B	10.87	19.57	23.91	13.04	17.39	13.04	2.17	46
C	9.09	13.64	40.91	11.36	15.91	9.09	0.00	44
D	12.70	15.87	25.40	12.70	15.87	14.29	3.17	63
E	10.26	11.54	26.92	16.67	17.95	14.10	2.56	78
F	12.50	11.36	28.41	15.91	12.50	17.05	2.27	88
Total failure percentage	11.41	14.13	28.26	14.40	15.49	14.13	2.17	368

Table 2 Failure factor's weight

Failure factor	Weight
Host hardware failure	3
System software failure	3
Application software failure	2
Human error	1
Network failure	1
Facility failure	1
Natural disaster	6

Table 3 DRc for case banks, annual average of failure factors present by days

Annual average Bank	Host hardware failure (FA1)	System software failure (FA2)	Application software failure (FA3)	Human error (FA4)	Network failure (FA5)	Facility failure (FA6)	Natural disaster (FA7)	Disaster recovery capacity (DRc)
A	0.5000	0.6667	1.0833	0.5833	0.5833	0.5833	0.0833	7.9167
B	0.4167	0.7500	0.9167	0.5000	0.6667	0.5000	0.0833	7.5000
C	0.5714	0.8571	2.5714	0.7143	1.0000	0.5714	0.0000	11.7143
D	0.6667	0.8333	1.3333	0.6667	0.8333	0.7500	0.1667	10.4167
E	0.6667	0.7500	1.7500	1.0833	1.1667	0.9167	0.1667	11.9167
F	0.9167	0.8333	2.0833	1.1667	0.9167	1.2500	0.1667	13.7500
Weight	3	3	2	1	1	1	6	
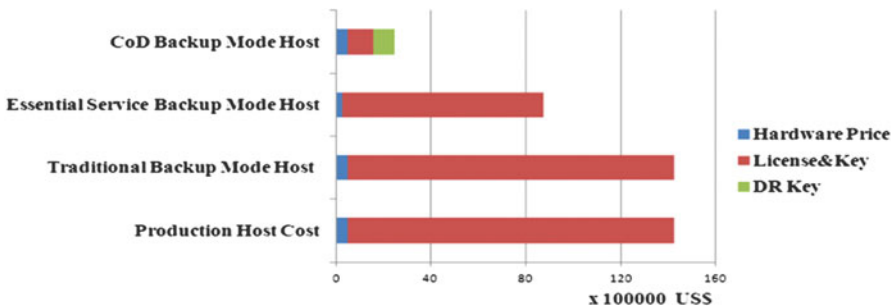
Fig. 4 Cost comparison of each backup mode

Besides the traditional hardware costs, the major cost of the current host based on the CoD mode is the system license and performance key prices. However, the cost of the backup host is only the base hardware, system license, and performance key required for standby operation, and additional disaster recovery key for backup purpose.

The cost comparison based on the reference of marketing price between the CoD mode and other two common backup modes is shown in Fig. 4. Since the traditional
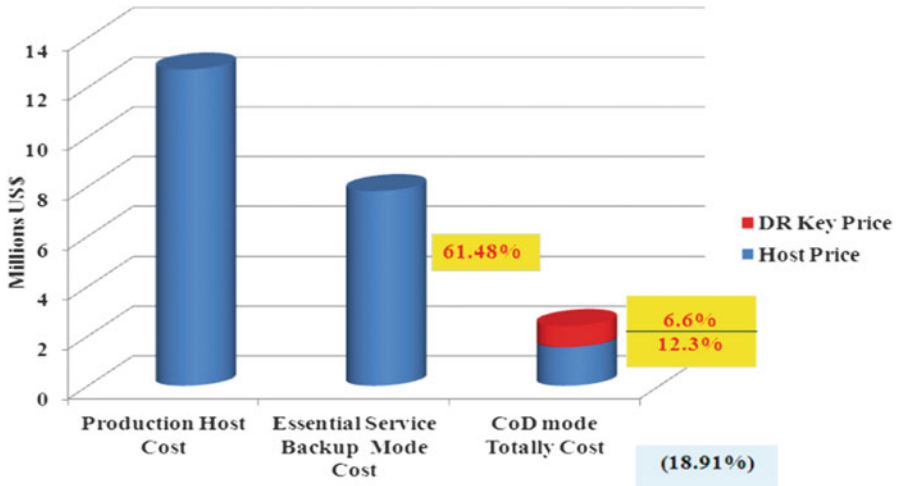
Fig. 5 Bank B cost comparison

mode needs to buy a same level host, it has almost the same cost with the production host. The essential service mode is to just back up the core operation by half performance, whose cost is about 50 % of the traditional mode. From this chart, it can be seen that the backup host on the CoD mode saves more than 60 % cost than the traditional model.

This chapter uses banks B and C as cases to estimate the feasibility. Bank B backup host is planned to be a simple remote backup host, which just stands by to back up the primary host daily. Referring to Table 3, it needs to buy an annual 8 days DR key, and the cost comparison is shown in Fig. 5. The total cost using the CoD mode is 18.91 % of the production host, which can reduce about 81 % price than the traditional mode. It is clear when using the CoD mode to design the backup host it can greatly reduce the cost. Through the disaster drilling, we can find the operating performance of the backup host, which is the same as the production host. So the simulation result is expected, and the backup host can take over all the service jobs when a disaster happens in the primary site.

The mainframe system is quite expensive. To use these resources, we can design the developing environment in the backup host to increase its operation rate.

Bank C backup host is planned to be a developing host daily and a role as the backup primary host. Its DRc is 11.71 days (refer to Table 3). It needs to buy an annual 12 days DR key. This bank needs to buy additional system license and performance key for development purpose. The cost comparison for each mode is shown in Fig. 6. The total cost using the CoD mode is 62.66 % of the production host price. The cost of the essential service backup mode is lower, but its performance is just about half of the production host when the backup is initiated for the disaster that happened, so the CoD mode is more adaptable for recovery. Using the remote backup host as a routine developing host, its operating rate can be greatly increased to reduce the idle and waste of resources.
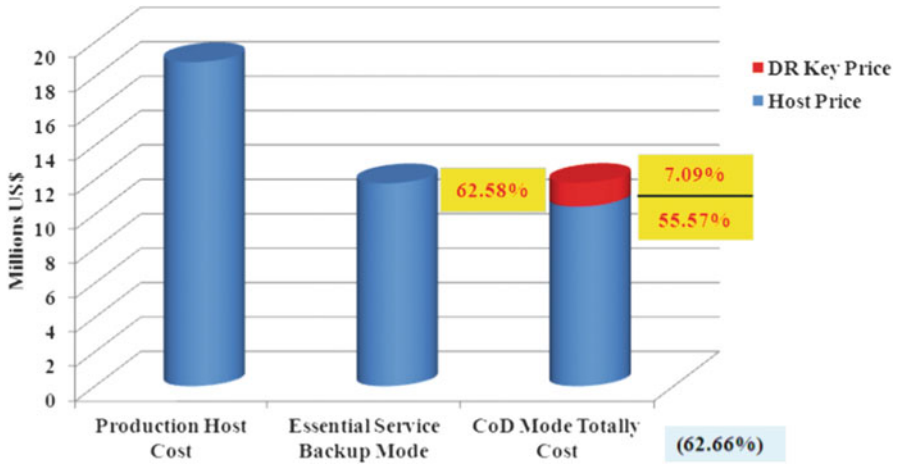
Fig. 6 Bank C cost comparison

4 Conclusion

Due to the banking concern, this chapter plans to use the composite remote backup mode to back up information system of production host for unexpected disasters. This chapter proposes using the CoD model to design the remote host, and according to the disaster recovery capacity formula (1) to calculate how many disaster recovery capacities are needed for the backup host that only needs to buy the cheaper performance key (DR key), which is a certain number of days and can open with the same performance level as the production host rather than buy similar processing capability of the host in a traditional mode.

Remote backup host cost using the CoD mode compared with other modes can save about 40–80 %. For a mainframe host that costs several hundred million dollars, it can save a considerable amount. This proves the feasibility of the proposed CoD model via the case banks B and C remote host plan and disaster recovery drill. Banks that need to set up remote backup host for protecting the information system can refer to this proposed method, which may reduce the setup cost and always keep the same performance level with the production host in disaster recovery time.

References

1. Snedaker S (2007) Business continuity and disaster recovery planning for IT professionals. Syngress Publishing Inc, Burlington
2. Patel S (2002) Dynamic capabilities of capacity on demand. HP Company

3. Wiboonrat M, Kosavisutte K (2008) Optimization strategy for disaster recovery. In: 4th IEEE international conference on management of innovation and technology, ICMIT 2008, Bangkok, 21–24 September 2008, pp 675–680
4. Lin G, Yu Zh, Li HB, Zhang LJ, Zhang JP (2010) A remote data disaster recovery system model based on undo. In: Sixth international conference on networked computing and advanced information management (NCM 2010), Seoul, 16–18 August 2010, pp 123–128
5. Yang P, Kong B, Li J, Lu M (2010) Remote disaster recovery system architecture based on database replication technology. In: 2010 international conference on computer and communication technologies in agriculture engineering (CCTAE 2010), Chengdu, pp 254–257

Part V
Intelligent Electronic Circuits and Systems

A Design of LED Panel Lamp for Indoor Illumination

Ming-Da Tsai, Jin-Jia Chen, and Kuang-Lung Huang

Abstract An LED panel lamp is presented for general indoor illumination. This lamp consists of arrayed LED light sources with each LED united with an evening lens so that the Lambertian distribution of LED light is altered, and the illuminance on a target plane can be uniform. The computer simulation result shows that the illuminance uniformity is 0.737, and the maximum illuminance is 140 lx on a detecting screen at 1.5 m away.

1 Introduction

In recent years, the crisis of energy resource and environment protection issue force the development of recycle, energy saving, and nonpollution consumptive production. Especially for the light sources, the high-power white-light LEDs, which have many versatile advantages of energy saving, long lifetime, good color rendering, small volume, and fast response, have attracted many applications in general indoor or outdoor lighting.

M.-D. Tsai (✉) • J.-J. Chen
Department of Electrical Engineering, National Changhua University of Education, Changhua 50007, Taiwan
e-mail: pilomida@hotmail.com

K.-L. Huang
Department of Electro-Optical and Energy Engineering, Mingdao University, Peetow, Changhua 52345, Taiwan

As compared with the conventional indoor illumination using fluorescent tubes, the LED light source has better lifetime, electro-optic efficiency, color rendering index, and small lamp volume that lead them to be the popular light source of panel lamps in the future. However, its light distribution is generally a Lambertian type [1] and cannot be directly used in a lighting system to achieve uniform illumination. Therefore, this chapter proposes an evening lens (similar structure has been used for LCD display backlighting purpose) incorporated with the LED light sources and a reflector to form a panel lamp so that a uniform illumination on a target plane at 1.5 m away can be obtained and also satisfies the general lighting requirement of illumination uniformity above 0.7.

2 Structure of the Proposed LED Panel Lamp

The structure of the proposed LED panel lamp is shown in Fig. 1, which consists of two parts, i.e., a reflector and an LED light source array with each LED having an evening lens. The evening lens can redistribute light rays emitted from the LED so that partial light rays will be directly refracted out from the evening lens to the irradiated target plane, while partial light rays will be first refracted by the evening lens and then be reflected by the reflector to the target plane. With appropriately adjusting the lens structure and the pitch between two successive LEDs, the output light rays from the LED panel lamp will uniformly irradiate the target plane. The construction of the evening lens and the reflector is stated as follows.
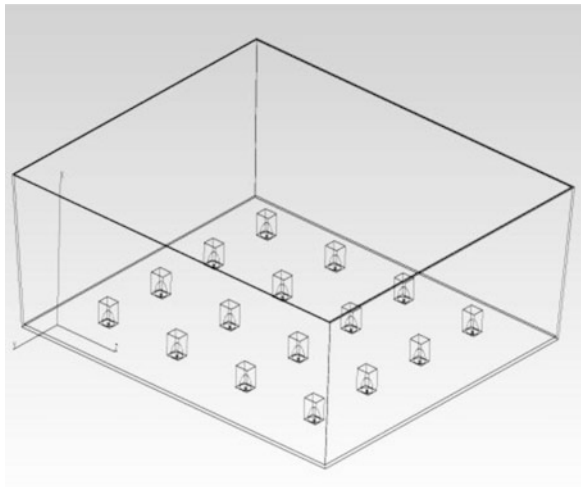
Fig. 1 Structure of the proposed LED panel lamp
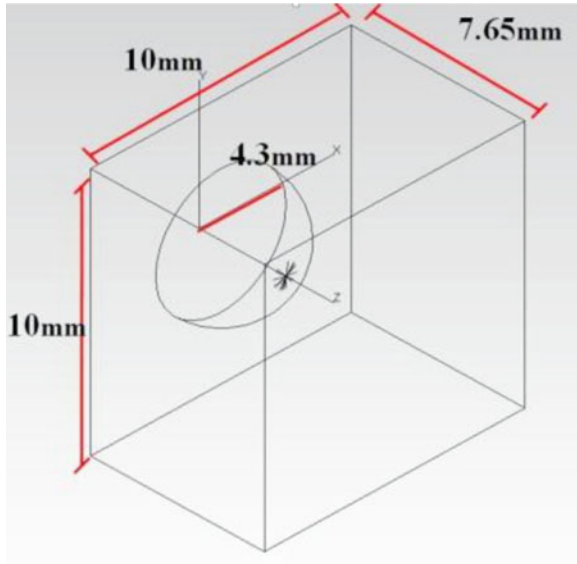
Fig. 2 The 3D scheme of the lens
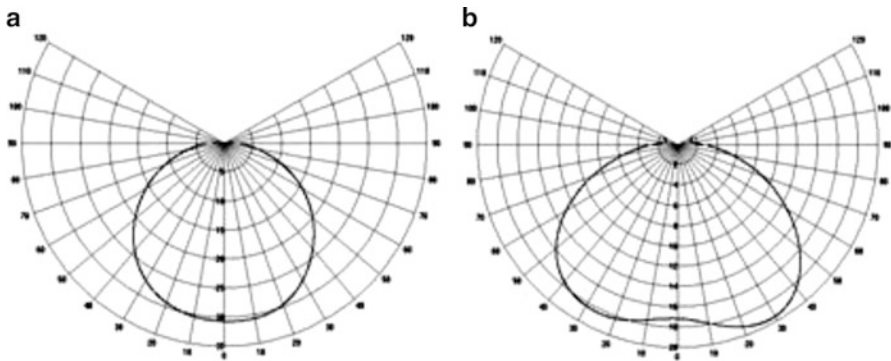
Fig. 3 (**a**) Polar candle power distribution of the LED light source and (**b**) that of the LED light source with the evening lens

2.1 Construction of the Evening Lens

The evening lens used in this chapter refers to the lens structure proposed by Chen and Chang [2] for the purpose of LCD display backlighting; however, the dimension of the lens is altered to fit the LED panel lamp for general lighting. The three-dimensional (3D) scheme of the lens is shown in Fig. 2. It looks like a squared penetrate lens with a half-spherical concavity of 4.3 mm radius at the bottom of the lens. The LED chip is placed at the center of the half-spherical concavity so that the light rays can be redistributed through the evening lens (as shown in Fig. 3).
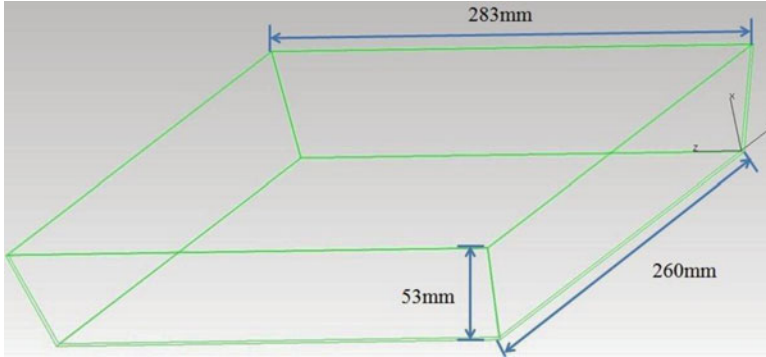
Fig. 4 Dimension of the reflector

2.2 Construction of the Reflector

To redirect light rays refracted out the evening lens from its lateral sides to the target plane, a square reflector is constructed with a TracePro program. As shown in Fig. 4, the dimension is 260 mm × 260 mm at the bottom, 283 mm × 283 mm at the upper opening, and 53 mm in height. For obtaining better optical efficiency, the inner surface of the reflector is coated with high reflective material that the reflectivity of its inner surface is 0.945.

3 Computer Simulation Results

Once the reflector is constructed, a 4 × 4 array of LED light sources with each LED having an evening lens is placed on the bottom of the reflector. The chip size of the LED light source is 1 mm × 1 mm with a Lambertian light output of 100 lm. In addition, the pitch of the LED array is 51 mm, and the target plane (or detecting screen) is located 1.5-m away.

The computer ray-tracing result of the constructed LED panel lamp is shown in Fig. 5, and the simulated illumination on the target plane located at 1.5 m away is shown in Fig. 6. The results show that the spread beam angle of the panel lamp is 89°, the maximum illuminance on the target plane is 140 lx, and the illuminance uniformity η is 0.737, which is calculated by using the following equation:

$$\eta = 100 \,\% \times \frac{L_{\text{ave}}}{L_{\text{max}}} \tag{1}$$

where L_{ave} is the average illuminance and L_{max} is the max illuminance. The simulated result satisfies the requirement for general lighting.
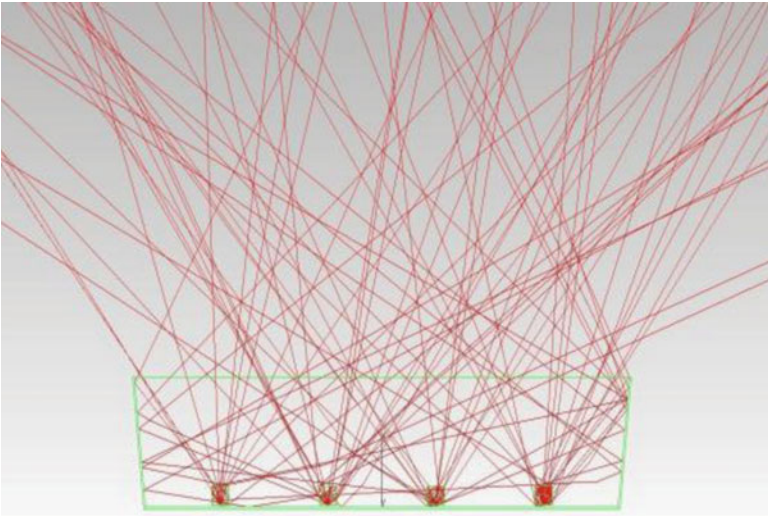
Fig. 5 Ray-tracing result of the proposed LED panel lamp
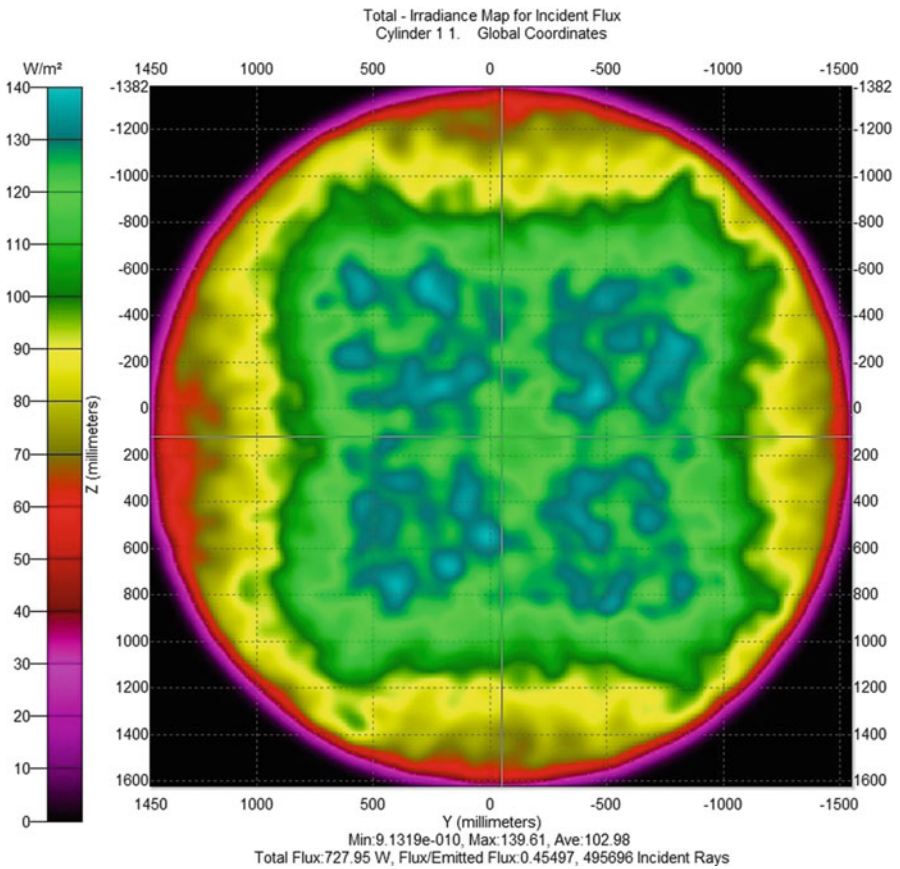
Fig. 6 Computer simulation illumination of the proposed LED panel
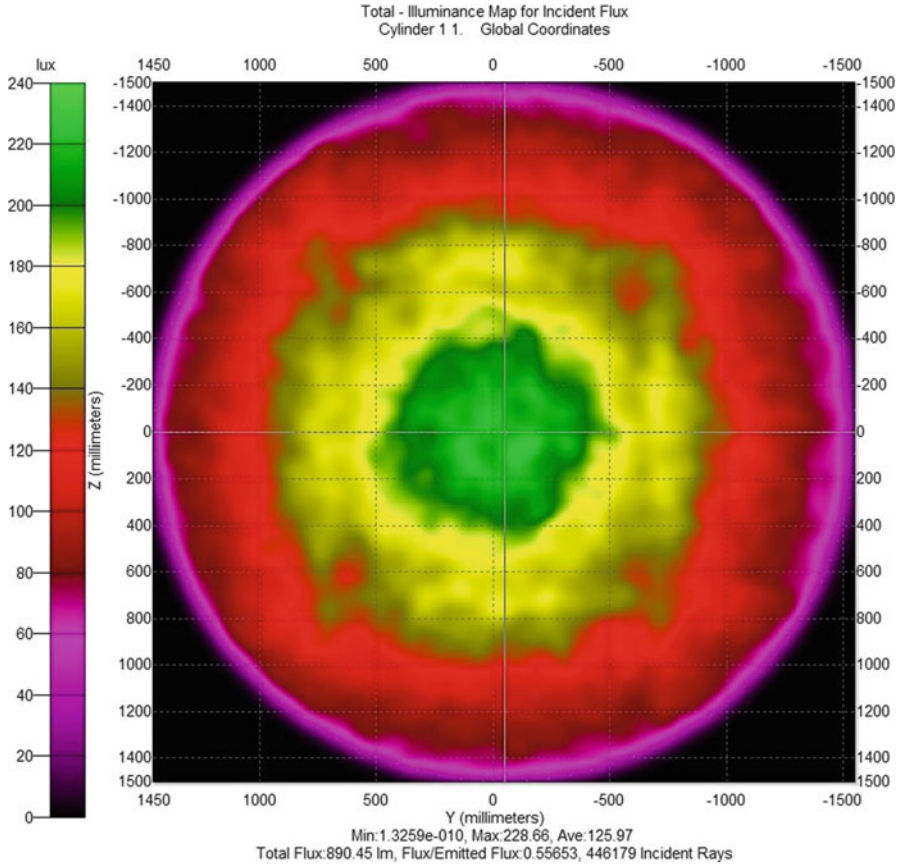
Fig. 7 Computer simulation illumination of conventional direct-backlighting LED panel lamp

Table 1 The effect of the evening lens on the illuminance parameters

Panel lamp	Average illuminance (lx)	Max illuminance (lx)	Illuminance uniformity
No lens	125.97	228.66	0.550
Lens	102.98	139.61	0.737

For comparing the performance of the proposed direct-backlighting LED panel lamp with that of the conventional one without LED evening lens, the simulated illumination of a conventional direct-backlighting LED panel lamp without evening lens is also shown in Fig. 7. From this figure, it can be seen that the maximum illuminance is greater than the proposed lamp; however, the illuminance uniformity is much inferior. In addition, the effect of the evening lens on the illuminance parameters is summarized in Table 1.

Table 2 The effect of the lens pitch on the illuminance uniformity

Lens pitch (mm)	Illuminance uniformity
30	0.686
40	0.699
50	0.730
51	0.737
60	0.630
70	0.594

Other than the evening lens, the pitch of the lenses (or LED light sources) also affects the illuminance uniformity [3, 4] of the LED panel lamp. The effect of the pitch on the illuminance uniformity is shown in Table 2. From the table, it can be seen that the pitch of 0.51 mm gets the best illuminance uniformity to satisfy the purpose of general lighting.

4 Conclusion

A direct-backlighting LED panel lamp is constructed to obtain uniform illumination on the target plane. This lamp is composed of a 4 × 4 array of LED light sources, with each LED having an evening lens and a reflector. The computer simulation result shows that the proposed LED panel lamp can achieve an illuminance uniformity of 0.737 and a maximum illuminance of 140 lx on a target plane at 1.5 m away if a lens pitch of 51 mm is used. Meanwhile, the performance of the proposed LED panel lamp is better than that of a conventional one without using the evening lens; therefore, it can be extended to be used for general lighting.

References

1. Zhen ZR, Hao X, Liu X (2009) Freeform surface lens for LED uniform illumination. Appl Opt 48:6627–6634
2. Chen J-J, Cheng K-H (2010) Light-emitting cover lens design for large-scale liquid crystal device television backlight modules. Opt Eng 49:053003
3. West RS, Takaaki Y (2003) High brightness direct LED backlight for LCD TV. SID, pp 1262–1265
4. Zhang Y (2011) Indoor illumination based on distributive LED lights. In: Proceedings of the ICCTA, 2011

Analysis of Voltage Variations of a Large-Scale Offshore Wind Farm Connected to Taipower Grid

Li Wang, Chun-Jui Yeh, Min-Han Hsieh, Cheng-Tai Wu, and Chieh-Lung Lu

Abstract When a high-capacity offshore wind farm (OWF) is connected to a power system, the power quality of the power system can be significantly deteriorated under various wind speeds. This paper presents the analyzed voltage variations of Taiwan Power System connected with a 100-MW OWF using a commercial power system simulation software. The ultrahigh voltage bus of ten onshore substations that are close to the potential OWF is selected as the connection point. The voltage variation results at the connection points under different lengths of submarine cable are accomplished and analyzed when the 100-MW OWF is connected to the selected substations. The simulated results can offer a reference for the development of OWFs in Taiwan in the near future.

Keywords Offshore wind farms • Grid connection • Voltage variations

1 Introduction

The fast development of industry and the excessive use of fossil fuels have led to a shortage of energy in recent years. In addition to the global climate anomaly changes, the health of human being can also be significantly threatened. Besides, the protest of the development of nuclear power generation systems becomes the topic of global concern after an earthquake happened in Fukushima, Japan, damaging nuclear power plants. Taiwan lacks of indigenous energy, and most energy relies on imports. Hence, research and development of the clean and pollution-free renewable energy resources for Taiwan are an important issue, while wind energy is one of the best candidates among various renewable energy resources [1].

L. Wang (✉) • C.-J. Yeh • M.-H. Hsieh • C.-T. Wu • C.-L. Lu
Department of Electrical Engineering, National Cheng Kung University, Tainan 70101, Taiwan
e-mail: liwangncku@gmail.com

At present, the development of onshore wind power generation systems in Taiwan has reached a bottleneck. However, offshore wind power generation systems in Taiwan are still under planning stages.

When a high-capacity renewable energy resource or a distribution generation (DG) system such as an offshore wind farm (OWF) is connected to a power system, the power quality at the point of common coupling (PCC) of the power system can be significantly deteriorated under various operating conditions [2, 3]. The effects of high-capacity renewable energy resource connected to a power system have to be evaluated before practical installation. This paper presents the simulation results of an OWF connected to the ultrahigh voltage bus of ten onshore substations that have higher potential for future development in Taiwan. The simulated voltage variation results of an OWF of 100 MW connected to Taiwan Power System through a submarine cable under different lengths are performed by using a power system simulation software.

2 System Configuration

The single-line diagram of the studied OWF system fed to Taipower grid is shown in Fig. 1. The rated power of each wind turbine generator (WTG) based on doubly fed induction generator (DFIG) is 5 MW, and each group has ten WTGs connected in series. The total capacity of the OWF containing two groups is 100 MW. The output of the OWF is connected to Taipower grid through an offshore step-up transformer of 23/161 kV, a submarine cable, and an underground cable. The 2012 off-peak forecasted load of Taiwan Power System is employed as the system loading basis in this paper. This paper selects the mode of power factor control for each wind DFIG that can maintain its output power factor at the target value.

3 Grid Code of Taipower System

According to [4], the specification states that "If the total capacity of the power generation equipment is more than 20,000 MW, it can be connected to ultra-high voltage systems." Hence, the choice of the connection point of the 100-MW OWF
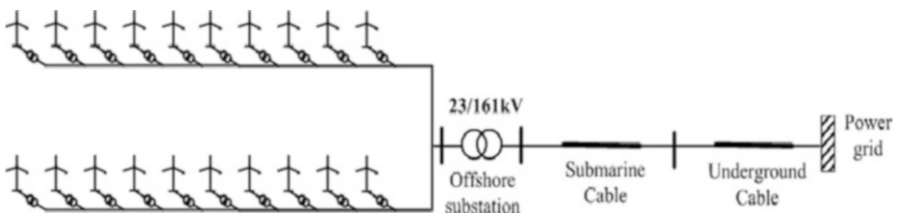
Fig. 1 Single-line diagram of the 100-MW offshore wind farm connected to Taipower grid

in this paper is the ultrahigh voltage buses of onshore substation of Taiwan. The selected ten ultrahigh buses for the connection points that are closer to the coast have enough carrying capability. The provision of [4] on voltage variations states that "When the power generation equipment connected to Taiwan Power System causes voltage variations at PCC, it should be maintained at the level of each less than 2.5 %." According to "Transmission System Planning Criteria of Taiwan Power Company (TPC)" [5], the system voltage limit criterion states that "The system voltage should be maintained between 0.95 p.u. and 1.03 p.u. under normal condition."

Based on the above two technical points for grid code of TPC, this paper discusses whether the voltage steady-state value and the voltage variations comply with the grid code issued by TPC after the 100-MW OWF is connected to the substation of Taiwan Power System.

4 Analysis of Simulation Results

The one-line power system diagram of Taichung administrative region is shown in Fig. 2. The scope of this region covers Taichung and Changhua. These selected ultrahigh buses as the connection points for connecting the 100-MW OWF contain Chung-gang E/S, Chung-ke E/S, Gang-gung D/S, Hai-wei D/S, Chuan-hsing E/S, Zhang-bin E/S, and Han-bau E/S. The simulated voltage variation results of each bus under different lengths of submarine cable are carried out using a commercial power system simulation software of PSS/E.
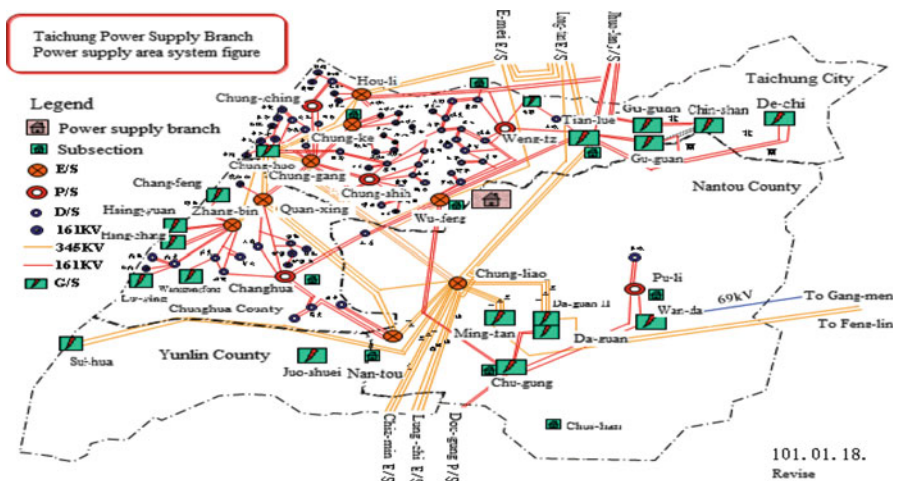
Fig. 2 Power system diagram of Taichung administrative region [6]

Table 1 Magnitude and phase angle of voltage as well as voltage variations at PCC under different lengths of submarine cable after the100-MW OWF is connected to Chung-gang E/S

Length of submarine cable (km)	20	40	60	80	100
Voltage value at PCC (kV)	157.07	157.33	157.77	158.15	158.54
Voltage value at PCC (p.u.)	0.9756	0.9772	0.98	0.9823	0.9847
Phase angle of voltage at PCC (p.u.)	−5.7	−5.8	−5.8	−5.8	−5.8
Rate of voltage variation at PCC (%)	0.4605	0.6267	0.9082	1.1512	1.4007

Table 2 Magnitude and phase angle of voltage as well as voltage variations at PCC under different lengths of submarine cable after the 100-MW OWF is connected to the Chung-ke E/S

Length of submarine cable (km)	20	40	60	80	100
Voltage value at PCC (kV)	158.59	158.98	159.85	160.56	161.28
Voltage value at PCC (p.u.)	0.985	0.9875	0.9929	0.9972	1.0017
Phase angle of voltage at PCC (p.u.)	−4.5	−4.5	−4.6	−4.6	−4.6
Rate of voltage variation at PCC (%)	0.9034	1.1516	1.7051	2.156	2.6150

Chung-gang E/S is located at Taichung Harbor and the length of the onshore cable is assumed to be around 13 km. Before the OWF is connected to Chung-gang E/S, the bus voltage of the Chung-gang H is 156.35 kV or 0.9711 p.u. Table 1 lists magnitude and phase angle of the voltage at PCC as well as the voltage variations under different submarine cable lengths after the OWF is connected to the Chung-gang E/S. It can be seen from Table 1 that the voltage at PCC increases with the increase of the length of the submarine cable, while the voltage magnitude and voltage variation at PCC are kept within the limitation of grid code of TPC.

Chung-ke E/S is located at Central Taiwan Science Park and the length of the onshore cable is assumed to be around 19 km. Before the OWF is connected to Chung-ke E/S, the bus voltage of Chung-ke H is 157.17 kV or 0.9762 p.u. Table 2 lists the magnitude and phase angle of voltage as well as voltage variations at PCC under different submarine cable lengths after the OWF is connected to Chung-ke E/S. It can be observed from Table 2 that the voltage at PCC can be maintained between 0.95 and 1.03 p.u. However, when the length of the submarine cable reaches 100 km, the voltage variation at PCC is higher than 2.5 % that violates the grid code of TPC.

Gang-gong D/S is a distribution substation and its voltage level decreases from 161 to 22.8 kV. The selected connection point is its UHV bus. The length of onshore cable is assumed to be about 7 km. Before the OWF is connected to the substation, the UHV bus voltage is 159.86 kV or 0.9929 p.u. After the OWF is connected to the UHV bus of Gang-gong D/S, the magnitude and phase angle of voltage as well as voltage variations at PCC under different lengths of submarine cable are listed in Table 3. Table 3 gives that the voltage variation at PCC is 2.6 % that violates the standard limitation of grid code of TPC when the submarine cable length is 100 km.

Table 3 Magnitude and phase angle of voltage as well as voltage variations at PCC under different lengths of submarine cable after the 100-MW OWF is connected to Gang-gong D/S

Length of submarine cable (km)	20	40	60	80	100
Voltage value at PCC (kV)	160.97	161.68	162.43	163.21	164.03
Voltage value at PCC (p.u.)	0.9998	1.0043	1.0089	1.0137	1.0188
Phase angle of voltage at PCC (p.u.)	−2.8	−2.8	−2.9	−2.9	−2.9
Rate of voltage variation at PCC (%)	0.6943	1.1384	1.6076	2.0955	2.6085

Table 4 Magnitude and phase angle of voltage as well as voltage variations at PCC under different lengths of submarine cable after the 100-MW OWF is connected to Hai-wei D/S

Length of submarine cable (km)	20	40	60	80	100
Voltage value at PCC (kV)	160.79	161.49	162.22	162.98	163.79
Voltage value at PCC (p.u.)	0.9987	1.003	1.0076	1.0123	1.0173
Phase angle of voltage at PCC (p.u.)	−2.8	−2.8	−2.8	−2.9	−2.9
Rate of voltage variation at PCC (%)	0.5817	1.0196	1.4762	1.9517	2.4584

Hai-wei D/S is also a distribution substation and the length of onshore cable is assumed to be about 3 km. Before the OWF is connected to the Hai-wei substation, the voltage of the UHV bus is 159.86 kV or 0.9929 p.u. After the 100-MW OWF is connected to the UHV bus of Hai-wei D/S, the magnitude and phase angle of voltage as well as voltage variations at PCC under different lengths of submarine cable are listed in Table 4. From the simulated results listed in Table 4, the voltage values and the voltage variations are within the specified limit when the OWF is connected to the substation and the length of submarine cable is less than 100 km.

Zhang-bin E/S is located inside Changhua Coastal Industrial Park. The distance from seashore is about 9 km. The voltage at the UHV bus of Zhang-bin E/S is 159.9 kV or 0.9931 p.u. before the OWF is connected to the UHV bus. After the OWF is connected to the UHV bus of Zhang-bin D/S, the magnitude and phase angle of voltage as well as voltage variations at PCC under different lengths of submarine cable are listed in Table 5. It is seen from Table 5 that the voltage variation at PCC is 1.9887 % that falls in the region limited in grid code of TPC after the 100-MW OWF is connected to the substation and the length of submarine cable is less than 100 km.

The length from coast to Quan-xing E/S is assumed to be 13 km. Before the OWF is connected to the UHV bus of this substation, the bus voltage is 160.28 kV or 0.9955 p.u. After the OWF is connected to the UHV bus of the Quan-xing E/S, the magnitude and phase angle of voltage as well as the voltage variations at PCC under different lengths of submarine cable are listed in Table 6. It can be discovered from Table 6 that the voltage magnitude at PCC falls in the limit region of the grid code of TPC after the OWF is connected to the UHV bus of Quan-xing E/S.

The distance from coast to Han-bao E/S is about 10 km. Before the OWF is connected to the UHV bus of this substation, the bus voltage is 160.69 kV or 0.9981 p.u. After the OWF is connected to the UHV bus of Han-bao E/S, the results of voltage magnitude, phase angle of voltage, and voltage variations at PCC under

Table 5 Magnitude and phase angle of voltage as well as voltage variations at PCC under different lengths of submarine cable after the 100-MW OWF is connected to Zhang-bin E/S

Length of submarine cable (km)	20	40	60	80	100
Voltage value at PCC (kV)	160.82	161.35	161.90	162.47	163.08
Voltage value at PCC (p.u.)	0.9989	1.0022	1.0056	1.0092	1.0129
Phase angle of voltage at PCC (p.u.)	−3.7	−3.7	−3.8	−3.8	−3.8
Rate of voltage variation at PCC (%)	0.5753	0.9068	1.2507	1.6072	1.9887

Table 6 Magnitude and phase angle of voltage as well as voltage variations at PCC under different lengths of submarine cable after the 100-MW OWF is connected to Quan-xing E/S

Length of submarine cable (km)	20	40	60	80	100
Voltage value at PCC (kV)	161.11	161.54	161.99	162.46	162.95
Voltage value at PCC (p.u.)	1.0007	1.0033	1.0061	1.0091	1.0121
Phase angle of voltage at PCC (p.u.)	−3.9	−4.0	−4.0	−4.0	−4.1
Rate of voltage variation at PCC (%)	0.51784	0.7861	1.0668	1.3602	1.6658

Table 7 Magnitude and phase angle of voltage as well as voltage variations at PCC under different lengths of submarine cable after the 100-MW OWF is connected to Han-bao E/S

Length of submarine cable (km)	20	40	60	80	100
Voltage value at PCC (kV)	162.18	162.98	163.81	164.68	165.60
Voltage value at PCC (p.u.)	1.0073	1.0123	1.0174	1.0229	1.0286
Phase angle of voltage at PCC (p.u.)	−4.1	−4.1	−4.2	−4.3	−4.3
Rate of voltage variation at PCC (%)	0.9272	1.4251	1.9416	2.4830	3.0555

different lengths of submarine cable are listed in Table 7. It is seen from Table 7 that the voltage variation exceeds the specified range and the voltage value is close to 1.03 p.u. after the OWF is connected to the substation and the length of submarine cable is 100 km.

5　Conclusion

When the studied 100-MW offshore wind farm (OWF) is connected to the bus of the selected substation through a step-up transformer, a submarine cable, and an underground cable, the length of the employed submarine cable can significantly affect the voltage magnitude and voltage variation at the connection point.

The operation of the OWF can lead to large voltage variations on nearby buses. The connected power system can also be severely influenced by the OWF operation. Hence, the power quality is one of the key issues of the studied power system to which a large-scale OWF is connected.

A commercial power system simulation software PSS/E is employed to simulate the voltage variations of a 100-MW OWF connected to the bus of selected substations under different lengths of submarine cables. The simulation results show that Chung-gong, Quan-xing, and Zhang-bin substations exhibit less voltage variations on the connection point after the 100-MW OWF is connected the bus of these substations.

References

1. Taiwan Power Company (2009) Wind power phase IV project feasibility study report, Taiwan Power Company Report, Taipei
2. Chompoo-inwai C et al (2005) System impact study for the interconnection of wind generation and utility system. IEEE Trans Ind Appl 41(1):163–168
3. Kim E-H et al (2012) Impact analysis of wind farms in the Jeju Island power system. IEEE Syst J 6(1):134–139
4. Taiwan Power Company. (2011) Grid-connection technical points for renewable energy power generation systems of Taiwan Power Company. http://www.taipower.com.tw/left_bar/rules_item/Regeneration_energy.htm. Retrieved 9 Jan 2011
5. Taiwan Power Company (2012) Transmission system planning criteria of Taiwan Power Company. http://www.taipower.com.tw/index.php?content=big/System_Plan_Criterion.htm. Retrieved 9 Jan 2012
6. Taiwan Power Company (2011) http://www.taipower.com.tw. Retrieved 17 Feb 2011

Source-End Layouts on ESD/LU Reliabilities in an HV 0.25 um 60 V nLDMOS

Shen-Li Chen, Min-Hua Lee, Tzung-Shian Wu, Yi-Sheng Lai, Chun-Ju Lin, and Hsun-Hsiang Chen

Abstract Latch-up (LU)/electrostatic discharge (ESD) protection inclinations of a high-voltage (HV) IC reliability are investigated in this chapter, where the test DUTs were fabricated by a 0.25 um 60 V BCD process. In order to effectively evaluate the LU and ESD reliabilities, the source-end layout in two manners were proposed and verified; all of them effectively improved the trigger voltage (V_{t1}) or the secondary breakdown current (I_{t2}) to enhance its ESD immunity. These two kinds of source-end layout are the P^+ of discrete distributed type and P^+ of bulk-contact numbers varied type, while these two different layout methods have their own advantages and disadvantages. It can be concluded that the ESD immunity level or the trigger voltage (V_{t1}) decreasing of a device can be improved by the source-end layout optimization in an HV process. Then, in this work, by using some layout techniques to improve the important reliability robustness, these strategies will be easily used and without added any additional process or mask in an HV process technology.

S.-L. Chen (✉) • M.-H. Lee • T.-S. Wu • Y.-S. Lai • C.-J. Lin
Department of Electronic Engineering, National United University, MiaoLi 36003, Taiwan
e-mail: jackchen@nuu.edu.tw

H.-H. Chen
Department of Electronic Engineering, National Changhua University of Education, Changhua, Taiwan

1 Introduction

Generally, for any HV integrated circuits, in order to achieve a high device breakdown voltage and low turned-on resistance, it often imposes a complex well engineering at the drain end [1–4]. In HV technologies, the holding voltage (V_h) of an ESD protection device is usually smaller than the specified operating voltages at I/O pads or the normal power supply voltage (VCC). Unfortunately, the LU effect will be a serious reliability concern of HV integrated circuits [5]. For example, system-level ESD events, electromagnetic coupling, or hot plug of ICs can induce fast transient noises on I/O pins and power supply lines, which can induce an LU catastrophe of HV integrated circuits. As a result, devising ESD protection circuits with high ESD robustness and high immunity against LU or electrical overstress (EOS) are the main design targets in HV technologies [6–8].

In recent years, power management ICs are in focus as the development project in the power industry. In order to reduce manufacturing costs, power management ICs and power transistors (Power MOS) are integrated into a BCD HV process, which plays an important role in HV components. In order to increase the driving capability, it is often to pay the cost of a large area to increase the current handling capability. In addition, HV components in order to achieve a high breakdown voltage, its composition often used a lightly doped process, which is not favorable to conduct the ESD current. So, a lot of literatures do a considerable number of studies recently in the layout arrangement of the HV components [9–12], which hopes to effectively improve the ESD capability and LU immunity. In this chapter, layouts of source-end region will be proposed; of course we want to know how these influence anti-latch-up and ESD protection abilities.

2 Layout Design of Test Devices

In the TSMC 0.25 um 60 V BCD process, an HV structure of nLDMOS device is shown in Fig. 1. Here, higher the operation voltage, the well structures of HV device will be toward more complex, which does effectively prevent a leakage current to affect the surrounding circuit. For this 60 V device, it added an NBL layer to increase its isolation capability. The P_{Base} layer (HVPB) under the source end is a selective P-type boron implanted layer, and a parasitic NPN bipolar junction transistor is also formed here.

Under a high-current injection, the Kirk effect is known to induce impact ionization at the drain side. Meanwhile, due to the high-current injection, the depletion region extended toward the drain region; nearly all the electrons emitted from source end can be swept to the drain side without suffering any strong recombination. These electrons emitted from the source end will enter the
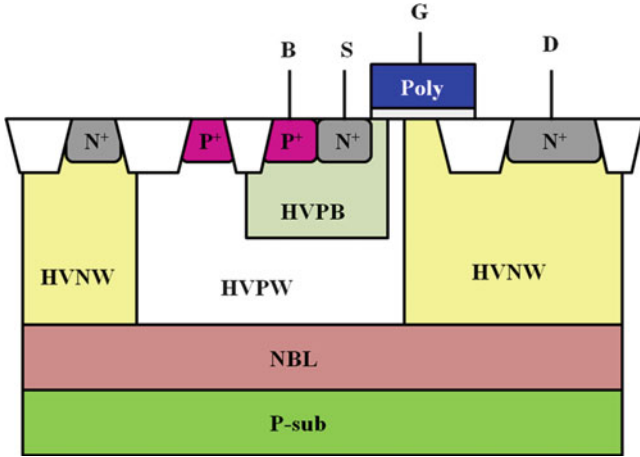
Fig. 1 Cross-sectional view of a 60 V HV nLDMOS

avalanche region at drain side, and thus a large number of electron–hole pairs generated. As a result, the electron density emitted from source end is one important factor that affects the snapback holding voltage of nLDMOS. This chapter will aim at improving ESD/LU immunity of HV devices, and the source-side layout arrangements are proposed. A multi-finger structure of MOSFET used in this work, the channel length (L) is kept to be 1 um, channel width (W_f) of unit finger is 50 um, and the total channel width (W_{tot}) is kept a constant value (300 um). The traditional nLDMOS (standard reference DUT) is a full and even distribution with P$^+$ bulk stripe in the source side. Then, two different source-end architecture structures of nLDMOS to affect the holding voltage and secondary breakdown current will be deliberated.

2.1 P$^+$ Discrete Distributed Types in the Source End

In order to validate the effect of increasing nLDMOS ESD handling capability in this work, we do changes for the source-region layout, as shown in Fig. 2. We reduce the P$^+$ area in source end; this purpose expects to enhance the ESD capability. The P$^+$ implant region in Fig. 2 is an ohmic contact directly connected to the HV-PW in the source region. That is, the original pickup stripe splits into several sections or portion, i.e., a P$^+$ stripe divided into a discrete distribution, increasing N$^+$ region to conduct the ESD current. It is classified into "the discrete distributed type (1)": *length of each P$^+$ piece, 3.3 um; spacing, 1.8 um; everyone 50 um channel width with eight segments*; "the discrete distributed type (2)": *length of each P$^+$ piece, 6.6 um;*
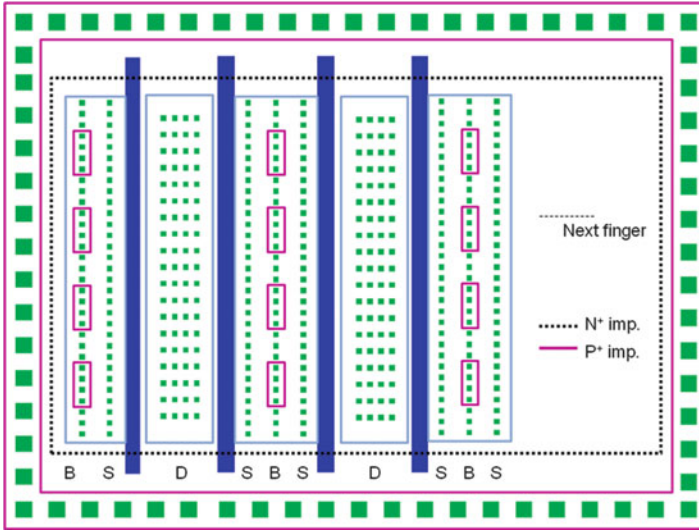
Fig. 2 Schematic layout of the P$^+$ bulk discrete distributed type

spacing, *1.8 um*; *everyone 50 um channel width with 4.5 segments*; and "the discrete distributed type (3)": *length of each P$^+$ piece, 9 um*; *spacing, 1.8 um*; *everyone 50 um channel width with 3.5 segments*.

2.2   P$^+$ Bulk-Contact Numbers Varied Types in the Source End

As indicated in Fig. 3, the contact point numbers of P$^+$ bulk area in the source end varied, just like the bulk contact(1), bulk contact(2), and bulk contact(3), respectively. Numbers of the P$^+$ bulk contact(1) are 17, numbers of the bulk contact(2) are 10, and numbers of the bulk contact(3) are 7; however, the numbers of traditional stripe be haven 67.

3   Test Equipment System

The transmission line pulse (TLP) system for DUTs experimental testing is controlled by the LabVIEW software. This machine can provide a continuous step-high square wave to a DUT, and shortly rising/falling time of the continuous square wave can also simulate transient noise of an ESD pulse. This HBM-like system has used the short square wave with 100 ns pulse widths and 10 ns rising/falling times to evaluate the voltage and current response of a DUT.
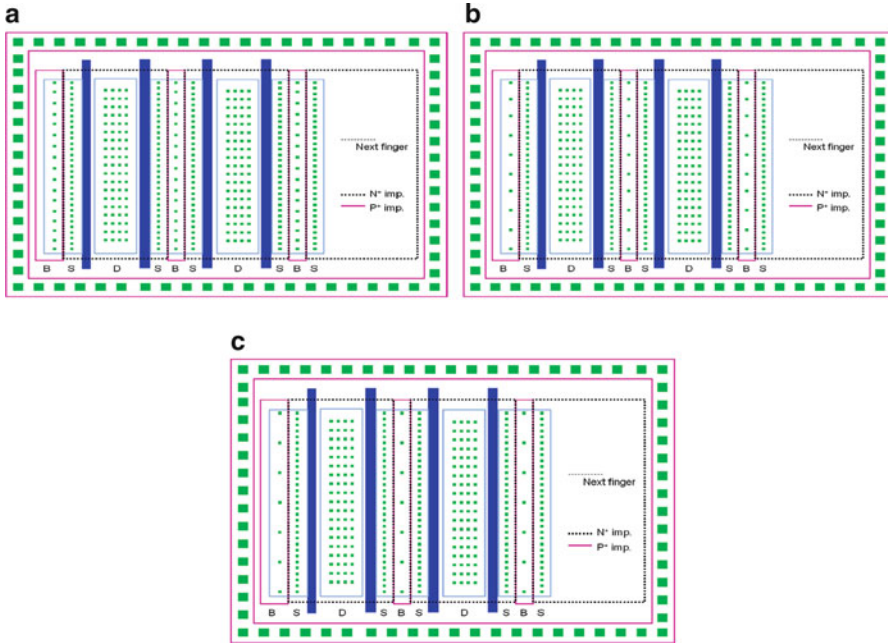
Fig. 3 Schematic layout of the different bulk-contact number types: (**a**) bulk contact(1), (**b**) bulk contact(2), (**c**) bulk contact(3)

4 Measure Results and Discussion

4.1 P⁺ Discrete Distributed Types in the Source End

In Fig. 4, these are the TLP measurement results of the nLDMOS with reducing P^+ bulk region in the source end shown in Fig. 2. It can increase the ability of ESD robustness, but the holding voltage (V_h) will be smaller because the P-bulk region is reduced and the impedance of parasitic bulk resistance (R_{bulk}) is increased. Then, it is to make the parasitical BJT turned on more easily and cause the holding voltage decreasing as compared with a traditional one shown in Table 1. On the other hand, a smaller trigger voltage can quicken its turned-on behavior of this parasitic BJT and can enhance ESD level.

From Table 1, reducing the P-type bulk region in the source end can effectively improve the ESD protection capability especially in the discrete type (1), whereas the I_{t2} is increased from 1.44 to 1.47 (A). It will somewhat sacrifice the LU immunity (low holding voltage), but these layout structures can effectively improve the ESD robustness, therefore, which can effectively reduce layout area of an HV ESD devices.
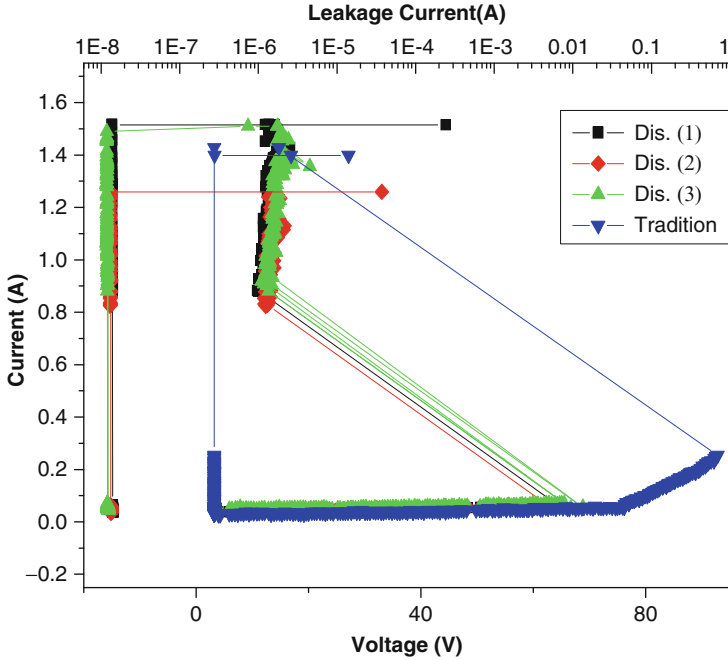
Fig. 4 Snapback *I–V* curves and leakage currents of nLDMOS DUTs with the source-end P⁺ discrete types

Table 1 Snapback key parameters of the source-end P⁺ discrete types

Sample type	V_{t1} (V)	V_h (V)	I_{t2} (A)
Tradition	91.83	14.61	1.44
Discrete(1)	64.16	11.29	1.47
Discrete(2)	63.8	12.08	1.27
Discrete(3)	62.73	12.15	1.42

These layout structures through the P⁺ discrete distributed types in source end to increase the ESD capability, no additional mask costs need and this implies that the new kind layouts can also deal with much higher current capability of the HV components, instead of to enlarge the unit width or finger numbers to increase its robustness.

4.2 *P⁺ Bulk-Contact Numbers Varied Type in the Source End*

Furthermore, Fig. 5 shows the snapback *I–V* curve and leakage current measured results with the source-end P⁺ bulk-contact numbers reduction shown in Fig. 3. These efforts can effectively increase an ESD-dissipated capacity; however, the
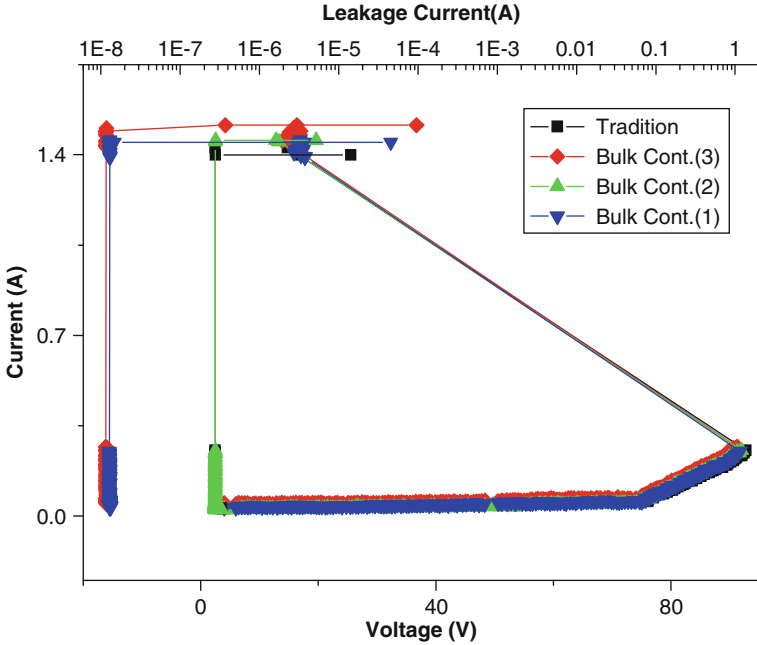
Fig. 5 Snapback *I–V* curves and leakage currents of nLDMOS DUTs with the source-end P$^+$ bulk-contact numbers varied types

Table 2 Snapback key parameters of the P$^+$ bulk-contact numbers varied types

Sample type	V_{t1} (V)	V_h (V)	I_{t2} (A)
Tradition	91.829	14.612	1.44
Bulk cont.(1)	91.336	13.816	1.452
Bulk cont.(2)	91.535	13.114	1.456
Bulk cont.(3)	91.507	13.296	1.485

bulk's parasitic resistance (R_{bulk}) will be increased, and the parasitic BJT is turned on more easily. Meanwhile, these downgradings of the holding voltage as compared with the traditional one are shown in Table 2. And the decline of trigger voltage (V_{t1}) may accelerate a parasitic BJT of HV nLDMOS, turned on fast to discharge the huge ESD current.

Comparing the measurement data shown in Table 2, to reduce the contact numbers of P$^+$ bulk in the source end, it can be noted that the I_{t2} value will be increased as the number of P$^+$ contact points decreased. This can effectively improve the ESD protection capacity, the indicators I_{t2} increased from 1.44 to 1.49 A, and this layout structure can effectively improve the ESD robustness of the HV components, which can minimize the original layout area.

Table 3 Source-end engineering impacted on LU/ESD reliabilities

Source-end eng	LU impact	ESD impact	Layout influence
P^+ discrete distributed type	Bad (V_h 23 %↓)	Good (V_{t1} 32 %↓, I_{t2} 2 %↑)	Cell area can be decreased
P^+ bulk-contact numbers varied type	Bad (V_h 10.3 %↓)	Good (V_{t1} 0.54 %↓, I_{t2} 3.1 %↑)	A minimum modification to increase ESD ability

5 Conclusion

From the TLP testing results of this work, the ESD reliability improved strategy of HV nLDMOS is not only one way, and the source-end engineering can be summarized as in Table 3. The kind (1) is a P^+ discrete distributed type in the source end, the ESD-dissipated capacity can be enhanced, but the holding voltage, that is, the latch-up immunity, will be substantially decreased. Finally, the kind (2) is a P^+ bulk-contact numbers varied type in the source end; it is a minimum modification as compared with a traditional one, and it is a good choice to increase ESD ability, but however, the holding voltage (LU immunity) is some degrees of diminution. Therefore, from above two-source engineering modifications, it is found that the relationship between holding voltage and ESD robustness is a complementary relation; therefore, we need to get an optimized arrangement.

References

1. Suzuki N, Yamaguchi H, Shiraki S (2005) In: The 17th international symposium on power semiconductor devices and ICs (USPSD), Santa Barbara, 2005, pp 179–182
2. Huang CT, Tsui B-Y, Liu H-J, Lin G-L (2007) In: IEEE conference on electron devices and solid-state circuits (EDSSC), Taiwan, 2007, pp 267–270
3. Miyamoto M. Sugii N. Kumagai, Y, Kimura Y (2010) In: IEEE 23rd international symposium on power semiconductor devices and ICs (ISPSD), San Diego, 2011, pp 168–171
4. Fathipour V, Malakoutian M, Fathipour S, Fathipour M (2011) In: 19th Iranian conference on electrical engineering (ICEE), Tehran, 2011, pp 1–5
5. Ker M-D, Hsu C-L, Chen W-Y (2010) In: IEEE international symposium on circuits and systems, Paris, 2010, pp 989–992
6. Minixhofer R, Feilchenfeld N, Knaipp M, Rober G, Park JM, Zierak M, Enichlmair H, Levy M, Loeffler B, Hershberger D, Unterleitner F, Gautsch M, Shi Y, Posch W, Seebacher E, Schrems M, Dunn J, Harame D (2010) In: 22nd international symposium on power semiconductor devices & IC's (ISPSD), Hiroshima, 2010, pp 75–78
7. Chen W-Y, Ker M-D (2011) IEEE Trans Electron Device 58(9):2944–2951
8. Salman AA, Farbiz F, Appaswamy A, Kunz H, Boselli G, Dissegna M (2012) IEEE international reliability physics symposium (IRPS), Anaheim, 2012, pp 3E.1.1–3E.1.6
9. Lee J-H, Chen SH, Tsai YT, Lee DB, Chen FH, Liu WC, Chung CM, Hsu SL, Shih JR, Liang AY, Wu K (2007) In: 19th international symposium on power semiconductor devices and IC's (ISPSD), 2007, pp 173–176

10. Chen W-Y, Ker M-D, Jou Y-N, Huan Y-J, Lin G-L (2009) In: IEEE international symposium on the physical and failure analysis of integrated circuits, 2009, pp 41–44
11. Chen W-Y, Ker M-D (2009) IEEE Electron Device Lett 1–3
12. Lee J-H, Su H-D, Chan C-L, Yang D, Chen JF, Wu KM (2010) In: 22nd international symposium on power semiconductor devices & IC's (ISPSD), 2010, pp 303–306

The Functional Catoptric LED Luminaire in T8 Form Factor

Chuang-Jan Chang, Yi-Hsuang Tseng, Chiang-Wei Huang, Bor-Jen Wu, and Shu-Lin Hwang

Abstract This chapter aims at enhancing the model validness in the LED luminaire simulation. Regarding the deviation between simulation outcomes and the real measured data, the optical parameters to model the simulation were adjusted or, even, added the newer ones. After recursive simulation, the updated or renewed model would progressively approach to the physical one. Our studies concluded that the formatting of scatter parameter, which ordinarily ignored, factors critically in pursuing a better emulation. Practically, a home-made catoptric LED luminaire is referred to find the suitable parametric set that would derive the candela profiles each other approached. Finally, the example of the desktop lamp having adjustable catoptric optics is instanced to demonstrate the achievements of this study.

Keywords Desktop lamp • LED luminaire • Luminaire's materials

1 Introduction

Haitz's law: "Every decade, the cost per lumen falls by a factor of 10, and the amount of light generated per LED package increases by a factory of 20". Recently, LED luminaire has made a breakthrough, like power saving, high lighting effect, long service life, mercury free, and adjustable color temperature. These advantages advance the LED luminaire to replace traditional lighting equipment.

C.-J. Chang • Y.-H. Tseng • C.-W. Huang • S.-L. Hwang (✉)
Department of Electronic Engineering, Ming Chi University of Technology,
New Taipei City 24301, Taiwan
e-mail: hwangsl@mail.mcut.edu.tw

B.-J. Wu
Nan Ya Photonics Inc, New Taipei City 24301, Taiwan

2 Background and Motivation

The LED luminaire is composed of multiple LED grains. Each grain is a compact module containing the diode(s) as the light emitting part, so it is as a device converting electric energy into luminous energy. For better luminous efficacy, LED lamps on the market are preferred to the direct-type illumination structure, i.e., the direction of the main flux from LED grain, with no purposely bending, illuminates the target directly [1]. Since they are not suitably shielded, the light spot from each LED grain cannot be prevented by the naked eyes when the lamp is lit, so it will discomfort the eyes due to factors such as glare. To solve this problem, usually the luminaire is shielded by some diffuser parts before luminous flux leaves the lamp body.

However, this addendum cost is due to the heavy degradation to the luminous intensity. Therefore, some alternative arts were proposed, and the possibility is the catoptric structure; it hides the grain's main flux by other optical reflector(s) before the luminous energy exits.

Software simulation forecasts the performance of the designed products before real implementation. Many photonic software packages had worked well in designing the LED grain. These tools adapted the simulation of the luminaire accordingly. Usually the luminaire was processed as a bundle of tens or hundreds of discrete LED grains. However, the parts outside the LED grains are not as ideal as those in the semiconductor industry. The peripheral components of a luminaire are various and hard to emulate exactly. This chapter surveyed the validness of the simulation model and took a home-made catoptric LED luminaire as the studied instance.

3 Experimental Methods and Results

The LED lamps deployed by the vender are firstly discussed, and then a home-made luminaire that can improve the lighting glare is summarized. This design is own parts that reflect the luminous flux before illuminating to the target. We will successively describe the experimental methods and results obtained. The flow diagram of Fig. 1 shows the research process of the entire experiment.

3.1 The Direct Luminous LED Luminaire

An on-the-shelf LED T8 luminaire was studied first [2]. As a regular case, the illuminating direction of LED grains is matched with that of the luminaire in order
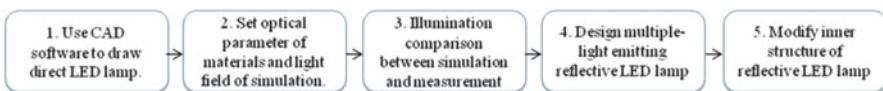
Fig. 1 Experimental flow diagram

Fig. 2 Direct LED luminaire
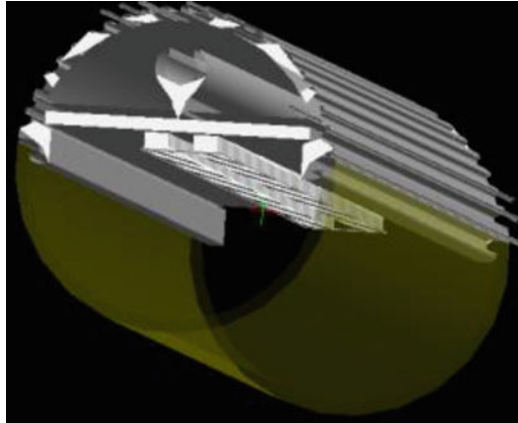
Table 1 Optical characteristics of PC material

Haze		91
Transparency	Total transmission index	63
	Diffused transmission index	57.5
	Horizontal transmission index	05.6
Refractive		01.59
Unit: %		

to maximize the luminous efficacy. The transmission exitance uses the PC material, expressed as yellow in Fig. 2, and its optical characteristics are listed in Table 1. This material will diffuse the luminous flux so that with no dazzling when people focus on the luminaire.

The simulation model was established with a 4 m*4 m analysis surface, and placed 0.5, 0.75, 1, 1.25 and 1.5 m, respectively, under the tested unit. Then, with a similar physical layout, the real device is measured by a luminous meter as well. The experimental values obtained show that the illumination of the physical measurement matches well with the simulation outcome, so the software simulation at this stage can evaluate the illumination of light sources (Fig. 3).

3.2 The Catoptric Luminous LED Luminaire

We also studied a home-made catoptric LED luminaire with T8 form factor compatible. A China patent [3] had claimed that the catoptric illumination of the LED luminaire can prevent lighting glare effectively. Referring to the patent context, and enhancing further, our mock up was fabricated, which is shown in Fig. 4. The array-arranged LED grains illuminated first to the cylindrical ceiling surface. For reducing the weight, the aforementioned patent claimed that a concrete PMMA solid bar is replaced by a hollow tube. The material characteristics of the internal structure are listed in Table 2.
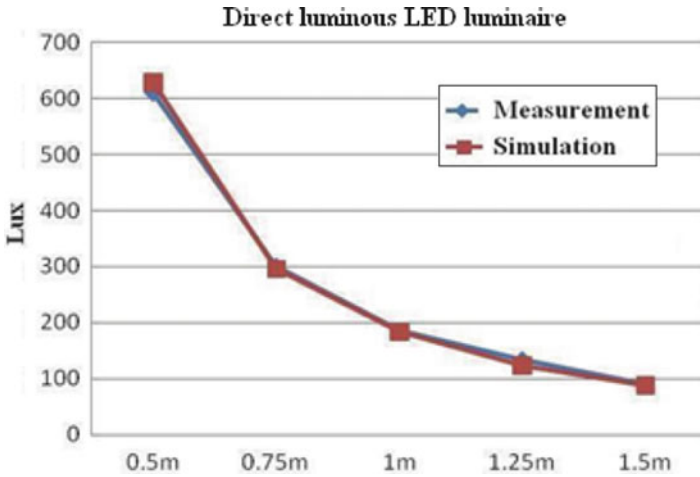
Fig. 3 Illumination comparison
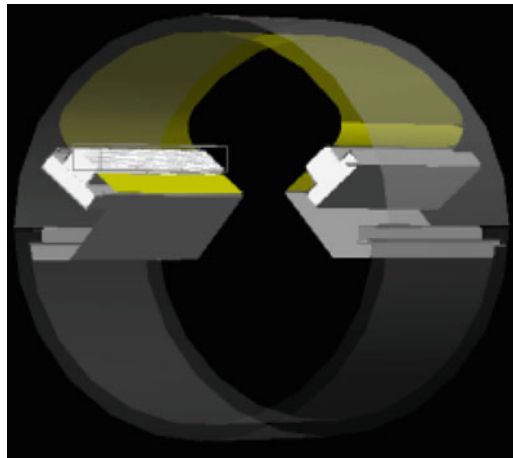
Fig. 4 Catoptric LED luminaire

Simulation modeling: The simulation in the last section is adapted to model our apparatus, and then to obtain the candle power distribution, as shown in Fig. 5. The blue profiles were from around 0°–180° axis, and the red one 90°–270°. There exists a bat wings distribution in the blue contour. The real physical measurement was taken and obtained as shown in Fig. 6. It is quite different from the simulated results.

Reviewing the physical measurement and as the guiding reference, the logic of losing the bat-wing profiles was reviewed. The inference was that the optical parameters fed to model the luminaire are not sufficient. The optical terms molded

Table 2 Material characteristics of luminaire

	Refractive	Reflective	Transmission	Purpose
TiO2	2.609	19.87	–	Light strip base
PC	1.59	–	90	Transmission face
TAIRILIN	–	96.5	–	Reflection face

Unit: %
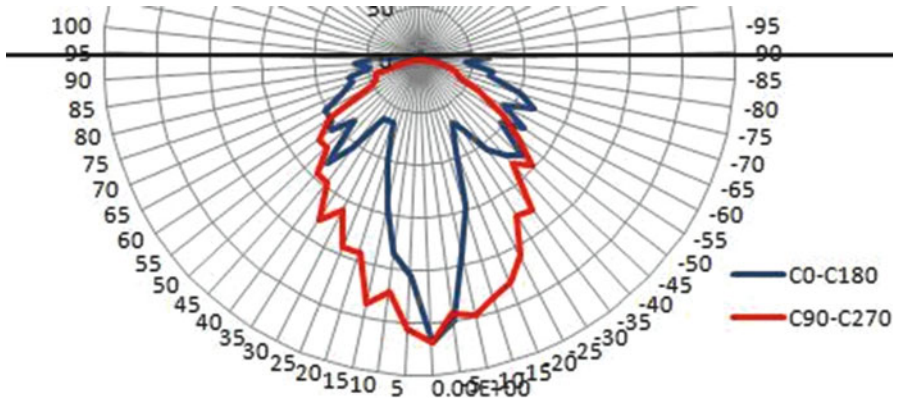
Fig. 5 Simulation
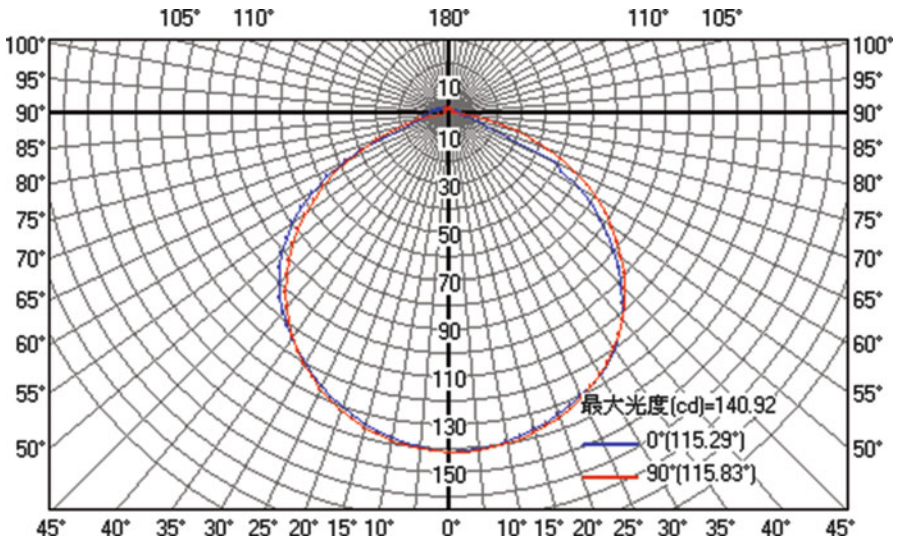
Fig. 6 Measurement
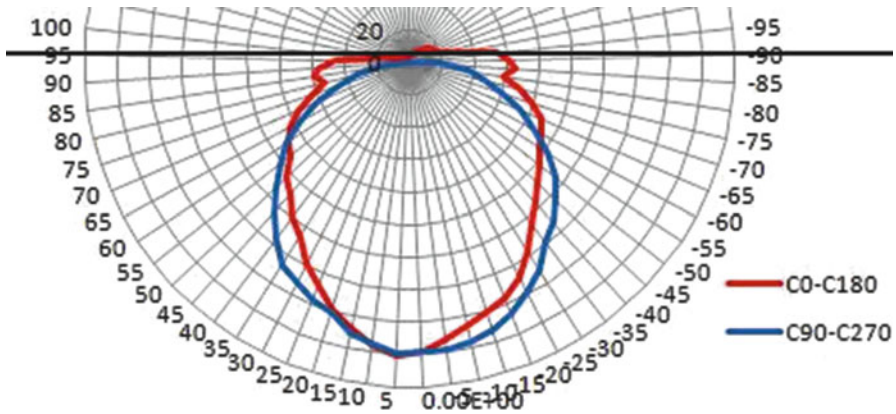
Fig. 7 Lambertian scattering
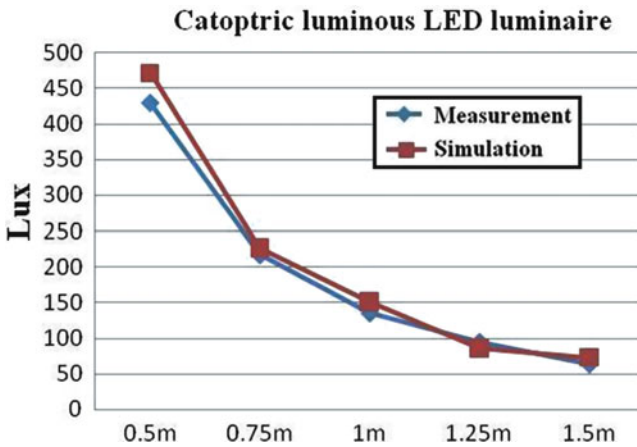
Fig. 8 Illumination comparison

were refraction and reflection in specular mode. They revealed that these worked well in modeling the illumination of the direct-type LED luminaire as given in the last section. We presumed that the light rays of the last experiment were just like glass materials. Therefore, the specular light tracing is sufficient. However, the composing parts in our mock-up were different. The mirror-like specular reflection could not dominate the optical property. Moreover, we are even without accurate data sheets. Therefore, a self-reasonable procedure is needed.

We postulate the scatter property must be extended, and the semi-circular ceiling, shown as the yellow face in Fig. 4, was deemed with white Lambertian scattering. The optical properties are renewed, and the simulation results are shown in Fig. 7. It shortened the deviation from the real case. Besides, the illumination intensity below the center was measured and is shown in Fig. 8. It is reasonable that
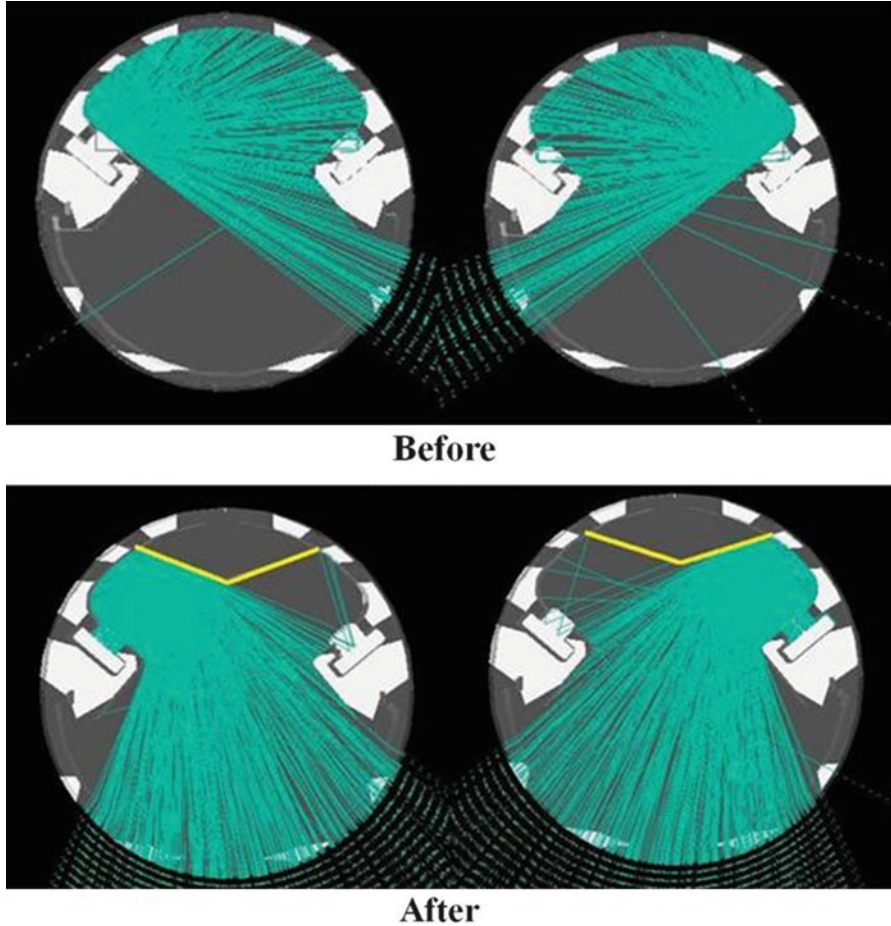
Before

After

Fig. 9 Light traces before and after modifying lamp

direct lighting luminaire will be brighter than the catoptric one. Consequently, we will discuss the advantage of the catoptric illumination structure, and, accordingly, the obtained scattering parameters will be considered as well.

3.3 Luminous Enhancement of the Catoptric Luminaire

The alternative catoptric structure that modified the luminous function was demonstrated. Comparing Figs. 3 and 8, it reveals that the luminous lighting of the catoptric LED lamp is inferior to the one of direct type. The attenuation is due to the indirect illumination causing a longer backward tracing, and a part of the lighting energy being blocked. This circumstance is observed by the beam distribution inside the luminaire, shown in the upper part of Fig. 9.
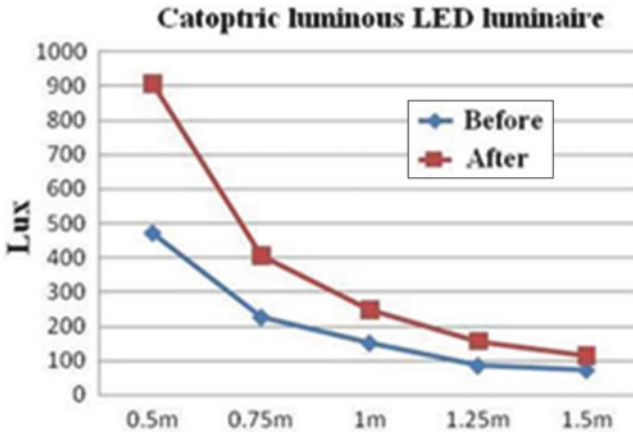
Fig. 10 Illumination comparison

It is intuitional that shortening the trace and guiding the blocked energy out improve the luminous efficacy. For this issue, the cylindrical roof is modified by adding two intersected plates with angle, as shown in the lower part of Fig. 9. In this way, the reflector will route out the light beams, thereby increasing the total luminous output. Figure 10 shows the downward illumination that has been increased by 435 lux at 0.5 m. Furthermore, adjusting the reflective geometry would accordingly modify the luminous function. In next section, the candle curves from various intersected angles will be demonstrated.

3.4 The Functional Catoptric Lamp and the Desk Lamp

The specified function could be achieved by adjusting the catoptric geometrical structure or changing the material with different optical properties. Various environments need their respected different illumination. However, the brighter the better is not always true. We took desk lamp as the survey instance. In a reading room, both too much or too low lighting will harm the eyes. JIS C8112 has formulated the minimum lighting flux needed for a desk lamp [4], but it did not limit the maximum ones due to this issue being controversial to the cost. In developing a LED luminaire, the preference is using as fewer LED grains as possible to comply with the regulation. In this study, we did not physically implement a catoptric luminaire with adjustable reflected plates installed. However, the simulation would guide us to figure out the suitable design. Here, we simulated in alternative skeletons adjusting the intersected angles to 124°, 144°, and 164° between the two embedded catoptric plates and alternative optical properties formulating a specular-dominated material and a Lambertion scattering–dominated material. The candle power profiles of each one are respectively shown in Figs. 11, 12, and 13.

Fig. 11 Each angle of reflector
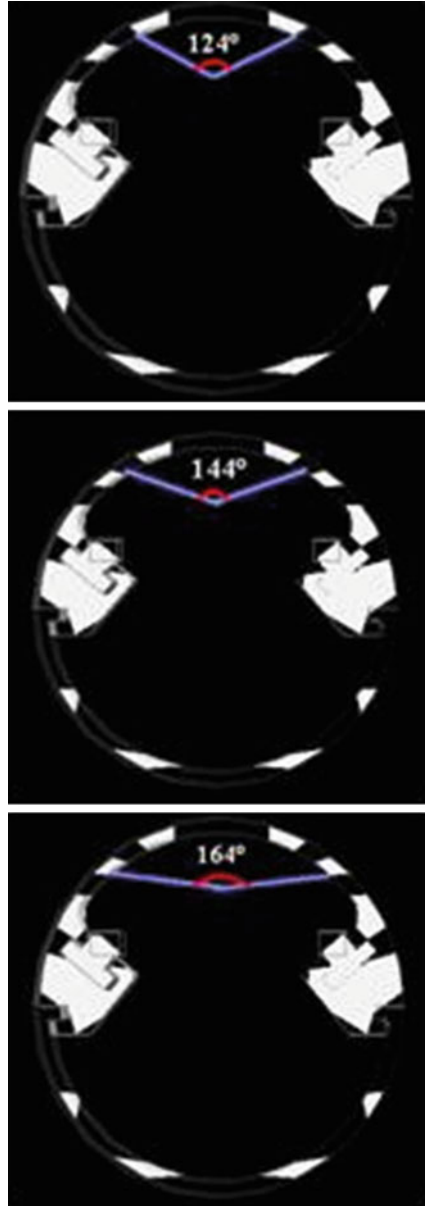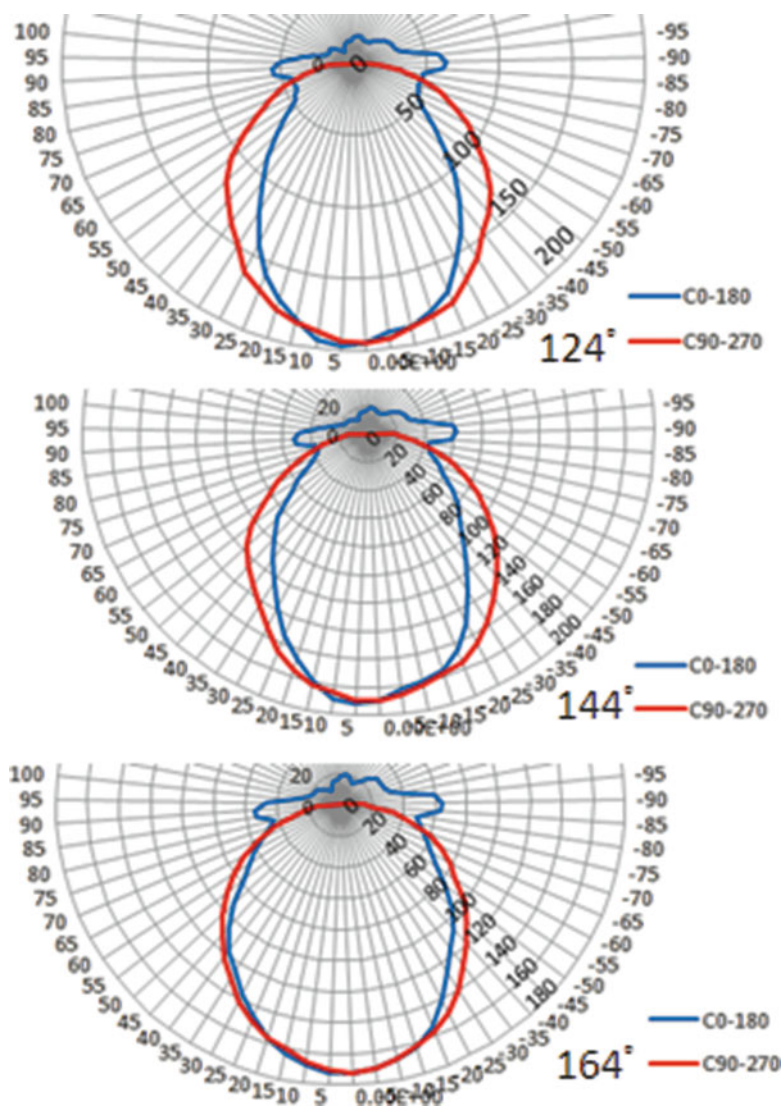
Fig. 12 Lambertion scattering
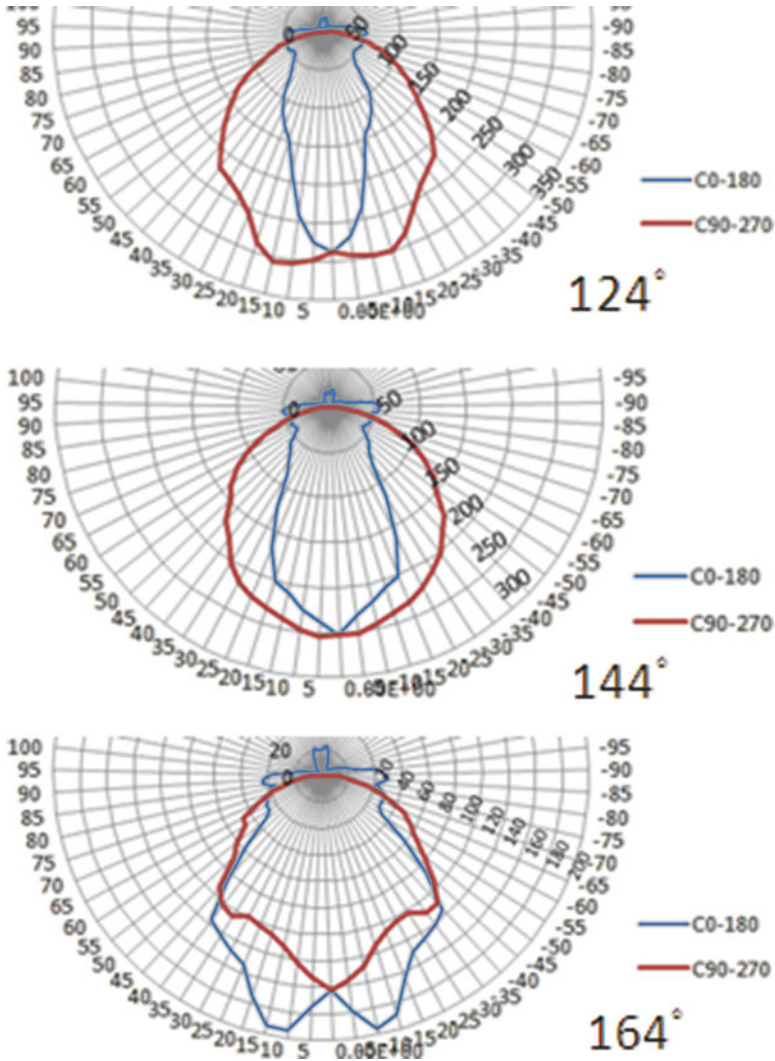
Fig. 13 Specular

In the simulation process, we can get the illumination profiles simultaneously. The 2 m*2 m analysis surface is placed under the luminaire 30 cm, and their 0°–180° Illumination is simulated as shown in Fig. 14. It clearly shows that the illumination increases significantly after adding the reflector. The maximum value is obtained when the intersected angle is at the minimum, and vice versa. For the reflector with a 154° included angle and 164° included angle, the range meeting the standard illumination of the desktop lamps is wider and can be used in a desktop lamp, as listed in Table 3.
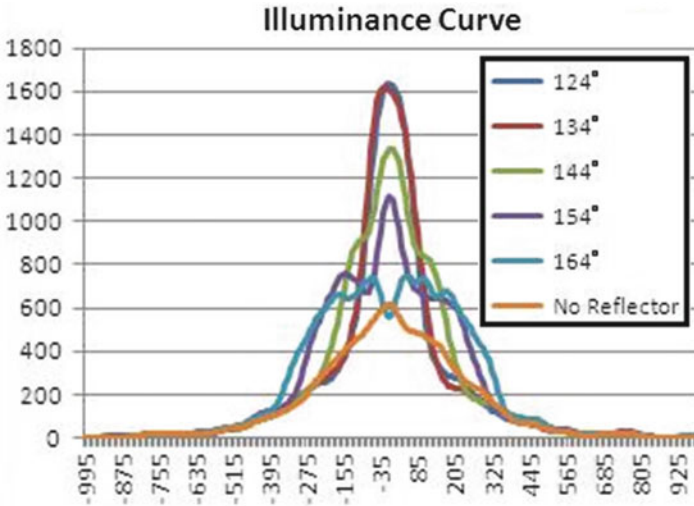
Fig. 14 Illumination of each angle

Table 3 Lighting range meeting desktop lamp standard

Included angle of reflector	124°	134°	144°	154°	164°	No reflector
Maximum illumination value, lux	1,638	1,619	1,329	1,118	733	616
Illumination range of grade AA, cm	24	25	35	48	52	13
Illumination range of grade A, cm	35	35	44	57	65	43

4 Conclusions

The LED luminaire has made a breakthrough in the artificial lighting area. The luminaire are made of different materials. The luminous property is different between the scattering effect and scatter-free effect. Therefore, it is important to select the materials and suitably set simulation parameters when designing lamps. The illumination distribution characteristics within the working range are one of the lighting quality indicators, and the lighting demands of the light field vary with the application. In this study, the LED T8 lamp is used in the desktop lighting so that when the lamp reaches the lampshade effect and the lamp's inner structure is changed, the light field can have more functions, and the grade AA stated in JIS C8112 "Table study lamps for fluorescent lamps."

References

1. Guan R, Tian D, Wang X (2008) Design and implementation of LED daylight lamp lighting system. In: ICEPT-HDP
2. Nan Ya Photonics Inc. http://www.nypi.com.tw/web/product_led_Tube.asp
3. Wang X (2010) A LED light bar. China Patent
4. J. C8112 (2008) JIS C8112 table study lamps for fluorescent lamps

A Sigma–Delta ADC Design for Audio Applications

Chin-Fa Hsieh, Chun-Sheng Chen, and Kang-Ni Lin

Abstract An analog-to-digital converter (ADC) that uses delta–sigma modulation technique is less restricting to analog circuit specification, consumes less circuit power, and achieves higher resolution. This chapter presents an oversampling, second-order, fully differential design for a sigma–delta ADC, which is suited to audio applications. The modulator architecture is first designed using the behavioral simulator in MATLAB and then the TSMC 0.18 μm single-poly six-metal process. Using a sampling frequency of 6.4 MHz, an oversampling rate of 128 and an input amplitude of −3 dB of the full swing, a signal-to-noise ratio (SNR) of 92 dB is achieved using behavioral simulations and a ratio of 89 dB from the circuit simulations. This is equivalent to 15-bit resolution.

Keywords ADC • Sigma–delta • Modulation

1 Introduction

Analog-to-digital converters (ADC) convert a measured analog signal to a digital representation and play a very important role in electronic systems. The performance of an ADC is usually evaluated based on its speed and resolution. With high speed and resolution, an ADC enhances a system performance, making it applicable in many fields. For example, a direct-conversion ADC (flash ADC) provides the highest conversion rate by using $2n - 1$ comparators in parallel to convert an analog signal into a digital signal and the comparator generates a code for each voltage range. Although very high-speed conversion is possible, this design results in large die area, high input capacitance, and high power dissipation. This type of ADC is often used for

C.-F. Hsieh (✉) • C.-S. Chen • K.-N. Lin
Department of Electronic Engineering, China University of Science and Technology,
Taipei 11581, Taiwan
e-mail: c0935@cc.cust.edu.tw

video, wideband communications, or other fast signals processing device [1, 2]. A Successive approximation register ADC (SAR ADC) uses a comparator to successively narrow the range of input voltages, step by step. It requires n comparative cycles for an n-bit output, so a SAR ADC saves power consumption and area, but its conversion rate is very slow because of the successive comparisons necessary to its operation [3].

Delta–sigma ($\Delta\Sigma$) modulators are widely used in digital audio applications. Their oversampling and noise-shaping features reduce the noise and move the in-band quantization error out of the band. The digital filter used filters the noise on high-frequency signals and significantly improves the resolution. Its conversion speed is between those of a flash ADC and a SAR ADC, but it has better resolution because of the oversampling. Because of these advantages, $\Delta\Sigma$ ADCs are mainly used when high resolution and high cost-effectiveness are important, such as for audio, in measurement instruments [4–6].

In this chapter, a $\Delta\Sigma$ modulator is firstly presented and then a second-order $\Delta\Sigma$ modulator is designed, using 0.18 um CMOS technology. The chapter is organized as follows. Section 2 describes the principle of a $\Delta\Sigma$ ADC. In Sect. 3, the circuit is designed. Simulation results are presented in Sect. 4. Finally, Sect. 5 gives a conclusion.

2 Principle of a $\Delta\Sigma$

Figure 1 shows a diagram of a $\Delta\Sigma$ ADC system. The modulator processes the signal generated by a sample and hold circuit. It converts a continuous analog signal into a high-speed discrete digital signal with high-frequency noise. After downsampling and noise filtering, these digital signals are processed in a digital system. The $\Delta\Sigma$ ADC uses oversampling to achieve a higher resolution than other types of data converter. For a first-order $\Delta\Sigma$ ADC, the SNR increases by 9 dB if the oversampling rate doubles, which is equivalent to an increase of 1.5 bits. A second-order $\Delta\Sigma$ modulator, as shown in Fig. 1, consists mainly of integrators and a quantizer. It includes two integrators. The SNR increases by 15 dB if the oversampling rate doubles, which is equivalent to an increase of 2.5 bits.
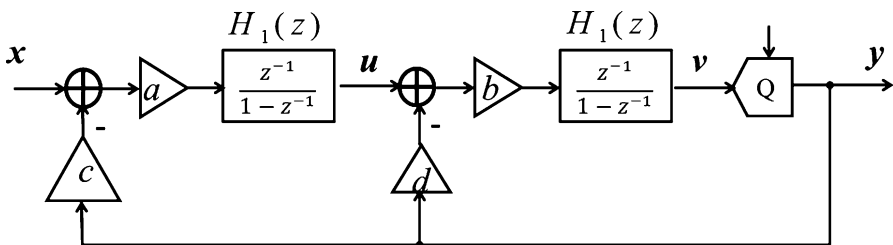
Fig. 1 A diagram of a $\Delta\Sigma$ modulator

3 Circuit Design

A block diagram of a second-order $\Delta\Sigma$ modulator is shown in Fig. 2. The architecture comprises a switched-capacitor integrator module, a common-mode feedback module, a quantizer module, and switches. The function of each part is described as follows:

3.1 Switched-Capacitor Integrator

The performance of a $\Delta\Sigma$ ADC depends on the accuracy of the switched-capacitor integrator, which requires nonoverlapping clock signals and a linear advantage on voltage.

The integrator shown in Fig. 2 is mainly composed of the switched-capacitor circuits and an operational amplifier. The integrator plays a very important role because its performance determines the performance of a modulator.

The operational amplifier, the most important component in a modulator, comprises three sub-circuits: the main amplifier, a bias circuit, and a common-mode
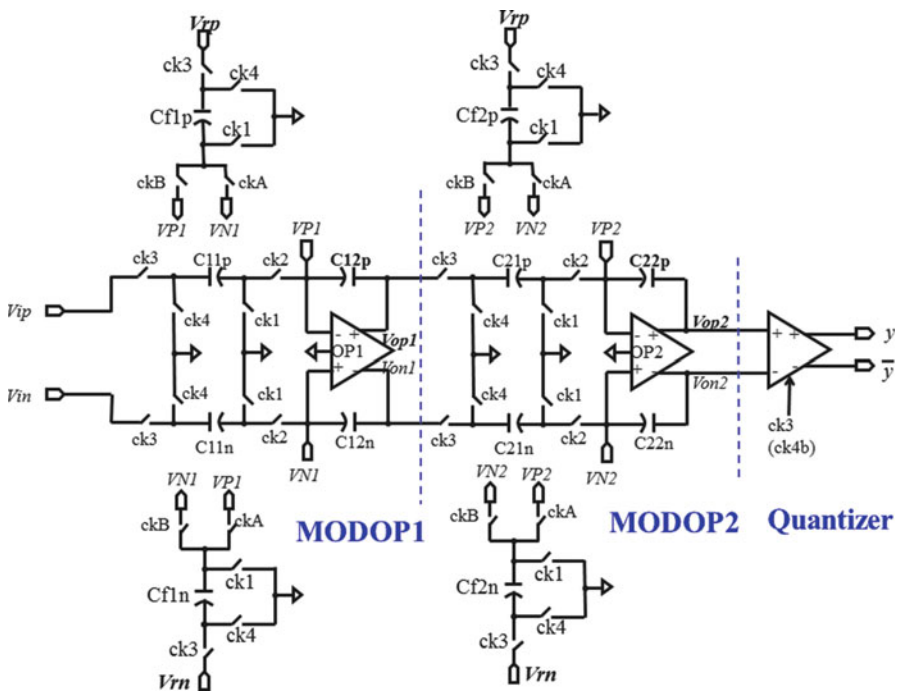
Fig. 2 A block diagram of a second-order $\Delta\Sigma$ modulator
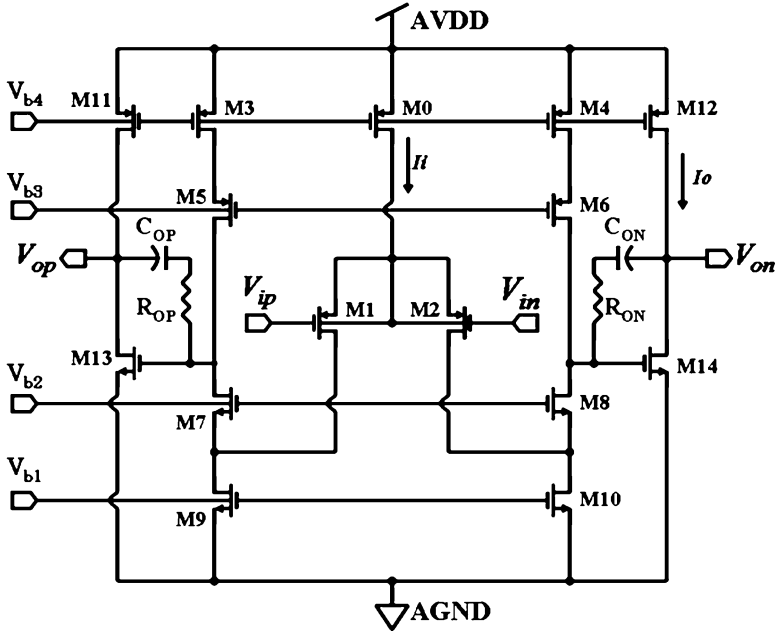
Fig. 3 Operational amplifier

feedback (CMFB) circuit, as shown in Figs. 3, 4, and 5, respectively. We select a fully differential operational amplifier for the input signal because it has a better performance than the single-end operational amplifier. The fully differential operational amplifier is a folded cascode two-stage architecture design which uses Miller compensation. A PMOS input pair is also used to minimize the flicker noise. The bias circuit provides bias voltages: Vb1, Vb2, Vb3, and Vb4 for the amplifier. If the output voltage of the operational amplifier is not properly stabilized at the common-mode level, there may be signal distortion [7, 8]. A CMFB is then required to calibrate the common-mode output offset. The CMFB measures the output common-mode level compared to a reference voltage and can send the error to the amplifier.

An analog switch is a very important component in a $\Delta\Sigma$ ADC. The design of this circuit must take account of the resistance characteristic: a very high resistance value when the switch is off and a very low value when it is on. A CMOS transmission gate has a lower resistance value than a single NMOS or a PMOS, so a CMOS transmission gate is used as the switch in a switched-capacitor circuit. It requires nonoverlapping clocks in the switched-capacitor circuit, so four-phase nonoverlapping clocks are designed.
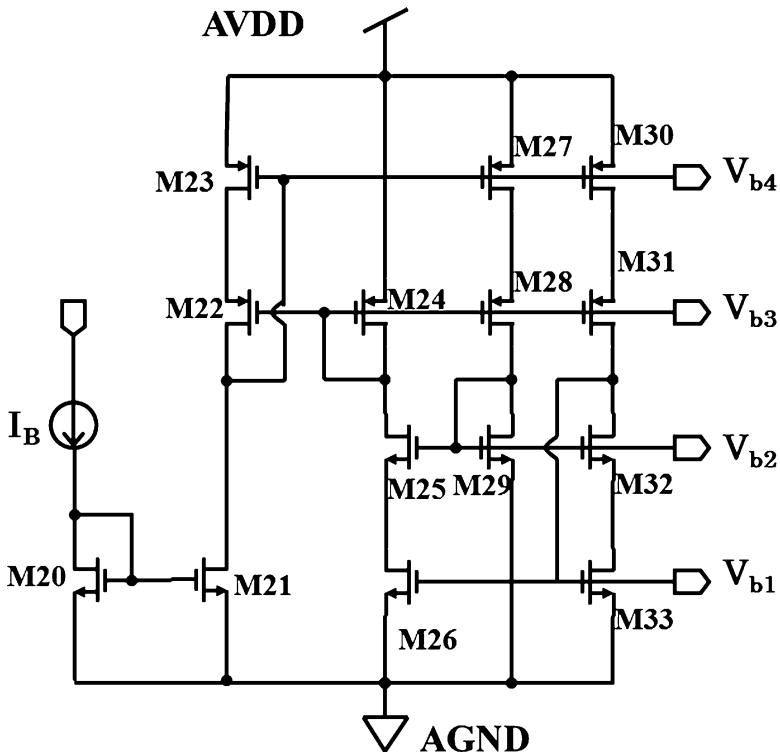
Fig. 4 Bias
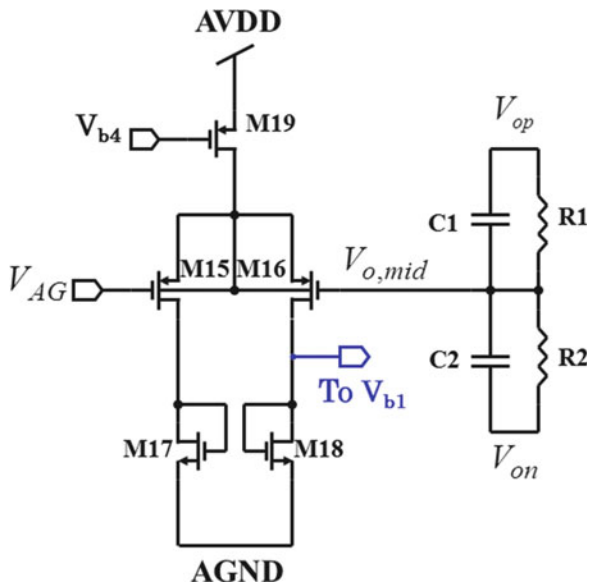
Fig. 5 CMFB

3.2   Quantizer

The quantizer comprises three sub-circuits: a comparator, a dynamic latch, and a static latch. Noise shaping reduces the effect of the quantization error on the efficiency of a modulator. A regenerative comparator is used. For half of one clock cycle, the regenerative comparator is in a pre-charging state, so in order to maintain the previous state and to produce the correct output waveform, a regenerative comparator must be connected with a RS latch circuit.

4   Simulation Result

The efficiency of the proposed modulator depends on the design of the operational amplifier. A fully differential operational amplifier has a higher DC gain, which is used to drive the signal. In order for the transistors to work properly, the voltage dropped from the gate to the source voltage must always be greater than the saturation voltage, so that all of the transistors in the saturation region work. This is verified by the simulations, using HSPICE. The frequency response is shown in Fig. 6 and Table 1. The simulation result shows that the DC gain, the unity-gain
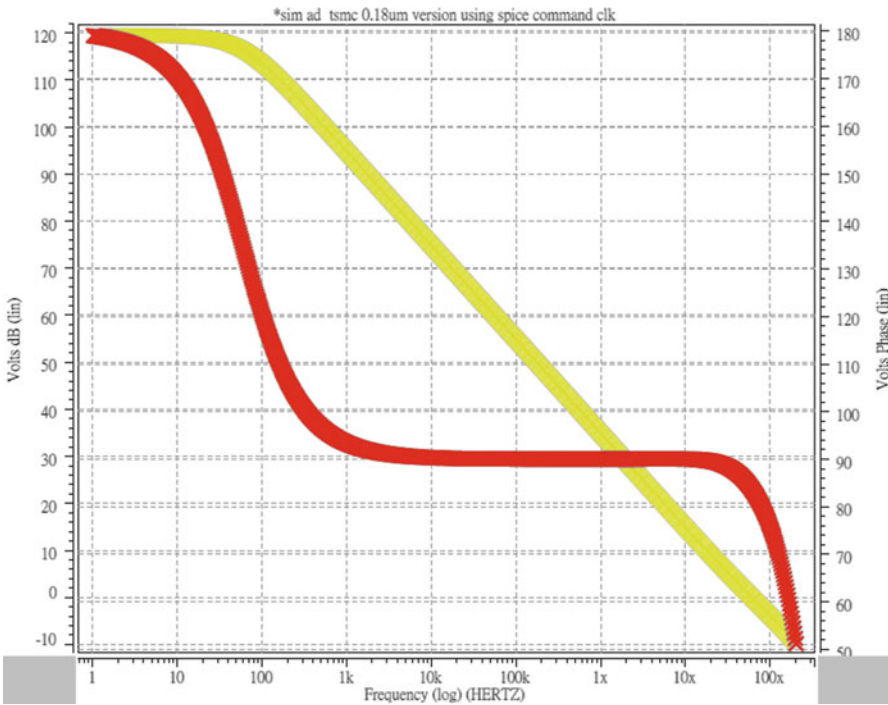
Fig. 6 Simulation result for the OP

Table 1 Simulation results for the OP

Parameter	Simulation result
Voltage	1.65 V
Gain	129 dB
UGBW	60.9 MHz
Phase margin	83.8
Load	4 pF

Table 2 Simulation results of modulator

Input level (dB)	Input voltage (V)	SNR (dB)
−3	0.707	89.6
−6	0.5	88.1
−10	0.35	85.9
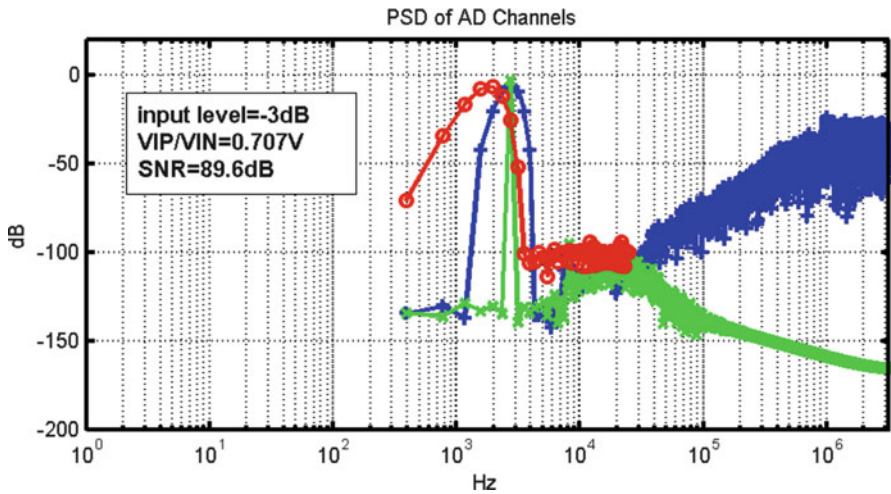
Fig. 7 Output spectrum

bandwidth, and the phase margin are 129 dB, 60.9 MHz, and 83.8°, respectively. The bias voltages for the amplifier, Vb1, Vb2, Vb3, and Vb4, are 0.81, 1.18, 1.93, and 2.46 V, respectively. In order to generate nonoverlapping clocks, we use appropriate size inverter chain to adjust time delay. CK1 and CK2 are the nonoverlapping clocks, with an interval of approximately 7.5 ns. The CLKA delay and the CLKB delay from CK1 and CK2 are approximately 2 ns.

The proposed $\Delta\Sigma$ ADC is simulated using different input voltage level. The effect of different input voltages on the SNR is shown in Table 2, which shows that the proposed modulator with an input level of −3 dB and a Vip/Vin of 0.707 V has SNR of 89.6 dB, giving an effective number of bits of approximately 15. Figure 7 shows the output spectrum. A comparison of the result with [9] and [10] is shown in Table 3.

Table 3 Results for comparison

	Ref. [9]	Ref. [10]	Proposed
Process (µm)	0.5	45	0.18
Supply voltage (V)	5	3.3	3.3
OSR	64	64	128
SNR	85 dB	92.1 dB@−2.1 dBFS	89.6 dB

5 Conclusion

This chapter presents a second-order $\Delta\Sigma$ modulator designed in TSMC 0.18 µm single-poly six-metal CMOS process. The sampling frequency is 6.4 MHz. It is simulated at different input voltage levels. The simulation result shows that the proposed modulator with an input level of -3 dB and a Vip/Vin of 0.707 V has SNR of 89.6 dB with an oversampling rate of 128. For an ADC, the $\Delta\Sigma$ modulation technique consumes less circuit power and achieves a higher resolution. The effective number of bits of the proposed architecture is approximately 15, making it very suitable for data conversion in audio applications.

References

1. Sall E, Vesterbacka M, Andersson KO (2004) A study of digital decoders in flash analog to digital converters. In: IEEE international symposium on circuits system, Vancouver, 2004
2. Kale AV, Palsodkar P, Dakhole PK (2012) Comparative analysis of 6 Bit thermometer-to-binary decoders for flash analog-to-digital converter. In: 2012 international conference on communication systems and network technologies (CSNT), Rajkot, 2012, pp 543–546
3. Cho SH, Lee CK, Lee SG, Ryu ST (2012) A two-channel asynchronous SAR ADC with metastable-then-set algorithm. J IEEE Trans VLSI Syst 20:765–769
4. Signore BP, Kerth DA, Sooch N, Swanson E (1990) A monolithic 20-b delta-sigma A/D converter. J IEEE Solid State Circ 25:1311–1317
5. Mahajan D, Kakkar V, Singh AK (2011) Analysis of delta sigma modulator In: 2011 international conference on computational intelligence and communication networks (CICN), Gwalior, 2011, pp 182–186
6. Fujimoto Y, Re PL, Miyamoto M (2005) A delta-sigma modulator for a 1-bit digital switching amplifier. J IEEE Solid State Circ 40(9):1865–1871
7. Pelgrom M, Duinmaijer A, Welbers A (1989) Matching properties of MOS transistors. J IEEE Solid State Circ 24(5):1433–1439
8. Kinget P (2005) Device mismatch and tradeoffs in the design of analog circuits J. IEEE Solid State Circ 40(6):1212–1214
9. Koppula RMR, Balagopal S, Saxena V (2012) Multi-bit continuous-time delta-sigma modulator for audio application: In: 2012 I.E. workshop on microelectronics and electron devices (WMED), Boise, 2012, pp 1–5
10. Kim JS, Kwon TI, Ahn GC, Kim YG, Kwon JK (2011) A $\Delta\Sigma$ ADC using 4-bit SAR type quantizer for audio applications. In: 2011 I.E. international SoC design conference (ISOCC), Jeju, 2011, pp 73–75

Applications of ZigBee on Building a Home Automation System

Shih-Ching Huang and Chin-Sung Hsiao

Abstract Application of wireless transmission technology to construct a family automation system is proposed and realized in this study. In this investigation, we make use of the advantages of ZigBee consisting of power saving, high reliability, and extensibility to build an automatic system so that the problems of the hardware complicity and the maintenance of the family household appliances network can be excluded.

1 Introduction

Real-time controller with microprocessor has been widely applied for automatic control that makes family automation in realization. Today the family entertainments, household appliances, and home safety systems can be mutually connected by the Internet, and these are able to be independently monitored or controlled in a remote site. Traditionally, a home space that only provides residing for humans has not been gratified due to the life quality promotion and the matured development of the wireless sensor network; therefore, a higher-realm spiritual life has become the main goal pursued by most people. To attain this function, the integration of hardware circuit and wireless technology to form a home automation system is feasible.

S.-C. Huang
Department of Computer Science and Information Engineering, Asia University,
Taichung 41354, Taiwan

C.-S. Hsiao (✉)
Department of Photonics and Communications Engineering, Asia University,
Taichung 41354, Taiwan
e-mail: cshsiao@asia.edu.tw

Home automation is equipped with microprocessors, relays, and wireless sensors [1, 2] to form a sensible system for control of the household appliances such as lighting, computer, home security, air-condition, and video and/or stereo. The applications of home automation are classified into three types: housework management, antitheft and security safety, and housing culture.

In this study, we employ ZigBee and electronic components to construct a home automation system. The core controller in the system named CC2420, a microchip, is fabricated by Chipcon Corporation and is certified by the global ZigBee alliance [3]. The IC2420 microchip with near-distance data transmission ability under the protocol of IEEE 802.15.4 has the ability to provide maximum supportable 65,536 interconnection points so that the system can provide versatile, easy operation, and unstained interfaces with which the user can monitor the states of the household appliances at anytime and from anywhere.

2 Structure of the Designed System

ZigBee is a wireless technology of low-speed transmission, short distance, and low-power consumption. The maximum transmittable distance of ZigBee is around 10 m, and the most operatable spectral bands are located in 900 MHz and 2.4 GHz based on 10–250 kbps. Additionally, ZigBee has the merit of text and graphic transmission with AES encryption [4]. The proposed home automation system is structured by three parts as shown in Fig. 1.
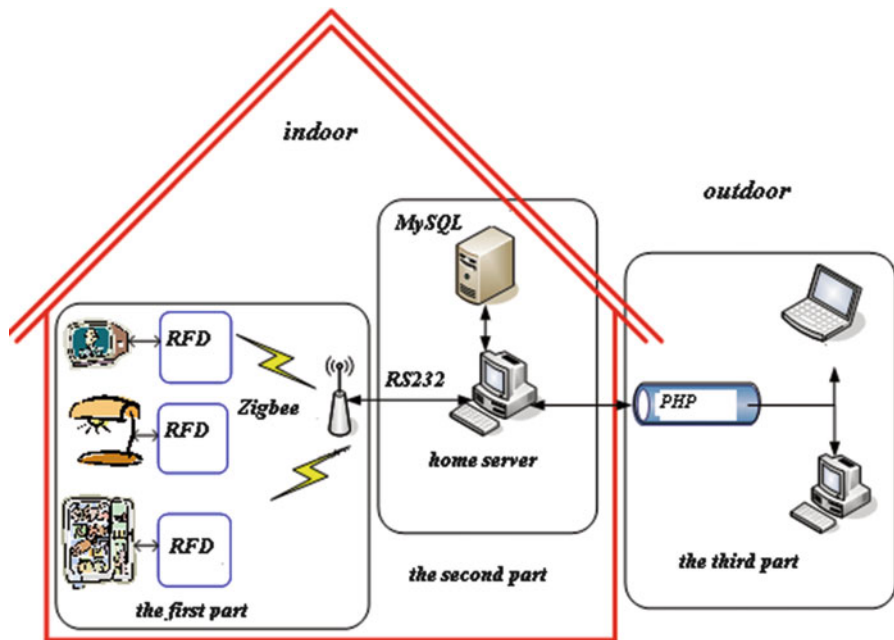
Fig. 1 Schematic structure for the proposed family automatic control system

Table 1 Household appliances server hardware specification

Item	Specification
Operating system	Windows XP Professional SP2
CPU	Inter(R) Pentium(R)M processor 1.86 GHz
Motherboard	ASUSTeK Computer Inc. M9V
Memory	1,024 MB
Display card	ATI Mobility Radeon X600 SE
Hard disk	80 GB
Network card	Realtek RTL8139 Family Ethernet

This first part includes a control circuit equipped with 8951 microprocessor to control the household appliances. The ZigBee household appliances network contains the RFD and coordinator, in which RFD is combined with the control circuit while the coordinator is connected to the home server to form a household appliances network to transmit and receive signals by wireless.

The second part is called the home server that includes a personal computer for data integration and a MySQL database for recording all control states and household appliances data. The home server platform transmits a control signal when new states of household appliances are reset.

This third part is the rear-end platform, where the users are capable of observing the available states of the household appliances at anytime via the Internet. This part is equipped with the Apache Server through which the users can operate via the PHP home page interface by the Internet.

2.1 Requirement of System Hardware

The proposed system hardware is equipped with a household appliances server, MySQL database, and PHP home page interface. The specifications of the household appliances server hardware are listed in Table 1.

2.2 Requirement of System Software

System software is classified into two parts described as follows.

2.2.1 Developed Port Software

Operating system: Windows XP Professional SP2
Home page server: Apache Server
Database: MySQL
System-developed program: Microsoft Visual Basic 2005
Home page–developed program: Dreamweaver 8
PIC microchip program: MPLAB IDE V7.43
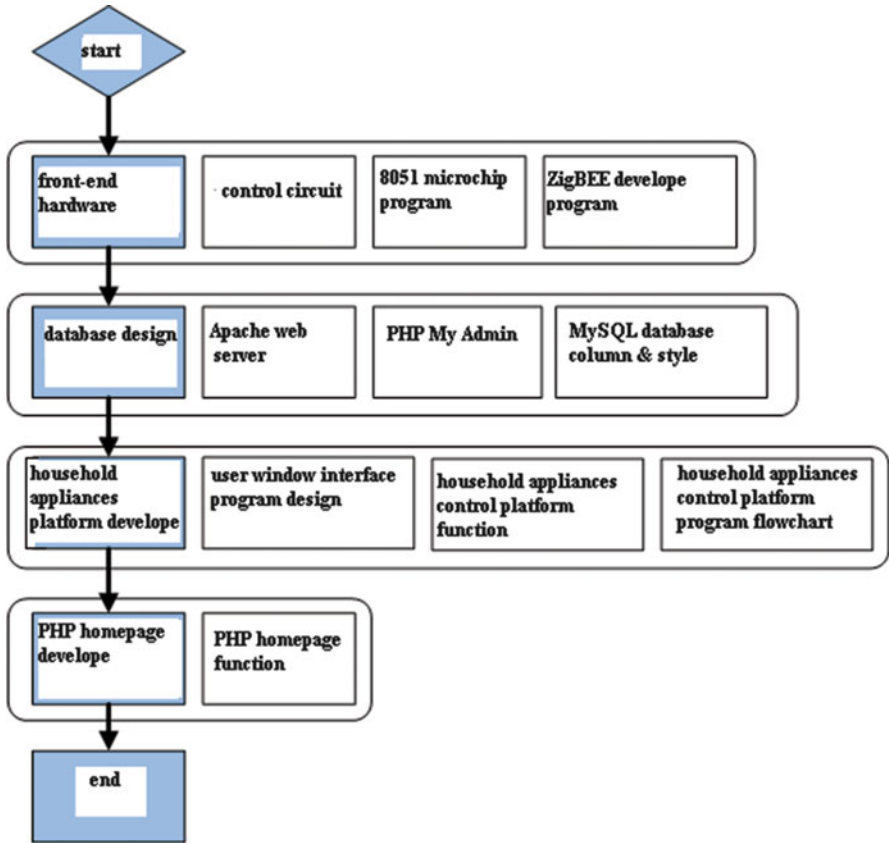
Fig. 2 The studied system flowchart

2.2.2 Server Port Software

Operation system: Windows XP Professional SP2
Home page server: Apache Server
Database: MySQL
Home page–developed program language: PHP

2.3 System Flowchart

The system flowchart in this study is assembled by four parts as shown in Fig. 2.
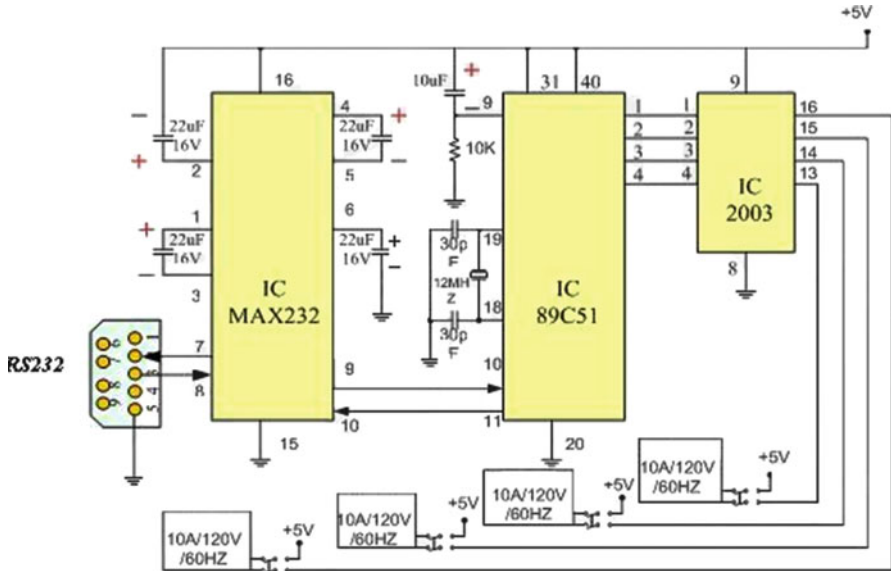
Fig. 3 Schematic diagram of the front-end control circuit

2.4 Front-End Hardware and Control Circuit

The function of this front-end hardware is for control signal when the state feedback signal is connected to ZigBee and personal computer. Figure 3 displays the front-end control circuit diagram congregated by microchip IC8951, ICMAX232, IC2003, resistors, capacitors, and relays. IC 8951 is a relay driver for switching the state of the household appliances as the coordinator sends a control code to RFD that actuates IC 8951. IC 8951 will retransmit the state code to RFD and then send to the coordinator at the relay with a switching action, and then the coordinator returns the state code to the household appliances server that makes a judgment to decide whether the switching state of the household appliances in the database is valid or not.

2.5 Function of the Household Appliance Platform

There are three blocks included in the household appliance control platform: household appliance information browses, input home page, and control home page.

2.5.1 Household Appliance Information Browses

The users need to connect to the MySQL database by the Internet to check the applied information, while the MySQL database is not available from Microsoft so the install of the ODBC package is required for the application of the MySQL database.

2.5.2 Input Home Page

The users need to establish the specified nameplate, position, state, and numbers of the designated household appliance in the MySQL database for adding or deleting information in the future.

2.5.3 Control Home Page

The users are able to select a port for data transmission when one of the household appliances is selected, which will automatically produce a control code for updated information transmission via RS-232, and this code is thus sent to the personal computer for state control.

3 Results

After completing the proposed control circuit, we here present the whole system operation procedure. First we need to log in to a ZigBee household appliances network before Internet transmission; this process is processed by setting the coordinator and RFD in the Windows XP operating system. Next, the control of the system is used for the household appliances control program execution that adds or deletes the names, numbers, positions, and the states of the household appliances to the system. Finally, the users are able to inquire the updated states of the household appliances only by virtue of wireless equipment. Figure 4 shows the accomplished diagrams of the control circuit and the ZigBee control board, respectively. With the presetting of the coordinator and RFD in the Windows XP operating system, the user can program on the household appliances control platform to give numbers and to stitch the states of the household appliances. Furthermore, the users can know the updated states of the household appliances via the PHP home page from anywhere by using a wireless mobile device.

Fig. 4 An accomplished control circuit board used to switch the state of the household appliances when the coordinator sends a control code to RFD that actuates the 8951 microprocessor

4 Conclusion

An intelligent household appliances monitor system that is constructed with a few ICs and electronic components and is controlled with ZigBee is proposed and completed. The present system with the advantages and unique characteristics of an intelligent house is realizable by embedding wireless technology so that users can randomly inquire the updated states of the household appliances with a notebook via the PHP home page Internet under IEEE 802.11 wireless environment. In conclusion, the merits of this proposed system include cost reduction, low-power consumption, easy maintenance of the system, window operation interface, extensibility, and easy installation.

References

1. Perrig A, Stankovic J, Wangner D (2004) Security in wireless sensor networks. J Commun ACM 47:53–57
2. Akyildiz IF, Su W, Sankarasubramaniam Y, Cayirci E (2002) Wireless sensor networks: a survey. Comput Netw 38:393–422
3. ZigBee Alliance. http://www.ZigBee.org/

Design of a Smart Battery System
for Laptop Computer

**Yu-Shan Cheng, Jing-Hsiau Chen, Yi-Feng Luo, Chun-Wei Ko,
and Yi-Hua Liu**

Abstract The performance and lifespan of Li-ion batteries are closely related to the quality of their charger. To enhance the charger's performance, the Smart Battery System (SBS) Specification presents one element of a complete system solution for rechargeable batteries used in portable electronic equipment. The SBS features charging characteristics that are controlled by the battery itself, in contrast to a charger with fixed charging characteristics that will work with only one cell type. Therefore, the smart battery/smart battery charger combination provides distinct advantages in system safety, performance, and cost.

In this chapter, a level 2 SBS is developed and implemented. The power stage is implemented using a level 2 SBC IC ISL88731 from Intersil Corp., and the host controller is realized by using the dsPIC microcontroller from Microchip Corp. The five-step constant-current charging pattern is implemented in the host controller. Comparing to conventional constant-current–constant-voltage (CC-CV) charging pattern, five-step constant-current charging algorithm has the advantages such as higher charging efficiency and shorter charging time.

Keywords Smart battery • Smart battery charger • Level 2 smart battery charger • Five-step constant-current charging algorithm

Y.-S. Cheng (✉) • J.-H. Chen • C.-W. Ko • Y.-H. Liu
Department of Electrical Engineering, NTUST, Taipei, Taiwan, R.O.C.
e-mail: M10107201@mail.ntust.edu.tw

Y.-F. Luo
Division for Biomedical and Industrial IC Technology, Green Electronics Design
and Application Department, ICL, ITRI, Hsinchu, Taiwan, R.O.C.

1 Introduction

Many electronic products rely on batteries as their primary or auxiliary power sources. Among rechargeable batteries, lithium-ion (Li-ion) batteries offer several advantages, including high energy density, low maintenance requirement, high open-circuit voltage (OCV), low self-discharge rate, and lack of memory effect, and have emerged as the major power source for today's electronic products [1–3]. The performance and lifespan of Li-ion batteries are closely related to the quality of their charger [4–8]. To enhance the charger's performance, the Smart Battery Charger (SBC) Specification presents one element of a complete system solution for rechargeable batteries used in portable electronic equipment such as laptop computer systems, cellular telephones, and video cameras. The electrical characteristics of the SBC feature charging characteristics that are controlled by the battery itself, in contrast to a charger with fixed charging characteristics that will work with only one cell type. Therefore, the smart battery/ smart battery charger combination provides distinct advantages in system safety, performance, and cost.

In this chapter, a smart battery system is developed and implemented. The hardware and firmware parts of the proposed system are described in detail. In this chapter, the power stage is implemented using a level 2 SBC IC ISL88731 from Intersil Corp. The host controller is realized using the dsPIC microcontroller from Microchip Corp. It reads the battery's charging requirements and controls the battery charger accordingly. The five-step constant-current charging pattern is implemented in the host controller. Comparing to conventional constant-current–constant-voltage (CC-CV) charging pattern, five-step constant-current charging algorithm has the advantages such as higher charging efficiency and shorter charging time. In order to validate the correctness of the proposed system, experiments on Li-ion battery modules for laptop computers are carried out. According to the experimental results, the charging time of the proposed system can be reduced, and the performance of the proposed charger can be improved.

2 Hardware Configuration

Figure 1 shows the block diagram of the proposed smart battery system. In Fig. 1, the input power of the proposed Li-ion battery charger is a commercially available adaptor for notebook computer, and the smart battery module used is a 12.6 V, 4 Ah lithium-ion battery pack for laptop computer. In Fig. 1, a level 2 smart battery charger which complies with the smart battery charger specification v1.1 is utilized as the power stage of the smart battery system, and the charging voltage/current is controlled by the dsPIC33FJ16GS502 microcontroller from Microchip Corp. Figure 2 shows the detailed schematic of the presented smart battery charger. In Fig. 2, the control IC
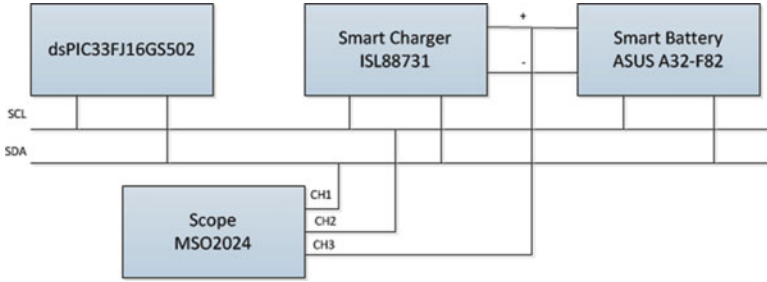
Fig. 1 Block diagram of the proposed smart battery system
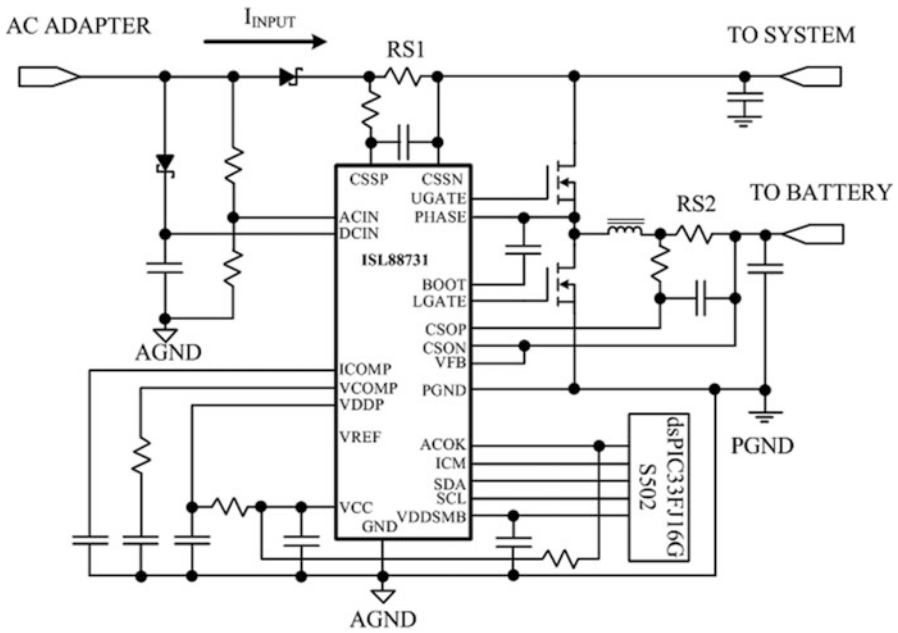
Fig. 2 Hardware configuration of the proposed smart charger

used in the proposed system is ISL88731 from Intersil Corp. The ISL88731 is a highly integrated Li-ion battery charger controller, programmable over the SMBus system management bus (SMBus). As shown in Fig. 3a, a synchronous buck-type DC/DC converter [9, 10] is used as the power stage. By adequately controlling the PWM gating signal, the power converter can transfer the required energy to the Li-ion battery pack. Using the state-average modeling techniques, the small signal model for a continuous conduction mode (CCM) buck converter can be expressed as Eq. (1), as shown in Fig. 3b:
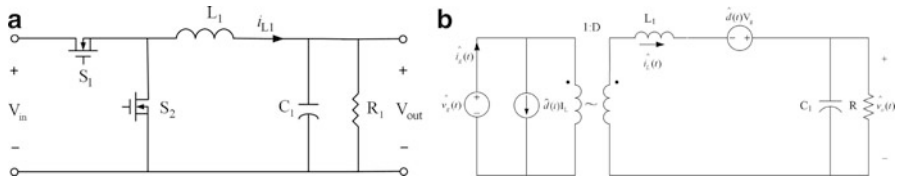
Fig. 3 Power stage of the proposed system. (**a**) Circuit topology and (**b**) Small signal model

$$G_{vd}(s) = \left.\frac{\hat{v}_o(s)}{\hat{d}(s)}\right|_{\hat{v}_g(s)=0} = V_g \cdot \frac{1}{1 + \frac{L_1}{R}s + L_1 C_1 s^2} \tag{1}$$

3 Software Configuration

In this section, the software configurations of the proposed charging system will be provided. Figure 4 shows the software flowchart of the proposed controller. According to the literatures, multistage constant-current charging algorithm has the advantages such as longer cycle life, higher charge/discharge energy efficiency, and shorter charging time. Therefore, five-step constant-current charging algorithm is implemented in the proposed smart battery charger system. Figure 5 illustrates the concept of the five-step constant-current charging pattern used in this chapter. From Fig. 5, the total charging time can be divided into five stages. In each stage, the charging current is set to a predetermined value. During charging, the voltage of the battery will increase. When the voltage reaches the preset limit voltage V_{limit}, the stage number will increase and a new charging current set value will be applied accordingly. This process will continue until the stage number reaches 5.

4 Experimental Results

In order to validate the effectiveness of the proposed system, experiments are carried out on commercially available Li-ion battery packs. Figure 6 shows the measured voltage/current profile for commonly utilized constant-current–constant-voltage (CC-CV) technique, and Fig. 7 shows the measured voltage/current profile for the proposed five-step constant-current charging algorithm. From Figs. 6 and 7, the presented smart battery charger can accurately follow the charging command. Table 1 shows the performance comparison between the CC-CV technique and the proposed five-step constant-current charging algorithm. From Table 1, the charging time can be reduced and the discharged capacity can be increased using the proposed algorithm.
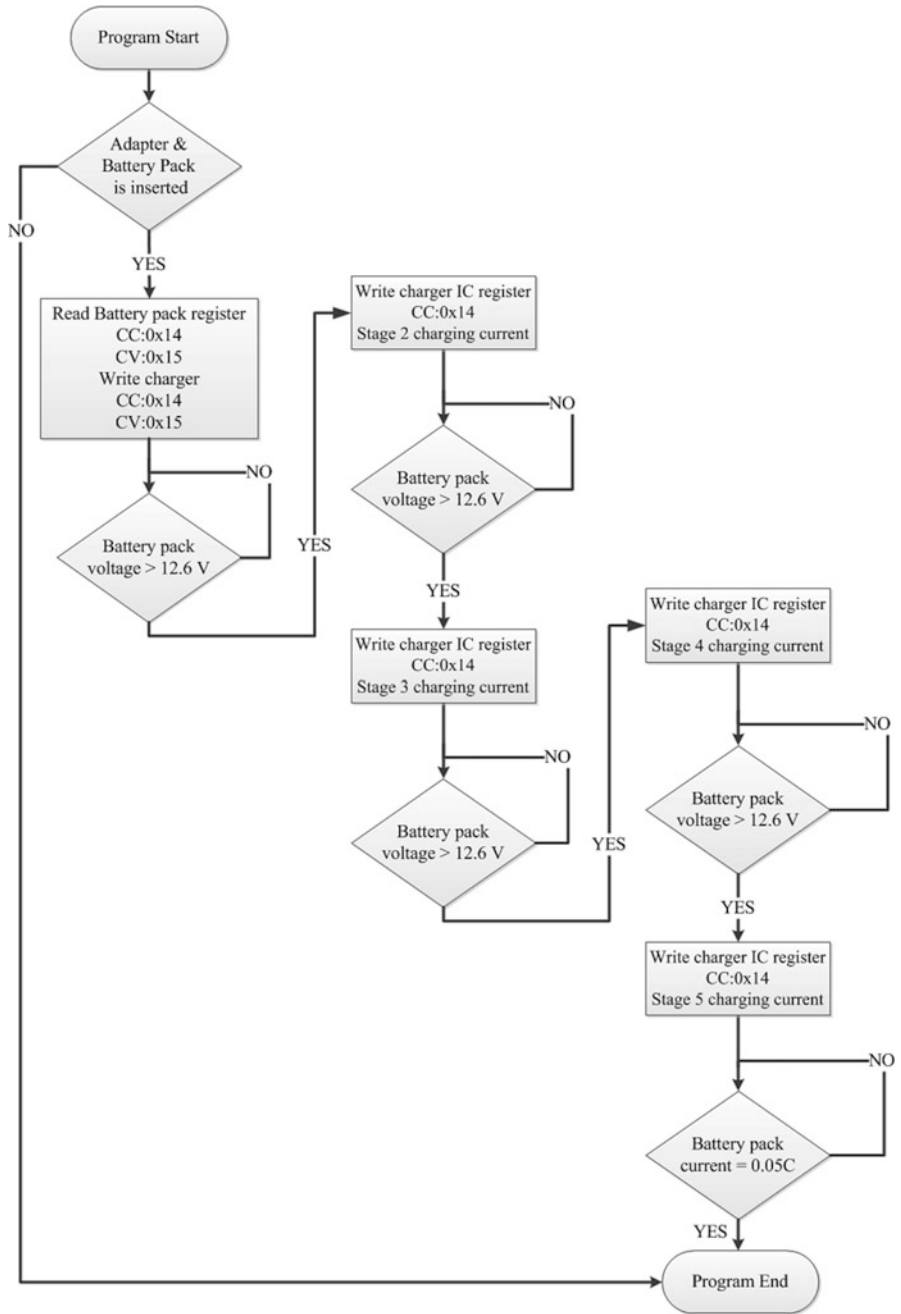
Fig. 4 Software flowchart of the proposed charger
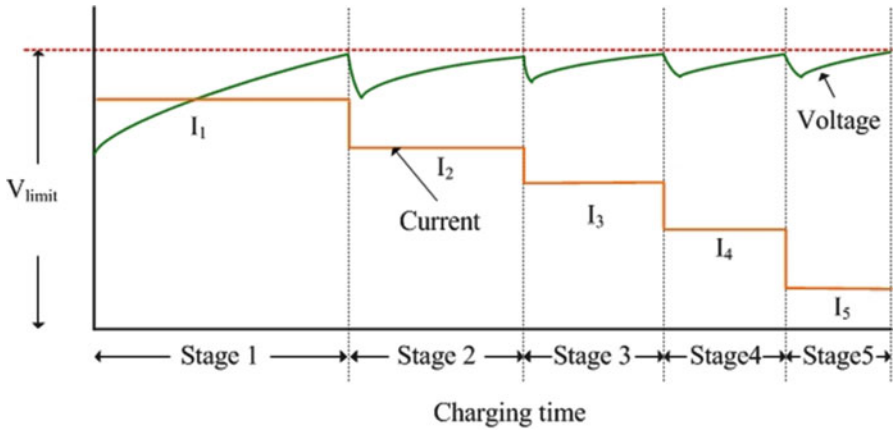
Fig. 5 Five-step constant-current charging algorithm
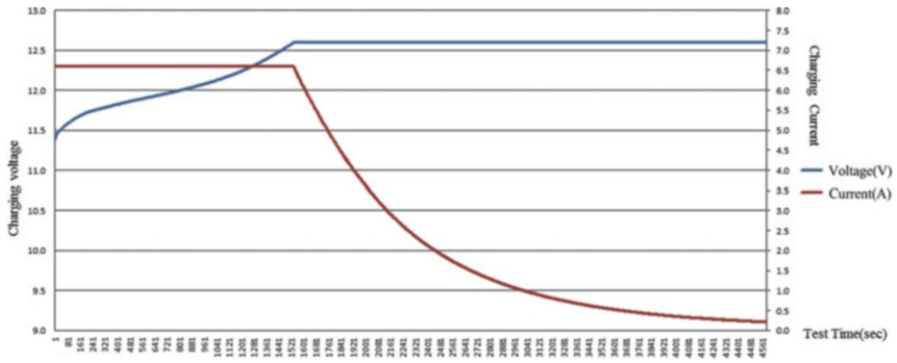
Fig. 6 Measured voltage/current profile for CC-CV technique
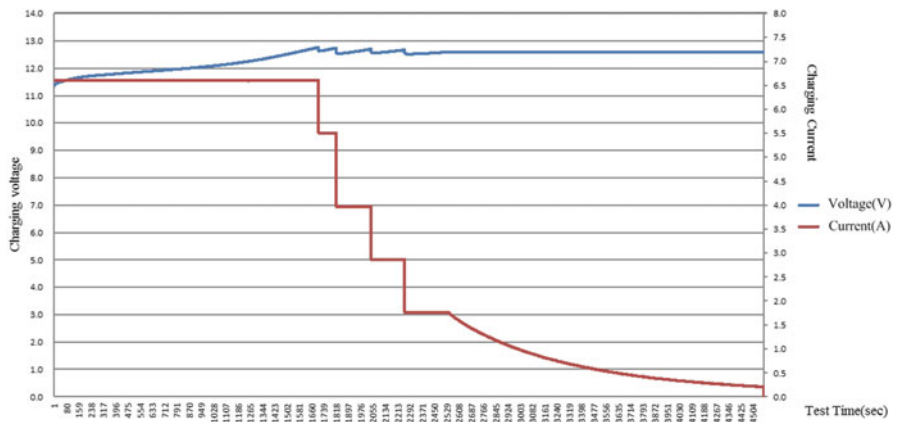
Fig. 7 Measured voltage/current profile for five-step constant-current charging algorithm

Table 1 Performance comparison between CC-CV method and the proposed method

	CC/CV CC-1.5C	Proposed algorithm
Capacity (mAh)	4,223	4,271
Charging time(min)	76.5	75.9
Discharge capacity (mAh)	4,197	4,249

5 Conclusion

In this chapter, a level 2 smart battery system is developed and implemented; five-step constant-current charging pattern is also implemented in the host controller. Comparing to conventional constant-current–constant-voltage (CC-CV) charging pattern, the proposed system can reduce the charging time for 0.7 % and increase the discharge capacity by 1.24 %.

References

1. Chen LR (2004) PLL-based battery charge circuit topology. IEEE Trans Ind Electron 51:1344–1346
2. Zhang SS (2006) The effect of the charging protocol on the cycle life of a Li-ion battery. J Power Sources 161(2):1385–1391
3. Wang JB, Chuang CY (2007) Design considerations of microprocessor-controlled multiphase battery charger with fast-charging strategy. IET Electr Power Appl 1(2):143–152
4. Ikeyaa T, Sawadab N, Murakamic JI et al (2002) Multi-step constant-current charging method for an electric vehicle nickel/metal hydride battery with high-energy efficiency and long cycle life. J Power Sources 105(1):6–12
5. Chiu HJ, Lin LW, Pan PL, Tseng MH (2006) A novel rapid charger for lead-acid batteries with energy recovery. IEEE Trans Power Electron 21(3):640–647
6. Lin CH, Chen CL, Lee YH, Wang SJ, Hsieh CY, Huang HW, Chen KH (2008) Fast charging technique for Li-ion battery charger. In: Proceedings of the IEEE electronics, circuits and systems international conference, 2008, pp 618–621
7. Svoboda V, Doering H, Garche J (2005) The influence of fast charging on the performance of VRLA batteries. J Power Sources 144(1):244–254
8. James M, Grummett J, Rowan M et al (2006) Application of pulse charging techniques to submarine lead-acid batteries. J Power Sources 162(2):878–883
9. Mohan N, Undeland TM, Robbins W (2003) Power electronics converters application and design, 3rd edn. Wiley, Hoboken
10. Erickson RW, Maksmovic D (2000) Fundamentals of power electronics, 2nd edn. Kluwer Academic Publishers, Norwell

A Novel Fuzzy Neural Network Controller for Maglev System with Controlled-PM Electromagnets

Seng-Chi Chen, Ying-Jyh Lin, Van-Sum Nguyen, and Ming-Mao Hsu

Abstract This chapter proposed an intelligent control method for the positioning of a hybrid magnetic levitation (Maglev) system, using the emerging approaches of fuzzy logic and artificial neural network (ANN). A Maglev system depends on controlling the air gap of the electromagnetic actuator. In practice, no precise mathematical model can be established because this hybrid Maglev system is inherently unstable in the direction of levitation, and the relationships between current and electromagnetic force are highly nonlinear. Fuzzy logic has emerged as a mathematical tool to deal with the uncertainties in human perception and reasoning. It also provides a framework for an inference mechanism that allows for approximate human reasoning capabilities to be applied to knowledge-based systems. Moreover, ANNs have emerged as fast computation tools with learning and adaptive capabilities. Recently, these two fields have been integrated into a new emerging technology called fuzzy neural networks (FNN) which combine the benefits of each field. In the method that is proposed herein, the control model uses Takagi-Sugeno fuzzy logic, in which the back-propagation algorithm processes information from neural networks to make suitable adjustments to the parameter of the fuzzy logic controller (FLC) and the control signal for object output tracking of the input. This method can then be applied to improve the control performance of nonlinear systems. System responses transient performance and steady-state performance various processes that are by using a FNN that must be trained through a learning process, to yield suitable membership functions and weightings. The result on the Maglev system of a simulation indicates that the system response satisfies the control performance without overshoot, zero-error steady state, and obtaining the rise time within 0.1 s. The proposed controller can be feasibly applied to Maglev systems with various external disturbances, and the effectiveness of the FNN with self-learning and self-improving capacities is proven.

S.-C. Chen (✉) • Y.-J. Lin • V.-S. Nguyen • M.-M. Hsu
Department of Electrical Engineering, Da-Yeh University, Changhua 51591, Taiwan
e-mail: amtf.csg@mail.dyu.edu.tw

1   Introduction

The Maglev technique has been adopted in industry to eliminate friction in mechanical contact, subsequently decreasing maintenance costs and achieving high-precision positioning, explaining its extensive use in various fields such as high-speed train suspension in Germany and Japan [1],magnetic bearings [2], vibration isolation systems, and magnetic suspension motors [3]. This work presents a position control scheme of the hybrid actuator by using the emerging approaches of the FNN. Fuzzy systems and neural network-based control methodologies have emerged in recent years as a promising means of solving nonlinear control problems [4–6]. The main method is based on the control model using Takagi-Sugeno fuzzy logic, in which the back-propagation algorithm processes information from neural networks to make appropriate adjustments to the parameter of the FLC and the control signal for object output tracking of an input [7, 8]. Simulation results of the Maglev system indicate that the system response satisfies the control performance without an overshoot, zero steady-state error. Additionally, this controller also satisfies the requirements of a real-time response and stability under the condition of disturbances or interferences with the control system.

2   Hybrid Maglev System

A hybrid electromagnet system consists of a permanent magnet and an electromagnet coil within an E-shaped core, as depicted in Fig. 1, which comprises of a hybrid electromagnet and a ferrous rail. The system forms two flux loops and the flux passes through a permanent magnet (PM), a ferrous plate, an air gap, and a core in each loop. Figure 2 displays the corresponding magnetic equivalent circuit. The magnetomotive force (MMF) of this hybrid electromagnet is the summation of the PM and the electromagnet MMF, where N_m denotes the coil turns and i represents the current through the coil. Moreover, the total reluctance of the magnetic path is

$$R = \frac{R_1 R_2}{R_1 + R_2} \tag{1}$$

with $R_1 = R_2 = R_{Pm} + R_{Fe} + R_x$, where R_{Pm}, R_{Fe} and R_x refer to the reluctances of the PM, ferrous rail, and air gap in the magnetic path, respectively. The reluctances are calculated as follows:
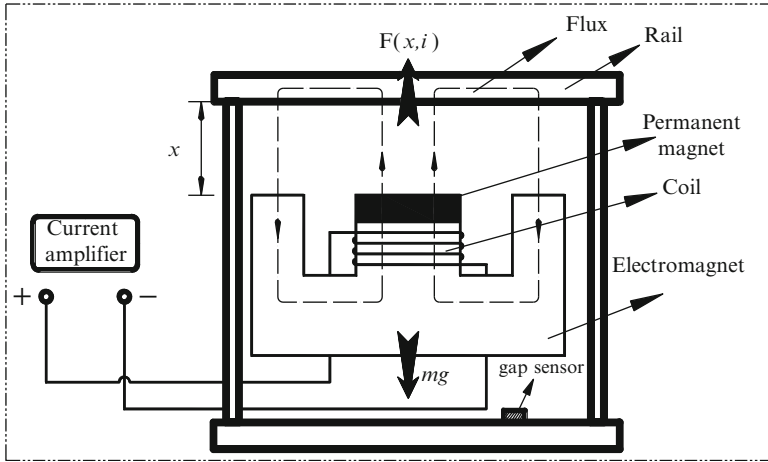
Fig. 1 Simplified model of the hybrid magnetic suspension system
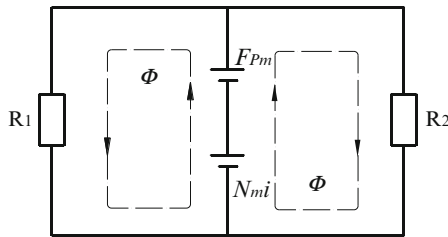
Fig. 2 The equivalent magnetic circuit of the hybrid electromagnet

$$R = \frac{1}{2}\left(\frac{h_{Pm}}{\mu_{pm}S_{Pm}} + \frac{l_{Fe}}{\mu_{Fe}S_{Fe}} + \frac{x}{\mu_0 S_x}\right) \tag{2}$$

where h_{Pm}, l_{Fe} and x denote the lengths of magnet, ferrous materials, and air gap, respectively. S_{Pm}, S_{Fe}, and S_x represent the corresponding cross-sectional areas; μ_{Pm}, μ_{Fe}, and μ_0 refer to the corresponding permeability.

The flux Φ produced against the magnetic reluctance R by this hybrid electromagnetic MMF can be denoted as

$$\Phi(x, i) = \frac{2(F_{Pm} + N_m i)}{\frac{h_{Pm}}{\mu_{pm}S_{Pm}} + \frac{l_{Fe}}{\mu_{Fe}S_{Fe}} + \frac{x}{\mu_0 S_x}} \tag{3}$$

with $F_{Pm} = H_c h_{Pm}$, where F_{Pm} denotes the MMF of the permanent magnet and H_c represents permanent magnetic coercive force. The attractive force between the hybrid magnetic and ferrous plate can be expressed as
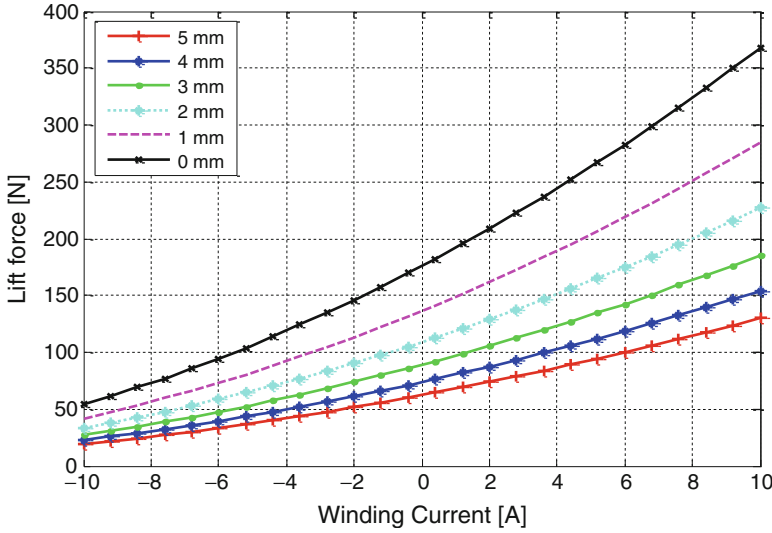
Fig. 3 The results of computation force

$$F(x, i) = \frac{B^2}{2\mu_0} S \tag{4}$$

where S denotes the sum of the cross-sectional area of each flux path and B represents air gap flux density. Figure 3 shows the relation of the lifting force $F(x, i)$, current i, and various air gap x. The mathematical model, which describes the dynamics of the electromagnetic levitation system, is determined using Newton's law. Additionally, the dynamic behavior of the hybrid Maglev system is governed by the following equation:

$$m \frac{d^2 x(t)}{dt^2} = mg + F(x, i) \tag{5}$$

where m denotes the suspended mass and g represents the gravitational acceleration.

The force in terms of deviation from equilibrium values x_0 and i_0 is written as

$$F(x_0 + \delta x, i_0 + \delta i) \cong F(x_0, i_0) + k_x \delta x + k_i \delta i \tag{6}$$

The linear gains are found as follows: k_x represents the slope of the force versus x along the curve $i = i_0$, and k_i refers to the change of force with a current for a fixed value of $x = x_0$. Setting $x = x_0 + \delta x, i = i_0 + \delta i$ instead of (5) leads to

$$m \frac{\mathrm{d}^2(x_0 + \delta x)}{\mathrm{d}t^2} = mg + F(x_0 + \delta x, i_0 + \delta i) \tag{7}$$

The linearized equation of motion about the equilibrium point in terms of δx is thus

$$m \frac{\mathrm{d}^2 \delta x}{\mathrm{d}t^2} = k_x \delta x + k_i \delta i \tag{8}$$

Laplace transformation of (8) yields

$$\frac{\Delta X(s)}{\Delta I(s)} = \frac{k_i/m}{s^2 - k_x/m} \tag{9}$$

Equation (9) indicates that the open-loop transfer function of the hybrid electromagnet system is unstable unless a feedback controller is used.

3 Design of a FNN Controller

Figure 4 shows the structure a FNN. Its input layer and output layer are all fuzzy measures. Also, the whole network comprises the following five layers:

1. The first layer: Every neuron is an input variable, namely, characteristics of the input. The input of neuron i is $I_i^{(1)} = x_i$, and the output is $O_i^{(1)} = x_i$, $(i = 1, 2, \ldots, m)$, where $I_i^{(q)}$ is the input data of neural i in layer q and $O_i^{(q)}$ is the output data of neural i in layer q.
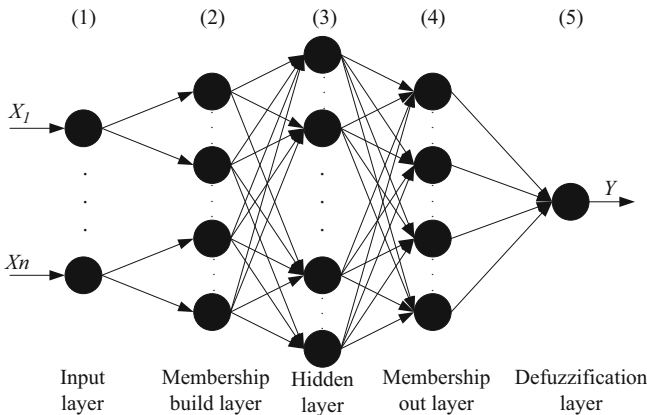
Fig. 4 Fuzzy neural network
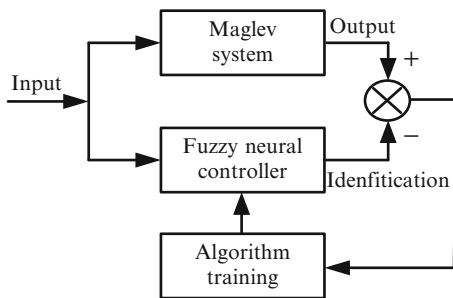
Fig. 5 Structure identification of fuzzy neural model

2. The second layer: This layer leads to defuzzification of input data. The input vector is $I_k^{(2)} = I_k^{(1)} = x_i$ and the output is

$$O_k^{(2)} = e^{-(x_i - c_{ij})^2 / 2\sigma_{ij}^2} \tag{10}$$

where c_{ij} denotes the center and σ_{ij} represents width of Gauss function.

3. The third layer: Neuron number is owing to fuzzy clustering. Input of the neuron i is $I_i^{(3)} = \sum_{j=1}^{L} w_{ij}^{(3)} O_j^{(2)} - \theta_i^{(3)}$ and the output is $O_i^{(3)} = f(net_i^{(3)})$, where $w_{ij}^{(q)}$ denotes the link weight of neuron i in layer q and neuron j in layer q- and $\theta_i^{(q)}$ is the threshold of neuron i in layer q. Gauss function is chosen $f(x) = 1/(1 + e^{-x})$.

4. The fourth layer: The output is the membership value of each class; the input of neuron i is $I_i^{(4)} = \sum_{j=1}^{M} w_{ij}^{(4)} O_j^{(3)} - \theta_i^{(4)}$ and the output is $O_i^{(4)} = f\left(net_i^{(4)}\right)$.

5. The fifth layer: This layer contains only one node whose output represents the result of centroid defuzzification.

$$O^5 = \frac{\sum_{j=1}^{J} O_j^4 . c_j}{\sum_{j=1}^{J} O_j^4} \tag{11}$$

where c_j is a parameter that can be tuned to improve the performance of the system. Figure 5 shows a fuzzy neural identification system with a general structure. The system was constructed based on the Sugeno-Takasi, in which the controller parameters are the network training algorithm. In the back-propagation learning algorithm, the error index should be defined first, in which the global error is

Fig. 6 Block diagram
of parameter identification
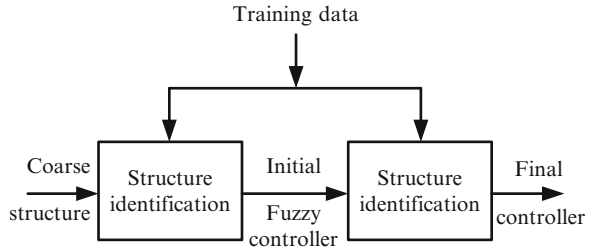
$$E = \frac{1}{2} \sum_{k=1}^{R} \sum_{i=1}^{N} (d_{ki} - y_{ki})^2 \tag{12}$$

where R denotes the number of training samples, d_{ki} represents the expected output of neuron i when using sample k to train the network, and y_{ki} refers to its practical output. Parameters that must be updated include weights $w_{ij}^{(3)}$ and $w_{ij}^{(4)}$ in layers 3 and 4. Adjust measures and modified formulate of this two layers are as follows:

$$\Delta w_{ij}^{(q)}(t) = \eta \left(-\frac{\partial E_k}{\partial w_{ij}^{(q)}(t)} \right) + \alpha \Delta w_{ij}^{(q)}(t-1) \tag{13}$$

$$\Delta w_{ij}^{(q)}(t+1) = w_{ij}^{(q)}(t) + \Delta w_{ij}^{(q)}(t) \tag{14}$$

where η denotes the learning speed and α represents the momentum modulus. The neural fuzzy learning scheme consists mainly of two steps. In the first step, the number of rules nodes and initial rule parameters are determined using structure identification [9, 10]; in the latter, all parameters are adjusted using parameter identification as shown in Fig. 6. This work adopts the hybrid learning algorithm, with details provided by Jang [11]. In parameter identification, the initial fuzzy rules are adjusted using the neural network techniques.

4 Simulation Results

The FNN controller is designed in the following steps:

1. Draw the Simulink model with FLC and simulate it with the given rule base.
2. Design the FNN controller by collecting the training data while simulating on Simulink model with FLC. Here, the training data is generated from the first FLC (with 25 rules and five membership functions for input e(t) and error rate de(t)). The number of data points generated is 525, in which Simulink is used to create the FNN model.
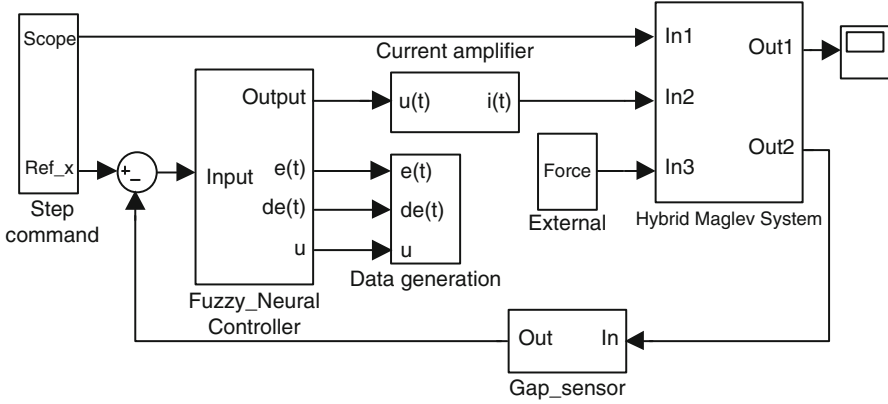
Fig. 7 Matlab-Simulink model for fuzzy and FNN controller
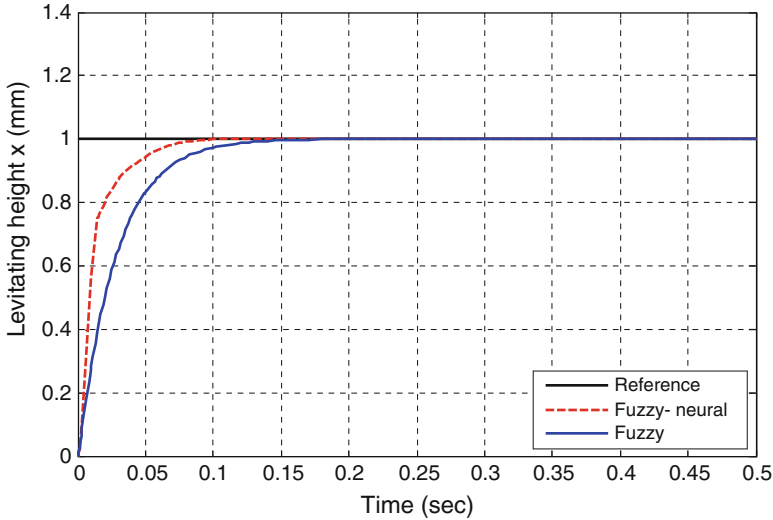
Fig. 8 Comparison of step response fuzzy and FNN controller

3. Load the training data collected in step 1 and generate a fuzzy inference system with Gauss membership functions. To validate the above-mentioned control strategies, Fig. 7 shows the complete Simulink block for the complete system, including the control design and the plant. Figures 8, 9 and 10 summarize the simulation results for step inputs as described in the following.
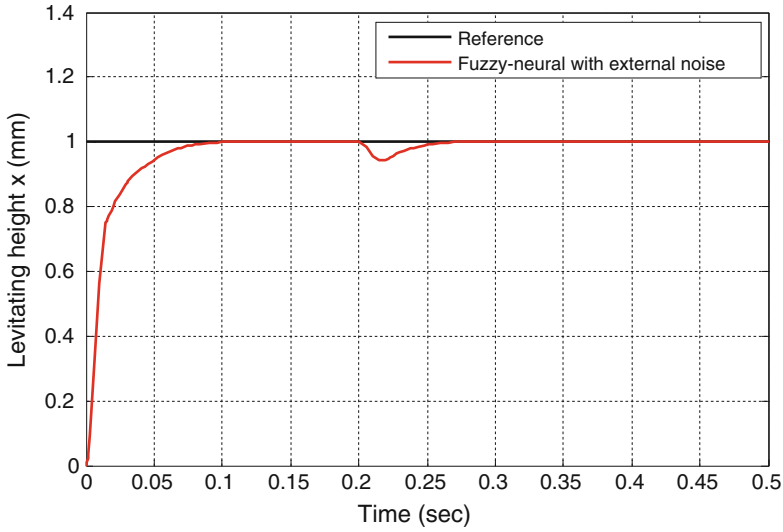
Fig. 9 Step response of system with external disturbance
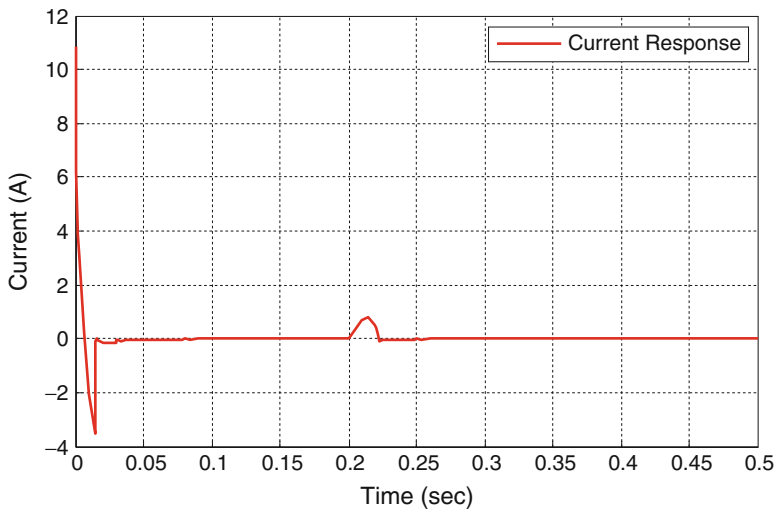
Fig. 10 Current response in system

Figure 8 depicts the performance of the proposed control design for reference input, indicating that the response is still slow when the FLC is applied to the Maglev system. However, when the FNN controller is integrated into the Maglev system, the response is significantly rapid. The system response to the step reference input is compared with that of the FLC and FNN controller. That comparison reveals that the FNN controller achieves a better response than the FLC.

Our results further demonstrate that a faster rise time implies a faster settling time, lower overshoot, and without steady-state error with external disturbance. Figures 9 and 10 indicate that the current response in the system is stable and balance at zero current point, as shown in the above Figs. 9 and 10. Consequently, the FNN control algorithms are highly effective for the position control of a magnetic levitation system.

5 Conclusions

This work describes a novel of position control scheme based on the Maglev system by using the emerging approaches of FNN. The proposed method can also improve the control performance of nonlinear systems. Simulation results indicate that the controller has a good response to a reference signal. Importantly, the proposed controller is better than the FLC in terms of transient performance and disturbance rejection. The proposed control method is also effective for both the Maglev system and other nonlinear systems.

References

1. Nakashima H (1994) The superconducting magnet for the maglev transport system. IEEE Trans Magn 30:1572–1578
2. Lin CT, Jou CP (2000) GA-base fuzzy reinforcement learning for control of a magnetic bearing system. IEEE Trans Syst Man Cybern B 30:276–289
3. Oshima M (2010) Decoupling method of radial forces in a dual rotor-type magnetic suspension motor. IEEE IPEC, pp 2197–2203
4. Dias JM, Dourado A (1999) A self-organizing fuzzy controller with a fixed maximum number of rules and an adaptive similarity factor. Fuzzy Set Syst 103:27–48
5. Nurnberger A, Nauck D, Kruse R (1999) Neuro-fuzzy control based on the nefcon-model: recent developments. Soft Comput 2:168–182
6. Chen SC, Tung PC (2000) Application of a rule self-regulating fuzzy controller for robotic deburring on unknown contours. Fuzzy Set Syst 110:341–350
7. Ordonez R, Passino KM (1999) Stable multi-input multi- output adaptive fuzzy/neural control. IEEE Trans Fuzzy Syst 7:345–353
8. Chen SC, Nguyen VS, Chang G (2012) Application of self-tuning fuzzy PID controller on magnetic levitation system. In: 2012 the 11th Taiwan power electronics conference & exhibition, National TsingHua University, Hsinchu, 2012
9. Chiu SL (1994) Fuzzy model identification based on cluster estimation. J Int Fuzzy Syst 2:267–278

10. Chopra S, Mitra R, Kumar V (2005) Identification of self-tuning fuzzy PI type controllers with reduced rule set. In: Proceedings of the IEEE international conference on networking, Sensing and Control, Arizona, 2005, pp. 537–542
11. Jang JS (1993) ANFIS: adaptive network based fuzzy inference system. IEEE Trans Syst Man Cybern 23:668–685

CMOS Transimpedance Amplifiers for Optical Wireless Communications

Roger Yubtzuan Chen and Zong-Yi Yang

Abstract CMOS transimpedance amplifiers (TIAs) suitable for optical wireless communications are presented. The shunt-feedback TIAs are designed using a feedforward current amplifier (CA). In the presence of a large input photodiode capacitance, the CA-based TIA posses a wide dynamic range with a relatively constant bandwidth. The optical wireless preamplifiers are validated by both simulation and measurement.

Keywords CMOS • Feedback amplifier • Optical wireless communications • Optical receiver • Transimpedance amplifiers • TIA

1 Introduction

Transimpedance amplifiers (TIAs) are adopted in optical receivers to sense the input current generated by the photodiode and generate an amplified output voltage. The commonly used TIA configuration is to apply a shunt-shunt feedback to close the loop around a voltage amplifier to allow absorbing the photodiode current and yielding better drive capability [1–8]. Because the impact of the usually non-negligible and even dominant photodiode capacitance, e.g., in optical transmissions with a large diameter photodiode to relax alignment requirement or optical wireless involving eye-safety regulations, can be suppressed by the lower input impedance, implementing a feedback TIA using a feedforward current amplifier (CA) is an attractive alternative [9].

In this chapter a CMOS feedback transimpedance amplifier consisting of a feedforward current amplifier (CA-TIA) is studied. In addition to low cost, CMOS

R.Y. Chen (✉) • Z.-Y. Yang
Department of Electronics Engineering, National Yunlin University of Science
and Technology, Doulio, Yunlin 64002, Taiwan
e-mail: chenry@yuntech.edu.tw

facilitates integration with back-end systems. The CA-TIAs are designed using a low-cost 0.35 μm CMOS and adopted in an optical receiver capable of rejecting low-frequency ambient noise in Sect. 2. Post-layout simulations are shown in Sect. 3. In Sect. 4 the experimental verification of the optical receiver front end are presented.

2 Circuit Description

The block diagram of the CA-based TIA is shown in Fig. 1. The photodiode is represented by a current source in parallel with its junction capacitance. A schematic diagram of the feedforward current amplifier is given in Fig. 2. A regulated cascade (RGC) [10] is added to increase the equivalent transconductance of the
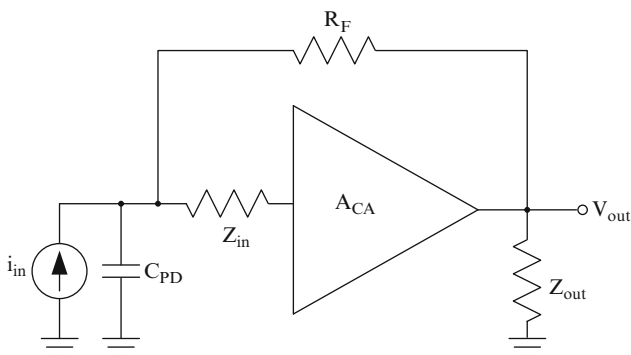
Fig. 1 Block diagram of a CA-TIA
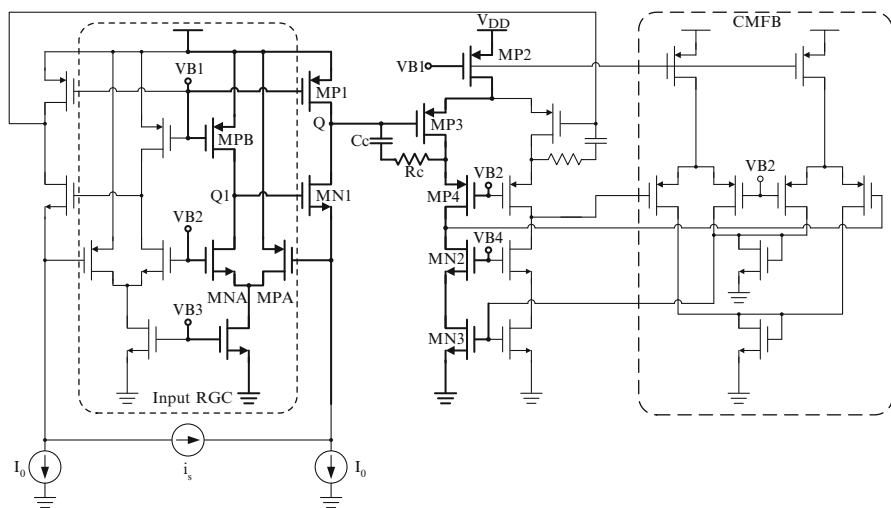
Fig. 2 Schematic diagram of a current amplifier
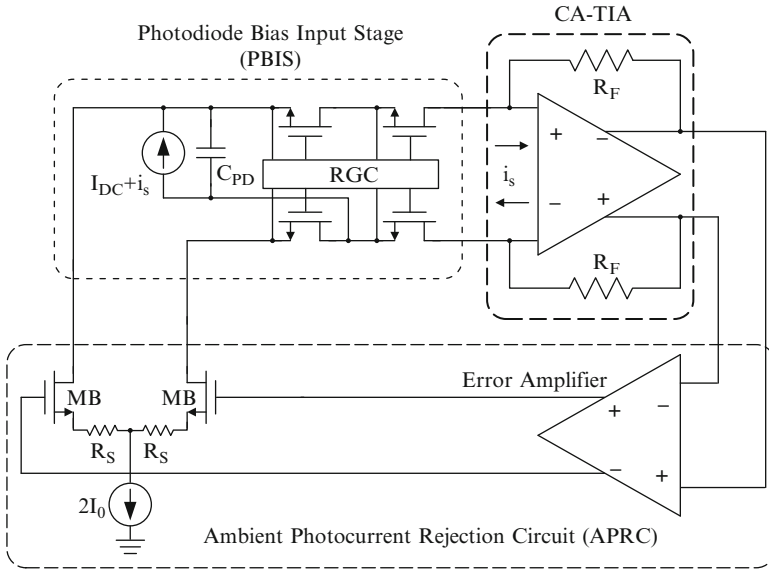
Fig. 3 The CA-TIA is employed to implement an optical preamplifier with ambient photocurrent rejection

input common-gate transistor MN1 and thus reduce the input impedance of the current amplifier. Hence, the effect of its input capacitance is suppressed and by contrast is less significant. In order to lower the minimum voltage level at the input node of the CA, i.e., to free the minimum input node voltage from the constraint imposed by the gain boosting transistor, a folded-cascode stage using an input PMOS transistor MPA is adopted [11], instead of a common-source NMOS transistor. In Fig. 2 a compensation network of $C_C - R_C$ is also added.

In the optical wireless receivers, an ambient photocurrent rejection circuit (APRC), as well as a photodiode bias input stage (PBIS), is applied to close the loop around the CA-TIA, as shown in Fig. 3 [5]. Note that the APRC, consisting of an error amplifier and a differential-pair transconductance amplifier, serves as a voltage–current feedback network of the optical preamplifier to direct the low-frequency ambient perturbation and bias current of the photodiode away from the TIA. The error amplifier is configured to have a bandwidth much smaller than that of the TIA. The ambient rejection loop introduces a zero at the cutoff frequency of the error amplifier and a pole frequency higher by the amount of the loop gain, and the transfer function of the optical preamplifier is described as

$$A_{\text{OPA}}(s) \approx \frac{(s + \omega_{z_{\text{OPA}}})A_{\text{TIA}}(s)}{(s + \omega_{p_{\text{OPA}}})} \tag{1}$$
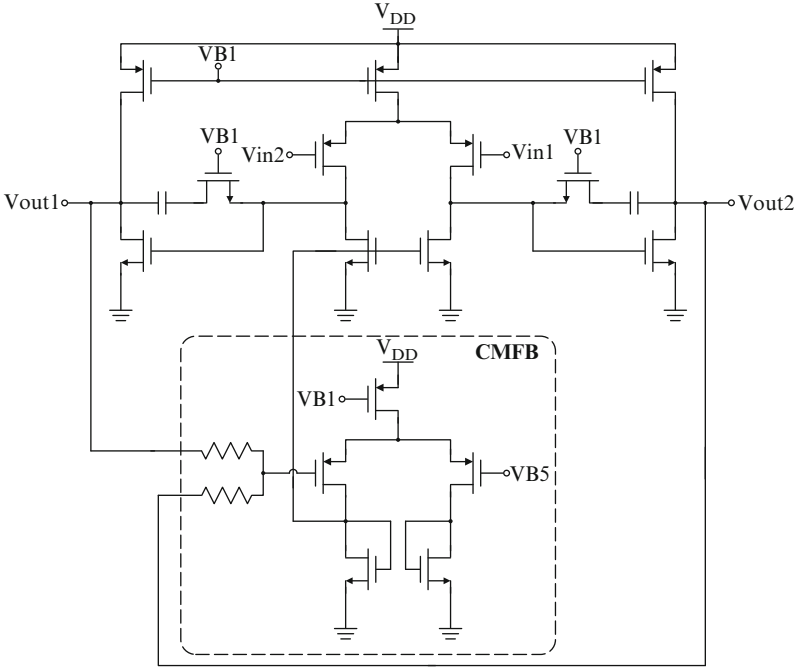
Fig. 4 Circuit diagram of the error amplifier

where $\omega_{p_{OPA}} \approx \omega_{p_{EA}} \times g_{m_{MB}} A_{EA0} R_F$ and $\omega_{z_{OPA}} = \omega_{p_{EA}}$, respectively. A_{EA0} and $\omega_{p_{EA}}$, respectively, denote the low-frequency gain and cutoff frequency of the error amplifier, and $g_{m_{MB}}$ is the equivalent transconductance of the differential pair of the APRC. Since $\omega_{z_{OPA}} < \omega_{p_{OPA}} < \omega_{3\,dB_{TIA}}$, the optical receiver front end acts as a band-pass filter to attenuate the low-frequency ambient photocurrents and degenerates into $A_{TIA}(s)$ at frequencies greater than the pole and zero. For our purpose, the bandwidths of the CA-TIA can be deduced from the upper cutoff frequency of the implemented optical preamplifier. The schematic diagram of the adopted error amplifier is shown in Fig. 4.

3 Simulation Verification

The optical receiver front end including the CA-TIA, shown in Fig. 3, is designed using a 0.35 μm CMOS. Due to the adoption of the fully differential CA-TIA and differential photocurrent-sensing APRC, the transimpedance gain at mid-band is $2R_F$. The frequency responses of the optical receiver front end are given in Fig. 5.
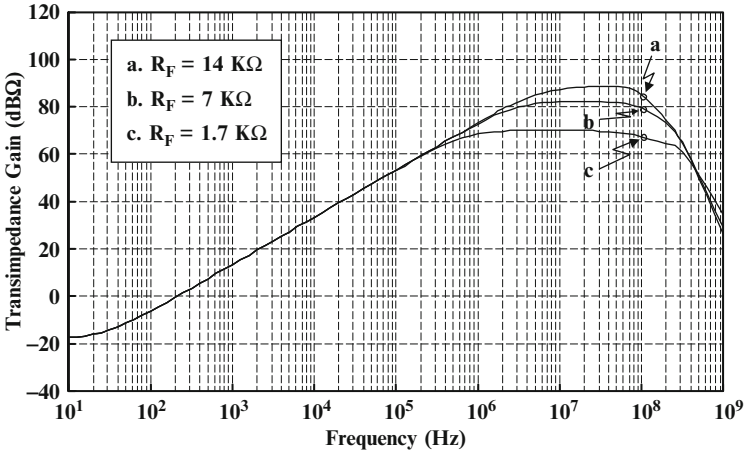
Fig. 5 Frequency responses of our CA-TIAs according to the post-layout simulation
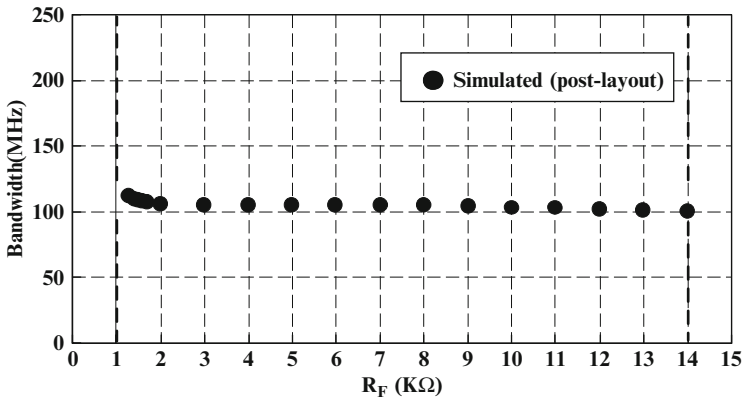
Fig. 6 Simulated bandwidths of the CA-TIA

As a function of R_F, the simulated bandwidths of CA-TIA in the variable-gain mode, i.e., 1.7 k$\Omega \leq R_F \leq$ 14 kΩ, are shown in Fig. 6. The variable-gain CA-TIA attains a constant bandwidth of roughly 104 MHz as its gain is varied from 70 to 88.2 dBΩ. A pair of source degeneration resistors R_S is added to the differential-pair transconductor as shown in Fig. 3 to reduce the input-referred thermal noise current of the CA.

4 Measurement Results

One microphotograph of the optical preamplifier is given in Fig. 7. The active area of the CA-TIA and optical preamplifier, respectively, is 170 μm × 175 μm and 475 μm × 345 μm. To emulate the signal current generated from the photodiode, a medium-sized NMOS transistor is implemented at the input of the optical preamplifier to serve as the input current source. An on-chip capacitor of 5 pF is laid out and then connected across the MOS transistor to act as the photodiode parasitic capacitance. All measurements are directly carried out on the prototypes wafer using on-wafer probes. The measured power consumptions of the CA-TIAs are equal to 8.75 mW. The optical preamplifiers dissipate roughly 15.85 mW of power.

Measured output noise spectra of the CMOS optical preamplifiers are presented in Fig. 8. The corresponding optical sensitivities, as a function of bit error rate (BER), are given in Fig. 9 assuming a typical, widely used photodiode PDCS75T with a responsivity of 0.9 A/W is utilized.

Figure 10 shows the measured output eye diagram (Agilent 54855A) of the optical preamplifier adopting the CA-TIA when a pseudorandom binary sequence (PRBS) with a bit rate of 100 Mb/s and test patterns up to $2^{15} - 1$, the longest available on the employed pulse/pattern generator (Agilent 81130A), are applied at its input.
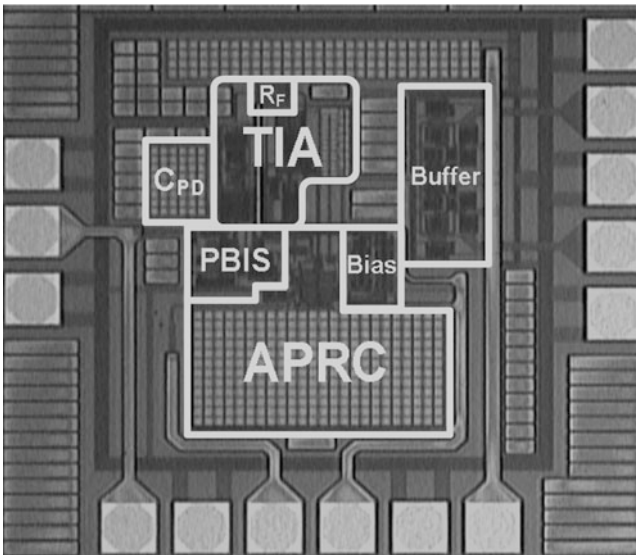
Fig. 7 Microphotograph of the optical preamplifier
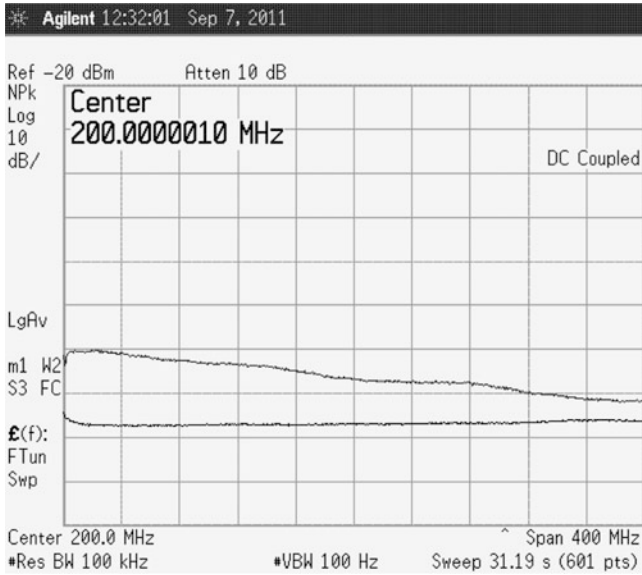
Fig. 8 Measured output noises of the optical preamplifier employing the variable-gain CA-TIA ($R_F = 7$ kΩ)
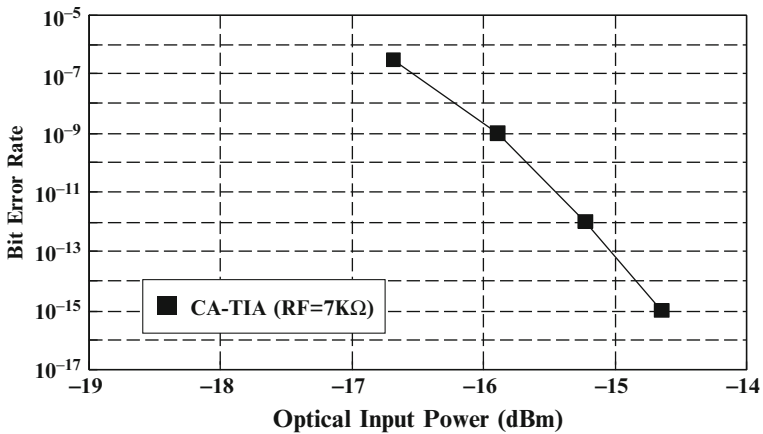
Fig. 9 For the optical receiver front ends utilizing the CA-TIAs, BER as a function of the average optical input power at a data rate of 100 Mb/s
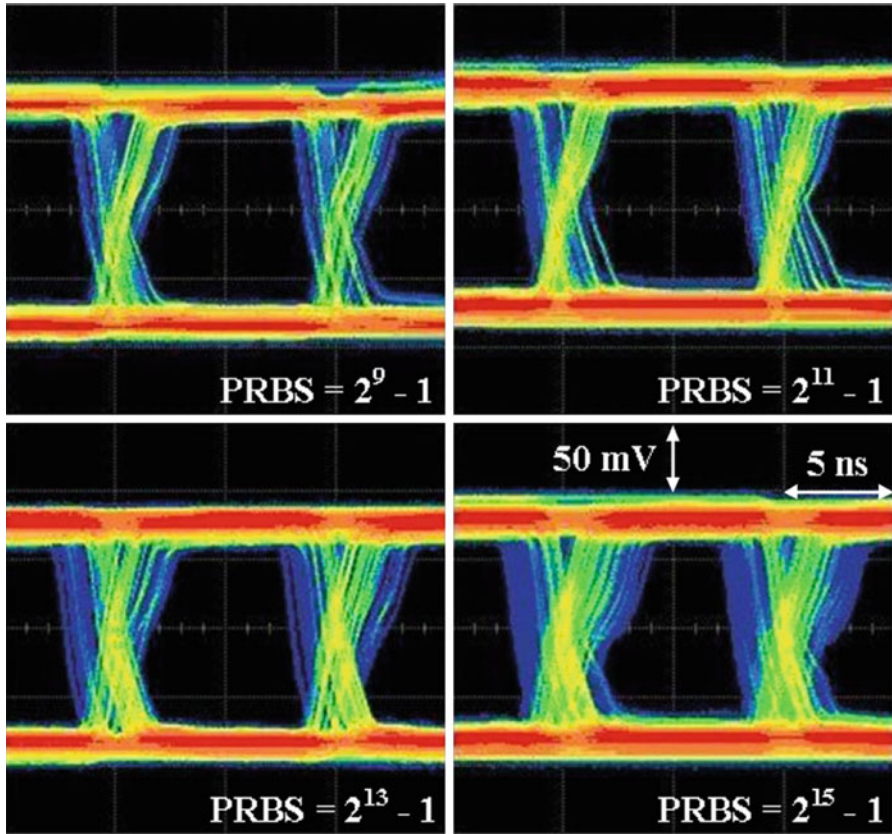
Fig. 10 Measured output eye diagram under an input PRBS with a bit rate of 100Mb/s

5 Conclusions

Transimpedance amplifiers and receiver front end are presented in 0.35 um CMOS. Both SPICE simulation and experimental characterizations, in terms of noise spectrum and eye diagram, are given. The presented CA-TIAs are suitable for optical wireless communications.

References

1. Sturn J, Leifhelm M, Schatzmayr H, Groiss S, Zimmermann H (2005) Optical receiver IC for CD/DVD/blue-laser application. IEEE J Solid State Circ 40(7):1406–1413
2. Hermans C, Steyaert M (2006) A high-speed 850-nm optical receiver front-end in 0.18-um CMOS. IEEE J Solid State Circ 41(7):1606–1614
3. Lu Z, Yeo KS, Ma JG, Do MA, Lim WM, Chen X (2007) Broadband design techniques for transimpedance amplifiers. IEEE Trans Circ Syst I 54(3):590–600
4. Chen W-Z, Gan R-M, Huang S-H (2009) A single-chip 2.5-Gb/s CMOS burst-mode optical receiver. IEEE Trans Circ Syst I 56(10):2325–2331
5. Phang K, Johns DA (1999) A CMOS optical preamplifier for wireless infrared communication. IEEE Trans Circ Syst II 46:852–859
6. Basu A, Robucci RW, Hasler PE (2007) A low-power, compact, adaptive logarithmic transimpedance amplifier operating over seven decades of current. IEEE Trans Circ Syst I 54(10):2167–2177
7. De Ridder T, Ossieur P, Yin X, Baekelandt B, Melange C, Bauwelinck J, Qiu XZ, Vandewege J (2008) BiCMOS variable gain transimpedance amplifier for automotive applications. Electron Lett 44(4):287–288
8. Wangtaphan S, Suadet A, Meksiri S, Kasemsuwan V (2008) A 1.0 volt thermal noise-canceling CMOS transimpedance-based amplifier. In: IEEE Asia Pacific conference on circuits and systems, Macao, Dec 2008, pp 692–695
9. Wilson B, Drew JD (1998) High-performance transimpedance formulation for MESFET- and HBT-based monolithic microwave integrated circuits. IEE Proc Circ Devices Syst 145 (6):429–436
10. Park SM, Yoo HJ (2004) 1.25-Gb/s regulated cascade CMOS transimpedance amplifier for gigabit Ethernet applications. IEEE J Solid State Circ 39(1):112–121
11. Chen RY, Hung CY, Hung TS (2004) A CMOS infrared optical preamplifier with a variable-gain transimpedance amplifier. In: IEEE Asia Pacific conference on circuits and systems, Tainan, Dec 2004, pp 265–268

Dependable Embedded Memory
for Intelligent Systems

Yen-Chieh Huang and Tsung-Chu Huang

Abstract Contiguity along Gray codes and neighborhood among cluster faults are naturally connected by a novel hypercube-based address remapping unit. A novel memory repair architecture based on redundant hypercube is proposed, which mainly consists of a modified ternary CAM with an address concentrator. A modified ESPRESSO tool is developed for redundancy analysis on clustered-fault repairing optimization. Based on the redundancy analysis for a two-dimensional Gray-code-ordered memory array, every clustered fault with a width of no more than w and a length of no more than l can be repaired by a single hypercube-based spare row with a degree of $\left(\lceil \log 2(w-1) \rceil + 1\right)\left(\lceil \log 2(l-1) \rceil + 1\right)$. Finally 100 % of repair rate can be obtained using only a few equivalent rows.

Keywords Memory repairing • Redundancy analysis • Remapping architecture • Hypercube • Cluster faults • Fault tolerant

1 Introduction

According to the International Technology Roadmap for Semiconductors (ITRS) in 2007, the relative silicon area occupied by embedded memories will approach 94 % by 2014. Although recent prediction of the ITRS on embedded memory has been a little adjusted, the percentages of embedded memory transistors will still take more

Y.-C. Huang (✉) • T.-C. Huang
Graduate Institute of Integrated Circuit Design, National Changhua University
of Education, Changhua, Taiwan
e-mail: endlessaquarius@gmail.com

than 87 and 80 % in a consumer chip and an MPU, respectively [1]. Owing to the crucial variation and increasing density in the nanotechnology revolution, the urgent desire for yield promotion has made the test and repairing an inevitable challenge for memory [2].

The authors in [3] and [4] have an elaborated survey on conventional memory repairing architectures, which are based on spare rows and/or columns [5–7]. They are quite straightforward since the spare rows and/or columns can be implemented adjacent to the main memory blocks to share bitlines (BLs) and/or wordlines (WLs), respectively, in a compact layout style. However, full spare rows and columns are obviously no longer efficient for repairing clustered faulty cells and scattered faulty cells due to address faults [6] and clustered faults [7]. Therefore, some infrastructures for remapping are proposed to split into shorter segments [7] and/or spare blocks [8, 9]. Especially the authors in [7] propose an approach to improve the repair rate by dividing the row/column blocks, and in the patent [9] the inventors propose the remapping technique via variable blocks. Both have considered clustered faults, but performance impact due to inserted gates and low efficiency are still the major issues, so that clustered faults have obviously become the major challenge of memory repairing.

The rest of this chapter is organized as follows. After definitions and basic concepts are clarified in Sect. 2, the proposed hypercube-based remapping architecture is introduced in Sect. 3. In Sect. 4 a modified Quine-McCluskey algorithm (MQMA) is proposed to optimize the repairing efficiency for 2D Gray-code-ordered memory arrays. Finally the conclusions are drawn in Sect. 5.

2 Definitions and Basic Concept

In this chapter a cell address A is defined by $2n$ binary bits, while an n-subcube Q_{2n}^n is represented by a ternary-valued address $Q = (Q_{2n-1}Q_{2n-2}\ldots Q_nQ_{n-1}\cdot Q_1Q_0)$ with n bits of "−" where all $Q_i \in \{0, 1, -\}$ and the dash "−" means the union of "0" and "1" instead of "X" usually a don't-care bit. The ternary-valued address Q can be also represented by a pair of binary numbers (A, K). The mask bits K_i ($i = 0 \ldots 2n - 1$) will mask the associated bits of base point A. The basic concept of this work is that the mask bits are employed as don't-care bits while matching and the matched address bits associated to the mask bits ($K_i = 1$) will be shifted and gathered together as the column address of the spare rows. Finally any one of the s spare physical rows can serve not only as a row and a column but also as an n-subcube (Fig. 1).

For example, when a faulty cell address (10110101) is accessed in a 4 × 4 memory and a spare cube (1- -101- -) is assigned to repair it, the address bits at the mask positions are shifted to a column address (0101) = 5. The 5th bit in the associated spare cube can then be used to replace the faulty cell.
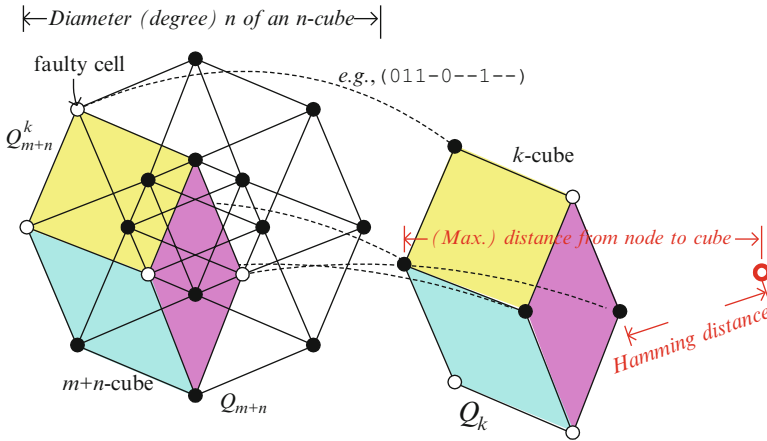
Fig. 1 Conceptual diagram of hypercube-based node repairing

3 Hypercube-Based Remapping Architecture

3.1 Block Diagram of Remapping Architecture

For explanation and comparison a conventional remapping architecture for a two-dimensional (2D) memory array, typically two binary content-addressable memories (BCAMs), are employed to check the column/row address inputs and to map to associated spare columns/rows, respectively, while the associated address is matched [5]. A row-major or column-major priority selector controlled by two row/column hit bits is employed to select the original cell or spare cell along the spare rows/columns.

Figure 2 shows the proposed remapping architecture. Compared with traditional architecture, except the masked address-bit concentrator (address concentrator) and the spare column address decoder, the other blocks look quite similar to conventional remapping architectures. However, the ternary content-addressable memory (TCAM) is designed to be able to pass out the matched mask pattern with the searching address for gathering the masked address bits by a bubble shifter-like address concentrator as the column address to the spare column address decoder. A priority encoder is embedded and hidden in the TCAM. When the address is matched, the Hit signal will be 1 and the data in the spare n-cube memory is selected to access.

3.2 Proposed TCAM for HYPERA

The TCAM can be designed in transistor level for compact layout or gate level using CMOS comparators with a register file (RF) for high speed. A mask-type TCAM can be modified for passing out required masked address bits. Typically
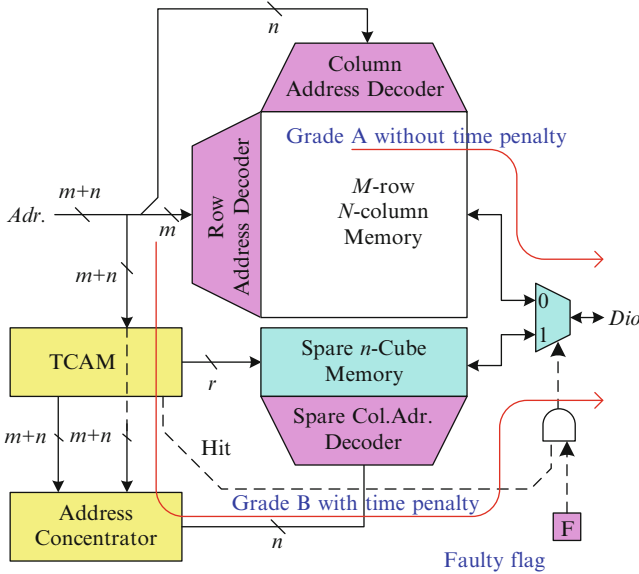
Fig. 2 Proposed hypercube-based remapping architecture

the jth address bit of the ith word, A_{ij}, is stored in the upper storage cell by bitlines in address write mode and the mask bit, K_{ij}, the lower storage by sharing the same bitlines in mask write mode. Both can be read in address/mask read mode. In the matching mode, the mask wordline MWL can be also selected by the output of the priority encoder following the TCAM so that the associated mask bit K_{ij} can be passed out along the pair of mask-bitlines KL.

3.3 Proposed Sorting Network as Concentrator

In communications an n-to-m channel concentrator where $1 \leq m < n$ means an $n \times n$ switch that receives n signal values from an arbitrary ordered set and routes the largest m of them to the output group [13]. In our architecture we require the masked address bits to be the column address to take its bijective property, and thus the device is called the masked address-bit concentrator and address concentrator in brief.

Intuitionally the address concentrator can be implemented by a binary-valued sorting network [13]. Typically a sorting network is composed of swappers. For a multiple-valued sorting network, the swapper is usually implemented by a 2×2 switch controlled by a magnitude comparator. However, for a binary-valued sorting network, the swapper can be designed by very few logic gates. Figure 3a shows the symbol of a descending swapper for comparing the jth and the $j + 1$ pairs of bits (A_j, K_j) and (A_{j+1}, K_{j+1}) where bits A denote the address bits and bits K the key bits. Both pairs will be exchanged only when $K_j < K_{j+1}$. Figure 3b shows its implementation in gate level.
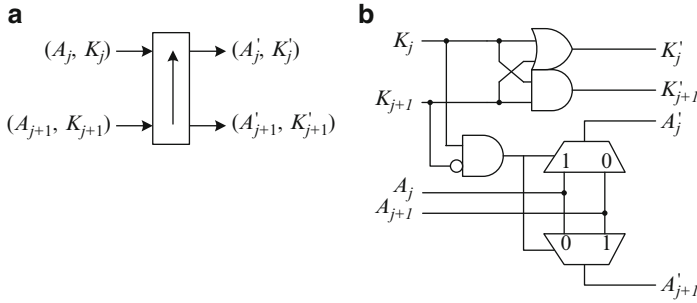
Fig. 3 A symbol of the descending swapper with a mask-bit K as the key

4 Hypercube-Based Redundancy Analysis

In our preliminary HYPERA in [10], a MQMA is proposed for optimizing the repair rate using an external system or embedded processors.

4.1 Modified Quine-McCluskey Algorithm (MQMA)

In the standard Quine-McCluskey Algorithm (QMA), a list of minterms with don't-cares are sorted by weights and then merged into implicants with incremented degrees. Finally the prime implicants are selected in a prime implicants chart according to an essential tabular procedure (ETP) [14]. For the proposed remapping architecture, it is also a covering problem. Of course we can map all good cell addresses into don't-cared minterms and then solve it using the QMA except the merged degrees need not be greater than that of the spare cubes, say n. However, this will arouse a dramatically huge numbers of subcubes to execute the ETP. Obviously an easy but exhaustive method to modify the QMA for our problem is as follows:

1. Let the maximum degree of spare subcubes be n. Initialize all faulty cell addresses as subcubes of degree $d_1 = 0$.
2. Sort all subcubes of degree d_1 by weight.
3. Select any pair of subcubes q_1 of degree d_1 and q_2 of degree $d_2 < d_1$ if $d_1 + d_2$; merge them into a subcubes q of degree d if $d_2 < n$.
4. Increment d_1 by 1 if $d_1 < n$ then go to step 2.
5. Execute the ETP for all subcubes over all minterms.

Example 1 Given clustered faults A and B in an 8×8 Gray-code-ordered array in Fig. 4, only two spare cubes $S_0 = $ 0-10- -, and $S_1 = $ 1-1- - - are required for repairing in proposed HYPERA.

Fig. 4 An example for
illustrating modified QMA
for HYPERA
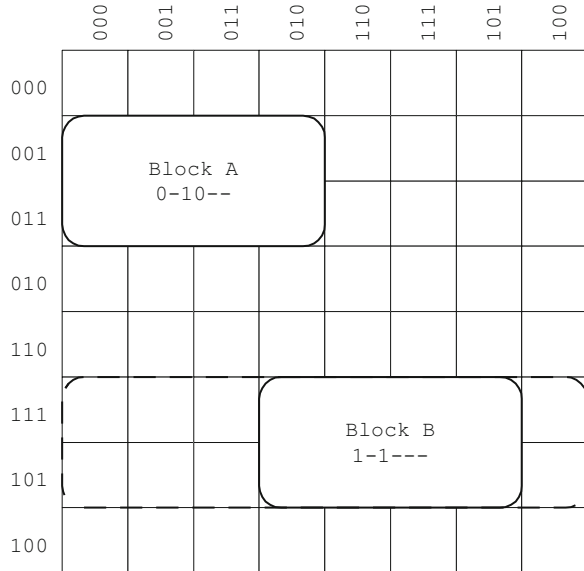
5 Conclusions

In this chapter a novel infrastructure for memory repairing is proposed. For the
hypercube-based remapping architecture, the redundancy analysis with an external
repairing algorithm is developed. According to the intrinsic property of a clustered
fault along the Gray-code-ordered memory array, the clustered faults and even all
row-/column-based line faults as well as some address scatter faults can be easily
covered by a hypercube-based spare row.

The repairing ability of a hypercube-based spare row is evaluated by external
repairing algorithms so far. Developing an efficient algorithm for built-in self-
repair will be our future work.

References

1. Allan A et al (2009) Test and test equipment. In: 2009 technology roadmap for
   semiconductors, p 29, TST-6, 2009
2. Zorian Y, Shoukourian S (2003) Embedded-memory test and repair: infrastructure IP for SoC
   yield. IEEE De Test Comput 20(3):58–66
3. Huang C-T, Wu C-F, Li J-F, Wu C-W (2003) Built-in redundancy analysis for memory yield
   improvement. IEEE Trans Reliab 52(4):386–399
4. Wang L-T, Wu C-W, Wen X (2006) VLSI test principles and architectures. Elsevier, New
   York. ISBN 10:0-12-370597-5

5. Kawagoe T, Ohtani J, Niiro M. Ooishi T, Hamada M, Hidaka H (2000) A built-in self-repair analyzer (CRESTA) for embedded DRAMs. In: Proceedings of the IEEE international test conference, Atlantic City, Oct 2000, pp 567–574
6. Hamdioui S, van de Goor AJ (2002) Efficient tests for realistic faults in dual-port SRAMs. IEEE Trans Comput 51(5):460–473
7. Lu S-K, Yang C-L, Hsiao Y-C, Wu C-W (2010) Efficient BISR techniques for embedded memories considering cluster faults. IEEE Trans VLSI 17(2):174–193
8. Shen YN, Park N, Lombardi F (1996) Spare cutting approaches for repairing memories.In: Proceedings of the IEEE international conference on computer design: VLSI in computers and processors, Austin, Oct 1996, pp 106–111
9. Lee M, Wu CW (2009) Method for repairing memory and system thereof.ROC Patent No. 200921690, disclosed on 16 May, 2009
10. Huang TC, Lu KY, Huang YC (2010) HYPERA: high-yield performance-efficient redundancy analysis. In: Proceedings of the IEEE 19th Asian test symposium, Shanghai, 1–4 Dec 2010, pp 231–235
11. Batcher KE (1968) Sorting networks and their applications. In: Proceedings of the AFIPS spring joint computer conference, Atlantic City, 1968, vol 32, pp 307–314
12. McCluskey EJ (1956) Minimization of Boolean functions. J Bell Syst Tech 35(5):1417–1444

Research and Development of Versatile Autonomous Vehicles for Education

Chien-Yuan Liu, Chih-Feng Huang, and Yann-Chang Huang

Abstract Autonomous vehicles are recently a popular research and development domain in academy and industry. In this research, Arduino was adopted as the system control unit for an autonomous vehicle. Infrared sensors, motors, and all required IO components were installed to form an electromechanical assembly of the vehicle. The versatile vehicle has three functionalities or operating modes, named tracking, obstacle avoiding, and remote operating. The verification results of the vehicle apparently showed that all kinds of operations conformed to the basic design. Furthermore, the expenses are obviously lower than marketing robotic vehicles.

1 Introduction

Microprocessor-based embedded systems have tremendous advancement in recent years. Thus, the applications of embedded systems are continuously extending in daily life from set-top boxes (STB), smart phones, and smart home controllers to interactive amusing devices. The trend shows the importance to learn embedded systems with more interesting motivation and better learning performance [1].

To accelerate the design speed and to decrease the learning barrier, an open source platform, named Arduino [2], was created in the past few years. Due to its quick evolvement, faster hardware and powerful software are swiftly created and

---

C.-Y. Liu (✉) • C.-F. Huang
Department of Computer Science and Information Engineering,
Cheng Shiu University, Kaohsiung 83347, Taiwan
e-mail: cyliu@csu.edu.tw

Y.-C. Huang
Department of Electrical Engineering, Cheng Shiu University, Kaohsiung 83347, Taiwan

added into the product portfolio. Therefore, it becomes a very popular embedded system for the project of intelligent and interactive applications.

Autonomous vehicles need high degree of the integration of software and hardware, containing a high-level language program for vehicle control, a microprocessor, motors, driver IC, power transistors, LED indicators, certain sensors, etc. The learners have to mount all components and to solder them into a workable circuit for a vehicle. Thus, it has been obviously that many robotic vehicles were produced for education [3–5].

2   Background Reviews

Piperidis et al. [4] designed a low cost, modular robotic vehicle for education. The feature of the robotic vehicle is modular construction compared to off-shelf commercial vehicles. However, the embedded system is a dedicated hardware and is not popular enough like some open source platforms. Stollenwerk [5] utilized open source Arduino as the developing platform. The implementation is successful in obstacle avoidance. However, it lacks of a wireless remote control capability. To enhance the functionality, wireless technology had been combined into smart embedded systems. Faludi [6] demonstrated how to integrate the applications with wireless sensor networks (WSN) and Arduino embedded systems.

3   Technology and Theorem

3.1   ZigBee

ZigBee is a technology pertained to the wireless personal area networks (WPAN) and WSN. The protocol stack of ZigBee was shown in Fig. 1. Low power consumption, short range, and low data rate are the advantages of ZigBee technology. In addition, even with low cost, it provides reliable wireless communication, flexible network topology, and secured data transmission. In ZigBee, there is exactly one coordinator, yet with many routers and end devices. Figure 2 showed different topologies auto-formed by ZigBee. Up to 65,536 nodes are allowed to flexibly compose one ZigBee network.

In the remote control of autonomous vehicles, one-hop communication is the basic requirement. Under this requirement, several wireless technologies can be adopted for the remote control, e.g., ZigBee, Bluetooth, Wi-Fi, or typical RF. However, when multi-hops are required to extend the moving range, ZigBee would become the best choice. Therefore, ZigBee was selected as the wireless connections for this development.
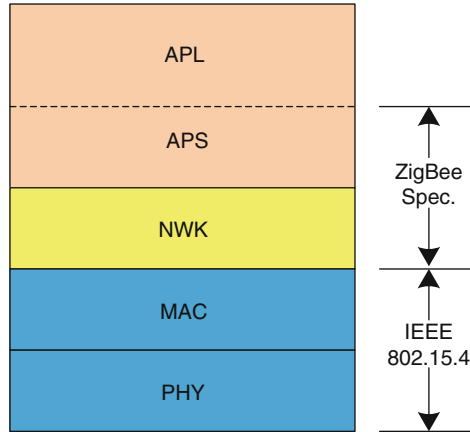
Fig. 1 ZigBee protocol stack
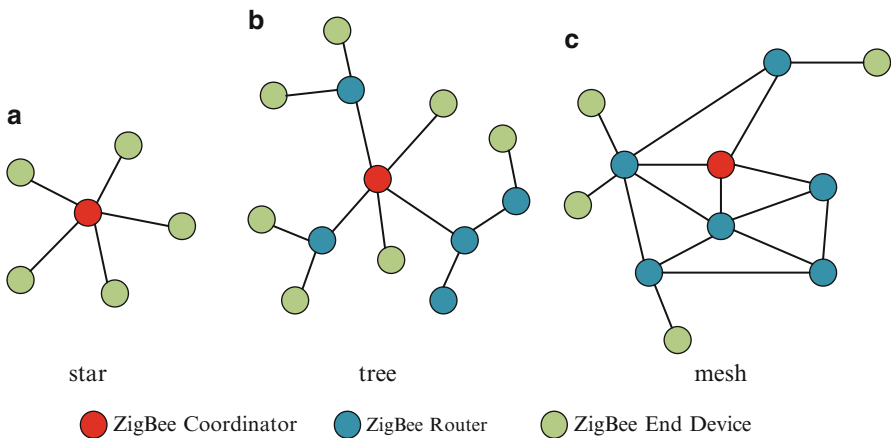
Fig. 2 ZigBee topologies

4 Arduino

Due to several advantages of Arduino platform, e.g., open-source software and hardware, inexpensive, cross operating system, and simple integrated develop environment (IDE), it has become one of the most popular electronic prototyping platforms in the world. Its IDE provides developers an efficient environment to code C-like firmware and to upload the firmware to a target board mounted with a microprocessor. The grade of microprocessor can range from an 8-bit microprocessor to a 32-bit multi-kernel CPU. Hardware vendors decide the computation power and IO capability of their compatible target boards. The compatibility means the
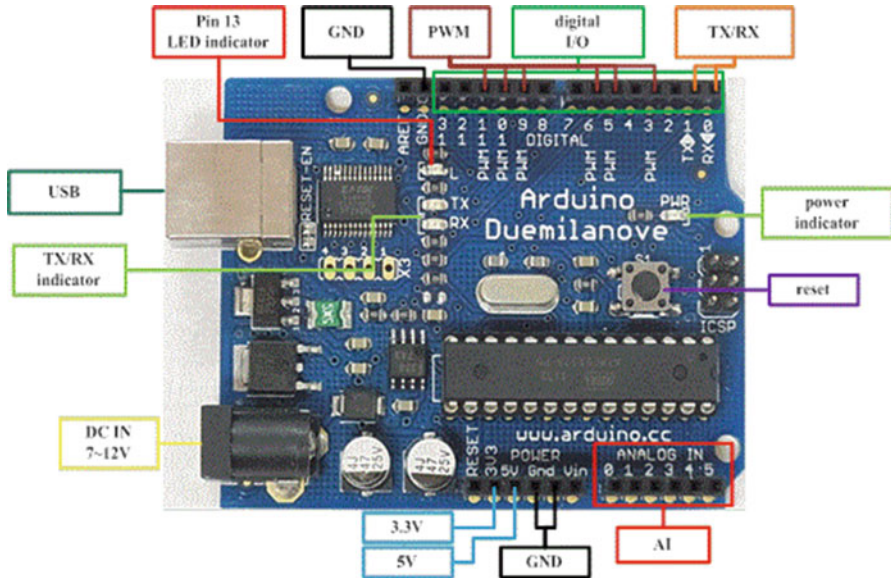
Fig. 3 Arduino Dueminalove board

location and dimension of IO pins on a PCB board layout shall be the same. Therefore, developers can independently choose a target board from various vendors. Currently, Arduino UNO or Dueminalove are the most popular ones. Hence, Dueminalove in Fig. 3 was chosen as the target board for this development.

4.1 Sensors

In this implementation, two types of sensors are utilized. The first one is a very short-range infrared sensor, named CNY70, as shown in Fig. 4. CNY70 emits 800 nm invisible infrared, then through the filter, it receives echo infrared by the photo transistor. It can detect a range from 1 to 5 mm. Another one is Sharp GP2D120 as shown in Fig. 5. Basic theorem of GP2D120 is similar to CNY70, except the detecting distance of GP2D120 is ranging from 4 to 30 cm.

5 System Design

5.1 Control Functionality

Figure 6 showed that there were three control modes specified in the system basic design, i.e., tracking mode, obstacle-avoiding mode, and remote operating mode. The control mode of autonomous vehicle is determined by the states of two pins of a dip
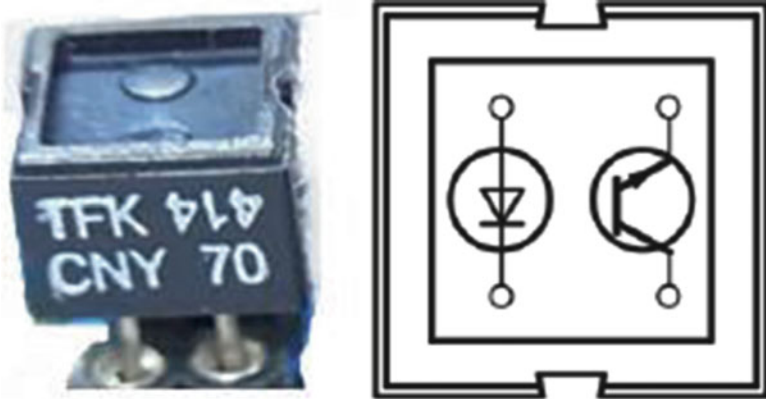
Fig. 4 CNY70

Fig. 5 Sharp GP2D120

switch soldered on the vehicle. However, the mode selection command transferred from operator's handheld remote can dominate the control mode preset by the states of the dip switches.

In tracking mode, the vehicle will utilize 3 CNY70 sensors installed on the bottom and near the front end. The total width of these three sensors is a little narrower than the track marked by a black PVC tape. In normal case, all 3 sensors will fall within the black tape. Assume that the right CNY70 moves outside the tape, it will detect a high reflection signal. This indicates that the vehicle should turn a little left to go back the normal track. Furthermore, if two sensors are off the track at the same time, this means the vehicle should make a greater directional changing to balance the offset situation.
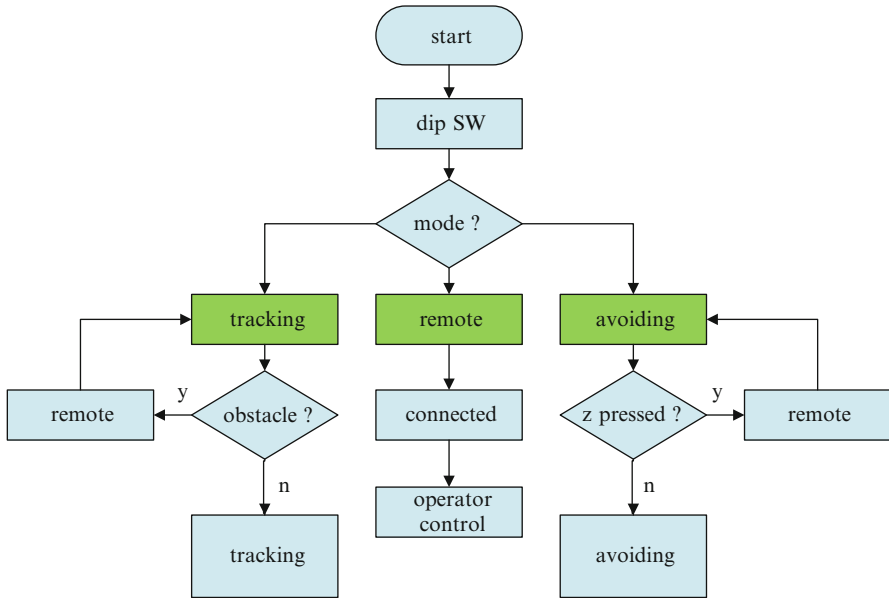
Fig. 6 Control flowchart

In obstacle-avoiding mode, the vehicle will utilize 2 GP2D120 sensors installed at the front end toward the direction of an obstacle. According to the reflection signals of these two front sensors, the vehicle can decide the direction and distance of the obstacle. Thus, it can make a proper turning command to avoid the approaching obstacle.

Using remote operating mode, an operator can move the vehicle in any direction with a joy stick soldered on a handheld remote controller. The remote controller is also developed by Arduino Dueminalove board. The directional coordinate (x, y) of joy stick is transformed into directional command and transferred to the vehicle via a ZigBee network.

5.2 System Configuration

Figure 7 showed the system configuration of the autonomous vehicle. In this system, all Arduino Dueminalove boards were laid and fabricated by this wok itself, including circuit laying, layout exposing, image developing, etching, slicing, drilling, and soldering. The layout of PCB was created by the Fritzing software tool. Figure 8 showed the layout and PCB designed and fabricated in this work. All components and devices were purchased from commercial markets with affordable cost.

Figure 9 illustrated the circuit of the remote controller. Figure 10 describes the circuit of L293D motor driver IC for the control of 2 DC motors. Figure 11
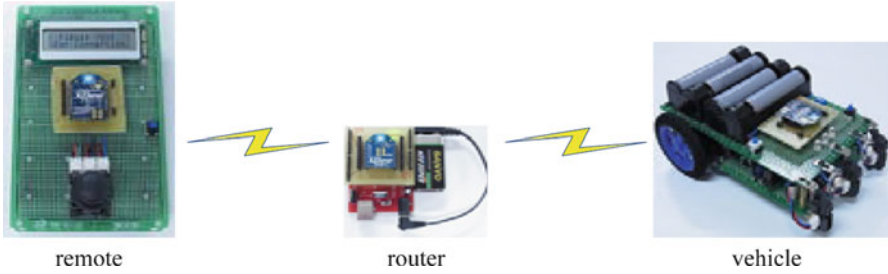
Fig. 7 System configuration
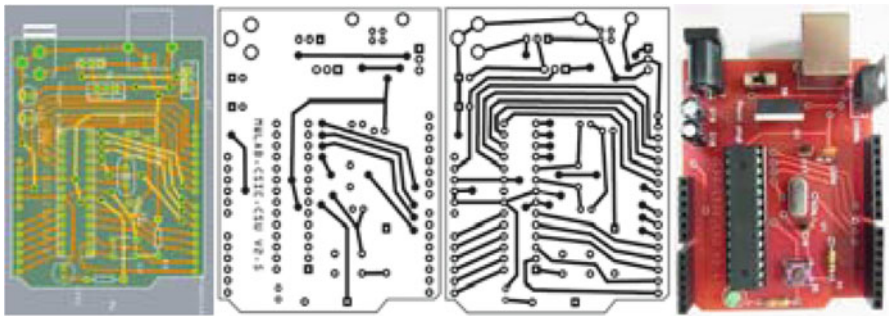
Fig. 8 Dueminalove compatible PCB

illustrated the driving circuit for the two high-power LED lamps. Figure 12 depicts the circuit of each mid-range infrared sensor. Figure 13 explains the circuit of very short-range infrared sensor. The firmware loaded in the CPU of the vehicle reads all required sensing signals via analog input (AI) pin and decides the motor rotation direction and speed via DO pins. Different control modes realized various control logics and procedures as illustrated in Fig. 6.

6 Development Results

Figure 14 showed the controller PCB on the vehicle. The grid holes PCB on the bottom was utilized as the base frame of the vehicle. The Dueminalove board was mounted at the middle-front segment of the frame. The grid holes PCB on the upper plane was utilized to mount two battery sets, the ZigBee chip, the power-on switch, and the starting button. The design of two battery sets was to separate heavy load of
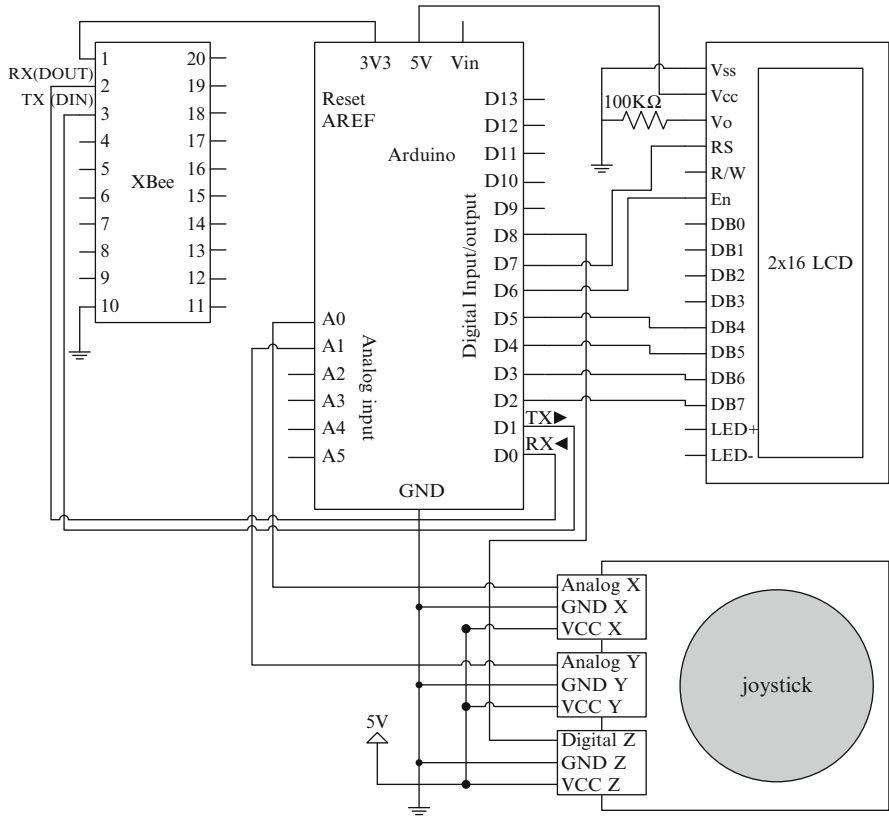
Fig. 9 Remote controller circuit
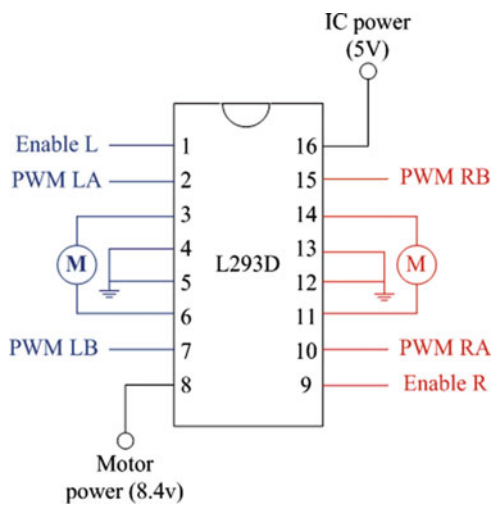
Fig. 10 Motor driver

Fig. 11 LED driver
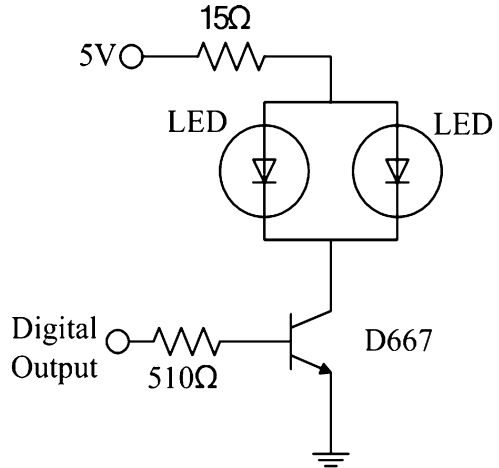
Fig. 12 GP2D120 circuit
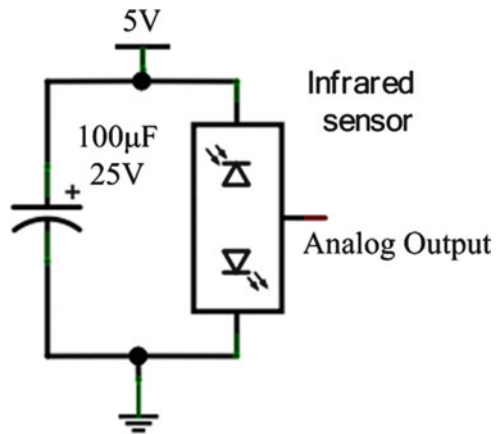
motors and light load of processing circuit. All external sensors and electronic components consume either DC 5 V or DC 3.3 V from output power pins on the Dueminalove board.

Figure 15 demonstrated the autonomous vehicle running on the tracking field for verifying the tracking functionality. The result of tracking verification showed that the vehicle can successfully track the black tape rail. Figure 16 demonstrated the vehicle running on the obstacle-avoiding field for verifying the obstacle avoidance functionality. The verification results showed that the vehicle can stably avoid bottle in the testing field. Meanwhile, the operator can wirelessly drive the car with the handheld remote controller as shown in Fig. 17.
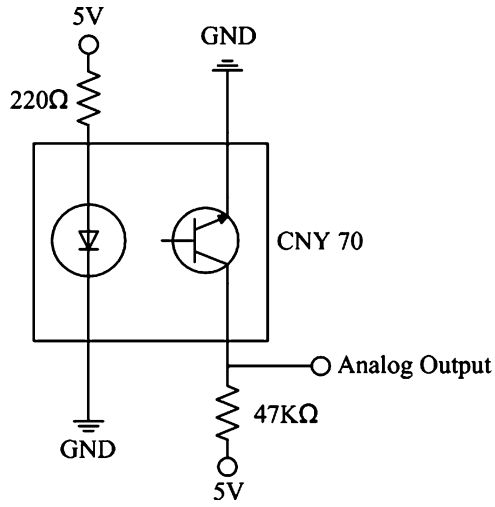
Fig. 13 CNY70 circuit
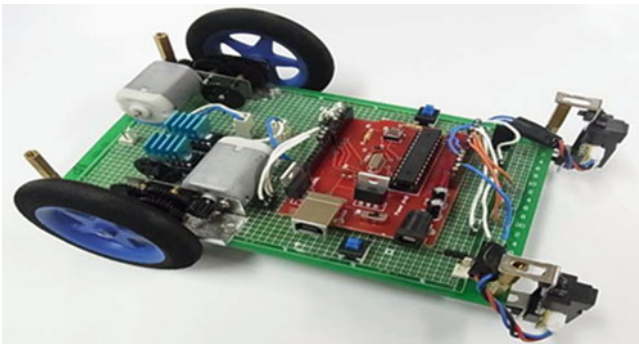
Fig. 14 Vehicle controller
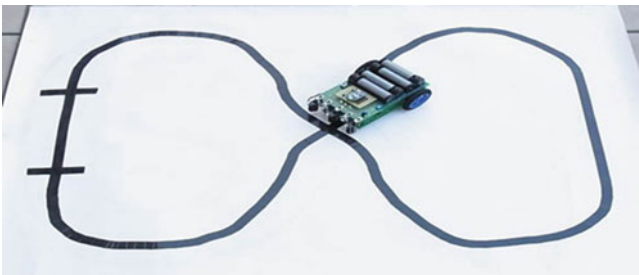
Fig. 15 Tracking field

Fig. 16 Obstacle-avoiding field
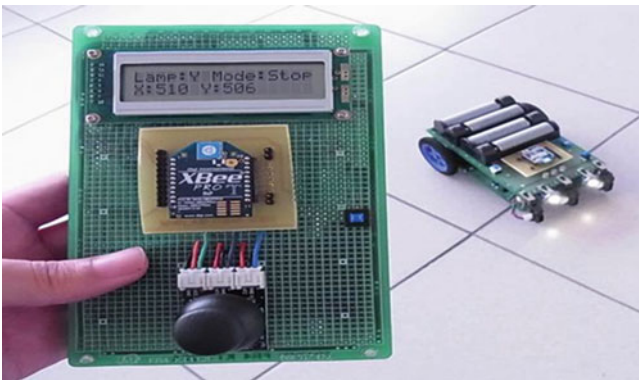
Fig. 17 ZigBee remote controller

7 Conclusions

The research and development was focus on the design and implementation of an autonomous vehicle for education. In this work, the vehicle was composed of usually low-cost components. Verification results showed that the tracking mode, obstacle-avoiding mode, and remote operating mode are controlled in conforming to the basic design specification. In the future, some advance functions should be added in order to extend the application domains, e.g., vision or voice.

References

1. Russell DJ (2010) Introduction to embedded systems: using ANSI C and the arduino development environment. Synth Lect Dig Circ Syst 5(1):1–275
2. http://www.arduino.cc/
3. Brunvand E, Stout P (2011) Kinetic art and embedded systems: a natural collaboration. In: Proceedings of the 42nd ACM technical symposium on computer science education, Dallas, Mar 9–12 2011
4. Piperidis S, Doitsidis L, Anastasopoulos C, Tsourveloudis NC (2007) A low cost modular robot vehicle design for research and education. In: Mediterranean conference on control and automation, T30-026, Athens, 2007
5. Stollenwerk A (2010) A modular, robust and open source microcontroller platform for educational robot usage. In: Proceedings of the 2010 workshop on embedded systems education, Scottsdale, 2010
6. Faludi R (2010) Building wireless sensor networks: with ZigBee, XBee, arduino, and processing, 1st edn. O'Reilly Media, Farnham
7. Mohamma T (2009) Using ultrasonic and infrared sensors for distance measurement. World Academy of Science, Engineering and Technology, No. 51

New Ultrasonic Parking Sensor System in Automobiles

Chih-Feng Huang and Chien-Yuan Liu

Abstract A highly accurate ultrasonic parking sensor system for use in air is described. The proposed system uses a method which combines both the time-of-flight (TOF) method and the phase-shift method. The proposed method can obtain larger range measurement and also get higher accuracy compared with the TOF method. A single-chip microcomputer-based two-frequency continuous signal generator and phase detector was designed to record and compute the TOF, two phase shifts, and the resulting distance. In the test embodiment to confirm concept feasibility, three cost 40 ± 2 kHz ultrasonic transducers allow flexibility on bumper for transmitting and receiving ultrasound. The ultrasound transducer on the middle of bumper is transmitting the ultrasound. Two ultrasound transducers on the left and right sides of bumper are receiving the ultrasound simultaneously for detecting multiple objects. Experiments were done in air using two-frequency continuous wave (TFcw) with the frequencies of 40 and 41 kHz. Distance resolution of 0.05 % of the wavelength corresponding to the frequency of 40 kHz was obtained. The range accuracy was found to be within ± 0.05 mm at a range of over 3,000 mm. The main advantages of this ultrasonic parking sensor system are high resolution for detecting multiple objects, low cost, narrow bandwidth requirements, and ease of implementation.

Keywords Phase-shift method • Time-of-flight method • Ultrasonic parking sensor system

C.-F. Huang • C.-Y. Liu (✉)
Department of Computer Science and Information Engineering,
Cheng Shiu University, Kaohsiung, Taiwan
e-mail: cyliu@csu.edu.tw

1 Introduction

The techniques of distance measurement using ultrasonic in air include the time-of-flight technique [1], binary frequency shift keying (BFSK) [2], and a multifrequency AM-based ultrasonic system [3]. In the TOF method, the pulse propagates through the transmission medium and is reflected by a suitable reflector. The time taken for the pulse to propagate from transmitter to receiver is proportional to the reflector's range. In this case, system errors are primarily due to amplitude degradation of the received signal. However, so the TOF method of range measurement is subject to high levels of errors (about 1 cm) when used in an air medium, thus limiting its applications.

Thus, in most applications of range measurement in air using ultrasonic, a phase-shift analysis of single-frequency continuous-wave transmission is used to reduce error [4]. The ranging distance L can be determined by the phase shift of a single frequency if the maximum ranging distance does not exceed a full wavelength; otherwise a phase ambiguity will occur.

Ultrasonic sensors are used as parking aids on many vehicles. Most ultrasonic parking sensors detect the objects by using the TOF method. Every ultrasonic sensor can transmit and receive the ultrasound and calculate the distance of the object. This method cannot detect the real positions of the objects. The new ultrasonic parking system can be used the multiple transmitter-receiver pairs for multiple object definition. This chapter presents methods for combining both the time-of-flight (TOF) method and the phase-shift method by using TFcw [5–7].

2 Method

The method underlying TFcw is as follows. The transmitted signals and the received signals are shown in Fig. 1. The U_T is the transmission signal of a TFcw which has two frequencies f_1 and f_2 shown in Fig. 1a. The U_R is the received signals corresponding to the transmitted signals as shown in Fig. 1b.
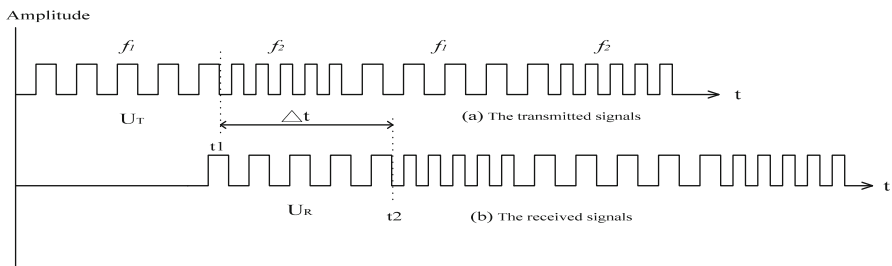
Fig. 1 Transmitted signals and received signals
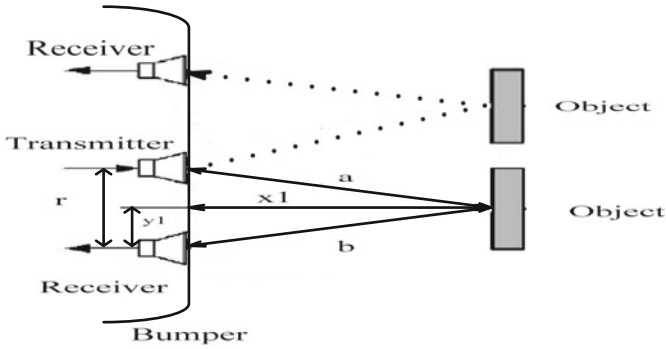
Fig. 2 The new ultrasonic parking system

There are two steps to processing of the received signal. The method to calculate the TOF is as follows. In Fig. 1 the elapsed time Δt, which is the round-trip travel time, can be calculated by received/transmitted signals and written as $\Delta t = t_2 - t_1$. Here t_1 is the time when f_1 changes to f_2 of the transmitted signals, and t_2 is the time when f_1 changes to f_2 of the received signals corresponding to the transmitted signals. The ranging distance can be expressed as $d = (c*\Delta t)/2$, where c is the sound velocity.

The phase-shift method by using TFcw is as follows. The phase shift can be detected by the received signals corresponding to the transmit signals. The first frequency (f_1) continuous wave is transmitted from an ultrasonic transducer. The first phase shift (θ_1), transmitted signal relative to received signal, is calculated by digitized phase information. Then the second frequency (f_2) continuous wave is transmitted, yielding the second phase shift (θ_2). The phase-shift difference ($\Delta\theta$) can be expressed using the following algorithm:

(a) If θ_2 θ_1, then $\Delta\theta = \theta_2 - \theta_1$.
(b) Else if $\theta_2 < \theta_1$, then $\Delta\theta = \theta_2 - \theta_1 + 2\pi$.

If the ultrasound velocity c is constant, the wavelengths λ_1 and λ_2 can be determined as $\lambda_1 = c/f_1$ and $\lambda_2 = c/f_2$. The frequency difference (Δf) is equal to $f_2 - f_1$. The final estimate of target distance can be expressed as

$$d = \frac{1}{2} * \text{int}[\Delta t * \Delta f] * \frac{c}{\Delta f} + \frac{1}{2} * \text{int}\left[\frac{\Delta\theta}{2\pi} * \frac{f_1}{\Delta f}\right] * \frac{c}{f_1} + \frac{1}{2} * \frac{\theta_1}{2\pi} * \frac{c}{f_1} \qquad (1)$$

The new ultrasonic parking system can be used the multiple transmitter-receiver pairs for multiple object definition by using the triangulation method as shown in Fig. 2. The ultrasound transducer on the middle of bumper is transmitting the ultrasound. Two ultrasound transducers on the left and right sides of bumper are receiving the ultrasound simultaneously for detecting multiple objects. If the distance between the transmitting transducer and the object is a, the distance between

the receiving transducer and the object is b, and the distance between the receiving transducer and the transmitting transducer is r, the distance between the bumper and the object can be expressed by using the following algorithm:

$$x_1 = \sqrt{a^2 - \frac{(r^2 + a^2 - b^2)^2}{4r^2}}$$

(2)

The coordinate of the object can be expressed as (x_1, y_1). The value of the horizontal coordinate is x_1 which can be used in Equation (2) to calculate. The value of the vertical coordinate is y_1 can be expressed by using the following algorithm:

$$y_1 = \sqrt{b^2 - x_1{}^2}$$

(3)

3   System Implementation

Figure 3 shows a block diagram of the TFcw ultrasonic parking system which consists of three ultrasonic transducers, a TFcw signal generation system, auto-gain-controlled amplifier, low-pass filter, frequency discrimination for TOF trigger signal, phase-shift meter, and microprocessor-based controller. A microprocessor controls the operation of the entire system:

The ultrasonic transducer has different responses to different frequencies. To avoid error from acoustic attenuation effects, the gain of the amplifier must change automatically when the frequency of ultrasound is varied. Therefore, the error effects related to acoustic attenuation are minimized in this auto-gain-controlled (AGC) amplifier module, and the received ultrasound is transferred in digital form by the AGC module. The microprocessor gets the elapsed time T_F and digital phase-shift data of θ_1, θ_2 and computes the phase-shift difference ($\Delta\theta$). Finally, the distance can be calculated by T_F, θ_1, and $\Delta\theta$.

4   Results and Discussion

The ultrasonic parking sensor test system consists of a constant temperature box, a brass plate (which is used as a reflector and mounted on a step motor's arm), an optical linear scale, and a PC. The reference scale of an optical linear measuring device (Pulscale model SJH5515AAR, Futaba, Japan) is mounted on the stepping motor. An optical sensor and its reflector are attached to each other and fixed in the stepping motor's arm. The stepping motor's arm changes the position of the reflector. Thus, for any given position, the PC is provided the optically measured
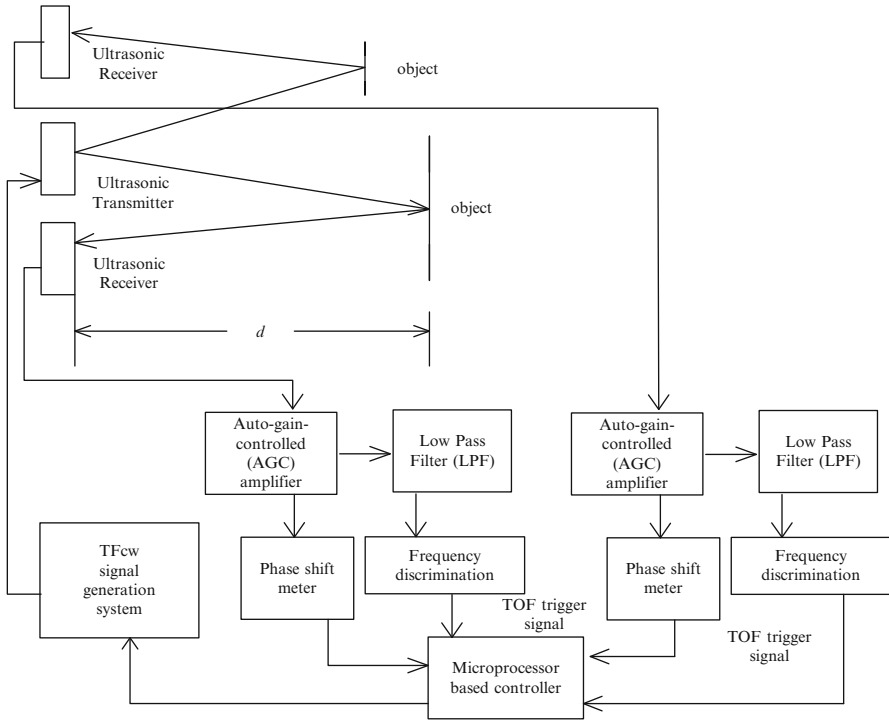
Fig. 3 Block diagram of the new ultrasonic parking system

distance, allowing the PC to calculate and display the error of distance that can be used for calibration.

Figure 4 shows the reconstructed distance calculated from TOF and the phase-shift difference when the actual distance moves from 100 to 3,000 mm. The standard error of measurement is calculated as follows:

$$\text{S.E.} = \sqrt{\sum \frac{\text{RP[i]} - \text{AP}}{\text{n}}} \tag{4}$$

where RP is the distance of the ultrasonic measurement, AP is the distance measured by the optical linear scale, and n is the number of measurements. The standard error is 0.05 mm. The range accuracy was found to be within $\pm$ 0.05 mm at a range of over 3,000 mm.

The new ultrasonic parking system can be used the multiple transmitter-receiver pairs for multiple object definition by using the triangulation method. The coordinate of the object 1 is (150, 200) cm and the coordinate of the object 2 is (60, 50) cm. The position of multiple objects is calculated by using the triangulation method as shown in Fig. 5.
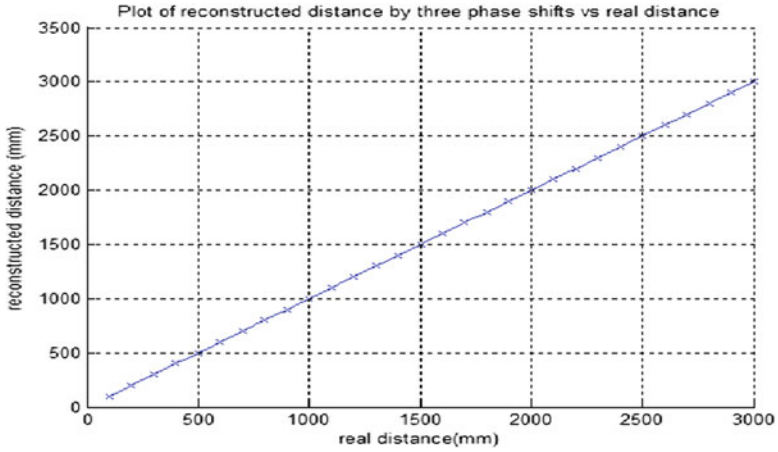
Fig. 4 The reconstructed distance vs real distance
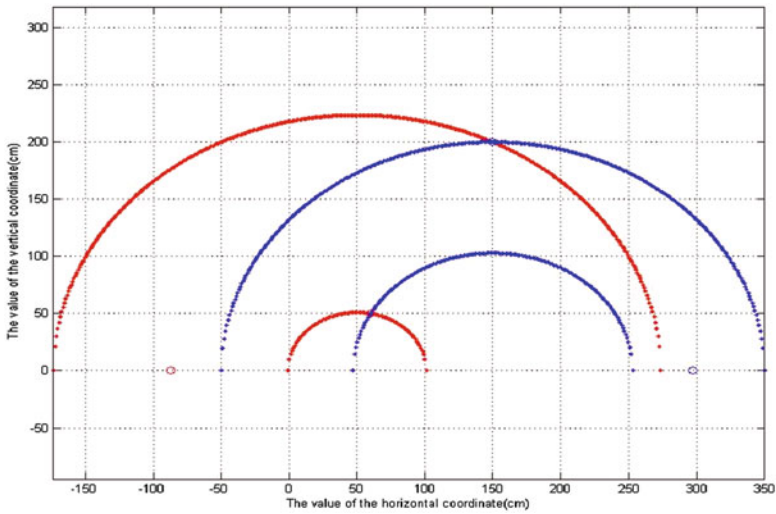
Fig. 5 The coordinates of multiple objects

References

1. Püttmer A, Nowottnick J, Hauptmann P (1998) High-accuracy measurement of pulse amplitudes for new applications of ultrasonic sensors. Sens Actuator A 68:454–459
2. Webster D (1994) A pulsed ultrasonic distance measurement system based upon phase digitizing IEEE Trans. Instrum Meas 43:578–582
3. Yang M, Hill SL, Bury B, Gray JO (1994) A multifrequency AM-based ultrasonic system for accuracy distance measurement. IEEE Trans Instrum Meas 43:861–866

4. Daniele M, Claudio N, Carlo O, Dario P, Andrea T (1992) Digital time-of-flight measurement for ultrasonic sensors. IEEE Trans Instrum Meas 41:93–97
5. Francis EG, Mihai V, Christian EE, Pascal D (1997) Accurate distance measurement by an autonomous ultrasonic system combing time-of-flight and phase-shift methods. IEEE Trans Instrum Meas 46:1236–1240
6. Huang CF, Young MS, Li YC (1999) Multiple-frequency continuous wave ultrasonic system for accurate distance measurement. Rev Sci Instrum 70:1452–1458
7. Huang SS, Huang CF, Huang KN, Young MS (2002) A high accuracy ultrasonic distance measurement system using binary frequency shift-keyed signal and phase detection. Rev Sci Instrum 73:3671–3677

Using the Gate-Diffusion Input Technique for Low-Power Programmable Logic Array Design

Shou-Hung Chiu and Kai-Cheng Wei

Abstract A novel low-power programmable logic array (PLA) structure based on gate diffusion input (GDI) is presented. The GDI technique allows reducing power consumption, propagation delay, and area of digital circuits. It also maintains low complexity of circuit design. In this chapter, we use the GDI technique to modify Kwang's PLAs. The conditional evaluation circuit in all product lines of Kwang's PLAs is replaced by a GDI circuit. To verify the proposed PLA, we use the MCNC PLA benchmark circuits to perform experiments. Simulation results show that the proposed scheme can reduce the number of transistors by 28.1 %, power consumption by 40.6 %, delay time by 15 %, and total power-delay product (PDP) by 49.5 % compared with Kwang's PLAs, which use the alu2 in MCNC benchmark for 0.18 μm CMOS technology.

Keywords Low-power CMOS • Programmable logic array • Gate diffusion input

1 Introduction

Programmable logic array (PLA) is extensively used for realizing arbitrary combinational and sequential logic function in very-large-scale integration (VLSI) systems. Because of its simplicity, flexibility, and regularity [1], PLA is still attractive to design high-performance digital circuits. Though the power consumption of conventional PLA should be reduced to make the PLA more suitable for applications in low-power systems. The main drawback of the conventional dynamic PLA [2] is that the operation speed is too slow and the power depletion too high. In Blair's PLA [3], it uses the pseudo-NMOS circuit; therefore, it obtains

S.-H. Chiu • K.-C. Wei (✉)
Department of Integrated Circuit Design and Information Engineering, National Changhua University of Education, Changhua 50007, Taiwan
e-mail: kcwei@cc.ncue.edu.tw

smaller and faster than an equivalent CMOS NOR gate. Unfortunately, the circuit has the short circuit current to consume the power during the evaluation phase. So, the power consumption of the PLA is still large. To solve this problem, Kwang's PLA [4] uses a conditional evaluation circuit in every product line, which compared with Blair's PLA can be reducing short circuit current. However, the design of PLA is still complex and requires a large area.

This chapter proposes a new PLA architecture with a GDI cell [5]. In this design, the number of transistors, dynamic switch power, and propagation delay compared with Kwang's PLA are reduced. We found that Kwang's PLA circuit can be improved to be faster and energy saving by removing the conditional evaluation circuit, since the conditional evaluation circuit will increase huge number of transistors. However, the more transistors in the PLA, the more power is needed.

2 PLA Structure and Design

Figure 1a shows the critical path model of Blair's PLA that is composed of foot NMOSs, which are two NOR-type dynamic logics connected in cascade. But the short circuit power consumption exists during the evaluation phase when the input is HIGH. Figure 1b shows the critical path model of Kwang's PLA with the conditional evaluation circuit. This configuration is similar to Blair's PLA except for the conditional evaluation circuit, which is composed of the inverter and NOR gate. The conditional evaluation circuit can eliminate the short circuit current during the evaluation phase when the input is HIGH. In Kwang's PLA, every product line PMOS (Pc) needs a NOR gate to control switch that will make the circuit more complicated. To solve this problem, we propose a new high-performance and low-power dynamic PLA design that uses a GDI cell scheme. Figure 1c shows that the critical path of the proposed PLA using a GDI cell design. The main feature of this circuit is using one GDI cell instead of all the conditional evaluation circuit in every product line. Therefore, it can reduce the number of transistors and power consumption.

Table 1a shows a conventional GDI cell [5] which can be designed with various logic functions using only two transistors, and it is suitable for designing fast, low-power circuits. The GDI cell contains three inputs: a common gate input G for nMOS and pMOS, input P to the pMOS, and input N to the nMOS, and the bulks of both nMOS and pMOS are connected to N or P, respectively. In Table 1b, the clocks CLKi and CLKii are LOW in the evaluation phase by using the GDI cell. The new GDI cell is different with conditional evaluation circuit that is not necessary to control every product line independently. It only needs one GDI cell to control all the PMOS (Pc) at the same time. Therefore, it can reduce the large number of transistors and eliminate the parasitic capacitance Cpc. The other
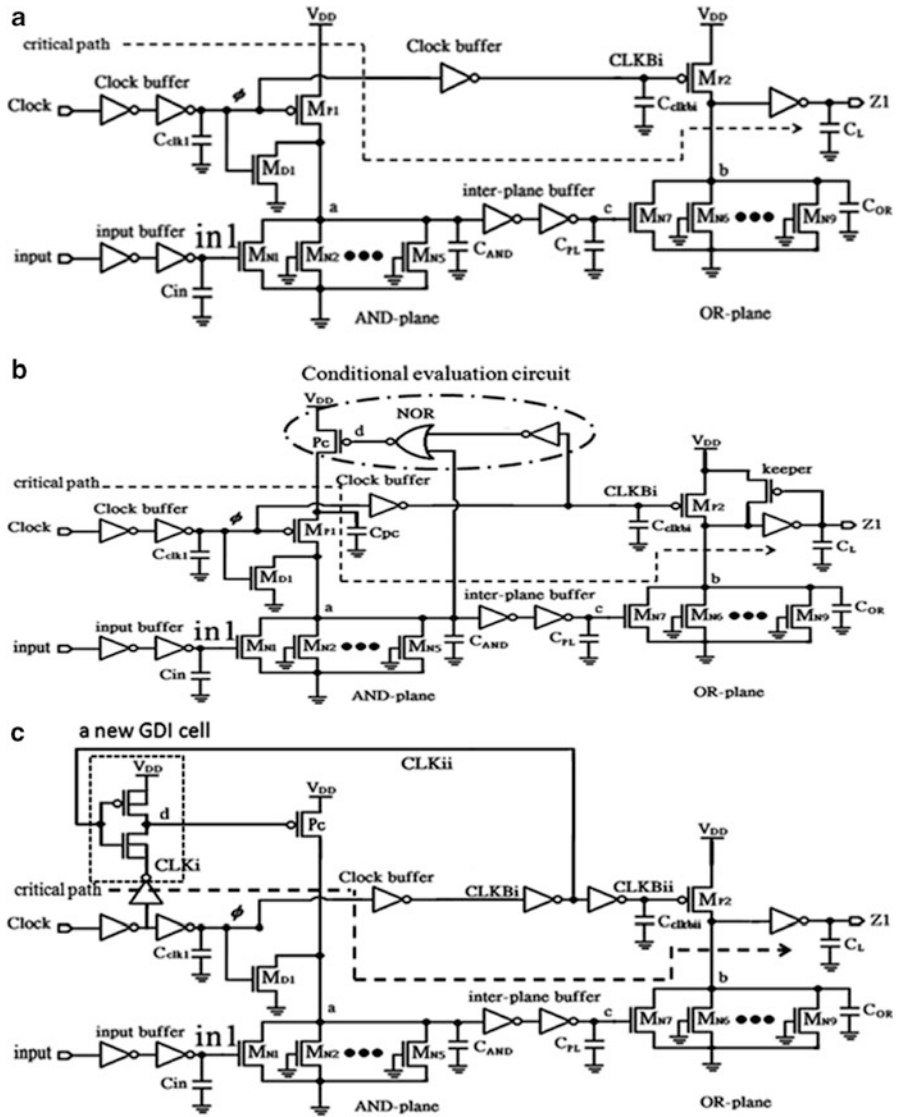
Fig. 1 The critical path model of (**a**) Blair's PLA, (**b**) Kwang's PLA, and (**c**) our proposed PLA

advantage is that it can reduce the charging time during the evaluation phase. In Kwang's PLA, the conditional evaluation circuit turns on the PMOS (Pc) to charge node "a" during the evaluation phase when all the input is LOW. Using the GDI cell, the PMOS (Pc) turns on only in the time interval when the CLKi is LOW and the CLKii is HIGH in the evaluation phase. It can reduce the power depletion of PMOS (Pc).

Table 1 The GDI cell configuration: (**a**) various logic functions of GDI cell for different inputs and (**b**) the new GDI cell configuration in our proposed PLA

N	P	G	OUT	Function
'0'	B	A	$\overline{A}B$	F1
B	'1'	A	$\overline{A}+B$	F2
C	B	A	$\overline{A}B+AC$	MUX
'0'	'1'	A	$\overline{A}$	NOT

CLKi	CLKii	node 'd'
0	0	1
1	0	1
1	1	1
0	1	0
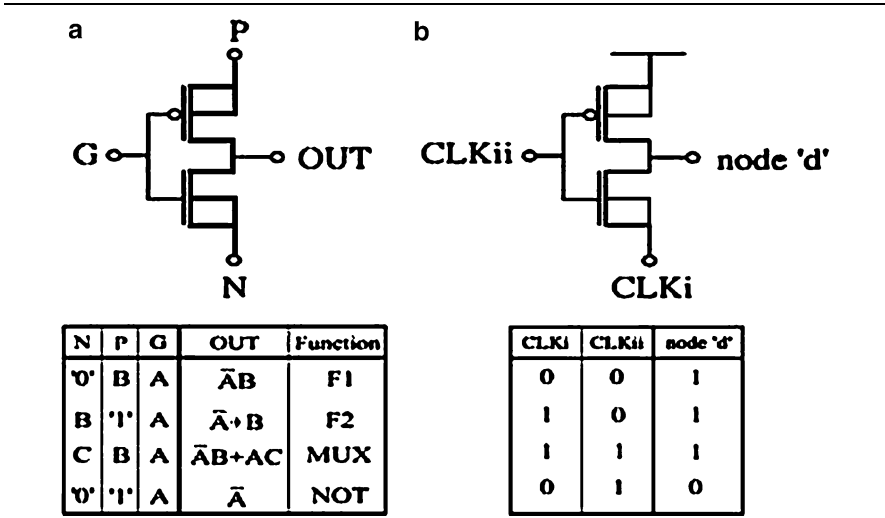
3 Simulation Results and Comparisons

The proposed PLA is implemented for a real chip from MCNC benchmark circuit alu2 by TSMC 0.18 μm CMOS technology with 1.8 V supply voltage. Figure 2 shows the signal propagation waveforms of the proposed PLA for the circuit alu2 simulate at 100 MHz. We can see that the nodes "a" and "c" are discharged to GND during the precharge phase. During the propagation time of clock delay chain (CLKii), the new GDI cell is LOW and PMOS (Pc) is opened to evaluate the PLA. After the propagation time of clock delay chain, the new GDI cell transforms into HIGH. By using this technique, the short circuit power consumption exists only in the short propagation time of clock delay chain.

Figure 3a shows the waveform of the new GDI cell with the alu2 circuit in the proposed PLA. It can be seen that the delay time generated by CLKi and CLKii created a LOW in Fig. 3b; it has enough time to drive the PLA. The comparison results of the number of transistors for various PLA are shown in Table 2. Compared to Kwang's PLA, the number of transistors of the proposed PLA was reduced the range from 21.5 to 28.1 %. The average power dissipation of the post-simulation for the various PLA in different circuits is shown in Table 3. The power savings of the proposed PLA range from 33.3 to 40.6 % compared to Kwang's PLA. The delay times for the various PLA in different circuits are shown in Table 4. Compared to Kwang's PLA, the delay time of the proposed PLA was reduced with the range from 15 to 23.1 % for the different circuits.
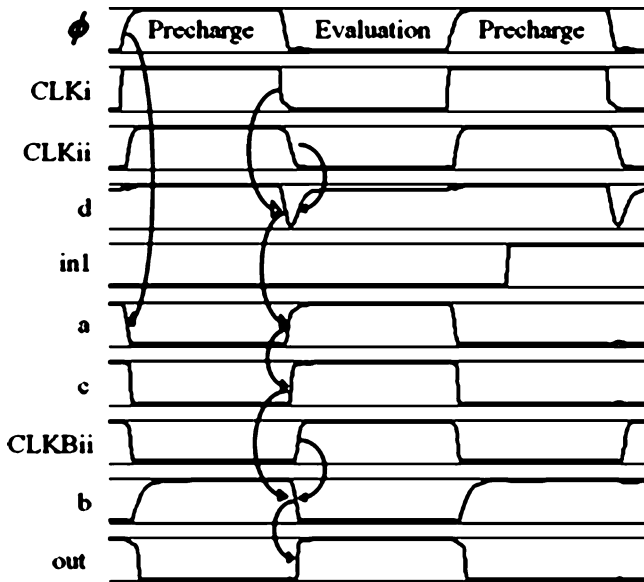
Fig. 2 The signal waveforms of the proposed PLA for the benchmark circuit alu2 simulating at 100 MHz
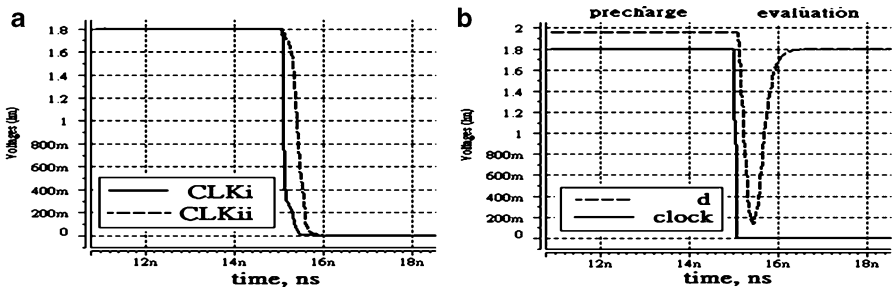
Fig. 3 The post-simulation clock waveform for the alu2 circuit at 100 MHz: (**a**) the waveform of GDI cell input and (**b**) the waveform of GDI cell output

Table 2 The comparison results of the number of transistors of various PLA

Circuit	I × O × P	Blair's [3]	Kwang's [4]	Our	Reduce ratio with (%) [3]	[4]
p82	5 × 14 × 21	377	484	371	1.6	23.3
b7	8 × 31 × 27	533	670	511	4.1	23.7
alu2	10 × 8 × 68	873	1215	873	0.0	28.1
in7	26 × 10 × 54	1005	1277	1003	0.2	21.5

Table 3 The post-simulation comparison results of power consumption at 100 MHz (units: mW)

Circuit	Blair's [3]	Kwang's [4]	Our	Reduce ratio with (%)	
				[3]	[4]
p82	6.74	0.51	0.34	95.0	33.3
b7	8.10	0.7	0.45	94.4	35.7
alu2	10.76	1.75	1.04	90.3	40.6
in7	10.60	1.4	0.93	91.2	33.6

Table 4 The post-simulation comparison results of delay time at 100 MHz (units: ns)

Circuit	Blair's [3]	Kwang's [4]	Our	Reduce ratio with (%)	
				[3]	[4]
p82	1.14	0.65	0.5	56.1	23.1
b7	0.78	0.7	0.55	29.5	21.4
alu2	1.14	1	0.85	25.4	15.0
in7	0.99	0.92	0.77	22.2	16.3
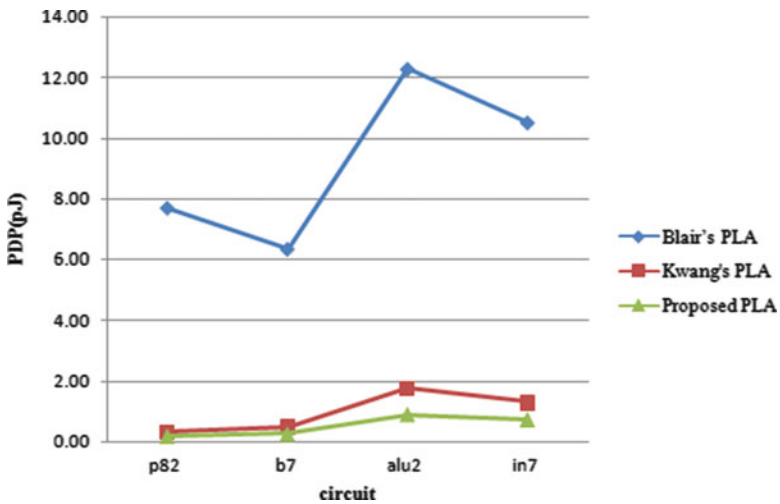
Fig. 4 The post-simulation performance comparison results of various PLAs at 100 MHz

The post-simulation of the performance comparison results of various PLA is shown in Fig. 4. The power-delay product (PDP) of the proposed PLA is reduced for the range from 92.8 to 97.8 % compared to Blair's PLA and the range from 44.4 to 49.5 % compared to Kwang's PLA for the different circuits.

4 Conclusion

A low-power and high-speed dynamic PLA using the GDI cell technique is proposed. In this design, the number of transistors, the power consumption, and propagation delay compared with Kwang's PLA are reduced. We found that Kwang's PLA circuit can be improved to be faster and energy saving by removing the conditional evaluation circuit because the conditional evaluation circuit will increase huge number of transistors. However, the more transistors in the PLA, the more power is needed. The main feature of this circuit is using one GDI cell instead of the conditional evaluation circuit in every product line. Therefore, it can reduce the number of transistors and power consumption. Compared to Kwang's PLA, the amount of transistors of the proposed PLA was reduced to 28.1 %, the power savings is 40.6 %, and the delay time was reduced to 23.1 %. The PDP of the proposed PLA is reduced to 92.8 % compared with Blair's PLA and reduced to 49.5 % compared with Kwang's PLA.

References

1. Posluszny S et al (1998) Design methodology for a 1.0 GHz micro processor. In: International conference on computer design: VLSI in computers and processors, ICCD 1998, pp 17–23
2. Weste N, Eshrahian K (1992) Principles of CMOS VLSI design-a system perspective, 2nd edn. Addison-Wesley, Reading
3. Blair GM (1992) PLA design for single-clock CMOS. IEEE J Solid State Circ 27(8):1211–1213
4. Oh KI, Kim LS (1994) A high performance low power dynamic PLA with conditional evaluation scheme. Proc IEEE Int Symp Circ Syst 2:881–884
5. Morgenshtein A, Fish A, Wagner IA (2002) Gate-diffusion input (GDI) – a power efficient method for digital combinatorial circuits. IEEE Trans VLSI Syst 10(5):566–581

Using LC-3 Soft Core on an FPGA Development Board for Microprocessor Labs

Yuan-Jhang Liao and Wing-Kwong Wong

Abstract In this study, a Little Computer 3 (LC-3) core is ported to Altera's Cyclone III FPGA on the DE0 development board. DE0 input/output devices such as seven-segment display, LED, switch, GPIO devices, and Lego Mindstorms NXT devices are added as memory-mapped devices. The LC-3 core was designed with VHDL on Quartus II 9.0 Web Edition. The input/output devices on DE0 can be manipulated by LC-3 instructions. With these additional devices in LC-3, more diversified and interesting labs can be designed. Students can first test their programs on the simulator and then on DE0. This should add more fun to learning assembly language programming and computer organization and flatten the learning curve.

Keywords LC-3 • FPGA • DE0 • NXT • Assembly language

1 Introduction

It is not difficult for engineering students to learn computer programming in high-level languages such as C, Java, and VB. However, they might not know much about computer organization and architecture even if they do well in programming in high-level languages. For the students who want to understand how a computer really works in hardware level, they must learn assembly language

Y.-J. Liao (✉)
Graduate School of Electronic Engineering, National Yunlin University of Science & Technology, Douliou, Yunlin 64002, Taiwan
e-mail: M10013246@yuntech.edu.tw

W.-K. Wong
Department of Electronic Engineering, National Yunlin University of Science & Technology, Douliou, Yunlin 64002, Taiwan

programming. LC-3 is an Instruction Set Architecture (ISA) with an assembler and simulator suite that students may use in learning the organization of a microprocessor. This study is about the design of such a course, which makes use of a soft processor LC-3 that runs on an FPGA platform.

1.1   Introduction to LC-3

The Little Computer 3 (LC-3) is developed by Patt and Patel [1]. LC-3 instruction set implements 15 types of instructions and specifies a word size of 16 bits for its registers and uses a 16-bit addressable memory. The register file contains eight registers, referred to by number as R0 through R7. All of the registers are general-purpose in that they may be freely used by any of the instructions. LC-3 is a 16-bit processor with a small instruction set that beginners can learn with a low hurdle. Students can develop an assembly program on an LC-3 Editor with an assembler and runs its object code on an LC-3 simulator [2].

1.2   Related Work

Google search shows that many universities use a 32-bit soft core NIOS II provided by Altera in their microprocessor lab courses (e.g., [3]). NIOS II is a good choice because it comes with an integrated development environment with an assembler and a C compiler that compiles C programs into NIOS instructions. In addition, there are several simulators that help the design of NIOS II assembly programs. However, there are many instructions in the instruction set of NIOS II, which might be difficult for beginning students to learn. Instead of using NIOS II in our course, we choose to use an LC-3 core, which is a 16-bit microprocessor, with only 15 instructions instead. LC-3 also comes with an assembler, a simulator, and a C compiler called LCC. Our course focuses on training students to do assembly language programming and to understand the basic organization of a small and simple microprocessor.

1.3   DE0 I/O Devices and Lego NXT Devices Combine with LC-3 Processor

This study is about the design of a course on microprocessor using a soft processor LC-3 that runs on an FPGA platform. I/O device of DE0 board and Lego NXT devices combine with the LC-3 core. Student can use LC-3 assembly language to

program their applications to control I/O devices. Lego NXT works with many peripheral devices such as light sensor, sound sensor, ultrasonic sensor, and inter-active servo motor. With these devices, more diversified and interesting labs can be designed. In one lab, we use LC-3 core with Lego Mindstorms NXT servo motors and light sensor. For example, students can write an application to control a robot car to follow a black strip on the floor.

2 Implementation

2.1 System Architecture

LC-3 processor can be downloaded to a DE0 board. Then student can program in LC-3 assembly language to access I/O devices of DE0 and Lego NXT devices. DE0 communicates with Lego NXT devices using Inter-Integrated Circuit (I^2C) proto-col. Some NXT devices are analog sensors, whose analog output signals must be digitized before they can be received by DE0, which cannot handle analog signals. An analog-to-digital converter must be used for this conversion (Fig. 1).

2.2 DE0 FPGA Board

DE0 board, manufactured by Altera, has many merits that allow users to implement a wide range of applications. For construction of the LC-3 experimental platform, the following hardware components provided by DE0 are used:

- Altera Cyclone® III 3C16 FPGA device
- Pushbutton switches
- 10 toggle switches
- 7-segment Displays
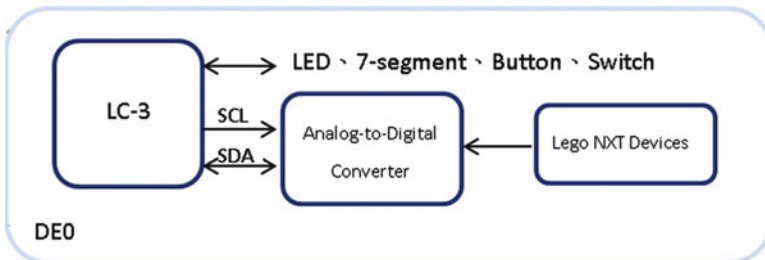
Fig. 1 LC-3 based on DE0

- Green LEDs
- Expansion Headers
- SD-card socket
- RS-232 port
- PS2 port
- VGA

Some DE0 hardware components are not implemented in our LC-3 core such as SD-card socket, RS-232, PS/2, and VGA.

2.3 Lego Mindstorms NXT Devices

Lego Mindstorms NXT is jointly developed by a well-known Danish toy manufacturer Lego (LEGO) and the Massachusetts Institute of Technology. Lego Mindstorms NXT is a programmable robotics kit released by Lego in late July 2006. In this study, we use two Lego NXT devices, a light sensor and two servo motors.

The servo motor is controlled by pulse-width modulation (PWM) signals. We can use LC-3 assembly language to generate PWM signals via GPIO to control a servo motor. We use a DC motor driver IC to amplify the PWM signals, because the GPIO output current 8 mA is not strong enough to drive the servo motor. DE0 also communicates with input sensors using I^2C protocol with GPIO.

For Lego NXT sensor, the light sensor output signal type is analog. We have to add an analog-to-digital converter (ADC) to convert analog signals to digital ones. NXT Solderless Prototype Board NPS1055 [4] can access digital or analog devices through designated addresses. The light sensor sends data to DE0 via an ADC module on NPS1055.

2.4 I/O Device Communicates with LC-3 Processor

I/O-mapped I/O and memory-mapped I/O [5] are two complementary methods of performing input/output between the CPU and peripheral devices in a computer. In this study, we use memory-mapped I/O to implement this LC-3 experimental platform, because a maximum total of 16 instructions are allowed for LC-3, and 15 instructions have been specified.

There are two special registers in LC-3's memory architecture: Memory Data Register (MDR) and Memory Address Register (MAR). MDR saves data to be written or read data. MAR points to the currently accessed address. Memory accesses must be made through MAR and MDR.

Fig. 2 LC-3 memory-mapped I/O architecture
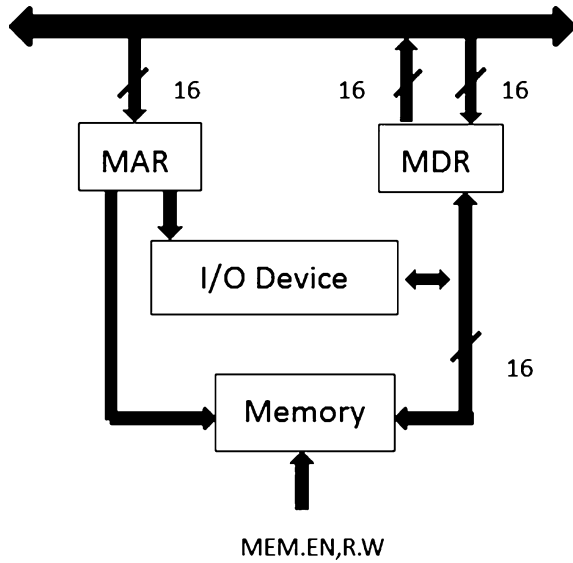
Fig. 3 LC-3 memory map
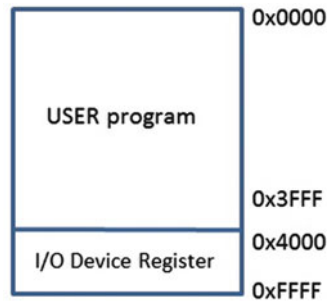
We add a decision circuit to the original memory architecture. If an address falls in the range reserved for I/O devices, then an I/O access will be made (Fig. 2).

The LC-3 memory has an address space of 2^{16} locations and addressability of 16 bits. Memory space within 0x0000 ~ 0x3FFF is reserved for user program and user stack, and 0x4000 ~ 0xFFFF is reversed for I/O addresses (Fig. 3).

In the following sample assembly program, a number is read from the input switches and written to the output LEDs on DE0 board using a load instruction and a store instruction, respectively. Then the number will be shifted left 10 times and shown on the LEDs.

```
        .ORIG       x0000                   ; Load program at x0000
Start   AND         R3, R3, #0
        LD          R1, SWaddr
        LDR         R1, R1, #0              ; R1 := values of switches
        LD          R2, LEDaddr
LOOPADD R3, R3, #1  ; increment counter
        ADD         R1, R1, R1              ; R1 shifts left
        STR         R1, R2, #0              ; LEDs := R1
        ADD         R4, R3, #-10               ; R4 := R3-10
        BRn         LOOP                    ; Exit loop after 10 times
        BRnzp       Start                   ; Repeat from Start forever
LEDaddr .FILL       xFFFC                   ; LED address
SWaddr  .FILL       xFFFD                   ; Switch address
        .END
```

2.5 I^2C *Protocol*

Inter-Integrated Circuit (I^2C) [6] is a multi-master serial single-ended computer bus invented by Philips that is used to attach low-speed peripherals to embedded system or other electronic devices. I^2C uses only two bidirectional open-drain lines, Serial Data Line (SDA) and Serial Clock (SCL). The I^2C reference design has a 7-bit or a 10-bit (depending on the device used) address space. Common I^2C bus speeds include the 100 Kbit/s standard mode and the 10 Kbit/s low-speed mode, but arbitrarily low clock frequencies are also allowed.

Lego NXT devices use I^2C protocol. We implement an I^2C driver for LC-3 using hardware description language (HDL). User can program their applications using special I/O addresses and the original LC-3 instructions to access Lego NXT devices.

3   Result

FPGA can implement any microprocessor core on board. In this design, LC-3 is realized on an Altera DE0 board and can communicate with some DE0 I/O devices and Lego Mindstorms NXT devices. Students do not need to know the complexity of I^2C but still can directly control Lego NXT devices.

In one lab, we use LC-3 core with Lego Mindstorms NXT servo motors and light sensor. Student can program to output PWM signals to GPIO to control two servo motors and read light sensor data. According to light sensor's data, the robot car controls the motors to track a black path to move forward, turn right, or turn left.
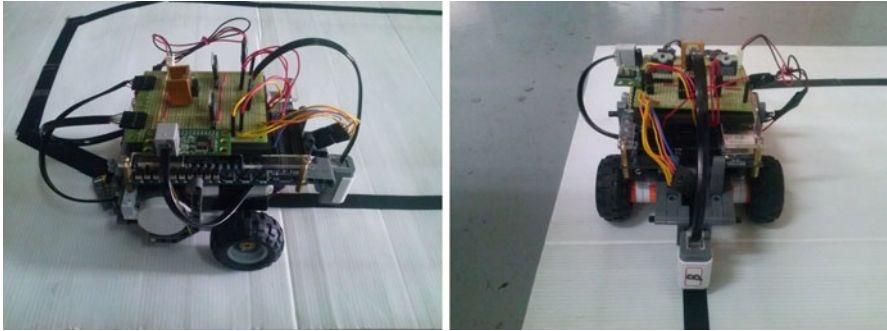
Fig. 4 The *front* and *right-side view* of the robot car with DE0

In the future, we will add interrupts, timers, and a small operating system to the core. Moreover, other Lego NXT devices would be added, allowing students to design more interesting applications (Fig. 4).

References

1. Patt YN, Patel SJ (2005) Introduction to computing systems. McGraw-Hill, New York/London
2. LC-3 simulator. http://highered.mcgraw-hill.com/sites/0072467509/student_view0/lc-3_simulator.html
3. Loo SM, Planting CA (2009) Use of discrete and soft processors in introductory microprocessors and embedded systems curriculum. ACM SIGBED Rev 6(1):1–10
4. Solderless Prototype Board NPS1055. http://www.hitechnic.com/cgi-bin/commerce.cgi?preadd=action&key=NPS1055
5. Memory-mapped I/O. http://en.wikipedia.org/wiki/Memory-mapped_I/O
6. I2C protocol. http://en.wikipedia.org/wiki/I%C2%B2C

Executing Linux-Based Software of Electronic Design Automation on Windows Platform of Microsoft

Hsin-Jung Wang and Zhi-Ming Lin

Abstract Due to developing history of EDA tools, current mainstream EDA tools are almost developed on Linux or UNIX. This chapter is a study of discovering some methods or techniques to execute such UNIX-based EDA tools on Microsoft Windows platform without rewriting the entire program. In this chapter, XCircuit, an electrical circuit schematic drawing program executing on UNIX, will be put into experiment for discovering a way to execute the program on Microsoft Windows platform. XCircuit is an open-source program and authorized by General Public License (GPL). This can avoid some problems that may be caused by proprietary software. XCircuit is expected to port and execute on Microsoft Windows XP during the porting experiment in this chapter.

Keywords EDA • GPL • UNIX

1 Introduction

The introduction will review the developing history of electronic design automation (EDA) accompanied by the history of computing hardware.

1.1 EDA in Early Days

Around 1970, a period where mainframes were used as major computing hardware, the earliest tools of EDA had been produced academically and introduced to the

H.-J. Wang (✉) • Z.-M. Lin
Department of Computer Science and Information Engineering, National Changhua University of Education, Changhua 50007, Taiwan
e-mail: m9956006@mail.ncue.edu.tw

world in the public domain. One of the most famous tools was produced by the University of California, Berkeley, the "Berkeley VLSI Tools Tarball," a set of UNIX utilities used to design early VLSI systems [1].

1.2 Midterm Development of EDA

After decades of development in computing hardware, EDA tools were still developed, maintained, and used on mainframes, minicomputers, or workstations, the high-end microcomputers designed for technical or scientific applications. This began to change in the year 2005. Intel and AMD, the top two leading manufacturers of microprocessors, introduced the multi-core microprocessor, which is used by normal personal computers, of their own.

1.3 Recent Development of EDA

After multi-core microprocessors were introduced to the market by Intel and AMD and recent developments of advanced manufacturing process of very-large-scale integration (VLSI), which is perfectly predicted by the well-known Moore's law, the computing performance of normal personal computers is finally competitive with workstations. This change does break the gap between normal personal computers and high-end personal computers, the workstations. This gives a chance for the developers to develop their EDA tools on normal personal computers. Besides, people can have more chances of obtaining and using these EDA tools since normal personal computers are widespread nowadays. Before this, no matter mainframes, minicomputers, or even workstations, they were never affordable for normal people other than government agencies, companies, researching organizations, or academic institutes.

1.4 Software Problems of EDA Caused by Developing History

Earlier the computing performance of normal personal computers was sufficiently good enough for the requirements of EDA tools, mainframes, minicomputers, or workstations that utilized these resource-consuming EDA tools. After restrictions were broken by the developments of advanced manufacturing process of VLSI, limits of hardware were eliminated. But problems of software arose. Because the EDA tools are all applications, they need a platform, or an operating system, to perform their designed functionality. This would become a tragedy because mainframes, minicomputers, and workstations are all powered by the UNIX or Linux platforms, but normal personal computers are usually powered by Microsoft

Table 1 A brief summary of mainstream EDA tools and the companies owing them

Company	Product	Supported platform		
		UNIX	Linux	Windows
Synopsys	HSPICE	Yes	Yes	Yes
Agilent	Advanced Design System	Yes	Yes	Yes
Cadence	Virtuoso	Yes	Yes	None
Mentor Graphics	Calibre	Yes	Yes	None
SpringSoft	Laker³ Custom Design Platform	Yes	Yes	None
	Laker Custom Layout Automation System	Yes	Yes	None
	Laker Advanced Design Platform	Yes	Yes	None

Windows platform. As people know, applications made for a specific platform cannot or have little chances to be used on other platforms. Otherwise, the application has different builds for different platforms.

1.5 Response of EDA Industry

The revolutions in computing hardware do attract the attention of some leading companies in the EDA industry, such as Synopsys and Agilent. They released new builds for normal personal computers using Microsoft Windows platform with the revolutionary trend in computing hardware. But there are other companies, such as Cadence and Mentor Graphics, that still release their products without the support of Microsoft Window platform. Table 1 provides a brief list of mainstream EDA tools used by the design flows of full-custom IC design of VLSI and the companies that own the EDA tools.

1.6 Do It Yourself

Without a doubt, commercial companies manufacturing EDA tools would have the ability to build applications that will work on different platforms. It would be an appealing thing if someone can perform a procedure to do the same thing and save the waiting period before the formal release of these commercial companies on a particular platform desired by someone. This can also avoid the risks if the commercial company has no such interests or plans to provide additional supports to the specific platform for their products. This will be discussed in the next section.

2 Experiment

The idea of the porting experiment is compiling XCircuit from source [3] on Microsoft Windows XP. We will also discuss the problems that would occur during porting. All these details will be discussed in the following sections.
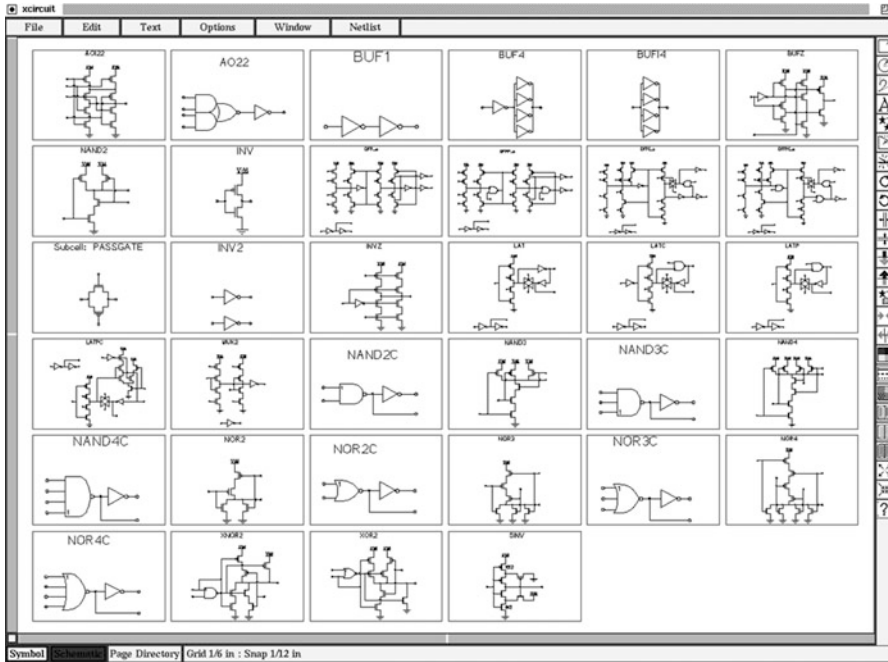
Fig. 1 Sample image of XCircuit provided by the author

2.1 XCircuit

XCircuit is a UNIX/X11 program developed and maintained by Tim Edwards. The program is a famous EDA tool in the free-software community. This program is similar to Laker Advanced Design Platform of SpringSoft for drawing publishable-quality electrical circuit schematic diagrams and related figures and producing circuit netlists through schematic capture. XCircuit regards circuits as inherently hierarchical and writes both hierarchical PostScript output and hierarchical SPICE netlists. Figure 1 shows a sample image of XCircuit provided by the author.

2.2 GPL

XCircuit is a free software licensed by General Public License (GPL); the complete document of GPL can be reviewed on the website of Free Software Foundation (FSF) [2]. The huge advantage of having a program licensed by GPL is that anyone can freely obtain and modify the source code of the program as and when desired.

This is of great convenience to the porting experiment of XCircuit between different platforms. Some restrictions and problems might occur and suffer when using proprietary software that will never exist.

2.3 C Language

Furthermore, XCircuit is programmed in C language, a programming language applied for various purposes. This can be realized because there are plenty of C-language compilers provided on different platforms. This also gives more advantages to the porting experiment of XCircuit because the situation of a shortage of compiler would never be considered. During the performed porting experiment, GNU GCC will be used as the compiler of the compiling process.

2.4 Compiling Environment

The compiling environment is summarized in Table 2.

3 Results

Figures 2 and 3 are the screenshots of XCircuit on Microsoft Windows XP that show the results of the porting experiment of XCircuit.

In Fig. 2, it can be easily recognized that the frame of the window is the classic style of Microsoft Windows XP. Moreover, the task of XCircuit listed in the applications tab of Windows Task Manager gives strong evidence that XCircuit is a task of Microsoft Windows XP. With these, it is clear that XCircuit can be truly executed on Microsoft Windows XP.

In Fig. 3, a simple work is done by using the drawing tools provided by XCircuit. This can be considered as the demonstration of functionality of XCircuit. The functions used to complete this work all performed well during the period of composition.

Table 2 A summary of compiling environment	Platform	Microsoft Windows XP
	CPU	Intel i7-870
	Cores of CPU	4
	Memory	8 GB
	Compiler	GNU GCC
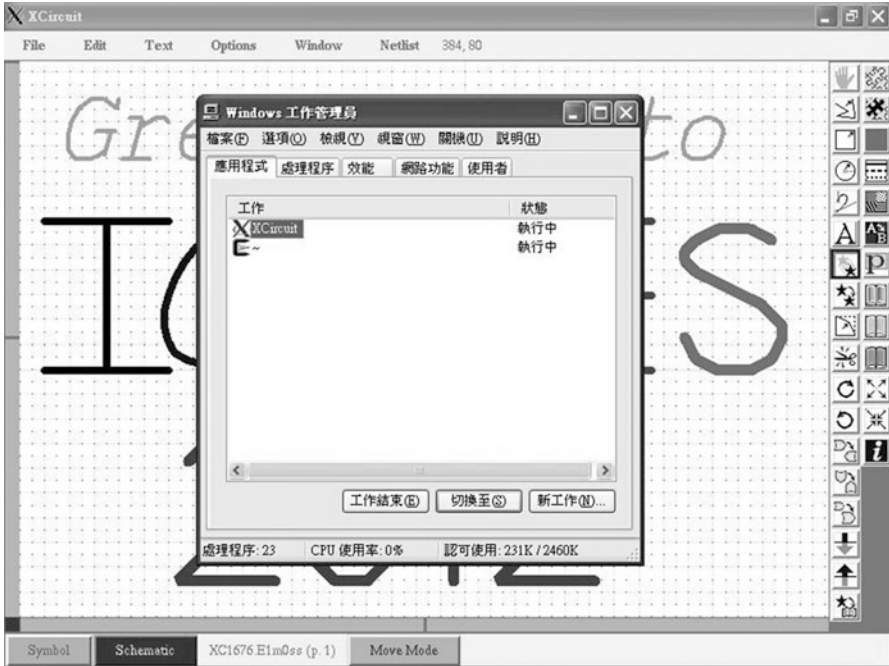
Fig. 2 Screenshot of XCircuit on Microsoft Windows XP
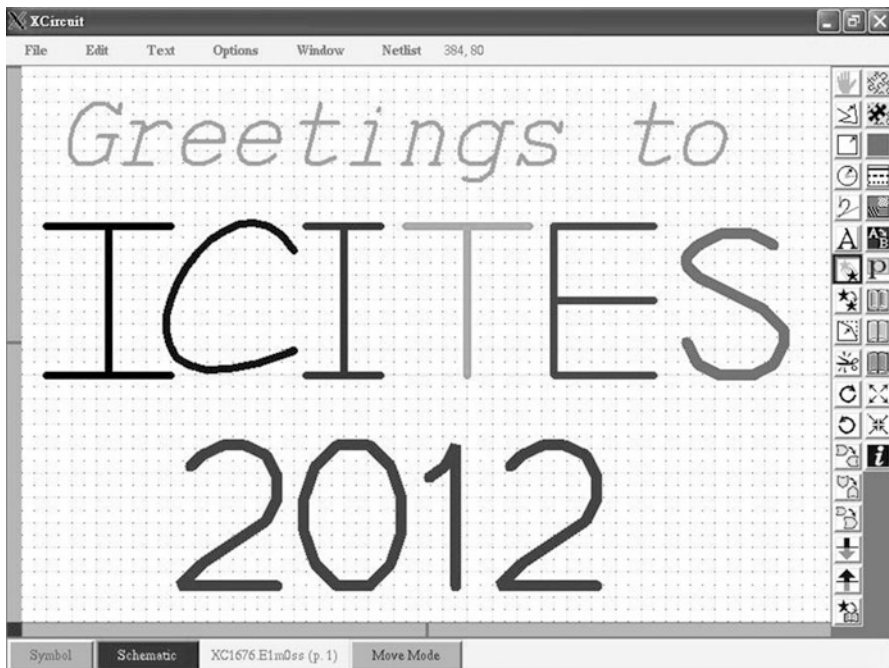
Fig. 3 XCircuit was practically used on Microsoft Windows XP

4 Conclusion

With all the achievements obtained earlier, it can be concluded that if an EDA tool that is open source or the source can be obtained by some approaches and is programmed in C language, then it can be ported to different platforms. This can be of benefit when some EDA tools are not available on a desired platform. After the study of the chapter, one can stop worrying about an EDA tool that has no corresponding release on a desired platform or will not be supported by an official platform. This problem can be solved just by taking a minimal effort to compile the program from the source since the requirements can all be achieved.

References

1. Chen D (2009) Design automation for microelectronics. Urbana
2. Free Software Foundation (FSF). http://www.fsf.org/
3. SourceForge. http://sourceforge.net/projects/xcircuit/

Design of a Transparent Pipeline Based on Synchronous Elastic Circuits

Ren-Der Chen and Sheng-Hung Chang

Abstract This chapter presents a transparent pipeline architecture based on the synchronous elastic circuits. Compared with a traditional synchronous pipeline, a transparent pipeline can reduce dynamic clock power dissipation by reducing the amount of clock pulses required for data latching. Moreover, with the help of the synchronous elastic properties, our design can also provide tolerance to variations in computation and communication delays. The proposed architecture has been implemented by the Verilog HDL and synthesized with Altera Quartus II. The experimental results performed on a five-stage pipeline have also shown the power efficiency of our architecture.

Keywords Elastic • Pipeline • Transparent

1 Introduction

In modern VLSI design, clock power plays an important role in chip power dissipation. Clock gating is an efficient technique widely used in low-power designs [1, 2]. Transparent pipelining is also a clock-gating solution for reducing dynamic power dissipation by reducing the amount of clock pulses that are redundant to the correct operation of a pipelined design [3–5]. In a traditional pipeline, the latches of a pipeline are assumed to be opaque by default to avoid data races between pipeline stages. But in a transparent pipeline, the internal latches are kept transparent by default to allow data items that are sufficiently separated to propagate through the pipeline without generating any clock pulses. Such separation often occurs in pipeline stalls of instruction execution caused by data dependencies. Since data

---

R.-D. Chen (✉) • S.-H. Chang
Department of Computer Science and Information Engineering, National Changhua University of Education, Changhua 500, Taiwan, R.O.C.
e-mail: rdchen@cc.ncue.edu.tw

races between latch stages can be avoided by properly separating data items in a transparent pipeline, a transparent latch needs to be clocked only when a true data race occurs. The number of required clock pulses can then be reduced by proper control of the gated clock signals. Therefore, the clock power can be significantly reduced by relaxing the clocking requirements of the latches in a pipeline.

Synchronous elastic circuits are a form of discretized asynchronous circuits [6–8]. The elastic property makes it possible to tolerate unpredictable timing variations in the computations and communications of a circuit and its environment. By this synchronous elasticity, there is no need to fix the communication delays as used in traditional designs. The implementation of elastic circuits relies on the clock-based synchronous handshake protocol to control the latching of data items. The handshake signals are based on *valid* and *stall* signals, and to achieve elasticity, no specific assumption is made about the implementation of the circuit. This chapter incorporates the concept of synchronous elasticity into the design of a transparent pipeline. The purpose is to reduce dynamic power dissipation and at the same time to tolerate variations in computation and communication delays. The synchronous handshake protocol is adopted to control the latches in the pipeline for data item propagation. Compared with traditional pipelines, however, these improvements are obtained at the expense of some additional area cost.

This chapter is organized as follows. Section 2 introduces the concept of transparent pipelines and elastic circuits. Section 3 gives the architecture of our elastic transparent pipeline. Section 4 includes the experimental results and discussions, and finally Section 5 concludes the chapter.

2 Transparent Pipelines and Elastic Circuits

A transparent pipeline keeps its latch stages transparent by default. Data races of two items propagating concurrently through the transparent pipeline can be avoided by forcing a latch stage between them to enter an opaque mode [3]. However, data items that are sufficiently separated in time can propagate through the pipeline without requiring the latch stages to be clocked. By reducing the number of clock pulses generated in the pipeline, clock power saving can be achieved. Figure 1 illustrates the behavior of a five-stage pipeline with three transparent stages, $S2$, $S3$, and $S4$. The other two stages $S1$ and $S5$ form the input and output environment, respectively, of the transparent pipeline and operate in the traditional opaque mode by default. It can be seen that only a total of six clock pulses is required for the two data items A and B to propagate through the pipeline, shown as the six shadowed data items in the figure. Due to the transparent property, there is no need to latch the data entering stage $S2$ for all the clock cycles. For example, when the valid data item A is latched in the first cycle in stage $S1$, it will then propagate through stages $S2$, $S3$, and $S4$ since these stages are transparent by default. In the second cycle, since there is no valid data item entering $S1$, the value of A can still be kept in $S1$. Stage $S2$, which is transparent at this time, can still get the valid data item A supported by $S1$. Therefore,

Cycle	Input (Data/Valid)	Pipeline stage				
		S1	S2	S3	S4	S5
0	A	-	-	-	-	-
	1	0	0	0	0	0
1	-	A	A	A	A	-
	0	1	0	0	0	0
2	B	A	A	A	A	-
	1	0	1	0	0	0
3	-	B	B	A	A	-
	0	1	0	1	0	0
4	-	B	B	B	A	-
	0	0	1	0	1	0
5	-	B	B	B	B	A
	0	0	0	1	0	1
6	-	B	B	B	B	A
	0	0	0	0	1	0
7	-	B	B	B	B	B
	0	0	0	0	0	1

Fig. 1 An example illustrating the behavior of a transparent pipeline
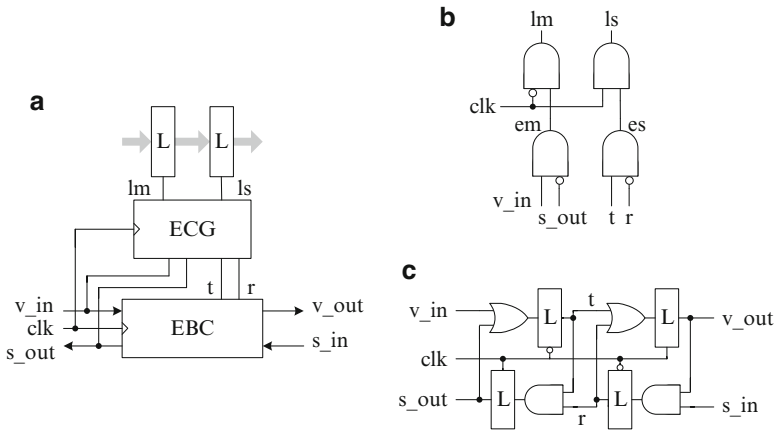
Fig. 2 (a) One elastic pipeline stage. (b) Elastic clock generation (ECG) unit. (c) Elastic buffer control (EBC) unit

there is no need for S2 to latch A in this cycle, i.e., no clock pulse is needed. For the traditional synchronous counterpart, it takes a total of 10 clock pulses (two for each stage) to propagate the same data items through the pipeline. The number of clock pulses for data latching can then be reduced for power saving by making a pipeline transparent.

Synchronous elastic circuits can tolerate unpredictable timing variations in the computations and communications of a circuit and its environment [6]. Figure 2a shows one stage of a synchronous elastic pipeline. It consists of two master-slave

data latches, an elastic clock generation (ECG) unit, and an elastic buffer control (EBC) unit. The ECG unit, shown in Fig. 2b, is responsible for generating the master and slave clock signals (*lm* and *ls*) for the data latches. When there is no valid data, signaled by the EBC unit in Fig. 2c, the two clock signals are gated in a logic-low state to make the data latches opaque. When a valid data item enters the elastic stage, the EBC unit will switch to clocked mode. A positive pulse will be generated on *lm* and then, after half a clock cycle, another positive pulse will also be generated on *ls* to latch the input data.

3   Elastic Transparent Pipelines

The architecture of the proposed elastic transparent pipeline is illustrated in Fig. 3. It is a five-stage elastic pipeline with three internal transparent stages. For the control part of the pipeline, the first opaque stage consists of an opaque clock generation (OCG) unit and an elastic buffer control (EBC) unit. The internal transparent stage consists of a transparent clock generation (TCG) unit and an EBC unit. The last stage is a traditional elastic stage consisting of an elastic clock generation (ECG) unit and an EBC unit. To make the pipeline work correctly, a transparent stage in transparent mode has to be able to detect when it should switch to clocked mode and when to switch back. The clocked mode should be entered when it is necessary to separate two or more data items propagating concurrently through the transparent stages of the pipeline. Otherwise, a transparent stage will operate in its transparent mode.

For a transparent stage s_i, there are two necessary conditions under which s_i has to enter clocked mode to separate data items in the transparent pipeline [3]. First, there is a valid data item present at the input of s_i. Second, there is another valid data item present at the input of any transparent stage upstream of s_i or present at the input of the outside environment. In circuit implementation, the first condition can be detected by feeding the input valid signal of the elastic buffer control (EBC) unit
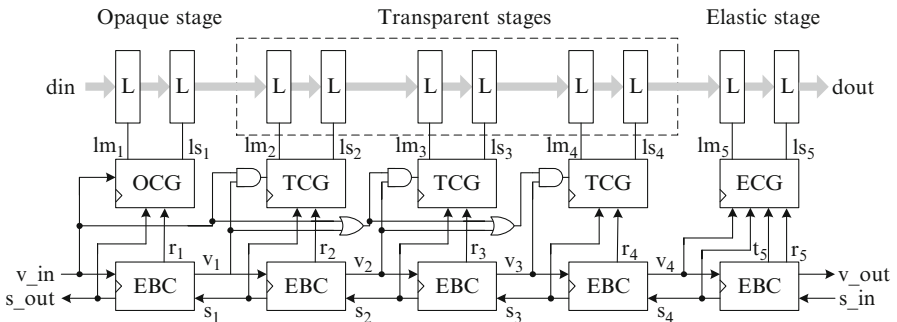
Fig. 3 Five-stage elastic transparent pipeline
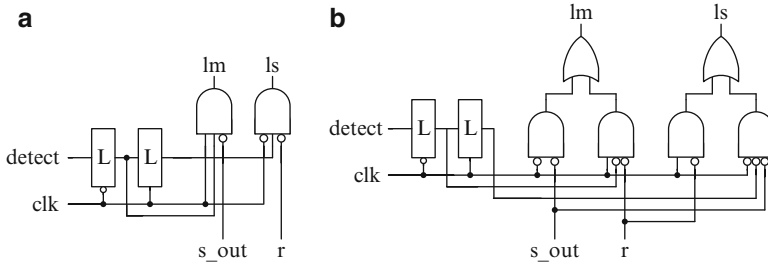
Fig. 4 (**a**) Opaque clock generation (OCG) unit of the opaque stage. (**b**) Transparent clock generation (TCG) unit of the transparent stage

of s_i into the corresponding transparent clock generation (TCG) unit, as shown in Fig. 3. For the second condition, it can be detected by feeding the input valid signal of each EBC unit upstream of s_i, through a series of OR gates, into the TCG unit of s_i. Since the two conditions have to be satisfied at the same time to switch to clocked mode, an AND gate is used here to serve the purpose.

The implementations of the opaque clock generation (OCG) unit and transparent clock generation (TCG) unit are given in Fig. 4a, b, respectively. Both of them contain one master and one slave latch internally for generating the clock-gated signals lm and ls. When the first opaque stage in Fig. 3 is in opaque mode, lm and ls are gated in a logic-low state, whereas when the transparent stage is in transparent mode, they are gated in a logic-high state to make the corresponding data latchestransparent. When the opaque stage switches to clocked mode for data latching, a positive pulse should be generated on lm and, after half a clock cycle, another positive pulse should also be generated on ls to latch the incoming data item. Similarly, when the transparent stage switches to clocked mode, a negative pulse should be generated on lm and then, after half a clock cycle, another negative pulse should also be generated on ls to latch data travelling through the transparent stages.

4 Experimental Results

The architecture of the proposed elastic transparent pipeline was implemented by the Verilog HDL and synthesized with Altera Quartus II 9.0. The experimental circuit was a five-stage pipeline with three internal transparent stages. Figure 5 shows the timing simulation result of this pipeline, which was simulated on the FPGA device Stratix III EP3SL50F484C2. For the four data items entering the pipeline, the number of clock pulses required to clock the data latch is four for the first and last pipeline stages. However, it takes only one, two, and three clock pulses for the second, third, and fourth transparent stages, respectively. For a five-stage traditional synchronous counterpart, the number of pulses for data latching is four for each
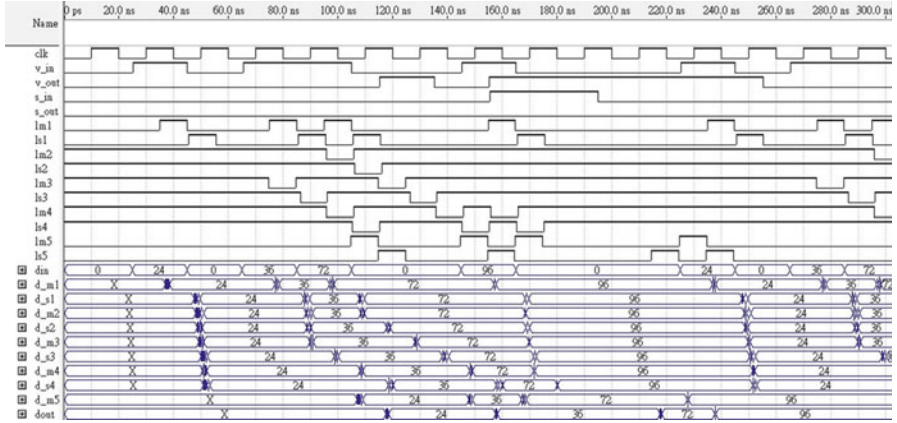
Fig. 5 Timing simulation waveform of a five-stage elastic transparent pipeline

Table 1 Comparisons of the three five-stage pipeline architectures

Design	Max. working freq. (MHz)	Combinational ALUTs	Registers	Dynamic power dissipation (mW)	Static power dissipation (mW)
[3]	125.0	19	5	50.02	377.96
[6]	80.0	26	0	38.33	386.01
Ours	66.6	35	0	4.74	380.87

stage. It is evident that the amount of clock pulses can be reduced by using the transparent pipelining technique. On the other hand, the simulation result also shows the property of synchronous elasticity since the data item 36 is stalled in the pipeline for two clock cycles due to the incoming stall signal *s_in*.

For the five-stage pipeline example, two other architectures, transparent pipeline [3] and elastic pipeline [6], were also implemented for comparison. Table 1 gives the experimental report of each design. The maximum working frequency of each design is given in the second column. For area comparison, only the control part of each design was compared, not including the same 32-bit data path. The comparison results are represented as combinational ALUs and registers in the third and fourth columns, respectively. The fifth and last columns show the comparisons of dynamic and static power dissipation, respectively, which were measured by running the data patterns in Fig. 5 for 1,000 clock cycles. As the table shows, by making an elastic pipeline [6] transparent, the dynamic power dissipation can be reduced from 38.33 to 4.74 mW at the expense of slower working frequency and larger circuit area in the control part. However, when the 32-bit data path is taken into consideration in a realistic pipelined circuit, the area overhead due to transparency will contribute only a small part to the whole design.

5 Conclusion

In this chapter, the concept of synchronous elasticity has been incorporated into the design of a transparent pipeline. By the transparent properties, the design can achieve clock power saving by reducing the amount of clock pulses required for data latching. By the synchronous elastic properties, the design can provide tolerance to variations in computation and communication delays. Finally, the timing simulation results have also shown the power efficiency of the proposed architecture.

References

1. Benini L, De Micheli G (1996) Automatic synthesis of low-power gated-clock finite-state machines. IEEE Trans Comput-Aided Des Integr Circuits Syst 15(6):630–643
2. Wu Q, Pedram M, Wu X (2000) Clock-gating and its application to low power design of sequential circuits. IEEE Trans Circuits Syst I Fundam Theory Appl 47(103):415–420
3. Jacobson HM (2004) Improved clock-gating through transparent pipelining. In: International symposium on low power electronics and design (ISLPED), Newport Beach, 2004, pp 26–31
4. Hill EL, Lipasti MH (2007) Transparent mode flip-flops for collapsible pipelines. In: 25th international conference on computer design (ICCD), Lake Tahoe, 2007, pp 553–560
5. Choi J-H, Kim B-G, Dasgupta A, Roy K (2010) Improved clock-gating control scheme for transparent pipeline. In: 15th Asia and South Pacific design automation conference (ASP-DAC), Taipei, pp 401–406
6. Carmona J, Cortadella J, Kishinevsky M, Taubin A (2009) Elastic circuits. IEEE Trans Comput Aided Des Integr Circuits Syst 28(10):1437–1455
7. Cortadella J, Galceran-Oms M, Kishinevsky M (2010) Elastic systems. In: 8th IEEE/ACM international conference on formal methods and models for codesign (MEMOCODE), Grenoble, 2010, pp 149–158
8. Casu MR (2011) Half-buffer retiming and token cages for synchronous elastic circuits. IET Comput Digit Tech 5(4):318–330

The Wireless Electric Guitar with Digitally Integrated Effector

Chun-Tang Chao, Kuo-An Li, and Nopadon Maneetien

Abstract This chapter presents the design and implementation of a wireless electric guitar with digitally integrated effector. Wireless audio modules are first employed so that electric guitar players no longer have to worry about stumbling on the stage. Furthermore, in a traditional analog way, electric guitar players may face many different kinds of effectors, such as distortion, flanger, and reverberation. It is hard for players to control them by pedals. The digitally integrated effectors are proposed and implemented by DE2-70 Multimedia Development Board. Finally, a little radio transmitter with multiple keys is equipped on the electric guitar such that the players can easily select the desired audio effect.

Keywords Wireless electric guitar • Effectors • DE2-70

1 Introduction

Compared to the classical guitar and acoustic guitar, electric guitar with powerful sound attracts a lot of young music fans [1]. The reason why electric guitar can capture the tone played is because of the magnetic pickup installed in it. The people familiar with the electric guitar often need to purchase many effects to make the sound effect more vivid. Figure 1 shows some single electric guitar effects.

Due to the inconvenience of the single effect, there is the advent of integrated effect, shown in Fig. 2. But it is bulky and must be controlled by pedal or button. For the guitar players, it is still not easy for them to do real-time manipulation. In this paper, we hope to improve these missing by applying modern digital technology.

C.-T. Chao (✉) • K.-A. Li • N. Maneetien
Department of Electrical Engineering, Southern Taiwan University of Science and Technology, Tainan 71005, Taiwan
e-mail: tang@mail.stust.edu.tw

Fig. 1 Single electric guitar effects, delay, flanger, and echo (*left to right*)

Fig. 2 Electric guitar analog integrated effects

Currently, only few researches have been on this topic [2]. On the other hand, there have been a lot of international researches on guitar effects [3–8]. This paper tries to use Altera DE2-70 to finish wireless electric guitar with integrated digital effects.

2 System Description

The FPGA-based digital integrated system will be first introduced. Then some topics such as wireless audio transmission, radio code transmission, and digitally integrated effectors will be described in subsections.

2.1 FPGA-Based Digital Integrated System

Figure 3 shows the wireless electric guitar system blocks. The Altera DE2-70 board is used to finish to DSP (digital signal processing), ADC, and DAC functions.
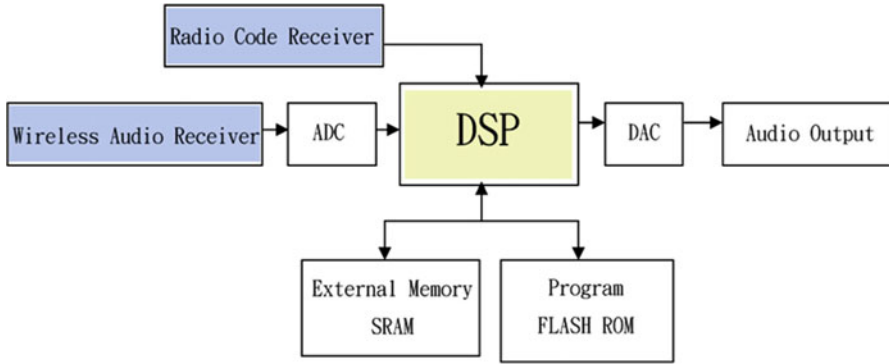
Fig. 3 The wireless electric guitar system blocks

Fig. 4 The 2.4 GHz wireless audio transmitter

2.2 Wireless Audio Transmission

To make the electric guitar wireless, we should eliminate the wire from guitar to speaker in the first step. In order to accelerate the realization of the creative concept in this paper, we directly use a commercially available Waveconn 2.4 GHz wireless stereo headphone and modify it. Figure 4 shows the 2.4 GHz wireless audio transmitter.

The corresponding and modified 2.4 GHz wireless audio receiver is shown in Fig. 5.

Before the receiver in Fig. 5 is connected to the DE2-70, the proposed preamplifier and anti-aliasing filter circuit is required (Fig. 6). It is worth mentioning that the operating amplifier design uses single power [10, 11].
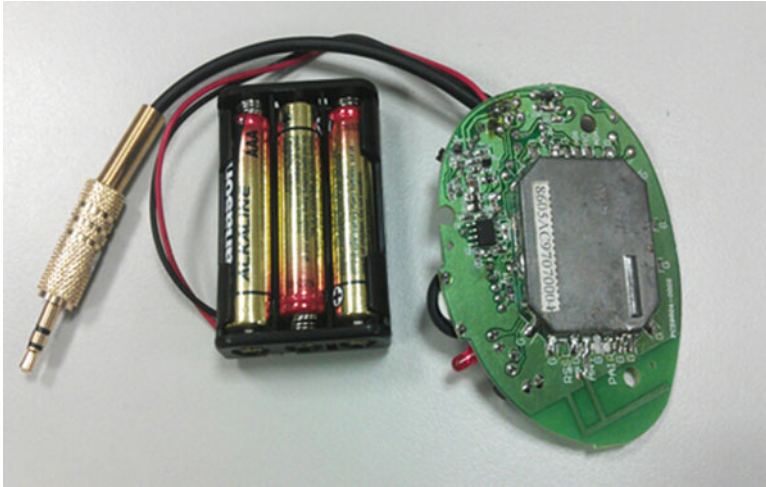
Fig. 5 The 2.4 GHz wireless audio receiver
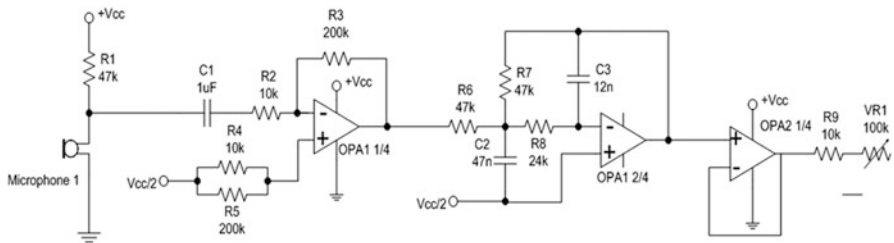
Fig. 6 Preamplifier and anti-aliasing filter circuit

2.3 Radio Code Transmission

To save development time, the applied radio code transmitter and receiver in Fig. 7 are also commercially available.

2.4 Digitally Integrated Effectors

In the subsection, some effects in the proposed system are discussed.

2.4.1 Flange Effect

Flange effect is like chorus, the difference is that the delay for flange is about 0–35 ms, while the delay for chorus is about 35–50 ms. To combine both flange and
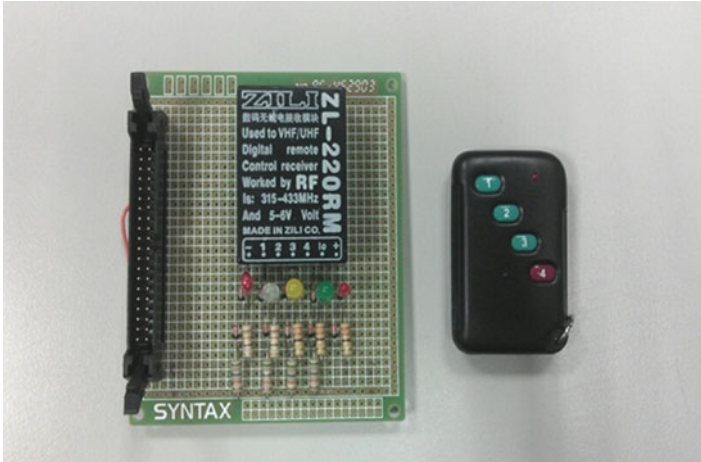
Fig. 7 Radio code transmitter and receiver (*right and left*)
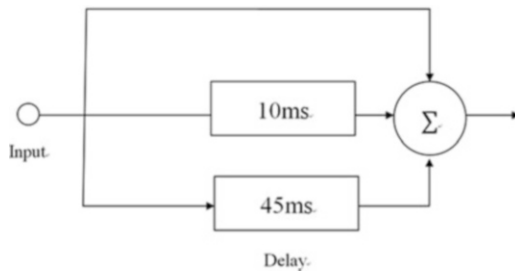
Fig. 8 Block diagram of Flange effect

chorus effect, we try to finish the system difference equation in (1) and its schematic diagram is shown in Fig. 8.

$$y[n] = x[n] + x[n - 128] + x[n - 768] \tag{1}$$

2.4.2 Reverberation Effect

This effect is similar to echo effect. The filter in (2) can produce "onefold echo" for the given input signal. If the sample frequency fs is 16 kHz, then the time difference between the input and the echo will be about 0.1 s:

$$y[n] = x[n] + 0.8 * x[n - 1,600] \tag{2}$$

To produce a more realistic "multiple-fold" echo [13], (2) can be modified as (3). The original FIR type in (2) becomes IIR type in (3):
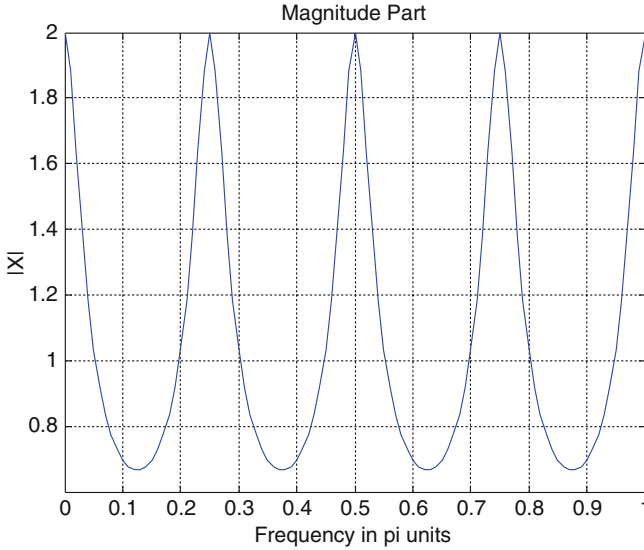
Fig. 9 Frequency gain response of digital comb filter

$$y[n] = x[n] + 0.8 * y[n - 1, 600] \tag{3}$$

The resulting Z transfer function is shown in (4), a so-called comb filter:

$$H(z) = \frac{1}{1 - 0.8z^{-1,600}} \tag{4}$$

Figure 9 shows a frequency gain response of digital comb filter with 8 time delay units.

To make the reverberation effect more apparent in software simulation, the echo effect in (2), (3) and (4) is modified from 0.1 to 0.5 s, and the feedback gain in (2), (3) and (4) is modified from 0.8 to 0.6. A 0.6 s short music is used as input, and the resulting output is shown in Fig. 10 in Matlab simulation.

2.4.3 Distortion Effect

When a sinusoid signal is taken as input of a clipping circuit, a severe distortion will occur and the resulting output is like a square wave. For auditory effect, it makes the original soft sound become rude. This sound effect can be thought as the most important one for some electric guitar players.

Before writing FPGA programs, the Matlab simulation can be applied to verify the distortion function. Figure 11a shows an input signal with hybrid frequency of 100 and 200 Hz; Fig. 11b is the resulting output.
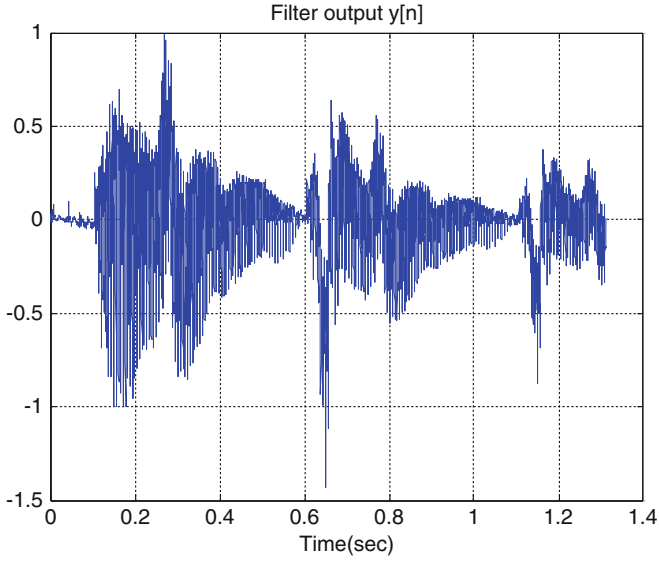
Fig. 10 Short music output by the reverberation effect
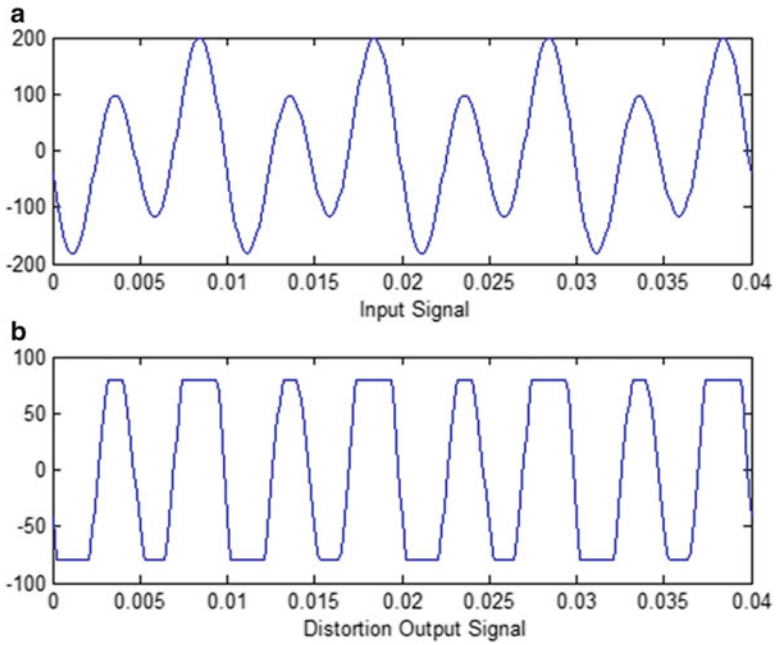
Fig. 11 The I/O of distortion effect

Fig. 12 The wireless electric guitar with digitally integrated effector

Figure 12 shows the implementation of the wireless electric guitar with digitally integrated effector. In the electric guitar body, there are wireless audio transmitter and radio code transmitter. On the other hand, the FPGA DE2-70 is connected to wireless audio receiver and radio code receiver.

3 Conclusions

This paper has implemented a wireless electric guitar with digitally integrated effectors. First, the wireless audio modules are employed to transmit electric guitar music. Secondly, the digitally integrated effectors are presented so that electric

guitar players do not need to face messy wires and many different kinds of effectors, such as distortion, flanger, and reverberation. The DE2-70 board is applied as the core processor. Finally, to make the electric guitar players select the desired audio effect in an easier and quicker way, a small radio code transmitter with keypads is mounted on the edge of electric guitar. Based on the proposed prototype system, the integrated digital effector with more practical effectors will be investigated in the future.

References

1. Tony Bacon, Dave Burrluck, Paul Day (2000) Electric guitars: the illustrated encyclopedia. Thunder Bay Press, San Diego
2. Li-Wei Hsiao (2010) Effect recognition and delay estimation for a guitar effector, Master thesis, National Taiwan University, Taipei
3. Kyungjin Byun, Nak-Woong Eum, Hee-Bum Jung, Koang-Hui Jeong, Jae-Eul Koo (2011) Development of portable sound effector. In: IEEE international conference on multimedia and expo (ICME), Barcelona, 2011
4. Jon Dattorro (1997) Effect design – part 1: reverberator and other filters. J Audio Eng Soc 45(9):660–684
5. Jon Dattorro (1997) Effect design – part 2: delay-line modulation and chorus. J Audio Eng Soc 45(10):764–788
6. Navarun Jagatpal, Fred Rassam, Young Jin Yoon, Elton Chung (2007) Guitar effects. http://www.scribd.com/doc/60888725/Guitar-Effects
7. Khan ARM, Thakare AP, Gulhane SM (2010) FPGA-based design of controller for sound fetching from codec using Altera DE2 Board. Int J Sci Eng Res 1(2):1–8
8. Verfaille Vincent, Zolzer Udo, Arfib Daniel (2006) Adaptive Digital Audio Effects (A-DAFx): a new class of sound transformations. IEEE Trans Audio Speech Lang Process 14 (5):1817–1831
9. Chirkal Technology CO., LTD., http://www.chirkal.com.tw/
10. Texas Instruments (2000) A single-supply op-amp circuit collection. Application report, SLOA058
11. Texas Instruments (2000) Active low-pass filter design. Application report, SLOA049A
12. Joyce Van de Vegte (2002) Fundamentals of digital signal processing. Pearson Education, Upper Saddle River
13. Jyh-Shing Roger Jang, Audio signal processing and recognition. Available at the links for on-line courses at the author's homepage at http://www.cs.nthu.edu.tw/~jang

Implementation and Study of Constant-Frequency LLC Resonant Converter

Shi-Yi Lin, Shih-Kuen Changchien, Chien-Ming Hong, and Yi-Nung Chung

Abstract This chapter presents an LLC resonant converter with constant frequency. Since LLC resonant converters possess the advantages of high efficiency and low electromagnetic interference, they are widely used in many applications. However, the EMI filter design becomes more complex because of the variable-frequency operation of LLC resonant converter. Therefore, in this chapter, a circuit configuration of a buck converter cascade an LLC resonant converter, buck-fed LLC resonant converter, is proposed to complete constant-frequency operation and simplify the EMI filter design. The buck converter is applied in the proposed converter as the input source for the LLC resonant converter. In addition, by adjusting the output voltage of the buck converter, the output regulation and constant-frequency operation of the proposed converter can be achieved. Finally, a prototype of the buck-fed LLC resonant converter with input voltage 380–400 V and output 24 V/10 A is implemented. The experimental results demonstrate the feasibility of the proposed converter.

Keywords Constant frequency • EMI filter • LLC resonant converter • Cascade • Buck-fed LLC resonant converter

S.-Y. Lin • Y.-N. Chung (✉)
Department of Electrical Engineering, National Changhua University of Education, Changhua 50007, Taiwan
e-mail: ynchung@cc.ncue.edu.tw

S.-K. Changchien
Department of Automation Engineering and Institute of Mechatronoptic Systems, Chienkuo Technology University, Changhua 50007, Taiwan

C.-M. Hong
Department of Electrical Engineering, Chienkuo Technology University, Changhua 50007, Taiwan

1   Introduction

DC-DC converters are commonly applied in many applications with constant-frequency operation. However, the greater switching loss and series electromagnetic interference (EMI) are the main drawbacks. Because of high efficiency, soft-switching, and sinusoidal voltage and current of the power paths, LLC resonant converters are widely used in many power conversion applications, such as PC power, LCD TV power, and LED backlight [1–4]. Generally, LLC resonant converters are operated with variable switching frequency to meet the output requirements [5]. However, base on variable-frequency operation, the EMI filters are relatively difficult designed for suppressing the harmonic and the electromagnetic interference noise of LLC resonant converters. As operation frequency range with load change and the operation frequency is lower in full load that LLC resonant converters make bigger in volume. Moreover, the higher switching frequency is necessary to LLC resonant converters for output requirements under no load or light load that the output voltage cannot be effectively regulated.

Several researchers proposed to discuss DC-DC resonant converters with constant frequency [6–8]. Agrawal proposed LLC series resonant converter (LLC-SRC) for more detailed analyses under constant frequency, but they were restricted in mathematical deduction and simulation, rather than actual designs to verify such a theory [9]. A lot of literatures discussed the applications of two-stage or multistage LLC resonant converters to multi-output, high-power, and high-efficiency power converter [10–12]. Some researchers also utilized a buck converter as the front stage, reducing the input voltage and regulating the output voltage to supply the second-stage circuit load for a half-bridge converter with synchronous rectifier [13].

Due to the constant-frequency operation for the LLC resonant converter, the design of EMI filter is regarded simpler. This study therefore proposes a two-stage LLC resonant converter with constant-frequency operation. The proposed constant-frequency LLC resonant converter named buck-fed LLC resonant converter is the combination of two power converters which are a buck converter and an LLC resonant converter. The cascade of the buck converter and LLC resonant converter regulates the output voltage of front-stage buck converter to be the input voltage of second-stage LLC resonant converter for achieving output regulation and constant-frequency operation.

2   Buck-Fed LLC Resonant Converter

Figure 1 shows the proposed constant-frequency LLC resonant converter, in which the front stage and the second stage are buck converter and LLC resonant converter, respectively. The buck converter is applied in the proposed converter as the input source for the LLC resonant converter to achieve the output regulation and constant-frequency operation of the proposed converter. In addition, the switching
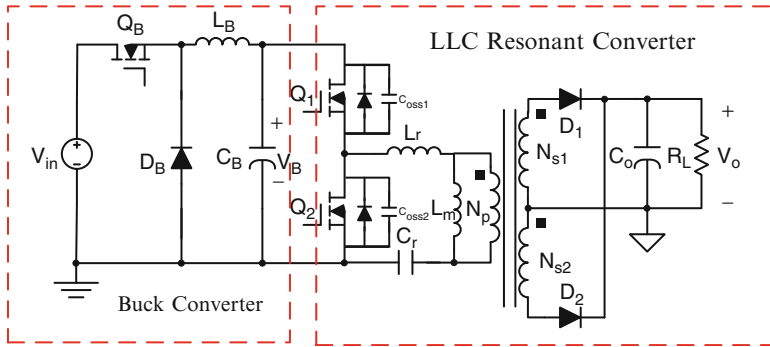
Fig. 1 Buck-fed LLC resonant converter
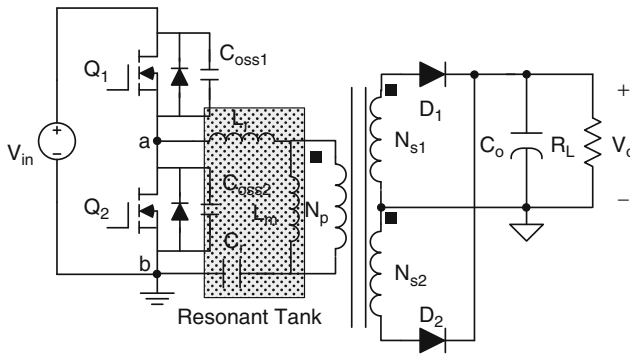
Fig. 2 LLC resonant converter

frequency, a constant frequency with dead time, is selected for LLC resonant converter. The output of the buck converter is adjusted by sampling and feedback of the proposed converter output voltage to achieve system stability and constant-frequency operation.

Figure 2 shows the LLC resonant converter, the second stage of the proposed converter. The resonant tank is a combination of magnetizing inductance on transformer primary side, L_m, resonant inductor, L_r, and resonant capacitor, C_r. The voltage and current of the power switches present sinusoid through resonance of the resonant tank components; therefore, zero voltage and zero current switching on power switches are completed during dead-time period.

According to [14, 15], the equivalent circuit model of LLC resonant converter is shown in Fig. 3. From this circuit model, the voltage gain of the output v_p and input v_{ab} can be obtained as follows:

$$G(j\omega) = \frac{v_p}{v_{ab}} = \frac{j\omega L_m / n^2 R_L}{j\omega L_r + \frac{1}{j\omega C_r} + (j\omega L_m / n^2 R_L)} \tag{1}$$
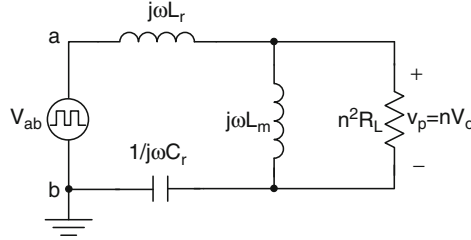
Fig. 3 Equivalent circuit model of LLC resonant converter
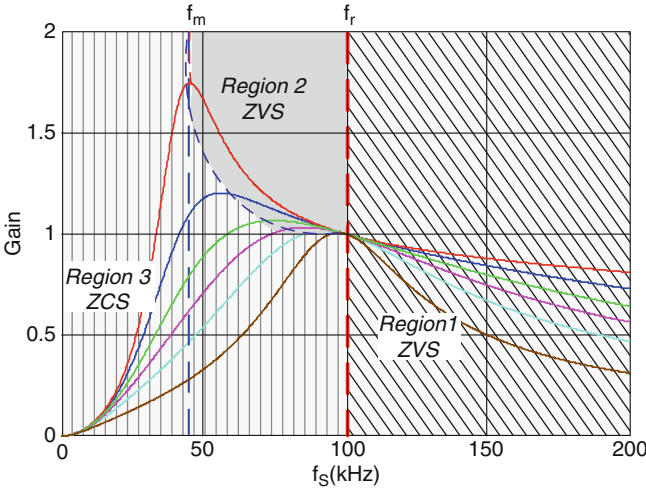
Fig. 4 Voltage gain of LLC resonant converter versus operation frequency

From Eq. (1), the voltage gain of LLC resonant converter can be derived as

$$|G(j\omega)| = \frac{1}{\sqrt{\left[\left(\frac{f_r^2}{f_m^2} - \frac{f_r^2}{f_s^2}\right) \cdot \frac{1}{k}\right]^2 + \left[Q_r \cdot \left(\frac{f_s}{f_r} - \frac{f_r}{f_s}\right)\right]^2}} \tag{2}$$

where $f_r = \dfrac{1}{2\pi\sqrt{L_r C_r}}$, $f_m = \dfrac{1}{2\pi\sqrt{(L_r + L_m)C_r}}$, $Q_r = \dfrac{\sqrt{L_r/C_r}}{n^2 \cdot R_L}$, and $k = \dfrac{L_m}{L_r}$.

Apparently, C_r, L_r, L_m, n, and R_L are the relevant parameters in the voltage gain of LLC resonant converter. From Eq. (2), the voltage gain of LLC resonant converter versus operation frequency can be shown in Fig. 4, where LLC resonant converter contains two resonant frequencies. Moreover, the first resonant frequency f_r is determined by L_r and C_r, and the second resonant frequency f_m is determined by L_m, L_r, and C_r.

From Fig. 4, the voltage gain and the two resonant frequencies could be divided into three regions. *Region 1* is the right half plane of f_r, the voltage gain less than 1,

and *Region 2* is between f_{r} and f_{m}, the voltage gain larger than 1. Such two regions are inductive zero voltage switching (ZVS) regions with lagging voltage, suitable for circuits with high voltage and low current. *Region 3* is the left half plane of f_{m}, the capacitive zero current switching (ZCS) region with leading voltage, suitable for circuits with high voltage and high current. This study proposes the high-voltage and low-current diagram that the transformer primary resonant components, dead time t_{d}, and output power P_{o} are the zero voltage switching condition in *Region 1*. As a result, general design of LLC resonant converter is operated in *Region 2*, with the zero voltage switching condition being the transformer primary resonant components and t_{d}, without considering the output power. The design of LLC resonant converter in this study is therefore operated in *Region 2*.

From Fig. 1, the relation between the output voltage V_{o} of LLC resonant converter and the output voltage V_{B} of the buck converter reveals

$$V_{\mathrm{o}} = \frac{V_{\mathrm{B}}\eta|G(j\omega)|}{2n} \tag{3}$$

when η is the efficiency of the front-stage buck converter.

$f_{\mathrm{r}}, f_{\mathrm{m}}, f_{\mathrm{s}}, V_{\mathrm{o}}$, and n are constants because the front stage and the second stage are operated under fixed frequencies; then Eq. (3) is shown as

$$V_{\mathrm{B}} = \frac{2nV_{\mathrm{o}}}{\eta} \cdot \sqrt{\left[\frac{4\pi^2(L_{\mathrm{r}}+L_{\mathrm{m}})C_{\mathrm{r}}f_{\mathrm{s}}^2 - 1}{4\pi^2 L_{\mathrm{r}}C_{\mathrm{r}}f_{\mathrm{s}}^2 k}\right]^2 + \left[\frac{\sqrt{L_{\mathrm{r}}/C_{\mathrm{r}}} \cdot V_{\mathrm{o}}}{n^2 I_{\mathrm{o}}}\left(\frac{\left(2\pi\sqrt{L_{\mathrm{r}}C_{\mathrm{r}}}f_{\mathrm{s}}\right)^2 - 1}{2\pi\sqrt{L_{\mathrm{r}}C_{\mathrm{r}}}f_{\mathrm{s}}}\right)\right]^2} \tag{4}$$

where $f_{\mathrm{r}}, f_{\mathrm{m}}, f_{\mathrm{s}}, V_{\mathrm{o}}$, and n are constants.

From Eq. (4), the larger I_{o} appears, the smaller V_{B} presents that the relations between the output of buck converter V_{B} and the output current I_{o} are acquired.

Figure 5 shows the relations between the output power of the proposed converter and the variation of V_{B}. With the design of $L_{\mathrm{r}}, C_{\mathrm{r}}, L_{\mathrm{m}}$, and f_{s}, the adjusted voltage, V_{B}, from no load to full load is restricted in the proper range for the design of front stage. According to the figure, the input voltage increases with the larger output power that the change of load is also controlled by the adjusted voltage, V_{B}.

3 Circuit Design and Experimental Results

In order to verify the feasibility of the proposed constant-frequency LLC resonant converter, the experimental results of the prototype buck-fed LLC resonant converter with input voltage 380–400 V and output 24 V/10 A is implemented to demonstrate the performances of the proposed converter.

Fig. 5 Output voltage of the buck converter versus output power
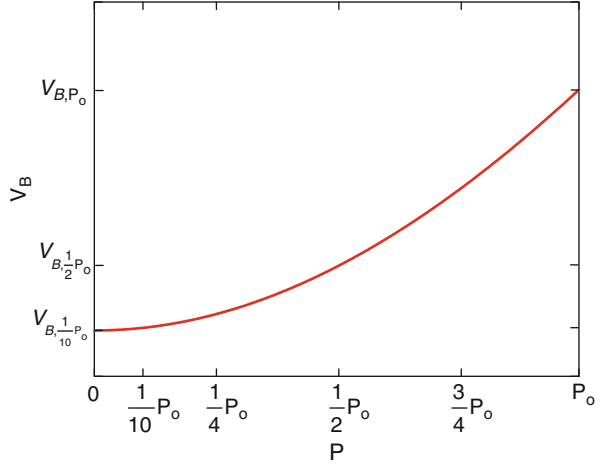
Table 1 Specifications of the buck converter

Parameters	Specifications
Input voltage, V_{in}	380–400 V
Output voltage, $V_{B, max}$	230 V
Output current, I_B	1.2 A
Maximum output power, $P_{B, max}$	280 W
Ripple current, ΔI_{LB}	0.6 A
Ripple voltage, ΔV_B	50 mV
Switching frequency, f_B	100 kHz

Table 2 Specifications of the LLC resonant converter

Parameters	Specifications
Maximum input voltage, V_{in}	230 V
Output voltage, V_o	24 V
Output power, P_o	240 W
Turns ratio, n	4
Switching frequency, f_s	100 kHz
Resonant frequency, f_r	80 kHz

3.1 Specifications of the Prototype Converter

The circuit specifications utilized for the verification of constant-frequency LLC resonant converter are shown below.

The specifications of front stage, the buck converter, are listed in Table 1. The specifications of second stage, the LLC resonant converter, are shown in Table 2.

3.2 Design of the Prototype Constant-Frequency LLC Resonant Converter

The component design for continuous conduction mode (CCM) is presented as follows:

1. Determine the maximum duty cycle.
   The duty cycle in DC-DC converters is not restricted. Actually, the switching capability of the switch should be taken into account, in which the maximal range of the duty cycle is 0.05–0.95. Comparison with current mode and voltage mode PWM control, the maximum duty cycle is less than 0.5, or the slope compensation is required for current mode PWM control. Such a restriction does not appear for voltage mode PWM control. With the change of input voltage, the maximum duty cycle is acquired as

$$D_{\max} = \frac{V_{\mathrm{B}}}{V_{\mathrm{in,min}}} \tag{5}$$

2. Determine the boundary condition and design the inductance.
   The variation of load, inductance, and switching frequency would affect the operation of DC-DC converters in continuous conduction mode or discontinuous conduction mode (DCM). The inductance and switching frequency are generally set constant values that the load is regulated for the operation mode.

   In terms of the operation in CCM, Eq. (6) is the design of inductance L_{B}:

$$L_{\mathrm{B}} > \frac{V_{\mathrm{o}}T_{\mathrm{B}}}{\Delta I_{\mathrm{LB}}}(1 - D_{\max}) \tag{6}$$

   where T_{B} is the period of the selected switching frequency and ΔI_{LB} is the current ripple of the inductance. To ensure the converter operating in CCM, the inductance, L, is slightly larger than the boundary in practice.

3. Output capacitor selection.
   The inductance in CCM is calculated by Eq. (6). Equation (7) calculates the output capacitance. Equations (8) and (9) show the calculation of the equivalent series resistance (ESR) and the current rating of the output capacitor:

$$C_{\mathrm{o}} = \frac{T_{\mathrm{B}}^{2}V_{\mathrm{B}}}{8L\Delta V_{\mathrm{B}}}(1 - D_{\max}) \tag{7}$$

   where ΔV_{o} is the output ripple voltage; then ESR and ΔI_{LB} are

$$\mathrm{ESR}_{\max} \leq \frac{\Delta V_{\mathrm{B}}}{\Delta I_{\mathrm{LB}}} \tag{8}$$

$$I_{\mathrm{C,\,rms}} = \frac{\Delta I_{\mathrm{LB}}}{2\sqrt{3}} \tag{9}$$
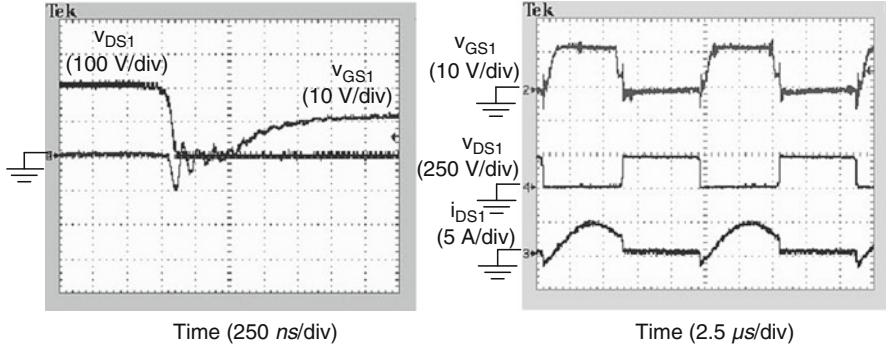
Fig. 6 Experimental results of power switch Q_1 under full-load condition

4. The selection of the power switch and diode.

   (a) Selection of power switch

      The voltage across power switch ($V_{DS} > V_{in, max}$), the current of power switch ($I_{DS} > I_{o,max}/n + \Delta I_{LB}/2$), parasitic capacitance C_{oss}, and on-state-resistance $R_{DS(on)}$ should be considered for the power MOSFET selection, where Δ_{iL} is the output ripple current.

   (b) Selection of diode

      Diode is required for delivering load through the current path that the voltage ($V_D > V_{in, max}/n + V_o$) and the current ($I_D > I_{peak} = I_{o, max} + n\Delta I_{LB}/2$) of the power diode should be considered.

3.3 Experimental Result

In the prototype of the buck converter, $L_B = 1.5$ mH, $C_B = 100$ μF, and $D_{max} = 0.61$ are adopted to implement the front stage. Also, IRF460 and STTH8R06 are applied for the power MOSFET and output diode, respectively. Besides, for the LLC resonant converter, $L_m = 160$ μH, $L_r = 32$ μH, and $C_r = 110$ nF are employed to implement the second stage. IRF460 and MBR20H200CT are used for the power MOSFETs and output diodes, respectively.

    Figure 6 shows the waveforms of v_{GS1}, v_{DS1}, and i_{DS1} of the power switch Q_1 in full load, in which Q_1 does not appear to have switching loss, achieving the zero voltage switching.

    Figure 7 shows the waveforms of v_{GS2}, v_{DS2}, and i_{DS2} of the power switch Q_2 in full load, in which Q_2 also does not reveal switching loss and the zero voltage switching is achieved.

    Figure 8 presents the waveforms of resonant capacitor voltage V_{Cr} and resonant inductor current i_{Lr}, in which resonant inductor current i_{Lr} equals to magnetizing inductance current i_{Lm} in dead time t_d that there is no current in the transformer
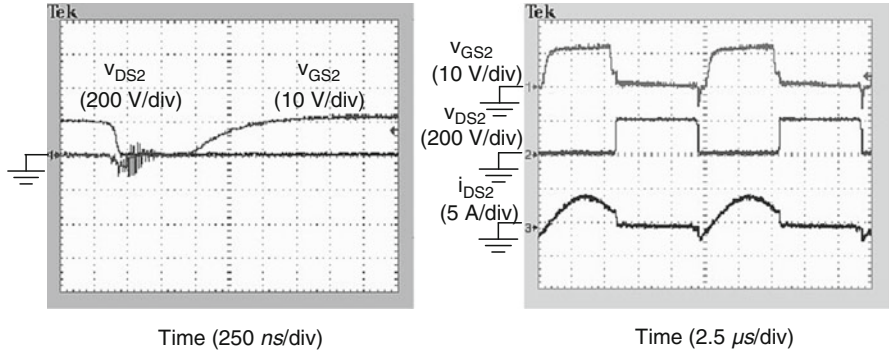
Fig. 7 Experimental results of power switch Q_2 under full-load condition
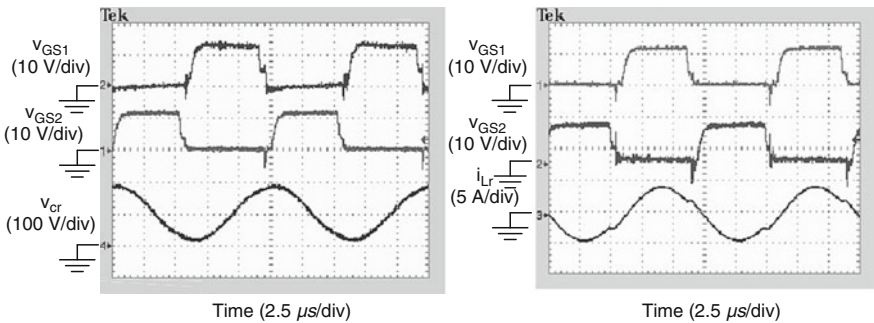
Fig. 8 Experimental results of V_{Cr} and i_{Lr} under full-load condition
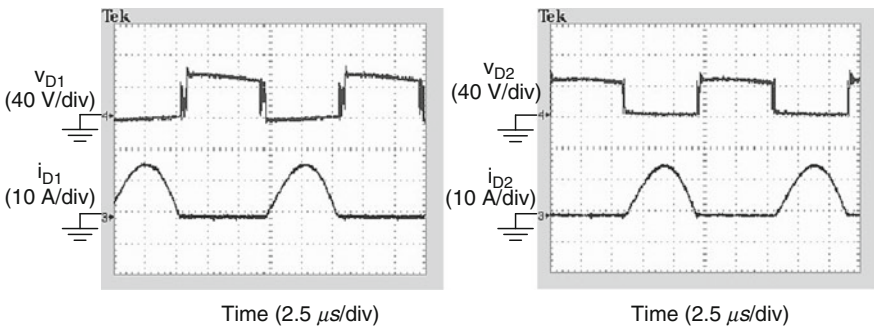
Fig. 9 Experimental results of v_{D1}, v_{D2} and i_{D1}, i_{D2} under full-load condition

primary current i_p, the transformer is open, and no energy is delivered to the secondary. As a result, there is no current in secondary diode current i_{D1} and i_{D2} and the zero current switching is achieved.

Figure 9 shows the waveforms of the secondary diode voltage stresses (v_{D1} and v_{D2}) and currents (i_{D1} and i_{D2}). When Q_1 or Q_2 is induced, i_{D1} and i_{D1} achieve the zero current switching.

Table 3 Measured data of the proposed converter

V_{in} (V)	I_{in} (A)	V_o (V)	I_o (A)	P_{in} (W)	P_o (W)	η (%)	V_B	D
400	0.08	24	1	32	24	75.0	197	0.49
400	0.15	24	2	60	48	80.0	202	0.51
400	0.21	24	3	84	72	85.7	207	0.52
400	0.28	24	4	112	96	85.7	211	0.53
400	0.35	24	5	140	120	85.7	214	0.54
400	0.41	24	6	164	144	87.8	219	0.55
400	0.48	24	7	192	168	87.5	222	0.56
400	0.55	24	8	220	192	87.3	224	0.56
400	0.62	24	9	248	216	87.1	227	0.57
400	0.70	24	10	280	240	85.7	229	0.57
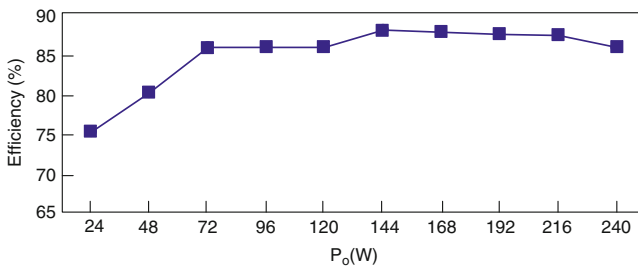
Fig. 10 Efficiency of the proposed converter versus output power

Also, from Figs. 6, 7, 8, and 9, the switching frequency of the LLC resonant converter can be seen at 80 kHz. Table 3 shows the measured data of the proposed buck-fed LLC resonant converter, where V_B is the output voltage and D is the duty cycle of buck converter. From Table 3, the relations between the output power and the efficiency can be revealed in Fig. 10. From Table 3 and Fig. 10, when the power is 144 W ($V_o = 24$ V, $I_o = 6$ A), the efficiency appears 87.8 %, while the efficiency reveals 85.7 % under the full load, 240 W ($V_o = 24$ V, $I_o = 10$ A).

4   Conclusion

A constant-frequency buck-fed LLC resonant converter is presented in this chapter. The cascade of the buck converter and the LLC resonant converter is used to regulate the output voltage of front-stage buck converter to be the input voltage of second-stage LLC resonant converter for achieving output regulation and constant-frequency operation. A 240 W ($V_o = 24$ V, $I_o = 10$ A) buck-fed LLC resonant converter is finally implemented. The experimental waveforms demonstrate that ZVS and ZCS of the power switches can be achieved for reducing the switching loss. According to the measured results, when the power is 144 W ($V_o = 24$ V, $I_o = 6$ A), the efficiency appears 87.8 %, while the efficiency reveals 85.7 % under the full load.

References

1. Erickson RW, Maksimovic D (2001) Fundamental of power electronics. Kluwer Academic Pub, Norwell
2. Mohan N, Undeland T, Robbins W (1995) Power electronics. Wiley, New York
3. Pressman AI (1991) Switching power supply design. McGraw-Hill, New York
4. Severns RP (1985) Modern dc-to-dc switchmode power converter circuits. Van Nostrand Reinhold Company, New York
5. Yang B (2003) Topology investigation of front-end DC-DC converter for distributed power system. Dissertation of Virginia Polytechnic Institute and State University, Blacksburg
6. Jain P, Sion H, Cardella M (1994) A constant frequency resonant DC/DC converter with zero switching loses. IEEE Trans Aerosp Electron Syst 30:534–544
7. Lee CQ, Sooksatra S, Liu R (1991) Constant frequency controlled full-bridge LCC-type parallel resonant converter. In: 16th annual conference of IEEE applied power electronics conference and exposition, pp 587–593
8. Glaser JS, Witulski AF, Myers RG (1994) Steady-state analysis of the constant-frequency clamped series resonant converter. IEEE Trans Aerosp Electron Syst 30:135–143
9. Sin K, Lee CQ (1989) Constant switching frequency LLC-type series resonant converter. In: 32nd midwest symposium on IEEE circuits and systems, Champaign, 1989, vol 1, pp 513–516
10. Liu R, Lee CQ, Upadhyay AK (1991) Experimental study of the LLC-type series resonant converter. In: 6th annual conference of IEEE applied power electronics conference and exposition, pp 31–37
11. Jin K, Ruan X (2006) Hybrid full-bridge three-level LLC resonant converter-a novel DC–DC converter suitable for fuel-cell power system. IEEE Trans Indus Electron 53(5):1492–1503
12. Ang Y, Bingham CM, Foster MP, Stone DA (2007) Modelling and regulation of dual-output LCLC resonant converters. In: 33rd annual conference of the IEEE. Industrial Electronics Society, Taipei, 2007, pp 2130–2135
13. Wu CM (2004) Study of buck-fed half-bridge converter with synchronous current-doubler rectification, Thesis of National Cheng Kung University, Tainan
14. Steigerwald RL (1988) A comparison of half bridge resonant converter topologies. IEEE Trans Power Electron 3(2):174–182
15. De Simone S, Adragna C, Spini C, Gattavari G (2006) Design-oriented steady state analysis of LLC resonant converters based on FHA. In: International symposium on power electronics, electrical drives, automation and motion, Naples, 2006, pp s41-16–s41-23

Part VI
Communications

Exercise Bracelet with Bluetooth Low Energy Module and Accelerometer for Sporting Events

Jung-Tang Huang, Wen-Chia Chao, and Chia-Hsiang Lee

Abstract While the wireless Bluetooth 4.0 technology has been introduced, this study focuses on its low power consumption and quick connection features to develop a system used in sporting events. The system includes a user bracelet, signal reading stations, and individual positioning program by using of the RSSI (received signal strength indication). The proposed system does effectively and accurately capture user's location, with different characteristics from regular positioning system as GPS and Wi-Fi, which can be applied in indoor and outdoor environments. Due to sporting events, the venue must maintain a certain space for movement, and the loss of multipath fading effects in the open spaces is much lower. Thus, the attenuation of the signal strength is much less, and it will more effectively target the user's position. The positioning method is similar to Zigbee by using the triangulation algorithm, but the biggest difference is the cellular phones in the market support Bluetooth rather than ZigBee.

Keywords Bluetooth 4.0 • Positioning • Exercise bracelet

1 Introduction

This study adopts Bluetooth 4.0 technology for short distance transmission. For the different sporting events, we designed a bracelet and read station for the event's timing and combined a 3-axis accelerometer to record the movement information of the bracelet wearer, with the algorithm designed to calculate the movement distance, speed, and other information for trainer to refer and match the analysis. Due to the spacious space of the sport event, the phenomenon of multipath fading

J.-T. Huang (✉) • W.-C. Chao • C.-H. Lee
Department of Mechanical Engineering, National Taipei University of Technology,
Taipei 10608, Taiwan
e-mail: jthuang@ntut.edu.tw

effects is not obvious when wearing the bracelet. Thus, after users pass by the reading station, it could use the RSSI (received signal strength indicator) value to locate their positions. But, due to the RSSI floating figures and the absolute value with noise [1], the distance information of the blind node must use at least three masternodes doing the positioning [2]. And we design algorithms to mitigate the error value to increase the positioning accuracy.

Comparing with the previous studies, the regular positioning technology using GPS (Global Positioning System) employs satellite to obtain the coordinates of the target [3]. However, this method is only available in the outdoor areas but not in the indoor area. Therefore, many different wireless locating methods based on Zigbee, RFID, Bluetooth, Wi-Fi, etc. [4–6] are developed for indoor positioning, which have their own pros and cons for selection and evaluation. In this study, the novel Bluetooth 4.0 (BT4) technology only using a 3 V coin cell battery [7] is proposed to operate the positioning system for sporting competition. In this release version, the literature article pointed out that the master and slave devices can keep connection and periodically transmit packets on one CR2032 coin cell battery to maintain the utilization rate nearly a year [8], with sending a small amount of data and transfer rates reaching to 1 Mbps. So the use of BLE in competition can effectively reduce the transmission of data time and thus record the accurate timing.

Sporting events and training were analyzed by using a 3-axis accelerometer for several years [9]. And the combined gyroscope can identify the direction and restore the more accurate positioning information of the subjects [10]. Using the original accelerometer values with the algorithm designed for motion analysis, the system can be applied to running, bicycle riding, swimming, and other activity [11] in terms of 3-axis data of the action, speed, and acceleration. With the information kept inside the flash memory of the MCU chip. After the sports, one can place the bracelet device near to the computer/mobile phone to transmit and record user's activity information and use these methods to build a personal exercise model which is used in sporting events and training program.

2   System Design

Our system is composed of static receiving read station and the bracelet sender worn by the user. The system reads the information from the bracelet at each station then transmits to the cloud database and unifies the integrated timing and information. Inside each bracelet, there is a control unit which is a microcontroller of CC2540 [12] from Texas Instruments. This microcontroller is a complete SoC (system on chip), which is a combination of a BLE transceiver and an 8051 microcontroller. And due to its 6×6 mm size, it significantly reduces the designed area of the bracelet.

The system reading station is accompanied with computer/phone for transceiving action. The PC portion is using the USB dongle designed by Texas Instrument as shown in Fig. 1. And the Bluetooth board developed by our research
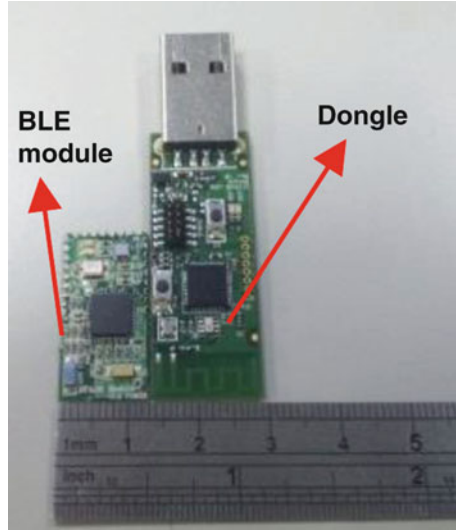
team will be applied in bracelet circuit. Since Bluetooth communication is a built-in function for the mobile devices, it is straightforward to develop the application program on the iOS/Android mobile phone operating system. Finally, through Wi-Fi/3G network supported by the computer/phone, data is sent to the cloud database and integrated into useful information and stored as part of the personal database, which builds up a health management program for reference analysis of the exerciser.

The circuit of the bracelet is worn by the user, shown in Fig. 2; the battery is placed in the back of the circuit board with the accelerometer (CMA 3000-D [13] VTI Technology) which contains SPI and I^2C interface for fast transfer. The chip's power consumption is quite small and can maintain for a long time. According to the referenced article [14], the analysis of physical activity by accelerometer is different from wear positions of the individual body parts, usually worn on the hands, waist and leg are the more appropriate locations for this device. One

example in this study is to let the bracelet be worn on the upper arm for measurement, which is expected to have less irregular jitter and vibration than wrist. And the position makes users feel less uncomfortable. Also, the fixed method is important, and because the value of the accelerometer will be impacted from different placement and gravity, the design of the bracelet should make the board to be attached nicely, without unnecessary shaking [15]. When sports bracelet is worn in a different location, the gravity (3-axis value) caused by the earth's gravitation will be various. In accordance with the CMA3000 datasheet, in the original flat state, there will be +1 g gravity offset along the Z axis. Therefore, for the position of wear in this study, the X-axis yields +1 g gravity offset, which is compensated with the data processing to obtain the correct accelerometer values.

3 Experimental Setup

The demonstrations of experimental test use the circular track and a swimming pool as shown in Fig. 3, for example. We set the starting point, relay station, and final point on the track. The set number of relay station depends on the distance of the track. When players pass the starting point, the starting point starts reading the players time data via Bluetooth for timing. As the players pass, relay station will record the individual player time. The final station records the time data, which is then employed to subtract from the records of previous few stations and get the total time period spent by the players. As shown in Fig. 4, at the indoor swimming pool, for example, due to the short distance of the track, the implementation way of our system is different. The short distance of back-and-forth track will not allow setting up relay stations. Both sides of the read station will be combined as the start and final function, then calculation of the two station time gets the players' time. While in large outdoor swimming, implementation method will be the same as to the general track-and-field events.

Fig. 3 Track-and-field event diagram
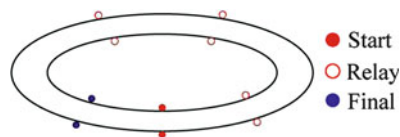
Fig. 4 Swimming event diagram
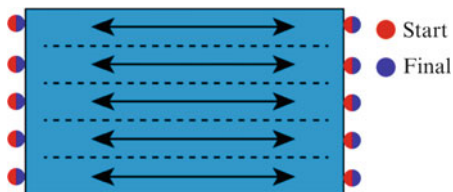
Fig. 5 System configuration diagram

The overall operation of Fig. 5 shows the user enters the scope of the read station. Reader station will work with the user Bluetooth bracelet device to quickly obtain information for record. The read station with Wi-Fi/3G network spread to cloud database. Therefore, it can increase the multi-record station and alternately record to avoid data missing, if a considerable number of users enter the range. The Bluetooth 4.0 can offer fast scanning service in 10 ms [16]. In game/training session, the user can go to the USER Login station game/training memory to record the original 3-axis accelerometer values sent to the USER Login station.

4 Experimental Results

While the Bluetooth wireless communications is used in sporting events/training, the wireless signal is highly sensitive to the surrounding environment inference and the signal strength is also vulnerable to air medium decay. However, according to the accurate RSSI offered by the Bluetooth 4.0, positioning or tacking of the blind node is possible and can be applied to indoor and outdoor sports occasions, mostly due to the smaller of the changing environment in open space. As shown in Fig. 6, the test in the free space, the RSSI is taken eight times at the same location, then recalculated in smooth algorithm to filter the original read RSSI values. It can be found obviously from the figure that the original RSSI value is beating severely and the ideal distance ratio is not so obvious. After smoothing, the RSSI value is closer to the ideal propagation curve. Therefore, we confirmed that this smoothing method can indeed improve the accuracy of the RSSI and increase its usability too.

As described previously, RSSI is a fluctuating value, which means every measured value has inherent error and the error range has proportional relationship with the distance as shown in Fig. 7. Therefore, take the circular track as an example, it has eight running tracks and its width is about 10 m. Comparing with ideal RSSI in Fig. 7, the RSSI at distance of 10 m has error up to ±3 dBm. In order to cover the whole width of the eight tracks and alleviate the large error of the RSSI, the read stations are installed along the two sides of the track; hence, the maximum reading distance is reduced from 10 to 5 m, which indicates that the RSSI error is around ±2 dBm accordingly and the positioning accuracy is enhanced.
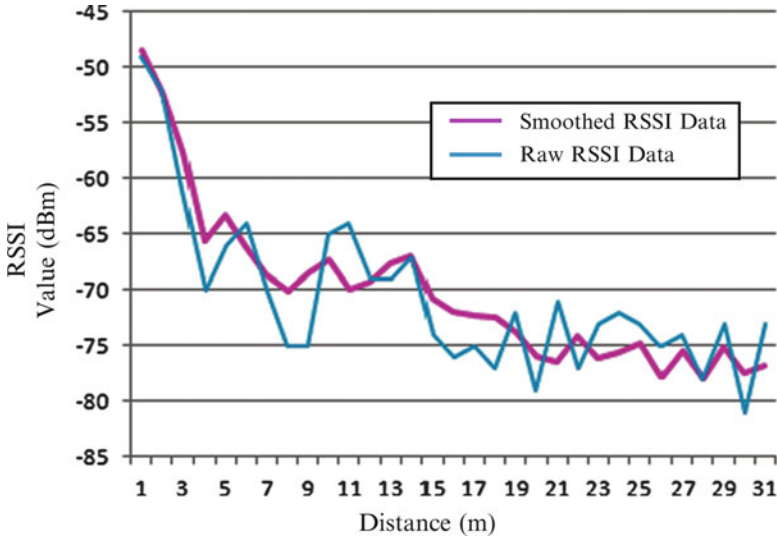
Fig. 6 Smoothed RSSI and original RSSI comparison
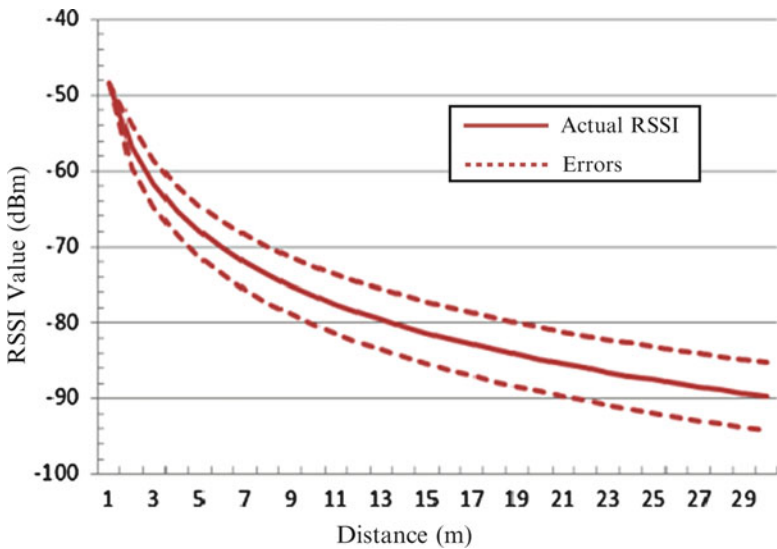
Fig. 7 Actual RSSI and errors comparison

Considering the fast rhythm of the sporting contest, Bluetooth 4.0 just can provide a quick scanning function to fetch data of several nodes in very short period. In this study, the read station can scan each target node and obtain its several RSSI values in a period of 100 ms, which are calculated to get the distance through algorithm in [17]. As shown in Fig. 8, three final read stations of C1, C2, and C3 can
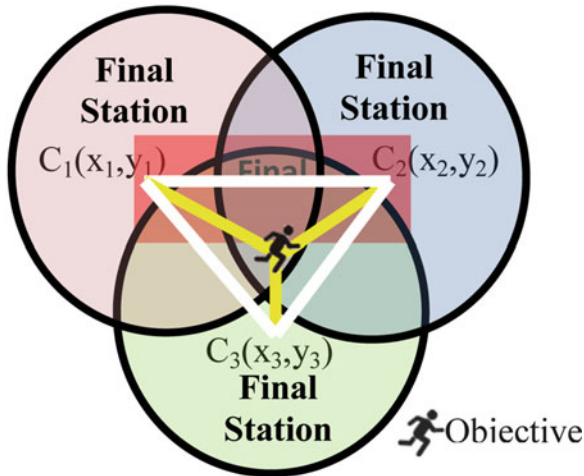
Fig. 8 Triangulation diagram

Table 1 Compare the actual and estimate result

Range (m)	Actual position	Estimate position	SQRT $(|\Delta X + \Delta Y|)$
3	(2, 1.1)	(2.3, 1.5)	0.77
3	(1.9, 1.8)	(1.4, 2.7)	1.18
5	(3.5, 2.9)	(2.9, 3.2)	0.94
5	(3, 0.4)	(3.1, 1)	0.83

read the RSSI value from the target node, respectively, and upload the data to the cloud database for computing the coordinates of the target node through triangulation algorithm [18, 19]. As shown in Table 1, we performed several experiments by setting up three reading stations at the vertices of the right triangle. Two cases of 3 and 5 m between each reading station are tested. The results indicate the error between the estimated and the actual location is less than 1 m. As described previously, in the near distance, the variance of the RSSI is smaller. Mostly the runners run on the inner track in a circular track so that their BT4 bracelet will be close to the read station installed near the side, and thus the RSSI is stronger to have higher accurate positioning.

5 Conclusion

In this chapter, we describe the personal bracelet with Bluetooth 4.0 communication module and the backhaul system for sporting events. We implemented the new Bluetooth 4.0 communication based on the CC2540 SoC solution architecture, which can effectively reduce the area. In the sporting event system, through the

fast communication between the user bracelet and read station, it can record the user's time and position when the user is entering the range of read station. Through the read station with Wi-Fi/3G, our system can upload users' exercise conditions and status to the cloud database for storage and further analysis to obtain their personal sporting model.

References

1. Sugano M, Kawazoe T, Ohta Y, Murata M (2006) Indoor localization system using RSSI measurement of wireless sensor network based on ZigBee standard. In: Proceeding of the IASTED international conference on WSN, Banff, 2006, p 1
2. Liu H (2007) Survey of wireless indoor positioning techniques and systems. IEEE Trans Syst Man Cybern 37(6):1067–1080
3. Radu S, He T, Stankovic JA (2004) Walking GPS: a practical solution for localization in manually deployed wireless sensor networks. In: 29th annual IEEE international conference on local computer networks, Tampa, 16–18 Nov 2004, pp 480–489
4. Pahlavan K, Li X, Mäkelä JP (2002) Indoor geolocation science and technology, IEEE Commun Mag 40(2):112–118
5. Ni M, Liu YH, Lau YC, Patil AP (2003) LANDMARC: indoor location sensing using active RFID. In: Proceedings of the first IEEE international conference on pervasive computing and communications, Fort Worth, 2003, pp 407–415
6. Evennou LF, Marx F (2006) Advanced integration of WIFI and inertial navigation systems for indoor mobile positioning. EURASIP J Appl Signal Process 164–164
7. Specification of the Bluetooth System, Covered Core Package version: 4.0 (30 June 2010)
8. Kamath S (2010) Measuring bluetooth low energy power consumption. In: Texas instruments application note AN092, Dallas, Oct 2010
9. Hawley J (1999) Guidelines for laboratory and field testing of athletic potential and performance. In: Maughan R (ed) Basic and applied sciences for sports medicine. Butterworth-Heinemann, Oxford
10. Luinge HJ, Veltink PH (2004) Inclination measurement of human movement using a 3-D accelerometer with autocalibration. IEEE Trans Neural Syst Rehabil Eng 12(1):112–121
11. James DA, Davey N, Rice T (2004) An accelerometer based sensor platform for insitu elite athlete performance analysis. In: Proceeding of the IEEE sensors conference, Vienna, Oct 2004, pp 1373–1376
12. CC2540 Development Kit User's Guide. http://www.ti.com/lit/ug/swru270b/swru270b.pdf
13. CMA3000-D0X Product Family Specification. http://www.vti.fi/sites/default/files/documents/cma3000_d01_datasheet_8277800a.03.pdf
14. Jamie AW, Lukowicz P, Troster G, Starner TE (2006) Activity recognition of assembly tasks using body-worn microphones and accelerometers. IEEE Trans Pattern Anal Mach Intell 28(10):1553–1567
15. Sun L, Zhang D, Li B, Guo B, Li S (2001) Activity recognition on an accelerometer embedded mobile phone with varying positions and orientations. In: Ubiquitous intelligence and computing, 2001
16. Specification of the Bluetooth System, Covered Core Package version: 4.0 (30 June 2010). http://www.bluetooth.com/Specification%20Documents/Core_V40.zip
17. Jain HV, Chakravarty S, Bhargava P, Position location monitoring using IEEE 802.15.4/ZigBeeR technology. Beyond Bits (IV):67–69. Freescale

18. Lau EEL, Chung WY (2007) Enhanced RSSI-based real-time user location tracking system for indoor and outdoor environments. In: International conference on convergence information technology, Washington, DC, 2007, pp 1213–1218
19. Sun G, Chen J, Guo W, Liu KJR (2005) Signal processing techniques in network-aided positioning. IEEE Signal Process Mag 22(4):12–23

Design and Implementation of an eBook Access Control Protocol

Hui-Wen Liao, Po-Hsien Wang, and Meng-Lieh Sheu

Abstract Electronic books have the advantages of being portable and low cost; however, there are drawbacks, such as they can be duplicated easily. This research designs and implements an eBook access control protocol and achieves authorized user access verification. This method includes network communication and RFID technique, mainly utilizing the feature of RFID tag that contains unique Tag ID, establishes a database of eBooks tag IDs on a Radius server, and allows access to these eBooks only by the user with legitimate RFID tag. This chapter presents function $F(\ )$ and $F^{-1}(\ )$, the inverse function of $F(\ )$. The Radius server uses $F(\ )$ to encrypt and send the data to the RFID tag; besides, it also can decrypt the data sent from RFID tag. $F^{-1}(\ )$ in the RFID tag can be used to decrypt and encrypt data to and from the Radius server. Furthermore, SSL over TCP/IP is applied to secure and protect data transfer between Radius server and eBook reader.

Keywords Electronic books • Access control • RFID • SSL

1 Introduction

The eBook is a text and/or image-based publication in digital form produced, published, and readable on computers or other digital devices, in which the texts, pictures, and graphs are stored in digital files. It differs from the traditional printed media for its abilities to add sounds, animations, videos, and other multimedia data to liven and further enhance published content. With eBook, readers have the ability to search the full texts using keywords to easily locate any specific

H.-W. Liao (✉)
Department of Information Technology, Ling Tung University, Taichung 40852, Taiwan
e-mail: hwliao@teamail.ltu.edu.tw

P.-H. Wang • M.-L. Sheu
Department of Electrical Engineering, National Chi Nan University, Nantou 54561, Taiwan

information. The eBook can be stored in hard disk, compact disk, cloud storage, or any other digital storage devices. These files of eBook can and do exist without any printed equivalents; the production of eBooks does not consume paper, ink, etc; hence, eBook is an environmental friendly technology. Furthermore, eBooks can be read on a plethora of devices, increasing accessibility and distribution.

The eBooks usually need dedicated eBook reading software (Reader software). Reader software can run on PCs, Notebooks, Tablet PCs, PDAs, smartphones, or a dedicated hardware device known as an eBook reader. These different platforms allow users to choose whichever device they prefer. Because eBooks are digital files, they can be easily reproduced or shared among users and that would lead to substantial profit losses. The potential eBooks piracy issue also makes publishers and authors reluctant to distribute digitally.

RFID (radio-frequency identification) technology like a raging fire spreads rapidly to several aspects of our daily lives. Its related technology and applications are constantly being developed and adapted by many industrial applications in their next generation systems; especially, in the logistics management. RFID technology uses electromagnetic waves to store, access, and exchange data. Using radio wave transmitting data, RFID replaces traditional analog approach like barcode scanning that is done one at a time. RFID technology has many advantages, such as it can retrieve multiple sets of data even under unfavorable conditions; the devices are generally small, reusable, easily accessed, and wireless and can operate over a wide range.

This chapter presents a solution, using RFID technology, to resolve the piracy problem on eBooks today. This chapter will also propose a complete RFID security solution to ensure that the RFID tags are not easily hacked or copied.

2 Related Work

In 2005, Bono et al. [1] successfully defeated a RFID device security known as a digital signature transponder (DST), manufactured by Texas Instruments. It proved that the RFID tag could be duplicated and subsequently used to defeat the security systems. RFID tags are used in many current commercial and private systems; their security vulnerability leads to a recent surge of RFID security-related developments [2]. To enhance RFID technology security, it needs to be done at the point of RFID tag authentication to prevent fake RFID tags from fooling the RFID reader; in addition, the security is needed to prevent fake RFID readers from obtaining any vital information in RFID tags [3].

In 2003, Weis et al. [4] proposed a security design revolving around a hash-based access control scheme. When server assigns a RFID tag, a key is generated and also hashed to produce metalID to be stored in the tag. To access, RFID reader uses the metalID from the tag, looks up the appropriate key in the back-end database, and transmits the key to the tag. The tag hashes the key and compares it to the stored metalID. If the values match, it unlocks itself and offers its full contents to any nearby readers. Although it is effective, this type of security is highly vulnerable to replay attacks [5].

In 2005, Yang et al. [6] proposed a simple and effective mutual authentication protocol, a more advanced security solution. The mutual authentication protocol is mainly used in RFID reader and RFID tag authentication. The RFID tag will authenticate the reader and obtain cryptic messages which will then be used in the index-pseudonym. Once these verifications are performed, the tag will respond with contents or refuse to respond if failed authentication. In this security mechanism, the message sent by the RFID tag will be changed; but Avoine [7] proved that this mechanism may still be cracked; if a hacker gets hold of the last communications sent between the RFID tag and RFID reader, the hacker could calculate the next message transmitted by the RFID tag.

In 2006, Chien [8] published a paper on a more secured RFID access control design that prevents falsifying the tag or RFID reader. Each signal sent by the tag also includes the current date so that they are varied each day, thus prevents replay attacks. The tag reader is also required to authenticate itself by hashing the key and date and sends the calculated value back to the tag for verification.

3 Research Methods

The following showcases our proposed research method; the first part introduces the system architecture and then describes the access control protocol.

The structure of this protective mechanism includes the Radius server, eBook reader, RFID reader, and RFID tag (as shown in Fig. 1). The eBook reader and Radius server use SSL over TCP/IP to communicate. Using this protection process, hackers cannot use network IDs of the RFID tag to track usage (user) or reading behavior and reduce the possibility of defeating the system security.

Using RFID Tag Standard ISO-15693 as an example, the tag has 112 bytes to store any extra data. The function $F(\ )$ on Radius server has 48 bytes permutation, and $F^{-1}(\ )$ in the RFID tag also has 48 bytes permutations; the remaining 64 bytes storage space in RFID tag is used by a cipher table of 64 groups keys with 4 bytes generated by shift operator; the Radius server also has this cipher table to ensure the legitimacy of this RFID tag. The simulation to verify the procedure between the eBook reader and the Radius server is shown in Fig. 2.
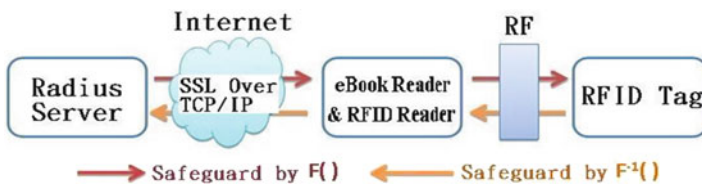
Fig. 1 The use of $F(\ )$ and $F^{-1}(\ )$ in the signals provides a confirmation code in order to verify and authenticate the Radius server and RFID tag key(s)
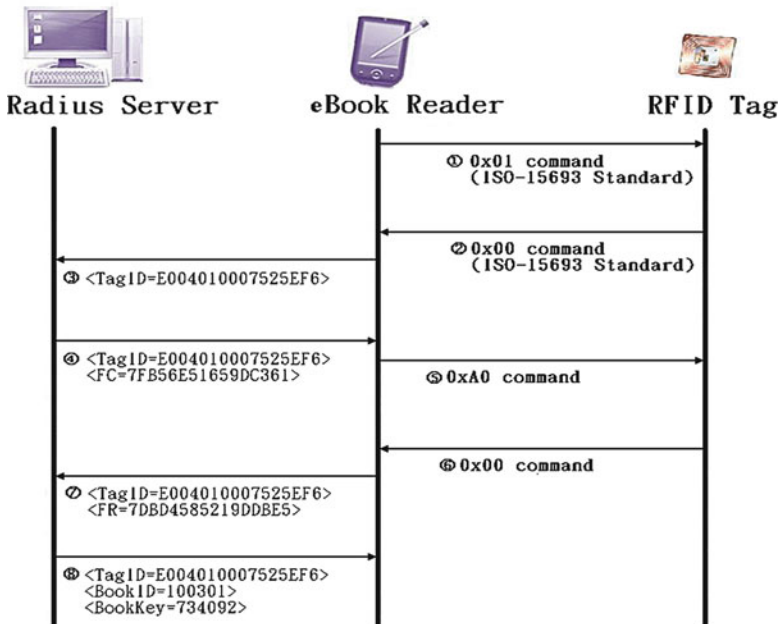
Fig. 2 For the verification process, it starts with the Radius server generating a random number R, then selects one of 64 groups $Key(n)$, encrypts the R and the $Key(n)$ via $F(R, Key(n))$, and sends $F(R, Key(n))$ to RFID tag through Internet; next, RFID tag uses $F^{-1}(F(R, Key(n)))$ to decrypted R and $Key(n)$, selects $Key(n + 1)$ information, encrypts R and $Key(n + 1)$ via $F^{-1}(R, Key(n + 1))$, and sends $F^{-1}(R, Key(n + 1))$ to Radius server; lastly, Radius server uses $F(F^{-1}(R, Key(n + 1)))$ to decrypt R and $Key(n + 1)$. If this $Key(n + 1)$ can be confirmed by Radius server, then the RFID tag is a legal ID; also, by verifying R is to confirm it is from the current verification process, not from the repeat attack

4 Implementation of eBooks Access Control Protocol

The following introduces the pseudo codes of the eBook reader (Sect. 4.1), the pseudo codes of the Radius server (Sect. 4.2), and implementing results (Sect. 4.3).

4.1 Pseudo Code of the eBook Reader

We need to establish legally authorized RFID Tags in order to confirm the eBook user. The following is the verifying procedure pseudo codes for the eBook reader access control process:

```
Begin
FIND_RFID:
wait ID of RFID Tag
   if ID of RFID Tag
       send ID of RFID Tag to Radius Server
       wait verification data from Radius Server
         if verification data
             send verification data to RFID Tag
             wait response of RFID Tag
             send response of RFID Tag to Radius Server
             wait key of eBooks
              if keys
                  break
              else
                go to FIND_RFID
         else
           go to FIND_RFID
     else
       go to FIND_RFID
End
```

4.2   Pseudo Code of the Radius Server

The eBook reader and RFID reader continuously detect the presence of a RFID tag. When the eBook reader receives a RFID tag ID, it sends that information to the Radius server via SSL over TCP/IP. If authentication is successful, then access will be granted to the local cache storage; if an eBook file is not there, then the Radius server would immediately download the eBook and display the content on the eBook reader screen. The following is the verifying procedure pseudo codes for the Radius server access control process:

```
Begin
wait for connection
receive ID of RFID Tag from eBook Reader
   if ID of RFID Tag registered
     send verification data to RFID Tag via eBook Reader
     wait response of RFID Tag
     if response is correct
      send key and book number of eBooks to eBook Reader
      stop
     else
      stop
   else
    stop
End
```

Fig. 3 The frame of successful verification. In the frame, each button represents a procedure

4.3 Implementing Results

The Radius server uses FreeBSD as the operating system and gcc (GNU Compiler Collection) to compile the software written in C language. The eBook reader adopts C# language developed in Microsoft Windows environment. Figure 3 shows the frame of successful verification.

5 Conclusions

The eBooks are environmental friendly, but more importantly, they offer a convenient platform to pass information and knowledge to the readers. Therefore, major publishers are becoming more receptive toward this new way of distribution. This study shows how RFID technology can be used to protect eBook contents, avoid piracy, and offer effective yet low-cost secured distributions. Certainly, publishers will not welcome high expenditure for data security because it will offset the savings from the eBook platform.

This chapter presents and implements an eBook access control protocol to protect legitimatization of RFID tag and to prevent data stealing by fake RFID reader. This access control protocol covers RFID readers and eBooks; it expands the scope of protecting the process between RFID tag and Radius server and ensures that RFID tag cannot be duplicated nor analyzed by unexpected user.

References

1. Bono S, Green M, Stubblefield A, Juels A, Rubin A, Szydlo M (2005) Security analysis of a cryptographically-enabled RFID device. In: 14th USENIX security symposium, Baltimore, 2005, pp 1–16
2. Spiekermann S, Evdokimov S (2009) Critical RFID privacy-enhancing technologies. IEEE Secur Priv Mag 7(2):56–62
3. Henrici D, Muller P (2004) Hash-based enhancement of location privacy for radio-frequency identification devices using varying identifiers. In: Proceedings of the second IEEE annual conference on pervasive computing and communications workshops, Los Alamitos, 2004, pp 149–153
4. Weis S, Sarma S, Rivest R, Engels D (2003) Security and privacy aspects of low-cost radio frequency identification systems. In: 1st international conference on security in pervasive computing, Boppard, 2003
5. Avoine G, Dysli E, Oechslin P (2005) Reducing time complexity in RFID systems. In: The 12th annual workshop on selected areas in cryptography, Kingston, 2005
6. Yang J, Park J, Lee H, Ren K, Kim K (2005) Mutual authentication protocol for low-cost RFID. In: Workshop on RFID and lightweight crypto, Graz, pp 17–24
7. Avoine G (2005) Cryptography in radio frequency identification and fair exchange protocols. Ph.D. thesis. No. 3407, Ecole Polytechnique Fédérale de Lausanne, Lausanne, 2005
8. Chien HY (2006) Secure access control schemes for RFID systems with anonymity. In: Proceedings of the 7th international conference on mobile data management, IEEE Computer Society, Washington, DC, 2006, p 96

Novel T-Shaped Non-orthogonal Dual-Mode Band-Pass Filters with Two Differently Structured Resonators

C.Y. Kung, C.F. Yang, Y.T. Hsieh, W.C. Chang, C.G. Kuo, and C.C. Diao

Abstract Novel dual-mode filters with two differently structured resonators were designed on Al_2O_3 ceramic substrates to achieve pattern minimization and better filter properties. The input/output microstrip lines were arranged in a straight line, making the designed filter easy to connect with other RF circuits. To promote a coupling effect between the input/output microstrip lines and the resonator, two additional coupling stubs were used to form modified T-shaped microstrip coupling lines. In a dual-mode filter, adding a perturbation stub could generate two degenerate modes and increased the bandwidth in the desired passband. To achieve this, the type-A dual-mode filter was designed on a square-ring resonator with two perturbation stubs. For the type-B filter, two open stubs, one perturbation patch, and one meandering loop ring resonator were investigated to achieve the same purpose but with a smaller pattern size than type-A. According to simulated results, the proposed filters with optimized parameters exhibited the wide passbands.

C.Y. Kung • C.F. Yang (✉)
Department of Chemical and Materials Engineering, National University of Kaohsiung, Kaohsiung, Taiwan, R.O.C.
e-mail: cfyang@nuk.edu.tw

Y.T. Hsieh • W.C. Chang
Department of Electronic Engineering, Southern Taiwan University, Tainan, Taiwan, R.O.C.

C.G. Kuo
Department of Industrial Education, National Taiwan Normal University, Taipei, Taiwan, R.O.C.

C.C. Diao
Department of Electronic Engineering, Kao Yuan University, Kaohsiung, Taiwan, R.O.C.

1   Introduction

Microstrip planar filters have garnered increased attention in recent years for their use in modern wireless communication networks [1, 2]. Compact size, wide bandwidth, small insertion loss, and high out-of-band rejection are requisite properties, and because dual-mode filters meet these demands, they have attracted interest in the investigation of band-pass filters (BPFs) [3, 4]. Each resonator of a dual-mode filter is regarded as a doubly tuned resonant circuit, so the required number of resonators can be cut in half [5]. Filters with ring-type dual-mode resonators are more compact than filters with patch-type dual-mode resonators, and they meet commercial requirements; various dual-mode microstrip line filters have been proposed in theory and experimentally, such as circular ring [6, 7] and square ring [5], triangular ring [8], and hexagonal ring [9]. To create a band-pass filter, the two degenerate modes of a dual-mode resonator are excited and coupled to each other by orthogonal feed lines and a variety of perturbations are added. There are many methods of creating perturbations, such as adding or subtracting a patch on the symmetrical line or on each side [10–12]. However, most dual-mode filters have the input/output microstrip lines along the orthogonal ($=90°$), while a few filters have them at an angle greater than $90°$ but less than $180°$ to excite two degenerate modes with a closer frequency in the resonators. In this way, the bandwidth of the dual-mode filter is improved but the complexity of the layout arrangement connecting it with other RF devices is increased. In this chapter, two new designs of dual-mode BPFs are investigated. The prototype type-A filter uses a square-ring resonator with two perturbation stubs to generate two degenerate modes. A square-ring resonator can be curved into a meandering loop resonator, or it can connect the open stubs for pattern miniaturization [5, 13]. In the type-B filter, two open stubs, one perturbation patch, and one meandering loop ring are adopted to design a new modified dual-mode band-pass filter to achieve the same result but with a smaller pattern size than the type-A filter. The principle advantage of this new type-B dual-mode microstrip filter over the prototype type-A filter is that it facilitates the practical minimization of a filter function response using a meandering loop ring resonator and two open stubs. Notably, the input/output microstrip lines are arranged in a straight line, making the designed filter easy to connect with other RF circuits. To promote a coupling effect between the input/output microstrip lines and the resonator, two additional coupling stubs are used to form modified T-shaped microstrip lines. Finally, the proposed filters are fabricated using a printing method that generates minimal environmental pollution and are verified by simulation and measurement.

2   Design of T-Shaped Square-Ring Dual-Mode BPF

The Al_2O_3 ceramic substrates have a comparably higher dielectric constant of 9.4, a dielectric loss of less than 0.001, and a low price. For these reasons, the filter was designed on 1 mm thick Al_2O_3 ceramic substrates for pattern minimization.

Fig. 1 The structure of the prototype ($F = 0$) and modified ($F \neq 0$) T-shaped non-orthogonal input/output dual-mode bandpass filter (type-A)
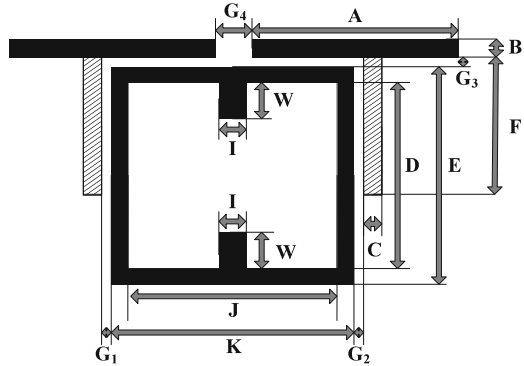
A printing method with low environmental impact was used to fabricate the proposed dual-band band-pass filter (the method did not require $FeCl_3$ solution to etch the Cu) [3, 14]. An Ansoft full-wave electromagnetic field simulator (HFSS) was used to adjust and optimize the pattern parameters. The proposed T-shaped square-ring dual-mode filter was based on a resonator with the length of 1 λ_g. According to the ε_r (9.4) of the Al_2O_3 substrates, the approximate fundamental guided wavelength of the 2.4 GHz 1 λ_g square-ring resonator was calculated using Eq. (1) [3], yielding a value of 40.77 mm:

$$V = \frac{C}{\sqrt{\varepsilon_r}} = f\lambda_g \tag{1}$$

Figure 1 shows the basic microstrip square-ring resonator; a single difference between the proposed resonator and a conventional microstrip square loop resonator is that the proposed filter has the structures of the prototype ($F = 0$) and modified ($F \neq 0$) non-orthogonal coupling designs. The proposed filters were arranged non-orthogonal input/output ports in a straight line with a gap (G_4) of 1.4 mm. These input/output ports were introduced to enhance the flexibility of the circuit layout. A 0.1 mm gap (G_3) between the square-ring resonator and the transmission lines was used for stronger coupling. Two perturbation stubs located along the symmetrical line of the square-ring resonator were used to excite two degenerate modes. A perturbation was formed by changing the length (W) of two open stubs, which can distinguish it from the other literatures using the square patch [10, 11]. The coupling length between the transmission lines and the resonator in the typical orthogonal input/output dual-mode filter was about the length of one side of the square ring. Thus, the prototype non-orthogonal input/output filter shown in Fig. 1 measured less than half a side length. If the coupling factor was weak, a ripple would exist in the passband, so to address this problem, the coupling effect needed to be enhanced. Additional coupling stubs ($F \times C$) were added to form the type-A filter, where gaps G_1 and G_2 were equal to G_3.

The simulated response of the prototype T-shaped dual-mode BPF as a function of perturbation length (W) is shown in Fig. 2. As the length of W increased, the left
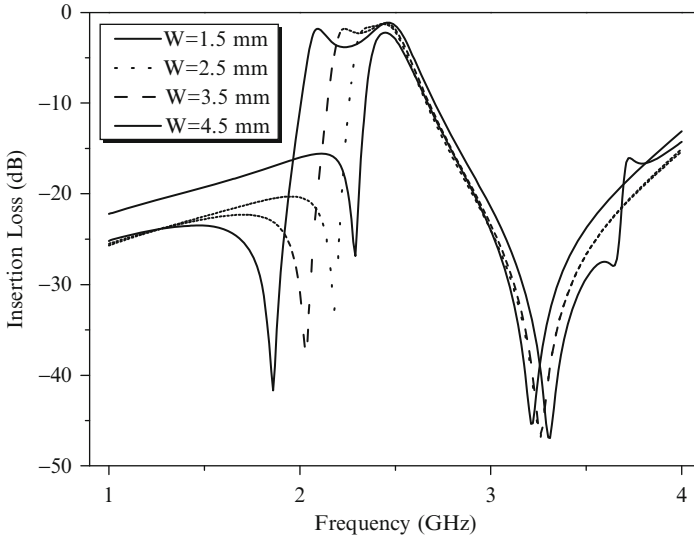
Fig. 2 Simulated results of prototype T-shaped non-orthogonal dual-mode bandpass filter as a function of perturbation length
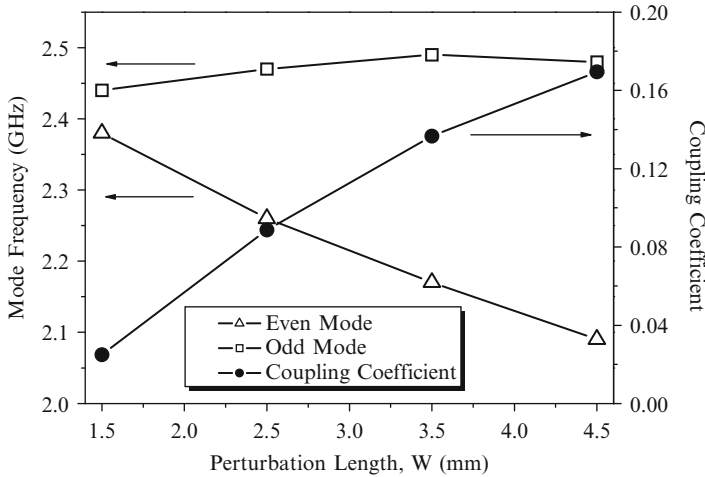
Fig. 3 Simulated coupling coefficient of two degenerate modes for type-A filter as a function of W

transmission zero changed from 26.86 to 41.67 dB and shifted from 2.29 to 1.86 GHz. Figure 3 shows the coupling coefficient of the two degenerate modes as a function of W. The coupling coefficient was calculated using Eq. (2) [15]:

$$C = \frac{f_a^2 - f_b^2}{f_a^2 + f_b^2} \tag{2}$$

where f_a and f_b are the resonant frequencies of the two splitting modes. As the length of W increased from 3 to 4.5 mm, the mode splitting linearly increased from 130 to 350 MHz. For the even mode the frequency decreased from 2.48 to 2.31 GHz, and for the odd mode it increased from 2.61 to 2.66 GHz. If no perturbation was added ($W = 0$ and $I = 0$), neither splitting of the resonant modes nor passband response was observed. As Fig. 3 shows, the coupling coefficient between the two degenerate modes was close to 0.111.

3 Miniature Modified T-Shaped Dual-Mode BPF

According to circuit theory, one line with characteristic impedance Z_0 can be divided into two lines with characteristic impedance $2Z_0$ using a shunt connection [20]. The coupling sections of the T-shaped structure were halved for impedance matching, and the filter structure was modified as shown in Fig. 4, with thinner C and H values. The effect of using different lengths of divided coupling lines is presented in Fig. 5. The insertion losses and ripples decreased as the coupling length of the T-shaped coupling lines increased from 4 to 5.5 mm, due to increased coupling strength. However, 6 mm was not feasible because G_4 was then equal to 0. In this study, $F = L = 5.5$ mm was selected because it yielded the lowest insertion loss, the best shape factor, deeper transmission zeros, and a smaller ripple in the passband.

To keep the resonant frequency unchanged, the length of the square-ring resonator was reduced and the pattern size was decreased. It is also known that a square-ring resonator can be curved into a meandering loop resonator for pattern miniaturization [13]. As can be seen from Fig. 6, an important difference between the proposed new resonator (type-B filter) and a conventional microstrip square loop resonator (type-A filter) is the use of one meandering loop ring resonator and two open stubs. The operating frequency was easily tuned using the length of the open stub (M) and of the meandering loop (P). The frequency modulation is sensitive to the open stub (M) and meandering loop (P) lengths. As M and P
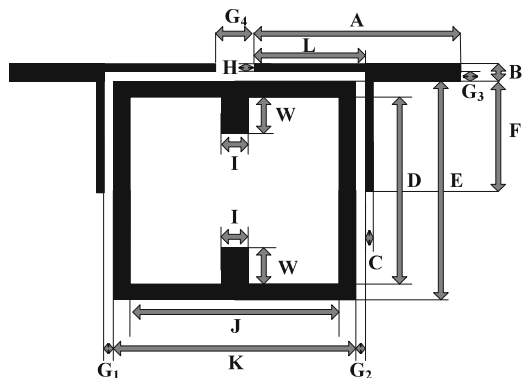
Fig. 4 The modified transmission line of the proposed dual-mode filter
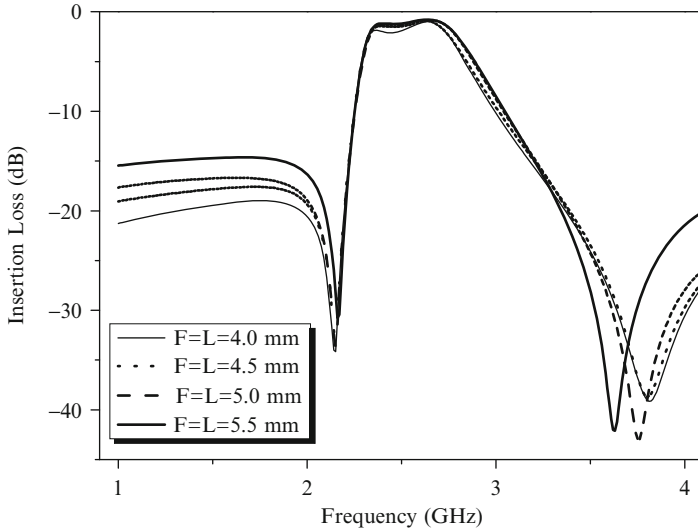
Fig. 5 Simulated results of modified transmission line dual-mode filter as a function of *F*'s lengths (*F* = *L*)
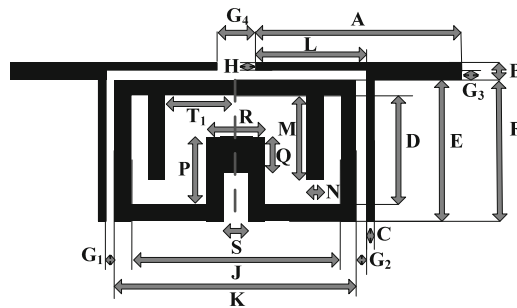
Fig. 6 The modified meandering loop T-shaped non-orthogonal input/output dual-mode band-pass filter with open stubs (type-B)

increase, the splitting of the two resonant modes increases, and both the bandwidth and the ripple during the passband also increase. Two methods can be used to address those problems. The first is tuning the perturbation length (*Q*). The splitting of the two resonant modes increases as *Q* increases, effectively increasing the bandwidth and the unwanted ripple in the desired passband. The second method is moving the stub position. Figure 7 shows the splitting of two resonant modes as a function of T_1, which is the distance between the open stub and symmetrical line. As T_1 increases to 3.5 mm, the splitting of the two resonant modes and the bandwidth in the desired passband decrease. As T_1 decreases to 2.5 mm, the splitting of the two resonant modes and the desired passband increase, but a ripple in the passband is also present. If the open stubs are close to the symmetrical line,
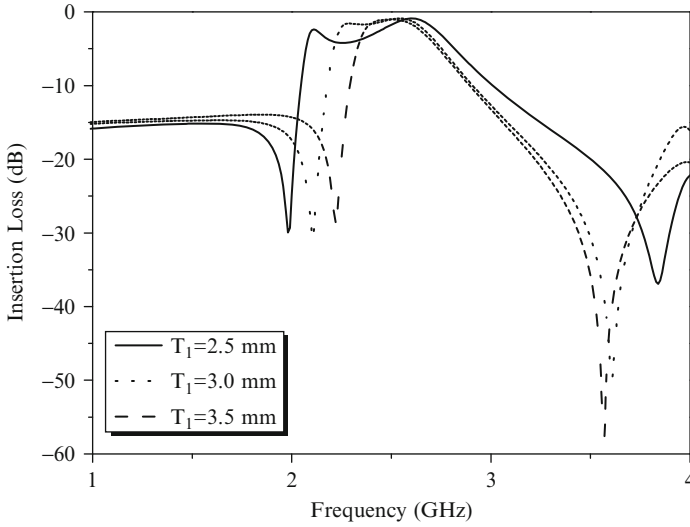
Fig. 7 Simulated results of the type-B filter, varying with different distances (T_1) between the open stub and symmetrical line
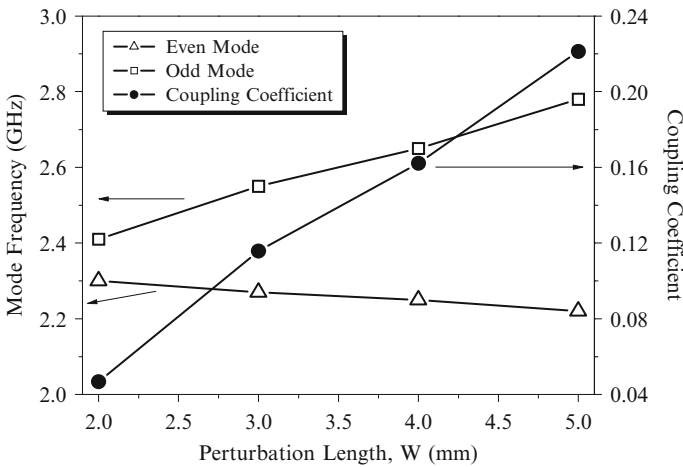
Fig. 8 Simulated coupling coefficient of two degenerate modes for the type-B filter as a function of perturbation length (Q)

they have large effects similar to perturbation and the two resonant modes have larger splitting. Conversely, if the open stubs are far away from the symmetrical line, they have few effects similar to perturbation and the two resonant modes approach to generate a wide passband.

Figure 8 shows the coupling coefficient of the two degenerate modes in the type-B filter as a function of perturbation length (Q). As Q increases from 2 to 5 mm,

the mode splitting linearly increases from 110 to 560 MHz, the frequency of the even mode decreases from 2.3 to 2.22 GHz, and that of the odd mode increases from 2.41 to 2.78 GHz. As Fig. 10 shows, the optimal coupling coefficient between the two degenerate modes of the type-B filter is 0.116 for the 2.4 GHz band.

4 Simulated and Measured Results

The optimal parameters for the proposed type-A filter are $A = 12$ mm, $B = I = 1$ mm, $C = 0.5$ mm, $D = J = 10$ mm, $E = K = 12$ mm, $F = 7.5$ mm, $W = 3.5$ mm, $G_1 = G_2 = G_3 = 0.1$ mm, and $G_4 = 1.4$ mm. The optimal parameters for the proposed type-B filter are $A = 10.2$ mm, $B = I = N = 1$ mm, $C = H = 0.5$ mm, $D = 6.5$ mm, $J = 10$ mm, $E = 8.5$ mm, $P = M = 5.5$ mm, $K = 12$ mm, $F = 8.1$ mm, $L = 5.6$ mm, $Q = T_1 = 3$ mm, $S = 2$ mm, $R = 4$ $W = 4$ mm, and $G_1 = G_2 = G_3 = 0.1$ mm. After the optimal parameters are found, the low environmental pollution of printing method was used to print the Ag/Pd paste according to the designed patterns on the Al_2O_3 ceramic substrate. After printing, the pattern was sintered at 700 °C for 15 min. Finally, two SMA connectors were welded as the input/output, and the microwave properties were measured by the Agilent-N5230A network analyzer. The fabricated type-A and type-B filters have the very small sizes of 25.4 × 13.1 mm (type-A) and 21.4 × 9.1 mm (type-B). The type-B filter shows a size reduction of 42 % compared with the size of type-A. Figures 9 and 10 compare the simulated and measured results for the proposed filters. For the type-A filter, the simulated results are $S_{21} = 1.31$ dB and BW = 480 MHz (20.43 %) at 2.35 GHz,
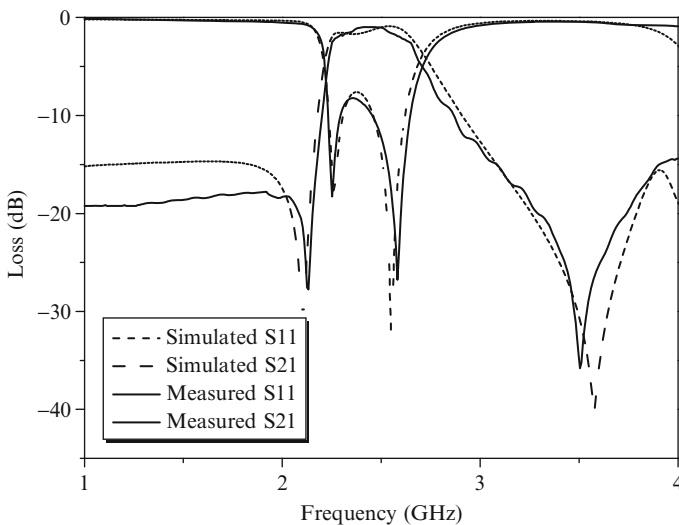
Fig. 9 Simulated and measured results for the type-A filter
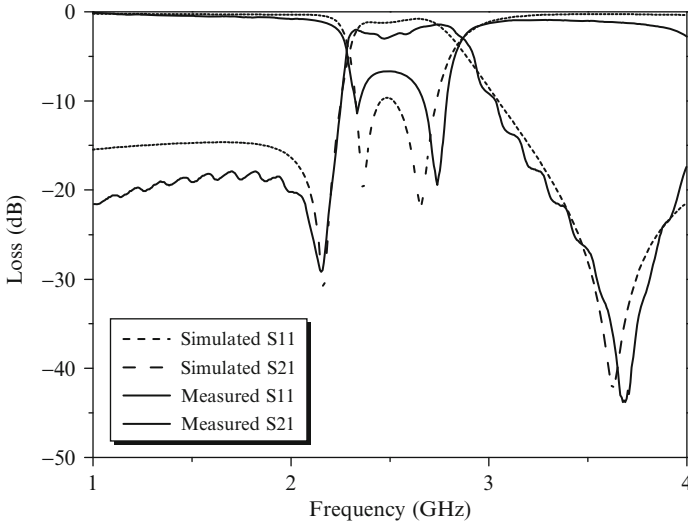
Fig. 10 Simulated and measured results for the type-B filter

and the measured results are $S_{21} = 1.73$ dB and BW = 450 MHz (18.83 %) at 2.39 GHz. The simulated out-of-band rejections are 29.79 dB at 2.11 GHz and 39.85 dB at 3.58 GHz. The measured out-of-band rejections are 27.76 dB at 2.13 GHz and 35.78 dB at 3.51 GHz. For the type-B filter, the simulated results are $S_{21} = 1.15$ dB and BW = 610 MHz (24.71 %) at 2.47 GHz, and the measured results are $S_{21} = 2.26$ dB and BW = 650 MHz (26.97 %) at 2.41 GHz. The simulated out-of-band rejections are 30.75 dB at 2.16 GHz and 42.09 dB at 3.63 GHz. The measured out-of-band rejections are 29.26 dB at 2.14 GHz and 43.81 dB at 3.69 GHz. However, the measured results still agree well with the simulated results.

5 Conclusions

In this study, dual-mode filters with two differently structured resonators were investigated. Both of them had the advantages of wide bandwidth, deep transmission zeros, compact size, simple pattern, and easy fabrication. They were indeed suitable for WLAN (2.4–2.4835 GHz) applications. The type-A filter had a 16.52 % bandwidth at a center resonant frequency of 2.36 GHz. Two transmission zeros with insertion losses of 29.79 and 39.85 dB were present on both sides. The type-B filter had a 26.97 % bandwidth at a center resonant frequency of 2.41 GHz. Two transmission zeros with insertion losses of 29.26 and 43.81 dB were present on both sides. The type-A filter was 25.4×13.1 mm and the type-B filter 21.4×9.1 mm (both without SMA). This study demonstrated that the type-B filter had a smaller size and wider bandwidth in the passband than the type-A filter.

References

1. Vegesna S, Saed MA (2010) Prog Electromagn Res B 20:245–262
2. Zhou Y, Lucyszyn S (2010) Prog Electromagn Res (PIER) 105:71–92
3. Kung CY, Chen YC, Wu SM, Yang CF, Sun JS (2011) J Electromagn Waves Appl 25:617–628
4. Lin XM (2010) J Electromagn Waves Appl 24:2029–2035
5. Chen CH, Chen HM, Lin YF, Yang CF (2008) Microw Opt Technol Lett 50:2117–2119
6. Mao RJ, Tang XH, Xiao F (2007) IEEE Microw Wireless Comput Lett 55:1539–1547
7. Hsieh LH, Chang K (2000) Electron Lett 36:1626–1627
8. Zhao LP, Dai XW, Chen ZX (2007) Prog Electromagn Res 77:417–424
9. Mo SG, Yu ZY, Zhang L (2009) Prog Electromagn Res 96:117–125
10. Gorrur A (2004) IEEE Trans Microw Theory Tech 52:671–677
11. Chiou YC, Yang PS, Kuo JT, Wu CY (2010) Prog Electromagn Res 108:23–36
12. Esfeh BK, Ismail A, Raja Abdullah RSA, Adamand H, Alhawari ARH (2009) Prog Electromagn Res B 16:277–290
13. Lin YF, Chen CH, Chen KY, Chen HM, Wong KL (2007) IEEE Microw Wireless Comput Lett 17:580–582
14. Yang CF, Cheung M, Huang CY, Sun JS (2010) J Electromagn Waves Appl 24:1697–1707
15. Zhang YP, Sun M (2006) IEEE Trans Microw Theory Tech 54:3779–3785

A Novel Method to Simplify the Structure of Dual-Band Bandpass Filters: Design the Resonators on Combined Substrates

Cheng-Yuan Kung, Yuan-Tai Hsieh, Chien-Chen Diao, Chia-Ching Wu, and Cheng-Fu Yang

Abstract Two dual-band bandpass filters are investigated both using two resonators parallel positioned along with microstrip lines. The proposed dual-band bandpass filter was based on $\lambda_g/2$ open-loop rectangle-ring resonator (Resonator L). A shorter open-loop rectangle-ring resonator (Resonator S) was parallel positioned at another side of the input/output microstrip lines with the same coupling conditions to the original longer resonator. If phase difference for signals in two paths was equal to 180°, the energy cancellation has happened, and no passband would be found. The longer resonator resonates at 1.23 and 2.4 GHz band. The shorter resonator resonates at 2.4 GHz band to enhance the bandwidth and out-of-band rejection by phase difference method. The bandwidth of 1.23 GHz band is produced by $\lambda_g/2$ fundamental response of Resonator L. The bandwidth of 2.4 GHz band is produced by combining 1 λ_g first spurious response of Resonator L and $\lambda_g/2$ fundamental response of Resonator S. The proposed filters are suitable to use for GPS (L2-band) and WLAN.

C.-Y. Kung • C.-F. Yang (✉)
Department of Chemical and Materials Engineering, National University
of Kaohsiung, Kaohsiung, Taiwan, R.O.C.
e-mail: cfyang@nuk.edu.tw

Y.-T. Hsieh
Department of Electronic Engineering, Southern Taiwan University,
Tainan, Taiwan, R.O.C.

C.-C. Diao • C.-C. Wu
Department of Electronic Engineering, Kao Yuan University, Kaohsiung, Taiwan, R.O.C.

1 Introduction

Microstrip planar multiband bandpass filters had found wide applications in modern microwave wireless communication systems because of low profile, compact size, easily fabricated, low cost, and easy integration [1, 2]. Many modified methods were investigated to improve the filtering characteristics [2–5]. In the past, the single-stage multiband bandpass filters had the shortcomings of and narrow bandwidths and inadequate out-of-band rejections. To solve these problems, filters needed to cascade more resonators to get wider bandwidth and larger out-of-band rejection. However, the insertion losses and the pattern sizes were greatly increased and that would limit their utility. Besides, the requirements of many modern wireless communication protocols were quite different, especially in bandwidth. The cascaded method usually increases the bandwidths of all operating bands, and it was difficult to control the bandwidths of each passband [6]. Some bandwidths were too large for its narrowband protocol, for example, Global Positioning System (GPS) and radio-frequency identification (RFID), and that would bring unwanted noise signal [7]. In this study, there are two microstrip planar dual-band bandpass filters investigated. The higher dielectric constant Al_2O_3 ceramic substrate ($\varepsilon_r = 9.4$) was used for pattern minimization. At first, the proposed filter was based on a longer open-loop rectangle-ring resonator with the dual resonant frequencies of 1.23 and 2.31 GHz. Another shorter open-loop rectangle-ring resonator was designed to resonate at 2.52 GHz and was parallel positioned at another side of input/output transmission lines to improve the bandwidth of 2.4 GHz band. Further, the different dielectric constant Teflon/Al_2O_3 combined substrate is used to regulate the different length of parallel positioned resonators and simply the filter circuits. The different resonant current distributions of two filters were investigated to demonstrate the proposed method. The low environmental pollution of printing method was used to fabricate the proposed dual-band bandpass filter. The proposed filters with two operating bands and deep transmission zeros could be used for GPS (L2-band, 1.227 GHz) and WLAN (IEEE802.11b/g/n, 2.4–2.4835 GHz) dual-band applications.

2 Design on Al_2O_3 Ceramic Substrate

The proposed dual-band bandpass filter was based on $\lambda_g/2$ open-loop rectangle-ring resonator (Resonator L) (the dot section) shown in Fig. 1. According to the dielectric constant of Al_2O_3 ceramic ($\varepsilon_r = 9.4$), the approximation of the fundamental guided wavelength could be calculated by Eq. (1) [8]:

$$V = \frac{C}{\sqrt{\varepsilon_r}} = f\lambda_g \tag{1}$$

Fig. 1 The proposed dual-band bandpass filter designed on Al_2O_3 ceramic substrate
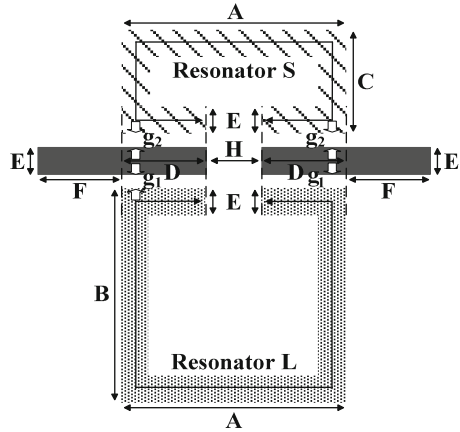
Fig. 2 The simulated frequency responses of two different resonators
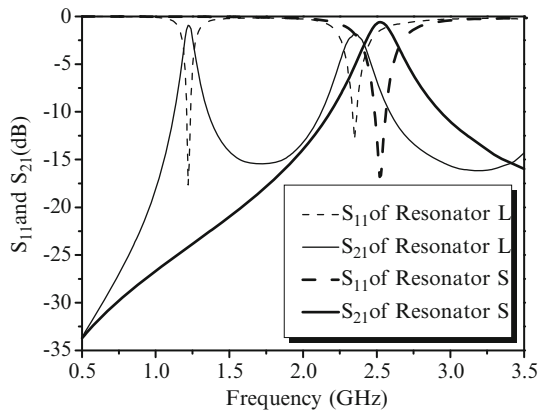
According to Eq. (1), the approximation of fundamental guided wavelength for our 1.23 GHz $\lambda_g/2$ open-loop resonator was 39.78 mm. As the fundamental resonance is set at 1.23 GHz, the approximation of the first spurious resonance would be closed to 2.31 GHz. It is 1 λ_g resonance, and its frequency is almost twice of $\lambda_g/2$ fundamental resonance. The optimal coupling parameters between input/output microstrip lines and resonators were 0.1 mm gap and 4 mm length. The resonant properties were showed in Fig. 2. However, even the bandwidth of 1.23 GHz band was adequate for GPS-L2-band protocol, and the bandwidths of 2.31 GHz were inadequate for the WLAN application. To improve the bandwidth of 2.4 GHz band independently, another resonator resonated closed to 2.4 GHz was needed. Figure 1 shows a shorter open-loop rectangle-ring resonator (Resonator S) (the oblique line section) was parallel positioned at another side of the input/output microstrip lines with the same coupling conditions to the original longer resonator. The resonant property of the shorter open-loop rectangle-ring resonator was also showed in Fig. 2. In this way, the bandwidth of second passband could be individually increased.

Table 1 Resonant properties of proposed filter against different C value

C value	5	5.5	6
f_0 of Resonator L	1.23 GHz	1.23 GHz	1.23 GHz
f_{s1} of Resonator L	2.31 GHz	2.31 GHz	2.31 GHz
f_0 of Resonator S	2.61 GHz	2.52 GHz	2.39 GHz
BW at 1.23 GHz	60 MHz	60 MHz	60 MHz
BW at 2.4 GHz	280 MHz	240 MHz	–
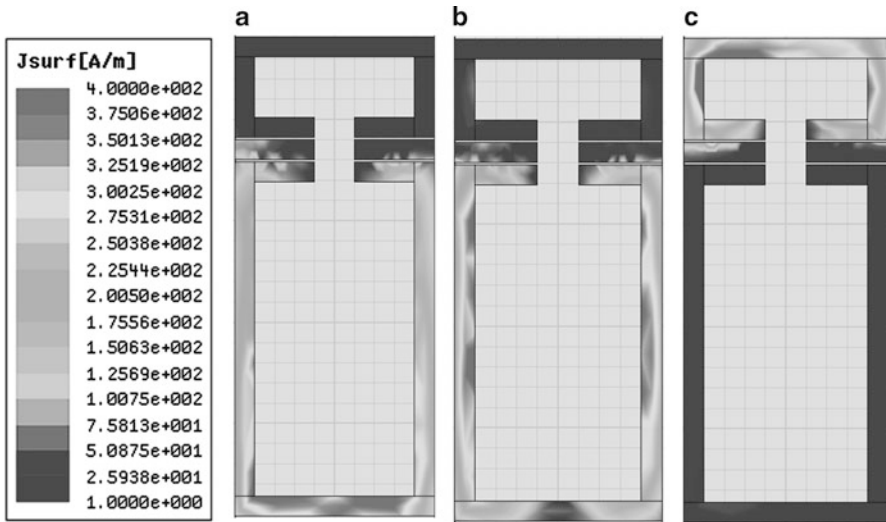
Fig. 3 The simulated resonant current distributions of two resonators at (**a**) 1.23 GHz, (**b**) 2.31 GHz, and (**c**) 2.52 GHz

According to the reference, if phase difference for signals in two paths was equal to 180°, the energy cancellation has happened, and no passband would be found [9, 10]. By suitable tuning, the signal could be coupled to different resonators and produced several resonant paths between the input/output transmission lines to enhance the bandwidths and produce the deep transmission zeros. The 2.4 GHz-band bandwidth of designed filter could be tuned by adjusting the length of Resonator S. Table 1 shows the resonant properties of proposed filter against different C value. As the C value increased from 5 to 6 mm, the responses of Resonator L had no apparent change, but the resonant frequency of Resonator S would shift to lower value. The bandwidths of 1.23 GHz band are the same, and those of 2.4 GHz band are decreased. Although the bandwidth of $C = 5$ mm was wider than that of 5.5 mm, the unwanted ripple would occur in the passband. If C was equal to 6 mm, the resonant frequencies of two resonators are two closed, the energy cancellation would happen, and no passband could be found around 2.4 GHz. As a result, $C = 5.5$ mm was the optimal value in this study.

For the first resonant mode, as Fig. 3a shows, two zero points are present in the front/end edges, and the maximum current density is present in the middle of resonator.

Fig. 4 The s voltage phase diagrams of two resonators
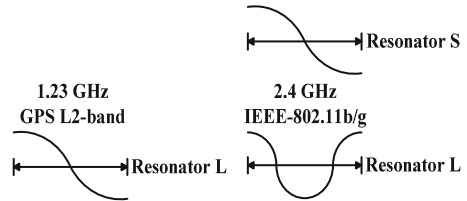
Fig. 5 The simulated and measured results of the proposed filter designed on Al_2O_3 ceramic substrate
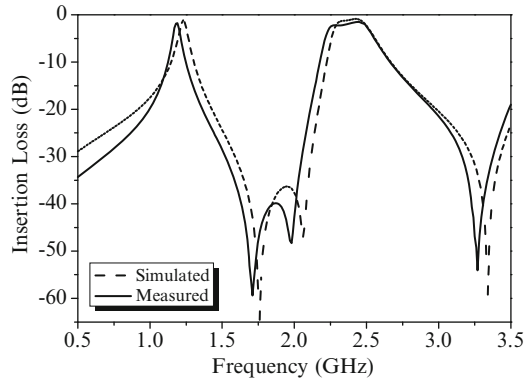
It means that the length of Resonator L is equal to the half-guided-wavelength route fundamental response for 1.23 GHz. Figure 3b shows that three 0 points and two maximum current density zones are distributed in Resonator L. It means that the length of Resonator L is equal to the full-guided-wavelength route of the first spurious response at 2.31 GHz. The current distribution of Resonator S in Fig. 3c presents the typical $\lambda_g/2$ fundamental response at 2.52 GHz. The voltage phase diagrams of two resonators at two resonant frequencies are shown in Fig. 4. The bandwidth of 1.23 GHz band is produced by $\lambda_g/2$ fundamental response of Resonator L. The bandwidth of 2.4 GHz band is produced by combining 1 λ_g first spurious response of Resonator L and $\lambda_g/2$ fundamental response of Resonator S. The structure with 180° phase difference was designed to achieve deep transmission zero and wider bandwidth for 2.4 GHz band.

The optimal parameters of the proposed filter designed on Al_2O_3 ceramic substrate are $A = 10$ mm, $B = 15.5$ mm, $C = 5$ mm, $D = 4$ mm, $E = 1$ mm, $F = 5$ mm, $H = 2$ mm, and $g_1 = g_2 = 0.1$ mm. Figure 5 shows the simulated and measured results of proposed filter. The simulated results are $S_{21} = 1.13$ dB, BW = 60 MHz (4.88 %) at 1.23 GHz and $S_{21} = 0.91$ dB, BW = 260 MHz (10.74 %) at 2.42 GHz. The measured results are $S_{21} = 1.77$ dB, BW = 60 MHz (4.96 %) at 1.21 GHz and $S_{21} = 1.96$ dB, BW = 310 MHz (12.55 %) at 2.45 GHz. The simulated transmission zeros are 64.55 dB at 1.76 GHz, 46.97 dB at 2.05 GHz, and 59.22 dB at 3.34 GHz. The measured transmission zeros are 59.39 dB at 1.71 GHz, 48.31 dB at 1.98 GHz, and 54.08 dB at 3.32 GHz, respectively. The fabricated filter is able to use in GPS-L2-band and WLAN systems.

3 Design on Teflon/Al$_2$O$_3$ Combined Substrate

Although the proposed dual-band bandpass filter designed on Al$_2$O$_3$ ceramic substrate has the good properties, it still has some disadvantages. First, the coupling length is not easy to tune because of the limits of its morphology. Second, there is waste space inside the loop ring. Third, as we know, Resonator L has almost double length to Resonator S. In this way, the first spurious resonance of Resonator L and the fundamental resonance of Resonator S could be united to lead the wide bandwidth and deep transmission zeros caused by phase difference. In order to couple the front/end stage of different length resonator with the same coupling length, two resonators must be curved as rectangle ring, but the corners will bring some inaccuracy. To solve the problem, the combined substrate method could be used to design two resonators with same parameters and different resonant frequencies. According to Eq. (1), the same length resonators designed on two substrates with four times of dielectric constant different would lead two times of fundamental frequency different. The proposed dual-band bandpass filter design on Teflon/Al$_2$O$_3$ combined substrate is shown in Fig. 6. The transmission lines and one resonator are positioned at Teflon side, and another resonator is designed at Al$_2$O$_3$ side.

Figure 7 shows the resonant properties of proposed filter vary on different width (J) of Resonator B. As Fig. 7 shows, the first operating band at 1.23 GHz band is
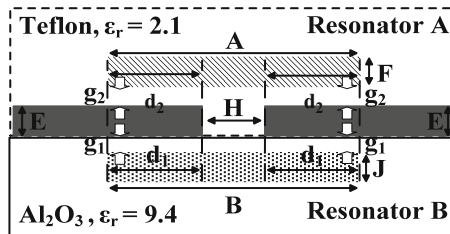
Fig. 6 The proposed dual-band bandpass filter design on Teflon/Al$_2$O$_3$ combined substrate
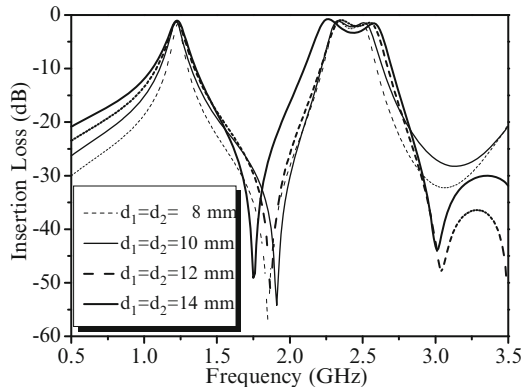
Fig. 7 The resonant properties of proposed filter vary on different width (J) of Resonator B

Fig. 8 The resonant properties of proposed filter vary on different coupling length ($d_1 = d_2$)
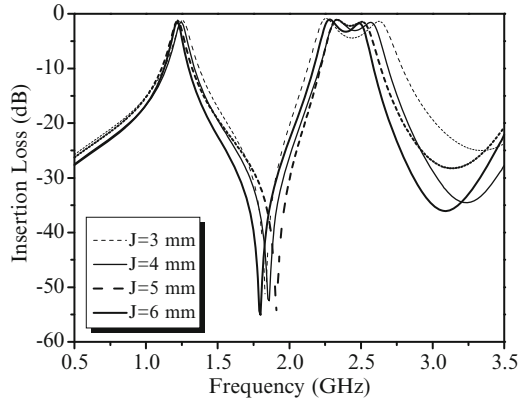
Fig. 9 The simulated and measured results of the proposed filter designed on Teflon/Al$_2$O$_3$ combined substrate
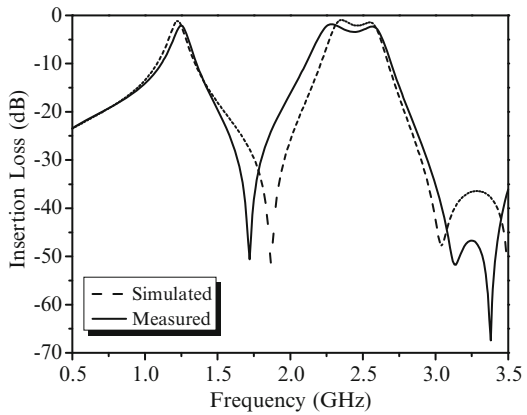
almost unchanged, but the second passband at 2.4 GHz band will increase with the J value increasing. The first spurious resonance shifts to higher value is the reason. Although the bandwidths of 2.4 GHz band will be enhanced, the ripple would become serious. In this study, $J = 5$ mm is adopted because of wide bandwidth and tiny ripple.

Figure 8 shows the resonant properties of proposed filter vary on different coupling length ($d_1 = d_2$). As Fig. 8 shows, both passbands will increase with the coupling length increasing from 8 to 14 mm. If the coupling length is longer than 12 mm, the out-of-band rejection, which is higher than the second passband, would present transmission zeros. If the coupling length is longer than 14 mm, the serious ripple would be presented in second passband. The coupling between transmission lines and resonators is too strong. In this study, $d_1 = d_2 = 12$ mm is selected because of good out-of-band rejection and acceptable ripple.

The optimal parameters of the proposed filter designed on Teflon/Al$_2$O$_3$ combined substrate are $A = B = 42$ mm, $E = 3.2$ mm, $F = 3$ mm, $J = 5$ mm, $H = 18$ mm, and $g_1 = g_2 = 0.1$ mm. Figure 9 shows the simulated and measured results of

proposed filter. The simulated results are $S_{21} = 1.17$ dB, BW $= 90$ MHz (7.32 %) at 1.23 GHz and $S_{21} = 1.91$ dB, BW $= 350$ MHz (14.22 %) at 2.46 GHz. The measured results are $S_{21} = 1.69$ dB, BW $= 80$ MHz (6.40 %) at 1.25 GHz and $S_{21} = 2.86$ dB, BW $= 430$ MHz (17.77 %) at 2.42 GHz. The simulated transmission zeros are 52.1 dB at 1.87 GHz and 47.75 dB at 3.04 GHz. The measured transmission zeros are 50.58 dB at 1.72 GHz, 51.73 dB at 3.14 GHz, and 67.45 dB at 3.38 GHz, respectively. The fabricated filter is able to use in GPS-L2-band and WLAN systems.

4 Conclusions

Two novel dual-band bandpass filters are investigated both using two resonators parallel positioned along with microstrip lines. The resonators have revealed even mode and odd mode with 180° phase difference around 2.4 GHz and present wide operating bandwidth and large out-of-band rejection. For the proposed filter designed on Al_2O_3 ceramic substrate, the measured results of the printed filter are $S_{21} = 1.77$ dB, BW $= 60$ MHz (4.96 %) at 1.21 GHz and $S_{21} = 1.96$ dB, BW $= 310$ MHz (12.55 %) at 2.45 GHz. The measured transmission zeros are 59.39 dB at 1.71 GHz, 48.31 dB at 1.98 GHz, and 54.08 dB at 3.32 GHz. For the proposed filter designed on Teflon/Al_2O_3 combined substrate, the measured results are $S_{21} = 1.69$ dB, BW $= 80$ MHz (6.40 %) at 1.25 GHz and $S_{21} = 2.86$ dB, BW $= 430$ MHz (17.77 %) at 2.42 GHz. The measured transmission zeros are 50.58 dB at 1.72 GHz, 51.73 dB at 3.14 GHz, and 67.45 dB at 3.38 GHz, respectively. The proposed filter reveals great filtering properties of GPS narrowband and WLAN wide band and deep transmission zeros.

References

1. Cheng CM, Yang CF (2010) IEEE Micro Wireless Compon Lett 20:268–270
2. Kung CY, Chen YC, Wu SM, Yang CF, Sun JS (2011) J Electromagn Waves Appl 25:617–628
3. Chen CH, Chen HM, Lin YF, Yang CF (2008) Micro Optic Tech Lett 50:2117–2119
4. Zhang YP, Sun M (2006) IEEE Trans Microw Theory Tech 54:3779–3785
5. Hsieh LH, Chang K (2000) Electron Lett 36:1626–1627
6. Zhou M, Tang XH, Xiao F (2008) IEEE Microw Wireless Compon Lett 18:779–781
7. Tu WH, Chang K (2005) IEEE Microw Wireless Compon Lett 15:268–270
8. Hong JS, Lancaster MJ (2001) Microstrip filters for RF/microwave applications. Wiley, New York
9. Rosenberg U, Amari S (2002) IEEE Trans Microw Theory Tech 50:2896–2902
10. Osipenkov V, Vesnin SG (1994) IEEE Trans Microw Theory Tech 42:1360–1336

Constructing an Integrated Communication and Oriented Protocols into EV Preliminary Operation: A Case Study of EV Surveillance Application

Chan-Wei Hsu, Yu-Chi Shiue, Shun-Li Wang, Hou-Yu Huang, and Cheng-Ruei Wei

Abstract EVs have been gradually applied into life, but the demand is uncertain, yet a developed and service infrastructure of charging stations is a prerequisite for growth in EV market. A preliminary operation is therefore constructed in long-term perspective, and this chapter presents a concept of surveillance, message broadcast, and data acquisition design for EV preliminary research. The platform integrated communication technologies and address oriented protocols for simulated scenarios. Mobile communication offers data exchange for remote surveillance when continuously linking. Each parameter acquisition is handled by OBU via CAN bus. To simulate different traffic conditions, DSRC is adopted as the bridge among roadside unit, server center, and vehicle. Server center plays the role of benefit evaluation which has the ability to provide statistic data for further analysis and assessment. Taking an EV as demonstrated vehicle, the power consumption and scheduled traffic condition are used to discuss and verify platform ability.

Keywords Charger point • DSRC • CAN bus

C.-W. Hsu (✉)
Research & Development Division, Automotive Research & Testing Center,
Changhua 50544, Taiwan
e-mail: winsonhsu@artc.org.tw

Y.-C. Shiue • H.-Y. Huang • C.-R. Wei
Green Vehicle Division, Automotive Research & Testing Center,
Changhua 50544, Taiwan

S.-L. Wang
Technical Service Division, Automotive Research & Testing Center,
Changhua 50544, Taiwan

1 Introduction

With increasing concern over the environment and strict emissions regulations, the electric vehicle has been investigated as an alternative form of transportation. Walgreens, which is a pharmacy chain, plans to offer electric vehicle (EV) charging stations at about 800 locations across the country by the end of the year in 2011, making it the nation's largest charging station retail host. The charging stations will feature either a fast DC charger that can add 30 miles of range in as little as 10 min of charging time, or a Level 2 charger that can add up to 25 miles of range per hour of charge [1]. However, the electric vehicle suffers from relatively short range and long charging times and consequently has not become an acceptable solution to the automotive consumer. Owing to the shortcoming of its characteristics, it is difficult to guarantee the applicability of electric vehicles [2]. Therefore, it is necessary for data collection and quality tracking for EV under qualitative concept.

This chapter presents an integrated system to construct an EV preliminary research field using hybrid communications, DSRC for controlling and simulating real traffic scenario, and RFID for ID certification. EV would be demonstrated in this study for power optimization with simulated traffic from statistic data analysis, and moreover, a charger point plays auxiliary role for assistant research. Many scheduled formats of broadcasting protocols are also taken into consideration, and furthermore, these formats will be open protocols under the Department of Industrial Technology Research.

2 Introduction

The EV preliminary operation platform is built of four main components, including ARTC server center, onboard unit (OBU), RSU devices, and charger station in demonstrated field. The architecture of the preliminary research platform is shown in Fig. 1 below. The ARTC server provides handling information and collecting database with long-term statistic data and short-term variation when EV drivers stop on the road, e.g., power on air condition, access charger point, or drive from one place to another place. Figure 1 shows that the communication bridge is Ethernet interface between server center and charger station.

Under data collecting demand, we have established some outstanding technology in mobile data surveillance system. The core technology is mainly focused on client and server architecture through the Internet. The client is designed and fabricated using microcontroller-based circuit with embedded firmware for connecting sensors and transducers into mobile communication, while the ARTC server is designed and constructed to access Internet performance to receive client data, including operation data strings and physical data collecting from the sensors or transducers. Hence, OBU is a mobile device which transmits relevant parameters. The communication also has high feasibility for operating different protocols. Through the Internet,
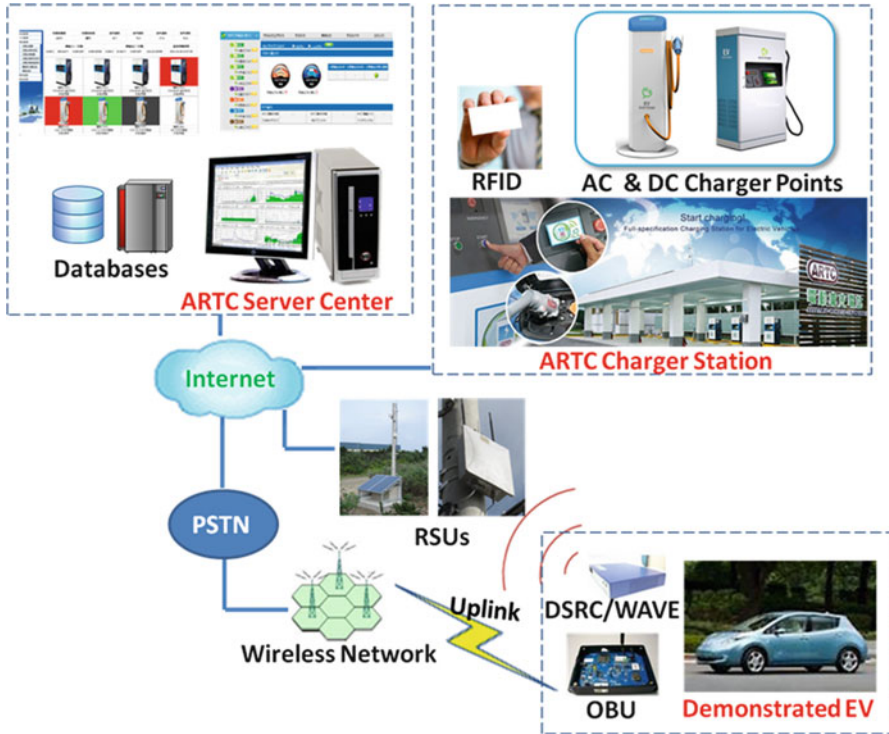
Fig. 1 This architecture shows EV preliminary operation platform that the communication bridge is Ethernet interface between server center and charger station

the reporting data will be collected onto ARTC server for further data mining. Along the Internet backbone, all data can be retransmitted to any authorized user with less than 2-s delays [3].

2.1 Onboard Unit

An OBU is built of the basic four parts of processing core: SD card for data logging, GPS module for positioning, HSPA module for data surveillance, and CAN interface for vehicular information. The MCU is chosen as core controller to handle real-time message. GPS data through universal asynchronous receiver and transmitter port, and furthermore, positioning data and dynamic data are well processed to server center. Besides, the core is designed to perform as supervisor core, where vehicular data and power information are on-line captured and processed back to the HSPA module. These power parameters are captured in CAN bus with controlled timing. Each packet is less than 8 bytes using standard ID (11 bit); moreover, the refresh time of packets is about 20 ms. In this study, the data rate is 500 kbps and its sampling

point is held in 75 %. In addition, the differential input resistance should be defined to decide bus loaded before connecting to a bus except terminal resisters [4]. Not only data acquisition but also diagnostic function is very important. The diagnostic function is implemented in serial and can interface. Besides, the OBU also presents another design concept to keep overall record. SD card is applied to an auxiliary role with respect to HSPA communication. The record data can be stored into SD card and can be easily read through any operation system in this research.

2.2   ARTC Server Center

In the planning of ARTC server center, the core technology may be aimed at the server system and its database in different types of position. All the demonstrated vehicles will be conformed and transmitted to the EV database under different filtering mechanisms. In real-time processing, RFID database in relationship to user information in ARTC server center operation will initiate a synchronized mechanism and provide user's authorization and authentication certification to charger station. Database management relating to security and performance is an important issue in the planning and implementation. The receiving EV data will need to design a very neat coding to build in the OBU system. This will speed up EV information in data mining, such as SOC, with current w.r.t time varying. Taking EV database as example, it is designed in following the concepts with real-time information, EV basic records, EV-type information, and its historical data. The historical data has the data table linkage and process for the proposed server center. Referring to Fig. 1, information acquisition and delivery is carried on through Internet. Real-time delay of 1–20 s is inevitable in abnormal state. The storage data in SD card will record alternatively, and OBU will transmit recorded data when communication slot is available.

2.3   Charger Station

The charger station supports multiple functions to access its charger points. This charging station has several mainstream charger interfaces of the world, including Taiwan standard, American SAE, European IEC type I, China GB, and Japan CHAdeMO. In Taiwan IDB standard, types 2A and 2B are compatible and the difference is the maximum current (32A and 80A@220 VAC). The interface voltage of CHAdeMO is located from 50 to 500 V and the maximum is 125 A, usu. 80 A. It also has household socket (110 V) for electric scooter charging. The charger is activated by an RFID tag, and the server center can record all the charging information automatically (duration, power, current, voltage, etc.). The RFID reader reads tag data and sends to server computer via TCP/IP for data process. The data frame includes destination address, source address,

data, and its checksum. For convenience, this kind of tag is inductively coupled transponders which operate passively. The mechanism can inform users where charging points are.

2.4 RSU Unit

In traffic simulation, this research has been undertaken. ARTC server uses Ethernet and DSRC channel interface to transmit data. DSRC are for data-only systems and operate on radio frequencies in the 5.725–5.875 MHz industrial, scientific, and medical (ISM) band. DSRC systems consist of roadside units (RSUs) and the onboard units (OBUs) [5]. The demonstrated EV also uses another DSRC OBUs to acquire necessary traffic data (speed, accidents, or events). During this setup, various traffic scenarios were simulated and many EV parameters were also captured and logged to ascertain the usability and reliability. The traffic information is handled by ARTC server center, and data broadcasting is finished from radio base station to nearest RSU.

3 Oriented Protocol Design

For data collection of preliminary research, OBU design plays the key role. In operation, OBU transmits data to server center through PSTN network via HSPA communication. Before transmitting to server, data frame is complied with database structure. To meet a real scenario, traffic conditions are simulated with Wi-Fi broadcasting. However, the broadcasting message should follow ISO 2735. In this chapter, the oriented protocol is adopted to define message frames. The EV data collecting platform has special function which it can simulate differential traffic scenarios. It depends on the ARTC broadcasting system, which follows SAE J2735 in protocol and refers to radio data system for broadcasting specification. Besides, the RDS specification also has been applied in traffic message channel (TMC). This oriented protocol is integrated with J2735 in message sets and TMC frame.

The purpose of SAE J2735 is to support interoperability among DSRC applications through the use of standardized message sets, data frames, and data elements. It provides information that is useful in understanding how to apply the various DSRC standards, along with the message sets, data frames, and data elements specified herein, to produce interoperable DSRC applications. But the relevant parameters in preliminary platform only adopt three message sets of J2735 [6], which selects MSG_Ala Carte about sending and receiving entities, MSG_BasicSafety in exchanging safety data regarding vehicle state, and MSG Common SafetyRequest in broadcasting.

4 EV Platform Implementation

This preliminary research mainly provides EV parameter status from network. Outside the charging station, the user can by way of Ethernet to obtain the real-time charging information. Users can use ARTC surveillance platform to check EV status. In addition, the surveillance platform also is compatible with explorer or chrome browsers. When EV drivers use charger points to charger, the charging function can show estimated finish time and charger point status. Besides, the web instrument can display its real-time voltage and current using TCP/IP connection. It also presented the charger power and state of charge in right down form.

This platform will provide five major functions, driving information monitor, charging information monitor, remote diagnostic, system performance trend forecast, and data report. The charging information is very important for preliminary research and the voltage variation research can be logged into database in which the server center uses chart or curve diagram to show its historical data, as shown in Fig. 2. In another concept about traffic simulation, some event (traffic jam, accident, or limited speed) is also logged into historical data which is labeled in chart using broadcasting mechanism. One case about traffic accident is shown in Fig. 3. On the other hand, the EV activation or utilization is also considered. To evaluate the charger station contribution, the activation chart is also available in ARTC web browser. In the upper part of Fig. 3, the chart demonstrated the station activation relative to time. In the lower part of Fig. 3, it converts to power efficiency. This index can estimate the remaining time so as to remind the driver with message or instrument display.

5 Discussion

In this chapter, the capability of EV preliminary research platform using mobile and DSRC communication is verified. The proposed system designs OBU device over HSPA technology and implements broadcast mechanism over DSRC to accomplish
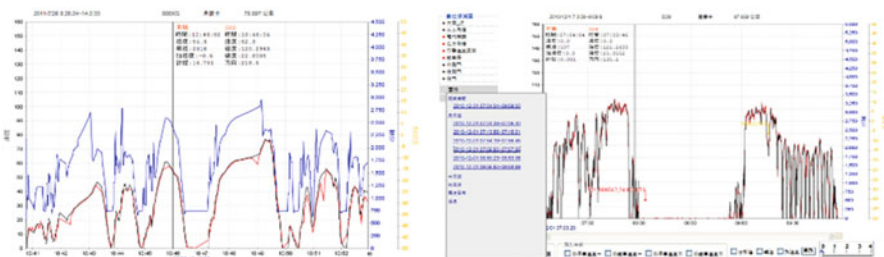
Fig. 2 The history record of charging voltage, and traffic events w.r.t. time are presented and traffic simulation event is also included into locus

Fig. 3 EV activation in historical data shows in plots from database table with charging points

traffic simulation. Data recorder plays an auxiliary role to record overall data. The web browser also helps EV driver or managers get on-line activation or state of charge. The implementation also extends the capability of EV research into real-time data collection in many varieties. In such support, the proposed system can surveillance EV parameters and demonstrate a completely testbed.

References

1. Environmental & Energy Management News. http://www.environmentalleader.com/
2. Liu H, Wu J, Chu L (2011) Design of remote monitoring and fault diagnosis system for electric vehicle. Electron Mech Eng Inf Technol 2:1079–1082
3. Fernandes P, Nunes U (2007) Vehicle communications: a short survey. In: IADIS international conference of telecommunications, networks and systems, Lisbon, 2007, pp 134–138
4. Lin CE, Li CC, Hou AS, Wu CC (2003) A real time remote control architecture using mobile communication. IEEE Trans Instrum Meas 52(4):995–1002
5. Szilagyi C, Koopman P (2010) Low cost multicast authentication via validity voting in time-triggered embedded control networks. Workshop on embedded system security, New York, 2010
6. Xu Q, Segupta R, Jiang D, Chrysler D (2003) Design and analysis of highway safety communication protocol in 5.9 GHz dedicated short range communication spectrum. Veh Technol Conf 4:2451–2455
7. (2006) SAE standard J2735: Dedicated short range communications (DSRC) message set dictionary, SAE handbook, Society of Automotive Engineers

The Design of Capacitive Coupling Bandpass Filter Using Stepped Impedance Resonator

Chien-Hung Chen, Hua-Ming Chen, Chien-Chen Diao, Wei-Kuo Chia, and Cheng-Fu Yang

Abstract In this chapter, the main focus is on the design of microstrip dual-band filter function. This chapter presents a new compact, low insertion loss, sharp-rejection, and capacitive coupling dual-band microstrip bandpass filter. The operation of filter was designed in dual band of WLAN 2.45 GHz and WiMax 3.5 GHz. In order to reduce the size, the proposed filter used skew symmetric feed and microstrip line ring structure. The proposed filter additional two winding-type L shape of the stepped impedance resonator increased high-frequency transmission zeros to achieve a good dual-band effect. The filter was using electromagnetic simulator Ansoft HFSS, which was used to adjust and optimize the associated parameters. The filter was fabricated by Rogers RT/duroid 6010 substrate and measured by Agilent-N5230A with the connectors. The dual-band bandpass filter experimental results are in good agreement with the full-wave simulation results. Experimental results are in good agreement with the full-wave simulation results.

Keywords Microstrip • Bandpass filter • Stepped impendence

C.-H. Chen
Department of Avionics Engineering, Air Force Academy, Kaohsiung, Taiwan, R.O.C.

H.-M. Chen
Institute of Photonics and Communications, National Kaohsiung University
of Applied Sciences, Kaohsiung 807, Taiwan

C.-C. Diao
Department of Electronic Engineering, Kao Yuan University, Kaohsiung, Taiwan, R.O.C.

W.-K. Chia
Department of Electronic Engineering, Fortune Institute of Technology,
Kaohsiung, Taiwan, R.O.C.

C.-F. Yang (✉)
Department of Chemical and Materials Engineering, National University
of Kaohsiung, Kaohsiung, Taiwan, R.O.C.
e-mail: cfyang@nuk.edu.tw

1 Introduction

In recent years, microwave wireless systems are growing rapidly to offer and satisfy lots of communication products. And the communication and contact of user have risen from wire to multiband wireless communication system very conveniently. However, people continually promote the needs of qualities of wireless communications, which will provide for multimedia information of voices, figures, and images in the future. Besides, it is the most important to combine the World-wide Interoperability for Microwave Access (WiMax) with wireless local area network (WLAN) communications. Due to the development of communications technology and the increase in operation band, it brings a great benefit to increase the band operation and add a good transmission zero of data. Therefore, some of wireless local area network (WLAN) standards, including IEEE 802.11 and WiMax, are offered. With the rapid development of modern mobile and wireless communication systems, the need for filters is challenged by not only its compact size but also the dual band.

In this chapter, a new resonator microstrip coupling step impendence band filter working at 2.4 and 3.5 GHz is introduced. The use of step impendence structure allows a wide stop-hand filter to be integrated into the circuit substrate, thus allowing for collocation of other microstrip circuit elements with the filter [1–7]. The first section describes how the filter was designed and presents the parameters of the filter. And then, the following section describes the simulated results with 3D full-wave electromagnetic analysis using HFSS. The last part gives a discussion of the effect of parameters of the filter, especially the depth of the performances. The filter is integrated in a standard printed circuit board (PCB) Rogers RT/duroid 6010.

2 Theory and Design

The function of the impedance converter that makes the energy can be sent without loss and reflected waves ($\Gamma = 0$). [1] If the general impedance mismatches, it will produce the reflected waves. The quarter-wave impedance converter is a very common impedance matching circuit, which is easy to design and has a simple structure.

In Fig. 1a, b, the load impedance Z_L and the feed line impedance Z_o are both known two real numbers. Between those two components is a period quarter-wave transmission line in which Z_1 is the characteristic impedance. Take advantage of quarter-wave transmission line and make the load match the transmission line to Z_o that cloud obtain ($\Gamma = 0$) and also in non-reflective state.

From the transmission line impedance formula:

$$Z_{in} = Z_1 \frac{Z_L + jZ_1 \tan(\beta l)}{Z_1 + jZ_L \tan(\beta l)} \tag{1}$$
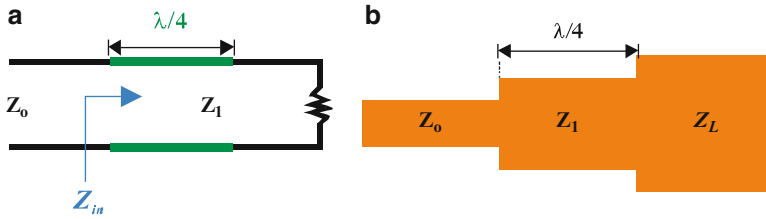
Fig. 1 (**a**) The circuit diagram and (**b**) The microstrip line of quarter-wave impedance converter
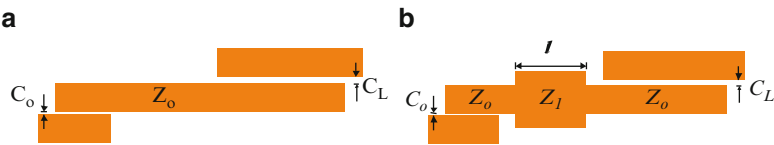
Fig. 2 (**a**) The drawing of different coupling segments of microstrip line and (**b**) microstrip line with stepped impedance

When $l = \lambda/4$ and $\beta\, l = \pi/2$, it will cause the imaginary part equal to 0:

$$Z_{\text{in}} = \frac{Z_1^2}{Z_L} \tag{2}$$

And there is a reflection coefficient formula:

$$|\Gamma| = \left| \frac{Z_{\text{in}} - Z_{\text{o}}}{Z_{\text{in}} + Z_{\text{o}}} \right| \tag{3}$$

In order to get no reflection ($\Gamma = 0$), the input impedance (Z_{in}) must be equal to output impedance (Z_{o}). Therefore, substituting into Eq. 3, the formula will be

$$Z_1 = \sqrt{Z_{\text{o}} Z_L} \tag{4}$$

In this study, the characteristic impedance of the resonator is 50 Ω. But both ends of the coupling length and spacing are not the same. In Fig. 2a, therefore, that must have the quarter-wave impedance to adjust the matching impedance.

By the reflection coefficient equations, the real part of Z_{in} and Z_{o} is the same, but the imaginary part is not. In the middle of the structure, those have to add with the imaginary part of the impedance converter to adjust the impedance matching. In order to match impedance, make stepped impedance in the structure shown in Fig. 2b. And then, following those equations cloud calculate the middle of structure required stepped impedance is 24 Ω, which the length l equals to $\lambda/30$.

3   Results and Discussion

Figure 3 shows the structure of capacitive coupling bandpass filter using stepped impedance resonator. The design was fabricated on a Rogers RT/duroid 6010 substrate of thickness $h = 0.635$ mm and relative permittivity $\varepsilon_r = 10.2$; the optimal design parameters of the filter are as follows: $L = 30$ mm and $W = 11.4$ mm. For the dual-band filter operation, the input/output (I/O) ports were spatially separated by $180°$ (parallel) and a perturbation element was introduced within the resonator at a symmetrical axis apart from both I/O ports [8–10]. In order to reduce experimental cut-and-try design cycles, the simulation software HFSS is used to provide the design dimensions.

It can be seen that the proposed resonator produces two different characteristics. The coupling coefficient is computed using the relationship between the splitting in the resonant frequencies of the two modes and the coupling coefficient k, as described by [1, 4]:

$$k = \frac{f_2^2 - f_1^2}{f_2^2 + f_1^2} \tag{5}$$

In Eq. 5, f_1 and f_2 are the resonant frequencies of mode 1 and mode 2, respectively. Comparing the resonant coupling coefficient of the different length of the coupling gap Fig. 4a G_1 and Fig. 4b G_2. From this evidence, it is concluded that the resonant coupling coefficient is predominantly affected by the coupling gap. The length of the coupling gap is designed in 0.1 mm.

The proposal stepped impedance capacitive-coupled dual-band filter was fed into a 50 Ω microstrip line skew symmetric and shunt-connected to the capacitive loads of the resonators. And there is an open resonator in two separate horizontal re-coupling two inverted L configuration of the resonator consisting. In order to achieve the miniaturization effect, make an annular manner. The experiment is designed for radio-frequency microwave capacitive microstrip coupling line applied to filter of high performance.
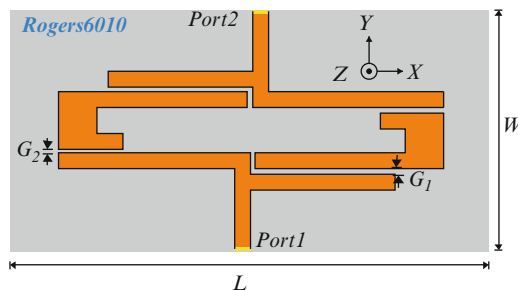
Fig. 3   The structure of capacitive coupling bandpass filter using stepped impedance resonator
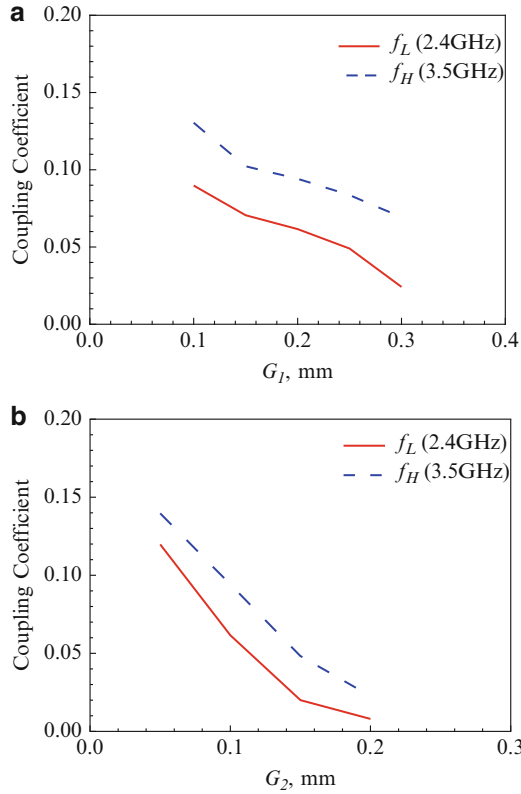
Fig. 4 Coupling coefficient of the proposal bandpass filter under different gaps (**a**) G_1 and (**b**) G_2

4 Conclusions

The bandpass filter was designed to integrate the recent advances made by the dual band and low cost in the rapidly expanding field of WLAN and WiMax operation. In this chapter, a small-size, microstrip filter for dual-band operation is proposed and successfully implemented in the letter.

Figure 5 shows the simulated and measured response of the proposal bandpass filter. The results of simulations and those of experiments are in good agreement. The characteristics of mode splitting have been described, and the transmission zeros are adjusted by shifts that the two inputs feed. The change in the return loss and insertion loss is reflected by a change in the coupling gap. There is an open resonator that could excite the low-frequency modal. There is a simple structure that has symmetry and easy control operation band and has a good independent modal in operating characteristics. Its advantages conform to the needs of modern wireless local area network that narrows the distance of oscillators and reduces the
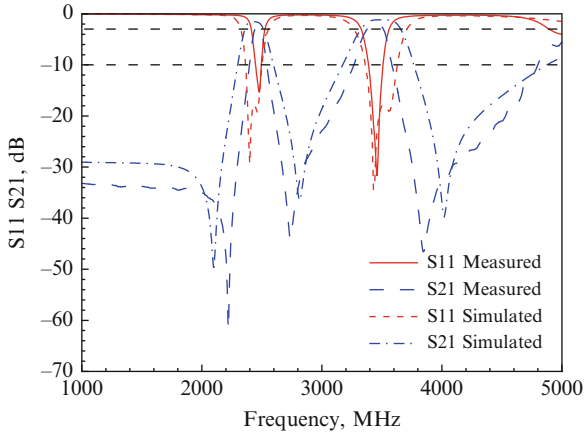
Fig. 5 Simulated and measured response of the proposal bandpass filter
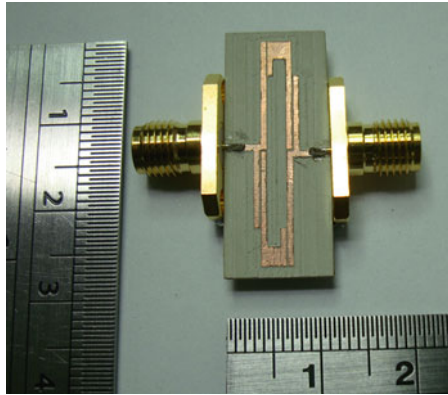
Fig. 6 Photograph of the proposed bandpass filter

size of filters drastically. Therefore, this design is smaller and cheaper than available before. This design regulates not only harmonic to increase or decrease electric transmission zero by aspect ratio of upper coupling to reach control of the effect of insertion loss of filters but also the length of coupling gap or microstrip line to adjust damage of the bandpass and the insertion. Figure 6 shows the photograph of the fabricated bandpass filter. The proposed filter has been designed and fabricated on the Rogers RT/duroid 6010 substrate and found to have two operation bands, which cover the 2.4 and 3.5 GHz for the operation of WLAN IEEE-802.11b/g/n and WiMax, making the application of the proposed RF module in future WLAN systems possible.

References

1. Hong JS, Lancaster MJ (2011) Microstrip filters for RF/microwave applications, 2nd edn. Wiley, New York
2. Hsieh LH, Chang K (2000) Electron Lett 36:1626–1627
3. Lin Y-S, Wang P-C, You C-W, Chang P-Y (2010) IEEE Trans Microw Theory Tech 58(12):3417–3426
4. Gorrur A (2004) IEEE Trans Microw Theory Tech 52:671–677
5. Cheng CM, Yang CF (2010) IEEE Microw Wirel Compon Lett 20(5):268–270
6. Sun S, Zhu L (2006) IEEE Wirel Compon Lett 15(10)
7. Rosenberg U, Amari S (2002) IEEE Trans Microw Theory Tech 50:2896–2902
8. Rebenaque DC, Pereira FQ, Garcia JP, Alvarez Melcon A, Guglielmi M (2004) IEEE Wirel Compon Lett 14(10)
9. Hsieh LH, Chang K (2002) IEEE Trans Microw Theory Tech 50:1340–1345
10. Gorur A (2002) IEEE Microw Wirel Compon Lett 12:386–388

Part VII
Materials and Mechanical Engineering

A Novel Power-Effective and Reliable Wireless Thermal Convection Angular Accelerometer Without Any Movable Parts and Grooved Cavity

Jium-Ming Lin and Cheng-Hung Lin

Abstract This chapter integrated an active RFID tag with a thermal convection angular accelerometer on a flexible substrate. The first new idea was to make the device directly on a flexible substrate without any movable parts, so it is very easy to make and reliable. The second idea used the flexible substrate such as polyimide, since its thermal conductivity is much lower than silicon, and thus, it can save more power. The third new idea and the most powerful one is that the angular acceler-ometer is integrated with an active RFID tag on the same flexible substrate; thus, the device becomes a more useful wireless angular acceleration sensor. By using the traditional square chamber filled with carbon dioxide, the device sensitivity is $18.8\ ^{\circ}C/(rad/s^2)$ and the response time is 158 μs.

1 Introduction

Conventional accelerometers are made on silicon [1–17], some of them used the thermal convection technologies [6–17], and the chamber is filled with air or CO_2. This chapter integrates RFID tag with thermal convection angular accelerometers on a flexible substrate as in Fig. 1. The first idea makes the device directly on a flexible substrate without any movable parts, so it is very easy to make and reliable. The second idea is to make the device on a flexible substrate as plastic or polyimide; the thermal conductivity of the polyimide (0.06–0.0017 W/(cm-K)) is about 25th of

J.-M. Lin (✉)
Department of Communication Engineering, Chung-Hua University, Hsin-Chu 30012, Taiwan
e-mail: jmlin@chu.edu.tw

C.-H. Lin
Ph.D. Program in Engineering Science, College of Engineering, Chung-Hua University, Hsinchu, Taiwan
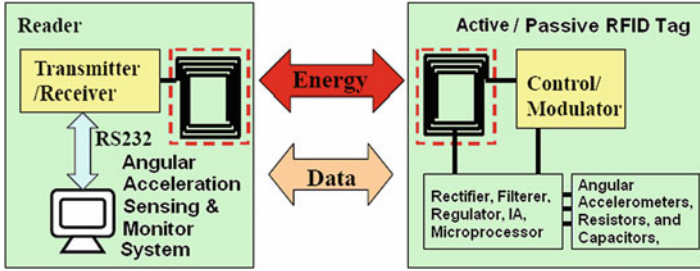
Fig. 1 Block diagram of the proposed RFID-based angular accelerometer

the silicon (1.48 W/(cm-K)), and thus, it can save more power and very useful. The third new idea and the most powerful one is that the angular accelerometer is integrated with an active RFID tag on the same flexible substrate; thus, the device becomes a more useful wireless angular acceleration sensor, and it can be applied in the fields of hospital monitoring, game, etc., so the new device is very easy for usage and fabrication. The heater operating temperature is 127 °C (400 K) without melting the polyimide substrate. By using the traditional square chamber filled with carbon dioxide, the device sensitivity is 18.8 °C/(rad/s^2) and the response time is 158 μs.

2 Fabrication and Packaging Steps

Step 1: Evaporate SiO$_2$ on both sides of substrate for thermal, electrical, and humidity isolation. Next is to cover photoresist (PR) on both sides to protect the layers of SiO$_2$. The result is in Fig. 2.

Step 2: Deposit a layer of p-type amorphous silicon with thickness 100–250 μm then, using an Nd-YAG laser, anneal it as a polysilicon thermistor. Next is to use mask #1 and PAEP to reserve the PR on the polysilicon thermistor. Finally, use KOH solution or RIE process to remove the layers of polysilicon without PR protection. After removing the PR, the result is in Fig. 3.

Step 3: Deposit Cr and Ni to make the heater and the supporting layers of RFID antenna and conductors connected to the power supply. Next is to use mask #2 and PAEP to reserve the PR on the heater, RFID antenna, as well as the conductors connected to the power supply. Finally, use sulfuric acid solution or RIE process to remove the layers of Cr and Ni without PR protection. After removing the PR, the result is in Fig. 4. Note that the temperature sensors can also be made by the E-beam evaporation process by using one set of the thermal pile materials as follows: K type (chromel and alumel), J type (iron and constantan), E type(chromel and constantan), and T type (copper and constantan).

Fig. 2 The result of Step 1

Fig. 3 The result of Step 2
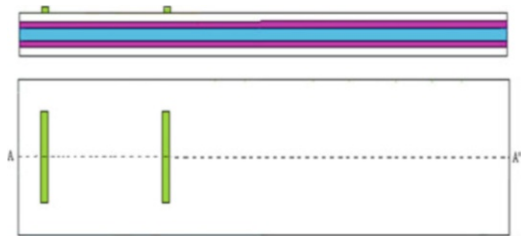
Fig. 4 The result of Step 3
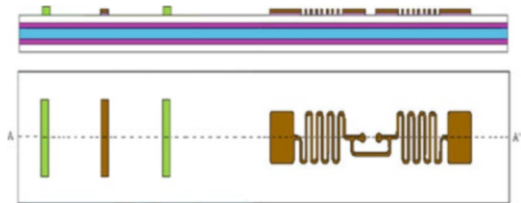
Fig. 5 The result of Step 4
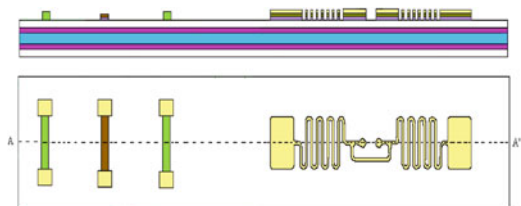
Fig. 6 The result of Step 5
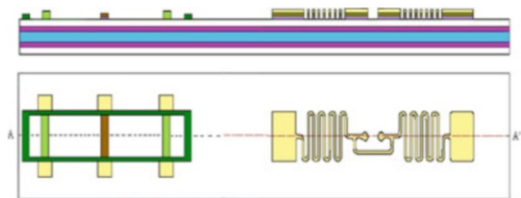
Step 4: Use mask #3 and PAEP to reserve PR on the heater, and then flash a layer of gold on Ni by electroless plating. Thus, the conductivity of the RFID antenna and the conductors connected to the power supply would be very good. In addition, the performance of the soldering process on the pads for packaging would also be increased. Then remove the PR. The result is in Fig. 5.

Step 5: Use screen printing method to put plastic or polymer as the sealing material around the accelerometer as dam bar as in Fig. 6, and the chip with metal bump is a flip chip bonded to RFID feed terminal by thermal compression method, and then make the underfill to increase the adherence of the chip.
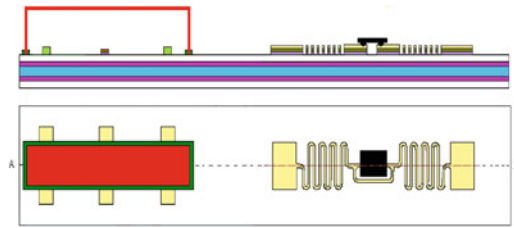
Fig. 7 The result of Step 6
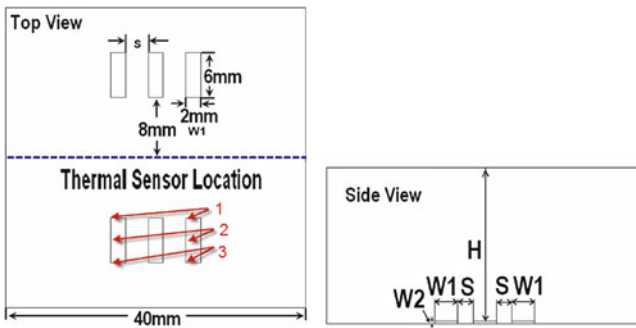
Fig. 8 Square chamber dimensions

Step 6: Finally, put a cap with square chamber on the dam bar as addressed in Hsu [18] before curing and sealing it, one can fill it with CO_2, and the result is in Fig. 7. The geometric definitions of heater, thermistor, and chamber dimensions are as in Fig. 8 ($H = 19.7$ mm, $W1 = 2$ mm, $W2 = 0.3$ mm).

3 Simulation and Discussion

In this section we use ESI-CFD + software package for 3D simulation. Firstly, the temperatures of the package boundaries and the heaters are set as 300 and 400 K, respectively. The thermal sensor can be at either one of the three points in Fig. 8 to be traded off later. The governing equations of mass, momentum, and energy are, respectively, as follows:

In the above equations, u is the velocity vector, t is the time, and Δ is nabla. ρ, p, and α are density, pressure, and acceleration, respectively, and c_P, T, and k are the fluid specific heat, temperature, and thermal conductivity, respectively. In addition, with the ideal gas constant R, one has the relationship of states ρ and p as follows:
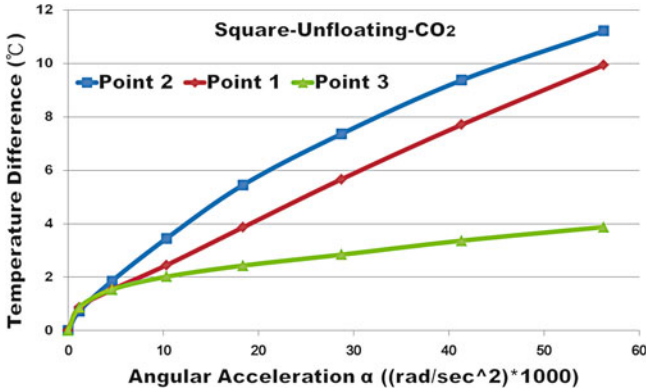
Fig. 9 The thermal sensor temperature differences vs. angular accelerations for the thermal sensors at points 1, 2, and 3

$$\nabla \cdot \bar{u} = 0 \tag{1}$$

$$\frac{\partial \rho}{\partial t} + \nabla \rho \bar{u} = 0 \tag{2}$$

$$\frac{\partial \rho \bar{u}}{\partial t} + \nabla(\rho \bar{u}\,\bar{u}) = \rho \beta (T - T_{\text{heater}}) \alpha \tag{3}$$

$$\rho c_{\text{P}} \bar{u} \nabla T = k \nabla^2 T \tag{4}$$

$$\rho = \frac{p}{RT} \tag{5}$$

Firstly, let the distance between heater and thermal sensors ($=S$) be 2 mm. The thermal sensor temperature differences vs. angular accelerations for the thermal sensors at points 1, 2, and 3 are as in Fig. 9. Note that the sensitivity is far better ($18.8\ ^\circ$C/(rad/s^2) to put the thermal sensors at point 2, and the linearity is also good.

So we put thermal sensors at this place for the following analysis of the step-input angular acceleration responses of gas velocity, static pressure, and total enthalpy; the results are as in Fig. 10a and b. The detailed response times of step-input angular accelerations for static pressure and total enthalpy are listed in Table 1, respectively. Note that the response time of step-input angular accelerations is 81 µs.

4   Conclusions

The contributions of this chapter are summarized as follows:

1. This is a brand new idea to make both heater and temperature sensors of a thermal convection angular accelerometer on a flexible substrate by using
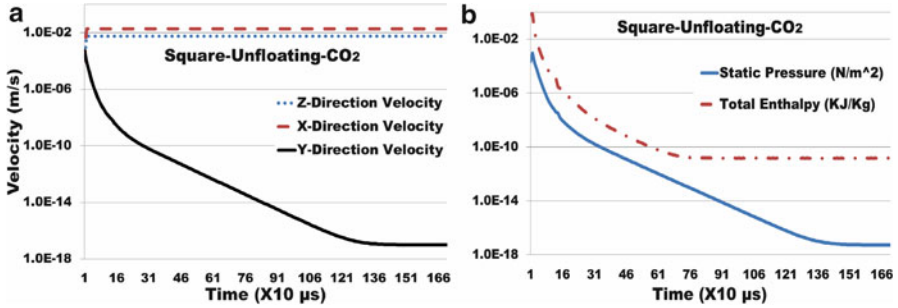
Fig. 10 The step-input angular acceleration responses of (**a**) gas velocity and (**b**) static pressure and total enthalpy

Table 1 The response times of step-input angular accelerations

Static pressure	Total enthalpy
158 μs	85 μs

lower-temperature process, such as evaporation, which is not proposed before. Besides, the device is without any movable parts and grooved cavity, so it is very reliable.

2. Thus, one can integrate the RFID tag with the thermal convection angular accelerometer on the plastic substrate to make a more powerful wireless angular acceleration sensor.
3. It is a new idea to use flexible substrate; its thermal isolation capability is better than the traditional silicon, and thus, the cost of power dissipation is lower for the new design.
4. The sensitivity and the response time of the new thermal convection angular accelerometer are 18.8 $°C/(rad/s^2)$ and 158 μs, respectively.

References

1. Lin L, Howe RT, Pisano APJ (1998) Microelectromechanical filters for signal processing. J Microelectromech Syst 7:286–294
2. Roylance LM, Angell JB (1979) A batch-fabricated silicon accelerometer. IEEE Trans Electron Devices 26:1911–1917
3. Zavracky PM, McClelland B, Warner K, Wang J, Hartley F, Dolgin B (1996) Design and process considerations for a tunneling tip accelerometer. J Micromech Microeng 6:352–358

4. Mineta T, Kobayashi S, Watanabe Y, Kanauchi S, Nakagawa I, Wuganuma E, Esashi M (1996) Three-axis capacitive accelerometer with uniform axial sensitivities. J Micromech Microeng 6:431–435
5. Spangler LC, Kemp CJ (1996) Integrated silicon automotive accelerometer. Sens Actuators A Phys 54:523–529
6. Zhao Y, Leung A, Rebeschini ME, Pucci GP, Dribinsky A, Cai BAY (2007) Method and circuitry for thermal accelerometer signal conditioning. U.S. Patent 7,305,881 B2, 11 Dec 2007
7. Zhao Y, Brokaw AP, Rebeschini ME, Leung AM, Pucci GP, Dribinsky A (2004) Thermal convection accelerometer with closed-loop heater control. U.S. Patent 6,795,752 B1, 21 Sept 2004
8. Liao KM, Chen R, Chou BCS (2006) A novel thermal bubble based micromachined accelerometer. Sens Actuators A Phys 130–131:282–289
9. Dauderstadt UA, Sarro PM, Middelhoek S (1995) Silicon accelerometer based on thermopiles. Sens Actuators A Phys 46:201–204
10. Dao R, Morgan DE, Kries HH, Bachelder DM (1996) Micromachined convective accelerometers in standard integrated circuits technology. U.S. Patent 5,581,034, 3 Dec 1996
11. Milanovic V, Bowen E, Tea N, Suehle JS, Payne B, Zaghloul ME, Gaitan M (1998) Convection-based accelerometer and tilt sensor implemented in standard CMOS. In: International mechanical engineering conference and exposition, MEMS symposia, Anaheim, 1998
12. Luo XB, Li ZX, Guo ZY, Yang YJ (2001) An optimized micromachined convective accelerometer with no proof mass. J Micromech Microeng 11:504–508
13. Lin L, Pisano AP, Carey VP (1994) Thermal bubble powered microactuators. Microsyst Technol 1:51–58
14. Tsai JH, Lin L (2002) Active microfluidic mixer and gas bubble filter driven by thermal bubble micro pump. Sens Actuators A Phys 97–98:665–671
15. Dido J, Loisel P, Renault A (2008) Thermal accelerometer with automatic zero control. U.S. Patent 7,426,862 B2, 23 Sept 2008
16. Courteaud J, Crespy N, Combette P, Sorli B (2008) Studies and optimization of the frequency response of a micromachined thermal accelerometer. Sens Actuators A Phys 147:75–82
17. Dauderstädt UA, de Vries PHS, Hiratsuka R, Korvink JG, Sarro PM, Baltes H, Middelhoek S (1996) Simulation aspects of a thermal accelerometer. Sens Actuators A Phys 55:3–6
18. Hsu TR (2002) MEMS and microsystems: design and manufacture. McGraw-Hill Companies, Boston

Parallel Operation of the Piezoelectric Energy Harvest Using the Taguchi Method

Po-Jen Cheng, Chin-Hsing Cheng, and Chuan-Wei Chen

Abstract This chapter investigates a technique for a piezoelectric generator system using the synchronized switch harvesting on inductor (SSHI) electronic interface. Piezoelectric materials can convert mechanical energy into electrical energy through direct piezoelectric effect. In order to increase the current capability of the power source, several piezoelectric generators are placed in parallel. However, the electricity generated by piezoelectric generator reduces when the piezoelectric materials are parallel connected. To raise the output power density of piezoelectric generator system, a SSHI is used in parallel with the harvesting structure. Two electronic interface structures, the bridge rectifier and the SSHI, are used to harvest the energy from the piezoelectric generator. The structure of the SSHI is better than that of the bridge rectifier. The Taguchi parameter design for the SSHI structure is utilized to harvest energy of piezoelectric generator system, and the results of measurement verify the feasibility of this structure in the experiment.

Keywords Synchronized switch harvesting on inductor (SSHI) • Piezoelectric generator • Taguchi method

P.-J. Cheng
Department of Electrical Engineering, Nan Jeon Institute of Technology, No. 178,
Chaoqin Rd., Yenshui Dist., Tainan City 73746, Taiwan

C.-H. Cheng (✉) • C.-W. Chen
Department of Electrical Engineering, Feng Chia University, No. 100, Wen Hwa Road,
Taichung 40724, Taiwan
e-mail: chcheng@fcu.edu.tw

1 Introduction

Energy recovery from wasted or unused power has been a topic of discussion in recent times. Unused power exists in various forms such as industrial machines, human activity, vehicles, structures, and environmental sources. Among these, some of the promising sources for recovering energy are periodic vibrations generated by rotating machinery or engines. Primarily, the selection of the energy harvester as compared to other alternatives such as battery depends on two main factors: cost-effectiveness and reliability [1, 2].

Piezoelectric generators are based on the electromechanical energy conversion taking place in a piezoelectric material. Such a generator usually includes a mechanical device designed to apply a driving stress on piezoelectric elements. The piezoelectric elements acting as the generator are connected together to an electrical network constituting the energy receiver [3]. Since a piezoelectric element subjected to a vibration generates an alternating voltage across its electrodes, most of the proposed electrical circuits include an AC-to-DC converter. Thus, the electrical energy is provided to a storage device, such as a capacitor or a battery, in order to feed the terminal electric load under a DC voltage [4–6]. This chapter proposes an approach for piezoelectric energy reclamation from mechanical vibrations. The approach is derived from the so-called synchronized switch harvesting on inductor (SSHI), a semi-passive technique that was developed to address the problem of vibration damping in mechanical structures. The technique is based on a nonlinear processing of the voltage delivered by the piezoelectric elements. This process increases the amount of electrically converted energy during a mechanical loading cycle of the piezoelectric element. The processing circuit has the principal advantage of being very simple: it comprises an electronic switching device connected in parallel with the piezoelectric element [7–10].

The Taguchi method can overcome the shortcomings of full factorial design when implementing fractional factorial design. The approach optimizes parameter design, but with fewer experiments. Taguchi's parameter design is intended to yield robust quality by reducing the effects of environmental conditions and variations due to the deterioration of certain components. This high quality is achieved by the selection of various design alternatives or by varying the levels of the design parameters for component parts or system elements. It can optimize performance characteristics by the settings of design parameters and reduce the sensitivity of the system performance to sources of variation [11].

2 Construction and the Principle of the Piezo-Generator

The experimental setup for the energy-harvesting scheme is shown in Fig. 1. To increase the efficiency of the harvest energy, parallel operation of the 11 sets of piezo-generators is investigated. There are two piezoelectric elements in one set. One is used as shake generator driven by the variable frequency signal generator;
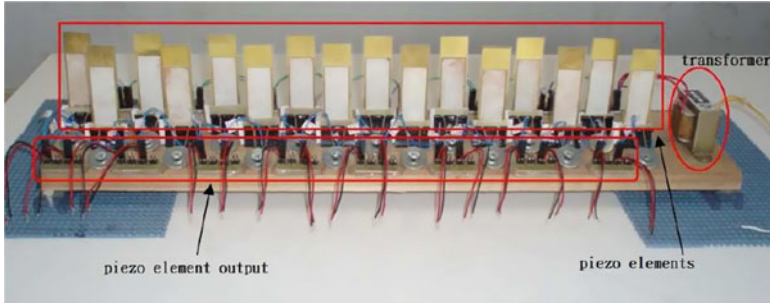
Fig. 1 Experimental setup for the energy-harvesting scheme

the other is used as piezo-generator to generate the energy for harvesting. The piezo-generator supplies an AC voltage. The AC signal must be rectified and the obtained DC signal, with some ripple, is regulated by rectifier circuit to drive a supercapacitor. A synchronized switch harvesting on inductor (SSHI) is applied to artificially increase the conduct duration of the rectifier and the average output power density of the piezo-generator [12].

3 Experimental Methodology

Essentially, traditional experimental design procedures are too complicated and not easy to use. A large number of experimental works have to be carried out when the number of the process parameters increases. To solve this problem, the Taguchi method uses a special design of orthogonal arrays to study the entire parameter space with only a small number of experiments [13, 14].

Based on the average output value at each parameter level, main effect analysis is performed. Furthermore, a statistical analysis of variance (ANOVA) is performed to see which process parameters are statistically significant. With the main effect and ANOVA analysis, the optimal combination of the process parameters can be predicted. Finally, a confirmation test is conducted to verify the optimal process parameters obtained from the parameter design.

4 Experimental Procedure

4.1 Establishment of Orthogonal Array

There are four factors, A, B, C, and D, corresponding to four design variables, as shown in Fig. 2 and Table 1, each at three levels, where A is the vibrating frequency of piezoelectric material, B is the duty cycle, C is the switching frequency of SSHI, and D is the inductance. A standard Taguchi's orthogonal array L-9 is used for numerical experiments [15].
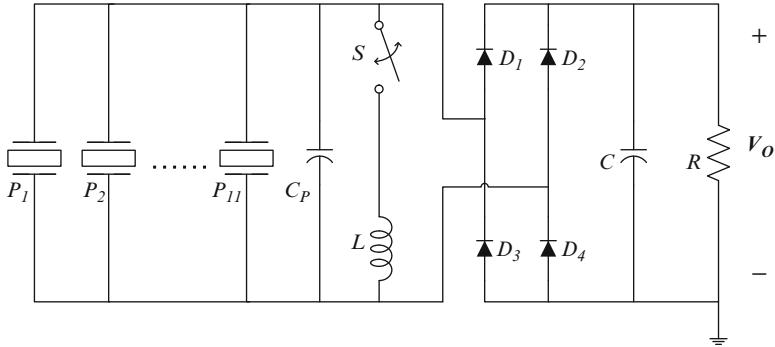
Fig. 2 The circuit for the parallel operation with SSHI

Table 1 Levels of design variables

Settings/ factors	Vibrating frequency of piezoelectric material A_i (Hz)	Duty cycle B_i (%)	Switching frequency of SSHI C_i (kHz)	Inductance D_i (mH)
1	85	10	40	0.67
2	90	20	50	2.9
3	95	30	60	10

4.2 Analysis of Means

There are nine experiments required to determine the optimum combination of the levels of these factors and to understand the contribution of each to produce the value of output power. The analysis of means (ANOM) is used to determine the optimal process parametric settings, and it is the process of estimating the main effects of each parameter. The effect of a parameter level is the deviation it causes from the overall mean response.

The means of all results can be calculated as

$$m_{\text{all}} = \frac{1}{9} \times \sum_{i=1}^{9} P(i) \tag{1}$$

4.3 Calculation of Average Effect

The average output power for all levels of factors can be obtained. Figure 3a illustrates the main factor effects on output power. It is seen that the factor-level combination (A_3, B_1, C_3, D_3) contributes to maximization of output power. In a similar way, the output efficiency can be obtained for all levels of all factors. The factor-level combination (A_1, B_1, C_3, D_3) contributes to maximization of the output efficiency as shown in Fig. 3b.
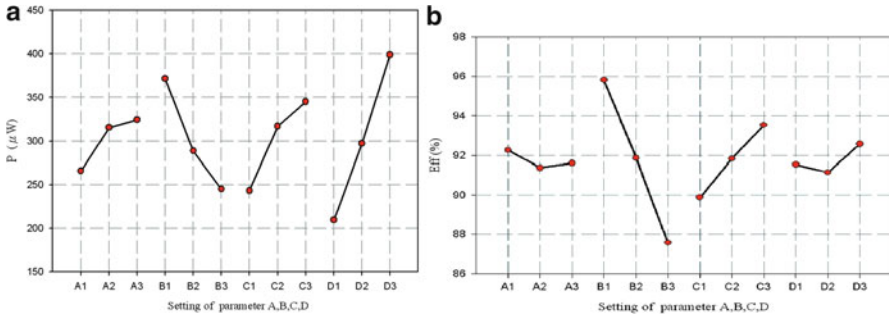
Fig. 3 Main factor effects on (**a**) output power and (**b**) output efficiency

4.4 Analysis of Variance

ANOVA is a computational technique which is used to estimate the relative significance of each process parameter in terms of percent contribution to the overall response. ANOVA is also required for estimating the variance of error for the effects and confidence interval of the prediction error.

To conduct ANOVA, the sum of squares (SS) is calculated first. It is a measure of the deviation of the experimental data from the mean value of the data. The sum of squares (SSF$_A$) due to various factors can be calculated as

$$SSF_A = 3 \sum_{i=1}^{3} \left(m_{A_i} - m_{\text{all A}} \right)^2 \tag{2}$$

It is noted in Fig. 3a that the best combination of design parameters for maximum output power is (A_3, B_1, C_3, D_3). From Fig. 3b the best combination of design parameters for maximum output efficiency is (A_1, B_1, C_3, D_3). All factors are used to regulate the values of output power and output efficiency. The vibrating frequency of piezoelectric material has larger effect on output power. Therefore, the best combination of design parameters for maximum output power and maximum output efficiency is determined to be (A_3, B_1, C_3, D_3).

There are three possible scenarios for the parallel operation of the system: (1) parallel operation directly, (2) parallel operation after rectification, and (3) parallel operation with SSHI. The output voltage is rectified by diode and stored in supercapacitor. The harvested energy for the parallel operation after rectification for 300 s is shown in Fig. 4. The harvested energy is higher than that of parallel operation directly. The harvested energy for the parallel operation with SSHI for 300 s is shown in Fig. 5. The harvested energy is the highest among the three methods.
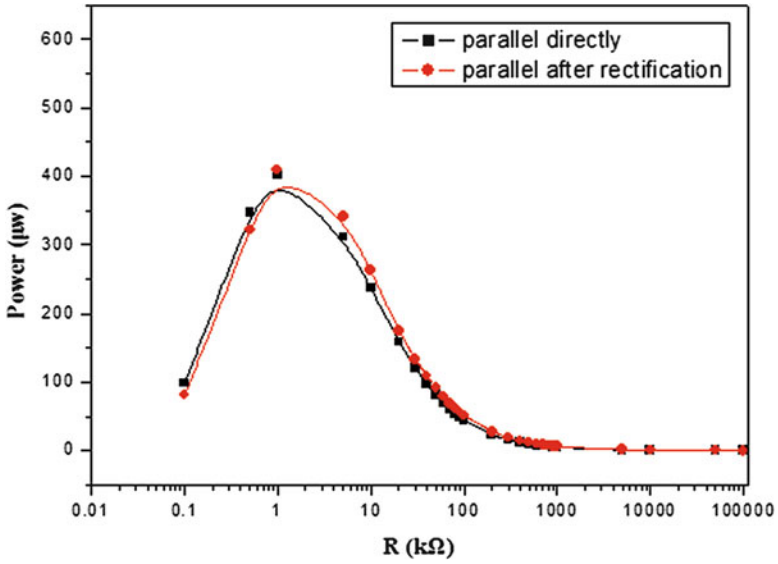
Fig. 4 Harvested power versus the resistive load for the parallel operation after rectification
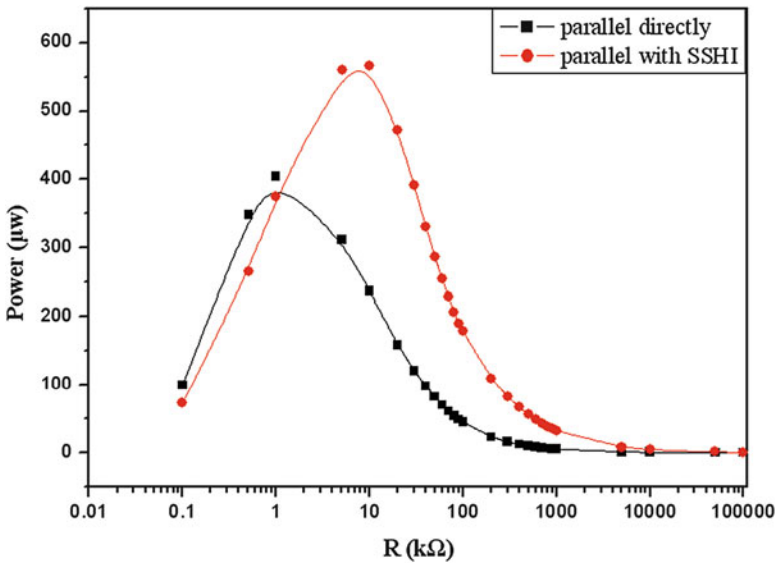
Fig. 5 Harvested power versus the resistive load for the parallel operation with SSHI

5 Conclusion

This chapter applied the Taguchi methods to the design optimization for parallel operation of the piezoelectric energy-harvest output power and output efficiency maximizations. A case with several piezoelectric generators in parallel was studied in order to increase the input current to the system. The proposed method in this chapter is effective for obtaining the design parameters with high output power and high efficiency.

References

1. Harb A (2011) Energy harvesting: state-of-the-art. Renew Energy 36:2641–2654
2. Priya S (2007) Advances in energy harvesting using low profile piezoelectric transducers. J Electroceram 19:165–182
3. Guyomar D, Badel A, Lefeuvre E, Richard C (2005) Toward energy harvesting using active materials and conversion improvement by nonlinear processing. IEEE Trans Ultrason Ferroelectr Freq Control 52:584–595
4. Lefeuvre E, Badel A, Richard C, Petit L, Guyomar D (2006) A comparison between several vibration-powered piezoelectric generators for standalone systems. Sens Actuators A 126:405–416
5. Ottman G, Hofmann HF, Bhatt A, Lesieutre G (2002) Adaptive piezoelectric energy harvesting circuit for wireless remote power supply. IEEE Trans Power Electron 17:669–676
6. Ottman G, Hofmann HF, Bhatt A, Lesieutre G (2003) Optimized piezoelectric energy harvesting circuit using step-down converter in discontinuous conduction mode. IEEE Trans Power Electron 18:696–703
7. Badel A, Guyomar D, Lefeuvre E, Richard C (2005) Efficiency enhancement of a piezoelectric energy harvesting device in pulsed operation by synchronous charge inversion. J Intell Mater Syst Struct 16:889–901
8. Richard C, Guyomar D, Audigier D, Ching G (1999) Semi passive damping using continuous switching of a piezoelectric device. In: Proceeding of the SPIE smart structures and materials conference on passive damping and isolation, San Diego, 1999
9. Richard C, Guyomar D, Audigier D, Bassaler H (2000) Enhanced semi passive damping using continuous switching of a piezoelectric device on an inductor. In: Proceeding of the SPIE smart structures and materials conference on passive damping and isolation, San Diego, 2000
10. Guyomar D, Richard C, Lefeuvre E, Petit L (2004) Piezoelectric non-linear systems for standalone vibration control and energy reclamation. In: Proceeding of the AC'04, Hildesheim, 2004
11. Taguchi G (1993) Taguchi methods: design of experiments. American Supplier Institute, Inc, Dearborn
12. Hu Y, Xue H, Hu T, Hu H (2008) Nonlinear interface between the piezoelectric harvesting structure and the modulating circuit of an energy harvester with a real storage battery. IEEE Trans Ultrason Ferroelectr Freq Control 55:148–160

13. Yang WH, Tang YS (1998) Design optimization of cutting parameters for turning operations based on the Taguchi method. J Mater Process Technol 84:122–129
14. Taguchi G (1990) Introduction to quality engineering. Asian Productivity Organization, Tokyo
15. Hwang CC, Lyu LY, Liu CT, Li PL (2008) Optimal design of an SPM motor using genetic algorithm and Taguchi method. IEEE Trans Magn 44:4325–4328

Effect of Anisotropy Parameters on the Initiation of Plastic Yielding in Thin Hollow Disks Subject to Thermomechanical Loading

Sergei Alexandrov, Elena Lyamina, and Yeau-Ren Jeng

Abstract A thin elastic–plastic annular disk subject to thermomechanical loading is considered. It is assumed that plastic yielding is controlled by Hill's quadratic orthotropic yield criterion. A distinguished feature of the boundary value problem considered is that there are two loading parameters. One of these parameters is temperature and the other is pressure over the inner radius of the disk. It is shown that the initiation of plastic yielding may occur either at the inner radius or at the outer radius of the disk depending on the value of anisotropy parameters.

Keywords Thin disks • Analytic solution • Plastic anisotropy • Parametric study

1 Introduction

A significant amount of analytical and numerical research for various material models has been carried out in the area of stress and strain analysis of thin disks. A review of previous works devoted to the problem of enlargement of a circular hole in thin plates has been given in Masri et al. [1]. The assumptions made

S. Alexandrov (✉)
Department of Mechanical Engineering and Advanced Institute of Manufacturing
with High-tech Innovations, National Chung Cheng University, Chia-Yi 62102, Taiwan

A. Ishlinskii Institute for Problems in Mechanics, Russian Academy of Sciences,
Moscow 119526, Russia
e-mail: sergei_alexandrov@yahoo.com

E. Lyamina
A. Ishlinskii Institute for Problems in Mechanics, Russian Academy of Sciences,
Moscow 119526, Russia

Y.-R. Jeng
Department of Mechanical Engineering and Advanced Institute of Manufacturing
with High-tech Innovations, National Chung Cheng University, Chia-Yi 62102, Taiwan

regarding yield criterion and strain hardening have a significant effect on the predicted response. Even though closed-form solutions involve more assumptions than numerical solutions, the former are necessary for studying qualitative effects and verifying numerical codes. In this chapter, the effect of temperature and pressure over the inner radius of a thin hollow disk on the initiation of plastic yielding is investigated. The outer radius of the disk is fixed. The state of stress is plane. The boundary value problem is axisymmetric. The classical Duhamel–Neumann law is adopted to connect strain and stress. Plastic yielding is controlled by the yield criterion proposed by Hill [2].

2   Statement of the Problem

Consider a thin disk of radius b_0 with a central hole of radius a_0, which is inserted into a rigid container of radius b_0 (Fig. 1). The disk is subject to thermomechanical loading by a uniform pressure P over its inner radius and a uniform increase of temperature T from its initial value. Both P and T are monotonically increasing functions of time. Also, $P = 0$ and $T = 0$ at the initial instant. Thus, both $P \geq 0$ and $T \geq 0$. The disk has no stress at the initial instant. Introduce a cylindrical coordinate system (r, θ, z) whose z-axis coincides with the axis of symmetry of the disk. Then, the equations for the inner and outer radii of the disk are $r = a_0$ and $r = b_0$, respectively. The strains are supposed to be small. Let σ_r, σ_θ, and σ_z be the normal stresses in the cylindrical coordinate system. The state of stress is plane, $\sigma_z = 0$. The boundary conditions can be written as

$$\sigma_r = -P \quad \text{for} \quad r = a_0, \tag{1}$$

$$u_r = 0 \quad \text{for} \quad r = b_0. \tag{2}$$

Here u_r is the radial displacement.

   The sum of the elastic and thermal portions of the strain tensor follows the classical Duhamel–Neumann law. In the case under consideration, this law reads
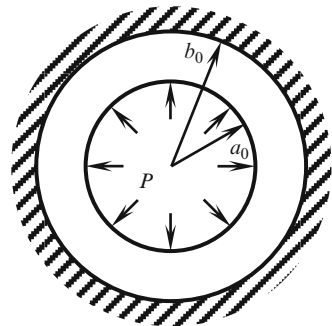
Fig. 1 Illustration of the structure

$$\varepsilon_r^e + \varepsilon_r^T = (\sigma_r - \nu\sigma_\theta)E^{-1} + \alpha T,$$
$$\varepsilon_\theta^e + \varepsilon_\theta^T = (\sigma_\theta - \nu\sigma_r)E^{-1} + \alpha T,$$
$$\varepsilon_z^e + \varepsilon_z^T = -\nu(\sigma_r + \sigma_\theta)E^{-1} + \alpha T \qquad (3)$$

where ε_r^e, ε_θ^e, and ε_z^e are the elastic portions of the strain tensor; ε_r^T, ε_θ^T, and ε_z^T are the thermal portions of the strain tensor; E is Young's modulus; ν is Poisson's ratio; and α is the thermal coefficient of linear expansion. It is assumed that the initiation of plastic yielding is controlled by the yield criterion proposed by Hill [2]. By assumption, the principal axes of anisotropy coincide with the base vectors of the cylindrical coordinate system. Therefore, the boundary value problem is axisymmetric. Under the assumptions made, the yield criterion becomes

$$(G+H)\sigma_r^2 - 2H\sigma_r\sigma_\theta + (H+F)\sigma_\theta^2 = 1 \qquad (4)$$

where G, H, and F are constants which characterize the current state of anisotropy. It is convenient to rewrite (4) as

$$\sigma_r^2 + p_\theta^2 - \eta\sigma_r p_\theta = \sigma_0^2,$$
$$p_\theta = \frac{\sigma_\theta}{\eta_1}, \quad \eta = \frac{2H}{\sqrt{(G+H)(H+F)}}, \quad \eta_1 = \frac{\sqrt{G+H}}{\sqrt{H+F}}, \quad \sigma_0 = \frac{1}{G+H} \qquad (5)$$

The only nontrivial equation of equilibrium is

$$\frac{\partial\sigma_r}{\partial r} + (\sigma_r - \sigma_\theta)r^{-1} = 0. \qquad (6)$$

3 Elastic Solution

When both T and P are small enough, the entire disk is elastic. For axisymmetric deformation and the plane strain conditions, the equations of linear thermoelasticity consisting of (3) and (6) have the general solution in the form

$$\frac{\sigma_r}{\sigma_0} = \frac{A}{\rho^2} + B, \quad \frac{\sigma_\theta}{\sigma_0} = -\frac{A}{\rho^2} + B, \quad k^{-1}u = (1-\nu)B\rho - (1+\nu)\frac{A}{\rho} + \tau\rho \qquad (7)$$

where $\rho = r/b_0$, $k = \sigma_0/E$, $\tau = \gamma TE/\sigma_0$, $u = u_r/b_0$, and A and B are constants of integration. When the entire disk is elastic, A and B are determined from the solution (7) using the boundary conditions (1) and (2) as

$$A = A_e = \frac{a^2[\tau - p(1-\nu)]}{a^2(1+\nu) + 1 - \nu}, \quad B = B_e = -\left[\frac{(1+\nu)pa^2 + \tau}{a^2(1+\nu) + 1 - \nu}\right] \tag{8}$$

where $p = P/\sigma_0$ and $a = a_0/b_0$. As a result of an increase in τ, or p or both, a plastic zone can appear at $\rho = \rho_c$. In order to find the value of ρ_c, it is necessary to substitute (7) and (8) into the yield criterion (5). As a result,

$$\Omega(\rho) = \frac{A_e^2}{\rho^4}\left(2 + \frac{1}{\eta_1^2}\right) + \frac{2A_eB_e}{\rho^2}\left(1 - \frac{1}{\eta_1^2}\right) + B_e^2\left(1 + \frac{1}{\eta_1^2} - \frac{\eta}{\eta_1}\right) - 1. \tag{9}$$

It is necessary to find a maximum of $\Omega(\rho)$ in the range $a \le \rho \le 1$. If the function $\Omega(\rho)$ has a local maximum or minimum at $\rho = \rho_m$, then $d\Omega(\rho)/d\rho = 0$ at this point. It follows from (9) that the equation $d\Omega(\rho)/d\rho = 0$ is equivalent to

$$A_e\left(2 + \eta_1^{-2}\right) + B_e\rho_m^2\left(1 - \eta_1^{-2}\right) = 0. \tag{10}$$

It is seen from this equation that $\Omega(\rho)$ is a monotonic function of ρ at $\eta_1 = 1$. In particular, $\eta_1 = 1$ for isotropic material. In this case, the function $\Omega(\rho)$ attains its maximum value at one of the ends of the interval under consideration. Differentiating the right-hand side of (9) with respect to ρ two times and replacing ρ with ρ_m by means of the solution to equation (10) show that the second derivative of the function $\Omega(\rho)$ is positive at $\rho = \rho_m$. Thus, the function $\Omega(\rho)$ attains a minimum at $\rho = \rho_m$ and the initiation of plastic yielding can occur at either $\rho = a$ or $\rho = 1$.

4   Initiation of Plastic Yielding

The yield criterion (5) is satisfied automatically by the following substitution:

$$\frac{\sigma_r}{\sigma_0} = 2 \cos \varphi\left(4 - \eta^2\right)^{-1/2}, \quad \frac{p_\theta}{\sigma_0} = \eta \cos \varphi\left(4 - \eta^2\right)^{-1/2} + \sin \varphi. \tag{11}$$

It follows from (7) that the stresses are constant over the entire disk if $A_e = 0$. It can be found from (8) that this special case is obtained at

$$\tau = p(1 - \nu). \tag{12}$$

The initiation of plastic yielding occurs in the entire disk simultaneously. Substituting (7), (8), and (12) into (11) determines the corresponding angle $\varphi = \varphi_{c1}$ as

Fig. 2 Variation of φ_{c1} and φ_{c1} with G/H
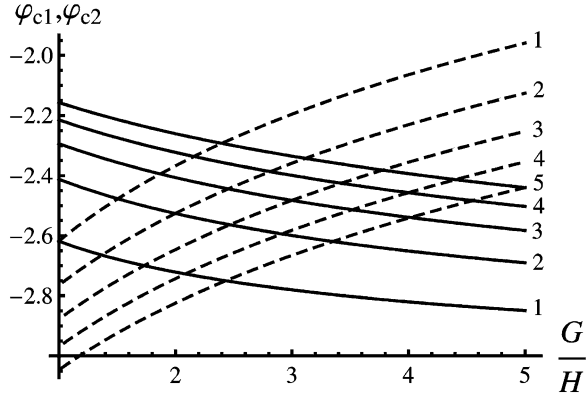
$$\varphi_{c1} = \arctan\left(\frac{2 - \eta\eta_1}{\eta_1\sqrt{4 - \eta^2}}\right) - \pi. \tag{13}$$

Another solution of special interest is when two plastic zones appear simultaneously at the inner and outer radii of the disk whereas the interior of the disk is elastic. Substituting (7) into (11) gives

$$\frac{A_e}{a^2} + B_e = \frac{2\cos\varphi_{c2}}{\sqrt{4 - \eta^2}}, \quad -\frac{A_e}{a^2} + B_e = \eta_1\left(\frac{\eta\cos\varphi_{c2}}{\sqrt{4 - \eta^2}} + \sin\varphi_{c2}\right) \tag{14}$$

where φ_{c2} is the values of φ at the inner radius of the disk at the instant of the initiation of plastic yielding. Since A_e and B_e are expressed through p and τ, the dependence of p on τ corresponding to the simultaneous initiation of plastic yielding at the inner and outer radii of the disk is determined from Eq. (14) once φ_{c2} has been found. The dependencies of φ_{c1} and φ_{c2} on G/H and several values of F/H are depicted in Fig. 2 (curve 1 corresponds to $F/H = 1$, curve 2 to $F/H = 2$, curve 3 to $F/H = 3$, curve 4 to $F/H = 4$, and curve 5 to $F/H = 5$). The solid lines correspond to φ_{c1} and the broken lines to φ_{c2}. The dependence between p and τ corresponding to the initiation of plastic yielding for several values of F/H and G/H is illustrated in Figs. 3, 4, 5, 6, and 7. Curve 1 corresponds to $G/H = 1$, curve 2 to $G/H = 2$, curve 3 to $G/H = 3$, curve 4 to $G/H = 4$, and curve 5 to $G/H = 5$. In all calculations $a = 0.5$ and $\nu = 0.3$.

5 Conclusions

The solution found shows the effect of plastic anisotropy of the initiation of plastic yielding in thin disks subject to thermomechanical loading. Two special cases of great interest have been identified. One of them corresponds to loading conditions

Fig. 3 Illustration of loading conditions corresponding to the initiation of plastic yielding at $F/H = 1$
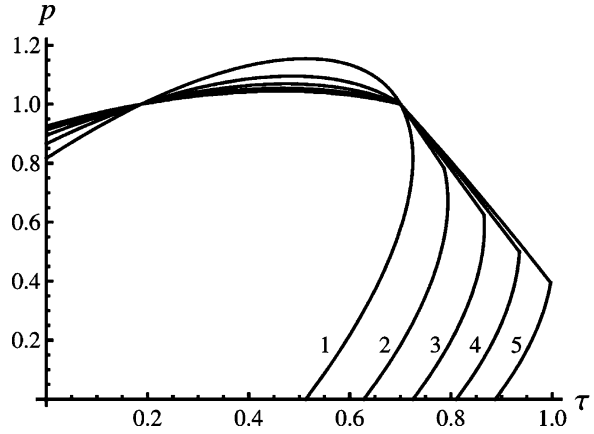
Fig. 4 Illustration of loading conditions corresponding to the initiation of plastic yielding at $F/H = 2$
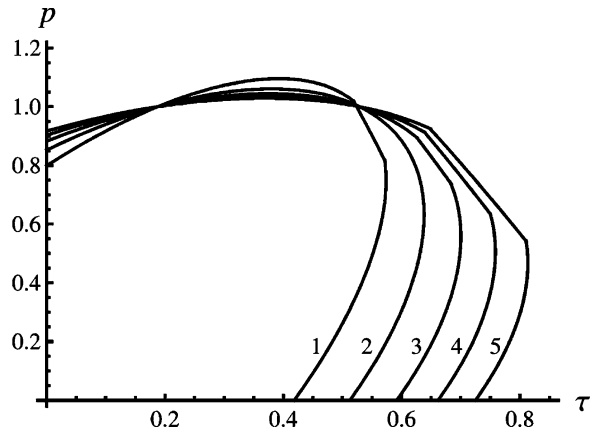
Fig. 5 Illustration of loading conditions corresponding to the initiation of plastic yielding at $F/H = 3$
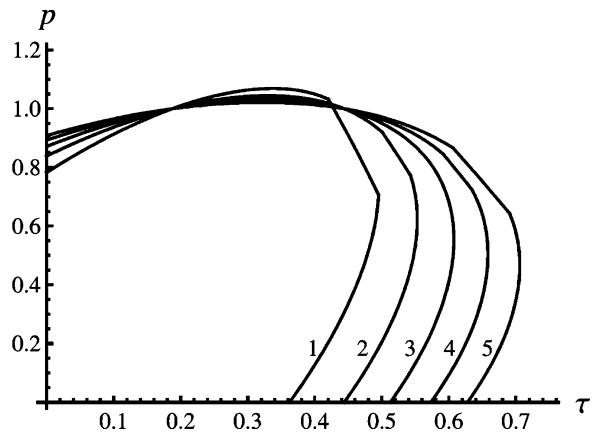
Fig. 6 Illustration of loading conditions corresponding to the initiation of plastic yielding at $F/H = 4$
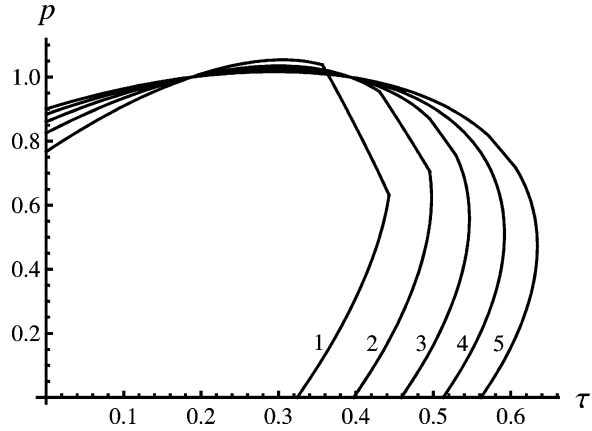
Fig. 7 Illustration of loading conditions corresponding to the initiation of plastic yielding at $F/H = 5$
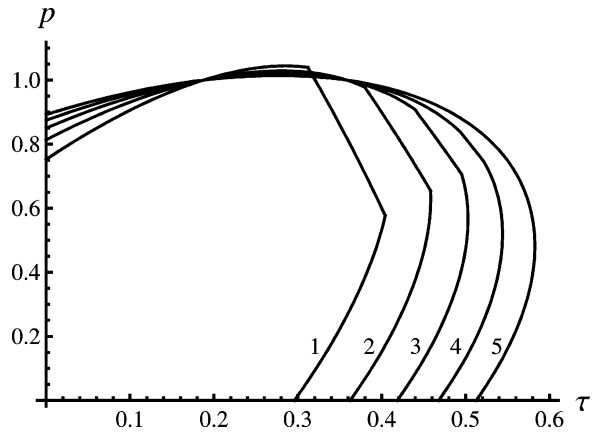
at which the entire disk becomes plastic simultaneously. The other case corresponds to loading conditions at which two plastic zones appear simultaneously. These special cases determine the complete qualitative structure of the solution (Figs. 3, 4, 5, 6, and 7).

References

1. Masri R, Cohen T, Durban D (2010) Enlargement of a circular hole in a thin plastic sheet: Taylor-Bethe controversy in retrospect. Q Mech Appl Math 63:589–616
2. Hill R (1950) The mathematical theory of plasticity. Oxford University Press, Oxford

Development of MEMS Gyroscope Module for Rotating Machine Performance Characterization

Guo-Hua Feng and Fu-Tun Chang

Abstract This chapter presents the development of a Micro Electro Mechanical System (MEMS) gyroscope-based sensing module and the experiments to verify the functionality of the sensing module in a rotating mechanism. The module integrated a MEMS gyroscope sensor, battery, microprocessor, signal processing circuitry, analog-to-digital converter, memory unit, remote switch to turn on/off the module operation, and signal output port. It has no wire connection for power supply and signal transmission, which avoids the wire twisting problem during spindle rotating test. The module is then firmly secured on a rotating platform to test its function. The measured angular velocities are verified the accuracy through the encoder readout of the driving motor. Also, using this sensing module to detect a rotating plate with intentionally run-out error setting, the acquired signals clearly exhibit the corresponding relationship. The preliminary results demonstrate the feasibility of the developed sensing module for dynamic characterization of rotating mechanism.

Keywords MEMS • Gyroscope • Rotating machine • Spindle dynamics measurement • Run-out error

1 Introduction

For current machining market, the development and production of high-speed machining center has a significant demand. This means the machining center should perform with a higher feed rate to machine a great amount of precision products. In order to achieve this demand, improving the operation capability of the spindle

G.-H. Feng (✉) • F.-T. Chang
Department of Mechanical Engineering and Advanced Institute of Manufacturing with High-tech Innovations, National Chung Cheng University, Chiayi 62102, Taiwan
e-mail: imeghf@ccu.edu.tw; frankca@ms57.hinet.net

during high RPM machining is very important [1]. Nowadays, the scheme to on-line monitor the performance of high-speed spindle is commonly acquired from the controller of the machining center through the feedback signals during the motor to drive the spindle [2].

In recent years, commercial MEMS gyroscopes have become reliable, and their tiny and low-cost properties attract many researchers and engineers' interests for industrial applications. In this study we focus on constructing a MEMS gyroscope-based sensing module and use this module on a rotating mechanism to obtain the signal directly during rotation. Through this study, we will evaluate the feasibility of using the developed module for characterization of a rotating mechanism and its potential for monitoring the performance of high-speed spindle in the future [3].

2   Experimental Setup and Method

Figure 1 shows the experiment setup for our constructed gyroscope sensing module to acquire the signals from a rotating plate. We installed the high-speed motion control card (PCI-DMC-A1, Delta Electronics Co., Ltd., Taiwan) into a personal computer's mainboard, and the company provided software so the angular velocity can be set as needed. A CANopen (Controller Area Network) communication cable was used to connect the personal computer and the servo driver (ASD-A2-0421F, Delta Electronics Co., Ltd., Taiwan) so that the motor (ECMA-C10604, Delta
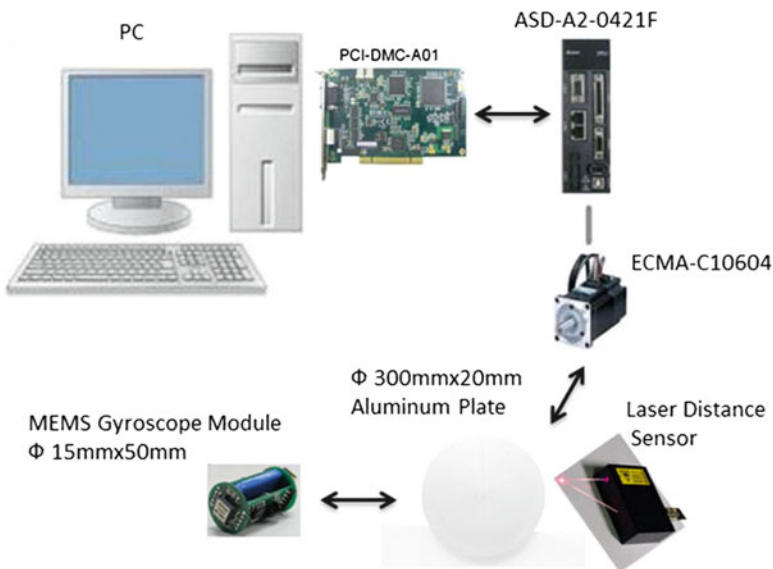
Fig. 1 The experimental setup of the developed MEMS gyroscope sensing module shows how to obtain the information from a rotating plate
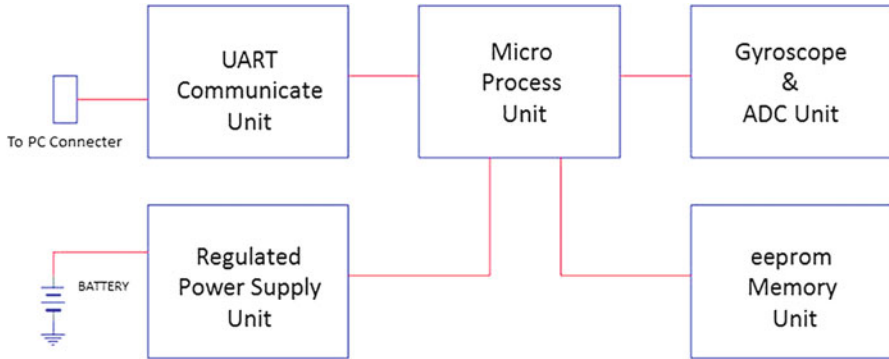
Fig. 2 The schematic diagram shows the designed independent gyroscope module

Electronics Co., Ltd., Taiwan) can be driven [4, 5]. We installed the self-made MEMS gyroscope module on a circular aluminum plate which was anchored on the servo motor. Then, the circular plate is calibrated by the laser triangular sensor in the direction of parallel and perpendicular to the axis of the servo motor to ensure no obvious run-out errors during the plate rotation.

Regarding the experiment method, we set the servo motor to rotate at desired angular velocities. We start and stop to record the signals from the constructed sensing module through its remote control function. When the yaw axis of the sensing module is set to be parallel to the servo motor shaft axis, the acquired data can be used to verify its accuracy through comparing the sensing angular velocity signals and the servo motor operation parameters setting.

2.1 Implementation of Gyroscope Module

The MEMS gyroscope device for our constructed sensing module is made by Analog Devices, Inc. (AXRS622). The main specifications can be found in its datasheet [6]. The operating voltage, positive analog supply, positive charge pump supply, and references supply for ratiometric output are set to 5 V in this study.

In order to apply the ADI gyroscope to a rotating mechanism, it is necessary to avoid wire connection for power supply and signal transmission. Therefore, we build an independent module including the following components: the self-power supply with regulated unit, gyroscope sensor, analog converting to digital signal unit, memory unit, remote unit, data output unit, and microprocessor unit. Figure 2 shows the schematic diagram of our designed sensor module. As for packaging, the sensing module is housed in a cylinder with the size about $\Phi 15 \times 50$ mm, which is suitable for the experiment performed in this chapter and is practical for future applications.
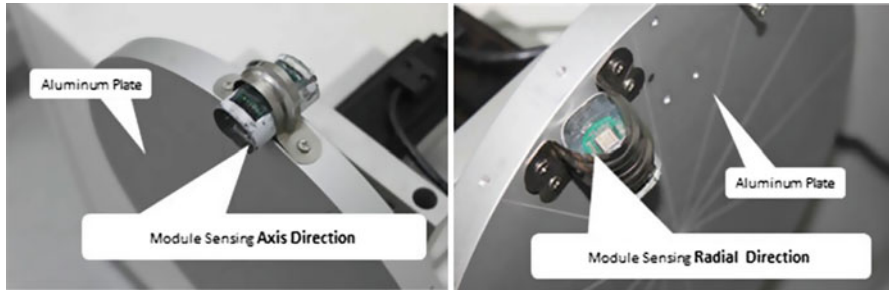
Fig. 3 The developed sensing module is installed at different locations on the circular plate

2.2 Specification of Rotating Machine Platform

ECMA servo motor is used to drive the circular plate of the experiment platform. The motor has its own incremental encoder of 20-bit resolution up to 1,280,000 pulses per revolution which can eliminate unstable commands at low-speed, smooth motor operation and enhance the accuracy of positioning.

2.3 Installation of Sensing Module

Figure 3 shows the installation of fabricated sensing module on the circular plate of experimental platform. The radius of the aluminum plate is 150 mm and the thickness is 20 mm. In this study, we can neglect the causes to gyroscope device performance by the centrifugal force balance because the experiment condition is under a low RPM and the mass inside MEMS gyroscope is really small. The issue of centrifugal force balance might be an interesting issue when we study the rotating mechanism under a high RPM.

When the circular plate rotates, the radial and axial errors will occur due to the geometrical error and accumulative geometric error from the platform. Normally, the geometrical error could be controlled by off-line measurement, and it belongs to statics measurement. For example, a circular plate that passed the Q.C. inspection may often cause the performance problems because of the accumulative geometric error. The accumulative geometric error will present on the final dynamic error and is complicated for study. However, this rotating dynamic error is possible to be measured using our developed sensing module.

3 Experiment Results and Discussion

Two kinds of experiments are executed in this study. One is to confirm the performance of fabricated sensing module meets the MEMS gyroscope specification provided by the manufacturer, and the other is to verify the feasibility that the module can monitor the run-out component of the rotating plate under varied rotation speeds.

For the first experiment, the yaw axis of sensing module is placed parallel to the shaft direction of the servo motor, and the data obtained from the module means the angular velocity of the aluminum plate. We set the angular velocity of servo motor from 5 to 45 rpm with an increment of 10 rpm in both clockwise and counterclockwise directions. Meanwhile, the sensing module is turned on to record the corresponding data as noted in Table 1. Based on the datasheet of ADXRS622 gyroscope, the typical sensitivity is 7.0 mV/°/s and the null voltage is 2.5 V when it does not rotate [6].

For example, if the gyroscope module is under a 5 rpm clockwise circumstance, we can calculate the output voltage from the equation as below:

$$5 \text{ rpm} = 5 \times 360°/60 \text{ s} = 30°/\text{s} \tag{1}$$

$$30°/\text{s} \times 7.0 \text{ mV}/°/\text{s} = 21 \text{ mV} = 0.21 \text{ V} \tag{2}$$

$$0.21 \text{ V} + 2.5 \text{ V} = 2.71 \text{ V} \tag{3}$$

Similarly, if the gyroscope module is under a 5 rpm counterclockwise circumstance, the 7.0 mV/°/s will become negative, so we can get the voltage 2.29 V.

After the experiment, we can verify that the measured angular velocities from the sensing module are the same as the rotational speeds we set on the testing motor (Table 1).

The second experiment tries to confirm the feasibility of the developed gyroscope sensing module to monitor the run-out error of the rotating plate under varied spin speed. In this experiment, the sensing module is placed on the edge of the circular plate with the yaw axis of gyroscope perpendicular to the radial direction of circular plate and to the motor shaft direction. We set the servo motor to rotate

Table 1 Results of the developed sensing module performance accuracy

	Clockwise rotation			Counterclockwise rotation		
RPM	Module output voltage	Theoretical voltage	Accuracy (%)	Module output voltage	Theoretical voltage	Accuracy (%)
5	2.71	2.71	100.00	2.29	2.29	100.00
15	3.12	3.13	99.68	1.87	1.87	100.00
25	3.53	3.55	99.44	1.44	1.45	99.31
35	3.95	3.97	99.50	1.02	1.03	99.03
45	4.37	4.39	99.54	0.61	0.61	100.00
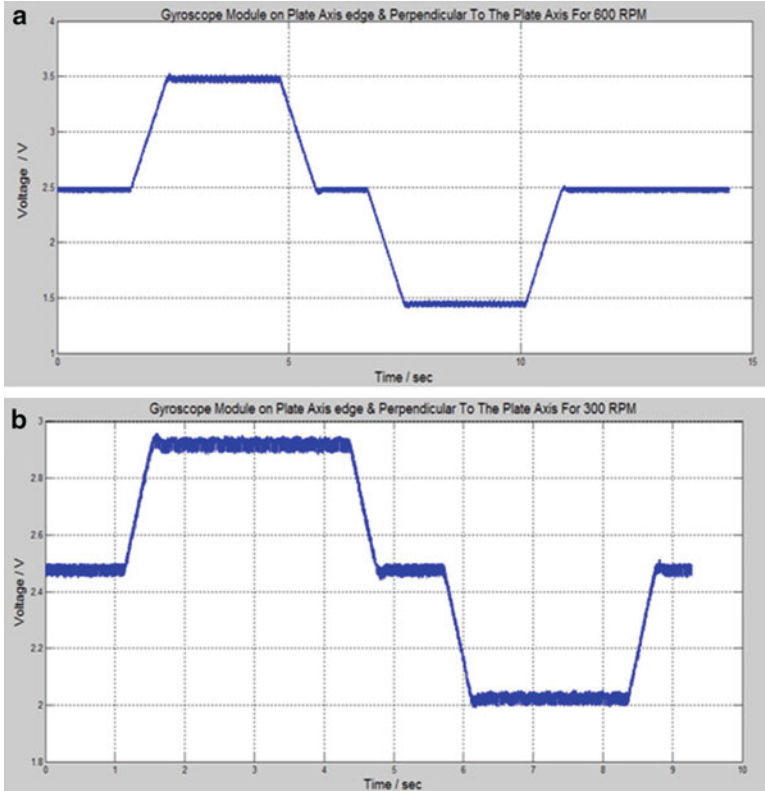
Fig. 4 Measured signals from the sensing module. The servo motor is set at (**a**) 600 rpm (*top subplot*) and (**b**) 300 rpm (*bottom subplot*)

at 300 and 600 rpm, respectively. Each setting has the following stages: stop, acceleration, 600 rpm (CW), deceleration, stop, acceleration, 600 rpm (CCW), and deceleration to stop.

Figure 4 displays the results acquired from the servo motor setting at 600 and 300 rpm, respectively. We realize that the gyroscope module can respond to the operation of a rotating mechanism when the servo motor has different operation settings. Figure 5 shows the period of 2.6–3.6 of the results in Fig 4, which the rotating plate runs at a constant speed at this period. Figure 5a, b exhibit periodical responses, which indicate the slightly back-and-forth rotation of the circular plate along the motor shaft direction during the plate rotation. Also, the waveform shown in Fig. 5a has double frequency compared to the waveform shown in Fig. 5b. This is coincident with the spin speed of the circular plate. Thus, applying the developed gyroscope module to measure a dynamic run-out error of a rotating mechanism can be feasible.
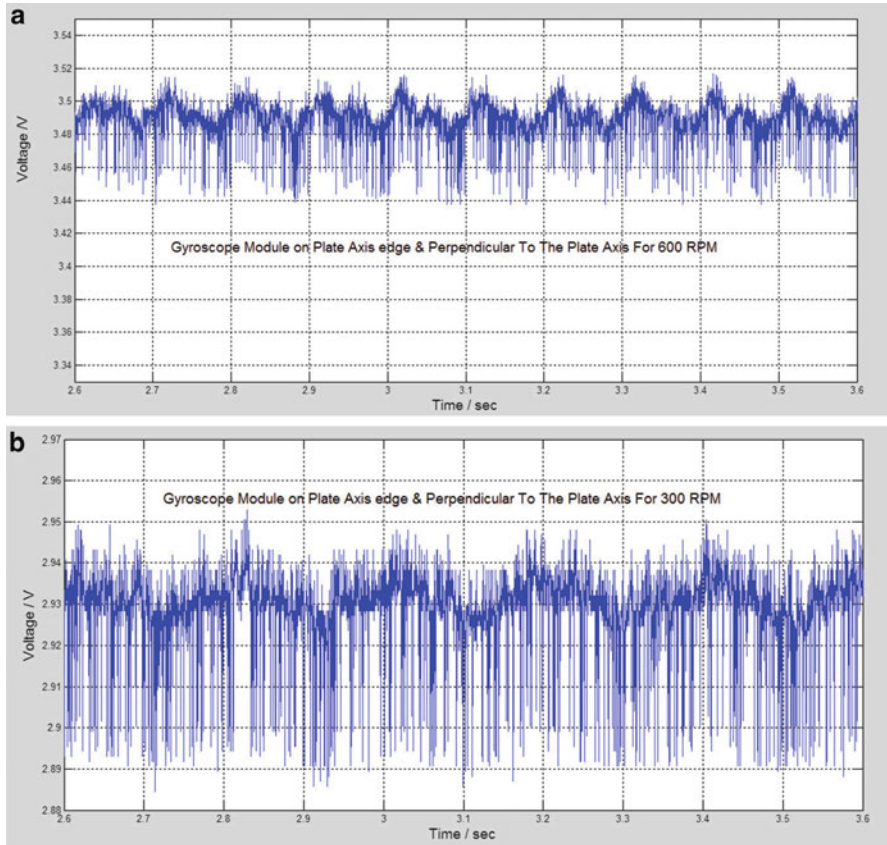
Fig. 5 Measured signals with zoom-in inspections of Fig. 4 during the period of 2.6–3.6 s. The servo motor is set at (**a**) 600 rpm (*top subplot*) and (**b**) 300 rpm (*bottom subplot*)

4 Conclusion

The MEMS-based gyroscope sensing module with battery power supply and no data transmission wires is constructed and is tested to monitor a dynamic rotating mechanism. Installing the sensing module at different positions and directions of the rotating mechanism, we can obtain the information about the dynamic performance of the rotating mechanism. Hence, the developed sensing module could allow us to further evaluate the performance of high-speed spindle.

References

1. Heng A, Zhang S, Tan ACC, Mathew J (2009) Rotating machinery prognostics: state of the art, challenges and opportunities. Mech Syst Signal Process 23(3):724–739
2. Al-Khazali HA, Askari M (2011) Modal analysis design to exposure gyroscopic effect in rotating machinery using experimental and analytical/computational techniques. Int J Eng Sci Technol (IJEST) 3(9):7234–7243
3. Gerdtman C, Bäcklund Y, Lindén M (2011) Development of a test rig for MEMS-based gyroscopic motion sensors in human applications. In: 15th Nordic-Baltic conference on biomedical engineering and medical physics (NBC), Aalborg, 2011, vol 34, pp 203–206
4. (2012) 1.1 connection example. In: PCI-DMC-A01User Manual version: 1.12.2, pp 1–1, Delta Electronics Co., Ltd.
5. (2012) ASDA-A2 series features. In: Delta AC servo system ASDA-A2 series, p 3, Delta Electronics Co., Ltd.
6. (2010) ADXRS622 SPECIFICATIONS. In: ADXRS622 Data Sheet Rev C, p 3, Analog Devices, Inc.

Design and Surface Roughness Analysis of Thin-Sheet Plastic Injection Forming

Dyi-Cheng Chen, Jun-Yan Pan, Juan-Wei Gao, and Wen-Jong Chen

Abstract This chapter selected plastic injection molding to investigate molding real production. Plastic products penetrate plastic injection forming. Recently, 3C products have required light and thin materials. In traditional plastic injection forming, several parameters can influence mold product precision, such as warping, sinking and residual stress, surface quality, size deviation, and shrinkage rate. Therefore, this chapter examines the sheet forming for plastic injections. The experiment investigates the runner gate number and appearance influencing plastic injection finished products. First, mold flow analysis software was used to search for optimum parameters. The primary test offers various parameters in runner and pouring gates and examines their influence on surface roughness in plastic injection thin sheets. The experimental results show useful insights into the optimal processing conditions for plastic injection forming of thin sheets and offer a reference for the industry.

Keywords Moldflow • Plastic injection forming • Surface roughness

1 Introduction

The warpage and surface roughness of injection-molded parts is a difficult problem for mold designers. Numerous factors exist that cause warpage and surface roughness, such as the processes of injection molding and the structure and material of molds. The runner system is important in plastic injection molding because it

D.-C. Chen (✉) • J.-Y. Pan • J.-W. Gao • W.-J. Chen
Department of Industrial Education and Technology, National Changhua University of Education, Changhua 500, Taiwan
e-mail: dcchen@cc.ncue.edu.tw

affects the part quality and material costs. The plastic injection forming that has been previously studied. Wang et al. [1] constructed a numerical model to analyze the heat transfer during the heating and cooling phases of the rapid heat cycle molding (RHCM) process. The model was then used to optimize the design of an RHCM mold with hot-fluid heating. Altan [2] proposed a method based on the Taguchi experimental design approach and the analysis of variance (ANOVA) technique to optimize the process parameters for plastic injection-molded components to minimize the shrinkage of the ejected parts.

Shelesh-Nezhad and Siores [3] presented an artificial-intelligence (AI) system based on rule- and case-based reasoning subsystems to determine the optimal process parameters in the plastic injection molding operation.

Zhai et al. [4] examined an approach that balanced the flow by adjusting the runner sizes. Considering the restraint conditions of mold and the characteristics of injection molding at the post-filling stage, some reasonable hypotheses have been assumed, and a stress model was constructed by Zhou and Li [5]. Fu et al. [6] studied X-ray imaging as a promising method for nondestructive evaluation and quality control for metal injection molding parts.

Therefore, this chapter examines sheet forming as the target of plastic injections. The experimental investigate runner gate numbers and appearance influence plastic injection finished products. The primary test has various parameters set on runner and pouring gates that influence their surface roughness in plastic injection of thin sheets. The experimental results show useful insights into the optimal processing conditions for plastic injection forming of thin sheets and offer a reference for the industry.

2 Research Approach and Steps

2.1 Structures and Designs of the Mold

References to mold in prior research were used to encode the first code to the gate shape, the second code for runner appearance, and the third code for the gate number, as shown in Figs. 1 and 2.

2.1.1 Gate Shape

According to the research, the design of the gate is divided into three types: (A) the conical gate (Fig. 3), (B) the semicircular gate (Fig. 4), and (C) the rectangular gate (Fig. 5).

Fig. 1 Photograph of mold and die
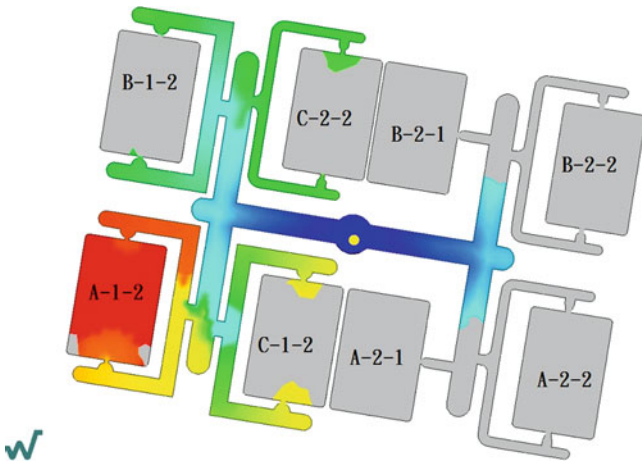
Fig. 2 Mold code
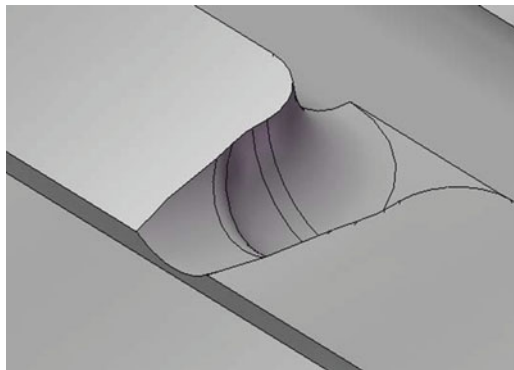
Fig. 3 Conical gate

Fig. 4 Semicircular gate
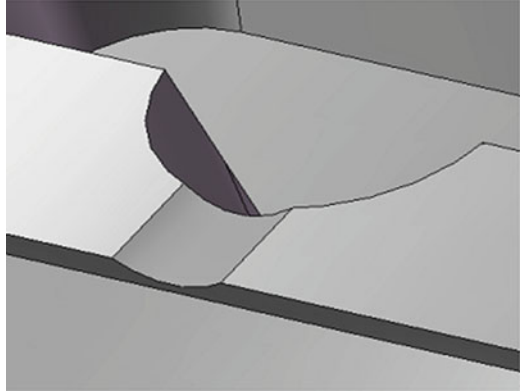
Fig. 5 Rectangular gate
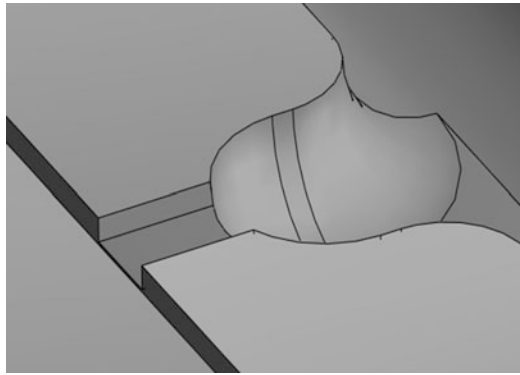
Fig. 6 Trapezoidal runner
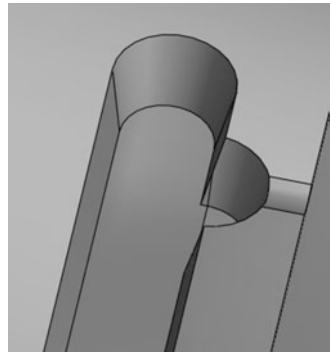
2.1.2 Runner Appearance

According to the research, the designed runner is divided into two types: (1) trapezoidal runners (Fig. 6) and (2) semicircular runners (Fig. 7).

Fig. 7 Semicircular runner
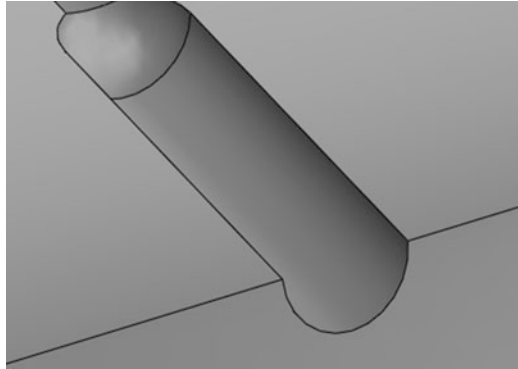
Table 1 Process parameters of plastic materials 180 °C

Code of product	Injection pressure (kg/cm^2)	Injection speed (mm/s)	Injection time (s)	Pressure of holding pressure (kg/cm^2)	Speed of holding pressure (mm/s)	Time of holding pressure (s)
180-1	70	100	4	100	100	7
180-2	65	100	4	100	100	7
180-3	60	100	4	100	100	7

Table 2 Surface roughness of plastic materials 180 °C for injection speed

Code of product	Injection speed	Ra (μm)	Rz (μm)
180-1	100	0.813	7.627
2-180-1	80	0.985	7.989
2-180-2	50	1.091	10.085

Table 3 Surface roughness of plastic materials 180 °C for pressure of holding pressure

Code of product	Pressure of holding pressure	Ra (μm)	Rz (μm)
180-1	100	0.813	7.627
3-180-1	80	1.074	11.499
3-180-2	50	2.214	16.789

2.2 Experimental Parameter Settings

2.2.1 Injection Molding Parameter Settings

This experiment used Gin-Jie Machinery Industrial Co., Ltd. Model JT-30 to set up the plastic injection molding machine and set the temperature in accordance with the Gin-Jie Machinery general thermoplastic rubber materials molding conditions. This study uses a PVC material barrel temperature of 150–180 °C based on the forming better pressure parameters, as shown in Tables 1, 2, 3, and 4.

Table 4 Surface roughness of plastic materials 180 °C for speed of holding pressure

Code of product	Speed of holding pressure	Ra (µm)	Rz (µm)
180-1	100	0.813	7.627
4-180-1	80	0.855	9.483
4-180-2	50	1.153	11.019

Scale (100 mm)
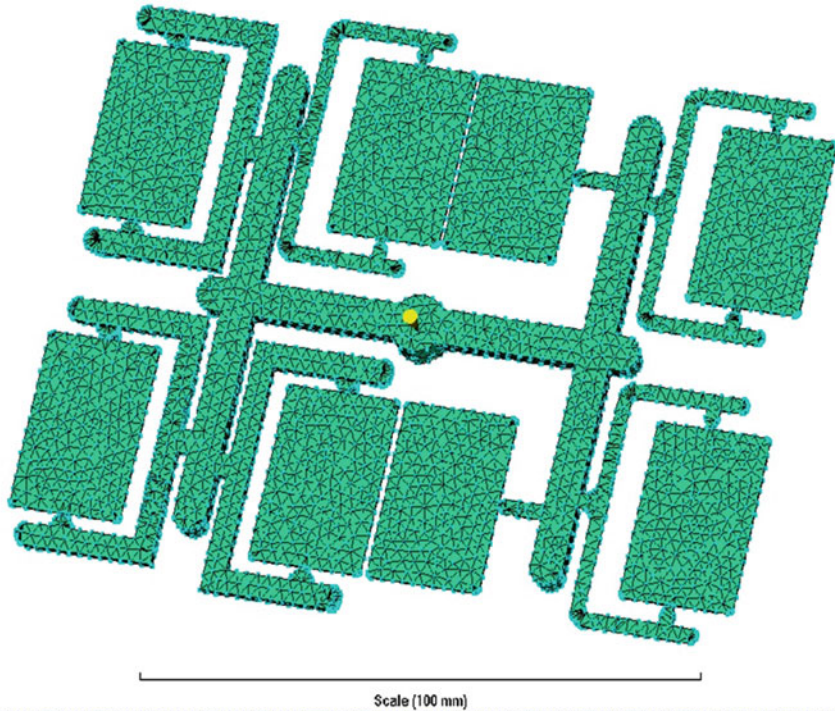
Fig. 8 Mold flow analysis grid chart

2.2.2 Mold Flow Analysis Parameter Settings

1. Grid Settings

   This study used Moldflow software to perform mold flow analysis. The actual injection molding experimental parameters imported into the mold flow analysis compared with the actual injections of the finished product. Figure 8 shows the mold flow analysis modeling grid chart, which is set to 2 mm global edge length, IGES merge tolerance is set to 0.25 mm, and the entire model is divided into a total of 18,539 units.

2. Material
   The material parameter is set to use plastic materials for Formosa Plastics PVC material.
3. Injection Parameters
   The injection parameters are set to the mold temperature, plastic temperature, injection time, injection pressure, and holding pressure parameters.
4. To Analyze the Options
   The parameters of the analysis were chosen, including the filling condition, pressure distribution, temperature distribution, and flow analysis.

3 Study and Discussion

3.1 Effects of the Mold Shape

1. The Impact of the Gate Appearance
   Figure 9 shows that of the A-1-2, B-1-2, and C-1-2, with the same runners and different gates; the B-1-2 is the worst semicircular gate. Number 180-2 forming showed the best results with the parameters and its encoding, a temperature of 180 °C, and injection pressure of 65 MPa.
2. The Impact of the Runner
   Figure 9 shows a C-1-2 trapezoidal sprue runner with the same gate perspective, two in the C-2-2 semicircular sprue fill time charts, a C-1-2 trapezoidal runner more complete filling.
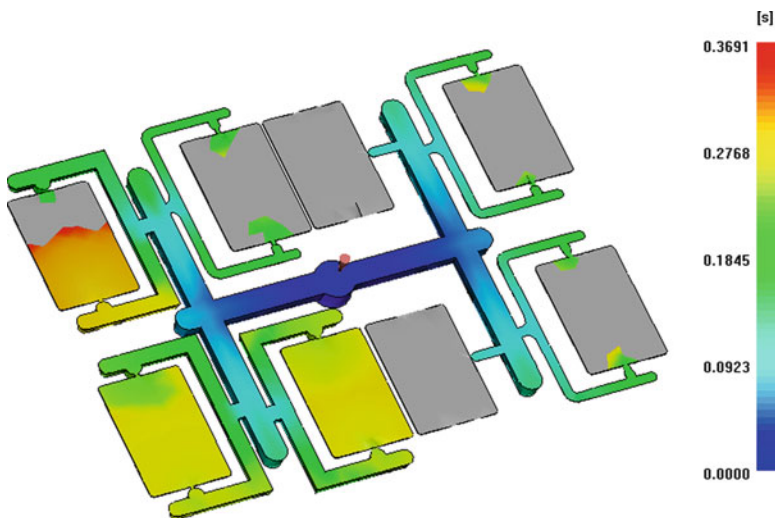
Fig. 9 Mold flow analysis of filling time
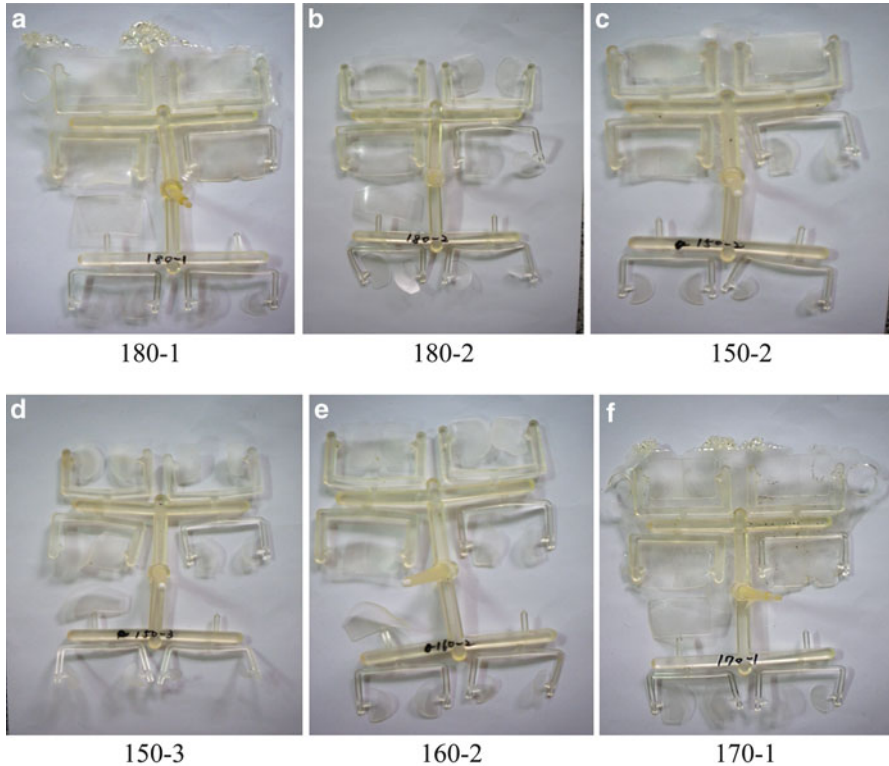
Fig. 10 Photograph of thin-sheet plastic component

3.2 Surface Roughness Analysis

This study changes the parameters to analyze the forming degrees. Number 180-2 showed the best parameters to analyze the impact of surface roughness.

1. Injection Pressure
   Table 1 shows 180-1 and 180-2, with the finished results shown in Fig. 10a and b. The pressure of 70 and 65, the pressure difference of only 5, but the 180-1 but serious overflow, its 150-2, 150-3 (finished; see Fig. 10c, d) of pressure, respectively, 95 and 90, the pressure difference is only 5,150-2 overflow many, but 150-3 but obviously insufficient injection pressure affect the large visible.
2. The Temperature Impact Plastic
   Injections 150-2, 160-2, 170-1, and 180-2 were compared. Figure 10b, c, e, and f show the four conditions for injection of extruded products. The results show that plastic temperature affects forming and is an important parameter.
3. The Speed of Injection Speed, Holding Pressure, and Holding Speed
   The injection speed does not have a significant impact on the shaping; Table 2 shows the results of 180-2, 2-180-1, and 2-180-2 after the measurement of

170-3 code

180-2 code
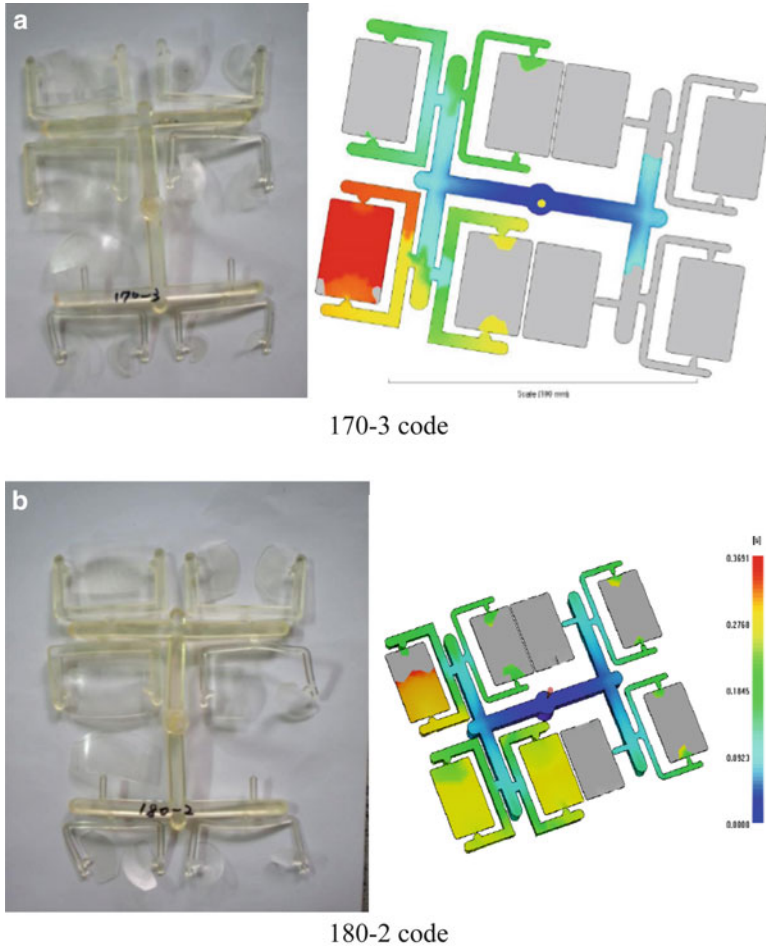
Fig. 11 Experiment compared with simulation of code mold flow analysis

surface roughness. Its value is the gradual rise in the roughness of the surface. Visible surface roughness increases with the speed of the decline.

Holding pressure and holding speed both. Its impact and other parameters of large, from Tables 3 and 4, shows that the speed of holding pressure and packing pressure improves roughness.

4 The Experiment Is Verified

According to the mold flow analysis, the parameters of injection verify the forming outcomes, such as Fig. 11a and b, which compare actual injections of the finished product with the filling simulation diagram. Although the mold flow analysis results
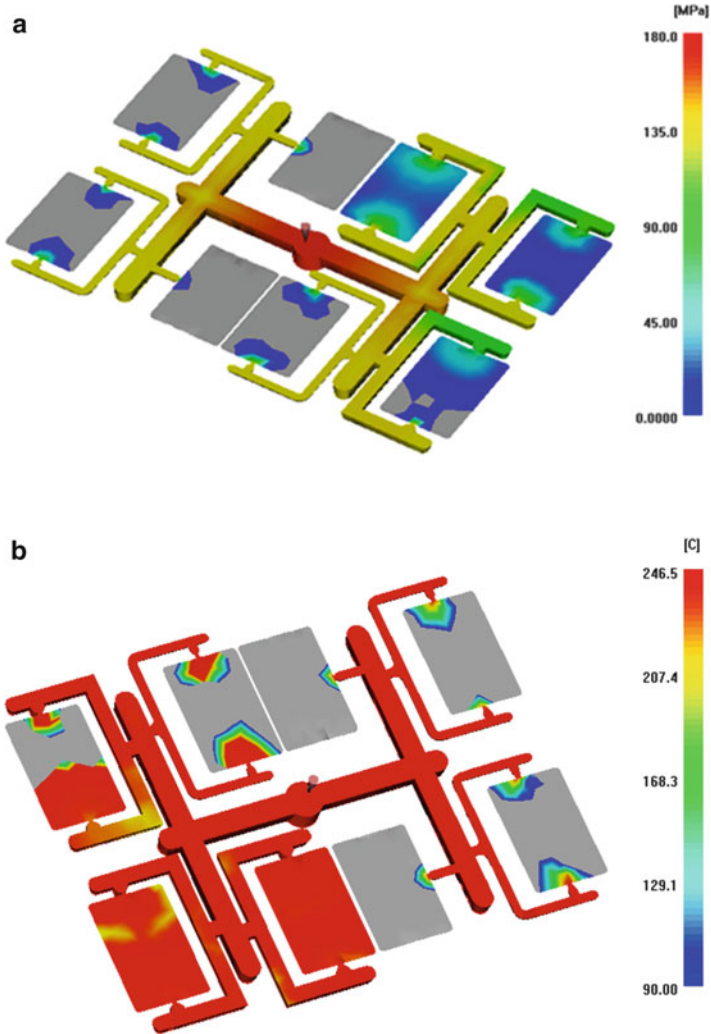
Fig. 12 Simulation of 180-2 code mold flow analysis. (**a**) Pressure simulation, (**b**) temperature simulation

and the actual injection results are not the same, they are similar. Therefore, first, an analysis of better forming parameters must be performed to reduce the expenditure of the cost and improve the quality of the finished product. Figure 12a and b show the pressure and temperature simulation with the best parameter results (coding 180-2 of Fig. 11b).

5 Conclusion

This chapter first used mold flow analysis. An analysis of better parameters for injection forming verification and measurement of the surface roughness was performed. The results can be summarized as follows:

1. The plastic temperature affects the formation of one of the important parameters.
2. The parameter's value is the gradual rise in the roughness of the surface. Visible surface roughness increases with the speed of the decline.
3. The first analysis of better forming parameters to reduce cost expenditures effectively and improve the quality of the finished product was performed with mold flow analysis.

References

1. Wang G, Zhao G, Li H, Guan Y (2010) Analysis of thermal cycling efficiency and optimal design of heating/cooling system for rapid heat cycle injection molding process. Mater Des 31:3426–3441
2. Altan M (2010) Reducing shrinkage in injection moldings via the Taguchi, ANOVA and neural network methods. Mater Des 31:599–604
3. Shelesh-Nezhad K, Siores E (1997) An intelligent system for plastic injection molding process design. J Mater Process Technol 63:458–462
4. Zhai M, Lam YC, Au CK (2009) Runner sizing in multiple cavity injection mould by non-dominated sorting genetic algorithm. Eng Comput 25:237–245
5. Zhou H, Li D (2005) Residual stress analysis of the post-filling stage in injection moulding. Int J Adv Manuf Technol 25:700–704
6. Fu YQ, Ji CH, Batchelor AW, LOh NH (1997) X-ray imaging of metal injection moulding parts. J Mater Sci Lett 16:1873–1875

A Comparison of Correlation Technique and Random Decrement Algorithm for Modal Identification from Nonstationary Ambient Vibration Data Only

Chang-Sheng Lin, Tse-Chuan Tseng, June-Rong Chen, and Dar-Yun Chiang

Abstract Modal identification from response data only is studied for structural systems under nonstationary ambient vibration. By assuming the ambient excitation to be nonstationary white noise in the form of a product model and introducing a technique of curve fitting, the practical problem of insufficient data samples available for evaluating nonstationary correlation functions or randomdec signatures can be approximately resolved by first extracting the amplitude-modulating function from the response and then transforming the nonstationary responses into stationary ones. Modal-parameter identification can then be performed using the Ibrahim time-domain method in conjunction with the correlation technique and random decrement algorithm, respectively. A comparison of correlation technique and random decrement algorithm is demonstrated through numerical simulations, which also confirm the validity of the proposed method for identification of modal parameters from nonstationary ambient response data.

Keywords Correlation technique • Random decrement algorithm • Ibrahim time-domain method • Curve-fitting technique • Nonstationary ambient vibration

C.-S. Lin (✉) • T.-C. Tseng
National Synchrotron Radiation Research Center, Hsinchu, Taiwan
e-mail: lin.changsheng@nsrrc.org.tw

J.-R. Chen
National Synchrotron Radiation Research Center, Hsinchu, Taiwan

National Tsing Hua University, Hsinchu, Taiwan

D.-Y. Chiang
National Cheng Kung University, Tainan, Taiwan

1   Introduction

A variety of methods have been developed for extracting modal parameters from structures undergoing ambient vibration. Ibrahim [1] applied the random decrement technique coupled with a time-domain parameter identification method [2] to process ambient vibration data. James et al. [3] developed the so-called natural excitation technique using the correlation technique coupled with time-domain parameter extraction. In the previous studies of modal-parameter identification from ambient vibration data, the assumption usually made is that the input excitation is a broadband stochastic process modeled by *stationary* white or filtered white noise. In this chapter, it is shown that if the input signals can be modeled as nonstationary white noise, which is a product of white noise and a deterministic time-varying function, the practical problem of insufficient data samples available for evaluating nonstationary correlation can be approximately resolved by first extracting the amplitude-modulating function from the response and then transforming the nonstationary responses into stationary ones. The correlation functions and randomdec signatures of the stationary response are treated as free-vibration response, and so the Ibrahim time-domain method can then be applied to identify modal parameters of the system. Numerical simulations will be performed to demonstrate a comparison of correlation technique and random decrement algorithm for modal identification and to confirm the validity of the proposed method for identification of modal parameters from nonstationary ambient vibration data.

2   Correlation Technique

James et al. [3] developed the so-called natural excitation technique (NExT) using the correlation technique. It was shown that the cross-correlation between two response signals of a linear system with classical normal modes and subjected to white-noise inputs is of the same form as free-vibration decay or impulse response. In combination with a time-domain parameter extraction scheme, such as the ITD method, this concept becomes a powerful tool for the identification analysis of structures under stationary ambient vibration. When a system is excited by stationary white noise, the cross-correlation function $R_{ij}(\tau)$ between two stationary response signals $x_i(t)$ and $x_j(t)$ can be shown to be [3]

$$R_{ij}(\tau) = \sum_{r=1}^{n} \frac{\phi_{ir}A_{jr}}{m_r\omega_{dr}} \exp(-\zeta_r\omega_r\tau) \, \sin\left(\omega_{dr}\tau + \theta_r\right) \tag{1}$$

where ϕ_{ir} denotes the ith component of the rth mode shape, A_{jr} a constant, and m_r the rth modal mass. The result above shows that $R_{ij}(\tau)$ in Eq. (1) is a sum of complex exponential functions (modal responses), which is of the same mathematical form as

the free-vibration decay or the impulse response of the original system. Thus, the cross-correlation functions evaluated of responses data can be used as free-vibration decay or as impulse response in time-domain modal extraction schemes so that measurement of white-noise inputs can be avoided.

3   Random Decrement Algorithm

The random decrement technique is a method that has been studied extensively for signature analysis of vibrating systems. Vandiver et al. [4] and Bedewi [5] showed that when excitation force is zero-mean, stationary, Gaussian white noise, the random decrement signature $\delta_{ij}(\tau)$ of response, could be denoted as follows:

$$\delta_{ij}(\tau) = \frac{R_{ij}(\tau)}{R_{ij}(0)} x_s, \tag{2}$$

where $R_{ij}(0) = R_{ij}(\tau = 0)$. Note that x_s is the threshold level for the acquisition of sample time history and generally defined as the root-mean-square value of system's stationary displacement response. Equation (2) signifies that the random decrement signature is in proportion to the cross-correlation function $R_{ij}(\tau)$. Since the correlation function has the same mathematical form as that of free-vibration response [3], the random decrement signature can also be treated as a free-vibration signal for modal-parameter identification.

4   Practical Treatment of Nonstationary Data

It has been shown in the previous studies [3–5] that by assuming the ambient excitation to be stationary white noise, the cross-correlation functions or randomdec signatures evaluated at a fixed time instant of responses can be used as free-vibration decay or as impulse response in time-domain modal extraction schemes. However, the practical problem for evaluating nonstationary randomdec signatures is that usually very limited data samples are available in engineering practice. The problem can be resolved by first extracting the modulating function from the response if the nonstationary excitation can be modeled approximately as the product model [6]. It has been shown in a previous paper of the authors [6] that the temporal root-mean-square functions of the response histories describe the same time variation as given by the envelope function. If the original nonstationary data could be represented by the product model with a slow varying envelope function, the temporal root-mean-square functions of the data also have the same nonstationary trends as that of the original data. The temporal root-mean-square function, and so the envelop function, can thus be determined by using the interval average and then applying curve fitting. This gives us the

deterministic envelope function which describes the slow variation in the amplitude of the ambient excitations. The approximate stationary responses can thus be acquired by dividing the nonstationary responses of each DOF with the associated modulating functions obtained through curve fitting. Then the randomdec signatures of the stationary response data can be obtained, which are in turn treated as the free decay responses corresponding to each DOF. The modal parameters of a system can then be obtained via a time-domain modal identification method, such as the ITD method [4].

5   Numerical Simulation

To demonstrate the effectiveness of the proposed method, we consider a linear 6-DOF chain model with viscous damping. A schematic representation of this model is shown in Fig. 1. The mass matrix M, stiffness matrix K, and the damping matrix C of the system are given as follows:

$$
M = \begin{bmatrix} 2 & 0 & 0 & 0 & 0 & 0 \\ 0 & 2 & 0 & 0 & 0 & 0 \\ 0 & 0 & 2 & 0 & 0 & 0 \\ 0 & 0 & 0 & 2 & 0 & 0 \\ 0 & 0 & 0 & 0 & 3 & 0 \\ 0 & 0 & 0 & 0 & 0 & 4 \end{bmatrix} N \cdot s^2/m,
$$

$$
K = 600 \cdot \begin{bmatrix} 1 & -1 & 0 & 0 & 0 & 0 \\ -1 & 2 & -1 & 0 & 0 & 0 \\ 0 & -1 & 2 & -1 & 0 & 0 \\ 0 & 0 & -1 & 2 & -1 & 0 \\ 0 & 0 & 0 & -1 & 3 & -2 \\ 0 & 0 & 0 & 0 & -2 & 5 \end{bmatrix} N/m,
$$

$$
C = 0.05M + 0.001K + 0.2 \begin{bmatrix} 1 & \cdots & 1 \\ \vdots & \ddots & \vdots \\ 1 & \cdots & 1 \end{bmatrix}_{6 \times 6} N \cdot s/m.
$$

Note that the system has nonproportional damping (and so complex modes in general), since the damping matrix C cannot be expressed as a linear combination of M and K. Consider that the ambient vibration input can be modeled as nonstationary white noise as represented by the product model. The stationary white noise
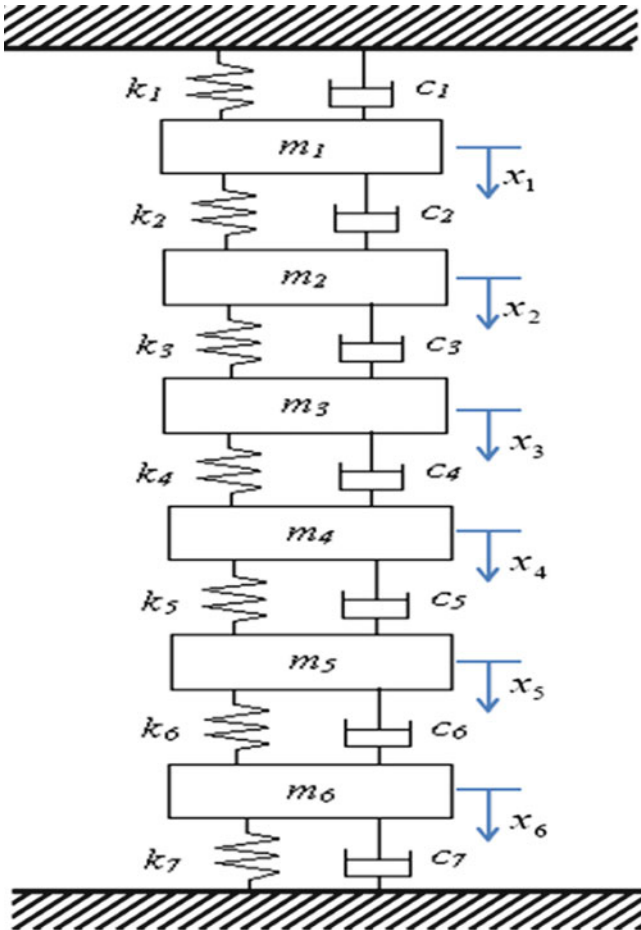
Fig. 1 Schematic plot of the 6-DOF chain system

is generated using the spectrum approximation method [7] as a zero-mean band-pass noise, whose standard deviation is $0.02 \, \text{N}^2 \cdot \text{s/rad}$ with a frequency range from 0 to 50 Hz. The sampling interval is chosen as $\Delta t = 0.01$ s, and the sampling period is $T = N_t \cdot \Delta t = 1,310.72 \, s$. The stationary white noise simulated is then multiplied by an amplitude-modulating function $\Gamma(t) = 4 \cdot (e^{-0.002t} - e^{-0.004t})$, as shown in Fig. 2, to obtain the nonstationary white noise, which serves as the excitation input acting on the 6th mass point of the system. The time signal of a simulated sample of the nonstationary white noise and the power spectrum of the corresponding stationary part are shown in Figs. 3 and 4, respectively.

The simulated displacement responses of the system were obtained using Newmark's method [8]. By examining the Fourier spectra associated with each of
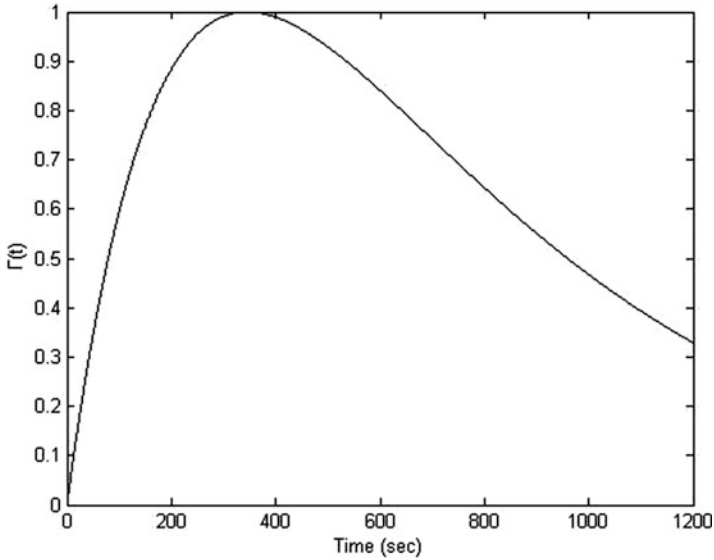
Fig. 2 A typical plot of the amplitude-modulating function
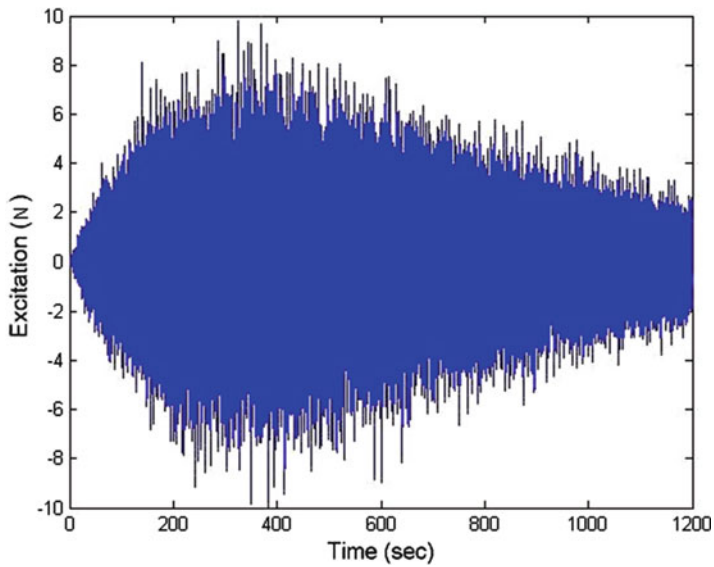
Fig. 3 A sample function of nonstationary white noise in time domain

the response channel, we chose the response of the 6th channel, $X_6(t)$, which contains rich overall frequency information, as the reference channel to compute the correlation functions and randomdec signatures, respectively, of the system. According to the theory presented in the previous sections, the nonstationary
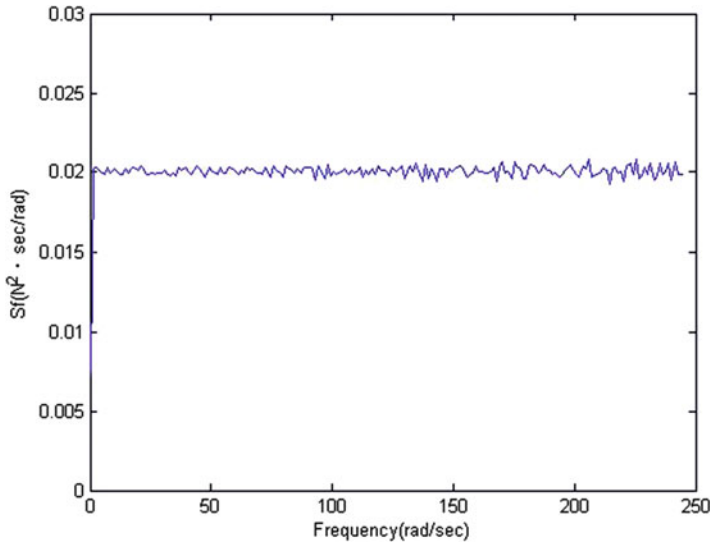
Fig. 4 Power spectrum associated with the stationary part of the simulated nonstationary white noise

Table 1 Results of modal-parameter identification of a 6-DOF system subjected to nonstationary white-noise input in the form of a product model through the correlation technique in conjunction with a technique of curve fitting

	Natural frequency (rad/s)			Damping ratio (%)			
Mode	Exact	ITD	Error (%)	Exact	ITD	Error (%)	MAC
1	5.03	5.03	0.06	5.24	5.12	2.29	1.00
2	13.45	13.43	0.16	1.07	1.06	0.93	1.00
3	19.80	19.74	0.28	1.13	1.09	3.54	1.00
4	26.69	26.53	0.60	1.43	1.41	1.40	0.98
5	31.66	31.41	0.80	1.66	1.65	0.60	0.94
6	33.73	33.38	1.03	1.74	1.70	2.30	0.95

problem may reduce to a stationary problem if we extract the amplitude-modulating function from the original nonstationary data. Therefore, we can follow the same procedures as those for stationary problems and the correlation functions and randomdec signatures, respectively, thus obtained are treated as free-vibration data. The Ibrahim time-domain method could then be applied to identify modal parameters of the system.

The results of modal-parameter identification are summarized in Tables 1 and 2, which shows that the errors in natural frequencies are less than 2 % and the maximum error in damping ratios is less than 40 %. Note that the "exact" modal damping ratios listed in Table 1 are actually the equivalent modal damping ratios

Table 2 Results of modal-parameter identification of a 6-DOF system subjected to nonstationary white-noise input in the form of a product model through the random decrement algorithm in conjunction with a technique of curve fitting

Mode	Natural frequency (rad/s)			Damping ratio (%)			MAC
	Exact	ITD	Error (%)	Exact	ITD	Error (%)	
1	5.03	5.04	0.11	5.24	4.99	4.77	1.00
2	13.45	13.41	0.30	1.07	0.94	12.15	1.00
3	19.80	19.74	0.30	1.13	1.25	10.62	1.00
4	26.69	26.59	0.37	1.43	1.11	22.38	1.00
5	31.66	31.42	0.74	1.66	1.02	38.55	0.99
6	33.73	33.21	1.53	1.74	1.48	14.94	1.00

obtained by utilizing ITD from the simulated free-vibration data of the nonproportionally damped structure. It is remarkable that the modes identified by the ITD generally include the vibrating modes of the structural system and some fictitious modes due to numerical computation. To keep track of the target modes, we utilize the Modal Assurance Criterion (MAC) [9] that has been extensively used in the experimental modal analysis. The value of MAC varies between 0 and 1. When the MAC value is equal to 1, the two mode-shape vectors represent exactly the same mode shape. In addition, we can distinguish the fictitious modes from the vibrating modes of the structural system if the mass matrix or the stiffness matrix of the structural system is available according to the orthogonality conditions, which show that vibrating shapes are orthogonal with respect to the stiffness matrix as well as to the mass matrix.

The identified mode shapes are also compared with the exact values in Fig. 5, where good agreement is observed. The errors of identified damping ratios and mode shapes are somewhat higher due to the fact that the system response generally has lower sensitivity to these modal parameters than to the modal frequencies. It should be mentioned that the choice of the reference channel for computing the correlation functions and randomdec signatures is important to the identification results. The reference channel is chosen as a response channel for which the Fourier spectrum has rich frequency content around the structure modes of interest. The richer the frequency content of the reference channel, the better the modal-parameter identification that can be achieved. It is remarkable that for the random decrement algorithm to be effective, we need generally more than 500 samples of time history for each response channel. We can then perform averaging over the samples to obtain good quasi free-vibration data for further modal-parameter identification. For this purpose, the random decrement algorithm generally requires response data to be much longer in time and therefore is practically less efficient when compared with the correlation technique.
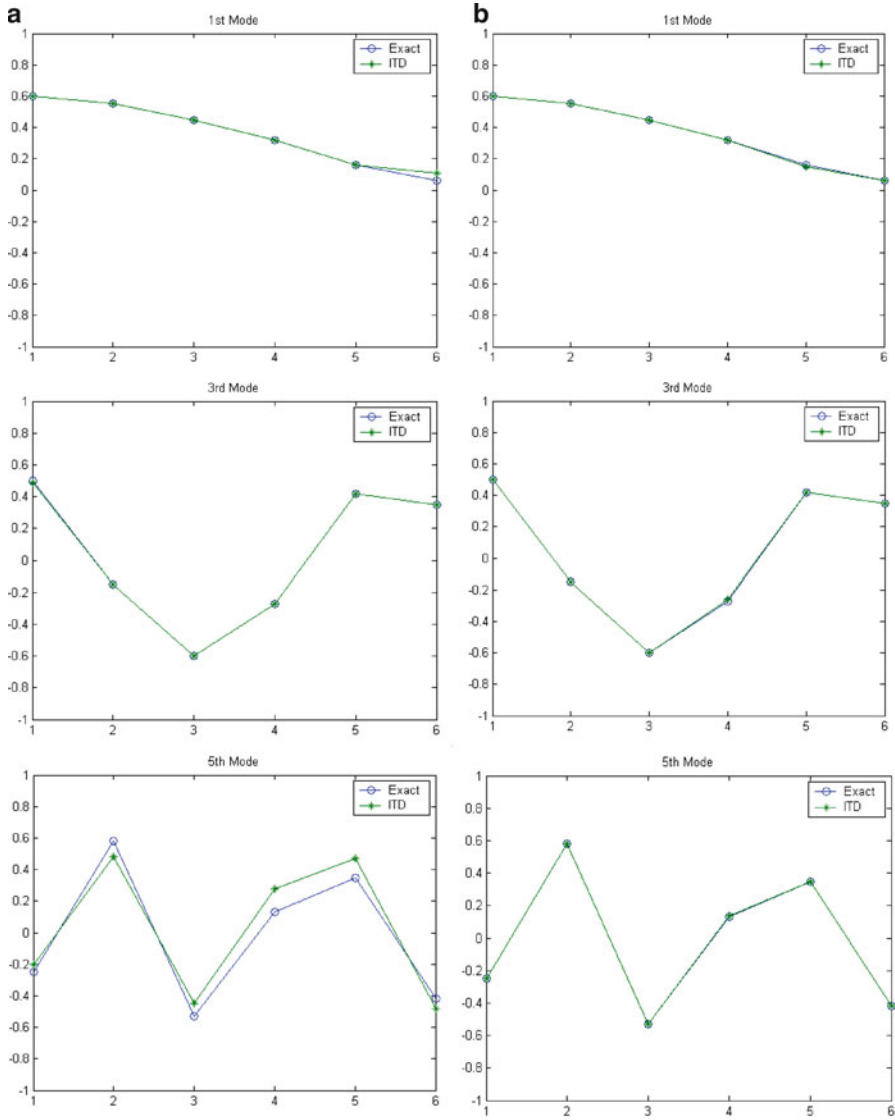
Fig. 5 Comparison between the identified mode shapes and the exact mode shapes of the 1st, 3rd, and 5th modes of the 6-DOF system subjected to nonstationary white-noise input. (**a**) Correlation technique. (**b**) Random decrement algorithm

6 Conclusions

Identification of modal parameters is considered from response data of structural systems under nonstationary ambient vibration. It is shown that if the original nonstationary data could be represented by the product model with a slowly varying envelope function, the temporal root-mean-square functions of the data also have the same nonstationary trend as that of the original data. The temporal root-mean-square function, and so the envelope function, can thus be determined by using interval average and then applying curve fitting. The practical problem of insufficient data samples available for evaluating nonstationary correlation functions and randomdec signatures, respectively, can be approximately resolved by first extracting the amplitude-modulating function from the response and then transforming the nonstationary responses into stationary ones. The correlation functions and the randomdec signatures of the stationary response are treated as free-vibration response, and so the Ibrahim time-domain method can then be applied to identify modal parameters of the system. The selection of reference channel for computing correlation functions and randomdec signatures is also important to the identification results. The richer frequency content the reference channel has, the better results of modal-parameter identification can be achieved. In addition, the random decrement algorithm generally requires response data to be much longer in time and therefore is practically less efficient when compared with the correlation technique.

References

1. Asmussen JC, Ibrahim SR, Brincker R (1996) Random decrement and regression analysis of bridges traffic responses. In: Proceedings of the 14th international modal analysis conference, Dearborn, 1996, vol 1. pp 453–458
2. Ibrahim SR, Mikulcik EC (1977) A method for the direct identification of vibration parameters from free response. Shock Vib Bull 47(4):183–198
3. James GH, Carne TG, Lauffer JP (1993) The natural excitation technique for modal parameter extraction from operating wind turbines. SAND92-1666. UC-261, Sandia National Laboratories, Sandia
4. Vandiver JK, Dunwoody AB, Campbell RB, Cook MF (1982) A mathematical basis for the random decrement vibration signature analysis technique. ASME J Mech Des 104:307–313
5. Bedewi NE (1986) The mathematical foundation of the auto and cross-random decrement techniques and the development of a system identification technique for the detection of structural deterioration. Ph.D. thesis, University of Maryland College Park, College Park
6. Chiang DY, Lin CS (2010) Identification of modal parameters from ambient vibration data using eigensystem realization algorithm with correlation technique. J Mech Sci Technol 24(12):2377–2382
7. Shinozuka M (1971) Simulation of multivariate and multidimensional random processes. J Acoust Soc Am 49(1):357–367
8. Newmark NM (1959) A method of computation for structural dynamics. J Eng Mech ASCE 85(EM3):67–94
9. Allemang RL, Brown DL (1983) A correlation coefficient for modal vector analysis. In: Proceedings of the 1st international modal analysis conference, Society for Experiment Mechanics, Bethel, 1983, pp 110–116

Effect of Annealing Temperature on the Mechanical Properties and the Spherical Indentation of NiTi Shape Memory Alloy

Tsung-Han Tan, Mei-wen Wu, and Chun-Ying Lee

Abstract NiTi alloy is one of the so-called shape memory alloys (SMAs). Its shape memory effect is derived from the phase transformation controlled by the temperature. With the similar spherical indentation produced in the measurement of Brinell hardness, a surface topography accompanied with residual stress is obtained on the polished NiTi alloy. Following the usual controlled heating performed in the SMA, the indented surface can nearly return to its flat surface configuration as the NiTi alloy goes through the martensite to austenite transformation. This study firstly focused on how to implement the SMA material tensile test at different controlled temperatures. Thus, the associated mechanical properties at different temperatures were obtained, and the effect of annealing temperature on the SMA's phase transformation was also investigated. The thus formed spherical indentations on shape memory alloys could have reversible depth change, i.e., deeper depth in the martensitic phase at low temperature and shallower depth in the austenitic phase at high temperature. Thus, by controlling the temperature of the NiTi alloy, a surface with tunable morphology was demonstrated.

Keywords Shape memory alloy • Superelasticity • Tunable surface morphology

T.-H. Tan • C.-Y. Lee (✉)
Department of Mechanical Engineering, National Taipei University of Technology,
Taipei 10608, Taiwan
e-mail: leech@ntut.edu.tw

M.-w. Wu
Chienkuo Technological University, Changhua 50015, Taiwan

1   Introduction

Due to the potential demand on the miniaturization and integration of biochips and other microchips for chemical analysis, the research in the microfluidic devices has been a popular topic recently [1]. The reduction of chip size down to 1 mm or less than 500 μm minimizes not only the required sample volume and testing time but also the operation cost. However, the effectiveness and accuracy of the test depends mostly on the fluidity and proper mixing of the reagent and sample inside microchannel. The low Reynolds number and diffusivity of fluid, worse for fluid with high molecular weight, poses a serious challenge on the device design. Among the different designs for the micromixers, they are categorized into active and passive devices. The active micromixer utilizes actuating forces, such as pressure, electrophoresis, or electric osmosis, to actuate the mixing. On the other hand, the passive design uses the geometrical shape of the microchannel to increase the interface interaction between two fluids [2–4]. Although the passive devices are simple to use and consume less energy, the controllability and mixing enhancement are not as effective as its active counterparts. Nevertheless, the complexity and high cost are the tradeoffs for using active devices.

The tuning of the surface profile of the microchannel wall can provide the tool to change the fluid flow pattern inside the duct. The use of shape memory material with controllable surface geometrical profile in the fabrication of microchannel wall has been proposed previously [5, 6]. In 2006, Zhang et al. disclosed the fabrication of shape memory surface, which had controllable indentation marks [7, 8]. Shape memory materials are the class of materials which geometrical shape can be controlled by temperature [9, 10], magnetic field [11, 12], etc. The underlined mechanism is associated with the phase transformation incurred during the change of controlled parameter. Basically, the transformation point is determined by the microstructure of the shape memory material which can be altered by the heat treatment [13]. Moreover, the shape memory effect can be trained by repetitive thermal and mechanical loading cycles [14, 15]. Thus, the study on the fabrication of a two-way shape memory surface using different heat treatments on the NiTi alloy was performed with its intended application in micromixer.

2   Experimental

2.1   Specimens

The NiTi wire with diameter of 1.0 mm used in this study was manufactured by Furukawa Electric Co. The as-received NiTi wire was previously fabricated from drawing process. Thus, the induced plastic deformation made the wire incapable of inheriting the shape memory effect. Therefore, an annealing treatment was required to restore the mechanical property of the NiTi wire. The NiTi wire was first

trimmed into segments of 120 mm long. The NiTi segments were then placed inside a heat treatment oven and started to heat up to annealing temperature. The specimens were remained at the annealing temperature for 1 h and then cooled to room temperature inside the oven. Six different annealing temperatures were investigated starting from 200 to 450 °C with interval of 50 °C. The annealed wire was laid down and embedded in mounting resin as the usual practice for microscopic examination. The embedded specimen was then polished with emery papers and alumina sol subsequently until a flat strip surface of NiTi wire appeared on the mounting surface. At both ends of the NiTi wire, the mounting resin was milled away and the wire ends revealed from the mounting block. The exposed ends of the wire were employed as the connections for the electric heating circuit.

2.2 Uniaxial Tensile Testing

The stress-strain curve of the NiTi wire at different controlled temperatures was measured by using an in-house uniaxial tensile testing machine. Since the mechanical properties of the NiTi wire were sensitive to the material temperature, the specimen was submerged in a constant temperature water bath to maintain the specimen at constant temperature during testing [16]. The specimen was clamped between two grips and submerged in the water bath. A servo motor drove the ball screw and the movable end grip to apply the tensile load on the specimen. The loading and displacement of the grip were measured by a load cell and an LVDT displacement meter, respectively. The water in the specimen bath was circulated continuously with a constant temperature water tank. The water medium had good heat capacity and thermal convection, and good control of the specimen temperature could be assured. However, because water medium was used in the temperature bath, the temperature tested was limited to the range from 0 to 90 °C. The measured loading and displacement of the wire specimen were recorded in a dynamic signal analyzer. By normalizing the load and displacement with respect to the specimen cross-sectional area and the grip length, the stress-strain curve could be constructed.

2.3 Micro-indentation and Training

In order to study the shape memory effect of the indentation on surface of the polished specimen, a simple indentation platform was built in this study. A spherical indenter mounted at the end of the press rod was driven by a rocker arm. A load cell installed between the press rod and the indenter was employed to measure the indentation load. Hence, the size of indentation could be controlled according to the designated load. The specimen was fixed on an $x-y$ platform such that the location of the indentation could be adjusted. By controlling the magnitude of the contact load, the spherical indentation in different sizes could be obtained.

Some of the indented specimens went through training process. The indented specimen still with the indenter pressed on at given load was dipped into two water baths alternatively. The lower temperature bath was maintained at 0 °C in water mixed with ice cubes. The other water bath was heated on top of a temperature-controlled hot plate at around 95 °C which was above the austenite finished temperature (A_f) of the NiTi alloy used herein. The training process continued for a preset times.

2.4 Structural Characterization and Morphology

After indentation, the surface morphology of the specimen was examined by optical microscope. In addition, surface contour of the indentation was measured by using a surfcorder (SEF3500 Kosaca Co., Japan). Beside the surface geometric characterization, the microstructural texture of the NiTi alloy after different annealing treatments was also performed by employing an X-ray diffractometer (Philips 1830/Mac, Holland). The X-ray was generated by a Cu–K$_\alpha$ target operated at 30 kV and 20 mA with a wavelength of 0.15418 nm.

3 Results and Discussion

3.1 Stress-Strain Curve at Controlled Temperature

The stress-strain curves of the annealed NiTi wires under uniaxial tensile testing at different temperatures are presented in Fig. 1. For detail discussion, take the 300 °C-annealed specimen (Fig. 1b) as the example. It is seen for temperatures under 50 °C the NiTi wire demonstrated the shape memory effect, i.e., after unloading, there was permanent deformation. This residual deformation could be recovered by heating the wire back to higher temperature. However, when the water
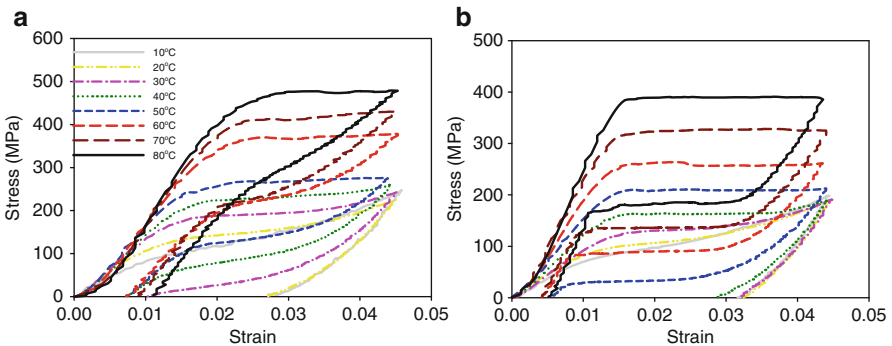
Fig. 1 The temperature-dependent stress-strain curves of NiTi wires annealed at (**a**) 200 °C and (**b**) 300 °C. All legends follow those indicated in (**a**)

bath temperature was higher than 50 °C, almost the deformation occurred due to loading could be removed during unloading. A small permanent deformation was still present which may be caused by the high strain induced by the clamping at the ends of the specimen. It is also shown in Fig. 1 that both the transformation stress and reverse transformation stress varied with the specimen temperature.

3.2 The Microstructure of the NiTi Wire

In order to determine the microstructure of the annealed NiTi wire, the X-ray diffraction patterns of the specimens were measured. The diffraction peaks corresponding to the different phases were presented in Ref. [17]. It was found that at room temperature, the most prevailing phase was austenite for all annealed specimens. However, the content of martensite increased gradually with the raise of annealing temperature from 200 to 400 °C. For NiTi wire annealed at 450 °C, the peak of the martensite diffraction slightly dropped. The residual austenite detected at room temperature denoted the M_f (finished temperature of martensitic transformation) of the specimen was lower than room temperature. In addition, the annealing at higher temperature caused more annealed microstructure which transformed into martensite when cooled to room temperature.

3.3 Phase Transformation Characteristics

By employing the DSC measurement, the transformation temperatures of the NiTi wires after annealing at different temperatures could be obtained. The results are shown in Fig. 2. It is seen that with higher temperature annealing, the R_s increased first but decreased later on. Similar trend was found for the R_f. By comparing the temperature range between R_s and R_f for different annealing temperatures, the span reached minimum at around 400 °C. This result was consistent with the XRD measurement where most martensite content was observed for annealing at 400 °C. Furthermore, the temperature span between A_s and A_f enlarged at 450 °C, and this might relate to the slight grain growth at this temperature. These results demonstrated the more effective phase control of this NiTi wire can be obtained by annealing at around 400 °C.

Another indicator for the phase transformation is stress-induced martensite in austenite. The corresponding transformation stress was distilled from the results of the stress-strain curves in Fig. 1. Basically, both the transformation stress and strain decreased with increased annealing temperature. It is understood that with higher annealing temperature, more ductility can be restored from the cold-worked NiTi wire during fabrication. Therefore, the transformation threshold was lowered. However, for tensile testing at 70 and 80 °C, an increasing trend was observed at 400 °C annealing. The mechanism for this phenomenon was still unclear and needs further investigation.
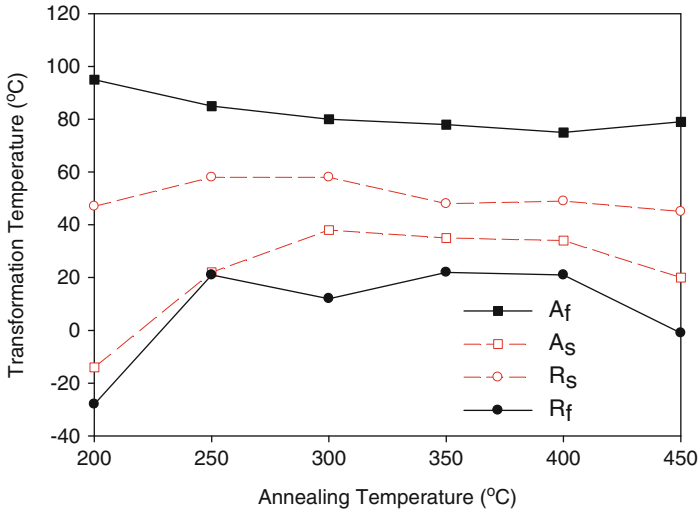
Fig. 2 The change of transformation temperature with the annealing treatment temperature
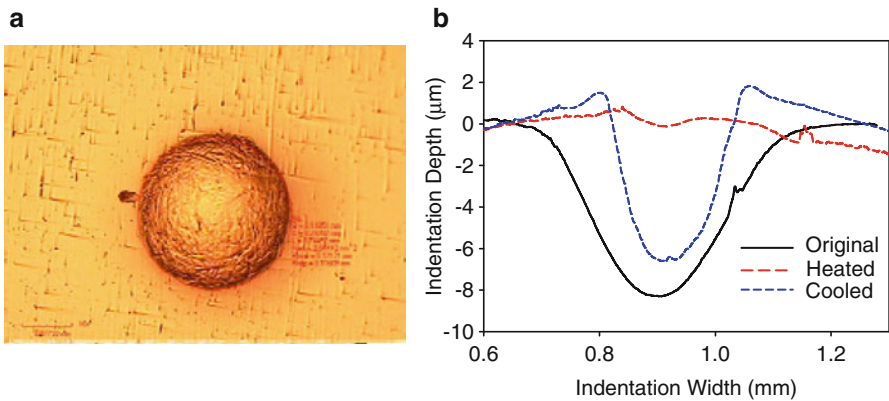
Fig. 3 (**a**) The typical OM picture of an indentation on NiTi alloy and (**b**) the associated diametrical line contour of the indentation at different temperatures

3.4 Surface Indentation on NiTi Alloy

Figure 3 presents the OM picture and the associated diametrical profile of a typical indentation fabricated in this study. In the measured contour, the diameter and depth of the indentation were determined accordingly. From the previous results on the effect of annealing temperature, the ones annealed at 350 and 400 °C demonstrated the best shape memory effect. Hence, the shape memory effect of

Table 1 The depth of indentation for specimens at different stages

Specimens	Indented (μm)	Heated (μm)	Cooled (μm)
350 °C (untrained)	11.40	2.02	1.90
350 °C (trained, 30 cycles)	16.86	4.92	5.12
350 °C (trained, 50 cycles)	16.04	5.88	6.34
400 °C (untrained)	18.48	0.6	1.28
400 °C (trained, 30 cycles)	16.08	0.6	1.48
400 °C (trained, 50 cycles)	17.92	5.16	5.12

the surface indentation was focused on the specimens treated at these two temperatures. In addition, in order to study the effect of shape memory training, the indented specimens also were treated with 30 and 50 training cycles. The change in the dimensions of the indentation was presented in Table 1. The indented, heated, and cooled specimens denoted the first indented specimen at room temperature, the indented specimen heated above 90 °C, and the cooled specimen back to room temperature, respectively. The results in Table 1 show that the indentation was nearly recovered upon first heating. However, the subsequent cooling back to room temperature barely changed the dimensions of the indentation and revealed unnoticeable two-way shape memory effect. Further cooling the 400 °C specimen to lower temperature with dry ice (−78.5 °C) was attempted, and the results are presented in Fig. 3b. In this case, the untrained specimen still barely showed the two-way shape memory effect. However, the 30-cycle trained specimen did improve its dimensional change between heated and cooled temperatures.

4 Conclusion

The effect of annealing temperature on the mechanical properties of the NiTi wire was investigated experimentally. The results from the isothermal uniaxial tensile testing showed that increasing the annealing temperature up to 400 °C could enhance the shape memory effect by decreasing the temperature span between the phase transformations. For the NiTi wire annealed at lower temperature, the residual cold work was not fully recovered such that the transformation stress was higher than annealed at higher temperature. For the indentation fabricated on the polished surface of the NiTi wire, the simple indentation only provided the surface with one-way shape memory effect, i.e., the indentation recovered upon the first heating above the A_f and no significant profile change upon subsequent cooling even lowered to −78.5 °C. Nevertheless, by training the indented specimen between cold and hot water baths alternatively for certain times, the surface indentation with two-way shape memory effect could be obtained. However, the effect could only be shown for lowering to the temperature of dry ice, not at room

temperature. This is still hard to apply in microfluidic devices now. Therefore, how to manipulate the two-way surface morphology control with lower temperature closed to room temperature can be topic for future study.

References

1. Nguyen N-T, Wu Z (2005) Micromixers – a review. J Micromech Microeng 15:R1–R16
2. Adeosun JT, Lawal A (2005) Mass transfer enhancement in microchannel reactors by reorientation of fluid interfaces and stretching. Sens Actuators B 110:101–110
3. Ansari MA, Kim KY, Anwar K, Kim SM (2010) A novel passive micromixer based on unbalanced splits and collisions of fluid streams. J Micromech Microeng 20:055007
4. Bhagat AAS, Peterson ETK, Papautsky I (2007) A passive planar micromixer with obstructions for mixing at low Reynolds numbers. J Micromech Microeng 17:1017–1024
5. Tseng L-Y, Yang A-S, Lee CY, Hsieh C-Y (2011) CFD-based optimization of a diamond-obstacles inserted micromixer with boundary protrusions. Eng Appl Comput Fluid Mech 5:210–222
6. Yang A-S, Lee CY, Tseng L-Y, Liao S-K (2011) Development of a novel SMA-tuned micromixer. In: 3rd international conference on ferromagnetic shape memory alloys, Dresden, 18–22 June 2011
7. Zhang Y, Cheng Y-T, Grummon DS (2006) Shape memory surfaces. Appl Phys Lett 89:041912
8. Zhang Y, Cheng Y-T, Grummon DS (2006) Two-way indent depth recovery in a NiTi shape memory alloy. Appl Phys Lett 88:131904
9. Wang ZG, Zu XT, Fu P, Dai J, Zhu YS, Wang LM (2003) Two-way shape memory effect of TiNi alloy coil extension springs. Mater Eng A360:126–131
10. Nemat-Nasser S, Guo W-G (2006) Superelastic and cyclic response of NiTi SMA at various strain rates and temperatures. Mech Mater 38:463–474
11. O'Handley RC, Murray SJ, Marioni M, Nembach MH, Allen SM (2000) Phenomenology of giant magnetic-field-induced strain in ferromagnetic shape-memory materials. J Appl Phys 87:4712–4717
12. Soderberg O, Ge Y, Sozinov A, Hannula SP, Lindroos VK (2005) Recent breakthrough development of the magnetic shape memory effect in Ni-Mn-Ga alloys. Smart Mater Struct 14:S223–S235
13. Huang X, Liu Y (2001) Effect of annealing on the transformation behavior and superelasticity of NiTi shape memory alloy. Scr Mater 45:153–160
14. Lach CL, Thrner TL, Taminger KM, Shenoy RN (2000) Effects of thermomechanical history on the tensile behavior of Nitinol ribbon. In: Christopher S. Lynch (ed.) Annual international symposium on smart structures and materials; active materials: behavior and mechanics, SPIE vol 4699, Paper No. 4699-45, San Diego, 17–21 Mar 2002
15. Zhang Y, Cheng Y-T, Grummon DS (2007) Two-way shape memory surfaces. United States Patent Application Publication, Pub. No.: US2007/0163686 A1
16. Shaw JA, Churchill CB, AIadicola M (2009) Tips and tricks for characterizing shape memory alloy wire: part 2-fundamental isothermal responses. Exp Tech 33:51–62
17. Uchil J, Braz Fernandes FM, Mahesh KK (2007) X-ray diffraction study of the phase transformations in NiTi shape memory alloy. Mater Charact 58:243–248

The Analysis of Engine Intake Air Cooling Device by Using Thermoelectric Module

Wang Jia-Wei and Ming-Hsien Hsueh

Abstract The intake air cooling device of the engine is discussed in this chapter. The thermoelectric module (T.E.M.) is applied on the device for the decrease of the intake air temperature to the engine. The device is placed between the engine and the air filter, and it can increase the efficiency of the induction system by reducing induction air heat and promoting more thorough combustion. The closed water cooling system can remove the heat produced from the thermoelectric module and increase the efficiency of the thermoelectric module. According to the device, it can increase the engine power about 60 % at most and decrease the intake air temperature by 14 %.

Keywords Thermoelectric module • Intake air • Water cooling system • Induction system

1 Introduction

In the internal combustion engine, the combustion of fossil fuel mixed with air in a combustion chamber applies direct force to some component of the engine [1]. In order to improve the volumetric efficiency of the internal combustion engine, there are several methods to increase the efficiency. The larger valves or multiple valves in the combustion engine can add the air volumetric to the combustion chamber [2]. The supercharger [3] or turbocharger [4] also provides more forced air to the induction system for the increase of the volumetric efficiency. The intercooler used in the forced induction (turbocharger or supercharger) can increase intake air charge density by rejecting heat to the atmosphere [5]. The variable valve timing [6] or lifting system [7] allows the lift, duration, or timing of the intake or exhaust

W. Jia-Wei (✉) • M.-H. Hsueh
Department of Mechatronics Engineering, Taipei Chengshih University of Science and Technology, No. 2, Xueyuan Rd, Peitou, Taipei 112, Taiwan, R.O.C.
e-mail: wangjiawei1860@126.com

valves to be changed while the engine is in operation in order to extend the time of intake gas into the combustion chamber.

The purpose of above researches improves the volumetric efficiency of the internal combustion engine. In this chapter, the thermoelectric module (T.E.M.) is applied in the inlet manifold of the engine to cool the inlet air to increase the intake air charge density. The thermoelectric cooling modules are widely used in the heat removal and cooling devices in engineering. The performance of the engine power and fuel consumption efficiency is discussed in this chapter to show the improvement of the induction system by the thermoelectric module.

2 T.E.M. Model and Physics

Thermoelectric module (T.E.M.) [8] is widely applied in heat removal and temperature control of scientific research, military affairs, semiconductor industry, and so on. A T.E.M. consists of equal number of P-type and N-type elements connected in series and parallel sandwiched in between two ceramic plates, as shown in Fig. 1. When the electric power is transported across two metallization junctions (from P to N or N to P), the heat will be absorbed into the cold junction and dissipated from the hot junction, i.e., Peltier effect. The temperatures of the cold junction and hot junction are defined as T_{cj} and T_{hj}, respectively. The temperature of the cold ceramic plate connected to cold junctions is defined as T_c and the hot ceramic plate connected to hot junction is T_h.

The thermoelectric performance of the T.E.M. is determined by three properties: the electrical resistivity (ρ), the Seebeck coefficient (α), and the thermal conductivity (k). These properties of the P and N arms are generally arbitrary functions of temperature. Because these parameters change slightly in the working temperature range for the commercial T.E.M., we assume that the three properties are independent of
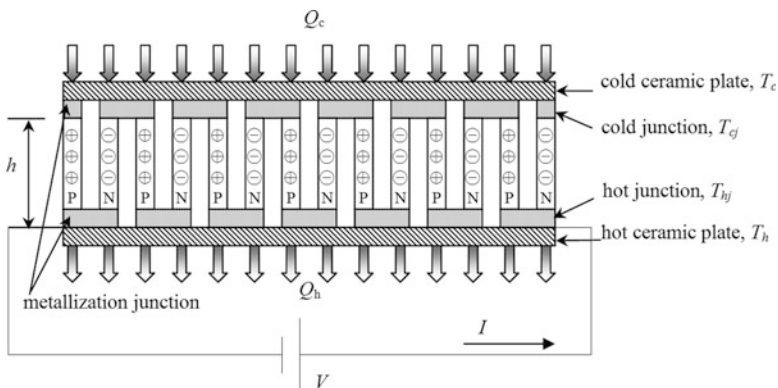
Fig. 1 Scheme of T.E.M. construction

temperature in this chapter. The three parameters of T.E.M. couple can be given as follows:

$$K = 2k \cdot \frac{S}{h} \tag{1}$$

$$R = 2\rho \frac{h}{S} \tag{2}$$

$$A = 2\alpha \tag{3}$$

where K, R, and A are the thermal conductance, electrical resistance, and Seebeck coefficient of the T.E.M. couple, respectively, and S and h are the cross-sectional area and the length of P- or N-type arms. The heat balance cooled or expelled by each TEC couple leads to the following equations:

$$Q_c = (T_c - T_{cj})K_c \tag{4}$$

$$Q_c = A \cdot I \cdot T_{cj} - \left[K(T_{hj} - T_{cj}) + \frac{1}{2}I^2 R \right] \tag{5}$$

$$Q_h = A \cdot I \cdot T_{hj} - \left[K(T_{hj} - T_{cj}) - \frac{1}{2}I^2 R \right] \tag{6}$$

$$Q_h = (T_{hj} - T_h)K_h \tag{7}$$

where Q_c represents the heat flow through the cold plate, Q_h is the heat flow through the hot plate, K_c is the thermal conductance of the cold ceramic plate, K_h is the thermal conductance of the hot ceramic plate, and I is the electric current that flows through the T.E.M. element. We assume that the thickness of the cold or hot ceramic plate is very thin, so the thermal conductance of the cold or hot ceramic plate can be limited to $K_c \rightarrow \infty$, $K_h \rightarrow \infty$. After being eliminated, the T_{cj} and T_{hj} from Eqs. 4, 5, 6, and 7 and the heat balance equations of the T.E.M. couple can be calculated by the following equations:

$$Q_c = A \cdot I \cdot T_c - \left[K(T_h - T_c) + \frac{1}{2}I^2 R \right] \tag{8}$$

$$Q_h = A \cdot I \cdot T_h - \left[K(T_h - T_c) - \frac{1}{2}I^2 R \right] \tag{9}$$

The voltage of the T.E.M. can be given as

$$V = I \cdot R + A \cdot (T_h - T_c) \tag{10}$$

The electric energy supplied into the T.E.M. can be calculated as

$$P = Q_h - Q_c = I^2 \cdot R + A \cdot I \cdot (T_h - T_c) \qquad (11)$$

3 Introduction of the Intake Air Cooling Device

The intake air cooling device for engine induction system by using the T.E.M. is illustrated in Fig. 2. The device includes the T.E.M. and heat exchange system, which consists of water block, hoses, water pump, radiator, and cooling fans. The coolant, which is a mixture of water and an agent that prevents freezing, runs through the heat exchange system and transfers the heat from the water block to the radiator. One side of the T.E.M. is fixed on the surface of intake air box and the other is stuck on the water block. When we supply the electric power to the device, the T.E.M., water pump, and cooling fans begin to be operated. The surface of the T.E.M. fixed to the induction box will absorb the heat of the intake air in the induction system to decrease the temperature of the inlet air. According to the physical property of thermal expansion and contraction, the cooled air can increase the oxygen index for
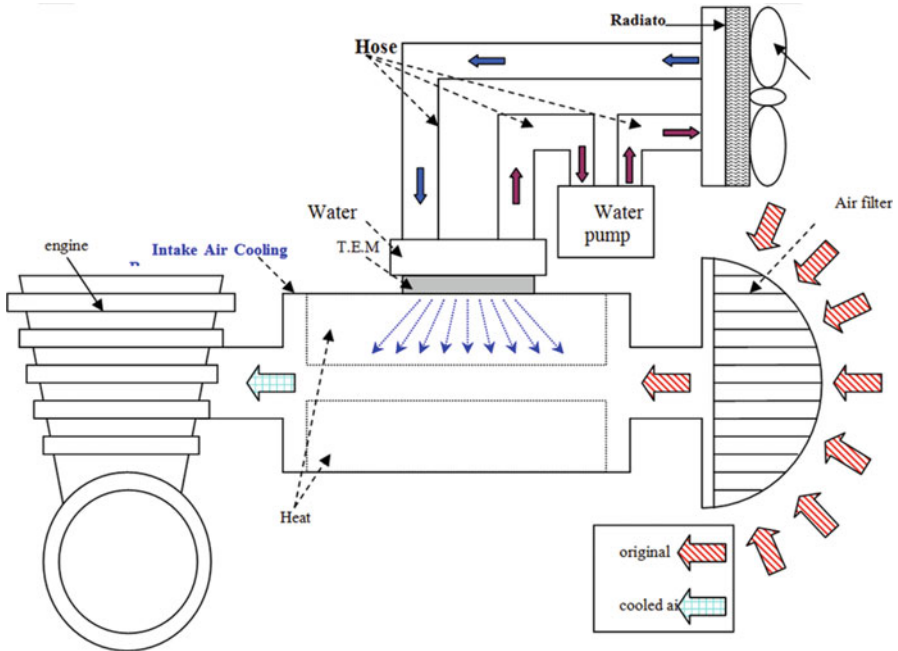
Fig. 2 The Simplified intake air cooling device

combustion of the engine and boost the engine power. The other surface of the TEC chip will expel the heat flow to the heat exchange system for keeping the efficiency of the TEC chip. The coolant absorbs the heat from the water block and flows to the water pump to be pressed into the radiator. The cooling fans dissipate the heat from the radiator to the surrounding and result in the temperature decrease of the coolant. The cooled coolant will return to the water block and restart to absorb the heat flow of T.E.M. The above procedure will execute with repetition to keep on absorbing the heat of the inlet air to increase the volumetric efficiency of the engine.

4 Experimental Method and Measurement Details

The intake air cooling device is shown in Fig. 3, and the intake air cooling box is shown in Fig. 4. In Fig. 4, the water blocks are stuck on the intake air cooling box, and T.E.M. is between the water block and the induction box. In this box, we used the DRIFT-0.6 type T.E.M. manufactured by Kryotherm Co., and the detail properties of the chip are shown in Table 1. The radiator, water pump, and cooling fans are shown in Figs. 5 and 6, in which the cooling fans are connected on the water pump for using the same power of the motor. The intake air cooling device is connected to the engine dynamometer shown in Fig. 7, which is a 2-l four-cylinder petrol power plant.

5 Results and Discussion

The inlet air temperature after cooling by the intake air cooling device is shown in Fig. 8, where the x-axis is the measuring time of the intake air and the y-axis is the intake air temperature. From the plot, it is obvious that the temperature of the intake air
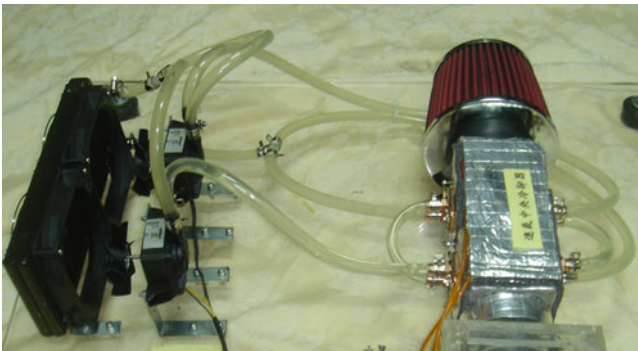
Fig. 3 The intake air cooling device
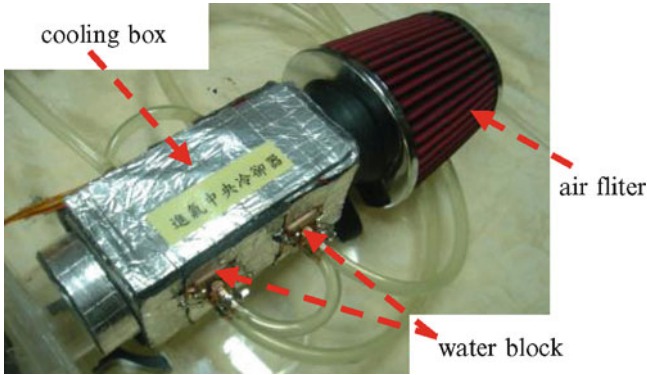
Fig. 4 The intake air cooling box

Table 1 Properties of the TEC chips

Type	Maximum voltage (V)	Short-circuit current (A)	Q_{max} (W) $T_h = 27°C$	ΔT_{max} (°C)	Dimensions (mm) Length	Width	Thickness
DRIFT-0.6	24.6	15.1	229.3	68	40	40	3.1

Fig. 5 The radiator and water pump

decreased from 28.6 to 24.7 °C for 14 % after 500 s. The result of engine power over experimental time before or after using the T.E.M. device is shown in Fig. 9. The power of the engine which intake air cooled by the T.E.M. device was larger than that which
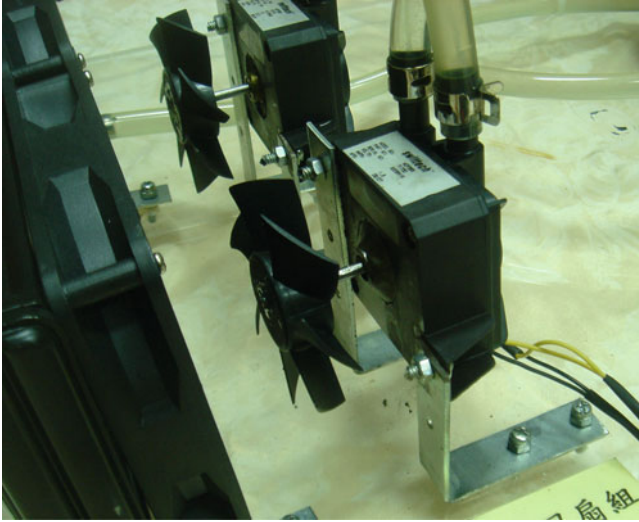
Fig. 6 The water pump and cooling fans

Fig. 7 The engine dynamometer

were not be cooled by the T.E.M., about 9–60 % in 500 s. In Fig. 9, we can find that the lower engine speed presents better performance than high engine speed because it needs more air into the induction system at the high engine speed for the combustion.
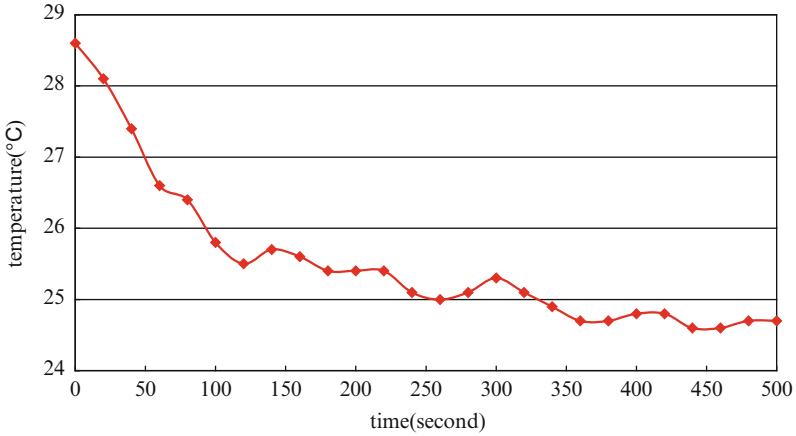
Fig. 8 The relation of intake air temperature and operation time
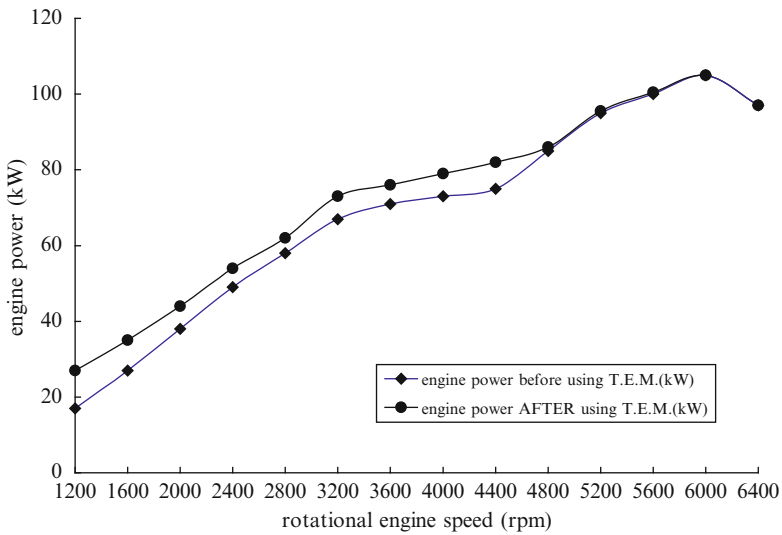
Fig. 9 The result of the engine dynamometer test

6   Summary

In this chapter, we invent a new method to absorb the heat from the induction system to increase the volumetric efficiency by using the intake air cooling device. The device effectively decreases the temperature of the intake air to the engine and increases the engine power with the T.E.M. and the closed water cooling system according to the experiments which we modeled in this chapter. By applying the T.E.M. in the induction system, we can improve the combustion efficiency of the internal combustion engine and increase the output of the engine.

References

1. Chiang J-S, Chuang S-H, Soon KK, Lee H-J (2004) Fuel efficiency test of internal combustion engine with gas-cushioned piston. Zhongguo Hangkong Taikong Xuehui Huikan/Trans Aeronaut Astronaut Soc Repub China 36(3):233–240
2. Ma J, Zhu GG, Schock H (2011) Adaptive control of a pneumatic valve actuator for an internal combustion engine. IEEE Trans Control Syst Technol 19(4):730–743
3. Merala R (1988) Modeling and simulation of a supercharger. J Dyn Syst Meas Control Trans ASME 110(3):316–323
4. Müller M (2009) Volumetric efficiency and pumping torque estimation and compressor recirculation control of turbocharged engines. SAE Int J Eng 2(1):344–356
5. Shibata Y, Nissan Motor Co Ltd, Hosaka S, Fujitani K, Himeno R (1990) Numerical analysis method for optimizing intercooler design in the vehicle development process, vol 900080, SAE technical paper series. SAE, Warrendale, 13 p
6. Parker PH (2000) Variable valve timing mechanism for the Rover K16 engine Part 2: application to the engine and the performance obtained. Proc Inst Mech Eng Part D J Automob Eng 214 (2):207–216
7. Yamada Y, Machida K, Yamazaki T (2009) Development of continuous variable valve event and lift control system for SI engine. SAE Int J Eng 1(1):949–959
8. Chein R, Huang G (2004) Thermoelectric cooler application in electric cooling. Appl Therm Eng 24(14–15):2207–2217

Effects of Deposition Temperature and Hydrogen Plasma on the Properties of the Radio-Frequency Magnetron Sputtering Deposition of ZnO-Al$_2$O$_3$ Films

Fang-Hsing Wang, Chia-Cheng Huang, Chien-Chen Diao, Chia-Ching Wu, and Cheng-Fu Yang

Abstract A 98 mol % ZnO–1 mol % Al$_2$O$_3$ (AZO) compound was sintered at 1,350 °C as a target and deposited on glass substrates using a radio-frequency magnetron (r.f.) sputtering system, under the 30 sccm 98 % Ar + 2 % H$_2$ ambient. The effect of deposition temperature (25–300 °C) on carrier concentration, carrier mobility, resistivity, and optical transmission spectrum of the AZO films was studied. The Burstein-Moss shift was observed and used to prove that defects in the AZO films decreased with increasing deposition temperature. The effect of hydrogen (H$_2$) plasma on carrier concentration, carrier mobility, resistivity, and optical transmission spectrum of the different temperature-deposited AZO films was also studied. The value variations in the optical band gap (E_g value) of the AZO films were evaluated from the plots of $I = I_0 e^{-\alpha t}$, where $\alpha^2 = h\nu - E_\mathrm{g}$. The measured E_g value of the as-deposited AZO films increased with increasing deposition temperature and had no apparent trend difference as the H$_2$ plasma was used.

Keywords AZO films • Deposition temperature • Hydrogen (H$_2$) plasma

F.-H. Wang • C.-C. Huang
Department of Electrical Engineering, National Chung Hsing University,
Taichung, Taiwan, R.O.C.

C.-C. Diao • C.-C. Wu
Department of Electronic Engineering, Kao Yuan University, Kaohsiung, Taiwan, R.O.C.

C.-F. Yang (✉)
Department of Chemical and Materials Engineering, National University of Kaohsiung,
Kaohsiung, Taiwan, R.O.C.
e-mail: cfyang@nuk.edu.tw

1 Introduction

TCO films are also the key components in flat panel displays and thin-film solar cells [1]. In the past, the indium tin oxide (ITO) was the most extensively used material because the ITO films yielded excellent electrical properties and optical transmittance characteristics in the visible region. The ever-increasing demand was caused by the large growth of flat panel displays and solar cell market, causing the price of ITO to rise quickly over the past years. This has caused the increased efforts to improve material properties and production processes for other TCO materials. Therefore, the Al-doped ZnO (AZO) films have been extensively studied in recent years because they combine attractive properties with high visible transparency and electrical conductivity [2]. Hydrogen (H_2) plays a very important role in many semiconductors and is an indispensable ingredient in integrated circuit fabrication, because it passivates the defects at the Si/SiO_2 interfaces [3]. Besides, H_2 also forms a strong bond with oxygen (O_2) and provides a powerful driving force for its incorporation in the crystallization of ZnO [4]. This incorporation is accompanied by remarkably large relaxations of the surrounding atoms. H_2 never forms an electrically neutral impurity inside a semiconductor or insulator [5]. It can either invariably give up its electron to become a donor with positive charge or it can acquire an additional electron to become an acceptor with negative charge. For that, H_2 is thought as an amphoteric impurity, it is H^+ in p-type (a donor) and H^- (an acceptor) in n-type to limit the conductivity [6], and the amphoteric behavior prevents H_2 from acting as a dopant. However, the experimental calculation results show that H_2 is exclusively positive charge state in ZnO. Recently, the deposition of AZO films in Argon (Ar) + H_2 ambient and at higher temperature significantly improves their electrical properties [7]. In this chapter, radio-frequency magnetron (r.f.) sputter 98 % Ar + 2 % H_2 ambient was used as the deposition atmosphere in order to study the effect of deposition temperature on the physical and electrical characteristics of the AZO films. The different temperature-deposited AZO films also underwent the post-H_2-plasma treatment. The results would show that the improved characteristics of the AZO films could be obtained by combining with the higher deposition temperature and the H_2-plasma passivation. Those results were compared by observing the surface morphology, mobility, carrier concentration, resistivity, and optical transmittance spectrum. Optical transmittance parameters were also used to investigate the effects of deposition temperature and the H_2-plasma treatment on the optical band gap (E_g) of the AZO films.

2 Experiment

The AZO powder (ZnO = 98.0 mol %, 99.999 % purity; and Al_2O_3 = 1 mol %, 99.999 % purity) was calcined at 1,100 °C and sintered at 1,350 °C to prepare the ceramic target. The AZO films were deposited on $25 \times 25 \times 2$ mm Corning 1,737

glass substrates by using the SYSKEY 13.56 MHz r.f. sputtering system. The base chamber pressure was less than 1×10^{-6} Torr, then argon (Ar) and H_2 were introduced into the chamber, and the pressure was controlled at 5×10^{-2} Torr, under the 30 sccm 98 % Ar + 2 % H_2 ambient. The r.f. power was 100 W and the deposition temperature (room temperature (RT ~ 300 °C)) was controlled by a thermocouple gauge, and the deposited samples were abbreviated as the as-deposited AZO films. After deposition, the plasma-enhanced chemical vapor deposition (PECVD) H_2 was treated on the as-deposited AZO films at 200 °C (the H_2-plasma-treated AZO films). The working pressure was maintained at 1 Torr under the 300 sccm H_2 flow rate, and the used power was 10 W. The thickness of the as-deposited AZO films was controlled by the deposition time, measured using a nano-view SEMF-10 ellipsometer, and confirmed by a field emission scanning electron microscope (FESEM). The carrier concentration and Hall mobility were obtained from Hall-effect measurement by the Van der Pauw method (Ecopia, HMS-3000), and the electrical resistivity was measured using a four-point probe. The optical transmittance spectra were recorded using a Hitachi U-3300 UV-Vis spectrophotometer in the 300–800 nm wavelength range.

3   Results and Discussion

The XRD patterns of the as-deposited and H_2-plasma-treated AZO thin films were investigated in Fig. 1. Only the (002) diffraction peak was observed in the as-deposited and H_2-plasma-treated AZO films. The 2θ value of the (002) diffraction peak for the as-deposited AZO films shifted upward (from 34.23° to 34.48°) as the
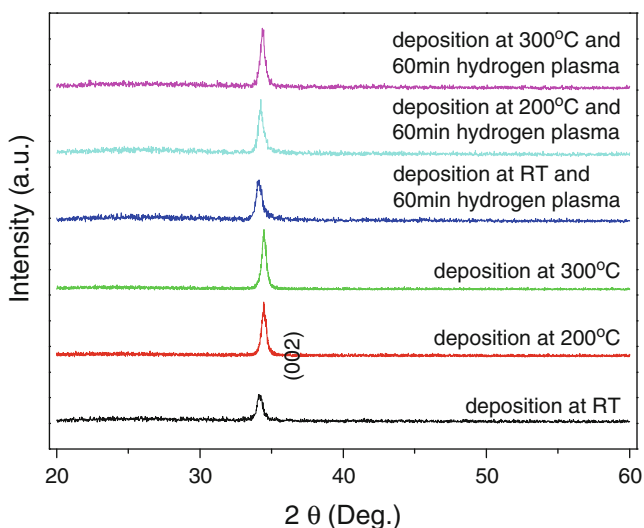
Fig. 1 X-ray diffraction patterns of the as-deposited and H_2-plasma-treated AZO films
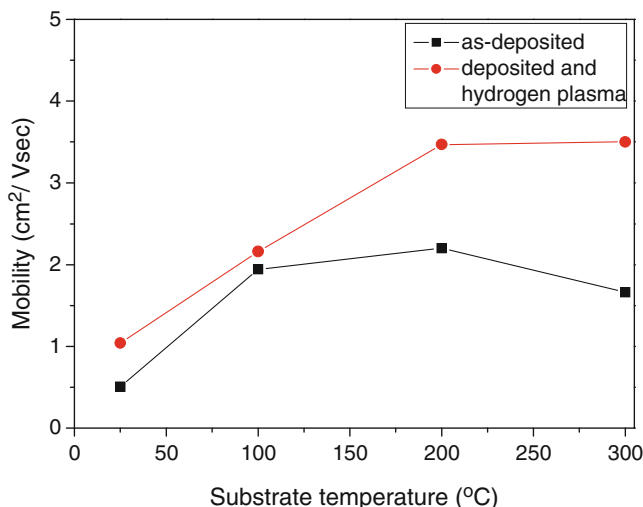
Fig. 2 Mobility of the as-deposited and H$_2$-plasma-treated AZO films

deposition temperature rose from RT to 300 °C. The ionic radii of Al^{+3} (0.053 nm) are smaller than that of Zn^{+2} (0.074 nm), suggesting that the Al^{+3} ions will dope onto the ZnO particles and substitute at Zn^{+2} sites, then the lattice constant of the AZO films decreases. The full width at half maximum (FWHM) values of the (002) peak were 0.54°, 0.45°, 0.41°, and 0.38° for RT-, 100, 200, and 300 °C-deposited AZO films, respectively. Those results indicate that the degree of crystallization for the AZO films increases with increasing deposition temperature. As the H$_2$ plasma is used to treat on the surfaces of the AZO films, the 2θ values have no apparent shift, but the FWHM values (0.59–0.44°) have obvious increase as compared with those of the as-deposited AZO films. The mobility, carrier concentration, and resistivity of the as-deposited and H$_2$-plasma-treated AZO films as a function of deposition temperature are shown in Figs. 2, 3, and 4. As Figs. 2 and 3 show, as the deposition temperature is equal and lower than 200 °C, the as-deposited AZO films exhibited a lower mobility and a lower carrier concentration in comparison with those of the H$_2$-plasma-treated AZO films. Figure 3 shows that for the as-deposited AZO thin films the carrier concentration increased with increasing deposition temperature and for the H$_2$-plasma-treated AZO thin films the variations in the carrier concentration were not obvious.

Many mechanisms, such as acoustical, impurity, and grain boundary scattering, will affect the mobility of the AZO films, and the grain boundary scattering is the most important mechanism. Varieties of structural defects, such as vacancies, interstitials, and impurities, exist as the AZO films are prepared by the sputtering process. All the defects are associated with dangling bonds, which act as traps for charge carries to reduce the drift mobility and lifetime of the carries. When the r.f. sputtering is used to deposit the AZO films on the glass substrates, many defects exist and inhibit electron movement. Three factors are believed to cause variable
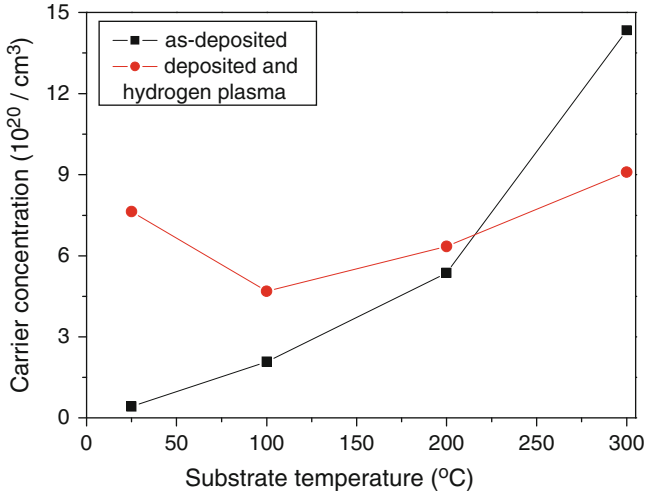
Fig. 3 Carrier concentration of the as-deposited and H_2-plasma-treated AZO films
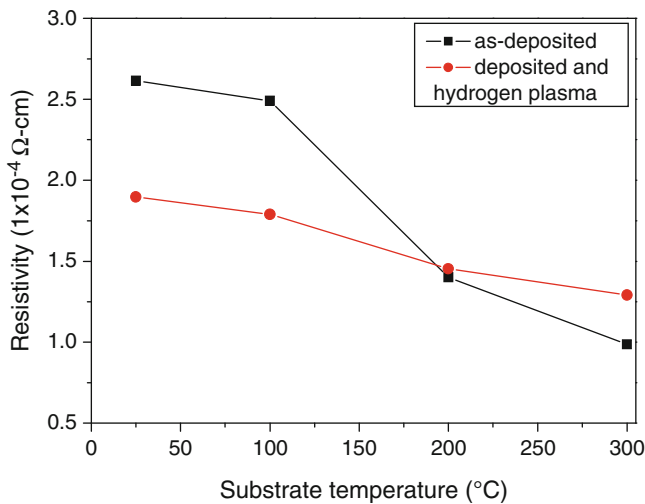
Fig. 4 Resistivity of the as-deposited and H_2-plasma-treated AZO films

mobility with increasing deposition temperature in the AZO films. First, the decrease of the O_2 vacancies may lead to a decrease in scattering centers and a resultant increase in mobility. The higher deposition temperature also provides more energy for deposition atoms to enhance movement of the AZO particles, which can smooth the surface and decrease the defects and O_2 vacancies in the AZO films. Second, as the deposition temperature increases, the density of the AZO films

increases and the barriers inhibiting electron transportation decrease [8]. Third, as the deposition temperature is too high, the AZO particles have the higher activation energy and the defects increase.

The variation in carrier concentration may be due to desorption of negatively charged O_2 species, which increases O_2 vacancies or interstitial zinc atoms, and the formation of shallow donors generated by incorporated H_2 [9, 10]. As a result, the H_2 ions forming during the plasma process can readily diffuse into the AZO films and terminate the dangling bonds associated with the structural defects. The deep-level defects can be concluded from the considerable performance of mobility and hence lifetime of electrons in the AZO films. Furthermore, H_2 can remove the desorption of O_2 species under air ambient from the grain boundary and surface via the formation of a strong bond between H_2 and O_2 to passivate the boundary and surface. A passivation will prevent the films from the oxidation and moisture to make the duration longer.

An improved resistivity of post-H_2-plasma treatment can be observed in the AZO films even at deposition temperatures of RT and 100 °C. The resistivity of the TCO films can be described in the following Eq. (1) [11]:

$$\rho = \frac{1}{n_e e \mu} \tag{1}$$

where n_e is the carrier concentration and is related to the O vacancies and Al-doping concentration and μ is the mobility and is related to the grain boundaries and impurity scattering. The electrical conductivity of the AZO films may be explained by the E_g values and the defects formed during the deposition process. The higher conductivity of the TCO films results mainly from deviations in stoichiometric compositions due to dopants or substitution atoms. Many methods can be used to improve the conductivity of the ZnO-based TCO films. Cai et al. [12] suggested that the H_2 in the plasma-treated ZnO film not only passivated most of the defects and acceptors but also introduced shallow donor states such as the VO-H complex and the interstitial H_2. Electrons generating from O_2 vacancies and Zn interstitial atoms resulting from the dopant primarily determine the conduction properties of the AZO films. Therefore, the electrical conductivity of the AZO films will be higher than that of the pure ZnO films due to the contribution of Al ions on the substitutive sites of Zn ions and Al interstitial atoms. The resistivity of the AZO films is shown in Fig. 4 as a function of deposition temperature for the as-deposited and the H_2-plasma-treated AZO films. Those results suggest that the decreased in resistivity is due to the increase of the carrier concentration as the higher deposition temperature or H_2 plasma are used. In this study, the 300 °C-as-deposited AZO films had the minimum resistivity of 0.98×10^{-4} Ω-cm. Figure 5a shows the UV-VIS spectrum of the as-deposited AZO films in the wavelength range of 300–800 nm. The optical band gap (E_g) value of the AZO films can be determined using the extrapolation
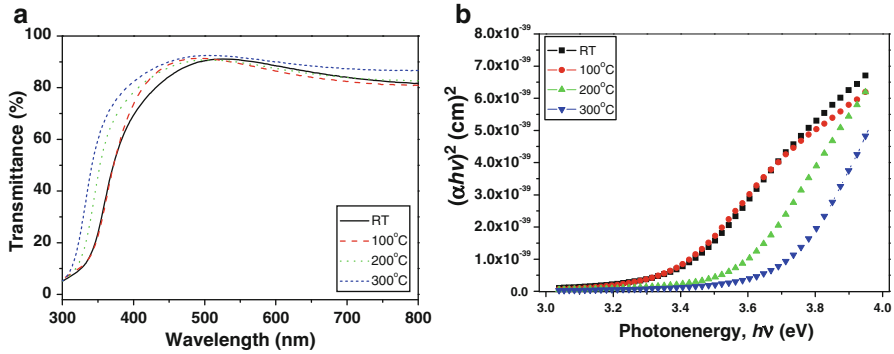
Fig. 5 (**a**) Transmittance and (**b**) $(\alpha h\nu)^2$ vs. $h\nu - E_g$ plots of the as-deposited AZO films

method from the absorption edge for direct interband transition, which can be calculated using the relation in Eq. (2) [13]:

$$(\alpha h\nu)^2 = c\left(h\nu - E_g\right) \tag{2}$$

where h is Plank's constant and ν is the frequency of the incident photon. The optical absorption coefficient, α, is defined as

$$I = I_0 e^{-\alpha t} \tag{3}$$

where I and I_0 are the intensities of the transmitted light and incident light and t is the thickness of the AZO films. The transmittance ratio is defined as I/I_0; therefore, α can be obtained from Eq. (3). The linear dependence of $(\alpha h\nu)^2$ to $h\nu$ indicates that the AZO films are direct transition-type semiconductors. α is calculated with Eq. (3) using normal incident transmission data of the as-deposited AZO films. Figure 5b illustrates the $(\alpha h\nu)^2$ versus $h\nu$ (energy) in accordance with Eq. (2), the E_g value can be found at $(\alpha h\nu)^2$ is zero, and the calculated E_g values of the as-deposited AZO films are shown in Fig. 6. The E_g value of the as-deposited AZO films increased from 3.33 to 3.62 eV as deposition temperature increased from RT to 300 °C.

The UV-VIS spectra of the H_2-plasma-treated AZO films are shown in Fig. 7 as a function of deposition temperature. As Fig. 7 shows, the transparency of the H_2-plasma-treated AZO films also increased as the deposition temperature rose. Figure 6 also shows that the calculated E_g value of the H_2-plasma-treated AZO films decreased from 3.42 to 3.48 eV with increasing deposition temperature. As those results suggest, the H_2 plasma on the AZO films is another reason to cause an increase in the E_g value of the AZO films. As the results in Figs. 3 and 6 are compared, the variation of the E_g value had the similar trend with that of carrier concentration that proves the Burstein-Moss shift theory.
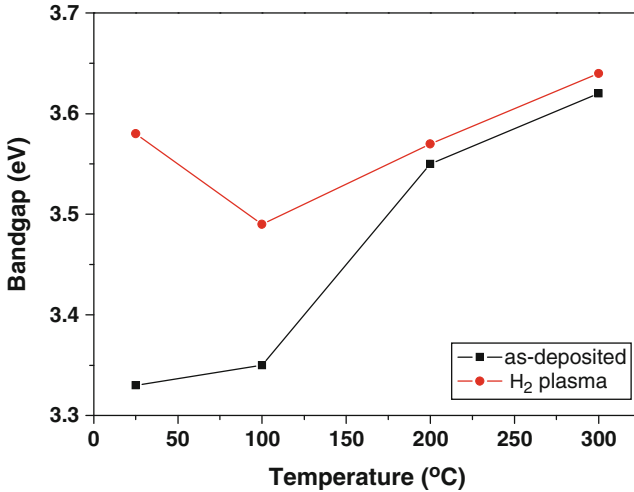
Fig. 6 Optical band gap of the as-deposited and H_2-plasma-treated AZO films
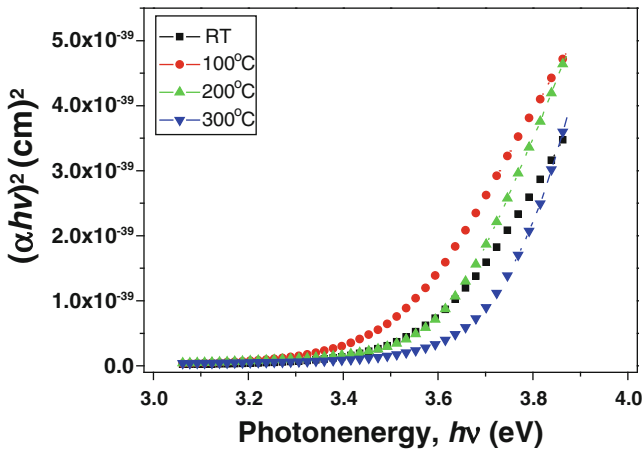
Fig. 7 $(\alpha h\nu)^2$ vs. $h\nu - E_g$ plots of the H_2-plasma-treated AZO films

4 Conclusions

As the deposition temperature of the as-deposited AZO films increased, the mobility first increased with increasing deposition temperature and reached a maximum of 2.2 cm^2/V s at deposition temperature of 200 °C, the carrier concentration reached a maximum of 14.3×10^{20}/cm^3 at deposition temperature of 300 °C, and the resistivity reached a maximum value of 0.986×10^{-4} Ω-cm at deposition temperature of 300 °C, respectively. As the deposition temperature of the

H_2-plasma-treated AZO films increased from RT to 300 °C, the mobility reached a maximum of 3.5 cm^2/V s at deposition temperature of 300 °C, the carrier concentration reached a maximum of 9.09×10^{20}/cm^3 at deposition temperature of 300 °C, and the resistivity reached a maximum value of 1.29×10^{-4} Ω-cm at deposition temperature of 300 °C, respectively. As the deposition temperature increased from RT to 300 °C, the calculated E_g values increased from 3.33 to 3.62 eV for as-deposited AZO films and from 3.42 to 3.48 eV for H_2-plasma-treated AZO films.

References

1. Gupta A, Compaan AD (2004) Appl Phys Lett 85:684–686
2. Zhang XY, Huang ZZW, Chan HL, Kwok KW, Choy CL (1999) J Eur Ceram Soc 19:985–988
3. Forbess MJ, Seraji S, Wu Y, Nguyen CP, Cao GZ (2000) Appl Phys Lett 76:2934–2936
4. Desu SB, Li TK (1995) Mater Sci Eng B 34:L4–L8
5. Wei YF, Kao CH, Yang CF, Huang HH, Huang CJ (2007) Mater Lett 61:4643–4646
6. Chevallier J, Theys B, Lusson A, Grattepain C (1998) Phys Rev B 58:7966–7969
7. Sun Y, Weifeng L, He Z, Liu S, Zou ZY, Guotong D (2006) Vacuum 80:981–985
8. Strzhemechny YM, Mosbacker HL, Look DC, Reynolds DC, Litton CW, Garces NY, Giles NC, Halliburton LE, Niki S, Brillson LJ (2004) Appl Phys Lett 84:2545–2547
9. Igasaki Y, Saito H (1991) J Appl Phys 69:2190–2195
10. Ohashi N, Wang YG, Ishigaki T, Wada Y, Taguchi H, Sakaguchi I, Ohgaki T, Adachi Y, Haneda H (2007) J Cryst Growth 306:316–320
11. Minami T, Sato H, Nanto H, Takata S (1986) Jpn J Appl Phys 25:L776–L779
12. Cai PF, You JB, Zhang XW, Dong JJ, Yang XL, Yin ZG, Chen NF (2009) J Appl Phys 105:083713
13. Kim KH, Wibowo RA, Munir B (2006) Mater Lett 60:1931–1935

The Influences of Post-annealing Temperature on the Properties of $Sr_{0.6}Ba_{0.4}Nb_2O_6$ Thin Films

Chin-Guo Kuo, Chien-Chen Diao, Chien-Hung Chen, Wen-Cheng Tzou, and Cheng-Fu Yang

Abstract   In this study, $Sr_{0.6}Ba_{0.4}Nb_2O_6$ (SBN) thin films were prepared by radio-frequency (RF) magnetron sputtering. After finding the optimal deposition parameters, the deposited SBN thin films were annealed in a conventional furnace. In comparisons of XRD patterns, the annealing process had improved the crystallization and also had large effects on the crystalline orientation of SBN thin films. As the annealing temperature was risen from 600 to 700 °C, the diffraction intensities of (410) and (001) peaks really increased. Annealed at 800 °C, SBN thin films showed a highly c-axis crystalline orientation in (001) peak. Effects of annealing temperature on the electrical characteristics were

C.-G. Kuo
Department of Industrial Education, National Taiwan Normal University,
Taipei, Taiwan, R.O.C.

C.-C. Diao
Department of Electronic Engineering, Kao Yuan University, Kaohsiung,
Taiwan, R.O.C.

C.-H. Chen
Department of Avionic Engineering, Chinese Air Force Academy, Kaohsiung,
Taiwan, R.O.C.

W.-C. Tzou
Department of Electro-Optical Engineering, Southern Taiwan University, Tainan,
Taiwan, R.O.C.

C.-F. Yang (✉)
Department of Chemical and Materials Engineering, National University of Kaohsiung,
Kaohsiung, Taiwan, R.O.C.
e-mail: cfyang@nuk.edu.tw

recorded and analyzed, including the polarization-applied electric field curves, the capacitance-voltage curves, and the leakage current density-electric field curves. As the annealing process was used to treat on the as-deposited SBN thin films, the Pr, Ps, and Ec values were really improved. The theorems to cause the drastic variations in the capacitances, the memory windows, and the flat-band shift voltages of SBN thin films were also discussed.

Keywords Annealing process • Leakage current density • Flat-band shift voltage

1   Introduction

The ferroelectric oxide materials, such as $SrBi_2Ta_2O_9$, $(Ba,Sr)TiO_3$, $(Ba,Zr)TiO_3$, and $PbZrTiO_3$, exhibit the high dielectric constants and are widely developed as ferroelectric thin films for the various possible applications. SBN ceramic is one of the most important ferroelectric materials for various applications due to its significant spontaneous polarization occurring along c- axis. SBN-based ceramics are relatively stable, less poison, and environmental friendly as compared with other lead-base ferroelectric materials. Ferroelectric $Sr_xBa_{1-x}Nb_2O_6$ ceramics ($0.2 \leq x \leq 0.8$) are attractive materials and considered very useful in diverse device applications, including memory devices [1] and saw devices [2]. Rare-earth alkali ions can be doped into $Sr_xBa_{1-x}Nb_2O_6$ crystals to improve the c-axis crystalline orientation of SBN thin films and then to expand their applications in the electro-optic and photorefractive coefficients. Eu^{+3} was used as dopant in $Sr_{0.61}Ba_{0.39}Nb_2O_6$ [3], and potassium was used as dopant in $Sr_{0.6}Ba_{0.4}Nb_2O_6$ (SBN) thin film [4]. But so far, only few studies are focused on the $Sr_xBa_{1-x}Nb_2O_6$-based thin films for possible applications in memory devices. Due to the anisotropic properties, it is desirable to obtain the highly oriented SBN thin films. For example, the c-axis-oriented SBN thin films were grown on silicon substrate by using sol-gel method [5] or grown on (100) MgO substrate [6]. However, highly c-axis-oriented $Sr_xBa_{1-x}Nb_2O_6$-based thin films prepared directly on silicon substrates using the post-annealing process are rarely been reported [7]. For SBN thin films, the effects of deposition parameters on the characteristics of SBN thin films were investigated. Post-annealing process in air or in oxygen atmosphere has improved the physical and electrical characteristics of ferroelectric thin film materials [8–10]. In this study, the results would show that the post-annealing process had improved the (001) orientation and the grain growth of SBN thin films. Our results significantly found that the capacitances, the memory windows, and the flat-band shift voltages (ΔV_{FB}) had drastic variations and the capacitance values increased in the inversion region. The theorems for annealing-induced changes in SBN-SiO$_2$ interfaces to cause those results were also investigated.

2   Experiment

SrCO$_3$, BaCO$_3$, and Nb$_2$O$_5$ powders were mixed and ball milled for 4 h in deionized water. After being dried and ground, SBN powder was calcined at 1,100 °C for 2 h, then ground again, and mixed with polyvinyl alcohol as a binder. SBN powder was then uniaxially pressed into pellets of 5 mm thickness and 52 mm diameter. After debindering, the pressed target was sintered at 1,340 °C in air for 2 h. SBN thin films were deposited onto Pt/Ti/Si and SiO$_2$/Si/Al substrates by RF magnetron sputtering method to form the metal-ferroelectric-insulator-semiconductor (MFIS) and metal-ferroelectric-metal (MFM) structures. The optimal substrate temperature and RF power for deposition of SBN thin films were 500 °C and 120 W, respectively. The oxygen concentration was changed from 0 to 60 % (flow rate, O$_2$/(O$_2$+Ar) in sccm), and the chamber pressure was changed between 5×10^{-3} and 5×10^{-2} Torr to find the optimal deposition parameters. After deposition, SBN thin films were annealed by changing the temperature from 600 to 800 °C for 30 min in air. Thickness and morphology of SBN thin films were characterized by field emission scanning electron microscopy (FESEM), and their crystalline phases and the preferred orientations were identified by X-ray diffraction (XRD) patterns. To finish the MFM and MFIS structures, an array of circular top contacts with a diameter of 1 mm was formed by deposition Al thin films. An HP 4194 impedance analyzer was used to measure the leakage current density-electric field (J-E, MFM structure) characteristics, and an HP4156B semiconductor parameter analyzer was used to measure the capacitance-voltage (C-V, MFIS structure) curves with a DC bias ranging from −20 to +20 V. The ferroelectric polarization-electric field (P-E, MFM structure) hysteresis loops were recorded at room temperature by a standard Sawyer-Tower equipment of RT 1000 at 50 kHz.

3   Results and Discussion

Figure 1 shows the effects of oxygen concentration (chamber pressure = 10 m Torr) on the deposition rate of SBN thin films. As the oxygen concentration changed from 0 (pure argon), 20, 40, to 60 %, the deposition rate of SBN thin films linearly decreased from 14.3, 10.2, 8.2, to 6.8 nm/min. The decrease in the deposition rate is caused by that, and as the concentration of oxygen increases, less argon can be used to remove SBN molecules from the surface of SBN ceramic target, and then the deposition rate decreases. The roughness of SBN thin films was 9.58, 5.96, 3.22, and 3.18 nm as oxygen concentration was 0, 20, 40, and 60 %, respectively. For that, the 40 % oxygen concentration is used because SBN thin films have the smooth surface and acceptable deposition rate.

Figure 1 also shows the variations in the deposition rates of SBN thin films as a function of chamber pressure (oxygen concentration = 40 %). The deposition rate increased from 5.13 to 8.20 nm/min as the chamber pressure increased from 5 to
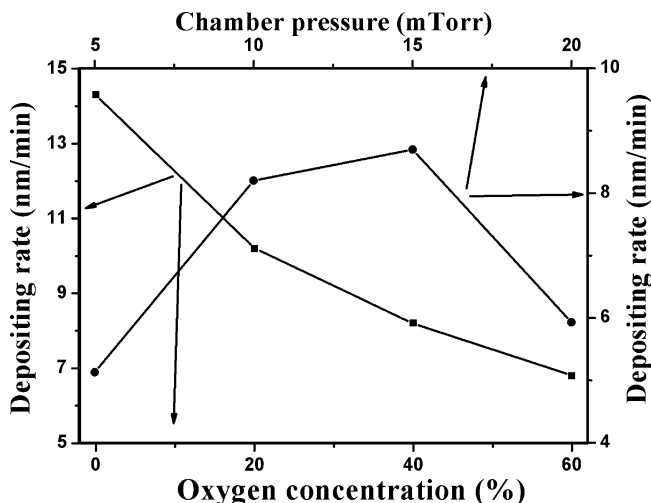
Fig. 1 Deposition rate of SBN thin films under different deposition parameters

10 m Torr. After reaching a maximum value of 8.70 nm/min at 15 m Torr, the deposition rate decreased to 5.93 nm/min as chamber pressure was further increased to 20 m Torr. Too much argon/oxygen mixing atmosphere has inhibited the deposition process of SBN thin films, because higher chamber pressure increases the colliding chances between the mixing atmosphere and SBN molecules, and the deposition rate decreases. However, the roughness of SBN thin films deposited under 5, 10, 15, and 20 m Torr was 3.13, 3.22, 4.12, and 3.15 nm. The 10 m Torr is used as the chamber pressure because the roughness of SBN thin film deposited under this condition is better than that of deposited under 15 m Torr.

The thicknesses of SBN thin films deposited under optimal parameters (as-deposited) and annealed under different temperatures were calculated by FESEM. The cross-section image of as-deposited SBN thin film is shown in Fig. 2a, the thickness was about 246 nm, and the thicknesses of annealed SBN thin films were also about 246 nm. For the as-deposited SBN thin films, the morphology revealed a smooth surface and the grain growth was not observed (not shown here). Annealed at 600 °C, as Fig. 2b shows, the grain size distributions of SBN thin films were 15–70 nm and the average grain size was approximate 38 nm. Annealed at 700 and 800 °C, as Fig. 2c and d show, the grain size distributions were 30–210 and 220–600 nm. Those results prove that the annealing process has improved the grain growth of SBN thin films. Figure 2c also shows that the 700 °C-annealed SBN thin film revealed a densified morphology. Figure 2d suggests that annealing SBN thin films at 800 °C is not necessary because the destruction in SBN thin films is really observable. The destruction may be caused by the melt of SBN thin films or by SBN thin films reacting with the substrate materials of SiO_2/Si or Pt/Ti/Si.
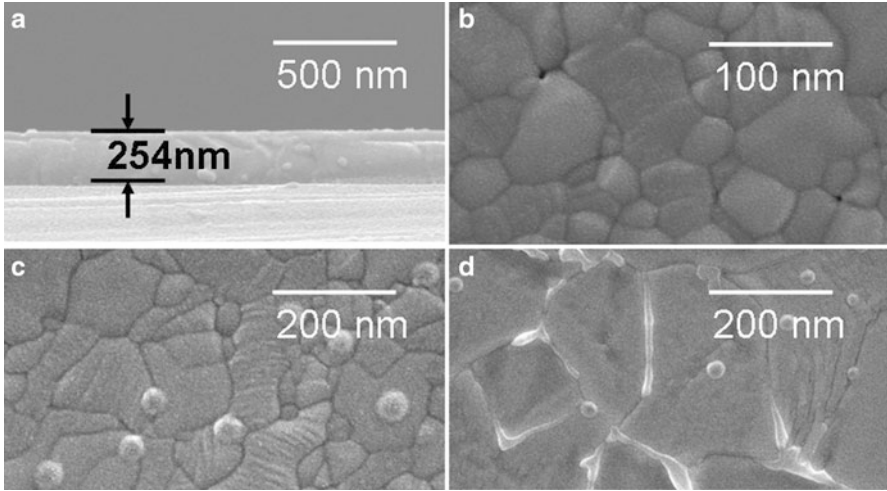
Fig. 2 (**a**) Cross section and surface observations of SBN thin films under different annealing temperatures: (**b**) 600 °C, (**c**) 700 °C, and (**d**) 800 °C
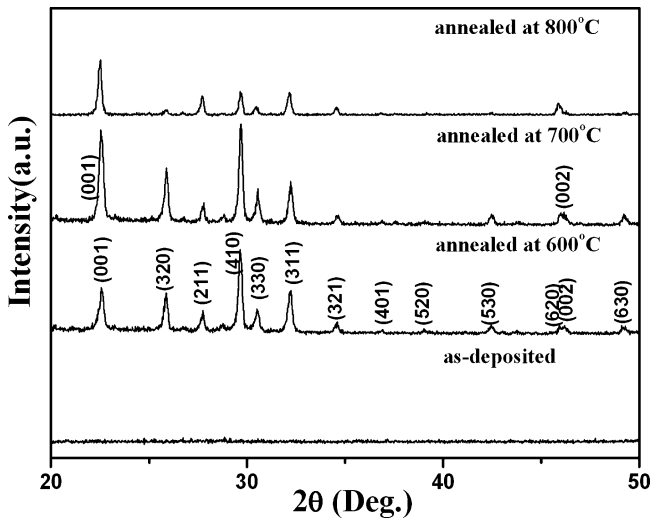
Fig. 3 XRD patterns of SBN thin films under different annealing temperatures

The XRD patterns of as-deposited and annealed SBN thin films are compared in Fig. 3. The as-deposited SBN thin film showed an amorphous structure and no crystallization was observed. After annealing, SBN thin films displayed the tetragonal tungsten bronze phase. When the annealing process was used, SBN thin films were crystallized with the preferred (410) orientation. Figure 3 also shows that the
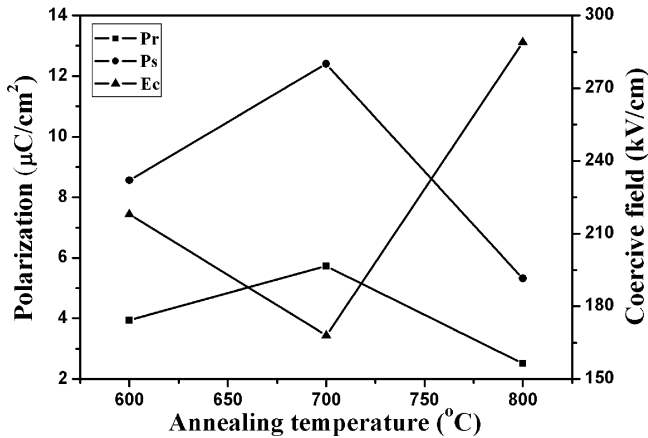
Fig. 4 Pr, Ps, and coercive field of SBN thin films

diffraction intensity for the (410) peak increased and full width at half maximum value (FWHM) for the (410) peak decreased from 0.22° to 0.20° as annealing temperature increased from 600 to 700 °C. This result suggests that the crystallization of SBN thin films is importantly improved under the annealing process. When SBN thin films were annealed at 800 °C, the diffraction intensities of (001) and (002) peaks increased and the diffraction intensity of (001) peak was stronger than that of mainly crystalline (410) peak. Those results demonstrate that the annealing process has improved the c-axis orientation of SBN thin films. From the results shown in Figs. 1 and 2, even the 800 °C-annealed SBN thin film has the highly c-axis orientation, the destruction is really observed on the surfaces.

From the P-E curves (not shown here), the remnant polarization (Pr), the saturation polarization (Ps), and the coercive field (Ec) of as-deposited SBN thin films were 1.22 $\mu C/cm^2$, 2.37 $\mu C/cm^2$, and 221 kV/cm, respectively. This result suggests that SBN thin films either crystallize on the crystalline SiO_2/Si or Pt/Ti/Si substrate or there is an additional injected charge being followed in addition to the polarization. Figure 4 shows that as the annealing process was used to treat on the as-deposited SBN thin films, the Pr, Ps, and Ec values were improved. As Fig. 4 shows, when the annealing temperature increased from 600 to 700 °C, the Pr and Ps values increased and Ec value decreased. Many reasons will affect the Pr, Ps, and Ec values of SBN thin films, including the pores, grain growth, and crystalline orientation. As the results of Figs. 2 and 3 are compared, except the increase of grain sizes and the decrease of pores, the increase of the c-axis orientation is another reason to cause the variations of Pr, Ps, and Ec values. Those results also prove that the Pr, Ps, and Ec values of SBN thin films are improved as the annealing process is used. Even the 800 °C-annealed SBN thin films had the maximum lotgering factor [11] in the (001) orientation, the Pr and Ps values decreased and Ec value increased. The theorem is that the destruction of SBN thin films has decreased the crystallization of SBN thin films because the diffraction intensity of the (001) peak decreases,
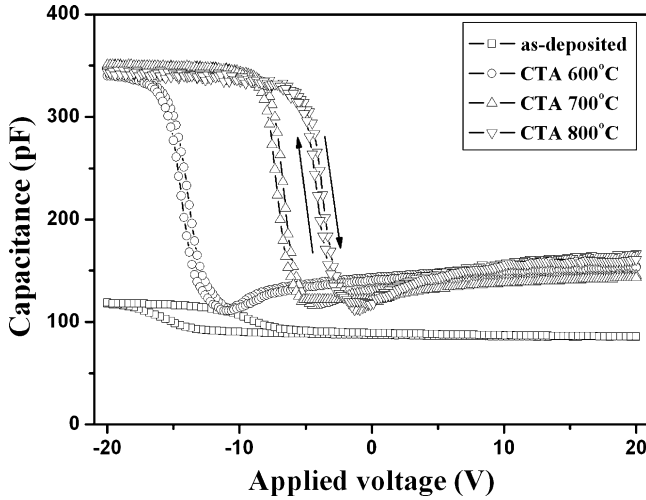
Fig. 5 C-V curves of SBN thin films under different annealing temperatures

and then the polarized characteristics are degenerated. 700 °C-annealed SBN thin films have the maximum Pr and Ps values of 5.73 and 12.4 $\mu C/cm^2$ and the minimum Ec value of 168 kV/cm.

To examine the characteristics of the C-V curves in the MFIS structure, the as-deposited and annealed SBN thin films were developed at 1 MHz, and the results were shown in Fig. 5. A smaller close hysteresis loop and an increase in capacitance were clearly observed in the annealed SBN thin films. For a ±20 V program and erase voltage, the capacitance of as-deposited SBN thin films increased from 80 to 120 pF, and the capacitances of annealed SBN thin films increased from 110 pF to around 350 pF. The increase in the capacitance of annealed SBN thin films is considerable. Because the grain sizes and the crystalline orientation of SBN thin films increase after annealing process, that will lead to the increase of polarization. The theorem is that the carriers tunneling through the SiO_2 layer are trapped and de-trapped at the trap levels distributed near the ferroelectric-SiO_2 interfaces. The trapped charges offset the memory effect, which is induced by the ferroelectric polarization, and then the movement of charges between the trap level and Si raises the inversion capacitance. The memory window of as-deposited SBN thin film was 10.3 V, and those of annealed SBN thin films were 1.2 V, which was independent of annealing temperatures and smaller than 3 V required for conventional flash memory devices. When the negative voltage is biased on the ferroelectric layer, the holes accumulate between the Si-SiO_2 interfaces. If there are defects that exist and the holes tunnel the Si-SiO_2 interface and inject into the SiO_2 layer, this will cause the C-V curves to change from clockwise to counterclockwise, then the memory window decreases [12]. The ΔV_{FB} values were −7.0, −12.3, −5.1, and −1.8 V for the as-deposited, 600, 700, and 800 °C-annealed SBN thin films, respectively. The variations of the ΔV_{FB} values are explained by the following
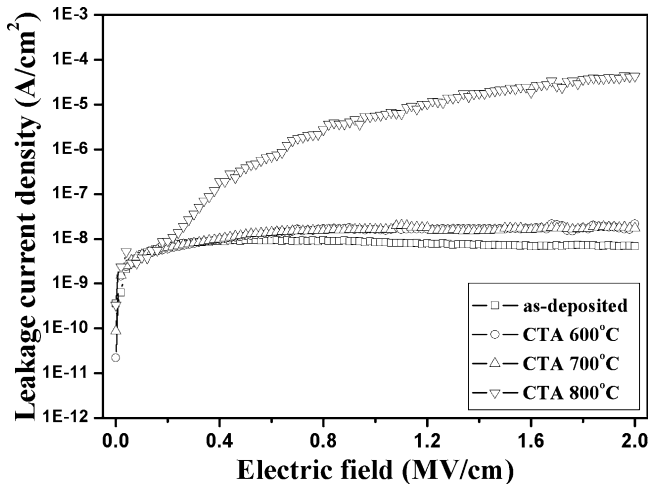
Fig. 6 J-E curves of SBN thin films different annealing temperatures

mechanism. When SBN thin films are used as the buffer layer, the electrical field in the high dielectric constant layer (as compared with SiO_2) increases. Increasing the electrical field in SBN layer decreases the needed switching voltage and the ΔV_{FB} values are shifted to less negative voltages.

The J-E characteristics of as-deposited and annealed SBN thin films are shown in Fig. 6. The leakage current density of the MFIS thin films plays an important role in alleviating the interdiffusion between elements of silicon substrate and SBN thin films under the differently deposited parameters. Annealed at 600 and 700 °C and even the electric field is increased from 0 to 2 MV/cm, the leakage current densities were smaller than 1×10^{-8} A/cm^2. Using 800 °C as annealing temperature, as the electric field increased from 0 to 2 MV/cm, the leakage current density increased from 1×10^{-9} to 3×10^{-5} A/cm^2. Annealing at 800 °C, the destruction of SBN thin films is really observed in Fig. 2a. For that, SBN thin films and SiO_2 layers will form an unknown phase, and the diffusion layer between the SiO_2-SBN interfaces and a partial of SiO_2 buffer layer is destroyed. The composites of the diffusion layer are not uniform and reveal a relatively low dielectric layer (as compared with SBN thin films). Because SBN thin films destruct and the defects existing in the diffusion layer increase, those reasons will cause the increase of leakage current densities.

4   Conclusions

SBN thin films were successfully deposited on Pt/Ti/Si and SiO$_2$/Si/Al substrates using a RF magnetron sputtering. The results showed that the grain growth, the crystalline orientation of (410) and (001) peaks, and the capacitance of SBN thin films were enhanced after annealing treatment. The memory window of SBN thin films was

10.3 V for as-deposited sample and decreased to 1.2 V as the annealed process was used. The flat-band shift voltages were -7.0, -12.3, -5.1, and -1.8 V for as-deposited, 600, 700, and 800 °C-annealed SBN thin films, respectively. SBN thin films annealed at 700 °C had the properties of a small leakage current density of 1×10^{-8} A/cm^2, a minimum Ec value of 168 kV/cm, and the maximum Pr and Ps values of 5.73 and 12.4 μC/cm^2, which were better than those of as-deposited, 600, and 800 °C-annealed SBN thin films.

References

1. Cheng HF, Chiou GS, Liu KS, Lin IN (1997) Appl Surf Sci 113/114:217–221
2. Xu Y, Chen CJ, Xu R, Mackenzie JD (1991) Phys Rev B 44:35–41
3. Li ST, Liu GK, Liu H, Fernandez FE (2000) J Alloy Compd 303–304:360–363
4. Shen ZR, Ye H, Mak CL, Yum TY, Wong KH (2007) Thin Solid Films 515:3475–3479
5. Shen Z, Ye H, Mak CL, Wong KH, Yum TY, Liu W, Zou T (2006) Mater Chem Phys 99:10–14
6. Li XT, Du PY, Ye H, Mak CL, Wong KH (2008) Appl Phys A 92:397–400
7. Infortuna A, Muralt P, Cantoni M, Tagantsev A, Setter N (2004) J Eur Ceram Soc 24:1573–1577
8. Shang JL, Zhang T, Wang H, Xie J, Hu GJ (2009) Appl Phys A 95:699–702
9. Diao CC, Yang CF (2010) Adv Appl Ceram 109:421–425
10. Zhong N, Shiosaki T (2007) Mater Lett 61:2935–2938
11. Lotgering FK (1959) J Inorg Nucl Chem 9:113–123
12. Watanabe Y (1998) Solid State Ionics 108:59–65

Improving the Properties of Sol–Gel Deposition SrBi$_4$Ti$_4$O$_{15}$ Thin Films by Post-annealing Process

Wen-Cheng Tzou, Ping-Shou Cheng, Wen-Chung Chang, Chien-Chen Diao, and Cheng-Fu Yang

Abstract In this study, the characteristics of the SrBi$_4$Ti$_4$O$_{15}$ (SBT) thin films were investigated by sol–gel method. Bi(NO$_3$)$_3$ and SrCO$_3$ were mixed with the ethylene glycol and acetic acid at 120 °C. After that, the titanium (IV) isopropoxide was added and mixed, and then the sol–gel precursor formula SrBi$_4$Ti$_4$O$_{15}$ + 4 wt% Bi$_2$O$_3$ (SBT) was obtained. After baking at 350 °C for 10 min, the one-layer SBT thin films were obtained. The spin coating and baking process were repeated twice for the two-layer SBT thin films. After deposition, the SBT thin films were annealed in a conventional furnace (CTA) at 600, 700, and 800 °C for 60 min in O$_2$ atmosphere. The cross sections and the surface morphologies of SBT thin films were investigated by using FE-SEM, and the crystalline structures were characterized by XRD patterns. It was found that the grain sizes increased and the pores decreased with rising CTA temperature. The effects of annealing temperature on the electrical properties of SBT thin films were also recorded and analyzed, including the capacitance–voltage curves and the leakage current density–electric field curves.

Keywords SrBi$_4$Ti$_4$O$_{15}$ + 4 wt% Bi$_2$O$_3$ • Anneal • Capacitance–voltage curve

W.-C. Tzou
Department of Electro-Optical Engineering, Southern Taiwan University,
Tainan, Taiwan, R.O.C.

P.-S. Cheng
Department of Electronic Engineering, National Kaohsiung University of Applied Sciences,
Kaohsiung, Taiwan, R.O.C.

W.-C. Chang
Department of Electronic Engineering, Southern Taiwan University, Tainan, Taiwan, R.O.C.

C.-C. Diao
Department of Electronic Engineering, Kao Yuan University, Kaohsiung, Taiwan, R.O.C.

C.-F. Yang (✉)
Department of Chemical and Materials Engineering, National University of Kaohsiung,
Kaohsiung, Taiwan, R.O.C.
e-mail: cfyang@nuk.edu.tw

1 Introduction

In the past years, the layer-structured ferroelectrics compound was one of the most technologically interesting thin film materials for the memory applications. The layer-structured bismuth oxides consisted of one to three slabs of perovskite-like layers, separated by fluorite-like $(Bi_2O_2)^{2+}$ layers, and had the general formula $A_{n-1}Bi_2B_nO_{3n+3}$, where A was usually a divalent ion, such as Sr^{2+}, Ba^{2+}, or Pb^{2+}, and B was Ti^{4+}, Nb^{5+}, or Ta^{5+} [1–3]. Within the bismuth family, $SrBi_2Ta_2O_9$ ceramics are received as an attracted candidate because of its excellent fatigue endurance against repetitive switching of polarization even when in the form of thin films. However, the remnant polarizations of $SrBi_2Ta_2O_9$ thin films are not sufficient for the applications in the high density of NvRAM, because the $SrBi_2Ta_2O_9$ ceramics exhibit lower Curie temperatures, leading to a temperature drift. $SrBi_4Ti_4O_{15}$ (SBT) ceramics are also a layer-structured bismuth compound ferroelectric and own the high Curie temperature of about 520 °C [4]. In the fluorite-like $(Bi_2O_2)^{2+}$ layers of ceramic-based compositions, the Bi_2O_3 vaporizes during the ceramic and the thin film fabrication processes that will degenerate the properties of ceramic and the deposition thin films. However, the addition of excess Bi_2O_3 content in bilayer-structured bismuth was also known to affect their ferroelectric properties and the crystalline structures. For example, the excess Bi_2O_3 had inhibited the formation of secondary phases ($SrBi_2O_4$ and $BiTaO_4$) in the $SrBi_2Ta_2O_9$ ceramics [5]. Also, the excess Bi_2O_3 had decreased the formed secondary phases ($Bi_2Ti_2O_7$ and $SrTiO_3$) in the $SrBi_4Ti_4O_{15}$ ceramics [6]. In this study, thin films based on SBT composition were investigated. The excess Bi_2O_3 content was also used in the SBT sol–gel source to decrease the effects of Bi_2O_3 vaporization on the properties of SBT thin films and to compensate the vaporization of Bi_2O_3 during the fabrication process of SBT thin films. $SrBi_4Ti_4O_{15} + 4$ wt% Bi_2O_3 was used as the formula to prepare the source composition in the sol–gel process. In our past experience, the thin film post-annealing was the most important process to improve the crystalline and electrical properties of the deposited ferroelectric thin films [7, 8]. The SBT thin films post-treated process, annealing in a conventional furnace (CTA), was also adopted to improve the properties of deposited SBT thin films. The effects of CTA temperature on the morphologies and electrical characteristics of SBT thin films were well developed.

2 Experiment

$Bi(NO_3)_3$ and $SrCO_3$ were added into the ethylene glycol and acetic acid and mixed at 120 °C, then the titanium(IV) isopropoxide was added and mixed, the sol–gel precursors were obtained, and the precursor formula was $SrBi_4Ti_4O_{15} + 4$ wt% Bi_2O_3 (SBT). The SBT thin films were deposited onto the SiO_2/p-Si(100)/Al

substrates for the metal–ferroelectric–insulator–semiconductor (MFIS) structure. For the one-layer samples, the deposition process was used in the two-step process, and the two-step spinner's speed and time were 800 rpm for 20 s and 5,000 rpm for 30 s, respectively. After deposition, the SBT thin films were baked at 120 °C for 10 min and 350 °C for 10 min, respectively. For the two-layer samples, the deposition process was repeated two times. After the SBT samples were prepared, the SBT thin films were annealed in a conventional furnace (CTA) from 600 to 800 °C for 60 min in O_2 atmosphere. The thicknesses of SBT thin films were characterized by field emission scanning electron microscopy (FE-SEM) from the cross-section observations. The thicknesses of one-layer SBT thin films were 53.6, 49.8, 45.3, and 40.1 nm for the as-deposited 600, 700, and 800 °C-annealed SBT thin films; the thicknesses of two-layer SBT thin films were 93.6, 90.6, 87.6, and 85.4 nm for the as-deposited 600, 700, and 800 °C-annealed SBT thin films, respectively. Apparently, the thicknesses of SBT thin films decreased with increasing annealing temperature. The surface morphologies of SBT thin films were also characterized by FE-SEM, and the crystalline structures were identified by X-ray diffraction (XRD) patterns. To finish the MFIS structure, an array of circular top contacts with a diameter of 1 mm was formed by deposition Al thin films. All the capacitance–voltage (C–V) characteristics were measured by an impedance analyzer (HP 4294A) at 1 MHz, with the initial dc bias at the top electrode scanned between −40 and 0 V. The leakage current density–electrical field (J–E) properties were measured by a semiconductor parameter analyzer (HP 4156).

3 Results and Discussion

The morphologies of SBT thin films with various annealing temperatures and layers are shown in Fig. 2. Even 600 °C-annealed SBT thin films exhibited a smooth surface, the grain growth was observed, and the pores were also observed. As the results in Fig. 1 were compared, the existence pores of two-layer SBT thin films were more than those of one-layer SBT thin films. Figure 1 also shows that the grain size increased with increased annealing temperature, suggesting that the crystallization degree of SBT thin films increases with increased annealing temperature. Because different morphologies are apparently observed, for that the annealing temperatures will have large effects on the electrical properties of SBT thin films.

The XRD patterns of as-deposited and annealed SBT thin films are compared in Fig. 2. No matter one-layer or two-layer were analyzed, as-deposited SBT thin films showed an amorphous structure, and no crystallization was observed. As the annealing process was used, the SBT thin films were crystallized with the preferred (119) orientation, and the diffraction intensity of (119) peak increased with increased annealing temperature. As annealing temperature increased from 600 to 800 °C, the full width at half maximum (FWHM) value by the (119) peak decreased from 0.42° to 0.36° for one-layer SBT thin films and decreased from 0.38° to 0.31° for two-layer SBT thin films. Those results suggest again that the crystallization of
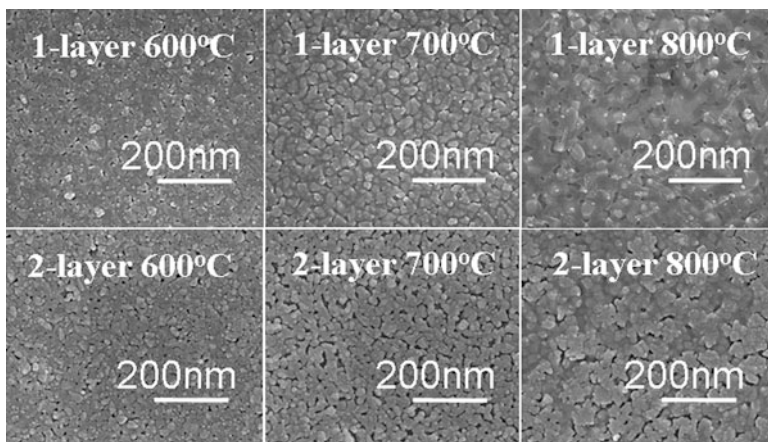
Fig. 1 Surface morphologies of SBT thin films as a function of annealing temperature
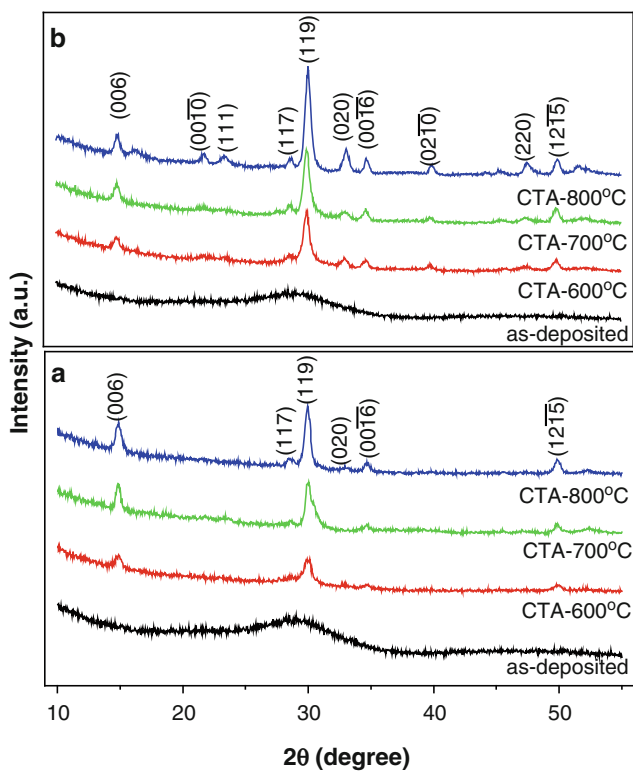
Fig. 2 XRD patterns of SBT thin films: (**a**) one-layer and (**b**) two-layer
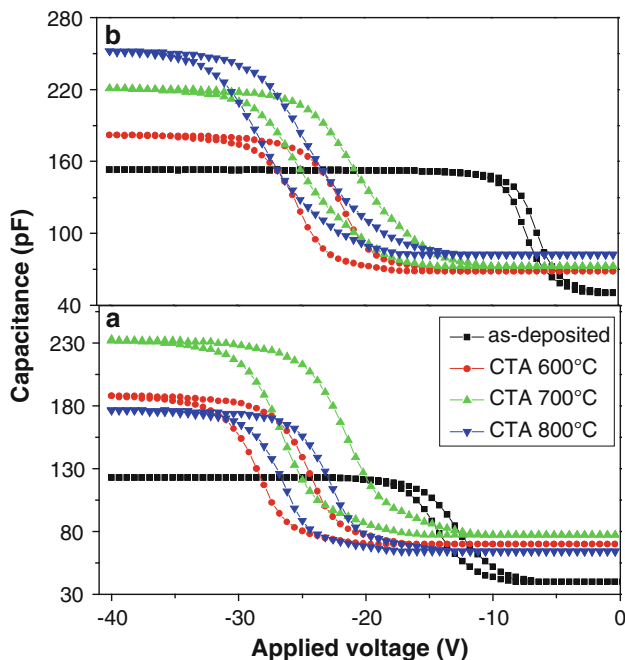
Fig. 3 *C–V* curves of SBT thin films: (**a**) one-layer and (**b**) two-layer

SBT thin films is importantly improved under the annealing process. When the SBT thin films were annealed, the diffraction intensities of (006) and (0010) peaks also increased with increased annealing temperature. Those results demonstrate that the annealing process has improved the *c*-axis orientation of SBT thin films. These results suggest that the annealing temperature affects the crystalline structure and then will affect the electrical properties of SBT thin films.

Figure 3 shows the capacitance (*C*)–voltage curves (*V*) of SBT thin films under different annealing temperatures and with different layers. With a −40 to 0 V program-erase voltage, the *C* value of as-deposited one-layer SBT thin films increased from 40 pF to around 124 pF, and the *C* values of annealed one-layer SBT thin films increased from 60–70 pF to around 180–230 pF; the *C* value of as-deposited two-layer SBT thin films increased from 45 pF to around 150 pF, and the *C* values of annealed two-layer SBT thin film increased from 70 pF to around 180–250 pF. Because the grain sizes and the crystalline orientation of SBT thin films apparently increase after annealing process, that will lead to the increase of polarization. For one-layer SBT thin films, the memory window of as-deposited film was 1.7 V, and those of annealed films were about 5.2–6.0 V; for two-layer SBT thin films, the memory window of as-deposited film was 1.1 V, and those of annealed films were about 4.2–5.0 V, respectively.
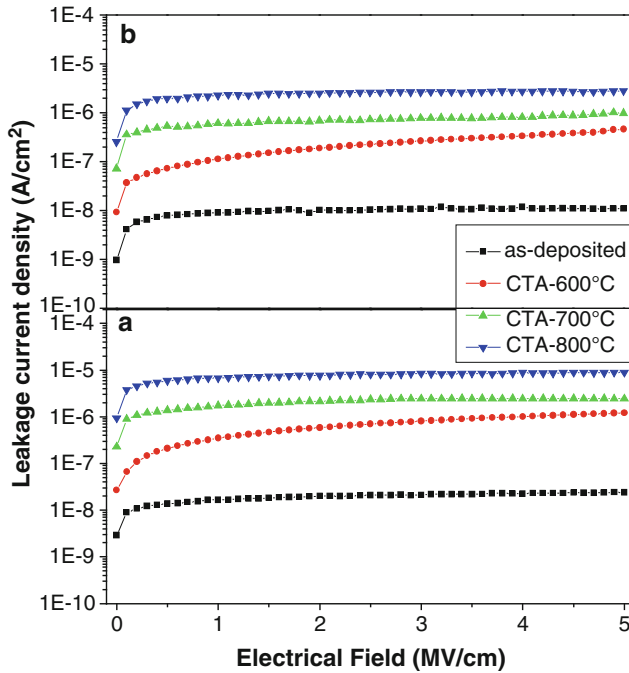
Fig. 4 *J–E* of SBT thin films: (**a**) one-layer and (**b**) two-layer

The smaller memory windows of as-deposited one-layer and two-layer SBT thin films are attributed to the fact that as-deposited SBT thin films are amorphous and less remanent polarization are residual in the thin films. For that, they only need the smaller coercive field to eliminate the remanent polarization. Because the crystallization of SBT thin films is improved, as Fig. 3 shows, the larger memory windows are attributed to the remanent polarization increases in the annealed SBT thin films and need the larger coercive field to eliminate the remanent polarization. For that as the annealing process is used to treat on the SBT thin films, the memory window is critically increased. For one-layer SBT thin films, the flat-band shift voltages (ΔV_{FB}) were -13.5, -22.0, -25.1, and -26.1 V for the as-deposited 600, 700, and 800 °C-annealed SBT thin films; for two-layer SBT thin films, the flat-band shift voltages were -5.50, -22.8, -23.2, and -22.5 V for the as-deposited 600, 700, and 800 °C-annealed SBT thin films, respectively. As the annealing temperature increases, the SBT thin films and SiO_2 layer form a defect layer with unknown phase between their interfaces. Because the composites of defect layers are not uniform and they are a relatively low dielectric layer, for that the ΔV_{FB} values are shifted to less negative voltage.

The leakage current behaviors of SBT thin films were investigated to determine the leakage current density (J) and electrical field (E) properties, and the results are shown in Fig. 4. The l J value of the MFIS thin films plays an important role in alleviating the interdiffusion between silicon and the SBT thin films under the

different CTA temperatures. For the as-deposited one-layer and two-layer SBT thin films, the saturation J values were 1.1×10^{-8} and 9×10^{-9}A/cm^2 as the electrical field increases from 0 to 5 MV/cm. When the annealing temperature was raised, the saturation leakage current densities really increased. It is believed that as the annealing temperature increases, the increased surface defects produce those results. When the same annealing temperature was used, the saturation J values of one-layer SBT thin films were larger than those of two-layer SBT thin films. Even the pores of one-layer SBT thin films are less than those of two-layer SBT thin films, the increase in the thickness is the main reason to cause the decrease of the saturation J values.

The linear variations of leakage current densities correspond either to the Schottky emission mechanism or to the Poole–Frenkel emission mechanism. The current density (J) in the Schottky emission mechanism is generated by the thermionic effect, which is caused by electron transport across the potential energy barrier via field-assisted lowering at a metal–insulator interface, as given by Eq. (1) [9]:

$$J = A^* T^2 \exp \frac{\left(\beta_s E^{1/2} - \phi_s \right)}{\left(k_B T \right)} \tag{1}$$

where $\beta_s = (e^3/4\pi\varepsilon_o\varepsilon)^{1/2}$ and e is the electron charge, ε_o is the dielectric constant of free space, and A^* is the effective Richardson constant. The current density (J) in the Poole–Frenkel emission mechanism is due to field-enhanced thermal excitation of trapped electrons from the insulator into the conduction band, as given by Eq. (2) [10]:

$$J = J_0 \exp \frac{\left(\beta_{PF} E^{1/2} - \phi_{PF} \right)}{\left(k_B T \right)} \tag{2}$$

where $J_o = \sigma_o E$ is the low-field current density, $\beta_{PF} = (e^3/\pi\varepsilon_o\varepsilon)^{1/2}$, σ_o is the low-field conductivity, ψ_{PF} is the height of trap potential well, and T is the absolute temperature.

Figure 5 shows the J–E characteristics with $\ln(J)$ as the vertical axis and $E^{1/2}$ as the horizontal axis. From the $\ln J$–$E^{1/2}$ curves of SBT thin films shown in Fig. 5, the leakage current densities are linearly related to the square root of applied electrical field. The experimental results in Fig. 5b indicate that the as-deposited and annealed two-layer SBT thin films exhibit the Poole–Frenkel emission mechanism under the low electric field of $E^{1/2} = 0$–10 (kV/cm)$^{1/2}$. This means that the carriers are transported through the SBT thin films by the field-enhanced Poole–Frenkel emission mechanism in the low electrical field region. Figure 5b also shows SBT thin films exhibiting the Schottky emission mechanism, as $E^{1/2} > 10$ (kV/cm)$^{1/2}$. These results suggest that the leakage current densities of SBT thin films are mainly caused by electron transport across the potential energy barrier. However,
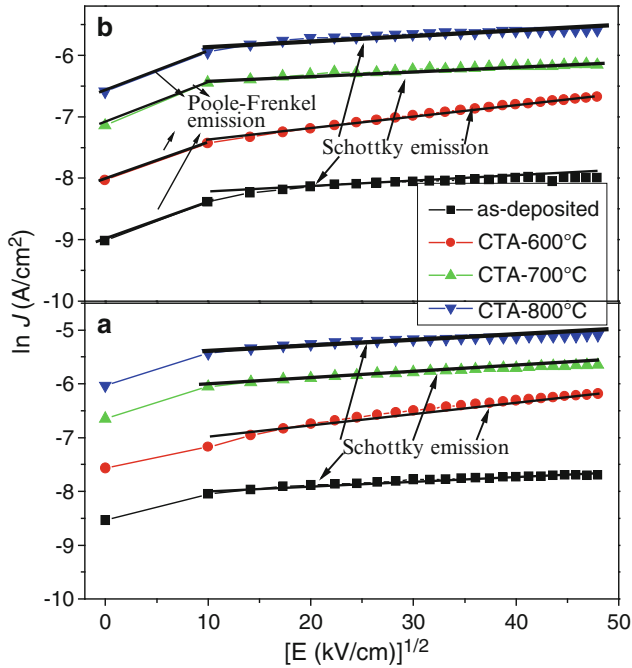
Fig. 5 log J–$E^{1/2}$ plots of SBT thin films: (**a**) one-layer and (**b**) two-layer

the results in Fig. 5a show that as-deposited and annealed one-layer SBT thin films mainly exhibit the Schottky emission mechanism. The Poole–Frenkel emission mechanism is not existed in the as-deposited and annealed SBT thin films.

4 Conclusions

In this study, the SBT thin films were successfully prepared by the sol–gel process; the influences of annealing temperature on the characteristics of SBT thin films were well explored. For as-deposited one-layer and two-layer SBT thin films, they revealed the amorphous phase. The crystallization and the grain sizes increased, and the pores decreased with raising annealing temperature. In the leakage current density versus electrical field (J–E) curves, the leakage current densities increased with raising annealing temperature and decreased with increasing layer of SBT thin films. The increase in leakage current densities with rising annealing temperature occurred because as the annealing temperature increased, the defects on the surfaces of SBT thin films increased. The memory windows of SBT thin films also increased after the CTA process. From the ln J–$E^{1/2}$ curves of SBT thin films, the Schottky emission mechanism dominated the leakage current densities of SBT thin films rather than the Poole–Frenkel emission mechanism.

References

1. Araujo CA, Cuchiaro JD, Mcmillan LD, Scott MC, Scott JF (1995) Nature 374:627–629
2. Zhang XY, Huang ZZ, Chan HL, Kwok KW, Choy CL (1999) J Eur Ceram Soc 19:985–988
3. Forbess MJ, Seraji S, Wu Y, Nguyen CP, Cao GZ (2000) Appl Phys Lett 76:2934–2936
4. Desu SB, Li TK (1995) Mater Sci Eng B 34:L4–L8
5. Wei YF, Kao CH, Yang CF, Huang HH, Huang CJ (2007) Mater Lett 61:4643–4646
6. Wei YF, Yang CF, Chen CY, Huang CJ, Kao CH (2009) Adv Appl Ceram 108:102–105
7. Chen KH, Diao CC, Yang CF, Wang BX (2009) Ferroelectrics 385:46–53
8. Chen KH, Yang CF (2009) Ferroelectrics 381:59–66
9. Hesto P, Barvotlin G, Vapaille A (1986) Instabilities in silicon devices. Elsevier, North-Holland, Amsterdam
10. Sze SM (1981) Physics of semiconductor devices. Wiley, New York

Water Tank Simulation of a Continuous Hot-Dip Galvanized Zinc Pot

Y.S. Lo, C.J. Fang, L.C. Tsao, and J.C. Leong

Abstract This work has simulated the flow field in a hot-dip galvanized zinc pot using a water tank simulation. The flow pattern was visualized using laser sheet flow visualization technique. The general flow pattern in the water tank was not sufficiently influenced by the belt speed. The traces of water on the snout side, in the snout region, and close to the surface, where the stabilizing roll and the belt were in contact, were closely examined. The water tank was also investigated numerically. The steady-state CFD solution also indicated that a change in the belt velocity has little influence on the overall flow pattern developed in the tank. The flow patterns obtained via CFD means had a close resemblance with those visualized through laser sheet technique.

Keywords Hot-dip galvanized zinc pot • Laser sheet • Flow visualization

1 Introduction

Galvanization is a process to apply a protective zinc oxide coating on the surface of steel or iron to prevent rusting and corrosion. Galvanized steel provides low-cost and effective performance by combining the corrosion resistance of zinc with the strength and formability of steel. In the hot-dip galvanization process, a moving

Y.S. Lo • J.C. Leong (✉)
Department of Vehicle Engineering, National Pingtung University of Science and Technology, Pingtung 91201, Taiwan
e-mail: jcleong@mail.npust.edu.tw

C.J. Fang
Department of New Materials Research and Development, China Steel Corporation, Kaohsiung 81233, Taiwan

L.C. Tsao
Department of Materials Engineering, National Pingtung University of Science and Technology, Pingtung 91201, Taiwan

steel strip is dipped into and withdrawn from a molten zinc pot of approximately 460 °C. Right after its removal from the pot, the steel strip passes through an air knife system mainly composed of a pair of gas-wiping jets produced where excess molten zinc that adheres to each side of the steel strip is blown off. When the strip is in the molten zinc pot, small intermetallic particles of Zn-Fe and Al-Fe will form, and this leads to a consistent production of dross within the pot. The motion of the steel strip in the molten zinc pot causes some of this dross to stick to the strip surfaces. This kind of surface defect affects the overall quality of the steel strip. Although it can be greatly reduced by the control of zinc temperature and aluminum additive concentration into the pot to suppress the formation of dross, a further understanding of the flow pattern within the molten zinc pot will help in reducing the surface defect. This problem has been investigated from the aspect of fluid mechanics [1–5].

In this study, the flow field in a hot-dip galvanized zinc pot was simulated using a water tank and a belt driven by a motor. In this study, the motor was regulated to give two different belt speeds. For validation, the water tank was also investigated numerically via FLUENT.

2 Methodology

The water tank employed in this study, as shown in Fig. 1, was based on a 1:10 reduced scale for a currently used CGL molten zinc pot. In order to visualize the flow patterns in the water tank, the tank was made of Plexiglas. The driven power was provided by a motor. The motor then conveyed its motion to a belt. The rotational speed of the motor was regulated via an inverter. To visualize the flow patterns of the
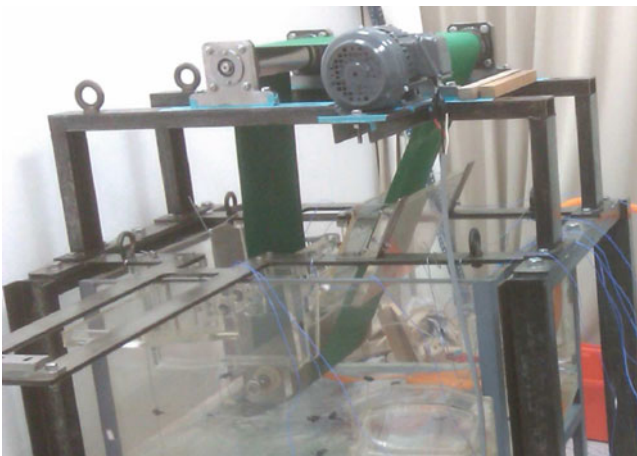
Fig. 1 Picture of the current experimental apparatus
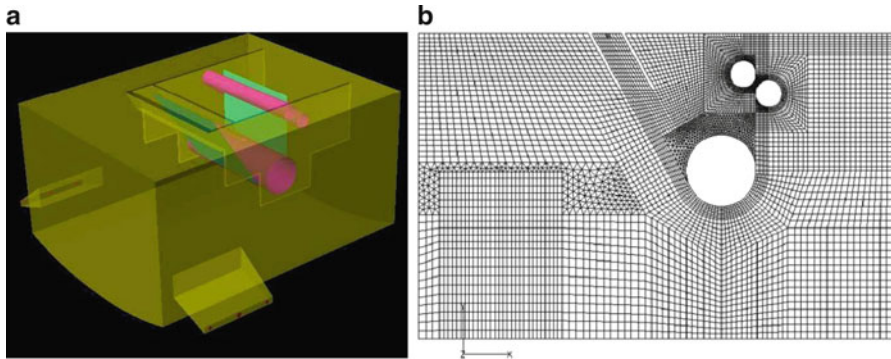
Fig. 2 CFD modeling: (**a**) schematics of the model, (**b**) layout of the grid system

300 L water in the water tank, 5 cc flow visualization particles were added into the water. With the help of a 200 mW green light laser sheet module, the traces of the visualization particles could be recorded using a digital camera. Two different motor rotational speeds were examined; these speed corresponded to a linear belt velocity of 0.40 and 0.96 m/s. At the lower belt velocity, an aperture size of F8.0 and an exposure time of 1/2 s were used for the photography device. At the higher belt velocity, the aperture size and exposure time were adjusted to be F4.5 and 1/6 s.

A virtual model of the water tank had been constructed, and various mesh systems were examined for appropriateness. For brevity, the continuity and Reynolds-averaged Navier-Stokes equations for this numerical work are not listed here. Furthermore, this work employed the RNG k-ε turbulence model Launder and Spalding originally developed [6] but modified by Yakhot and Orzag [7]. Their model introduced the turbulence kinetic energy k and the turbulence dissipation rate ε. As a matter of fact, the RNG k-ε turbulence model was preferred over the standard k-ε turbulence model in this study for its higher accuracy in modeling flow circulation.

The geometry of the water tank model is depicted in Fig. 2a. Because the geometrical shape involved in the water tank was quite complicated, a combination of structured and unstructured grids was employed. The layout of the grid system (340,000) on the center plane of the tank is shown in Fig. 2b.

3 Results and Discussions

When the belt linear velocity was 0.40 m/s, the traces of the visualization particles close to the moving belt were longer in length, as shown in Fig. 3a. At the region close enough to the left vertical wall of the water tank, the fluid elements were observed to move almost horizontally towards the belt. When these fluid elements were close enough to the moving belt, they were dragged along by the belt to move in the direction almost parallel to the belt motion. When the belt linear velocity was
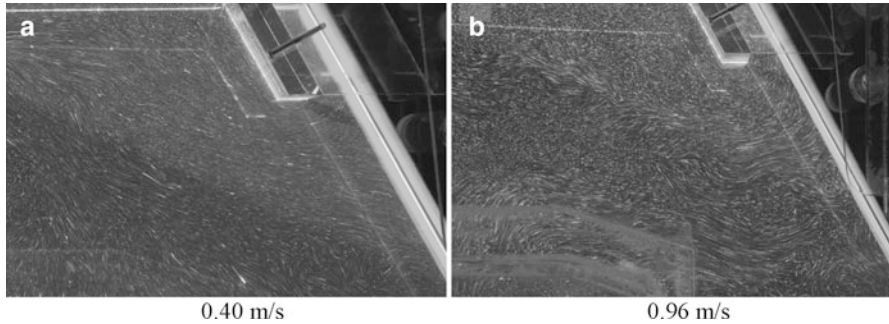
Fig. 3 Pictures taken at the *upper left* region of the water tank at different belt linear speeds
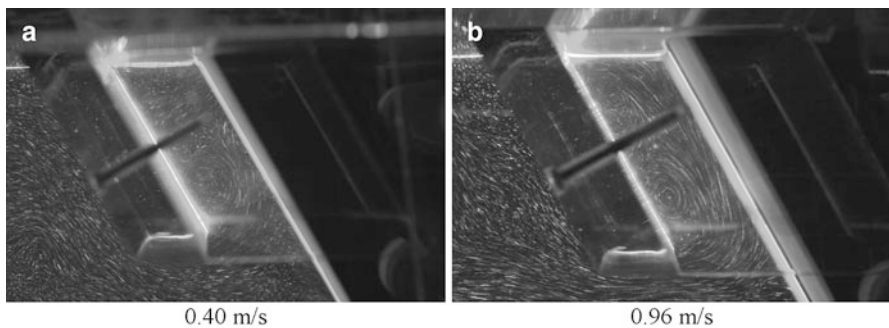
Fig. 4 Pictures taken at the snout region of the water tank at different belt linear speeds

increased to 0.96 m/s, most of the traces of the visualization particles appeared to be short, while only a relatively small portion of them actually elongated, as shown in Fig. 3b. Those elongated traces indicated that the fluid elements flowed faster as a result of the increase in belt speed and thus the increase in the shearing effect it imposed. However, the flow instability kicked in leading to the generation of a great deal of three-dimensional eddies. When this happened, part of the fluid barely flowed towards the belt. Instead, these eddies formed blockages and only allowed a narrow stream of fluid to flow from the left towards the belt.

The flow in the snout region belt is presented in Fig. 4. Regardless of the belt linear speed, there always occurred a recirculation cell filling the space between the snout wall and the moving belt. The flow in this region was mainly attributed to the presence of wall effect and shear stress effect. In this region, some of the fluid elements were forced to flow along with the belt creating a localized low-pressure region within the snout. As a result, some fluid elements at the snout opening would flow into the snout region. When this happened, an obvious recirculation cell would evolve at the sharp corner of the snout. At a belt linear speed of 0.96 m/s, the traces of the visualization particles were much longer and clearer.
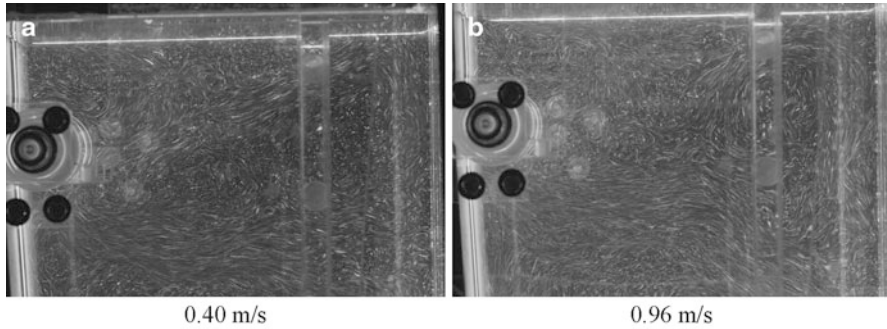
Fig. 5 Pictures taken at the *upper right* region of the water tank at different belt linear speeds
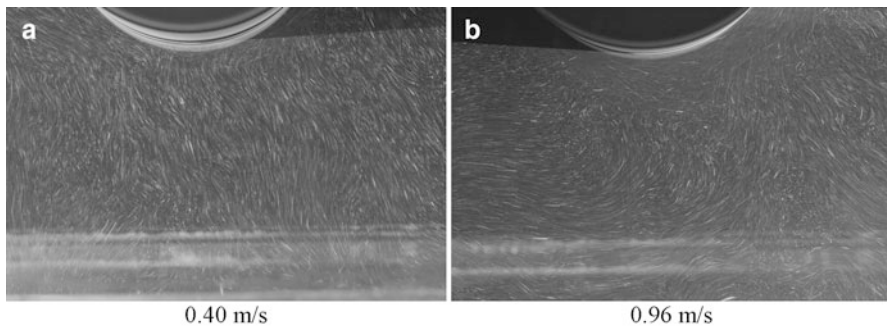
Fig. 6 Pictures taken at the region *right* below the sink roll at different belt linear speeds

Figure 5 shows the flow patterns at the upper right region of the water tank. It was found that there existed two obvious streams of fluid ejecting from the stabilizing roll to the wall of the water tank. Since the stabilizing roll rotated in the clockwise direction, the fluid at the upper sharp corner between the belt and the stabilizing roll was forced to move either vertically upwards or almost tangentially along the stabilizing roll. At the lower sharp corner, the fluid was squeezed and eventually forced to form a strong current flowing away from this corner. These two aforementioned currents then met somewhere to the lower right of the stabilizing roll. Soon after they met, these two currents were repelled from the roll, one to the upper right, while the other to the lower right, as shown in Fig. 5a. When the belt linear velocity was increased to 0.96 m/s, the amount of eddies in the fluid had apparently increased. Not only so, two large flow circulation cells were observed between the aforementioned currents.

At the bottom of the sink roll, it was observed that there existed a buoyant flow rising from the base of the water tank. At a belt linear speed of 0.40 m/s, this stream of flow was rather clear, as shown in Fig. 6a. When the belt speed was increased, the flow dragged along from the left portion of the tank was forced to spin around the sink roll. In this situation, the shear flow deformed the buoyant flow from the base and caused the buoyant flow to be less obvious, as shown in Fig. 6b.
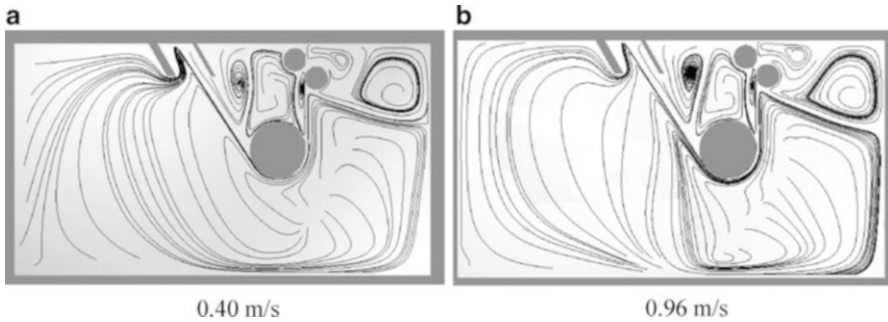
Fig. 7 Flow patterns in the water tank obtained through CFD means

The flow patterns obtained through computational means are shown in Fig. 7. The overall flow fields are quite similar to those displayed in Figs. 3, 4, 5, and 6. The main difference between these results is the formation of small eddies and localized highly nonperiodic flow circulation. Since the CFD simulation employed the Reynolds-averaging technique, temporal fluctuation in the velocity field was actually filtered out leaving no trace of small eddies and localized highly nonperiodic flow circulation. Both the experimental and numerical results confirmed that some water would be entrained into the snout before it was dragged out of the snout along with the belt. As the belt speed increased, more water at the base was attracted to the sink roll. The currents emitted from the stabilizing roll as well as the flow recirculation cell in between them were also clearly observed in both Figs. 5 and 7.

4 Conclusions

This work has visualized the flow of water in a water tank simulation for a molten zinc pot. Experimental results showed that the flow field outside of the snout was quite stable at a low belt speed. As the speed increased, a large amount of eddies formed in this region influencing the stability of the fluid flow. On the opposite side of the tank, a great deal of eddies was also observed. At the entry region, water flowed stably, but its flow pattern was greatly affected by the small eddies when the belt moved at high speeds. Both experimental and CFD results had demonstrated the important characteristics of the fluid in the water tank. These include the shear flow next to the moving belt, the entrainment of water into the snout, the buoyant flow at the base of the tank below the sink roll, and the formation of eddies at the exit region.

References

1. Shin DS, Choi JH, Lee S-J (2000) Velocity field measurements of flow inside snout of continuous hot-dip galvanizing process using a single-frame PIV technique. ISIJ Int 40 (5):484–490
2. Kim YH, Cho YW, Chung S-H, Shim J-D, Ra HY (2000) Numerical analysis of fluid flow and heat transfer in molten zinc pot of continuous hot-dip galvanizing line. ISIJ Int 40(7):706–712
3. Lee SJ, Kim S, Koh MS, Choi JH (2002) Flow field analysis inside a molten Zn pot of the continuous hot-dip galvanizing process. ISIJ Int 42(4):407–413
4. Jiang Z, Feng T (2007) Fluid dynamics analysis of a zinc pot in a continuous galvanising line. Millennium Steel 2007:197–203
5. Park HS, Han K-A, Lee J, Shim J-W (2008) Numerical simulation of zinc flow and temperature distribution in a galvanizing zinc pot. ISIJ Int 48(2):224–229
6. Launder BE, Spalding DB (1974) The numerical computation of turbulent flows. Comput Method Appl Mech Eng 3(2):269–289
7. Yakhot V, Orszag SA (1986) Renormalization group analysis of turbulence. I. Basic theory. J Sci Comput 1(1):3–51

The Finite Element Analysis Study of the Laser Lift-Off (LLO) of III-Nitride Compound

Yan-Hsin Wang and Wei-Li Chen

Abstract ANSYS was used to simulate the temperature field of the nitride semiconductor compound in the laser lift-off (LLO) process. One-dimension thermal conduction model is formulated. When the fluence is 107 mJ/cm^2, the InN temperature starts to rise up, coupled with a large temperature gradient across the InN film, to above 600 °C for a region within 108 nm below the irradiated InN/sapphire interface. The diameter of the beam spot is 300 μm, but the diameter of the decomposed area is around 100 μm for InN due to Gaussian beam shape. For GaN, LLO can be achieved by using either a single pulse of 350 mJ/cm^2 fluence or multiple pulses of fluence down to 95 mJ/cm^2. The result shows that when six successive 95 mJ/cm^2 pulses are used, the thermal stress can be greatly reduced from 0.929 GPa in the case of a single 350 mJ/cm^2 pulse to 0.332 GPa.

Keywords Laser lift-off • ANSYS • Temperature field • InN • GaN

1 Introduction

When the photon energy of the UV laser is greater than the bandgap of GaN, the photon absorption primarily caused interband absorption, called interband LLO. By contrast, the laser photon energy is below the absorption edge of GaN for intraband LLO. These processes were applied to separate GaAs thin films grown

---

Y.-H. Wang
Department of Mechatronics Engineering, National Changhua University of Education,
Changhua 50007, Taiwan

Taichung Thermal Power Plant, Taiwan Power Company, Taichung 43401, Taiwan

W.-L. Chen (✉)
Department of Electronic Engineering, National Changhua University of Education,
Changhua 50007, Taiwan
e-mail: weili@cc.ncue.edu.tw

on GaAs substrates [1]. A sacrificial ZnO buffer layer was also used in the lift-off of very thick GaN (200–400 μm) [2]. Kelly et al. [3] reported the pulse laser-assisted thermal etching of GaN using the third harmonic of a Q-switched Nd:YAG laser. The 3.49 eV (355 nm) radiation is just above the absorption edge of GaN. The lift-off of thin (~5 μm) GaN film from its sapphire substrate was first successfully done by illuminating the substrate-film interface with high-power laser pulses. Wong et al. [4, 5] reported successful laser lift-off of GaN thin films by illuminating KrF excimer laser pulses ($\lambda = 248$ nm, laser intensity >400 mJ/cm^2, pulse duration = 38 ns) through the transparent sapphire substrate. Ho et al. [6] adopted the pulsed second harmonic Nd:YAG laser with longer wavelength ($\lambda = 532$ nm, laser intensity = 12.4 mJ/cm^2, pulse width = 10 ns) to perform GaN lift-off.

This study aims to explore the thermal behavior of the nitride semiconductor LLO procedures using a commercially available finite element analysis (FEA) software (ANSYS). One-dimension thermal conduction model in nitride layer for LLO technique is formulated with a single or multiple 355 nm pulses.

2 Simulation

The basic principle of FEA is to disassemble complicated structures into simple unit elements, and heat transmission is presented by equations. The heat equation can then be solved analytically with the assumption of a one-dimensional heat flow, as shown in Fig. 1. It is assumed that there is no phase change during the laser pulse illumination.

Both the meshing model of the film and the Gaussian distribution of laser energy were created by the ANSYS Parameter Design Language. The thermal and mechanical properties of GaN used in the analytical model were temperature dependent. The parameters of InN were set to be temperature independent. The simulation was first carried out by using a single laser pulse for lift-off. The study also involves the situation of illuminating repeated pulses on GaN with lower energy density.
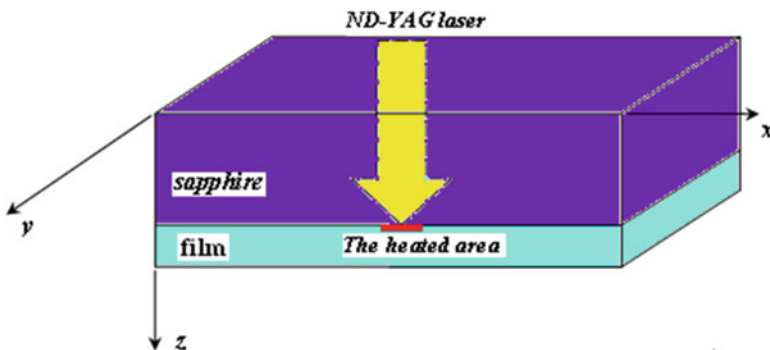
Fig. 1 The model of the heat conduction for LLO. Laser pulse enters the sample via the sapphire substrate and thermally decomposes a GaN film at the substrate interface

Table 1 The thermal and mechanical parameters of GaN used in simulation [7–12]

		Temperature (°C)								
Properties		27	77	127	177	227	327	427	527	627
Specific heat, C_p (J/kg°C)		488		498.8		509.5	520.2	530.9	541.6	552.3
Thermal conductivity, k (W/m°C)		1.66	1.55	1.45	1.37					
Thermal expansion coefficient $(\times 10^{-6})$	α_a	4.17		5.0		5.45	5.65	5.75	5.83	5.9
	α_c	3.9		4.5		4.9	5.15	5.3	5.4	5.5
Young's modulus, E (GPa)		288.1		287.2		286	284.8	283.5	282.3	281.1
Poisson ratio, ν						0.23				
Density, ρ (kg/m^3)						6,150				

The temperature-dependent thermal and mechanical properties of the GaN are listed in Table 1 [7–12]. The material and thermal parameters of the InN, including density, thermal conductivity, and specific heat, are set to be 6,810 kg/m^3, 300 J/kg°C, and 45 w/m°C, respectively [7, 13, 14]. The length, width, and height of the film applied in the calculation were 162, 330, and 15 μm, respectively.

The grid size of the element unit was set as 0.2 μm to guarantee sufficient resolution for the heat-affected zone. The established 3D mesh model of a film and the type of element used for analysis is solid 70. Transversal cross section of the film was designed as a two-dimensional approach and adopted four-node, plane strain, quadratic, and thermal structural element (PLANE 13).

The initial temperature was 27 °C. The simulated laser system used in the present work provided a pulse energy with a Gaussian intensity profile whose beam diameter is 300 μm. The pulse length and repetition rate were 35 ns and 1 kHz, respectively. The laser heat source was converted into the heat flux to act on the interface. The temperature variation at the film/sapphire interface was simulated by a transient form, and the full Newton-Raphson method was used to accelerate the convergence rate. The ANSYS program calculated the temperature distribution with an ending time up to 35 ns in every zeros, and therefore, the temperature distribution and heat effect of the laser light could be studied.

3 Results and Discussion

Simulation results revealed that 305 and 93 mJ/cm^2 laser fluence for 35 ns pulse duration were required to raise the interface temperature to achieve the decomposition of InN (~600 °C) [15] and GaN (≥900 °C) [4], respectively. It should be reminded that the optical intensity used in the simulation is the net power entering
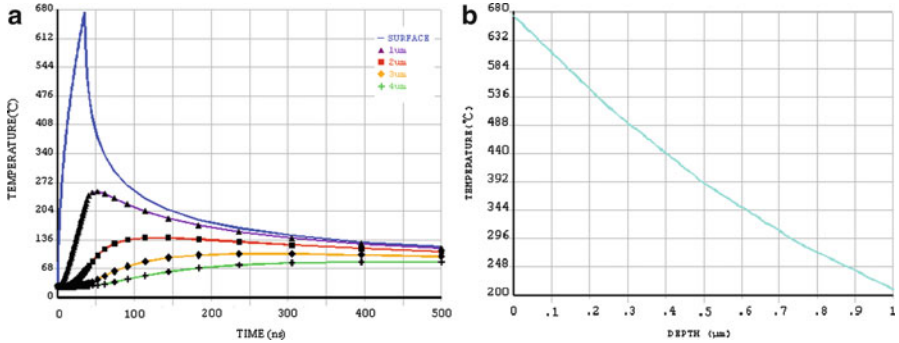
Fig. 2 (**a**) The temperature evolution for various depths. (**b**) The vertical temperature distribution at beam center after irradiated by a 35 ns laser pulse of 107 mJ/cm^2 fluence

GaN and InN, which is 15 % below the initial laser output intensity because of the losses caused by reflections at the air/sapphire and sapphire/film interfaces. To guarantee successful LLO, 350 and 107 mJ/cm^2 were adopted for subsequent simulations.

The planar temperature field shows circular symmetry. The Gaussian beam diameter is 300 μm. For the case of InN, a laser fluence of 107 mJ/cm^2 will cause the InN/sapphire interface temperature to rise above 600 °C, which will trigger InN decomposition, within a circular region of 100 μm in diameter. Figure 2a illustrates the temperature evolution for various depths. The highest temperature (673 °C) occurs at the interface at the end of 35 ns illumination. As the location moves away from interface, it requires longer time to allow heat transfer to reach peak temperature. Figure 2b shows the temperature distribution along vertical axis at the beam center. The decomposition zone of InN will be limited within 108 nm from InN/sapphire interface. This distance gradually decreases as the location moves away from spot center. Usually the device epistructure is located more than 1 μm from the interface. Because the peak temperature at such a depth has dropped down to 245 °C, the device structure will not be degraded due to LLO process.

Figure 3 shows the simulated cross-sectional temperature field of a GaN/sapphire structure at beam center after a single pulse. The interface temperature rises to its maximum, 1,032 °C, at the end of 35 nm pulse. The laser fluence used in simulation was 350 mJ/cm^2. The depth of the region with a temperature above GaN decomposition temperature (≥900 °C) is 188 nm at beam center. These cases employing repeated pulses with lower laser power density were also simulated. The time duration between pulses is 1 ms. Figure 4 indicates that two successive pulses with a fluence of 250 mJ/cm^2 can raise the temperature to 1,030 °C, and the depth of decomposition zone extends to 238 nm. Compared with Fig. 3, the thermal stress declined from 0.929 to 0.784 GPa in Fig. 4. When the number of successive pulses is increased and the fluence of each pulse is reduced, the depth of the decomposition zone is extended, and the thermal stress is decreased. Table 2 shows the result in the case of six successive pulses of 95 mJ/cm^2 fluence. The thermal stress greatly drops
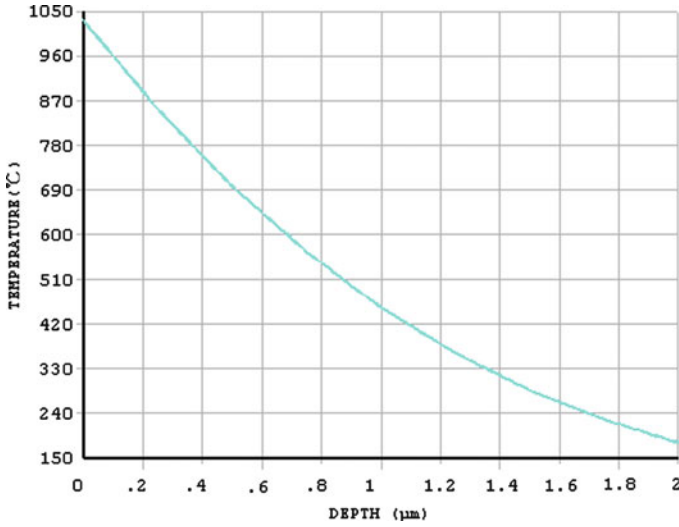
Fig. 3 The cross-sectional temperature field of GaN film after irradiated by a single pulse of 350 mJ/cm^2 fluence
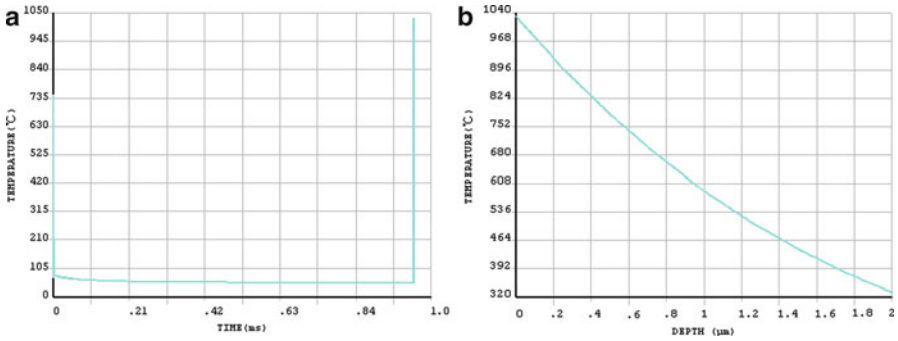
Fig. 4 (**a**) The temperature evolution at the spot center irradiated by two successive pulses of 250 mJ/cm^2 fluence. The time duration between pulses is 1 ms. (**b**) The temperature field at the GaN/sapphire interface at the end of the second pulse

Table 2 LLO used repeated pulses for the temperature profile of different energy density

Energy density (mJ/cm^2)	The number of pulses	Highest temperature (°C)	Thermal stress (GPa)	The depth of highest temperature (nm)
350	1	1,032	0.929	188
250	2	1,030	0.784	238
180	3	1,077	0.653	475
140	4	1,074	0.503	600
95	6	1,055	0.332	787

to 0.332 GPa, while the depth of the decomposition zone reaches 787 nm. The thermal stress was greatly reduced by using more low-power pulses due to longer time of heat conduction and thicker region of decomposition. Usually the device structure is more than 3 μm away from the GaN/sapphire interface; thicker decomposition zone will not cause damage to device structure.

4 Conclusion

The temperature fields of the GaN and InN films during LLO process have been simulated using ANSYS. The temperature of simulated InN/sapphire interface is 673 °C after 107 mJ/cm^2 fluence illumination, exceeding the decomposition temperature of InN. The laser beam size is 300 μm, while the diameter of the decomposition zone is 100 μm at interface, and the thickness of decomposition zone is 108 nm at bean center. When six low-power density (95 mJ/cm^2 fluence) multiple pulses are adopted for GaN LLO, the thermal stress drops from 0.929 GPa for the case of single pulse to 0.332 GPa.

References

1. Yablonovitch E, Sands T, Hwang DM, Schnitzer I, Gmitter TJ, Shastry SK, Hill DS, Fan JCC (1991) Van der Waals bonding of GaAs on Pd leads to a permanent, solid-phase-topotaxial, metallurgical bond. Appl Phys Lett 59:3159–3161
2. Detchprohm T, Amano H, Hiramatsu K, Akasaki I (1993) The growth of thick GaN film on sapphire substrate by using ZnO buffer layer. J Cryst Growth 128:384–390
3. Kelly MK, Ambacher O, Dalheimer B, Groos G, Dimitrov R, Angerer H, Stutzmann M (1996) Optical patterning of GaN films. Appl Phys Lett 69:1749–1751
4. Wong WS, Sands T, Cheung NW (1998) Damage-free separation of GaN thin films from sapphire substrates. Appl Phys Lett 72:599–601
5. Wong WS, Kneissl M, Mei P, Treat DW, Teepe M, Johnson NM (2001) Continuous-wave InGaN multiple-quantum-well laser diodes on copper substrates. Appl Phys Lett 78:1198–1200
6. Ho HP, Lo KC, Siu GG, Surya C, Li KF, Cheah KW (2003) Raman and photoluminescence spectroscopy of free-standing GaN separated from sapphire substrates by 532 nm Nd:YAG laser lift-off. Mater Chem Phys 81:99–103
7. Piprek J (2003) Semiconductor optoelectronic devices: introduction to physics and simulation. Academic, Amsterdam/Boston
8. Reeber RR, Wang K (2001) High temperature elastic constant prediction of some group III-nitrides. MRS Internet J Nitride Semicond Res 6:1–5
9. Zou J, Kotchetkov D, Balandin AA, Florescu DI, Pollak FH (2002) Thermal conductivity of GaN films: effects of impurities and dislocations. J Appl Phys 92:2534–2539
10. Nipko JC, Loong C-K, Balkas CM, Davis RF (1998) Phonon density of states of bulk gallium nitride. Appl Phys Lett 73:34–36

11. Kisielowski C, Kruger J, Ruvimov S, Suski T, Ager JW III, Jones E, Liliental-Weber Z, Rubin M, Weber ER, Bremser MD, Davis RF (1996) Strain-related phenomena in GaN thin films. Phys Rev B 54:17745–17753
12. Roder C, Einfeldt S, Figge S, Hommel D (2005) Temperature dependence of the thermal expansion of GaN. Phys Rev B 72:085218–085223
13. Krukowski S, Witek A, Adamczyk J, Jun J, Bockowski M, Grzegory I, Lucznik B, Nowak G, Wroblewski M, Presz A, Gierlotka S, Stelmach S, Palosz B, Porowski S, Zinn P (1998) Thermal properties of indium nitride. J Phys Chem Solids 59:289–295
14. Davydov VY, Emtsev VV, Goncharuk IN, Smirnov AN, Petrikov VD, Mamutin VV, Vekshin VA, Ivanov SV, Smirnov MB, Inushima T (1999) Experimental and theoretical studies of phonons in hexagonal InN. Appl Phys Lett 75:3297–3299
15. Liang LW, Tsen KT, Poweleit C, Ferry DK, Tsen S-WD, Lu H, Schaff WJ (2005) Non-equilibrium carrier transport in a high-quality InN film grown on GaN. Phys Status Solidi (c) 2:2289–2300

Combining Quality Function Deployment and TRIZ to Solve the Drainer Problems

Chia-Pao Chang and Ying-Hsiang Lin

Abstract A drainer is a very common article in a bathroom or balcony. Wherever the weep hole exists, there is always a drainer. But, the general drainer cannot obstruct cockroaches and stench from the drain. TRIZ method was used to resign and improve the stench and cockroaches problem in this study. In order to solve previous problem, we use quality function deployment (QFD), tech/physical contradictions, and invention principles to find the key point problems and improve them. This study adds a light float in the drainer. When water pours into the drainer, the float in the drain will be opened by water buoyancy. Contrariwise, when water flows out, the float and drain close directly by gravity. Therefore, this drainer can effectively keep from insect pests and bad odor, no matter the water exist or not.

Keyword Quality function deployment • Tech/physical contradictions • Invention principles

1 Introduction

The main function of a drainer is to drain off water. However, the long-term use of water pipes or the connection and integration of drainage pipes of the apartment buildings can easily result in odors and the breeding of mosquitoes, cockroaches, and moldy gases, having a considerable adverse impact on environment quality.

In response to the above mentioned needs and problems, types of drainers have been developed and marketed as briefly summarized as below:

1. *The traditional water trap drainer*: The disadvantage is that the water in the trap will dry if the drainage hole has not drained off water for a long time. As a result,

C.-P. Chang (✉) • Y.-H. Lin
Department of Industrial Engineering and Management, National Chin-Yi University of Technology, Taichung, Taiwan, R.O.C.

the pest control and deodorant functions will be gone. Therefore, this type of drainer is not suitable for being installed in holes that do not drain off water frequently.

2. *The manual-type drainer*: The opening and closing of the drainer is manually adjusted and its disadvantages are:

   (a) Manual
   (b) Completely unable to block odors, which may also come in if it is left open unintentionally
   (c) Requiring regular cleaning as there may be scaling between two layers of iron pieces

3. *Water falling-type drainer* (*spring door*): By using the gravity, it will open if the weight of the water has reached the threshold level. It closes when there is no water flow and thus it can effectively prevent odors and pests. The disadvantages are that the water flow will be very slow and it requires regular cleaning. Hence, it is suitable for places of little drainage. Moreover, although the pest control effects are very good, it cannot prevent odors as it is contained by spring and rubber. The elasticity of rubber and spring will lose to create gaps. As a result, the odors will come out.

4. *Water seal-type drainer*: Water seal-type drainer has a built-in water trap. The functions of the water trap include pest control and odor prevention. However, the amount of water is not high and the water will dry up within 1 or 2 days. As a result, the water seal will dysfunction and the foreign matters will produce smell.

TRIZ theory provides a complete set of creative thinking models and tools that can quickly and efficiently solve the problem. In this study, we use 39×39 contradiction matrix of TRIZ and 40 inventive principles to solve the common problems of drainer in each household for an improvement plan.

2 Research Method

After the observation of many invention-related issues in the innovation process, Altshuller summarized the first breakthrough discovery, the technical contradiction. The so-called technical contradiction means when the innovator attempts to improve a technical system parameter A, it will result in the worsening of parameter B. For example, when reducing the product weight can make the product lighter and easier to carry, it will also make the product thinner and more fragile. When using better replacement material, the cost will increase. The TRIZ innovative invention is a new way of thinking which is beyond the contradiction to allow the two contradictory parameters to develop in the positive direction [1].

2.1 Research Process

The issues of an object were identified firstly and then the technical contradictions were found out. After learning the technical contradictions, we then can develop the 39×39 contradiction matrix in search of the 40 inventive principles that can possibly solve the technical contradiction. Next, the feasible 40 inventive thinking solutions and logic thinking are employed to consider the listed programs and select the most appropriate solution to solve the problem.

2.2 Quality Function Deployment

Quality function deployment (QFD) is a "method to transform user demands into design quality, to deploy the functions forming quality, and to deploy methods for achieving the design quality into subsystems and component parts, and ultimately to specific elements of the manufacturing process," as described by Dr. Yoji Akao, who originally developed QFD in Japan in 1966, when the author combined his work in quality assurance and quality control points with function deployment used in value engineering. QFD helps transform customer needs (the voice of the customer [VOC]) into engineering characteristics (and appropriate test methods) for a product or service, prioritizing each product or service characteristic while simultaneously setting development targets for product or service [2].

2.3 Contradiction Matrix

Altshuller observed each technical contradiction and developed a system accordingly. The first system regarding innovation and invention is known as the contradiction matrix. When studying a patent, he would confirm and sum up the technical contradictions and the applied innovative inventive principles for this patent. Based on the summaries of a large number of patents, he summed up 39 engineering parameters and 40 innovative inventive principles and developed the 39×39 matrix, which is a matrix using i to represent the improved characteristic and j to represent the avoidance of worsening result.

Each box grid represents a type of inventive problems, and each inventive problem has corresponding i and j coordinates. In the box grid of specific i and j, there are identification codes of inventive principles to solve the problems [3, 4].

2.4 Forty Inventive Principles

Forty principles provide TRIZ users a way of thinking from principle to application. Each inventive principle is a simple basic concept, and the derived thoughts from

the principle can cover a wide range. Different principles' layers and details can produce different architectures and contents. Each principle and thought can empower the innovator with new answers, "think about each principle and then find out the answer" [5].

3   Actual Case of Improved Design

A drainer plays an important role in each household. Although it is inconspicuous, it is essentially important. The traditional drainer design does not prevent insects and pests. Therefore, the drainer design should be improved to address the above two problems. In this way, there will no cockroach or smell that may disrupt the living environment.

3.1   Knowing Improving Direction by Performing QFD

According to the weights of executing QFD, the rank of quality characteristics was shown as follows: (1) practicability 3.069, (2) structure complexity 1.619, (3) size of top lid 1.123, (4) convenience 0.913, (5) size of passageway 0.90, (6) area of top lid 0.77, (7) easy disassemblies 0.596, (8) durability 0.59, and (9) inside materials. Therefore, there are three key points to improve drainers: First is practicability, second is water flow rate, and the final is disassemblies of parts.

3.2   Technical Contradiction of the Improvement Case

The main purpose is to improve the drainer design to prevent cockroach and foul smell from entering the living environment via drainer, in other words, to increase the drainer productivity. The best method to realize this purpose is to increase the blocking of the drainer to separate the drainage pipes and the living environment to prevent any channel to the living environment. However, the blocking of the drainer channels will affect the smooth drainage. Such changes are not expected; therefore, the existing technical contradictions are as follows: the technical contradiction 1: "system complexity" vs. "easy to operate and use."

   The technical contradiction 2: "productivity" vs. "system side effect."

3.3   Development of Contradiction Matrix

As shown in Table 1, the appropriate *i* (improved characteristic) and *j* (avoidance of worsening result) are found in the matrix. No. 36 column is "system complexity"

Table 1 Drainer design case's contradiction matrix

The avoidance of worsening result (*j*)		1	...	31	...	33	...	39
Improved characteristic (*i*)		Weight of the moving object	. . .	System side effect	. . .	Easy to operate and use	. . .	Productivity
1	Weight of the moving object							
. ..	. ..							
36	System complexity					15, 25, 23		
. ..	. ..							
39	Productivity			3, 7, 10, 15				

and No. 39 column is "productivity," while No. 31 row is "system side effect" and No. 33 row is "easy to operate and use." The table presents contradiction 1 "system complexity" and "easy to operate and use" and contradiction 2 "productivity" and "system side effect," and the box grids of intersecting columns and rows represent the principles that can be used to solve the existing contractions.

According to the analysis of the feasible improvement concepts and programs based on the recommended principles, it is preliminarily concluded by assessment that No. 3 principle "local quality," No. 7 principle "overlay architecture," No. 10 principle "pre-role," and No. 15 principle "dynamic" are the best suggestions that can be improved by current technologies.

3.4 Thinking and Improvement

First, No. 3 principle "local quality" should be taken into consideration to allow the functionality of each part of the system to reach the optimum state (local). Regarding how to isolate the drainage pipes and the living environment, No. 10 principle "pre-role" should be considered to place the object or system in advance to function at the most convenient time and place. It is recommended to introduce a certain object to realize the isolation of the drainage pipes and the living environment in advance. Next, by following No. 7 principle "overlay architecture," an object or a system is placed inside another object or system. Regarding the matter or object that can isolate the drainage pipes and the living environment, we can introduce a plug to isolate the drainage pipes and living environment to realize the function of preventing cockroach and foul smell.
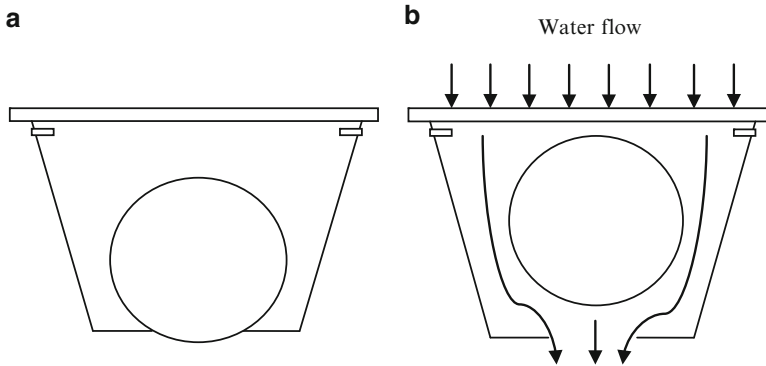
Fig. 1 Inside of the drainer in case of (**b**) with and (**a**) without water

According to No. 15 principle "dynamic," the freedom of movement capabilities should be enhanced. Under different conditions, the object or system characteristics should be able to (automatically) change to realize the optimal effects. In case of having no water, the plug should be able to block the drainage holes to realize the function of isolating the drainage pipes and living environment. However, when there is water, it should be able to smoothly drain off the water. The issue of switching the two functions of the drainer should be considered to find out the key.

After taking advantage of the buoyant force, a drainer device was designed. In the drainer, the plug object floating ball is installed. In usual situation without water (Fig. 1a), the floating ball can completely block the drainage holes to isolate drainage pipes and living environment. When the drainer is draining off the water (Fig. 1b), the floating ball will float due to the buoyant force of the water. The floating ball will expand under the buoyant force without blocking the drainage holes to realize the function of smooth drainage.

4 Conclusions

TRIZ innovation theory can be applied in a lot of things, not just only one product. It can be applied to many things. Regardless of what industry, problems will arise inevitably. The understanding and learning of TRIZ is like the opening of an extra window, and you can have a wider vision than others. It can guide us to quickly find where the problem lies, to analyze problems, identify the key, and then employ the thinking logic of TRIZ before taking appropriate solutions. By the method of a design process and the concept of logical thinking provided by TRIZ, this study explores the feasibility to solve the problems in improvement design by the

procedure from considering the problem to solving the problem. The characteristic of water buoyancy is employed to improve the drainer to realize the functions of preventing insects and pests like cockroach or the foul smell of drainage pipes from entering the household through drainage pipes via drainer to cause adverse impact on living environment and smoothly draining off the water, making the drainer of improved design to have new concepts.

References

1. Darrell M (2007) Hands-on systematic innovation for business & managers. IFR Press, Clevedon, pp 4–5
2. QFD Team of China Productivity Center (1992) The application of quality function deployment. China Productivity Center
3. Darrell M (2007) Hands-on systematic innovation for business & managers. IFR Press, Clevedon, pp 117–119
4. Clarke DW Sr (2005) 40 principles extended edition: TRIZ keys to technical innovation. Technical Innovation Center, Worcester, pp 11–13
5. Clarke DW Sr (2005) 40 principles extended edition: TRIZ keys to technical innovation. Technical Innovation Center, Worcester, pp 17–18

A Study on Improving Polishing Process Effectiveness for Silicon Reclaim Wafer

Chia-Pao Chang, Wei-Ling Wang, and Yung-Ching Kuo

Abstract   In this study we improve the capacity of the polishing process of silicon reclaim wafer by applying the six sigma approach and the five steps of DMAIC. Based on the Taguchi experiment approach, a four-factor three-level experiment is designed by experimental design method using the existing polishing parameters, in particular such processing conditions as the cylinder head down force of the main process section, the PP rpm, LP rpm, and the flow of polishing slurry. The four factors are as follows: cylinder head down force, PP rpm, LP rpm, and the slurry flow. By studying the correlation between various parameters in the polishing process and the polishing result, the polishing factors' effect on the material removal rate (MRR) and wafer's total thickness variation (TTV) after the polishing process is analyzed, to obtain the optimized parameters for the improvement of the quality of polishing process and enhancement of process yield rate.

Keywords   Silicon reclaim wafer • Polishing process • Taguchi experiment method

1   Introduction

With the rapid development of semiconductor processing technology, that is, very-large-scale integration (VLSI) circuit, especially the continuous improvement of the processing technology of the 12-in. (300-mm diameter) silicon wafer, the quality of over 100 processes during the manufacturing process of the semiconductor IC has to be ensured, as any change in parameters of each process has great influence on the final yield rate of the wafer production. To make sure each process is strictly monitored, lower-cost testing wafers have to be used to ensure correctness of the process parameters and guarantee the yield rate of production.

C.-P. Chang (✉) • W.-L. Wang • Y.-C. Kuo
Department of Industrial Engineering and Management, National Chin-Yi University of Technology, Taichung 41170, Taiwan, R.O.C.

Therefore, reclaim wafers made of recycled control wafers and dummy wafers are used. The most important polishing process among the silicon reclaim wafer processes (chemical mechanical polishing, CMP), or the planarizing technique of the chemical mechanical planarization process, is an anisotropic etching technique in the domain of mechanical function. The basic principle of the polishing process is mainly to pour the polishing slurry onto the PU pad of the polishing machine for polishing action on the wafers. The objective of the process is to remove the oxidized materials on the surface and planarize it to reduce the extent of defects and TTV of the wafer.

Nonetheless, as the size of wafers is becoming larger, it is a greater challenge to achieve the high-precision silicon wafer processing technique even in a single process of treating the large-size silicon wafer surface. Furthermore, the requirement to improve the wafer quality after the polishing process and enhance the yield rate is an even more important concern of the manufacturers of silicon wafer semiconductor. In order to ensure the precision of silicon wafer surface processing, two-step (rough polishing and refine polishing) or three-step (rough polishing, fine polishing, and final polishing) or four-step (rough polishing, fine polishing, refine polishing, and final polishing) processing will be carried out [1].

In the chemical mechanical planarization (polishing) of the wafer semiconductor processing, chemical mechanical polishing slurry in the form of acid or alkali fluid that contains suspended abrasive particles, oxidant, and active agent is poured between the rotary work bench carrying the silicon wafer on one side and the polishing pad on the other side, so that the polishing pad is rotating against the wafer, and hence global planarization is achieved through the alternative action of the chemical etching and the removal mechanism that grinds the two materials. Many defects on the surface of the wafer are removed in the polishing process, and thus it helps improve the product yield rate. However, some defects will be created during the process as well, such as scratches, residual slurry, particles, erosion, and dishing [2].

Preston equation has always been used to describe the relationship between polishing speed and pressure, as expressed below:

$$\text{R.R.} = K\text{p}(PV) \tag{1}$$

In the equation, R.R. means removal rate, Kp is a constant, P represents the down force on the polishing surface, and V is the sliding speed between the polishing surface and the polishing pad. Polishing rate will increase with the rise in pressure and rotational speed [3].

Chemical mechanical polishing slurry is composed of fine suspended colloidal silica that contains SiO_2 and $NaOH$ (or KOH, NH_4OH, HNO_3) or other organic acid. The SiO_2 particle size, concentration, and pH value in the slurry are the major factors that affect the removal rate and quality of polishing. And the mechanical reaction mechanism means the removal of the oxidized layer with the mechanical friction between the polishing pad, colloidal silica, etc., and the wafer, and it also provides the kinetic source for corrosion oxidation [4].

2 Research Method

In this study, relevant literature of both domestic and overseas research was compiled, and a certain wafer manufacturer was taken as example, using the DMAIC steps and experimental design analysis. Results of the experiment were provided as a reference for improvement of the process.

2.1 Defining the Question

By observing the result of the daily monitored MRR of the polishing process by the 12-in. wafer polishing machine SpeedFam, it was found that the MRR had a declining trend. Controllable factors that affect the polishing process were analyzed, after eliminating the effect of other uncontrollable factors.

2.2 Measurement

Among the parameters of the rough polishing process, major processes that affect the polishing result are the cylinder head down force, PP rpm, LP rpm, and slurry flow. The process may be divided into six processing sections (by time). As a basic concept of polishing, the chemical mechanism and mechanical mechanism of polishing have the best result under high temperature (low slurry flow) and high pressure.

2.3 Data Analysis

Table 1 shows the experimental factors and levels. As the original pressure setting of the main processing section (the fourth section is defined as the main processing section due to the largest pressure and longest polishing time) was down force setting at 230 kg, the maximum down force was set at 250 kg considering the load of the machine. Maximum slurry flow was set at 8 L/min, and maximum PP rpm and LP rpm range at 60 rpm.

In this study the polishing pad model used in the experiment was SUBA-800 50″D PS, and the slurry model was BINDZIL 999. The thickness of test film collected was 760–780 um, and TTV was measured before and after polishing. The cylinder head with non-crystallized surface and relevant polishing consumables were replaced with new ones, and the slurry was also replaced with new slurry after completion of each production lot on a component ratio of 1:20 (slurry:DI). Polishing experiments were carried out according to the experimental configuration parameters in the L9 (3^4) orthogonal arrays, together with a brand-new rough

Table 1 Experimental factors and levels

Level factor	Controllable factor	Level 1	Level 2	Level 3
A	Down force (kg)	210	230	250
B	Slurry (L/min)	4	6	8
C	L.P. (rpm)	40	50	60
D	P.P. (rpm)	60	50	40

Then, the L9 (3^4) orthogonal arrays were used to configure the 9 sets of experimental parameters
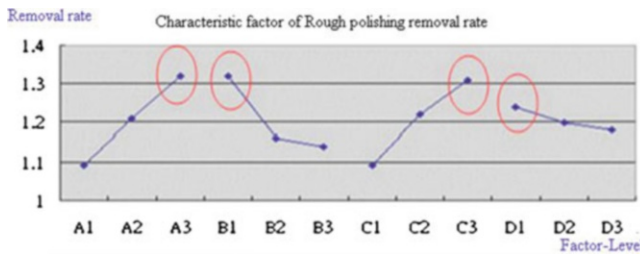
Fig. 1 Characteristic factor of rough polishing MRR

polishing pad. The central removal rate was largest when the processing down force was higher (250 kg), slurry flow was lower (4 L/min), LP rpm was faster (60 rpm), and PP rpm was faster (60 rpm). (1) When the slurry flow is higher, the change in central removal rate is not significant. (2) When the PP rpm becomes slower, the change in central removal rate is not significant. (3) Processing pressure and LP rpm are the controlled factors that have the most significant effect on the change of the central removal rate.

The effect of cross multiplication of various controlled factors on the TTV divergence was concluded: (1) Change in TTV is the smallest when the processing pressure is higher (210 kg), slurry flow is higher (6–8 L/min), LP rpm is slower (40 rpm), and PP rpm is slower (40 rpm). (2) Change in TTV is not significant when the processing pressure becomes higher. (3) Change in TTV is not significant when the slurry flow becomes higher. (4) LP rpm and PP rpm are the controlled factors that have the most significant effect on the change of TTV.

2.4 Improvement

The MRR and geometric accuracy difference ($\triangle$TTV) of various factors and levels were calculated according to the above-mentioned nine sets of experimental parameters, and the resulting data were plotted on the cause and effect diagram like Figs. 3 and 4, for determination of various polishing factors' influence on the MR and TTV of rough polishing. Figure 1 shows the polishing factors' influence on the MRR of rough polishing: (1) Factor A: Large, processing temperature becomes relatively higher. (2) Factor B: High, greater removal mass, but the effect of greater

slurry flow on the removal mass is not significant. (3) Factor C: The faster the LP rpm, the higher the processing temperature, and the greater the removal mass. (4) Factor D: Removal mass is largest when PP rpm is at 60 rpm, but its effect on the change of removal rate is not significant. Therefore, the combination of levels that meets the larger the better (LTB) criterion of MRR is A3B1C3D1 (down force, 250 kg; flow, 4 L/min; LP rpm, 60 rpm; PP rpm, 60 rpm).

The polishing factors' influence on the geometric accuracy (TTV) is described as follows: (1) Factor A: Change in TTV is smallest when the down force of the main process is at 210 kg, and the processing temperature is low. (2) Factor B: The smaller the slurry flow, the higher the processing temperature, and the bigger the TTV change, but the effect of greater slurry flow on TTV is not significant. (3) Factor C: The lower the processing temperature, the smaller the TTV change. (4) Factor D: Change in TTV is smallest when PP rpm is at 40 rpm, but the processing temperature is high. Therefore, the combination of levels that meets the smaller the better (STB) criterion of △TTV is A1B2C1D3 (down force, 210 kg; flow, 6 L/min; LP rpm, 40 rpm; PP rpm, 40 rpm).

2.5 Control

The above experimental results were introduced to the change in the processing parameters, and the process stability was monitored by the polishing statistical process control (SPC) approach. Moreover, polishing stability was observed and maintained through the inspection items of the machine for the polishing process, for example, PH value of slurry and processing temperature calibration at the machine. When the observed data have reached stable levels, these process parameters may be established as standardized operational processing criteria, to ensure the control of the parameters and the normal operation of mass production.

3 Results

After adopting the new parameters, the mean value of MRR increases from 0.96 to 1.15 (Fig. 2), and the trend of △TTV transforms from divergent to convergent (Fig. 3).

4 Conclusion

The DMAIC steps of the six sigma approach were used in this study for improvement of the polishing process parameters for silicon reclaim wafers. A four-factor three-level experiment was designed by means of experimental design method, and the effect on the removal rate and change in wafer thickness after the polishing process
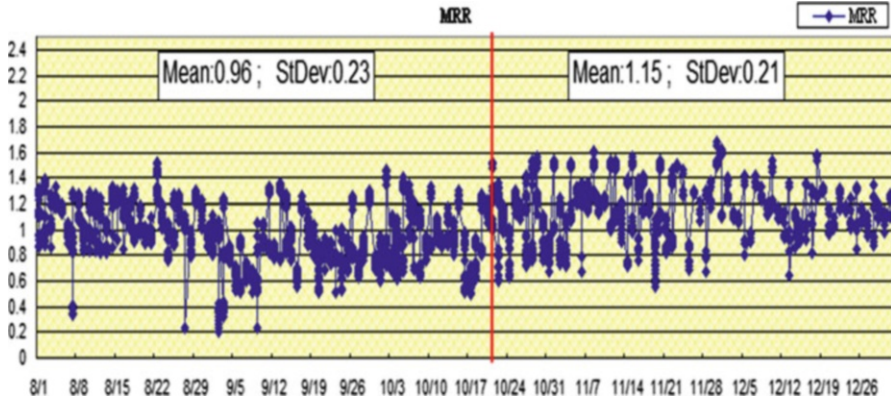
Fig. 2 MRR before and after changing processing parameters
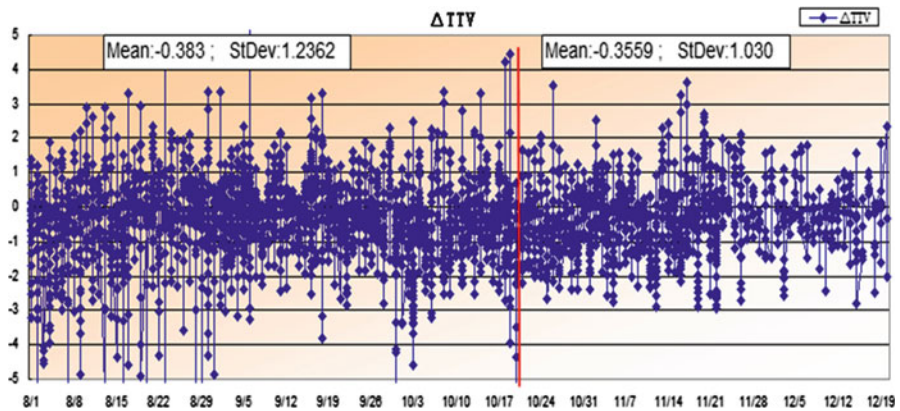
Fig. 3 TTV before and after changing processing parameters

was considered. It is known from the research results that the optimized parameters of the polishing process are down force setting at 230 kg, slurry flow at 5 L/min, LP rpm at 50 rpm, and PP rpm at 50 rpm during the polishing process stage, so that the MRR and TTV stability of the process may be improved.

References

1. Chang JC (2009) The manufacturing technology of silicon wafers. Chemistry Industry Publishing Ltd.
2. Hong X (2002) Introduction to semiconductor processing technology. Pearson Education
3. Chou SW (2005) A study of the dynamic and static mechanical properties of The CMP Pad. Master thesis. National Tsing Hua University, Hsinchu City

4. Chiu JB, Su AJ, Yu CC, Shen SH (2004) Planarization strategy of Cu chemical mechanical polishing: interaction between plated copper thickness and removal rate. J Electrochem Soc 151:G217–G222
5. Li MS (1999) Materials technology of silicon wafers. Chuan Hwa Publishing Ltd.
6. Singh RK, Bajaj R (2002) Advances in chemical-mechanical planarization. MRS Bull 27:743–747
7. Patrick WJ, Guthrie WL, Standley CL, Schiable PM (1991) Application of chemical mechanical polishing to the fabrication of VLSI circuit interconnections. J Electrochem Soc 138:1778–1784
8. Preston FW (1927) The theory and design of plate glass polishing machines. J Soc Glass Technol 11:214–256

Detection of CO Concentration by Using SnO$_2$ SPR Apparatus and Common-Path Heterodyne Interferometer

Ke-Ming Chen, Chih-Hsiung Shen, and Jing-Heng Chen

Abstract A conception by using integration of chemical microsensors and surface plasmon resonance (SPR) is proposed to sense carbon monoxide (CO). The research is based on the common-path heterodyne interferometer which contains nondestructive, high-sensitivity, and high accuracy optical sensing system and combines the tin dioxide which is chemical stability to sense CO as analyte of SPR. Under this configuration, the method can measure tiny phase differences for SnO$_2$ with different CO concentration. The minimum resolution of gas concentration is verified with a best value of 0.0207 ppm occurring in pH 9.

Keywords SPR • SnO$_2$ • Carbon monoxide

1 Introduction

Carbon monoxide (CO) gas sensing is an important technique applied to detect CO concentrations in domestic and industrial environments and especially in the underground rapid transit system. Several methods had been proposed for the purpose. Recently, an attractive approach has been proposed by integrating surface plasmon resonance (SPR) apparatus and chemical sensing film. The applied sensing materials can significantly determine the sensitivity and selectivity of detected combustible, toxic, and pollutant gases. Metal oxide compounds, such as SnO$_2$ and SnO$_2$-TiO$_2$, have been utilized as sensing materials for detection of carbon monoxide [1]. The tin dioxide (SnO$_2$) has become a primary choice due to its high sensitivity, good stability,

K.-M. Chen (✉) • C.-H. Shen
Department of Mechatronics Engineering, National Changhua University
of Education, Changhua 50007, Taiwan
e-mail: m0151017@mail.ncue.edu.tw

J.-H. Chen
Department of Photonics, Feng Chia University, Taichung 40724, Taiwan
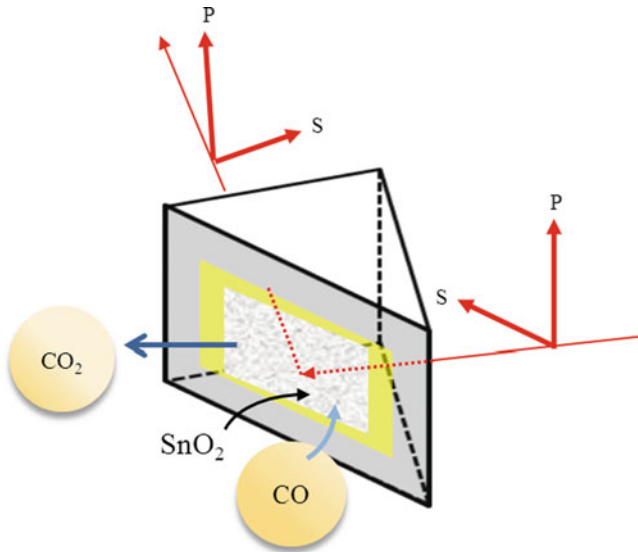
Fig. 1 The schematic diagram of the experiment

and low cost. Over two decades, the phenomena of SPR have been widely applied for detection of biomedical and chemical reactions because of its high-sensitivity, label-free, real-time response. In these applications, the refractive index variations of analyte coated on golden film are concerned. Several SPR techniques are implemented by measuring the intensity, wavelength, and phase of reflected detection light [2]. However, the environment vibrations and light source intensity stability can influence the measurement results.

Accordingly, in this research, we propose a new method for carbon monoxide gas sensing by combing a common-path heterodyne interferometer [3] and SPR apparatus coated with a film of tin dioxide. In order to show the feasibility of the method, different pH values of prepared SnO_2 were investigated to obtain an optimal condition. Relations between carbon monoxide concentration and the phase differences were obtained. The experimental results show that pH value of 9 gives a highest sensitivity and best measurement resolution in CO concentration (Fig. 1).

2 Principle of Sensing Mechanism

2.1 SPR System Setup

We proposed a sensing mechanism for gas concentration detection with SPR which is based on the changes of analyte dielectric constant. There is a schematic diagram of the optical setup of SPR used in this research, as shown in Fig. 2. The laser passes
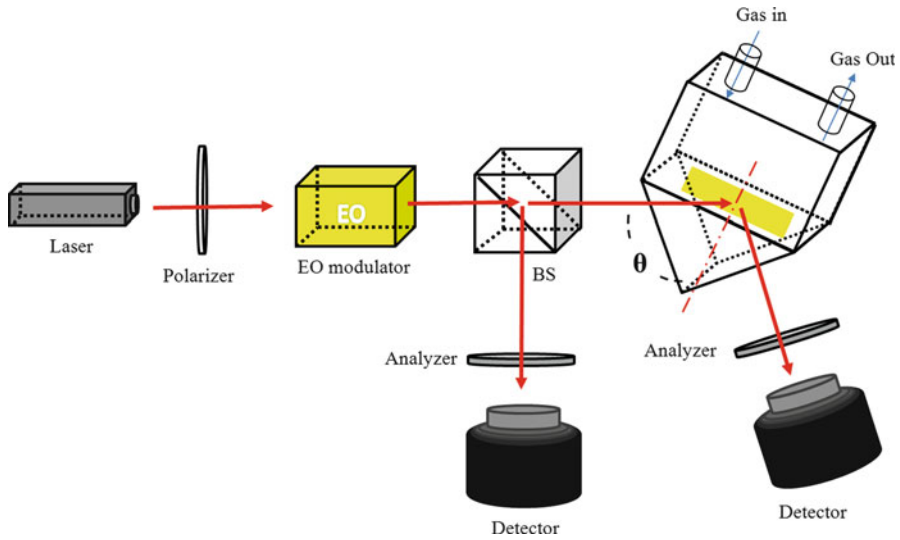
Fig. 2 The configuration of common-path heterodyne interferometry

through the polarizer which can adjust the relative magnitude of the p and s wave components to change the beam into linear polarized light. The linear polarized light acts as a heterodyne light source by electro-optic modulator. The heterodyne light enters the center of beam splitter and is divided into reflection and transmission lights. On the other hand, the transmission light is impinged on the analytes that cause refractive index changes by the gas concentration and gives phase differences between p and s waves. The higher gas concentration gives larger phase differences. Finally, both reflection and transmission light travel through an analyzer which is at 45° with respect to x-axis and enter into photodetectors. Therefore, gas concentration can be measured accurately by the common-path heterodyne interferometry [3].

2.2 Surface Plasmon Resonance

Surface plasmon resonance (SPR) is described as an electromagnetic wave that propagates along the surface of a thin metal layer, and the wave may produce a surface plasmon. It is the density of longitudinal electric charges that shakes the phenomenon and usually stimulates photon and phonon by the optical structure and then arouses the vibration of free electrons shaking to generate surface plasmon wave [4]. The approach is based on prism couplers with Kretschmann mode to excite the surface plasmon. Surface plasmon resonance is the result of optical excitation of a surface plasmon wave along the interface between a highly

conductive metal and a dielectric material [5]. The TM-polarized wave vector of the surface plasma wave can be expressed as follows:

$$k_{sp} = \frac{\omega}{c} \sqrt{\frac{\varepsilon_m \varepsilon_a}{\varepsilon_m + \varepsilon_a}} \tag{1}$$

where ω is the frequency of the incident wave, c is the speed of light, ε_m is the dielectric constant of the metal, and ε_a is the dielectric constant of the analyte.

The structure had coated a metal layer on the corner of the right angle prism, and the metal film thickness is d. For convenience, we will set Sample 1 as prism, Sample 2 as metal film, and Sample 3 as analyte; those reflective indexes are, respectively, n_1, n_2, and n_3. Surface plasmons will be excited when the linear polarizer polarized the incident light into the resonance angle of SPR. The reflection coefficient of p- and s- polarized light can be expressed as

$$r_q = \frac{\left(r_{12}^q + r_{23}^q e^{i2k_z d}\right)}{\left(1 + r_{12}^q + r_{23}^q e^{i2k_z d}\right)}, q = p, s, \tag{2}$$

where r_{12}^q and r_{23}^q are according to the Fresnel's equations, k_z is z-propagating wave vector of incident light in Sample 1, and k_0 is the vacuum wave vector. Therefore, the phase differences between p and s polarizations of the reflection light at the boundary of a surface plasmon resonance can be expressed as [6]

$$\varphi = \arg(r_p) - \arg(r_s). \tag{3}$$

The sensitivity of gas concentration is defined as

$$S = \frac{1}{\varphi} \frac{\partial \varphi}{\partial C} = \frac{1}{\varphi} \left(\frac{\partial \varphi}{\partial K_{sp}} \frac{\partial K_{sp}}{\partial \varepsilon_a} \frac{\partial \varepsilon_a}{\partial C}\right) = (S_s \cdot S_C), \tag{4}$$

where C is the gas concentration, $S_s \left(= \frac{1}{\varphi} \left(\frac{\partial \varphi}{\partial K_{sp}} \frac{\partial K_{sp}}{\partial \varepsilon_a}\right)\right)$ is the system sensitivity, and $S_c \left(= \frac{\partial \varepsilon_a}{\partial C}\right)$ is the sensitivity of material.

3 Experimental Results and Discussion

The phase differences concerning surface plasmon resonance of carbon monoxide sensing is measured under the common-path heterodyne interferometer structure. The gold film is coated on the corner of the right angle prism, because it is much more stable than other metals. We place the prism on 4-axis rotation stage whose resolution is 0.0025° (SHOT-204MS, Sigma Koki, Inc.) and set the incident angle in 64.25° which is in the resonance angle. The sensing material SnO_2 prepared
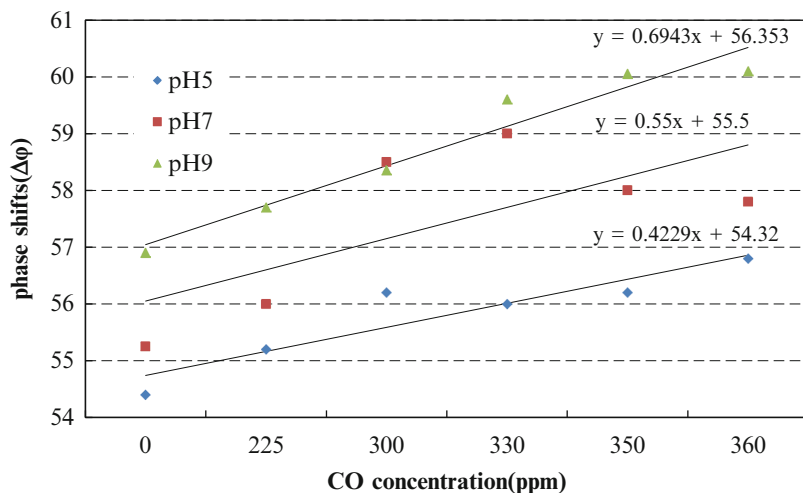
Fig. 3 The relation between CO concentration and phase shifts

using SnCl$_4$·5H$_2$O diluted in water and then mixing with aqueous solution of NH$_4$OH promotes the hydrolysis and condensation with deionized water and ammonia. After the solution aging for 12 h, the solution will precipitate, and then the fabricated of SnO$_2$ have been done. The sensing film would be spin coated on the outside of the metallic film with the first turn 500 rpm 10 s and the second turn 1,200 rpm 25 s and heat at 90 °C for 1 h and 20 min.

The laser passes through the polarizer and then the laser experiences spatial phase retardation by electro-optic modulator (Mode 4002, New Focus) which is driven by function generator. The laser is split into two beams by a beam splitter. The reflected light passes through an analyzer and then enters a photodetector as a reference signal. The transmission light enters in the prism to excite the SPW. While light leaves the prism, the phase changes on account of the SnO$_2$ film. At last, the transmission light passes through an analyzer and then enters a photodetector as a test signal. Ultimately, we can analyze the signals by DAQ lock-in-amplifier (USB-6259 BNC, Compact DAQ, National Instruments) on computer.

The phase would alter from the changes of SnO$_2$ refractive index. While the chamber fills with the CO gas, SnO$_2$ will react with the carbon monoxide. The electrical property would be changed when the surface of SnO$_2$ is exposed to the CO gas. SnO$_2$ would release electron to push reducing reactions of CO. The reducing reactions from CO$_2$ and the electrons are injected into SnO$_2$ [7]. As a result, the refractive index of SnO$_2$ changes along with the phase shifts.

According to above descriptions, we aim to measure phase shifts based on the changes of SnO$_2$ which is sensitive to carbon monoxide. After being measured on the proposed experimental condition, the relation of phase shifting caused by CO concentration changing is sketched in Fig. 3. As the concentration of CO increases, the refractive index of SnO$_2$ decreases. As the different pH value, the minimum

resolutions are 0.0236°, 0.0182°, and 0.0144° corresponding to the pH values 5, 7, and 9. Moreover, the minimum resolutions of gas concentration detection are derived as 0.0558, 0.033, and 0.0207 ppm which are highly sensitive than other research works.

4 Conclusions

Tin dioxide has been used for CMOS MEMS as sensing materials; sometimes, it would mix with some molecules to increase the sensing capability. Under surface plasmon resonance system, we can measure the changes of SnO_2 film easily, because of its high-sensitivity and low-resolution measurement. Furthermore, the integration of surface plasmon resonance and common-path heterodyne interferometer enhances stability that can avoid the external perturbation from environment.

Eventually, the experimental results show that the resolutions are 0.0558, 0.033, and 0.0207 ppm corresponding to pH 5, pH 7, and pH 9 [8]. This experimental method is a novel approach which combines the surface plasmon resonance and common-path heterodyne interferometer to measure the gas concentration by chemical sensing film. Through observing the influence when SnO_2 is exposed to the carbon monoxide, we can demonstrate the relation between phase shifts and concentration. This measuring system could be extended more thoroughly in the predictable future.

References

1. Po-Hao Hsu, Meng-Hung Tsai, Chih-Hsiung Shen, Shu-Jung Chen (2010) A new approach of thermal type microsensor with photonic crystal
2. Nelson SG, Johnston KS, Yee SS (1996) High sensitivity surface plasmon resonance sensor based on phase detection. Sens Actuators B Chem 35(1–3):187
3. I-Hsuan Shao, Chih-Hsiung Shen, Jing-Heng Chen (2011) A new measurement architecture of thermal properties of electronic film based on surface plasmon resonance of common-path heterodyne interferometer
4. Stemmler I et al (1999) Sens Actuators B 54:98–105
5. Nelson SG, Johnston KS, Yee SS (1996) High sensitivity surface plasmon resonance sensor based on phase detection
6. Kun-Huang Chen (2004) The principle of surface plasmon resonance heterodyne interferometer and its applications
7. Hsu-Pei Chen, Chun-Ming Cheng, Chih-Hsiung Shen, Shu-Jung Chen (2011) A new stack electrode type CMOS compatible gas sensor

8. Ming-Ji Tsai (2012) Study on sensitivity-tunable optical humidity sensor based on total internal reflection
9. Homola J, Koudela I, Yee SS. Surface plasmon resonance sensors based on diffraction gratings and prism couplers: sensitivity comparison
10. Maier SA (2007) Plasmonics fundamentals and applications. Springer, New York
11. Salamon Z, Tollin G (1999) Surface plasmon resonance, applications

Magnetic Field Correction Based on Intelligent Shimming Method

Jui-Che Huang and Ching-Shiang Hwang

Abstract An APPLE-II elliptically polarized undulator (EPU) is commonly used in third-generation electron accelerator storage ring to provide varied polarization soft X-ray. When electron beam passes through an undulator, the radiation is generated and collimated. In order to have high photon flux, these collimated photons need to be coherent. Therefore, prefect magnetic fields are necessary for electron beam trajectory and phase. EPU46 consists of 1,320 magnet blocks to create sinusoidal magnetic field, and four-phase modes generate various polarization on synchrotron soft X-ray. The objective functions are to minimized electron trajectory/angle deviation and phase error. Without intelligent optimization method, field correction becomes a tedious and time-consuming work. In this chapter, a field shimming adapted with Genetic Evolutionary algorithm is developed; the methodology and results are presented.

Keywords Elliptically polarized undulator • Magnetic field correction • Genetic Evolutionary algorithm

1 Introduction

An insertion device is a key component in modern third-generation synchrotron light sources. Elliptically polarized undulator is one of insertion device type to stimulate highly brilliant, forward-directed synchrotron radiation emission by forcing a stored charged particle beam. For a soft X-ray beamline, an "APPLE-II" EPU has the widest range of tunable energy and a large rate of circular polarization for a synchrotron light source. Therefore, NSRRC decided to install an elliptically polarized undulator of period length 46 mm (EPU46) in Taiwan Photon Source

J.-C. Huang (✉) • C.-S. Hwang
Magnet Group, National Synchrotron Radiation Research Center, HsinChu 300, Taiwan
e-mail: huang.juiche@nsrrc.org.tw

Table 1 Main parameters of EPU46

Type	Elliptically polarized undulator outside the vacuum
Magnet	Pure, Nd-Fe-B
Period	46 mm
Range of gap	$15 \leq G \leq 100$ mm
Maximum field strength	$B_y = 0.75$ T, $B_x = 0.43$ T
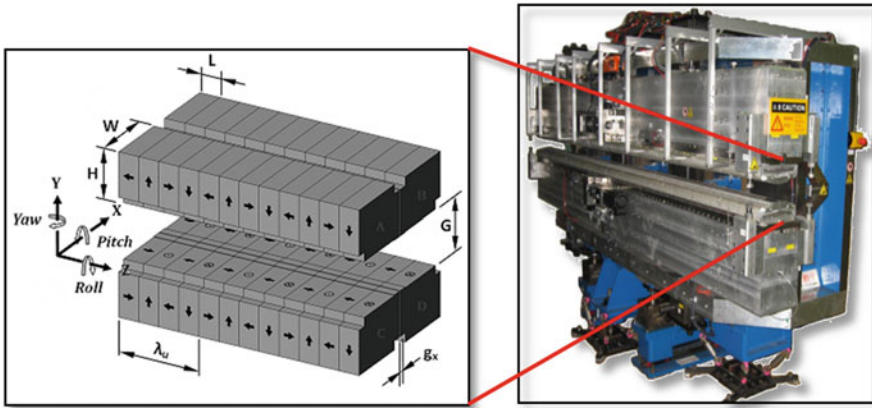
Fig. 1 Sketch of an EPU46 magnet array

(TPS) in 2013. This 4-m EPU46 is dedicated to provide great flux at photon energies between 0.30 and 1.5 keV. The key parameters of EPU46 are shown in Table 1.

To achieve high brilliant X-ray and high electron beam stability, magnetic field along the undulator is critical. Shimming techniques are commonly used in in-air undulator which adds the shim pads to correct the magnetic field and improved magnetic performance that will allow the use of higher photon energy range of X-ray with satisfactory flux intensity. Huang et al. [1, 2] specify procedures to manually correct magnetic field. By tuning the magnet blocks position, the magnetic field properties can be corrected. To correct the field of an EPU, two objective functions are concerned. One is r.m.s. electron trajectory, and the other is phase error in four-phase modes (Fig. 1).

2 Objectives Function and Impact Factors

Phase error is key objective function to calculate the phase with respect to idea value, and it is shown in Eq. 1; a large phase error results in a flux spectrum intensity smaller than the ideal case, especially in the high harmonics:

$$\phi(z) = \frac{2\pi}{\lambda_r} \left[\frac{Z}{2\gamma^2} - \frac{\int x'^2 dz}{2} \right],$$ (1)

in which x' is the angle that the electron makes with the undulator axis; it is rewritten as

$$x'^2(z) = \left(\frac{dx}{dz} \right)^2 = \beta_x^2(z') + \beta_y^2(z').$$ (2)

$\beta_{x,y}$ is the relative horizontal or vertical velocity of the electron, and λ_r is the radiation wavelength. Another objective function is r.m.s. trajectory. The trajectory is double integral of magnetic field along the longitudinal direction and shown in Eq. 3. Large r.m.s. trajectory means

$$\text{Trajectory of X, Y}(z) = \int \int B(y, x) dz.$$ (3)

2.1 First Field Integral Deviation

The deviation of the first field integral $(dI_{x,y}/<I_{x,y}>)$ at each half period was calculated in Eq. 4, and this is most crucial and basic parameter on the field properties. For example, if the deviation is accumulated along the longitudinal direction, this function ES (Eq. 5) will have a strong connection to the objective function, phase error. In the manually shimming procedures, the ES function reflects a positive or negative trend of the first field integral; one can readily determine whether the positive or negative first field integral has to be corrected. This is very effective method to reduce a large phase error value. The final condition of the deviation of the first field integral should be controlled within 0.5 %:

$$I_{n(x,y)} = \int_{Z}^{Z+\frac{\lambda_u}{2}} B_{x,y} dz,$$ (4)

$$\text{ES}(n) = \sum_{m=1}^{n} \left(\frac{\left| I_{n(x,y)} \right| - <I_{x,y}>}{<I_{(x,y)}>} \right)_m,$$ (5)

in which n indicates the nth pole.
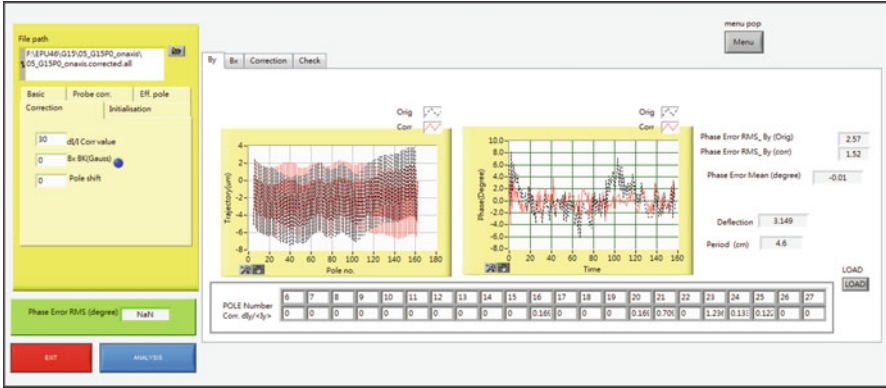
Fig. 2 User interface of field correction analysis program

2.2   Kicker Value

The kicker value explains how the extra first integral from the average results in the trajectory wander. In some case, a small variation of $dIx,y/<Ix,y>$ does not ensure a small phase error. From Eq. 1, the phase error depends on the angle that the electron makes with the undulator, and it is also related to the deviation of the trajectory length over a half period. Kicker value reflects the turning point of the trajectory, and the kicker value shall be minimized to keep straightness of electron beam trajectory;

$$Kicker = \frac{I_{n(x,y)} - (-1)^n < I_{x,y} >}{< I_{x,y} >} \tag{6}$$

Before applied to intelligent shimming method, a standard code of magnetic field analysis is developed in NSRRC. Analysis code will calculate trajectory, first integral field deviation, kicker, phase error, and all parameters related to undulators based on the magnetic field input. In order to manually correct the field, the relationship between shim pad thickness and first field integral deviation is required. The user has to correct the magnet pole with large kicker value based on its first integral deviation. To select the effective pole to straighten the trajectory and reduce the phase error is highly based on experiences, or user can try and error by using analysis code. Figure 2 shows the user interface of field correction program, and user can input the pole and shim pad thickness to predict the electron beam trajectory, phase error, and other parameters. However, this is still a time-consuming work.

To improve the efficiency of field correction, introducing an optimization process to the field correction is necessary. Many searching methods have been used, and Genetic evolutionary algorithms are regarded as one of the most efficient

methods and are widely used in engineering applications. Therefore, Genetic evolutionary algorithms adapt to magnetic field analysis code for intelligent field correction purpose.

3 Genetic Evolutionary Algorithm

Genetic Evolutionary algorithms (GEA) are inspired from natural selection and survival of the fittest in the biological world. GEA are inspired from natural selection and survival of the fittest in the biological world. Pedro and Fernando [3] used GEA in many intelligent control applications, and as a result, GEA can also provide an efficient search method to find optimized phase error from pole shimmed. Here details of how the GEA has been adapted for use with magnetic field analysis code and predictions for optimized combination are shown in Fig. 3:

1. Randomly create initial population (generation initial population).
2. Evaluate the individual fitness of the population (evaluation fitness).
3. Select pairs of best-ranking individuals to reproduce (select and weight).

   (a) Apply crossover operator for random chromosome exchange (crossover).
   (b) Apply random mutation for new child organism's chromosome (mutation).

4. Repeat steps 2 and 3.
5. Until terminating condition (iteration >1,000 or 50 successive iterations s no better solutions).
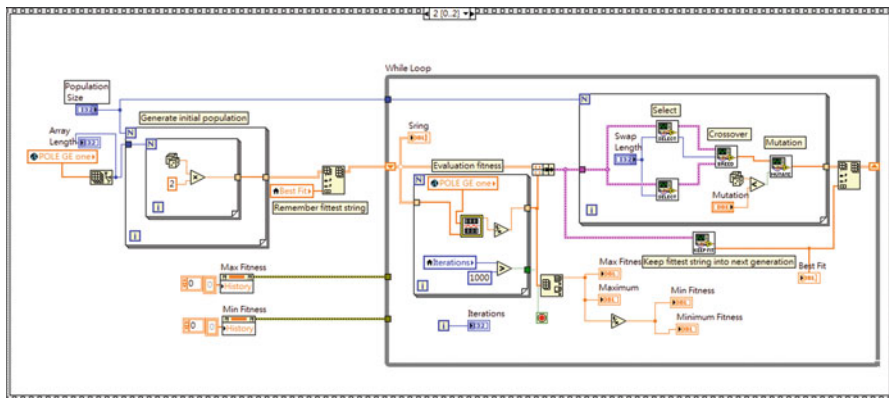
Fig. 3 Field correction adapted with Genetic Evolutionary algorithms

4 Results

The current work initializes 20 random samples of shimming pad thickness as a population. The individual fitness was evaluated by the field analysis code, and the smaller values of r.m.s trajectory/phase error were given a stronger position to be selected for the next generation. Swap length is set up at 5 and mutation rate is 0.1. Based on the kicker value, the criterion was first set up to be greater than 30, and there are 29 magnet poles that can be shimmed. In test one, all 29 poles need to be corrected and minimum phase error is 2.38. Second test corrected all 152 poles by GEA and no pole number limitation. The GEA can use all combination of 152 poles; however, there are only 48 poles that are shown to be corrected, and minimum phase error is 2.05 (Fig. 4 shows results). Results demonstrate that user shall use all 152 poles for intelligent shimming program and the program will not confuse user by giving a small shim pad thickness to be corrected.

All optimization methods are trying to find a global optimized solutions, sometimes it may end up with a local optimized solution. In order to improve this situation, the program will first use r.m.s. trajectory as an objective function, and the best solutions from GEA will bring it into second optimization process which uses phase error as an objective function. The results shown in Fig. 5, the correction will result in decrease of kicker values but not for all first integral deviation. Following the GEA suggestions to insert/remove shim pads, both r.m.s. trajectory and r.m.s. phase error efficiently decrease. After several iterations, the final results can be achieved and the results are shown in Table 2 and Fig. 6. Figure 6 black line shows
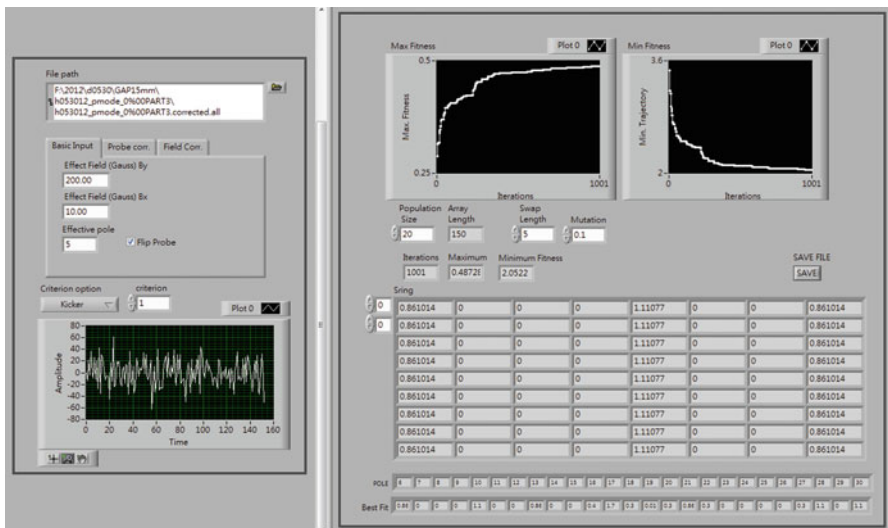
Fig. 4 Magnetic field correction based on intelligent shimming method
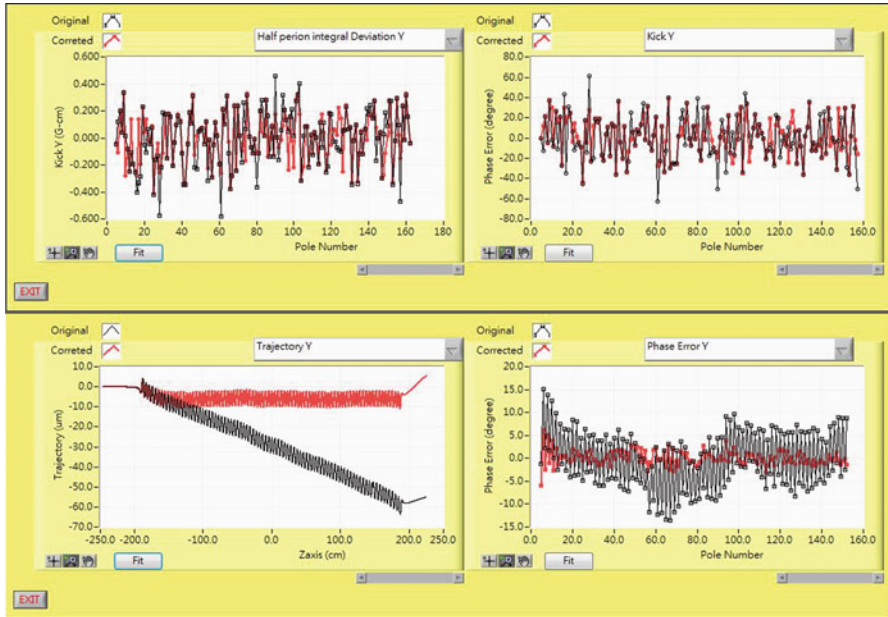
Fig. 5 Magnetic field correction based on intelligent shimming method

Table 2 Magnetic field performance using GEA correction

Polarization mode	r.m.s. trajectory (µm)		r.m.s. phase error (degree)		r.m.s. dB/B (%)	
	Before	After	Before	After	Before	After
Linear polarization	33.96	3.26	8.9	3.3	0.21	0.20
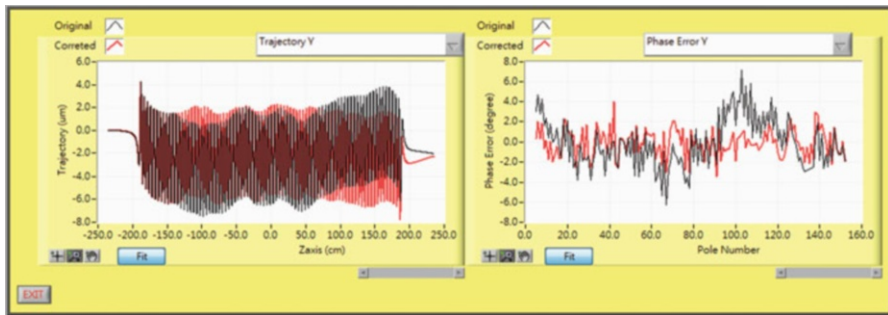
Fig. 6 Corrected results with GEA optimization work

the corrected results. The mechanical correction results have slight differences with respect to predicted value, so the GEA can always predict a better solution. For the engineering point of view, the results satisfy the specifications, so there is no further correction.

5   Conclusion

A field shimming adapted with Genetic Evolutionary algorithm is developed in LabVIEW program:

1. Genetic Evolutionary algorithm is successfully applied to magnetic field correction. The time of field correction can be dramatically reduced.
2. GEA optimization work shall first be applied to r.m.s. electron trajectory and followed by phase error optimization.
3. In the final correction, the r.m.s. trajectory and r.m.s. phase error are reduced by 30 μm and 5.6°, respectively, but the peak field deviation is no change.

References

1. Huang JC, Hwang CS et al (2012) Field correction of an elliptically polarized undulator. IEEE Trans Appl Supercond 22(3):4100705
2. Huang JC, Hwang CS et al. (2012) Performance of the elliptically polarized undulator in NSRRC. In: 11th international conference on synchrotron radiation instrumentation, Lyon, 2012
3. Pedro PC, Fernando RF (2010) Intelligent control systems with LabVIEW™. Springer, Heidelberg, pp 123–154

Innovative Designs for Quartz Crystal Microbalance

Chih-Chi Lai, Shu Jung Chen, and Chih-Hsiung Shen

Abstract Quartz crystal microbalance (QCM) is a piezoelectric sensor with multiple application such as antigen-antibody interactions, detection of virus capsids, protein adsorption, and DNA and RNA hybridization. The material of QCM model with diameter of 4.5 mm in this research is AT-cut quartz since the resonance mode of AT-cut crystal is thickness-shear mode (TSM). The principle of QCM is sensing the change of resonance frequency caused by the variation of mass. Based on the theory of electricity, decreasing the separation distance and expanding the effective area of electric field are feasible solutions for improving QCM. According to these concepts, novel groove designs for QCM with gold electrodes were proposed to develop electric field distribution. Complete analysis for piezo-electricity and electricity of QCM was simulated via analysis software CoventorWare 2010. The analysis results reveal that innovative designs in this research fulfill the advantages such as larger effective area, lower crystal impedance, and higher quality factor.

1 Introduction

1.1 History and Feature of QCM

Request for real-time biomedical sensor with high accuracy and high sensitivity keeps increasing with each passing day. Considering the features like low cost, label-free, nondestructive, high quality factor, and high sensitivity, quartz crystal

C.-C. Lai (✉) • S.J. Chen • C.-H. Shen
Department of Mechatronics Engineering, National Changhua University of Education, Changhua 50007, Taiwan
e-mail: m0051009@mail.ncue.edu.tw

microbalance (QCM) is an excellent option for real-time precision sensor. QCM is a bulk acoustic wave (BAW) sensor with versatile utilizations such as antigen-antibody interactions, detection of virus capsids, protein adsorption, and DNA and RNA hybridization [1]. Quartz Micro-Electro Mechanical Systems (QMEMS) technology then become a common research. Hence, several kinds of configuration were then developed from the conventional BAW device in order to realize the miniature for QCM sensor and other BAW component. For instance, the "grooved resonators" and the "ring-supported resonators" delivered by Mitsuo Nakazawa are inventive structure designs of the BAW resonator [2]. The "ring-supported resonators" is then commonly referred to as "inverted mesa technology" [3]. These designs are then applied to liquids operation or gravimetric sensors and demonstrated to be high sensitive [4, 5]. The material of QCM model in this research is chosen to be AT-cut quartz with gold electrode since AT-cut quartz crystal is least affected by temperature in general temperature range. The cutting angle for AT-cut crystal is $(-35° \ 15')$ from z-axis of the quartz crystal [6]. Usually, AT-cut QCM is a thin quartz plate with metal electrodes on both sides of a circular plate. Once the electrodes are applied for outer voltage, a shear resonance which is normally called thickness-shear mode (TSM) will then occur on the surface of crystal [7].

1.2 Conventional QCM Design

The other improvement for QCM is improving electrode geometry. The "closed ring electrode" design makes the resonance energy concentrate on TSM and finally leads to an efficient enhancement for QCM [8]. There are many electrode geometries published by Chao Zhang and John F. Vetelino such as "small," "closed ring," and "open ring" electrode design [8]. It is mentioned that the "small" electrode design isn't functional and the "open ring" electrode is excellent in liquid sensing while not excited in air. The "closed ring" electrode is, however, between the former two designs. Soon after a few years, we prefer to apply QCM on gas sensing. Hence, the "closed ring" electrode design was chosen to be the standard conventional electrode geometry in this research (Fig. 1).

2 Theory and Innovative QCM Design

2.1 Sensing Principle

Designs for QCM and solutions for developing electricity in this research are based on Sauerbrey's equation which indicated that frequency shift of a quartz crystal
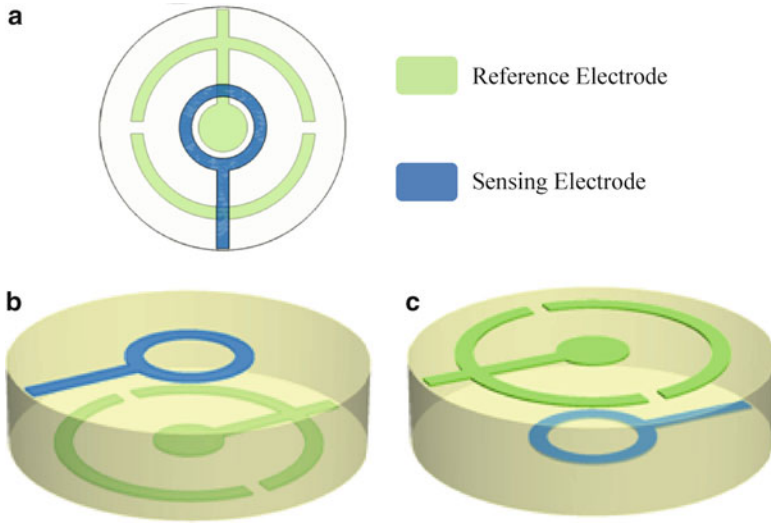
Fig. 1 (**a**) Top view of closed ring geometry, (**b**) side view of closed ring geometry(not actual proportion), (**c**) opposite side view of closed ring geometry (not actual proportion) [6]

resonator has a proportional relationship with the incremental loading mass as Eq. (1) indicated [9]:

$$\Delta f = - \frac{2f_q{}^2}{A_{pze}(\rho_q\mu_q)^{\frac{1}{2}}}\Delta m \tag{1}$$

In Eq. (1), Δf is frequency shift, f_q is the fundamental resonant frequency of the quartz, μ_q is the shear modulus of quartz ($\mu_q = 2.947 \times 1{,}011$ g/cm·s^2), ρ_q is the density of quartz ($\rho_q = 2.648$ g/cm^3), A_{pze} is the piezoelectrically active area, and Δm is the incremental loading mass. The resonance frequency f_q is an important factor in TSM and is inversely proportional to the thickness of quartz. From Sauerbrey's equation, it is easy to realize that the principle of AT-cut QCM is sensing the change of mass of resonance frequency caused by the variation of mass. The fundamental resonant f_q can be represented in other form as indicated in Eq. (2):

$$f_q = \frac{\upsilon_q}{2t_q} \tag{2}$$

where υ_q is a constant wave velocity in quartz, f_q is the fundamental resonant frequency of the quartz, and t_q is the thickness of quartz. Obviously, the thinner the thickness is, the higher the frequency become.
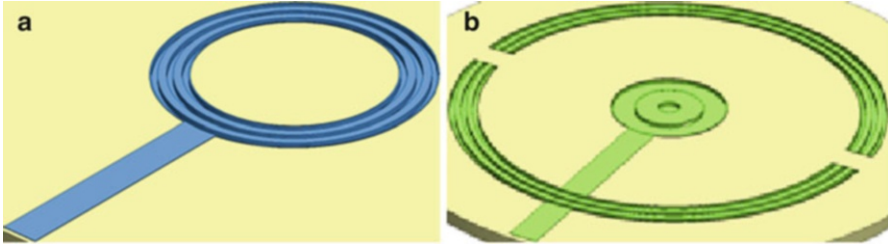
Fig. 2 Multi-groove on (**a**) sensing electrode and (**b**) reference electrode [10]

2.2 Multi-groove Design

Based on the theory of quartz crystal resonator mentioned above, there are two main purposes for ameliorating QCM in the following section: shorten the separation distance of electric field and expanding the effective area of electric field line between the electrodes. Not long ago, the novel "multi-groove structure design" was applied to the "closed ring" electrode geometry [10]. The multi-groove structure leads to a new idea of structure design and successfully increases the electricity of QCM. According to the former electrode geometry design and groove design, we intend to progress the groove design to a further stage and finally come up with a forward-looking groove configuration: "grooves array." This forward design and the former design will then be compared with each other for electricity and mechanical characteristic through piezoelectric analysis. The "grooved resonators" delivered by Mitsuo Nakazawa only apply groove structure on QCM surface without electrode and therefore can solely modify the mechanical characteristic to enhance the frequency shift. Multi-groove design sketched as Fig. 2, however, utilizes three concentric grooves to quartz surface contact with gold electrodes. This clever idea not only modifies the mechanical characteristic but also enhances the electricity.

2.3 Grooves Array Design

By slicing the multi-concentric groove to several pieces, number of grooves becomes "grooves array" which can exactly provide extra electric field area as shown in Fig. 3. The conventional design, multi-groove design, and grooves array design with different depths of grooves are then simulated through piezoelectric analysis via CoventorWare 2010 for mechanical characteristic and electricity to optimize the design for QCM.
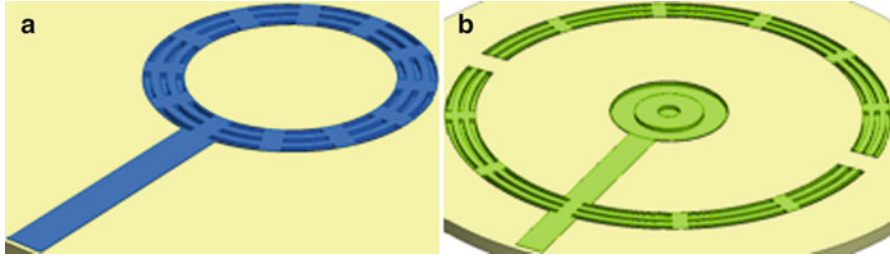
Fig. 3 Grooves array on (**a**) sensing electrode and (**b**) reference electrode
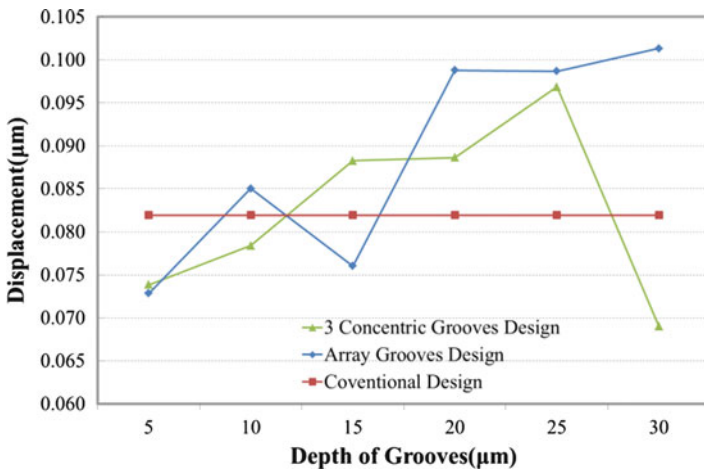
Fig. 4 Displacement vs. depth of grooves

3   Simulation Results and Discussions

For the mechanical characteristic, the simulation results show that the conventional QCM has a displacement of 0.082 μm, multi-groove design has a maximum displacement about 0.096 μm, and grooves array design has a maximum displacement about 0.100 μm which is at most 21.9 % better than the conventional QCM. Obviously, once the depth of grooves is deeper than 20 μm, the displacement of QCM with grooves array performances at most better than the QCM with multi-groove and the conventional QCM as shown in Fig. 4. For the charge accumulation, the charge of conventional design is 485,043 C which is taken as the reference value in Fig. 5 and is extremely smaller than the charge of the innovative designs. The maximum charge of multi-groove is about 17×10^6 C. The maximum charge of QCM with 15 μm array grooves is 26.59 % better than the QCM with multi-groove.
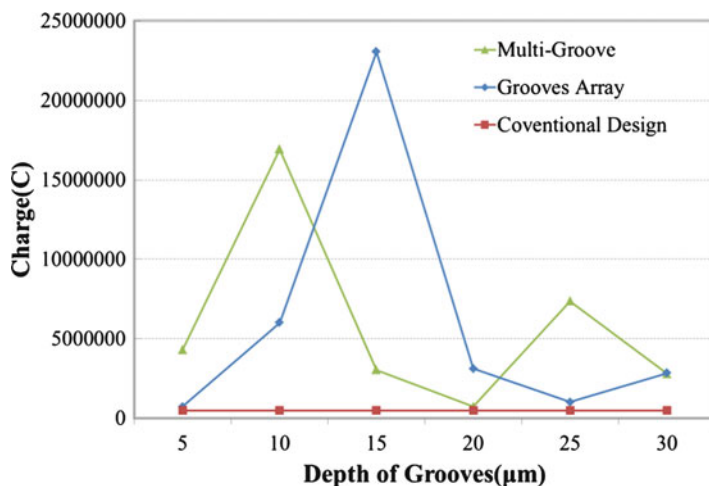
Fig. 5 Charge vs. depth of grooves

The piezoelectric results reveal that the grooves array design is a feasible idea to enhance both of the mechanical and electric performance indicated as Fig. 5.

4 Conclusions

As an extension of grooved designs, an innovative grooves array design is proposed in this chapter and compared with the former designs for charge accumulation and piezoelectric displacement. Grooves designs with gold electrodes configuration are discussed and simulated via CoventorWare 2010 for mechanical characteristic and electricity. The multi-groove design and grooves array design, as we expected, are well functional in air surroundings. Namely, the innovative design can efficiently shorten the distance of electric field and generate extra affective area of electric field line. The grooves array design with depths of grooves has a mechanical performance at most 21.9 % better than the conventional QCM and is 26.59 % better than multi-groove design for the charge accumulation.

References

1. Cathy I. Cheng, Yi-Pin Chang, Yen-Ho Chu (2012) Biomolecular interactions and tools for their recognition: focus on the quartz crystal microbalance and its diverse surface chemistries and applications. Chem Soc Rev 41:1947–1971

2. Nakazawa M (1981) Force and acceleration frequency effects in grooved and ring supported resonators. In: Annual frequency control symposium, USAERADCOM, Ft. Monmouth, NJ C7733
3. Vig JR, LeBus JW, Filler RL (1977) Chemically polished quartz. In: Proceedings of the 31st annual frequency control symposium, Springfield, 1977, pp 131–143
4. Zuxuan Lin, Yip CM, Scott Joseph I, Ward MD (1993) Operation of an ultrasensitive 30-MHz quartz crystal microbalance in liquids. Anal Chem 65:1546–1551
5. Kreutz C, Lörgen J, Graewe B, Bargon J, Yoshida M, Fresco ZM, Frèchet JMJ (2006) High frequency quartz micro balances: a promising path to enhanced sensitivity of gravimetric sensors. Sensors 6:335–340
6. Janshoff A et al (2000) The quartz-crystal microbalance in life science. Angew Chem 39:4004–4032
7. Martin SJ, Frye GC, Ricco AJ (1993) Effect of surface roughness on the response of thickness-shear mode resonators in liquids. J Am Chem Soc 65:2910–2922
8. Chao Zhang, Vetelino JF (2001) Bulk acoustic wave sensors for sensing measurand-induced electrical property changes in solutions. IEEE Trans Ultrason Ferroelectr Freq Control 48(3):773–778
9. Sauerbrey GZ (1959) Use of quartz crystal vibrator for weighting thin film on a microbalance. Z Phys 155:206–210
10. Zong-Han Liu, Chih-Hsiung Shen (2012) New groove structures for miniature quartz crystal microbalance with low crystal impedance. Adv Mater Res 538–541:2461–2465

Semi-active Control of Tunable Hybrid Shape Memory Material for Vibration Attenuation

Jinsiang Shaw and Jiun-Du Huang

Abstract Vibration absorber has been used as an effective tool in the vibration reduction of structure-suffered single-frequency excitation. An absorber consisted of a spring element made of hybrid shape memory materials was proposed. A cantilevered beam fabricated by superelastic (SE) core and shape memory polymer (SMP) sleeves was employed as the spring element of the absorber. By controlling the electric current through the SE core and thereby the temperature of the SMP sleeves, the natural frequency of the absorber was tunable. In this study, an absorber with actively tunable frequency capability may offer more powerful solution. The fabricated hybrid shape memory material absorber was capable of changing its natural frequency by more than 45 %. By applying semi-active controllers including fuzzy logic control and self-tuning control to the tunable vibration absorber, system resonance can be avoided, thus ensuring adaptability and robustness of the damping system.

Keywords Semi-active control • Shape memory material • Vibration attenuation

1 Introduction

The operation of precision machinery may encounter vibration problem when under external force excitation. Therefore vibration control is crucial in improving the machine precision level and keeping steady-state operation for manufacturing; the product yield rate thus can be increased. To solve the vibration problem, one can apply a passive control method, such as redesigning the system so that the structure natural frequency is far away from the excitation frequency, in order to avoid the

J. Shaw (✉) • J.-D. Huang
Institute of Mechatronic Engineering, National Taipei University of Technology,
Taipei 10608, Taiwan
e-mail: jshaw@ntut.edu.tw

resonance phenomenon, or employing a vibration absorber [1] to minimize the main structural vibration; one can use an active control method, for example, adding an actuator in the system to provide a counter force [2]; and one can employ a semi-active control method, such as using MR (magnetorheological fluid) mount [3] or adjustable vibration absorber [4], by varying the control input based on the applied excitation frequency to adjust the system parameters (stiffness/damping ratio, etc.) so that vibration attenuations can be achieved.

Sun et al. [5] and Williams et al. [6] surveyed some adjustable vibration absorber design methods including adjustable shape memory alloy (SMA) vibration absorber. Williams et al. [4, 6, 7] used SMA for an adjustable vibration absorber and can tune the absorber frequency up to 17 % change by applying varying electric currents to the absorber. Chen [8] designed a cantilevered beam made of superelastic (SE) SMA core and shape memory polymer (SMP) sleeves as a vibration absorber. Experiments showed that this adjustable hybrid shape memory material vibration absorber was feasible in vibration reduction when its frequency was properly tuned.

In this chapter, a vibration absorber, similar to that in [8], consisted of a spring element made of hybrid shape memory materials and a mass is proposed. By controlling the applied electric current through the SE core and thereby the temperature of the SMP sleeves, the natural frequency of the absorber can be varied. The aim of the chapter is to develop semi-active controllers to find the applied current to the absorber so that vibration amplitude at the main system can be attenuated when it undergoes external force excitations.

2   System Description

A schematic diagram of the designed hybrid shape memory material vibration absorber is shown in Fig. 1. The cantilevered spring element is made of superelastic SMA wires wrapped by SMP material. By adjusting the applied current to the SMA wire, the natural frequency (damping ratio as well) of the vibration absorber can be accordingly tuned. Figure 2 depicts relations of SMP material Young's modulus and damping ratio with temperature. Therefore by controlling temperature of the SMP material, one can tune properties of the vibration absorber. This vibration absorber is then attached to a main system of another cantilevered beam at the free end, as illustrated in Fig. 3, for vibration attenuation purpose. The cantilevered end of the main system is clamped to a shaker which can simulate external force applied to the system. Figure 4 shows the experimental setup for the vibration control evaluation using the hybrid shape memory material vibration absorber.

Noncontact displacement sensor is employed to measure vibration signal at the main mass. By feeding back this signal to the controller, a suitable control signal based on certain control algorithm is output via a D/A converter to a current amplifier for applying electric current to the absorber for vibration absorption purpose.
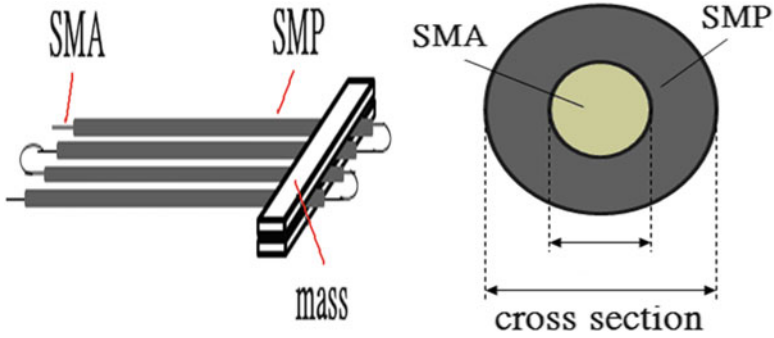
Fig. 1 Diagram of beam element as a vibration absorber
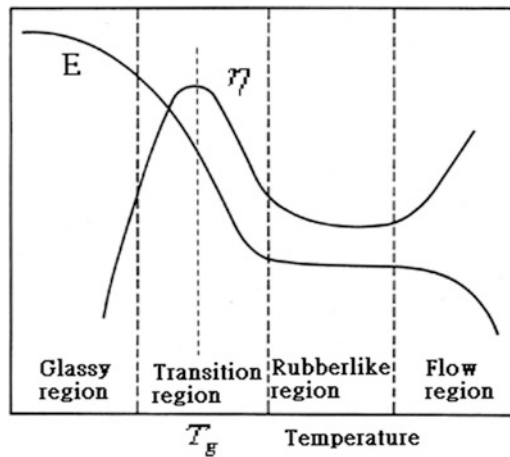
Fig. 2 Young's modulus and damping ratio as a function of temperature
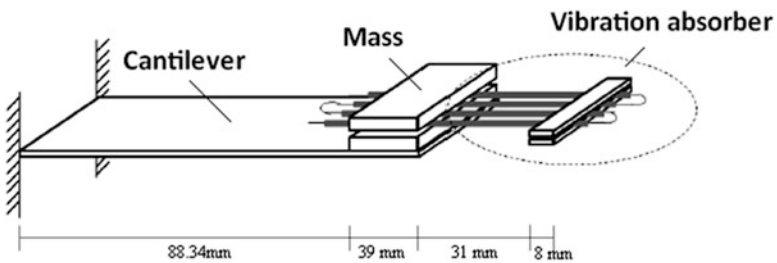
Fig. 3 Schematic diagram of the vibration system
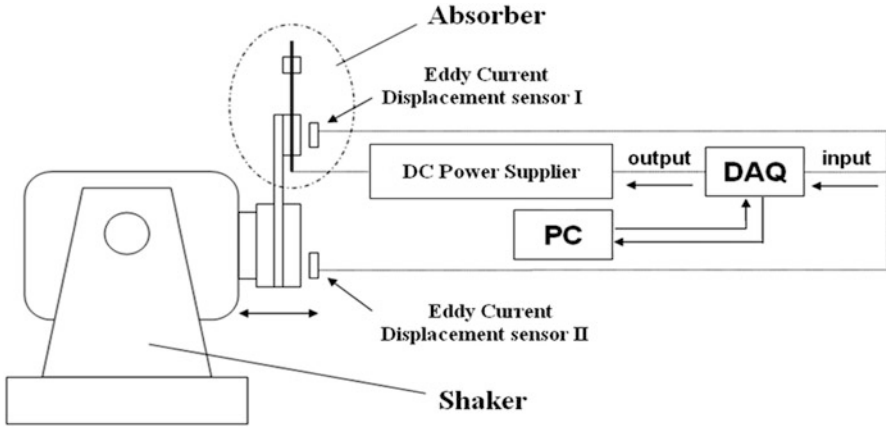
Fig. 4 Schematic diagram of vibration control experiment

3 The Controller Design

3.1 Fuzzy Logic Controller

It is well known that a vibration absorber is most effective when its natural frequency is tuned to be exactly that of the forcing frequency. It is therefore important to investigate frequency responses of the main system under different applied currents to the vibration absorber, as shown in Fig. 5, which is obtained experimentally. Within the applicable range of currents [0 A, 1.8 A], six frequency responses are shown from which the optimal control currents for obtaining the least vibration amplitude can be deduced for a specified range of excitation frequency. The optimal control currents based on the frequency response plot of Fig. 5 are shown in Fig. 6. Since only six finite different currents are employed for the frequency response plot, a fuzzy logic controller [9] is thus employed for obtaining a smoother control actions based on the results in Fig. 6. The corresponding designed fuzzy control rule reads like this:

Rule-j: if excitation frequency $\omega \in [\omega_{lower}^j, \omega_{upper}^j]$, then control current is i_j.

It is noted that there are eight such control rules. Mandanni-type inference engine is used in this chapter for computing the control output. More specifically, a trapezoidal membership function $A(\omega)$ is adopted for the input excitation frequency, with the upper base length equal to 80 % length of $[\omega_{lower}^j, \omega_{upper}^j]$. A fuzzy singleton membership function with value at i_j is used for the output current. Finally, center of area (COA) is applied for the defuzzification method to obtain the crisp control current:

$$i = \frac{\sum_{j=1}^{8} \mu_{A_j}(\omega) \cdot i_j}{\sum_{j=1}^{8} \mu_{A_j}(\omega)} \tag{1}$$

Fig. 5 Frequency responses
of the main system for various
applied optimal currents
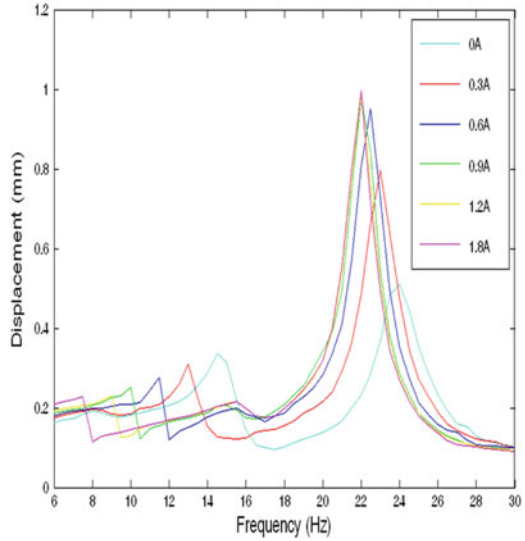
Fig. 6 The optimal currents
needed for best attenuation
at different frequency ranges
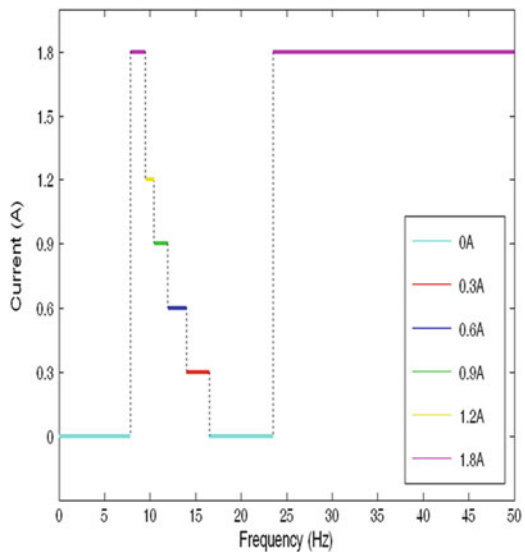
3.2 Self-Tuning Controller

In this section, self-tuning control is to be developed for finding the optimal control
current when the main system is under forced harmonic excitation. In each of the
eight sections in frequency axis in Fig. 6, vibration amplitudes vary with the applied
current from 0.A to 1.8A. It is concluded that only four patterns for amplitude
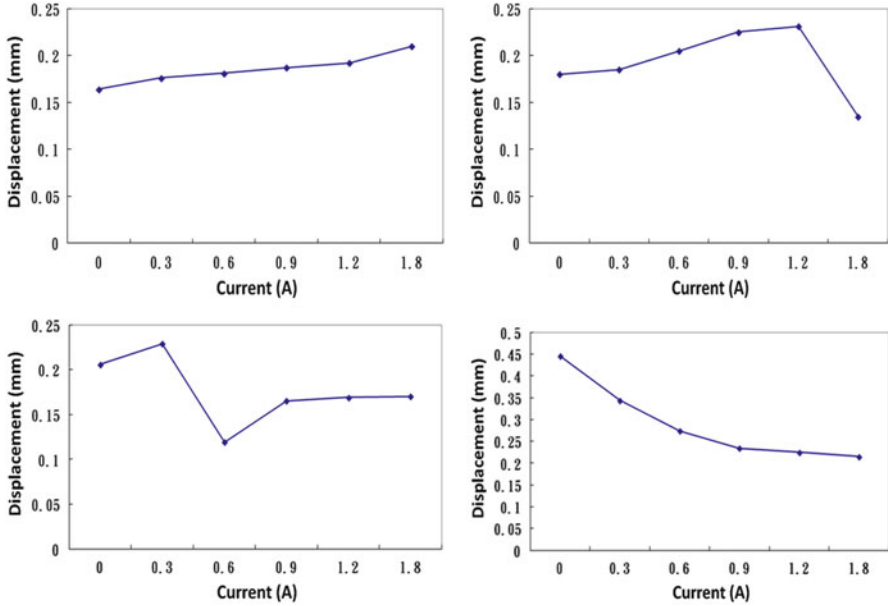
Fig. 7 Vibration amplitudes as a function of current at different excitation frequency

variation are observed, as shown in Fig. 7. The vibration amplitude can increase or decrease monotonically with the applied currents. It can also increase first with the applied current to the maximum value and then decrease to the button with/without increase again. Based on these observed phenomena, a self-tuning controller can be readily derived using only four rules to quickly infer the optimal control current by a few trials of applied currents beginning from 0.A to the system, regardless of the knowledge of excitation frequency.

4 Experimental Results

The two controllers discussed in the previous section are employed for evaluating vibration control performances of the vibration absorber. The results are compared with that of uncontrolled system (0.A applied) as well as that obtained in Fig. 5, whose optimal control currents are given in Fig. 6. Vibration attenuation results with these different control algorithms are shown in Fig. 8. The developed fuzzy logic controller and self-tuning controller indeed have the capability of attenuating vibration amplitudes in the tested frequency range by adjusting absorber natural frequency so that system resonance can be avoided and robustness of the damping system can be assured.
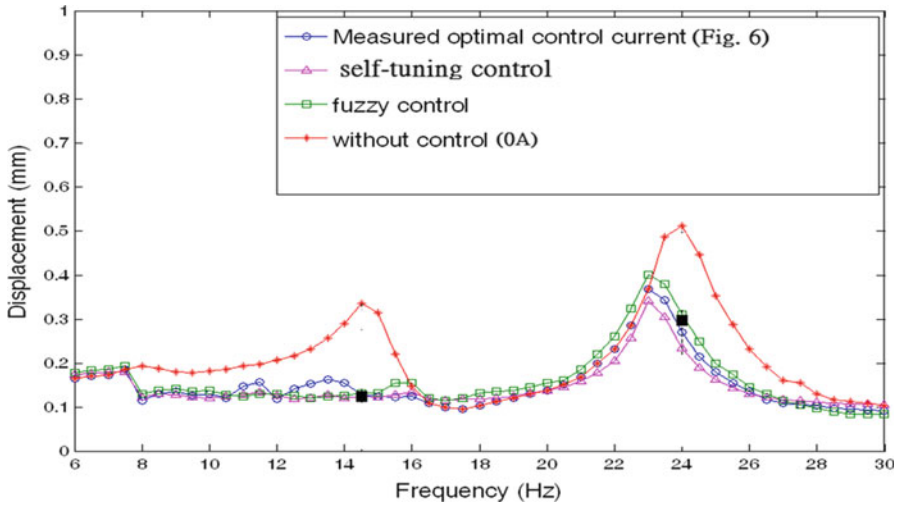
Fig. 8 Vibration attenuation results with different control algorithms

5 Conclusions

A cantilevered beam fabricated by superelastic SMA core and SMP sleeves was employed as the spring element of a vibration absorber. By controlling the electric current through the SE core and thereby the temperature of the SMP sleeves, the natural frequency and damping ratio of the absorber was tunable. Fuzzy logic controller is employed by knowing the input excitation frequency for computing an optimal control current to the absorber so as to attenuate vibration amplitudes. The self-tuning controller based on vibration amplitude variations as applied current increases can rapidly find the final control current for vibration attenuation. Experiment results show effectiveness of the proposed controllers in reducing vibration amplitude to get to the level that could possibly be obtained.

Since SMA core is wrapped by SMP sleeves, heat dissipation could be a problem when the system is in operation. Hence, good cooling system should take into account in design stage for better control of the vibration absorber, especially when response time is a stringent concern.

References

1. Den Hartog JP (1956) Mechanical vibrations. McGraw-Hill, New York
2. Shaw J (2001) Active vibration isolation by adaptive control. J Vib Control 7(1):19–31

3. Shaw J, Pan R (2012) Fuzzy sliding mode control of an MR mount for vibration attenuation. J Chin Soc Mech Eng 33(1):21–28
4. Williams KA, Chiu GT, Bernhard RJ (2002) Adaptive-passive absorbers using shape-memory alloys. J Sound Vib 249:835–848
5. Sun JQ, Jolly MR, Norris MA (1995) Passive, adaptive, and active tuned vibration absorbers – a survey. J Mech Des 117B:234–242
6. Williams KA, Chiu GT, Bernhard RJ (2005) Dynamic modeling of a shape memory alloy adaptive tuned vibration absorber. J Sound Vib 280:211–234
7. Williams KA, Chiu GT, Bernhard RJ (2005) Nonlinear control of a shape memory alloy adaptive tuned vibration absorber. J Sound Vib 280:1131–1155
8. Chen JC (2011) Control of tunable hybrid shape memory material vibration absorber used in vibration reduction. Master thesis, National Taipei University of Technology, Taiwan
9. Zadeh LA (1965) Fuzzy set. Inf Control 8:338–353

Simultaneous Thickness Measurement and Material Composition Analysis Using X-Ray Fluorescence Technique

Hsiao-Wen Wu and Xuan-Loc Nguyen

Abstract In this chapter, a methodology for simultaneous thickness measurement and material composition analysis using X-ray fluorescence (XRF) technique is present. This research bases on the fundamental parameter (FP) method to reconstruct the composition and thickness of target layers. A monochromatic nondivergent incident radiation is used as a source for generating the emission of characteristic secondary spectrum from a material. The reference set in which material composition is known was used to calibrate and validate measurement of concentrations of elements. XRF measurements of the thickness are correlated as a function of process parameters given by receiving spectra from inspecting target. The method can provide a real-time measurement with high accuracy in determining thickness and material composition.

Keywords X-ray fluorescence (XRF) • Fundamental parameter (FP) • Thickness measurement • Material composition analysis

1 Introduction

The XRF spectroscopy has recently become a powerful and versatile technique for material analysis and characterization. The technique can probably be considered as the most useful nondestructive analytical tool for many industrial applications. XRF analysis is based on the fact that the emissions of characteristic or secondary X-rays from a material excited by bombarding with high-energy electrons or other X-ray are

H.-W. Wu
Department of Electronics Engineering, Tung Nan University, Shen-keng, Taiwan

X.-L. Nguyen (✉)
Research and Development Division, Allied Engineering and Consultant,
Inc., Taipei, Taiwan
e-mail: aoi@aecteam.com

characteristic of the element involved. If the incident beam has enough energy, it can bombard and push an orbital electron out of the inner shell of the target atom. The vacancy created by this electron can be filled by one of the electrons from the higher shells, which emits a photon with energy equal to the difference in binding energy of the two shells. The intensity of secondary ray is proportional to both the elemental concentration and the strength of the incident beam.

For the last few decades, many significant researches have been proposed using XRF technique to determine the concentrations of various elements as well as structural parameters of inspecting target [1, 2]. In 1955 Sherman [3] derived the basic equation for expressing measured characteristic intensities. Criss and Birks [4, 5] showed how to put Sherman's equation in practice, in which the method is generally known as fundamental parameter (FP) method. In this approach, most of the developed methods assume that the measured intensities are corrected for background and line overlap. This technique includes the influence of all other present elements in the sample on the inspecting element. The FP method requires accurate information about attenuation and XRF production cross sections, fluorescence yields, and line energies. Therefore, the acquisition of these parameters has been an active research topic in this field, which provides many available tabulations, either obtained from experimental data or quantum mechanical calculations [6, 7]. The other form of FP method is called Fundamental Algorithm method, which was first proposed by Rousseau [8]. The method proposed an explicit expression from Sherman's equation without any approximation. The algorithm combines the practical flexibility of the influence coefficient concept and the theoretical exactness of the FP method [9, 10].

This chapter presents a method for simultaneous thickness measurement and material composition analysis based on FP method. The significant contribution of this research is to implement thickness measurement and material composition analysis in the same probe lab equipment. The use of FP computations has brought real-time analysis to XRF analytical system with massive on-line disk storage, RAM, and multi-core CPUs.

2 Methodology

2.1 Fundamental Parameter Method

When the element composition is excited by a radiation source, the generated characteristic photons are isotropically emitted in all directions. A portion of emitting beam is directed to detector. Supposing the incident beam strikes the surface of element composition at an angle, ψ_1 it hits the analyte i and the characteristic photons leave the composition to get into the detector at an angle ψ_2, shown in Fig. 1. The Sherman's equation describing the relationship between the primary intensity emitted by a specimen and its composition is given by [11]
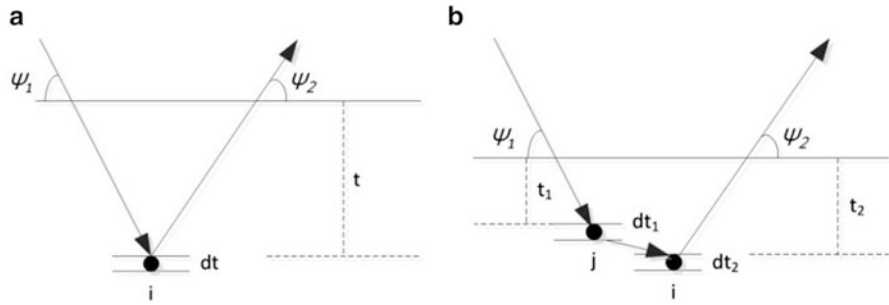
Fig. 1 Schematic of the fluorescence radiation: (**a**) primary fluorescence radiation; (**b**) secondary fluorescence radiation

$$P_i = \frac{I_0 C_i \mu_{i,0} Q_{i,0} (\csc \psi_1)(\Omega/4\pi)}{\mu_{M,0} \csc \psi_1 + \mu_{M,i} \csc \psi_2}, \tag{1}$$

where

P_i is the primary intensity of analyte i

I_0 is the intensity of incident beam with wavelength λ_0

C_i is the concentration of analyte i

$Q_{i,0}$ is the excitation factor depending on the excited line and fluorescence yield of analyte i being bombarded by the beam with wavelength λ_0

$\mu_{i,0}$ is the mass attenuation coefficient of analyte i for beam with wavelength λ_0

$\mu_{M,0}$ is the mass attenuation coefficient of the element composition for beam with wavelength λ_0

$\mu_{M,i}$ is the mass attenuation coefficient of the element composition for characteristic radiation with wavelength λ_i

Ω is the solid angle as viewed by the detector

The mass attenuation coefficient $\mu_{M,0}$ of element composition for wavelength λ_0 depends on mass attenuation $\mu_{i,0}$ of each element i that is calculated as

$$\mu_{M,0} = \sum_{i=1}^{n} \left[\mu_{i,0} C_i \right]. \tag{2}$$

The excitation factor $Q_{i,0}$ depending directly to the absorption jump ratio r_i of analyte i, fluorescence yield ω_i and transition probability f_i is given as follows:

$$Q_{i,0} = \omega_i \frac{r_i - 1}{r_i} f_i \tag{3}$$

In the condition when the energy of characteristic photons of an element j is strong enough to excite atoms of an analyte i, shown in Fig. 1b, the secondary fluorescence is included in calculating the intensity:

$$S_i = \frac{I_0 C_j \mu_{j,0} Q_{j,0} (\csc \psi_1) \left(\frac{\Omega}{4\pi}\right) \mu_{i,j} C_i Q_{i,j}}{2 \left(\mu_{M,0} \csc \psi_1 + \mu_{M,i} \csc \psi_2\right)}$$

$$\times \left(\frac{\sin \psi_1}{\mu_{M,0}} \ln \left[1 + \frac{\mu_{M,0}}{\mu_{M,j} \sin \psi_1} \right] + \frac{\sin \psi_2}{\mu_{M,i}} \ln \left[1 + \frac{\mu_{M,i}}{\mu_{M,j} \sin \psi_2} \right] \right) \quad (4)$$

where
S_i is the secondary intensity of analyte i
C_j is the concentration of element j
$\mu_{j,0}$ is the mass attenuation coefficient of element j for beam with wavelength λ_0
$Q_{j,0}$ is the excitation factor depending on the excited line and fluorescence yield of element j being bombarded by the beam with wavelength λ_0
$\mu_{M,j}$ is the mass attenuation coefficient of the element composition for characteristic radiation with wavelength λ_j

The total excited characteristic intensity is then given by adding the primary and secondary fluorescence:

$$I_{i,0} = P_{i,0} + \sum_{j=1, j \neq i}^{n} S_{j,i}. \quad (5)$$

2.2 Iteration Process for Concentration Calculation

Since the intensity and concentration of element in composition have cross relation, an iteration equation is used at present in calculations to converge element concentrations to the correct value. Steps for iteration process can be described as follows:

Step 1: The element concentrations are initialized by the intensity after normalized to unity.
Step 2: The intensities of elements are then calculated by FP method.
Step 3: The element concentrations are calculated again by a converging function:

$$C_{i,\text{new}} = \frac{\overline{I_{i,0FP}} \, C_i \left(1 - \overline{I_{i,0}}\right)}{\overline{I_{i,0FP}} \left(C_i - \overline{I_{i,0}}\right) + \overline{I_{i,0}} (1 - C_i)} C_i, \quad (6)$$

where

$\overline{I_{i,0}}$ is the normalized intensity of incident beam with wavelength λ_0 from measurement

$\overline{I_{i,0FP}}$ is the normalized intensity of incident beam with wavelength λ_0 from FP calculation

Step 4: Error evaluation values between C_i and $C_{i,\text{new}}$ are estimated to decide whether to stop the iteration process.

2.3 Thickness Measurement by Calibration of Standard Samples

For measuring thickness of an unknown target, a set of standard samples are used to find the relation between intensity response and thickness of each material. The relation between measured intensity and sample thickness can be described as follows:

$$d_i = f\left(I_{i,0}\right) \tag{7}$$

By calibration process, a polynomial function is used to fit the curve response of intensity from thickness of each element. This function is then used during on-line measurement process.

3 Experimental Results and Analysis

3.1 Material Composition Analysis

The geometry and the shielding arrangement of the experimental setup employed in the present study are as shown in Fig. 2. The spectra were recorded by a detector having energy resolution of 150 eV. Example of an alloy was used in the experiment, shown in Fig. 3, where Fe (67.9 %), Cr (24.8 %), Ni (6.36 %), and Mo (0.854 %) were detected. Many alloys were also tested to evaluate the capability of the method, where a maximum error in material composition analysis was found at 8.2 %.

3.2 Thickness Measurement

For each element, a set of standard thickness samples is used to find the polynomial fitting function between intensity and thickness. An example of curve response of
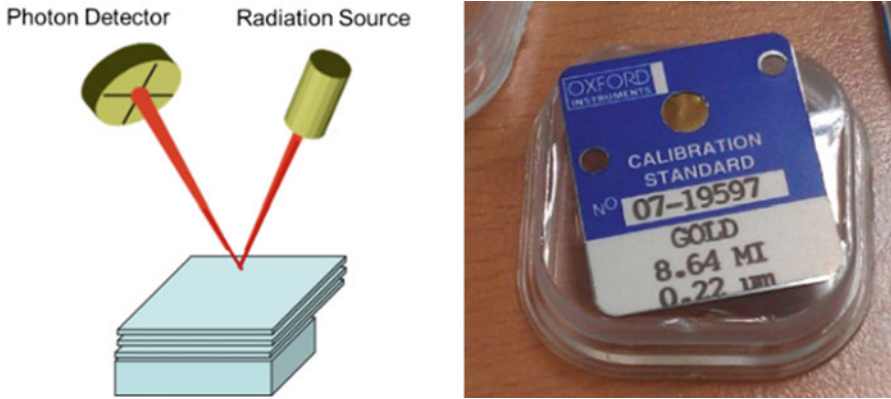
Fig. 2 Experimental setup used for measurements of material composition and thickness
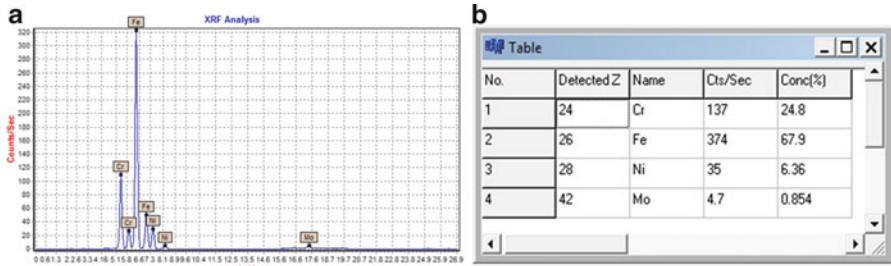
Fig. 3 Experimental result for material composition analysis of an alloy: (**a**) spectral data with peak detection; (**b**) concentration analysis for material composition
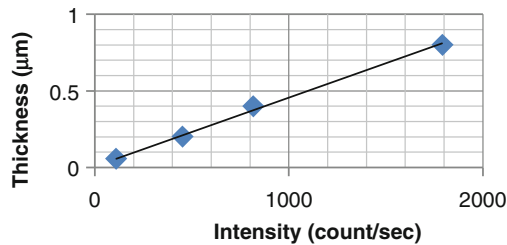
Fig. 4 Calibration result for intensity and thickness on standard gold samples

gold is shown in Fig. 4, where four standard samples of pure gold with thickness of 0.05, 0.2, 0.4, and 0.8 µm were conducted in calibration. Two standard coating samples were also used to verify the measurement capability of the method, shown in Table 1, where variety of coating material is retrieved.

Table 1 Experiment result on standard thickness samples

Substrate	Coating	Sample (serial number)	Measured thickness (μm)	Standard thickness (μm)
Ni	1. Sn	08-20823	0.052	0.05
	2. Au	08-20744	6.035	5.92
Sn	1. Pd	08-21913	0.106	0.11
	2. Ni	07-20243	10.837	10.7
	3. Au	07-19949	0.897	0.80

4 Conclusions

A method for measuring coating thickness and composition is developed using X-ray fluorescence. The contribution of this work is that we combine the thickness measurement and material composition analysis in the same system and methodology. The technique is nondestructive and noncontact, which is suitable for many applications such as monitoring the elemental content of iron slags during recycling and refining and preventing overcoating and undercoating during coating process. As demonstrated in the experiment, the method is capable of analyzing the complex layer structures found in the current and future high-technology markets.

References

1. West M, Ellis AT, Potts PJ, Streli C, Vanhoof C, Wegrzynek D, Wobrauschek P (2010) Atomic spectrometry update–X-ray fluorescence spectrometry. J Anal At Spectrom 25:1503–1545
2. Evans EH, Day JA, Palmer CD, Smith CMM (2009) Atomic spectrometry update: advances in atomic spectrometry and related techniques. J Anal At Spectrom 24:711–733
3. Sherman J (1955) The theoretical derivation of fluorescent X-ray intensities from mixtures. Spectrochim Acta 7:283–306
4. Criss JW, Birks LS (1968) Calculation methods for fluorescent X-ray spectrometry, empirical coefficients vs. fundamental parameters. Anal Chem 40:1080–1087
5. Criss JW, Birks LS, Gilfrich JV (1978) Versatile X-ray analysis program combining fundamental parameters and empirical coefficients. Anal Chem 50:33–37
6. Krause M (1979) Atomic radiative and radiationless yields for K-shells and L-shells. J Phys Chem Ref Data 8:307–327
7. Elam W, Ravel B, Sieber J (2002) A new atomic database for X-ray spectroscopic calculations. Radiat Phys Chem 63:121–128
8. Rousseau RM (2001) Concept of the influence coefficient. Rigaku J 18:8–14
9. Rousseau RM (1984) Fundamental Algorithm between concentration and intensity in XRF analysis, part 1: Theory. X-Ray Spectrum 13:115–120
10. Rousseau RM (1984) Fundamental Algorithm between concentration and intensity in XRF analysis, part 2: Practical application. X-Ray Spectrum 13:121–125
11. de Vries JL, Vrebos BAR (2002) Quantification of infinitely thick specimens by XRF analysis. In: van Grieken RE, Markowicz AA (eds) Handbook of X-ray spectrometry, 2nd edn. Marcel Dekker, Inc., New York, pp 341–405

Integration Design and Installation of Girder Systems in the Injection Section of Taiwan Photon Source

Keng-Hao Hsu, Wei-Yang Lai, Yung-Hui Liu, Che-Kai Chan, Chih-Sheng Yang, Chih-Sheng Chen, His-Cho Ho, Pei-Lung Sung, Shen-Yaw Perng, Tse-Chuan Tseng, Din-Goa Huang, and June-Rong Chen

Abstract The electron beam is injected from the end of the transport line into the injection section of the storage ring in Taiwan Photon Source (TPS). A girder system for the injection section has been designed to support AC/DC septum magnets, four kicker magnets (K1–K4), and vacuum chambers. The girder system includes three girders, a Rapson-slide mechanism, and stages for the septum/kicker magnets. To improve the reliability and the stability of the injected electron beam, the girder systems are designed and installed in the injection section of TPS, as described in this chapter. The positioning accuracy of installing three girders and the stages for septum/kicker magnet are, respectively, within 0.3 and 0.05 mm.

Keywords TPS • Injection section • Girder system

1 Introduction

Taiwan Photon Source (TPS), a 3-GeV synchrotron facility, is under construction at National Synchrotron Radiation Research Center (NSRRC) for completion in 2013. The electron beam is injected from the end of a transport line into the injection section of the storage ring. A girder system for the injection section has been designed to support and to position AC/DC septum magnets, four kicker

K.-H. Hsu (✉) • W.-Y. Lai • Y.-H. Liu • C.-K. Chan • C.-S. Yang • C.-S. Chen • H.-C. Ho
P.-L. Sung • S.-Y. Perng • T.-C. Tseng • D.-G. Huang
National Synchrotron Radiation Research Center, Hsinchu 30076, Taiwan
e-mail: khhsu@nsrrc.org.tw

J.-R. Chen
National Synchrotron Radiation Research Center, Hsinchu 30076, Taiwan

National Tsing Hua University, Hsinchu 30013, Taiwan
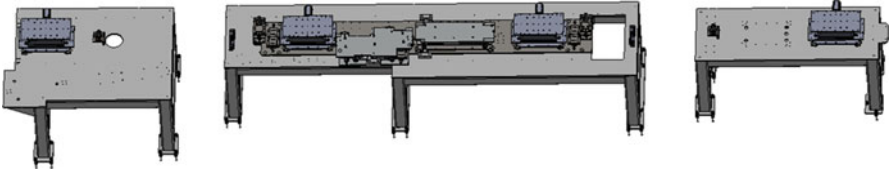
Fig. 1 Girder systems of the injection section of TPS storage ring

magnets (K1–K4), and vacuum chambers [1] within 0.1 mm. The girder system, shown in Fig. 1, includes three girders, a Rapson-slide mechanism, a stage for an AC septum magnet, a stage for a DC septum magnet, and four one-axis goniometer stages for the kicker magnet. In this chapter, the integration design and installation of the girder system in the injection section of Taiwan Photon Source are described.

2 Design of Girder Systems

2.1 Girder

Girders in the injection section are supposed to support firmly the adjustable stages for magnets, the Rapson-slide mechanism, the supports for vacuum chambers, and so on. A girder is designed to be composed of structural rectangular steel tubes and a steel plate (SS400, thickness 20 mm). To decrease the deformation of the desk of the girder, rectangular steel tubes are adopted as beams under the steel plate. The distance from the ground to the bottom of the beam is more than 840 mm. The space under the desk of the girder is supposed to place the power supply for the pulsed magnet. The surface of the desk of the girder was machined to control its flatness within 0.05 mm for the installation of a Rapson-slide mechanism and stages for adjustable stages. Seven linear grooves in the middle girder (length 5 m), which supports an aluminum adjustable plate, were machined to install linear guideways of the Rapson-slide mechanism.

2.2 Rapson-Slide Mechanism

To achieve highly efficient injection during top-up operation, a strict requirement is that the four kicker magnets have identical waveforms. The performance of the kicker power supply can be more reliable and stable with operation at a lower voltage, and
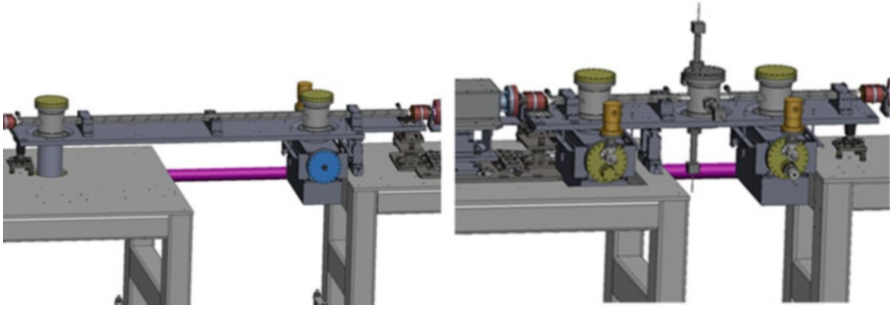
Fig. 2 Two rotatable aluminum plates are designed to load and to steer the vacuum chamber located between the injection kickers

some approaches implementing DC bumps [2, 3] or moving the AC/DC septum magnet [4] were adopted to decrease the operating voltage of the kicker power supply.

An aluminum plate (length 4.11 m), shown in Fig. 1, is precisely machined to control its flatness within 0.05 mm for placement of the injection kickers (K2, K3) and the AC septum magnet. The plate is adjustable; two linear guideways mounted parallel on the plate serve to guide the adjustable plate for motion in the transverse direction that is perpendicular to the beam orbit. A sliding rod is attached to each end of the adjustable plate to connect the rotating plates as shown in Fig. 2. During tuning of the adjustable plate, the sliding rods drag the rotating plates, causing them to rotate about the pivots.

2.3 Stage for the DC Septum Magnet

The stage for the DC septum magnet is designed as shown in Fig. 3. The height, pitch, and roll of the stage are adjusted with five, fine, M30 screws. Three of those screws are primary, and the others are auxiliary used to support the middle plate of the stage. Fifteen fine nuts are thinned to fit the screws. The surge, sway, and yaw of the stage are adjusted on pushing eight fine M12 screws fixed in the side plate that is fixed to the top plate of the stage. Six M16 screws serve to lock the DC septum magnet from the top plate of the DC septum stage. Four fiducial holes in the top plate of the stage enable alignment with a laser tracker. Three pins serve to position the DC septum magnet after alignment of the top plate of the stage. The bottom plate of the stage can be also shifted 5 mm as the adjustable aluminum plate in the transverse direction with two linear guideways mounted parallel in the middle girder.
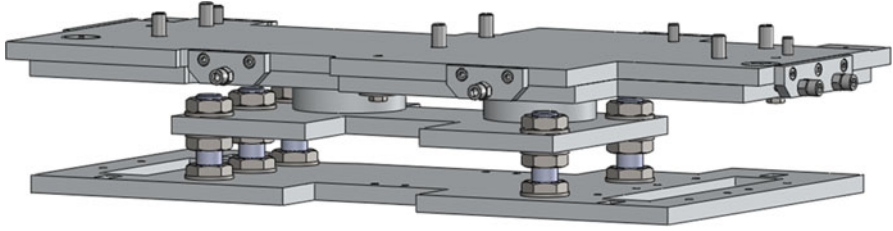
Fig. 3 Design of the stage for DC septum magnet
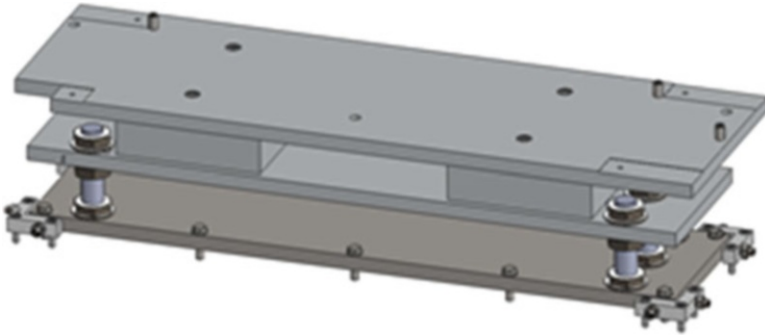
Fig. 4 Design of the stage for the AC septum magnet

2.4 Stage for the AC Septum Magnet

The stage for the AC septum magnet is designed to support and to position the AC septum magnet as shown in Fig. 4. Five, fine, M30 screws serve to adjust the height, pitch, and roll of the stage. Fifteen nuts are thinned to fit the screws. Four L-type blocks in the four corners of the stage serve to adjust the surge, sway, and yaw of the stage. An L-type block is mounted on the adjustable aluminum plate with three M8 screws. Two fine M10 screws per block are used to push the bottom plate of the stage for the AC septum magnet. After pushing the stage into the correct position, two fine M10 nuts per L-type block are tightened, and ten M10 screws are used to fix the stage on the adjustable plate.

2.5 One-Axis Goniometer Stage for the Kicker Magnet

To minimize the vertical orbit transient [5, 6] caused by misalignment and a horizontal stray field, four precise one-axis goniometer stages for the kicker magnet were designed [7], as shown in Fig. 5, and manufactured.
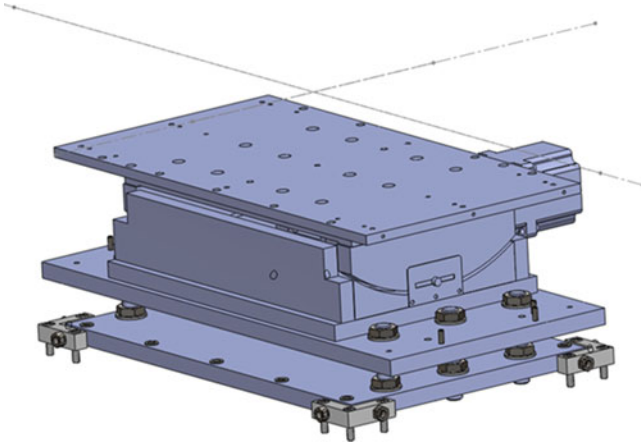
Fig. 5 Design of the one-axis goniometer stage for the kicker stage magnet in TPS

The one-axis goniometer stage is designed to position the kicker magnet and the support of the ceramic chamber, respectively. The stage is driven with a stepping motor through a ball screw to tilt the kicker magnet precisely in the roll direction.

3   Installation of the Girder System

After manufacture and inspection of the components of the girder system in the injection section, the girders are installed in our assembly factory in Chutung town in Hsinchu County. The girders are installed on the ground with 48M20 screws with corresponding nuts and ball washers. To increase the stability of the girder, the feet of girder were grouted with unshrinking concrete. The position of the girder was aligned within 0.3 mm with a laser tracker.

The adjustable aluminum plate was then installed in the middle girder of the injection section and aligned with four fiducial holes on it within 0.05 mm. The Rapson-slide mechanism, stages for the kicker, AC/DC septum, and injection vacuum system were installed on the aluminum plate or girder in sequence. The measurement results of stage for kicker magnets are listed in Table 1 within 0.05 mm. All these were aligned with a laser tracker. The kicker magnets and AC/DC septum magnets were then placed directly on the corresponding stages that were already aligned into their correct position as shown in Fig. 6.

Table 1 The measurement results of four kicker stages (K1–K4)

Fiducial pt.	Measurement (mm)			Position accuracy (mm)		
	X	Y	Z	X	Y	Z
K1-p1	10,155.989	−214.992	81.976	−0.0113	0.0082	−0.0245
K1-p2	10,155.987	−484.995	81.961	−0.0128	0.0050	−0.0394
K1-p3	10,756.037	−215.015	81.984	0.0374	−0.0151	−0.0158
K1-p4	10,756.045	−485.025	81.974	0.0452	−0.0245	−0.0257
K2-p1	6,556.034	−214.981	82.011	0.034	0.019	0.011
K2-p2	6,556.019	−484.997	82.029	0.019	0.003	0.029
K2-p3	7,156.041	−214.988	81.984	0.041	0.012	−0.016
K2-p4	7,156.039	−485.022	82.043	0.039	−0.022	0.043
K3-p1	3,755.989	−215.008	82.043	−0.011	−0.008	0.043
K3-p2	3,755.974	−485.034	82.027	−0.026	−0.034	0.027
K3-p3	4,356.007	−215.011	81.993	0.007	−0.011	−0.007
K3-p4	4,355.997	−485.045	82.010	−0.003	−0.045	0.010
K4-p1	155.980	−214.976	82.024	−0.020	0.024	0.024
K4-p2	155.994	−485.005	81.964	−0.006	−0.005	−0.036
K4-p3	755.990	−214.960	81.969	−0.010	0.040	−0.031

X: longitudinal direction, Y: transverse direction, Z: vertical direction
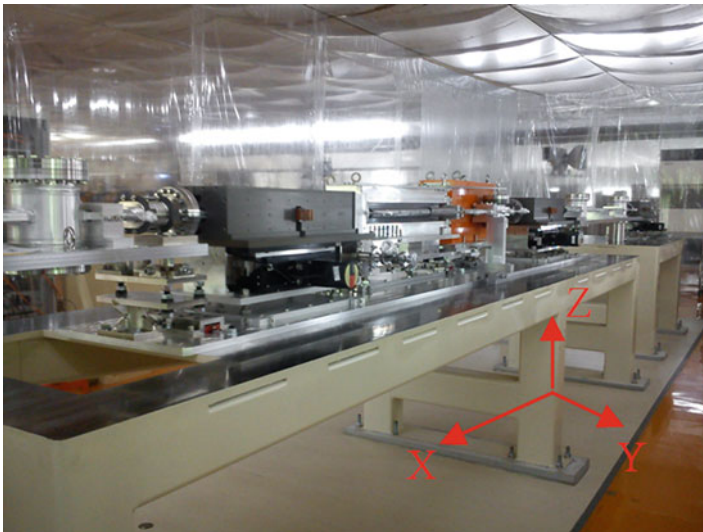
Fig. 6 The girder systems in the injection section were installed in the assembly factory in Chutung town in Hsinchu County

4   Conclusion

The integration design and installation of the girder systems for the injection section of Taiwan Photon Source are described in this chapter. The Rapson-slide design of the injection section decreases the operating voltage of the kicker magnets, which increases the reliability of the top-up operation. The design of the one-axis goniometer stage for the kicker magnet will minimize the magnitude of the horizontal stray field of the kicker magnet due to misalignment.

After manufacturing and diagnosing the components of the girder system, the injection girder system, vacuum system, and magnets are installed sequentially for some tests in our Chutung factory. The measurement results of positioning accuracy of three installed girders and the stages for the septum/kicker magnet are, respectively, within 0.3 and 0.05 mm. These results meet the requirement of the original specification.

References

1. Liu YH, Yang CS, Hsu KH, Chan CK, Chen CS, Kuo CY, Hsueh HP, Kuan CK (2011) TPS SR Kicker prototype installation status. In: The 2st international particle accelerator conference, San Sebastian, 2011
2. Blednykh A, Casey B, Dalesio B, Faussete R, Ferreira M, Fliller R, Ganetis G, Heese R, Hseuh H-C, Job PK, Johnson E, Kosciuk B, Kowalski S, Padrazo D, Parker B, Pinayev I, Sharma S, Singh O, Spataro C, Shaftan T, Wang G, Wileke F (2011) Progress with NSLS-II injection straight section design. In: Proceedings of the particle accelerator conference, New York, 2011, pp 2528–2531
3. Wang GM, Shaftan T, Kramer SL, Fliller R, Guo W, Heese R, Yu LH, Parker B, Willeke FJ (2011) Implementation of a DC Bump at the storage ring injection straight section. In: Proceedings of the particle accelerator conference, New York, 2011, pp 2378–2380
4. Kempson VC, Dobbing JA, Duller GMA, Hauge N, Hilleke G, Hansen C (2006) Pulsed magnets and pulser units for the booster and storage ring of the diamond light source. In: Proceedings of European particle accelerator conference, Edinburgh, 2006, pp 3341–3343
5. Huang I, Shin S, Kim M, Kim C, Lee EH, Ha T, Joo Y, Kim S-H, Lee B-J (2012) Injection transient motion at PLS-II. In: Proceedings of the international particle accelerator conference, New Orleans, 2012, pp 688–689
6. Fukami K, Hesegawa M, Mitsuda C, Nakanishi T, Oishi M, Ohshima T, Shoji M, Soutome K, Yonehara H, Zhang C (2008) Remote tilt-control system of an injection bump magnet in the spring-8 storage ring. In: Proceedings of European particle accelerator conference, Genoa, 2008, pp 2172–2174
7. Hsu KH, Wu MH, Lai WY, Tsai YL, Liu YH, Yang CS, Chan CK, Chen CS, Tseng TC, Sung PL, Perng SY, Wang HS, Lin CS, Chen ML, Huang DG, Chen JR (2012) Design and diagnostics of a precise 1-Axis goniometer stage for a kicker magnet in the injection section of the TPS storage ring. To be published in Proceedings of 7th MEDSI conference

FTIR Characterizations of the Gamma-Ray-Irradiated Silica Nanoparticles/γ-APTES Nanocomposite with UV Annealing

Po-Yen Hsu, Jing-Jenn Lin, Bo-Wei Lai, You-Lin Wu, Cheng-Fu Yang, and Shou-Sheu Lin

Abstract We report the effect of UV annealing on post-γ-ray-irradiated spin-coated γ-APTES and γ-APTES + NPs + UV. The structure changes of the membranes were characterized using Fourier transform infrared spectroscopy (FTIR) and atomic force microscopy (AFM). We found that the absorption peaks of the Si-O-Si-related bonds of the FTIR spectrum varied with time after 10 kGy γ-ray irradiation. The absorption peak of the NH_3^+ bonds of the post-irradiated membranes showed less sensitive to hydrogen ions. The AFM surface morphologies showed great grain reconstructions after γ-ray irradiation for all the membranes. However, following the UV annealing process, both the FTIR spectrum and AFM surface morphologies showed that only the spin-coated γ-APTES + NPs + UV membrane could be restored to the pre-irradiated status. It is believed that the nanocomposite of silica NPs mixed with γ-APTES forms a lot of γ-APTES/SiO_2 interfaces which enhance the post-irradiation UV oxidation and hence restore the membrane from degradation.

Keywords Spin coated • γ-APTES • Nanocomposite • Irradiation

P.-Y. Hsu
Winbond Electronics Corporation, Hsinchu, Taiwan

J.-J. Lin (✉)
Department of Applied Materials and Optoelectronic Engineering,
National Chi Nan University, Puli, Nantou, Taiwan
e-mail: cclin@ncnu.edu.tw

B.-W. Lai • Y.-L. Wu
Department of Electrical Engineering, National Chi Nan University, Puli, Nantou, Taiwan

C.-F. Yang
Department of Chemical and Materials Engineering, National University
of Kaohsiung, Kaohsiung, Taiwan

S.-S. Lin
Computer and Communication Engineering, National Kaohsiung First University
of Science and Technology, Kaohsiung, Taiwan

1 Introduction

The fabrication of implantable biomedical devices requires sterilization, for which EO gas and plasma are widely used. Gamma-ray is another excellent sterilization method in that it provides much deeper penetration than other methods [1–3]. However, gamma-ray sterilization could degrade implantable biosensors, and exploring the effects of radiation on biomaterials and methods to restore them could contribute to the development of ultrasensitive implantable biosensors.

Among biomaterials, 3-aminopropyltriethoxysilane (γ-APTES) easily absorbs biomolecules including deoxyribonucleic acid (DNA), protein, and cells and is thus widely used in the modification of solid-state biosensor surfaces [4–6]. In our previous studies, we reported the development of γ-APTES + silica nanoparticles (NPs) coated polysilicon wire (PSW) biosensors [7–9], in which the γ-APTES membrane can act as a hydrogen ion receiver when coated on the PSW surface. The absorption of ions induces channel conductivity changes in the PSW. However, for implantable PSW biosensors, the key concern is the effect of sterilization. This work reports on the effect of UV annealing effect on post-irradiated γ-APTES + NPs + UV. Our results show the PDMS-treated silica NPs can potentially be used as material for implantable biosensors.

2 Experiments

The preparation method of the γ-APTES and γ-APTES + NPs solutions can be found in our previous study [7–9]. The γ-APTES and γ-APTES + NPs prepared for FTIR analysis were spin coated on the thermally grown SiO_2 surface at 3,000 rpm for 30 s, then cured at 120 °C for 5 min on a hot plate. The samples coated with γ-APTES + NPs were subjected to UV light (wavelength = 365 nm) illumination for 120 s. The scanning range for the FTIR analysis ran from 700 to 4,500 cm^{-1} with a resolution of 4 cm^{-1}, and 30 scans were recorded for each absorbance spectra using the HORIBA FT720 FTIR system. The γ-APTES- and γ-APTES + NPs + UV-coated Si samples were irradiated by ^{60}Co with 10 kGy. The post-^{60}Co-irradiated UV annealing was performed in open air at room temperature.

The surface morphology of each Si sample modified with γ-APTES or γ-APTES + NPs + UV sensing membrane was measured with the SEIKO 300HV AFM system, with measurements conducted under a tapping mode with a resonant frequency of 130 kHz, a force constant of 15 N/m, a speed of 0.7 Hz, and a scan area of 3 μm × 3 μm. This work used a Si tip with a radius of less than 7 nm for all surface morphology and topography measurements.

3 Results and Discussion

Figure 1 shows the FTIR spectra of the γ-APTES with 10 kGy γ-ray irradiation. The major peak observed in the spectra is the stretching vibration of the Si-O-Si and Si-O bond from 1,033 to 1,133 cm^{-1}, which is mainly the adsorption of the pre-irradiated γ-APTES. In addition, the NH$_2$, NH$_3^+$, CH$_3$, and OCH$_2$CH$_3$ rocking vibration were, respectively, observed at 1,577; 1,488; 1,346; and 1,199 cm^{-1}. It is clearly seen that the molecular structure of the γ-APTES has changed following γ-ray irradiation. Following 10 kGy γ-ray irradiation, the intensity of the absorption peak of the Si-O-Si decreased, while the intensity of the Si-O increased. It is believed that the Si-O-Si bond was broken during γ-ray irradiation. It is also found that the intensities of the absorption peaks of the NH$_2$ and OCH$_2$CH$_3$ increased on the FTIR spectrum. However, the intensities of the NH$_3^+$ and CH$_3$ were almost unchanged.

Figure 2 shows the FTIR spectra of the post-irradiation γ-APTES + NPs + UV membrane. The spectra intensities of the major peaks for the Si-O-Si and Si-O bonds decreased following γ-ray irradiation. Comparing Fig. 2 with Fig. 1, we find the radiation effect changes with UV illumination of the Si-O-Si and Si-O bonds of the γ-APTES + NPs. The absorption peak intensities for NH$_2$, NH$_3^+$, CH$_3$, and OCH$_2$CH$_3$ of γ-APTES + NPs + UV trend similarly to those of γ-APTES following γ-ray irradiation. Figure 3a, b shows the pre- and post-γ-ray-irradiated AFM surface morphology images of the Si samples coated with γ-APTES and γ-APTES + NPs + UV, respectively. Before irradiation, no obvious aggregations were observed in the AFM surface morphologies of the γ-APTES and γ-APTES + NPs + UV. However, after irradiation, aggregations were found in the AFM images. The aggregations grew quickly over the first 3 days following irradiation and finally stopped growing after the 6th day. It is clear that all the membranes exhibited great AFM surface morphology changes which were consistent with the FTIR spectrum variations after γ-ray irradiation.
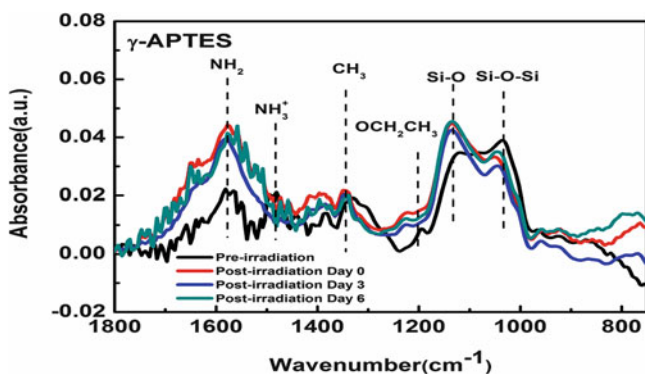
Fig. 1 FTIR characterization of the γ-APTES by 10 kGy γ-ray irradiation by post-irradiation day
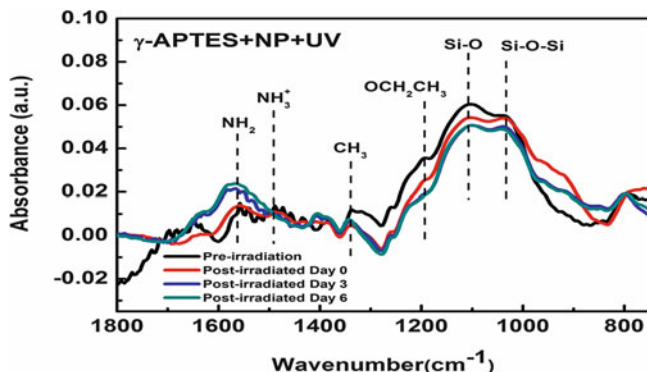
Fig. 2 FTIR characterization of the γ-APTES + NPs + UV by 10 kGy γ-ray irradiation by post-irradiation day
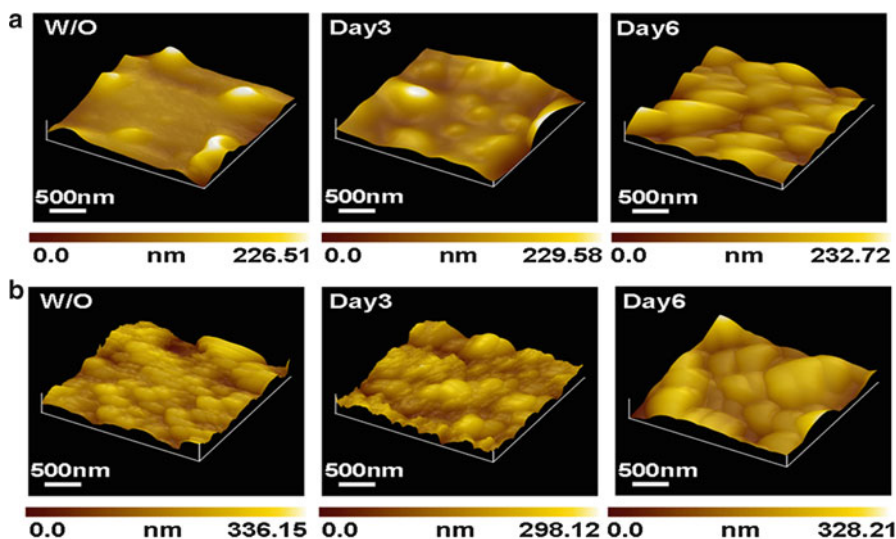
Fig. 3 Time-dependent AFM surface morphology images of the pre- and post-irradiation Si wafer coated with (**a**) γ-APTES and (**b**) γ-APTES + NPs + UV

Figure 4 shows the annealing effect on the post-irradiated γ-APTES sensing membrane with different UV annealing times. The FTIR spectra intensities of the major peaks for the Si-O-Si and Si-O bonds remain nearly unchanged by the UV annealing processes. The same results were also found for the absorption peaks of NH_3^+, CH_3, and OCH_2CH_3. However, for the NH_2 bond, the absorption peak decreased with increased UV illumination time. Figure 5 shows the UV annealing
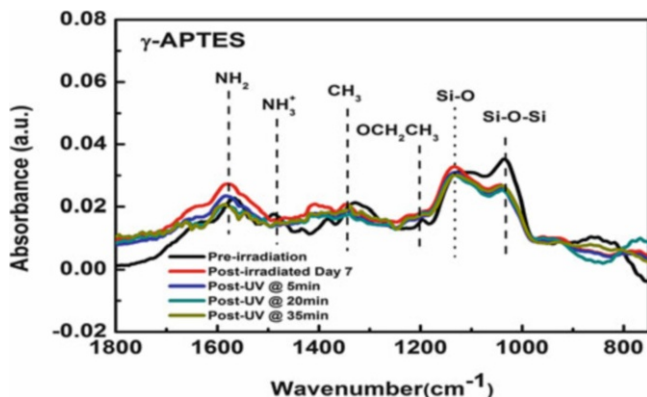
Fig. 4 FTIR characterization of the effect of UV annealing on γ-APTES by 10 kGy γ-ray irradiation by post-irradiation day
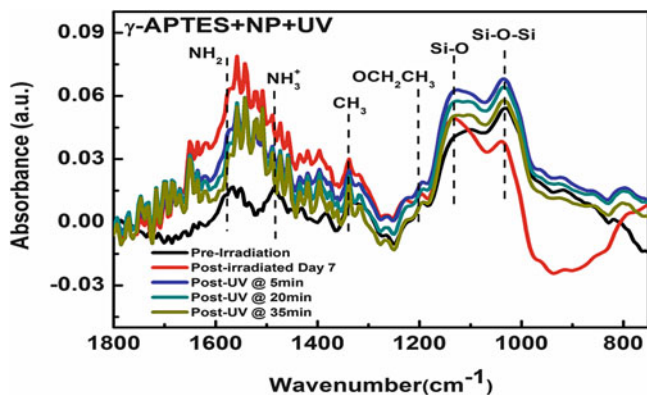
Fig. 5 FTIR characterization of the effect of UV annealing on γ-APTES + NPs + UV by 10 kGy γ-ray irradiation by post-irradiation day

effect of different annealing times on the post-irradiated γ-APTES + NPs + UV sensing membrane. The intensities of the absorption peaks for Si-O-Si and Si-O bonds from 1,033 to 1,133 cm^{-1} are clearly restored by the UV annealing process. The intensity of the absorption peak for Si-O-Si decreased following 10 kGy γ-ray irradiation. Following the UV annealing process, the intensities of the Si-O-Si and Si-O bonds were stronger than in the pre-irradiation γ-APTES + NPs + UV sensing membrane. It is believed that the broken bonds of the SiO$_2$/Si interface of the γ-APTES/silica NPs can be restored by UV oxidation processes. We also found the intensities of the absorption peaks for NH$_2$, NH$_3^+$, CH$_3$, and OCH$_2$CH$_3$
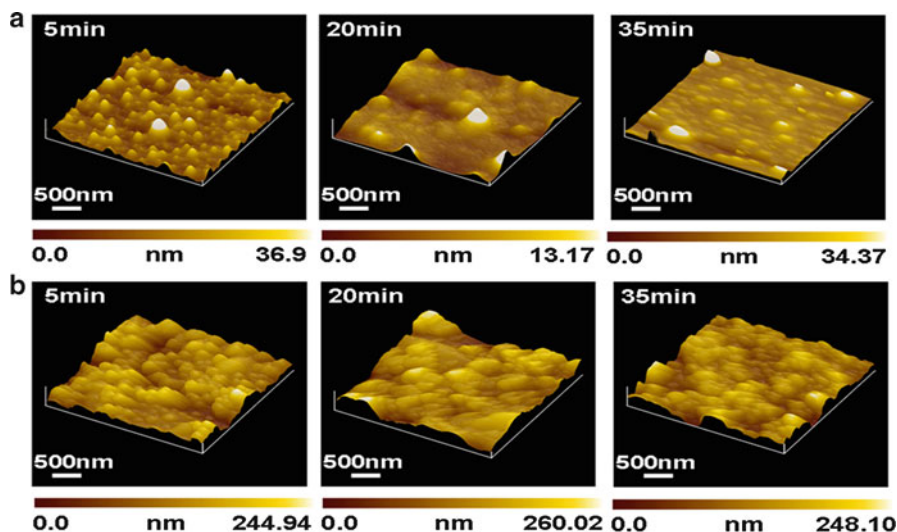
Fig. 6 Annealing time-dependent AFM surface morphology images of the post-irradiation Si wafer coated with (**a**) γ-APTES and (**b**) γ-APTES + NPs + UV

decreased with increased UV annealing time. Figure 6a, b respectively shows the AFM surface morphology images of the γ-APTES and γ-APTES + NPs annealed by post-sterilization with UV treatments. It is clear that the polymerization of the γ-APTES was not affected by UV treatment with different annealing times. But, for the γ-APTES + NPs + UV as a sensing membrane, increased UV annealing time reduced the polymerization effect, and they tend to restoration to the pre-sterilization status after 35-min UV annealing.

4   Conclusions

This chapter reports the effects of UV annealing on post-γ-ray-irradiated γ-APTES, γ-APTES + NPs, and γ-APTES + NPs + UV sensing membranes. The FTIR spectra show that the damage to the γ-APTES + NPs + UV caused by γ-ray irradiation can be restored by UV annealing. It is believed that the spin-coated γ-APTES + NPs + UV membrane has potential for use in implantable biomaterial applications.

References

1. Humenyuk I, Temple-Boyer P, Sarrabayrouse G (2008) The effect of γ-sterilization on the pH-ChemFET behaviour. Sens Actuat A Phys 147:165–168
2. Vaddirajua S, Tomazos I, Burgess DJ, Jain FC, Papadimitrakopoulos F (2010) Emerging synergy between nanotechnology and implantable biosensors: a review. Biosens Bioelectron 25:1553–1565
3. Markus H, John H, Ian S, Maren D, Martin FS, Herwig GP, Stefan T (2010) Appl Phys Lett 96:092110 0
4. Cui Y, Wei Q, Park H, Lieber CM (2001) Nanowire nanosensors for highly sensitive and selective detection of biological and chemical species. Science 293:1289–1292
5. Hahm JI, Leiber CM (2004) Direct ultrasensitive electrical detection of DNA and DNA sequence variations using nanowire nanosensors. Nano Lett 4:51–54
6. Lin CH, Hung CH, Hsiao CY, Lin HC, Ko FH, Yang YS (2009) Poly-silicon nanowire field-effect transistor for ultrasensitive and label free detection of pathogenic avian influenza DNA. Biosens Bioelectron 24:3019–3024
7. Hsu PY, Lin JJ, Wu YL, Hung WC, Cullis AG (2009) Ultra-sensitive polysilicon wire glucose sensor using a 3-aminopropyltriethoxysilane and polydimethylsiloxane-treated hydrophobic fumed silica nanoparticle mixture as the sensing membrane. Sens Actuat B 142:273–279
8. Wu YL, Hsu PY, Lin JJ (2011) Polysilicon wire glucose sensor highly immune to interference. Biosens Bioelectron 26:2281–2286
9. Wu YL, Lin JJ, Hsu PY, Hsu CP (2011) Highly sensitive polysilicon wire sensor for DNA detection using silica nanoparticles/γ-APTES nanocomposite for surface modification. Sens Actuat B Chem 155:709–715

Improvement of Radiation-Induced Degradation in MOSFET by Using Glass Fiber/Epoxy/Silica Nanoparticles/γ-APTES Composite as Shielding Materials for High-Energy Radiation

Po-Yen Hsu, Shou-Sheu Lin, Cheng-Fu Yang, and Jing-Jenn Lin

Abstract Our recent study showed that the trapping charges of the polysilicon wire sensor caused by γ-ray radiation primarily concentrated in the γ-APTES/silica nanoparticles composite layer covered on the sensor. In this chapter, we investigate the shielding effect of the glass fiber/epoxy/silica nanoparticles/γ-APTES composite materials for high-energy radiation in commercially available MOSFET. The use of glass fiber/epoxy/silica nanoparticles/γ-APTES composite plate shielding during irradiation improved the post-irradiated degradation of transfer characteristics by three orders of magnitude for the pMOSFET and half an order of magnitude for the nMOSFET, respectively, as compared to the pMOSFET and nMOSFET with the glass fiber/epoxy or glass fiber/epoxy/silica nanoparticles or without shielding.

Keywords γ-APTES • Nanoparticles • Radiation • Shielding

P.-Y. Hsu
Winbond Electronics Corporation, Hsinchu, Taiwan

S.-S. Lin
Computer and Communication Engineering, National Kaohsiung First University
of Science and Technology, Kaohsiung, Taiwan

C.-F. Yang
Department of Chemical and Materials Engineering, National University
of Kaohsiung, Kaohsiung, Taiwan

J.-J. Lin (✉)
Department of Applied Materials and Optoelectronic Engineering, National Chi
Nan University, Nantou, Taiwan
e-mail: cclin@ncnu.edu.tw

1 Introduction

Since the first proposed radiation effects of the MOS device by Naval Research Laboratory in the early 1960 [1], the studies of radiation effects in MOSFET have attracted many researchers for more than three decades. Techniques for developing radiation hardness in silicon-based [2, 3] or compound semiconductor electronic devices [4] are well established. For silicon-based semiconductor components covered with silicon dioxide insulator, the primary radiation-induced damages were confirmed by electron paramagnetic resonance (EPR) as the formation of E′- and Pb centers in the strained region of the oxide [5, 6]. The transformation and migration of the trapped charges will finally build up in the strained region of the oxide and the interface of the SiO_2/Si. As feature sizes shrink for the integrated circuit, the thickness of the silicon dioxide is continuously thinning to below 10 nm, the problem of radiation-induced trapped charges vanishes naturally, and the radiation effects mainly cause the isolation island, especially the bird's beak region [7]. As the feature sizes further shrink, the high-k materials are used to overcome the tunneling current, and the radiation issue needs to be reconsidered when increasing thickness of the insulator.

As protection from high energy of radiation for most non-aerospace grade, commercially available MOSFET is very weak. The use of package often increases the effect of radiation dosage [8]. We recently published results of the γ-ray sterilization effects in pH-sensitive polysilicon wire (PSW) sensors using a mixture of 3-aminopropyltriethoxysilane (γ-APTES) and polydimethylsiloxane (PDMS)-treated hydrophobic fumed silica nanoparticles (NPs) as a sensing membrane [9]. The previous study showed that the trapping charges caused by γ-ray radiation primarily concentrated in the γ-APTES + NPs layer covered on the PSW sensor. Figure 1a, b is an example of 358-nm-wide PSW sensor showing the channel current change ΔI as a function of glucose concentration before and after γ-ray irradiation for the γ-APTES/ native-oxide/PSW and γ-APTES + NPs/native-oxide/PSW sensors. Figure 2a, b is another example of 5-μm-wide PSW showing the channel current I_{DS} as a function of drain-to-source voltage V_{DS} before and after hydrolyzation of the post-irradiated membranes. The I_{DS} returned to its original pre-irradiation value after the removal of the post-irradiated γ-APTES + NPs membrane. Mixing the PDMS-treated silica NPs into γ-APTES can provide many γ-APTES/SiO_2 interfaces for the accumulation of trapping charges, thus protect the device from radiation damages. In this chapter, we investigate the shielding effect of the glass fiber (GF)/epoxy/silica NPs/γ-APTES composite materials for high-energy radiation.

2 Experiments and Results

The epoxy, silica NPs, and γ-APTES were mixed and degassed by a noncontact defoaming mixer. The mixed weight ratio of the epoxy, silica NPs, and γ-APTES is 100:1:1. The epoxy/silica NPs/γ-APTES composite resin and glass fiber (GF) were

Fig. 1 Example for illustrating the channel current change ΔI of a 358-nm-wide PSW as a function of glucose concentration over time before and after γ-ray irradiation for the (**a**) γ-APTES/native-oxide/PSW and (**b**) γ-APTES + NPs/native-oxide/PSW glucose sensors
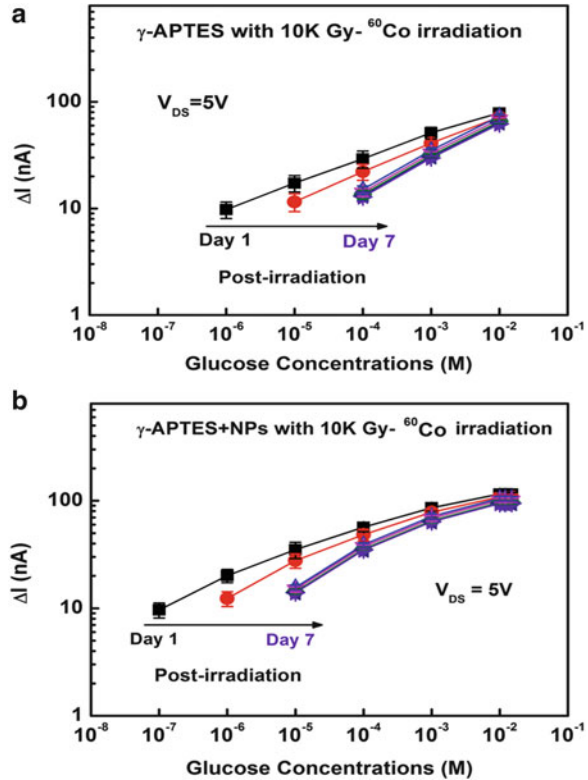
made into a prepreg with 5 layers of fiber, and then cured for 3 h in a curing oven. After curing, the plate of GF/epoxy/silica NPs/γ-APTES was cut into pieces with size of 4 cm $\times$ 4 cm, and then each six of the cut plate were made into a cubic shape box. Following the same procedures, cubic boxes made of GF/epoxy/silica NPs or GF/epoxy composite without adding γ-APTES or γ-APTES + silica NPs were also prepared for comparison. After finishing the preparation of the shielding boxes made of the GF/epoxy/silica NPs/γ-APTES, GF/epoxy/silica NPs, or GF/epoxy composite materials, two batches of the commercial MOSFETs (CD4007) were put inside these three types of boxes. Another batch of MOSFETs without shielding box was used as control elements. The four batches of MOSFETs were then subjected to the γ-ray irradiation with total dose of 10 kGy. Finally, the pre- and post-irradiation transfer characteristics of the nMOSFETs and pMOSFETs inside the boxes made of different composite materials were compared.

Figure 3 shows the transfer characteristics of the pMOSFET before and after irradiation for shielding with GF/epoxy/silica NPs/γ-APTES, GF/epoxy/silica NPs, and GF/epoxy composites, respectively. The control pMOSFET without shielding is also shown for comparison. It is found that pMOSFETs with GF/epoxy/silica NPs
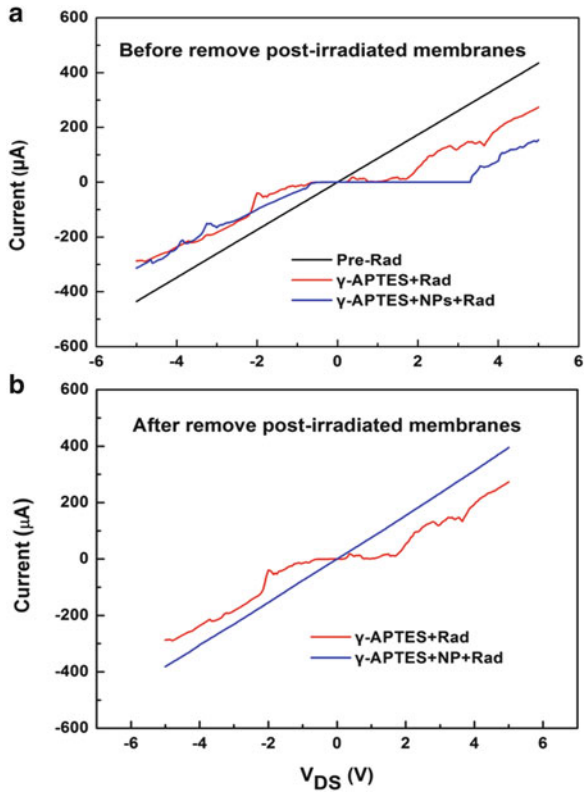
Fig. 2 Example for illustrating the channel current I_{DS} of a 5-µm-wide PSW as a function of drain-to-source voltage V_{DS} before and after γ-ray irradiation and the removal of the post-irradiated sensing films for the (**a**) γ-APTES/native-oxide/PSW and (**b**) γ-APTES + NPs/native-oxide/PSW sensors
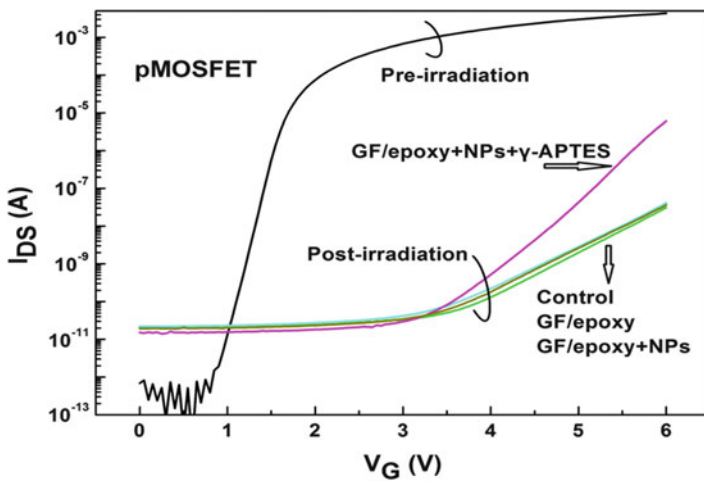
Fig. 3 Transfer characteristics of the pMOSFET before and after irradiation for shielding with GF/epoxy/silica NPs/γ-APTES, GF/epoxy/silica NPs, and GF/epoxy composites

Fig. 4 Transfer characteristics of the nMOSFET before and after irradiation corresponding to Fig. 3
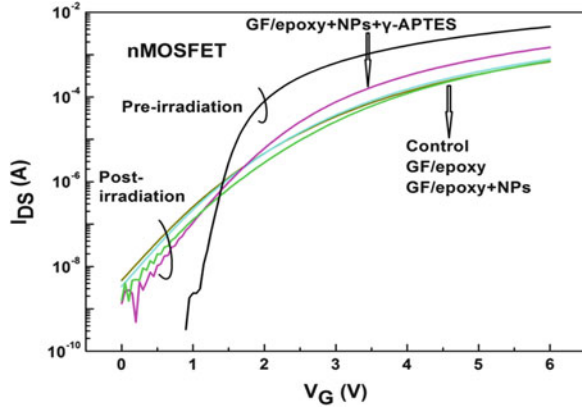
or GF/epoxy shielding have nearly no effect on the improving of radiation-induced degradation. The post-irradiated drain current I_D of the GF/epoxy/silica NPs/γ-APTES-shielded sample at $V_{DS} = 6$ V is larger than the others by three orders of magnitude. Figure 4 is the transfer characteristics of the nMOSFET before and after irradiation corresponding to Fig. 3. The post-irradiated drain current I_D of the GF/epoxy/silica NPs/γ-APTES-shielded sample at $V_{DS} = 6$ V increases by half an order of magnitude. The improvement difference between p- and nMOSFET is possible because the donor-type interface traps are induced by the radiation.

3   Conclusions

It was found that the radiation-induced degradation of the MOSFETs can be improved with the shielding of GF/epoxy/silica NPs/γ-APTE composite. No apparent effect on improvement of the radiation-induced degradation in MOSFET by using GF/epoxy/silica NPs or GF/epoxy shielding. Because epoxy resin is often used in electronic package, our investigation provides a possible way to reduce radiation-induced damage for the epoxy-based electronics package by using the epoxy/silica nanoparticles/γ-APTES composite materials.

References

1. Hughes HL, Giroux RR (1964) Space radiation affects MOSFET's. Electronics 37:58
2. Ma TP, Dressenforder PV (1989) Ionizing radiation effects in MOS devices and circuits. Wiley, New York

3. Listvan MA, Vold PJ, Arch DK (1987) Ionizing radiation hardness of GaAs technologies. IEEE Trans Nucl Sci 34:1663–1668
4. Markus H, John H, Sharp ID, Maren F, Martin S, Herwig GP, Stefan T (2010) Real-time x-ray response of biocompatible solution gate AlGaN/GaN high electron mobility transistor devices. Appl Phys Lett 96:092110
5. Revesz AG, Goldstein B (1969) Electron paramagnetic resonance investigation of the Si–SiO interface. Surf Sci 14:361
6. Marquardt CL, Sigel GH (1975) Radiation-induced defect centers in thermally grown oxide films. IEEE Trans Nucl Sci NS-22:2234
7. Benedetto JM, Boesch HE, McLean FB, Mize JP (1985) Hole removal in thin-gate MOSFET's by tunneling. IEEE Trans Nucl Sci NS-32:3916
8. Sarrabayrouse G, Siskos S (1998) Radiation dose measurement using MOSFETs. IEEE Instrum Meas Mag 1(3):26–34
9. Lin J-J, Hsu P-Y (2011) Gamma-ray sterilization effects in silica nanoparticles/γ-APTES nanocomposite-based pH-sensitive polysilicon wire sensors. Sensors 11:8769–8781. doi:10.3390/s110908769

An Invention of Pneumatically Powered and Charged LED Flashlight

Kuo-Yi Li

Abstract The present invention pertains to a pneumatically powered and charged LED flashlight that conquers the flashlight of the firefighter deficient in electricity in the emergency rescue work especially in a dark fire scene. A high-pressure air in the air bottle is able to drive an operation of a volute magnet unit in order to generate sufficient electricity for 30 min within 20 s. The present product attains rapid electricity generation with an effort-saving operation, low electricity use, and waterproof effect, which is an excellent green firefighting device.

Keywords Pneumatically • Power generation • LED • Flashlight

1 Introduction

The firefighter in the dark disaster occasions like a mining pit and a tunnel requires proper lighting equipment to attain the rescuing mission. The flashlight is one of the commonly used lighting appliances [1, 2]. The batteries are used to allow the flashlight to function. However, the overused batteries not only consume energy but incur serious contamination to the environment [3, 4]. Time-saving is a matter of critical importance in a rescuing mission, so it is impossible for firefighters to leave the disaster site and replace batteries out of the site if the flashlight lacks electricity suddenly [5]. The present invention uses the air bottle with every firefighter to quickly charge the flashlight and provide sufficient luminance. Therefore, the present invention solves the sudden insufficiency of electricity of the flashlight. The study of the energy saving and carbon reduction as well as relevant patents related to chargeable flashlights is described as follows.

K.-Y. Li (✉)
Department of Industrial Engineering and Management, National Chin-Yi University of Technology, Taichung, Taiwan
e-mail: kyli@ncut.edu.tw

1.1 Study of the Energy Saving and Carbon Reduction for Flashlight

The definition of energy saving and carbon reduction is to save the energy and decrease the discharge of carbon dioxide in order to minimize the break in the hole of the atmospheric envelope and mitigate the influence of the worsened warm effect [6, 7]. To attain a light device facilitating the saving energy and reducing carbon, traditional tungsten-filament bulbs and incandescent light bulbs are gradually substituted by LED bulbs. The LED bulb has a small bulk, a low power consumption, a low electricity consumption, a long life, and a property of being friendly to the environment. The deficiencies of the LED bulbs are a low efficiency, a small luminous flux, an insufficient light effect, and a poor average luminance [8, 9]. With regard to the environmental protection issue, white LEDs, the superior lighting equipment in the next generation, can be recycled and will not contaminate the environment. With the development of light technology, the evaluation of future light source should not only focus on the light efficiency but emphasize the light effect, light comfort, light bio-effect, and evaluation of light safety, environmental protection, and source consumption [10, 11].

1.2 Study of Relevant Patents Related to Charging Flashlights

In order to solve the sudden insufficiency of electricity in time of rescuing in underground disaster places, some firms develop the flashlight with an electricity generation function. In TIPO patent search system, some relevant patents are found, and the features as well as disadvantages are briefly described as follows. (1) A utility innovation patent of "An LED flashlight capable of manually charging and generating electricity" as invented by Wen-Song Li is disclosed. The disclosure has small electricity power and low luminance [12]. (2) A utility innovation patent of "An LED flashlight capable of manually charging and supplying the outside with electricity" as invented by Yu-Chi Chen is disclosed. The disclosure uses the manual gear set to generate electricity but provides small electricity power and slow charging speed [13]. (3) A utility innovation patent of "A self-generating flashlight" as invented by Wen-Li Chou is disclosed. The disclosure uses the rectilinear motion of the hand pull unit to drive the dynamoelectric gear and generate electricity, which however spends labors and provides small electricity power [14]. The typical flashlights can be generally classified into manual-swinging flashlights, hand-pressing flashlights, pulling flashlights, and reciprocating sway flashlights. These flashlights cannot provide much electricity and charge quickly, so they are not suitable for the emergency rescue in disaster occasions.

2 Research Method

2.1 Experimental Research Method

According to the research goal, the present invention adopts an experiment research method to study the problem of the suddenly insufficient electricity of flashlights. The experimental research method is a stricter method by detecting the concatenation of independent variables and dependent variables under a well-controlled situation. The experimental result can attain the explanation, the prediction, and the goal of controlling phenomenon [15–17]. According to the spirit of the experimental research method, the present invention tests correlated parameters related to the operation, such as air flow velocity, air flow quantity, turning number of the coil, and electricity power, in order to find a safety protection device with superior functions. First, conduct an original base of the structure of the LED flashlight product and apply an Inventor software to design the interior structure of the product, including the combination view of product, the perspective view, the plan assembly view, and the schematic view of the operation. After completing the layout of the LED flashlight product via the Inventor software, convert the drawing data of all components into IGES format or STL format, which can be thence saved in the RP or the CNC machine to execute the pattern manufacture. Therefore, the present invention adopts the RP and the CNC 3D to accomplish the pattern manufacture for a reference of processing a substantial product.

2.2 TRIZ Method

TRIZ method, resolving theory of inventive problems, is a polybasic methodology and a systematized analyzing method that comprises many inventive tools, such as 40 inventive principles, contradiction matrix, substance-field analysis, 76 standard solutions, and ARIZ (Algorithm for Inventive Problem Solving) [18–20]. The present pneumatic powered and charged LED flashlight experiences the inventive problem-solving phase, an original setting of product phase, an embodiment stage, a product layout phase, a model-making stage, a substantial manufacturing stage, a marketing stage, etc. All the processes use the 40 inventive principles and the contradiction matrix to optimize the product. The 40 inventive principles include forty principles, such as the division principle, the separation principle, the merging principle, and the universal principle. The contradiction matrix is divided into a technique contradiction and a physical contradiction. Wherein the technique contradiction functions when one parameter in the system is improved and the other parameter is set to be contrary to the previous parameter. The physical contradiction functions when the same parameters are in conflict and has to increase some specific parameters [21–23]. To idealize the innovation of the pneumatically powered and charged LED flashlight, five correlated inventive principles like the

division principle, the merging principle, the universal principle, the dynamic principle, and the change of parameters principle are adopted to execute the analysis. In the 39 parameters of the contradiction matrix, the present invention follows the spirit of the contradiction matrix in order to decline the influence of conflict items and attain the goal of the optimized layout.

3 Product Design

3.1 Product Structure and Functions

Referring to Fig. 1, the product mainly includes a main body, an electricity generation coil, a volute blade magnet unit, a rectifier, a chargeable lithium battery, a quick air inlet joint, and an air discharge switch. In use, the present invention has to connect the inlet port at the tail end of the pneumatically powered and charged LED flashlight to the quick joint of the air bottle. By using the high-pressure air of the air bottle to quickly strike the electricity generation coil of the flashlight in a
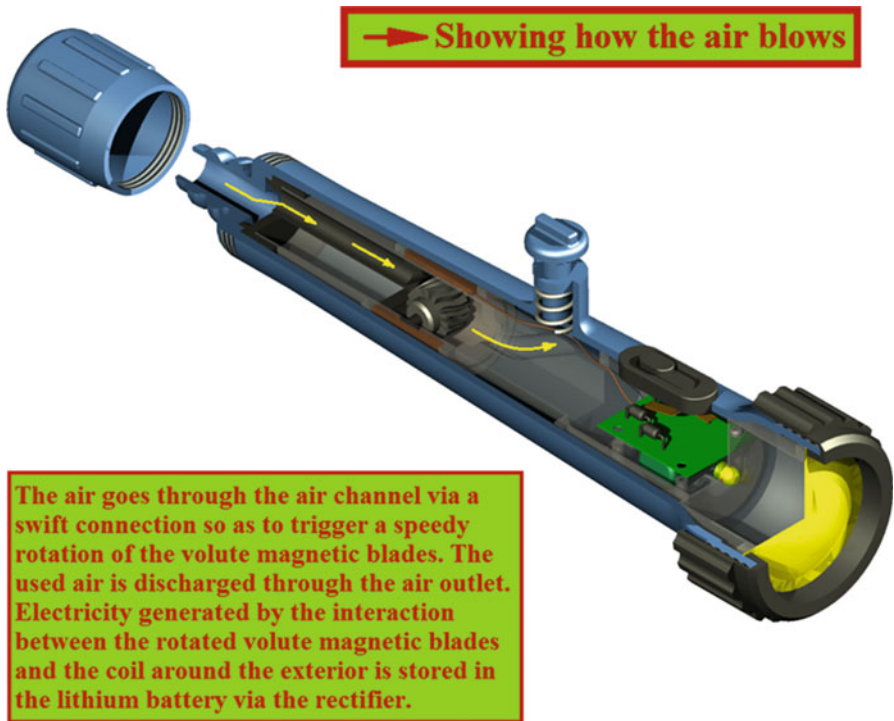
Fig. 1 The present pneumatically powered and charged LED flashlight

short period of time, a mutual motion between the coil and the electromagnet is caused to generate electricity, which is sent to the rectifier and thence stored in the lithium battery of the flashlight. The product can generate the power electricity within 20 s, which supplies the LED bulbs with the use time of about 30 min for firefighters to continue the rescue work. The product, an excellent firefighting device, has features of rapid generation and charge of electricity, an operation with less labor, a low electricity use, and a waterproof effect. The present product is not only adapted to firefighters but suited to where the pressured-gas device is arranged. The present invention with a simple configuration and a rapid charging effect is extremely adapted for the emergency rescue.

3.2 The Computer Animation and Pattern Manufacture

The present pneumatically powered and charged LED flashlight adopts an Inventor software to establish 2D and 3D drawings. The computer animation is used in both of the original setting phase and the embodiment stage. A simple edition of the animation is made in the original setting phase. The use of the computer animation is convenient to discuss the product configuration with the flashlight user and shorten the time of developing products. The use of the computer animation in the embodiment stage is convenient to discuss the product model with model technicians and properly remind them that the flashlight may have a wall with a smaller thickness. Therefore, the pattern manufacture can be successfully completed. The computer animation includes the arrangement of the projection, films, 3D data, music, and subtitles. The "Ulead VideoStudio" software is then used to complete the animation. Before converting the 2D and 3D data designed by the Inventor software into IGES format and STL format, it is better to communicate with the model technicians via the computer animation for decreasing the error of component tolerance and intensity. The present invention adopts a specific RP machine to manufacture patterns of the main body and the sealing cover. The inner components of the main body are more complicated in the manufacture due to the use of the supporting material. By means of the prior communication of the computer animation, the pattern manufacture is successfully completed. The CNC 3D process is applied to make the discharging switch and the air inlet joint. Due to the animation communication, the pattern manufacture is successfully completed.

3.3 Features of the Product

The features of the present invention are as follows:

Rapidly generating and charging electricity: The present invention applies the air bottle with the firefighter to inject high-pressure air that quickly strikes the

volute magnet blade unit. Therefore, the present invention can generate the power electricity within 20 s supplying the LED bulbs with the use time of 30 min for firefighters to continue the rescue work.

Operation with less labor: The traditional flashlights, such as manual-swinging flashlights, hand-pressing flashlights, pulling flashlights, and reciprocating sway flashlights, are operated by using the palm to execute labored and tedious actions for the electricity generation. In contrast, the present invention saves labor and attains an efficient operation by using the high-pressure air to quickly generate electricity.

Low consumption of electricity: By comparing with the traditional bulb, the adoption of the LED bulb in the present invention facilitates less consumption of electricity power under the same luminance to efficiently prolong the rescue time in disaster occasions.

Providing a waterproof effect: The light device must have the waterproof effect since there is water in the disaster place during the rescue. Therefore, at the air inlet port of the flashlight and the contact end of the LED head light, a silicone rubber member is used to firmly cover the joint part for a preferable waterproof effect.

4 Conclusion

The chargeable flashlights in the market may generate electricity and provide lighting effect but have problems of spending labor and time in the operation and smaller electricity power. They are not adapted for the emergency rescue. The present pneumatically powered and charged LED flashlight is designed to solve the sudden deficiency of electricity in dark disaster occasions and avoid interrupting the rescue. By applying high-pressure air in the air bottle with the firefighter that quickly strikes the volute magnet blade unit, the present invention can generate the power electricity within 20 s supplying the LED bulbs with the use time of 30 min. The product, an excellent firefighting device, has features of rapid generation and charge of electricity, an operation with less labor, a low electricity use, and a waterproof effect. The present invention is now registered in a Utility Innovation Patent No. M437418 in Taiwan. The present invention also obtained the gold medal from the Inventeco and the Taipei international invention shows of 2012. The present invention deserves to be widely applied in the market of firefighting devices.

References

1. Elvidge CD, Imhoff ML, Baugh KE, Hobson VR (2001) Night-time lights of the world: 1994–1995. ISPRS J Photogramm Remote Sens 56(2):81–99
2. Vianello C, Fabiano B, Palazzi E, Maschio G (2012) Experimental study on thermal and toxic hazards connected to fire scenarios in road tunnels. J Loss Prev Process Ind 25(4):718–729

3. Sun L, Qiu K (2011) Vacuum pyrolysis and hydrometallurgical process for the recovery of valuable metals from spent lithium-ion batteries. J Hazard Mater 194:378–384
4. Li J, Shi P, Wang Z, Chen Y, Chang CC (2009) A combined recovery process of metals in spent lithium-ion batteries. Chemosphere 77(8):1132–1136
5. Mattsson B, Juås B (1997) The importance of the time factor in fire and rescue service operations in Sweden. Accid Anal Prev 29(6):849–857
6. Eyre N (2001) Carbon reduction in the real world: how the UK will surpass its Kyoto obligations. Clim Policy 1(3):309–326
7. Boyd R, Ibarraran ME (2002) Costs of compliance with the Kyoto Protocol: a developing country perspective. Energy Econ 24(1):21–39
8. Kawagoshi Y, Oki Y, Nakano I, Fujimoto A, Takahashi H (2010) Biohydrogen production by isolated halotolerant photosynthetic bacteria using long-wavelength light-emitting diode (LW-LED). Int J Hydrog Energy 35(24):13365–13369
9. Yam FK, Hassan Z (2005) Innovative advances in LED technology. Microelectron J 36(2):129–137
10. Tianhu L, Luoguangyi YS (2012) Layer illumination management technology based on LED. Energy Procedia 16:477–482
11. Chen HC, Wu GY (2010) Investigation of irradiance efficiency for LED phototherapy with different arrays. Optics Commun 283(24):4882–4886
12. Li WS (2004) LED flashlight capable of manually charging and generating electricity. Taiwan Utility Innovation patent No. M245355, Taichung
13. ChenYC (2006) LED flashlight capable of manually charging and supplying the outside with electricity. Taiwan Utility Innovation Patent No. M288917, Taipei
14. Chou WL (2004) Self-generating flashlight. Taiwan Utility Innovation Patent No. M250091, Taipei
15. Chang SH (2005) Research method. Tsang Hai Book Publishing Company, Taichung
16. Kuo SY (2006) Psychological and educational research. Chin Hua Book Publishing Company, Taipei
17. Babbie E (2002) The basics of social research. Thomson Learning Inc., Wadsworth
18. Althuller G (2005) 40 principles: TRIZ keys to technical innovation. Technical Innovation Center, Worcester
19. Deimel M (2011) Relationships between TRIZ and classical design methodology. Procedia Eng 9:512–527
20. Orloff MA (2003) Inventive thinking through TRIZ: a practical guide. Springer, New York
21. Rousselot F, Merk CZ, Cavallucci D (2012) Towards a formal definition of contradiction in inventive design. Comput Ind 63(3):231–242
22. Yoon J, Kim K (2011) An automated method for identifying TRIZ evolution trends from patents. Expert Syst Appl 38(12):15540–15548
23. Prickett P, Aparicio I (2012) The development of a modified TRIZ Technical System ontology. Comput Ind 63(3):252–264

The Invention in the Safety Protection Device of the Table Saw

Kuo-Yi Li

Abstract The goal of the present invention is to design a safety protection device of the new table saw, which applies a transparent safety guard and the spring to form a protection space around a cutting tool of the table saw. The operator clearly sees the processing procedures via the LED unit and the transparent safety guard and prevents hands from touching the cutting tool. A dust-collecting apparatus under the table saw is arranged to gather dust and debris. Therefore, the accidents of cutting and kickback injuries are prevented.

Keywords Table saw • Safety • Safety guard • Safety protection device

1 Introduction

The table saw is one of the common cutting machines that are widely adapted to cut woods and thin boards. However, even a slight incautious operation easily leads to the injury of the fingers [1, 2]. In light of the statistics of national occupational accidents from the Council of Labor Affairs (CLA) in 2011, the proportion of the injury to fingers is 37.46 %. The main reason for this injury is that the cutting machines do not equip themselves with any protection devices. Therefore, it suggests that the employer should install protection devices on the machines [3, 4]. Due to the table saw having a sharp serrated sheet and cutting tools in a high-speed rotation, the cutting and kickback injuries are easily caused, and the generation of debris and dust is adverse to the environment [5]. To prevent these problems, I have designed a safety protection of

K.-Y. Li (✉)
Department of Industrial Engineering and Management, National Chin-Yi University of Technology, Taichung, Taiwan
e-mail: kyli@ncut.edu.tw

the new table saw and expect to decrease the frequency of accidents. The study of potential damages of the table saw and relevant patents in relation to the safety protection devices is described as follows.

1.1 Potential Damages of the Table Saw

In the processing of the table saw, install a disc saw on a working base and move the workpiece along a guiding board to a cutting space of the disc saw so that the operator executes the cutting operation under the protection of a safety guard [6]. With respect to the accidents due to the table saw, the statistics show that the proportion of injury to the upper limb is 71.6 % and the proportion of injury to the fingers is 57.8 % [7].

The problem found on the centrifugal force derived from the high-speed rotation of the cutting tools is that the serrated sheet may sometimes rupture and scatter [8]. When the table saw is used to cut the plywood, the plywood may become recovered and suddenly clamp the rotated serrated sheet to result in the rupture or scattering of the sheet and hurt the operator [9]. When the table saw operates, the unsafe behavior will cause the accident, especially for the cutting injury to fingers. The unsafe environment means the environmental sanitation of the working place will have the problem of debris and dust contamination when no dust-collecting apparatus is installed [10, 11].

1.2 Study of Patents in Relation to Safety Protection Devices of the Table Saw

To prevent the operation of the table saw from hurting hands, some firms develop safety protection devices for the table saw. In the TIPO patent search system, some relevant patents are found, and the features as well as disadvantages are briefly described as follows. (1) A utility innovation patent submitted by Shia et al. and titled by a protection device and a disc saw equipment with a protection device is disclosed. This patent discloses to boost the blade of the protective guard and expose the disc cutting blade when the equipment cuts the wood. The cutting tool in the disclosure may easily hurt operator's hands [12]. (2) A utility innovation patent submitted by Tsai and titled by a safety debris-free apparatus of the disc saw is disclosed. This disclosure may have a partial protection effect but still has problems, such as failure to protect the operator during the entire process and the poor debris-free effect [13]. (3) A utility innovation patent submitted by Yan and titled by a table-typed safety device of the disc saw is disclosed. This disclosure may have a partial protection effect but still has problems, such as failure to protect the operator during the entire process and the easy-scattering debris [14]. These kinds of safety protection devices for the table saw restrict the damage inside the safety protection device to avoid hurting operators [15].

2 Research Method

2.1 Experimental Research Method

According to the research goal, the present invention adopts an experiment research method to study the problem of the safety guard of the table saw. The experimental research method is a stricter method by detecting the concatenation of independent variables and dependent variables under a well-controlled situation. The experimental result can attain the explanation, the prediction, and the goal of controlling phenomenon [16–18]. According to the spirit of the experimental research method, the present invention tests correlated parameters related to the operation, such as blade rotation speed, cutting direction, feeding velocity, and protection space, to find a safety protection device with superior functions. After completing the layout of the safety protection device of the table saw via the Inventor software, convert the drawing data of all components into IGES format or STL format, which can be then saved in the RP or the CNC machine to execute the pattern manufacture. Therefore, the present invention adopts the RP and the CNC 3D to accomplish the pattern manufacture for a reference of processing a substantial product.

2.2 TRIZ Method

The TRIZ method, resolving theory of inventive problems, is a polybasic methodology and a systematized analyzing method that comprises many inventive tools, such as 40 inventive principles and contradiction matrix. TRIZ consists of five basic elements, namely, a technology system, an innovative grade, an idealized principle, a contradiction, and an evolution of technology system. These elements develop the current technology [19–21]. The first commonly used principle in the TRIZ method is the 40 inventive principles, which include 40 principles, such as the division principle, the separation principle, and the universal principle. The secondary commonly used principle is the contradiction matrix, including 39 elements, such as the weight of the moving object, speed, and temperature [22, 23]. To idealize the innovation of the safety protection device, five correlated inventive principles like the division principle, the merging principle, the universal principle, the dynamic principle, and the change of parameters principle are adopted to execute the analysis. In the 39 parameters of the contradiction matrix, the present invention follows the spirit of the contradiction matrix in order to decline the influence of conflict items and attain the goal of the optimized layout.

3 Product Design

3.1 Product Structure and Functions

The present invention mainly comprises a height-adjusting shank, a sliding seat, a compressed spring, a light unit, a transparent safety guard, and a fixing pin. Referring to Fig. 1, a dust-collecting apparatus, a dust-gathering tube, a disc saw protection seat, etc., are disposed under the main body. The transparent safety guard is formed into a U-shaped contour, with its bottom extending to two sides. The safety guard driven by the compressed spring presses the workpiece during the entire process and forms a protection space to keep the operator's hands out of the disc saw and keep the operator from the cutting and kickback accidents. The safety guard is made of a transparent acrylic material. On the top-front side of the safety guard, an LED is disposed to clearly see the processing of the disc saw within the safety guard and prevent accidents efficiently. In a normal cutting process, the fixing pin fixing on the sliding rail and the safety guard fixing on the top of the disc saw prevent the operator's hands from touching the cutting tools
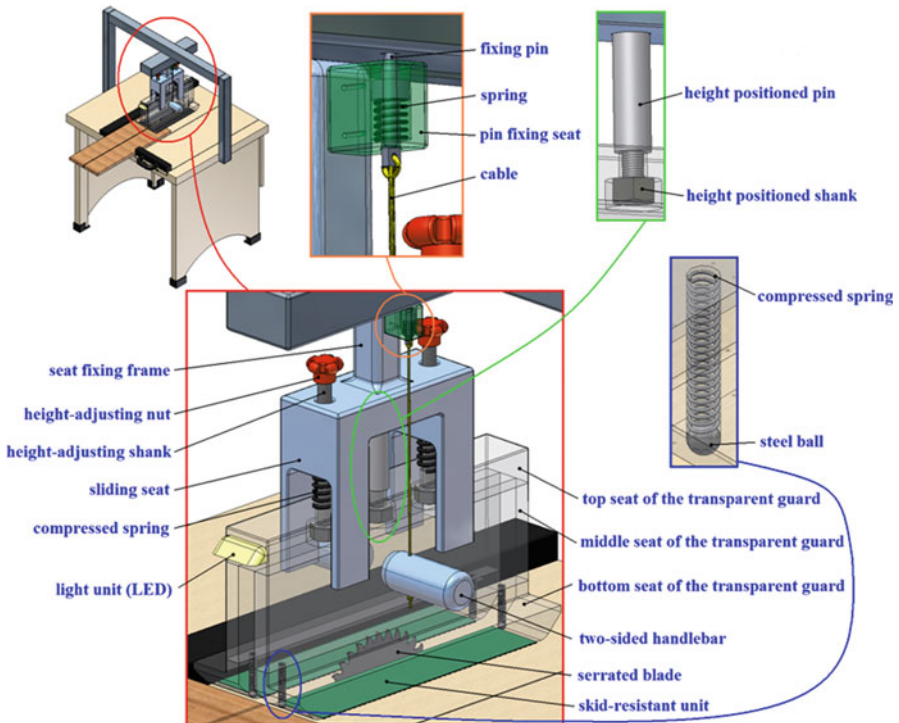
Fig. 1 Safety protection device of the table saw

efficiently. While cutting an end of the workpiece longitudinally, the operator's hands grasp the handlebars and press downward to allow the cable to depart the fixing pin from the rail, which render the workpiece able to be pressed by the safety guard and moved forward to complete the end process. Because the operator's hands are put on the handlebar of the safety guard, the hands are efficiently prevented from touching the cutting tools.

3.2   Computer Animation and Pattern Manufacture

The use of the computer animation in the embodiment stage is convenient to discuss the product model with model technicians in order to prevent the errors in the pattern manufacture. The computer animation includes the arrangement of the projection, films, 3D data, music, and subtitles. The "Ulead VideoStudio" software is then used to complete the animation. Before converting the 2D and 3D data designed by the Inventor software into IGES and STL formats, it is better to communicate with the model technicians via the computer animation for decreasing the error of component tolerance and intensity. The present invention adopts a specific RP machine to manufacture patterns of the sliding seat and the fixing pin. The inner components of the main body are more complicated in the manufacture due to the use of the supporting material. By means of the prior communication of the computer animation, the pattern manufacture is successfully completed. The CNC 3D process is applied to make the U-shaped safety guard and the left and the right extension parts. Due to the animation communication, the pattern manufacture is successfully completed.

3.3   Features of the Product

The features of the present invention are as follows:

Obviousness of the dangerous region: The U-shaped safety guard is made of a transparent acrylic material. A light device is disposed on the top-front side of the safety guard to clearly see the processing of the cutting device and prevent accidents.

Prevent hands from touching the cutting tools to ensure the operator's safety: Between the U-shaped safety guard and the sliding seat, the spring and the bolt are used to allow the safety guard to press the workpiece during the entire cutting process. The extension part at two sides of the bottom of the U-shaped safety guard forms a safety protection space in the workpiece cutting position to avoid the accidents.

Assure the safety of the lateral cutting: While proceeding a lateral cutting, the operator pushes the workpiece at the right of the U-shaped safety guard without touching the workpiece by hands.

Assure the safety of the longitudinal cutting: When cutting the end of the workpiece, the operator holds two handlebars at two sides and presses downward to allow the workpiece to be pressed by the safety guard and moved forward to complete the cutting without hurting the hands.

Keep the operator from debris and dust: A dust-collecting device is disposed below the table saw to efficiently gather cutting debris into a debris receptacle, which keeps the operator from dust contamination.

4 Conclusion

Typical table saws may cooperate with different safety devices, but those devices may hurt the operator's hands due to the fact that the workpiece boosts the safety guard in the cutting process to cause the interstice between the disc saw and the working base. The two-sided extension part extending from the bottom of the present U-shaped safety can overcome this problem. Further, the configuration of fixing pin and the sliding seat solves the kickback of the material in the process of longitudinally cutting the end. The features of the present invention are listed as follows:

1. Superior protection efficiency: The extension part at two sides of the bottom of the U-shaped safety guard forms a safety protection space in the workpiece cutting position to prevent the hands from touching the cutting tool, avoid the kickback of the material, and attain a protective effect.
2. Concise and good configuration: Height and sliding seat can be adjusted according to user's demands. The present invention attains an easy operation.
3. Low manufacture cost: The present invention comprises simple components that are easy to assemble and lowers the manufacture cost efficiently. By these features, the present invention is submitted as a utility innovation patent whose application number is 101218058. The present invention also obtained the gold medal from the Ukraine international invention show in 2012.

References

1. Shields BJ, Wilkins JR, Smith GA (2011) Nonoccupational table saw-related injuries treated in US Emergency Departments, 1990–2007. J Trauma-Inj Infect Crit Care 71(6):1902–1907
2. Frank M, Lange J, Napp M, Hecht J, Ekkernkamp A, Hinz P (2010) Accidental circular saw hand injuries: trauma mechanisms, injury patterns, and accident insurance. Forensic Sci Int 198(1):74–78

3. Council of Labor Affairs Executive Yuan (2011) Investigation of injury location due to occupational accidents. Annual report of Labor statistics in year 2011, Taipei
4. Liu LW, Hsu CF (2009) Study of the prevention and reestablishment method in insurance of occupational accidents in different countries. Labor safety sanitation research (IOSH97-H302), Taipei
5. Pon HT, Lan HF, L HH, Yah MC (2011) Bio-material practice. College of Agriculture, National Pingtung University of Science and Technology, Pingtung
6. Demaine ED, Demaine ML, Kaplan CS (2001) Polygons cuttable by a circular saw. Comput Geom 20:69–84
7. Ratnasingam J, Ioras F, Abrudan IV (2012) An evaluation of occupational accidents in the wooden furniture industry-a regional study in South East Asia. Safety Sci 50(5):1190–1195
8. Cheng LF (2009) Safety protective standard for tool machines and establishment of inspection process- take cutting center machines as an example. Master thesis, In-service Master Program of Graduate Institute of Economic Management, Feng Chia University, Taichung
9. Hsien HL (2003) Industrial safety sanitation. Wu Nan Book Publishing Company, Taipei
10. Lindroos O, Aspman EW, Lidestav G, Neely G (2008) Accidents in family forestry's firewood production. Accid Anal Prev 40(3):877–886
11. Igathinathane C, Melin S, Sokhansanj S, Bi X, Lim CJ, Pordesimo LO, Columbus EP (2009) Machine vision based particle size and size distribution determination of airborne dust particles of wood and bark pellets. Powder Technol 196(2):202–212
12. Shia YJ, Cheng ST, Wu CM, Huang YT, Huang SC (2010) A protection device and a disc saw equipment with a protection device. Taiwan Utility Innovation Patent No. M388982, Hsinchu
13. Tsai YS (1988) A safety debris-free apparatus of the disc saw. Taiwan Utility Innovation Patent No. 095622, Tainan
14. Yan AA (1991) A table-typed safety device of the disc saw. Taiwan Patent No. 160241, Hsinchu
15. International Organization for Standardization (2002) Safety of machinery guards general requirements for the design and construction of fixed and movable guards. International Standard No. 14120, ISO
16. Chang SH (2005) Research method. Tsang Hai Book Publishing Company, Taichung
17. Kuo SY (2006) Psychological and educational research. Chin Hua Book Publishing Company, Taipei
18. Babbie E (2002) The basics of social research. Thomson Learning Inc, Wadsworth
19. Althuller G (2005) 40 Principles: TRIZ keys to technical innovation. Technical Innovation Center, Worcester
20. Deimel M (2011) Relationships between TRIZ and classical design methodology. Procedia Eng 9:512–527
21. Orloff MA (2003) Inventive thinking through TRIZ: a practical guide. Springer, New York
22. Rousselot F, Merk CZ, Cavallucci D (2012) Towards a formal definition of contradiction in inventive design. Comput Ind 63(3):231–242
23. Yoon J, Kim K (2011) An automated method for identifying TRIZ evolution trends from patents. Expert Syst Appl 38(12):15540–15548

Applying the Principles of Lean Manufacturing to Optimize Conduit Installation Process

Jun-Ing Ker and Yichuan Wang

Abstract To meet the ever-increasing demand for concrete shelters that house telecommunication equipment, the construction company under study has hired several new employees and grouped them to work in teams; however, the expected increase in production has not been achieved consistently. The objective of this study is to apply the principles of lean manufacturing to identify root causes for productivity variations in their conduit installation process and suggesting ways of improvement. By observing the conduit installation process on-site and timing each task, non-value-added activities that prohibit productivity were recognized, including rework, talking, employee interference, and gathering materials and tools. Based on the findings, we suggested the company to implement training modules to help standardize work methods, prepare assembly kits, move supply carts closer to the work sites, and optimize team size. These suggestions help reduce the non-value-added procedures and add time to productive work.

Keywords Lean manufacturing • Time study • Root cause analysis • Conduit installation process optimization

1 Introduction

Telecommunication companies rely on strong concrete shelters to protect their people, revenue, and equipment from extreme weather, vandalism, and the destructive effects of time. To meet the ever-increasing demand for concrete shelters,

J.-I. Ker (✉)
Industrial Engineering, Louisiana Tech University, Ruston, LA 71272, USA
e-mail: ker@latech.edu

Y. Wang
Department of Aviation and Supply Chain Management, Auburn University,
Auburn, AL 36830, USA

the construction company under study has hired several new employees and grouped them to work in teams; however, the expected increase in production has not been achieved. The main thrust of our study consists of applying the principles of lean manufacturing to identify root causes for productivity variation in their conduit installation process and suggest ways of improvement to increase productivity.

Construction projects generally can be divided into repetitive and non-repetitive activities [1]. The construction of the shelters in this study is a non-repetitive process, which creates a volatile working environment, as the company has to deal with an array of clients demanding hundreds of building models that are often different in sizes and facilities equipped inside. Three main manufacturing segments involved in the interior fabrication of a shelter are conduit installation, wire pulling, and electrical wiring. Due to the extensive nature of construction, this study focused on the conduit installation process. The purpose of this project is to identify the root causes leading to productivity variation and suggest areas of improvement to improve the productivity.

2   Theory Building

To understand the conduit installation process, we conducted time studies. The time study procedure involves defining the task, deciding number of observations needed for each task, computing the average observed cycle time, and determining performance rating [2]. Cycle time refers to the length of time to complete a process. It is an important metric in practicing lean manufacturing as the reduction in cycle time often results in higher productivity [3]. Activities within the cycle time can be divided into two groups: value added and non-value added. Non-value-added tasks add no value to the overall product, and the elimination of these activities is one way to decrease the cycle time.

Another approach to reducing cycle time is by improving the learning rate of the newly hired workers. The learning curve expresses the relationship between experience and efficiency described by a power function, commonly referred to as Henderson's Law. Some basic guidelines exist for estimating the learning percent – the percentage of time reduced from each iteration. Usually statistical analysis of time data is implemented along with this formula

$$C_n = C_1 n^{-a}. \tag{1}$$

A common tool utilized in this project for comparison among data is percent difference denoted by the formula

$$\% \text{ difference} = \frac{(N_o - N_1)}{N_o}, \tag{2}$$

where N_o is the number of tasks completed in the original cycle and
   N_1 is the number of tasks completed in the new cycle.

3   Methodology

In this project, the conduit installation process was divided into eight tasks: work, walking, measuring, viewing plans, retrieving tools/equipment, talking, rework, and employee interference. Most of these tasks are self-explanatory; however, a few need clarification. Work refers to anything directly related to constructing the building, including cutting conduit, bending conduit, and drilling holes. The plans for each building in fabrication are taped to various interior walls for reference. The task viewing plans involves the time taken to interpret the construction instructions throughout the day. Talking among employees consists of both personal and work-related. Rework entails any action that needs to be repeated due to error. Employee interference occurs when someone's work is disrupted by another employee's actions or equipment.

The following steps were followed to achieve the project goal: (1) observe/record workers, (2) divide procedure into subcategories (tasks), (3) identify non-value-added procedures, (4) analyze task distribution and respective times, (5) identify reasons for productivity variations, (6) propose ways to eliminate non-value-added time and variations, (7) present time savings, and (8) estimate projected productivity increase.

3.1   Procedure

We first examined the production schedule and chose shelters of similar models to begin the time study. When conducting time study, one observer was assigned to observe one to two workers per day. It was found that experienced workers worked faster than newly hired workers.

For analytical purposes, special attention was given to the follow circumstances during time studies:

1. Talking to other employees: Note personal versus work related.
2. Walking to supply and conduit carts: Activities include walking to (W), getting equipment (E), and walking back (W).
3. Location of supply and conduit carts: Note the locations of two material supply carts in reference to the main door and generator room door.
4. Walking to retrieve extra tools or materials: Activities include walking to (W), getting equipment (G), and walking back (W).
5. Employee interference: Interference can be disguised as other tasks. For example, employee A cannot work in his designated area because employee B is in the way; therefore, employee A is forced to work outside the building creating excessive walking in and out.
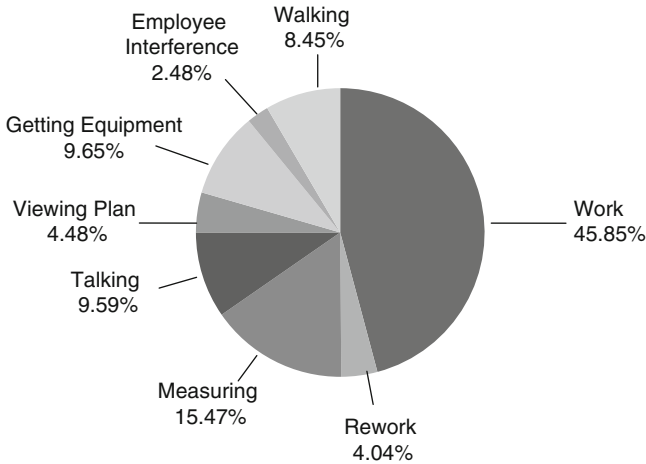
Fig. 1 Conduit installation task time distribution

3.2 Data

After all the data was entered, an overall task and time distribution table was generated to show the initial state. This time distribution is seen in Fig. 1. Four non-value-added activities were identified, including rework, talking, employee interference, and gathering materials and tools. These non-value-added activities account for about 34 % of total task time.

4 Recommendations

Based on the findings, four suggestions were offered to the case company: (1) implement training modules, (2) prepare assembly kits, (3) move supply carts, and (4) optimize team size.

4.1 Training Module

Currently there is no standard training procedure for conduit installation resulting in large task time variations between new employees and experienced workers. While this is expected, more intense standardized training can eliminate a portion of this gap. Figure 2 shows the results from the comparison of two workers with over 10 years of experience and two workers with less than 6 months of experience. It can be seen that the experienced workers spent more time on working and less time on talking, measuring, and performing rework.

Fig. 2 Productivity variations between new and experienced workers
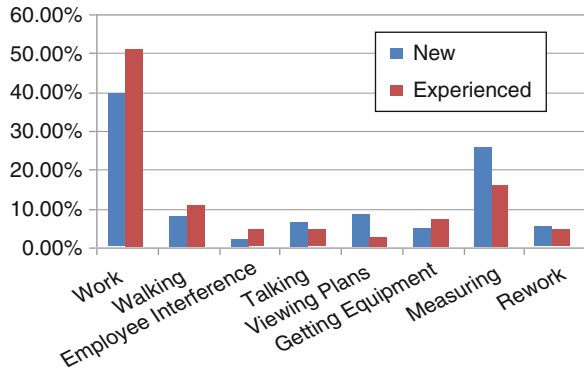
By implementing a separate training area with one designated experienced trainer for a week, the trainee will have the opportunity to familiarize himself with the tools and basic techniques needed. To calculate how much time this would save, a learning curve was generated. From examining basic guidelines published for various industries, a 95 % learning curve was deemed efficient [4]. This 95 % learning curve means that when the number of iterations performed doubles, the total completion time will be reduced by 5 %. Since a new employee takes approximately 6 h to complete the conduit process on the first shelter attempted, the learning curve is

$$C_n = 6n^{-074}. \tag{3}$$

By assembling a total of five buildings, one building per day for 1 week, the employee will reduce the total competition time by 11.23 % or 69.65 min. This is found by using Eq. 2 to calculate the percent difference as shown below.

$$C_5 = 6(5)^{-.074}$$

$$C_5 = 5.33 \text{ h}$$

$$\% \text{ difference} = \frac{(C_1 - C_5)}{C_1}$$

$$\% \text{ difference} = \frac{(6 - 5.33)}{6} = 11.23 \%$$

4.2 Moving Supply Carts

The current placement of supply carts varies. On average, an employee takes twelve trips to the supply carts during the work period. By moving the supply cart and

Fig. 3 Conduit installation
new task time distribution
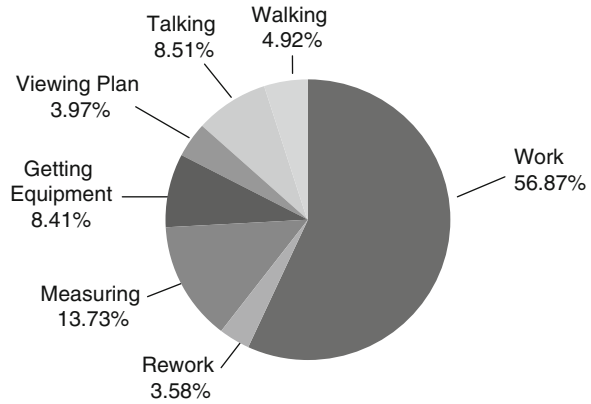
conduit cart in between the building doors, the time spent on walking will be reduced by 50 % for employees working in the generator room and 25 % for employees working in the main room. This will result in a time saving of 12.58 min.

4.3 Assembly Kits

Employees often are required to leave the work area to retrieve materials and tools needed. Since the production schedule is known in advance, assembling kits with all needed materials and tools specified for the building can be prepared prior to the conduit installation operation. This will decrease time spent on walking, talking, and getting materials and tools and result in a saving of 67.70 min.

4.4 Optimum Team Size

Since the productivity varies among teams, some require more workers than others. Given the restricted work space, too many employees generate clutter and thus, create interference with productivity. With the implementation of the previous suggestions, the team size can be reduced, decreasing employee interference, talking, and labor cost. A proposed size of four workers would be sufficient, placing one in the generator room and three in the main room. An exact savings of labor cannot be found given insufficient financial information. However, the time saved is found by summing all the interference time found during observation. This generated a total saving of 53.68 min.

By implementing all four suggestions, the results display a total possible savings of 3.394 h. In other words, a total of 11.02 % of the observed time (30.8 h) can be turned into productive work. Figure 3 shows new task time distribution resulting from these time savings.

5 Conclusion

Assuming the employees at case company work 40 h a week and the project observations are a good representation of their normal production conditions, by implementing the lean manufacturing principles, the case company has the potential to save 229.17 h per year. The time saved can then be allotted to complete an additional 45 conduit installations per year.

References

1. Harmelink DJ, Rowings JE (1998) Linear scheduling model: development of controlling activity path. J Constr Eng Manage 124:263–268
2. Heizer J, Render B (2000) Principles of operations management. Pearson College Division, Upper Saddle River
3. Shah B, Ward PT (2003) Lean manufacturing: context, practice bundles, and performance. J Oper Manage 21:129–140
4. Goldberg MS, Touw A (2005) Statistical methods for learning curves and cost analysis. The CNA Corporation, Alexandria

Portable Measurement System for Static and Dynamic Characterization of MEMS Component

Hsiao-Wen Wu, Liang-Chia Chen, Abraham Mario Tapilouw, Xuan-Loc Nguyen, and Jin-Liang Chen

Abstract MEMS performance can be determined from the static and dynamic characteristic. These two parameters can be measured by various measuring systems. In this chapter, a portable measurement system which is able to measure static and dynamic characteristic of MEMS in 2-D and 3-D aspects is presented. Nanoscale static microstructure profiles are measured by means of white-light interferometry with nanometer scale accuracy. Key for dynamic characteristic measurement is the employment of stroboscopic lighting which is synchronized with the excitation signal of the measured sample. The system is capable of measuring multimode resonant frequencies and also mode reconstruction for both in-plane and out-of-plane vibration. The main advantage of the system is its versatility and portability for testing different vibration modes with improved reliability and repeatability. Achievable repeatability of the resonant frequency measurement can reach 0.012 kHz for in-plane vibration, while the repeatability of the out-of-plane resonant frequency is 0.216 kHz for a controlled environment and 0.354 for an environment with disturbance from air conditioner.

Keywords MEMS • In-plane • Out-of-plane • Resonant frequency measurement

H.-W. Wu
Department of Electronics Engineering, Tung Nan University, Taipei, Taiwan

L.-C. Chen
Department of Mechanical Engineering, National Taiwan University, Taipei, Taiwan

A.M. Tapilouw
Graduate Institute of Automation Technology, National Taipei University
of Technology, Taipei, Taiwan

X.-L. Nguyen (✉) • J.-L. Chen
Research and Development Division, Allied Engineering and Consultant, Inc, Taipei, Taiwan
e-mail: aoi@aecteam.com

1   Introduction

Microelectromechanical systems (MEMS) are the integration of mechanical elements, sensors, actuators, and electronics on to a silicon substrate through microfabrication technology [1]. The mechanical and chemical processes during MEMS fabrication affect the final shape and characteristics of the MEMS. Undesired defects can significantly affect the performance of the MEMS during its operation in dynamic modes, either vibrating in in-plane direction or out-of-plane. Thus, static and dynamic characteristics of MEMS must be accurately measured during inspection. Static characteristic includes dimension measurement and surface profilometry which can be performed by common phase-shifting interferometry (PSI) or vertical scanning interferometry (VSI) systems.

   Dynamic characteristic of MEMS can be generally divided into two categories, in-plane and out-of-plane vibration. There are many developed methods for measuring dynamic out-of-plane vibratory modes of micromechanical devices employing single-beam laser Doppler vibrometers [2]. However, these techniques are valid only for slow point-type scanning measurement and would be pretty time-consuming. Laser phase-shifting interferometry can also be combined with stroboscopic lighting [3–5] for measuring the surface of the vibrating MEMS.

   In this chapter, a MEMS measurement system is introduced. The system is capable of measuring resonant frequency of in-plane and out-of-plane vibration. Surface profile measurement can also be performed by means of white-light interferometry both in static and dynamic condition. Comparison of the measurement repeatability of resonant frequency performed in two conditions is presented, one is when the room air conditioner is turned off and the other one is when the room air conditioner is turned on. The experimental results show that the developed system for resonant frequency measurement is not affected severely by the acoustical noise and vibration from the air conditioner.

2   Measurement Principles

The developed testing platform employs a replaceable microscopic objective for different applications with a tunable field of view (FOV). The microscope is equipped with a motorized X-Y stage and also a nanoscale piezo translator for performing vertical scanning and phase-shifting interferometry measurement. Figure 1a shows the picture and the schematic of the optional features of the system.

   The key element of the developed system is the stroboscopic lighting which is employed in dynamic measurements such as automatic resonant frequency detection and also dynamic profile measurement [6–9]. Synchronization of the signal generators is crucial to resonant frequency detection, in-plane and out-of-plane
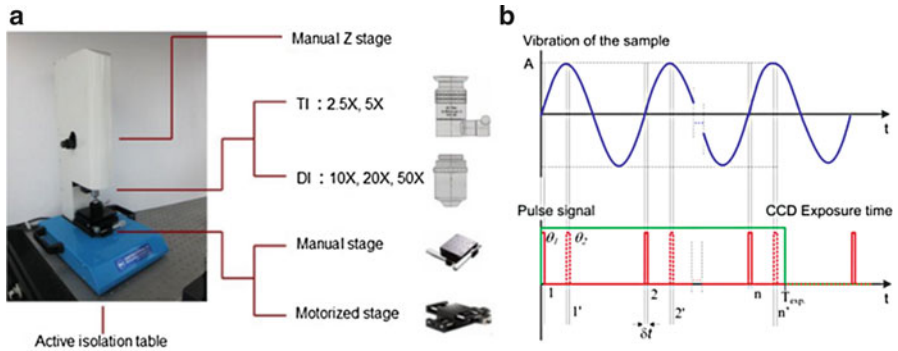
Fig. 1 The developed system and its stroboscopic measuring principle: (**a**) developed MEMS testing platform (courtesy of AEC corp.), (**b**) synchronization signal of the sample and stroboscopic lighting in the system

measurement. Figure 1b shows the sinusoidal signal for exciting the sample and also pulse signaling for the stroboscopic lighting.

Phase delay between the vibration signal and the pulse signal (θ) is varied to enable reconstruction of the vibrational mode of the sample. Phase delay θ_1 is applied to the pulse signal to perform reconstruction of the object at 0°, and phase delay θ_2 is applied to perform reconstruction of the object at 90°. By applying different phase delays between the pulse light and the vibration signal in one period, the vibrating object can be three-dimensionally reconstructed and the dynamic characteristics of the object being excited a periodical signal can be observed and derived automatically. This principle is applied for analyzing vibrating objects both for in-plane and out-of-plane directions.

2.1 Resonant Frequency Detection

In-Plane Resonant Frequency Detection. In-plane resonant frequency is detected by firstly defining the Region of Interest (ROI) at the vibration region of the sample, frequency scanning range, and frequency scanning pitch. The vibration is quantified by calculating its magnitude and phase from the series of images captured at a certain frequency. After the scanning process is finished, Bode plot is generated for determining the resonant frequency.

In the detection process, template matching technique is applied for the measurement of motion vectors. The matching process includes the matching of the template at every possible orientation of the sample. A matching score based on normalized cross correlation is evaluated at each orientation, and the highest
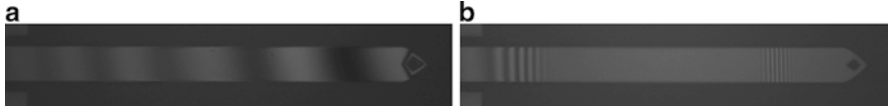
Fig. 2 Interferogram of AFM cantilever beam vibrating at (**a**) not resonant frequency and (**b**) resonant frequency

matching score determines the motion vector. The formula of normalized cross correlation is given as follows:

$$c = \frac{n \sum_{i,j} A_{ij}B_{ij} - \sum_{i,j} A_{ij} \sum_{i,j} B_{ij}}{\sqrt{n \left(\sum_{i,j} A_{ij}^2\right) - \left(\sum_{i,j} A_{ij}\right)^2} \sqrt{n \left(\sum_{i,j} B_{ij}^2\right) - \left(\sum_{i,j} B_{ij}\right)^2}}, \tag{1}$$

where c is cross correlation, n is the pixel number of template or source image, and A_{ij}, B_{ij} are intensities of the template and source image at position (i, j) of image coordinate, respectively.

In order to overcome rotation variant problem in template matching, a set of templates at different orientation is employed for matching. During the searching process, all the template patterns are used to compare with a source image. Resolution of the image is also another limitation for resolution of template matching. This limitation can be overcome by resampling the image into higher resolution by means of interpolation and then Gaussian smoothing filter to minimize the high-frequency noise of the image. Motion vectors are calculated by performing template matching with the new image. By doing so, resolution of the template matching can be increased to sub-pixel resolution.

After obtaining of the motion vectors, sinusoidal fitting technique is applied to the data to calculate magnitude and phase of the vibration. Magnitude and phase information are needed to construct a Bode plot for determining resonant frequency.

Out-of-Plane Resonant Frequency Detection. Resonant frequency in mechanical system is the frequency which induces vibration to unstable maximum amplitude. In interferometry system, this phenomenon could be clearly observed and automatically detected by the change of the interferogram pitch during vibration. The higher vibration amplitude, the smaller interferometric fringe pitch is.

As an example for demonstrating the change in the interferogram when it is vibrating in the resonant frequency, a contact mode cantilever beam is employed for experiment. Cantilever beam was chosen because of the simple structure and known mechanical characteristic. However, this resonant detection technique is also applicable for other samples such as membrane. Figure 2a shows the interferogram of the sample when the vibration frequency is not the resonant

frequency. In contrast, Fig. 2b shows the interferogram of the sample when vibrated at its resonant frequency. It can be observed that the pitch of the interferogram fringe is clearly reduced and became smaller when the sample was vibrating at its resonant frequency.

Based on this phenomenon, resonant frequency detection is performed by analyzing the spatial frequency of the interferogram at different stimulating frequency of the sample. Fast Fourier transform (FFT) is employed for accurately extracting the frequency components of the interferogram fringes.

Frequency scanning is performed in two stages, coarse and fine scanning. With the coarse scanning result obtained, fine scanning is then performed around the result with smaller frequency scanning pitch. Within this range, the same spectrum analysis algorithm is performed to obtain the final frequency scanning result, and the fine peak is calculated by using a centroid detection method.

3   Measurement Results

In-Plane Resonant Frequency Detection. The tested sample is an electrostatic comb drive and an actuator where two comb structures can be moved together by applying a voltage and an excited frequency. Nominal resonant frequency of the comb drive was 2.7 kHz. The sample is excited with sinusoidal signal with amplitude 5 V. Figure 3a shows the image of the comb drive, and Fig. 3b shows captured images under microscopic optical system, respectively.

Repeatability test of the measurement is performed by measuring the sample 30 times. The measurement results are shown in Fig. 4. The average of measured
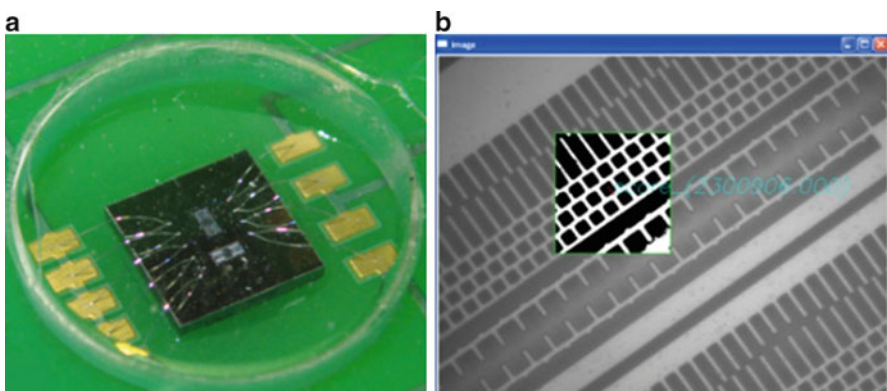
Fig. 3 In-plane measurement of a MEMS comb drive: (**a**) image of a MEMS comb drive, (**b**) vibrating parts of the comb drive captured by the microscopic system
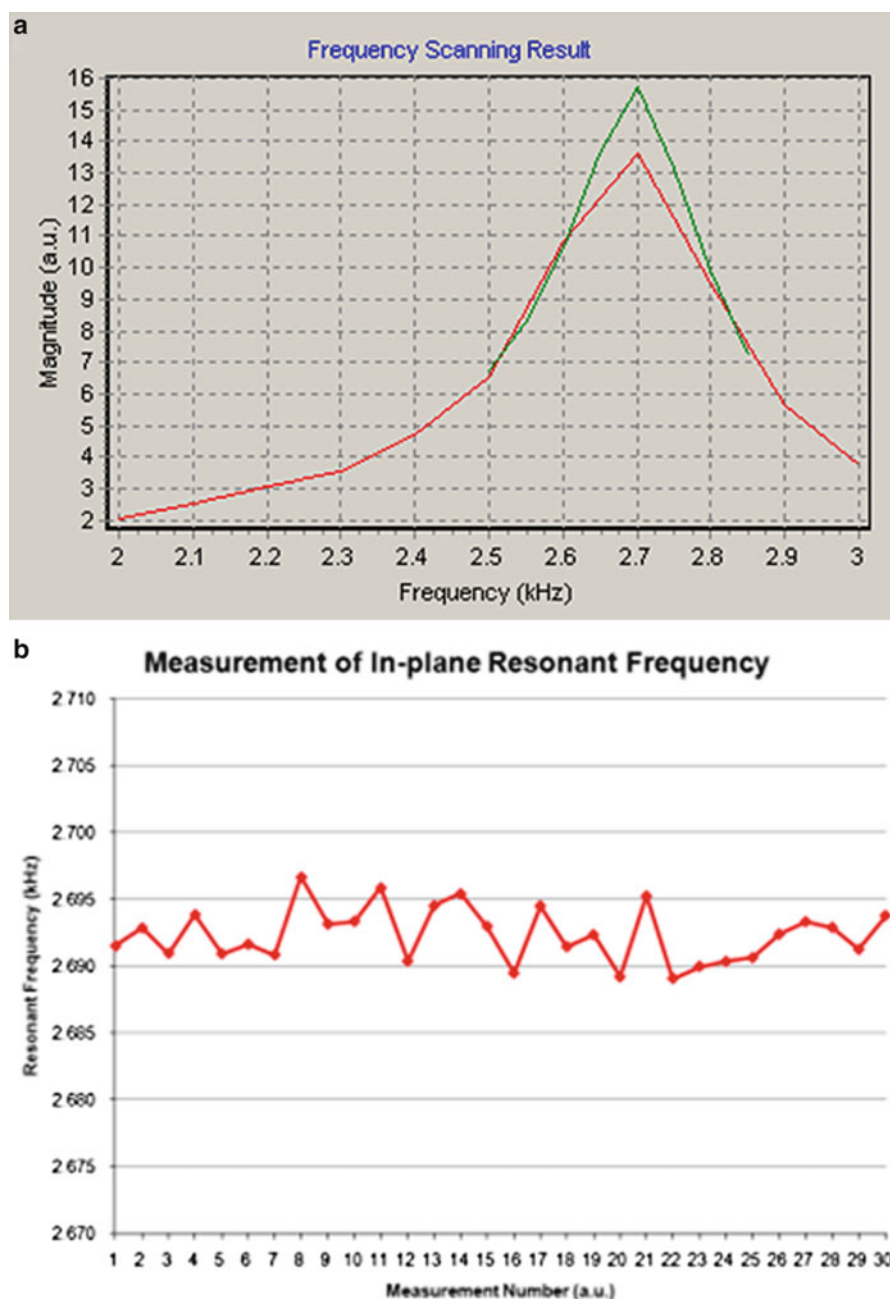
Fig. 4 (**a**) Measurement result of in-plane resonant frequency and (**b**) repeatability measurement result of in-plane resonant frequency measurement
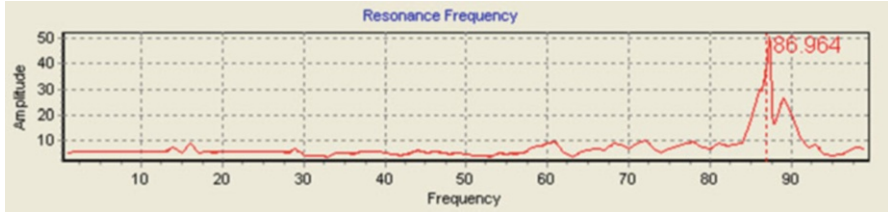
Fig. 5 Resonant frequency measurement result of AFM cantilever beam

resonant frequency was 2.692. The repeatability of the measurement was 0.012 kHz for six times standard deviation (Six Sigma).

Out-of-Plane Resonant Frequency Detection. The measurement for out-of-plane resonant frequency detection is performed in two conditions. The first experiment was performed with air conditioner in the room turned off to minimize the disturbance to the system, while the second experiment was performed with air conditioner in the room turned on. This test was performed to the out-of-plane resonant frequency detection because the detection is based on interferogram which is sensitive to environmental disturbance.

The measurement result of the AFM cantilever beam is shown in Fig. 5. In this result, the scanning result was 86.964 kHz, and the measurement is performed in the experiment room with air conditioner turned off.

The repeatability measurement results at the two conditions are shown in Fig. 6. The average resonant frequency when the air conditioner was turned off was 86.992 kHz, and the repeatability was 0.216 kHz (Six Sigma). Meanwhile, the average measured resonant frequency when the air conditioner was turned on was 86.970 kHz, and the repeatability was 0.354 kHz (Six Sigma).

These experiment results show that the environment disturbance doesn't affect the measurement result significantly and the system is still capable of measuring resonant frequency accurately. However, further study and extensive experiment is still needed to investigate the limit of the environment disturbance acceptable by the system.
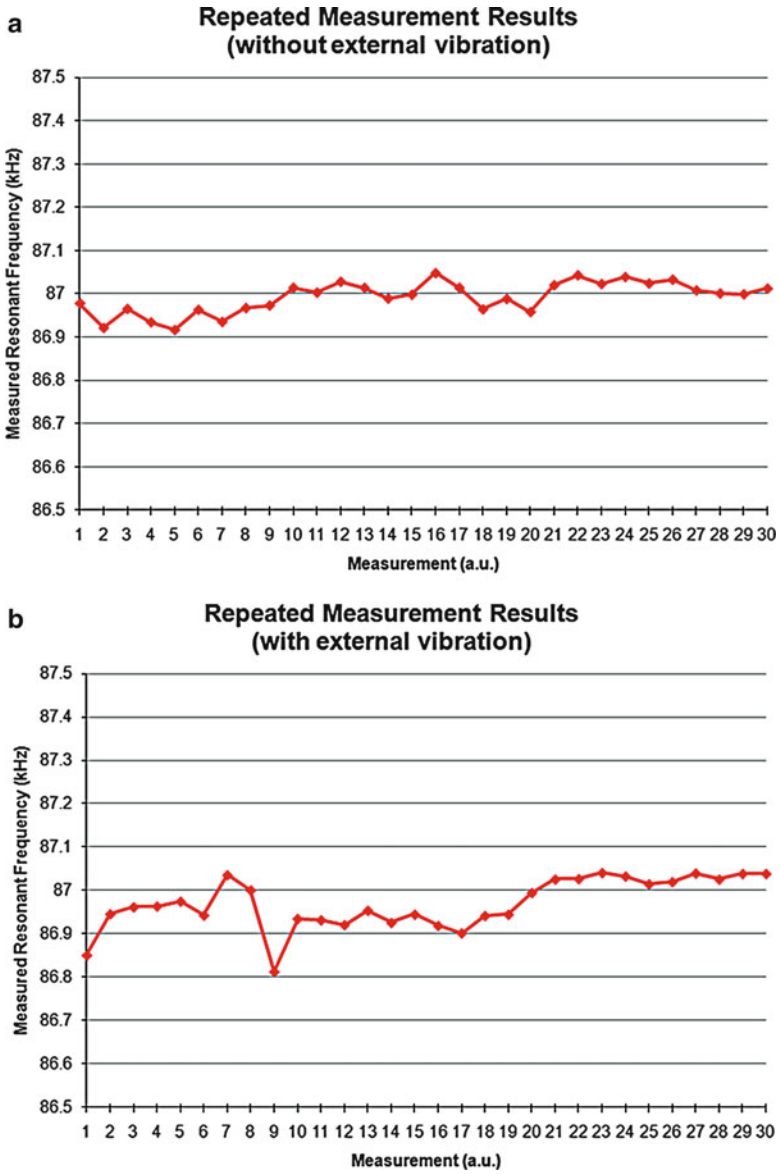
Fig. 6 Repeatability measurement results of out-of-plane resonant frequency measurement when (**a**) air conditioner was turned off and (**b**) air conditioner was turned on

4 Conclusions

A system for measurement of dynamic characteristic of MEMS component has been developed successfully. The system was validated for measuring resonant frequency of in-plane and out-of-plane vibration. Repeatability of the in-plane measurement was 0.012 kHz with the average measured resonant frequency of 2.692 kHz. The measurement repeatability of the out-of-plane resonant frequency measurement was 0.25 % for a static measurement where environment disturbance was minimal and was increased moderately up to 0.4 % for the measurement in an environment with disturbance from air conditioner. The repeatability of the measurement was calculated for six times standard deviation (Six Sigma). The results demonstrate that the system is still reliable when environmental disturbance exists.

References

1. Coppola G, Ferraro P, Iodice M, De Nicola S, Finizio A, Grilli S (2004) MEMS inspection by digital holographic. In: 24th international conference on microelectronics, 2004, Nis, Serbia and Montenegro, vol 211 pp 213–216
2. Speller K, Goldberg H, Gannon J, Lawrence EM (2002) Unique MEMS characterization solutions enabled by laser doppler vibrometer measurements In: SPIE'2002, pp 478–485
3. Bosseboeuf A, Gilles JP, Danaie K, Yahiaoui R, Dupeux M, Puissant JP, Chabrier A, Fort F, Coste P (1999) Versatile microscopic profilometer-vibrometer for static and dynamic characterization of micromechanical devices. In: SPIE'1999, pp 123–133
4. Petitgrand S, Yahiaoui R, Danaie K, Bosseboeuf A, Gilles JP (2001) 3D measurement of micromechanical devices vibration mode shapes with a stroboscopic interferometric microscope. Opt Lasers Eng 36:77–101
5. Rembe C, Kant R, Muller RS Optical measurement methods to study dynamic behavior in MEMS. In: SPIE'2001, pp 127–137
6. Chen L-C, Huang Y-T, Nguyen X-L, Chen J-L, Chang C-C (2009) Dynamic out-of-plane profilometry for nano-scale full-field characterization of MEMS using stroboscopic interferometry with novel signal deconvolution algorithm. Opt Lasers Eng 47:237–251
7. Liang-Chia C, Yao-Ting H, Huang-Wen L, Jin-Liang C, Calvin CC (2008) Innovative automatic resonant mode identification for nano-scale dynamic full-field characterization of MEMS using interferometric fringe analysis. Meas Sci Technol 19:125303
8. Liang-Chia C, Yao-Ting H, Kuang-Chao F (2007) A dynamic 3-D surface profilometer with nanoscale measurement resolution and MHz bandwidth for MEMS characterization. Mechatronics IEEE/ASME Trans 12:299–307
9. Liang-Chia C, Xuan-Loc N, Hsin-Sing H, Jin-Liang C (2010) Dynamic surface profilometry and resonant-mode detection for microstructure characterization using nonconventional stroboscopic interferometry. Ind Electron IEEE Trans 57:1120–1126

Effects of BaTi$_4$O$_9$ Concentration on Dielectric Constants of the Polyetherimide/BaTi$_4$O$_9$ Composites

Wei-Kuo Chia, Chia-Ching Wu, Cheng-Fu Yang, Chien-Chen Diao, and Chean-Cheng Su

Abstract In this chapter, the poly(ether imide) (PEI)/BaTi$_4$O$_9$ (BT4) composites were investigated for the applications of the high dielectric constant embedded capacitors or flexible organic substrates. BT4 ceramic was sintered at 1,275°C and ground into microscale power. After that, BT4 ceramic power was mixed with PEI to form PEI/BT4 composites, the effects of the concentration of BT4 filler on the physical and dielectric properties were developed. Thermogravimetric analysis (TGA) was used to determine the weight loss, thermal degradation temperature (T_d), and endothermic-exothermic peak of the PEI/BT4 composites. The Lichtenecker mixing rule was used to predict the variations of dielectric constants of the PEI/BT4 composites, and the mixing rule would fit the measured results. The dielectric constants of the PEI/BT4 composites with various concentrations (0–70 wt%) of BT4 filler were measured, and the dielectric constants were almost unchanged as the measured frequency increased, because the PEI was a nonpolarized material. This research proved that we could investigate the PEI/BT4 composites with stable frequency-dependent properties.

Keywords Polymer-ceramic composite • Dielectric constant • Thermogravimetric analysis

W.-K. Chia
Department of Electronic Engineering, Fortune Institute of Technology,
Kaohsiung, Taiwan, R.O.C.

C.-C. Wu • C.-C. Diao
Department of Electronic Engineering, Kao Yuan University, Kaohsiung, Taiwan, R.O.C.

C.-F. Yang (✉) • C.-C. Su
Department of Chemical and Materials Engineering, National University
of Kaohsiung, Kaohsiung, Taiwan, R.O.C.
e-mail: cfyang@nuk.edu.tw

1   Introduction

Recently, with the trend of the increase of clock speed and the drop of power supply voltage for high-speed circuits, the elimination of power/ground bounce noise (P/GBN) becomes more important. Several forms of electromagnetic bandgap (EBG) substrates are proposed to efficiently suppress the P/GBN in high-speed digital circuits. The EBG substrates are organic materials compositing periodical cells of metallic or dielectric elements. The EBG characteristics are dependent on the material structure such as dimensions, periodicity, and dielectric constant [1, 2]. Many different structures of EBG substrates were researched. Compared to other EBG structures, the high-k ceramics embedded into a low-k host to fabricate an EBG structure has a preferable feature of compactness [3–6].

Polymer is a suitable material for its inertness to the electroless plating solution and its compatibility with printed wiring boards (PWBs). For this reason, the polymer/ceramic composites have been of great interest as EBG substrate materials, because the polymer/ceramic composites not only reveal process mixing ability of polymers with high dielectric constant ceramics but have good compatibility with printed circuit boards (PCBs) [7–9]. Hence, the polymer/ceramic composites are important materials used to develop the embedded technology. In this investigation, poly(ether imide) (PEI) is an amorphous high-performance polymer with high thermal durability ($T_g = 220$ °C) and good mechanical properties because of resisting scratching and chemical corrosion and ignition. Self-synthesized $BaTi_4O_9$ (BT4) ceramic powder was chosen as the dielectric ceramic filler to form the PEI/BT4 composites, and the filler concentration was varied in the PEI/BT4 composites. The dielectric constant (ε_r) and loss tangent (tan δ) of the PEI/BT4 composites as a function of ceramic filler concentration and measured frequency were discussed.

2   Experimental Procedures

Raw materials of $BaCO_3$ and TiO_2 with purity higher than 99.5 % were weighed according to the composition of $BaTi_4O_9$ (BT4) and ball-milled with deionizer water for 1 h. The slurry was dried for 24 h at 120 °C and ground, then the powder was calcined at 1,100 °C for 2 h and ground again. After that, the calcined power was pressed into disks and sintered at 1,275 °C for 10 min. After sintering, the BT4 ceramics were ground into the fine powder by using a ball-milling-grinder for 5 h, and then the BT4 ceramic powder was used as the precursor to prepare the PEI/BT4 composites. The crystalline structure of BT4 ceramic power was determined by X-ray diffraction (XRD) patters. At first, the PEI and commercial KD1 dispersant were dissolved in dichloromethane by ultrasonic machine, and 10–80 wt% BT4 ceramic powder was mixed with the solution to form the PEI/BT4 mixing solutions. The amount of dispersant set for BT4 powder was 0.2–1.2 wt%.

A viscosity test was conducted under the different concentrations of dispersant to decide the optimum amount of dispersant. The mixing solutions were poured in the mold and roasted at 60 °C to vaporize the solvent, and then the PEI/BT4 composites were obtained. The microstructures of PEI/BT4 composites were observed via the scanning electron microscopy (SEM). Thermogravimetric analysis (TGA) was used to determine the temperature range of weight loss and the thermal degradation temperature (T_d) of the PEI/BT4 composites. The glass transition temperature (T_g) of the PEI/BT4 composites was obtained by using the differential scanning calorimeter (DSC) thermal analysis, and the heat temperature was proceeded from 30 to 300 °C at a heating rate of 10 °C/min. A HP 4294A LCR meter (Agilent Technologies Inc., Englewood, CO) was used to measure the capacitance of the PEI/BT4 composites using the metal/composites/metal sandwich structures. The measurements were performed from 100 to 100 MHz. Several samples were measured and an average of the capacitance values was taken. The dielectric constant (ε_r) of the composites film was calculated as

$$\varepsilon_r = \frac{Cd}{\varepsilon_0 A},\tag{1}$$

where C is a capacitance value of the structures, d is thickness of the composite film near the capacitor measured, A is area of the top electrode that defines the parallel plate capacitor, and ε_0 is permittivity of vacuum space (8.854 $\times$ 10^{-12} F/m). The measurement is averaged over different capacitors to get stable statistics.

3 Experimental Procedures

The disperse properties of BaTi$_4$O$_9$ (BT4) powder mixing with poly(ether imide) (PEI) will influence the dielectric properties of the PEI/BT4 composites [10]. The particle sizes of the obtained BT4 ceramic powder are in the range of 1–5 μm, as shown Fig. 2a. The fine powder (about 1–2 μm) easily forms agglomerates because of the existence of the van der Waals force. In addition, the theoretical densities of PEI and BT4 ceramic are 1.28 and 2.45 g/cm^3, respectively. The phenomenon of concentration gradient occurs as the difference of theoretical density of PEI and BT4 is large (about 1.17 g/cm^3). The suspension made of BT4 powder, DK1 dispersant, and dichloromethane (CH$_2$Cl$_2$) solvent are ball-milled, then a viscosity test is conducted under different concentration of dispersant, and the results are shown in Fig. 1. As the concentration of dispersant increases from 0.2 to 0.4 wt%, the viscosity vertically decreases; as the concentration of dispersant is higher than 0.4 wt%, the viscosity has no apparently change. For that, the 0.6 wt% DK1 dispersant is used for the different shear rate with low viscosity.

Figure 2 shows the XRD patterns of the BT4 ceramic powder and PEI/BT4 composites. There are many secondary phases existing in the BaO-TiO$_2$ system, including BaTiO$_3$, BaTi$_3$O$_7$, BaTi$_5$O$_{11}$, BaTi$_4$O$_9$, and Ba$_2$Ti$_9$O$_{20}$, respectively.
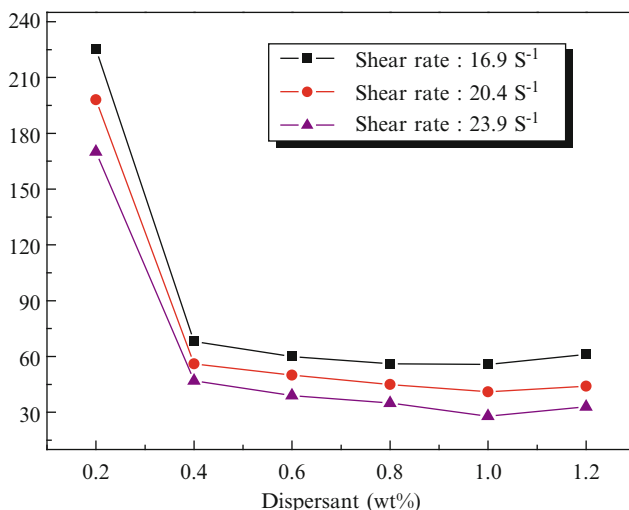
Fig. 1 Viscosity changes of the PEI/BaTi$_4$O$_9$ composites as a function of dispersant content
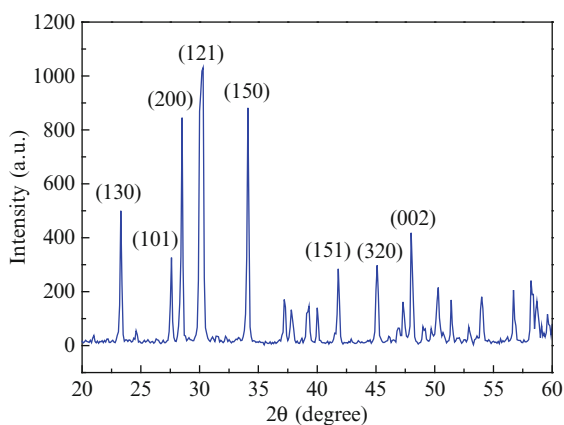
Fig. 2 XRD patterns of BaTi$_4$O$_9$ ceramic powder

For that, the phase control of BT4 ceramic is very important. In Fig. 2, only the orthorhombic BT4 phases existed and no satellite phases were observed in the BaTi$_4$O$_9$ ceramic powder. Also, only the BT4 phase existed in the XRD patterns of the PEI/BT4 composites, and the crystalline intensity of BT4 phases increased with increasing BT4 concentration. The SEM images of the BT4 ceramic powder and PEI/BT4 composites shown in Fig. 3 proved that the BT4 powder was well dispersed in PEI as the 0.6 wt% concentration of DK1 dispersant was added. Figure 3b, c shows the SEM surface morphologies of the PEI/BT4 composites with 20 and 70 wt% of BT4 ceramic powder, respectively. As Fig. 3b, c shows, the
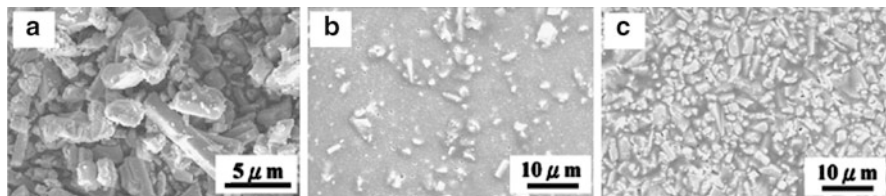
Fig. 3 SEM morphologies of (**a**) BaTi$_4$O$_9$ ceramic powder and of the PEI/BaTi$_4$O$_9$ composites with (**b**) 20 wt% and (**c**) 70 wt% BaTi$_4$O$_9$ ceramic powder
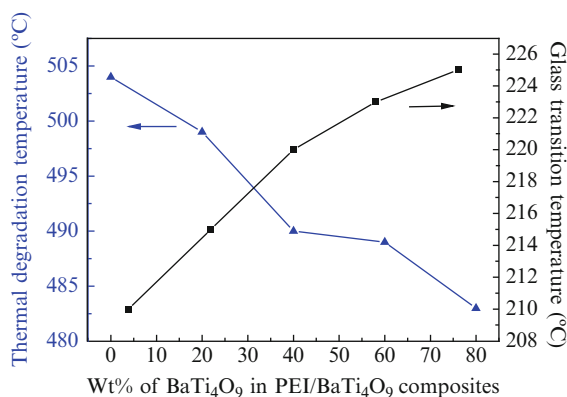
Fig. 4 Thermal degradation temperature (T_d) and glass transition temperature (T_g) of the PEI/ BaTi$_4$O$_9$ composites

black region was the PEI and the white and gray particles were the BT4 powder. As the concentration of BT4 ceramic powder increased, the more BT4 ceramic powders were revealed.

The onset of degradation temperatures of PEI mixing with 0–80 wt% BT4 ceramic powder is measured, and the results are shown in Fig. 4. The solid–liquid coexisting area of the PEI/BT4 composites obtained was at the range of 210–240 °C, and the range of solid–liquid coexisting temperature is appropriated to press the PEI/ BT4 composites into a plate-form sample. Thermal degradation temperature (T_d) of the PEI/BT4 composites was dependent on the concentration of BT4 ceramic powder. As the results shown in Fig. 4, the T_d was shifted to lower temperature as the concentration of BT4 ceramic powder increased. As the concentration of BT4 ceramic powder increases, the three-dimensional barrier between the molecules increases, and that could lead to the volume of freedom increases and the molecular structure will become weaker. For that, as the concentration of BT4 powder increases, the T_d is shifted to lower temperature.

Fig. 5 Measured and predicted dielectric constants of the PEI/BaTi$_4$O$_9$ composites
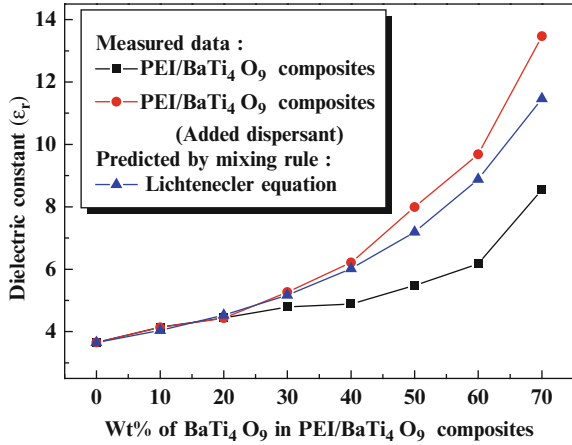
For PEI with 80 wt% BT4 ceramic powder, the onset of degradation temperature and weight loss is not apparently observed in the TGA plot. To obtain the more accurate conditions of heat press process, the differential scanning calorimeter (DSC) analysis was used to find the glass transition temperature (T_g) of the PEI/BT4 composites. From Fig. 4, the T_g value increased as the concentration of BT4 ceramic powder in the PEI/BT4 composites increased. The high volume of BT4 ceramic powder in the PEI/BT4 composites could lead to large limits of cross-linking of PEI. In the sample, motion of the molecular chain needs a high energy in the non-cross-linking area, and it results the composite with a higher T_g value. Based upon the above results, the optimum T_g value of heat press condition is set to 230 °C in this study.

The dielectric properties of the PEI/BT4 composites are shown in Fig. 5. Measured at 1 MHz, the dielectric constant of the PEI/BT4 composites increased as the concentration of BT4 ceramic powder increased. The dielectric constants of PEI and BT4 ceramic measured at 1 MHz were 3.65 and 39, respectively. Because the dielectric constant of BT4 ceramic is higher than that of PEI, for that, the dielectric constants of the PEI/BT4 composites will increase with increasing concentration of BT4 ceramic powder. As Fig. 5 shows, the dielectric constants of the PEI/BT4 composites increased from 3.92 to 13.8 as the concentration of BT4 ceramic powder increased from 10 to 70 wt%. The logarithmic mixing rule is composed of dielectric spheres with dielectric constant ε_2 dispersed in a continuous medium with dielectric constant ε_1, where $\varepsilon_2 > \varepsilon_1$. The logarithmic mixing rule can be used to predict the dielectric constant of the PEI/BSTZ composites, and the results are also shown in Fig. 5 to compare with the measured results. The mixing rule is as follow [11]:

$$(V_1 + V_2) \log \varepsilon = V_1 \log \varepsilon_1 + V_2 \log \varepsilon_2, \qquad (2)$$

Fig. 6 Dielectric constants
of the PEI/BaTi₄O₉
composites as a function
of measured frequency
and BT4 concentration
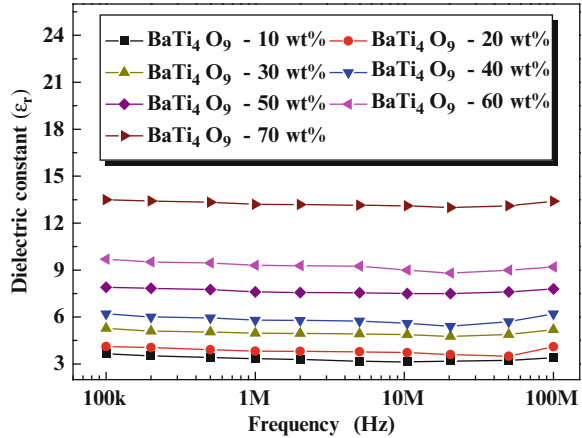
where $V_1 = W_1/D_1$ and $V_2 = W_2/D_2$ represent for the volume fraction of PEI and dispersed dielectric material, and ε_1 and ε_2 represent the dielectric constants of PEI and dispersed dielectric material, respectively, and the $V_1 + V_2 = 1$. As shown in Fig. 5, the predicted dielectric constants are in good agreement with the measured values of the PEI/BT4 composites as the KDI dispersant added.

As the concentration of BT4 ceramic power is lower than 45 wt%, the measured results are matched and slightly smaller than the predicted results; as the concentration of BT4 ceramic powder is more than 45 wt%, the measured dielectric constant is more than the predicted value, and the difference is more apparent as more concentration of BT4 ceramic powder is added. The theoretical prediction in the dielectric constant of a composite is based on that assuming a high dielectric constant ceramic powder is uniformly dispersed in a low dielectric constant polymer, as shown in Fig. 2b. As the concentration of BT4 ceramic powder is more than 45 wt%, the finer BT4 ceramic powder can fill the interstitial sites of coarser BT4 ceramic particles; the fill density and boundary of grain contact of BT4 powder increases as shown in Fig. 2c. For this reason, it will cause the measured dielectric constants to be more than the predicted ones.

From Fig. 6, as the measured frequency increased from 100 to 100 MHz, the dielectric constants of the PEI/BT4 composites were almost unchanged at lower measured frequency and slightly increased at higher measured frequency. Because as the BT4 ceramic powder is mixed with nonpolarization PEI to form PEI/BT4 composites, the less ionic dipoles are available to form the switchable dipoles.

4   Conclusions

In this study, the BaTi₄O₉ (BT4) powder was uniformly dispersed in the poly(ether imide) (PEI) and revealed fewer pores as compared to those of other reports. Measured from 10 to 100 MHz, as the concentration of BT4 ceramic powder in

the PEI/BT4 composites increased from 0 to 70 wt%, the dielectric constant increased from 3.92 to 13.8. Also, the dielectric constants of the PEI/BT4 composites were almost unchanged as the measured frequency increased. This research proved that we could investigate the PEI/BT4 composites with stable dielectric characteristics, and the PEI/BT4 composites could be the good candidates for the applications of the future 3C systems.

References

1. Coccioli R, Yang FR, Ma KP, Itoh T (1999) Aperture-coupled patch antenna on UC-PBG substrate. IEEE Trans Microw Theor Tech 47:2123–2130
2. Cheype C, Serier C, Thevenot M, Monediere T, Reineix A, Jecko B (2002) An electromagnetic bandgap resonator antenna. IEEE Trans Antennas Propag 50:1285–1290
3. Chappell WJ, Gong X (2003) Wide bandgap composite EBG substrates. IEEE Trans Antennas Propag 51:2744–2750
4. Yang F, Samii YR (2003) Reflection phase characterizations of the ground plane for low profile wire antenna applications. IEEE Trans Antennas Propag 51:2936–2946
5. Lee Y, Yeo J, Ko K, Lee Y, Park W, Mittra R (2004) A novel design technique for control of defect frequencies of an electromagnetic bandgap (EBG) super-strate for dual-band directivity enhancement. Microw Opt Technol Lett 42:25–31
6. Lee YJ, Yeo J, Mittra R, Park WS (2005) Application of electromagnetic bandgap (EBG) superstrates with controllable defects for a class of patch antennas as spatial angular filters. IEEE Trans Antennas Propag 53:224–235
7. Bhattacharya SK, Tummala RR (2000) Next generation integral passives: materials, processes, and integration of resistors and capacitors on PWB substrates. J Mater Sci Mater Electron 11:253–268
8. Bhattacharya SK, Tummala RR (2001) Integral passives for next generation of electronic packaging: application of epoxy/ceramic nanocomposites as integral capacitors. Microelectron J 32:11–19
9. Rao Y, Ogitani S, Kohl P, Wong CP (2002) Novel polymer–ceramic nanocomposite based on high dielectric constant epoxy formula for embedded capacitor application. J Appl Polym Sci 83:1084–1090
10. Paik KW, Cho SD, Lee JY, Hyun LG (2002) International symposium on electronic materials and packaging. In: IEEE, vol 341
11. Kingery WD, Bowen HK, Uhlmann DR (1976) Introduction to ceramic, 2nd edn. Wiley, New York, p 947

Design the Bandwidth of Zero-Phase Filter of Iterative Learning Controller by Improved Particle Swarm Optimization

Shu-Ting Li, Jen-Ai Chao, Yi-Hao Li, and Yi-Cheng Huang

Abstract This chapter utilized the IPSO technique with bounded constraints for adjusting the gains of PID controller, ILC controller, and the bandwidth of zero-phase Butterworth filter. Simulation results show that IPSO-ILC-PID controller will have chance of producing high frequencies in the error signals when the filter bandwidth is fixed for every repetition. Since the conventional ILC iterative learning process has the potential to excite rich frequency contents and try to learn the error signals, however, the learnable and unlearnable error signals should be separated for bettering control process. Thus, the adaptive bandwidth of a zero-phase filter in ILC-PID controller with IPSO tuning characteristic is proposed here. Simulation results show that the new controller can cancel the errors as repetition goes. The frequency response of the error signals is analyzed by the EMD and the HHT method. Errors are reduced and validated by good ILC learning with adaptive filter bandwidth.

S.-T. Li • Y.-H. Li • Y.-C. Huang (✉)
Department of Mechatronics Engineering, National Changhua University
of Education, Changhua 50007, Taiwan
e-mail: ychuang@cc.ncue.edu.tw

J.-A. Chao
Chienkuo Technology University, Changhua 50007, Taiwan

1 Introduction

Conventional proportional-integral-derivative (PID) controllers are widely applied in control systems. PID gains must be well tuned to obtain better dynamic performance, guarantee security, and sustainably utilize equipment and plants [1]. Kennedy and Eberhart introduced PSO in 1995 [2]. It does not require strong assumptions about linearity, differentiability, convexity, separability, or nonexistence of constraints to solve the problem efficiently [3]. Iterative learning control (ILC) [4] aims to iteratively reduce the tracking error, over a finite time interval, by incorporating past experience in the actual control input.

In the existing literature [5], three digital learning compensators have the unit-gain feature. The first one is the linear phase lead learning compensator [6]. The linear phase lead will provide phase compensation increasing linearly with frequency, which will be excessive at high frequency, and cutoff has to be introduced to stop phase compensation at high frequencies. The second one is the learning compensator using the partial isometry of system Markov parameter matrix, calculated by singular value decomposition [7].

The third learning law is the phase cancelation learning law that constructs its learning compensator (matrix) by calculation of an inverse discrete Fourier transform (IDFT) from the phase characteristics of the plant. Again, the computation burden may be heavy. Computational enhancement was proposed in Lee-Glauser et al. [8] to reduce the calculation cost. Still, adaptive learning gain or the cutoff bandwidth searched by intelligence method at every repetition time was discussed less.

This study utilized the bounded constraints technique of IPSO through the experience by conducting the experiment of real-time implementation [9]. This chapter utilizes the new IPSO [9] to tune the gains of PID and ILC and bandwidth of zero-phase filter at every repetition. The transient response of the ILC algorithm is improved by using the gain tuning of designed IPSO. Root mean square (RMS) serves as the minimization criterion for the tracking error when the IPSO is lunched by every repetition.

1.1 *Transfer Function of Linear Synchronous Motor*

Figure 1a presents a sketch diagram for single axis of a linear synchronous motor (LSM). The transfer function of the moving coil is approximated by a first-order lag system with resistance R_{25} and inductance L. Moving the coil generates a back electromotive force. The open loop transfer function F with input voltage V_a is approximated by a third-order lag system [10].
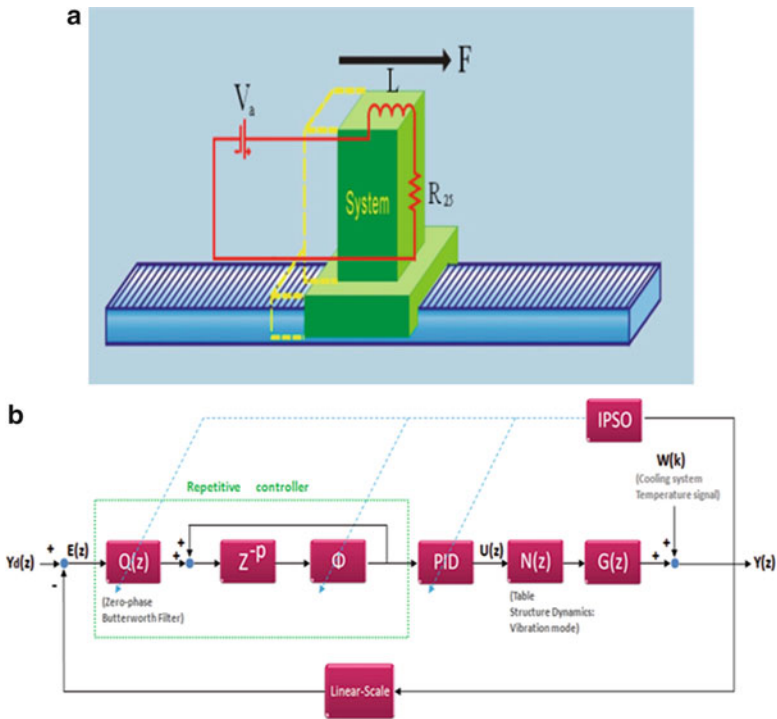
Fig. 1 (**a**) Simplified LSM model. (**b**) Illustration for the IPSO-PID-ILC control block diagram

The transfer function in Fig. 1 is obtained as follows:

$$G(s) = \frac{K_f}{(M + m)s(R_{25} + sL) + K_f K_v} \tag{1}$$

where M is the payload mass on the force (moving part of the LSM) and is the linear motor forcer mass, R_{25} is the armature resistance, L is the inductance, K_f is the thrust constant, K_v is the contrary EMF constant, and $V_a(s)$ is the input voltage.

Figure 1b shows the control block diagram for IPSO-PID-ILC controller. This chapter uses the IPSO method to search the bandwidth of zero-phase Butterworth filter $Q(z)$ online and has the ability to cancel out the unlearnable error signals after next repetition for ILC control law.

1.2 Particle Swarm Optimization

Based on a flock of flying birds, the PSO algorithm simulates the behavior of a swarm as a simplified social system [2, 11]. Since each particle remembers its worst

experience, it can explore the search space effectively to identify the most promising solution region. Thus, the PSO algorithm is derived as follows:

$$V_{id}(t) = w \times V_{id}(t-1) + c1 \times \text{Rand}() \times (P_{id} - X_{id}) + c2 \times \text{Rand}() \times (P_{gd} - X_{id}) \qquad (2)$$

$$X_{id}(t) = X_{id}(t-1) + V_{id}(t) \qquad (3)$$

where $V_{id}(t)$ is the current velocity of i particle, $i = 1, \ldots, n,$ in which n is the population size, the subscript d is the dimension of the particle, P_{id} is the best previous position of the ith particle, P_{gd} is the best previous position among all the particles in the swarm, and X_{id} is the current position of the ith particle. The constants C_1 and C_2 represent the weighting of the stochastic acceleration terms pulling each particle toward P_{id} and P_{gd} positions. Low values allow particles to roam far from the target regions before being tugged back. On the other hand, high values result in abrupt movement toward, or past, target regions. Therefore, previous approaches often set the acceleration constants $c1$ and $c2$ to 2.0. Rand() represented the uniform random number between 0 and 1.

A parameter called inertia weight W can help balance the global and local search. This study sets the $W_{\max}$ to be 1 for global searching. The inertia weight is set according to the following equation:

$$W = W_{\max} - \frac{W_{\max} - W_{\min}}{N_{\max}} \times N_{\text{iter}} \qquad (4)$$

where $N_{\max}$ is the maximum number of iterations and N_{iter} and is the current number of iterations [12]. Equation (1) restricts the value to the range $[W_{\max}, W_{\min}]$. This study sets the maximum and minimum values of the inertia weights as 1 and 0.2, respectively.

1.3   Iterative Learning Controller

In Arimoto et al. (1984) [13], the input update utilizes the derivative of the previous error signal, and the learning law is termed P-type ILC. In some repetitive or periodic systems, iterative control can be used to perform the system tracking. The control algorithm for these simplified systems without any frequency concerned filter design can be represented as

$$u_{j+1}(kT) = u_j(kT) + \phi e_j(kT) \tag{5}$$

$$e_j(kT) = y_d(kT) - y_j(kT) \tag{6}$$

where $u_{j+1}(kT)$ represents the input at time k and iteration j, $e_j(kT)$ is the difference between the actual output and the desired output at time k and iteration j, and φ is the learning gain.

2 Simulation Results

Figure 2a plots the trajectory responses and error with IPSO-ILC-PID (with fixed cut off frequency) and IPSO-ILC-PID-filter (dynamic bandwidth filter at every repetition). It is obvious that the IPSO-ILC-PID-filter (the letter w in plot indicates the dynamic bandwidth filter) controller produces less error than conventional ILC-PID controller with fixed cutoff frequency at 30 Hz zero-phase filter. Tracking error of IPSO-ILC-PID control without filter design reveals the output delay with large phase lag and error in magnitude when compared with IPSO-ILC-PID-filter control. This is caused by less dynamic bandwidth adjustment without the IPSO tuning. Table 1 shows the comparisons of IPSO-ILC-PID and proposed IPSO-ILC-PID-filter control systems in repetition three with maximum tracking error and the RMS (root mean square) error measures. Figure 2b shows the ILC learning convergence in RMS error measure. It elucidates that the convergence rate of IPSO-ILC-PID-filter controller is better than the one of IPSO-ILC-PID controller. This is because the merit of IPSO tuning for every learning iteration and the new control law $\left\| 1 - \phi Q_{\text{zero−phase−filter}}(s)G_{\text{plant}}(s) \right\|_\infty < 1$ should separate the unwanted unlearnable error signals in every repetition.

Figure 3a shows the Hilbert-Huang spectrum (HHS) for the error data at repetition 6 with respect to the IPSO-ILC-PID and IPSO-ILC-PID-filter controllers. In Fig. 3a (or Fig. 3b), from top to bottom, shows the error by the time frequency, error history in time, error spectrum by marginal frequency (integration by HHS), and the conventional fast Fourier transform. In comparisons between Fig. 3a, b, the proposed IPSO-ILC-PID-filter control law shows the good learning ability at repetition 6. In Table 2, the RMS tracking errors (RMS_w) by dynamic cutoff frequency filter design (f_c) are lower than the RMS tracking errors with fixed cutoff frequency at 30 Hz when the command is varied from 1 to 5 Hz.
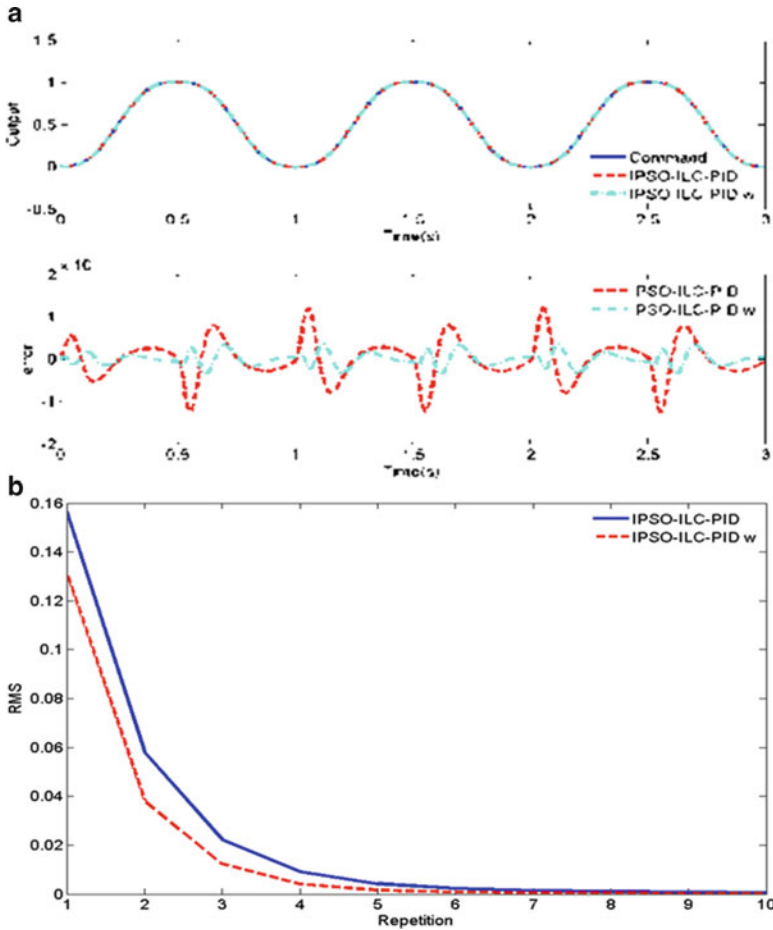
Fig. 2 (**a**) Simulation results of the trajectory output and tracking error compared with the IPSO-ILC-PID and IPSO-ILC-PID-filter controllers. (**b**) Simulation results of the RMS convergence error the IPSO-ILC-PID and IPSO-ILC-PID-filter controllers, respectively

Table 1 Comparisons of IPSO-ILC-PID and proposed IPSO-ILC-PID-filter in Fig. 3

	K_P	K_I	K_D	ILC gain (Π)	F_C (Hz)	MAX error	RMS
IPSO-ILC-PID	0.493	0.096	5.607	0.81	30	0.0017	6.6027×10^{-4}
IPSO-ILC-PID-filter	0.12	1.0625	6.604	1.2406	21.0026	5.2062×10^{-4}	1.8263×10^{-4}
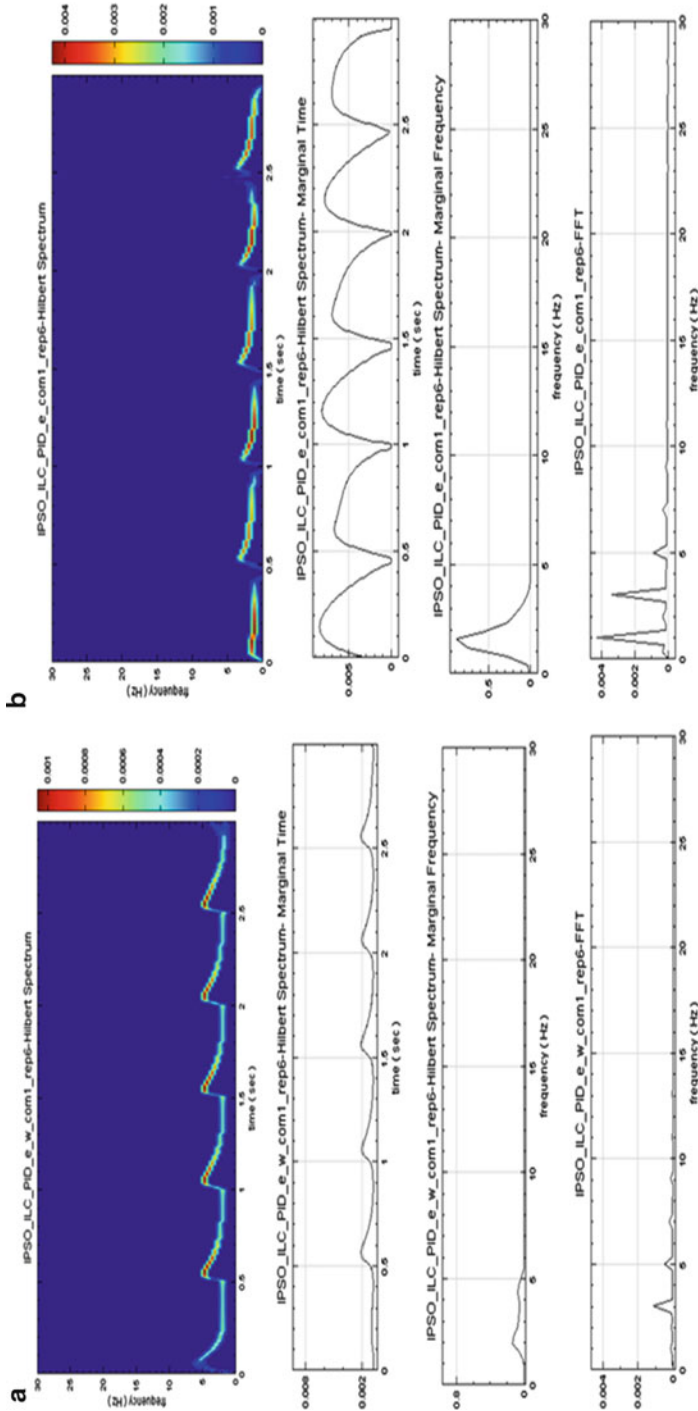
Fig. 3 (**a**) Simulation results of the error IPSO-ILC-PID-filter controller with repeat6, (**b**) Simulation results of the error IPSO-ILC-PID controller with repeat6

Table 2 Comparisons of IPSO-ILC-PID and proposed IPSO-ILC-PID-filter control

Run	1 Hz			3 Hz			5 Hz		
	f_c (Hz)	RMS_w	RMS	f_c (Hz)	RMS_w	RMS	f_c (Hz)	RMS_w	RMS
Rep1	5.172	0.157	0.182	5.172	0.471	0.545	4.183	0.719	0.793
Rep 3	21.339	0.008	0.035	21.339	0.024	0.105	3.229	0.036	0.198
Rep 6	31.103	0.001	0.004	31.103	0.003	0.012	14.586	0.004	0.027
Rep 10	21.003	0.0002	0.001	21.003	0.001	0.002	50.556	0.001	0.004

3 Conclusion

This chapter utilized the improved particle swarm optimization (IPSO) technique with bounded constraints for adjusting the gains of PID controller, ILC controller, and the bandwidth of zero-phase Butterworth filter. The proposed IPSO-ILC-PID controller shows more bettering tracking control than the conventional ILC-PID controller. Simulation results show that IPSO-ILC-PID-filter controller will have a chance of reducing the high frequencies in the error signals when the filter bandwidth is adaptive tuned at every repetition. The learnable and unlearnable error signals can be separated by each control process. Thus, the adaptive bandwidth of a zero-phase filter in ILC-PID controller with IPSO tuning characteristic is promising in this research.

References

1. Hongqing F, Long C (2009) Application of an enhanced PSO algorithm to optimal tuning of PID gains. In: Proceedings of 2009 Chinese control and decision conference, Guilin, 17–19 June 2009, pp 35–39
2. Kennedy J, Eberhart R (1995) Particle swarm optimization. In: Proceedings of the IEEE international conference on neural networks, Perth, 1995, pp 1942–1948
3. Solihin MI, Akmeliawati W, Akmeliawati R (2009) Self-erecting inverted pendulum employing PSO for stabilizing and tracking controller. In: Proceedings of international colloquium on signal processing & its applications (CSPA), Kuala Lumpur, 6–8 Mar 2009, pp 63–68
4. Middleton RH, Goodwin GC, Longman RW (1989) A method for improving the dynamic accuracy of a robot performing a repetitive task. Int J Robot Res 8(5):67–74
5. Ye Y, Tayebi A, Liu X (2009) All-pass filtering in iterative learning control. Automatica 45(1):257–264
6. Elci H, Longman RW, Phan MQ, Juang J-N, Ugoletti R (2002) Simple learning control made practical by zero-phase filtering: application to robotics. IEEE Trans Circ Syst I Fundam Theory Appl 49:753–767
7. Jang HS, Longman RW (1996) Design of digital learning controller using a partial isometry. Adv Astronaut Sci 93:137–152

8. Lee-Glauser GJ, Juang JN, Longman RW (1996) Comparison and combination of learning controllers: computational enhancement and experiments. AIAA J Guid Control Dyn 19(5):1116–1123
9. Huang YC, Li YH, Li ST (2012) Design and experiment of iterative learning controller based on particle swarm optimization approach with new bounded constraints technique. J Appl Mech Mater (EI)
10. Yajima H, Wakiwaka S, Senoh K, Minegishi N, Fujiwara K (1997) Consideration on high-response of a linear DC motor. IEEE Trans Magn 33(5):3880–3882
11. Shi Y, Eberhart R (1998) A modified particle swarm optimizer. In: Proceedings of the IEEE international conference on evolutionary computation, Anchorage, 1998, pp 69–73
12. Gaing ZL (2004) A particle swarm optimization approach for optimum design of PID controller in AVR system. IEEE Trans Energy Convers 19:384–391
13. Arimoto S, Kawamura S, Miyazaki F (1984) Bettering operation of robots by learning. J Robot Syst 1:123–140
14. Jang HS, Longman RW (1994) A new learning control law with monotonic decay of the tracking error norm. In: Proceedings of the 32nd allerton conference on communication, control, and computing, University of Illinois, Urbana, 1994, pp. 314–323
15. Jang HS, Longman RW (1996) An update on a monotonic learning control law and some fuzzy logic learning gain adjustment techniques. Adv Astronaut Sci 90:301–318

Prognostic Diagnosis of Hollow Ball Screw Pretension on Preload Loss Through Sensed Vibration Signals

Yi-Cheng Huang, Yu-Shi Chen, Shi-Lun Sun, and Kuan-Heng Peng

Abstract The pretension for a ball screw is a way to improve the position accuracy. Hollow ball screw without a cooling system has the thermal deformation effect due to increase in temperature. It will reduce precision accuracy in machine tool when the ball screw nut preload or ball screw pretension is lost. The purpose of this study is to use vibration signals for the prognostic analysis for the ball screw pretension. Features of different pretension conditions by 0, 5, 10, and 20 μm are discriminated by empirical mode decomposition (EMD), fast Fourier transform (FFT), and marginal frequency method. Temperature effects with long-term operation were discussed. This study experimentally extracts the characteristic frequencies for bettering pretension through the vibration signals. This diagnosis results realize the purpose of prognostic effectiveness on knowing the hollow ball screw preload loss based on pretension data and utilizing convenience.

Keywords Hollow ball screw • Vibration signals • Hilbert–Huang transform • FFT

1 Introduction

High-lead ball screw is used widely in industrial machines and equipment for linear actuation. The positioning accuracy of feed system is an important factor in machine tools. However, the ball screw thermal displacement is a key factor.

When a machine has been operated for a long time, it produces thermal displacement effects as general. There are two conventional ways to improve the thermal displacement: control the temperature rise and compensate the thermal displacement. Controlling the temperature rise is the most efficient way.

Y.-C. Huang (✉) • Y.-S. Chen • S.-L. Sun • K.-H. Peng
Department of Mechatronics Engineering, National Changhua University
of Education, Changhua 50007, Taiwan
e-mail: ychuang@cc.ncue.edu.tw

But it is costly and difficult to maintain the temperature variation. The use of the thermal displacement compensation method is as follows. First is to let the temperature of the machine reach a steady state by warming up the machine. Then the motor encoder or the optical scale signals are manipulated and can be feedback to the controller. Last but not least is to do the ball screw pretension for absorbing the thermal displacement caused by temperature rise. Pretension is effective to improve the thermal displacement. However, discussion for monitoring the status of the pretension failure is less in recent years. Large pretension may cause preload loss. Therefore, predicting the signals to determine the onset of pretension loss or preload loss of ball screws has recently become an urgent necessity in the industry. These signals often require conventional fast Fourier transform (FFT), short-time Fourier transform, or discrete wavelet transform for fault diagnosis in the frequency and time domains [1]. Huang and coworkers [2, 3] developed a new approach to signal analysis to avoid generating unphysical results from the Complex Trace formalism [1]. The Complex Trace formalism defines the concepts of instantaneous amplitude, phase, and frequency such that the original signal can be expressed in terms of a Fourier-like expansion based on these concepts [2]. This process and the definition of instantaneous frequency work well for mono-component signals. In many real applications, the signals are multi-component and often corrupted by noise. Researchers have recently used HHT in numerous applications, including fault diagnosis in electrical machines, rolling bearing failure analysis in mechanical engineering, and brain activity signal monitoring in bioengineering [4, 5]. HHT provides both the time and frequency analysis is used for identification pretension failure. The characteristics of pretension according to temperature changes and the amount of displacement under long-time operation are explored in this study.

2 Theoretical Backgrounds

2.1 Empirical Mode Decomposition Method

Empirical Mode Decomposition Method (EMD) is the first step of Hilbert–Huang transform. It lets complex signal be decomposed into multiple intrinsic mode function combination. Then vibration signals can be decomposed by the characteristic time scale of signals.

This step is called the sifting process. In the sifting process, surges are eliminated and smooth amplitude waveform in more symmetrical is made. The sifting process is repeated to get the new mean values of the new upper and lower envelopes until satisfying the conditions of intrinsic mode function.

2.2 Hilbert–Huang Transform

Hilbert–Huang transform (HHT) is a method to decompose a signal into intrinsic mode functions (IMF) and obtain instantaneous frequency data. It is designed to work well for data that are nonstationary and nonlinear.

3 Experimental Setup

An in-house experiment platform was designed and assembled in Fig. 1. This apparatus was fabricated as the industrial standard for one axis of a tapping machine. This experimental machine was installed in the test bed by fixed and simple supported bearing-fit status. It is applicable to the general speed and high precision. The amount of vibration generated by the supporting end of the machine should be greater than the fixed one. However, the supporting end frame is designed strong enough for not sliding when ball screw pretension is applied. The pretension value is set as 0, 5, 10, and 20 μm for experiments.

4 Experimental Results

The vibration signals from the ball screw contain different excitation sources when the motion table is moving. Therefore, determining the attached accelerometer position that reveals the signals is very important to effectively capture the screw pretension features.
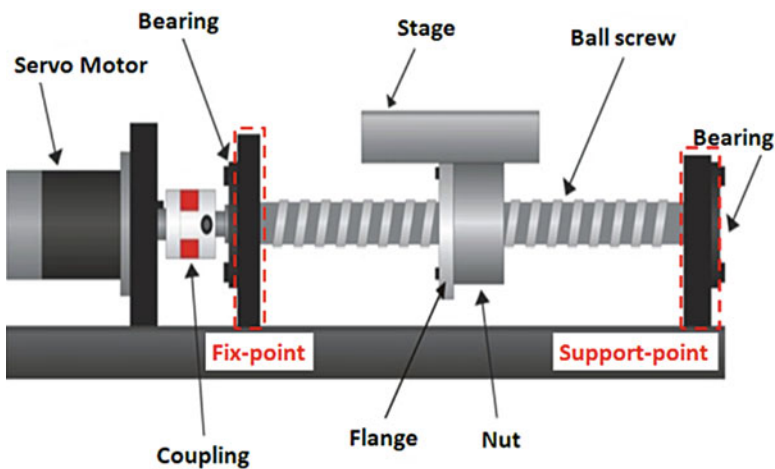
Fig. 1 Basic introduction and schematic diagram of lead screw
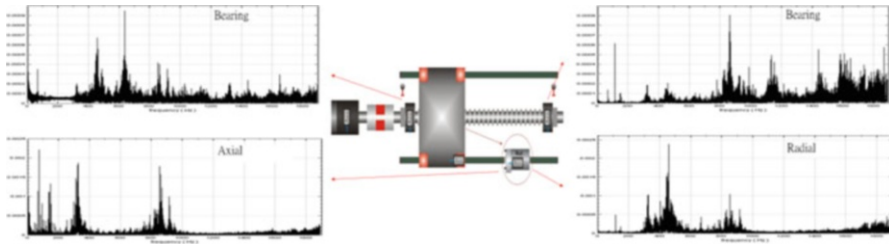
Fig. 2 Dynamic measurement signal distribution diagram

Vibration signals on top of the left and right in Fig. 2 contain rich structural frequency, some modulated signals, and excitation signals from the motor when the accelerometer is attached to the fixed end and supporting end bearings. The signals with respect to axial and radial vibration measurements are shown in the bottom of the left and right in Fig. 2 when the accelerometer sensors are attached to the ball nut. The FFT signals are more focused around the 320 and 850 Hz range.

In Fig. 3, the main frequency distribution was observed around the bandwidth of 300–330 and 850 Hz. Some structure vibration modes and ball bearing frequencies are below 300 Hz. According to previous research results [7], 320 Hz is defined as the characteristic frequency for ball screw preloading. The total stiffness of the ball screw includes the ball bearings, ball nut, and ball screw. Nevertheless, the position of the table counts for the effect on the ball screw stiffness when all the mechanical elements are connected in series. When the pretension is applied to the ball screw, one frequency peak roughly about 312 Hz in the range of 300–330 Hz is observed. As the pretension changes from 5, 10, to 20 μm, the FTT signal about 312 Hz changes. It is obvious that once the pretension is applied the characteristic frequency of the phenomena moves to the left. That is, the characteristic frequency for ball screw stiffness changes when the pretension and preload effects are coupled. To more clearly understand the frequency change, a magnified observation of Fig. 3a is selected in Fig. 3b. The magnitude of the frequency at 320 Hz is reduced significantly when the pretension value reaches 20 μm. Frequency distribution becomes larger at 312 Hz than the one at 320 Hz. Screw pretension in terms of the amount of 20 μm might be too large and renders to preload loss. The characteristic frequency at 312 Hz is selected for the following analysis.

The merit of HHT used here is to decompose the vibration signals to multiple IMFs by EMD processes as shown in Fig. 4. The time frequency of different IMFs can be abstracted into the marginal spectrum (based on frequency domain analysis). It is found that the first and second groups of IMFs are contributed by higher frequency signals (Fig. 4, from the top two IMFs). These cover a lot of random signals and make the magnitude in IMF1 and IMF2 relatively small. The fourth and fifth groups of IMFs contain low-frequency signals as interpretation having structure modes dynamics and ball running frequencies. As mentioned, the third group of IMF around 300–330 Hz contains the characteristic signal of preload and when pretension is presented.
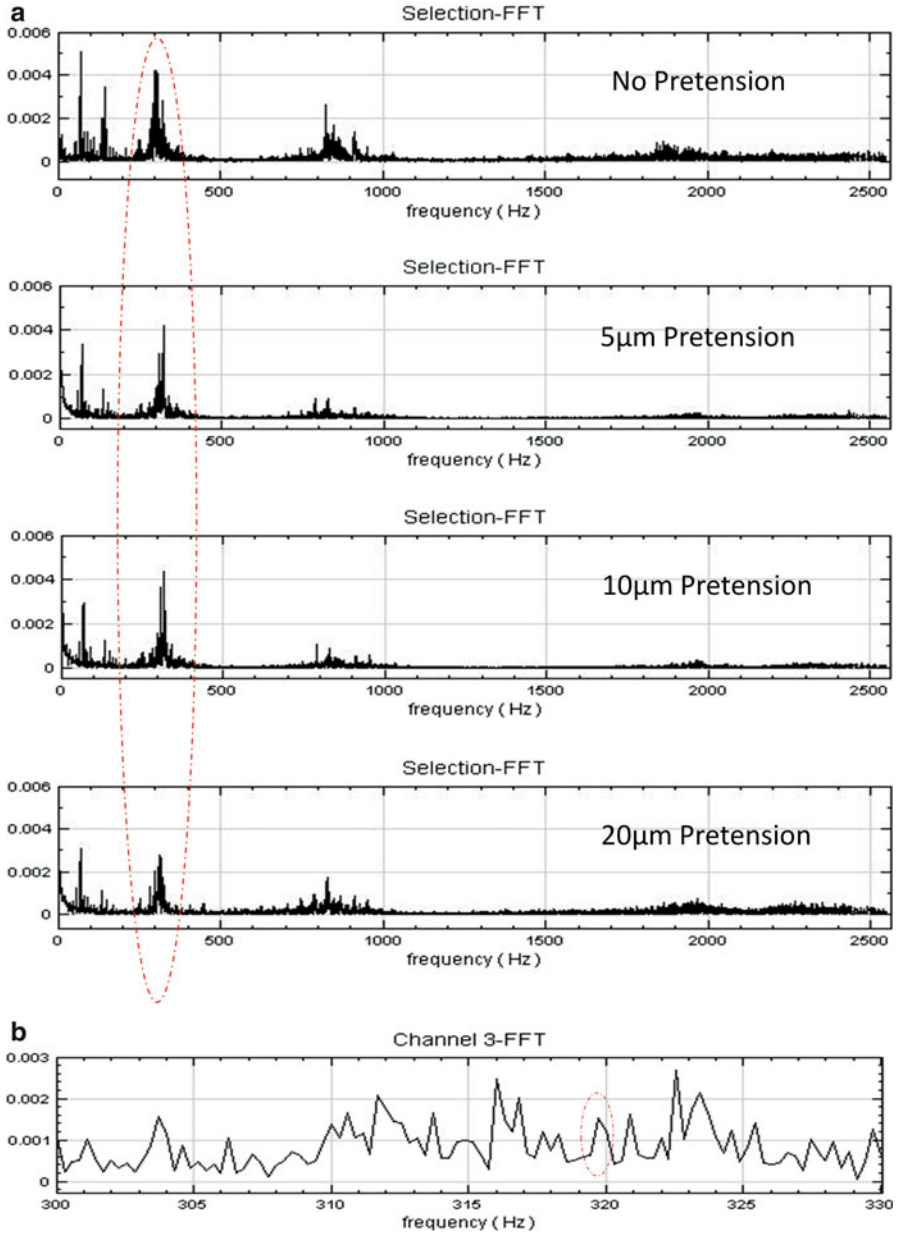
Fig. 3 (a) Axial vibration signals from the ball nut with pretension value of 0, 5, 10, and 20 μm, respectively. (b) Enlarged view of the frequency in 300–330 Hz
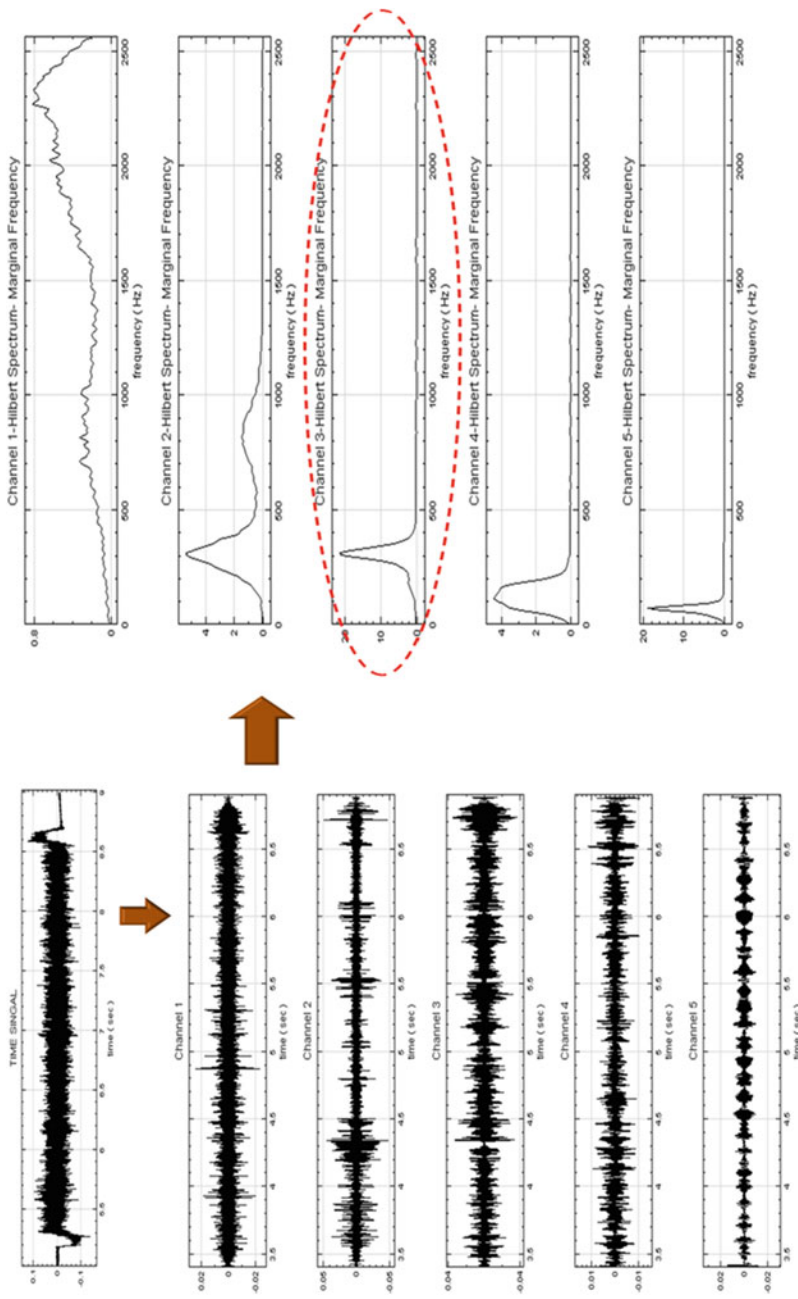
Fig. 4 Marginal spectrum for the first to fifth intrinsic mode functions
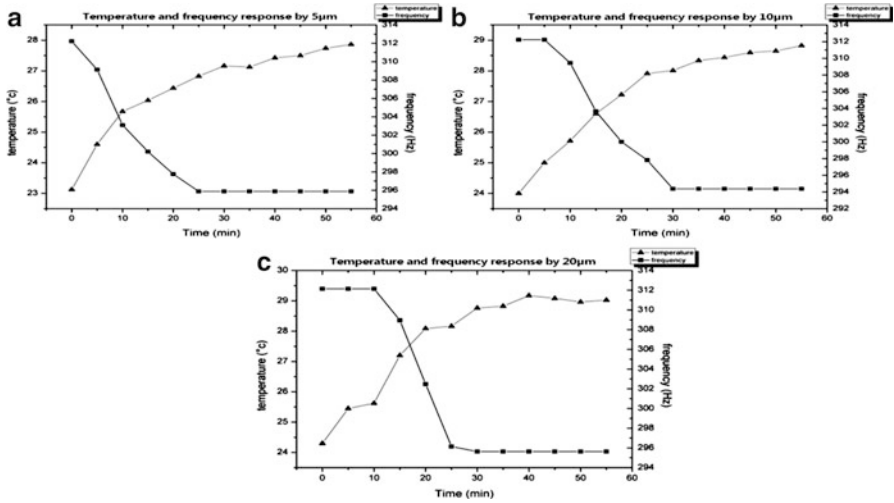
Fig. 5 Temperature and frequency response with time by 5, 10, and 20 μm pretensions
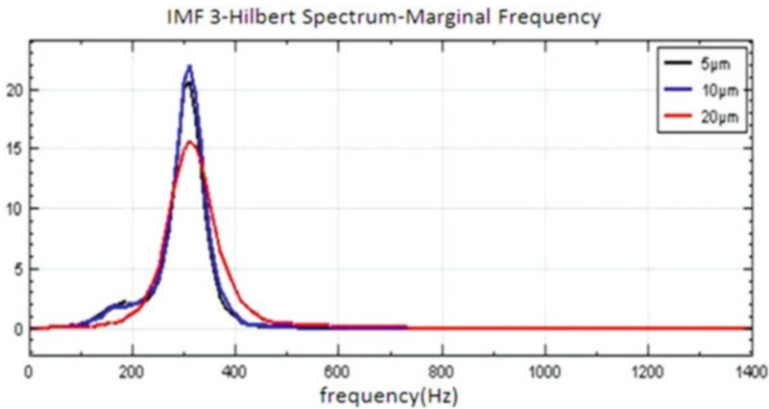
Fig. 6 Marginal frequency of IMF3 by 5, 10, and 20 μm pretensions

The long-term machine operation for the temperature influence is explored in Fig. 5a, b, and c with 5, 10, and 20 μm pretensions, respectively. Temperature data are acquisitioned averaged from the ball screw teeth by thermocouples. It is shown when reciprocating table in motion for one hour, all the heat generation increases through the ball screw by enhanced pretension value from 5, 10, to 20 μm. Moreover, the characteristic frequency about 312 Hz decreases about 10 %. This discloses the total stiffness of the ball screw changes and followed by preload loss, since temperature causes the stress variations and affects the stiffness thereafter. Observation in Fig. 6 elucidates the amplitude of Hilbert spectrum in marginal frequency of the IMF 3 decreases as the pretention value increases from 5 to 10 μm and 20 μm.

This corresponds to the prognostic diagnosis for preload loss with sensed vibration signals when the characteristic frequency of the pretension frequency decreases significantly.

5   Conclusion

This study examines a signal analysis technique to detect machinery states. The highly nonlinear processing EMD/HHT method is used for detecting the complexity of a ball screw preload and pretension system. An experiment measure of ball screw pretension was used to quantify the ball screw dynamical complexity and identify the irregularity caused to preload loss. Experimental results reveal evidence of a preload loss when the pretension value of the ball screw feed drive system is large to 20 μm. Experimental results also show a clear inclination in temperature and declination in featured frequency by increased pretension. It has been successfully demonstrated that the preload loss of a ball screw can be prognostic by the vibration signals sensed at the ball nut based on the pretension value for a long-time operation. Experimental results successfully show that the proposed methodology can determine the machinery state when the ball screw is in operation. Applying signal analysis techniques of EMD/HHT achieves the purposes of diagnostic effectiveness and useful application.

References

1. Denkena B, Harms A, Jacobsen J, Möhring H-C, Lange D, Noske H (2006) Life-cycle Oriented Development of Machine Tools. In: 13th cooperative institutional research program international conference on life cycle engineering, pp 693–698
2. Huang NE, Shen SSP (2005) Hilbert–Huang transform and its applications. World Scientific Publishing, Singapore
3. Huang NE, Shen Z, Long SR, Wu MC, Shih HH, Zheng Q et al (1998) The empirical mode decomposition and the Hilbert spectrum for nonlinear and nonstationary time series analysis. Proc R Soc A 454:903–995
4. Peng ZK, Tse PW, Chu FL (2005) A comparison study of improved Hilbert–Huang transform and wavelet transform application to fault diagnosis for rolling bearing. Mech Syst Signal Process 19:974–988
5. Costa M, Goldberger AL, Peng C-K (2005) Multiscale entropy analysis of biological signals. Phys Rev Express 71:021906-1–021906-18
6. Antonino-Daviu J, Jover Rodriguez P, Riera-Guasp A, Arkkio M, Roger-Folch J, Perez RB (2009) Transient detection of eccentricity-related components in induction motors through the Hilbert–Huang transform. Energy Convers Manage 50:1810–1820
7. Huang YC, Shin YC (2012) Method of intelligent fault diagnosis of preload loss for single nut ball screws through the sensed vibration signals. In: International conference on machine learning and data analysis, 65, World Academy of Science, Engineering and Technology, Tokyo, Japan, pp 1394–1401

Simulation and Experiment of Langevin-Type Piezoelectric Ultrasonic Horn for Micro Tool Motion

Yi-Cheng Huang, Guan-Zhang Ding, Bo-Hsuan Chen, and Yu-Jui Huang

Abstract The principle of a piezoelectric transducer used in this chapter is to transfer the high frequency of electrical energy to mechanical energy. Since the output displacement of piezoelectric transducer is too small, the need of amplifying the displacement of the tool is based on the design of horn shape. Since resonance frequency of the horn should be compatible with the vibration frequency of the piezoelectric vibrator. This chapter is first to conduct experiment to measure the vibration frequency and amplitude of a piezoelectric transducer (PZT) for ultrasonic vibration. According to the experimental result, the resonant frequency of the horn for amplifying the displacement of the PZT is achieved thereafter. Theoretical calculation and ANSYS simulation can be used for figuring out the geometrical shape of the piezoelectric actuated horn. In the simulation, the horn modal frequency and harmonics analysis via the ANSYS simulation reach the error less than 3 %. Experimental results will be compared and validated with the simulated results.

Keywords Piezoelectric transducer • Modal analysis • Harmonic analysis • Horn design • Tool motion

Y.-C. Huang (✉) • G.-Z. Ding • B.-H. Chen
Department of Mechatronics Engineering, National Changhua University
of Education, Changhua 50007, Taiwan
e-mail: ychuang@cc.ncue.edu.tw

Y.-J. Huang
Department of Power Mechanical Engineering, National Tsing Hua University,
Hsinchu 30013, Taiwan

1   Introduction

In recent years, usage of piezoelectric ultrasonic transducer is increasing. For the medical field, introduction of such transducers have been brought into cutting medical tissues applications [1]. The main ultrasonic principle is converting high-frequency power to mechanical vibration power by the vibrator, and then steady amplitude of mechanical vibration is reached thereof. Since the output amplitude of transducer is very small, the ultrasonic horn is usually designed and operated in harmonization to amplify the output amplitude. The horn resonant frequency should be compatible with the excited transducer frequency; otherwise, this will cause the vibration modal change, affecting the energy transferring and leading to an amplification decline. The ultrasonic vibration system is composed by the vibrator, horn, and the tools for micro cutting or machining. In theory, the stepped horn provides the largest amplification displacement. In order to increase the amplitude of the piezoelectric vibrator, stepped horn is the most common solution and capable of generating highest amplification. Such horn tends to have stress concentration as general. Hence, shaped shape for smooth connection is usually utilized for stress concentration reduction. Reliable performance of horns is normally associated with the amplitude of vibration, uniformity of vibration amplitude at the working surface, and the avoidance of modal participation by non-tuned modes at the operating frequency [2]. Therefore, theoretical calculation and ANSYS simulation are used for designing the geometrical shape of the piezoelectric actuated horn in this study. Simulation results will be investigated by conducting experimental results for validation PZT with horn for application on tool displacement.

1.1   *The Finite-Element Method and Modal Analysis*

The finite-element method (FEA) was applied on actual structural engineering analysis problems since 1950. FEA is a methodology that divides a complex structure of entities (ideal model) into many small elements with restrictions. Mechanical equilibrium equation for each element can be obtained by mechanics methodology. It makes the structure system satisfied the continuous condition. Therefore, the actual overall structure of mechanical equilibrium equation can be obtained. Besides, the natural vibration characteristics of the mechanical structure can be solved via FEA. It is capable of obtaining the system mode shapes of the overall structure under specific boundary conditions.

1.2   *Harmonic Analysis*

Harmonic analysis is a way for confirming the response of a structure suffering a given excitation wave. To understand the reaction of ultrasonic horn under a

periodic force of PZT, the ultrasonic horn shape is simulated with modal analysis. The purpose of the analysis is to understand the output displacement of the horn under a periodic sine wave excitation from the output of the Langevin-type PZT.

2 Simulation and Experimental Results

2.1 Experimental Setup

Figure 1 shows the schematic diagram for measuring the ultrasonic motion of the Langevin-type PZT. Laser Doppler-vibration meter is utilized to measure the oscillation. When the frequency of piezoelectric vibrator is excited at 37.573 kHz, the measured displacement is from -0.85 to $+0.88$ μ based on integration of the velocity records. According to this measurement results, the theoretical design and simulation analysis for the shaped horn design can be followed thereafter.

2.2 Theoretical Geometry Calculation for Horn Shape

As stated the horn is designed to amplify the amplitude of the piezoelectric vibrator output. Change of the cross-sectional area to achieve the purpose of enlarging displacement is used as usual. Stepped type has the highest amplification among all the various horn types, but there is a stress concentration problem. Therefore, a smooth geometrical profile is usually utilized to connect the piezo terminal section ($D1$) to the reduced section ($D2$) as shown in Fig. 2. In this study, $D1 = 45$ mm, $D2 = 25$ mm, $D3 = 5$ mm, and $L3 = 5$ mm with the theoretical amplification rate of 3.22.
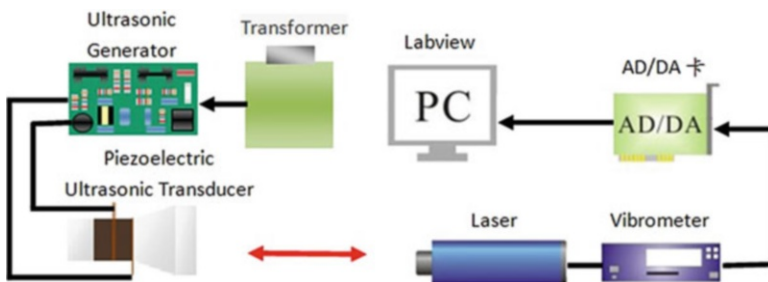
Fig. 1 Schematic diagram of the Langevin-type PZT measurement system
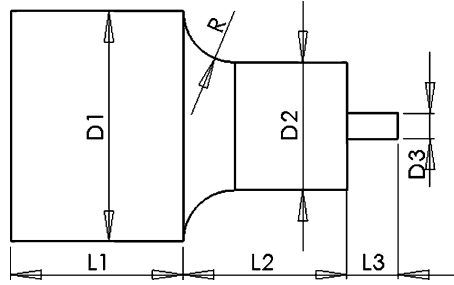
Fig. 2 Dimensional drawings of the horn shape
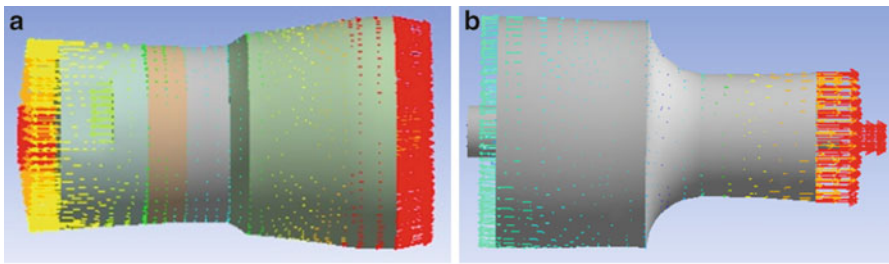
Fig. 3 (**a**) ANSYS simulation for the piezoelectric modal frequency at 39,646 Hz. (**b**) ANSYS simulation for the excited frequency at 36,963 Hz along with resonance mode in axial displacement

2.3 *Piezoelectric Resonance Modal Excitation to the Designed Horn Shape*

ANSYS simulation for the Langevin-type piezoelectric modal frequency results in 39,646 Hz and creates the axial displacement of vibrator as shown in Fig. 3a. The simulation frequency with the experimental resonance at 37,573 Hz is about 5.1 % in frequency error. This error may cause by the ideal contact between each material setting. The material excepted by the piezoelectric body is chosen to be the aluminum alloy (6061T6) which has the same sonic speed as the ultrasonic horn. In ANSYS modal analysis, the resonance frequency of the designed horn shape is excited by 39,646 Hz and results in axial displacement mode at 37,500 Hz. This leads to an error of 1.4 % when the theoretical analysis is compared. Figure 3b shows the horn is oscillated at 36,963 Hz, whereas experimental result is measured at 37,500 Hz with 1.7 % error.
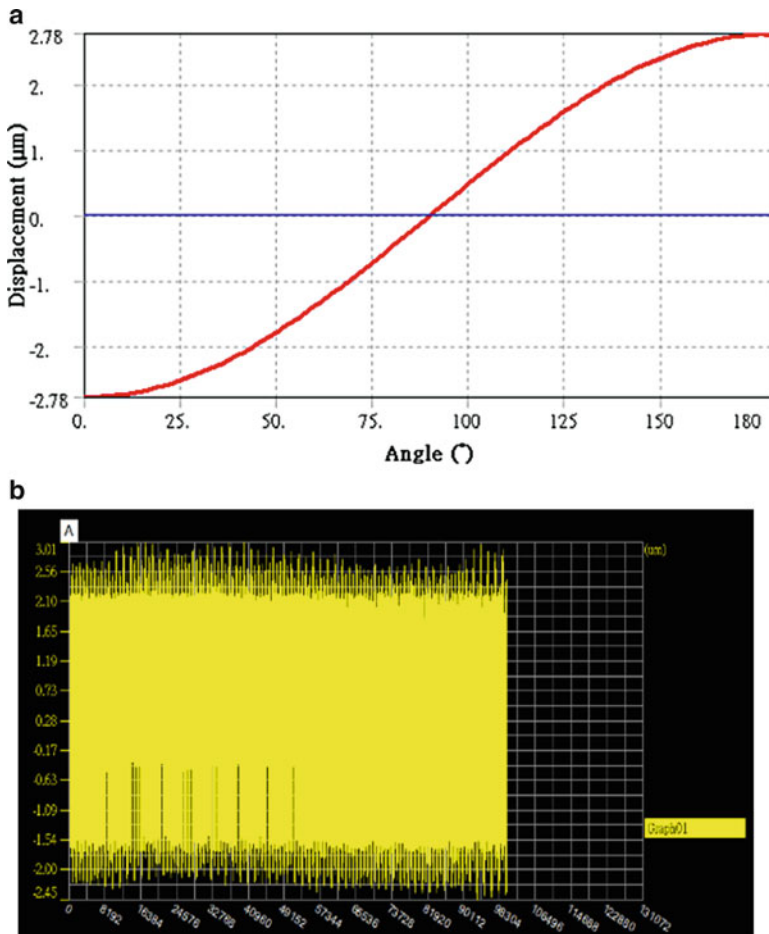
Fig. 4 (**a**) The numerical simulation for the displacement of the horn tip (tool) with one half of the sinusoidal excitation. (**b**) Experimental results for the displacement of the horn tip (tool) with one half of the sinusoidal excitation

2.4 Shaped Horn Harmonic Excitation to the Tool Tip

According to the experiment for the output of the Langevin-type PZT, the displacement is reciprocating between 0.85 and +0.88 µ with modal frequency at 37,500 Hz. The average maximum reciprocating displacement is 1.73 µm. Then the amplitude at the end of horn should be 1.73 µm*3.22 (= 5.57 µm). In simulation, applying the displacement of 0.865 µm on the horn in the x-axis and then examining the displacement of the horn tip (tool) can be depicted in Fig. 4a.

As in Fig. 4a, the maximum reciprocating displacement of the end point tip (tool) is 5.56 μm. As stated above, an error of 3.1 % is reached when the simulated amplification rate of 3.22 is compared with the theoretical one. Moreover, from the experimental measurement results, as shown in Fig. 4b, the peak-to-peak output displacement is 5.46 μm with an error of 1.7 % when the theoretical one is 5.56 μm. This is convinced that through theoretical calculation followed by ANSYS simulation, the experimental results consolidate the design procedure, and identifying or tuning the excitation frequency from experiment measurement of PZT, designing the horn shape and the tip motion in desired (axial) motion is established very accurately.

2.5   Arc Linked Stepped Horn

It is known that the size of horn is used for connecting the machining tool or cutting tool. In some cases, it can be part of the horn shape for amplification concern. Hence, an arc linked stepped horn (Fig. 5b) is numerical simulation. Modal frequency of a stepped ultrasonic horn can be numerical simulation first through the ANSYS. In Fig. 5a, the horizontal axis represents the size of tip (tool) in mm and the vertical axis represents the simulated frequency by ANSYS (Hz). When the material is 6061T6 aluminum alloy with the diameter ratio of 1:10, the displacement is simulated as 71.56 μm in Fig. 5a. Simulation result reveals the feasibility of the corresponding chart on top of Fig. 5a as look-up chart. In consequence, it was proved experimentally at the bottom of Fig. 5a.

3   Concluding Remarks

In this chapter PZT is used to driving the tip (tool) motion for machining metal or cutting tissue. Since the output displacement of PZT is too small, amplifying the horn shape followed by the displacement of the tool is designed through the ANSYS simulation and experimental validations. This chapter shows that one can first to conduct experiments to measure the PZT frequency and amplitude under the best ultrasonic vibration. Then the resonant frequency on the horn shape for amplifying the displacement of the PZT is achieved thereafter. Theoretical calculation and ANSYS simulation can be used for figuring out the geometrical shape of the piezoelectric actuated horn. In ANSYS simulation and theoretical calculation, the horn modal frequency and harmonics analysis reach the error of 3.1 %. Moreover, the Langevin-type PZT with horn shape modal frequency and harmonics analysis reach the error of 0.6 %.
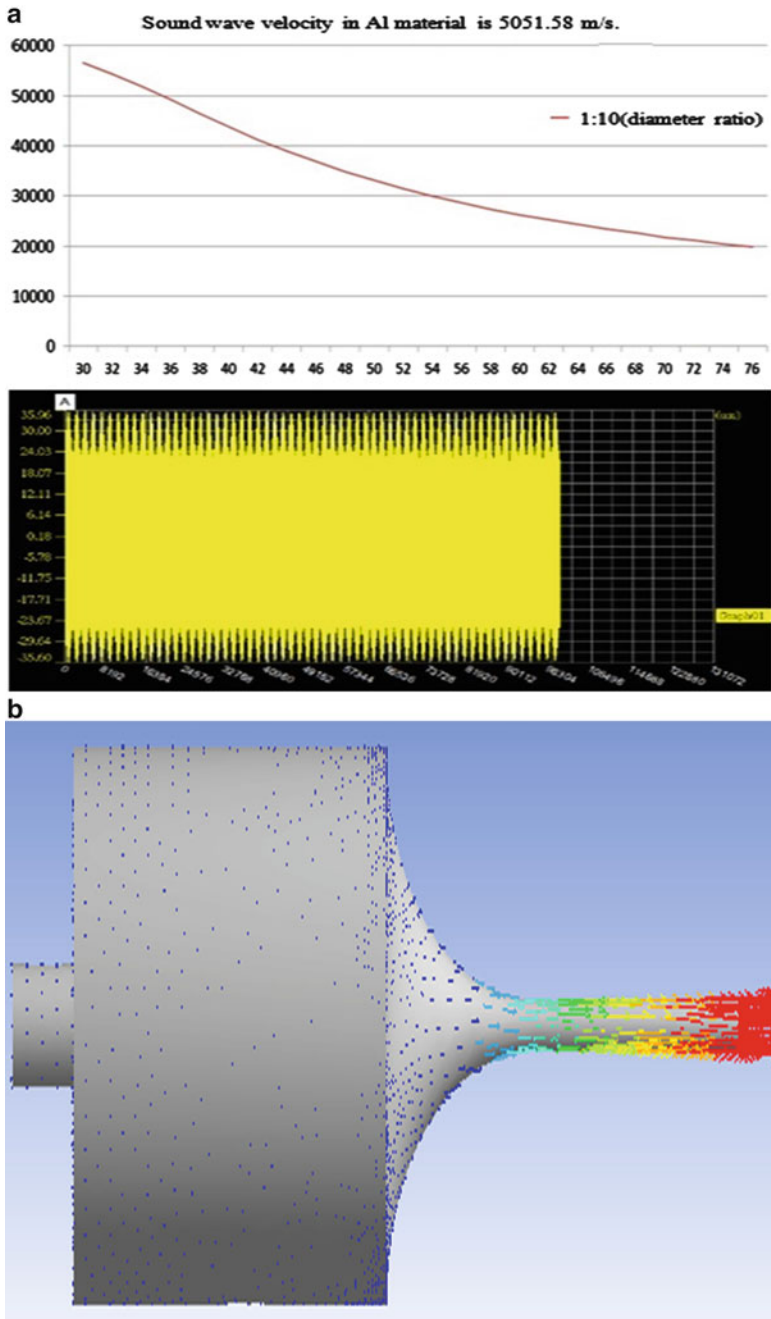
Fig. 5 (**a**) *Top*: ANSYS simulation (diameter ratio with output end and input end: 1:10); *bottom*: experimental results. (**b**) The 36,762 Hz frequency in (**a**) with resonance mode in axial displacement

References

1. Chen L, Ru CH, Rong WB, Liu Y, Sun L (2010) Design, modeling and control of a piezoelectric ultrasonic microdissection technique for the molecular analysis of tissue. Smart Mater Struct 19:1–7
2. Cardoni A, Lucas M (2002) Enhanced vibration performance of ultrasonic block horns. Ultrasonics 40(1–8):365–369
3. Ding G-Z, Huang, Y-C (2012) Design of a piezoelectric ultrasonic horn shape and its simulation. J Appl Sound Vib 4(2)

A New Low-Temperature Fabrication Method of Dye-Sensitized Solar Cells

Yeong-Lin Lai, Shin-Hong Chen, Jiong-Heng Lu, Jia-Shan Ting, and Tsung-Yen Tsai

Abstract A new fabrication method of dye-sensitized solar cells (DSSCs) is presented in this chapter. The traditional fabrication methods of dye-sensitized solar cells (DSSCs) using high-temperature processes for working electrodes have been ameliorated. In the new method, TiO_2 powder was ground with polydimethylsiloxane (PDMS) for the fabrication of working electrodes and graphite powder was ground with PDMS for relative electrodes. The mixtures for both the working and relative electrodes were coated on ITO-glass substrates by the doctor blade technique. PDMS was able to enhance the adhesion of the film and the substrate as well as reduce film cracks. The process temperature of the proposed fabrication method was 150 °C. The low process temperature allows the usage of the plastic substrate for the DSSC. This leads to the advantages of low costs and substrate flexibility. The proposed method demonstrates a promising future for the flexible applications of DSSCs.

1 Introduction

The energy crisis is worsening in recent years because that several energy reserves are decreased all over the world. According to the statistics form 2012 BP Statistical Review of the World Energy, the total reserves-to-production ratio of the oil is about 54.2 years and those of the natural gas and the coal are 63.6 and 112 years, respectively [1]. In order to solve the energy problem, solar cells are the top choices

Y.-L. Lai (✉) • S.-H. Chen • J.-H. Lu • J.-S. Ting • T.-Y. Tsai
Department of Mechatronics Engineering, National Changhua University
of Education, Changhua 50007, Taiwan
e-mail: yllai@cc.ncue.edu.tw

of green energies. There are many types of solar cells. Different types of solar cells have different efficiency values. The photoelectric conversion efficiency of silicon-based solar cell is able to reach 25 %, that of GaAs compound-based solar cells attends 28.8 %, and that of dye-sensitized solar cells (DSSCs) is 11 % [2].

DSSC is a low-cost and low-pollution technology for solar cell industry. To make the porous TiO_2, a sintering step at the temperatures higher than 450 °C was used in traditional methods [3–11]. By the sintering process, the DSSC efficiency can attain to 9 % [6]. However, the high sintering temperature limits the substrates chosen because some substrates cannot suffer such high temperature. Only the substrates which can bear high temperature, such as ITO [12] and FTO [13–15] glasses, can be chosen. The glass substrates are, however, not flexible. This restricts the DSSC for flexible applications. For the use of flexible substrates like conductive plastics, the low-temperature (<450 °C) methods are needed.

In this chapter, polydimethylsiloxane (PDMS) is used as a binder to reduce the process temperature of the TiO_2 working electrodes of DSSCs and enhance the adhesion property of the TiO_2 film on the substrate.

2 Experimental

Figure 1 shows the DSSC structure with a TiO_2-PDMS mixture. When the TiO_2 absorbs the photons, electrons are stimulated. The electrons move from the working electrode through the external circuit, load, relative electrode, and electrolyte and finally come back to the working electrode.

2.1 Reagents

The chemicals used include Degussa P-25 TiO_2 (80 % anatase and 20 % rutile) nanopowder, PDMS, Triton X-100 solution, graphite (SHOWA, 80 % coal), and deionized (DI) water. The PDMS (Sylgard 184) was mixed by prepolymer and curing agent at a 10:1 mixing ratio.

2.2 Substrate Clean

The substrates were glasses with ITO (In_2O_3:Sn). Substrates were dipped in acetone for 10 min with ultrasonic cleaning, then in isopropanol and DI water, respectively. Finally, the substrates were dried by a nitrogen flow and heated at 100 °C for 5 min in order to remove residual moisture.
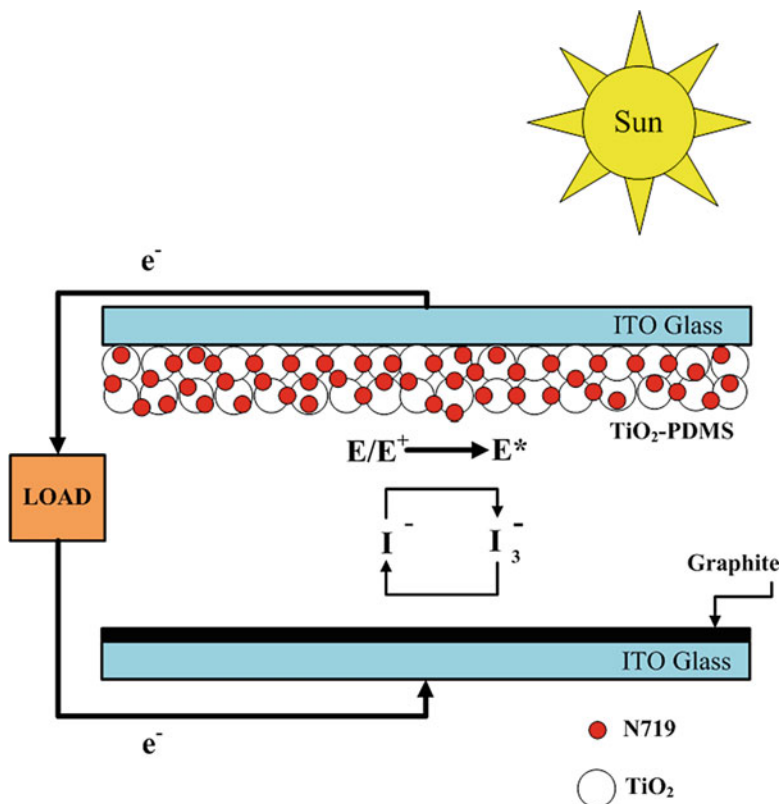
Fig. 1 DSSC structure with TiO$_2$-PDMS mixture

2.3 Electrode Preparation

Figure 2 shows the TiO$_2$-PDMS mixture in which 3-g TiO$_2$ powder was ground with 4.5-g DI water, and 0.4-g PDMS. Triton X-100 solution was also added in the mixture. For relative electrodes, 2-g graphite powder was ground with 4.5-g DI water, 0.4-g PDMS, and Triton X-100 solution. The active region of DSSC was surrounded by the Scotch (3M) tape. TiO$_2$-PDMS and graphite-PDMS mixtures were coated by the doctor blade technique. Then the tape was removed and the electrode was heated at 150 °C for 25 min for drying. The TiO$_2$-PDMS electrode was dipped in N719 dye for 18 h.

2.4 Cell Fabrication and Measurement

Two PE membranes were used to prevent the short circuit of the working and relative electrodes. The electrolyte (KI) was filled in between the working and relative electrodes.

Fig. 2 TiO$_2$-PDMS mixture

The DSSC was exposed by an AM-1.5 light simulator with a light intensity of 100 mW/cm^2 to measure the cell efficiency. With the use of current–voltage (I–V) measurement instrument (KEITHLEY 2400) and software, the electrical characteristics of the open voltage, short current, fill factor, and efficiency were obtained.

3   Results and Discussion

A novel method for the fabrication of DSSCs was proposed. TiO$_2$ was mixed with PDMS to form a colloid mixture. Degussa P-25 TiO$_2$ powder was used because of its photocatalytic property. The PDMS polymer acted as a binder between TiO$_2$ powder and substrate.

It is a challenge to obtain a crack-free TiO$_2$ film at a low temperature using the doctor blade method. The addition of the PDMS material was used to reduce the cracks. The surface morphology of the TiO$_2$ film was observed by scanning electron microscopy (SEM). Figure 3 shows the SEM picture of the TiO$_2$ film prepared at low temperature. Nanoscale of the TiO$_2$ film was obtained.

Figure 4 shows the I–V characteristics of the DSSC. The open-circuit voltage and the short-circuit current were 610 and 1.42 mA, respectively.
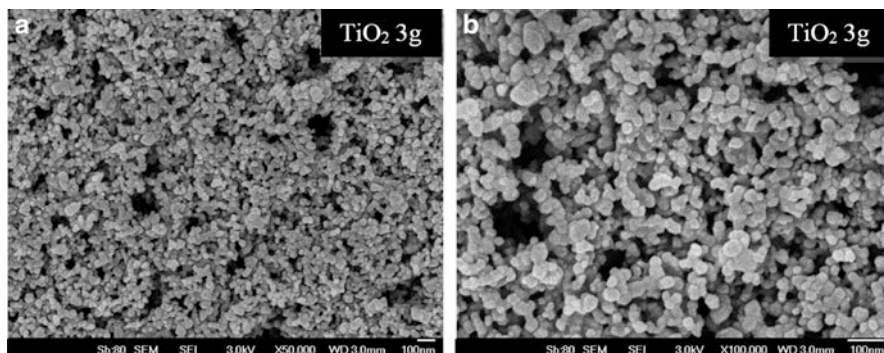
Fig. 3 FE-SEM micrograph of TiO$_2$ and PDMS mixture
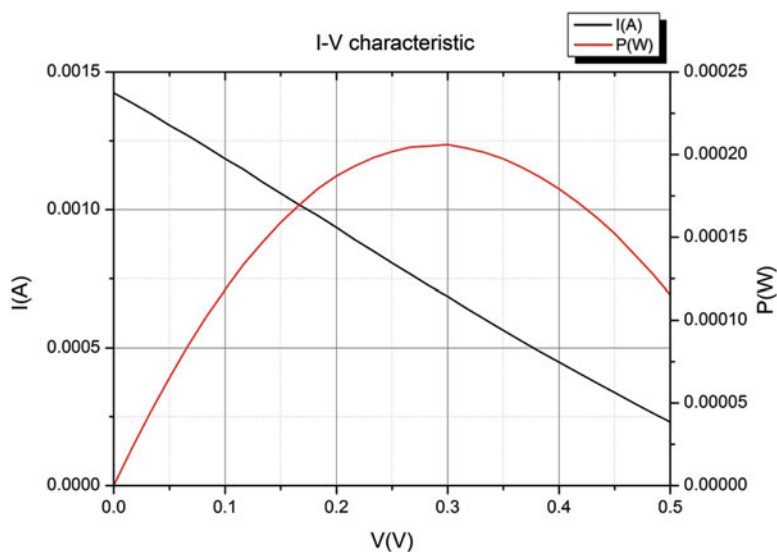
Fig. 4 *I–V* characteristics of DSSC

4 Conclusion

A new TiO$_2$-PDMS working electrode technique has been proposed for DSSCs. The TiO$_2$-PDMS mixture was made by the TiO$_2$ powder, DI water, PDMS material, and Triton X-100 solution. Both the material and electrical characteristics of the DSSCs were investigated. The good characteristics of the DSSCs have been achieved using the technique.

References

1. BP statistical review of world energy, http://www.bp.com/statisticalreview
2. Green MA, Emery K, Hishikawa Y, Warta W, Dunlop ED (2012) Solar cell efficiency tables (version 40). Prog Photovolt Res Appl 20:606–614
3. Chapin DM, Fuller CS, Pearson GL (1954) A new silicon P-N junction photocell for converting solar radiation into electrical power. J Appl Phys 25:676
4. Shanmugam M, Bills B, Baroughi MF (2010) Overview of atomic layer deposited metal oxides for treating nanoporous TiO_2 photoelectrode for dye sensitized solar cells. In: 35th IEEE photovoltaic specialists conference, IEEE Press, New York, pp 3248–3252
5. Jumi Kim MJS, Kim HJ. Hong B (2010) Effect of plasma rteatment with avrious gases on nanocrystalline TiO_2 for dye-sensitized solar cell (DSSC). In: 35th IEEE photovoltaic specialists conference, IEEE Press, New York, pp 3242–3247
6. Alivov Y, Fan ZY (2010) Dye-sensitized solar cells using TiO_2 nanoparticles transformed from nanotube arrays. J Mater Sci 45:2902–2906
7. Fujihara K, Kumar A, Jose R, Ramakrishna S, Uchida S (2007) Spray deposition of electrospun TiO_2 nanorods for dye-sensitized solar cell. Nanotechnology 18:365709–365714
8. Mor GK, Shankar K, Paulose M, Varghese OK, Grimes CA (2006) Use of highly-ordered TiO_2 nanotube arrays in dye-sensitized solar cells. Nano Lett 6:215–218
9. Ngamsinlapasathian S, Sreethawong T, Suzuki Y, Yoshikawa S (2005) Single- and double-layered mesoporous TiO_2/P25 TiO_2 electrode for dye-sensitized solar cell. Sol Energ Mater Sol Cells 86:269–282
10. Schmidt-Mende L, Grätzel M (2006) TiO_2 pore-filling and its effect on the efficiency of solid-state dye-sensitized solar cells. Thin Solid Films 500:296–301
11. Park JH, Jun Y, Yun H-G, Lee S-Y, Kang MG (2008) Fabrication of an efficient dye-sensitized solar cell with stainless steel substrate. J Electrochem Soc 155:F145–F149
12. Jinting Jiu IS, Wang F, Motonari A (2006) Dye-sensitized solar cells based on a single-crystalline TiO_2 nanorod film. J Phys Chem B 110:2087–2092
13. Balraju P, Suresh P, Kumar M, Roy MS, Sharma GD (2009) Effect of counter electrode, thickness and sintering temperature of TiO_2 electrode and TBP addition in electrolyte on photovoltaic performance of dye sensitized solar cell using pyronine G (PYR) dye. J Photochem Photobiol A Chem 206:53–63
14. Song MY, Kim DK, Ihn KJ, Jo SM, Kim DY (2005) New application of electrospun TiO_2 electrode to solid-state dye-sensitized solar cells. Synth Met 153:77–80
15. Lee H-S, Bae S-H, Jo Y, Kim K-J, Jun Y, Han C-H (2010) A high temperature stable electrolyte system for dye-sensitized solar cells. Electrochim Acta 55:7159–7165

A Cell Culture System with Programmable Physical Stimulation for Human Mesenchymal Stem Cell Differentiation and Promotion

Tzu-Yu Chuang, Yu-Sheng Chuang, Nancy Wang, and Kerwin Wang

Abstract It is important to study the osteoblast and chondrocyte differentiations of human mesenchymal stem cells (hMSCs) due to a significant demand for prerequisite regenerative medicine. Many physical stimulators would also promote cell differentiation. This study presents a time-efficient cell differentiation system to induce and evaluate the stem cell differentiation process under given physical stimulations. In this system, all the driving signals of physical stimulations can be controlled independently by a reprogrammable microcomputer for physical stimulation studies. This chapter focuses on the design methodology and characterization of this cell culture system.

Keywords hMSCs • Cell culture • Programmable • Physical stimulation

1   Introduction

It is important to study the differentiation of osteoblasts due to a great need for orthopedic therapy in regenerative medicine [1]. Slow differentiation process and low throughput in stem cell culturing set limitations in clinical applications. Optimizing differentiation process would be a great benefit to regenerative

T.-Y. Chuang • Y.-S. Chuang • K. Wang (✉)
Department of Mechatronics Engineering, National Changhua University
of Education, Changhua 50007, Taiwan
e-mail: kerwin@cc.ncue.edu.tw

N. Wang
Graduate Institute of Biotechnology, National Changhua University
of Education, Changhua 50007, Taiwan

therapies. Recently, there are lots of researches concerning influence of cell cultured with physical stimulations including different optical wavelengths, alternative electric currents, and fluidic stresses. Effects from each single stimulator have been demonstrated individually in an independent platform [2–5]. In order to design a system which could culture cells in an array with multiple stimulation factors, this chapter presents a novel combination of a microcomputer and a 4-by-6 well-array cluster. In each column of well array, cells are stimulated by predetermined physical signals which are controlled by a microcomputer (ATmega168). Optimized differentiation conditions can be screened and determined from this platform.

2 Platform Design

The proposed cell culture system consists of a 4-by-6 well array in which 40,000 human mesenchymal stem cells (hMSCs) are cultured in each well. Each column of this array is equipped with a 4-by-1 stimulator array which is installed to a transparent lid except the control column. In column 1, buzzers are equipped with micro glass tubes to produce acoustic waves. The acoustic waves induce the fluidic stress and are transmitted to activate cell differentiation. In column 2 and column 3, each column delivers current pulses to stimulate cells through a gilded electrodes pair. In columns 4 and 5, cells are exposed to selected wavelengths of lights using pulse-width modulator. Column 6 is a control group for comparison. A detailed configuration of this platform is shown in Fig. 1.

Cells are cultured in osteogenic medium containing DMEM medium with β-glycerol phosphate (10 mM), ascorbate-2-phosphate (50 μg/ml), penicillin (100 U/ml), and streptomycin (100 U/ml). For chondrocyte differentiation, cells are cultured in DMEM medium with proline, ITS (5 μg/ml), ascorbate-2-phosphate (50 μg/ml), penicillin (100 U/ml), and streptomycin (100 U/ml). Cells are kept in a 5 % CO_2 incubator for 4 days.

3 Stimulating Signals

Two kinds of square pulses are generated in column 2 and column 3 by microcomputer with duration of 12 and 8 ms, respectively. The periods of both channels are 1,240 ms which is adjustable from microcomputer programming. The duty cycles are around 0.65–0.97 %. The voltage difference between two electrodes is 4.91 V, and the resistance between the culture medium-immersed electrodes is 188.7 Ω. The current between two electrodes is around 25 mA. Detailed waveforms of these electrical signals are shown in Fig. 2.
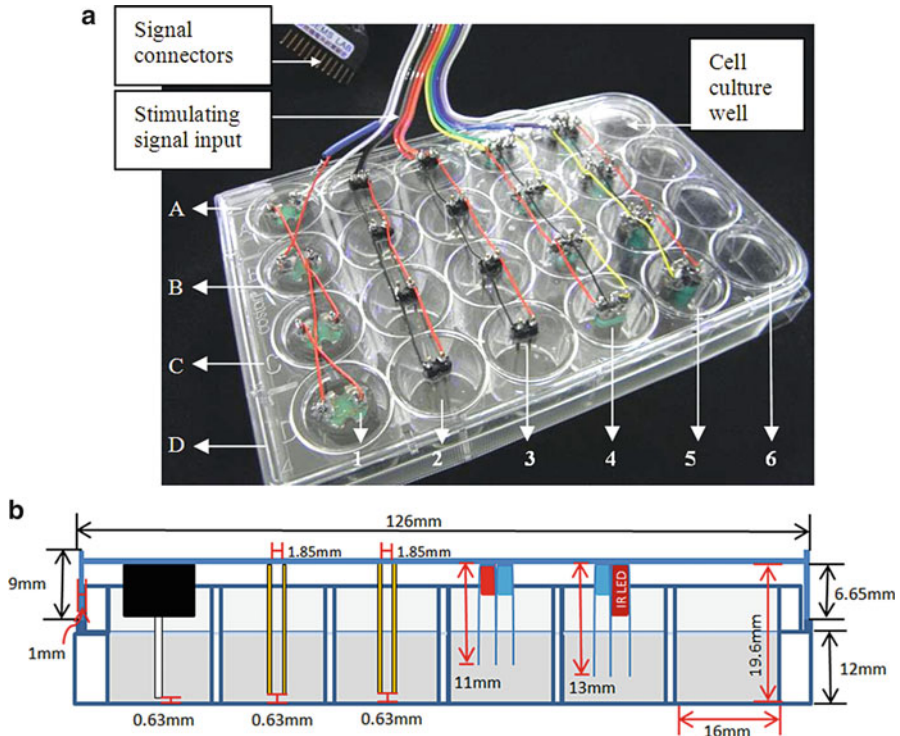
Fig. 1 (**a**) The stimulator array consists of a set of oscillatory flow generators, a 4-by-1 pulsed electrode pair array, and a dual-color LED array. An oscillating acoustic wave for fluidic stress test is produced by buzzers at 2,160 Hz; the intensity is around 43 dB. The current between two electrodes is between 25 mA. All the programmable driving signals are controlled independently by a microcomputer (ATmega168) for physical stimulation study; (**b**) this schematic diagram presents the structure of the cell culturing test platform

A buzzer connected with a capillary can generate a fluidic stress pulse. The acoustic waves, generated from a metal sheet, inside of the buzzer, can produce fluid oscillating waves in the capillary. The oscillating wave signal is controlled by a microcomputer. The fundamental oscillation frequency of the buzzers is around 2,160Hz; the intensity is controlled at 43 dB. Its configuration is detailed in Fig. 3a. A set of LEDs, connected with a black heat shrink tube, yields optical stimulation. The black tube is installed to confine the illuminated area of the LED's light. The tubes are chemically inert to culture medium. The LEDs' lighting duration is 160 ms, which is controlled by the microcomputer. The luminance of two-color LED is adjusted to same intensity. In the experiment, three different wavelengths, 470, 630, and 850 nm, have been tested. The configuration is presented in Fig. 3b.
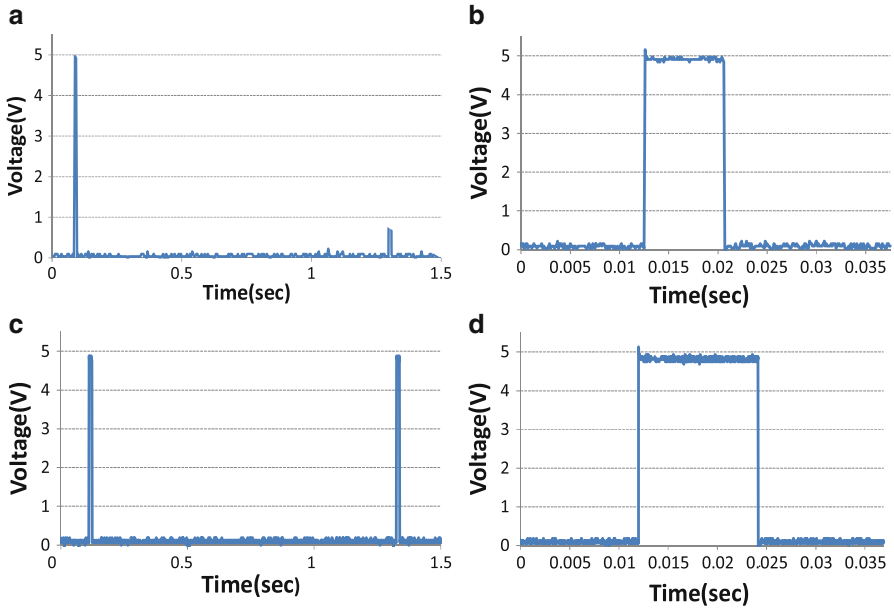
Fig. 2 (**a**, **c**) Shows the time periods between two pulses signals of column 3 and column 2, respectively. (**b**, **d**) Presents the duration of each pulse; the pulse durations of column 3 and column 2 are 8 and 12 ms, respectively
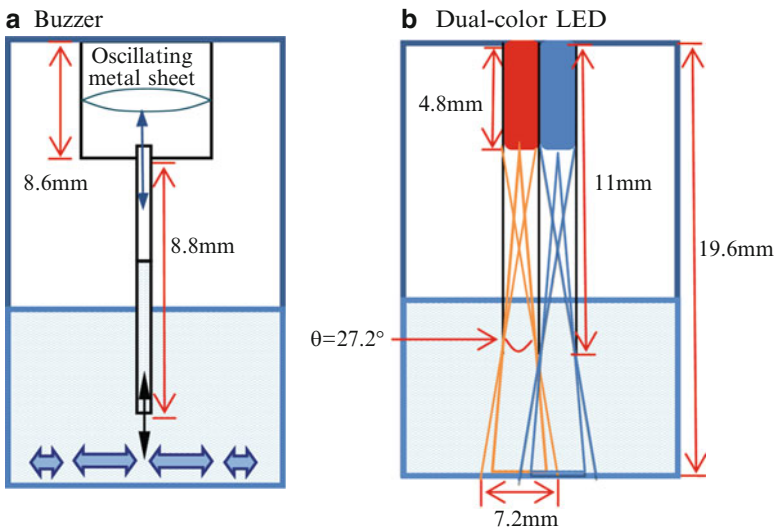
Fig. 3 (**a**) When the buzzer is acting, the fluidic level in the capillary will oscillate up and down, which generates a fluidic stress wave near the *bottom* of the cell culturing well in radial direction. The oscillating wave signals can promote the circulation and diffusion of cell culture medium. (**b**) The LED illuminator is applied to evaluate the bio-photonic interaction to the tested cells
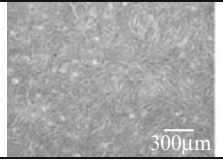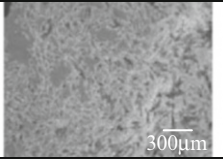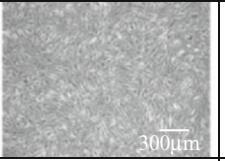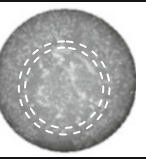
Osteoblast differentiation with cell culture medium			
Control group	Electrical stimulation (duration=8ms, duty cycle is around 0.65%)	Optical stimulation (λ=470nm/850nm Duration=160ms, duty cycle=12.9%)	Fluidic oscillation
300μm	300μm	300μm	
The control group is prepared to minimize the effects of unwanted variables other than a single independent variable.	This image shows the morphological changes of hMSCs undergoing ostegenic differentiation.	A morphological change presents an increased cell number and size.	There is no cell living under the edges of the microtube (dash white circles) in which they would face stronger mechanical stress.

Fig. 4 Osteoblast differentiation under different physical stimulations

4 Results

Stimulating hMSCs under given physical conditions with proposed cell culture platform would induce hMSC differentiating into either osteoblasts or chondrocytes (Fig. 4); the cell population growth rates are also increased, which has raised new possibilities for hMSC differentiation studies.

5 Summary

This chapter presents a cell culture system in which cells are cultured and stimulated by three kinds of physical stimulators. Because the culture system is controlled by a microcomputer, the physical stimulators are reprogrammable. One can easily and simultaneously observe hMSC differentiation progress under various influences from multiple stimulations.

References

1. National Center for Biotechnology Information. http://www.ncbi.nlm.nih.gov/
2. Hartig M, Joos J, Wiesmann H (2000) Capacitively coupled electric field accelerate proliferation of osteoblast-like primary cells and increase bone extracellular matrix formation in vitro. Eur Biophys J 29:499–506

3. McCullen SD, McQuilling JP, Grossfeld RM, Lubischer JL, Clarke LI, Loboa EG (2010) Application of low-frequency alternating current electric fields via interdigitated electrodes: effects on cellular viability, cytoplasmic calcium, and osteogenic differentiation of human adipose-derived stem cells. Tissue Eng Part C Method 16(6):1377–1386
4. Hronik-Tupaj M, Rice WL, Cronin-Golomb M, Kaplan DL, Georgakoudi I (2011) Osteoblastic differentiation and stress response of human mesenchymal stem cells exposed to alternating current electric fields. Biomed Eng Online 10:9
5. Cohen DM, Chen CS (2008) Mechanical control of stem cell differentiation. StemBook. Harvard Stem Cell Institute, Cambridge, MA. http://www.ncbi.nlm.nih.gov/pubmed/20614621

A Spray Method for Dye-Sensitized Solar Cells

Yeong-Lin Lai and Yi-Hsien Huang

Abstract A new spray method was applied for the working electrode of dye-sensitized solar cells (DSSCs), instead of the doctor-blade method, to make the film on the working electrode uniform. The working electrode was soaked to the dye which was heated to 60 °C, and then the dye was vibrated by a resonator. This procedure was capable of making the dye be well adsorbed into the working electrode. The solar photovoltaic conversion efficiency is increased from 0.26 % for the doctor-blade method to 2.65 % for the proposed spray method. The TiO_2 pastes were widely spread on the fluorine-doped tin oxide (FTO) substrate, even with a curved surface, using the spray method to achieve an efficient and simple manufacture technology of DSSCs with the advantage of low cost.

Keywords Dye-sensitized solar cell (DSSC) • Spray method • Working electrode

1 Introduction

Since 1990s, because of the advantages of dye-sensitized solar cells (DSSCs), such as inexpensive price, flexibility, and simple manufacture, more and more study for DSSCs has been increasing [1–5]. Although there is, yet, no breakthrough for the efficiency of DSSCs to surpass silicon solar cells, the much less cost of DSSCs in manufacture makes the DSSCs superior. The efficiency of DSSCs can be raised by solving the problem of electrolyte volatilization and chemical corrosion in electronic packaging. DSSCs will play an important role in solar cell area in the coming future [6–9].

Y.-L. Lai (✉) • Y.-H. Huang
Department of Mechatronics Engineering, National Changhua University
of Education, Changhua 50007, Taiwan, R.O.C.
e-mail: yllai@cc.ncue.edu.tw

The traditional film coating methods of DSSCs include screen printing, sol–gel, magnetron sputtering, and spin coating [10–12]. In addition to the traditional methods, a new spray method for the DSSC has been developed in this study. The spray method proposed is simple and convenient without the use of complex instruments. It also saves a lot of time and equipment costs and achieves a good efficiency.

In this work, the baking varnish spray gun collocated with gas air compressor was utilized for the spraying of films on the fluorine-doped tin oxide (FTO) substrates. The DSSCs with good characteristics were successfully manufactured.

2 Experimental

2.1 Structure

The structure of the DSSC contains a working electrode, an electrolyte, and a counter electrode, as shown in Fig. 1. The dye sensitizer was added in the working electrode of the DSSC to enhance the absorption of the visible light. The DSSC is able to transfer the solar energy to the electric energy. The characteristics of the DSSC can be improved by ameliorating the process of the working electrode.

2.2 Materials

The FTO glass plates were used for the substrates of the working electrode and the counter electrode. The materials of the working electrode included TiO_2 (Degussa P-25), ethyl cellulose, terpineol, ethyl alcohol, and N719 dye.
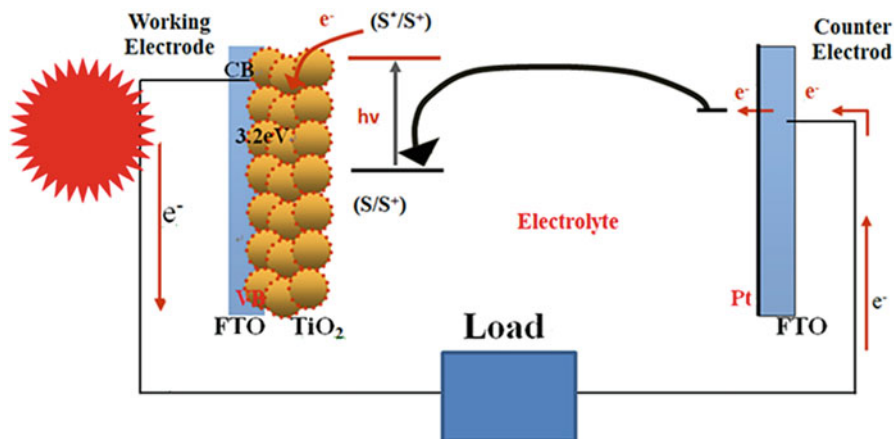
Fig. 1 Structure of DSSC

2.3 Preparation of TiO₂ Screen-Printing Pastes

The procedures of the preparation of TiO$_2$ screen-printing pastes include mixing the materials of the working electrode, placing the materials on the direct-controlled magnetic stirrers, stirring and heating the mixture at 80 °C for 20 min, and vibrating the materials with an ultrasonic cleaner for 30 min.

2.4 Preparation of Counter Pt-Electrodes

The counter electrode was dripped on the FTO glass plate by Eversolar Pt-100 (Everlight Chemical Industrial Corporation), and the plate is then sintered at 450 °C for 30 min.

2.5 Dye

The N719 dye was heated and resonated at 60 °C for 2 h and finally attached the electrodes.

2.6 DSSC Assembly

Figure 2 shows the assembly process of DSSC. The first step is cutting out an open window with an area of 0.9 × 0.9 cm^2 from a 30-μm-thick Surlyn film. The hollow section is for the filling of the electrolyte. The second step is drilling two 0.1-cm-diameter holes with a 0.5-cm distance between each other on the substrate. The third step is dropping the liquid platinum on the substrate to accomplish the counter electrode. The paste was sprayed on the 0.9 × 0.9-cm^2 area of the substrate as the working electrode. The fourth step is stacking the counter electrode, surly film, and working electrode to form a semifinished solar cell. The final step is to inject the electrolyte from the hole of the counter electrode substrate, seal the hole by UV glue, and solidify the paste by exposing with an ultraviolet exposure machine.

3 Results and Discussion

Under a solar simulator (AM1.5), the solar cell was measured by a current–voltage (I–V) instrument (Keithley 2400) for the open-circuit voltage (V_{oc}), short-circuit current density (J_{sc}), fill factors, maximum power voltage, maximum power
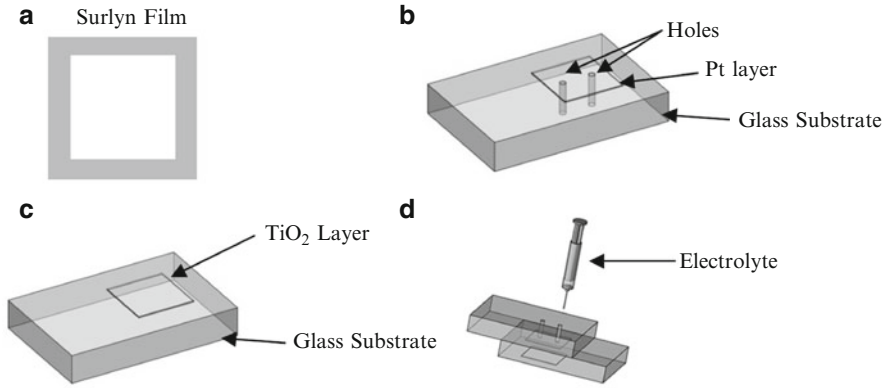
Fig. 2 DSSC assembly process: (**a**) Cut out an open window from a Surlyn film. (**b**) Counter electrode. (**c**) Working electrode. (**d**) Assembly and electrolyte injecting
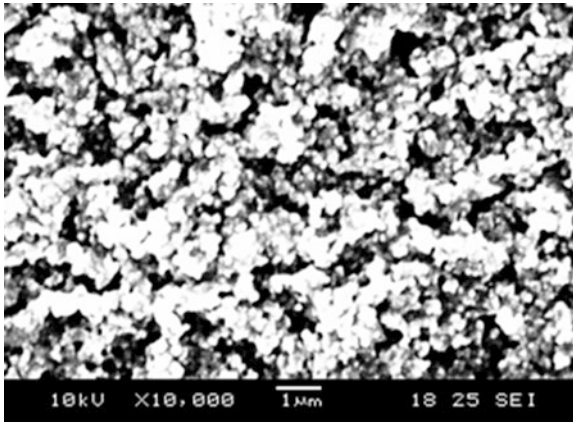
Fig. 3 SEM image of TiO$_2$ for porous and high specific surface area

current, and photo conversion efficiency (η). The efficiency and fill factors (FF) can be calculated according to Eqs. (1) and (2), respectively, as follows:

$$\eta = \frac{(I \times V)_{\text{max}}}{P_{\text{light}}} \tag{1}$$

$$\text{FF} = \frac{(I \times V)_{\text{max}}}{(I_{\text{sc}} \times V_{\text{oc}})} \tag{2}$$

The TiO$_2$ film has an important effect on the performance of the DSSC. The film manufactured has the structure with porous and high specific surface to absorb more photon within a constant geometric surface area as shown in Fig. 3. The conductive
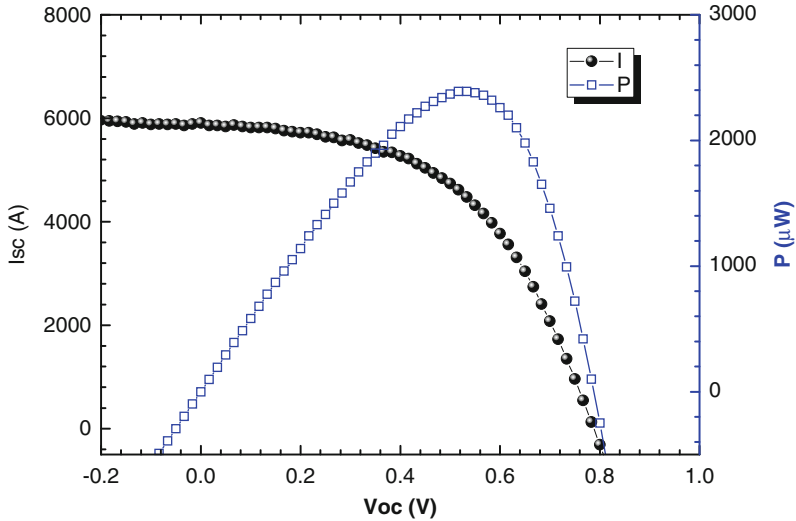
Fig. 4 *I–V* characteristics of DSSC

Table 1 Parameters of DSSCs based on the time of spraying

	J_{sc} (mA/cm^2)	V_{oc} (V)	Fill factor	Efficiency (%)
10 s	2.40	0.706	0.47	0.81
15 s	2.54	0.729	0.48	0.90
25 s	6.56	0.788	0.51	2.65
30 s	5.93	0.771	0.49	2.26

substrate and TiO_2 film must be contacted with each other in order to let the electrons transfer to the external electric circuit. Since the conductance of electrons will be influenced by the thickness of film, the thickness must be appropriate.

The distance between spray gun and the substrate was 15 cm. The TiO_2 paste was sprayed uniformly on the working electrodes. Figure 4 shows the *I–V* characteristics of the DSSC. Table 1 lists the solar cell parameters of the DSSC as a function of the time of spraying. It can be found from Table 1 that when the spraying time is 25 s, the current density is 6.56 mA/cm^2, the open-circuit voltage is 0.788 V, and the filling factor is 0.51 %. On the basis of all the data for calculation, the η value of DSSC is 2.65 %.

4 Conclusion

In contrast to the conventional doctor-blade method, the spray method developed costs less and is able to be applied to large-area working electrode manufacturing. In the mean time, the time for producing the working electrode is decreased, and the efficiency of DSSC is enhanced dramatically by the spray method.

References

1. Xiao Y, Wu J, Yue G, Xie G, Lin J, Huang M (2010) The preparation of titania nanotubes and its application in flexible dye-sensitized solar cells. Electrochim Acta 55:4573–4578
2. Chen HW, Huang KC, Hsu CY, Lin CY, Chen JG, Lee CP, Lin LY, Vittal R, Ho KC (2011) Electrophoretic deposition of TiO$_2$ film on titanium foil for a flexible dye-sensitized solar cell. Electrochim Acta 56:7991–7998
3. Weerasinghe HC, Huang F, Cheng YB (2012) Fabrication of flexible dye sensitized solar cells on plastic substrates. Nano Energy (in press online)
4. Chang H, Chen TL, Huang KD, Chien SH, Hung KC (2010) Fabrication of highly efficient flexible dye-sensitized solar cells. J Alloy Compd 504:S435–S438
5. Chen L, Tan W, Zhang J, Zhou X, Zhang X, Lin Y (2010) Fabrication of high performance Pt counter electrodes on conductive plastic substrate for flexible dye-sensitized solar cells. Electrochim Acta 55:3721–3726
6. Huang LT, Lin MC, Chang ML, Wang RR, Lin HC (2009) Thin film encapsulation of DSSCs on plastic substrate. Thin Solid Film 517:4207–4210
7. Ni M, Leung MKH, Leung DYC, Sumathy K (2006) An analytical study of the porosity effect on dye-sensitized solar cell performance. Sol Energy Mater Sol Cell 90:1331–1344
8. Hara K, Nishikawa T, Kurashige M, Kawauchi H, Kashima T, Sayama K, Aika K, Arakawa H (2005) Influence of electrolyte on the photovoltaic performance of a dye-sensitized TiO$_2$ solar cell based on a Ru(II) terpyridyl complex photosensitizer. Sol Energy Mater 85:21–30
9. Mikroyannidis JA, Suresh P, Roy MS, Sharma GD (2011) New photosensitizer with phenylenebisthiophene central unit and cyanovinylene 4-nitrophenyl terminal units for dye-sensitized solar cells. Electrochim Acta 56:5616–5623
10. Meng L, Ren T, Li C (2010) The control of the diameter of the nanorods prepared by Dc reactive magnetron sputtering and the applications for DSSC. Appl Surf Sci 256:3676–3682
11. Lee Y, Chae J, Kang M (2010) Comparison of the photovoltaic efficiency on DSSC for nanometer sized TiO$_2$ using a conventional sol–gel and solvothermal methods. J Ind Eng Chem 16:609–614
12. Dinh NN, Quyen NM, Chung DN, Zikova M, Truong VV (2011) Highly-efficient electrochromic performance of nanostructured TiO$_2$ films made by doctor blade technique. Sol Energy Mater Sol Cell 95:618–623

An Intelligent Approach for High Material Removal Rate Machining

Jhy-Cherng Tsai and Shen-Jhy Wang

Abstract Machining is one of the most important manufacturing processes. Material removal rate (MRR) is a crucial issue in machining, but it is limited by machining stability lobe which depends on cutting dynamics. This chapter investigates an intelligent approach for increasing MRR. The approach increases the MRR by identifying the stability limit rather than constructing the whole stability lobe. Experiments are conducted using a machining center by machining the standard ISO test model with three typical materials: the aluminum alloy, the brass, and the SKD11 molding alloy. The results show that the average MRR for machining each material is increased to 281, 280, and 141 %, respectively. The merit of this approach is to reach high MRR by identifying chatter frequency without exhaustively finding the detailed stability lobes.

Keywords High removal rate machining • MRR • Stability • Chatter

1 Introduction

Machining, in particular metal cutting, is one of the most important manufacturing technologies and has been widely employed in manufacturing process for material removal. It is a crucial issue how to maintain high machining quality and high productivity while reducing the machining cost in the cutting process.

Among many measurements of cutting process, material removal rate (MRR), which counts the material removed by the process in a specific time period, is the most commonly used index in measuring the efficiency of a machining process. High MRR implies the process can be completed in a short time, thus reducing

J.-C. Tsai (✉) • S.-J. Wang
Department of Mechanical Engineering, National Chung-Hsing University,
Taichung 40227, Taiwan
e-mail: jctsai@mail.nchu.edu.tw

machining cost. As a result, high MRR is the goal for high efficiency machining. However, machining under large MRR often results in vibration and noise, i.e., chattering. Chattering is a response of the machine tool, in the form of vibration, corresponding to the cutting dynamics. Once chatter occurs, it results in poor surface finish, sometimes even damage, on the workpiece and damage on the cutter and machine spindle which further reduces machining quality and processing efficiency. One way to avoid chattering is to reduce the DOC that reduces cutting force. The maximum DOC without chattering is called the critical DOC which is a characteristic of a machine tool and depends on the structure characteristics. The characteristic, however, could become complicated when it is coupled with the cutting process [1].

As the critical DOC is crucial for determining the cutting efficiency, it is important to identify the critical DOC in machining process. In industrial practice, the critical DOC is often tested by experience or by the trial and error method. The test process is not only time-consuming, if not impossible, but also not precise because the stable/unstable cutting zone is not linear and is difficult using interpolation at various speeds. It is an important issue to develop strategies for improving cutting efficiency without losing the machining quality using a systematic method. This chapter aimed to investigate strategies for improving the machining performance, i.e., machining with higher MRR, based on chatter identification but not tested against the whole stability lobe.

2 Stability Analysis of a Machining System

MRR of a typical milling operation is a function proportional to WOC, DOC, as well as to the feed per cutting edge, spindle speed, and the number of cutting edge. It appears that higher MRR can be achieved by increasing these parameters. However, these parameters are limited either by the cutting capacity, the feeding system of machine tool, the strength of cutter, the limit of spindle speed, the horse power of the spindle, or by the cutting limit due to self-excited vibration chattering.

Chatter is a self-excited vibration of the machining system which is caused by the energy into the machining system. When the system is unable to dissipate the input energy, the accumulated energy is then presented in the way of vibration. A direct approach to avoid chattering is to reduce the machining parameters. It, however, reduces the MRR, resulting in lower production capacity at the same time, and is therefore not commonly employed in practice. It is necessary to understand the behavior of chatter in order to increase the MRR while it keeps stable machining.

The self-excited vibration, i.e., chatter, is caused by the coupled effect of the machine tool and the machining process. The vibration grows with the machining time as the exciting source is generated in the cutting process. It is a combined effect of the machine tool structure dynamics and the machining process dynamics.
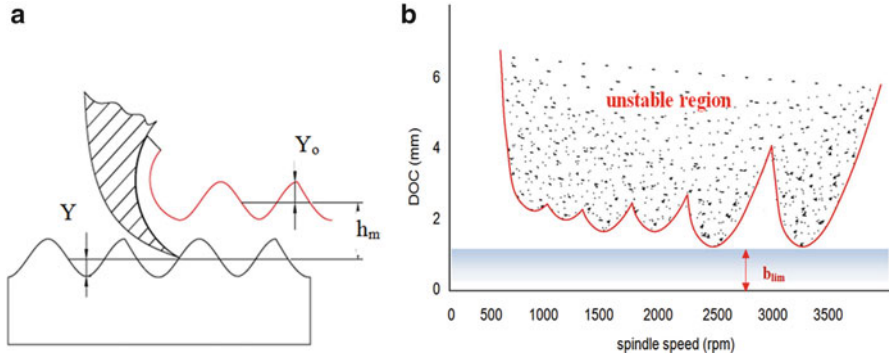
Fig. 1 (a) Regeneration of waviness in machining [2] and (b) stability lobe and conservative limit of stable machining

As the source of chatter is within the machine tool system, the vibration is more intense due to regenerative effect.

The regenerative effect is illustrated as in Fig. 1 where the cutting process generates a surface with waviness on the workpiece as shown in Fig. 1a. When the cutting edge passes through the workpiece, the cutting force is proportional to the thickness of the material removed or the DOC. The cutting force is therefore represented as the following equation:

$$f(t) = K_s(y_0(t) - y(t - T)), \qquad (1)$$

where K_s and $y_0(t) - y(t - T)$ are the specific cutting energy per unit width and the DOC, respectively. The DOC varies with time t, thus leading to the variation of cutting force.

Merritt modeled the machining system, including the machine tool and the cutting process, as a mass-damper-spring system [3]. Based on the model, the dynamic equation of the machining system is equivalent to the following second-order ordinary differential equation, where m, c, k are the mass, the viscous friction coefficient, and the stiffness of the system, and $x(t)$ and $f(t)$ are the displacement of the mass and the external force:

$$m\ddot{x}(t) + c\dot{x}(t) + kx(t) = f(t). \qquad (2)$$

Taking Laplace transformation of the equation, the transfer function $X(s)/F(s)$ can be represented as follows, where $\omega_n = \sqrt{k/m}$ and $\xi = c/2\sqrt{mk}$ are the natural frequency and the damping ratio of the machine tool structure:

$$\frac{X(s)}{F(s)} = \frac{1}{ms^2 + cs + k} = \frac{1}{k} * \frac{\omega_n^2}{s^2 + 2\zeta\omega_n s + \omega_n^2}. \qquad (3)$$

   Merritt [3] then established a block diagram to represent the machining system. The instantaneous DOC and overlapping factor are the two factors affecting the characteristics of the system. The block diagram then leads to the corresponding stability diagram. The stability limit of this system depends on the governing equation (3). As a result, the stability lobe is plotted as shown in Fig. 1b where the region under the lobe is stable cutting and the region above the lobe means unstable cutting. The instantaneous limit of DOC is determined by the cutting speed and the waviness of the machined surface [3]. Once the DOC is higher than the limit, the system becomes unstable and the vibration occurs. The vibration amplitude increases with time because of the feedback gain.

   The maximum DOC without the chattering is the critical DOC at certain speed. It means the machining process is stable when the DOC is lower than the critical DOC. The limit of DOC for stable cutting $b_{\lim}$ based on the theory can be derived as shown in the following equation [4, 5]:

$$b_{\lim} = \frac{-1}{2K_s \ \mathrm{Re}(G_m(j\omega))_{\mathrm{neg}}}, \tag{4}$$

where $b_{\lim}$ is the limit of DOC without chattering and $\mathrm{Re}(G_m(j\omega))_{\mathrm{neg}}$ is the negative real part of the frequency response function of the machining system.

3 High MRR Machining Approach and Verification

Although higher MRR can be achieved by increasing the DOC, the WOC, the feed per cutting edge, the spindle speed, or the number of cutting edge, only process parameters can be adjusted in machining process once the cutter and workpiece are determined. While $b_{\lim}$ in Eq. (4) is a conservative limit of DOC, a strategy of machining without sacrificing MRR but to avoid chattering is to change cutting speed, i.e., to change the cutting frequency, while increasing the DOC. This is because high DOC can be achieved at the stable region. As illustrated in Fig. 2, assume the maximum spindle speed at 3,400 rpm. The DOC at 3,400 rpm is limited by the stability lobe as shown in point B. Although the MRR at B is high, the MRR at D is even higher because the DOC at D is much higher than that at B. It shows that higher MRR can be achieved at lower spindle speed [6].

   The next step is to find the machining parameters at D as illustrated in Fig. 2. The machining process starts at high speed in order to obtain high MRR; the DOC is set at low in the beginning, shown as point A in the figure, to avoid chattering. The DOC is then increased gradually to obtain higher MRR until chatter occurs as cutting limit is reached, shown as point B in the figure. The spindle speed is then changed to the chattering frequency to make the waviness of two machined surfaces in phase. The DOC is set to the one at condition B, shown as point C in the figure,
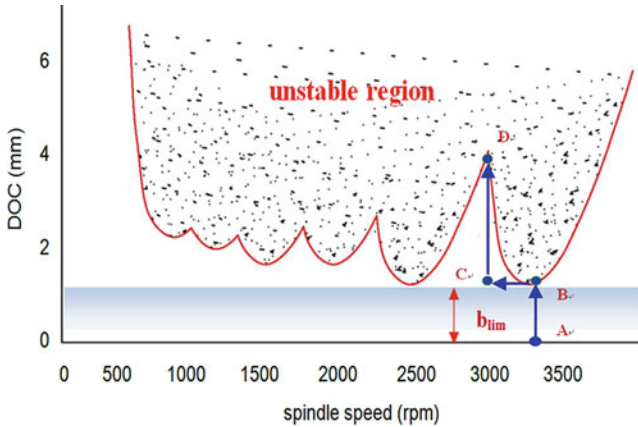
Fig. 2 Stability lobe with multimode and parameter selection strategy for high MRR
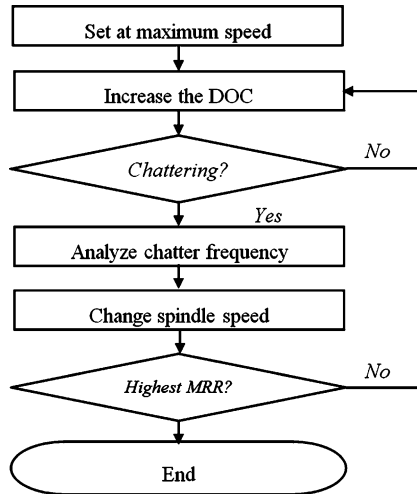
Fig. 3 Procedure for identifying high MRR

and then again increased gradually until the chatter occurs again, shown as D in the figure. The MRR at D is higher than that at B because of higher DOC.

Based on this procedure, an approach to reach higher MRR is shown in Fig. 3. To reach high MRR, it starts at maximum spindle speed, say 3,400 rpm at this example. The DOC is then increased gradually until chatter occurs. The chatter frequency is measured and analyzed. The spindle speed is then changed to the chatter frequency in order to make both cutting frequency and chatter frequency in phase. The machining process is again tested against the DOC using the new spindle speed until the highest MRR is reached.

Table 1 Comparison of machining time

Material	Process	Rough machining	Finish machining	Total machining time	MRR improvement (%)
Aluminum alloy	Original	119 min 46 s	24 min 54 s	144 min 40 s	281
	Improved	30 min 56 s	20 min 33 s	51 min 29 s	
Brass	Original	138 min 56 s	31 min 30 s	170 min 26 s	280
	Improved	37 min 1 s	23 min 42 s	60 min 43 s	
SKD11	Original	241 min 33 s	44 min 2 s	285 min 35 s	141
	Improved	185 min 40 s	18 min 5 s	202 min 45 s	

Experiments are designed to verify this machining approach for achieving high MRR. The materials used in the experiments include aluminum alloy, brass, and SKD11 molding steel. They are selected in order to test the machining strategy for different types of materials, from soft and sticky to hard material. The blocks are machined according to the ISO machining test.

The machine tool used in this test is the LH1608V vertical-axis machine by Awea Machinery Industry Co. Ltd. The recommended maximum spindle speed and feed are 4,000 rpm and 0.3 mm/tooth, respectively. As an example of aluminum alloy as shown in the first row in Table 1, the original machining time, with a set of machining parameters determined by a CAD/CAM system and adjusted by experience, is 144 min and 40 s that includes 119 min 46 s for rough machining and 24 min 54 s for finish machining. Chatter frequency is picked by a microphone.

A preexperiment is first conducted to determine the best DOC for the machining system. Taking aluminum alloy as an example, the DOC is increased gradually until chatter occurs at DOC 7 mm. The measured chattering frequency is converted to the equivalent spindle speed at 3,744 rpm. The spindle speed is adjusted to that speed, and the DOC is again gradually increased to test the limit DOC. Chatter did not occur until the DOC reaches the limit of cutting edge at 9 mm.

The machining parameters of the ISO test are set based on these parameters from the preexperiments. The average MRR is increased to 281 %. The experimental data for machining brass and SKD11 molding steel are conducted in the same way. The results are listed in Table 1 with the corresponding improvement of MRR. This result further shows the merit of this machining strategy.

4   Conclusions

As machining is one of the most important manufacturing technologies and has been widely employed in manufacturing process for material removal, it is an issue to maintain high productivity while increasing the machining performance. Machining performance of a machine tool, however, is often limited by cutting stability, a characteristics combining structure dynamics and process dynamics. This chapter presents an approach to achieve high MRR machining, measured by

the machining time, of a machine tool. The approach tests the machining limits of the machine tool to find the maximum DOC at high spindle speed. Chatter occurs when the limit of DOC is reached. The chattering frequency is then used for adjusting the spindle speed at a higher DOC, which results in higher MRR at lower spindle speed. Experiments are designed and conducted to machine stocks of aluminum alloy, brass, and SKD11 molding steel according to the ISO machining test. The average MRR for these three tests are increased to 281, 280, and 141 %. The merit of this approach is to reach high MRR by identifying chatter frequency without exhaustively finding the detailed stability lobes.

References

1. Altintas Y, Weck M (2004) Chatter stability of metal cutting and grinding. CIRP Ann Manuf Technol 53(2):619–642
2. Smith S, Tlusty J (1990) Update on high speed milling dynamics. ASME J Eng Ind 112:142–149
3. Merritt HE (1965) Theory of self-excited machine-tool chatter. J Eng Ind 87:447–454
4. Tarng YS et al (2000) Chatter suppression in turning operations with a tuned vibration absorber. J Mater Process Technol 105(1):55–60
5. Saleh K, Sims ND (2012) The self-excitation damping ratio in variable speed milling. In: Proceedings of the world congress on engineering, vol III. London, 2012
6. Tsai J-C, Wang S-J, Chen F-J (2012) Machining performance improvement based on chatter identification. In: Proceedings of the 9th international conference on machine tools, automation and robotics technology, Prague, 2012

The Position and Correction System
of Laser PSD

**Hsueh-Cheng Lin, Mei-Ling Chen, June-Rong Chen, His-Chou Ho,
Keng-Hao Hsu, Din-Goa Huang, Chien-Kuang Kuan, Wei-Yang Lai,
Chang-Sheng Lin, Chia-Jui Lin, Hung-Ming Luo, Shen-Yaw Perng,
Pei-Lun Sung, Tse-Chuan Tseng, Huai-San Wang, and Meng-Hsiu Wu**

Abstract A laser PSD positioning system is included in the TPS girder auto-alignment system that is designed for aligning and positioning the straight-segment girders of TPS storage ring. The laser PSD positioning system consists of lasers, PSD, and lenses. This chapter describes the process of assembly, installation, adjustment, and the measurement result of the laser PSD system. Installing the laser PSD system consists of several steps. The first step is to assemble lenses and PSD in mechanism, lens PSD module. The tilt angles of lens on the lens PSD module are fine tuned and the PSD position value is adjusted to zero. The positioning fixture is designed and contains six touch sensors (absolute length gauges) for detecting the position of the lens PSD module. The lens PSD module is installed and adjusted on a girder absolute position precisely by the positioning fixture. So each module is adjusted to with equal distance to the vertical and horizontal reference plane of girder. The laser is adjusted according to the position of the PSD. Finally, use the absolute length gauges to correct the PSD. According to the aforementioned process of assembly and all parameters of PSD module, the girder can be aligned and positioned within 20 um precision scale.

Keywords Positioning lens module fixture • PSD • TPS • Absolute length gauges

1 Introduction

This chapter describes the design and assembly of the state of the PSD system applied to the Taiwan Photon Source (TPS) [1]. The storage ring has a circumference of 518 m and contains 24 sections of straight sections (6 long and 18 short)

H.-C. Lin (✉) • M.-L. Chen • J.-R. Chen • H.-C. Ho • K.-H. Hsu • D.-G. Huang • C.-K. Kuan
W.-Y. Lai • C.-S. Lin • C.-J. Lin • H.-M. Luo • S.-Y. Perng • P.-L. Sung • T.-C. Tseng
H.-S. Wang • M.-H. Wu
Precision Machinery Group, National Synchrotron Radiation Research Center,
Hsinchu, Taiwan, R.O.C.
e-mail: lin.andy@nsrcc.org.tw

Fig. 1 Main portions
of optical components

and 24 bending sections (one section consists of 3 girders). This laser positioning system will be installed on the girders located on both sides of each straight section (Fig. 1).

In addition to the described PSD system previously, the fourth set of system called PSD4; after all the experience of reflection of the laser light, that laser signal is received via the software conversion and displayed on a computer screen. Then, it distinguishes the position of the laser light and adjusts to the precise location.

In the assembly and adjustment process, the details of the procedures are very complicated and many errors and unexpected problems occur, which are eventually overcome to develop the SOP process for reference.

This positioning system can locate the girder at the micrometer scale [2], and this chapter presents the details of the design and installation of the laser positioning system.

2   System Design and Assembly

The laser positioning system is constructed by several main portions, including laser, PSD, beam splitters, outer covering, and isolation tubes (Fig. 2). Both laser and PSD are held on girder by rigid holder. The laser, with Gaussian distribution during working propagation distance, plays a role as a reference line of the girders of the straight section. There are two working distances for the long-straight section of TPS, 13 and 19 m long, respectively.

Optical components contain optical lens (beam splitter). The reflection rates of 23, 33, 50 %, each with an antireflection lens (glass window), are combined into three groups. This experiment, in order to pass the laser light, uses a different refractivity of the lens (beam splitter and glass window) mounted on every lens holder, and to adjust the lens to complete installation in girder as TPS straight-section calibration basis. Complete the initial installation and adjust the lens module installed on the girder side. Then adjust the lens module at girders on both sides of the offset, and finally, the laser light through the lens by the lens module gets reflected. At last the laser light is received and four 4-Quadrant Detectors are seen on the computer screen by PSD4 as shown in Fig. 2.
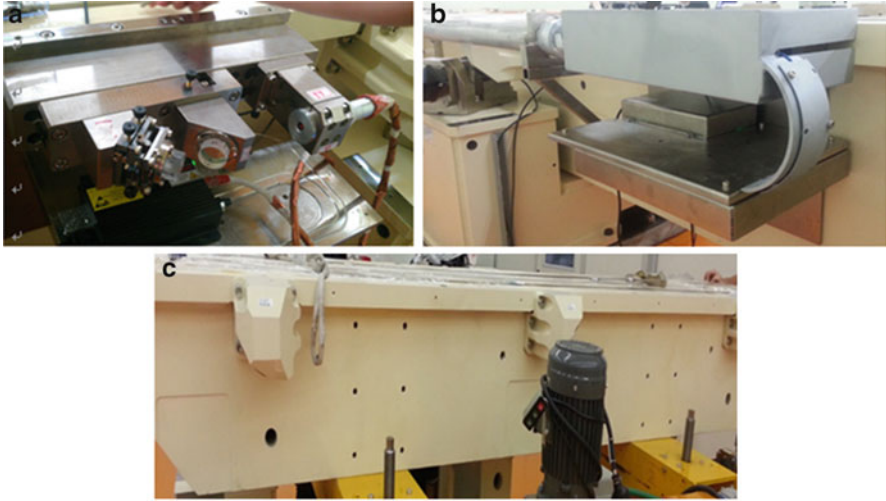
Fig. 2 Main portions of laser positioning system: (**a**) PSD and laser, (**b**) outer covering and isolation tube, and (**c**) girder
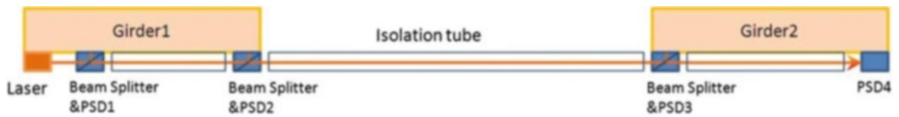
Fig. 3 Architecture of laser positioning system

A laser isolation tube without interference of the external environment, the system is covered by isolation tube to eliminate air disturbance and temperature variation. The isolation tube is composed of thermal isolation material. The beam slitter and PSD4 receive and reflect the final laser through software conversion and displayed on a computer.

Figure 3 shows a schematic diagram of a TPS system wherein a straight section, the content contains the location and function of the various components of the structure, in simple terms, the present system is to be issued by the laser light source, via the reflectance 23 % beam slitter and PSD1 received and refracted via beam slitter and PSD2 receiving and refraction again.

2.1 Preparation of Parts

The optical lens of the PSD system was bought from a company in the United States, such as Fig. 3, the optical lens is mounted on a small holder, the side coated with a strong UV glue, and then irradiated with UV light. The UV glue after solidification waits for a few minutes, and then the lens group is installed in the lens holder.

Fig. 4 The adjustment jig of PSD lens module and PSD displayed position on screen
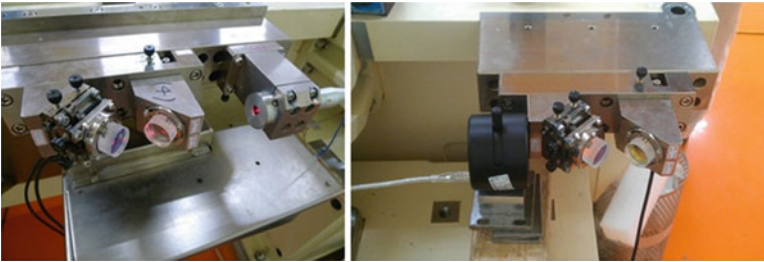
Fig. 5 Schematic diagram of the measurement for laser beam profile

The PSD is installed in the bottom of the lens holder, and then the lens module is installed in the lens module fixture. Adjust the fine-pitch screws so that the lens can effectively pass the laser via the beam splitter to glass window, and adjustment data are received and displayed on the screen by the 4-Quadrant Detector of PSD (Fig. 4).

2.2 Installation and Adjustment

The lens module system is installed on the girder sides of the fixed position and arranged with the installation as shown in Fig. 3, and in accordance with the index of refraction it is not the same sequence to the lens module mounted in the appropriate position.

The above are installed in the laser PSD1, such as Fig. 1, and the position of the laser light of the PSD in each group is adjusted, followed by the inspection of the beam profile, and the cross-sectional view of the light measuring laser light, such as Fig. 5.
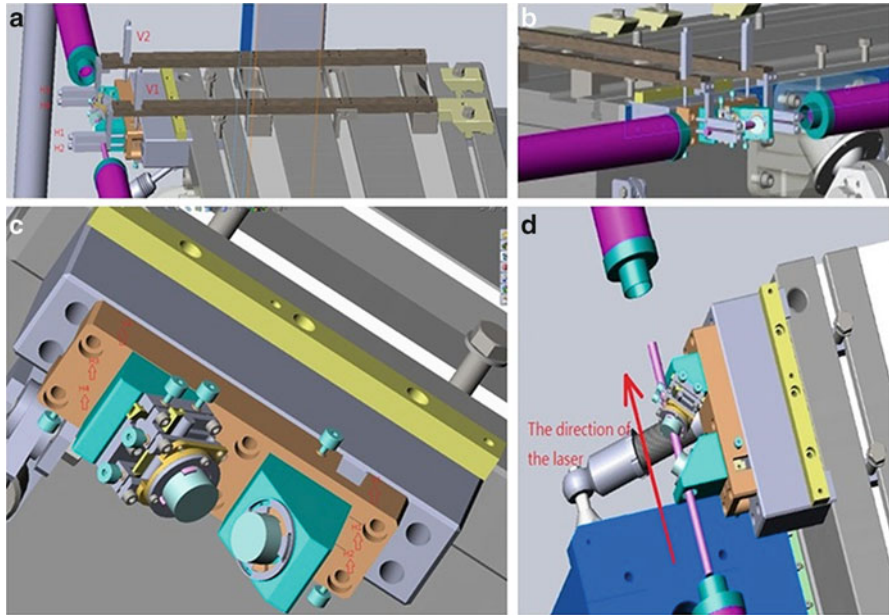
Fig. 6 Schematic diagram of the positioning fixture with laser receiver through the lens holder and refraction

2.3 Assembly and Application

The positioning fixture is designed and contains six touch sensors for detecting the position of the lens PSD module. The front end of the positioning fixture is installed with six touch sensors, including two in the vertical direction and four in the horizontal direction measurement. The positioning fixture is mounted on the relative position to the girder. This fixture can verify the distance of the PSD in two-dimensional space. The adjustment result of each PSD will be recorded via software data conversion. Figure 6a shows the diagram of the positioning fixture for measuring the position of the PSD system.

The lens PSD module is adjusted in accordance with the measured data of the touch sensors. By adjusting the fine-pitch screws and adding shims to correct the position of lens module to the ideal position the accuracy of the touch sensor is 1.2 um. Then assemble the touch sensors and fixtures of position jig, and after repeatedly operating jig, the average error is lower than 5 um, such as Fig. 6.

Figure 6a shows an illustration of a lens module mounted on the girder and using the positioning fixture to position. Six touch sensors installed in the front end of the fixture are used to measure and adjust the position of the lens module. Figure 6c shows an illustration of the measurement points on the lens module of touch sensors. After positioning and adjusting the lens module, the laser is mounted and adjusted by
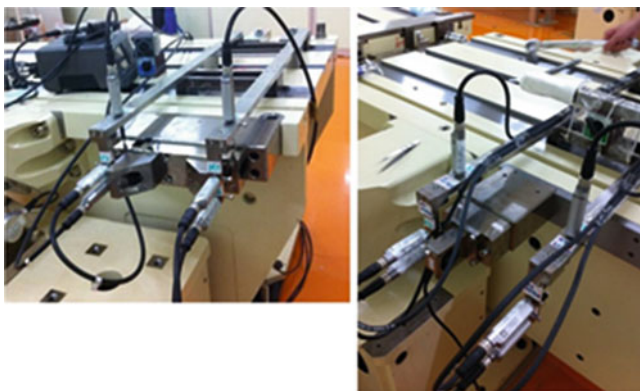
Fig. 7 Measuring the lens module by the positioning fixture

Fig. 8 The repeatability of the experiment data table
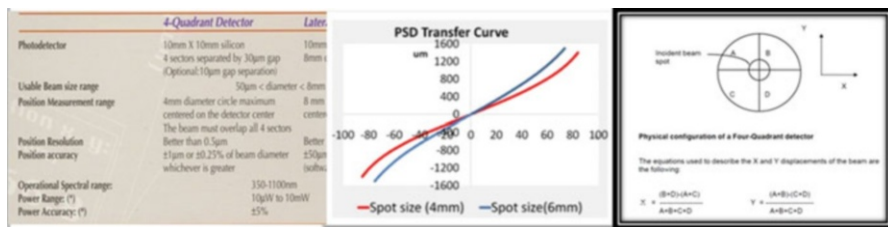
Fig. 9 Resolution, the transfer curve, and 4-Quadrant Detector of PSD

relating to the position of the lens module. The light path of the laser is parallel and collinear through the lens PSD module, such as Fig. 6b, d (Figs. 7 and 8).

Finally, adjust the PSD system to the cover housing and install an isolation tube to the stability of the light source, and finally test the laser stability.

PSD is a 4-Quadrant Detector with 0.5 um resolution and 1 um position accuracy. The X &Y displacement of PSD is calculated by 4 detectors. The transfer curve of PSD displacement is not linear and relative to beam power distribution. An absolute touch sensor is set up to calibrate the PSD transfer function.

The results of the entire test, from the PSD1 light source via PSD2 and PSD3 of light refraction, and finally received by PSD4, the overall margin of error is about 20 um (Fig. 9).

3   Conclusion

This system mainly focuses toward the development of high stability and high precision direction. The relative position accuracy of a laser PSD system can reach 2 um every 4 h. In order to position the straight-section girder accurately, the lens module is adjusted in advance and positioned on girder precisely. The absolute position accuracy of the laser PSD system can reach 20 um scale by comparison with laser tracer. The National Synchrotron Radiation Research Center will put in more efforts toward the development of high positioning, higher precision direction technology, and expects to effectively enhance the performance of the TPS.

References

1. Lai WY, Tseng TC, Wang HS, Chen JR (2009) Design and prototype tests of auto-alignment of a whole-ring girder. In: Particle accelerator conference
2. Wang HS, Ho HC, Tseng TC, Lin CJ, Hsu KH, Wang DJ, Chen JR et al (2008) Design and test of a PSD system for TPS girder. In: International conference on mechanical engineering design of synchrotron radiation equipment and instrumentation
3. Hsu KH, Chen ML (2010) Design improvements and tests of a laser positioning system for TPS girder system. MEDSI

Study of Cutting Parameter Effect on Spindle Vibration for Tool Breakage Monitoring in Drilling

Yu-Wei Hsu and Ming-Chyuan Lu

Abstract The cutting parameter effect including tool diameter and feed rate on the spindle vibration signal for tool breakage monitoring was studied. The vibration signal obtained from the accelerometer installed on a fixture connected to the spindle housing was considered as the input signal for the monitoring system. The monitoring system was integrated by a signal transformation module, feature selection module for creating the features related to the breakage event, and a classifier module for classifying the tool breakage event based on the selected features. The linear discriminate function was adopted as the classifier in this chapter. To collect the vibration signals for analyzing the signals and system performance affected by cutting parameter, an experiment was implemented on a tapping machine along with 2 mm/3 mm diameter drill and aluminum alloy workpiece. In feature analysis, various wavelet coefficients for the collected signals were analyzed for system performance with various tool diameters and feed rates. The results show that the system developed by combined signals obtained from various cutting parameters is not reliable to detect tool breakage when implementing with any cutting parameters included in the model development. However, 100 % classification rate can be obtained for all case based on the model developed by type 3 signals and with properly choosing wavelet coefficient as features.

Keywords Tool breakage monitoring • Vibration • Drilling

1 Introduction

Tool condition monitoring system draws much more attention in the past decade due to the high demand on the improvement of cutting efficiency to meet the energy-saving requirement and high competition in industry. A number of researches

Y.-W. Hsu (✉) • M.-C. Lu
Department of Mechanical Engineering, National Chung Hsing University,
Taichung 402, Taiwan

focusing on the cutting tool condition monitoring have been reported for the past 40 years [1, 2]. The indirect sensing technologies such as power, cutting force, vibration, and acoustic emission signals are the candidates for detecting tool condition. By considering the development of smart spindle and low-cost development of MEMS accelerometer, the vibration sensor system on the spindle housing provides an advantage of easy and cost-effective installation. Some works have been reported for to study the vibration signal for tool condition monitoring, but most of them focus on the tool vibration in turning or the workpiece vibration in milling [3–5].

By investigating the system development for industry, only some of the systems were developed for industry applications with simple processes at fixed cutting condition such as drilling a hole on an engine head. To extend the tool breakage system to applications with varied cutting parameters and tool size, the vibration signals obtained from the spindle housing are investigated in this study by changing the tool size and cutting condition, followed by the discussion of feature extraction for the system development.

2 System Development

For a sensor-based tool condition monitoring system, the time-domain signals usually hold lower sensitivity to the tool breakage change and are frequently transformed into the feature space for the following classifier design. In this study, the wavelet transformation of original time series signals was conducted to provide the features for the tool breakage monitoring. After that, the wavelet coefficients sensitive to the tool breakage were selected and considered as the valuable feature for identifying the tool condition.

A tool breakage monitoring system is shown in Fig. 1. The models in the system include the signal transformation, the feature selection, and the classifier design. The discrete wavelet transformation was adopted in this study for the signal transformation. For the classifier design, Fisher linear discriminant function was studied for monitoring the tool breakage based on the spindle vibration signals.

3 Experimental Setup

To analyze the spindle vibration signal and establish the classifier model for the tool breakage monitoring system, an experiment was implemented on a tapping machine. The system setup is shown in Fig. 2. A Kistler accelerometer (5141A2) with bandwidth from 5 Hz to 8 kHz was installed on the fixture connected to the spindle housing in the z direction. The vibration signal was collected by NI PCI-6251 data acquisition card with sampling rate of 60 kHz. The cutting conditions and workpiece for various experiments are shown in Table 1. In tests, more than eight tests for each type of cutting conditions were conducted for analyzing the signal and system performance.
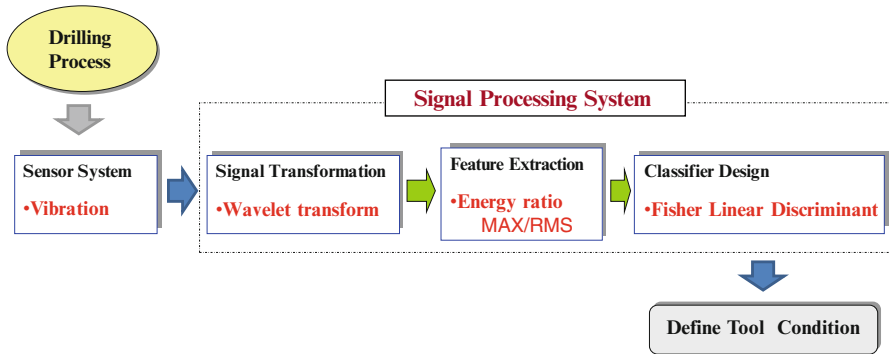
Fig. 1 Schematic of tool breakage monitoring system
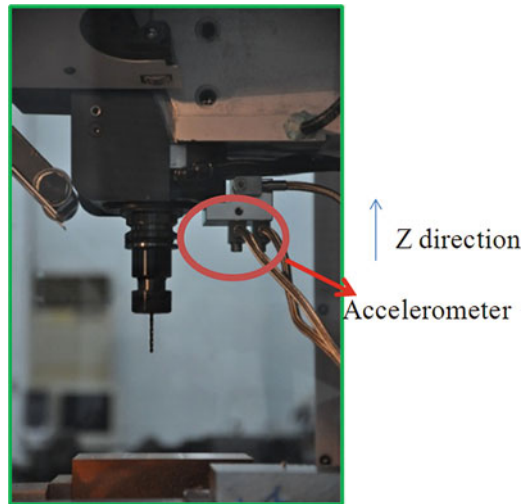
Fig. 2 Schematics of experimental setup for tool-wear monitoring in the micro milling

Table 1 Work material and cutting parameters for three types of drilling processes

	Tool diameter (mm)	Spindle speed (rpm)	Feed rate (mm/min)	Hole depth (mm)	Material
Type 1	2	3,600	320	12	Al 6061
Type 2	3	3,600	280	12	Al 6061
Type 3	3	3,600	320	12	Al 6061

4   Results and Discussions

4.1   Signal Analysis

The tool breakage and the corresponding vibration signals for the micro drilling were shown from Figs. 3 and 4, respectively. From the time-domain signals in Fig. 4, the breakage signals can be identified for all case with various cutting conditions. However, the tool breakage signal varies from each test, and the noise level might be at the same level as tool breakage signal. These situations will make the monitoring system failed if only setting up a threshold for detecting the tool breakage condition. To obtain the features closely related to the breakage event and remove the effect of the noise, signals collected from the cutting were transformed to time-frequency domain by wavelet transform.

After transforming the time-domain signals by wavelet transformation, the wavelet coefficient is shown in Fig. 5 for test with type 3 cutting conditions. The energy ratio of breakage/normal tool was observed to increase for D1 and D2 coefficients.

4.2   Tool Breakage Classification

As for the evaluation of the effect by the selected two features on the tool breakage monitoring for each cutting condition, the data obtained from the half of tested data were selected as the training data for developing Fisher linear discriminant classifier model and the other data for verifying the accuracy of the model.

The classification rate for each cutting condition with five kinds of selected features is illustrated in Table 2. The results show that 100 % classification rate can be obtained for properly selecting features. However, the optimum selected feature combination is different from other cutting conditions. By considering the model developed based on the signals from all three cutting conditions, the 100 % classification rate cannot be obtained as expected. The classification rate for each feature selection varied from 91 to 97.5 % as shown in Table 3.
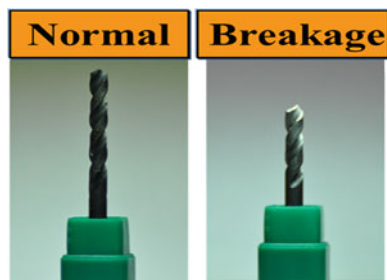
Fig. 3 Tool breakage conditions
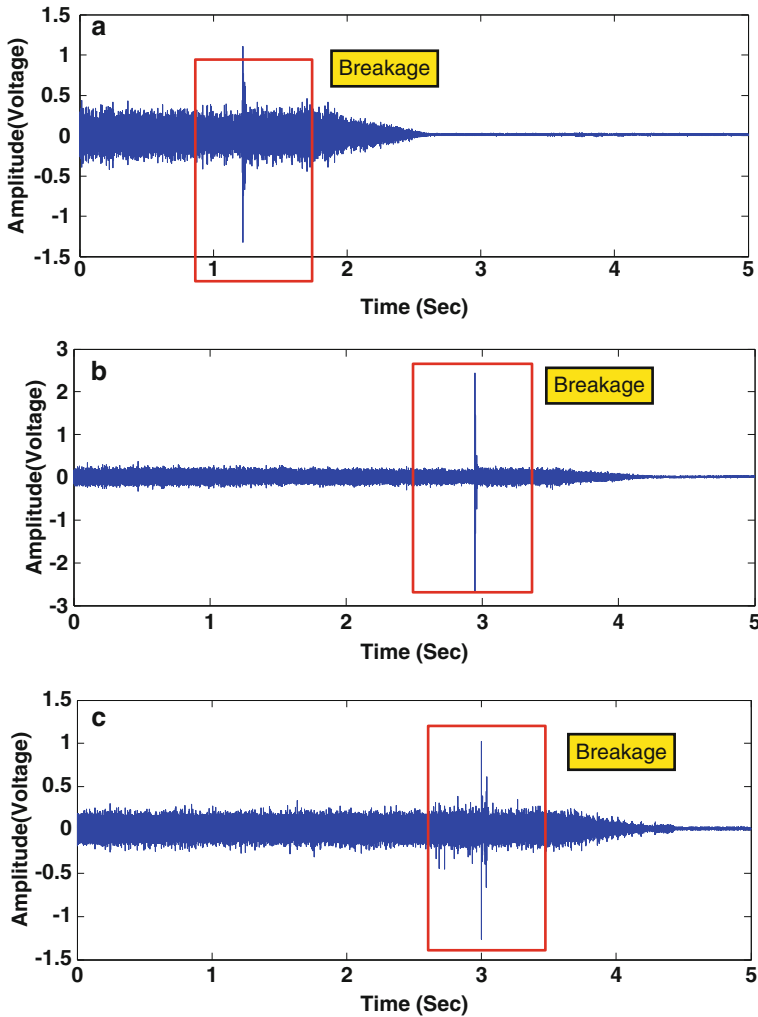
Fig. 4 Spindle vibration signals for tool breakage (**a**) type 1, (**b**) type 2, and (**c**) type 3

To further investigate the cutting parameter effect on monitoring performance, the signals with the cutting conditions that vary from those for developing the model were tested. The classification rates for all three models are shown in Table 4. From Table 2, the combination of D1 and D2 features seems to show a best chance to make the system work reliable for all cases with model developed by signals with single cutting conditions. However, low classification rates were obtained by all three types of models. This result might be caused by that classification function created from signals for each cutting condition that vary to each other, and the misclassification will occur when the signals with cutting condition other than those for model development were tested. Based on the results shown in Table 4, two models
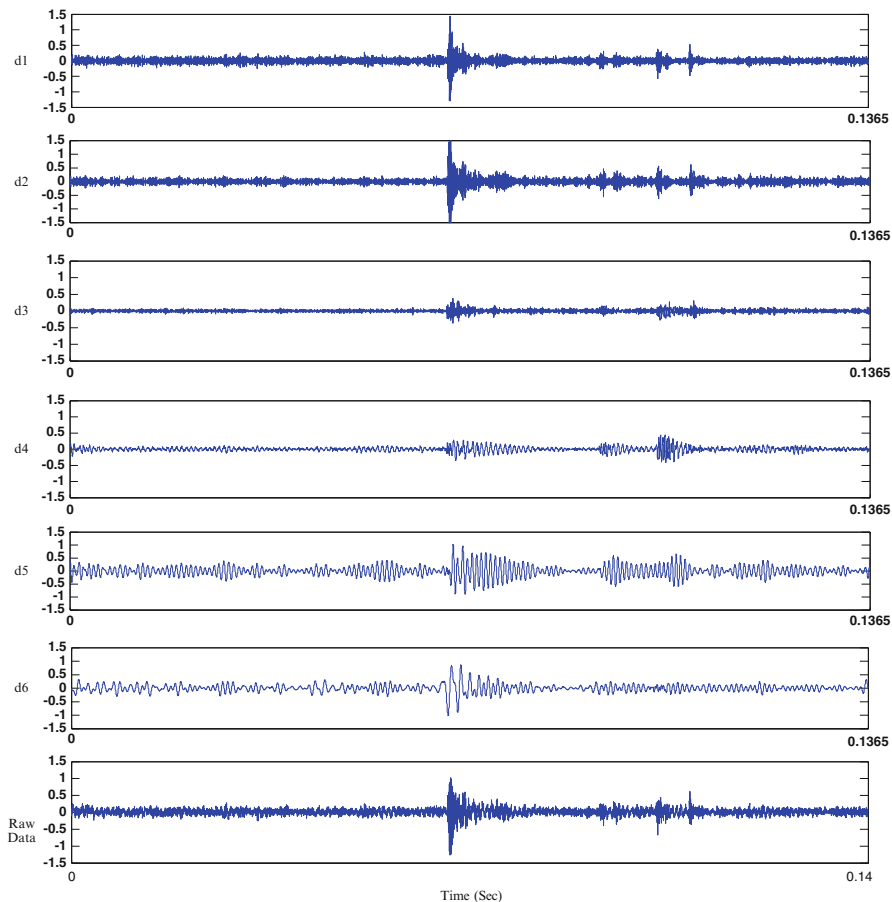
Fig. 5 Discrete wavelet transform for spindle vibration signals with tool breakage (type 3)

Table 2 Classification rate for various cutting parameter model and tests

Selected feature	D1D2	D1D5	D2D5	D1D6	D2D6
Type 1	100	100	100	90	**90**
Type 2	**100**	**90**	**90**	**100**	**90**
Type 3	100	100	90	100	**100**

Unit: (%)

Table 3 Classification rate for mixed-parameter model and tests

Selected feature	D1D2	D1D5	D2D5	D1D6	D2D6
Classification rate	**97.5**	**91**	**91**	**92**	**94.5**

Unit: (%)

Table 4 Classification rate for type 3 parameters model and tests

Signals for model development	Signals for test	Selected feature		
		D1D2	D1D5	D2D6
Type 1	Type 2	69	94	100
	Type 3	68	100	96
Type 2	Type 1	60	**100**	83.5
	Type 3	96	**100**	91
Type 3	Type 1	77	65.5	**100**
	Type 2	100	94	**100**

Unit: (%)

developed by D1/D5 features for type 2 cutting conditions and by D2/D6 features for type 3 cutting conditions can provide a much more reliable tool breakage monitoring condition. By comparing this result with those shown in Table 2, the model developed by D2/D6 features based on signal for type 3 cutting conditions can provide 100 % classification rate for all cutting conditions in this study.

By further investigating the tool size effect on the monitoring system, the low classification rate can be found to exist when testing type 1 signals with model developed by type 2 or type 3 signals. At the same time, low classification rate was also obtained for testing type 2 and type 3 signals with D1/D2 features based on model developed by type 1 signals. Moreover, no 100 % classification rate can be obtained by adopting model developed by type 1 signals. These observations might provide a conclusion that the change of tool size will affect the signals more significantly than feed rate for monitoring tool breakage condition in this study.

5 Conclusion

The cutting parameter effect including tool diameter and feed rate on the spindle vibration signal for tool breakage monitoring was studied in this chapter. The spindle vibration signals were analyzed first followed by the investigation of the effect on system performance by selected features. The results show that the features obtained by wavelet transform provide the higher signal/noise ratio than time-domain signal. For the system performance, the system developed by combined signals obtained from various cutting parameters is not reliable to detect tool breakage when implementing with any cutting parameters included in the model development. However, 100 % classification rate can be obtained for all case based on the model developed by type 3 signals and with properly choosing wavelet coefficient as features. By comparing tool size and feed rate effect on system performance, the tool size change demonstrates more significant effect than feed rate on the tool breakage monitoring.

References

1. Dornfeld D, Min S, Takeuchi Y (2006) Recent advances in mechanical micromachining. Ann CIRP 55(2):745–768
2. Dimla E, Dimla DE Snr (2000) Sensor signals for tool-wear monitoring in metal cutting operations – a review of methods. Int J Mach Tool Manuf 40:1073–1098
3. Issam AM (2003) Drilling wear detection and classification using vibration signals and artificial neural network. Int J Mach Tool Manuf 43:707–720
4. EL-Wardany TI, Gao D, Elbestawi MA (1996) Tool condition monitoring in drilling using vibration signature analysis. Int J Mach Tool Manuf 36(6):687–711
5. Al-Habaibeh A, Gindy N (2000) A new approach for systematic design of condition monitoring systems for milling processes. J Mater Process Technol 107:243–251

An Investigation into Electrode Wear in Layer-Cut EDM Process

Pei-Lun Song, Yo-Ming Chang, and Yao-Yang Tsai

Abstract This chapter discusses the influence of the peak current, pulse duration, and machining depth of each path on the electrode wear and carbide accumulation in layer-cut electrical discharge machining (EDM) process. During the layer-cut EDM process, the simple electrode runs through the planned path from the top layer to lower layer gradually to obtain any expected cavity, which is similar to the end milling process. It has the merits of end milling such as high flexibility machining by using tool and path but also has the strength of EDM such as easy to machining high hardness material. However, the electrode wear is the key problem that influences the precision for the development of layer-cut EDM process. The result shows that the steady linear electrode wear could be obtained using the pulse duration of 150 μs. The suitable parameters would be the basis of electrode compensation in the layer-cut EDM process.

1 Introduction

In the electrical discharge machining (EDM) process, it was made insulated between the electrode and workpiece by fill with nonconductive dielectric fluid or gas. There was no electric current flow or discharge spark that happened at the initial status. Then, the electrode approached the workpiece gradually. When the gap was small enough to make the electric field intensity higher than the insulation intensity of dielectric fluid, the momentary discharge spark happened at the shortest distance between electrode and workpiece. At this moment, the electric energy became the

P.-L. Song • Y.-M. Chang • Y.-Y. Tsai (✉)

Department of Mechanical Engineering, National Taiwan University, Taipei 10617, Taiwan

e-mail: yytsai@ntu.edu.tw

heat energy. The exploded discharge spark could make the temperature reach 6,000–10,000 °C. Thus, a tiny part of surface of electrode and workpiece melted or vaporized. Besides, the melted material would be removed by the dielectric fluid. Finally, the cavities would be made at the surface. This material removal process happened 10,000–100,000 times per second for the purpose of machining. EDM has been developed to machining extreme hard materials by electro-thermo removal process. The EDM process uses electrical discharge spark companying with an extremely high temperature to carry out material removal. Material of any hardness can be cut as long as it is electric conductive. It can diminish mechanical stresses, distortions, and vibration problems. This will be useful for the mold and die manufacturing industries.

Electrode and workpiece were connected to the positive and negative of a DC power, respectively.

If EDM can be performed as the end milling process, then any complex cavity and shape can be obtained. However, the high electrode wear ratio (EWR) and low material removal rate are the key problems of the EDM process especially for machining material with high melting point. There is an urgent need to develop the working technique for some special materials. It would make the precision inaccurate and decrease the machining efficiency when the electrode wore. Many electrodes are generally used for rough and finish machining in order to avoid inaccuracy caused by the electrode wear. It must change a new electrode to machining when the old one wore too much. Since many electrodes must be made, the wasted time and materials are considerable. Therefore, a layer-cut EDM process has been developed. The principle of layer-cut EDM is machining along a planned path by one electrode with a simple shape. Using a planned path to machine complex workpiece decreases the cost of making precise electrodes [1]. However, in the EDM filed, the electrode wear is still a big problem even though using a simple shape electrode to machine. Therefore, the solution of electrode wear is studied extensively [2, 3]. The parameters of the EDM process are very complicated. Generally, the voltage, current, pulse duration, and gap situation influence the results of machined workpiece like machining time, electrode wear, material removal rate, and surface roughness [4, 5]. Change of any one of these parameters would make the result different. Therefore, this chapter studied the machining situation and result of machined workpiece by planned experiments with changing parameters.

2 Experimental

EDM process was performed on a commercial EDM machine (CR-6 Creator Precision Co. Ltd.), and its controller has the built-in CNC code for simulating the milling situation of the planned path. XY stage was set up on the machine for cutting path. Layer-cut EDM processes were performed on a stainless steel SUS304 with size of $30 \times 10 \times 5$ mm to investigate the electrode wear.

Table 1 Experimental conditions

Working factor	Working condition
Electrode:	Copper
Workpiece:	Stainless steel (SUS304)
Dielectric fluid:	Kerosene
Polarity:	Electrode($-$); workpiece($+$)
Power voltage [V]:	130
Peak current [A]:	1, 5, 10
Pulse duration [μs]:	0.5, 1, 1.5
Machining depth [mm]:	50, 150, 250
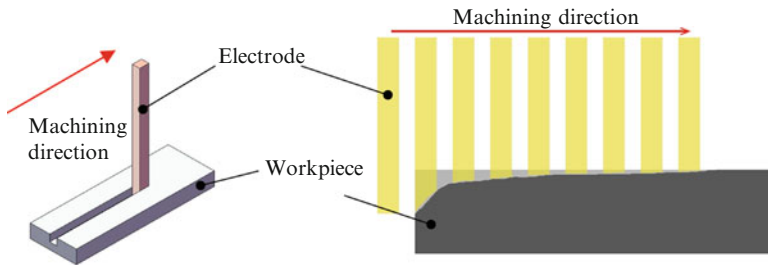
Fig. 1 Schematic diagram of machining process

Copper rods with side width of 1.5 mm were chosen as the electrodes, and commercial kerosene was used as dielectric fluid. The current, pulse duration, and machining depth are the various parameters in the experiment, as shown in Table 1. In order to reduce the dynamical effect from flushing condition, flushing motion was not adopted.

The wear characteristic in the EDM process is usually described by EWR. The electrode wear ratio is defined as the ratio between the amount of electrode removal and the amount of workpiece removal, that is, the weight of electrode wear divided by the weight of the removed material. Small wear ratio means workpieces removal is high with low electrode wear. Before and after the experiments, the workpieces and electrodes were all cleaned in an ultrasonic cleaner (LEO801 PANDA Co.) and used precise scale weight (AL204 Mettler Toledo, 0.01 mg accuracy) to measure their weights. The cutting path had the length of 15 mm from the side of workpiece. The machining depth for each path was pointed as listed in Table 1 from the start point but real cutting depth would become small as a result of perpendicular electrode wear. Figure 1 diagrammatically shows the electrode bottom would be rising because of electrode wear along the machining direction. For some case, the cutting path with the length of 15 mm perhaps could not be completed if extreme electrode wear makes the total consume of electrode wear over the pointed machining depth before the end of path. The perpendicular length wear of electrode was measured.

3 Results and Discussion

The electrode wear of different pulse duration and peak current for changing machining depth are shown in Fig. 2. More electrode wear was found when using low peak current because the low discharge energy could not remove the material effectively for smaller pulse duration. The discharge energy is decided by peak current and pulse duration. Changing the pulse duration would change the discharge energy and energy intensity of each pulse [6, 7]. EWR is smaller during short pulse duration. The reason is that shorter pulse duration can give more effective discharge energy on workpiece. However, EWR increases with increasing peak current until 5A and then decreases except for the machining depth of 1.5 mm when the pulse duration is 250 μs as shown in Fig. 2c. It is also found that there was obviously carbide accumulation for the pulse duration of 250 μs. Thus, the material removal rate decreases and the planned path could not complete because of the extreme electrode wear. When the peak current was 5A, the discharge energy may be not enough to remove the material which was under the carbide accumulation. Therefore, EWR of 5A was more than that of 10A and 1A. For the peak current of 10A, the discharge energy should be high enough to remove material effectively, so its EWR is the minimum.

Besides, Fig. 3 shows the relationship between wear ration and machining depth for different peak current and pulse durations. It is easy to find that EWR is independent or linear-dependent on the machining depth. And it also can be found that EWR increases by certain scale with varying peak current when the
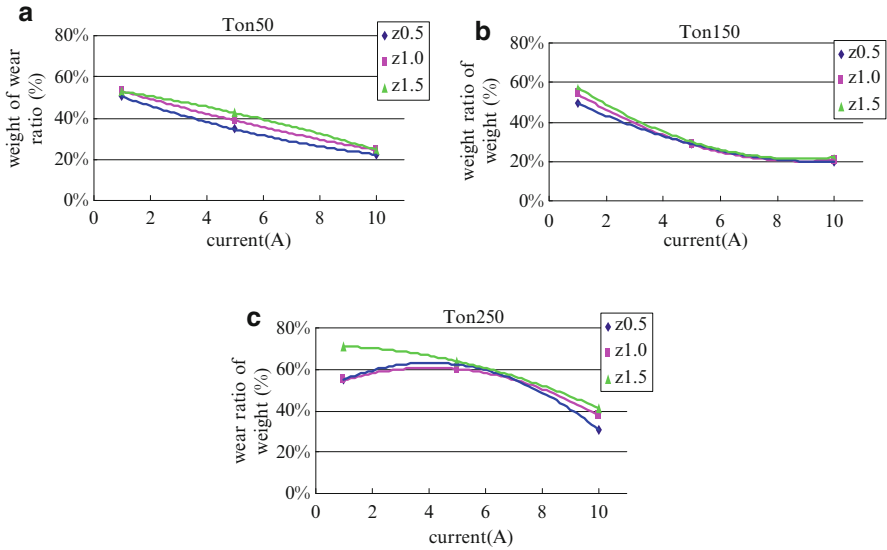
Fig. 2 Relationship between peak current and EWR for different machining depths and pulse durations: (**a**) pulse duration 50 μs, (**b**) pulse duration 150 μs, and (**c**) pulse duration 250 μs
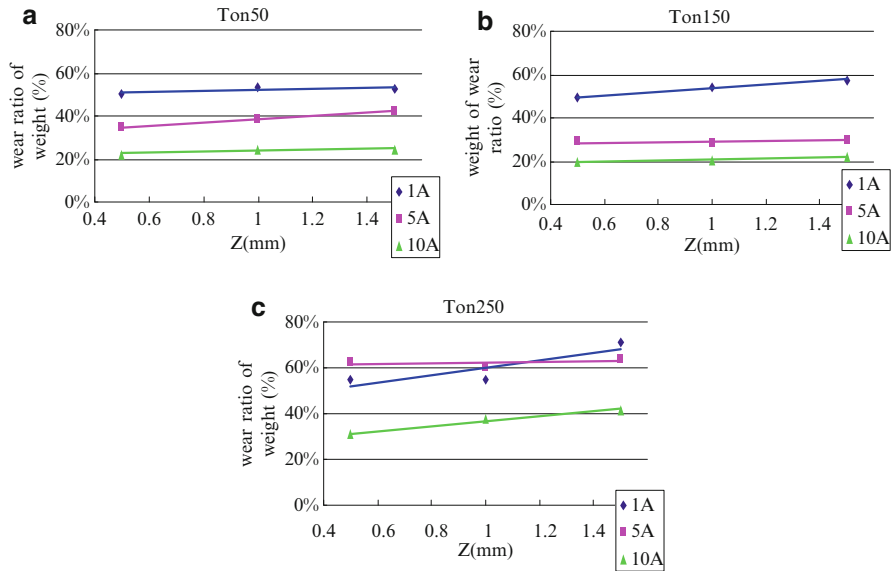
Fig. 3 Relationship between machining depth and EWR for different peak current and pulse durations: (**a**) pulse duration 50 μs, (**b**) pulse duration 150 μs, and (**c**) pulse duration 250 μs

machining depth increased. These results will be helpful for establishing the basis of electrode wear compensation in the layer-cut EDM process.

When the pulse duration is too long, the energy intensity becomes little and work temperature is not high enough. Therefore, its electrode wear is fairly large and more carbide accumulation for long pulse duration. Figure 4 shows the machined result of different pulse durations when the peak current is 5A and machining depth is 1 mm. It can be noticed the planned path could not be completed because of the extreme electrode wear and more carbide accumulation on the machined surface when the pulse duration was 250 μs. From the profile measurement shown in Fig. 5, the outline slope of front part is more than the one behind it. This means that the carbide accumulation should be caused by the long pulse duration. When the electrode wore at a certain extent, the decrease in the actual machining depth made the carbide accumulation decrease. Therefore, the carbide accumulation of the behind part is also less.

4 Summary

The layer-cut EDM process is an EDM technique using simple shape electrodes such as cylindrical or tubular electrode to machine the workpiece along the planned path layer by layer. The electrode and workpiece in this study were copper and
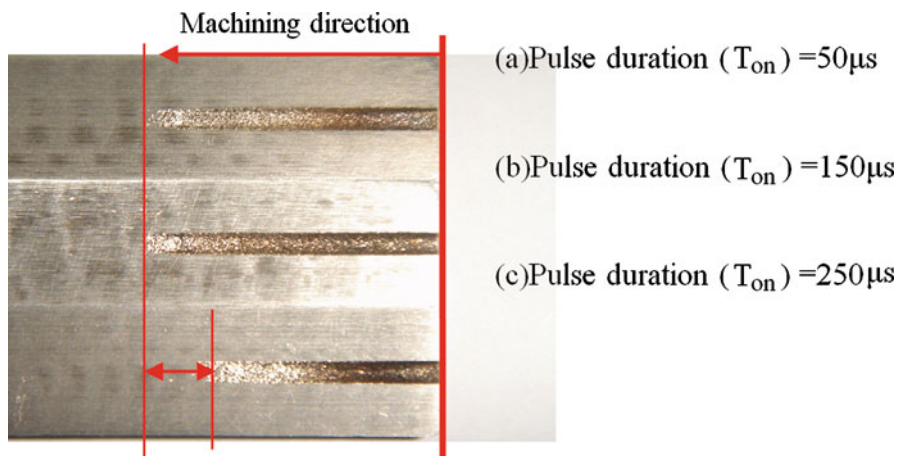
Fig. 4 Machined length and its surface for different pulse durations (T_{on}) when peak current $= 5A$, machining depth (z) $= 1$ mm

stainless steel, respectively. The suitable parameters were obtained and would become the basis of electrode compensation in the layer-cut EDM process. Summarizing the mean features of the results, the following conclusions may be drawn:

(a) Peak current and pulse duration are the most influencing factors on electrode wear. There are different tendencies for different pulse durations since changing the pulse duration would change the discharge energy and energy intensity of each pulse. Short pulse duration can give more effective discharge energy on workpiece, so EWR is smaller. And increasing peak current can decrease the electrode wear. Reversely, electrode wear increases when the pulse current is too small, as a result of the energy of discharge pulse not being enough to remove the material.

(b) If the pulse duration is too long, the energy intensity becomes little and the work temperature is not high enough. Therefore, it is easy to find carbide accumulation on the machined surface.

(c) In this study, the pulse duration of 150 μs can obtain a small linear wear stably. This condition is easier to be compensated in the layer-cut EDM process.
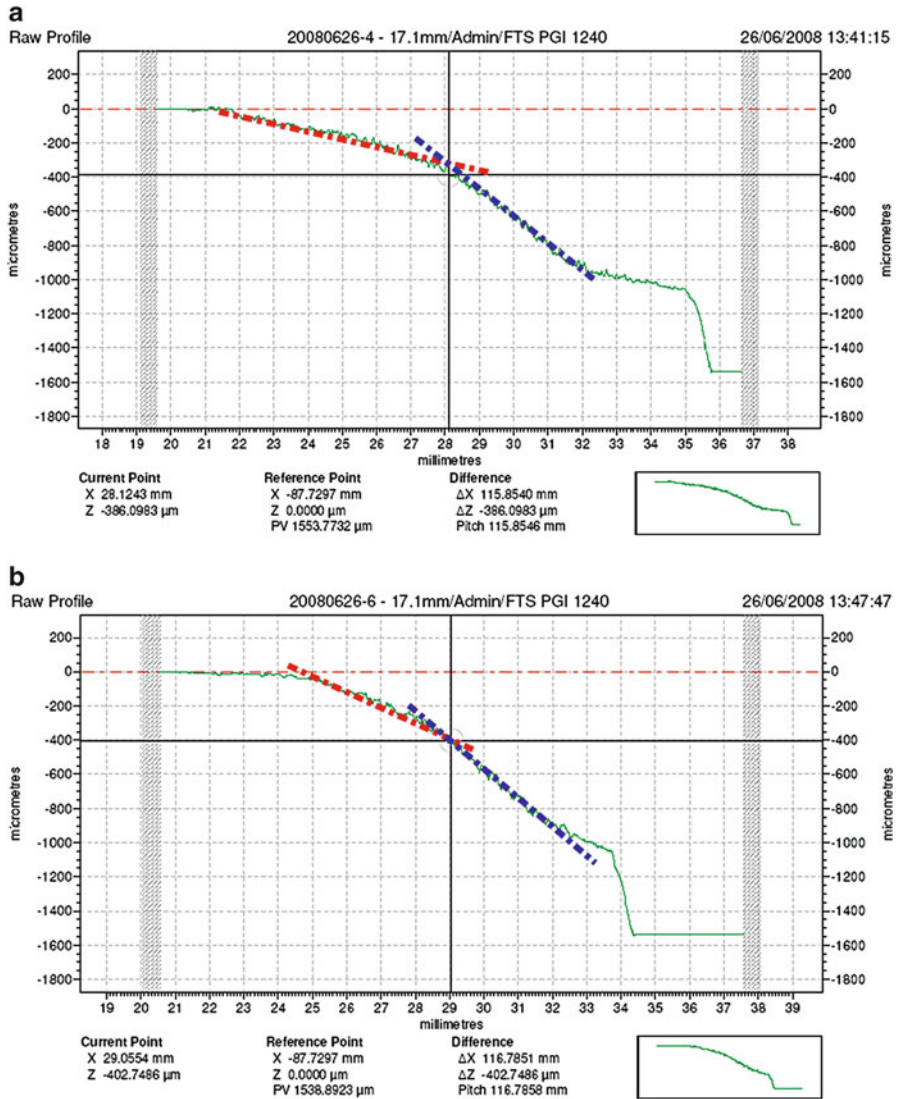
Fig. 5 Profile measurement when peak current = 5A, machining depth (z) = 1 mm: (**a**) pulse duration 50 μs and (**b**) pulse duration 250 μs

References

1. Yu ZY, Masuzawa T, Fujino M (1998) Micro-EDM for three-dimensional cavities – development of uniform wear method. Ann CIRP 47(1):169–172
2. Lo, C-Y (2007) A study on electrode wear sensing and compensation in micro-EDM. Master thesis of Department of Mechatronic Engineering, Huafan University, Taiwan
3. Chen M-C, Mei C-C (2006) The construction of the linear compensation and the machining on EDM Milling. In: 23th proceedings of the Chinese Society of Mechanical Engineers, D6-002, Tainan
4. Son SM, Lim H, Kumar A, Rahman SM (2007) Influences of pulsed power condition on the machining properties in micro EDM. J Mater Process Technol 190:73–76
5. Blatnik O, Valentincic J, Junkar M (2007) Percentage of harmful discharges for surface current density monitoring in electrical discharge machining process. Proc Inst Mech Eng Part B J Eng Manuf 221:1677–1684
6. Yeo SH, Kurnia W, Tan PC (2007) Electro-thermal modeling of anode and cathode in micro-EDM. J Phys D Appl Phys 40:2513–2521
7. Perez R, Rojas H, Walder G, Flükiger R (2004) Theoretical modeling of energy balance in electroerosion. J Mater Process Technol 149(198–203)

Precision Motion Control: Intelligent Mechanisms, Morphing Mechanisms

R.W. Longman, M.S. Chew, and M.Q. Phan

Abstract Engineering advances are often made at the boundary between two fields. This chapter considers synergy between the design of mechanisms used in manufacturing equipment and the design of control systems. Mechanism design often assumes constant velocity of the input shaft, but variations in inertia seen by the driving motor produce speed fluctuations. Typical feedback control cannot fix this, but smart control methods such as iterative learning control and repetitive control can. They can make the mechanism perform in hardware as it was intended to perform. With appropriate sensors they can also fix errors in manufacture and can also make hardware behave as if it were an improved design. The improvement in performance is achieved in software. We call these mechanisms/control systems intelligent mechanism or morphing mechanisms. Examples are discussed.

Keywords Mechanisms • Precision motion control • Iterative learning control • Repetitive control • Intelligent mechanisms • Morphing mechanisms

1 Introduction

Manufacturing can often benefit from high-precision motion control as an aid in producing high-quality competitive products. It can also benefit from high-speed motions that can speed up manufacturing and, as a result, increase productivity.

R.W. Longman (✉)
Department of Mechanical Engineering, Columbia University, New York, NY 10027, USA
e-mail: rwl4@columbia.edu

M.S. Chew
Lehigh University, Bethlehem, PA 18015, USA

M.Q. Phan
Thayer School of Engineering, Dartmouth College, Hannover, NH 03755, USA

Iterative learning control (ILC) and repetitive control (RC) are two forms of intelligent control that can be helpful in each of these objectives [1–5].

Very often significant research advances are made at the boundary between fields. The field of kinematics of mechanisms is a motion control field. This chapter discusses the potential for combining mechanism theory with intelligent control to enhance high-precision motion. The aim is to achieve the benefits of each. The concept of using pure control for automobile valve trains appeared long ago and has been studied extensively. But it has not seen significant applications in practice. The cam offers some practical advantages. We consider cams here but for applications where one aims for constant rotation speed that is controlled by a feedback control system. Then, one is able to make use of the advantages of intelligent control methods at the same time as benefiting from the advantages that the kinematics of cams offer. Using other examples we will show similar synergies with other kinds of mechanisms when combined with ILC and RC. The result of this synergy we wish to refer to as intelligent mechanisms and morphing mechanisms [6–8]. One can consider that control forms a bridge between mechanisms and intelligence.

As one might expect, finding ways to exploit the potential synergy can require expanded research in the fields involved. The preponderance of results in ILC and RC makes use of linear theory. Kinematics of mechanisms usually introduces nonlinearities. As with many forms of control applied to the world, one can often make use of linear control methods on nonlinear problems as in [4]. Some publications that deal with the extension of ILC and RC to nonlinear problems include [9–13]. Other publications develop ILC methods that take advantage of the form of nonlinearities in multibody dynamics models of robots.

2 Optimized Trajectories and Making the World Perform Them

Robotics forms one very special class of mechanisms. An important field of robotics is the choice of trajectory. Routine approaches create practical and easily computed trajectories between taught points. But these trajectories can be optimized. A logical objective is to aim for minimum time, with the benefit of increase productivity. The author and coworkers have produced a series of publications that develop understanding of how each of the motors of a robot can contribute through the interaction forces between the joints in order to produce minimum time motions, for example, [14]. Sometimes, the results initially seem counterintuitive. Figure 1 shows an example of time-optimal lifting of a robot arm confined to a vertical plane, for an elbow robot. Note that the optimal shoulder joint motion at first goes the "wrong" direction, away from the desired final angle for that joint.

If one wants to produce this desired trajectory in hardware, one immediately thinks of simply commanding the desired joint history to the feedback controllers for each joint. However, feedback controllers essentially never actually produced
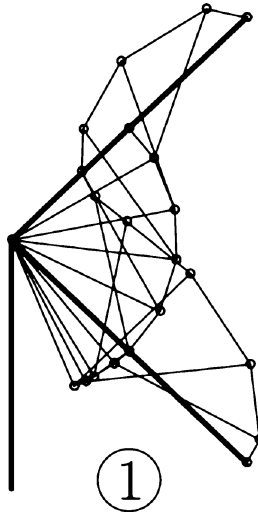
Fig. 1 Time-optimal lifting of an elbow robot
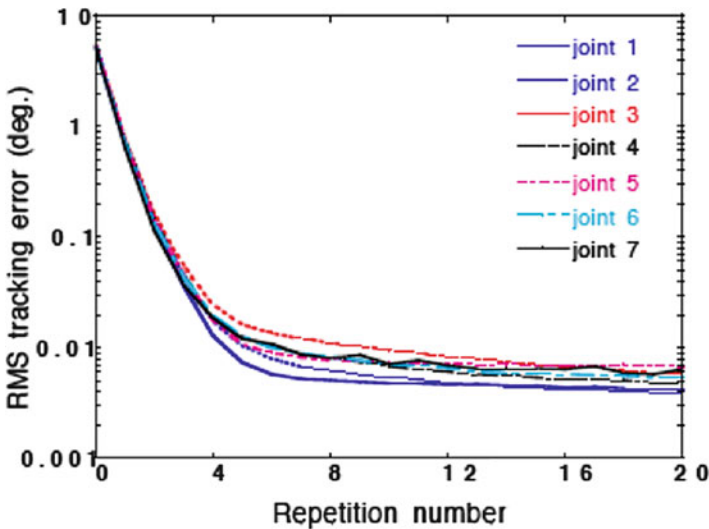
Fig. 2 RMS error verses iterations/repetitions for learning

the commanded trajectory. One measure used in evaluating the performance of a feedback control system is the bandwidth, which describes which frequency components of a command will be handled reasonable well and which components will not be handled well. Iterative learning control (ILC) examines the error in tracking the desired trajectory in the previous run and makes adjustments to the command of this run, iterating with the real world, aiming to converge to zero tracking error. This can be very effective. Figure 2 shows the root mean square error
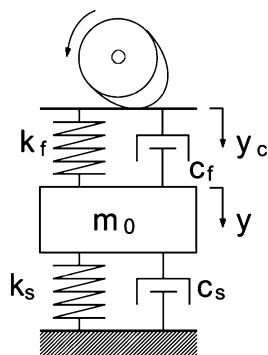
in a high-speed command given to all seven joints of a Robotics Research Corporation robot for each iteration for learning. After about 12 iterations, the RMS error is decreased by about a factor of 1,000. This produces high-precision motion by software modifications.

The use of optimal control theory to design cams is studied in a series of works by the authors and others; see, for example, [15–18]. In many applications, one would optimize the performance for a chosen operating speed. In applications where a typical feedback control system is used to produce this operating speed, there are implementation difficulties. Figure 3 shows a simple model of a cam with a flat-faced follower. It is clear that the radial distance to the contact point changes as the cam rotates. And this presents a varying torque load to the motor actuator of the speed control system. This represents a disturbance torque and will result in a periodic fluctuation in the speed of rotation of the cam, varying throughout each rotation. The result is that whatever optimized lift curve the cam designer produced, it will be distorted by the varying operating speed. The hardware is not producing the performance the designer intended. The optimization could be based on lift area, residual vibrations, Hertzian contact stress, energy loss per rotation, etc.

This time the logical control method to fix the situation is repetitive control. In the case of the robot maneuver above, the robot is returned to the same starting point before each maneuver, and then one wishes to follow the finite time trajectory, which is an ILC problem. On the other hand, RC is designed to eliminate periodic errors in the output of a control system, in this case periodic errors produced by a periodic disturbance torque. It can also be used to make a feedback control system converge to zero tracking error of a periodic command. Instead of looking at the error at each time step of the previous run, and adjusting the command accordingly in this run, RC looks back at the error in the previous period.

The simplest form of ILC or RC adjusts the command at each time step by looking at the error at the appropriate time step of the previous run or period, and changing the command by a gain times the error observed. However, at frequencies for which the phase lag from command to output gets too large, this fails, and one needs to adjust the command change to counteract the phase change, using a compensator.

3   What Can Intelligent Control Do for Mechanisms?

Various publications discuss some of the potential applications [15–25]. The cam problem as stated above was simply to achieve constant angular velocity of the input shaft. A large number of mechanism have this same assumption and can be treated similarly, for example, slider cranks, four-bar linkages, and noncircular gearing. Cardan joints represent a similar problem where one wants to have constant velocity of the output shaft by varying the velocity of the input shaft appropriately. Another version of this objective occurs in tooth meshing that can create speed variations of an output shaft. Experiments using timing belts and gears showed very good results [15]. Figure 4 shows the velocity spectrum of the output shaft of a system with a double reduction timing belt drive. The best RC law tested eliminated all of the peaks associated with tooth meshing and rotation of each gear [25]. Another rather different application is for active balancing of rotating machinery which is treated in [22], in order to reduce joint forces. Reference [20] considers straight line motion of a 4-bar linkage (Figs. 5 and 6). One can make such a mechanism perform very close to straight line motion, but it is not exact, and RC can fix the associated errors as shown in Figs. 7 and 8. Active control is applied to the link L to vary its length to fix structural error.
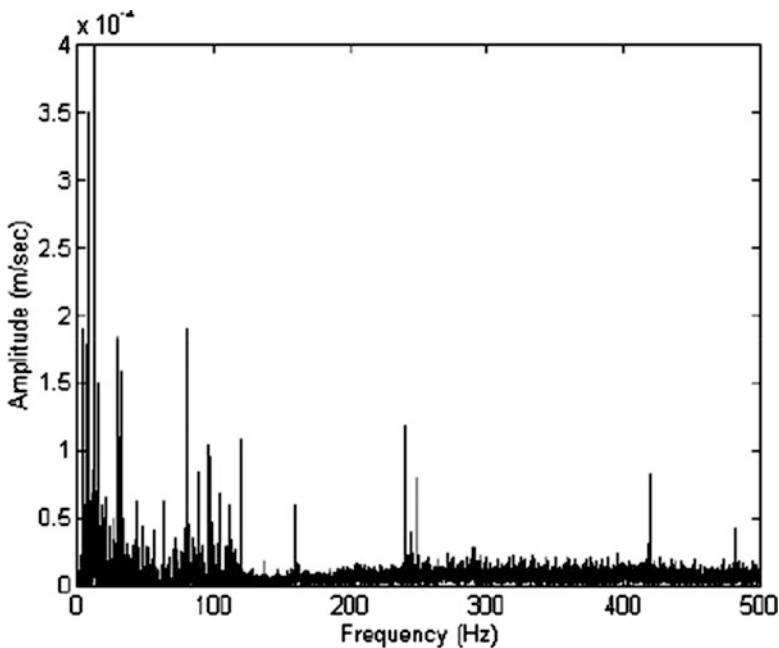
Fig. 4 Velocity variation spectrum in timing belt system
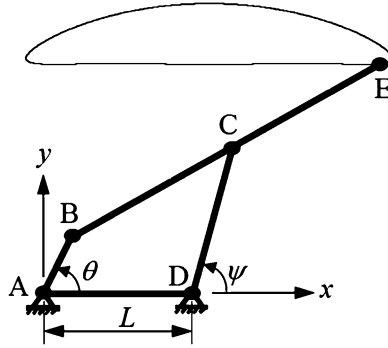
Fig. 5 Adjustable 4-bar mechanism
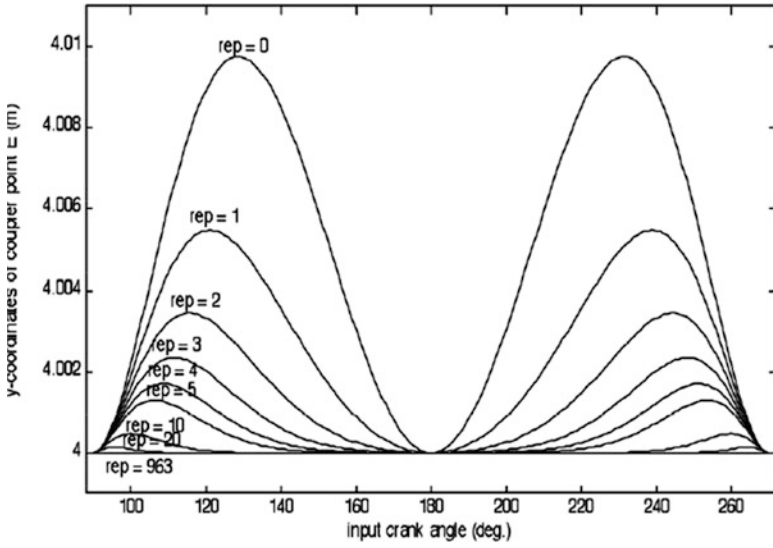
Fig. 6 The learning history for the 4-bar mechanism
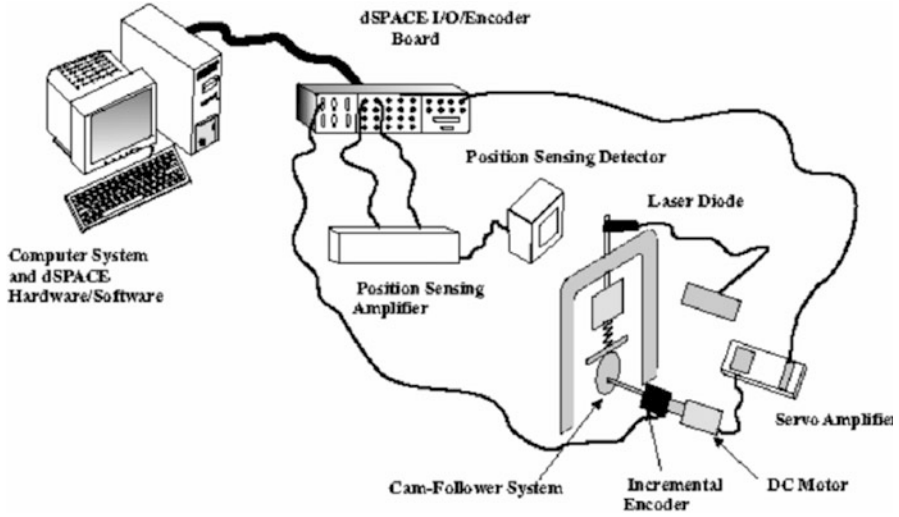
Fig. 7 Cam morphing experiments
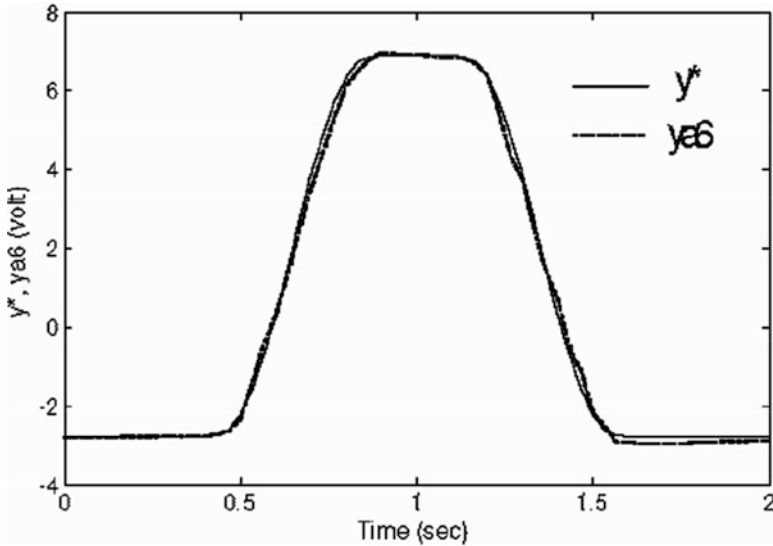
Fig. 8 Cam lift curve after six iterations compared to desired *curve*

References

1. Bien Z, Xu J-X (eds) (1998) Iterative learning control: analysis, design, integration and applications. Kluwer Academic Publishers, Boston
2. Moore K, Xu J-X, guest editors (2000) Special issue on iterative learning control. Int J Control 73(10): 819–823
3. Longman RW (2000) Iterative learning control and repetitive control for engineering practice. Int J Control 73(10): 930–954. Special issue on iterative learning control
4. Elci H, Longman RW, Phan MQ, Juang J-N, Ugoletti R (2002) Simple learning control made practical by zero-phase filtering: applications to robotics. In: Basu S, Swamy MNS (guest editors) IEEE transactions on circuits and systems I: fundamental theory and applications, Piscataway, June 2002, vol 49(6), pp 753–767. Special issue on multidimensional signals and systems
5. Longman RW (2010) On the theory and design of linear repetitive control systems. Eur J Control 16(5): 447–496. Special section on Iterative Learning Control, Guest Editor: Ahn H-S
6. Chew MS, Longman RW, Phan MQ (2004) Intelligent mechanisms. In: Proceedings of the 28th biennial mechanisms and robotics conference. ASME design engineering technical conference DETC2004-57553, Salt Lake City, 28 Sept–3 Oct 2004
7. Phetkong N, Chew MS, Longman RW (2005) Morphing mechanisms part 1: using iterative learning control to morph cam follower motion. Am J Appl Sci 2(5):897–903
8. Phetkong N, Chew MS, Longman RW (2005) Morphing mechanisms part 2: using repetitive control to morph cam follower motion. Am J Appl Sci 2(5):904–909
9. Xu J-X, Tan Y (2003) Linear and nonlinear iterative learning control (Lecture notes in control and information sciences), Springer, Berlin
10. Longman RW, Chang C-K, Phan M (1992) Discrete time learning control in nonlinear systems. A collection of technical papers, 1992 AIAA/AAS astrodynamics specialist conference, Hilton Head, Aug 1992, pp 501–511
11. Li J, Longman RW, Schulz VH, Bock HG (1998) Implementing time optimal robot maneuvers using realistic actuator constraints and learning control. Adv Astronaut Sci 99:355–374
12. Longman RW, Mombaur KD, Panomruttanarug B (2008) Designing iterative learning control subject to actuator limitations using QP methods. In: Proceedings of the AIAA/AAS astrodynamics specialist conference, Hawaii, Aug 2008
13. Longman RW, Mombaur KD (2009) Iterative learning control in nonlinear systems using state estimation for relinearization. Adv Astronaut Sci 134:1721–1735
14. Giese G, Longman RW, Bock HG (2004) Mechanical assessment of time-optimal robot motion. Comput Mech 33(2):121–128
15. Chew M, Freudenstein F, Longman RW (1983) Application of optimal control theory to the synthesis of high-speed cam-follower systems. Part I: optimality criterion. ASME Transactions. J Mech Transm Autom Design 105(3): 577–584, Sept 1983
16. Chew M, Freudenstein F, Longman RW (1983) Application of optimal control theory to the synthesis of high-speed cam-follower systems. Part II: system optimization. ASME Transactions. J Mech Transm Autom Design 105(3): 585–591, Sept 1983
17. Mennicke S, Longman RW, Chew M-S, Bock HG (2004) High speed automotive cam design using direct multiple shooting optimal control techniques. In: Proceedings of the 28th biennial mechanisms and robotics conference, ASME design engineering technical conference DETC2004-57415, Salt Lake City, Sept–Oct 2004
18. Mennicke S, Longman RW, Chew M-S, Bock HG (2004) A CAD package for high-speed cam design based on direct multiple shooting optimal control techniques. In: Proceedings of the 30th ASME design automation conference, ASME design engineering technical conference DETC2004-57410, Salt Lake City, Sept–Oct 2004
19. Chew M, Phan MQ (1994) Application of learning control theory to mechanisms, part 1 – inverse kinematics and parametric error compensation. In: Proceedings of the ASME 23rd biennial mechanisms conference, Minneapolis, 1994, DE-vol 71, ASME 1994, pp 25–32

20. Phan MQ, Chew M, Synthesis of Four-Bar Function Generators by an iterative learning control procedure. In: Proceedings of the ASME 24th biennial mechanisms conference, Irvine, 1996, 96-DETC/MECH-1219
21. Chen HJ, Longman RW, Chew M (2004) Eliminating structure error in real-time adjustable four-bar path generators using iterative learning control. In: ASME DETC 2004, Salt Lake City, 2004
22. Thuemmel T, Brandl M (1996) Active balancing of joint forces in high-speed linkages by redundant drives and learning control. In: Proceedings of the ASME design engineering technical conference, Irvine, 18–22 Aug 1996, 96-DETC/MECH-1572
23. Chew M, Phan MQ (1994) Application of learning control theory to mechanisms, part 2 – reduction of residual vibrations in high-speed electromechanical bonding machines. In: Proceedings of the ASME 23rd biennial mechanisms conference, Minneapolis, 1994, DE-vol 71, ASME 1994, pp 33–40
24. Chew M, Wongratanaphisan T, Lu YC (1998) Learning control of a high-speed cam dynamic system in the presence of viscous damping and Coulomb friction, theory and experiment. In: Proceedings of 1998 ASME design engineering technical conference, Atlanta, 1998, DETC 98/MECH-5971
25. Hsin YP, Longman RW, Solcz EJ, de Jong J (1997) Experiments bridging learning and repetitive control. Adv Astronaut Sci 95:671–690

Index